IFMBE Proceedings

Dössel • Schlegel (Eds.)

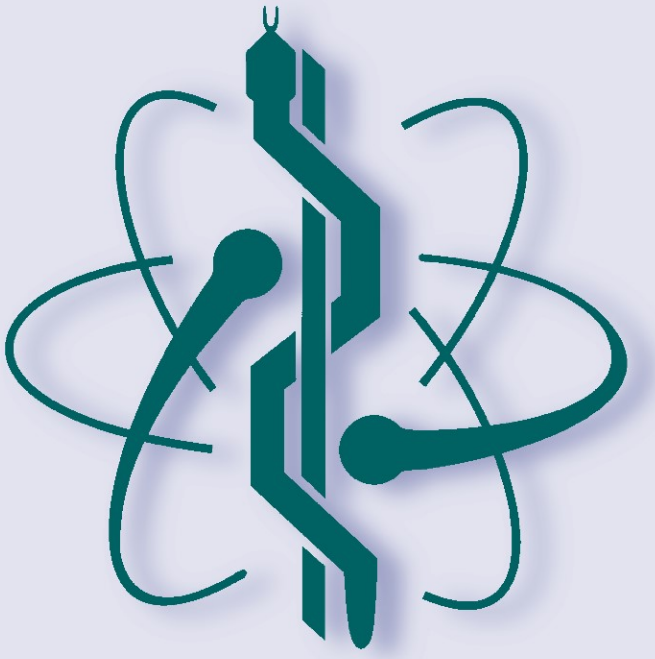
Volume 25/8

World Congress on Medical Physics and Biomedical Engineering

7–12 September 2009

Munich, Germany

Micro- and Nanosystems in Medicine, Active Implants, Biosensors



Springer

IFMBE Proceedings Volume 25/VIII

Series Editor: R. Magjarevic

11th International
Congress of the IUPESM

MEDICAL PHYSICS AND BIOMEDICAL ENGINEERING

WORLD CONGRESS 2009



For the benefit
of the Patient.

Sept 7–12, 2009
Munich, Germany

IUPESM
IOMP IFMBE

International Organization for Medical Physics
IOMP

The International Federation for Medical and Biological Engineering, IFMBE, is a federation of national and transnational organizations representing internationally the interests of medical and biological engineering and sciences. The IFMBE is a non-profit organization fostering the creation, dissemination and application of medical and biological engineering knowledge and the management of technology for improved health and quality of life. Its activities include participation in the formulation of public policy and the dissemination of information through publications and forums. Within the field of medical, clinical, and biological engineering, IFMBE's aims are to encourage research and the application of knowledge, and to disseminate information and promote collaboration. The objectives of the IFMBE are scientific, technological, literary, and educational.

The IFMBE is a WHO accredited NGO covering the full range of biomedical and clinical engineering, healthcare, healthcare technology and management. It is representing through its 58 member societies some 120.000 professionals involved in the various issues of improved health and health care delivery.

IFMBE Officers
President: Makoto Kikuchi, Vice-President: Herbert Voigt, Former-President: Joachim H. Nagel
Treasurer: Shankar M. Krishnan, Secretary-General: Ratko Magjarevic
http://www.ifmbe.org

Previous Editions:

IFMBE Proceedings WC 2009, "World Congress on Medical Physics and Biomedical Engineering",
Vol. 25, 2009, Munich, Germany, CD

IFMBE Proceedings SBEC 2009, "25th Southern Biomedical Engineering Conference 2009",
Vol. 24, 2009, Miami, FL, USA, CD

IFMBE Proceedings ICBME 2008, "13th International Conference on Biomedical Engineering"
Vol. 23, 2008, Singapore, CD

IFMBE Proceedings ECIFMBE 2008 "4th European Conference of the International Federation for Medical and Biological Engineering", Vol. 22, 2008, Antwerp, Belgium, CD

IFMBE Proceedings BIOMED 2008 "4th Kuala Lumpur International Conference on Biomedical Engineering",
Vol. 21, 2008, Kuala Lumpur, Malaysia, CD

IFMBE Proceedings NBC 2008 "14th Nordic-Baltic Conference on Biomedical Engineering and Medical Physics",
Vol. 20, 2008, Riga, Latvia, CD

IFMBE Proceedings APCMBE 2008 "7th Asian-Pacific Conference on Medical and Biological Engineering",
Vol. 19, 2008, Beijing, China, CD

IFMBE Proceedings CLAIB 2007 "IV Latin American Congress on Biomedical Engineering 2007, Bioengineering Solution for Latin America Health", Vol. 18, 2007, Margarita Island, Venezuela, CD

IFMBE Proceedings ICEBI 2007 "13th International Conference on Electrical Bioimpedance and the 8th Conference on Electrical Impedance Tomography", Vol. 17, 2007, Graz, Austria, CD

IFMBE Proceedings MEDICON 2007 "11th Mediterranean Conference on Medical and Biological Engineering and Computing 2007", Vol. 16, 2007, Ljubljana, Slovenia, CD

IFMBE Proceedings BIOMED 2006 "Kuala Lumpur International Conference on Biomedical Engineering",
Vol. 15, 2004, Kuala Lumpur, Malaysia, CD

IFMBE Proceedings WC 2006 "World Congress on Medical Physics and Biomedical Engineering",
Vol. 14, 2006, Seoul, Korea, DVD

IFMBE Proceedings BSN 2007 "4th International Workshop on Wearable and Implantable Body Sensor Networks",
Vol. 13, 2006, Aachen, Germany

IFMBE Proceedings ICBMEC 2005 "The 12th International Conference on Biomedical Engineering",
Vol. 12, 2005, Singapore, CD

IFMBE Proceedings EMBEC'05 "3rd European Medical & Biological Engineering Conference, IFMBE European Conference on Biomedical Engineering", Vol. 11, 2005, Prague, Czech Republic, CD

IFMBE Proceedings ICCE 2005 "The 7th International Conference on Cellular Engineering",
Vol. 10, 2005, Seoul, Korea, CD

IFMBE Proceedings NBC 2005 "13th Nordic Baltic Conference on Biomedical Engineering and Medical Physics",
Vol. 9, 2005, Umeå, Sweden

IFMBE Proceedings Vol. 25/VIII
Olaf Dössel · Wolfgang C. Schlegel (Eds.)

World Congress on Medical Physics and Biomedical Engineering 7–12 September, 2009 Munich, Germany

Micro- and Nanosystems in Medicine, Active Implants, Biosensors

Springer

Editors

Prof. Dr. Olaf Dössel
Univ. Karlsruhe
Inst. Biomedizinische Technik
Kaiserstr. 12
76128 Karlsruhe
Germany
E-mail: olaf.doessel@ibt.uni-karlsruhe.de

Prof. Dr. Wolfgang C. Schlegel
Deutsche Krebsforschungszentrum (DKFZ)
Abt. Medizinische Physik in der
Strahlentherapie
Im Neuenheimer Feld 280
69120 Heidelberg
Germany
E-mail: w.schlegel@dkfz-heidelberg.de

ISSN 1680-0737
ISBN 978-3-642-03886-0 e-ISBN 978-3-642-03887-7

Also available as set Vol. I–XIII ISBN 978-3-642-03897-6

DOI 10.1007/978-3-642-03887-7

Library of Congress Control Number: 2009934297

© International Federation for Medical and Biological Engineering 2009

This work is subject to copyright. All rights are reserved, whether the whole or part of the material is concerned, specifically the rights of translation, reprinting, reuse of illustrations, recitation, broadcasting, reproduction on microfilm or in any other way, and storage in data banks. Duplication of this publication or parts thereof is permitted only under the provisions of the German Copyright Law of September 9, 1965, in its current version, and permissions for use must always be obtained from Springer. Violations are liable to prosecution under the German Copyright Law.

The use of general descriptive names, registered names, trademarks, etc. in this publication does not imply, even in the absence of a specific statement, that such names are exempt from the relevant protective laws and regulations and therefore free for general use.

The IFMBE Proceedings is an Offical Publication of the International Federation for Medical and Biological Engineering (IFMBE)

Typesetting: Data supplied by the authors
Production & Cover design: Scientific Publishing Services Pvt. Ltd., Chennai, India.

Printed on acid-free paper

9 8 7 6 5 4 3 2 1

springer.com

Preface

Present Your Research to the World!

The World Congress 2009 on Medical Physics and Biomedical Engineering – the triennial scientific meeting of the IUPESM - is the world's leading forum for presenting the results of current scientific work in health-related physics and technologies to an international audience. With more than 2,800 presentations it will be the biggest conference in the fields of Medical Physics and Biomedical Engineering in 2009!

Medical physics, biomedical engineering and bioengineering have been driving forces of innovation and progress in medicine and healthcare over the past two decades. As new key technologies arise with significant potential to open new options in diagnostics and therapeutics, it is a multidisciplinary task to evaluate their benefit for medicine and healthcare with respect to the quality of performance and therapeutic output.

Covering key aspects such as information and communication technologies, micro- and nanosystems, optics and biotechnology, the congress will serve as an inter- and multidisciplinary platform that brings together people from basic research, R&D, industry and medical application to discuss these issues.

As a major event for science, medicine and technology the congress provides a comprehensive overview and in–depth, first-hand information on new developments, advanced technologies and current and future applications.

With this Final Program we would like to give you an overview of the dimension of the congress and invite you to join us in Munich!

Olaf Dössel
Congress President

Wolfgang C. Schlegel
Congress President

Preface

Welcome to World Congress 2009!

Since the first World Congress on Medical Physics and Biomedical Engineering convened in 1982, medically and biologically oriented engineers and physicists from all continents have gathered every three years to discuss how physics and engineering can advance medicine, health and health care and to assess the clinical, scientific, technical and professional progress in their fields. In the tradition and the mission of our professions, which are the only ones involved in the whole loop of health and health care from basic research to the development, assessment, production, management and application of medical technologies, the theme of WC 2009 is "For the Benefit of the Patient". Thus, in addition to scientific aspects, the Congress will focus on all aspects of safe and efficient health technology in both industrialized and developing countries, including economic issues, the perspectives that advanced technologies and innovations in medicine and healthcare offer for the patients and the development of societies, the progress of MBE and MP, including health policy and educational issues as well as the need for the regulation and classification as health professionals of those biomedical/clinical engineers and medical physicists who are working in the health care systems.

The World Congress as the most important meeting of our professions, bringing together physicists, engineers and physicians from all over the world, including the delegates of the 138 constituent organizations of the IUPESM representing some 140,000 individual members, is the best place to discuss these issues, thereby contributing to the advancement of the physical and engineering sciences, our professions and thus to global health.

It gives me great pleasure to welcome you to this important event. I wish you a rewarding and enjoyable congress and a most pleasant time in Munich, the ‘metropolis with heart’ that has so much to offer.

Joachim H. Nagel
President of the IUPESM

Preface

Let's talk!
Is our level of communication between Medical Physics, Biomedical Engineering, Clinical Engineering, Medical Informatics, Tissue Engineering, etc. and Medicine good enough? We would like to answer: yes, we are quite good, but not good enough! There is a lot of room for improvement. Let' start right on the spot - on the World Congress on Medical Physics and Biomedical Engineering 2009. And please remember: communication is 50% talking and 50% listening.

Let's work together!
Do we have a perfect level of collaboration in our field? OK, we are quite good, but we can do better. Just to give an example: there should be no funded project in Medical Physics or Biomedical Engineering where there is no medical partner. And vice versa: medical doctors should join their forces with physicists and engineers if they are aiming at improvements on medical devices or healthcare systems. Let's start right here in Munich, September 2009, with innovative projects and innovative ways of cooperation.

Let's get to know each other!
It's known for more than thousand years: people who know each other personally and from face to face can talk with better mutual understanding, collaborate with less friction losses, are much more successful ..... and have much more fun. Plenty of chances to make new friends and to refresh old relations on World Congress on Medical Physics and Biomedical Engineering 2009!

And here are the numbers:
More than 3000 scientists working in the field of Medical Physics and Biomedical Engineering meet in September 2009 in Munich. They come from more than 100 nations. They submitted about 2800 contributions. 10 plenary talks and 46 keynote lectures bring us to the top level of science in our field. 75 companies show their latest achievements in the industrial exhibition. It's definitely the largest market place of ideas and innovations in Medical Physics and Biomedical Engineering of the year 2009.

August 2009 Olaf Dössel

Table of Contents

Silicon Eye 1
Sandeep Thuvvakkadan and Vignesh Janardhanan Nair

Automated Assembly of Dynamic Micro-Bead Arrays Using a Multi-arm Laser Manipulator with Computer Vision 5
Y. Tanaka, H. Kawada, S. Tsutsui, M. Ishikawa, and H. Kitajima

A Nano-porous Aerogel Biochip for Molecular Recognition of Nucleotide Acids 8
Yen Kuang Li, Den-Kai Yang,Yun-Chu Chen, Hung-Ju Su, Jui-Chuang Wu, and Yui Whei Chen-Yang

Biodegradable Polymeric Implants as Drug Delivery Systems for Brain Cancer Therapy 11
Norased Nasongkla

CH_2-Symmetric/CH_2-Antisymmetric Stretch Ratio Sensor for Cell Analysis 15
S. van den Driesche, W. Witarski, and M.J. Vellekoop

Optimization of Ligand Surface Concentration for Biosensor Based on Imaging Ellipsometry 19
Yu Niu and Gang Jin

Are Defibrillation Thresholds Ruled by a Hyperbolic Strength Duration Relationship? 22
Werner Irnich

Development of a Patient Controlled, Telemetric Bolus System for an Implantable Infusion Pump 26
A. Knopp, K.-H. Otto, S. Klein, and B. Nestler

Finite Element Modelling of Microphysiometry on Cellular Specimen 30
M. Brischwein, D. Grundl, X. Zhang, and Wolf

CD146 Detection with Real-Time Total Internal Reflection Imaging Ellipsometry 34
Li Liu, Yu Niu, YongHong Meng, She Chen, XiYun Yan, and Gang Jin

Space Saving Mixed Signal FPGAs for Improving Processing Power and Memory Capacity as a Replacement for μCs in Portable Biosensor Devices 37
M. Schmidhuber, J. Bähr, F. Ilchmann, J. Wiest, and B. Wolf

Nanomaterial Based Electrochemical Transducing Platforms for Biomedical Applications 41
A. de la Escosura-Muñiz, A. Ambrosi, M. Maltez, B. Pérez-López, S. Marín, and A. Merkoçi

Sensor Chips for Multiparametric Real Time Monitoring of Cell Metabolism and Drug Response 45
M. Zottmann, J. Wiest, T. Flurschütz, M. Schmidhuber, and B. Wolf

Microfluidic Platform for the Initiation and Investigation of Cellular Interactions on a Single-Cell Level 49
M. Kirschbaum, M.S. Jäger, and C. Duschl

Esophageal Flow Control Module for Treatment of Obesity 53
S.S.R.F. Rosa, J.C. Carvalho Júnior, L.M. Brasil, A.F. Rocha, and J.C. Carvalho

Basic Concepts for Active Implantable Valve Development 57
M. Biehl and O. Scholz

Estimation of Magnetic Nanoparticle Diameter with a Magnetic Particle Spectrometer 61
S. Biederer, T. Knopp, T.F. Sattel, K. Lüdtke-Buzug, B. Gleich, J. Weizenecker, J. Borgert, and T.M. Buzug

Fate of Drug Loaded-LNCs in Cell Culture Medium – Impact on Drug Delivery Strategies 65
H.W. Rohm, T. Perrier, N. Lautram, K.-P. Schmitz, P. Saulnier, and M. Löbler

Speeding Up Sensor Response Times by Modifying the Geometry of the Fluidic Channel of a Disposable Array Compatible Sensor Housing for Surface Acoustic Wave Biosensors 69
B.E. Rapp, F.J. Gruhl, K. Länge, and M. Rapp

Surface Acoustic Wave (SAW) Biosensor Chip System – A Promising Alternative for Biomedical Applications 73
F.J. Gruhl, B.E. Rapp, M. Rapp, and K. Länge

Multiparametric NeuroLab with Integrated MEA & Life Support 77
F. Ilchmann, J. Meyer, M. Schmidhuber, M. Zottmann, B. Becker, and B. Wolf

QCM Based on Flow System for Cardiovascular Disease 80
K. Wong-ek, O. Chailapakul, J. Prommas, K. Jaruwongrungsee, N. Nuntawong, and A. Tuantranont

Automated 24 Well Neuro-Screening System with Life Support 84
F. Ilchmann, B. Becker, D. Grundl, J. Meyer, and B. Wolf

Manufacture of SU-8 Micro-Grippers for Mechanical Characterization of Gut Epithelial Cells 87
R.E. Mackay, H.R. Le, R.P. Keatch, and Q. Zhao

Mathematical Methods for Interpretation of Metabolic Signals from Living Cells on Biohybrid Sensor Chips 91
T. Flurschütz, D. Grundl, M. Zottmann, J. Wiest, and B. Wolf

Electroactive Nanoporous Valve for Controlled Drug Delivery 95
R. Kurz, A. Sickinger, and A. Robitzki

Fieldbus Controlled Live Support System for Cell-Based Biohybrid Measuring Systems 98
F. Demmel, D. Grundl, M. Schmidhuber, J. Wiest, and B. Wolf

Traveling-Wave Electrohydrodynamics: A Versatile Method for Collecting Nanoscaled Objects from Fluids 101
M. Boettcher, M.S. Jaeger, M. Stuke, and C. Duschl

Preparation of Functional Magnetic Cationic Polymeric Liposomes via a Simple Process 104
X.F. Liang, H.J. Wang, and J. Chang

Fluorescent Gold Nanoclusters for Biomedical Applications 108
Cheng-An J. Lin, Chin-Hsien Lee, Hung-I Yeh, and Walter H. Chang

Microelectrode Array (MEA) High Resolution Electrophysiological Mapping of Cardiac Cell, Tissue and Organ Preparations 112
T. Meyer, U. Kraushaar, and E. Guenther

α-Fetoprotein Analysis in Human Serum through Quartz Crystal Microbalance 116
S.L. Huang, C.S. Lin, Y.S. Lu, S.B. Jong, M.H. Yang, H.Y. Chang, H.Y. Hsun, and Y.C. Tyan

Development of a Generic Multiple Frequency Signal Generator for BioMEMS 120
N.A. Kadri, K.F. Hoettges, and M.P. Hughes

Precise Deposition of Electrospun Nanofibers and Electrospraying of Nanoparticles as Enabling Techniques for Biomedical Engineering Applications 124
S. Neubert, M. Eblenkamp, D. Pliszka, S. Sundarrajan, S. Ramakrishna, and E. Wintermantel

Nanomaterials for Positive Contrast Imaging of MR-Visible Implants 128
I. Slabu, G. Güntherodt, T. Schmitz-Rode, M. Hodenius, N. Krämer, G.A. Krombach, J. Otto, U. Klinge, and M. Baumann

Femtosecond Laser Microstructuring and Bioactivation of Titanium Surfaces for Middle Ear Ossicular Replacement Prosthesis 132
J. Ilgner, S. Biedron, D. Klee, E. Fadeeva, B. Chichkov, and M. Westhofen

Automation of Chemosensitivity Testing - Enabling Personalized Cancer Therapy 136
B. Becker, D. Grundl, S. Etzbach, M. Zottmann, M. Brischwein, and B. Wolf

A Novel Fabrication Route to Integrating Label-Free Detection of DNA Hybridization in Microfluidic Channel 140
J.H. Jiang, M.L. Bo, D.C. Jiang, J. Wang, L. Yang, K.-L. Paul Sung

Concept of a Microfluidics and Tunneling Effect-Based BioMEMS to Detect Cells 144
Shengbo Sang, Ulrike Fröber, and Hartmut Witte

Simulation of Drug Release for the Development of Drug-Eluting Stents – Influence of Design and Manufacturing Parameters on Drug Release Kinetics 148
N. Grabow, S. Siewert, K. Sternberg, H. Martin, and K.-P. Schmitz

Application of an Electronic Nose to Diagnose Liver Cirrhosis from the Skin Surface 150
K. Witt, T. Jochum, W. Poitz, K.J. Bär, and A. Voss

Development and Fabrication of Multielectrode Arrays for Immuno-Assisted Whole Cell Detection Systems 153
A. Steude, O. Pänke, S. Schmidt, and A.A. Robitzki

Sample Preparation on-Chip: Accumulation, Lysis of and DNA Extraction from Bacteria 157
M. Moschallski, C. Dorrer, M. Kubon, P. Rothacher, J. Weile, B. Hagmeyer, K. Fuchsberger, K.-H. Boven, A. Moeller, R. Mohrlok, and M. Stelzle

Towards Artificial Liver Sinusoids by Dielectrophoretic Cell Assembly in Microfluidic System for Use in Substance Screening 161
J. Schütte, B. Angres, K. Benz, C. Freudigmann, B. Hagmeyer, F. Holzner, M. Kubon, J. Böttger, R. Gebhardt, H. Becker, and M. Stelzle

Application of Supported Phospholipids Bilayer Bilayers for Biosensor Based on Imaging Ellipsometry 165
Y.Y. Chen, Y.B. Zhang, C.X. Wang, Z.J. Ding, C.H. Huang, W.R. Chang, and G. Jin

Chitosan Cushioned Air Stable Single PEGylated Phospholipid Bilayers 169
Y.B. Zhang, Y.Y. Chen, Z.J. Ding, C.X. Wang, C.H. Huang, and G. Jin

Application of Carbonyl Iron Powder as a Novel Mediator for Arterial Embolization Hyperthermia—Feasibility Investigation 172
Lingyun Zhao, Wei Jiang, Yongjian Jin, Xiaowen Wang, Xufei Wang, and Jintian Tang

Development of a Multifunctional Microfluidic System for Studies of Nerve Cell Activity during Hypoxic and Anoxic Conditions 176
Nazanin Bitaraf, Ahmed Ahmed, Michael Druzin, and Kerstin Ramser

A Novel Microfluidic Based Technique for Encapsulation of Langerhans' Islets Using High Viscosity Alginate and $BaSO_4$ Nanoparticles 180
F. Ehrhart, Patrick Stumpf, S. Wiedemeier, E. Weyand, R. Danzebrink, M.M. Weber, J. Metze, V. Sukhorukov, U. Zimmermann, and H. Zimmermann

Analysis of Chemotactic Activity of Mammalian Cells in a Microfluidic Device 183
A. Lankenau, A. Renner, and C. Duschl

An Adjustable Optofluidic Micro Lens Enhancing Single Cell Analysis Systems 185
M. Rosenauer and M.J. Vellekoop

Artificial Urinary Bladder – Focal Technical Challenges 189
M. Roth, D. Kirchleitner, D. Jocham, and H. Wassermann

Design and Performance of an Improved Active Subretinal Chip 192
Steffen Kibbel, Alex Harscher, Walter-G. Wrobel, Eberhart Zrenner, and Albrecht Rothermel

An Intelligent Implant System for Monitoring and Biofeedback Therapy of Snoring 196
Dan Anker Hofsøy, Johannes Clauss, and Bernhard Wolf

Driving Force of a Neutrophile in Liquid Using Concentration Marangorni Effect for Developing Microcapsule for Drug Delivery Systems 200
M. Tamagawa and K. Matsumura

Cellular Uptake of Gold Nanoparticles into Normal and Cancer Cells 202
Jade Trono, Kazue Mizuno, Noritaka Yusa, Takehisa Matsukawa, and Mitsuru Uesaka

Study to Trap Fluid Microcapsules in Artificial Blood Vessel by Producing Local Acoustic Radiation Force 206
Kohji Masuda, Ryusuke Nakamoto, Yusuke Muramatsu, Yoshitaka Miyamoto, Keri Kim, and Toshio Chiba

Diamond Microelectrodes for Amperometric Detection of Secretory Cells Activity 208
A. Pasquarelli, V. Carabelli, Y. Xu, Z. Gao, A. Marcantoni, E. Kohn, and E. Carbone

Local Electrical Stimulation of Single Myocytes Using Three-Dimensional Electrode Arrays with Small Interelectrode Distances 212
D. Braeken, R. Huys, D. Jans, Josine Loo, D.R. Rand, G. Borghs, G. Callewaert, and C. Bartic

On-Surface Amplification of L-Glutamate Using a Patterned Bi-enzymatic System 216
D.R. Rand, D. Braeken, Y. Mulla, G. Borghs, and C. Bartic

The Role of Microrheological Red Blood Cell Properties in Efficiency of Drug Transport and their Delivery to Cellular Targets 220
A.V. Muravyov, S.V. Cheporov, F.A. Chuchkanov, and A.A. Muravyov

A Polymer Based Local Drug Delivery System on Plasma Activated Silicon Implant Surfaces ... 223
H.W. Rohm, K. Sternberg, T. Stöver, G. Paasche, S. Barcikowski, A. Hahn, and K.-P. Schmitz

Particle-Size Distribution of Dextran- and Carboxydextran-Coated Superparamagnetic Nanoparticles for Magnetic Particle Imaging ... 226
K. Lüdtke-Buzug, S. Biederer, T.F. Sattel, T. Knopp, and T.M. Buzug

Size Depended Electrical Properties of Hydroxyapatite Nanoparticles ... 230
V. Bystrov, N. Bystrova, Yu. Dekhtyar, A. Karlov, A. Katashev, C. Meissner, E. Paramonova, N. Polyaka, and A. Sapronova

Microscale Organization of Chondrocyte Array in Hydrogel by Dielectrophoresis ... 233
S. Miyata and Y. Takeuchi

Iron Oxide Nanoparticles Conjugated with Trastuzumab as an Immunospecific Probe for Detecting HER2 Antigen ... 235
S. Rasaneh, H. Rjabi, and H. Babaei

Determination of Tannic Acid Precipitated with Bovine Serum Albumin by Visible Light Scattering by a Flow-Injection System ... 237
Tzong-Jih Cheng, Chien-Yu Chung, Po-Chung Chen, and Richie L.C. Chen

Magnetron Enhanced Plasma-Polymerization for Biocompatible Sensor Coatings and Membranes on Polymeric Based Materials ... 241
F. Olcaytug, L. Ledernez, G. Dame, P. Zahn, H. Yasuda, and G. Urban

Fully Electronic Cellular Migration Assays with Field-Effect Transistor Arrays ... 242
S. Ingebrandt, S. Schäfer, R. Stockmann, and A. Offenhäusser

Artificial Urinary Diversion System – Kinematic Requirements on Fixation ... 245
D. Kirchleitner, M. Roth, D. Jocham, and H. Wassermann

Compact Drug Delivery System for Analysis Arrays ... 248
M. Scheuenpflug and T.C. Lueth

Effect of Polymer Molecular Weight on Morphology and Particle Size of Chitosan Microspheres Prepared via Spray Drying Method ... 251
S. Taranejoo, M. Rafienia, M. Janmaleki, M. Kamali, and L. Sadeghzadeh

The Use of Body Motion for Powering Biomedical Devices ... 253
E. Romero, R.O. Warrington, and M.R. Neuman

Economic Feasibility Studies in the Field of Active Implants and Biosensors over Simulations: A Methodology for Structured and Valid Results ... 257
Ch. Elsner, D. Häckl, and H. Wiesmeth

Dual Phosphatidylglyceroglycerol-Based Thermosensitive Liposomes for MR-Guided Chemothermotherapy ... 259
T. Wang, M. Hossann, M. Peller, H.M. Reinl, M. Reiser, R.D. Issels, and L. H. Lindner

Monitoring Adherent Cell Cultures in Microtiter-Plates by a Wireless Sensory System ... 261
J. Wissenwasser, M. Milnera, L. Farmer, C. Höpfner, M. Vellekoop, and R. Heer

In-vitro Characterization of an Implantable Thermal Flow Sensor for Hydrocephalus 265
J. Burger, T. Bork, A. Hogg, M. Lempen, D. Mueller, D. Joss, T. Bardyn, P. Buechler, H. Keppner, and Y. Tardy

Concentration-Dependent Multi-parametric Functional Screening of CNS Drugs with Neuronal Networks on Microelectrode Arrays 269
O.H.-U. Schroeder, A. Gramowski, K. Jügelt, and D.G. Weiss

Electric Field Characteristics of Bipolar Impedance Sensors 273
P. Kassanos, R.H. Bayford, and A. Demosthenous

Hemodynamic Response with an Artificial Myocardial Assistance in Chronic Animal Examination 277
Y. Shiraishi, T. Yambe, Y. Saijo, M. Shibata, H. Liu, T. Sugai, A. Tanaka, S. Konno, A. Baba, T. Fujimoto, K. Imachi, M. Yoshizawa, S. Nitta, H. Sasada, K. Tabayashi, Y. Sato, M. Umezu, and D. Homma

Implantable Sensor System for the Monitoring of Bone Healing 281
M. Sattler, J. Clauss, M. Schmidhuber, J. Belsky, and B. Wolf

Spontaneous Activity of Rat Embryonic Cardiac Myocytes 285
D. Jans, D. Braeken, D. Rand, C. Bartic, and G. Callewaert

The Design and Construction of a Set of Modular Synthetic BioLogic Devices for Programming Cells 289
B. Wang, R. Kitney, M. Buck, M. Jovanovic, N. Joly, and E. James

An Innovative Rotational Magnetic System to Enhance Cell Transfection with Magnetic Nanoparticles 293
Dahmani Ch., Helling Fl., Weyh Th., and Plank Ch.

PROTMINE: A Web Service Based Tool to Interpreter Clinical Proteomic Data 297
M. Giacomini, S. Ravaschio, S. De Nadai, A. Petretto, and G. Melioli

Silicon Based Multi Parametric Biohybrid Microsensor Chips 299
Y. Eminağa, J. Wiest, M. Remm, M. Brischwein, and B. Wolf

Stent-Based Plasmid Gene Delivery into Porcine Coronary Artery 303
L.H. Zhang, T. Luo, C. Zhang, P. Luo, X. Jin, H.F. Sun, C.X. Song, and R.L. Gao

Disruption of Microvessels by Focused Ultrasound with Microbubbles to Cause the Extravasation of Macromolecules and Observed by Two-Photon Fluorescence Microscopy 306
Kuo-Wei Lu , Chi-Hsun Huang, Chun-Chin Wang, and Win-Li Lin

Micro– and Nanosensors for Medical Applications 310
Urban Gerald A.

Ferroelectric Nanoparticles for Contrast Enhancement Microwave Tomography: Feasibility Assessment for Detection of Lung Cancer 311
S. Semenov, N. Pham, and S. Egot-Lemaire

MEA Neurosensor, the Tool for Synaptic Activity Detection: Acute Amyloid-β Oligomers Synaptotoxicity Study 314
I. Benilova, I. Kuperstein, K. Broersen, J. Schymkowitz, F. Rousseau, C. Bartic, and B. De Strooper

Development of Tri-component Copolymer Rods as Implantable Drug Delivery Systems for Liver Cancer Therapy 317
N. Nasongkla, P. Akarajiratun, and S. Hongeng

Microchip-Integrated EOSCs (Electrolyte Oxide Semiconductor Capacitors) as Devices for High Efficiency and Selective Electroporation of Mammalian Cells 321
M. Maschietto, S. Girardi, M. Dal Maschio, and S. Vassanelli

Sensors for Healthcare Monitoring – Proteins, Viruses and Blood-Group-Typing 325
F.L. Dickert, P.A. Lieberzeit, A. Seifner, R. Schirhagl, and Christof Jungbauer

The Interaction between Charged Macroions Induced by Rod-Like Ions 329
K. Bohinc, A. Iglič, S. Maset, and S. May

Integration of Micro Fluidic Bio-chip Design and Automatic Fluorescent Identification for Rapid Sperm Mobility Assessment 332
Li-Chern Pan, Fang-Chi Hsu, Yun-Ying Wu, Fan-Gang Tseng, Da-Jen Yao, Yieh-Loong Tsai, and Jiann-Loung Hwang

Interfacing Metallic Ohmic Contacts in Biocompatible Ceramic Substrates with Diamond Surfaces for Biosensing Applications 336
M.A. Neto, E.L. Silva, A.J.S. Fernandes, F.J. Oliveira, and R.F. Silva

Chemical Modification of Surfaces for Biochemical and Medical Sensor Applications 339
V.C. Ayala, K. Moosmann, O. Prucker, J. Rühe, and L.M. Reindl

Minimizing Stress Exposure to Cells Using Novel Microfluidic Cell Capture Devices 343
G. Kijanka, I.K. Dimov, R. Burger, and J. Ducrée

Development of EGFR-Targeting Nanomedicine for Effectively and Noninvasively Treats Lung Cancer Patients by Aerosol Delivery 347
Ching-Li Tseng, Yueh-Hsiu Wu, Su-Wen Yu, Kai-Chiang Yang, and Feng-Huei Lin

Amperometric Microbiosensors Based on PQQ-Dependent Glucose Dehydrogenase towards the Development of an ATP Biosensor for in vitro Analysis 351
C. Weber, E. Gauda, E. Hecht, B. Mizaikoff, and C. Kranz

Remote Controlled Drug Release Induced by a Rotating Magnetic Field 355
W. Andrä, T. Gesener, A. Raabgrund, and M.E. Bellemann

Microfluidics for Drug Delivery 359
S. Haeberle, D. Hradetzky, A. Schumacher, M. Vosseler, S. Messner, and R. Zengerle

Cell Based Assays for Label Free Investigation of Living Cells 363
J. Wiest, M. Schmidhuber, D. Grundl, F. Demmel, M. Zottmann, H. Grothe, M. Brischwein, and B. Wolf

Silicon Based Devices for Intracellular Applications 365
R. Gómez-Martínez, M. Duch, A. Sanchez, J.A. Plaza, and J. Esteve

Cell Select – A New Concept for Collecting of Rare Cell Populations *in vivo* 369
S. Pietschmann, R. Martin, T. Schoen, J.P. Spatz, and U. Pison

Combined AFM-SECM: Towards a Novel Platform for Imaging Microbiosensors 372
Justyna Wiedemair, Jong-Seok Moon, D.E. Eaton, Boris Mizaikoff, and Christine Kranz

Microfluidic Platform for Investigating Small Blood Vessels 376
Conrad Lochovsky, Andrei Vagaon, Sanjesh Yasotharan, Darcy Lidington, Julia Voigtlaender-Bolz, Steffen-Sebastian-Bolz, and Axel Günther

Characterization of Electron Conduction in Unsaturated Organic Monolayers on Silicon(111) Using Electrical Impedance Spectroscopy 378
T.C. Chilcott, H.G.L. Coster, and D. Zamri

The Study of Micro Liter Insulin Injection System by Osmotic Pressure for Diabetes Therapy 382
Toshiaki Nagakura, Kazuki Inada, Yuuto Susuki, Naohiro Yoshida, Akira Yamada, Masashi Ikeuchi, and Koji Ikuta

Amperometric Monitoring of Substance-P Levels in Biological Fluids 384
J. Horak, B. Enderle, H. Bakirci, and G.A. Urban

High Throughput Microelectrode Array Platforms for Quantitative Pharmacology, Toxicology, and Drug Development Using Spontaneously Active Neural Tissue 385
Guenter W. Gross

Author Index 387

Silicon Eye

Author 1 ;

Sandeep Thuvvakkadan

Bio Medical department

D.S.E.C

Perambalur, Tamilnadu, India

E mail: Sandeep_t@37.com

Author 2;

Vignesh Janardhanan Nair

Bio Medical department

D.S.E.C

Perambalur, Tamilnadu, India

E mail: vignesh.229@gmail.com

Silicon eye can be otherwise called as a complete eye implant. The project overview is given in brief by the description of main components.

Here in the silicon eye, a biconcave gel lens is used in connection with a micro controller. A porous silicon nano photodiode is placed before the gel lens. This specially designed transparent diode will help in identifying the intensity of light receiving in the beginning of the processing chain. An effective drainage system (with the help of two valves) will control the working of gel lens. All these components together form the primary circuit to enable the process of auto focusing. The micro controller is connected with all main components of the system. The primary circuit is connected to a secondary circuit which consists of an artificial silicon retina and a chemical synapse. By the combined and co-ordinate working of both these will enable vision. The power supply, which all the electrical components here need is given by a series of nano paper batteries placed beneath the retinal layer (carbon nano tubes can also be implemented instead or along with it). The converted electrical impulses (from intensity of light received) will be carried to the visual area of brain through optic nerve by the effective interaction with a number of artificial chemical synapses.

Finally this silicon eye will be an effective implant for the damaged eye. And we are sure that this will be a great breakthrough in the modern medicine.

MATERIALS AND METHODS WITH DESCRIPTION

A. *Lens*

This is one of the main parts of the silicon eye. We believe that this is the main thing that we have thought in a different way from the existing technologies.

The lens is made of a special gel. We prefer this gel to be ideally transparent and also it shouldn't decrease the speed of light that passes through it. Silicon hydro gel is a suitable substance. Because it is a substance which is having high oxygen permeability. The substance used for making the contact lenses can also be tried.

O. Dössel and W.C. Schlegel (Eds.): WC 2009, IFMBE Proceedings 25/VIII, pp. 1–4, 2009.
www.springerlink.com

The preferred lens is made almost in a biconcave shape. We are designing the lens in such a way that, there are two pin holes on the lens; one at the top and one at the bottom. Now we are going to discuss about the drainage that used for the auto focusing of the gel lens.

The ductless lachrymal gland is connected to the top of the lens through a tiny tube. Thus we are making the ductless lachrymal gland to a ducted gland. The excess fluid after use is drained to the eye through another tube from the lower part of the lens. This will enable the eye to keep wet every time for the easy movement of eye lids. Now we are going for the explanation for the process of auto focusing,

As we have already explained above there is a drainage system using two tubes through which the fluid flows in out of the lens.

Now consider, the person wearing silicon eye is looking at an object; the porous silicon nano photo diode* will identify the intensity of light and it will create a specific electrical impulse and send that information to the micro controller**.

B. **Porous silicon nano photo diode(P.S.N.P.D);*

A specially made photo diode uses silicon. The need of this device here is, it will identify the intensity of light and pass information to a micro controller. As it name indicate this is porous in nature. I.e. it will pass the light without much difficulty. That's what we need too.

C. ***Micro controller(M.C);*

It is type of micro processor. In this device specific data will be encoded. The function of this is that, when a specific intensity of light is identified by the P.S.N.P and will send a particular electrical impulse to this M.C. Now this impulse is processed in M.C as follows;

- The intensity of light is identified.
- The system verifies and compares the pre coded data with the received intensity.
- Acquires the data with respect to the intensity of light received.
- Produces a new impulse for transmission to the valve system at the opening of the lachrymal gland.

Drainage system;

The drainage system is for, the working of auto focusing lens i.e. the process of focusing with respect to the object distance. Let us consider an object at a certain distance from the lens, the microprocessor sends a specific coded data to the first valve (let it be valve 1). The opening of this valve is related to the intensity of light falling on the porous silicon nano photo diode. If the intensity is high (or low), the valve 1 will regulate the secretion.

Thus a certain quantity of fluid enters the lens, which will result in the change of shape of lens from concave to convex or vice versa. That means the rays of light will converge or diverge in accordance with the intensity of light falling on the gel lens to take place the process of auto focusing.

I. *Working of the valve system*

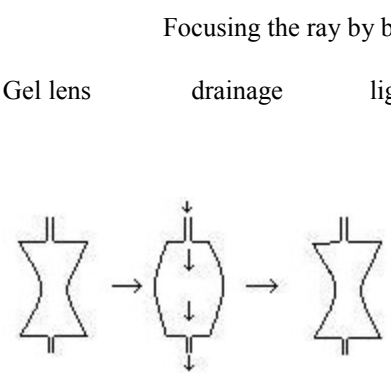
As we have early pointed out there are two tiny tubes used in the drainage. A group of valves that are controlled by several controlling units' (microcontroller) controls the flow of the lachrymal secretion through the tiny tubes. The detailed description of these valves is given below;

1. *Valve 1:*

This first valve is placed at the opening of lachrymal gland. Its function is to regulate the flow of fluid from the gland. It will work according to the data received from the micro controller. That means, when a small intensity of light is identified by the micro controller it will send specific information to the valve 1 and a respective process takes place vice versa too. Thus, the valve may open with respect to the impulse received from the M.C. The working means, opening and closure of the valve. Thus, it will help in the filling of the lens with the fluid. Moreover, in that way only, the process of auto focusing takes place. It is because of the reason that when fluid fills inside the lens, the previously made concave lens will slightly transform its shape to almost a convex shape. Thus, the light rays may diverge or converge with respect to the distance of the object observing the person.

2. *Valve 2:*

The second valve is placed at the bottom of the gel lens. The main function of this valve is to regulate back flow of the glandular secretion in gel lens and it will act as the outlet for the fluid from lens. The working of this valve 2 is controlled by the special sensors placed on the valve it self. The sensor at the valve 2 is a specially designed to identify the secretion level. Its function is to identify the level of secretion inside the gel lens.



A Rough diagram of the process of focusing

Power supply

For the uninterrupted power supply for the proper working of the entire system, we are taken the following measures

1. Nano paper battery

The nano paper battery will act as the primary source energy. This specially designed nano, power producing device is completely made of cellulose. Therefore, there will not be any problem of biocompatibility. As the name implies, this setup is like a paper only. So we can place this battery in between the choroid and sclera without much difficulty.

The main advantages of using this type of battery is that,

The most important thing is its nano size.

- Surgery can be done easily, since it is having only that much size.
- Due to its biocompatibility, we can use two or more batteries as supply according to the need.
- It can be easily replaced, if needy.

WORKING OF THE SILICON EYE

Here we are developing a lens, which is made up of silicon hydro gel. The gel should be ideally transparent and it will not reduce the intensity and speed of light considerably. A suitable gel substance is silicon hydro gel. This gel substance is coated with a transparent metal alloy, which is made up of indium tin oxide (ITO). This must be flexible i.e. it bears a sort of elasticity. We will enclose the gel inside ITO in almost a biconcave shape. For that purpose we are making some layers of ITO, it can be directly vaporized. However, at the top and bottom surface of the concave lens is solidified with a suitable metal alloy. Then we give drainage through the gel lens by using a tiny tube, which is connected to lachrymal gland. The tube must be hollow with opening at both ends and flap at mouth. The microcontroller controls Opening and closure of the flap.

The light through the pupil incident on the porous silicon nano photo diode, which is placed just before the gel lens and this, will identify the intensity of light and passes the information to the micro controller. If the object is near to us then the intensity of light will be high and vice versa. If the light intensity is high (or low) then the flap will open in accordance with that. This process of focusing takes place continuously. As a result, the biconcave lens will bulge out and it will become convex. This way the focusing will take place. To give power for the system we will use nano paper battery. The secretion going out through the drainage should be lesser than the secretion comes into the lens. All required program to control the opening and closure of the flaps are coded in the micro controller.

After the process of focusing, the light will fall on the artificial silicon retina. This will convert the received intensity of light to a specific electrical impulse. This impulse is traveled through the artificial chemical synapse to reach the area of vision in brain. Then brain enables the vision.

ADVANTAGES:

- The whole system is easy and convenient to carry.
- Most effective conduction process is employed.
- Simple power production from body fluids itself.
- For the additional power needed, a compact nano paper battery is used in extra.
- The clarity of the picture is almost near to, a normal man’s vision. Nevertheless, the persistence of vision will be somewhat higher than in a normal eye.

CONCLUSION:

Nowadays no such devices are available which have the ability to provide the vision to the blinds. This is an effective one and without much time delay a blind can enjoy the beauty of vision.

REFRENCES

1) www.wikipedia.com, the online encyclopedia,2)Human anatomy by Dr B.D.Chourasya

3) Nanostructure Science and Technology ,Di Ventra, Massimiliano; Evoy, Stephane; Heflin, James R. (Eds.)

Automated Assembly of Dynamic Micro-Bead Arrays Using a Multi-arm Laser Manipulator with Computer Vision

Y. Tanaka[1], H. Kawada[2], S. Tsutsui[2], M. Ishikawa[1], and H. Kitajima[2]

[1] AIST, AIST Shikoku, Takamatsu, Japan
[2] Kagawa University/Faculty of Engineering, Takamatsu, Japan

Abstract— **Dynamic microarrays have great flexibility and potential as tools for advancing research in diagnostics and biomedical fields. In contrast with static microarrays such as DNA-chip using micro-spots of the bio-molecules, dynamic microarrays use a mobile substrate, usually micro-beads coated with bio-molecules. To realize the dynamic microarray, micro-bead handling techniques are essential, allowing us to transport the selected bead, and immobilize them for signal detection. Laser manipulation, known as optical tweezers, is one of the most suitable techniques for arranging and handling micro-beads. We have developed a multi-arm laser manipulation system with an excellent user-interface and real-time image processing functions. In this paper, we report a new approach for fully-automated assembly of a versatile dynamic micro-bead array. The beads, dispersed in a pipetted liquid on a cover glass, can be simultaneously trapped and sorted into a desired order, using multiple optical tweezers to transport the beads along collision-less paths guided by both computer vision and knowledge database techniques. Two typical examples are demonstrated. One is the fully-automated assembly of a 3x3 micro-bead array and its handling in 3D space. The other is the collision-free sorting of an array's elements. We also describe the experimental apparatus used in these demonstrations.**

Keywords— **Optical tweezers, Micromanipulation, Dynamic microarray, μTAS, Hough Transform.**

I. INTRODUCTION

Micro/Nano systems for biomedical fields, such as the so-called Lab-on-a-Chip and bio-MEMS, is currently an area of intensive research. DNA-chips, using micro-spots of bio-molecules, represent a widely-used group of static microarrays for basic studies in biomedical fields, diagnostics, drug discovery, etc. Compared with static microarrays, dynamic microarrays using mobile substrate, usually micro-beads coated with bio-molecules, have several advantages as tools for advancing research in biomedical fields [1]. To realize the potential of dynamic microarrays, micro-bead handling techniques allowing us to transport the selected beads and immobilize them for signal detection are necessary. Laser manipulation, also known as optical tweezers [2, 3], is one of the most suitable techniques for manipulating and handling micro-beads. To achieve fully-automated manipulation for assembling micro-bead arrays, we developed a multi-arm laser manipulator based on the Time-Sharing Synchronized Scanning (T3S) approach for generating multiple laser trapping positions [4]. The multi-arm laser manipulator has an excellent user-interface and real-time image processing functions. In Section II, we propose a new approach for automated assembly of versatile dynamic micro-bead arrays. The system configuration is also described in this section. In Section III, we demonstrate two typical examples based on the proposed approach. One is the fully-automated assembly of a 3x3 micro-bead array and its handling in 3D space. The other is the collision-free sorting of an array's elements.

II. PC-CONTROLLED DYNAMIC MICROARRAYS

A. Approach using laser multiple-trap techniques

For assembling dynamic microarrays, several approaches including hydrodynamic [1], dielectrophoresis [5], and mechanical [6, 7], have been demonstrated. Laser trapping is one of the most suitable approaches and has several advantages: (i) no physical contact means we can manipulate the beads in a closed space such as Lab-on-a-Chip, and since no adhesion between manipulator and beads occurs, we can achieve more precise positioning; (ii) we can simultaneously manipulate multiple beads using single laser source; (iii) it is not necessary to redesign hardware configurations, namely, mechanical and fluidic parts, for handling beads of different size and number (a reusable platform can greatly reduce the cost of operation); (iv) an objective lens can be used as both a manipulating and an observing apparatus. We can control both operations under the same coordinate system, which makes using computer vision techniques for fully-automated applications easier when compared with competitors' systems. Figure 1 illustrates our approach for assembling dynamic bead arrays using laser multiple-trap techniques. Our approach consists of three control stages: Stage 1, image recognition and automated trapping; Stage 2, automatic transportation; and Stage 3, automatic sorting by color/size. First, in Stage 1, beads with specified properties are recognized, and then all

O. Dössel and W.C. Schlegel (Eds.): WC 2009, IFMBE Proceedings 25/VIII, pp. 5–7, 2009.
www.springerlink.com

the beads are trapped simultaneously. Secondly, in Stage 2, all the trapped beads are transported simultaneously to latticed positions along the collision-less path. Finally, in Stage 3, the beads are sorted to arrange in the specified order under the collision-free interchange algorithm based on group theory.

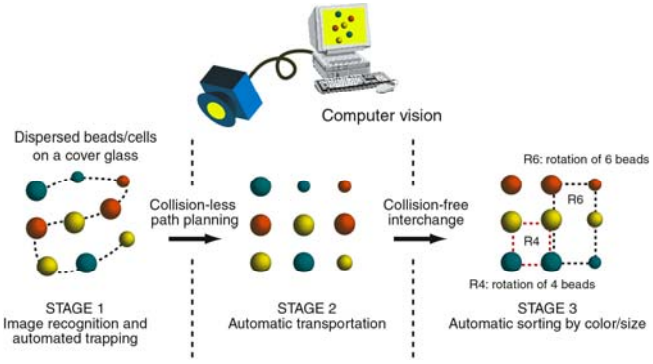


Fig. 1 Scheme of automated assembly of a dynamic beads array

B. *Experimental system*

To manipulate many micro-beads using laser multiple-trap techniques, we have used Time-Sharing Synchronized Scanning (T3S) Optical Tweezers [4]. This additional optical structure is linked to a commercially-available inverted microscope. Figure 2 schematically shows the experimental setup. The focal positions of the time-shared beam on the XY-plane are controlled by the 2-axis steering mirror. This mirror can tilt at a considerable rate just as a piezoelectric mirror can. The Z-coordinate is controlled by the lens L1 mounted on a PC-controlled linear stage, which can be moved parallel to the optical axis.

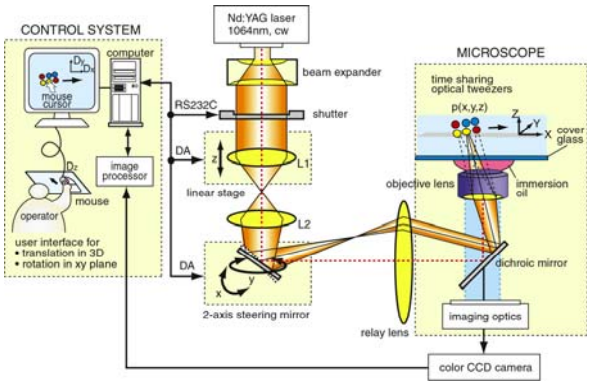


Fig. 2 Schematic of experimental setup

Thus, an assembled bead-array can be translated in 3D and rotated in XY-plane at a specified Z-coordinate using a PC 3-button mouse. An image processor digitizes the images from a color CCD camera in real time for feature recognition. Developed software for image processing and device control is executed by a personal computer (PC).

III. DEMONSTRATIONS

A. *Fully automated assembly of dynamic bead array*

Here, we demonstrate the fully-automated assembly of a 3x3 micro-bead array using computer vision techniques in order to explore the future possibilities for a laser-controlled, flexible microarray chip, or so-called "dynamic microarray". Figure 3 is a sequence of images recorded with the CCD camera showing the result of the fully-automated assembly of the dynamic array. First, the positions of the micro-beads dispersed in the pipetted water on a cover glass were detected by the circular Hough transform technique [8]. Nine beads nearest to the center position, o, were simultaneously trapped at the initially detected position of each bead using the T3S optical tweezers (Fig. 3(a)). Second, nine trapped beads were simultaneously transported to pre-designated destinations, where the beads formed a 3x3 array, along the collision-less paths (Fig. 3(b)). After forming the 3x3 array, the array could be translated in XY-plane (Fig. 3(c)), rotated (Fig. 3(d)), lifted off/down the cover glass (Fig. 3(e)), and expanded (Fig. 3(f)) using the PC 3-button mouse.

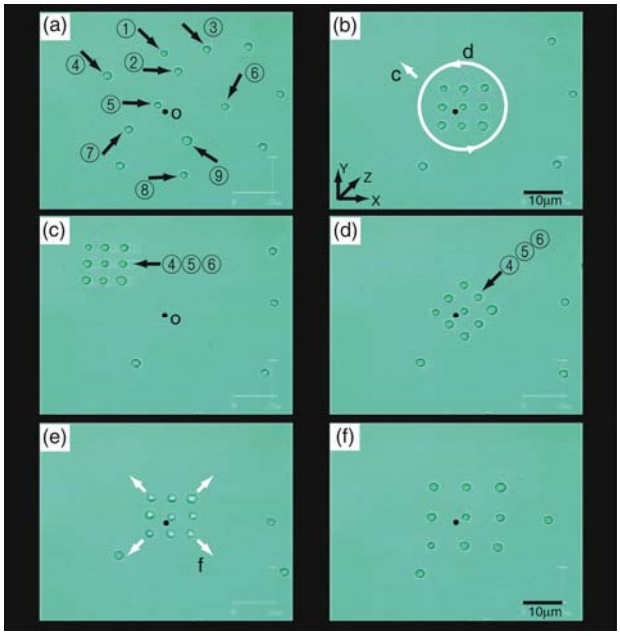


Fig. 3 Automated assembly of a 3x3 array and its translations in 3D space

B. Collision-free sorting of the array's elements

Rearrangement of the beads at arbitrary lattice positions is important for signal analysis applications of dynamic microarrays. Here, we demonstrate the automatic sorting of an array's elements by size. Figure 4 is a sequence of images recorded with the CCD camera showing the result of automated assembly of a 3x3 array and subsequent automatic sorting by size. First, nine beads were detected and transported to form the 3x3 array in a manner identical to Subsection A (Fig. 4(a), (b)). Next, the successive rotations of 4/6 beads at lattice position (R4/R6 in Fig. 1) were carried out, like solving the Rubik's Cube puzzle, in order to interchange the array's elements under the collision-free paths (Fig. 4(c)-(e)). Note that a mathematical proof based on the group theory shows that the procedure of rotations, R4 and R6, can exchange two beads at arbitrary lattice positions. This procedure continued until the sorting was completed (Fig. 4(f)).

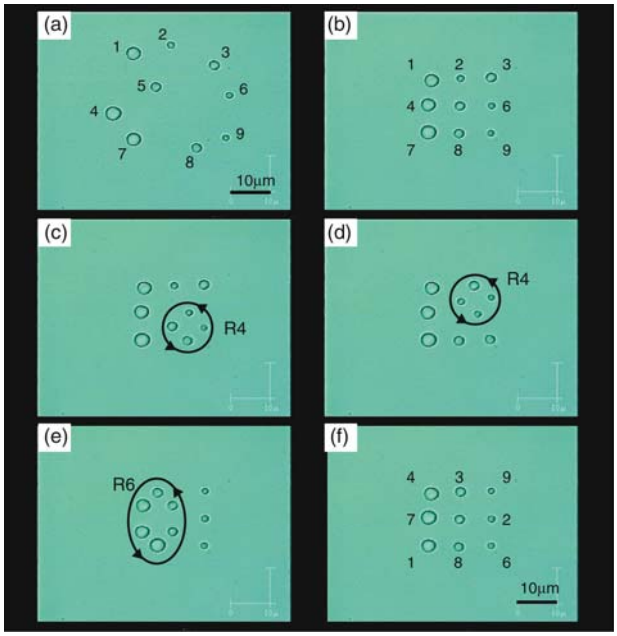


Fig. 4 Automated assembly of a 3x3 array and its sorting by size

IV. Conclusions

We have proposed a new approach for automated assembly of PC-controlled dynamic micro-bead arrays, and demonstrated two typical examples of fully-automated assembly. Although the demonstrations performed are indeed simple, laser-controlled dynamic arrays have great flexibility and potential as research tools in various fields, including biomedical applications. Furthermore, multi-arm laser manipulators combined with visual-feedback control or knowledge-database control may not only enable the assembly of dynamic micro-beads array, but also be applied to other biomedical and industrial fields.

Acknowledgment

This work was partly supported by Grants-in-Aid for Scientific Research (C, #20560252) from the Japan Society for the Promotion of Science, and also by Research for Promoting Technological Seeds from the Japan Science and Technology Agency.

References

1. Tan W-H and Takeuch S (2007) A trap-and-release integrated microfluidic system for dynamic microarray applications. PNAS 104:1146-1151
2. Ashkin A (1970) Acceleration and trapping of particles by radiation pressure. Phys. Rev. Lett. 24(4): 156-159
3. Grier DG (2003) A revolution in optical manipulation. Nature 424:810-816
4. Tanaka Y, Kawada H, Hirano K, Ishikawa M and Kitajima H (2008) Automated manipulation of non-spherical micro-objects using optical tweezers combined with image processing technique. Opt. Express 16(19): 15115-15122
5. Chiou PY, Ohta AT and Wu MC (2005) Massively parallel manipulation of single cells and microparticles using optical images. Nature 436:370-372
6. Noda H, Kohara Y, Okano K and Kambara H (2003) Automated bead alignment apparatus using a single bead capturing technique for fabrication of a miniaturized bead-based DNA probe array. Anal. Chem. 75: 3250-3255
7. Onal CD and Sitti M (2007) Visual servoing-based autonomous 2-D manipulation of microparticles using a nanoprobe. IEEE Trans. Control Sys. Tech. 15: 842-852
8. Ballard DH, Brown CM (1982) Computer vision. Prentice-Hall, New Jersey

- Author: Yoshio Tanaka
- Institute: AIST, AIST Shikoku
- Street: 2217-14 Hayashi-cho
- City: Takamatsu
- Country: 761-0395 JAPAN
- Email: yo-tanaka@aist.go.jp

A Nano-porous Aerogel Biochip for Molecular Recognition of Nucleotide Acids

Yen Kuang Li[1], Den-Kai Yang [2],Yun-Chu Chen [1], Hung-Ju Su [3], Jui-Chuang Wu [2*], Yui Whei Chen-Yang [1*]

[1] Department of Chemistry, Chung Yuan Christian University, 200 Chung-Pei Road, Chung-Li, Taoyuan County 32023, Taiwan, Republic of China

[2] R&D Center for Membrane Technology and Department of Chemical Engineering, Chung Yuan Christian University, Chung Li, Taoyuan County 32023, Taiwan, Republic of China

[3] Biomedical Engineering Center, Industrial Technology Research Institute, Chu Tung, Hsin Chu 31040, Taiwan, Republic of China

Abstract—**A nano-porous aerogel was produced in regular atmospheric conditions using the sol-gel polymerization of tetraethyl orthosilicate (TEOS) to build a three-dimensional (3D) structure for recognizing nucleotide acids. The Fourier transformation infrared spectroscopy and Brunauer-Emmett-Teller instrument had been used to characterize this 3D aerogel and concluded that it had a high porosity and large internal networking surface area to capture nucleotide acids. The functionality of molecular recognition on nucleotide acids was demonstrated on human gene ATP5O.**

Keywords— **Aerogel, molecular recognition, DNA detection. 3D biochips.**

I. Introduction

Silica aerogel is a material with high porosity, large surface area, low density, and low thermal conductivity. These unique characteristics guarantee this advanced material in the applications of thermal insulation, electrical batteries, nuclear waste storage, catalysis, acoustic insulation, and adsorbents [1]. In addition, silica aerogel also holds promises as biocompatible scaffolds to be applied on virus detection [2], protein entrapment [3], protein incorporation [4], hybridization array [5, 6], and building potential matrices in the further design of biosensors. The modern exciting application on capturing comet dust further pushed this material into the outer space (www.nasa.gov).

Unlike the traditional supercritically-dried technique [5], this contribution adopted a process to prepare the aerogel in the regular atmospheric condition. We also demonstrated the functionality of molecular recognition on detecting a sequence-specific deoxynucleotide acid (DNA) target and compared the results with those using traditional planar slides.

II. Exeperimental

A. Materials

The networking precursor of the aerogel, tetraethyl orthosilicate (TEOS), the solvent, methanol, and the surface modifying reagent of aerogel, 3-Glycidoxypropyltrimethoxysilane (GLYMO), were all obtained from Acros Company. The DNA targets were PCR (Polymerase Chain Reaction) products amplified from the human gene ATP5O in total RNA. Table 1 lists its gene information and the primers participating in the PCR process. Both probe and primer sequences are listed in Table 1. The conformations of DNA probe immobilization and probe-target hybridization are shown in Fig. 1.

Table 1 Genetic information of materials

ATP5O	
Length	313 bases
Definition (NCBI gene bank)	ATP synthase, H+ transporting, mitochondrial F1 complex, O subunit (oligomycin sensitivity conferring protein)
ATP5Oc (probe)	
Sequences	amine-C_6-5'(GTGATTGGACGCGGTGA)-(GTCTTGACAGACATGTCAACATATTTCTCGCCAATGCGCACAATCATTCCACCCAAGATT)3'
PCR Primers	
ATP5O-F1	TTCTGCTGCATCAAAACAGAAT
ATP5O-R1	ATGGCAGAAAACCAACACTTTT
cy3-ATP5O-F2	CGATTAAGCA CAAGGAG ATACC

B. Instrument

Fourier transformation infrared (FTIR, BIO-RAD-FTS-7) spectrometer was used to verify the removal of the template from the aerogel. The BET specific surface area and the pore volume of the as-prepared aerogels were deter-

O. Dössel and W.C. Schlegel (Eds.): WC 2009, IFMBE Proceedings 25/VIII, pp. 8–10, 2009.
www.springerlink.com

mined from the nitrogen adsorption/desorption isotherm by the Barrett-Joyner-Halenda (BJH) method using a Micrometrics ASAP 2020 analyzer. PCR was performed on GeneAmp_PCR, System 9700. The microarray scanner (GenePix 4000B, Molecular Devices) was used to excite and read the labeling fluorescence.

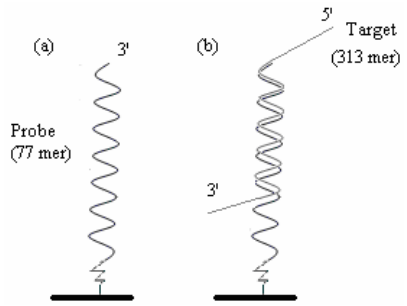


Figure 1. The Conformations of DNA Probe Immobilization and Probe-Target Hybridization. (a) To compare with experimental results, the 77-mer probe, ATO5Oc, was immobilized on both planar slide and aerogel surfaces. (b) The upper 60-mer of the probe was designed specifically to recognize the DNA sequence of the target. The lower 17-mer provided a space to prevent the target-substrate interface from a steric hindrance.

C. Procedure

The silica-aerogel was prepared in the sol-gel process by mixing TEOS, methanol, network template, and water. It was then cured at the ambient temperature for 1 week. The as-prepared silica aerogel was finally obtained by freeze drying, and Fourier transformation infrared (FTIR) analysis was utilized to confirm the removal of the ionic-liquid template. To capture the NH_2-modified DNA probe, the aerogel product was grained into powder and stirred in 5% GLYMO solution for 1 hr to modify the surface from -OH to epoxy functional group. The internal volume and porosity using Brunauer-Emmett-Teller (BET). The results were compared with those obtained prior to modification.

The epoxy-modified aerogel was dropped onto slides in the array aligned by a grid paper placed underneath. The slides were then baked at 100°C for 90 minutes and ready for DNA-probe immobilization.

The oligonucleotide probe was dropped on both commercial and aerogel slides in 1 µl. The slides were then incubated in a humid box at 30°C for 16-17 hours to immobilize the probes on the planar slides or aerogel. A wash step was conducted to remove the free probes in 0.5% SDS by shaking at 80rpm for 15 minutes. The slides were then immersed in the blocking buffer at 60°C for 45 min and finally rinsed with ddH_2O and spun to dry. DNA target was mixed with 1X hybridization buffer to the final concentrations of 40, 60, 80, and 120 nM. One micro-liter of the target solutions were dropped onto planar slides and aerogel dots at the previously-immobilized probes. All chips were then enclosed in a humid box and incubated at 50°C for 16-17 hours and then washed. They were initially immersed in 2X SSC/0.2X SDS at 42°C at 80 rpm for 10 min, then changed to 2X SSC in the same condition, and finally 0.2X SSC at room temperature. After rinsing with ddH_2O and spun to dry, the slides were scanned for fluorescence analysis.

III. Results and Discussion

Figure 2 shows the FTIR spectrum for the as-prepared silica aerogel before and after template removal. The characteristic template band was found to be absent revealing that the template was entirely removed from the wet aerogel by our extraction process.

Figure 3 shows the nitrogen adsorption/desorption isotherm of the silica aerogel product. The measurement indicated that its specific surface area was 813 m^2/g, pore volume was 0.78 cm^3/g, and the average pore-diameter was 4.2 nm. Its large surface area granted the assurance that the detection signal of the captured biological samples on the surface can be tremendously intensified.

As shown in Figure 4, ATP5Oc-immobilized aerogel was utilized to recognize the target human gene ATP5O and compared the results side-by-side with commercial planar slides. The positive control on the leftmost bottom of aerogel was the brightest over those on planar slides and the flat surface reached its accommodation saturation for target molecules; whereas the aerogel still kept capturing DNA targets.

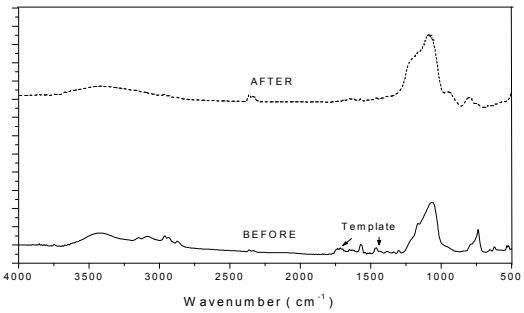


Figure 2. FTIR analysis of the aerogel product before and after template removal. The disappearance of the characteristic peaks in the spectrum indicates that the template was successfully removed.

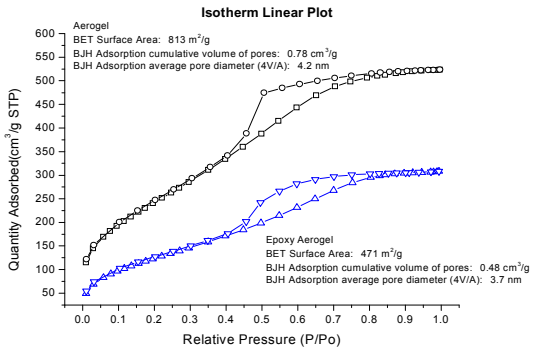


Figure 3. Nitrogen Isotherm of the Silica Aerogel Product. The specific surface area was 813 m^2/g, pore volume was 0.78 cm^3/g, and average porosity was 4.2 nm.

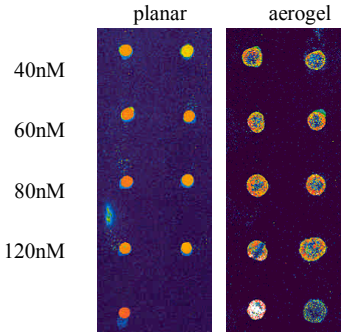


Figure 4. Molecular Recognition Test of ATP5O on Aerogel. Human gene ATP5O (313b) was recognized on the aerogel surfaces over various target concentrations

IV. Conclusions

In this study, mesoporous aerogels are prepared at room temperature by the sol-gel polymerization. The as-prepared aerogel was characterized and concluded that it had a high porosity and large internal networking surface area. The as-prepared aerogel was further arrayed onto slides and successfully recognized a short-size human gene ATP5O by an immobilized oligonucleotide probe on the aerogel surface.

Acknowledgment

The authors gratefully acknowledge the support of the National Science Council of the Republic of China under Grant No. NSC 97-2622-E-033-008-CC1.

References

1. Pierre A, Pajonk G. Chemistry of aerogels and their applications. Chem. Rev. 2002;102:4243-65
2. Power M, Hosticka B, Black E, Daitch C, Norris P. Aerogels as biosensors: viral particle detection by bacteria immobilized on large pore aerogel. J. Non-Cryst. Solids 2001;285:303-8.
3. Li Y, Chou M, Wu T, Jinn T, Chen-Yang Y. A Novel Method for Preparing a Protein-Encapsulated Bioaerogel: Using a Red Fluorescent Protein as a Model. Polymer. 2007;48(1): 456-457
4. Wallace J, Rice J, Pietron J, Stroud R, Long J, Rolison D. Silica nanoarchitectures incorporating self-organized protein superstructures with gas-phase bioactivity. Nano Lett. 2003;3:1463-67
5. Phinney J, Conroy J, Hosticka B, Power M, Ferrance J, Landers J, Norris P. The design and testing of a silica sol -gel-based hybridization array. Journal of Non-Crystalline Solids 2004;350:39-45
6. Saal K, Taette T, Tulp I, Kink I, Kurg A, Maeeorg U, Rinken A, Lohmus A. Sol -gel films for DNA microarray applications. Materials Letters 2006;60(15): 1833-1838

Author: Jui-Chuang Wu
Institute: Chung Yuan Christian University
Street: 200 Chung Pei Rd.
City: Chung Li, Tao Yuan
Country: Taiwan
Email: ray_j_wu@cycu.edu.tw

Biodegradable Polymeric Implants as Drug Delivery Systems for Brain Cancer Therapy

Norased Nasongkla

Department of Biomedical Engineering, Faculty of Engineering, Mahidol University, Nakorn Pathom, Thailand

Abstract— **Brain cancer therapy has been a challenging task due to its fatal outcome and limited accessibility. Recent advance in DDS leads to the utilization of polymers for the local delivery of anticancer agents directly to brain tumors. Polymer has received a growing attention as a material for drug delivery systems (DDS), especially brain cancer because of its biodegradable and biocompatible properties. Ease of polymer synthesis makes it possible to tune polymer properties to provide different drug release profiles and degradation mechanisms. This review aims to provide the information concerning biodegradable polymeric implants. The main focus is on systems that currently reach the *in vivo* study or are using in clinic.**

Keywords— **Polymer, implant, drug delivery system, brain cancer, tumor.**

Tremendous efforts have been made to create drug delivery systems that can deliver therapeutic agents to brain tumor and increase chemotherapeutic efficacy while reducing the negative side effects. In the late 19th century, Paul Ehrlich, the German scientist, originated the concept of "Magic bullet" for the targeted drug delivery from his experience in bacteria research.

Several great reviews on drug deliverys for brain cancer therapy have been reported. [1-3] This review aims to provide not only updated success and application of polymer implantation for brain cancer therapy but also the insight information on the design, problem and consideration that must take into account for the future development. First, obstacles in drug delivery to brain will be reviewed, followed by the in-depth summary on the utilization of polymers as drug delivery systems with the emphasis on Gliadel® wafers.

Even though many kinds of drug delivery systems have been developed for brain cancer therapy, for example, polymeric implants, liposomes and nanoparticles, little success have been accomplished. This is because brain cancer chemotherapy encounters very challenging obstacles: 1) *Drug elimination*: small molecules are secreted by kidney without any restriction. Chang et al.[4] reported that the renal elimination in a rat model of low molecular weight dextrans with a radius lower than 2.0 nm (Mw ~10 kDa) occured without any molecular restriction. On the other hand, the renal clearance of larger dextrans gradually decreased and approached zero at a radius higher than 4.4 nm (Mw ~40 kDa). For example, carmustine (BCNU) has a short elimination half-life (15 minute) [5]; 2) *Side effect*: side effect is the major obstacles for cancer treatment, especially chemotherapy. For example, 7-Ethyl-10-hydroxy-camptothecin (SN-38) has the side effect in category 3 (severe) and 4 (life threatening) as categorized by the National Cancer Institute Common Toxicity Criteria, USA. The symptom is such as severe diarrhea [6,7] and neutropenia.; 3) *Physiological barriers*: drugs are required to pass many physiological systems. For brain cancer, drugs must travel through the blood brain barrier (BBB). Inside the brain tumor, drugs will encounter the interstitial hypertension [8-11] which is the elevated pressure inside tumors. Due to this effect, the diffusion through the brain tumor will be dramatically limited. BBB is formed by tight junctions of endothelial cells in the central nervous system (CNS) which can inhibit the access of therapeutic agents to the brain. Many attempts have been made to overcome these problems but unfortunately end with the failure to successfully treat the brain cancer. Therefore, there is a need to develop drug delivery systems that can overcome these obstacles and efficiently deliver drugs to the brain. The ideal design of drug delivery system to use for brain cancer chemotherapy would be one that is able to directly deliver anticancer drugs in the brain, i.e. intracranial delivery.

The well known advantages of drug delivery over conventional chemotherapy are lowering the adverse effects and prolonging blood circulation time of therapeutic agent in body. Polymers have emerged as widely used delivery carriers for different kinds of anticancer drugs and have been successfully used as materials for a variety of drug delivery systems, for example, polymer implant[12,13] and microparticles for brain cancer therapy. Besides unique properties such as thermoplastic property, viscoelastic, biocompatible and adjustable thermal properties, polymers should be biodegradable. These polymers can be hydrolyzed and eventually decomposed. Therefore, there is no need to remove them after all of drugs diffuse out. Each polymer has different hydrolysis rate as the following sequence: polyanhydride > polyorthoester > polyester > polycarbonate > polyamide > polyurethane > polyurea.

POLYANHYDRIDE

Polyanhydride is successfully used for brain tumors therapy. Its fast hydrolysis rate produces a different degradation mechanism (surface erosion) from a common diffusion-controlled mechanism. The steady drug concentration is achieved from the controllable degradation rate of the polymer matrices and can be controlled by the copolymer

O. Dössel and W.C. Schlegel (Eds.): WC 2009, IFMBE Proceedings 25/VIII, pp. 11–14, 2009.
www.springerlink.com

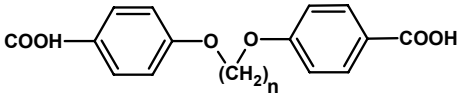
ratio of monomers. Polyanhydride can be made by polymerization of the two carboxylic acid containing monomer.

A) Aliphatic monomer

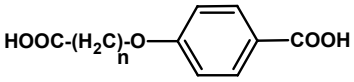
$HOOC\text{-}(CH_2)_4\text{-}COOH$ = adipic acid

$HOOC\text{-}(CH_2)_8\text{-}COOH$ = sebacic acid

B) Aromatic monomer

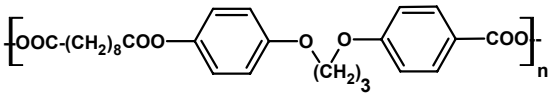


n = 1; bis(*p*-carboxyphenoxy)methane
n = 3; 1,3-bis(*p*-carboxyphenoxy)propane
n = 6; 1,3-bis(*p*-carboxyphenoxy)hexane



n = 1; *p*-carboxyphenoxy acetic acid
n = 4; *p*-carboxyphenoxy valeric acid
n = 8; *p*-carboxyphenoxy octanoic acid

C)



sebacic acid 1,3-bis(*p*-carboxyphenoxy)propane

Fig. 1 Chemical structure of A) aliphatic andydride monomers; B) aromatic anhydride monomers; and C) poly[1,3-bis(carboxyphenoxy) propane-*co*-sebacic-acid] (PCPP-SA).

Poly(bis(*p*-carboxyphenoxy)propane-sebacic acid) (pCPP:SA = 20:80) is used as a material for Gliadel®, a polymer wafer approved by the US food and drug administration in 1996 for the brain tumor treatment.[14-16] This system can be placed inside the brain cavity after brain surgery and can release drug within 2-3 weeks. It has a disc-shape with 1.4 cm in diameter and 1 mm in thickness. Gliadel wafers are prepare by spray drying pCPP-SA microspheres with BCNU-polymer solution.[12] The final formulation contains 3.85% BCNU which are homogenously distributed and within the pCPP-SA matrix. BCNU was found to stay as a solid solution form in the polymer matrix. This is confirmed by the presence of the single melting peak at 58 ^{o}C between that of pCPP:SA = 20:80 (approximately 65 ^{o}C) and BCNU (32 ^{o}C).[17] The fast hydrolysis of pCPP:SA leads to the surface eroding mechanism (the hydrolysis occurs simultaneously to the diffusion of water into the polymer surface as shown in Figure 2).

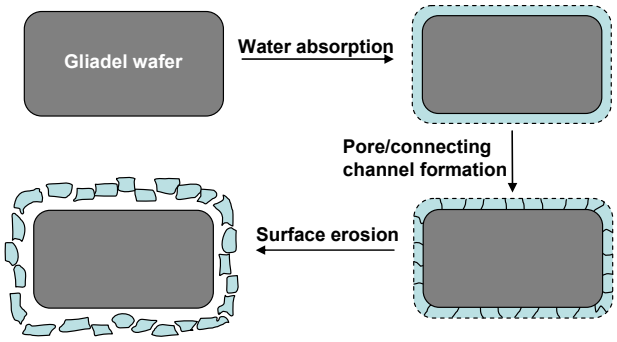


Fig. 2 Mechanism of surface erosion.

Westphal et al. [18] conducted a 30-month trial in two hundred forty patients and reported that the median survival time for the BCNU wafer and the placebo are 13.9 and 11.6 months, respectively. The BCNU wafers provide 29% risk reduction (P = 0.03) for the Gliadel® group against the placebo. These results are in agreement with results from the long time study (2-3 years) in which the median survival time for the BCNU wafer and the placebo are 13.8 and 11.6 months, respectively and 27% risk reduction. Even though the promising brain cancer therapy, Gliadel® were found to cause adverse effects such as CSF leak (5% vs. 0.8% for BCNU wafer vs. placebo) and intracranial hypertension (9.1% vs. 1.7% for BCNU wafer vs. placebo). Other adverse effects are seizures, brain oedema, healing abnormalities and intracranial infection.[18-20]

Recently, Gliadel® was reported as a contraindication when it is conducted in conjunction with the large opening of the ventricle.[21] The fatal consequences were found in three patients with glioblastoma multiforme whom were implanted with Gliadel®. The lateral ventricles of these patients were opened and wafers were hold in the resection cavity by the fibrin glue. Patients then had severe hydrocephalus and subsequently death possibly due to the obstruction of ventricular system. This report raises the concern on the use of fast hydrolysis polymer as a material for brain implantation. Therefore, it is very interesting to investigate how the slower hydrolysis polymer, i.e. polyester behaves once implanted into a brain.

Besides pCPP:SA, another polyanhydride, fatty acid dimer-sebacic acid (FAD-SA) copolymer, has been developed to deliver hydrophilic agents such as 4-hydroperoxycyclophosphamide (4HC) [22,23] and platinum drugs.

POLYESTER

Polyester is one of the most used materials for drug delivery systems. Generally, polyester can be made by ring

opening polymerization which can efficiently control the degree of polymerization and produce a narrow molar mass distribution.

This polymer does not have very fast hydrolysis as a result it is degraded by the bulk eroding mechanism (Figure 3). For this mechanism, the degradation takes place simultaneously through out the sample. Generally, drugs can be released from polyester by diffusion-based drug release.

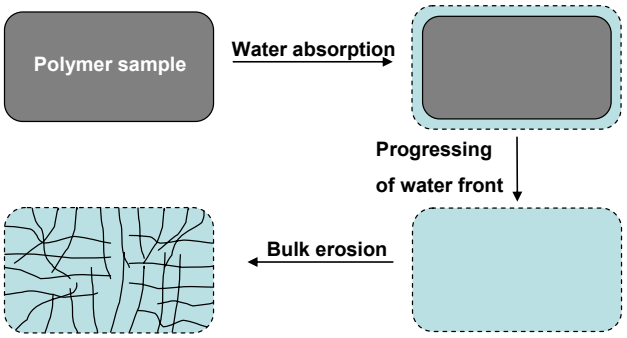


Fig. 3 Mechanism of bulk erosion.

The degradation of polyester has the characteristic mechanism so-call "autocatalytic effect" in which an acid, by product, can accumulate inside the sample and causes the inside out degradation as shown in Figure 4.

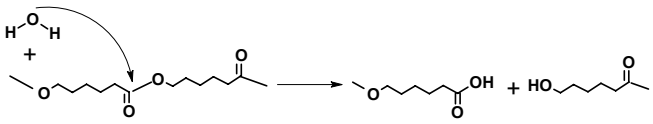


Fig. 4 Hydrolysis of polyester. An acid, by product of polyester degradation, can accumulate inside the sample and causes the inside out degradation so-call "autocatalytic effect".

Poly(lactic-co-glycolic acid) (PLGA) is the most widely used polyester for drug delivery systems, especially for cancer therapy because of its well-known biocompatible and biodegradable properties. [24-26] PLGA is a random copolymer of lactic acid and glycolic acid. Chemcial properties such as hydrophilicity, degradation rate, crystallinity can be controlled by the copolymer ratio between lactide (decrease hydrophilicity and degradation) and glycolide.

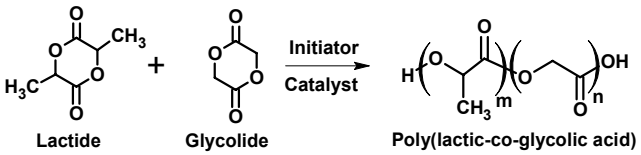


Fig. 5 Chemical structure of poly(lactic-co-glycolic acid) (PLGA). Its property can be controlled by the copolymer ratio between lactide and glycolide during the polymerization.

Similar approach has been performed to produce BCNU wafers from PLGA. Antitumor efficacy study in subcutaneous rat tumor model showed that this BCNU-PLGA wafer can delay the tumor growth. Nevertheless, tumors started to grow after 25 days. [27,28] There has been no report on PLGA wafers behavior and safety in the brain. A long term study in animal should be carried out to address this issue.

A variety of drug delivery systems for brain cancer therapy have been developed from polymers as shown in Table 1. Among them, PLGA microparticles have gained considerable attention with the ease of administration and great cancer treatment. Their microscale structure should be able to avoid the blockage of ventricles as reported in macroscopic systems such as wafers.

Table 1 Drug delivery systems for brain cancer

Formulation	Polymer	Drugs	*In vitro* study	*In vivo* study	Ref
Gliadel® (Wafer)	CPP: SA	BCNU	-	- Sprague-Dawley rats - Fisher 344 rats - Human	[12], [17], [18-20]
Disk	FAD-SA	4HC	-	- F98 & 9L gliomas in rat	[22,23]
Wafer	PLGA	BCNU	9L gliosarcoma cells	9L gliosarcoma cells in F 344 rats	[27,28]
Microparticle	PLGA	5-fluorouracil	-	- Phase II - C6 glioma in rats	[32] [33]
Micro/ nanofibers	PLGA	Paclitaxel	C6 glioma	-	[34]
Microparticle	PLGA	Temo-zolomide	C6 glioma	-	[35]
Microparticle	PLA/ PLGA	Cisplatin	C6 glioma	-	[36]

Conclusion

Rational designs as mentioned in this review must be considered to produce efficient drug delivery systems for brain cancer therapy. Antitumor activity in parallel with safety of the systems must be seriously considered.

References

1. Sawyer AJ, Piepmeier JM, Saltzman WM (2006) New methods for direct delivery of chemotherapy for treating brain tumors. Yale J Biol Med 79:141-152
2. Gutman RL, Peacock G, Lu DR (2000)Targeted drug delivery for brain cancer treatment. J Control Release 65:31-41
3. Lesniak MS (2005) Novel advances in drug delivery to brain cancer. Technol Cancer Res Treat 4:417-428

4. Chang RL, Ueki IF, Troy JL, Deen WM, Robertson CR, Brenner BM (1975) Permselectivity of the glomerular capillary wall to macromolecules. Ii. Experimental studies in rats using neutral dextran. Biophys J 15:887-906
5. Williams J, Lansdown R, Sweitzer R, Romanowski M, LaBell R, Ramaswami R, Unger E 2003 Nanoparticle drug delivery system for intravenous delivery of topoisomerase inhibitors. J Control Release 91:167-172
6. Araki E, Ishikawa M, Iigo M, Koide T, Itabashi M, Hoshi A (1993) Relationship between development of diarrhea and the concentration of sn-38, an active metabolite of cpt-11, in the intestine and the blood plasma of athymic mice following intraperitoneal administration of cpt-11. Jpn J Cancer Res 84:697-702
7. Iyer L, King CD, Whitington PF, Green MD, Roy SK, Tephly TR, Coffman BL, Ratain MJ (1998) Genetic predisposition to the metabolism of irinotecan (cpt-11). Role of uridine diphosphate glucuronosyltransferase isoform 1a1 in the glucuronidation of its active metabolite (sn-38) in human liver microsomes. J Clin Invest 101:847-854
8. Jain RK (1998) The next frontier of molecular medicine: Delivery of therapeutics. Nature Medicine 4:3
9. Gutmann R, Leunig M, Feyh J, Goetz AE, Messmer K, Kastenbauer E, Jain RK (1992) Interstitial hypertension in head and neck tumors in patients: Correlation with tumor size. Cancer Res 52:1993-1995
10. Leunig M, Goetz AE, Dellian M, Zetterer G, Gamarra F, Jain RK, Messmer K (1992) Interstitial fluid pressure in solid tumors following hyperthermia: Possible correlation with therapeutic response. Cancer Res 52:487-490
11. Leunig M, Yuan F, Menger MD, Boucher Y, Goetz AE, Messmer K, Jain RK (1992) Angiogenesis, microvascular architecture, microhemodynamics, and interstitial fluid pressure during early growth of human adenocarcinoma ls174t in scid mice. Cancer Res 52:6553-6560
12. Dang W, Daviau T, Brem H (1996) Morphological characterization of polyanhydride biodegradable implant gliadela during in vitro and in vivo erosion using scanning electron microscopy. Pharm Res 13:9.
13. Dang W, Daviau T, Ylng T, Zhao Y, Nowotmk D, Clow CS, Tyler BM, Brern H (1996) Effects of gliadel ® wafer initial molecular weight on the erosion of wafer and release of bcnu. Journal of Controlled Release 42:9
14. Wu MP, Tamada JA, Brem H, Langer R (1994) In vivo versus in vitro degradation of controlled release polymers for intracranial surgical therapy. J Biomed Mater Res 28:8
15. Madrid Y, Langer LF, Brem H, Langer R (1991) New directions in the delivery of drug and other substances to the central nervous system. Adv Pharmacol 22:25
16. Brem H, Langer R (1996) Polymer-based drug delivery to the brain. Science & Medicine 3:9
17. Dang W, Daviau T, Brem H (1996) Morphological characterization of polyanhydride biodegradable implant gliadela during in vitro and in vivo erosion using scanning electron microscopy. Pharmaceutical Research 13:9
18. Westphal M, Hilt DC, Bortey E, Delavault P, Olivares R, Warnke PC, Whittle IR, Jaaskelainen J, Ram Z (2003) A phase 3 trial of local chemotherapy with biodegradable carmustine (bcnu) wafers (gliadel wafers) in patients with primary malignant glioma. Neuro Oncol 5:79-88
19. Brem H, Piantadosi S, Burger PC, Walker M, Selker R, Vick NA, Black K, Sisti M, Brem S, Mohr G, et al. (1995) Placebo-controlled trial of safety and efficacy of intraoperative controlled delivery by biodegradable polymers of chemotherapy for recurrent gliomas. The polymer-brain tumor treatment group. Lancet 345:1008-1012
20. Subach BR, Witham TF, Kondziolka D, Lunsford LD, Bozik M, Schiff D (1999) Morbidity and survival after 1,3-bis(2-chloroethyl)-1-nitrosourea wafer implantation for recurrent glioblastoma: A retrospective case-matched cohort series. Neurosurgery 45:17-22
21. Gallego JM, Barcia JA, Barcia-Marino C (2007) Fatal outcome related to carmustine implants in glioblastoma multiforme. Acta Neurochir (Wien) 149:261-265
22. Buahin KG, Judy KD, Hartke C, Domb AJ, Maniar M, Colvin OM, Brem H (1992) Controlled release of 4-hydroperoxycyclophosphamide from the fatty acid dimer-sebacic acid copolymer. Polymers for Advanced Technologies 3: 6
23. Judy KD, Olivi A, et al (1995) Effectiveness of controlled release of a cyclophosphamide derivative with polymers against rat gliomas. J Neurosurg 82:481-486
24. Weinberg BD, Blanco E, Gao J (2007) Polymer implants for intratumoral drug delivery and cancer therapy. J Pharm Sci 97: 1681 - 1702
25. Wang F, Blanco E, Ai H, Boothman DA, Gao J (2006) Modulating beta-lapachone release from polymer millirods through cyclodextrin complexation. J Pharm Sci 95:2309-2319
26. Qian F, Nasongkla N, Gao J (2002) Membrane-encased polymer millirods for sustained release of 5-fluorouracil. J Biomed Mater Res 61:203-211
27. Chae GS, Lee JS, Kim SH, Seo KS, Kim MS, Lee HB, Khang G (2005) Enhancement of the stability of bcnu using self-emulsifying drug delivery systems (sedds) and in vitro antitumor activity of self-emulsified bcnu-loaded plga wafer. Int J Pharm 14:8
28. Lee JS, An TK, Chae GS, Jeong JK, Cho SH, Lee HB, Khang G (2005) Evaluation of in vitro and in vivo antitumor activity of bcnu-loaded plga wafer against 9l gliosarcoma. Eur J Pharm Biopharm 59:169-175
29. Hornstein MD, Surrey ES, Weisberg GW, Casino LA (1998) Leuprolide acetate depot and hormonal add-back in endometriosis: A 12-month study. Lupron add-back study group. Obstet Gynecol 91:16-24
30. Wheeler JM, Knittle JD, Miller JD (1993) Depot leuprolide acetate versus danazol in the treatment of women with symptomatic endometriosis: A multicenter, double-blind randomized clinical trial. Ii. Assessment of safety. The lupron endometriosis study group. Am J Obstet Gynecol 169:26-33
31. Dlugi AM, Miller JD, Knittle J (1990) Lupron depot (leuprolide acetate for depot suspension) in the treatment of endometriosis: A randomized, placebo-controlled, double-blind study. Lupron study group. Fertil Steril 54 :419-427
32. Menei P, Capelle L, Guyotat J, Fuentes S, et al (2005) Local and sustained delivery of 5-fluorouracil from biodegradable microspheres for the radiosensitization of malignant glioma: A randomized phase ii trial. Neurosurgery 56:242-248
33. Menei P, Boisdron-Celle M, Croue A, Guy G, Benoit JP (1996) Effect of stereotactic implantation of biodegradable 5-fluorouracil-loaded microspheres in healthy and c6 glioma-bearing rats. Neurosurgery 39:117-123
34. Xie J, Wang CH (2006) Electrospun micro- and nanofibers for sustained delivery of paclitaxel to treat c6 glioma in vitro. Pharm Res 23: 1817-1826
35. Zhang H, Gao S (2007) Temozolomide/plga microparticles and antitumor activity against glioma c6 cancer cells in vitro. Int J Pharm 329: 122-128.
36. Xie J, Tan RS, Wang CH (2008) Biodegradable microparticles and fiber fabrics for sustained delivery of cisplatin to treat c6 glioma in vitro. J Biomed Mater Res A 85: 897-908.

CH_2-Symmetric/CH_2-Antisymmetric Stretch Ratio Sensor for Cell Analysis

S. van den Driesche[1], W. Witarski[2], and M.J. Vellekoop[1]

[1] Institute of Sensor and Actuator Systems, Vienna University of Technology, Vienna, Austria
[2] Institute of Virology, Slovak Academy of Sciences, Bratislava, Slovakia

Abstract— **Here we report on a novel infrared sensor system for measuring the CH_2-symmetric/CH_2-antisymmetric stretch ratio of cell samples. Based on IR absorbance spectra of healthy and malignant breast [1], blood [2] and brain [3] cells found in literature we hypothesized the possibility of disease stage cell discrimination by only comparing a few absorbance peaks in the lipid absorbance wavelength region between 3 and 4 µm. By comparing the lipid CH_2-symmetric and CH_2-antisymmetric stretch ratios (with baseline correction and normalization) of three defined epithelial kidney cell lines, healthy MDCK and carcinoma A-498 and Caki-1 with the developed sensor, significant stretch ratio differences have been found between healthy and tumor cell types (and even between the two tumor types). The developed LED-photodiode based infrared absorbance sensor could be used for quick pre-screening of biopsy samples which, compared to labeling and staining techniques, does not require highly trained personnel and is much cheaper than liquid nitrogen cooled FTIR spectroscopes.**

Keywords— **Infrared absorbance sensor, Label-Free, Cell analysis**

I. Introduction

In recent years cancer is becoming the number one disease of dead causes [4]. The development of diagnostic tools plays an important role in understanding the fundamentals of tumor development and in selecting the proper treatment. Normally the screening of biopsies for possible malignant cells is done by visual inspection of slides with labeled or stained cells. The labeling and staining techniques are expensive and the visual inspection is time consuming, performed only by highly trained personnel and also results in false positives and negatives (e.g. for cervical tumor screening the interobserver reproducibility is very low [5]).

Infrared spectroscopy, IR absorbance due to specific molecular vibrations, is an interesting diagnostic tool without the need of added labels with the ability to analyze cell components such as DNA, RNA, proteins and lipids. By comparing the IR absorbance spectra of healthy and malignant cells, published in literature (e.g. in breast [1], blood [2] and brain [3]), we hypothesized a new concept to distinguish cell types. It concerns a few-wavelength based cell type discrimination concept in the wavelength region between 3 and 4 µm. In this region specific lipid absorbance peaks [6] can be found (CH_2-and CH_3-symmetric and antisymmetric stretch).

To test the few-wavelength hypothesis we recorded and compared our own data set of healthy (MDCK) and carcinoma (A-498 and Caki-1) epithelial kidney cell lines with a Fourier transform infrared (FTIR) spectroscope. The IR absorbance ratio CH_2-symmetric/CH_2-antisymmetric stretch (3.51/3.42 µm) differs between the cell types. This ratio is increased in the carcinoma cell lines compared to the healthy MDCK cell line (Fig. 1). This confirms that it is possible to distinguish between healthy and carcinoma epithelial kidney cell lines by only measuring the IR absorbance at a few wavelengths. To compare the lipid CH_2 stretch ratio of different samples baseline correction and normalization is required. This is normally done with the software package supplied with the IR spectroscope. Instead of recording the whole IR spectra between 2 and 20 µm with an expensive FTIR spectroscope, comprising of an liquid nitrogen cooled detector, we developed a smaller, faster and cheaper sensor system based on LED light sources, narrow bandpass filters and a room temperature operable photodiode detector which could be used to discriminate between healthy and tumor cell types.

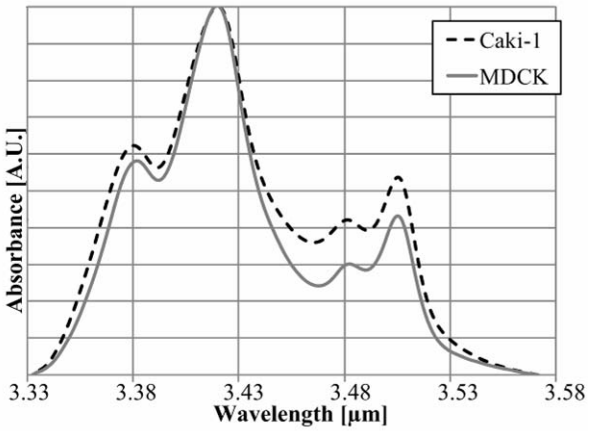


Fig. 1 Normalized and baseline corrected IR Absorbance spectra of epithelial kidney cells MDCK and Caki-1 recorded with a Bruker Equinox 55 spectrometer (240 scans per spectrum, 4 cm-1 resolution and 1 mm beam diameter). The absorbance peak at 3.51 µm is increased in the Caki-1 carcinoma cell line compared to the healthy MDCK cell line.

O. Dössel and W.C. Schlegel (Eds.): WC 2009, IFMBE Proceedings 25/VIII, pp. 15–18, 2009.
www.springerlink.com

II. MATERIALS AND METHODS

A. Sample preparation

The investigated epithelial kidney cell lines, healthy canine MDCK (ATCC CCL-34) and two human carcinoma A-498 (ATCC HTB-44) and Caki-1 (ATCC HTB-46), were cultivated under the same conditions in monolayer on IR transparent calcium-fluoride (CaF_2) slides at 37°C and 5% CO_2. The culture medium consisted of Dulbecco's Modified Eagle Medium (DMEM), 2 mM L-glutamine, 10% fetal calf serum (FCS) and antibiotics (100 units/ml penicillin, 100 µg/ml streptomycin and 0.25 µg/ml Amphotericin B) all obtained from Lonza. Before the IR absorbance measurements the sample slides were washed twice in phosphate buffered saline (PBS) to remove detached cells and medium components and dried for 3 hours in a sterile laminar flow cabinet to remove the water fraction.

B. Detection method

To determine the IR absorbance ratio between CH_2-symmetric and CH_2-antisymmetric stretch (3.51/3.42 µm) out of the total absorbance signal and to compare different samples baseline correction and normalization is required. For normalization and baseline correction the IR absorbance values at two additional wavelengths (at 3.33 and 3.57 µm) are recorded (Fig. 2). This way the non-functional absorbance values under the base line can be calculated and subtracted from the total absorbance signal resulting in the functional values. By dividing the functional absorbance value from the CH_2-symmetric with the antisymmetric stretch band the normalized ratio will be obtained which can be used for sample comparison.

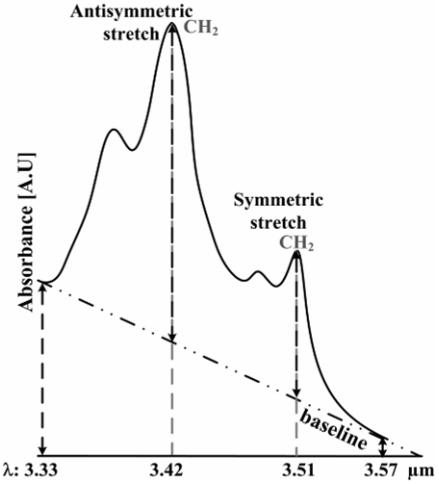


Fig. 2 Ratio determination. From each sample the absorbance at 3.33 and 3.57 µm is used for the base line (dashed black arrows) calculating the absorbance ratio 3.51/3.42 µm (dashed black grey arrows).

C. Sensor

The developed sensor (Fig. 3) measures the infrared absorbance values at four specific wavelengths (3.33, 3.42, 3.51 and 3.57 µm). The emitted light of two LED IR sources (center wavelength at 3.4 and 3.6 µm) are collimated by plano-convex lenses and directed at a filter wheel with narrow bandpass filters (NBP). This way, from each LED multiple wavelengths can be selected (in our case 3.33 and 3.42 µm from the 3.4 µm LED and 3.51 and 3.57 µm from the 3.6 µm LED). After passing the NBP the selected wavelengths are focused on a 1.5 mm aperture by a beam-splitter and another plano-convex lens.

To detect the transmitted light through a sample by a room temperature operable photodiode (PD) two additional plano-convex lenses are used.

By manually rotating the filter wheel the two other filters can be selected. To prevent the LEDs and PD shifting their center wavelength, they are all built into housings containing a thermocooler. The two LEDs are emitting 8 µs pulses alternately at a carrier frequency of 2 kHz (one LED at the up flank the other at the down flank of the carrier signal). The amplified photodiode signal (PD connected to a current to voltage amplifier) is only recorded when an LED is emitting. This is realized by connecting the carrier signals of both LED drivers and the amplified photodiode signal to a data acquisition board which is programmable with a Matlab script. This method is used to measure the IR absorbance values at two wavelengths simultaneously.

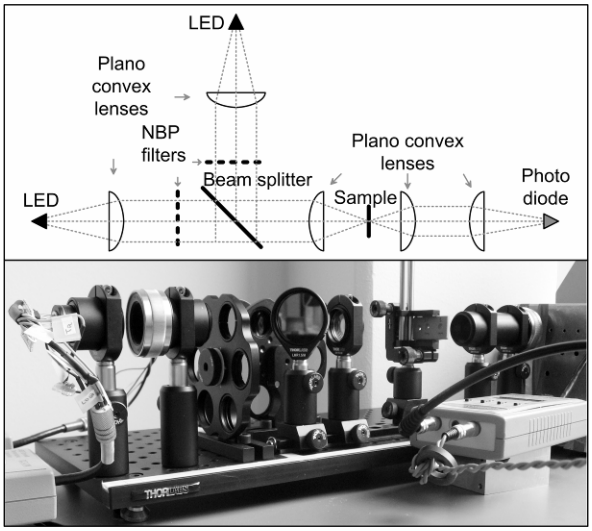


Fig. 3 Sensor concept. Two LEDs operated in alternating pulse mode both emitting in a broad range so that with changeable narrow band pass filters (NBP) two wavelengths can be used (3.33 and 3.42 µm for LED1 and 3.51 and 3.57 µm for LED2). A beam-splitter is used to focus the two beams on the same spot of the sample. The photodiode (PD) is used as detector and can be operated at room temperature.

D. Data analysis

The absorbed IR light by the sample is determined by comparing the transmittance difference of an empty calcium-fluoride slide and one containing the sample of interest. 8 µs LED pulses are sampled at a rate of about 10 sample points per pulse. To get the proper information out of a pulse the mean voltage of the four second highest values is used (Fig. 4). By averaging the values of multiple pulses more accurate absorbance values can be obtained.

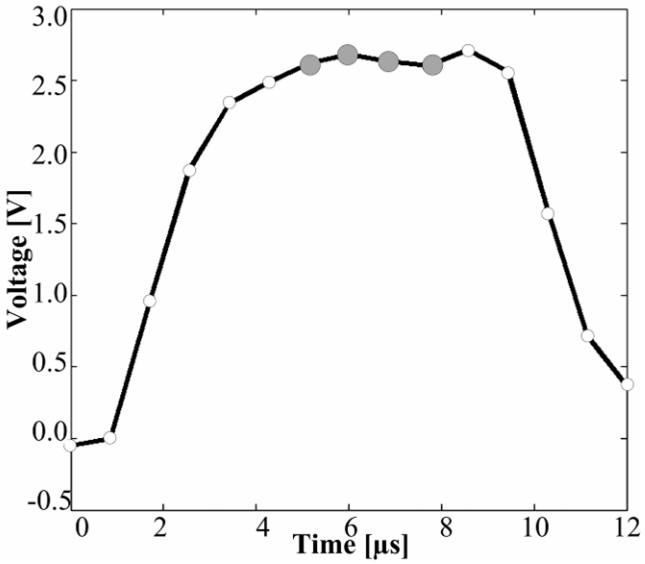


Fig. 4 Amplified photodiode signal of a single 8 µs LED pulse. By averaging the voltage values of the four second highest sample points (gray dots) one voltage value will be assigned to the pulse for further comparison.

III. RESULTS

The developed sensor system, measuring the infrared absorbance at four wavelengths to determine the lipid CH_2-symmetric / CH_2-antisymmetric stretch ratio, has been used to distinguish healthy from carcinoma epithelial kidney cell lines. The absorbance measurements were made after 3 hours of sample drying. Fig.4 shows the baseline corrected and normalized CH_2 stretch ratio of MDCK, A-498 and Caki-1. For every cell line the average value of four 1.5 mm diameter spots measured four times each were compared. Because the pulsed LEDs were operating at a frequency of 2 kHz it was easy to record multiple pulses to get more accurate data values. For these measurements 500 pulses per wavelength were recorded, resulting in a total of 8000 recorded pulses per wavelength per cell line.

As can be seen in Fig.5 there is a significant ratio difference between the healthy MDCK and carcinoma, A-498 and Caki-1, cell lines. Even between A-498 and Caki-1 a ratio difference of about 20% is detected.

Directly after the measurements the samples were stored in a closed polystyrene box at room temperature. Six days later the same samples were measured again for their CH_2 stretch ratios (the same way, four spots, measured four times). This resulted in comparable lipid CH_2 stretch ratios as measured earlier (0.49, 0.59 and 0.71 for MDCK, A-498 and Caki-1, respectively).

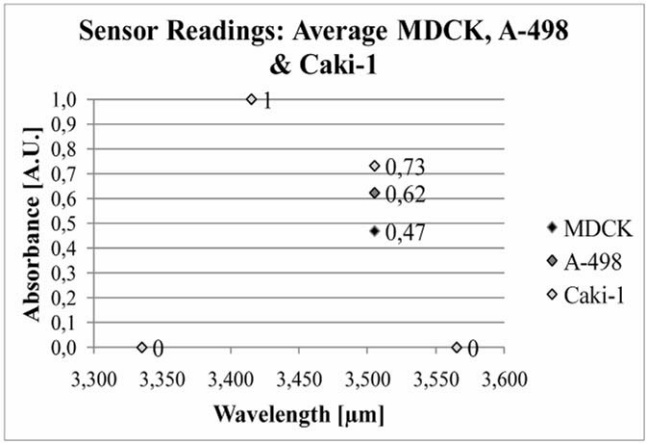


Fig. 5 CH_2-symmetric / CH_2-antisymmetric stretch ratio of three epithelial kidney cell lines MDCK (healthy) and two carcinoma A-498 and Caki-1. The absorbance values at wavelengths 3.33 and 3.57 µm are used as baseline points (set to zero). Next, the baseline corrected absorbance points at 3.42 and 3.51 µm are normalized so that different measurements can be compared. The stretch ratios of the carcinoma cell lines are higher compared to the healthy cell line (0.62 and 0.73 compared to 0.47).

IV. DISCUSSION

When cytology or histopathology techniques are used for cancer prevention programs the outcome of such tests depends on the judgment of the cytotechnologist and pathologist. A study of the interobserver reproducibility for cervical cancer [5] showed strong irreproducibility and false negativity.

Infrared spectroscopy has the potential to detect components such as DNA, RNA, proteins and lipids label-free but due to the requirement of a liquid nitrogen cooled detector and high price it not a potential device for easy prescreening purposes.

With the developed LED-photodiode based infrared absorbance sensor it is possible to determine the ratio between lipid CH_2-symmetric and antisymmetric stretch with baseline correction and normalization.

The compared samples used for the presented experiments were all epithelial kidney cell lines but not originated from the same species instead we compared healthy canine cells with two human carcinoma cell types. From the results it can be concluded that the developed sensor has the potential for detecting the lipid CH_2 stretch ratio which otherwise only could be detected with an infrared spectroscope. By comparing FTIR spectroscope recorded absorbance spectra of healthy and malignant blood, breast and brain cells found in literature differences in lipid CH_2 stretch ratios between healthy and malignant cell type can be derived. This indicates the potential of the developed sensor. Because of the relatively cheap design and the lack of necessary expensive chemicals the sensor could be interesting for fast prescreening of biopsy material (e.g. blood, breast and kidney).

V. Conclusions

A significant difference between CH_2-symmetric and CH_2-antisymmetric stretch ratios of healthy versus carcinoma (and even between two carcinoma) epithelial kidney cell lines have been detected with a novel infrared sensor system based on two LED light sources and a room temperature operable photodiode as detector.

The developed sensor could be used for quick prescreening of biopsy samples which compared to labeling and staining doesn't require highly trained personnel and is much cheaper than liquid nitrogen cooled FTIR spectroscopes.

Acknowledgment

This project is a part of an EU Marie Curie Research Training Network (MRTN) "On-Chip Cell Handling and Analysis" CellCheck. Project no. MRTN-CT-2006-035854. We thank Dr. K. Futschik, Institute of Electrical Measurements and Circuit Design, TU Vienna for support and use of the biology lab to prepare the samples.

References

1. Fabian H, Thi NA, Eiden M, et al. (2006) Diagnosing benign and malignant lesions in breast tissue sections by using IR-microspectroscopy. Biochim Biophys Acta 1758(7):874-882
2. Maziak DE, Do MT, Shamji FM, et al. (2007) Fourier-transform infrared spectroscopic study of characteristic molecular structure in cancer cells of esophagus: an exploratory study. Cancer Detect Prev 31(3):244-253
3. Krafft C, Thümmler K, Sobottka SB, et al. (2006) Classification of malignant gliomas by infrared spectroscopy and linear discriminant analysis. Biopolymers 82(4):301-305
4. CDC/National Center for Health Statistics at http://www.cdc.gov/nchs
5. Stoler MH, Schiffman M, (2001) Interobserver reproducibility of cervical cytologic and histologic interpretations: realistic estimates from the ASCUS-LSIL Triage Study. JAMA 285(11):1500-1505
6. Tamm LK, Tatulian SA, (1997) Infrared spectroscopy of proteins and peptides in lipid bilayers. Q Rev Biophys 30(4):365-429

Author: Sander van den Driesche
Institute: Institute of Sensor and Actuator Systems, Vienna University of Technology
Street: Gusshausstrasse 27-29/366
City: Vienna
Country: Austria
Email: sander.driesche@tuwien.ac.at

Optimization of Ligand Surface Concentration for Biosensor based on Imaging Ellipsometry

Yu Niu[1, 2], Gang Jin[1,*]

[1] Institution of mechanics, Chinese academy of Sciences, Beijing, China.
[2] Graduate University of Chinese academy of Sciences, Beijing, China.
[*]Corresponding author: Tel./Fax.: +86-10-82544138, E-mail: gajin@imech.ac.cn

Abstract— **the biosensor based on imaging ellipsometry for bio-molecular interactions has been developed for more than ten years and used to several biological applications successfully, such as detection of five markers of Hepatitis B, tumor markers and virus infection. Ligand surface concentration which might be related with its spatial configuration and bioactivity is an important factor to affect the biosensor sensitivity and dynamic range. In this investigation, IgG and its corresponding antibody are selected as a couple of model molecules for the optimization of ligand surface concentration. The optimization result of ligand surface concentration is achieved by analyzing the surface concentration increase of antigen-antibody complex on sensing surface with various ligand surface concentrations.**

Keywords—**biosensor, protein micro-array, Imaging ellipsometry, ligands surface concentration.**

I. Introduction

The concept of biosensor based on imaging ellipsometry for visualization of bio-molecular interactions was proposed in 1995 [1]. Imaging ellipsometry which has the advantages of ellipsometry and microscopy simultaneously is used to measure the amount of protein in an adsorbed layer accurately without any labeling [2]. This allows the application in a broad range of various biological systems, especially for the detection of interactions between protein molecules [3, 4]. So far, several bio-molecules, like five markers of Hepatitis B, Tumor markers, and Virus, have been tested successfully with the biosensor [5-7].

Ligand surface concentration is intimately associated with the amount of complex formation, and consequently, it has been proved that a remarkable factor can influence the biosensor sensitivity and dynamic range. In common sense, the amount of captured target bio-molecule might be proportional to the surface concentration of ligand, so the ligand surface concentration is usually used at its saturation level. However, the phenomenon is observed through the interaction between Bovine serum albumin (BSA) and its corresponding antibody that the surface concentration of BSA/anti-BSA binding complex rises firstly and then declines, as the surface concentration of BSA simply increases [8]. It is suggested that ligand surface concentration at its saturation may not be the optimization result.

In this investigation, IgG and its corresponding antibody, as a couple of model molecule are studied to optimize the ligand surface concentration.

II. Materials and methods

A. Principles

The label-free biosensor which functions as a kind of immunoassays is composed of two parts, micro-fluidic reactor system and Imaging ellipsometry reader.

A 48 channel integrated micro-fluidic reactor system which is served as micro-reactor system can be used to fabricate protein micro-array for high throughput detection [5]. By this reactor, ligands could be delivered individually to each unit and covalently immobilized on surface simultaneously to form ligands with a fixed pattern. After that, these ligands with good bioactivity can be reacted with different analytes under dynamic condition. During the whole process, the protein micro-array is stored in the packaging system which is full of buffer so that proteins are not exposed to denaturing conditions.

With a visualization of imaging ellipsometry, which has a high spatial resolution in the order of sub-nanometer in vertical and micron in lateral, the changes of surface concentration which is resulted from the interaction between ligand and analyte can be determined sensitively and accurately. The results of imaging ellipsometry shown in gray scale were processed to be the surface concentration of the adsorption layer.

B. Reagents and solutions

Chemicals used for PBS buffer (pH=7.4) preparation were all of analytical grade or better. Aminopropyltriethoxysilane (APTES) were purchased from Acros Organics. Succinic anhydride was purchased from Beijing hengye zhongyuan chemical Co., Ltd. 1-(3-Dimethylaminopropyl)-

O. Dössel and W.C. Schlegel (Eds.): WC 2009, IFMBE Proceedings 25/VIII, pp. 19–21, 2009.
www.springerlink.com

3-ethylcarbodiimide hydrochloride (EDC) and N- hydroxydroxysuccinimide (NHS) were purchased from Sigma. Rat-IgG and Anti-Rat-IgG antibody were purchased form Sigma.

C. Substrates

Silicon wafer was used as solid surface for imaging ellipsometry biosensor. Due to the need of 48 throughputs, the silicon slides were cut into 25×13 mm2 rectangle pieces. Then, aiming at washing out the organic and inorganic pollution, silicon wafers were cleaned with a mixture of 30% H2O2 and concentrated H2SO4 (1:3 v/v) for 30 minutes [9]. After thoroughly rinsing with deionized water and pure ethanol, these silicon wafers were treated with an ethanol solution of APTES (5% APTES and 95% pure ethanol) and the incubation last 2 hours at room temperature [10]. Following by intensively rinsing with pure ethanol, the silicon wafers silanized with APTES were reacted with oversaturated succinic anhydride in ethanol for at least 3 hours. After the final rinsing with pure ethanol, the silicon wafers were stored in pure ethanol for ligands immobilization.

D. IgG adsorption and IgG/Anti-IgG interaction

Surface concentration of IgG adsorption is intimately associated with IgG solution concentration, so several surface concentration of IgG can be achieved by controlling the solution concentration. In order to form significant variation among surface concentration of IgG adsorption, IgG solution is diluted with PBS buffer to 0.004mg/mL, 0.016mg/mL, 0.064mg/mL, 0.25mg/mL, 1mg/ml and 4mg/mL, respectively. IgG diluted solution at each concentration is used in four units in which two for analyte test and others as negative control.

The whole processes are listed as follows: Firstly, the modified surface is incubated with a mixture solution of EDC and NHS at the concentration of 0.2mol/L and 0.05mol/L for 5 minutes. In order to lessen the impact caused by non-specific adsorption, a step of blocking by Gelatin follows that IgG is immobilized to form a sensing surface with different surface concentration. The anti-IgG antibody solutions at 0.01mg/mL and 0.2mg/mL are delivered and react with IgG ligands on sensing areas.

III. Results

IgG at different surface concentration is assembled on the substrate, and then is exposed to Anti-IgG solution at the concentration of 0.01mg/mL and 0.2mg/mL. With a visualization of imaging ellipsometry, the surface concentration of the adsorption layer can be quantitatively shown in gray scale. After a logarithmic transformation of IgG solution concentration, the surface concentration trends of IgG adsorption and complex are present in Fig.1.

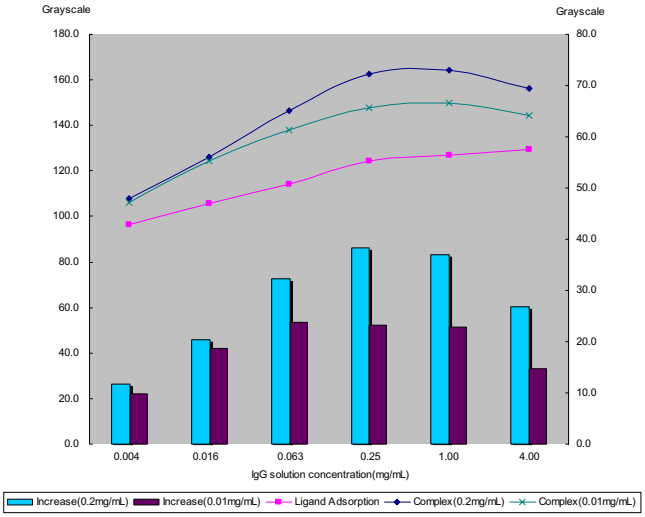


Fig.1 the results of IgG adsorption and IgG/anti-IgG binding complex

The surface concentration of IgG adsorption increases with the rise of its solution concentration but the increasing rate decreases when IgG solution concentration is beyond 0.25mg/mL. The trend suggests that the amount IgG adsorption approaches to saturation when its solution concentration is beyond 0.25mg/mL.

Unlike the trend of IgG adsorption, when solution concentration of Anti-IgG antibody is select at 0.01mg/mL, the surface concentration of IgG/Anti-IgG complex firstly goes up dramatically and then declines slightly, while the maximum is at the IgG solution concentration of 1.0mg/mL. However, the increase which can reflect the amount of binding antibody displays different trend. Firstly, the increase rises as solution concentration grows from 0.004mg/mL to 0.016mg/mL. Then, it keeps steady when solution concentration increases from 0.064mg/mL to 1.0mg/mL. Finally, it decreases sharply at solution concentration of 4.0mg/mL.The same trend repeats when anti-IgG antibody is selected at 0.2mg/mL, but the increase begins to remain steady at solution concentration of 0.25mg/mL.

In order to improve sensitivity and dynamic range of the biosensor, the surface concentration of ligand should be optimized at the point where the IgG/Anti-IgG binding complex reaching to the maximum. Therefore, when anti-IgG solution concentration is at 0.01 mg/mL and 0.2 mg/mL, the optimization range of IgG solution concentration should be from 0.064mg/mL to 1.0mg/mL and from 0.25mg/mL to 1.0mg/mL, respectively. It is obviously indicated that optimization surface concentration of ligand may change ac-

cording to analyte at different concentration. Furthermore, the surface concentration optimized by analyte at higher concentration is involved in the range which is achieved by lower concentration and can be applied under the condition of lower analyte concentration test.

In the condition that IgG surface concentration is at 4.0mg/mL, a sharp drop of the amount of binding antibody comes to both concentrations of Anti-IgG antibody. It can be foreseen that ligand surface concentration approaching to saturation may change its spatial configuration, cause steric exclusion and decrease its bio-activity. Meanwhile, rinsing process may affect more when ligand surface concentration is approaching saturation. Therefore, ligand surface concentration should be optimized below saturation adsorption concentration.

IV. Conclusions

The optimizing ligand surface concentration should be lower than the saturation adsorption concentration; meanwhile, comparing to analyte at lower concentration, the result optimized by higher analyte concentration owns a wider application scope.

Acknowledgment

The Chinese Academy of Sciences KJCX2-YW-M03 and KJCX2-YW-M04, National Basic Research Program of China 2009CB320302 and “863” program is acknowledged for financial supports.

References

1. Jin G, Tengvall P, Lundstrom I, et al. (1995) A biosensor concept based on imaging ellipsometry for visualization of biomolecular interactions. Anal. Biochem. 232:69-72.
2. Jin G, Jansson R, Arwin H (1996) Imaging ellipsometry revisited: Developments for visualization of thin transparent layers on silicon substrates. Rev. Sci. Instrum. 67:2930-2936.
3. Jin G, Wang Z H (2002) Micro-systems for optical protein-chip. International Journal of Nonlinear Sciences and Numerical Simulation 3:191-194.
4. Wang Z H, Jin G (2003) A label-free multisensing immunosensor based on imaging ellipsometry. Anal. Chem. 75:6119-6123.
5. Wang Z H, Meng Y H, Ying P Q et al. (2006) A label-free protein microfluidic array for parallel immunoassays. Electrophoresis 27:4078-4085.
6. Qi C, Duan J Z, Wang Z H et al. (2006) Investigation of interaction between two neutralizing monoclonal antibodies and sars virus using biosensor based on imaging ellipsometry. Biomed. Microdevices 8:247-253.
7. Jin G (2008) Development of biosensor based on imaging ellipsometry. Physica Status Solidi A: Applications and Materials Science 205:810-816.
8. Ying P Q, Jin G, Tao Z L (2004) Competitive adsorption of collagen and bovine serum albumin - effect of the surface wettability. Colloids and Surfaces B: Biointerfaces 33:259-263.
9. Wang Z H, Jin G (2003) Feasibility of protein A for the oriented immobilization of immunoglobulin on silicon surface for a biosensor with imaging ellipsometry. J. Biochem. Biophys. Methods 57:203-211.
10. Wang Z H, Jin G (2004) Covalent immobilization of proteins for the biosensor based on imaging ellipsometry. J. Immunol. Methods 285:237-243.

Are Defibrillation Thresholds Ruled by a Hyperbolic Strength Duration Relationship?

Werner Irnich

Justus-Liebig-University, University Hospital, Giessen Germany

Abstract— **Our defibrillation theory claims that mean voltage is a hyperbolic function of pulse duration if voltages below the rheobase are avoided. To verify this theory, two animal experiments were carried out. The 'rheobase condition' demands that pulses are truncated when the trailing edge voltage reaches the rheobase. This creates a relationship between the time constant, pulse duration, and chronaxie. The integral over voltage pulse is a linear function of pulse duration from which the hyperbolic threshold function between mean voltage and pulse duration is derived. In this study, we determined defibrillation thresholds in swine. Parameters measured were: leading and trailing edge voltages and currents, pulse durations, and failure or success of shock. A step-up test was used; the lowest successful shock was defined as the 'threshold'. Waveforms truncated according to theory yielded lower stored energy than either ½ optimal duration or fixed 65% tilt pulses. Plots of voltage integral vs. pulse duration produced a strong linear correlation. Mean defibrillation voltage vs. pulse duration formed a hyperbola. Ranking of stored energy showed that lower capacitances reduce energy to the detriment of increased peak voltages. These are the first experiments in which defibrillation pulses were adjusted according to theory. Truncation above or below the rheobase increased stored energy. The experimental results are consistent with theory. The algorithm for optimal truncation should be incorporated into ICD. If the energy required is lower at smaller output capacitances, a compromise between clinical and technical aspects can be attained. The current concept of 'constant tilt' in ICD should be abandoned in favour of 'optimal truncation'. Additional studies are needed to determine the applicability of this theory to humans.**

Keywords— **Defibrillation threshold, hyperbolic strength duration relationship, chronaxie, rheobase, rheobase condition**

I. Introduction

Defibrillation with square wave pulses has a hyperbolic strength duration relationship [1, 2]. Does such a hyperbolic relationship also exist for the exponentially decaying pulses that are commonly used in ICD today? In several papers we have hypothesized that exponentially decaying pulses obey a hyperbolic strength duration relationship in analogy to electrical stimulation [3, 4, 5]. Our theory can be characterized by formulating the hypothesis that the timely averaged voltage of the defibrillation pulse is a hyperbolic function of the effective pulse duration and that the pulse duration is effective as long as the voltage is not below the rheobase level ('rheobase condition'). Truncation of the pulse at the rheobase is also the optimal state of defibrillation as a voltage below the rheobase may be 'refibrillating' requiring higher energies for defibrillation. A voltage pulse ending at voltages higher than the rheobase is not desirable as it leaves useful energy on the capacitors and, thus, is not optimal. As long as the voltage is above the rheobase, the shape of the voltage pulse plays no role with regard to the threshold.

To verify this theory, two animal experiments were carried out. The aim was to demonstrate that the results of animal experiments are consistent with our defibrillation theory.

II. Theoretical Background

The 'rheobase condition' demands that a pulse is truncated if the trailing edge voltage reaches the rheobase (**RB**). This condition is the foundation on which a relationship between the time constant **RC** and the pulse duration **PD** with the chronaxie (**CX**) as a parameter can be determined mathematically for exponentially decaying pulses. The integral over a voltage pulse at threshold level **IntU** is, according to the theory outlined above, a linear function of the pulse duration **PD** (Eq. 1):

$$\mathbf{IntU} = \int^{\mathbf{PD}} \mathbf{U(t)dt} = \mathbf{U_{RB}} * \mathbf{t_{CX}} * (\mathbf{1} + \mathbf{PD}/\mathbf{t_{CX}}) \qquad (1)$$

where pulse duration **PD** ≤ optimal truncated.

If this linear function **IntU** is divided by the pulse duration **PD**, a hyperbolic relationship with the mean voltage $\bar{\mathbf{U}}$ is formed (Eq. 2):

$$\bar{\mathbf{U}} = \mathbf{1/PD} * \int^{\mathbf{PD}} \mathbf{U(t)dt} = \mathbf{U_{RB}} * (\mathbf{1} + \mathbf{t_{CX}/PD}) \quad (2)$$

An integral over a function divided by its duration is generally defined as the 'mean value'. Equation 2 claims that a hyperbolic threshold relationship only exists between mean voltage $\bar{\mathbf{U}}$ and pulse duration **PD**. However, if the mean value of the voltage $\bar{\mathbf{U}}$ of an exponential pulse is a hyperbolic function of the pulse duration **PD**, the relationship between leading edge voltage and pulse duration cannot be hyperbolic [5].

To determine optimal truncation, we have previously developed an algorithm with which a relationship between time constants and optimal pulse durations (or tilts), with the chronaxie as a parameter, can be calculated [4, 6, 8] (Eq. 3 and 4):

$$\mathbf{PD/ms} = \mathbf{2.3ms} * (\mathbf{RC/2ms})^{\mathbf{0.56}}, \qquad (3)$$

and for the trailing to leading edge voltage ratio $\mathbf{U_{trail}/U_{lead}}$:

O. Dössel and W.C. Schlegel (Eds.): WC 2009, IFMBE Proceedings 25/VIII, pp. 22–25, 2009.
www.springerlink.com

$$(U_{trail}/U_{lead}) = EXP(1.15 * (RC/2ms)^{-0.44}) \quad (4)$$

As a by-product of our theory it follows that the stored energy has its minimum at the chronaxie and then increases with increasing pulse duration [4].

III. Materials and Methods

Animal experiment # 1: 12 swine weighing between 19.5 and 28.2kg, mean value 24.7kg were used. A Ventritex generator HVS-02, output: 50V to 900V in steps of 10V, pulse duration in steps of 0.1ms between 1ms and 20ms, and with output capacitance of 150µF was used. Thresholds with three different biphasic waveforms were compared: 1) optimally truncated pulse duration, 2) half optimal pulse duration, and 3) 65% tilt of the first phase. The duration of the second phase was equal to that of the first phase in all waveforms. The study was carried out at the University of Alabama at Birmingham, Cardiac Rhythm Management Laboratory, Birmingham, AL, USA.

Animal experiment # 2: 10 swine weighing between 34 and 40kg, mean value 37.7kg were used. A high voltage generator with different output capacitances of nominal values of: 75µF, 110µF, 195µF, and 280µF generated exponential defibrillation waveforms with different time constants:

- Biphasic optimized truncated pulses.
- Biphasic pulses with half the optimized pulse durations.
- Polarity of the shocks: positive and negative output pulses of the above mentioned waveforms were applied.

All waveforms had equal phase 1 and 2 duration throughout the experiment.

To expedite the testing of 16 waveforms within one animal, testing started with the highest capacitance (lowest voltage) and progressed in order to successively lower capacitances at higher voltages. This study was carried out at Boston Scientific CRM, St. Paul, MN, USA.

A step-up test procedure with 10% voltage steps was used in both experiments as follows:

Induce VF and wait 10s. Start with shock intensity below the expected threshold. If the first shock fails, administer a second shock of the same intensity within 10s. If the second shock also fails, deliver a shock of increased intensity that was not included in the threshold determination. If the very first shock of a defibrillation threshold sequence succeeds, reduce intensity by two steps and repeat the sequence. The threshold was defined as the lowest successful trial whether with the first or second shock (Birmingham protocol [9]).

Measured values: The following six parameters were measured using battery operated oscilloscopes (Tektronix THS720A and TPS2014): 1) leading and 2) trailing edge voltage, 3) leading and 4) trailing edge current, 5) pulse duration, 6) failure (0) or success (1 for first, 2 for second trial) of defibrillation.

Ten parameters were calculated from the measured values: 1) resistance, 2) time constant, 3) ratio of measured trailing and leading edge voltage, 4) capacitance, 5) integral over voltage pulse, 6) mean voltage, 7) stored energy, 8) delivered energy, 9) ratio U_{trail}/U_{lead} for optimal truncation from time constant to adjust the succeeding pulse, 10) ratio U_{trail}/U_{lead} from time constant to adjust the succeeding pulse with half the optimized pulse duration. These parameters served for further evaluation of the measurements.

IV. Statistical Analysis

It was assumed that the distribution of thresholds was lognormal. The data were transformed by taking their logarithm for statistical analysis. A T-test was used to prove the assumption that there was no difference between the distributions of the observed data under different conditions (null hypothesis, H_0). As the analysis was done in an exploratory manner, the computed p-values are only a measure of the reproducibility of the observed results under the assumption of no difference. All reported p-values are based on two-sided tests. SPSS software, version 11.0 (SPSS Inc., Chicago, IL, USA) was used for statistical analysis.

V. Results and Discussion

A total of 196 thresholds were determined in the two animal experiments. Comparison of 80 thresholds of all waveforms with both polarities (160 measurements, 80 ratios) revealed that, under the chosen study design (anode and cathode consisting of the same material in experiment # 2), the ratio of negative to positive thresholds was 0.9914 and both were congruent within 0.89%. Thus, the threshold measurements of both polarities were combined to give one mean value for each capacitance.

Fig. 1 shows that the waveform truncated according to theory yielded the lowest stored energy ('Optibip 1').

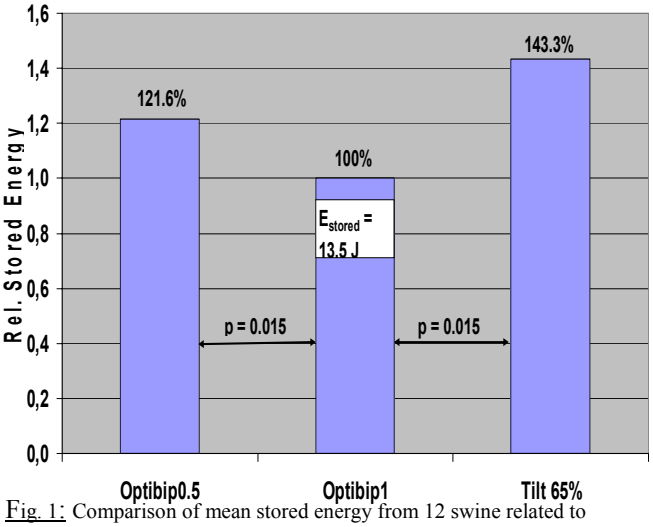


Fig. 1: Comparison of mean stored energy from 12 swine related to waveform: 'Optibi 1' is a biphasic waveform with optimal truncation and 'Optibi 0.5' is a biphasic waveform with half the optimal duration. The sored energy of waveform '65% Tilt' is 143.3% that of Optibip 1 and 121.6% that of Optibip 0.5. The differences are significant.

The voltage integral thresholds for all swine in experiment # 2 as a function of averaged pulse durations are summarized in Fig. 2. The linear approximation has a

correlation coefficient of 0.987 and is consistent with theory. Decreasing the pulse duration significantly reduced the voltage integral threshold as predicted by Equation (1). The slope of the straight line in Fig. 2 is equal to the rheobase. . A rheobase of 156.7V and a chronaxie of 2.44ms can be deduced from the linear approximation.

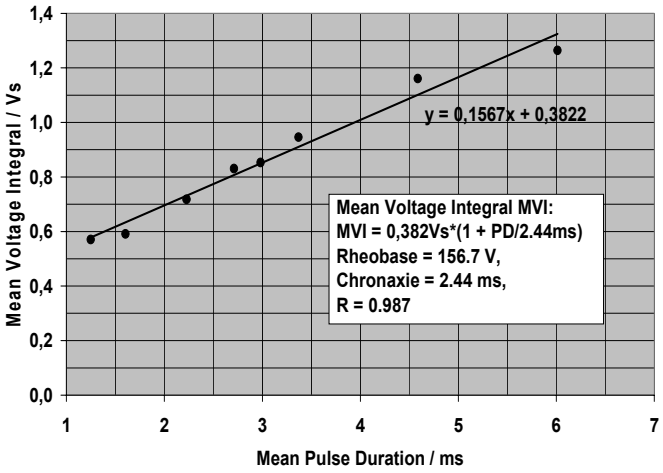


Fig. 2: Mean voltage integral thresholds versus mean pulse durations in 10 swine: only pulses with optimized or half the optimized pulse durations were considered. Each point summarizes 20 threshold measurements.

During electrostimulation, a prolongation of the pulse duration beyond optimal pulse duration would leave the leading edge voltage constant and thereby the stored energy. An effect like 'refibrillation' does not exist in electrostimulation. Therefore, the difference in energy between 65% tilt and optimized truncation in Fig. 1 may be attributed to the effect of 'refibrillation'. The voltage integral thresholds with halved pulse duration were all significantly lower than optimized pulses.

Dividing the voltage integral thresholds of Fig. 2 by the corresponding pulse duration, gives a mean voltage threshold that according to theory should form a hyperbola. Fig. 3 demonstrates that the threshold points are very close to the theoretical hyperbola that has been known to exist for electrostimulation since the study by Lapicque just 100 years ago [7]. Between the lowest voltage (210V at 6ms) and the highest voltage (417V at 1.3ms), there is a 99% increase in voltage with decrease in pulse duration to 22%.

The leading edge voltages demonstrate an interesting aspect. Reducing pulse duration to half the optimal increases the leading edge voltage by only 10% for 75µF, 110µF, and 195µF output capacitors, but by 20% for 280µF. Increase in leading edge voltage with reduction of capacitance is not as dramatic as often argued. Thus there is an increase of only 75% between the 6ms pulse of 280µF and the 1.3ms pulse of 75µF.

Comparison of the stored energy thresholds demonstrates that, in accordance with theory, the half optimized pulse durations require higher stored energies than the corresponding optimal waveforms. The opposite is true for the delivered energy. If the aim is to achieve the lowest delivered energy, pulse duration should be reduced to a minimum at the highest voltages. Wastage of stored energy would be the consequence. Prolongation of the pulse duration beyond optimal truncation increases the delivered

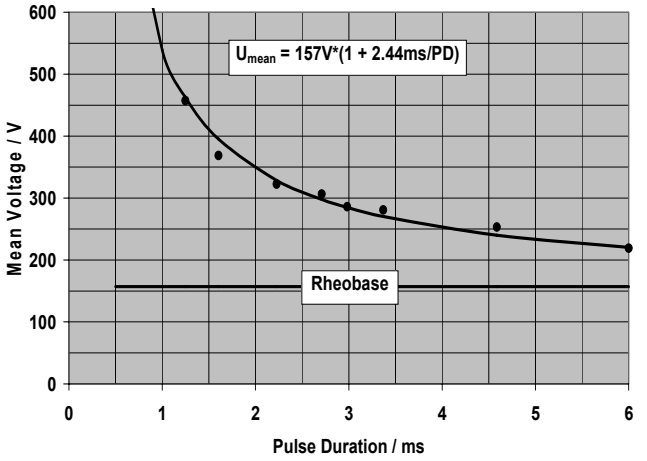


Fig. 3: Mean voltage as a function of mean pulse duration: The values of Fig. 2 divided by the pulse duration represent the mean voltages. The points derived from 20 threshold measurements per point are close to a theoretical hyperbola with a rheobase of 157V and a chronaxie of 2.44ms.

energy without increasing efficacy, to the detriment of the stored energy. Therefore, as a measure of defibrillation threshold, delivered energy does not reflect efficient defibrillation physiology.

Behind the currently used concept of 'constant tilt' is the hypothesis that the delivered energy should be constant under all circumstances. The usefulness of this hypothesis has never been proven experimentally though this would not be difficult to do.

Our results clearly demonstrate that a decreasing time constant decreases the delivered energy threshold. The optimal tilts of the output capacitors that we used in order to reach optimal stored energy varied between 42.2% and 63.7%. Thus, the current practice of 'constant tilt output' contradicts not only theory but also experimental results.

We tried to fit the linear voltage integral threshold curve of Fig. 2 with the corresponding exponential 'Blair equation' [10]. The result is shown in Fig. 4. One can argue that the Blair curve only minimally deviates from measured points. However, as the 'membrane time constant' and the lowest possible threshold (corresponding to the rheobase) are not linked, as is the case in the Lapicque equation, equivalence to the 'Rheobase condition' cannot be formulated with the 'Blair model'. Moreover, it is questionable whether the Blair equations needs peak voltages or mean voltages to formulate the strength duration relationship. The Blair equation, therefore, is not suitable for calculating refibrillation free defibrillation.

This is the first time in animal experiments that the pulse durations (or trailing edge voltages) have been adjusted to the time constant according to the above defibrillation

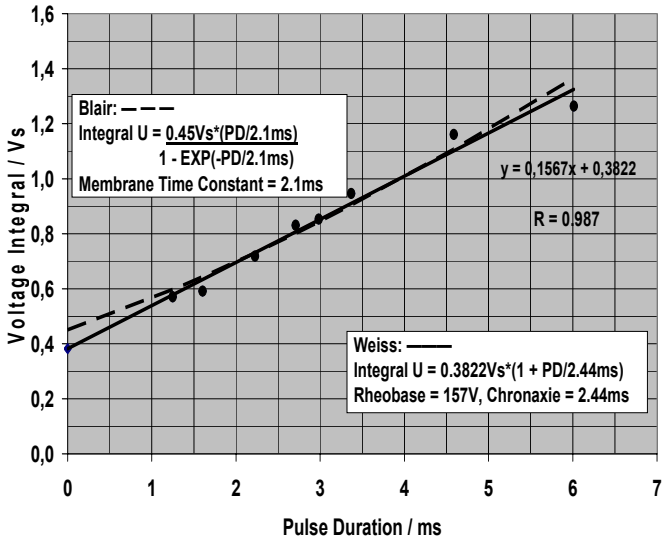


Fig. 4: Approximation of the voltage integral thresholds by the Blair-equation: Blair deviates from a straight line for short and long pulse durations indicating that the lowest possible threshold is higher than the rheobase and that the membrane time constant is shorter than the chronaxie.

theory so that the trailing edge voltage did not fall below rheobase and it is also the first time that defibrillation thresholds have been measured with durations shorter than the chronaxie. For durations below 2ms the leading edge voltages do not increase exorbitantly.

To summarize: the 'rheobase condition' and 'strength' expressed as mean voltage are the deciding differences in determining the strength duration relationship as compared to other authors. This explains why a hyperbolic relationship with exponentially decaying pulses has not previously been found.

VI. Conclusions

To answer our original question (see title): Yes, the results confirm the theory that average defibrillation voltage thresholds form a hyperbolic 'strength duration relationship' with pulse duration under the condition that the trailing edge of the defibrillation voltage does not fall below the rheobase voltage.

An algorithm {Eq. (3) and (4)} that was developed for calculating optimal truncation on a beat-to-beat basis, proved to be very helpful. Incorporation of this algorithm into ICDs is recommended.

As defibrillation thresholds are dependent on waveforms, the stored energy decreases with decreasing output capacitance. Reduction of the output capacitance reduces the energy required and could render the device smaller.

The current usage of the 'constant tilt concept' in ICD should be abandoned in favour of the 'optimal truncation concept'. Additional studies are needed to determine the applicability of this theory to humans.

Acknowledgement

We cordially thank Cheryl R. Killingsworth, DVM, Ph.D. and Gregory. P. Walcott, MD. from the Cardiac Rhythm Management Laboratory, Birmingham, AL, U.S.A. and Stephen Hahn PhD. and Allan Shuros from Boston Scientic, CRM, St. Paul, MN, U.S.A. for their valuable scientific support and assistance. We are also indebted to Rolf-Hasso Boedecker, PhD. from the Department of Medical Statistics, Justus-Liebig-University, Giessen, Germany for the statistical analysis of the data.

References

1. Koning G, Schneider H, Hoelen AAJ (1975): Amplitude duration relation for direct ventricular defibrillation with rectangular current pulses. Med Biol Eng Comput 13:388–395
2. Tacker WA, Geddes LA (1980) Electrical defibrillation, Chapter 1, Boca Raton, FL, CRC Press
3. Irnich W (1990) The fundamental law of electro-stimulation and its application to defibrillation PACE 13: 1433-1447
4. Irnich W (1995) Optimal truncation of defibrillation pulses. PACE 18: 673-688
5. Irnich W (2008) The hyperbolic strength duration relationship of defibrillation thresholds. IEEE Trans BME 55: 2057 – 2063
6. Irnich W (2003) How to program pulse duration or tilt in implantable cardioverter defibrillators. PACE 26: 453 – 456
7. Lapicque L (1909) Définition experimental de l'exabilité. Soc Biol 77: 280-283
8. Irnich W (2007) Viewpoint: Tilt or pulse duration - Which is the decisive parameter in defibrillation? PACE 30: 1181–1182
9. Irnich W, Walcott GP, Ideker RE (2007) The Birmingham Protocol for investigating defibrillation thresholds. Ital J Arrythmol Card Stim; 10 Suppl 2: 57, Abstract
10. Blair HA (1932) On the intensity-time relations for stimulation by electric currents. I. J Gen Physiol, 15, 709-729

Author: Prof. Dr.-Ing. Werner Irnich
Institute: Justus-Liebig-University, University Hospital
Street: Friedrichstr. 18
City: 35392 Giessen
Country: Germany
Email: werner@irni.ch

Development of a Patient Controlled, Telemetric Bolus System for an Implantable Infusion Pump

A. Knopp[1], K.-H. Otto[2], S. Klein[1], and B. Nestler[1]

[1] Center of Biomedical Engineering, University of Applied Sciences Luebeck, Luebeck, Germany
[2] tricumed Medizintechnik GmbH, Kiel, Germany

Abstract— **For patients suffering from chronic pain implantable infusion pumps are highly advantageous as they ease the pain by delivering a drug continuously at a constant rate (basal rate). Furthermore lower drug doses are needed, which reduces the side effects and the costs. However, if the pain level rises temporarily and an additional amount of drug (bolus) is needed, the patient has to attend a physician.**

In order to improve the pain therapy a bolus system, which can be controlled by the patient, should be integrated into the infusion pump. The bolus should be triggered telemetrically by the patient via an external control unit to reduce the infection risk. In this work a first concept of such a system has been developed and tested. To lower costs, power consumption and failure risk only passive electrical components, which drive a miniature valve have been used. First tests showed the telemetry system can successfully drive the valve against a required pressure of 2.4 bars and over a transmission distance of 5 cm (distance between sending and receiving coil).

Keywords— **Telemetry, transcutaneous power transmission, implantable infusion pump, bolus, magnetic induction.**

I. Introduction

Referring to a study 8.1 % of the population in the USA suffers from continuous or frequent pain [1]. This chronic pain limits the physical, emotional and social live and thus, reduces the quality of life. Furthermore it is cost intensive as a high number of these people need a therapy or cannot work anymore.

Today, there are several therapies. But general treatments like orally administered or injected pharmaceuticals are expensive and have several side effects because a high volume of drug is necessary to enable a pain relief. By contrast, an implantable infusion pump enables the injection of the drug directly at the spot of pain. Consequently, less time and drug is needed to achieve a pain relief. However, not every patient suffering from chronic pain is suitable for a pain therapy with an implantable infusion pump.

The infusion pump used is pressure controlled consisting of a drug reservoir and a propellant chamber separated by a titanium bellow as shown in Fig. 1. The propellant chamber is filled with an inert two-phase mixture (n-Butane) and is present in liquid and gaseous state of aggregation. At a temperature of 37 degrees Celsius the mixture has a vapor pressure of 2.4 bar, which drives the pump. The advantage of this kind of driving system compared to an electrically controlled infusion pump is a better ratio of drug volume to driving system, lower manufacturing costs, and a longer product life time.

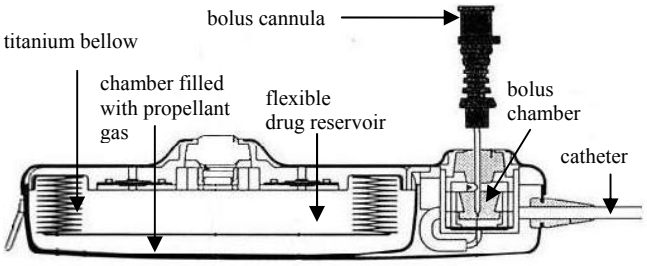


Fig. 1 Infusion pump showing the current bolus system consisting of a bolus chamber filled through the bolus septum via a syringe [2].

One of the main drawbacks of a gas controlled infusion pump is the lack of a patient controlled bolus system, which could enable the injection of an additional bolus if the patient would demand a higher amount of drug (e.g. during a temporarily increase of pain). Today, if the patient suffers from a sudden increase of pain he/ she has to consult a physician who then injects an additional amount of drug into the bolus chamber connected directly to the outlet of the infusion pump. This is time-consuming and decreases the patient's quality of life. To enable a higher flexibility of therapy the functionality of the infusion pump has to be improved by developing a patient controlled bolus system.

II. Development of the Bolus System

A. General Requirements

Three important specifications influence the development. First of all, the actuation and controlling of the bolus system have to be wireless. Additionally, a successful transcutaneous power transmission over a minimum distance of 50 mm is required. Furthermore, as few as possible active

O. Dössel and W.C. Schlegel (Eds.): WC 2009, IFMBE Proceedings 25/VIII, pp. 26–29, 2009.
www.springerlink.com

components actuating the bolus system have to be used to reduce the final power consumption and the rate of failure.

B. Telemetric Transfer of Energy

The telemetric transfer of energy is based on electromagnetic induction using two coupled coils. This is well-known and part of several medical applications [3, 4].

For this stage of the development requirements like MRI-compatibility, or biocompatibility were not taken into account.

As the receiving coil is part of the implantable infusion pump its shape and size is limited by the infusion pump's geometry resulting in an outer diameter of 70 mm. The height of the coil was set to 3 mm assuming an integration of the receiving coil into the base plate of the infusion pump. To assemble the coil a coil body of PMNA was used to carry the windings. Finally, the coils can be assumed to be short cylindrical, air coils.

Several coil setups were considered according to the optimal number of windings, input parameters and induced voltage before assembling both coils. The calculations to determine the magnetic field strength *H* were based mainly on the Law of Biot-Savart

$$\mathbf{H} = \frac{\mathbf{I}}{4\pi} \oint \frac{\vec{ds} \times \vec{r}}{r^3}, \qquad (1)$$

and a vector calculation to determine the entire magnetic induction of the receiving coil. The vector *r* points to a point *P* (point at receiving coil), and gives the distance between the point of origin (sending coil) and point P. The coil is supplied with a current *I*, and *ds* is a short segment of the wire. Finally, the initial parameters given in Table 1 were chosen. During the first development the geometry of both, the sending and the receiving coil were set to be identically.

Table 1 Initial parameters of sending and receiving coil

Feature	Value
Core material	Air
Wire material	Copper
Number of turns	~ 360
Outer diameter d_o [mm]	70
Inner diameter d_i [mm]	57
Diameter of coil wire [mm]	0.2
Inductance [mH]	13.7
Resistance sending/ receiving coil [Ω]	35.8 / 36.5

C. Actuation of the Valve

It was decided to use a miniature ball-valve as the bolus releasing component. A market research on geometry, safety and power consumption led to the micro valve *SMLD 300* (Fritz Gyger AG, Gwatt/ Thun, Switzerland), a normally-closed, electromagnetically driven valve [5].

The circuit controlling the valve (actuation circuit) consists of two main parts. First, the rectifier also called Villard cascade, which enables a full-wave rectification. The advantage of this particular rectifier is a large output voltage compared to the peak value of the input voltage (v_{ind}). During the first positive half-wave the capacitor C1 is charged, during the second half-wave the capacitor C2 is charged and the charge of C1 is added. To avoid a discharge of C1 and C2, diode D2 is connected reverse-biased. Second, a switch is integrated into the circuit controlling the opening and closing of the valve. If the switch is closed the resulting voltage of the rectifier (actuation voltage v_{act}) is transferred to the valve and the valve opens.

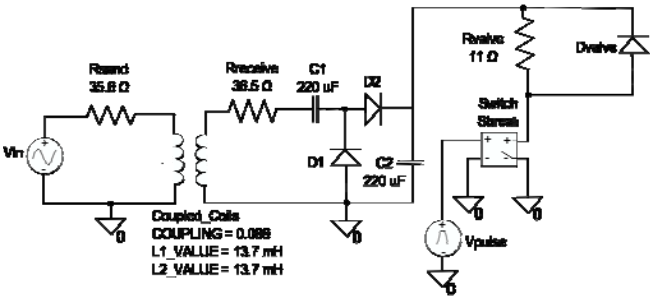


Fig. 2 Schematic arrangement of the bolus system including the sending and the receiving coil

According to Fig. 2 a voltage source (V_{in}) supplies the primary coil with a sine wave of a certain amplitude and frequency. A magnetic field develops, which again induces a voltage in the secondary coil (Coupled_Coils). Both coils form a non-ideal transformer and enable the transcutaneous power transmission. The induced current is given to the rectifier. The resulting DC supplies the valve (R_{valve} and D_{valve}) if the switch (Switch) is closed. The switch is implemented via a transistor, which again is driven by a second voltage source (V_{pulse}) providing a square wave with a duty cycle of about 10 %.

In order to enlarge the induced voltage a series resonant circuit was integrated into the circuit on the primary side. A series resonant circuit is used because its impedance becomes almost zero (depending on the ohmic resistance of the circuit) leading to a very high current supplying the sending coil and thus increasing the induced voltage. It was chosen to apply a frequency of 20kHz. Taking into account the inductance of the sending coil of 13.7 mH and the frequency of 20 kHz a capacitance of 4.6 nF results.

D. Optimization of the Actuation Circuit

An important result of the measurements (III.A) was the influence of several input and setup parameters (e.g. input frequency and amplitude, loading capacitors C1 and C2) on the voltage transferred to the valve (v_{act}). If the switching frequency f_{switch} is constant and the amplitude of the input signal is increased an increase of v_{act} can be observed caused by a higher charge of the capacitors within the same time. Therefore, a higher voltage is given to the valve. As given by the valve's specification the valve closes below a certain threshold voltage. If then a higher or lower voltage v_{act} is given to the valve more or less time is needed to go below this threshold. Consequently, this leads to a longer or shorter opening of the valve resulting in a change of the final bolus volume.

To ensure a stable amount of the bolus independent of changing input parameters the actuation voltage has to be stabilized. The final solution is a non-inverting Schmitt trigger composed of an operational amplifier and resistors, and the integration of an n-channel, enhancement-mode MOSFET replacing diode D1. The Schmitt trigger enables the setting of an upper and a lower threshold to control the actuation voltage. The MOSFET is needed to counteract the constant charge of the capacitors by short-circuiting the capacitors while the switch is closed. The optimized circuit was only simulated but indicated a constant actuation of the valve and thus, a constant bolus volume.

III. Measurements and Results

A. Influence of Relative Position of Sending and Receiving Coil

To analyze the influence of an alternating coil position during the energy transfer, a radial, an angular and a combination of these misalignments of the sending and the receiving coil Cs and Cr were examined at a coil distance of 50 mm (Fig. 3).

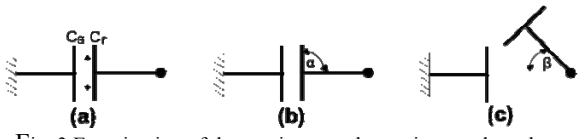


Fig. 3 Examination of the maximum voltage given to the valve applying a radial (a), an angular (b) or a combination of radial and angular misalignment (c) of sending coil Cs and receiving coil Cr to analyze the influence on the bolus injection

The position of the sending coil was fixed and was supplied with a sinusoidal signal of 10 V amplitude and a frequency of 20 kHz.

The induced voltage at the receiving coil was measured. The actuation circuit was not integrated into the measurement setup. The measurement data given in Fig. 4 show that a small misalignment of some degrees or centimeters, respectively, does not influence the transmission significantly. Only a coaxial misalignment in combination with an angular misalignment impacts the induced voltage strongly. This result is promising as it indicates that a successful transmission is still possible even if the coils are not hold exactly inline, which again eases the handling of the bolus injection system.

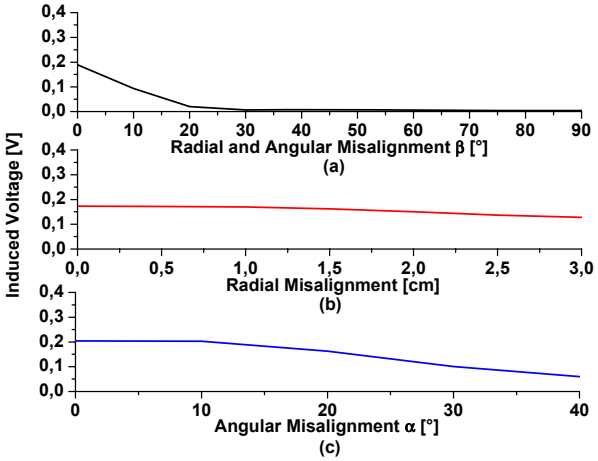


Fig. 4 Influence of induced voltage applying a coaxial combined with an angular misalignment (a), radial (b) and angular misalignment (c) of the sending and receiving coil

B. Flow Measurement

The valve SMLD 300 was connected to a pressure source providing a constant pressure of up to 2.4 bar. The flow was measured via a liquid mass flow meter (Model # N-565, Upchurch Scientific, Oak Harbor, USA) providing a working range of ± 8500 nl/min. The valve was opened every 20 s (f_{switch} = 50 mHz), the input signal given to the sending coil was a sine wave with an amplitude of 15 V and a frequency of 20 kHz. At all measurements, the switch used to open the valve was supplied via an external power source and not via the induced voltage.

Fig. 5 illustrates the results of the flow measurement. The progress of the flow was as expected. At the beginning of each switching cycle a sharp increase (opening of valve) followed by a less sharp decrease of the flow to 0 µl/ min (closing of valve) can be observed. The maximum flow

could not be measured as it was out of the sensor's working range.

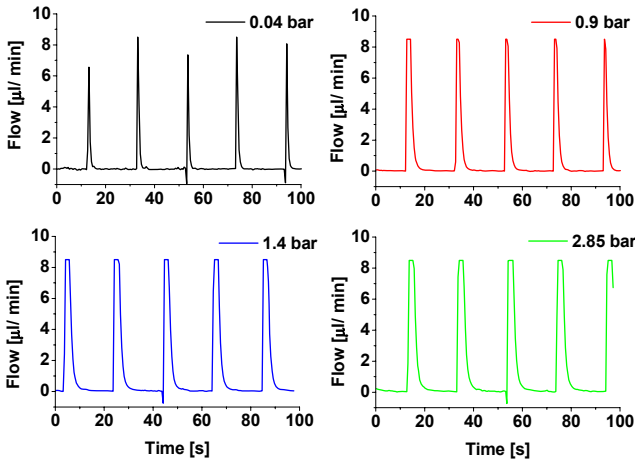


Fig. 5 Flow measurement to analyze the actuation circuit and the valve SMLD 300 with f_{in} = 20 kHz, f_{switch} = 50 mHz. The coil distance was set to 20 mm.

The final flow measurement, setting a coil distance of 50 mm and a working pressure of 2.4 bar, showed a successful switching of the valve and thus, a successful release of a bolus volume.

IV. Conclusion

It could be shown that a transcutaneous power transmission under the specified conditions using only a few active components is possible (distance less than 50 mm, pressure difference of 2.4 bar across the valve). As described in II.C the current actuation circuit had to be improved. A theoretical solution is given but has not been implemented, yet. A research on more appropriate electrical components (small in size, low power consumption) is also necessary. Furthermore all measurements were carried out in air and the influence of tissue on the transcutaneous power transmition must still be analyzed.

Acknowledgment

The authors want to thank the state Schleswig-Holstein and the German Federal Ministry of Education and Research (BMBF) for partly funding this project.

References

1. Von Korff M, Dworkin SF, Le Resche L (1990) Graded chronic pain status: An epidemiologic evaluation. Pain 40: 279-291
2. tricumed Medizintechnik GmbH(2007) The new generation of infusion pumps equipped with a positioning system for the refilling. Internal Information
3. Casadei F, Baldinger E (1970) Induktiv ladbarer Herzschrittmacher für die Langzeitimplantation. ZAMP 22: 1-14 DOI 10.1007/BF01624047
4. Faschingbauer M, Seide K, Weinrich N et al. (2007) Fixateur interne mit Telemetriesystem. Trauma und Berufskrankheit 9: 88-97 DOI 10.1007/s10039-007-1228-1
5. Fritz Gyger AG SWISS Mikroventil SMLD 300 at http://www.fgyger.ch (February 2009)

Corresponding Author:

Author: Anja Knopp, M.Sc.
Institute: Luebeck University of Applied Sciences, Center of Biomedical Engineering
Street: Moenkhofer Weg 239
City: Luebeck
Country: Germany
Email: knopp@fh-luebeck.de

Finite Element Modelling of Microphysiometry on Cellular Specimen

M. Brischwein[1], D. Grundl[1], X. Zhang[1], Wolf[1]

[1] Heinz Nixdorf Lehrstuhl Medizinische Elektronik, Technische Universität München, Deutschland

Abstract— **Cell or living tissues are cultured in microreaction chambers. Cell metabolic rates are monitored in real time with electric or optic microsensors for pH value and dissolved oxygen operating within these chambers. One of the most important application areas is the improvement of cancer treatment by in-vitro analyzing the individual chemosensitivity profiles prior to the application of chemotherapy. However, in a clinical setting any in-vitro diagnostic approach requires strict measures of data quality control. In order to identify operational faults in sensor readings, the signals were simulated in a 3-D finite element model (FEM) of diffusion. The program chosen was COMSOL. The model is not only used for the filtering of false data but also for the analysis of material effects (e.g. gas diffusion and absorption through polymers), for optimising the microchamber geometry and for investigating the kinetics of cell metabolism within different distributions of cell densities.**

Keywords— **microphysiometry, FEM, cell assay, pH, oxygen**

I. Introduction

Microscaled culture environments are at the heart of "cell-on-a-chip" systems. Systems using such environments are constructed for a simultaneous culturing and monitoring of small quantities of living cells. "Monitoring" may include the use of chip-based sensors for physico-chemical parameters such as pH and oxygen. Given an appropriate surface area to volume (SAV) ratio, the cells are able to control their microenvironment during culture. Sensor based monitoring of pH and oxygen values allows to observe changes in cell metabolic rates in real time, which in turn reflect changes in cellular signaling and physiology. The necessary SAV ratios to achieve a sufficient sensitivity/time resolution of measurement can be derived from typical metabolic rates found in animal and human cell cultures, which are in the order of 10^{-16} – 10^{-17} moles of released protons (per cell · second) and roughly the same amount of moles consumed dissolved oxygen. The aim is to obtain a drop of ≈ 0.1 pH units and ≈ 10% oxygen saturation within 5-10 minutes.

The system described and modeled in this paper is described in [1]. It is working with optochemical sensors (Presens GmbH, Regensburg) for pH and dissolved oxygen. The sensors are spotted on a glass chip substrate, which forms the bottom of the microreaction chamber. 24 chips are integrated into a 24 well plate, each well representing a single micro-reaction chamber. The top walls of the chambers are formed by the protrudings of a cover lid constructed for the multiwell plate.

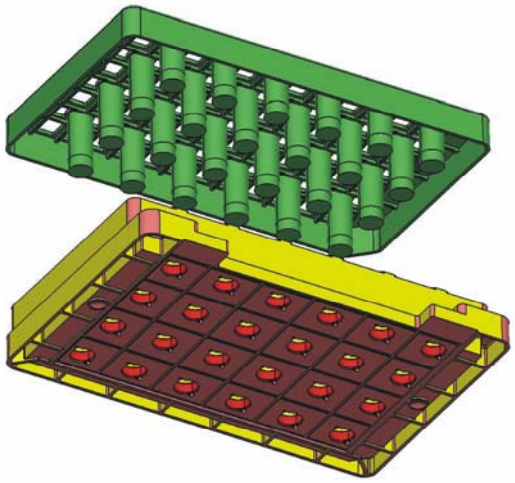


Fig. 1: The multiwell pate with bottom glass chips and cover lid. It contains 24 microreaction chambers, each connected to additional two vessels for the access of the pipetting robot.

To achieve an interfacing between macro- and microfluidics, each of the microreaction chambers is connected with two hydrostatic vessels, serving as the access ports to a pipetting robot. However, in this paper only the liquid volumes of the chambers in the resting intervals of the liquid system are considered, not any parameters of (laminar) flow.

II. Materials and Methods

A. Geometry

Each of the spotted sensors has a diameter of 2 mm with a height of ≈ 0,1 mm. The cell growth area on the chip has a diameter of 7,7 mm. The surface of the optochemical

O. Dössel and W.C. Schlegel (Eds.): WC 2009, IFMBE Proceedings 25/VIII, pp. 30–33, 2009.
www.springerlink.com

sensors is not grown by cells. The height of the chamber, resulting from the distance between glass chip and cover lid is adjusted to 0,5 mm. A cross section of the geometry is shown in Fig. 2 (all figures indicated in mm).

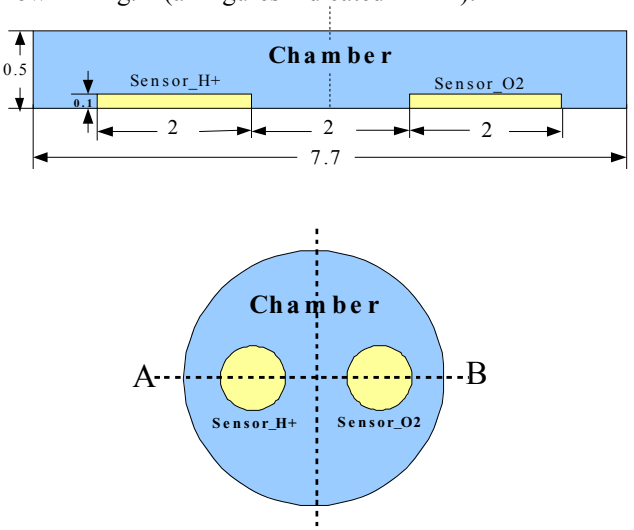


Fig. 2: 3D-geometry of the cell culture containment used for modeling with a chamber height of 0.5 mm and diameter of 7.7 mm. Top figure: Cross section. Bottom figure: Top view on the cell culture surface, with two axes of symmetry.

In the first step, the model was used to simulate the signals of optochemical sensors. The cell culture was modelled as a homogeneous monolayer on the substrate with a density of 10^3 cells per mm^2 and a height of 5 µm. The oxygen consumption rate was set to 10^{-16} moles O_2 sec^{-1} and the proton extrusion rate to 10^{-16} moles H^+ sec^{-1} (both values per single cell). The optochemical sensors are not grown with cells. The local distribution of pH values and oxygen saturation was now integrated on the sensor surfaces to obtain the synthetic sensor signals as a function of time.

B. Simulation

The simulation program was COMSOL Multiphysics 3.4. A mesh of 20797 triangular elements was applied. The diffusional equation (Fick`s 2nd law) is:

$$\frac{\partial c}{\partial t} + \nabla \cdot (-D \nabla c) = R \qquad \text{[Eq. 1]}$$

with c representing the concentration of protons (i.e. hydronium ions) or dissolved oxygen, The coefficient of diffusion (in water, 37 °C) is $13{,}94 \cdot 10^{-5}$ cm^2 sec^{-1} for protons and $3{,}149 \cdot 10^{-5}$ cm^2 sec^{-1} for oxygen. The reaction rate R stands for the rate of proton release or the rate of oxygen uptake by the cell layer (with $R \neq 0$ in the volume elements occupied by the cell layer). The starting condition was a pH value of 7,4 and a dissolved oxygen concentration of 0,214 mmol/L.

C. Implementation of the buffer capacity

For proton diffusion, the buffer capacity of the medium has to be taken into account. This was accomplished by multiplication of the cellular proton release rate R with a factor $\delta c_{free}/\delta c_{added}$, with δc_{free} describing the concentration change of "free" protons relevant for the pH value and δc_{cadded} describing the concentration change of protons added by cell metabolism. The remaining part of protons is bound to buffering species in solution. Using the definition of the buffer capacity

$$\beta = \frac{\partial c_{added}}{\partial \log c_{free}} \qquad \text{[Eq. 2]}$$

and the relationship $\delta \log c_{free}/\delta c_{free} = (\ln 10 \cdot c_{free})^{-1}$, the pH-dependent proportion $\delta c_{free}/\delta c_{added}$ is $2{,}3 \cdot c_{free} \cdot \beta^{-1}$. The rate R multiplied by this proportion is inserted into Eq. 1.
On the one hand, the buffer capacity β of typical cell culture media such as Dulbeccos Modified Eagles Medium (DMEM) is due to phosphate and amino acids such as histidine, cysteine and glutamine, on the other hand, it is due to proteins of the serum component [2]. The total buffer capacity was measured by titration of the culture medium (including 5% of fetal calf serum) with defined amounts of hydrochloric acid. The result is an approximately linear relationship between ΔpH and Δc_{added}. Therefore, the buffer capacity was assumed to be constant in the relevant range of pH (i.e. 7,4 to 6,5). A value of $\beta \approx 1{,}14 \cdot$ mmol/L was obtained by linear regression of the slope $-(\Delta c_{added}/\Delta pH)$.

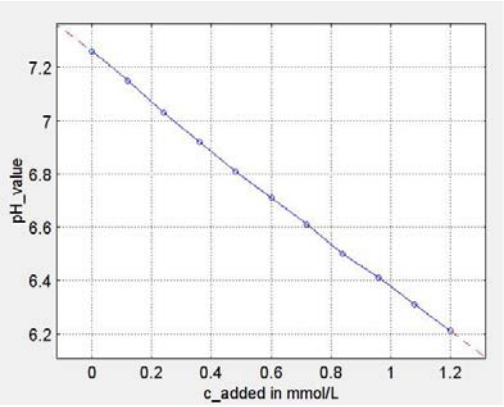


Fig. 3: Experimental determination of the buffer capacity β of the used DMEM cell culture medium with 5% serum.

III. Results

Based on the simulated distribution of pH (Figs. 3a and 4a) and oxygen (Fig. 3b and 4b) on the surface of the sensors, the kinetic sensor signals were obtained by the calculation of the surface integrals (Figs. 5a and 5b).

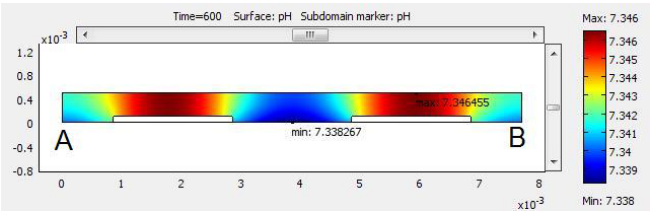


Fig. 3a: Calculated distribution of pH (initial value: 7,4, homogeneous) after 10 minutes from starting conditions. For the section plane, see Fig. 2

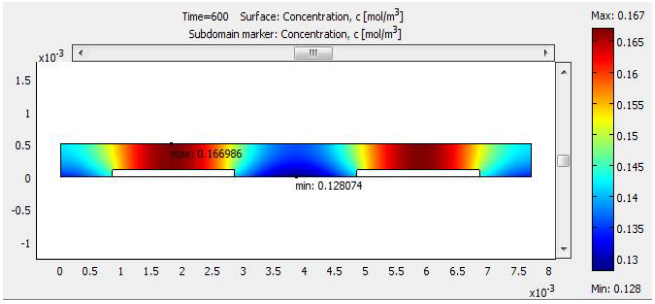


Fig. 3c: Calculated distribution of dissolved oxygen concentration (initial value: 0,214 mM, homogeneous) after 10 minutes from starting conditions. For the section plane, see Fig. 2.

Three-dimensional distributions of pH and oxygen are shown in Figs. 4 and 5.

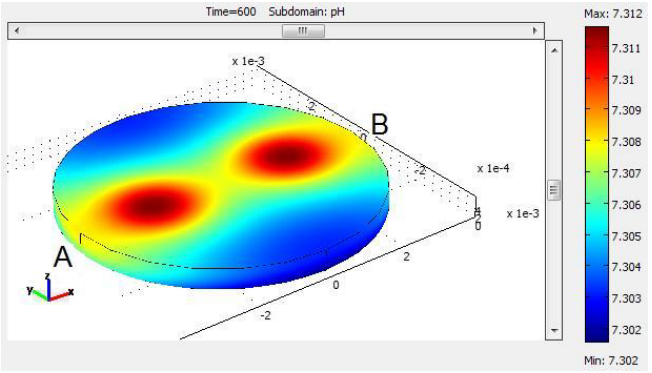


Fig. 4a: Simulated 3D model of pH after 10 minutes from starting conditions

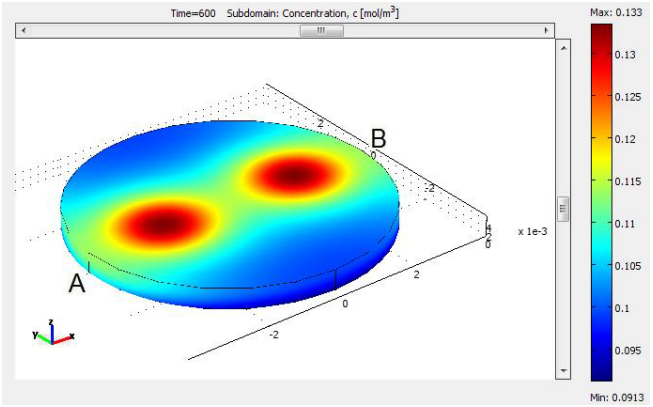


Fig. 4b: Simulated 3D model of dissolved oxygen concentration (initial value: 0,214 mM, homogeneous) after 10 minutes from starting conditions

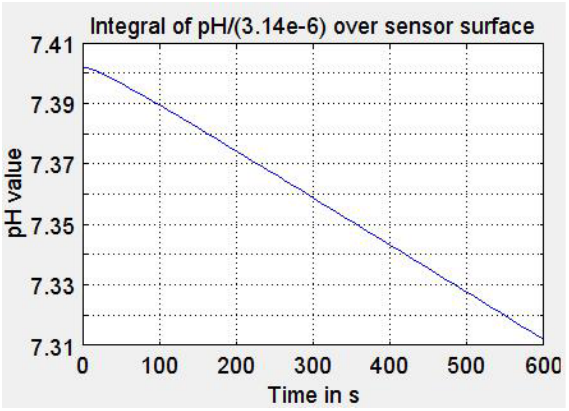


Fig. 5a: Kinetics of pH sensor derived for t=0 to t=10 minutes, calculated by the integration of pH on the sensor surface.

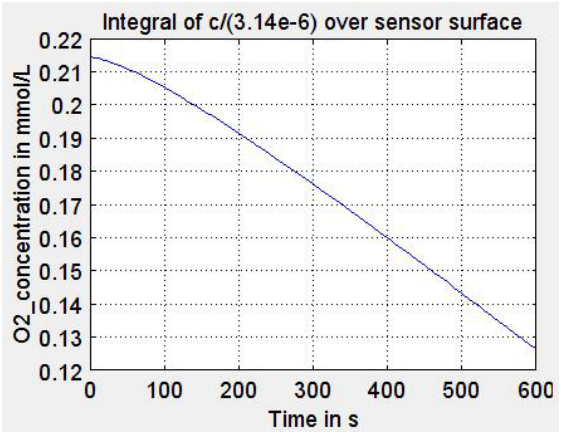


Fig. 5b: Kinetics of dissolved oxygen sensor derived for t=0 to t=10 minutes, calculated by the integration of oxygen concentration on the sensor surface.

IV. Discussion

By comparison with real kinetic sensor data (not shown in this paper) it appears that the model can correctly simulate the spatio-temporal distribution of the investigated physico-chemical parameters. Examples for time plots of real sensor data are found in a parallel paper, published by Flurschütz et al. in this conference proceedings.

This paper is a summary on first results. In the next steps, the model will be refined to simulate different locations of the sensors within the microchamber and non-homogeneous distributions of the cell metabolic activity. The latter is particularly relevant for the intended short-term cultures of tissue specimen within the chamber microenvironments. In this context however, not only the simulation of diffusion in resting fluid microcontainments, but also the pattern of a liquid flow for a controlled exchange of media is extremely important [3] and will be investigated in future work.

An alternative approach for the consideration of the buffer capacity in proton diffusion was proposed by Junge and Mc Laughlin [4]. They calculated an apparent diffusion constant for protons as a function of the buffer capacity β and the diffusion constants of buffering species with varying mobility (i.e. proteins and small organic compounds). Although its application depends on the knowledge – or at least the estimation – of all relevant diffusion constants, it is part of the subsequent work to simulate that approach as well. Moreover, this model will imply the introduction of hydroxide ion diffusion, ocurring in parallel and in counter direction to proton diffusion. Hydroxide ion diffusion is an issue to consider near pH $\approx$ 7, where H_3O^+ and OH^- ions are both present in appreciable concentrations.

V. Conclusions

It appears from the presented first simulation results that the model used is in principle valid and can be used for the optimisation of microchamber geometries, material selection and strategies for cell immobilisation and cell culturing. Equally important as the investigation of diffusional phenomena for the theoretical calculation of sensor raw data is the analysis of fluid exchange patterns by (laminar) flow, because only a well defined fluid exchange guarantees homogeneously distributed starting values of pH and oxygen concentration at the beginning of the resting intervals, as a condition for this simulation.

References

1. Bernhard Becker et al. (2008) Automated multi-parametric label free 24 channel real-time screening system NBC 14th Nordic-Baltic Conf. on Biomed. Eng. and Medical Physics 2008, Riga, NBC 2008, Proceedings 20:186-189
2. Owicki J.C. and Parce W. (1992) Biosensors based on the energy metabolism of living cells: The physical chemistry and cell biology of extracellular acidification. Biosensors & Bioelectronics 7:255-272
3. Walker, G.M., Zeringue, H.C., Beebe, D.J. (2004) Microenvironment design considerations for cellular scale studies. Lab on a Chip 4:91-97
4. Junge, W. and Mc Laughlin, S. (1987) The role of fixed and mobile buffers in the kinetics of proton movement. Biochimica et Biophysica Acta 890:1-5

Author: Dr. Martin Brischwein
Institute: Heinz Nixdorf-Lehrstuhl für Medizinische Elektronik, TU München
Street: Theresienstrasse 90
City: München
Country: Germany
Email: brischwein@tum.de

CD146 detection with real-time total internal reflection imaging ellipsometry

Li Liu[1,3] ,Yu Niu [1,3],YongHong Meng[1],She Chen[1],XiYun Yan[2] , Gang Jin[1]*

[1]Institute of Mechanics, Chinese Academy of Sciences, Beijing 100190, China
[2]Institute of Biophysics, Chinese Academy of Sciences, Beijing 100101, China
[3]Graduate School, Chinese Academy of Sciences, Beijing 100049, China
*Corresponding author: E-mail: gajin@imech.ac.cn; Tel./Fax.: +86-10-82544138

Abstract — **Biosensor with the total internal reflection imaging ellipsometry (TIRIE) uses an evanescent wave as optical probe to monitor bio-molecular interaction with a high sensitivity due to its property of phase sensitive. Here, the biosensor is applied for a quantitative detection of CD146 with concentrations of 0.1 to 100 ng/mL in order to realize a high sensitive quantitative detection. Moreover, the regression curve between the signal of biosensor (y) and CD146 concentration (x = lnC+2.4) is deduced as a linear y=1.0544x+0.7839.**

Keywords—**TIRIE biosensor, CD146 detection**

I. Introduction

Adhesion molecule CD146 (100-130kDa) belongs to the immunoglobulin super family and it is originally identified as a biomarker for melanoma [1] . Recently, CD146 is found as novel target molecule on endothelial cell and involved in tumor angiogenesis [2] . Also CD146 is considered as critical molecule in cell invasion [3; 4; 5] and anti-CD146 antibody could inhibit tumor metastasis and angiogenesis through its down regulation of NFk [6; 7] . In this paper we attempt to detect the CD146 molecule in positive serum with the TIRIE biosensor.

TIRIE is imaging ellipsometry performed in the total internal reflection mode which is introduced previously [8] .The biosensor with TIRIE using evanescent wave as optical probe to observe bio-molecular interaction has high sensitivity due to its phase sensitive [9] , otherwise avoids the solution disturbance and transparency influence. It is a powerful tool for the visualization and analysis of bio-molecular mono-layers. It can be operated in real time mode for the bio-molecular interaction process detection. Its properties are fast sampling for a large field of view, non-disturbance, qualitative and quantitative detection with label free and low reagent and specimen consumption. Its multi-channel micro-reactor has functions of the solution delivery, the ligand immobilization, the surface blocking, and a high throughput detection.

II. Materials and methods

A. Materials

The SF10 glass slides were purchased from Changchun institute of Optics, Fine Mechanics and Physics, Chinese Academy of Sciences (China). The 11-mercaptoundecanoic acid (MUA) was purchased from Sigma (USA).1-(3-Dimethylaminopropyl)-3-ethylcarbodiimide hydrochloride (EDC) and N- hydroxy-droxysuccinimide (NHS) were purchased from ACROS. All chemicals for preparing Phosphate-buffered Saline (PBS, 10mM phosphate, 0.1M NaCl, pH 7.4) and PBS solution with 1% Tween 20 (PBST) were purchased from sigma. Deionized water (resistivity18.3 MΩcm) was produced by ion exchange demineralization, followed by passing through a Milli-Q plus system from Millipore (Millipore, Bedford, MA). Mouse monoclonal antibody to CD146 AA1 was provided by institute of Biophysics of Chinese Academy of Sciences. All human sera were supplied from Anzhen Hospital (China).

B. Substrate

The SF10 glass slide was used as substrate and prepared by the evaporation of 2nm of chromium on surface then added by the evaporation of 30nm of gold. The gold surface was immersed into a 1mM MUA- ethanol solution for at least 18 Hs, followed by a thorough rinsing with both ethanol and deionized water. The MUA mono-layer with carboxyl group was self-assembled on the gold surface.

C. TIRIE setup

The schematic of the biosensor is shown in Figure 1. The TIRIE biosensor system is based on imaging ellipsometer under the total internal reflection condition equipped with a

O. Dössel and W.C. Schlegel (Eds.): WC 2009, IFMBE Proceedings 25/VIII, pp. 34–36, 2009.
www.springerlink.com

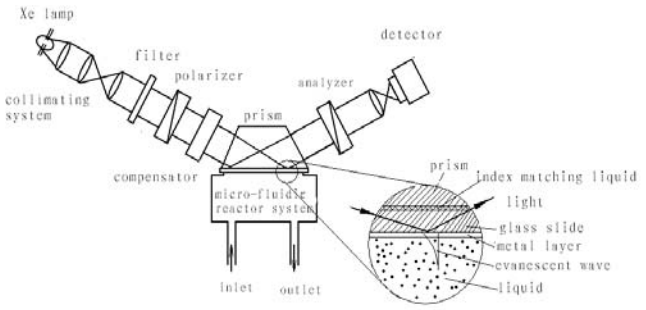


Figure 1.Schematic of the TIRIE biosensor. The zoom shows the details of the environment around the protein chip.

coupling prism and micro-fluidic reactor system. The principle of the TIRIE is briefly described here, and more details can be found elsewhere [10; 11]. Light beam with wavelength 633nm from light source goes through the polarizer and the compensator and then passes a 59° prism. The substrate equipped with the protein micro-array on chip mounted on the flow cell of the micro-fluidic reactor system contacts the prism bottom. For the prism and the glass slides coupling, an index matching liquid is used between them (refractive index n=1.73). After reflection from the bio-chip surface the light beam goes through the analyzer and then focused on a sensing area of the charge coupled device (CCD) camera. The video signal corresponding to the biomolecular mass surface concentration distribution was captured, digitized and stored in gray-scale format (8bits 0-256 grayscale) in a computer.

III. Results and Discussion

The goal of the experiment is to detect the target CD146 molecule with low concentrations in normal serum and obtain a regression curve of biosensor signal versus the concentration of target molecule. The ligand of target molecule is AA1 the monoclonal antibody of CD146. The immobilization condition of the ligand is determined by an optimization result of the concentration (mouse ascites diluted 200 times with PBS buffer) and the immobilization time is10 min. In our experiment, the concentration of CD146 in sera is 0.1, 1, 10, 20, 40, 100 ng/mL, respectively. All results of CD146 real-time detection processes are shown in Figure 2. The zoom in Figure 2 is the analysis of regression curve of Region 7 and Region 8 which show the dynamic process of CD146 with different concentrations reacting with its specific antibody on surface. Curve markers from g to a correspond to different concentrations of CD146 from low to high. The signal in grayscale before and after the interaction is shown in Table 1. The data in the region 8 is averaged over the last 300 S indicated in the Figure 2.

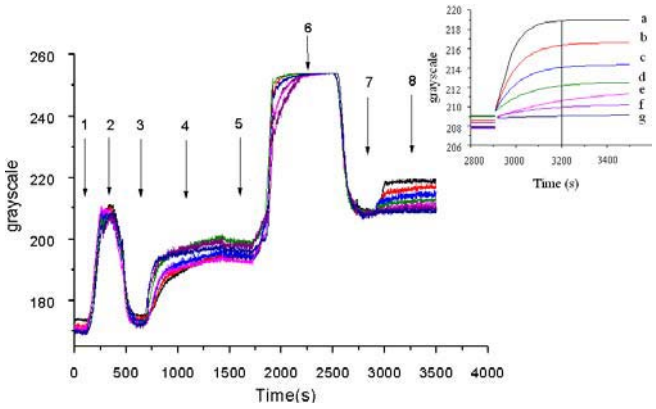


Figure 2. the real-time curves of the dynamic process for the CD146 binding with its antibody AA1 in various concentrations. The 1st region was the baseline. The 2nd region was corresponding to the NHS-EDC activation of carboxyl group assembled on the gold substrate; 3rd -PBS rising; 4th - AA1(1:200) immobilization on gold-coated substrate surface; 5th -PBS rinsing, 6th - blocking , 7th -PBS rinsing and 8th -CD146 binding with its antibody. Curve a-f was related to the several CD146 concentrations of 100, 40, 20, 10, 1, 0.1 ng/ml. The curve g was the reference.

Table 1: the surface concentration in grayscale before and after CD146 binding with its antibody

Concentration(C) (ng/ml)	7th Region	8th Region	Difference between ligand and interaction region
100	209.1±0.7	218.4±0.4	9.3±1.1
40	208.8±0.4	216.5±0.5	7.7±0.9
20	208.0±0.5	214.4±0.6	6.4±1.1
10	209.0±0.4	212.4±0.4	3.4±0.8
1	208.1±0.5	211.6±0.5	3.5±1.0
0.1	208.4±0.3	209.9±0.3	1.5±0.6
0	208.2±0.2	209.1±0.3	0.9±0.5

Though the signal of the biosensor is quite low at the concentration 0.1ng/ml but significant compared with the reference. It confirms that the sensitivity of the biosensor reaches the order of ng/mL. For quantification, the regression curve is established between the signal of biosensor and the concentration of CD146(C). The relationship between the signal in grayscale difference (y) and the concentration appears a logarithm formulation (x=lnC+2.4) especially in lower concentration showed in Figure 3. The signal variation is proportional to the concentration as expected in the regressive fitting curve and the relationship between the signal in grayscale difference(y) and concentration of CD146 (x) is y=1.0544x+0.7839.

The signal corresponds to 10ng/mL appears abnormal in regression curve. The signals of 10ng/mL and 20ng/mL

are so quite close that it's hard to distinguish. Maybe it's impacted by the ununiformity among independent channels or the stochastic noise, so that the improvement of the uniformity among independent channels and the ratio of signal and ratio is required. The work for the improvement is on the way, and some improved results could be foreseen.

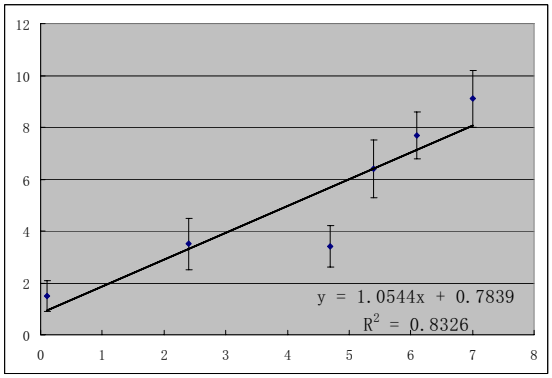


Figure 3. the regressive fitting curve between the signal in grayscale difference(y) in Table 3 and the concentration (C) of CD146 (x).. Here, the relationship between x and the concentration of CD146 is x = ln C+2.4.

IV. Conclusion

CD146 with concentration of 0.1-100 ng/ml range in serum has been detected with the TIRIE biosensor dynamically and quantitatively. The concentration of the detected sample is lower than the standard sample 243ng/mL which confirmed the biosensor could be applied in CD146 of low concentration detection. A linear relationship y=1.0544x+0.7839 between the biosensor signal (y) and the concentration of CD146 with logarithm formulation (x=lnC+2.4) has been obtained by regression curve which would be used as a reference of calibration for further CD146 detection. The total internal reflection biosensor shows a potential for clinic application.

References

[1]Johnson J P, Rothbacher USers C (1993) The progression associated antigen muc18 - a unique member of the immunoglobulin supergene family. Melanoma Res. 3:337-340.

[2]Bu P C, Zhuang J, Feng J et al. (2007) Visualization of cd146 dimerization and its regulation in living cells. Biochim. Biophys. Acta-Mol. Cell Res. 1773:513-520.

[3]Lehmann J M, Holzmann B, Breitbart E W et al. (1987) Discrimination between benign and malignant-cells of melanocytic lineage by 2 novel antigens, a glycoprotein with a molecular-weight of 113,000 and a protein with a molecular-weight of 76,000. Cancer Res. 47:841-845.

[4]Lehmann J M, Riethmuller GJohnson J P (1989) Muc18, a marker of tumor progression in human-melanoma, shows sequence similarity to the neural cell-adhesion molecules of the immunoglobulin superfamily. Proc. Natl. Acad. Sci. U. S. A. 86:9891-9895.

[5] Kang Y Y, Wang F C, Feng J et al. (2006) Knockdown of cd146 reduces the migration and proliferation of human endothelial cells. Cell Res. 16:313-318.

[6]Yan X Y, Lin Y, Yang D L et al. (2003) A novel anti-cd146 monoclonal antibody, aa98, inhibits angiogenesis and tumor growth. Blood 102:184-191.

[7]Bu P C, Gao L Z, Zhuang J et al. (2006) Anti-cd146 monoclonal antibody aa98 inhibits angiogenesis via suppression of nuclear factor-kappa b activation. Mol. Cancer Ther. 5:2872-2878.

[8]Chen Y YGang J (2006) Biosensor based on total internal reflection imaging ellipsometry. The Ninth World Congress on Biosensors.Canada: Biosensors & Bioelectronics, 219:

[9]G. Jin R J, H.Arwin (1996) Imaging ellipsometry revisited:Developments for visualization of thin transparent layers on silicon substrates. Rev.Sci.Instrum 67:2930-2936.

[10]Arwin H, Poksinski MJohansen K (2004) Total internal reflection ellipsometry: Principles and applications. Appl. Optics 43:3028-3036.

[11]Wang G L, Arwin HJansson R (2004) Optimization of off-null ellipsometry in sensor applications. Appl. Optics 43:2000-2005.

Space saving Mixed Signal FPGAs for improving processing power and memory capacity as a replacement for µCs in portable biosensor devices

M. Schmidhuber[1], J. Bähr[1], F. Ilchmann[1], J. Wiest[2] and B. Wolf[1]

[1] Heinz Nixdorf-Lehrstuhl für Medizinische Elektronik, Technische Universität München, Deutschland
[2] cellasys GmbH im Innovationszentrum Medizinische Elektronik, München, Deutschland

Abstract—**Living cells are extremely complex microsystems, which internally use biochemical and electronic signals for signal processing. These nonlinear and kinetic reactions are conceived as a quantitative collaboration of the cell as a biological system, whose output signals can be indicators for growth, mitosis, morphology, but could also be a quantity for the vitality of the surrounding micro environment on equal terms. These assays based on whole cell analysis techniques are very sensitive when exposed to external influences. The effect of different substances and toxic agents can be observed marker-free and in real time. The potential to understand the dynamics of the cellular processes justified the development of a handheld lab on chip system (see Fig. 1). The cells are regarded here as signal converters. The presented work herein is concerned with the conceptual development of a Handheld device, that have been optimized for the use in mobile biomedical multi-parametric analytics. On the electrochemical basis of sensor chips on a ceramic substrate made in thin-film technology, the measurement of cellphysiological parameters in the extracellular surrounding became possible. Sensors for pH, oxygen partial pressure, impedance, electrical potentials and temperature for the simultaneous in-vitro measurement of metabolic, morphologic and electrophysiological parameters were combined with a miniaturized mixed signal electronic, to allow local (Point of Care) analyses. A focus was put on the simulation of the various circuit parts, as well as the measurement of the electrical impedance. On this basis it was possible for the first time that food analysis could be shown without complex laboratory-technical investigation. The presented measurement results prove that this system approach with the acquired concepts is a serious alternative to commercially available solutions.**

Keywords— **Cell based system, live cell analysis, Point-of-Care, environmental monitoring, yeast cells.**

I. Introduction

Cell based biosensor systems using miniaturized electrochemical [1,2] or optical sensors have been introduced in different applications [3]. With the possibility of mobile devices [4] this systems can be used in wireless networks for applications in homeland security, water quality analysis [5] or in the health technologies [6]. For these applications the biosensor devices have to be operated automatically and autonomous. I.e. the biosensor devices have to be embedded into a software controlled systems which takes care of configuration, data processing and interpretation. Also aspects as improving operating time and flexibility due to miniaturization have to be considered. Here the electronic modules of an existing biosensor device shall be replaced by new concepts. A main focus was laid on the digital part of the device in which on the one hand measurement values are accomplished and on the other hand the data are processed. The use of a Mixed-Signal FPGA makes it possible to realize a System on Chip (SoC) which combines the needs out of the analogue world together with the digital signal and operational processes. The paper presented here should give an overview of design considerations made when going through the design flow of programming an FPGA.

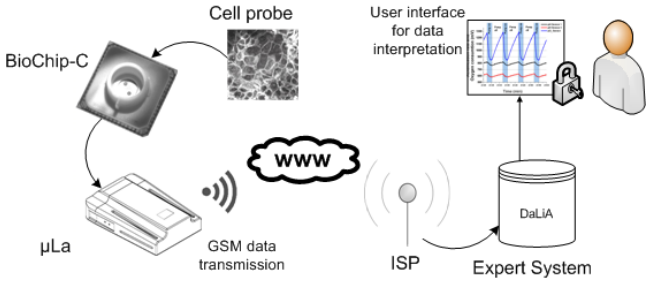


Fig. 1 Signaling circle of using living cells as a signal converter on external influences: The Biosensor (BioChip-C) is inserted in the device (µLa), data are sent wirelessly to an interpretation system where the users can access to.

II. FPGA (Field Programmable Gate Array)

An FPGA is a programmable integrated circuit of digital technique. In FPGAs it is possible to form specific configurations of internal structures for the most complex circuits. These are of small complexity, like e.g. a parallel counter, but also cover highly complex circuits, like microprocessors. A FPGA consists of many logic elements, mainly flip-flops and LUTs (LUT: Look Up Table), that can be linked to a special designated function by combining "electronic switches" according to the function required by the devel-

O. Dössel and W.C. Schlegel (Eds.): WC 2009, IFMBE Proceedings 25/VIII, pp. 37–40, 2009.
www.springerlink.com

oper. Current FPGAs consists of up to a few ten thousand of logic elements.

In most FPGAs RAM cells are available, that can be controlled by logic cells. So operations that need memory elements (FIFOs (FirstIn-FirstOut), RAM) can be easily carried out.

The FPGAs examined here belong to the family of Flash FPGAs: The current configuration is stored in a Flash memory, which ensures, that the information (ROM) is not erased again after switching off the device. Thus these components do not need external configuration memory and are immediately ready for operation after power on. The ICs contains up to 1 MByte Embedded Flash.

III. Design Study Actel Fusion

Due to the results of the comparison between FPGAs and microcontrollers previously made a design study with the Actel FUSION family was accomplished. Altium designer as an engineering tool for simulation and PCB layout together with the Actel Libero FPGA development software was used. Above all the flexibility and the possibility to reach very small dimensions justify this decision. The goal was to determine how far the PCB size and the power consumption can be reduced, if a design with an FPGA would be realized. Also good signal integrity was one of the main interests.

A. Main components and sub-assemblies

The used FPGA "Actel FUSION AFS600FG256" consists of 13824 flip-flops, 10 analogue Quads, 512kB Flash memory, a RTC counter, an integrated 1,5V voltage regulator, 40 analogue and up to 172 digital I/Os. The BGA256 package takes 289mm² (17mm x 17mm).

For the operation of the RTC counters an oscillator with 32.768kHz is necessary, which is stabilized by two capacitors. The voltage reference MAX6133 has a drift of only 5ppm per degree and is offered in the µMAX package with a surface of 3mm x 5mm. The power dissipation in stand by mode is about 40µA, but can go up to 15mA in full load operation. In order to keep the output voltage stable, 0.1µF ceramic capacitors are needed, preferred in 0402 package with a surface of 1mm x 0.5mm. The used D/A converter AD5664 from Analog Devices offers a four channel 16bit resolution output. It needs 0.44mA in normal operation and 0.2µA in the power down mode at 3.3V operating voltage. The ChipScale QFN package has the dimensions 3mm x 3mm. That converter is directly connected to the SPI interface of the FPGA. The operational amplifiers (OpAmp) MAX4252 are used as unity gain drivers, in order not to pull down the analogue outputs. Also passive RC-filters were used in order to minimize the noise. The OpAmp is available in 10 pin UCSP package with the dimensions of 2mm x 1.5mm. Its characteristics are distinguished by very small self-noise, very small offset, and Rail to Rail capability.

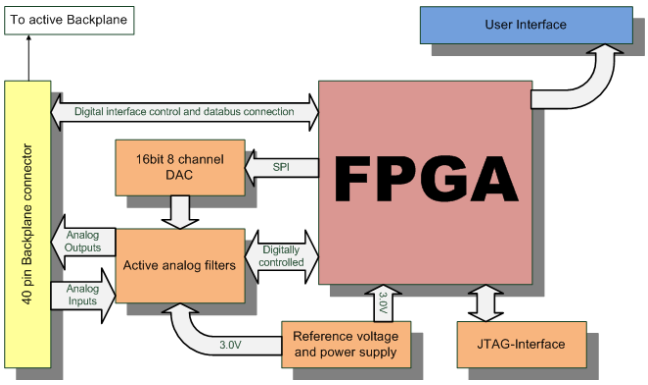


Fig. 2 Internal structure of the FPGA PCB: The electrical signals are combined in the backplane interface connector, the internal data acquisition is made by active filter structures. Analogue outputs are generated by a 16bit DAC.

B. Description of the FPGA system components

The logic blocks within the FPGA were realized with the development software Libero of Actel. This software is a collection of tools for the complete design flow. The following software tools were used within this work:

- Actel Project manager: Administration and overview of the individual components
- Smart Design: Block oriented design, configuration of the analogue blocks
- CoreConsole: Design of the processor subsystem, IP core data base
- Synplify AE: Synthesis tool
- Actel designer: Compiling, place and route, back annotate, generation of the programming file
- Smart power: Analysis of the current/power dissipation

The integration of the analogue components, like A/D converters, real time clock and the voltage supervisor circuitry was realized with SmartGen, whereas the processor sub-system was designed using the IP-core generator CoreConsole.

C. System Design of the FPGA PCB

The measured values shall be stored in the Flash memory as well as a time stamp. If the memory is full, is a connection to a PC over a serial interface is established and the

measured values are transferred. For the realization of the analogue part the following modules are used:

- The ADC module controls the four A/D-channels, the internal supply voltage supervisor and the initialization of the real time counters. The clock of the ADC system is adjusted to 40MHz. Thus the A/D converter can operate with the maximum possible frequency of 10MHz and the full 600ksps sampling rate. Each channel is scanned with 105ksps and the 12bit output resolution is fully available.
- The Crystal module controls the integration of the 32.768kHz oscillator frequency to the real time counters.
- The Flash system module ties up the Flash memory to the remaining system components and also contains the configuration data that the FPGA needs for initialization.
- The voltage regulator module activates the internal 1,5V voltage regulator for the supply of the digital FPGA components.
- The PLL module generates the clock pulses out the internal RC-oscillator, which operates at 100MHz. The overall system is clocked with 10MHz. The implemented soft-core processor has a maximum operating frequency of 25MHz. Aiming a current saving design, 10MHz represents a compromise between speed and power dissipation. The only exception is the ADC module, which is driven with 40MHz because of the maximum sampling rate.

D. Active filter structures

In this project active filter structures have been developed. They are primarily used to reduce the noise for the measurement signals, which mostly result from external influences. Active low-pass filters of 2nd order are used.

At low frequencies (1Hz to 1MHz) the necessary inductance values and thus the coils become very large. Within this project 22 of these filter structures must be accommodated on a PCB surface of 50mm x 50mm. Active filters were therefore preferred. The simplest low-pass filter is made of an RC element. For preventing load effects operational amplifiers used as impedance converters are inserted between the separate stages.

Compared with an ideal low-pass filter, an RC element has some disadvantages:

- The transition of the cut-off region into the transmission band is not sharply limited
- The phase response is nonlinear and caused thereby signal disturbances
- The amplitude in the transmission band varies long before the cut-off frequency f_c

The amplitude and phase response of a low-pass filter can be optimized according to the following three criteria:

- Greatest possible flatness of the transmission band
- The transition from the transmission band to the cut-off region must be as sharp as possible
- Linear phase response

For these optimizations the transfer function must have complex poles. The transfer function represents a cascade of filter stages of 2nd order, whereby the filter coefficients have positive real values. These coefficients specify the location of the complex poles for each filter stage. There are three different types of filter coefficients which fulfil the optimization criteria above:

- Butterworth coefficient: maximum flatness of the transmission band
- Tschebyscheff coefficient: sharp transition between transmission band and cut-off area
- Bessel coefficient: Linearization of the phase response to f_c

With passive RC elements no further optimization is possible, due to the absence of complex poles. Therefore active filter structures (operation amplifiers as active elements) are used. For this project an active Butterworth filter of 2nd order was developed. The maximum flatness of the gain response assures a minimum signal distortion of the measuring signals. Butterworth filter are particularly used for anti-alias applications (e.g. signal acquisition with AD-converters). For 2nd order low-pass filter two different topologies exist: Sallen key topology and multiple feedback topology. In this project the preference was given to the first one, as this is most suitable for „Unity Gain“- filters (gain = 1).

The heart of the filter structure within here is the operational amplifier LTC6079 of Linear Technology. Its package is available in SSOP16 with a surface of approx. 30mm^2. They convince through very small offset of maximally 25µV, an extremely small drift of 0.7µV/°C, a very small noise and a low power consumption of 54µA per OpAmp. The exact characteristics can be found in the data sheet.

E. Calculation of the estimated power demand

Smart power calculates the power consumption of the entire FPGA, separated into individual modules and individual supply voltage rails. The operating frequency and the activity factor "alpha" are taken into account. This factor contains the amount of the statically power consumption and the energy dynamically needed by the single modules

within the system, which are active at different operating times. The value is set internally to 0.6 in the software tool.

F. Summary of Design Alternatives

Small circuit layouts can be obtained with all alternatives. Especially by using the SoC structure of the Actel FUSION FPGA only very few external components are needed. Other solutions need more external components and thereby more PCB space. The current consumption is around 30-40mA. Particularly the MSP430 is characterised by a very small supply current. But also the energy consumption of the FPGA board can be drastically lowered by using different current savings modes.

There are fundamental differences with the attainable miniaturization, regarding the current consumption and not least with the price. While microcontroller implementations are much more current-saving and low-priced, FPGAs offer more flexible solutions and usually smaller structures. With FPGAs it is possible to test different realization possibilities very fast. Finding thus the optimal solution, a microcontroller based approach is not always ideal in the development stage due to the fixed PCB layout and its proprietary pin assignment. The realization with the Actel FUSION FPGA pointed out that nearly a complete SoC with a Mixed-Signal FPGA can be realized. The restriction by the lower resolution of the internal A/D converters can be resolved by oversampling. The signals which shall be measured change temporally very slowly. Thus it is possible to reach an effective resolution of 16bit by oversampling, digital filtering and reduction. The capacity of the FPGAs offers sufficient memory to realize this filter in software. A further possibility to reduce the current consumption is to use sleep modes: After the measurement procedure followed by processing the data the FPGA could be set into sleep mode and – if needed further on– woken up again at the next measurement interval. The very high speed of operation makes it possible to spend approx. 60 per cent of the time in the sleep.

IV. CONCLUSIONS

Tests have been made with the developed FPGA solution together with the adaption circuitry for the multiparametric biosensor. The analogue signals could be detected without relevant noise. A Crosstalk analysis with impact on the reference voltage supply showed an average disturbance of 100µV. This has no impact on the resolution of the measurement values of the biosensor as the accuracy is determined by the sensor itself. In the handheld biosensor device

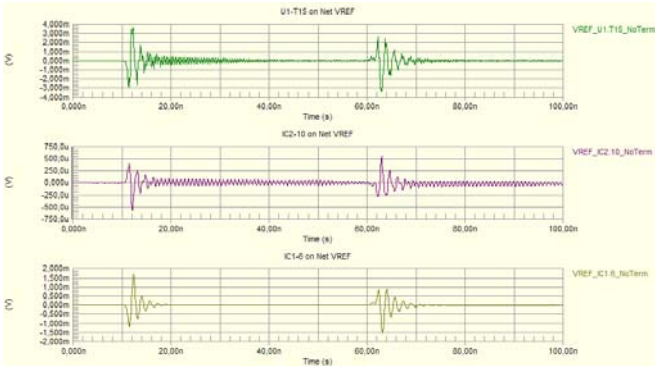


Fig. 3 PCB Crosstalk analysis of the reverence voltage signal network layer on peak disturbance of digital layers.

pH values can be distinguished up to 0.05, the oxygen sensor can detect changes in the medium with a resolution up to 5% (assuming 100% dissolved oxygen in the solution).

ACKNOWLEDGMENT

The authors want to thank the Heinz Nixdorf-Stiftung, the Bayerische Forschungsstiftung, SHZ Softwarehaus Zuleger GmbH, Sendsor GmbH, cellasys GmbH and Heraeus Sensor Technology for support of the project.

REFERENCES

1. B.Wolf, M.Kraus, M.Brischwein, R.Ehret, W.Baumann, M.Lehmann. Biofunctional hybrid structures - cell-silicon hybrids for applications in biomedicine and bioinformatics. Bioelectrochemistry and Bioenergetics, 1998, 46:215-25.
2. M.Brischwein, E.R.Motrescu, E.Cabala, A.M.Otto, H.Grothe, B.Wolf. Functional cellular assays with multiparametric silicon sensor chips. Lab Chip, 2003, 3:234-40.
3. L. Bousse Whole cell biosensors. Sensors and Actuators, B-Chemical, 1996, 34:270-275.
4. J.Wiest, T.Stadthagen, M.Schmidhuber et al. Intelligent Mobile Lab for Metabolics. Analytical Letters, 2006, 39,8:1759-1771.
5. Dissertation T. Stadthagen: Entwicklung eines online Gewässermonitoringsystems mittels Biosensorchips zum Nachweis ausgewählter Xenobiotika, 2007.
6. A.M.Otto, M.Brischwein, E.R.Motrescu et al. Chips statt Mäuse: Zellen auf bioelektronischen Sensorchips als Alternative zu Tierversuchen. ALTEX, 2004, 21:70-6.

Author: Michael Schmidhuber
Institute: Heinz Nixdorf-Lehrstuhl für Medizinische Elektronik
Street: Theresienstr. 90, Bld. N3
City: D-80333 München
Country: Germany
Email: schmidhuber@tum.de

Nanomaterial based electrochemical transducing platforms for biomedical applications

A. de la Escosura-Muñiz[1,2], A. Ambrosi[1], M. Maltez[1], B. Pérez-López[1], S. Marín[1], A. Merkoçi[1,3]

[1] Nanobioelectronics and Biosensors Group, Institut Català de Nanotecnologia, Barcelona, Spain
[2] Instituto de Nanociencia de Aragón, Universidad de Zaragoza, Zaragoza, Spain
[3] ICREA, Barcelona, Spain

***Abstract*— Recent advances of our research in the development of novel nanomaterial based electrochemical transducing platforms for biomedical applications are outlined. The objective has been to design platforms with interest for future applications in low cost, user-friendly and efficient electrochemical based sensors and biosensors that can be used even by non professional people for fast diagnostic at home or doctor's office as well as other applications where either an emergency exists or an alternative method toward the sophisticated and expensive laboratory instrumentation is being required.**

Keywords— **Biosensors, nanomaterials, nanoparticles, carbon nanotubes, lab-on-a-chip, screen-printing technology, electrochemical detection.**

I. INTRODUCTION

Nanotechnology based biosensors represent a novel generation of biosensors in the cutting edge technologies such as biotechnology and nanotechnology. In the medical diagnostics area, nanotechnology-based biosensors could be used, for example, to replace more costly and tedious laboratory methods for monitoring a patient's blood for proteins, chemicals, and pathogens. The research in this area aims to be the driving force for analytical oriented applications of current nanotechnology and nanoscience research.

The objective in this area is to study the biocompatibility of nanomaterials along with their properties such as: a) ability to be immobilized onto several electrodic transducing platforms so as to generate a high-conductive surface area interface that enables the sensitive / catalytic detection of ionic, molecular and biomolecular analytes; b) ability to act as effective labels for the amplified simultaneous analysis of analytes; c) possibility to enable the design of biomaterial architectures with pre-designed and controlled electrochemical functions ability including switching on-off properties that can easily be applied for several bioelectronics based detection systems that involve biomolecules such as DNA, proteins, cells and other receptors; d) ability to be integrated into novel lab-on-a-chip systems with interest for in-field screening of analytes along with other applications; e) ability to be integrated into nanobioelectronic based actuators / devices including nanomotors with special interest in future f or connection of biosensing / diagnostics with drug delivery / therapy applications. Both top-down and bottom-up approaches to develop nanobioelectronics based (bio)sensors and biodevices will be used.

II. DESIGN, PREPARATION AND CHARACTERIZATION OF NANOMATERIALS FOR SENSORS AND BIOSENSORS APPLICATIONS

Quantum Dots with electrochemical properties [1] as well as other nanoparticles with special interest for biosensor applications have been developed. Different methods of synthesis for the production of electroactive nanocrystals (NCs) for use as labels in bioensing systems are being used. They are based on two general ways of controlling the formation and growth of the nanoparticles: (a) physical restriction of the volume available for the growth of the individual nanoparticles by using templates such as reverse micelles; (b) arrested precipitation that depends on exhaustion of one of the reactants. Simple strategies for producing silver and gold nanoparticles (AgNP and AuNP) along with the corresponding core shell nanoparticles (Au–Ag and Ag–Au) by reduction of the metal salts are also used [2].

The obtained NPs are characterized by transmission electronic microscopy (TEM), UV–Vis absorption spectroscopy as well as electrochemical methods so as to see their future applications in sensing and biosensing including DNA sensors and immunosensors.

Alternative detections of nanoparticles with interest for future applications in biosensing systems are being studied too. ICP-MS, for example, offers great opportunities for such applications [3].

In figure 1 are shown some images and diagrams related to the synthesis and characterizations of nanoparticles.

O. Dössel and W.C. Schlegel (Eds.): WC 2009, IFMBE Proceedings 25/VIII, pp. 41–44, 2009.
www.springerlink.com

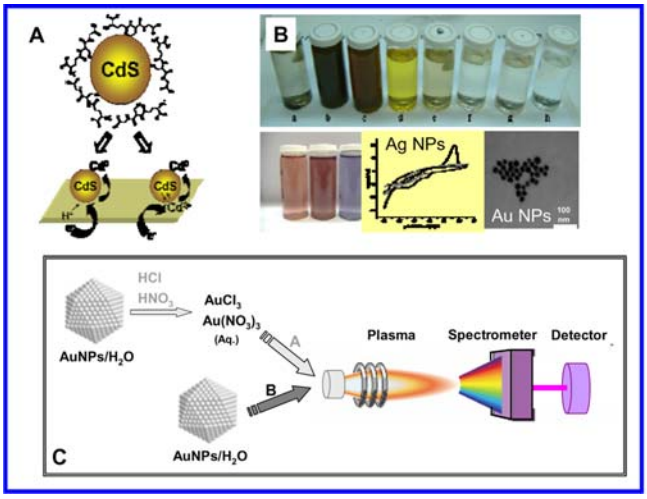


Figure 1: Synthesis and characterization of nanoparticles for biosensing. Scheme of quantum dots (CdS) electrochemical detection (A); different solutions of nanoparticles, electrochemical signal from silver nanoparticles and a TEM image of gold nanoparticles (B); scheme of gold nanoparticles detection using ICP-MS (C).

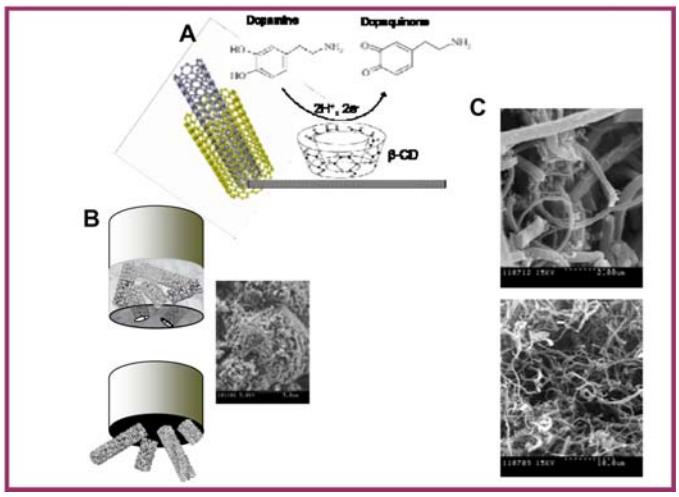


Figure 2: Scheme of the electrochemical fundament and some SEM images of electrochemical sensors based on carbon nanotubes for the detection of dopamine (A) and NADH (B,C).

III. ELECTROCHEMICAL SENSORS BASED ON CARBON NANOTUBES

The ability of carbon nanotubes to be immobilized onto several electrodic transducing platforms so as to generate a high-conductive surface area interface that enables the sensitive / catalytic detection of biomolecular analytes is studied. The introduction of CNT with catalytic properties into electrochemical sensors and biosensors decrease overpotentials of many analytically important electrochemical reactions, and even realize the reversibility of some redox reactions, which are irreversible at common unmodified electrodes.

The improvement of the performance (sensitivity, selectivity, response range etc.) of various kinds of biosensors with special interest in applications in clinical analysis, i.e. for the detection of dopamine [4] and NADH [5,6] have been achieved. Some schemes and images related with these studies are shown in figure 2.

IV. NANOPARTICLE BASED ELECTROCHEMICAL DETECTION (BIO)SYSTEMS AND BIOSENSORS FOR DNA, PROTEIN AND CELL DETECTION WITH INTEREST FOR USER-FRIENDLY DIAGNOSTICS, SECURITY AND QUALITY CONTROL FOR VARIOUS APPLICATIONS

DNA sensors and immunosensors are playing a growing role in various fields where an accurate, low cost, fast and on-line measuring system is required. To improve the electrochemical assay sensitivity and to achieve a better and more reliable analysis there is a great demand for labels with higher specific activity.

The most used labels for electrochemical sensors up to date have been enzymes as well as small molecules like electroactive indicators (dyes, etc.). In principle nanoparticles provide a novel platform for improving specific activity of a label as well as affinity to the tracer molecules (DNA probes or other biomolecules). Nanosized particles have a chemical behavior similar to small molecules and can be used as specific electrochemical labels. Nanoparticles in general and quantum dots (QDs) particularly, may be expected to be superior in several ways. Compared to existing labels, nanoparticles in general and QDs especially, are more stable and cheaper. They allow more flexibility, faster binding kinetics (similar to those in a homogeneous solution), high sensitivity and high-reaction rates for many types of multiplexed assays, ranging from immunoassays [7] to DNA analysis [8-10] and cell analysis. In addition the use of electrocatalytic effects of nanoparticles (i.e. AuNP electrocatalysis to silver enhancement) have been successfully applied [11]. Recently a similar indirect detection method, based on catalytic effects of AuNP, has been also applied to detect tumor cells.(ICN Patent, 2008, Submitted). Some images and schemes related with this application are shown in figure 3.

These biosensors have a great interest for future applications in genetic screening for cystic fibrosis or other similar cases. Binding nanoparticles to a specific antibody for cancer cells could make cancer detection much easier. Based on these ideas specific optical & electrochemical biosensors are being designed.

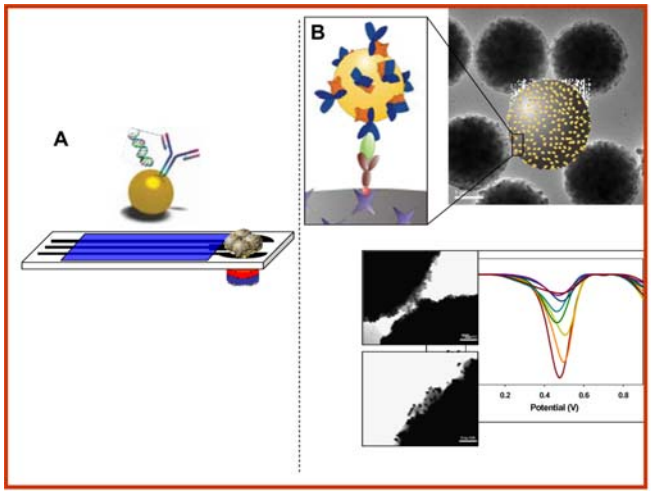


Figure 3: Scheme of the cell analysis based on gold nanoparticles (A); scheme of the magnetosdandwich assay developed for protein detection, some TEM images and the electrochemical signal form gold nanoparticles (B).

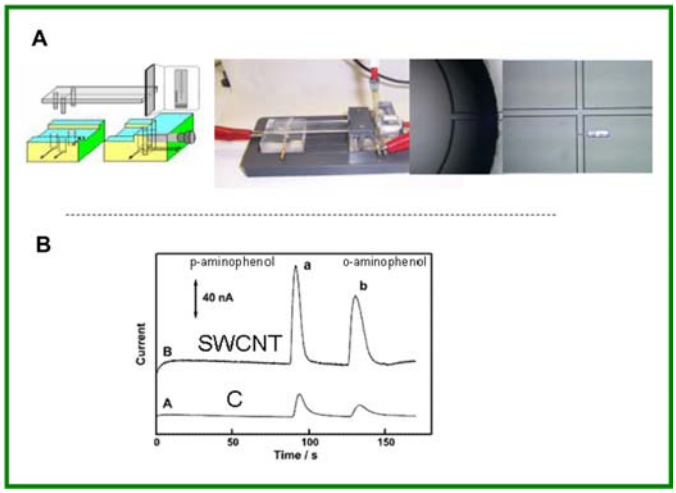


Figure 4: Scheme of the developed lab-on-a-chip systems (A); electropherograms for analytes separation/detection, and the improving of using carbon nanotubes modified electrodes (B).

V. LAB-ON-A-CHIP SYSTEMS WITH INTEREST FOR IN-FIELD SCREENING OF ANALYTES AND OTHER APPLICATIONS

Lab-on-a-chip (LOC) technology, based for example on capil-lary zone electrophoresis with electrochemical detection offers tremendous potential for obtaining desired analytical information in a simpler, faster and cheaper way compared to traditional batch/laboratory-based technology. It is par-ticularly attractive for multiple DNA recognition applica-tions (i.e. point-of-care) thanks to the high-throughput, automation, versatility, portability, re-agent/sample economy and high-performance of such mi-cromachined devices.

The LOC research aims to create and characterize portable bioanalytical systems where nanoparticles and carbon nanotubes, bringing special advantages, will be involved. In this way, a microchip system for the detection of neurotransmitters has been reported [12]. In figure 4 are shown some figures and schemes related to this study.

The developed systems will be able to perform "point-of-care" analysis with interest in clinic analysis between other fields. The developed lab-on-a-chip devices hold special interest in space exploration and will be carried out in collaborations with specialized institutes. It represents also a novel analytical technology in the context of systems biology to a better understanding of health and disease and intervention strategies and will be developed in collaboration with other institutes

VI. CONCLUSIONS

Novel nanomaterials for biosensors applications along with novel biosensor designs with interest for health protection are being developed. The promising results obtained for synthetic samples open the door to further applications in real clinical samples with interest for the rapid, simple and low cost diagnostics.

ACKNOWLEDGMENT

MEC (Madrid) for the projects MAT2008-03079/NAN, CSD2006-00012 ''NANOBIOMED'' (Consolider-Ingenio 2010) and Juan de la Cierva scholarship (A. de la Escosura) is acknowledged.

REFERENCES

1. Merkoçi A, Marcolino-Junior LH, Marín S, Fatibello-Filho O, Alegret S (2007) Detection of cadmium sulphide nanoparticles by using screen-printed electrodes and a handheld device. Nanotechnology 18, 035502.
2. Douglas F, Yañez R, Ros J, Marín S, de la Escosura-Muñiz A, Alegret S, Merkoçi A (2008) Silver, gold and the corresponding core shell nanoparticles: synthesis and characterization. Journal of Nanoparticle Research 10, 97–106.
3. Allabashi R, Stach W, de la Escosura-Muñiz A, Liste-Calleja A, Merkoçi A (2009) ICP-MS: a powerful technique for quantitative determination of gold nanoparticles without previous dissolving. Journal of Nanoparticle Research, DOI 10.1007/s11051-008-9561-2.
4. Alarcón-Angeles G, Pérez-López B, Palomar-Pardave M, Ramírez-Silva MT, Alegret S, Merkoçi A (2008) Enhanced host–guest electrochemical recognition of dopamine using cyclodextrin in the presence of carbon nanotubes. Carbon 46, 898 –906.

5. Pumera M, Merkoçi A, Alegret S (2006) Carbon nanotube-epoxy composites for electrochemical sensing. Sensors & Actuators B 113, 617–622.
6. Pérez-López B, Sola J, Alegret S, Merkoçi A (2008) A Carbon Nanotube PVC Based Matrix Modified with Glutaraldehyde Suitable for Biosensor Applications. Electroanalysis 20, 603 – 610.
7. Ambrosi A, Castañeda MT, Killard AJ, Smyth MR, Alegret S, Merkoçi A (2007) Double-Codified Gold Nanolabels for Enhanced Immunoanalysis. Analytical Chemistry 79, 5232-5240.
8. Pumera M, Castañeda MT, Pividori MI, Eritja R, Merkoçi A, Alegret S (2005) Magnetically Trigged Direct Electrochemical Detection of DNA Hybridization Using Au67 Quantum Dot as Electrical Tracer. Langmuir 21, 9625-9629.
9. Castañeda MT, Merkoçi, A, Pumera M, Alegret S (2007) Electrochemical genosensors for biomedical applications based on gold nanoparticles. Biosensors and Bioelectronics 22, 1961–1967.
10. Marín S, Merkoçi A (2009) Direct electrochemical stripping detection of cystic-fibrosis-related DNA linked through cadmium sulfide quantum dots. Nanotechnology 20, 055101.
11. De la Escosura-Muñiz A, Maltez-da Costa M, Merkoçi A (2009) Controlling the electrochemical deposition of silver onto gold nanoparticles: Reducing interferences and increasing the sensitivity of magnetoimmuno assays. Biosensors and Bioelectronics, In press.
12. Pumera M. Llopis X, Merkoçi A, Alegret S (2006) Microchip Capillary Electrophoresis with a Single-Wall Carbon Nanotube/Gold Electrochemical Detector for Determination of Aminophenols and Neurotransmitters. Microchim Acta 152, 261–265.

Author: Arben Merkoçi
Institute: ICREA & Institut Català de Nanotecnologia
Street: ETSE - Campus UAB
City: Bellaterra - Barcelona
Country: Spain
Email: arben.merkoci@cin2.es

Sensor chips for multiparametric real time monitoring of cell metabolism and drug response

M. Zottmann[1], J. Wiest[2], T. Flurschütz[1], M. Schmidhuber[1], B. Wolf [1]

[1] Heinz Nixdorf Lehrstuhl Medizinische Elektronik, Technische Universität München, Deutschland
[2] cellasys GmbH, München, Deutschland

Abstract— **Monitoring of metabolic parameters like O_2-consumption and extracellular acidification provides first line information of cell vitality and effects responding to drug addition. For this purpose, a bioelectronic test system based on multiparametric sensor chips has been developed. Cells are directly cultivated on the sensor chips which possess sensors for pH and pO_2 measurement and two IDES-sensors for additional detection of cell impedance changes. A fluidic system supplies the cell culture with fresh medium and enables addition and removal of test substances. Sensors are read out in real-time and data is converted to rates of O_2-consumption and extracellular acidification. Individual cell cultures can be monitored continuously from hours up to weeks. For experiments, the human cell line MCF-7 was treated with different concentrations of cisplatin (5µM and 10µM) and monitored for three days. For comparison, a WST test and cell count was performed in standard cultures every 24 hours. With the sensor chips first drug mediated effects were detected after 15 hours. In contrast to WST assay or CASY cell count with a series of end point measurements, sensor chips allow detection of drug mediated effects online and in real time.**

Keywords— **sensor chips, real time monitoring, cisplatin, MCF-7**

I. Introduction

Test series with cellular assays are an inevitable step for research and development of new drugs. A variety of test assays based on different cell parameters like cell count, DNA synthesis or staining of global cell components are presently in use for the screening of drug efficiency. The disadvantage of these standard methods is the impairment of cell vitality or requirement of cell death, respectively. Hence, a follow-up of the drug effects or a kinetic analysis need multiple parallel cultures depending on the number of time points to be analyzed.

In contrast to assays with a series of end point measurements, sensor chips allow detection of drug mediated effects online and in real time [1]. As cells will respond to modulations in their signaling network by adjusting their energy metabolism [2], the introduced bioelectronic test system makes use of the analysis of changes in metabolic activity and morphology in individual cell cultures.

II. Materials and Methods

A. Cellchip system

The IMOLA (Intelligent MObile LAb) is a mobile device with integrated life support system for measurement setups with biochips (Fig. 1). Cells are directly cultivated on ceramic-based multiparametric sensor chips (Biochip-C), which are inserted in the IMOLA and connected to the fluidic perfusion system. In current experiments six IMOLAs were used in parallel to receive redundant data. A laptop or PC using the IMOLA software allows to configure the measurement settings via wireless data transmission and stores the collected data.



Fig. 1: IMOLA module with supply and waste bottle.

The cell culture area on the chip has a diameter of 6 mm and includes the various sensor types (Fig. 2). Cells are growing directly on the sensors. During measurements, the height of the culture volume is adjusted by a spacer ring to 0.2 mm, which results in a fixed total volume of 7 µl. A high number of cells in this small volume enables quick and sensitive recording of cell metabolic rates [3]. The fluidic system is connected to a perfusion pump, which exchanges the medium of the culture volume in a stop & go mode.

O. Dössel and W.C. Schlegel (Eds.): WC 2009, IFMBE Proceedings 25/VIII, pp. 45–48, 2009.
www.springerlink.com

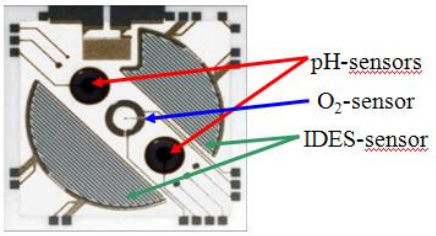


Fig. 2: Biochip-C with sensors for pH, pO_2 and impedance measurement.

Cellular vitality is determined by measuring the respiration of O_2 (mitochondrial activity) and extracellular acidification. For measurement of the pH value a metal oxide sensor is used. Changes in dissolved oxygen are measured by a three electrode amperometric dissolved oxygen sensor [4]. Cell proliferation and changes in adhesion forces of the cell culture are determined with an interdigitated electrode structure (IDES) [5], which uses a 100mV AC signal with 10 kHz. A Pt1000 sensor allows readout of the temperature on the chip.

B. Cells and media

The human adherent mamma carcinoma line MCF-7 was used. For experiments, cells were trypsinized and seeded on the chips at $3*10^4$ cells per chip in 300µl DMEM (Dulbecco´s modified eagle medium) with 5% FCS and 3.7 g/l $NaHCO_3$. Chips were then incubated under standard conditions (37°C, 10% CO_2) until the measurement started.

During the measurements, modified culture medium (DMEM with 5% FCS and 50 µg/ml gentamicin, without $NaHCO_3$) was used to ensure sensitivity of pH measurement. Chemicals were purchased from Sigma.

C. Drugs

Cisplatin is an alkylating-like chemotherapeutic substance used for the treatment of a variety of cancer types. Platinum complexes cause cross linking of DNA, interfering with cell division by mitosis, and blocks DNA-repair mechanisms, which results in a cytostatic effect. For experiments, concentrations of 0.1 up to 10 µM were used.

D. Experiments

MCF-7 cells were seeded directly on the biochips at a number of $3*10^4$ cells in 300µl culture medium. The biochips were placed in a petridish and incubated for 3 days under standart conditions until subconfluence of about 80% was reached.

On the 4th day chips were prepared for measurement with the IMOLA. First cell growth on the chips was controlled using a reflected light microscope. Spacer rings and fluidic heads were added to the chips, reducing the volume of media in the cell chamber to 7µl. Chips were inserted in the IMOLA, connected to the fluid perfusion system and the measurement was started. After 18 to 24 hours cisplatin was added in two different concentrations (5 and 10 µM).

E. WST-Test and cell count

WST-test is based on the reduction of WST-1 to the colorimetrically differentiated formazan, catalyzed by mitochondrial reductase in active cells. The amount of formazan dye was quantified by measuring the absorbance at 450 nm in a multiwell plate reader. Cell count was accomplished after WST-test with a CASY-cell counter.

Cells were seeded on four 24-well-plates at a number of $0.5*10^4$ cells in 500µl medium per well. After an incubation period of 3 days cisplatin was added at concentrations of 0.1 up to 10 µM. As a control, 3 wells were left without drug.

III. RESULTS

A. Measurements with sensor chips

The cellular respiration and extracellular acidification of MCF-7 cells growing on sensor chips was monitored for 3 days. After 18 hours, supply bottles with fresh medium containing 0, 5 or 10 µM of cisplatin respectively, were affiliated to the IMOLA modules. Figure 3 shows the extracellular acidification rates of three MCF-7 cultures treated with the different drug concentrations.

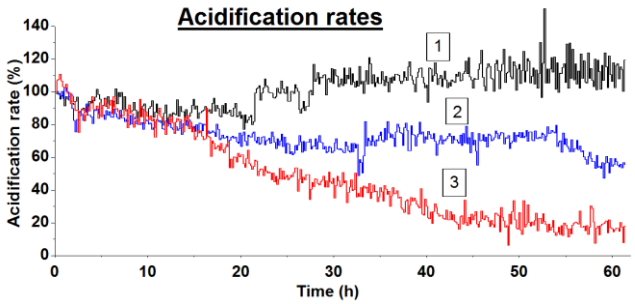


Fig. 3: Acidification rates of MCF-7 cultures on sensor chips. Signals of cultures without drug addition (1), 5µM cisplatin (2) and 10 µM cisplatin (3).

The control culture with no cisplatin added displays a continuing gain of acidification to the end of the measurement. Both cultures with drug addition show a does-

dependent constant decrease of acidification rates after a lag phase of 15 hours.

B. WST-test and cell count

After three days of incubation, cisplatin was added in concentration from 0.1 up to 10 µM to the 24-well-plates. First WST-test and cell count was accomplished on the day of drug addition to receive values of cultures before treatment. Subsequently, WST-Tests and cell count was performed every 24 hours. Figure 4 and 5 show the results of both test methods. For comparison to sensor chip results, only data of 5 and 10 µM are presented.

WST-test reveals a constant increase of cell activity in control wells without drug addition and in wells treated with 5 µM of cisplatin, with a smaller accession of activity at 5µM cisplatin. Cell activity increase in wells treated with 10 µM of cisplatin stagnates after two days.

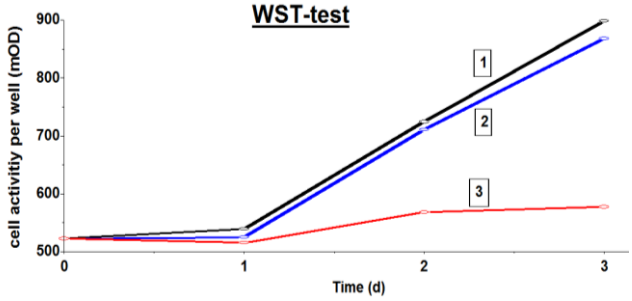


Fig. 4: Cell activity measured by WST-test.
Data of wells without drug addition (1), 5µM cisplatin (2) and 10 µM cisplatin (3).

CASY-cell count yields a constant increase of cell number in wells without drug addition, while both drug concentrations show a reductive effect on cell proliferation. There is stagnation of cell number in wells treated with 5 µM and a minor reduction in wells with 10 µM of cisplatin.

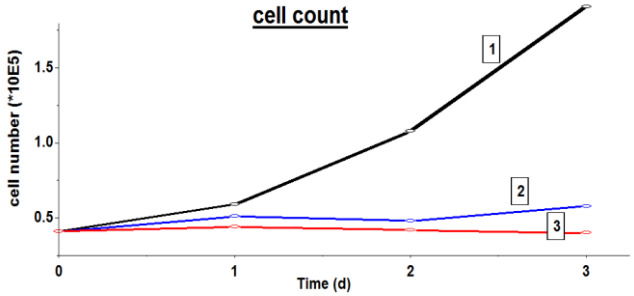


Fig. 5: Cell number measured with CASY. Data of wells without drug addition (1), 5µM cisplatin (2) and 10 µM cisplatin (3).

Both methods showed distinct differences between drug treated and control cultures after more than 24 hours.

IV. DISCUSSION

The presented results are a comparison of standard cellular assays and a novel test method based on multiparametric sensor chips. While cell count via CASY evaluates drug effects by the number of surviving cells, WST-test measures the activity of a cell culture determining the activity of mitochondrial reductases. The presented sensor chips allow for determination of changes in cell energy metabolism via measurement of extracellular acidification and respiration online and in real time. All test methods showed a response of MCF-7 cells to the addition of cisplatin at concentrations of 5 and 10 µM.

Results of CASY cell count showed a dose dependent diminution of cell proliferation in wells treated with cisplatin. This agrees with cisplatin having a disruptive effect on cell division. Wells with 10 µM of cisplatin even show a continuous decline in cell number after 24 hours of treatment.

In contrast to CASY results, WST-test does not indicate a distinct effect on cells treated with 5µM cisplatin. The mitochondrial reductases activity in wells with 5µM is close to the activity in control cultures, whereas wells with 10 µM cisplatin only show a neglect able increase of activity after drug addition. This effect can not jet be explained, but a calculation of activity / cell reveals a dose dependent increase of single cell activity with increasing cisplatin concentration (data not shown).

Real time measurements with sensor chips describe a dose dependent effect of the tested drug on MCF-7 cells. After a lag phase of 15 hours, cell cultures treated with cisplatin reduce the extracellular acidification rates while the rates of the control culture continue to increase. This is coherent with metabolism kinetics described in previous papers [6].Compared with WST test data, there is a distinct difference between activity of cultures with 5µM and control cultures. IDES sensors also showed a decrease in surface coverage, indicating a reduction of cell number (data not shown).

V. CONCLUSIONS

The known sensitivity of MCF-7 cells on cisplatin and dose dependent effects could be shown with all three test methods. Compared to both standard tests, which were carried out every 24 hours, multiparametric sensor chips allow online monitoring of an individual cell culture in real

time. Thus, first effects of the chemotherapeutic drug could already be recognized after 15 hours.

Sensor chip test systems are suitable tools for a variety of applications like pharmaceutical drug screening or environmental monitoring. One main target for future application is personalized cancer therapy. Predictive chemosensitivity assays with individual cancer biopsy material could avoid unnecessary chemotherapeutic treatment and allow selection of more effective drugs prior to the beginning of the chemotherapy.

Acknowledgment

Authors would like to thank cellasys GmbH and HP Medizintechnik for their support.

References

1. B. Wolf et al. (1998) Biofunctional hybrid structures – cell-silicon hybrids for applications in biomedicine and bioinformatics. *Bioelectrochemistry and Bioenergetics*, 46, 215-225
2. M. Kraus, B. Wolf (1996) Implications of Acid Tumor Microenvironment for Neoplastic Growrh and Cancer Treatment: A Computer Analysis. *Tumor Biology*, 17, 133-154
3. J. Wiest, T. Stadthagen et al (2006) Intelligent Mobile Lab for Metabolics in Environmental Monitoring. *Analytical letters*, 39: 1759-1771
4. J. Wiest, M. Brischwein et al. (2005) Planar Microsensors for Measurement of Cellular Respiration. *SENSOR 2005 Proceedings II*, 249-254
5. J. Ressler et al. (2004) New concepts for chip-supported multi-well-plates: Realization of a 24-well-plate with integrated impedance-sensors for functional cellular screening applications and automated microscope aided cell-based assays, *Proceedings of the 26th Annual International Conference of the IEEE EMBC*; 2074-2077
6. A. M. Otto, M. Brischwein, E. Montrescu, B. Wolf (2004) Analysis of Drug on Tumor Cell Metabolism Using Electronic Sensor Chips. *Arch. Pharm. Pharm. Med. Chem*., 337, 682-686

Author: Marlies Zottmann
Institute: TU München, Heinz Nixdorf-Lehrstuhl für medizinische Elektronik
Street: Theresienstr. 90
City: 80333 München
Country: Germany
Email: zottmann@tum.de

Microfluidic platform for the initiation and investigation of cellular interactions on a single-cell level

M. Kirschbaum, M.S. Jäger and C. Duschl

Fraunhofer Institute for Biomedical Engineering, 14476 Potsdam, Germany

Abstract— **Cellular interactions as they occur in the stem cell niche or in context with leukocyte activation are effective mechanisms for the regulation of cellular states *in vivo*. The analysis of the underlying principles is of high clinical interest. Unfortunately, conventional applications used for addressing the related questions often pool biological data of cellular subpopulations or provide only end point analyses of signal transduction processes. This leads to blurred data or ignores important information from the dynamics of cellular behaviour, respectively. Here, we present a novel microfluidic platform for the initiation and analysis of cellular interactions on a single-cell level. We used the system to stimulate single T cells with anti-CD3/anti-CD28-presenting microbeads and analyzed the cytosolic calcium signal simultaneously. T cell activation was examined 16 - 24 h after stimulus presentation and was correlated with the previously recorded calcium signal. A significant difference between the calcium patterns of activated and non-activated cells was detected. This shows that the dynamics of a cellular response can provide useful information about the specific physiological state of a cell. The described technique accounts for this finding and could help to diversify our view of intercellular communication.**

Keywords— **T cell activation, single-cell manipulation, calcium imaging, lab-on-a-chip, dielectrophoresis.**

I. Introduction

Controlling cellular states of *e.g.* stem- or immune cells is one of the most challenging fields of biomedical research and is assumed to be mediated by interaction of the cells with specific surface molecules present in their microenvironment. Although intensively investigated, the underlying mechanisms of activation or differentiation processes are still poorly understood [1]. However, the investigation of the involved signaling cascades is difficult and often constrained by insufficient techniques that pool biological data of thousands of cells. This leads to blurred results and a loss of important information about differences in timing and response patterns of individual cells. To overcome these limitations, investigation on a single-cell level is strongly desired. However, working with single cells over prolonged periods of time is demanding, in particular with non-adherent cells like lymphocytes. Moreover, the investigation of cell- or surface-mediated signal transduction processes in these cells requires (i) cell handling to be contactless because the manipulation with mechanical forces runs the risk of initiating undesired signaling cascades and (ii) to make the stimulated single cells available for a broad spectrum of downstream analyses after their manipulation.

Here, we present a novel dielectrophoresis-based microfluidic chip system that allows the contactless manipulation of single cells with very high accuracy. The technique enables to initiate cell-cell or cell-surface interactions on a single-cell level and to analyze the immediate cellular reactions to the stimulus simultaneously. Additionally, the cells can be isolated from the fluidic system so that long-term responses can be evaluated several hours or days after stimulus presentation. This enables to observe and to control the complete signal transduction process from stimulus presentation up to late events in the signaling cascade like protein expression or proliferation.

In order to demonstrate the potential of the system, we used T cell activation as an example of surface-mediated cell programming. T cells can be activated by contacting them with antibodies against the T cell receptor complex [2] (TCR). TCR engagement leads to a rapid rise of the cytosolic calcium level which mobilizes transcription factors that modify protein expression [3]. The shape of the cytosolic calcium signal depends on numerous factors like calcium buffers, mitochondria, and K^+ channels [4] and thus, can provide important information about the physiological state of an individual cell. Several hours after bead stimulation, analysis of T cell activation is possible by detecting the activation marker molecule CD69 in the outer leaflet of the cell membrane [5, 6].

We used anti-CD3/anti-CD28-presenting microbeads to trigger activation of single Jurkat T cells. We monitored the cytosolic calcium level simultaneously and deposited the cells into a microplate after imaging procedure. Activation of the cells was analyzed after over night incubation and was matched with the previously recorded calcium pattern. To our knowledge, this is the first time that short term calcium signals were related to long term responses, *i.e.* the expression of membrane proteins, on a single-cell level.

II. Materials and Methods

Cells: Cultivation of Jurkat T lymphocytes E6.1 was previously described [7]. For calcium imaging, 10^6 cells / ml were loaded by incubating them for 1 h in 2 µM Fura-2/AM (Invitrogen) at RT. After that, the cells were washed and used within the next 2 h. Vitality and activation state of the chip-manipulated cells was analyzed after over night incubation in a microwell. The cells were stained with 2 µg ml^{-1} anti-CD69:FITC (BD Biosciences) for fifteen minutes and analyzed in a LSM510 (Zeiss, Oberkochen, Germany). Cells were counted as vital if they showed a spherical mor-

O. Dössel and W.C. Schlegel (Eds.): WC 2009, IFMBE Proceedings 25/VIII, pp. 49–52, 2009.
www.springerlink.com

phology without blebs in the brightfield image. T cells were counted as activated, if their outlines were visible in the fluorescence image.

Beads: Particles for triggering T cell activation were produced by coating 10 µm polystyrene beads with anti-CD3 and anti-CD28 antibodies (Diaclone) as described elsewhere [7].

Chips: Microchips were described in detail earlier [7]. Briefly, they are produced by sandwiching a 30 µm thick SU-8 polymer between two glass slides so that the resist forms the sidewalls of a microchannel. The inner faces of the top and bottom slides of the channel are equipped with congruent, 15 µm wide microelectrodes. For dielectrophoretic manipulation, a radio-frequency generator (Cytocon 400, Evotec Technologies GmbH, Hamburg, Germany) is used to apply an a.c. voltage of 1 – 5 MHz to these electrodes. This creates an inhomogeneous field that prevents cells and particles from passing between them. Depending on the shape of the electrode structure, particles are held against the fluid flow or shifted laterally and thus, can be positioned in the microchannel. Inlets and outlets of the channel are connected to standard HPLC tubing. Syringe pumps (WPI, Berlin, Germany) were used to control fluid flow in the microchannel.

Calcium imaging: Intracellular calcium concentration of the Fura-loaded cells was detected by ratiometric fluorescence microscopy (excitation at 340 nm and 380 nm; emission at 515 nm; Cell-R, Olympus, Hamburg, Germany). Calcium traces were analyzed for the parameters *response latency* (*i.e.* the time between contact formation and initial calcium rise), *maximum peak height* (*i.e.* the maximum value of the calcium trace between initial calcium rise and subsequent decay) and rising time (*i.e.* the time between initial calcium rise and maximum peak).

III. Results

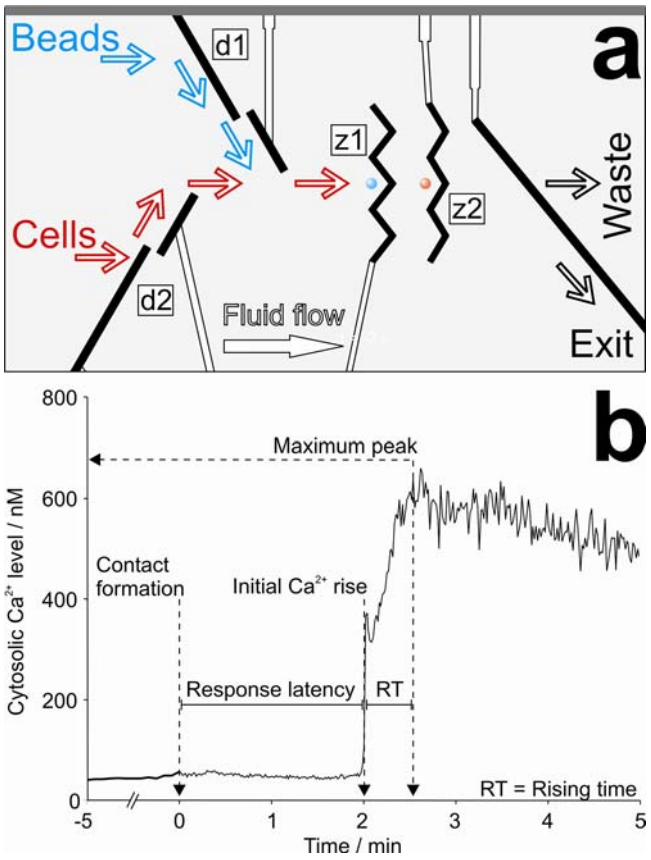


Fig. 1 Pair formation procedure. (a) Fura-loaded cells and beads enter the chip through two separate inlets and are transported hydrodynamically to the central part of the channel. Here, the dielectrophoretic deflection elements d1 and d2 are used to direct the particles to the consecutively arranged zigzag electrodes z1 (bead) and z2 (cell), where they are held against the fluid flow going from left to right. The cell-bead contact is initiated by inactivating electrode z1, so that the fluid flow shifts the bead towards the cell stored in zigzag electrode z2. $[Ca^{2+}]_i$ is monitored during the whole pair formation procedure. After calcium imaging, the cell-bead pair is directed to the exit of the channel and deposited into a well of a 96-well plate. Unprocessed particles are discarded to the waste outlet. (b) Typical course of a bead-induced calcium signal. Before contact formation, $[Ca^{2+}]_i$ is at baseline level. After initiation of the cell-bead contact it stays there for one or two additional minutes until it rapidly increases to several hundred nM followed by a slow decay. The traces were analyzed for the parameters *maximum peak height*, *response latency* and *rising time* (details see text).

A. General experimental procedure

Cells, particles and culture medium were brought into the dielectrophoresis chip through three separate inlets of the chip system. Due to the dimensions of the microchannel fluid flow is laminar, and thus, hydrodynamically transported particles moved in parallel trajectories. Dielectrophoretic manipulation of the particles took place in the central part of the channel. Here, cells and beads were contacted with each other, while the cytosolic calcium level ($[Ca^{2+}]_i$) was monitored simultaneously. While unprocessed particles were discarded to the waste outlet, the formed cell-bead pairs were directed to the sampling outlet of the channel, where a fast sheath flow accelerated them to the exit of the tubing system. There, the sheath flow formed a droplet that contained the cell-bead pair. By collecting the droplet in a microwell the pair was isolated from the fluidic system and cultivated further. Vitality and activation state of the cells were analyzed the next day and matched with the previously recorded calcium signal.

B. Pair formation procedure and calcium imaging

After having been forwarded to the central part of the microchannel, cells and beads approached deflection electrodes d1 and d2, respectively. These electrodes were used to direct both, single beads and cells to the zigzag electrodes z1 and z2, respectively (Fig. 1a). Here, the two particles were stored for 5 min. while $[Ca^{2+}]_i$ of the cell was analyzed in order to determine its baseline level. After this, the bead was released from its position and was hydrodynamically transported to zigzag electrode z2 with the cell stored there. As a consequence, cell and bead got into contact and formed a cell-bead pair. $[Ca^{2+}]_i$ was monitored continuously during the contact formation procedure.

A typical Ca^{2+} trace is shown in Fig. 1b. During the first five minutes before bead stimulation, the calcium concentration is at baseline level. After contact formation, it stays at baseline level for one or two additional minutes until it rapidly rises to a concentration of several hundred nM followed by a slow decay. The traces were analyzed for *maximum peak height*; *response latency* and *rising time* (see methods section for details).

C. Survival- and activation rate of the manipulated T cells

After over night incubation of the isolated cell-bead pairs, survival- and activation rates of the cells were analyzed. While 74% of all analyzed cells were vital one day after chip manipulation, 50% of all vital cells showed a brightly stained membrane after antibody staining against the activation marker molecule CD69 (Fig. 2c).

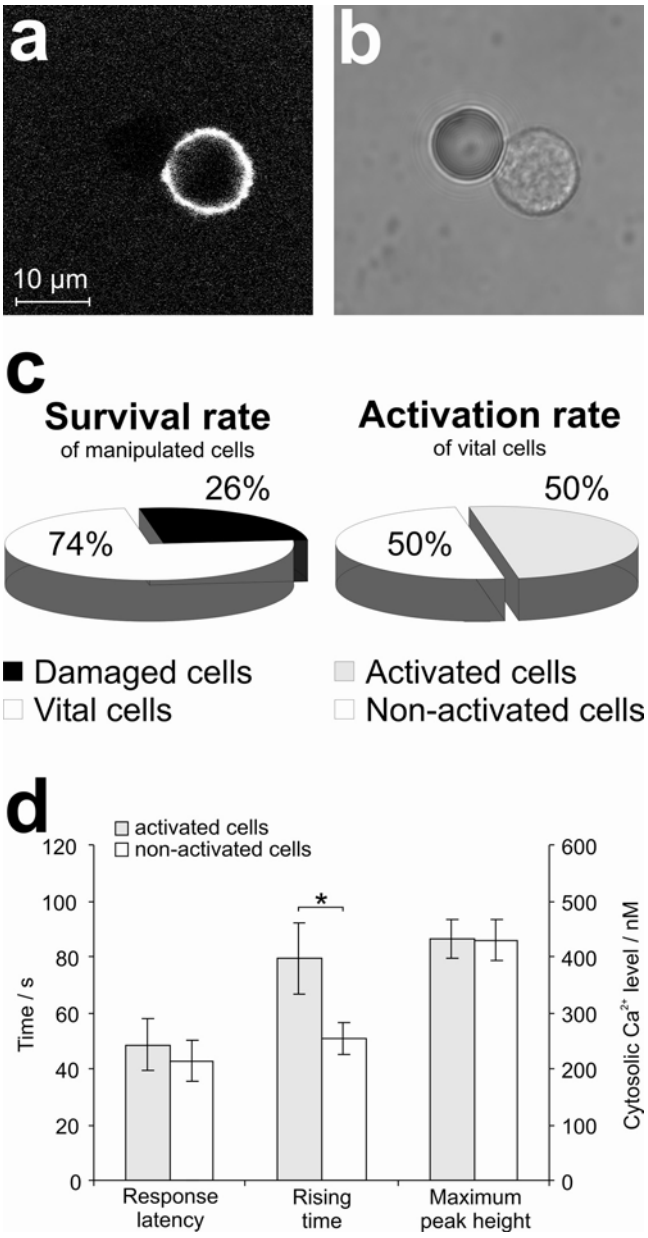


Fig. 2 Analysis of T cell activation. (a) Fluorescence image of an activated T cell after staining with fluorescently labeled antibodies against the activation marker CD69. (b) Corresponding brightfield image. (c) Survival- and activation rates of the bead-stimulated T cells were analyzed 16-24 h after their isolation from the chip system. While the vitality of all manipulated cells was analyzed, only vital cell were examined for their activation state. (d) Correlation of the calcium signal with T cell activation. The mean *response latency*, *rising time* and *maximum peak height* of the previously recorded calcium signals were evaluated for activated and non-activated T cells. Error bars, s.e.m.; n = 17; $*P < 0.05$.

D. Correlation of the calcium signal with T cell activation

To investigate, if the calcium signals elicited by bead stimulation provide early information about a later reaction of the cells, the previously recorded calcium signals of activated and non-activated cells were compared. While *response latency* (50 s vs. 43 s) and maximum *peak height* (430 nM

vs. 430 nM) differed only marginally in both populations, rising time was significantly increased in activated cells compared to non-activated cells (80 s vs. 51 s; $p < 0.05$; Fig. 2d).

IV. Discussion

We contacted single T cells with surface-modified microbeads in a novel lab-on-a-chip environment. The system provides particle manipulation at high resolution in both, a spatial and a temporal manner. This enabled us to monitor the cytosolic Ca^{2+} level before, during and after the contact formation procedure and to align it to the time point of bead contact at subsecond resolution. After the imaging procedure the manipulated cells were isolated from the fluidic system. This allowed us to cultivate them further, to analyze their activation state several hours after bead stimulation and to match the gained information with the previously recorded calcium signal. As a consequence, we detected a significant difference in the calcium traces of activated and non-activated cells. This shows, that calcium signals in T lymphocytes can provide early information about a later reaction of the cell.

The physiological compatibility of dielectrophoretic manipulation was described before [8] and is confirmed by the high survival rate of the bead-contacted single cells (74%) one day after manipulation.

Working on physiological cell models is very important in clinical research. Ongoing experiments show that the same approach can be used for the contact formation of arbitrary cell types like antigen-presenting cells and primary T cells (data not shown). Moreover, the system allows clustering of more than two cell types. This could be used for the creation of a defined microenvironment for individual cells and thus, could help to regulate stem cell differentiation in context with the formation of autologous tissue grafts.

V. Conclusion

We presented a novel microfluidic approach for the investigation of cell- or surface mediated signal transduction processes on a single-cell level. The big advantage of the described technique emerges from the possibility to precisely initiate cell-cell or cell-bead contacts in combination with the isolation of the manipulated cells from the chip system. This enables to analyze and to correlate short-term responses to a given stimulus (*e.g.* cytosolic calcium signals) with downstream analysis of the single cells on DNA, RNA or protein level several hours or days after their stimulation. Taken together, the described technique opens up new possibilities for the investigation of intercellular communication and therefore could lead to new insights into the mechanisms underlying lymphocyte activation or stem cell differentiation.

VI. Acknowledgments

For financial support we acknowledge the European Commission in the framework of the integrated Project "Cell-PROM" (NMP4-CT-2004-500039) and the German Research Foundation (DFG, FU 345/12-1). We thank Richard Kroczek (Robert Koch Institute, Berlin, Germany) for scientific advice, Steffen Howitz (GeSiM mbH, Grosserkmannsdorf, Germany) for chip processing support and Beate Morgenstern (Fraunhofer-IBMT, Potsdam, Germany) for cell culture assistance.

VII. References

1. Winslow MM, Crabtree GR (2005) Science 307:56-57
2. Frauwirth KA, Thompson CB (2002) J Clin Invest 109:295-299
3. Macian F (2005) Nat Rev Immunol 5:472-484
4. Quintana A, Griesemer D, Schwarz EC, Hoth M (2005) Pflugers Arch 450:1-12
5. Castellanos MC, Muñoz C, Montoya MC, Lara-Pezzi E, López-Cabrera M, de Landázuri MO (1997) J Immunol 159:5463-5473
6. Sancho D, Gómez M, Sánchez-Madrid F (2005) Trends Immunol 26:136-140
7. Kirschbaum M, Jaeger MS, Schenkel T, Breinig T, Meyerhans A, Duschl C (2008) J Chromatogr A 1202:83-89
8. Jaeger MS, Uhlig K, Schnelle T, Mueller T (2008) J Phys D: Appl Phys 41:175502

ESOPHAGEAL FLOW CONTROL MODULE FOR TREATMENT OF OBESITY

S.S.R.F. Rosa[1], J. C. Carvalho Júnior[4], L. M. Brasil[2], A.F. Rocha[3] and J. C. Carvalho[4]

[1] University of Brasília (UnB), Gama College (FGA), Gama, Brazil
[2] University of Brasília (UnB), Gama College (FGA), Gama, Brazil
[3] University of Brasília (UnB), Department Engineering, Brasília, Brazil
[4] University Federal of Goiás (UFG), Medicine Department, Goiânia, Brazil

Abstract — **Obesity is considered a serious public health problem. Many of the current methods for treatment involve surgery, but none of them offers completely satisfactory results. This paper presents a new approach to the treatment of obesity, which is based on a module that limits the flow in the esophagus without impairing food absorption or causing damage to the esophagus wall. The module was built using natural latex, and it had nearly a cylindrical shape, with a central lumen having a 1 cm radius. It was tested in a medium-sized canine. In the test, the module was placed in the region between the atlas and the fourth cervical vertebra. It was placed in the esophagus by videoendoscopy and remained in place for seven days. It was monitored by successive x-ray tests, and, finally, it was withdrawn by videoendoscopy. After that, a videoendoscopy exam demonstrated that there was no damage to the esophagus wall. Metabolic tests have shown that the module did not cause negative changes in the physiological parameters of the animal. Moreover, no behavioral changes in the dog were observed during or after the test. During the test, the animal lost 4.0% of its weight. These results suggest that the module has a good potential as a tool for obesity treatment.**

Keywords — **Esophagus, active implant, flow control, obesity.**

I. Introduction

Food ingestion in humans is influenced by non-biological variables that include social, economic, and cultural factors, as well as convenience and time of day. However, physical and biological factors such as sight, smell, taste and the metabolic state of the organism regulate appetite. In today's society there is a tendency for many people to overeat, which results in the so-called obesity disease. This is an important problem in public health due to its great prevalence and high recurrence rate.

Several treatment techniques for controlling obesity are described in the literature [1], [2], [3], [4] and each one has advantages and disadvantages. In [5] and [3], it is stated that about 65% of techniques are based on gastric bypass or gastroplasty with a "Y".

According to [6], this type of procedure is a mechanical factor of restriction of absorption which can lead to the reduction of exogenous hormones and to B_1 vitamin deficiency, which can cause Wernicke Encephalopathy Syndrome. Other less mentioned problems are also generated by obesity, such as psychological and social disturbances that are caused by a physical limitation, low self-esteem and difficulty in integrating into one's environment. Therefore, there is a real need to create other therapeutic techniques for controlling obesity, since the existing ones cannot achieve their expected goals without causing damage or requiring high costs.

In this article we propose a module for esophageal flow control (EFC), which is a new device for controlling weight that is applied to the esophagus without altering the digestive tract. This system should not affect the working of the hormonal mechanisms that are activated by the ingestion of food. The EFC promotes reduction in food flow, while preserving all the physiological processes of digestion. In the course of its development, it was defined that the module's material should have biocompatible physical and chemical characteristics and low antigenicity. Also, the module should be waterproof, flexible and be easy to apply and remove. With that in mind, the raw material extracted from natural rubber latex (*Hevea brasiliensis*), was chosen. This material is used in esophageal prostheses, among other applications [7].

II. Materials and methods

The goal was to develop the module and to test it in a medium-sized canine, in a 7 day period. The experiment would allow for preliminary testing of the technique as well as the identification of shortcomings of the module. These results should be useful for the further development of the module. In this section, we describe the different stages of this paper.

A) Manufacturing the EFC module

The raw material that was chosen was extracted from natural rubber latex, *Hevea brasiliensis*. From the natural

O. Dössel and W.C. Schlegel (Eds.): WC 2009, IFMBE Proceedings 25/VIII, pp. 53–56, 2009.
www.springerlink.com

latex, a final compound was prepared that has given the EFC module the essential characteristics of elasticity, smoothness, as well as being waterproof and hypoallergenic. This compound was achieved by the addition of chemicals in accordance with [7].

The module was prepared by taking the following steps: filtering and further dilution of the compound in bi-distilled water at a temperature of 20°C.

The module, shown in Figure 1a, was designed to fit the anatomy and characteristics of the wall tissue of the esophagus of a dog, especially the longitudinal grooves of the esophageal mucous membrane [7]. It has three distinct elements: the external and internal tubes, and the valve. This shape was proposed in such a way that the module could be submitted to a suitable pressure and have a coefficient of friction sufficient to keep the module positioned against the esophagus wall, without the need of another support technique.

The mould used for forming the external tube of the module was made from tubes of Tecnil (manufactured by DRACMA, São Paulo, Brazil), with dimensions of 15cm in length and 2cm in diameter, having eight external longitudinal grooves. This mould, with latex in its wall, is shown in Figure 1A. The mould used to form the internal tube was a glass tube containing boron-silicate (manufactured by NORMAX, Marinha Grande, Portugal) with a 1cm external diameter. This mould, with latex in its wall, is presented in Figure 1b. The valve was also made of latex, and was formed by a more complex process. It has a structure that is similar to the valves used in soccer balls in Figure 1c.

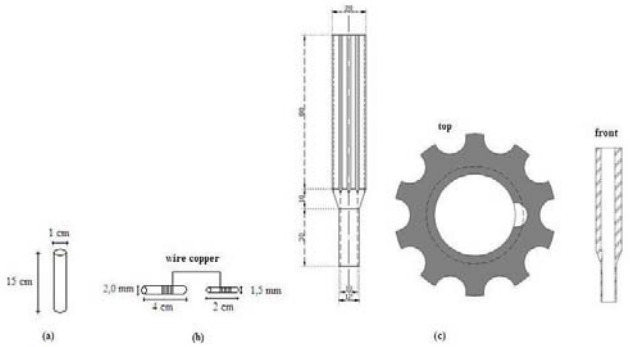


Fig. 1 *(a)* Mould used to form the internal tube, *(b)* valve and *(c)* glass mould used to form the external tube.

The moulds were previously cleaned and sterilized in an autoclave, and then received successive, gradual and uniform baths, followed by drying periods, until a latex compound was obtained. The moulds were first immersed in latex and then subjected to a temperature of 70°C, in a thermostatic oven, for curing, in five-minute intervals. Then, the thermostatic stove was turned off for 20 minutes, and, in this period, the mould remained inside the stove. These steps of bathing and drying were repeated until a thickness of 2 mm of the external module and 1.5mm at the surface of the glass tube were reached. After the internal and external tubes were ready, these two parts were assembled one inside the other.

The module remained for 24 hours at room temperature for the process to be finished. Then a 27G scalp (Embramed, Cotia, Brazil) was introduced in the valve of the EFC to be used in the filling of the module. After placing the scalp, three more latex immersion baths were performed with subsequent heating in the stove, to finally obtain the EFC module for final implementation , Figure 2.



Fig. 2 An esophageal flow control module measuring 8cm in length, with a scalp inserted in the valve**.**

An electronic system, with a man-machine interface, was especially projected to inflate the EFC. This machine contains a pressure sensor with a precision of 1mmHg, and it allows the automatic inflation of the module using carbon dioxide (CO_2). The doctor chooses the desired pressure value through commands on the screen.

When the module was finished, it was submitted to visual inspection for detection of defects. As such, tests were done for assessing wall resistance and deformation in the walls after inflation under pressures of 80mmHg and 100mmHg. A subsequent immersion in water allowed the search for leaks.

B) Test of the EFC in a dog

The testing procedure was approved by the committee of ethics in research of the Federal University of Goiás. The animal was previously subjected to the procedures for vaccination, control of ecto and endoparasites, in addition to laboratory tests, hematology and clinical chemistry, for verification of its health. The module was inserted, by endoscopy, in a male adult mixed race dog, with a body weight of 12.7 kg. The characteristics of the module used are shown in Table 1.

Table 1 Characteristics and dimensions of EFC module

Characteristic	Details	Dimensions
Shape	Cylindrical	External diameter: 2.5cm 1.5mm thick
External surface	Wavy, with longitudinal grooves	5.0mm salience and 5.0mm space between them.
Internal surface	Smooth	1.0cm diameter hole 2.0mm thick
Color	Yellow	-
Length	-	8.0cm
Characteristic	Details	Dimensions
Shape	Cylindrical	External diameter: 2.5cm 1.5mm thick

The application of the module was preceded by food restriction of 12 hours. Diazepam was used in pre-anesthesia in the proportion of 0.5mg/kg and the anesthesic propofol, in the proportion of 6.0mg/kg, for induction, and 0.5mg/kg/min to maintain anesthesia, all done intravenously.

Before the examination, under food restriction of 12 hours, the animal was anesthetized with the association of cloridrates levomepromazine, tiletamine and zolazepam at doses of 0.5, 2.5 and 2.5mg/kg per body weight, administered intramuscularly, all in the same syringe.

After loss of reflexes, the animal was subjected to endoscopic examination, initially to assess the physiological macroscopic conditions and anatomy of the esophagus, then, the unfilled EFC module was placed. The module was introduced slowly and positioned between the atlas and the fourth cervical vertebrae. Once in the desired position, the module was slowly inflated until it reached the specified pressure of 60mm Hg. The scalp was carefully removed to prevent damaging the esophageal wall and pressure loss in the module.

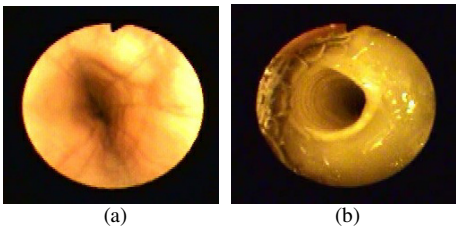
Later, the animal received a puréed diet in liquid form prepared in a blender in the proportion of 400g solid food to 1 L of water. The amount provided was calculated according to the body weight of the animal, as instructed by the manufacturer of the dog food.

During the seven days subsequent to the placement of the module, the behavior of the animal was evaluated by a veterinarian for food ingestion, vomiting, coughing and loss of body weight with observations recorded daily on the dog's chart. To confirm the continuation of the module's positioning, radiological examinations were performed on the latero-side incidence of the right cervical region immediately after the placement of the module and two days from the withdrawal of the module. The removal of the module followed a protocol that was very similar to the one used for its placement.

III. Results

The dog was submitted to a food restriction of 12 hours as a prophylaxis for vomiting in the trans-anesthetic, given that it could interrupt the endoscopy procedure and cause discomfort to the animal. Moreover, this procedure prevents a potential cause for the development of pneumonia caused by aspiration.

The result of the application methodology through endoscopy was positive because it promoted the evaluation of the integrity of the esophagus prior to the placement of the module. Also, the use of this technique facilitated the installation of the module in a slow and monitored way that allows for accurate positioning without damaging the mucous membrane. Through video-endoscopy, the module in the esophagus was shown on the computer screen, reducing its diameter from 3cm to 1cm, as exhibited in Figure 3.



(a) (b)

Fig. 3 *(a)* Photo of the endoscopic appearance of the dog's esophagus wall. *(b)* EFC Module with 60mm Hg in the esophagus.

In the seven days following the placement of the module, its retention within the esophagus was accompanied by x-ray examinations and a perfect accommodation between the atlas and fourth cervical vertebrae was found. The radiographic visualization of the piece was possible because the esophagus was distended by the presence of the module filled with gas and can be seen in a radiolucent image in the dorsal trachea in Figure 4.

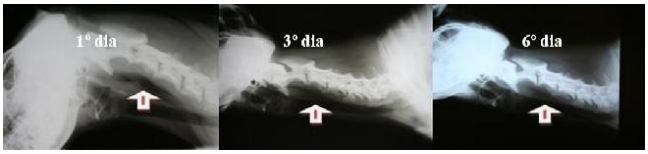


Fig. 4 Lateral radiographic images of the cervical region of a dog, registered on the first, third and sixth days after the placement of the EFC. The arrow indicates the radiolucent area, interposed between the cervical vertebrae and trachea, which corresponds to the region in which the module is positioned in the esophagus.

After the application of the module, the dog was put in an individual cage and its recovery from the procedure was monitored. In the first 15 hours there was salivation, coughing and isolated events of moderate choking. Such occurrences were possibly related to the period of the esophagus accommodating the object inserted in lumen.

After the first meal, a radiographic exam was made to check the position of the EFC module. The result of the exam confirmed positive expectations, indicating, among other things, that the consistency of the food was appropriate to pass through the inner portion of the module without sending the module to the stomach. The quality of the food could also be assured. In subsequent evaluations of the animal, excessive salivation, episodes of regurgitation or apparent discomfort in the animal were not observed.

During the seven days there were no changes regarding the intake of food, vomiting and coughing. This data suggest that the size of the module, the pressure on the walls of the esophagus and the place of installation were appropriate for maintaining the device in a dog of medium size with a body weight of approximately 12 kg.

After seven days, the animal was again subjected to a video-endoscopy exam for the removal of the module. During the examination it was observed that the module was properly positioned, confirming what was seen on the x-rays. Moreover, the presence of food remains wasn't observed in the cranial portion of the esophagus or around the module. After the removal of the module, no damage to the wall of the esophagus was found along its length.

Meanwhile, during the process of removing the EFC module, which was inflated using a pressure of 60mm Hg, some difficulty was encountered because it was very slippery. In the process of introducing the endoscopic nippers to pull the module out, the module slipped and lodged itself in the stomach of the animal. Ten days after of that occurrence, the EFC was expelled orally and it was observed that its integrity was seriously compromised. It is believed that other animals that were living with the dog may have bitten and damaged it.

Analyzing the issue of the module's displacement, it can be assumed that the application of a long nylon wire introduced in the module could be used for external fixation at the same region in the side of the face or the animal's neck. This procedure could be tested in order to prevent the device moving to other regions of the esophagus or even into the stomach.

Considering the variable of weight loss during the experiment which wasn't the main target as other data and conclusions were the objectives of this research, there was a weight loss of about 4% during one week of observation. However, this result should be carefully checked and validated in further studies using this approach. Nonetheless, these preliminary results are encouraging and are a good justification for the testing of this new method in a larger group of dogs in order to track various other parameters related to the module and the physiology of the animal.

IV. CONCLUSION

The use of the esophageal flow control module caused no apparent damage to or changes in the esophagus wall. Moreover, it promoted weight loss in the animal without impairing the physiological parameters or causing apparent behavioral changes. Thus, the results hint that the esophageal flow control module is a multidisciplinary approach that has good potential for treating obesity in humans and animals.

ACKNOWLEDGMENT

We would like to thank the Brazilian Ministry of Science and Technology (CAPES) for the financial support.

REFERENCES

1. Almeida N. (2006) O balão intragástrico nas formas graves de obesidade. Journal Port. Gastrenterol. 13:220-225.
2. Martin L.F., Tan T.L. & Horn J.R. (1995) Comparison of the costs associated with medical and surgical treatment of obesity. Surgery 118:599-607.
3. Martins M.V.D.C. (2005). Porque o "by-pass" gástrico em Y de roux é atualmente a melhor cirurgia para tratamento da obesidade. Revista Bras. Videocir. 3(2):102-104.
4. Miguel P.R., Rosa A.L.M., Reusch M. & Carlos J.R.C.B. (1998) Esofagomanometria e Phmetria de 24 horas para avaliar a fundoplicatura de Lind laparoscópica na doença do refluxo gastroesofágico. Revista Col. Bras. Cir. 25(4):241-245.
5. Buchwald H. & Williams S.E.(2004) Bariatric surgery worldwide 2003. Obesity Surg. 14(9):1157-1164.
6. Singh S. & Kumar A. (2007) Wernicke encephalopathy after obesity surgery: A systematic review. Neurology, 68:807–811.
7. Mrué F. (1995) Substituição do esôfago cervical por prótese biossintética de látex: estudo experimental em cães. Dissertação de Mestrado, Faculdade de Medicina da Universidade de São Paulo, Ribeirão Preto.

Author: Suélia de Siqueira Rodrigues Fleury Rosa
Institute: University of Brasília (UnB)
Street: Gama College – Ae . 02 Lt 14.
City: Gama- DF
Country: Brazil
Email: rodrigues.suelia@gmail.com

Basic Concepts for Active Implantable Valve Development

M. Biehl[1] and O. Scholz[1]

[1] Fraunhofer Institute for Biomedical Engineering, Biomedical Microsystems Department, 66386 St. Ingbert, Germany

Abstract— **Based on fundamental considerations concerning implantable valve actuating mechanisms and a review of recent low-energy actuators, we propose four concepts to adjust or switch an implantable valve. The Bellow-Concept makes use of a standard actuator and hermetic encapsulation with flexible bellows, where force can be transmitted by deflection of the bellows. The Shape-Memory-Alloy-Concept considers a biocompatible Shape-Memory-Alloy (SMA) actuator, which can be directly immersed in body liquids. The Stepper-Motor-Concept makes use of a hermetically encapsulated rotatory actuator, with the rotatory action being transmitted magnetically through the rigid encapsulation wall. Finally, the Magnetic-Spring-Concept proposes a hermetically encapsulated linear actuator and linear magnetic force transmission through the rigid encapsulation wall. We found the Magnetic-Spring-Concept the smallest and most simple one.**

Keywords— **Active implant, small actuator, implantable valve.**

I. Introduction

Active, electronically controlled medical implants need, at least for some of their components, a hermetic encapsulation, on the one hand to prevent parts susceptible to moisture from being corroded by body liquids, on the other hand to protect the human organism against toxic ingredients of the implant. In pace makers, for example, battery and electronics are encapsulated within a hermetic housing, with special feedthroughs providing electrical contact between implant electronics within the housing and stimulation electrodes outside. Concerning an active valve implant, it is not electrical energy, which must be provided outside the hermetic housing, but mechanical energy. This small difference will make the development of an active valve implant much more challenging. In the following, we discuss the technical possibilities from a basic point of view, review some suitable actuating mechanisms and deduce some proposals for realization.

II. Basic concepts for implantable valve actuation

Fluidic valves provide control of liquid outlet, which can be achieved either by adjusting the flow – examples are given in Fig. 1 with plunger-, stop-cock- and squeeze valve – or by adjusting the opening pressure, as exemplified with the ball-valve in Fig. 1. The ball-valve consists of a ball shaped closure member, which is pressed against the valve seat via a preloaded spring. The preload of the spring determines the opening pressure; it can be adjusted by moving the counter bearing at the end of the spring in axial direction. Many implantable valves, e.g. for hydrocephalus therapy, are preferably pressure-controlled, hence we concentrate in the following on mechanisms to adjust the opening pressure of a ball-valve via the preload of the associated spring.

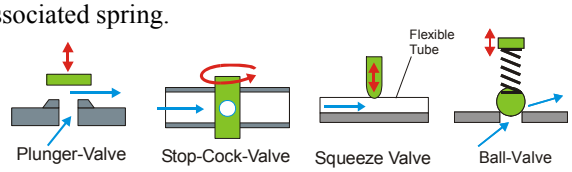


Fig. 1 Examples for valve control mechanisms: Three flow controlling valve types on the left side and pressure controlling valve (right)

The perhaps most challenging issue for an active valve implant is the transmission of energy supplied by implant electronics to a mechanical action for adjustment. The energy of an active implant is stored in terms of electrical energy. The energy storage, together with valve control electronics, must necessarily be encapsulated within a hermetically sealed metallic or ceramic housing, as any humidity intruding into this housing from patient's body would eventually damage the implant electronics. Mechanical energy, however, is needed within an actuator chamber containing body liquids. The valve actuator, which must be addressed by the hermetically sealed implant electronics, simultaneously has to transmit mechanical energy into a liquid-filled compartment. We found three basic principles to approach this challenge (Fig. 2):

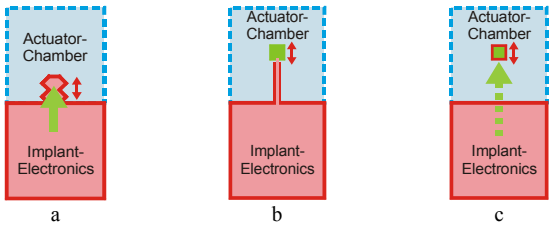


Fig. 2 : Basic principles for energy transmission out of a hermetic housing

O. Dössel and W.C. Schlegel (Eds.): WC 2009, IFMBE Proceedings 25/VIII, pp. 57–60, 2009.
www.springerlink.com

The first possibility (Fig. 2 a), we call it "Flexible-Wall-Concept", is to integrate the actuator together with implant electronics within the hermetic housing. The housing must therefore be equipped with a flexible wall, which can transmit the mechanical energy released by the actuator into the liquid filled chamber. With the hermetic housing enclosing the actuator, all concerns of intruding humidity or missing biocompatibility of the encapsulated valve components can be dispelled.

The second possibility, the "Implantable-Material-Actuator-Concept", means to position the actuator completely outside the electronic housing in direct contact to body liquids (Fig. 2 b). This requires the actuator to be biocompatible and resistant against humidity. Further, in order to connect the actuator to implant electronics electrically, hermetic feedthroughs throughout the wall of the hermetic housing are essential. A challenge may be that the electrical contacts within the body liquid must be encapsulated adequately in order to achieve a sufficient electrical insulation of the electrified parts. Otherwise, electrical discharge and corrosion might lead to an early failure of the implant.

The third principle, we name it "Contactless-Force-Transmission-Concept", uses an actuator, which can be split in two parts without mechanical contact to each other (Fig. 2 c). One part of actuator is in contact with body liquids, the other part of actuator is hermetically sealed within the electronics housing. Energy is transmitted without mechanical contact throughout the rigid wall of the electronics housing. The actuator part exposed to body liquids must be biocompatible and resistant against humidity – a requirement, which can be fulfilled by hermetic encapsulation with titanium, for example. Quite difficult is the question of contactless mechanical force transmission. The most obvious solution is force transmission by magnetic fields, but also ultrasound might be suitable to transmit an actuating effect into a liquid filled chamber.

III. Actuating principle overview

The actuator is one of the most crucial parts of an active valve. Which actuating principle might be the most suitable one, depends on the chosen mechanism of liquid control and energy transmission through the wall of the hermetic housing. The following section summarizes some established actuating principles, which can be realized at small size and might be suitable for an implantable valve.

Electromagnetic actuators, such as rotary motors and limited motion drives, are the most common actuators in mechatronics, by far [1]. Rotatory motors have the advantage that they are ubiquitous and versatile, can perform binary, discrete or continuous actuation, have long operational lifetimes and are quite efficient at small sizes. With the stepper motor ADM0620, the company ARSAPE offers a tiny version with a diameter of 6 mm and a length of 9.3 mm only, which might be interesting for implant actuation.

Limited motion drives, as voice coils and solenoid actuators, are simple, versatile and commonly used for valve actuation. At small size, however, actuation efficiency is small compared to other actuating mechanisms [2], position control proves to be difficult and large friction forces must be accepted.

A general disadvantage of electromagnetic actuators is the fact that inductive heating might occur and unintended powering of the conductive coils in magnetic resonance imaging (MRI) apparatus might lead to heating and damage [3]. Due to ferromagnetic components, MRI compatibility certainly is a critical concern for electromagnetic actuators in active implantable valves, as high field MRI is increasingly available and routinely used for diagnostics and control.

Piezoelectric actuators use the physical effect that piezoelectric crystals will undergo a relative change of length and thickness, if a voltage is applied between each two opposite surfaces [4]. Large displacements at small voltages can only be achieved with ultrasonic drives. They do not use single displacements, but mechanical oscillations in the ultrasonic range. Ultrasonic motors have an excellent efficiency, can apply and hold large force, the latter without energy supply, and they are MRI compatible. An example for a commercially available, mm-sized ultrasonic motor is the Squiggle®-motor. In its most tiny version, it has a size of 1.55 x 1.55 x 6 mm only, offers millimeters of stroke, sub-micrometer precision and can exert a force of 200 mN. It withstands high shock and has low power requirements for battery-driven devices.

Shape-Memory-Alloy (SMA) actuators exploit the temperature dependence of the crystalline structure of certain alloys. In cold martensitic state, the material can be deformed very easily; if it is heated again, it regains its original shape with considerable force. These actuators provide the highest ratio of releasable mechanical energy per volume of all actuator mechanisms, by far. Hence, they can most easily fulfill the requirement for small actuator size. Shape-Memory-Actuators can be produced in various shapes like wire, spring or beam. As they are metallic materials, heating can easily be performed by current flow. A special advantage is the fact that there are alloy compositions, which are considered to be biocompatible. Nickel-titanium alloys, for example, are successfully used in long-term implanted stents for many years. So far, this

application exploits the superelastic properties, not so much the actuator properties; applications of SMAs as actuators in medical implants, however, are proposed in literature [5][6][7]. As these materials are not ferromagnetic, an interaction with MRI-typical magnetic fields is not expectable.

IV. Proposals for Realization

The suitable actuating principles identified above can now be assigned conveniently to the three basic concepts for implantable valve actuation worked out in section II. Each of the following design drafts concentrates on the mechanical actuating principle only - battery and electronics are omitted for simplicity.

Concerning the Flexible-Wall-Concept, the flexible part of the wall must be some kind of metallic bellow, which is welded with the metallic housing. Other deformable materials like silicone cannot be used due to their high vapor permeability. A suitable actuator must overcome the restoring force of the quite stiff bellow, but needs not be biocompatible. Further, a compensation possibility for ambient pressure variations should be provided, as absolute pressure, which acts on the hermetic package and therewith on the actuator, can vary enormously. Our proposal, the so-called “Bellow-Concept”, is depicted in Fig. 3.

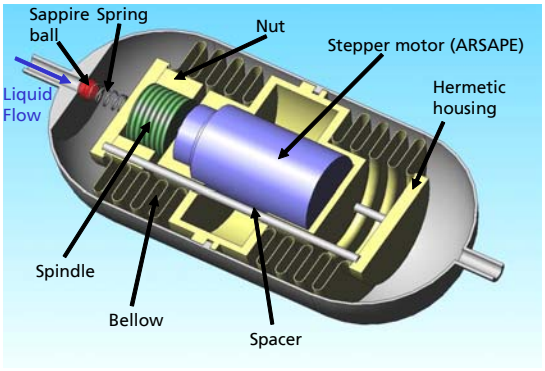


Fig. 3 : Bellow-Concept

The small stepper motor ARSAPE ADM0620 can apply enough force to slightly deflect a thin-walled bellow via a suitable nut-spindle-mechanism, which transforms the rotary movement of the motor to a linear movement. Thus, the front surface of the hermetic housing is shifted towards the valve seat to control the preload of the spring. Motor, spindle and electronics are encapsulated within the hermetic housing, which is fixed to the outer housing of the valve in such a way that its both ends remain movable towards the latter. The rigid spacer interconnection ensures that ambient pressure, acting on both ends simultaneously, but in opposite direction, will not additionally load the motor.

For the Implantable-Material-Actuator-Concept, bio-compatible nickel-titanium SMA materials might be suitable. Fig. 4 shows an embodiment with two parallel SMA wires acting in opposite directions – if one of them contracts on heating, it elongates the other cold one, and vice versa. The SMA wires are combined with a compliant bistable elastic mechanism, which acts on a piston to preload the spring, thus forming a bistable valve. Such a combination of SMA actuator and compliant mechanism has been shown to be highly efficient [8]; a disadvantage is that only two opening pressures can be adjusted.

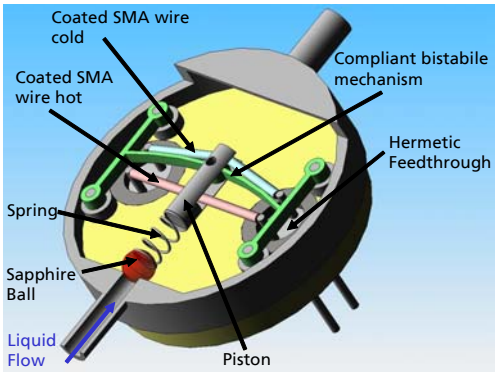


Fig. 4 : Shape-Memory-Alloy-Concept

For realization of the Contactless-Force-Transmission-Concept we found two solutions, both based on electromagnetic force transmission. The first solution, called “Stepper-Motor-Concept” (Fig. 5), uses rotatory electromagnetic actuation, similar to that of a stepper motor. Specifically, electrified coils, magnetic core and electronics of the stepper motor (i.e. the stator) are integrated within a hermetic housing. The rotor of the stepper motor bears several permanent magnets in circular arrangement within a separate hermetic housing, which may come in contact with body liquids. The encapsulated rotor is merged with an eccentric stepper wheel to transform rotatory to linear movement, thus defining the preload of the spring. Additionally, an integrated ball bearing reduces friction.

The functional principle of the second solution, called “Magnetic-Spring-Concept” (Fig. 6), is based on the repulsive force between two permanent magnets, which significantly increases with decreasing distance. Thus, by varying the distance between the two magnets with a linear actuator, which is integrated together with one of the magnets in the hermetic housing, the repulsive force can be adjusted. If, in turn, the repelled magnet outside the hermetic housing presses against the closure member of the

valve, the valve opening pressure can be influenced. This effect is similar to that of a mechanic spring positioned between linear actuator and closure member of the valve, with the decisive distinction that, in case of magnetic spring, the wall of a rigid hermetic encapsulation can be brought between actuator and closure member. Hence, actuator and electronics, which normally are sensitive to humidity and not biocompatible, can be hermetically encapsulated - nevertheless, a controlled force transmission onto the valve closure member is possible. As the actuator only needs to supply the force to press the closure member against the valve seat, a tiny actuator, like the smallest Squiggle®-motor, will be sufficient.

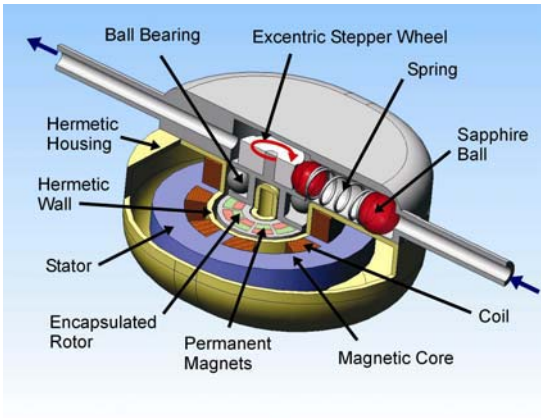


Fig. 5 : Stepper-Motor-Concept

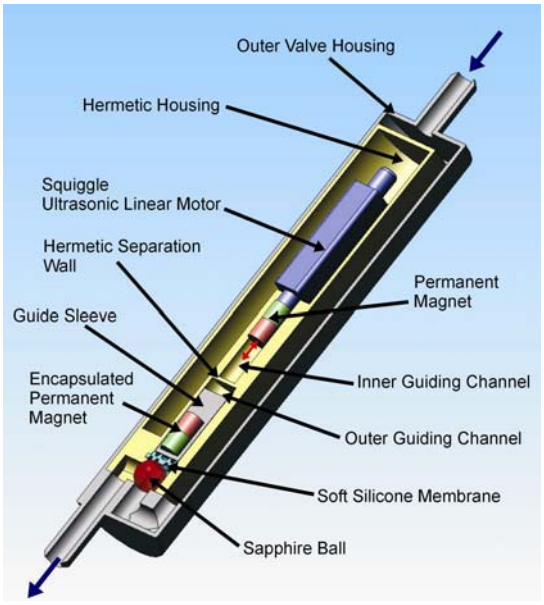


Fig. 6 : Magnetic-Spring-Concept

Conclusions

Comparing the four different design proposals, we conclude that the Magnetic-Spring-Concept is the smallest, the most versatile and the simplest one to be realized. The Bellow-Concept is quite large and needs unnecessary amounts of energy to deflect the stiff metallic bellows. The Shape-Memory-Alloy-Concept is the only one without ferromagnetic components, thus being definitely MRI compatible. However, it can only operate in a binary way, and the fabrication of SMA actuators can be very challenging due to largely varying properties of the SMA material. The Stepper-Motor-Concept is quite complicated, and a high development effort can be expected for such a custom specific motor. To sum it up, we assume that the Magnetic-Spring-Concept is the most promising one, which could be worth being pursued in future.

Acknowledgment

The authors would like to thank the Johnson & Johnson company, 325 Paramount Drive Raynham, MA, for co-funding this work. Special thanks go to Alan Dextradeur for his open interest as well as the provision of helpful information and proposals.

References

1. Pawlak A M (2007) Sensors and Actuators in Mechatronics: Design and applications. Delphi Corporation, Troy, Michigan
2. Smith S T, Seugling R M (2006) Sensor and actuator considerations for precision, small machines. Precision engineering 30(3):245-264
3. Szczesny S, Jetzki S, Leonhardt S (2006) Review of Current Actuator Suitability for Use in Medical Implants, Proc. of the 28th IEEE EMBS Annual International Conference, New York City, USA, 2006, pp 5956-5959
4. Janocha H (2004) Actuators. Basics and Applications. Springer, Berlin Heidelberg
5. Reynaerts D et al (1999) Shape memory micro-actuation for a gastro-intestinal intervention system. Sensors and Actuators 77:157-166
6. Pemble C M et al (1999) A miniature shape memory alloy pinch valve. Sensors and Actuators 77:145-148
7. Reynaerts D. et al. (1997) An implantable drug delivery system based on shape memory alloy micro actuation. Sensors and Actuators A 61: 455-462
8. Hiroya Ishii et al. (2004) SMA actuated compliant bistable mechanisms. Mechatronics 14:421-437

Author: Oliver Scholz
Institute: Fraunhofer Institut für Biomedizinische Technik (IBMT)
Street: Ensheimer Straße 48
City: 66386 St. Ingbert
Country: Germany
Email: oliver.scholz@ibmt.fraunhofer.de

Estimation of Magnetic Nanoparticle Diameter with a Magnetic Particle Spectrometer

S. Biederer[1], T. Knopp[1], T.F. Sattel[1], K. Lüdtke-Buzug[1], B. Gleich[1,2], J. Weizenecker[2], J. Borgert[2], and T.M. Buzug[1]

[1] Institute of Medical Engineering, University of Lübeck, Lübeck, Germany
[2] Philips Research Europe, Sector Medical Imaging Systems, Hamburg, Germany

Abstract— **Magnetic particle imaging is a new tomographic imaging technique, which allows for measuring the spatial distribution of magnetic nanoparticles. It achieves high sensitivity and high spatial resolution, while keeping acquisition time short.**

As can be observed in simulations, the diameter of the nanoparticles has a high impact on the imaging quality in magnetic particle imaging. Thereby, only the iron core of the particle contributes to the measured signal. Thus, the diameter of the iron core is important for magnetic particle imaging, not the total size of particles. The coating of the iron core is essential for biocompatibility of particles with the human body. Most common techniques measure the total size of the particles. In this work, a method is presented to measure the iron-core size exploiting the non-linear magnetization curve of the particles.

For this purpose, a magnetic particle spectrometer is used to measure the non-linear magnetization of the particles. Based on these measurements and the Langevin theory of paramagnetism, the particle-core size can be calculated. This, in turn, allows for more realistic simulations of the imaging performance in magnetic particle imaging.

Keywords— **magnetic particle imaging, magnetic nanoparticles, MPI, spectrometer, SPIO, medical imaging.**

I. INTRODUCTION

A new tomographic imaging technique called magnetic particle imaging (MPI) [1] was presented by Gleich and Weizenecker in 2005. The spatial distribution of magnetic nanoparticles (e.g. super-paramagnetic iron oxide particles, SPIOs) can be determined based on their non-linear magnetization curve. For this purpose, a time varying magnetic field is applied to the nanoparticles. An additional magnetic field is generating a field-free point (FFP). This field is zero at the FFP and high at all other positions in the field of interest. By moving the FFP through the field of interest, spatial encoding is achieved. As shown in [2], MPI achieves high sensitivity and high resolution, while the acquisition time remains short. Thus, real-time applications are feasible [3]. Gleich and Weizenecker proposed a tube like MPI-scanner geometry [1], where the specimen lies within a symmetric coil assembly. An alternative geometry was presented by Sattel et al [4], where all field generating and signal receiving objects are situated on a single side allowing for scanning larger specimen.

In simulation studies [2,5], the Langevin theory of paramagnetism is used to simulate the magnetic behavior of the nanoparticles. Thereby, the iron-core diameter of the nanoparticles is a very important parameter, because it determines how many harmonics can be measured and, in turn, the theoretically achievable spatial resolution of MPI. This is caused by the fact that Particles with a larger iron core have a steeper magnetization curve.

Common techniques for measuring the particle size like photon cross correlation spectroscopy (PCCS) estimate only the total size of the particles, which is of less interest for the MPI image quality than the iron-core diameter. Currently, the iron-core diameter can only be measured by a time consuming measurement with an electron microscope.

To achieve a high correlation between simulated and measured MPI signals, it is essential to know exactly the iron-core diameter. However, time consuming measurements are inconvenient during the particle-development process. Thus, it is indispensable to measure easily the iron-core diameter. Therefore, in this work, a method is presented allowing for measuring the iron-core diameter with acceptable effort.

With a magnetic particle spectrometer (MPS) [6] the magnetization of superparamagnetic nanoparticles can be measured. Exploiting the measured MPS signal and the Langevin theory of paramagnetism, the distribution of the iron-core diameter can be estimated.

This work starts with a mathematical model for the particle size distribution and for the nanoparticle's magnetization curve. Then, the experimental spectrometer is described. Based on the measured magnetization and the mathematical models, the particle size distribution is estimated for the commercially available contrast agent Resovist®.

O. Dössel and W.C. Schlegel (Eds.): WC 2009, IFMBE Proceedings 25/VIII, pp. 61–64, 2009.
www.springerlink.com

II. THEORY

A. Particle Size Distribution

It is assumed that the particle size distribution is log-normal distributed. Mostly, the particle size distribution is modeled by the log-normal distribution, because it describes the results of the particle growth process best [7]. The probability density function of the log-normal distribution is given by

$$f(D) = \frac{1}{\sigma D\sqrt{2\pi}} \exp\left(-\frac{1}{2}\left(\frac{\ln(D) - \mu}{\sigma} \right)^2 \right), \qquad (1)$$

where μ and σ are the parameters of the distribution and D is the diameter of the nanoparticles. The expectation value $E(X)$ is given by

$$E(X) = e^{\mu + \sigma^2/2}, \qquad (2)$$

and the variance $Var(X)$ by

$$Var(X) = \left(e^{\sigma^2} - 1 \right) e^{2\mu + \sigma^2}. \qquad (3)$$

B. Magnetization

When a time varying magnetic field with field strength $H(t) = H_0 \sin(2\pi f_0 t)$ and frequency f_0 is applied to magnetic nanoparticles, the change in magnetization induces a voltage in a recording coil, which can be can be measured. Since the magnetization curve of magnetic nanoparticles is non-linear, the spectrum of this magnetization does not only contain the fundamental frequency f_0 but also multiples of f_0, so-called harmonics. Figure 1 shows this behavior.

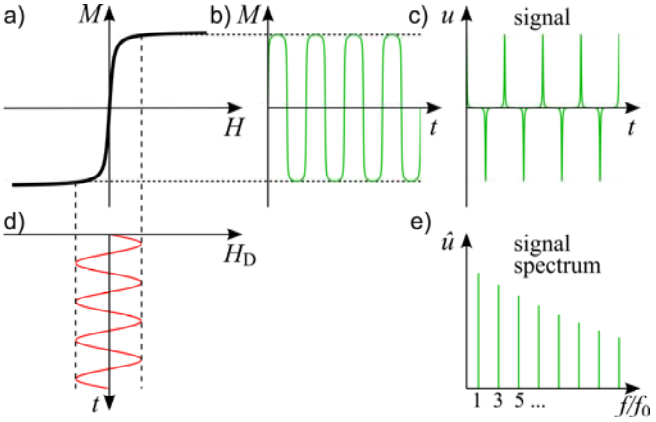


Fig. 1 Physical effect exploited in MPI. A sinusoidal magnetic field H(t) d) results in a magnetization b). The derivation -dM(t)/dt of the magnetization c) can be recorded. Due to the non-linear magnetization curve a), the spectrum of the recorded signal e) does not only consist of the fundamental frequency but also of harmonics.

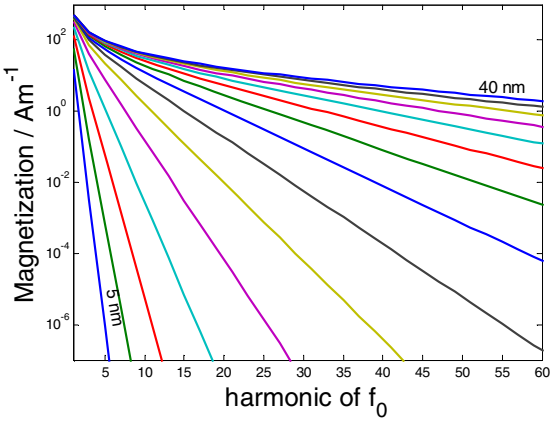


Fig. 2 Magnetization of the even harmonics for diameters from 5 nm up to 40 nm in steps of 2.5 nm.

The Langevin theory of paramagnetism [8] can be used to describe the non-linear magnetization curve of the particles by

$$M_D(t) = m_s c \left(\coth\left(\frac{m_s \mu_0 H(t)}{k_B T} \right) - \frac{k_B T}{m_s \mu_0 H(t)} \right), \qquad (4)$$

where T denotes the temperature (e.g. about 310 K within a patient), μ_0 the permeability of vacuum, k_B the Boltzmann constant, c the particle concentration, and $m_s = 1/6\pi D^3 M_s$ the saturation magnetic moment. The particles are characterized by their iron-core diameter D and the saturation magnetization M_s (e.g. 0.6 T/μ_0 for magnetite [9]).

Through the process of particles synthesis, the diameter D is not a single value rather a distribution given by equation 1. The total magnetization $\tilde{M}(t)$ can be calculated by summation of all magnetizations $M_D(t)$ of a single diameter D weighted with the probably density function $f(D)$, so that

$$\tilde{M}(t) = \sum_D f(D) \cdot M_D(t). \qquad (5)$$

The magnetization $M_D(t)$ of the even harmonics for different diameters D are shown in figure 2. It can be seen, that for larger diameters the magnetization level increases.

III. MATERIAL AND METHODS

The magnetization $M_{meas}(t)$ is measured with a magnetic particle spectrometer (MPS) [6]. It directly measures the physical effect exploited in MPI as shown in figure 1. For this purpose, an excitation field is generated by a transmit coil, while the change in magnetization of the nanoparticles

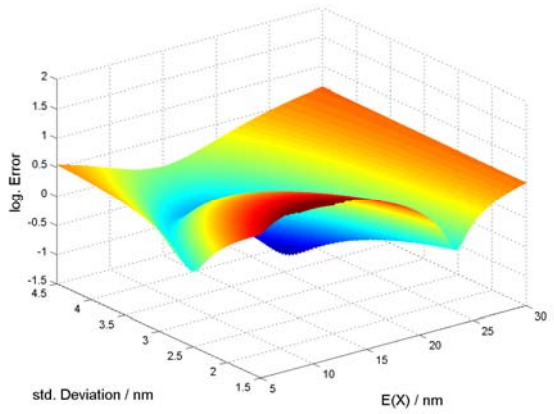


Fig. 3. The logarithmic error of the simulated and measured magnetization for different expectation values and standard deviations.

induces a voltage in a receive coil. To obtain the magnetization, the induced voltage is integrated over the time t. The fundamental frequency of the excitation field is chosen as $f_0 = 25$ KHz. Up to 100 harmonics are measured simultaneously and used to estimate the particle size distribution.

To find the simulated magnetization $\tilde{M}(t)$, which fits best to the measured one, the parameters μ and σ of the log-normal distribution have to be calculated. This can be done either by testing all possible values for μ and σ or by a multidimensional optimization. In this work, the GNU Scientific Library (GSL) [10] is used, which employs the simplex algorithm of Nelder and Mead [11]. The logarithmic error is plotted for different μ and σ in figure 3. It can be seen, that exactly one minimum exists. At that point, the simulated total magnetization $\tilde{M}(t)$, is almost equal to the measured magnetization $M_{meas}(t)$.

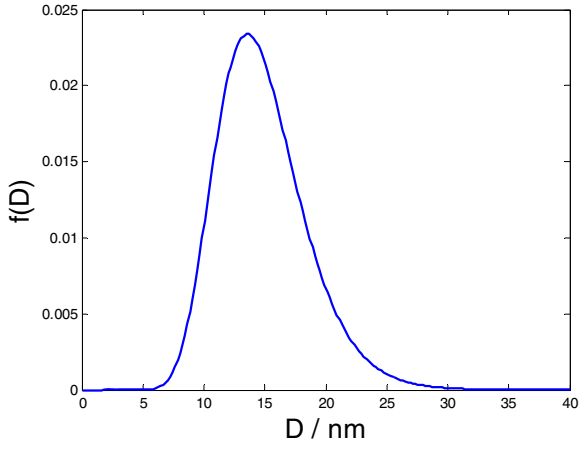


Fig. 4 Estimated particles size distribution of Resovist.

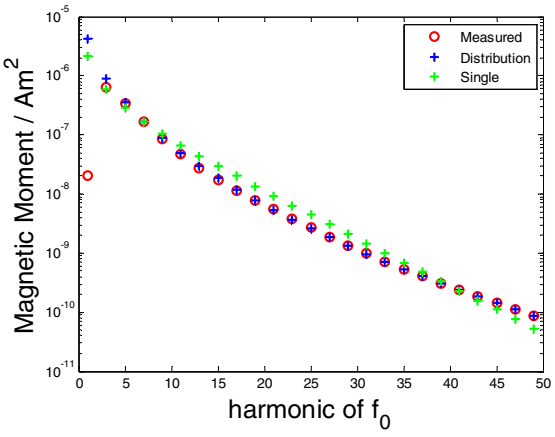


Fig. 5 Magnetic moment of the even harmonics for the measurement (red), simulations with a particle size distribution (blue), and simulation with a single diameter (green)

IV. Results and Discussions

As nanoparticles Resovist® (Schering AG) with a concentration of 500 mmol (Fe)/l is used. To achieve a reasonable magnetic moment, the volume of Resovist is chosen as 10 µl. To increase the SNR of the measurements the acquisition time of the MPS is set to 30 s according to 750,000 transmit periods. The field strength is set to 20 mT/μ_0, which ensures that the magnetization of Resovist is almost driven in saturation.

In figure 4, the estimated particle-core size distribution is shown. The particle size distribution of the present lot of Resovist was evaluated by an expectation value of 14.8 nm and a standard deviation of 3.7 nm. The expectation value is higher than values found in the literature, which are between 4 and 8 nm. The deviations probably result from an imperfect particle model of the nanoparticles. For example, anisotropy and hysteresis are not taken into account in the Langevin theory of paramagnetism.

The spectrum of the measured magnetic moment is shown in figure 5. For comparison, the simulated magnetic moment using a single diameter of 24.2 nm is shown as well. The simulated magnetic moment, using a particle size distribution, shows a much higher correlation between measurement and simulation than the correlation using a single diameter.

V. Conclusions

In this paper, a novel method to estimate the particle size distribution of different superparamagnetic nanoparticles is

presented. As an example, the particle size distribution of Resovist is evaluated. Thereby, variances to iron core sizes given in literature were observed. We assume that the deviations result from not described physical effects. Thus, further investigations on the particle model are necessary.

However, an improvement in the similarity of measured and simulated magnetic moment is recognizable, when a particle size distribution is used instead of a single diameter. The estimated distribution of the particle size can be used to improve the accuracy of magnetic particle imaging simulations in a way that the magnetization of the particles can be modeled more physically realistic.

ACKNOWLEDGMENT

This work was financially supported by the Innovation Foundation (ISH) of the state of Schleswig-Holstein, Germany (project id 2007-60).

REFERENCES

1. Gleich B, Weizenecker J (2005) Tomographic imaging using the nonlinear response of magnetic particles. Nature 435:1214-1217
2. Weizenecker J, Borgert J, Gleich B (2007) A simulation study on the resolution and sensitivity of magnetic particle imaging. Phys Med Biol 52:6363-6374
3. Gleich B, Weizenecker J, Borgert J (2008) Experimental results on fast 2D-encoded magnetic particle imaging. Phys Med Biol 53:N81-N84
4. Sattel T F, Knopp T, Biederer S, Gleich B, Weizenecker J, Borgert J, Buzug T M (2009) Single-Sided Device for Magnetic Particle Imaging. Journal of Physics D: Applied Physics, 42, 2:5
5. Knopp T, Biederer S, Sattel T, Weizenecker J, Gleich B, Borgert J, Buzug T M (2009) Trajectory Analysis for Magnetic Particle Imaging. Physics in Medicine and Biology, 56, 2:385-397
6. Biederer S, Sattel T, Knopp T, Lüdtke-Buzug K, Gleich B, Weizenecker J, Borgert J, Buzug T M (2008) A Spectrometer for Magnetic Particle Imaging. Proc. 4th European Congress for Medical and Biomedical Engineering, Springer IFMBE Series, 22:2313-2316
7. Kiss L B, Söderlund J, Niklasson G A, and Granqvist C G (1999) New approach to the origin of lognormal size distributions of nanoparticles. Nanotechnology 10:25–28
8. Chikazumi S, Charap S H (1964) Physics of Magnetism. Wiley, New York
9. Landholt S, Bornstein R (1977) Numerical Data and Functional Relationship in Science and Technology, Springer, Berlin
10. Galassi M, Davies J, Theiler J, Gough B, Jungman G, Booth M and Rossi F (2004) GNU Scientific Library Reference Manual 2nd edn (Bristol: Network Theory Ltd) at http://www.gnu.org/software/gsl/
11. Nelder J A und Mead R (1965) A Simplex Method for Function Minimization. Computer Journal, 7:308-313

Corresponding author:

Sven Biederer
Institute of Medical Engineering
University of Luebeck
Ratzeburger Allee 160
23538 Lübeck
Germany
biederer@imt.uni-luebeck.de

Fate of drug loaded-LNCs in cell culture medium – impact on drug delivery strategies

H. W. Rohm[1], T. Perrier[2], N. Lautram[2],K.-P. Schmitz[1], P. Saulnier[2], M. Löbler[1]

[1] Universität Rostock/Institut für Biomedizinische Technik, Rostock, Germany
[2] INSERM U64610, Angers, France

Abstract— **Drug delivery, mediated by nanoparticles, relies on nanoparticle stability without drug leakage into the surrounding medium. Furthermore, nanoparticles have to be taken up by the cells and the payload has to be discharged into the cytoplasm. In order to test nanoparticle mediated drug delivery we prepared TETD loaded nanoparticles which were stable in phosphate buffered saline. After mouse fibroblasts were confronted with these nanoparticles cells died at the expected TETD concentration. Since nanoparticles could be visualized inside the cells by confocal laser scanning microscopy it was assumed that cytoplasmic drug delivery was successful. However, after measurement of the amount of free TETD in cell culture medium after transfer of the nanoparticles revealed that TETD was completely discharged from the nanoparticles within several hours. In conclusion, the observed cytotoxicity of TETD loaded nanoparticles is most likely due to premature release of the TETD into the cell culture medium acting through the same pathway as TETD applied directly to cells. Therefore it is essential to test for nanoparticle stability when transferred into another medium.**

Keywords— **Nanoparticle, drug delivery, endocytosis, drug release, TETD**

I. Introduction

Nanoparticle mediated drug delivery to a cellular or tissue target is an attractive approach for delivery of toxic drugs to individual cells such avoiding systemic flooding of an organism with all their side effects. Such targeted drug delivery requires that (i) the payload is contained within the nanoparticle until the target cell or tissue is reached since premature leakage of the drug would result in systemic distribution of the payload (ii) the nanoparticle is taken up by the cell and the payload is released into the cytoplasm, provided that is the site of action of the drug. It has been shown previously that nanoparticle mediated drug delivery was up to two orders of magnitude less effective than direct application of the drug to the cells [1]. From this observation it was concluded that only a small portion of the payload reaches its target within the cytoplasm. This could either be due to partial release of the TETD into the cytoplasm after uptake of the nanoparticle or to premature release of as little as 1 % of the payload extracellularly which is sufficient for the observed toxicity. In order to test nanoparticle mediated drug delivery we have chosen nanoparticles that did not release their TETD payload for up to one week when stored in phosphate buffered saline (see results). Nanoparticle uptake was followed by a fluorescence tag and presumed drug delivery to the cytoplasm by a cell viability assay.

II. Materials and Methods

Sephadex G-25, rhodamine isothiocyanate (RITC), fluorescein-5-isothiocyanate (FITC), nile red were purchased from Sigma (Saint Quetin de Fallavier, France). 3,3´-dioctadecyloxacarbocyanine perchlorate (DiO) and 1,1'-dioctadecyl-3,3,3',3'-tetramethyl-indodicarbocyanine, 4-chlorobenzenesulfonate salt (DID) were obtained from InVitrogen.

1,2-Distearoyl-*sn*-Glycero-3-Phosphoethanolamine-*N*-[Amino(Polyethylene-Glycol)2000] (DSPE-PEG2000-amino) furnished by Avanti® Polar Lipids Inc. (Alabaster, USA)

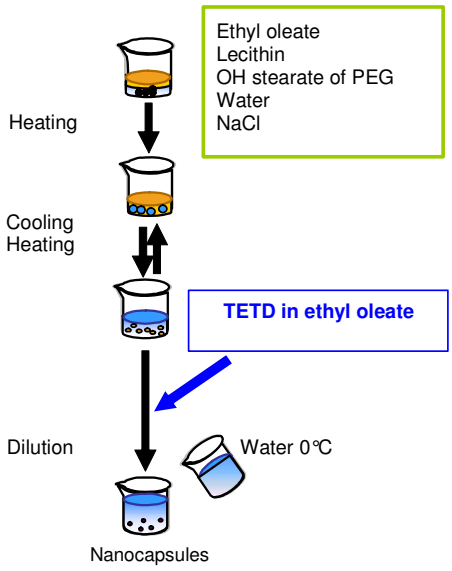


Fig. 1 Formulation of TETD loaded LNCs.

O. Dössel and W.C. Schlegel (Eds.): WC 2009, IFMBE Proceedings 25/VIII, pp. 65–68, 2009.
www.springerlink.com

Labrafac® WL 1349 (Gattefossé S.A., Saint-Priest, France) is a mixture of capric and caprylic acid triglycerides. NaCl was purchased from Prolabo (Fontenay-sous-Bois, France) and water was obtained from a Milli-Q-plus® system (Millipore, Paris, France). Lipoïd® S75-3 (Lipoïd GmbH, Ludwigshafen, Germany) is a soybean lecithin made of 69 % of phosphatidylcholine, 10 % phosphatidylethanolamine and other phospholipids, and Solutol® HS 15 (BASF, Ludwigshafen, Germany) is a mixture of free polyethylene glycol 660 (PEG) and polyethylene glycol 660 hydroxystearate.

After weighting, all components were mixed under magnetic stirring at an agitation speed of 200 rpm at room temperature. After progressive heating at a rate of 4°C/ min, a short interval of transparency at temperatures close to 70 °C could be observed, and the inverted phase (water droplets in oil) was obtained at 85 °C. At least three temperature cycles alternating from 60 to 85 °C at the same rate were applied near the phase inversion zone to obtain a stable water-in-oil emulsion. LNCs were impregnated with TETD by addition of TETD in ethyl oleate. Thereafter, the mixture underwent a fast cooling-dilution process: it was diluted 1:3.5 with 12.5 ml cold water at 2 °C and stirred for 30 min, leading to the formation of LNC with the desired size (Fig. 2).

Tetraethyldiuram disulfide (TETD) was measured by means of HPLC (Knauer, Berlin, Germany). The column used was Eurospher-100 C18, 4 mm ID, 120 mm at a temperature of 23 °C. A mixture of 80 % methanol and 20 % water (v/v) was used as mobile phase at a flow rate of 1.0 mL/min. The sample volume was 50 µL and the UV detector was set to a wavelength of 217 nm. A calibration in the range of 0.1 to 20 µg TETD/mL was performed. For all determinations the NP suspensions were diluted 1:10 with PBS (PAA Laboratories, Cölbe, Germany).

The overall amount of TETD was determined by applying the diluted suspension directly to the measurement. For the determination of the free amount of TETD 200 µL of diluted NP suspension were placed in a centrifugal filter device (Microcon, 50,000 MWCO). It was centrifuged at 5000 g for 10 min and the filtrate was subjected to HPLC to measure the amount of “free” TETD.

L929 mouse fibroblasts (DSMZ, Braunschweig, Germany) were cultured in DMEM culture medium (AppliChem, Darmstadt, Germany) containing 4.5 mg/ml Glucose , 10 % FCS, 100 U/mL Penicillin G, 100 µg/ml Streptomycin (PAA Laboratories), and $NaHCO_3$, 3.7 g/L at 37 °C, 5 % CO_2, and 98 % humidity. Cells were harvested by trypsination (PAA Laboratories) and seeded at 2000 cells/well into a 96 well microtiter plate (Greiner Bio-one, Frickenhausen, Germany). After one day cell culture medium was replaced by 200 µL of freshly prepared nanoparticle suspension in cell culture medium. After 48 h of cell growth under the above conditions cell culture medium was replaced by 10 % CellQuanti-Blue reagent (BioAssay Systems, Hayward, CA, USA, purchased through Biotrend Chemikalien GmbH, Köln) in cell culture medium and incubated for another 2 h. Cellular reductases reduce the CellQuanti-Blue reagent resazurin to resorufin which was quantified by fluorescence measurements (Fluostar Optima, BMG, Offenburg, Germany; excitation wavelength 544 nm, emission wavelength 590 nm). The effective concentration of TETD which reduced cell viability by 50 % (EC_{50}) was determined graphically.

Nanoparticle suspensions were diluted into cell culture medium to yield suspensions of 10^{12} Nanoparticles/mL which were further diluted with cell culture medium.

Uptake of nanoparticles into cells was followed by confocal laser scanning microscopy (Olympus FV100) at excitation wavelength of 510-560 nm and emission wavelength of 575-590 nm.

TETD stock solution, 10^{-4} M in DMSO (Sigma-Aldrich, Taufkirchen, Germany) was diluted into cell culture medium and applied to adherent cells in the same way as described for the nanoparticle suspensions. Cell viability is calculated in relation to the negative control lacking test substances.

III. Results

All the particles were characterized in term of size and zeta potential using a NanoZS apparatus (Malvern) after dispersion of 50 µl of the mother suspension in 3 ml of appropriate aqueous medium. All zeta potential values are comparable in relation with similar conductivity values (Fig. 2).

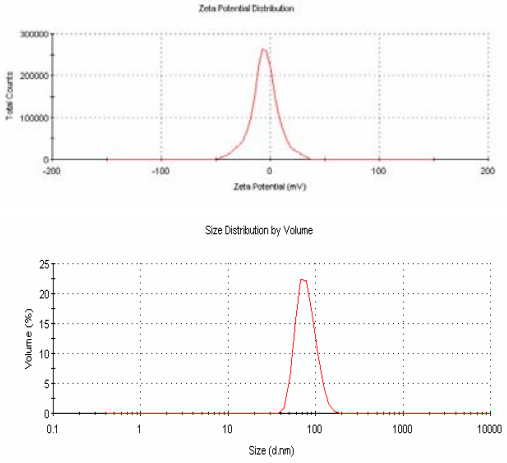


Fig. 2 Zeta potential and size distribution by volume of LNCs.

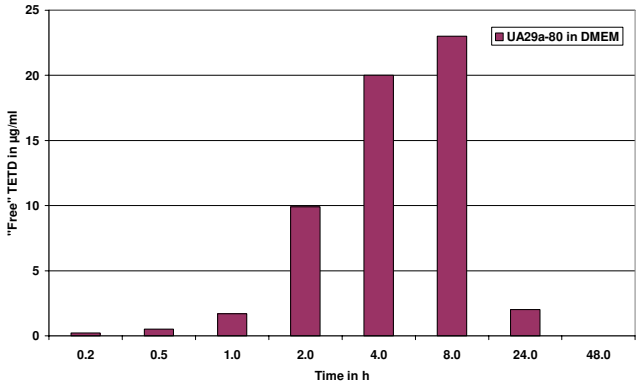


Fig. 3 Amount of "free" TETD in cell culture medium up to 48h after addition of the TETD containing UA29a nanoparticles.

HPLC measurements show that the LNC nanoparticles contain at least 80 % of the nominal TETD content and that as little as 1 % of the TETD leaks from the particles during a 14 d storage in PBS at room temperature. In contrast, nanoparticles readily release their TETD payload when transferred into cell culture medium. After 8 h in cell culture medium DMEM nanoparticles release at least 30 % of their payload (Fig. 3).

After 24 h the amount of "free" TETD in DMEM has decreased to 2.5 % and after 48 h TETD is no longer detected (Fig. 3). It is known that TETD is not stable in DMEM but follows a reductive pathway to N,N-Diethyl-thiocarbamate (DETC) which is consecutively converted into CS_2 and$(C_2H_5)_2NH$ [2]. This TETD reduction occurs within 6 h after transfer of TETD into DMEM cell culture medium, whereas no TETD reduction is observed in PBS (Fig. 4).

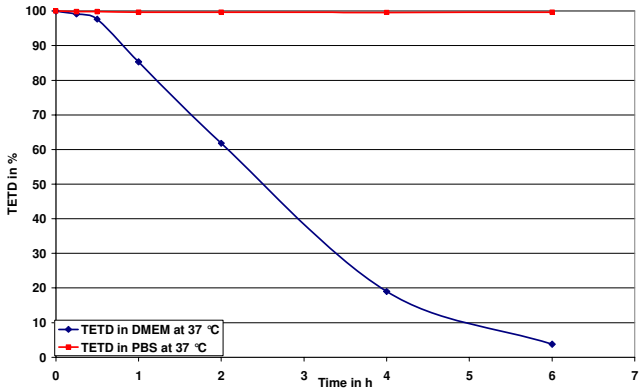


Fig. 4 Stability of TETD in DMEM and PBS at 37 °C

Confocal laser scanning microscopy shows endosomal uptake of nanoparticles UA at NPs /ml) into the cells (Fig. 4).

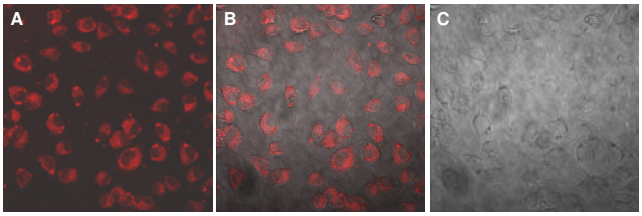


Fig. 5 Confocal laser scanning micrograph of L929 cells that have ingested DilO tagged LNCs. Fluorescent nanoparticles are endocytosed and accumulate in a perinuclear region (A, B). DIC micrograph shows viable cells (C). Superposition of the fluorescence (A) and the DIC (C) images (B).

The cytotoxicity assay shows that cytotoxicity is caused by the nanoparticles at the same TETD concentration as applied directly to the cells (Fig. 5). From this observation one might conclude that nanoparticle mediated drug delivery has been successful. Only complete extracellular discharge of TETD could account for the observed cytotoxicity. TETD loaded nanoparticles were diluted into cell culture medium and TETD release measured by HPLC. Within minutes all TETD was discharged into the cell culture medium such that the cytotoxicity of the TETD nanoparticles is most likely due to premature release of TETD from the nanoparticles. The same nanoparticles without a payload are cytotoxic at high concentrations only (Fig. 6).

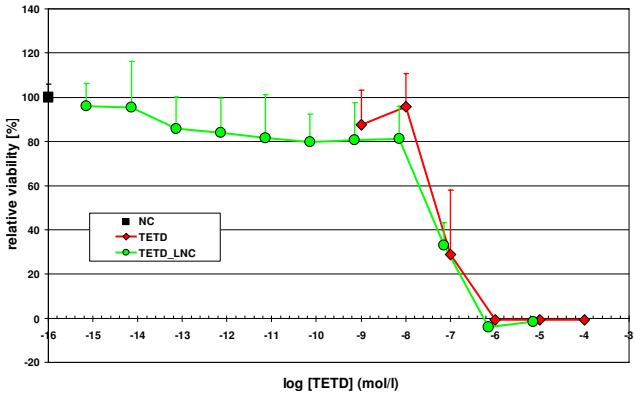


Fig. 6 Cell viability of L929 cells is plotted against the TETD concentration applied directly (◆) or through nanoparticles (●). Data of three batches of TETD loaded nanoparticles each run in quadruplicate were pooled. Standard deviations are calculated from twelve measurements or 10 independent measurements for TETD.

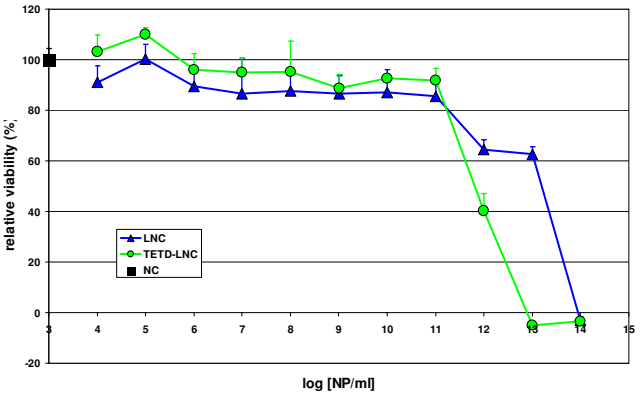


Fig. 7 Cell viability of L929 cells is plotted against the concentration of nanoparticles UA31a (◆) and UA31b (■). Standard deviations are calculated from four parallel measurements.

This nanoparticle suspension was applied to the cells and cell death was plotted against the total TETD concentration and the concentration of free TETD (Fig. 5). It is obvious that cell death could simply be attributed to the free TETD (EC_{50}=7.94x10^{-8} M) present in the nanoparticle suspension.

IV. Discussion

In DMEM medium 95 % of the TETD is degraded to DETC (Fig. 3) within 6 hours. Whereas TETD released from UA29a Nanoparticles can be detected as long as 24 h after addition of the LNCs to the cell culture medium. This delayed degradation of TETD can be attributed to the LNC nanoparticles which seem to protect the TETD molecules.

The release of TETD from the LNC capsules into cell culture medium (Fig. 3) is underestimated since TETD is quickly degraded as soon as it is in contact with the cell culture medium (Fig. 4). When the rapid degradation of TETD is taken into account about 60 % of the TETD is released from the nanoparticles within 8 h. The rapid degradation of TETD is of no concern during the in vitro cytotoxicity experiments since direct application of TETD in culture medium shows biological activity (Fig. 5). In addition, the degradation product DETC induces cytotoxicity which is about ten times less than that of TETD (unpublished observation). The in vitro cytotoxicity assay on TETD containing nanoparticles (Fig. 5) might be misleading as it clearly demonstrates biological activity of the nanoparticles. The conclusion that cytotoxicity is brought about by NP uptake and TETD release into the cytoplasm is not valid since TETD is rapidly released from the nanoparticles when transferred into DMEM cell culture medium. Therefore it is essential to characterize nanoparticles with respect to their stability in a physiological environment such as cell culture medium or serum.

V. Conclusions

Nanoparticle stability upon transfer from storage medium to application medium needs to be monitored in order to detect premature release. Nanoparticle mediated drug delivery requires that (i) the target is known, (ii) the drug reaches the target, (iii) the endosomes release at least the drug at sufficiently high concentrations to show a biological effect.

Acknowledgment

The technical assistance of Gabriele Karsten is gratefully acknowledged. This work is supported financially through the EU (NMP4 -CT-2006-02556).

References

1. Löbler M, Rohm HW, Schmitz KP, Johnston AH, Newman TA, Ranjan S, Sood R, Kinnunen PKJ (**2008**): Drug delivery by nanoparticles – facing the obstacles. IFMBE Proceedings 22, 2335–2338.
2. Hu P, Jin L, Baillie TA (1997) : Studies on the metabolic activation of disulfiram in rat. Evidence for electrophilic S-oxygenated metabolites as inhibitors of aldehyde dehydrogenase and precursors of urinary N-acetylcysteine conjugates. J. Pharm. Exp. Ther. 1997, 281, 611-617.

corresponding author:

- Author: Marian Löbler
- Institute: Universität Rostock,
- Insititut für Biomedizinische Technik
- Street: Friedrich-Barnewitz-Str. 4
- City: 18119 Rostock
- Country: Germany
- Email: Marian.loebler@uni-rostock.de

Speeding up sensor response times by modifying the geometry of the fluidic channel of a disposable array compatible sensor housing for surface acoustic wave biosensors

B. E. Rapp[1], F. J. Gruhl[1], K. Länge[1] and M. Rapp[1]

[1]Institute for Microstructure Technology (IMT), Forschungszentrum Karlsruhe, Germany

Abstract— **We describe an array compatible sensor housing for surface acoustic wave (SAW) based biosensors. The sensor housing is produced by injection molding as a mass market compatible production technology and embedded into this sensor housing by a fully automated assembly unit. A major advantage of our sensor housing is the fact that the sensitive sensor surface remains accessible for surface modification even after the embedding of the sensor into the housing. Single sensor housings can be combined to flexible sensor arrays by means of a second component, the fluidic cover. In order to speed up sensor response times we will demonstrate a design feature of this setup that allows us to easily decrease the height of the flow channel above the sensor by a slight geometric modification of the fluidic cover. We will compare five different modifications of our setup, each featuring a different sample channel height. Reducing the flow channel's height significantly reduces diffusion effects due to a reduced thickness of the Nernst diffusion layer above the sensor. This directly translates into decreasing sensor response times. The reduction of the flow channel's height allows furthermore the significant reduction of the effective sample volume above the sensor from 4.8 µl (former flow cell setup) down to 160 nl. We will compare these modifications with the initial housing setup and with a formerly used setup featuring a flow cell with respect to effective sample volume and sensor response times.**

Keywords— **microfluidics, biosensor, surface acoustic wave, disposable**

I. Introduction

One of the most discussed topics within the biomedical research community is the need for cheap and reliable sensors elements. In addition to being cheap and robust these sensor components have to be implemented as disposable components. The reason for this that reusing sensor components increases the risk of carryover effects between two experiments. This would significantly increase the costs of such experiments as cleaning and regeneration steps have to be implemented.

Biosensors based on surface acoustic waves (SAW) have proven to be a highly suitable choice of sensor elements to fulfill the requirements of this kind of applications [1]. SAW biosensors are cheap components which can be used

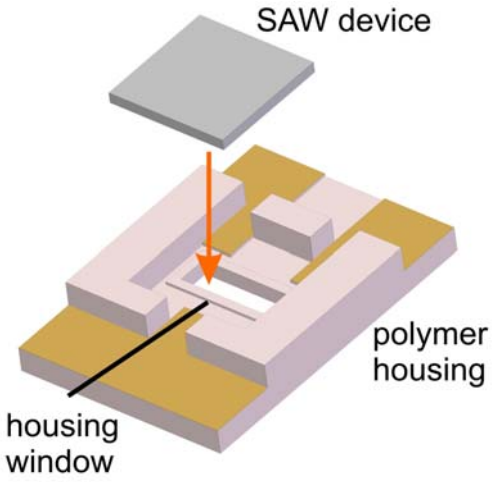


Figure 1. 3D CAD view of the designed sensor housing



Figure 2. SAW biosensor embedded in the designed polymer housing

O. Dössel and W.C. Schlegel (Eds.): WC 2009, IFMBE Proceedings 25/VIII, pp. 69–72, 2009.
www.springerlink.com

as single use disposables In order to transform laboratory setups into market compatible sensor systems, one major issue that needs to be addressed is the sensor packaging [2]. If the sensor is to be used as single use component the housing too needs to be implemented as a cheap disposable component. Besides protection of the sensor element such a housing should provide suitable electronic and fluidic interconnection of the sensor element to the sensor system. Furthermore the housing should be designed in a way that the deposition of a bioactive sensing layer on the sensitive sensor surface is possible even after the embedding. The latter is a crucial requirement for a biosensor as most surface modification protocols rely on the sensor surface being accessible for, e. g. cleaning or plasma activation steps [3].

II. MATERIALS AND METHODS

We previously reported the benefits of inserting SAW devices into disposable polymer housings. We manufacture these housings by mass market compatible manufacturing technologies as, e. g., injection molding [4]. We presented a disposable polymer housing for a SAW resonator with an effective sample volume above the sensor of 1.55 µl. The housing consists of polycarbonate and features an opening called the housing window (see fig. 1+2). This window guarantees that even after embedding of the SAW sensor into the polymer housing the sensor's sensitive surface remains accessible through this window for surface modification.

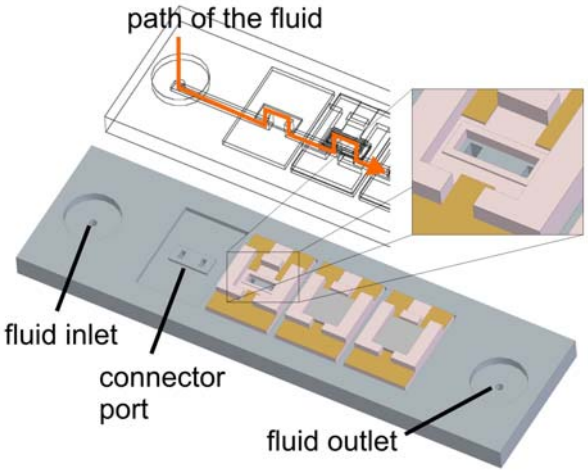


Figure 3. 3D CAD view of the fluidic cover, the path of the fluid is highlighted in the transparent view of the cover, three sensor chips are placed on the cover (in the enlarged image, the SAW device is not shown)

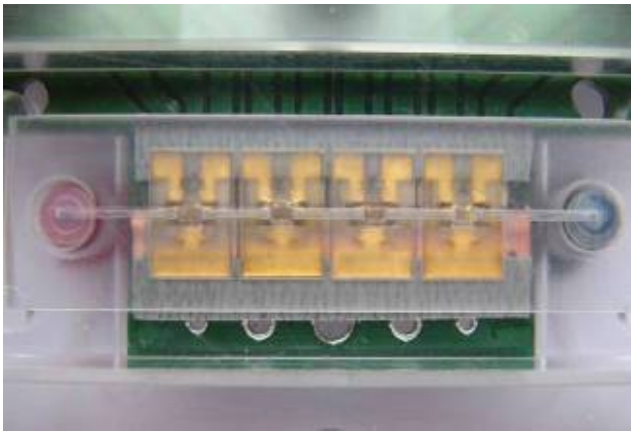


Figure 4. Fluidic cover with four attached SAW biosensors embedded in polymer housings

The fluid that is to be analyzed is guided to the housing window and thus to the SAW sensor by means of a second component the so called fluidic cover (see fig. 3+4). This component contains the fluidic channel that is used to guide the fluids of interest. The fluidic cover features four connector ports to which a housing with embedded SAW sensor can be attached. At each of these connector ports, the liquid is transferred out of the fluidic cover into the window of the attached housing with SAW sensor. There the liquid is guided across the sensitive surface of the sensor before being transferred back into the fluidic cover and guided directly to the next connector port of the sensor array. By this means it is possible to create flexible sensor arrays by combining SAW sensors embedded in housings with different biochemical sensing layers. The fluidic cover as well as the polymer housings and the SAW sensors are cheap mass market compatible components that can be disposed after each experiment allowing the setup to be used for single use applications as required, e. g., for biomedical applications.

For the designed sensor housing the volume within the housing window defines the effective sample volume above the sensor. With a length of 3.1 mm, a width of 1 mm and a height of 500 µm the effective sample volume sums up to 1.55 µl.

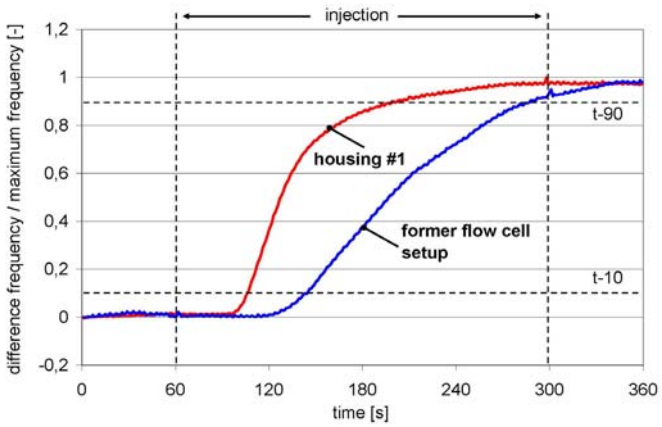


Figure 5. Experimental comparison of the former flow cell setup (effective sample volume above the sensor 4.8 µl) and the housing version #1 (effective sample volume above the sensor 1.55 µl), analyte: bovine serum albumin (BSA, 4 mg/ml in phosphate buffer), carrier: phosphate buffer, each experiment was repeated three times

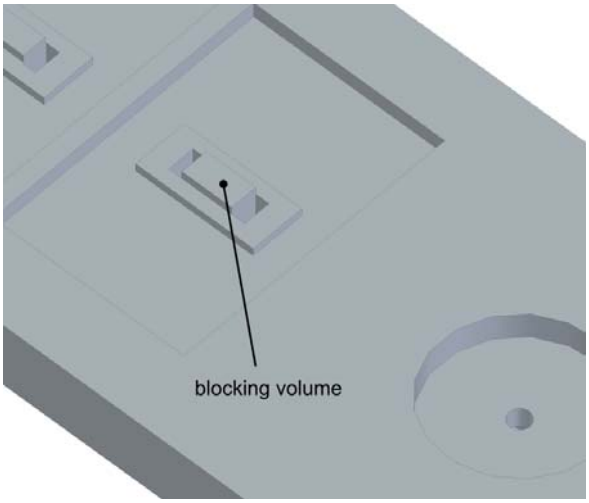


Figure 6. 3D CAD view of the modified fluidic cover, the blocking volume is located on the fluidic connector ports between the inlets of the two channels, it will locally reduce the sample volume above the SAW sensor in the attached sensor housing

III. RESULTS AND DISCUSSION

We compared the sensor housing described in the previous section to a formerly used setup with a flow cell which features an effective sample volume of 4.8 µl. For these experiments we used protein adsorption experiments. We have previously reported this type of experiments to be very suitable for the demonstration of diffusion effects which are mainly influenced by the thickness of the Nernst diffusion layer [5]. Bovine serum albumin (BSA) was dissolved in phosphate buffer to a concentration of 4 mg/ml and inserted into a 200 µl sample loop attached to a flow injection analysis (FIA) system. Prior to the experiment phosphate buffer was pumped via the FIA system through the sensor cell in order to allow the sensor to reach a stable baseline. After that the experiment was started. The FIA was switched to injection mode between 60 s and 300 s thus injecting the protein solution to the SAW sensor. BSA is known to adsorb permanently onto the surface of a SAW device, resulting in a measurable sensor signal. Two important parameters were characterized: the time it takes the sensor to show the first response due to BSA adsorption after the beginning of the injection and the time it takes the sensor signal to rise to a defined value. For this, two values were evaluated: the time the signal has reached 10 % of the maximal value (t-10 value) and the time the signal has reached 90 % of the maximal value (t-90 value). We have found that the reduction of the flow channel's height directly above the sensor significantly increases the sensor response times (small t-10 and t-90 times, see fig. 5). The height of the flow channel is a good means of manipulating the thickness of the Nernst diffusion layer above the sensor surface. By further reduction of the channel's height, we expect to further reduce the diffusion effect thus speeding up sensor response times even more. We will show comparative measurements with five different modifications of the initial sensor housing setup (see table 1). In order to do so, we implemented different fluidic covers that feature blocking volumes on the fluidic connector ports between the inlets of the two channels (see fig. 6). By doing so we will be able to locally reduce the height of the flow channel directly above the sensor to any value needed. Implementing a blocking volume of 300 µm height would reduce the initial height of the flow channel above the sensor from 500 µm to 200 µm (modification #3).

Table 1 Modifications of the initial sensor housing setup – each modification features a different flow channel height above the sensor and thus a different effective sample volume above the sensor

Item	Channel length [mm]	Channel width [mm]	Channel height [µm]	Effective sample volume [µl]
Flow cell	4.0	1.0	1200	4.8
Initial system as described in [4]	3.1	1.0	500	1.55
Modification #1	3.1	1.0	400	1.24
Modification #2	3.1	1.0	300	0.93
Modification #3	3.1	1.0	200	0.62
Modification #4	3.1	1.0	100	0.31
Modification #5	3.1	1.0	50	0.16

IV. CONCLUSION

We compared experimental results obtained using the initial sensor's polymer housing with a formerly used flow cell setup. We have found that reducing the flow channel's height reduces not only the effective sample volume but also the sensor response times due to smaller diffusion effects. Based on these promising results we further investigate the effect of the reduction of the flow channel's height with respect to sensor response times. In order to do so we intend to compare five different modifications of the initial sensor housing featuring different flow channel heights starting from 500 µm down to 50 µm and effective sample volumes above the SAW sensor of 1.55 µl down to 0.16 µl, respectively. We will compare these housing combinations with the formerly used flow cell setup and demonstrate how sample consumption and sensor response times can effectively be decreased by our flexible sensor housing design.

REFERENCES

1. Länge, K., Rapp, B. E., Rapp, M. (2008) Surface Acoustic Wave Biosensors - a Review. Anal. Bioanal. Chem. 391: 1509-1519.
2. Lec, R. M. (2001) Piezoelectric Biosensors: Recent Advances and Applications", IEEE International Frequency Control Symposium and PDA Exhibition (Seattle, USA). 419-429.
3. Länge, K., Grimm, S., Rapp, M. (2007) Chemical modification of parylene C coatings for SAW biosensors. Sens. Actuat. B 125: 441-446.
4. Rapp, B. E., Länge, K., Rapp, M. (2008) An array compatible polymer housing for a Love wave surface acoustic wave (SAW) biosensor allowing the elimination of conductivity sensitivities of SAW resonators., International Meeting on Chemical Sensors IMCS (Columbus, USA).
5. Länge, K., Blaess, G., Voigt, A., Götzen, R., Rapp, M. (2006) Integration of a surface acoustic wave biosensor in a microfluidic polymer chip. Biosens. Bioelectron. 22: 227–232

Corresponding author:

Author: Bastian E. Rapp
Institute: Institute for Microstructure Technology (IMT), Forschungszentrum Karlsruhe
Street: Hermann-von-Helmholtz-Platz 1
City: 76344 Eggenstein-Leopoldshafen
Country: Germany
Email: bastian.rapp@imt.fzk.de

Surface Acoustic Wave (SAW) Biosensor Chip System – a Promising Alternative for Biomedical Applications

F.J. Gruhl, B.E. Rapp, M. Rapp, K. Länge[1]

[1] Institute for Microstructure Technology (IMT), Forschungszentrum Karlsruhe, Germany

Abstract— **Surface acoustic wave (SAW) biosensors based on horizontally polarized surface shear waves enable label-free, sensitive and cost-effective detection of biomolecules in real time. Binding reactions on the sensor surface are detected by determining changes in surface wave velocity caused mainly by mass loading in the sensing layer. Typically SAW devices are coated with biochemically sensitive layers including analyte-specific capture molecules or ligands. For the development of an array, single SAW devices first are embedded in polymer housings, however, the sensitive sensor area still remains accessible for surface modification. Advantages of those SAW biosensor chips are simple handling and low consumption of chemicals used in the coating process. An integrated microfluidic chip connects eight SAW biosensor chips to an array. An additional feature of the microfluidic chip is the direct connection between sample and biosensor chips allowing small sample volumes. This SAW biosensor chip array enables simultaneous analysis of multiple analytes in one sample. A potential application of such an array is the use in future point-of-care (POC) devices. First affinity experiments using this set-up will be shown.**

Keywords— **Biosensors, label-free, surface acoustic wave, immobilization, biomedical applications.**

I. Introduction

In many cases it is possible to diagnose diseases, such as cancer or rheumatic diseases, via determining concentrations of specific protein markers in blood, i.e., a marker profile. Such a marker profile can also be used for monitoring the success of the therapy applied to cure those diseases. For example, therapy of breast cancer patients often has to be modified to achieve best possible chances for healing. In many cases, the critical time already lies within the first six weeks after therapy start [1]. For such POC applications based on the detection of multiple proteins analytes in one sample a cost-effective and rapid analysis system with small sample consumption is required.

SAW biosensors allow the label-free, sensitive and cost-effective detection of biomolecules. They have been applied successfully to detect proteins, DNA and bacteria [2]. For the detection of proteins the sensor surface is modified with capture molecules or ligands binding specifically to the analyte. Unspecific binding reactions were prevented by coupling the binding molecules via an intermediate hydrogel layer, such as dextran, on the sensor surface. This is a crucial issue for all biosensors based on label-free detection of analytes in serum samples due to the high protein background. Our current SAW biosensor system consists of a SAW device embedded in a flow cell and an external flow injection analysis (FIA) system. This set-up was used successfully in several affinity binding experiments [2,3], however, it is not suited for medical applications: Aside from the SAW device itself it consists of non-disposable components making it inappropriate for a POC device.

We developed disposable SAW biosensor chips consisting of single SAW devices embedded in polymer housings. An integrated microfluidic polymer chip connects eight of the biosensor chips to an array. Besides, the microfluidic chip offers a direct connection of the chips to the sample and replaces the previously used external FIA system making the whole set-up suitable for medical applications. The set-up was applied successfully in an affinity binding experiment.

II. Materials and methods

A. SAW device, instrumentation and fluidic system

The shear horizontal SAW resonator type E062 was designed in a former cooperation with Siemens, Munich, Germany and delivered by EPCOS, Munich, Germany. The resonator is based on a small (4 x 4 mm²) 36°YX-$LiTaO_3$ device with gold transducers and has a frequency of operation of 428.5 MHz. SAW measurements were performed in an oscillator circuit developed in-house with the SAW resonator as frequency-determining element. Details of the set-up have been described earlier [4].

A flow cell was designed in which the SAW device was mounted upside down onto isolated contact pads on the electronic board and coupled capacitively. A flow channel (volume 4.8 µl) between the contact pads allowed the fluid to pass along SAW device. Binding experiments were performed using an external FIA system equipped with two peristaltic pumps and injection valve.

O. Dössel and W.C. Schlegel (Eds.): WC 2009, IFMBE Proceedings 25/VIII, pp. 73–76, 2009.
www.springerlink.com

The core of our SAW biosensor chip array is the integrated microfluidic polymer chip. This disposable component allows the connection of up to 8 SAW biosensor chips – which are simply clipped into corresponding cavities – as well as it provides a direct connection with the sample resulting in an integrated microfluidic system. Details of the complete set-up have been published earlier [5].

B. Preparation of the sensor surface

Parylene coating: All SAW devices used in the following experiments were first coated with 0.1 µm parylene C to obtain a chemically homogeneous surface. This improves success and reproducubility of further preparation steps. Details of the process have been published earlier [6].

Covalent binding of hydrogel: Aminodextrane (AMD) with M_r 3.000 was used as intermediate hydrogel layer. The parylene C layer was activated by oxidation via plasma treatment and subsequent silanization with (3-glycidyloxypropyl)trimethoxysilane. After rinsing with acetone the sensors were treated overnight with an aqueous solution of hydrogel, c = 2 mg/ml. Then sensors were rinsed thoroughly with bidestilled water and dried.

Immobilization of non biotinylated bovine serum albumin (BSA) and biotinylated BSA (b-BSA): The affinity system of streptavidin with biotin was used for examplary measurements. BSA and b-BSA were immobilized on the AMD coated sensors. The amino groups were converted to carboxyl groups via glutaric anhydride dissolved in dimethyl formamide, c = 2 mg/µl. Protein immobilization was performed on-line by means of the external FIA system. Phosphate-buffered saline (PBS) was used as carrier stream. First, the carboxylized surface was activated with a solution of 0.05 M N-hydroxy succinimide and 0.2 M N-(3-dimethylamino-propyl)-N'-ethylcarbodiimide hydrochloride in bidistilled water and rinsed with PBS. Second, the surface was incubated with a solution of 1.8 µM b-BSA or BSA in acetate buffer, pH 5, and rinsed with PBS. Third, the remaining reactive groups on the surface were deactivated by flushing with a solution of 1 M ethanolamine, pH 8.5. After rinsing with PBS, the sensor was immediately used for the assay.

C. SAW measurements: streptavidin assay

Experiments were performed with PBS, pH 7.4, as carrier stream. The flow rate was set to 0.05 ml/min. Samples were loaded in the sample loop, injected into the carrier stream via the injection valve, and transported to the sensor. The injection interval was set to 60-300 s. After each injection the sensor was rinsed with PBS.

Sensors with covalently immobilized b-BSA or BSA were used. Samples containing, c = 0 (0.5; 1; 5; 10) µg/ml streptavidin were injected in the carrier stream.

III. Results

A. SAW biosensor with flow cell and external FIA system: affinity binding experiment

SAW measurements based on the affinity system streptavidin/biotin were performed with SAW biosensors integrated in the flow cell with the external FIA system. Biotinylated BSA and non biotinylated BSA, respectively, were immobilized on the SAW sensor surface via an intermediate AMD layer, samples contained streptavidin. Each sensor was tested by injection of several concentrations of streptavidin, c = 0 (0.5; 1; 5; 10) µg/ml. Exemplary signal responses are shown in Figure 1, the signals were reproducible (data not shown). Using a sensor with immobilized binding partner, i.e., b-BSA, the SAW signal response increases with higher concentrations of streptavidin until saturation is reached (Fig. 1 line (1)). The SAW signal does not significantly increase when streptavidin is injected using a sensor with immobilized BSA (Fig. 1 line (2)). This experiment shows the ability of our SAW biosensors to detect proteins specificly, directly and label-free.

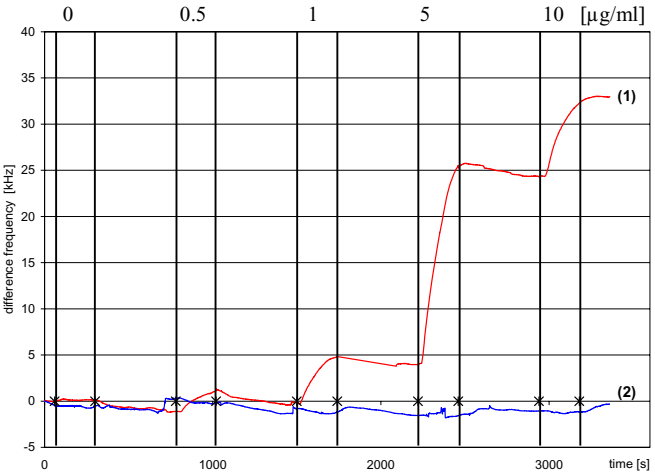


Fig. 1 Streptavidin assay. Typical measurement curves of the SAW biosensor. Biotinylated BSA (1) and non biotinylated BSA (2) immobilized on sensor surface coated with AMD 3.000. Different concentrations of streptavidin (0 – 10 µg/ml) were used as analyte.

A. SAW biosensor chip array with integrated microfluidic system: development and experiments

The set-up described above enables a single measurement per sample. But for many biomedical applications an array of several sensors is required, which have to be disposable components to avoid carry-over effects. Our biosensor chip system consists of an array of 8 SAW biosensors. For such a system two conditions were necessary: a simple handling of SAW sensors without loss of ability to individually modify the surface and an integrated microfluidic system.

In our case, a SAW device first is embedded in polymer housing. The housing features a window framing the sensitive area of the sensor (Figure 2). Therefore, after embedding, the SAW device's surface still is accessible for a variety of surface modification steps and sensor preparation can be performed.

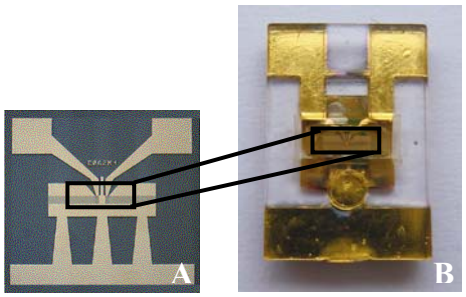


Fig. 2 SAW device E 062, 4 x 4 mm² (A). And SAW sensor embedded in polymer housing (B). The sensitive area of SAW device remains free (black rectangle).

The integration of a microfluidic system by means of a microfluidic polymer chip connects the 8 SAW biosensor chips directly with the sample (Fig. 3). The complete microfluidic chip can be disposed after each experiment. So the set-up of our SAW biosensor chip system consists of two disposable components: the biosensor chips and the microfluidic platform.

Fig. Disposable microfluidic polymer chip. The interconnection between the 8 SAW biosensor chips and the sample.

A preliminary measurement making use of solutions of different conductivity was performed with the complete SAW biosensor chip array. Phosphate buffer was used as carrier stream, bidistilled water was used as sample. The signal responses of 8 parylene C coated SAW biosensor chips are shown in Figure 4. The signal responses of the first 4 biosensor chips (C1 – C4) started immediately after beginning of the injection interval. The delayed signal response of the last 4 biosensor chips (C5 - C8) results from the channel geometry. Still, the experiment demonstrates that the delay time could be reduced using the complete system SAW biosensor chip array with integrated microfluidic system.

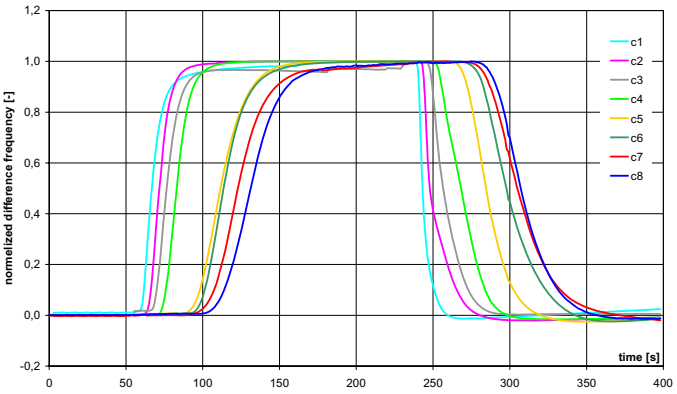


Fig. 4 Normalized measurement curves of the array with 8 biosensor chips (c 1 – c 8), coated with 0.1 µm parylene C. Phosphate buffer was used as carrier stream, bidestilled water as sample. Injection interval: 60 – 300 s.

IV. Discussion

In this work, the ability of the use of SAW biosensor for specific protein detection was shown with measurements in a flow cell as part of an external FIA system. Significant streptavidin signals were obtained only when the corresponding binding partner, b-BSA, was immobilized on the SAW biosensor surface. Aside from being specific, direct and label-free, the protein binding is monitored time-resolved enabling the determination of kinetic parameters of the binding reaction.

However, the SAW set-up with flow cell and external FIA system is not suitable for medical applications. It contains mainly non-disposable components which could lead to carry-over effects between different measurements. An additional disadvantage are the comparatively large dimensions of flow cell (and tubing) leading to a significant delay of signal response times and increase of sample volumes. In consequence, the flow cells are not array compatible.

Therefore, the benefits of inserting SAW devices in disposable polymer housings are not only simple handling and reduction of coating chemicals but also the array compatibility of those chips. In combination with the microfluidic polymer chip providing a direct connection between chips as well as sample and chips, sample volumes are kept low and the complete microfluidic detection system is disposable. Furthermore, the compact set-up is user-friendly and inexpensive. In consequence, the SAW biosensor chip system offers a suitable platform for biomedical applications. In the next step, the SAW biosensor chip array is optimized for biological applications with regard to real samples and required detection limits.

V. Conclusions

We presented a cost-effective SAW biosensor chip array included in a microfluidic system for future POC devices. In particular, this set-up offers a simple and cost-effective method for the detection of multiple protein analytes out of one sample, i.e., a protein marker profile. Such a profile could give a quick answer about the state of health of a patient (Figure 5) allowing an immediate adaptation of therapy.

Fig. 5 Model of a potential marker profile. Concentration of distinct proteins (here: 8) in serum can give quick information about state of health of patients.

References

1. Lüftner D., Lüke C. et al (2003) Serum HER-2/*neu* in the management of breast cancer patients. Clin. Biochem. 36: 233-240
2. Länge K., Rapp B. E. et al (2008) Surface acoustic wave biosensors: a review. Anal. Bioanal. Chem 391: 1509-1519
3. Länge K., Rapp M. (2008) Influence of intermediate aminodextran layers on the signal response of surface acoustic wave biosensors. Anal. Biochem. 377: 170-175
4. Länge K., Bender F. et al (2003) A surface acoustic wave biosensor concept with low flow cell volumes for label-free detection. Anal. Chem. 75: 5561-5566
5. Rapp B. E., Carneiro L. et al (2009) Microfluidic injection analysis (FIA) System allowing Diffusion Free and Indirect pumping of Liquids by Using Tetradecanes as Intermediary Liquid. Lab Chip 9: 354-356
6. Bender F., Länge K. et al (2004) On-line monitoring of polymer deposition for tailoring the waveguide characteristics of Love-wave biosensors. Langmuir 20: 3215-2319

Author: Friederike Gruhl
Institute: Institute for Microstructure Technology, Forschungszentrum Karlsruhe
Street: Hermann-von-Helmholtz -Platz 1
City: Eggenstein-Leopoldshafen (Karlsruhe)
Country: Germany
Email: Friederike.Gruhl@imt.fzk.de

Multiparametric NeuroLab with integrated MEA & life support

F. Ilchmann[1], J. Meyer[2], M. Schmidhuber[1], M. Zottmann[1], B. Becker[1] and B. Wolf[1,2]

[1] Heinz Nixdorf Lehrstuhl Medizinische Elektronik, Technische Universität München, München, Germany
[2] IMETUM - Zentralinstitut für Medizintechnik, Technische Universität München, Garching, Germany

Abstract— **The biology of neuronal cells is more complex than analyses of single molecular components can reveal. To understand the interactions of living neurons in their natural environment it is important to look at the functional mechanisms of cells. Stable culturing of neuronal networks over long periods of time requires strict control over biochemical parameters of the medium. Therefore the quantitative analysis of micro-environmental conditions and cell metabolic rates is essential in interpreting the changing patterns of electrophysiological activity. Changes in spontaneous spike production and oxygen consumption measured at the site of the network monolayer can provide rapid indications of metabolic disturbances. The developed biosensor supported neuro screening system NeuroLab helps to perform high content screening studies on living cells in a near invivo environment.**

Keywords— **MEA, recording chamber, sensor, pH, high content screening**

I. Introduction

The utilization of cultured neuronal networks grown on sensor chips with multi-electrode arrays (MEAs) for toxicological studies is a well established method [1]. Stable culturing of neuronal networks over long periods of time requires strict control over biochemical parameters of the culture-medium. Therefore the quantitative analysis of micro-environmental conditions and cell metabolic rates is essential in interpreting the changing patterns of electrophysiological activity. Changes in spontaneous spike production and oxygen consumption measured at the site of the network monolayer can provide rapid indications of metabolic disturbances.

The NeuroLab offers the possibility to handle different sensors and providing accurate temperature control of both sensor chip and medium [2]. The multiparametric glass sensor chip integrates different sensors for extracellular cell recordings, i.e. a microelectrode array, an amperometric sensor to measure changes in dissolved oxygen, a pH and a temperature sensor. By including all necessary circuits for easy computer readout and temperature control, the NeuroLab allows convenient handling.

II. Materials and Methods

A. Sensor chip

A glass-based sensor chip has been designed, including MEA and sensors for oxygen, pH and temperature. In addition to the obvious benefit for microscope inspection from both sides, glass-based sensor chips with metal oxide pH sensors need no silicon MOS technology. Glass chips are therefore not sensitive to electrostatic discharge, resulting in easier handling precaution. In addition, manufacturing costs are much lower for small quantities of large area chips making them ideal suited for one-time use.

For the detection of electrophysiological activity, a microelectrode array is placed in the centre of the sensor chip. It consists of 64 electrodes arranged in an 8 x 8 array.

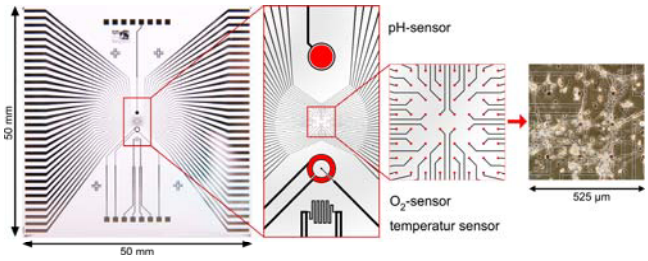


Fig. 1 Multiparametric NeuroChip with stepwise magnification

To monitor the microenvironmental parameters of the living cell culture, three sensors were placed in immediate vicinity of the MEA resulting in accurate measurement of the cellular parameters.

For measuring the pH-value, a ruthenium oxide (RuO_2) spot is applied on the surface of the sensor chip. Together with a reference electrode integrated in the fluidic system, pH measurement of the culture medium is possible.

Changes in the oxygen concentration can be monitored with a planar amperometric oxygen sensor. It consists of three electrodes (working-, quasi-reference- and auxiliary-electrode) without membrane structures. The diameter of the working electrode is ≈ 30 µm, the working potential -600 mV [3].

O. Dössel and W.C. Schlegel (Eds.): WC 2009, IFMBE Proceedings 25/VIII, pp. 77–79, 2009.
www.springerlink.com

The temperature of the cell culture medium is measured by a platinum resistor integrated on the sensor chip surface.

All conducting paths consist of thin platinum layers. The sensor chip is coated with an insulation layer which is opened only on the active sensor surface and the contact strips (shown in red in Figure 1). Due to the transparent substrate, all kinds of microscope monitoring are possible, making these chips powerful tools for neurobioinformatics [4].

B. Recording Hardware

For multiparametric measurements with the sensor chip, a recording chamber was developed (Figure 2) [5]. The measured parameters are directly amplified and converted to RS232 standard for computer readout within the platform. Furthermore, an integrated regulated heating foil underneath the sensor chip ensures stable temperature control for cell cultivation and enables the user to operate the chamber outside an incubator.

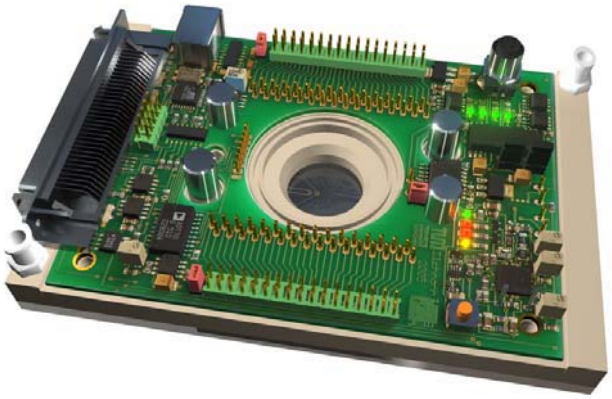


Fig. 2 NeuroLab with inserted sensor chip.
For better understanding, the picture shows an unveiled version

The complete recording chamber consists of only three parts relevant for the user's handling. The aluminium baseplate with integrated Kapton-heaters and additional temperature sensors forms the sensor chip carrier. A cut-out underneath the chip allows microscopic monitoring of the sensor chip from both sides at any time.

The second part of the NeuroLab made of biocompatible plastics forms the vessel for the cell culture medium on top of the sensor chip. It includes a micro-fluidic system that supports the cell culture with fresh culture-media supplied by an external syringe pump. A removable heated ITO-coated glass cap within the NeuroLab seals the cell culture from environmental impacts guaranteeing safe handling and protection against contaminations while allowing easy agent addition. That way, contamination-free recording periods of several days are possible. All parts in contact with the cell-medium can be fully cleaned by steam sterilization, as they are not carrying any electronic components.

C. Electronics

The upper part of the NeuroLab is the electronic circuit-board itself, fixed on a thin mounting plate. Gold-plated spring contact pins connect the MEA as well as the sensors and the heating elements. Thereby, reliable and constant contact resistance is achieved without the risk of damaging the glass sensor chip.

Sensor amplification forms the most important part, decisive for a precise measurement with low noise level. After A/D conversion, a microcontroller sends the measured data via RS232 interface to an external computer. Recorded MEA signals are preamplified and routed to an external amplifier for further signal processing.

The third part of the electronic section is the heating regulation circuit which works with an accuracy of up to 0,01°C using a proportional-integral-derivative (PID) controller.

Several LEDs give feedback to the user showing measurement and power supply status. In addition, separate over- and undertemperature outputs indicate when the chamber temperature is out of range. Integrated electromagnetic shielding keeps the sensor signals, including MEA, from external noise influence. The entire circuit board is coated to protect against moisture, making it especially suitable for laboratory work.

D. Experimental setup

For experiments, the NeuroLab with the culture is placed on an inverted phase contrast microscope inside a Faraday cage for electrical shielding. The space between the culture medium and the cover cap is perfused with a sterile 8 % CO_2-air mixture at a flow rate of 80 mL / min for pH stabilization. The cage is connected via a cable to the ground of the NeuroLab. Thus the culture medium becomes the reference ground for the amplifier. A CO_2-air mixer for pH control and a syringe pump for constant water supply are placed right outside the Faraday cage to minimize electrical interference. A constant, slow water addition (200 µL / hr) is necessary in order to prevent evaporation of the heated



Fig. 3 NeuroLab experimental setup with phase contrast microscope

culture medium and subsequent osmolarity changes that would affect the electrical activity of the neuronal cultures. The microscope is equipped with an epifluorescent system for simultaneous electrical and optical measurements. The monochromator, camera cooler and controller are positioned on the table below the microscope.

E. NeuroLab software

For easy interpretation of micro-environmental condition changes, an analytic software for easy signal interpretation has been developed. It is capable of controlling the external life support systems for the cell culture as well as recording all measured parameters. Scalable graphical plots allow both real-time and long-term monitoring. Using Plexon's MEA Workstation data acquisition software, activity can be easily analyzed (Figure 4).

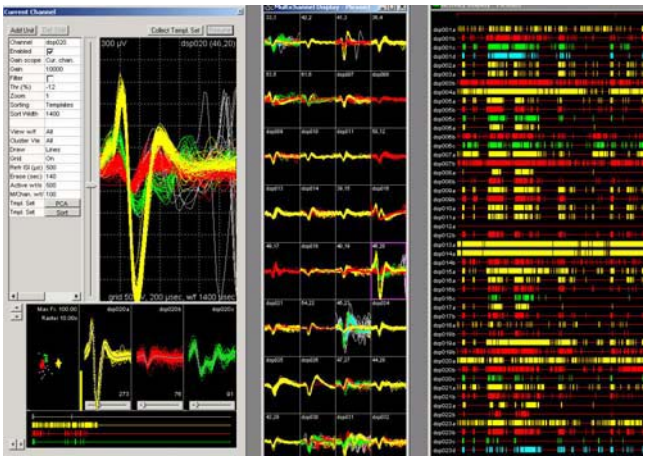


Fig. 4 Typical recordings done with Plexon's MEA Workstation data acquisition software

III. CONCLUSIONS

Studies conducted utilizing the NeuroLab showed excellent multiparametric recordings for up to nine days with parallel documentation of vital parameters. Currently, the NeuroLab serves for two experimental settings: First, to measure effects of electromagnetic pulses similar to those used in Transcranial Magnetic Stimulation (TMS), and second, to examine neurodegenerative proteins contributing to Alzheimer's and Parkinsons's disease. The measured data provide an ideal basis for further studies on metabolism dependant activity. The compact design allows integration in any laboratory environment.

ACKNOWLEDGMENT

The authors express their personal appreciation of the valuable assistance given them in their research by many students at the Heinz Nixdorf Lehrstuhl für Medizinische Elektronik [6]. Financial support by the Heinz Nixdorf Foundation is kindly acknowledged.

REFERENCES

1. G. Gross, F. Schwalm (1994) A closed chamber for long-term electrophysiological and microscopical monitoring of monolayer neuronal networks, Neuroscience Methods 52: 73-85
2. F. Ilchmann, D. Grundl, V. Lob,, B. Becker, B. Wolf (2008), Zell-Chipsysteme - Mikrosensorarrays für die biologische Grundlagenforschung und Diagnostik, GIT Laborfachzeitschrift, 52 Jahrgang, 3, 285-260
3. J. Wiest, M. Brischwein, J. Ressler, A. M. Otto, H. Grothe, B. Wolf (2005) Cellular Assays with Multi-parametric Bioelectronic Sensor Chips CHIMIA Vol. 59: No. 5, 243-246
4. F. Ilchmann, V. Lob, J. Meyer, H. Ressler, B. Wankerl, J. Wiest, B. Wolf (2008), Automated Cell Analytics, Application on Sensor Chips, Screening-trends in drug discovery, Volume 9, 21-23
5. J. Wiest, D. Grundl, M. Schmidhuber, M. Brückl, V. Lob, F. Ilchmann, M. Brischwein, H. Grothe, A.M. Otto, B. Wolf (2008), Real-time and marker-free investigation of living cells, Clinical Chemistry and Laboratory Medicine, 46, 9, A160
6. Heinz Nixdorf Lehrstuhl Medizinische Elektronik at http://www.lme.ei.tum.de

Author: Florian Ilchmann
Institute: Heinz Nixdorf Lehrstuhl Medizinische Elektronik
Technische Universität München
Street: Theresienstrasse 90, N3
City: 80333 Munich
Country: Germany
Email: Ilchmann@tum.de

QCM BASED ON FLOW SYSTEM FOR CARDIOVASCULAR DISEASE

K. Wong-ek[1], O.Chailapakul[1], J. Prommas[2], K. Jaruwongrungsee[3], N. Nuntawong[4], and A. Tuantranont[3]

[1] Nanoscience and Technology Graduate Program, Chulalongkorn University, THAILAND
Email: wongek@tu.ac.th
[2] Biosensor Laboratory, Faculty of Medical Technology, Mahidol University, THAILAND
[3]Nanoelectronics and MEMS Laboratory, National Electronics and Computer Technology Center
[4]Photonic Technology Laboratory, National Electronics and Computer Technology Center
Pathumthani, THAILAND

Abstract— **Quartz Crystal Microbalance (QCM) is a special sensor which has acoustic impedance detector by mass loading. In this study Cardiac Troponin T (CTnT) which elevates in all patients with AMI diagnosed by World Heath Organization (WHO) criteria is used as immunoligical assay onto sensor. Detection of the Troponin T is developed based on antigen - antibody system on QCM sensor as solid support and signal transduction for immobilization to monitor risk marker of myocardial infarction. To immobilize antibody, the sensor is functionalized with Polyvinyl chloride (PVC) doped COOH by spray coating technique. The modified sensor testing results can be given in short response time and a direct conversion of mass accumulation into a frequency shift representing a measurable electrical signal. The relationship between the Cardiac Troponin T concentration and the response current could be observed in the minimum concentration range at 5 ng/ml.**

Keywords— **Quartz Crystal Microbalance; Cardiac marker; Acute Myocardial Infarction, Biosensor; Flow injection**

I. INTRODUCTION

Cardiac troponins are part of the new definition of acute myocardial infarction (AMI) by the European Society of Cardiology and the American College of Cardiology (ESC/ACC). They are released into the blood circulation from injured heart muscle cells [1] during cardiac ischemia with no overlap with skeletal muscle troponins under normal conditions. [2] Multiple studies have demonstrated that both cTnI and cTnT are important prognostic indicators in patients presenting chest pain, even when MB fraction of creatine kinase (CK) is not elevated. [3] Particularly, the troponins T is wider accepted as a tool to stratify patients with chest pain, moreover the detection of cardiac troponin might also be useful prognosticator in high risk patients. There are several methods being able to detect troponin T such as enzyme linked immunosorbent assay (ELISA), radioimmunoassay (RIA) which are normally used but there are suffered from relatively low throughput, high reagent and large amount of sample consumption. Development of fast and sensitive CTnT detecting sensor by Quartz Crystal Microbalance (QCM) with Immunoassay method for the quantification of CTnT protein is great importance because QCM have advance capability in consuming less amount of reagent; therefore less amount of sample is required. Approach for cTnT detection using QCM technique, which has more potential to be truly direct measurements, as well as rapid, specific and user-friendly should be explored.

In 1959, Sauerbrey derived the equation of frequency shift of the quartz resonator in gas phase:

$$\Delta f = -\frac{2 f_O^2}{\sqrt{\rho_q \mu_q}} \frac{\Delta M}{A} \tag{1}$$

where: Δf is the frequency shift of the resonator, f_0 is the fundamental frequency, ρ_q is the density of quartz (2.648 g/cm^3), μ_q is the shear modulus of quartz (2.947×10^{11} g/cm×s^2), ΔM is the mass deposited on the surface of electrode and A is piezoelectrically active area (for the $2/\sqrt{(\rho_q\ \mu_q)}$ can be expressed as a constant, k, which is 2.26×10^{-7}). This equation can describe the additive mass rigidly deposited on the electrode surface. It can also be approximately applied for humidity and gas sensing. Although the water molecules and gas molecules deposited on the electrode are not rigid material, they can be absorbed by the hygroscopic and gas sensing layer, which is rigidly deposited on the electrode surface.

A modified QCM biosensor, combining the specificity of antibodies [4] with the sensitivity of the quartz crystal microbalance will provide a potentially rapid and direct measurement of CTnT concentration. The bioprobes on gold sensor is expected to have high active region per antigen antibody reaction. The sensor is mass sensitive detectors based on oscillating silver quartz crystal with some certain frequency. Due to complex binding, crystal

O. Dössel and W.C. Schlegel (Eds.): WC 2009, IFMBE Proceedings 25/VIII, pp. 80–83, 2009.
www.springerlink.com

frequency will decrease with amount of deposited material and could be used to measure change in its mass.

In this work, surface of QCM is coated with Polyvinyl chloride (PVC) doped COOH, 1-Ethyl-3-[3-dimethylaminopropyl]carbodiimide Hydrochloride (EDC) and *N*-hydroxysuccinimide (NHS), Protein G and CTnT Antibody to detect human CTnT which are specific biochemical assays to provide evidence of acute myocardial infarction (AMI). By our knowledge, CTnT detection based on QCM has not been developed before. The deposited QCM is used as an immunosensor and the relationship of frequency change relative to CTnT concentrations are characterized. [5] and [6]

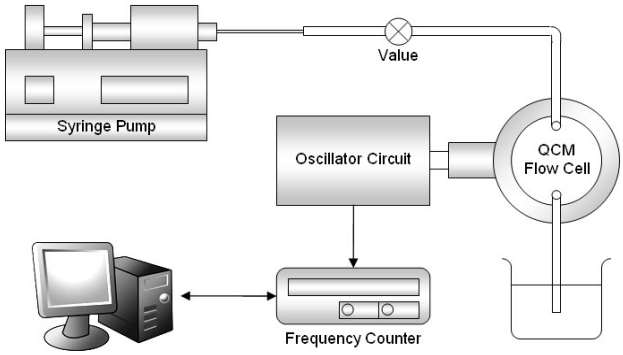


Figure 1 Diagram of developed flow injection system.

II. Materials and Experimental

A. Reagents and coating materials

Polyvinyl chloride (PVC), EDC/NHS and Protein G from Streptococcal bacteria are purchased from Sigma-Aldrich Chemical Co. Inc. Biotech grade Tetrahydrofuran (THF) (Merck, Damstadt, Germany) is used as a solvent of PVC-COOH and is prepared by dissolving 0.25 mg in 10 ml of THF with constant stirring for 10 minute at room temperature. The 1M phosphate buffer saline (PBS, pH 7.4) is used as a buffer solution. Monoclonal antibody 9G6 and Human Cardiac Troponin T are purchased from Abcam Co.Inc.. The mouse monoclonal antibody is of the IgG and is produced for use only in these experiments. Gold surface AT-cut QCM which are 5 MHz frequency range from Stanford Research System, Inc. are used. In this study, flow system is shown in diagram of figure 1. This system is developed by Nanoelectronics and MEMS Laboratory (NECTEC, NSTDA Thailand).

B. Immobilization procedures

Immobilization of the CTnT – QCM sensor is done by multiple coating steps. Firstly, QCM has to be cleaned prior coating by 1:1 of 30% H_2O_2 and 96% H_2SO_4 (Piranha solution). Then spray coating technique is provided in active zone of the QCM surface in a solution of 2.5% PVC-COOH. Then sensor is five times washed in HNO_3 solution to eliminate excess polymer and rinses with PBS buffer and dry with Nitrogen gas (N_2) before used. The flow system which has a peristaltic pump and manual switching valve connects to laptop with Window XP operating system sent frequency shift directly in every second controlled by developed program. All process are used flow rate at 0.5 µl per second [7]. After a QCM is placed, EDC/NHS is injected to QCM chamber system which performed by 1 ml of 25 mM EDC in distilled water mixed with 1 ml of 50 mM NHS in DI, then flowed for 30 minutes in chamber and then followed by 30 minutes flow of PBS solution [8]. After removing excess reagent, the 2 ml of 3 µg/ml CTnT antibody is injected and flowed for 30 minutes, and then washed by rinsing PBS buffer for 5 minutes. Figure 2 represents to Scanning Electron Microscope (SEM) image of Protein that adsorbs onto QCM surface.

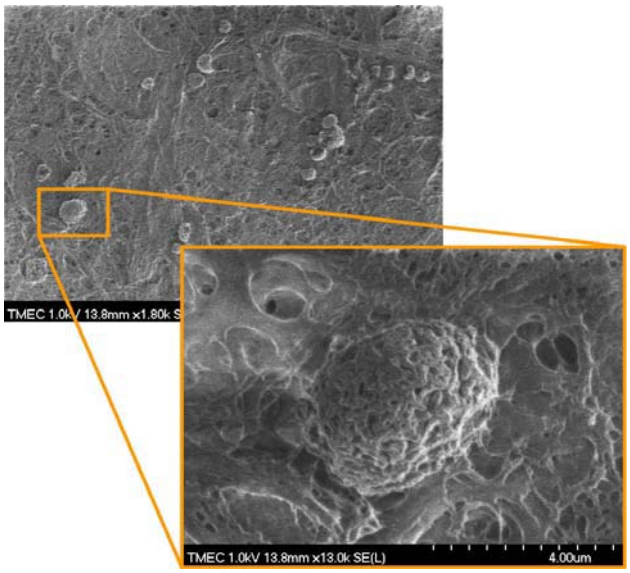


Figure 2 SEM image of the QCM sensor electrode surface after immobilized with protein G.

C. Analytical procedure

To detect QCM sensor antigen-antibody binding step, CTnT antigen 1 ml of 50 ng/ml is injected into the chamber

then flowed for 60 minutes (loop system) and then rinsed with PBS to remove excess conjugated product. The testing data of frequency shift collects to computer via GPIB port and show in figure 3.

D. Reusability

After application is done, modified QCM could be regenerating a cross-linker layer by rinsing sensor with 0.1M Sodium hydroxide. The protein layer is removed from surface by changing pH-value to alkaline area and rearranged crosslinker layer by change environment to pH 7.4 which possible to use for new detection.

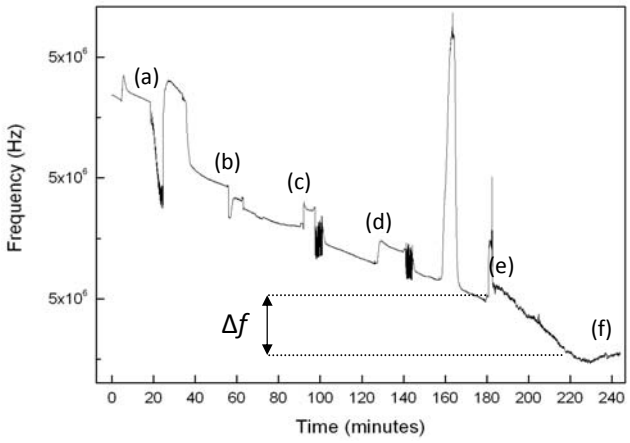


Figure 3 Frequency response for modified QCM sensor as a function of 50 ng/ml CTnT detection (a) EDC/NHS adsorption, (b) Protein G coating, (c) Ab coating, (d) Casine blocking reagent coating (e) Ab-Ag complex and (f) steady-state measured with modified QCM flow injection system.

III. Results and Discussion

In this research, the developed QCM sensor is characterized by acoustic resonant frequency analysis. The frequency shift response of QCM sensor which includes antibody-antigen binding immobilized on sensor surface is shown as steps (a)-(d) in Figure. 3. Protein G coating in step (b) is used to increase an ability of CTnT adsorption due to its potential of binding between the Fc region together with CTnT antibody. The sensor coated with protein G should exhibits a good response to the CTnT antigen with short response times. It can be seen after step (e) that the Ab-Ag binding can respond well to the controlled relative concentration of CTnT at 50 ng/ml, which produce the frequency shift after steady state of Δf = 400 Hz. The noise level of this measurement is less than ±10 Hz. The total

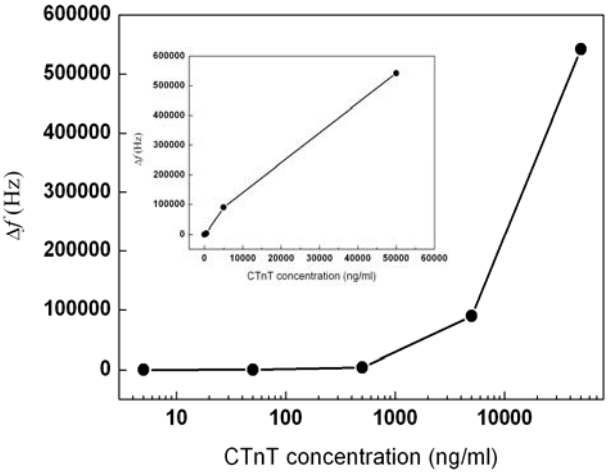


Figure 4 Linear-logarithmic relation between CTnT concentration and frequency shift plotting (inset) linear-linear relation

response time for the preparation step (a)-(d) of each sample is 2 hours and from antibody reacts with CTnT antigen from (e) to (f) is 60 minutes. The frequency responses from other tests are found to be stable and proportional to the CTnT concentration down to detection limit at CTnT concentration of 5 ng/ml.

Figure 4 shows the relation between frequency shift and CTnT concentration. The frequency response can be quantified from CTnT with concentration of 5 ng/ml, which is corresponding to a frequency shift of 23 Hz. The frequency shift increase drastically to around 90 kHz while the CTnT concentration reach 5 µg/ml. With CTnT concentration of 50 µg/ml, the frequency shift increase to around 542 kHz, this is close to the upper limit of system (using 5 MHz QCM) delectability at around 1 MHz.

IV. Conclusions

In conclusion, we have developed a Cardiac Troponin T sensor by spray coating technique of PVC-COOH with attachments of cross linker reagents onto a commercial quartz crystal resonator. To improve surface capability of antibody-antigen binding complex, we use a flow injection system in this experiment. The modified QCM electrode is shown an effectiveness of increased adsorption ability for protein-G. The sensitivity of coated sensor is increased tremendously compared to uncoated sensor. The frequency shift has found to be proportional to CTnT concentrations. The highest sensitivity of modified CTnT-QCM detection is 5 ng/ml with noise level less than ±10 Hz.

ACKNOWLEDGEMENTS

This research is supported by National Electronics and Computer Technology Center research grant of National Science and Technology for Development Agency, Ministry of Science and Technology, Thailand.

REFERENCES

1. Hougen HP, Valenzuela A, Lachica E, Villanueva, E. (1992) Sudden cardiac death: a comparative study of morphological, histochemical and biochemical methods. Foren Sci Int. 52, 161-169.
2. Mair J, Dienstl F, Puschendorf B. (1992) Cardiac troponin T in the diagnosis of myocardial injury. Critical reviews in clinical laboratory sciences. 29, 31-57.
3. De Winter RJ, Koster RW, Sturk A, Sanders GT. (1995) Value of myoglobin, troponin T, and CK-MBmass in ruling out an acute myocardial infarction in the emergency room. Circulation. 92, 3401-3407.
4. B. Cummins, M.L. Auckland, P. Cummins. (1987) Am. Heart J. 113.1333–1344.
5. J. Rabe, S. Buttgenbach, J. Schroder, and P. Hauptmann, "Monolithic miniaturized quartz microbalance array and its application to chemical sensor systems for liquids," IEEE Sensors Journal, Vol. 3, pp. 361 - 368, August 2003.
6. Masashi Kikuchi, Katsuya Omori, and Seimei Shiratori, "Quartz Crystal Microbalance (QCM) Sensor for Ammonia Gas using Clay/ Polyelectrolyte Layer-by-Layer Self-Assembly Film," IEEE Sensors Proceedings 2004, vol. 2, pp. 718-721, October 2004.
7. M. Michalzik, R. Wilke, S. Buttgenbach, "Miniaturized QCM-based flow system for immunosensor application on liquid," Sensors and Actuators B, pp. 410-415, April 2005
8. Y. Jimenez, R. Fernandez, R. Torres, and A. Arnau, "A contribution to solve the problem of coating properties extraction in quartz crystal microbalance applications," IEEE Transactions on Ultrasonics, Ferroelectrics, and Frequency Control, Vol. 53, pp. 1057 - 1072, May 2006.

Automated 24 well neuro-screening system with life support

F. Ilchmann[1], B. Becker[1], D. Grundl[1], J. Meyer[2] and B. Wolf[1,2]

[1] Heinz Nixdorf Lehrstuhl Medizinische Elektronik, Technische Universität München, Germany
[2] IMETUM - Zentralinstitut für Medizintechnik, Technische Universität München, Garching, Germany

Abstract— **Pharmacological research requires devices capable of performing parallel analyses to deliver a high quantity of comparable data for statistical evaluation. To understand the interactions of living neurons in their natural environment it is important to look at the functional mechanisms of cells. Stable culturing of neuronal networks over long periods of time requires strict control over biochemical parameters of the medium. Therefore the quantitative analysis of micro-environmental conditions and cell metabolic rates is essential in interpreting the changing patterns of electrophysiological activity. The presented neuro screening system is capable of measuring and reading out results of 24 neurochips simultaneously. With integrated biosensors for pH, pO2 and multi electrode arrays (MEAs) on each sensor chip, changes in spontaneous spike production and oxygen consumption can be measured at the site of the network monolayer to provide rapid indications of metabolic disturbances. As long-term monitoring of living cells demands a constant microenvironment in the wells, the screening system includes a pipetting robot able to deliver and remove culture medium or drug solutions to and from the wells. To achieve stable climatic conditions for the cell culture, the measuring unit and liquid handling robot are located in a climate chamber. The automated measuring system can also be combined with optical detection methods by integration of a microscope – allowing electrochemical and optical analysis methods at the same time.**

Keywords— **MEA, high content screening, liquid handling robot, sensor, automated microscope**

I. Introduction

The utilization of cultured neuronal networks grown on sensor chips with MEAs for pharmacological studies is a well established method and has yielded extensive knowledge in neurological research [1]. The functional properties of living neurons can best be examined by intelligent incubation methods that combine two requirements: First to cultivate cells in a quasi in-vivo physiological environment and second to read out their electric and metabolic signals automatically in real time.

However, parallel recordings have always been difficult to achieve due to signal interference and the need for large electronics. The newly introduced system integrates 24 separate cell cultures on the area of a standard multiwell plate together with the detection and amplification circuitry for both metabolic and MEA sensors. In combination with the automated robotic fluidic and sampling system and a microscope, a highly sophisticated system for high-throughput laboratory screenings is presented (Figure 1 + 5).

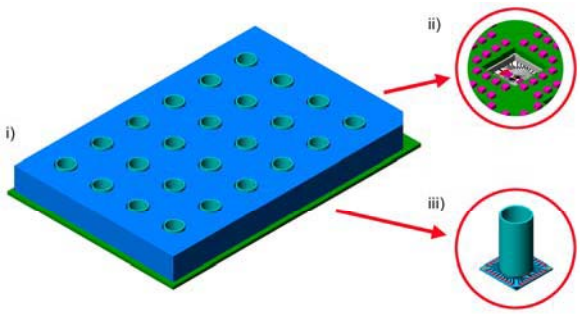


Fig. 1 NeuroPlate: i) baseplate with inserted sensor chips and electronic module, ii) enlargement of amplifier section, iii) sensor chip

II. Materials and Methods

A. Sensor chip

The core of the NeuroPlate recording system is comprised of 24 interchangeable glass sensor chips with 12 mm edge length (Figure 2). Each disposable chip includes its own culture well for up to 750 µl of culture medium. Through 32 thin film Au microelectrodes on an area of 1 mm², neuro-electrical signals can be monitored. A special sandwich type coating ensures high impedance of the signal deflecting electrodes.

For measuring the pH-value and the oxygen concentration, optical sensor spots have been integrated. The chip is designed to withstand humidity for up to three month in an incubator for cell growth and extended studies [2].

O. Dössel and W.C. Schlegel (Eds.): WC 2009, IFMBE Proceedings 25/VIII, pp. 84–86, 2009.
www.springerlink.com

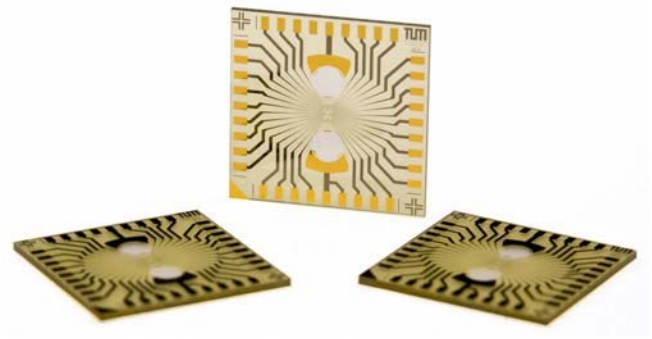


Fig. 2 NeuroChip with culture vessel removed

B. NeuroPlate

The NeuroPlate itself is reusable and can carry up to 24 sensor chips. As the user selects the cell culture chip individually, a huge variety of experimental setups is possible. For example, different cell age groups or tissues can be selected and compared in parallel (Figure 3).



Fig. 3 NeuroChip with culture vessel removed

Part of the NeuroPlate are highly integrated variable gain amplifiers and active filters allow precise amplification of up to 20,000 V/V in a range from 150 Hz to 8 kHz. All 768 (24 wells x 32 electrodes) channels can be addressed individually for different gain factors and customized readout. As the digitizing circuit is part of the NeuroPlate, there is no need for extensive wiring. The digital signal is processed on FPGAs providing digital filters and further signal processing (Figure 4). Special shielding technology is implemented to make low-noise recording possible. A single high-speed USB interface connects the NeuroPlate to an ordinary computer for activity and micro-environmental condition analysis [3].

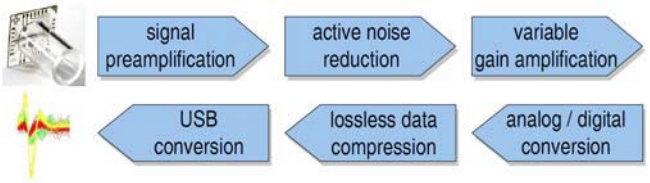


Fig. 4 Signal path within the NeuoPlate for all 786 channels

C. Intelligent Microplate Reader

Once the NeuroPlate is populated with 24 selected cell culture chips, the plate is inserted into the Intelligent Microplate Reader (IMR) (Figure 5).



Fig. 5 NeuroPlate inside the Intelligent Microplate Reader Lab. Picture shows robot with the climate chamber removed

The concept of the IMR pursues a modular configuration [4]. Consisting of a robotic liquid handling system and an automated microscope, long time monitoring of living cell cultures becomes a manageable task. The robot moves between seven user programmable positions and transports culture media and drug solutions to / from the desired vessels of the NeuroPlate. Besides the described setup, the system can handle standard 24 and 96 microwell plates for different experimental configurations. A fully controlled climatic chamber guarantees life supporting conditions for extended measurement periods (Figure 6).



Fig. 6 IMR software for robot control and sensor visualization

In addition to the electrical MEA signal recording, the current configuration allows optical readout of the pH-value and the oxygen concentration. All measured parameters are directly amplified, converted and read out via USB. The built-in automated fluorescence microscope enables the user to acquire cell culture images at any time of the experiment, making documentation and interpretation of the results much easier and more reliable. For robot control and signal interpretation, an analytic software has been developed (Figure 7).

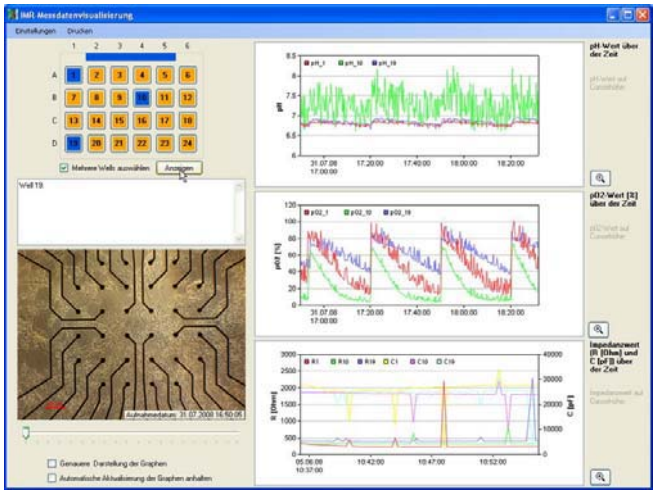


Fig. 7 IMR software for robot control and sensor visualization

III. CONCLUSIONS

Studies conducted utilizing the NeuroPlate and the IMR system showed excellent multiparametric recordings for up to four days with parallel documentation of vital parameters and cell culture images. All parameters are obtained marker-free, so cells do not need to be labelled [5]. No matter if high throughput or redundancy is desired, the presented system is an ideal basis for further studies on metabolism dependent activity in pharmacological research. The compact design allows integration in any laboratory environment.

ACKNOWLEDGMENT

The authors express their personal appreciation of the valuable assistance given them in their research by many students at the Heinz Nixdorf Lehrstuhl für Medizinische Elektronik [6]. Financial support by the Heinz Nixdorf Foundation is kindly acknowledged.

REFERENCES

1. G. Gross, F. Schwalm (1994) A closed chamber for long-term electrophysiological and microscopical monitoring of monolayer neuronal networks, Neuroscience Methods 52: 73-85
2. F. Ilchmann, D. Grundl, V. Lob,, B. Becker, B. Wolf (2008), Zell-Chipsysteme - Mikrosensorarrays für die biologische Grundlagenforschung und Diagnostik, GIT Laborfachzeitschrift, 52 Jahrgang, 3, 285-260
3. F. Ilchmann, V. Lob, J. Meyer, H. Ressler, B. Wankerl, J. Wiest, B. Wolf (2008), Automated Cell Analytics, Application on Sensor Chips, Screening-trends in drug discovery, Volume 9, 21-23
4. B. Bernhard, V. Lob, N. Janzen, D. Grundl, F. Ilchmann, B. Wolf (2008) Automated multi-parametric label free 24 channel real-time screening system, NBC 14th Nordic-Baltic Conference on Biomedical Engineering and Medical Physics, Riga, NBC Proceedings 20, 186-189
5. J. Wiest, D. Grundl, M. Schmidhuber, M. Brückl, V. Lob, F. Ilchmann, M. Brischwein, H. Grothe, A.M. Otto, B. Wolf (2008), Real-time and marker-free investigation of living cells, Clinical Chemistry and Laboratory Medicine, 46, 9, A160
6. Heinz Nixdorf Lehrstuhl Medizinische Elektronik at http://www.lme.ei.tum.de

Author: Florian Ilchmann
Institute: Heinz Nixdorf Lehrstuhl Medizinische Elektronik
Technische Universität München
Street: Theresienstrasse 90, N3
City: 80333 Munich
Country: Germany
Email: Ilchmann@tum.de

Manufacture of SU-8 Micro-Grippers for Mechanical Characterization of Gut Epithelial Cells

R.E. Mackay, H.R. Le, R.P. Keatch, and Q. Zhao

Division of Mechanical Engineering & Mechatronics, University of Dundee, Dundee, United Kingdom

Abstract— **This paper describes the manufacture of an integrated micro-electro-mechanical system (MEMS) to be used for small scale tissue manipulation. The micro-grippers are to be used to test the mechanical cell adhesion properties of the gut epithelium. In the majority of sporadic colon cancers the Adenomatous Polyopsis Coli (APC) protein is mutated or missing. Mutations of APC occur extremely early in the development of cancer, before formation of polyps. The following paper looks at the manufacturing processes for SU-8 micro-grippers. The micro-gripper structure has been successfully fabricated as a single structure not incorporating conduction paths. A number of sacrificial layers have been examined for compatibility with the SU-8 development. The sacrificial layer will be removed to leave a suspended structure. Stiction is a challenge to overcome in wet etch processes. An electroless coating process for Ni-P sacrificial layer has been developed. Coating Ni-P onto bare silicon substrates is a challenging problem. Sensitization and activation steps are needed to coat non-conductive surfaces. Sensitizers for Ni-P coatings of $SnCl_2$ and 3-aminopropyltriethoxysilane were tested to look at adhesion of Ni-P to the substrate. Results have shown Ni-P can be applied to SiO_2 surfaces at a thickness high enough to be utilized as a sacrificial layer for micro-grippers.**

Keywords—**Micro-electro-mechanical systems, micro-gripping, biomechanics, SU-8, Nickel-phosphorus.**

I. Introduction

The majority of sporadic colon cancers occur when the adenomatous polyopsis coli (APC) protein is mutated or lost [1]. APC supports cell migration and cell adhesion [2]. Loss of cell migration causes a build up of cells in a highly toxic environment. This causes mutations to occur within the cells. APC loss occurs early in the progression of colon cancer and occurs before the formation of polyps [3]. This project aims to characterize the mechanical properties of the gut epithelium cells and tissue, in particular looking at cell adhesion forces with the APC protein active or inactive.

Micro-gripping of constructs smaller than 50μm diameter is a challenging problem. Several types of micro-grippers have been reported. Shape Memory Alloy grippers can only be used for a limited number of cycles before the shape memory alloy fails or loses its shape memory effects [4]. Piezoelectric actuators show high gripping forces with accurate displacement; however they need high operating voltages (10-100V) and require amplification methods to obtain large displacements [5].

Thermoelectric bimorph micro-grippers are of great interest. Luo et al [6] developed three types of micro-grippers, including bimorph grippers, whilst examining temperature rise and displacement. The results show small actuations of bimorph micro-grippers which operate in a small power range, however Type III micro-grippers, initially developed by Lin et al [7] with two horizontal hot arms yields largest displacement for given power input. This paper will develop the manufacturing techniques of the Type III tweezers to allow them to be used within tissue engineering conditions. SU-8 is to be utilized as the structural material for the micro-grippers. SU-8 is a non-conductive polymer however by adding a conductive metal circuit to the micro-grippers actuation is possible [8; 9]. A number of materials will be investigated as sacrificial layers; photoresist, Al, Al-Ti and Ni-P. Ni-P is a material currently utilized for biocompatible coatings of medical devices. The use of Ni-P as a bioMEMS material could simplify the fabrication process because it is conductive.

II. Design Concepts

A. Design Concept for the System

The design concept is shown in Figure 1. The structure will be manufactured using well established MEMS processes on a silicon chip. The structure includes a stage with incorporated micro-grippers for holding cell or tissue samples. A piezoelectric actuator will be used to stretch the tissues (which is attached to the right end of the tissue specimen). The deflection of the spring structure will be measured using an optical fiber sensor; critical forces can then be derived. Removal of the substrate under the micro-grippers will reduce stiction in biological environment and allow for smooth actuation.

B. Design of the Micro-Gripping System

A schematic of the micro-tweezers is shown in Figure 2. Design and finite element analysis was shown in previous publications [10; 11].

O. Dössel and W.C. Schlegel (Eds.): WC 2009, IFMBE Proceedings 25/VIII, pp. 87–90, 2009.
www.springerlink.com

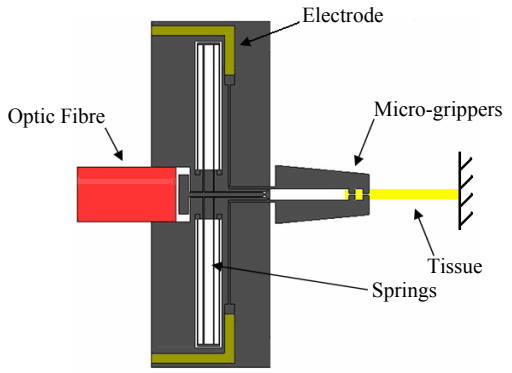


Figure 1. Schematic of System

III. Experimental Procedures

SU-8 micro-grippers are to be manufactured using a three mask process (Fig. 2). Currently two types of SU-8 have been used for spin coating, SU-8 2007 and SU-8 2015 (Chestech Ltd., UK). SU-8 was spun onto 100 mm wafers with a thermally grown 200nm $Si0_2$ layer. Wafers were cleaned using acetone (VWR Internationl, UK) and then dried with N_2; they were then rinsed with iso-propanol (IPA, VWR Internationl, UK) and dried with N_2. Wafers were placed in an oven and heated to a temperature of 200^0C; the heating step helped increase adhesion of SU-8 to SiO_2. Spinning of SU-8 is done in three stages; the first stage helps spread the SU-8 at a low speed and acceleration. Stage 2 spin speed is selected according to the data sheet for a specific thickness. Stage 3 spin speed is higher still but for a short time period, around three seconds to help edge bead removal. The edge bead removal step is important to ensure the mask and wafer is in full contact for patterning. This results in a more precise structure being formed. After spinning the SU-8 resist, the sample is soft baked. Soft bake occurs for 1 min at 65^0C and 3 mins at 95^0C. A hotplate is used instead of an oven to ensure complete diffusion of solvent from the SU-8. The wafer is then placed in an OAI J500 mask aligner. The wafer height is raised to ensure full contact with the mask. The mask is placed chrome down to ensure highest resolution of the micro-grippers. The sample is then exposed to UV light with an intensity of 595mJ/cm^2 for 30 seconds. A post exposure bake (PEB) is used to cure the SU-8 subjected to UV light; PEB parameters are equivalent to soft bake parameters. EC solvent (Chestech Ltd., UK) was used to develop structures; the sample was developed for i.e. 3 minutes. Finally the SU-8 structure was rinsed with IPA and dried with N_2. SU-8 structures were examined using a Dektak stylus and optical microscope.

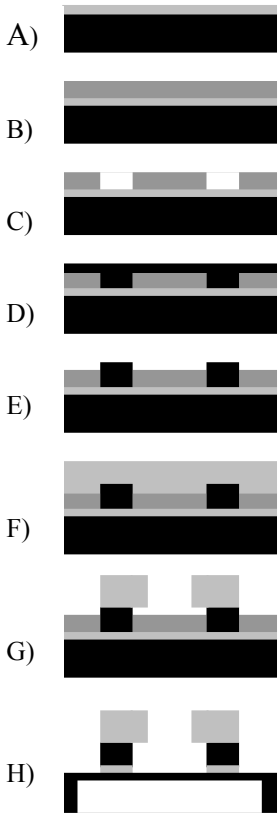


Figure 2. - Microgripper fabrication: (A) Si wafer with 200nm layer SiO_2 is coated with Ni-P (B), Sacrificial layer is patterned and etched (C), the Cu/Cr electrode path is deposited on the sacrificial layer (D), this is patterned and etched (E). SU-8 is spin coated (F), this is patterned and developed (G). Finally the sacrificial layer is removed and Si etched to leave a suspended structure (H).

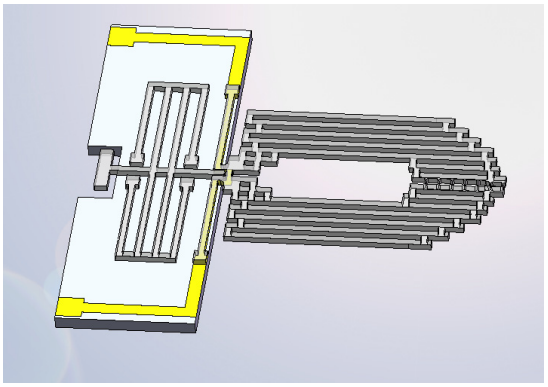


Figure 3. Suspended Micro-gripper Structure.

The final micro-gripper structure will incorporate suspended gripper arms (Fig. 3). To avoid stiction of the SU-8 micro-grippers to the Si substrate a sacrificial layer of high thickness (~6µm) is to be used. A number of materials were researched for the sacrificial layer. Initially Shipley S1818 was chosen as a sacrificial layer. Maximum thickness using S1818 was 2.5µm. The anchors were patterned using S1818; SU-8 was spun and developed on top of the patterned S1818. EC solvent is used to develop SU-8 structures; the EC solvent quickly removed the patterned S1818. S1818 was too thin a sacrificial layer and stripped easily in EC solvent which is utilized to develop SU-8. Stiction of the final structure to the substrate is seen (Fig. 4). Aluminium sacrificial layers from 1µm up to 2µm were evaporated and patterned. Al etchant does not attack the structure. Wet etching of such a thin sacrificial layer again resulted in stiction (Fig. 5). A sacrificial layer incorporating 2µm Al with a 400nm Ti layer was used to increase residual stresses and introduce a radius of curvature along the gripper arms and springs. After wet etching micro-grippers did show some signs of lift-off, however after a time micro-grippers again adhered to the wafer. Two surface treatments, perfluorohexane and dichlorodimethylsilane (DDMS, Sigma-Aldrich Company Ltd., UK), were deposited onto the structures using plasma enhanced chemical vapour deposition (PECVD) [12]. Perfluorohexane treatments showed no signs of releasing the structure. Both chemicals caused increased hydrophobicity of SU-8 and SiO_2, however only DDMS showed signs of lift off.

A thicker sacrificial layer >2µm is needed to avoid stiction after the wet etch phase. A possible solution was to use an electroless Ni-P coating.

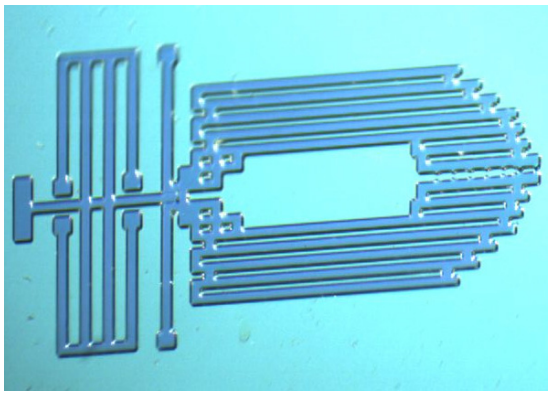


Figure 4. SU-8 Micro-gripper structure 25µm thickness.

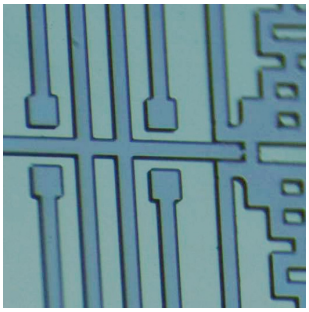


Figure 5. SU-8 Flexure springs, anchors and hinges.

Electroless Ni-P coatings can be coated using an autocatalytic process. Autocatalytic deposition can only occur on catalytic surfaces, e.g. Ni, Pd or steel. The SiO_2 layer needs to be activated or coated with a catalytic material before Ni-P can be deposited. A number of groups have used $SnCl_2$ (Sigma-Aldrich Company Ltd., UK) as a sensitizer and $PdCl_2$ (Chestech Ltd., UK) as an activator [12; 13]. Self assembled monolayers (SAMS) were investigated to increase adhesion between Ni-P and SiO_2 [14; 15].

IV. Results

Early results of SU-8 manufacture can be seen in figures 4 and 5. Structures were fabricated using SU-8 2015, structure of thickness up to 45µm have been successfully manufactured. Figure 5 shows the good resolution of the structures formed.

SU-8 patterned on top of 2µm Al and 400nm Ti layer with PECVD of DDMS showed good lift off of gripper arms.

Sacrificial layers of Ni-P have been created up to a thickness of 20µm. Sensitization was found to be an important step. Immersion of wafers in $SnCl_2$ solution followed by immersion in $PdCl_2$ allowed SiO_2 to be coated with Ni-P. Low adhesion between the wafer surface and Ni-P occurred resulting in the Ni-P layer peeling off the wafer during rinsing after removal from Ni-P bath. Sensitization using SAMS followed by immersion in $PdCl_2$ showed greater adhesion of Ni-P to SiO_2 (Fig. 6). Ni-P layers were created up to 20µm in thickness. A small number of samples coated evenly and Ni-P had adhered well to the SiO_2 substrate. Many samples, once removed from the Ni-P bath were unevenly coated with a very thin layer of Ni-P.

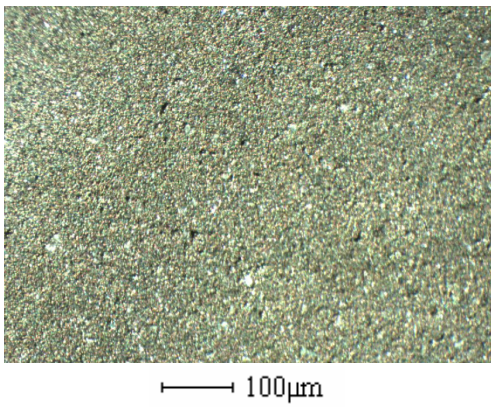


Figure 6. Ni-P Sacrificial Layer x50 magnification

V. CONCLUSIONS

SU-8 2015 has been utilized to successfully create the micro-gripper structure. Finding an appropriate sacrificial layer that is compatible with the SU-8 processing steps has been a challenging problem. A novel Ni-P sacrificial layer which is biocompatible has been examined. Bonding of Ni-P to SiO_2 has been a problem; however use of self assembled monolayers has yielded some promising results. Thin sacrificial layers, 2.5µm or lower showed no lift off. The sacrificial layer incorporating 2µm Al and 400nm Ti showed lift off with DDMS chemical treatment.

ACKNOWLEDGMENT

Financial support of EPSRC and IDB Technologies Ltd. towards a PhD Studentship for R.E.M. is acknowledged. The authors would like to thank Dr Chaozong Liu for PEVCD at Robert Gordon University. The authors want to thank Prof. I Nathke for biological input to project. The authors are grateful of the assistance of Ms. Chen Liu with the electroless process and constructive discussions with Drs. R. Keatch and K Donnelly.

REFERENCES

1. Nathke IS. The adenomatous polyposis coli tumor suppressor protein localizes to plasma membrane sites involved in active cell migration. The Journal of Cell Biology 1996;134(1):165-79.
2. Kawasaki Y, Sato R, Akiyama T. Mutated APC and Asef are involved in the migration of colorectal tumour cells. Nat Cell Biol 2003 Mar;5(3):211-5.
3. Nathke IS. THE ADENOMATOUS POLYPOSIS COLI PROTEIN: The Achilles Heel of the Gut Epithelium. Annual Review of Cell and Developmental Biology 2004 Nov 30;20(1):337-66.
4. Kohl M, Just E, Pfleging W, Miyazaki S. SMA microgripper with integrated antagonism. Sensors and Actuators A: Physical 2000 May 22;83(1-3):208-13.
5. Nah SK, Zhong ZW. A microgripper using piezoelectric actuation for micro-object manipulation. Sensors and Actuators A: Physical 2007 Jan 8;133(1):218-24.
6. Luo JK, Flewitt AJ, Spearing SM, Fleck NA, Milne WI. Comparison of microtweezers based on three lateral thermal actuator configurations. Journal of Micromechanics and Microengineering 2005;15(6):1294-302.
7. Lin LL, Howe RT, Pisano AP. A passive, in situ micro strain gauge. 1993 p. 201-6.
8. Nguyen NT, Ho SS, Low CL-N. A polymeric microgripper with integrated thermal actuators. Journal of Micromechanics and Microengineering 2004;14(7):969-74.
9. Chronis N, Lee LP. Electrothermally Activated SU-8 Microgripper for Single Cell Manipulation in Solution. Microelectromechanical Systems, Journal of 2005;14(4):857-63.
10. Mackay RE, Le Huirong. Development of Micro-Tweezers for Tissue Micro-Manipulation. 2008 The 2nd International Conference on Bioinformatics and Biomedical Engineering p. 1551-4.
11. Mackay RE, Le HR. Micro-gripping of Small Scale Tissues. 2008. IFMBE Proceedings 4th European Congress for Medical and Biological Engineering.
12. Yan XZ, Hansen O, Knieling T, Wang C, Rombach P, Lang W, et al. Vapor-Phase Self-Assembled Monolayers for Anti-Stiction Applications in MEMS. Microelectromechanical Systems, Journal of 2007;16(6):1451-60.
13. Davidoff C. Metallizing nonconductors. Metal Finishing 2007;105(10):324-30.
14. Tsai TK, Chao CG. The growth morphology and crystallinity of electroless NiP deposition on silicon. Applied Surface Science 2004;233(1-4):180-90.
15. Yoshino M, Nonaka Y, Sasano J, Matsuda I, Shacham-Diamand Y, Osaka T. All-wet fabrication process for ULSI interconnect technologies. Electrochimica Acta 2005 Nov 10;51(5):916-20.
16. Gao J, Tang F, Ren J. Electroless nickel deposition on amino-functionalized silica spheres. Surface and Coatings Technology 2005 Dec 21;200(7):2249-52.

Mathematical methods for interpretation of metabolic signals from living cells on biohybrid sensor chips

T. Flurschütz[1], D. Grundl[1], M. Zottmann[1], J. Wiest[2], and B. Wolf[1]

[1] Heinz Nixdorf-Lehrstuhl für Medizinische Elektronik, TU München, Munich, Germany
[2] Innovationszentrum Medizinische Elektronik – cellasys GmbH, Munich, Germany

Abstract— **Within the past few years, sensor chips have been developed that permit monitoring of physiological parameters of living cells – e.g. pH and pO_2 of the nutrient solution – in real-time. Long term experiments, in which these parameters are screened, produce large amounts of data. Their evaluation is usually carried out by hand in an error-prone and time consuming process.**

To avoid these problems an automated software solution is needed. Due to the periodic measuring procedure that is common for sensor chip-based systems, the data itself is also periodic. This was taken into account to reduce its size and complexity: by capturing the essential information within each period, time series were computed that offer a more direct insight into the cells' state of vitality. At the same time the data needed for further evaluation was strongly reduced and freed from the influence of sensor drift.

An experiment with human breast adenocarcinoma cells of type MCF-7, in which the mentioned parameters were recorded for several days, is used to demonstrate this fact. The impact of a cytostatic drug on the cells' vitality was measured by employing gradient and amplitude analysis as well as other mathematical methods. This process was carried out automatically using the R environment for statistical computing.

This approach not only delivers interpreted and therefore more meaningful data. The possibility to automate this process also offers simpler and faster means of evaluating an experiment while helping to avoid human errors. The described methods can be adapted to other sensor chip-based systems.

Keywords— **biohybrid sensor chip, cell based assay, data processing, mathematical methods**

I. Introduction

We have developed systems that allow monitoring physiological parameters of living cells in real-time. They are based on silicon, glass or ceramic chips that integrate sensors on their surface to permit measuring pH value and dissolved oxygen concentration in the medium, as well as impedance. Cells grow on such a surface, forming a biohybrid sensor chip, which makes it also possible to employ such sensors to record electrophysiological parameters, e.g. nerve cells' action potentials.

While impedance depends on cell adhesion and morphology, pH and dissolved oxygen concentration are affected by the cells' metabolites and therefore their metabolic activity [1]. This paper focuses on the latter.

The measuring procedure within such a system consists of two phases that are repeated throughout the measurement: First the medium is altered by the cells' metabolites, then it is exchanged (stop-and-flow). Each repetition of the stop-and-flow procedure is called a measurement period. Figure 1 shows three measurement periods within the raw signal.

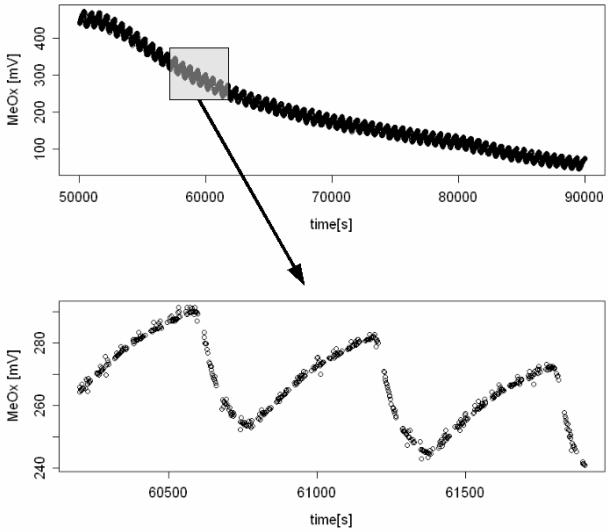


Fig. 1: Raw data from a sensor chip's metal oxide sensor. Its value is proportional to the pH of the medium.

As shown in [1] and [2], the rate at which measured pH and oxygen change within each measurement period can be treated as indicators for the cells' physiological state.

The systems developed at LME deliver up to 20 values for pH and oxygen per minute. An experimental setup will usually make use of several sensor chips (6-24) over many days, yielding large amounts of data. The measured values then give valuable insight into the current state of cell activity. Determining the rate of acidification and oxygen consumption manually takes long and is prone to errors. To

O. Dössel and W.C. Schlegel (Eds.): WC 2009, IFMBE Proceedings 25/VIII, pp. 91–94, 2009.
www.springerlink.com

avoid this, one aim is to compute these figures automatically and therefore in a fast and reliable way.

Besides the metabolic rates, additional information is required, as the course of measured values within a measurement period may not have as little curvature as those shown in figure 1. Figure 4 depicts this case schematically: Both pH and dissolved oxygen concentration may asymptotically approach a limiting value. In the course of automating the evaluation process, this information must be preserved.

A third issue is also covered in this context: As can be seen in figure 1, the data is influenced by sensor drift, which is a common problem that can not always be solved within the system itself. To improve the results of the above mentioned computations, a drift correction is desired.

II. MATERIALS AND METHODS

A. Cell based data

For demonstration purposes, data originating from an experiment with adenocarcinoma cells of type MCF-7 and a cytostatic drug are used.

The cytostatic drug was added to the media in concentrations of 5µM and 10µM after 18 hours. A reference culture was also monitored for comparison.

B. R for application of statistical methods

The evaluation of experimental data was decided to be automated using a scripting language that allows applying mathematical methods without need of implementing them.

For this purpose the R language and environment for statistical computing was chosen [3]. Similar to the commonly used tool Matlab, it provides language syntax as well as a development environment. It is free software designed for tasks in statistics and implements a large variety of methods, including least squares regression and the lowess algorithm.

C. Linear least squares regression for computation of rates

As mentioned earlier, the rate at which measured pH and dissolved oxygen concentration change, can be seen as an indicator for the cells' current state. The larger their metabolic activity, the faster the measured values rise. A straight forward approach for computing the slope within a time window of a measurement period's stop-phase is linear regression [4].

For one independent variable x_i, linear regression models the relation between x_i and the response variable y_i through a line equation [5]

$$y_i = \alpha + \beta x_i + \varepsilon_i \tag{1}$$

where ε_i is an error component.

Approximate values for α and β can be found by minimizing the mean square error

$$\sum_i (y_i - \alpha - \beta x_i)^2 \rightarrow \min \tag{2}$$

In the context of cell based data, x_i can be chosen to denote time and y_i to denote measured pH or dissolved oxygen concentration. By applying linear least squares regression, a least squares estimate of the measured values slope is obtained.

D. Lowess for noise reduction

Lowess (robust locally weighted regression) is an approach to scatterplot smoothing introduced in [6]. It employs weighted least squares regression, which works similarly to (ordinary) least squares regression: it assumes the same model (see equation (1)), but does not treat each pair (x_i,y_i) equally. Instead each independent variable and response variable are assigned a weight w_i [5,6]. Thus it minimizes the weighted mean square error.

$$\sum_i w_i (y_i - \alpha - \beta x_i)^2 \rightarrow \min \tag{3}$$

The weights make it possible to define the influence of a variable – or in this case of a measurement point. For each point (x_i,y_i) a smoothed value $\hat{y}_i$ is obtained in the following steps:

- Weighted least squares regression is performed in a neighbourhood of (x_i,y_i) where each neighbour x_k is given a weight depending on its distance $|x_i-x_k|$. The larger the distance, the smaller the weight w_k.
- New weights are computed, depending on the residuals ε_k. The larger ε_k, the smaller the weight.
- Weighted least squares regression is performed with the new weights.
- The last two steps are repeated as often as demanded by the user, iteratively diminishing the influence of outliers.

The algorithm determines a line equation for each point (x_i,y_i). By evaluating this equation at x_i, the smoothed value $\hat{y}_i$ is obtained. For more details, see [6].

III. RESULTS

For each of the tasks addressed above, it is reasonable to smooth the data, as it is influenced by different kinds of noise, depending on the employed measuring method. R provides different possibilities of smoothing, including the often employed lowpass filter.

Low-pass filtering in this special context faces two conflicting goals: the smoother the resulting values, the more distorted the discontinuity due to the exchange of medium will be (see figure 1). It will be smoothed and its peak shifted in time. Less smoothing on the other hand will increase the influence of outliers.

In experiments with data produced by sensorchip-based systems, the lowess algorithm performed well in both smoothing the data while maintaining the discontinuity. It is therefore applied to each measurement period in a first step.

The slope of the measured pH and oxygen values after exchange of medium is achieved by linear regression within a time window of each measurement period. The smoothed values of pH and pO_2 are used to minimize the influence of noise.

An R-framework was implemented to read data produced at LME and apply this concept. An example for the output of such an analysis is depicted in figure 2. It shows the acidification rate of the MCF-7 cells over time. After 14 hours the cytostatic drug was added in a concentration of 5µM (boxes in figure 2) to one cell culture and 10µM (crosses in figure 2) to the other. It can be observed, how the cells' metabolic activity is thereupon inhibited depending on the dose of the drug, while it remains generally unchanged for the untreated culture (circles in figure 2).

In comparison with the raw example data in figure 1, it can be seen that the computed time series is easier to interpret and also reduces the data volume – in this concrete case by a factor of approximately 170.

As mentioned above, a measurement period may asymptotically approach a limiting value. This can be the case for example, if the time, during which the cells metabolize, is chosen too long. In this case the dissolved oxygen in the medium may be consumed, before fresh medium is supplied. Similar effects can be observed for acidification.

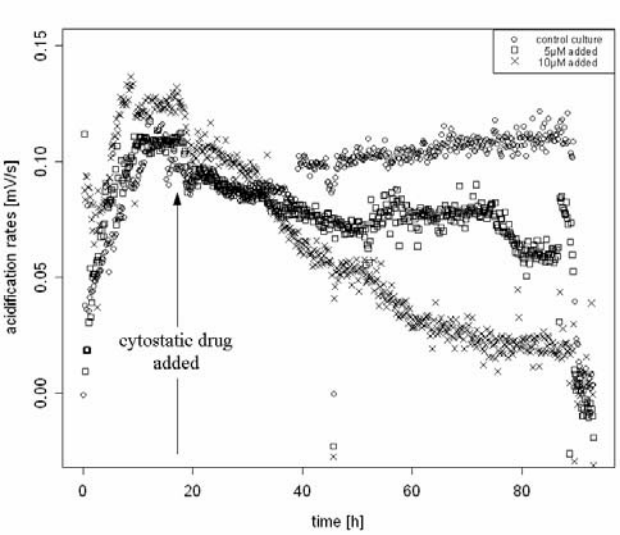


Fig. 2 Cellular acidification rates for three different concentrations of a cytostatic drug

To make such behaviour visible to the user and protect the cells from taking damage, a second characteristic figure besides the slope was defined: assuming linear behaviour, the previously computed slope would lead to a certain peak value at the time when the medium is about to be exchanged. The real peak may have a similar value, or – e.g. in the case just described – be lower.

Be A_e the linearly extrapolated amplitude as shown in figure 4 (gray box) and A_m the measured amplitude (gray circle), then the curve's shape can be characterized by $Rate_{amp}=A_e/A_m$.

This value has an optimum at 1, which means the course of the observations was linear. Smaller values indicate negative curvature; larger values would indicate that the slope increased further.

As the input of fresh medium restores a similar value for pH and pO_2 in each measurement period, any major fluctuation in the course of these points is predominantly caused by drift of the sensors. As a consequence, the change in level, that is hereby measured, can be treated as an error.

Smoothing as the first step performed in the course of evaluation allows for the detection of a minimum between each two measurement periods. This minimum can be seen as a reference value, or the "level" of the measurement.

The drift can now be modeled by piecewise linear approximation between the reference points and subtracted from the original signal. The impact on the acidification rates of the raw data in figure 1 is shown in figure 3: the original rate (crosses) is influenced by the drift; the values of the corrected rate (boxes) differ by up to 20%.

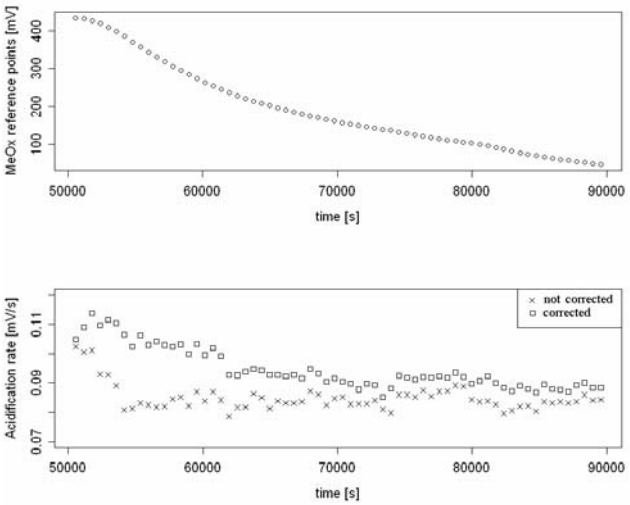


Fig. 3: Impact of drift correction on the computed acidification rate. Top: Reference points obtained from the raw data in figure 1. Bottom: corrected and unaltered acidification rates. The pH is proportional to the mV value measured by the metal oxide sensor.

IV. DISCUSSION AND CONCLUSION

We used R to automatically characterize the cells' metabolic activity over time in two figures. One figure – the slope of acidification and oxygen concentration – can be seen as an indicator of vitality. The other – the rate of amplitudes – shows, to what extent the course of measurement values asymptotically approaches a limiting value. Also the sensor drift as a source of error was eliminated.

The validity of acidification and oxygen consumption rates has been demonstrated in former publications [2]. Automated evaluation in the fashion described above adds the advantages of fast and reproducible computation as well as noise reduction, reliability and data reduction. The next task in this field will be to consider the pH buffer capacity of the medium in the calculations.

The rate of amplitudes was introduced as an intuitively understandable figure characterizing the curvature of the data points. It can contribute to maintaining adequate conditions for the cells throughout an experiment and will be evaluated in the near future.

The influence of drift, as a common source of error, was reduced by taking into account the nature of the measuring procedure.

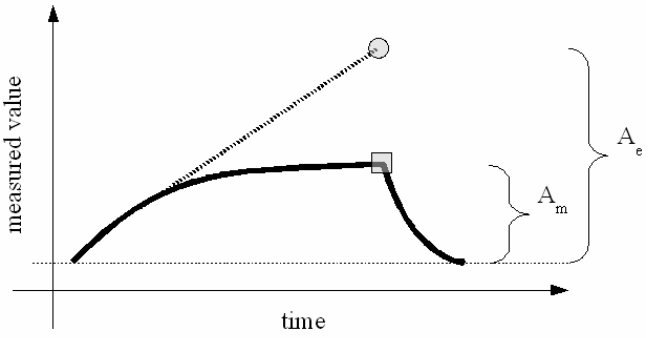


Fig. 4 Measured and extrapolated amplitude (schema)

V. ACKNOWLEDGEMENTS

We want to thank the Federal Ministry of Education, Science, Research and Technology as well as the Heinz Nixdorf Foundation for the financial support.

VI. REFERENCES

1. Kraus M, Wolf B (1995) Structured Biological Modelling, A New Approach to Biophysical Cell Biology. CRC Press Inc., Boca Raton
2. Brischwein M, Motrescu E, Cabala E et al. (2003) Functional cellular assays with multiparametric silicon sensor chips. The Royal Society of Chemistry, Cambridge
3. The R Project for Statistical Computing at http://www.r-project.org
4. Cabala E (2007) Monitoring multiparametrischer komplexer Mikrosensorarrays für zelluläre Analytik. At http://mediatum2.ub.tum.de
5. Kotz S et al (1981) Encyclopedia of Statistical Sciences. Wiley, New York
6. Cleveland W S (1979) Robust Locally Weighted Regression and Smoothing Scatterplots. Journal of the American Statistical Organization, Alexandria

Author: Thomas Flurschütz
Institute: Heinz Nixdorf-Lehrstuhl für Medizinische Elektronik, Technische Universität München
Street: Theresienstraße 90, Building N3
City: Munich
Country: Germany
Email: thomas.flurschuetz@mytum.de

Electroactive Nanoporous Valve for Controlled Drug Delivery

R. Kurz, A. Sickinger, and A. Robitzki

Center for Biotechnology and Biomedicine (BBZ), University Leipzig,
Division of Molecular biological-biochemical Processing Technology, Leipzig, Germany

Abstract— **Drug delivery is still a big challenge in the effective pharmaceutical treatment of diseases. The ultimate aim is the delivery of any active pharmaceutical ingrediant (API) in an appropriate therapeutic concentration at the right location without systemic adverse effects in a safe and reproducible manner. A promising technology is the use of implantable drug delivery systems. Here we report a new electroactive nanoporous valve for a drug delivery implant based on the electroactive polymer polypyrrole in a nanoporous membrane for a controlled continuous release of an API. The release is controlled by the opening of the nanopores of carrier substrate comprising the conducting polymer polypyrrole / sodium dodecylbenzenesulfonate (PPy/DBS) that is located in the nanopores on a gold layer, as conductor. The composition of a conducting redox-polymer (PPy) with the charged counterion DBS allows an overall volume change of this polymer depending on the redox-state of the PPy and therefore the opening or closing of the nanopores for the controlled release of an API.**

Keywords — **Drug Delivery, Electroactive Polymer, Nanopores, Polypyrrole**

I. Introduction

Treating illness in therapies is accompanied by more or less severe side affects caused by the high (systemic) concentration of an active pharmaceutical ingrediant (API). Also the variation in concentration over time due to the repeated medication is obstructive. A device, containing the API, placed appropriate to the demand and the electronically controllable release of APIs would eliminate these drawbacks.

A promising technology is the use of implantable drug delivery systems. This systems can be placed directly in treated areas of the body and allow a drug to be delivered for longer periods of time. There are different approaches to release the active pharmaceutical ingrediant from the drug reservoir of this implants such as electrochemical dissolution of thin anodic gold membranes [1] or electrostatic peristaltic micromachined pumps [2]. Furthermore different types of valves that use the electroactive polymer polypyrrole (PPy) as actuator have been decribed in the literature such as bilayer flaps [3-5].

Here we present a novel electroactive valve with variable nanopores and a microdevice for testing the electroactive nanoporous valve. The valve consists of an Al_2O_3 disc with 200 nm wide nanopores is covered with a layer of gold and afterwards a layer of polypyrrole is electrochemically deposited. Polypyrrols ability in changing his volume due to its redox state by stimulated incorporation of ions opens and closes the nanopores by applying an appropriate electrical field.

II. Material and methods

A. Fabrication

As nanoporous substrate an anodic etched Al_2O_3 disc (Anodisc 13, Whatman) with 200 nm wide pores was used. A gold layer of approximately 60 nm was applied to the Al_2O_3 disk via high frequency sputtering in 2×10^{-2} mbar argon atmosphere and serves as conducting layer. The gold plated Al_2O_3 disk is immersed into aqueous pyrrol solution (0.1 M) containing sodiumdodecylbenzenesulfonate (0.1 M) as doping agent that was aerated with nitrogen. The PPy/DBS layer was established by electrochemically polymerisation via cyclic voltammetrie (3 scans with 50 mV/s in the range from -1 V to 0.8 V vs. Ag/AgCl).

B. Assembly

The test device (Fig. 1) consists of a reservoir with three ring electrodes and two caps. The outermost electrodes establish the contact to the gold/PPy layer and the middle platinium electrode serves as counter electrode. The membrane disk fits into the reservoir on the electrode and is fixed by the cap. The connectors of the cap (volume of the cap) are in line with a peristaltic pump and flow through cell within a photometer to read the absorbance of released test specimen. The electrodes are connected to the control unit (not shown).

C. Diffusion measurement

The micro device is loaded with 1%- bovine serum albumin (BSA) solution in 0.9 % aqueous sodium chloride and the outlets embedded into the loop of a rotary pump and a flow cell. The UV-absorbance of BSA is measured at a wavelength of 280 nm.

O. Dössel and W.C. Schlegel (Eds.): WC 2009, IFMBE Proceedings 25/VIII, pp. 95–97, 2009.
www.springerlink.com

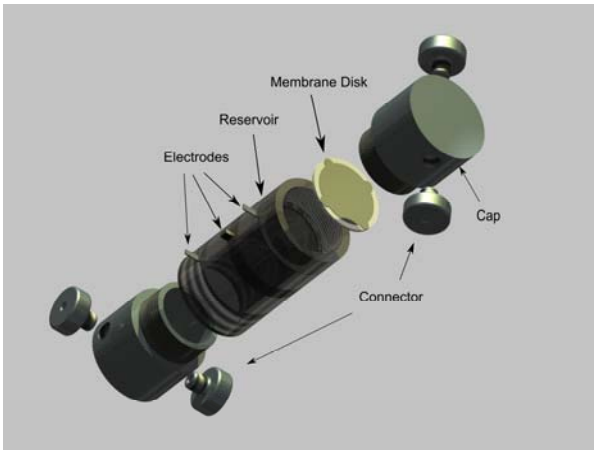


Fig. 1 Assembly of the test device with the internal ring electrodes, the reservoir for the API, the nanoporous membrane disc that acts as valve and the cap with connectors for the tube to the rotary pump and a photospectrometer.

III. Results

A valve with nanopores and controllable diffusion properties has been fabricated and demonstrated. With the use of conducting polypyrrol it is possible to control the diffusion of particles through nanopores by an electrical field. Dependent on the applied field it is possible to influence the redox state of the polymer and to control the opening in the nanopores by (de)swelling.

Porous Membranes: In an Al_2O_3 disk the pores are straight and the diameters have a very low variance (Fig. 2). In Figure 3 the Transmission Electron Microscopy (TEM) picture reveals in the lower left part the gold layer on the Al_2O_3, and also shows the nanopores in the gold layer.

The gold layer serves as conducting material and as electrode for the electrochemical polymerization of the PPy. This gold layer expands some nanometers into the pores but does not completely cover the openings. For deposition of DBS-doped PPy the use of cyclic voltametry allows fine tuning of the resulting layer. The cyclic voltammogram shows consecutive growing oxidize and reduce peaks correlated to the thickness of the PPy layer (Fig 4).

Principle of operation: Due to the preparation of PPy the entire polymeric chain has a positive charged backbone and therefore, bulky negatively charged ions ($-RSO_3^-$) are incorporated into the polymer for electro neutrality (Fig 5). By applying a negative electrical field to the PPy the polymer incorporates small positive ions for electrochemical neutrality and this results in a swelling of the whole polymer. The procedure is reversible with a reversed field.

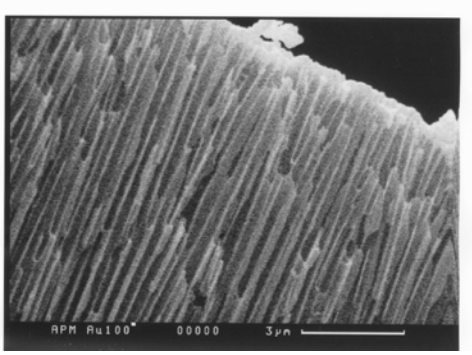


Fig. 2 TEM-picture of the breaking edge of the nanoporous Al_2O_3 membrane with 200 nm wide hexagonal nanopores.

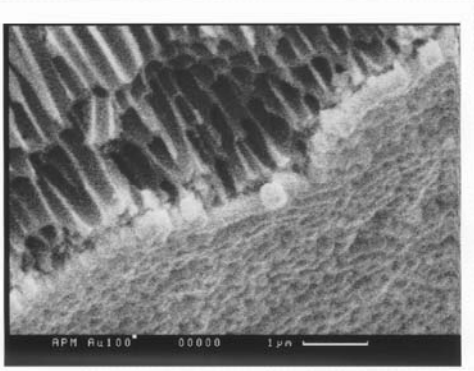


Fig. 3 TEM-picture of the breaking edge of gold sputtered nanoporous Al_2O_3 membrane.

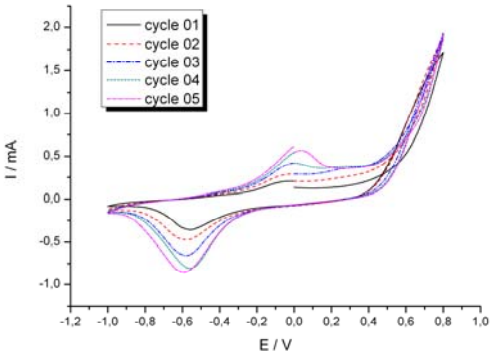


Fig. 4 Cyclic voltammogram of electrochemical deposition of PPy/DBS.

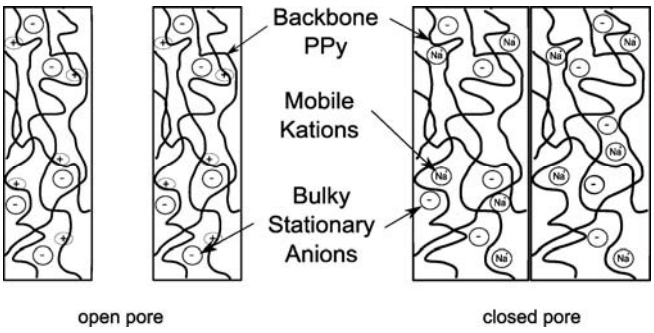


Fig. 4 Scheme of the molecular function of a nanopore. The oxidized state of the PPy in its positive charge is resulting in a shrunken PPy/DBS. In its reduced state small mobile kations (sodium) are incorporated, the polymers swells and the nanopore closes.

Proof of concept: The controlled diffusion through the pores has been verified with a 1 %- bovine serum albumin in a 0.9 % sodium chloride dissolution. For open pores a voltage of +0.8 V is applied to the membrane to get the PPy in a high oxidized state (detraction of electrons from the polymer). The characteristic of diffusion is shown in Fig. 6 (solid line). By applying -0.8 V to the membrane the diffusion is significantly reduced (doted line).

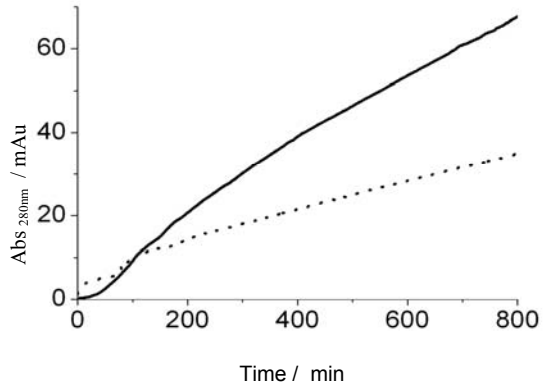


Fig. 6 Diffusion of BSA through the nanoporous valve by applying an electrical field to the PPy/DBS. The line shows the diffusion at oxidized (open) state of PPy/DBS and the dotted line the reduced (closed) state.

IV. Discussion

We established a method for preparation of a new electroactive valve for controlled drug delivery implants, based on nanoporous Al_2O_3 discs. We could show the forming of a conducting nanoporous gold layer and the electropolymerisation of Pyrrol doped with DBS as electro active polymer via EDX spectra (data no shown). In contrast to valves based on micromachined peristaltic pumps [2] or electro active polymers with flaps [3, 5] our valve has no mechanically mobile parts and depends only on availability of small mobile kations. We could show via cyclic voltammetry the oxidative and reductive states of the PPy/DBS on the gold layer.

We have also developed a micro device for testing the different nanoporous discs due basis of a flow cell at UV-absorption. Using the reference compound albumin we could show the different release rates across the nanoporous valve dependent on different redox states. The PPy/DBS pore in its oxidised state allows a significantly higher diffusion of albumin then the reduced form. So we could give the proof of concept for the function of the nanoporous valve.

V. Conclusions

In conclusion we developed a novel nanoporous valve based on the electroactive polymer PPy/DBS. We could show the proof of concept with the release of albumin at different redox states. Our nanoporous valve offers the possibility of a controlled release of drugs with different rates, depending on the redox state of the PPy/DBS, and the initial thickness of the PPy/DBS layer.

Acknowledgment

This work was funded by the BMBF (Translational Centre for Regenerative Medicine Leipzig. 1122MB) and the European Regional Development Fund (BBZ) of the Free State of Saxony. We thank Heinz-Georg Jahnke for helpful discussions.

References

1. Santini J T, Cima M J et al. (1999) A controlled-release microchip. Nature 397:335-338
2. Teymoori M M, Abbaspour-Sani E. (2005) Design and simulation of a novel electrostatic peristaltic micromachined pump for drug delivery applications. Sensors and Actuators A 117:222-229
3. Jager E W, Smela E et al. (2000) Microfabricating conjugated polymer actuators. Science 290:1540-1545
4. Xu H, Wang C et al. (2006) Polymer actuator valves toward controlled drug delivery application. Biosens Bioelectron 21:2094-2099
5. Smela E (2003) Conjugated Polymer Actuators for Biomedical Applications. Advanced Materials 15(6):481-494

Use macro [author address] to enter the address of the corresponding author:

Author: Dr. Randy Kurz
Institute: Center for Biotechnology and Biomedicine (BBZ)
Street: Deutscher Platz 5
City: Leipzig
Country: Germany
Email: randy.kurz@bbz.uni-leipzig.de

Fieldbus controlled live support system for cell-based biohybrid measuring systems

F. Demmel[1], D. Grundl[1], M. Schmidhuber[1], J. Wiest[2], B. Wolf[1]
[1] Heinz Nixdorf-Lehrstuhl für Medizinische Elektronik, TU München, Munich, Germany
[2] Innovationszentrum Medizinische Elektronik – cellasys GmbH, Munich, Germany

Abstract— **In biological research, the determination of the vitality of cells and its interactions with substances is important. To measure the vital parameters of living cells, the Intelligent Mobile Lab (IMOLA) with the BioChip-C has been developed. With this modular high-content screening system the metabolic cell activity can be measured label free and in real time. This way it is possible to determine the cellular respiration, the extracellular acidification, the adhesion and the morphology of cells in-vitro. On the basis of the obtained bioelectronic signals the dynamics of the cells' reaction on certain drugs can be studied. The fields of application are environmental monitoring, toxicology, cell biology and pharmacology.**

Several IMOLA systems can operate simultaneously to form a parallel and redundant assay. To improve the reproducibility and to minimize possible malfunctions, a high grade of automation is required. The individual modules are cross-linked to each other and controlled by a personal computer. The communication is realized via the Controller Area Network (CAN), an established industrial field bus system with the advantage of high data transfer rates, low fault liability and automatic error correction.

A live support system supplies the cell culture with nutrient or drug media. The medium selection is accomplished by integrated valves and occurring air bubbles in the measuring chamber are avoided by a bypass system. To guarantee a sterile working environment, the design of the fluidic system is enclosed and inert. A high precision peristaltic pump is used to transport the medium.

For controlled environmental conditions, the system is mounted in an incubator. An integrated sensor on the cell chip continuously detects the temperature in the cell chamber.

With the introduced high-content screening system, a user-friendly, reliable and highly automatic test-platform is available. It enables standardized and reproducible assays.

Keywords— **cell chip, fieldbus network, drug screening, cell assay**

I. Introduction

In biological and medical research, cells are increasingly used as a signal converter as well as a link between biology and electronics [1]. In the past, we have developed the Intelligent Mobile Lab (IMOLA), a compact, modularly usable, high-content screening system, that enables the user to measure functional parameters of cells online and in real time [2]. The heart and also the key technology of the system is the BioChip-C [3], a chip based on a ceramic thin-film technology. The sensors on the chip surface capture different parameters of the cell vitality. An oxygen sensor measures the respiratory activity, two impedance sensors determine the cell morphology and adhesion on the sensor surface, a PT-1000 element is used to record the temperature and with two pH sensors the extracellular acidification can be determined. The structure of the BioChip-C is shown in Figure 1. The living cell cultures are directly cultivated in a micro-volume on the surface of the chip.

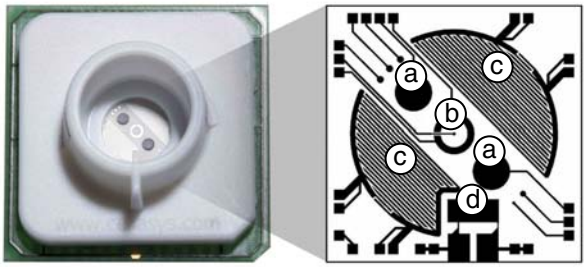


Fig. 1 Ceramic based cell chip *BioChip-C*, with integrated micro sensors – a) pH sensor; b) O2 sensor; c) impedance; d) temperature – *cellasys GmbH*

On the basis of the obtained parameters pH, temperature, oxygen concentration and impedance the dynamic response of cells to specific nutrient or drug media can be studied. The fields of application for such systems range from environmental monitoring, clinical studies, cell biology over pharmacology to chemo-sensitivity tests.

A. Problems and solutions

Biological assays are usually carried out in parallel and redundantly to save time on the one hand and to improve the reproducibility of such tests on the other hand. With this approach a higher efficiency in the daily laboratory work can be achieved. Parallel measurements in real-time with several IMOLA Systems cause a large amount of measuring data. The generated data must be transferred and stored through suitable measures in a correct and reliable way. In addition, the control of the system via an ergonomic user interface is essential.

Experiments with living cells require a sterile working environment. To keep the cell cultures on the BioChip-C alive, they must automatically be supplied with culture

O. Dössel and W.C. Schlegel (Eds.): WC 2009, IFMBE Proceedings 25/VIII, pp. 98–100, 2009.
www.springerlink.com

media or ingredients in regular time intervals. Thus an integrated live support system with an appropriate fluidic is necessary. Error-free measurements also require the avoidance of air bubbles in the measuring chamber.

Research on living cells is usually done at an ambient temperature of 37°C. These in-vitro conditions must be achieved and observed as accurately as possible. Even at an ambient temperature of 38°C cells are in a fever-like condition. Thus the shown cell-based measuring system must be operated at defined ambient conditions.

II. Materials and Methods

A. Structure of the n-fold IMOLA System

Several IMOLA systems operate simultaneously for parallel and redundant cell assays. Due to the high degree of automation, potential sources of error can be minimized and a high grade of reproducibility is achieved. Figure 2 shows a schema of the n-fold IMOLA system.

The System can be divided in three subsystems (Fig. 3):

- Cell-based measuring system
- Live Support System
- Climatic control

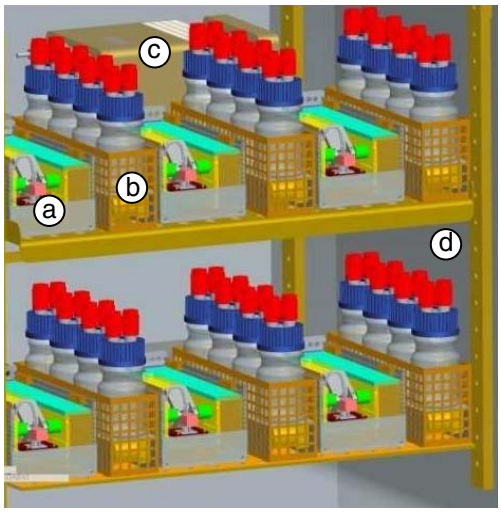


Fig. 2 Schematic of an n-fold IMOLA system - a) Intelligent Mobile Lab with the cell chip for screening vital parameters of living cells; b) live support module to select different media/agents; c) peristaltic pump to transport the media; d) incubator to regulate the environmental contitions - *cellasys GmbH*

The individual modules are interconnected to each other and communicate via a standardized field bus system. A central computer controls the whole system, the data recording and the data analysis. The supply of the cell cultures with growth media and agents is accomplished by a live support module. Individual media selection is realized by automated valves. Occurring air bubbles are detected optically and are lead out of the tubing system via a bypass. The entire system is installed in an incubator for climatisation.

B. Communication via fieldbus system

All components (IMOLA, live support system, peristaltic pump) have to communicate with each other and exchange data with the controlling computer. In the presented application, the Controller Area Network (CAN) had been chosen. This is a standardized field bus system which is established in automotive und automation industry. Due to a high grade of dissemination, different CAN modules are cheaply available at the market. Because of the linear bus topology the complexity of the network structure is reduced. Data transfer rates up to 1 MBit/s are supported and a fault management system is integrated. So an error free und reliable data transfer is guaranteed. By using a differential transmission method the CAN field bus is also robust against external interferences. [4]

The IMOLA and the used peristaltic pump are equipped with a serial port for communication. To connect them to the fieldbus the CAN-Dongle has been developed. It is a very compact, universal interface converter between serial transmission layer and the Controller Area Network [5]. The IMOLA Support System (ISS-3) already has an integrated CAN interface and can be directly connected to the existing bus system. By using the industrial established controller area network, the communication system is modular and easy to extend with additional components.

C. Live Support System

The Intelligent Mobile Lab requires a live support system for the automated supply of living cells with nutrients or test reagents. For each IMOLA a separate live support module is provided. In four vessels in the upper part of the module, the corresponding media can be stocked. Valves in the lower section of the module are used, to select one particular medium. Occurring air bubbles are detected in an optically way. The measurement is based on the fact, that a medium-filled tube has a different optical refractive index than an air-filled tube. If an air bubble within the fluidic appears, it will be automatically redirected to a bypass system, so that

it can't reach the cell culture in the measuring chamber and distort the test results. A peristaltic pump is used to transport the media through the fluidic. This allows setting up the flow rate and other important parameters precisely. The entire structure of the fluidic is an inert, enclosed system, which is autoclavable. This way a sterile working environment can be guaranteed. The electronic control of the peripheral components (valves, air bubble detectors) is done by the IMOLA Support System (ISS-3).

D. Climatic control

An ambient temperature of 37°C is required in order to create in-vivo near conditions for the living cell cultures. Thus the entire n-fold IMOLA system is operated in an incubator. Due to the precise temperature control, a constant climatization regardless of outside influences can be guaranteed. With the help of a PT-1000 element on the BioChip-C, the temperature of the cell cultures in the measuring chamber is continuously observed.

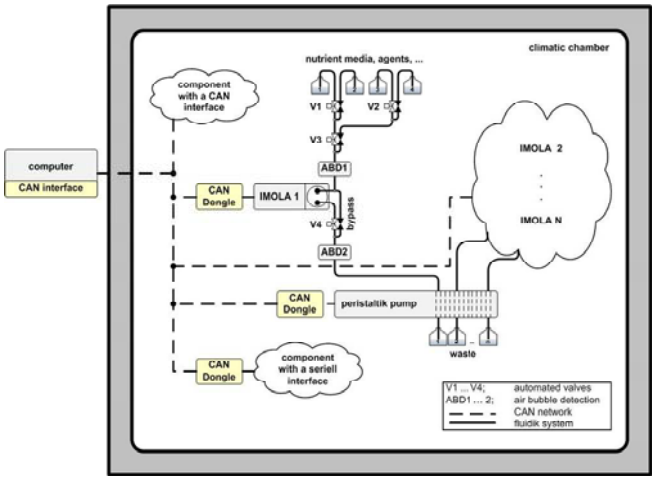


Fig. 3 Flowchart of an n-fold IMOLA system showing the CAN network, the fluidic network of the live supply system and the climatic control

III. Discussion and conclusion

With the Intelligent Mobile Lab and its associated BioChip-C a required platform has been created to use living cells as an interface between biology and electronics. The operation of several Intelligent Mobile Labs simultaneously allows the user to carry out parallel and redundant assays.

Here, the use of Controller Area Network (CAN bus) as communication system is very beneficial. Thanks to the fast and secure data transmission with integrated automatic fault correction, up to 256 IMOLA systems can be operated safely and in parallel. With the CAN-dongle it is easily, to integrate any components with a serial interface into the existing field bus system. For example, additional sensors for temperature, pressure and flow rate may be considered.

With the live support module a compact and user-friendly system is available, which contains all the major components for the supply of cells with culture media or ingredients. The desired medium is chosen automatically via valves, air bubbles in the measuring chamber and the associated measurement errors are avoided.

Due to the high degree of automation it is possible, to carry out several assays automatically over a long time period. Possible sources of error, for example due to improper operation will also be minimized. The user is disburdened and can achieve a high throughput of different assays in a short time.

References

1. Wolf, B., Kraus, M., Brischwein, M., Ehret, R., Baumann, W., and Lehmann, M. (1998) Biofunctional hybrid structures - cell-silicon hybrids for applications in biomedicine and bioinformatics. Bioelectrochemistry and Bioenergetics 46: 215-225
2. Wiest, J., Stadthagen, T., Schmidhuber, M., Brischwein, M., Ressler, J., Reader, U., Grothe, H., Melzer, A., and Wolf, B. (2006) Intelligent mobile lab for metabolics in environmental monitoring. Analytical Letters 39: 1759-1771.
3. Ressler J.: Ceramic-Based Multi-Parametric Sensorchip For Cost-Effective Monitoring Of Living Cells Or Tissue, 06.09.2005, 7th International Conference on Cellular Engineering 2005, Seoul
4. Konrad Etschberger. Controller-Area-Network. Carl Hanser Verlag München, 2000
5. Grundl, D., Wiest, J..: „Integrating RS-232 devices into CAN networks". CAN-Newsletter 09/2007, S. 37f

Author: Franz Demmel
Institute: Heinz Nixdorf-Lehrstuhl für Medizinische Elektronik
Technische Universität München
Street: Theresienstraße 90, Building N3
City: 80333 Munich
Country: Germany
Email: franz.demmel@mytum.de

Traveling-wave electrohydrodynamics: a versatile method for collecting nanoscaled objects from fluids

M. Boettcher[1], M. S. Jaeger[1], M. Stuke[2] and C. Duschl[3]

[1] Medical Technology, Saarland University, Saarbruecken, Germany
[2] Laser Chemistry, Max Planck Institute for Biophysical Chemistry, Goettingen, Germany
[3] Cellular Biotechnology & Biochips, Fraunhofer Institute for Biomedical Engineering (IBMT), Potsdam, Germany

Abstract— **Numerous methods for the manipulation of micro- and nanoparticles have attracted wide interest in medicine and biotechnology. Especially, lab-on-chip systems (LOC) found their applications due to their fine fluid channels being of the same length scale as the objects under test.**

An attribute of these micrometer-sized channels is a laminar fluid flow. In conventional LOCs, these flows are often generated by external pressure-driven pumps. An alternative path to establish the fluid transport is a high-frequency electric traveling-wave.

The full potential of these electrohydrodynamic traveling-waves has not yet been fully exploited. When originally employed to transport fluids through microfluidic devices - even those of physiological electric conductivity -, new applications were discovered. One example is the mixing of parallel laminar streams in a limited channel section which otherwise requires fluidic systems with special structures and geometries. A further new application is the accumulation of micro- and nanometer-sized particles by establishing vortical flows. These flows arise at the boundaries of an electrode array. We used a polydimethylsiloxane (PDMS) channel system with integrated parallel linear electrodes. When an electrical field is applied, a temperature gradient results and stationary vortices occurred.

Our goal is to optimize these vortices to manipulate especially nanometre-sized particles e. g. viruses. For that, it is essential to get a better understanding of the vortices. We use the traveling-wave mechanism to accumulate artificial fluorescent beads. The advantage of our system is the defined accumulation of nanometre-sized particles in the absence of any filtering material.

Keywords— **traveling-wave, electrohydrodynamic, microfluidic, lab-on-chip, nanoparticles**

I. Introduction

We investigate the mechanism of electrohydrodynamic traveling-waves with respect to their applicability to accumulate nanoscaled particles in microfluidic channels. The method is based on the electric manipulation of a fluid by high-frequency fields in the megahertz range. Melcher and Firebaugh were the first to describe in detail the stimulation of fluid movement by applying a phase-shifted electric traveling-wave [1, 2]. The basic idea was to develop a pump mechanism without any moving parts for electrically slightly conducting fluids. Later works showed their high applicability to further miniaturization of fluid devices [3-5]. These and the contributions by Mueller and coworkers [6] already showed the possibility for another application: the collecting of a limited amount of micro- and even nanoparticles by a vortical fluid movement in a system, the physical dimensions of which - in particular their small Reynolds numbers - ensure laminar fluid movement.

The principle of traveling-wave-based fluid flow is the introduction of dielectric inhomogeneities into the fluid. The ohmic heating above an electrically actuated microelectrode array results in the establishment of a thermal gradient. Due to the temperature dependance of fluid parameters like electric conductivity and permittivity, this gradient effects further inhomogeneities along the z axis of the microfluidic channel (see Fig. 1). The resulting differences in charge mobility cause a fluid flow. The free charges in the fluid follow the traveling-wave with a phase shift depending on the frequency of the signal induced by the electrode array which moves through the channel in the x direction. This array is an arrangement of four linear and parallel elements on the bottom. They cross the channel orthogonally. The driving signals for the wave are applied with 90° phase shifts between the single electrodes.

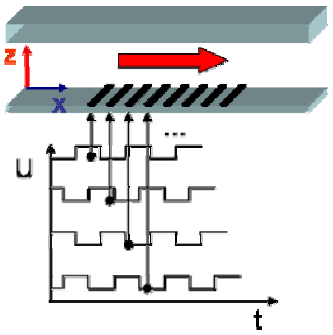


Fig. 1 Scheme of the traveling-wave mechanism for electrohydrodynamic fluid flow.

At the two upstream and downstream boundaries of the array, the total length of which is only a fraction of the

O. Dössel and W.C. Schlegel (Eds.): WC 2009, IFMBE Proceedings 25/VIII, pp. 101–103, 2009.
www.springerlink.com

whole area of the channel, vortices arise. The cause of this is the limited extension of the thermal gradient along the x direction.

Here, we show that these vortices could be a versatile tool to accumulate nanometer particles. By modifying the form, size and arrangement of the electrodes in the array, we modify the accumulation of different particles and their respective accumulation spots.

II. Materials and methods

A. Lab-on-chip device and periphery

Our system consisted of a single channel with dimensions of 300 µm in width, 30 µm in height and 1.5 cm in length and with fluidic interfaces on both ends. A positive silicon master with a thin polytetraflouroethylene (PTFE) layer was molded in PDMS. Through four ceramic connectors, this cast was coupled to a polymethylmethacrylate (PMMA) support. Then, the channel was sealed with a 170 µm glass slide which allows the usage of inverted microscopy methods for observation. On the inner face of the slide, 200 nm thick platinum microelectrodes on an adhesive layer of titanium extend into the channel. For preventing electric loss in the feed lines, a layer of silicon nitride was additionally deposited onto the electrodes. This layer was removed at the electrodes in the channel and at two ends of the slide for electrical contacting. Fabrication of the glass slide with the electrode and passivation layer is photolithographical. The dimensions of the microelectrodes are 10 µm in width and the interelectrode distance also is 10 µm. The electrode length was identical to the channel width. On the lower side of the PMMA support, a circuit board with two contact banks was attached to supply the electrodes with phase-shifted signals. On the upper side of the PMMA support, the fluidics were connected with standard HPLC tubings. Figure 2 shows a picture of our LOC device (GeSiM, Grosserkmannsdorf, Germany).

The PMMA support with the PDMS, the glass slide and the circuit board were clamped into a frame (Fig. 2) and mounted onto an inverted microscope for observation (IX71, Olympus, Hamburg, Germany). The electrodes were driven with a computer-controlled 32 channel high-frequency generator (Evotec Technologies, Hamburg, Germany).

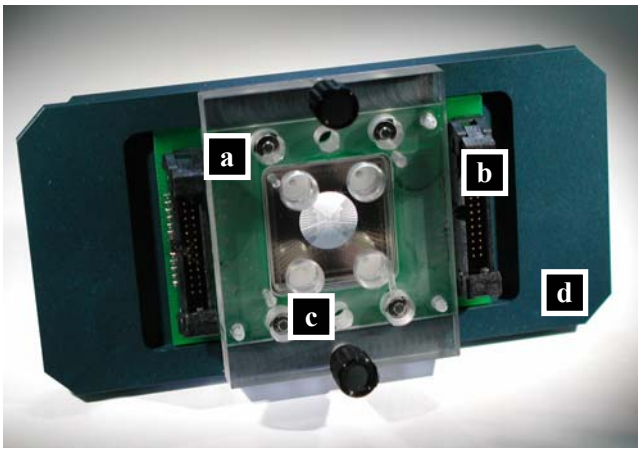


Fig. 2 Our LOC device consists of (a) the PMMA support, (b) the circuit board, (c) fluid connectors, (d) a frame and on the lower side the channel with electrodes (centre).

B. Particles and suspensions

We used a sodium chloride solution with an electric conductivity of 300 mS / m and 0.5% of an antiadhesive additive (Evotec Technologies, Hamburg, Germany) to suspend test particles in. For testing our electrode arrays, we used yellow-green fluorescent polystyrene (PS) particles with diameters of 2 µm, 1 µm and 200 nm (Polyscience Inc.).

III. Results

Our experiments addressed several questions: we tested the influence of the particle dimensions and additionally modified the form and arrangement of the electrodes.

First, we tested the vortex patterns with different particle sizes in a standard electrode array for a traveling-wave pump (Fig. 1). The array was driven with a frequency of 10 MHz and a voltage of 10 V_{pp}. The phase shift between two neighboring electrodes was 90°. We used 1 µm and 200 nm particles separately and as a mixture. We observed different localizations of these two types of particles: while particles of 1 µm in diameter preferentially accumulated in the middle of the array, the smaller 200 nm particles accumulated in the two vortices on the both ends of the array (see Fig. 3). A mixture shows the same behavior.

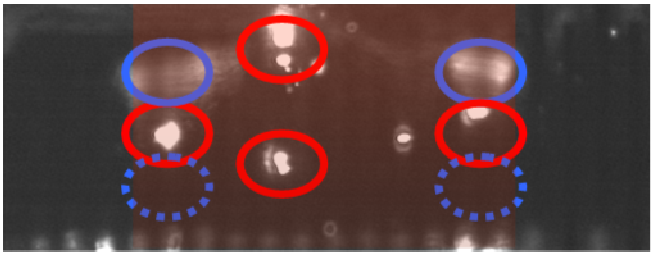


Fig. 3 The image shows the separation of a mixture of 1 µm and 200 nm particles in a microfluidic channel. The areas of particle accumulation are marked in blue for the small particles and in red for the 1 µm particles. The microfluidic channel extends from the left to the right. The electrodes cross this orthogonally. The highlighted light red region marks the active electrode array.

Secondly, the influence of the phase shift was tested by driving the array either in groups of four electrodes at 90° or in groups of two electrodes with a shift of 180°. This modification in electrode control only had a small effect on the pattern formation.

Thirdly, the parameters of electrode form and arrangement were tested by different kinds of arrays (Fig. 4). Linear electrodes with two active parts were formed by an interruption in the passivation layer. They accumulated the 2 µm particles in separate spots (see Fig. 4C). An electrode array with a v-shape shows no accumulation pattern. Instead, all particles in the immediate vicinity continually moved as a cloud above the array. All these tested arrays were driven with 1 MHz and $10V_{pp}$. The electrodes were feed with 90° phase shifts.

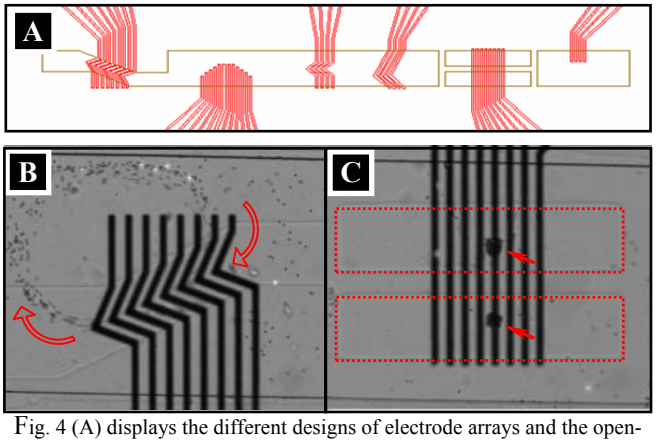


Fig. 4 (A) displays the different designs of electrode arrays and the opening in the passivation layer. (B) shows the movement of 2 µm particles in a vortex. (C) indicates the accumulation of 2 µm particles in the middle of two arrays. The width of each single electrode is 10 µm.

IV. Discussion

These experiments indicate the high applicability of traveling-wave as a method to separate micro- and nanometer particles and especially the accumulation them [7].

The modification of the array parameters are an effective method to exert an influence on the accumulation locations and patterns. We verified that traveling-wave-driven particle accumulation is a versatile tool to filter nanoparticles from suspensions.

Acknowledgment

We thank Steffen Howitz (GeSiM, Grosserkmannsdorf, Germany) for the technical support with the fluid device "MicCell". We acknowledge the German Research Foundation (DFG) for the financial support (JA 17 17 / 1 - 3).

References

1. Melcher J R (1966) Traveling-wave induced electroconvection. Phys. Fluids 9:1548–1555
2. Melcher J R, Firebaugh M S (1967) Traveling-wave bulk electroconvection induced across a temperature gradient. Phys. Fluids 10: 1178-1185
3. Hagedorn R, Fuhr G, Mueller T, and Gimsa J (1992) Traveling-wave dielectrophoresis of microparticles. Electrophoresis 13:49–54
4. Fuhr G, Hagedorn R, Mueller T, Benecke W, and Wagner B (1992) Microfabricated electrohydrodynamic (ehd) pumps for liquids of higher conductivity. J. Microelectromech. Syst. 1:141–146
5. Felten M, Geggier P, Jaeger M, and Duschl C (2006) Controlling electrohydrodynamic pumping in microchannels through defined temperature fields. Phys. Fluids 18: (051707)
6. Mueller T, Fiedler S, Schnelle T, Ludwig K, Jung H, and Fuhr G (1996) High frequency electric fields for trapping of viruses. Biotechnol. Tech. 10:221–226
7. Pethig R, Talary M S, and Lee R S (2003) Enhancing traveling-wave dielectrophoresis with signal superposition. IEEE Eng. Med. Biol. Mag. 22:43–50

To whom correspondence should be addressed:

Author: Magnus Jaeger
Institute: Medical Technology, Saarland University
Street: Am Muehlenberg 13
City: 14476 Potsdam
Country: Germany
Email: m.jaeger@mx.uni-saarland.de

Preparation of functional magnetic cationic polymeric liposomes via a simple process

X.F. Liang, H.J. Wang and J. Chang*

Institute of Nanobiotechnology, School of Materials Science and Engineering, Tianjin University and Tianjin Key Laboratory of Composites and Functional Materials, Tianjin, P. R. China

Abstract **We are reporting a simple and rapid method to prepare superparamagnetic, controlled size and monodispersed magnetic cationic polymeric liposomes (MCPL) by octadecyl quaternized carboxymethyl chitosan (OQCMC) and cholesterol. Hydrophilic Fe_3O_4 ferrofluid (LM) and hydrophobic magnetic nanoparticles (BM) can be encapsulated into this cationic polymeric liposomes, simultaneously or respectively. The size of these stable hydrophilic magnetic nanospheres with controlled size ranges from 10nm to 120nm. A model hydrophobic drug indomethacin can be successfully filled in MCPL with high drug loading capacity 22%. The drug encapsulated MCPL have a long and controlled sustained release profile by changing the number of polymeric lipid layer.**

Keywords **Polymeric liposomes, Magnetic nanoparticles, drug delivery, Chitosan.**

I. Introduction

Magnetic particles have been widely applied to various aspects in biotechnology and biomedicine fields, such as biosensor, MRI contrast agent, targeted drug delivery, and hyperthermia[1-3]. To be successfully used in the above areas, the current research has been focused on requirements as no sedimentation, nano-sized distribution, high and uniform superparamagnetic content, and providing hydrophilic surfaces with various functional groups for covalent coupling to antigens, antibodies, enzymes, etc[4]. However, no method can fulfill all the above mentioned requirements excepted to produce functionalized monodisperse nanoparticles completely encapsulating magnetic cores, and with controlled size and biocompatible surface[5].

The common route for synthesizing magnetic polymer particles is monomer polymerization including different polymerization methods, such as emulsion or dispersion polymerization[6-10]. Nanocrystals coated with porous silica shells were also a kind of desirable way to obtain superparamagnetic organic/inorganic hybrid spheres for biomedical applications[11,12]. Cationic polymeric liposomes (CPL), representing a new class of biomaterials with characteristics both of biomembrane and of synthetic polymers (chemical and physical stability), have a broad application areas including drug delivery and biodetection[13-15]. But, there are a very few studies about CPL and cationic magnetic liposomes[16] in recent years. Herein, we developed a new process to obtain monodispersed, nanoscale, superparamagnetic magnetite/polymeric liposomes spheres by using liposome method. In our former study, polymeric liposomes with functional groups formed from OQCMC and cholesterol were prepared by using different methods of liposome[14].

II. Writing the paper

A. Experimental method

- Materials
- Magnetic polymeric liposomes (MPL) preparation
- Characterization techniques
- Drug release in vitro

1. Materials

Chitosan was supplied by Yuhuan Aoxing biochemistry Co. Ltd in Zhejiang province in China, with a deacetylation degree of above 99% and molecular weight (M.W.) was $5\ 10^4$. Octadecyl quaternized carboxymethyl chitosan (OQCMC), hydrophobic magnetic nanoparticles (BM), hydrophilic magnetic nanoparticles (LM), are all prepared in our lab. All other chemicals were of reagent grade and were used as received.

2. Magnetic polymeric liposomes (MPL) preparation

Drug-encapsulating MCPL with one layer of OQCMC/Chol film was prepared as follows. Reverse-Phase Evaporation (REV) Method: OQCMC and cholesterol (total lipid 30 mg) were dissolved in 4 ml chloroform at room temperature to obtain the organic phase A1. Then, 6 ml deionized water was prepared to obtain aqueous phase B1. 8 mg BM and 8 mg indomethacin were added to above organic phase A1 with continuous stirring. Then, aqueous phase B1 was mixed with this organic phase A1. The mixture was sonicated for 5min using a bath-type sonicator. The organic solvents were evaporated on a rotary evaporator to form a gel-like highly concentrated magnetic polymeric liposomes suspension that can be diluted with a suitable aqueous

O. Dössel and W.C. Schlegel (Eds.): WC 2009, IFMBE Proceedings 25/VIII, pp. 104–107, 2009.
www.springerlink.com

buffer solution. The resulted magnetic polymeric liposomes were collected by magnet and washed three times by water. MCPL-B with two layers of OQCMC/Chol film were also prepared by REV method. Here, the above organic phase A1 was separated into two sections. 8 mg BM and 8 mg indomethacin were added to one section of A1 with continuous stirring. After preparing, suspension of MCPL-B(one layer) was used as aqueous phase B2. Then, the aqueous phase B2 was mixed with the other section of A1. To prepare the MCPL-B with three layers of OQCMC/Chol film, the above organic phase A1 was separated into three sections. MCPL-L was obtained by adding LM into aqueous phase by REV method. Magnetic polymeric liposomes encapsulating LM and BM were obtained by adding LM and BM into organic phase and aqueous phase, respectively.

3. Characterization techniques

The morphologies of different MCPL were observed by using Transmission Electron Microscopy (TEM). TEM observation of the liposomes was carried out at an operating voltage of 200 kV with JEOL-100CXII (Japan) in bright field mode and by electron diffraction. The average particle size and size distribution were determined by Dynamic Light Scattering Nanoparticle Size Analyzer LB-550 (Horiba) and quasielastic laser light scattering with a Malvern Zetasizer (Malvern Instruments Limited, United Kingdom) at 25 . Zeta potential was measured by using a Zetasizer S (Malvern, UK). The magnetic properties of magnetic polymeric liposomes were determined through VSM (vibrating samples magetometer, LDJ9600-1).

4. Drug release in vitro

The measurement of IMC content in polymeric liposomes were performed by UV/Vis spectroscopy (JASCO V-570, Tokyo, Japan) at a fixed wavelength of 320 nm. After preparing drug-encapsulating magnetic polymeric liposomes, the mixture solution was centrifuged to remove any unencapsulated IMC (4000 rpm for 10 min). Drug content was determined by calculate the weight of IMC encapsulated in magnetic polymeric liposomes.

In vitro drug release experiments of IMC loaded polymeric liposomes and different magnetic polymeric liposomes were carried out in shaking condition at 100 rpm and 37! 0.5 . The drug-loaded samples were enclosed in dialysis membrane and then incubated in 10 ml medium of PBS buffer solution (pH 7.4). The release medium was exchanged completely at regular time points. The amount of IMC released at certain set times was determined by UV/Vis spectroscopy at 320nm (with PBS as reference). Each experiment was repeated three times.

B. Results and discussion

- Process for preparing MCPL
- TEM analysis of different MCPL
- Particle size distribution and Zeta potential of MCPL
- Magnetic characterization of MCPL
- The application of MCPL as drug vector

1. Process for preparing MCPL

A two-step synthesis was used to derive MCPL. LM and BM (magnetic nanoparticles modified by oleic acid with an average particle size ~8nm) were initially synthesized by chemical coprecipitation method[17] in our lab. This was a simple and rapid synthesis of water-soluble magnetic nanoparticles system through encapsulation hydrophilic or hydrophobic magnetic nanoparticles into polymeric surfactant/cholesterol micelles. These novel polymeric surfactant/cholesterol micelles can be defined to a kind of multifunctional polymeric liposomes system, which cholesterol can be replaced by other lipid molecules. Scheme 1 illustrates the preparation procedure. Cholesterol, which is a cell membrane constituent, can modulate membrane fluidity, elasticity, and permeability by stabilizing the polymeric liposomes system.

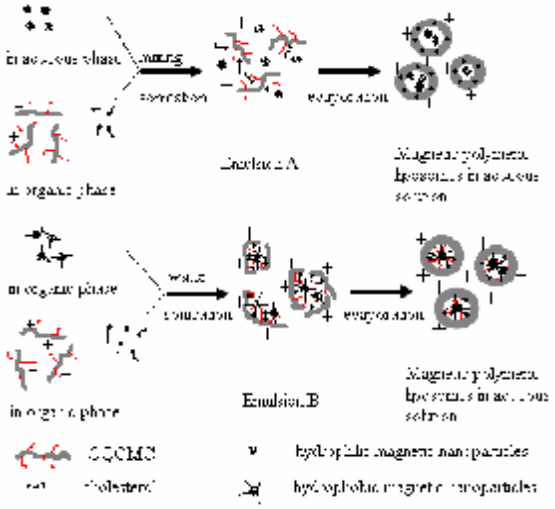


Fig. 1 Schematic diagram showing the preparation of MCPL with hydrophilic and hydrophobic magnetic nanoparticles.

2. TEM analysis of different MCPL

Figure 1a shows the transmission electron microscopy (TEM) image of LM in deionized water. Figure 1b shows TEM image of BM (8nm). Figure 1c shows TEM images of as-synthesized CPL (Fe_3O_4/liposomes) nanospheres encapsulated LM (MCPL-L). The synthesized magnetite nanopar-

ticles could not be dispersed into deionized water, while the MCPL nanoparticles could spontaneously disperse into water and form a stable dispersion. Figure 1d shows TEM image of CPL encapsulated BM (MCPL-B). In figure 1b, nanosized Fe_3O_4 crystals on the order of 8 nm are randomly arranged in organic solvent. After encapsulated by polymeric liposome and was dispersed in aqueous solution, the size of the monodispersed spheres is mostly in the range of 10~20nm and the nanospheres all assume well proportioned spherical geometry in a single layer on the sample substrate. TEM image of CPL encapsulated hydrophilic and hydrophobic magnetic nanoparticles (MCPL-L/B) simultaneously is shown in figure 1e. The size of MCPL had not changed a lot after encapsulating of different magnetic nanoparticles at one time. Also, these MCPL can be encapsulated by OQCMC/Chol film layer by layer. Herein, a novel stepwise layer-by-layer synthesis strategy[18] was used to achieve multilayer magnetic polymeric liposomes. Figure 1f, 1g show polymeric liposomes encapsulated BM by two layers and three layers of polymeric lipid film, respectively. MCPL-B(two layers) had no distinctly difference from MCPL-B(one layer)(figure 2d). However, the shape of MCPL-B(three layers) is not irregular and have a larger diameter compared with MCPL-B encapsulated by one or two layers.

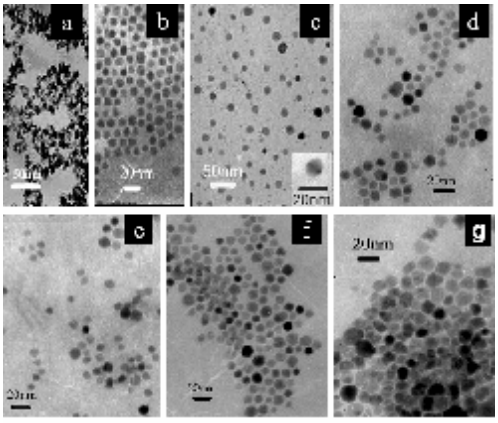


Fig. 2 TEM images of (a) LM, (b) BM(8nm), (c)MCPL-L (with a higher magnification), (d) MCPL-B(one layer), (e) MCPL-L/B, (f) MCPL-B(two layers), (g) MPL-BM(three layers).

3. Size and Magnetic characterization of MCPL

For comparison, Dynamic Light Scattering was used to further determine the particle size of MCPL. The experimental results on as-synthesized nanoparticles indicate that the mean hydrodynamic size of MCPL-B is 43.1! 1.5 nm, whereas the diffusion coefficient is 1.3758E-14 m^2/s, almost consistent with the monodispersed nanoparticles shown in figure 2d. The mean diameters of MCPL-L and MCPL-B/L are 101.5! 1.3 nm and 93.4! 1.4 nm, respectively. The unique characteristics of as-prepared Fe_3O_4/polymeric liposomes nanospheres with mono dispersion and functional groups are the result of the new preparation method. In this novel approach, both LM and BM can be encapsulated simultaneously. Zeta potential of MCPL can reach +40mv. After encapsulating with OQCMC/Chol polymeric liposomes film, the surface zeta potentical of hydrophilic Fe_3O_4 nanopartilces have change into positive. But, there are not distinct difference of Zeta potential for OQCMC, OQCMC/Chol polymeric liposomes and MCPL-L. The superparamagnetic MCPL-L, with saturation magnetization value of 28 emu/g at 300 K, was stable in aqueous solution[19]. The room-temperature magnetization curves of BM and MCPL-B show a typical superparamagnetic behavior at room temperature without any hysteresis loop.

4. The application of MCPL as drug vector

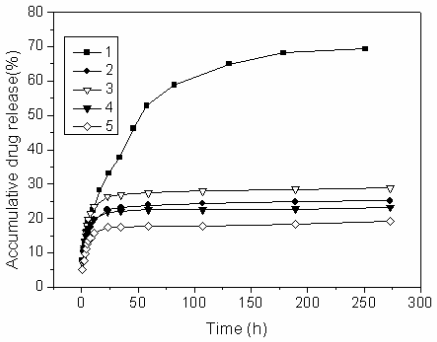


Fig. 3 In vitro release of IMC in PBS (pH 7.4 and 3.3) at 37! 0.5 . 1, polymeric liposomes in PBS(pH 3.3); 2, polymeric liposomes in PBS(pH 7.4); 3, MCPL-B in PBS(pH 7.4); 4, MCPL-B(two layers) in PBS(pH 7.4); 5, MCPL-B(three layers) in PBS(pH 7.4).

To investigate MCPL as a candidate of drug carriers for delivery, we selected indomethacin (IMC) as a model hydrophobic (lipophilic) drug. IMC is more easily encapsulated into MCPL with lower cholesterol content. Approximately, 22% drugs can be encapsulated into MCPL-B (OQCMC/Chol: 5/1) and the drug encapsulation efficiency of IMC can reach 95%. Figure 3 shows the release of IMC from MPL-BM with one, two and three layers of OQCMC/Chol film. In order to decrease the drug leakage of IMC, method of adding the membrane thickness of polymeric lipid during preparation was chosen. About 25.1% and 28.9% of IMC was released from polymeric liposomes and MCPL after 273h in pH 7.4, respectively. A more sus-

tained drug release was achieved for the MCPL-L with thick layer. About 23.3% and 19.1% of IMC was released at 273h for MCPL-B(two layers) and MCPL-B(three layers), respectively. MCPL-B(three layers) can release less IMC in first 59 h compared with MCPL-B with one layer and it could delay the drug release in vivid fashion.

III. CONCLUSIONS

In conclusion, we have developed a new simple and rapid method to obtain cationic monodispersed hydrophilic magnetic nanospheres that exhibit superparamagnetic, monodispersed, and controlled size using polymeric surfactant OQCMC and cholesterol. This functional MCPL system can encapsulate hydrophobic drug indomethacin with high encapsulating efficiency. The release rate of indomethacin can be controlled by changing the number of polymeric lipid layer. These magnetic polymeric liposomes nanospheres are likely to find many biomedical applications.

ACKNOWLEDGMENT

We thank National Natural Science Foundation of China (No.50873076,30772245,30876203) and key project of National High Technology Program (No.2007AA021808) for financial support.

REFERENCES

1. Xu H, Cui L L, Tong N H et al. (2006) Development of High Magnetization Fe_3O_4/Polystyrene/Silica Nanospheres via Combined Miniemulsion/Emulsion Polymerization. *J. AM. CHEM. SOC.* **128:** 15582-15583
2. Kim J, Lee J. E, Lee J et al. (2006) Magnetic Fluorescent Delivery Vehicle Using Uniform Mesoporous Silica Spheres Embedded with Monodisperse Magnetic and Semiconductor Nanocrystals. *J. AM. CHEM. SOC.* **128:** 688-689
3. Gao J H, Zhang W, Huang P B et al. (2008) Intracellular Spatial Control of Fluorescent Magnetic Nanoparticles. *J. AM. CHEM. SOC.* **130:** 3710-3711
4. Chen M H, Kim Y N, Li C C et al. (2008) Preparation and Characterization of Magnetic Nanoparticles and Their Silica Egg-yolk-like Nanostructures: A Prospective Multifunctional Nanostructure Platform. *J. Phys. Chem. C.* **112:** 6710-6716
5. Hor"k D, Babi%M, Mackov" H et al (2007) Preparation and properties of magnetic nano- and microsized particles for biological and environmental separations. J. Sep. Sci. 30: 1751(1772
6. Liu H B, Guo J, Jin L et al. (2008) Fabrication and Functionalization of Dendritic Poly(amidoamine)-Immobilized Magnetic Polymer Composite Microspheres. *J. Phys. Chem. B.* **112:** 3315-3321
7. K)+ov" J, - panov" A, Bohuslav R et al. (2005) Magnetic hydrophilic methacrylate-based polymer microspheres for genomic DNA isolation. J. Chromatogr. A. 1064: 247-253
8. Lu Y, Yin Y. D, Mayers B. T et al. (2002) Modifying the Surface Properties of Superparamagnetic Iron Oxide Nanoparticles through A Sol-Gel approach. *Nano Lett.* **2:** 183-186
9. Im S H, Herricks T, Lee Y T et al. (2005) Synthesis and characterization of monodisperse silica colloids loaded with superparamagnetic iron oxide nanoparticles *Chem. Phys. Lett.* **401:** 19-23
10. Stjerndahl M, Andersson M, Hall H E et al. (2008) Superparamagnetic Fe_3O_4/SiO_2 Nanocomposites: Enabling the Tuning of Both the Iron Oxide Load and the Size of the Nanoparticles. *Langmuir.* **24:** 3532-3536
11. Yi D K, Selvan S T, Lee S S et al. (2005) Silica-Coated Nanocomposites of Magnetic Nanoparticles and Quantum Dots. *J. AM. CHEM. SOC.* **127:** 4990-4991
12. Sadasivan S, Sukhorukov G B (2006) Fabrication of hollow multifunctional spheres containing MCM-41 nanoparticles and magnetite nanoparticles using layer-by-layer method. *Journal of Colloid and Interface Science.* **304:** 437(441
13. Gerelli Y, Bari M T D, Deriu A et al. (2008) Structure and organization of phospholipid/polysaccharide nanoparticles. *J. Phys.: Condens. Matter.* **20:** 104211-104219
14. Liang X F, Wang H J, Luo H et al. (2008) Characterization of novel multifunctional cationic polymeric liposomes formed from octadecyl quaternized carboxymethyl chitosan/cholesterol and drug encapsulation. *Langmuir.* **24:** 7147(7153
15. Dennis C, Jamesa H (1985) Polymeric liposomes as stable gas carriers *European Patent.* WO8504326
16. Yanase M, Shinkai M, Honda H et al. (1998) Intracellular hyperthermia for cancer using magnetite cationic liposomes: an in vivo study. *Jpn. J. Cancer Res.* **89:** 463(469
17. Sun S H, Zeng H, Robinson D B et al. (2004) Monodisperse MFe_2O_4 (M = Fe, Co, Mn) Nanoparticles *J. AM. CHEM. SOC.* **126:** 273-279
18. Wang Q B, Liu Y, Lin C X et al. (2007) Layer-by-layer growth of superparamagnetic, fluorescent barcode nanospheres *Nanotechnology.***18:** 1-7
19. Liang X F, Wang H J, Tian H et al. (2008) Synthesis and characterization of novel magnetic cationic polymeric liposomes. *Chemical Journal of Chinese Universities*. 29: 858-861

Author: J. Chang*
Institute: School of Materials Science and Engineering, Tianjin University
Street: 92, Weijin Road.
City: Tianjin
Country: P. R. China
Email: jinchang@tju.edu.cn

Fluorescent Gold Nanoclusters for Biomedical Applications

Cheng-An J. Lin[1],Chin-Hsien Lee[1], Hung-I Yeh[2], and Walter H. Chang[1]

[1] Department of Biomedical Engineering, Chung Yuan Christian University, Chung-Li 32023, Taiwan, R.O.C.
[2] Cardiac Medicine, Mackay Memorial Hospital, Taipei, Taiwan, R.O.C

Abstract— **Synthesis, characterization, and bioconjugation of fluorescent gold nanoclusters (FGNCs) are reported. The gold nanocluster is synthesized by etching gold nanoparticle. When the gold nanocluster is capped with reduced dipoic acid (DHLA, dihydrolipoic acid) that the nanocluster has the fluorescent property. The fluorescent gold nanoclusters have the emission in the range of 600~800 nm that is suitable for cell labeling, and its size and hydrodynamic radius are around 1.8 nm and 1.8~3.4 nm. The FGNCs can also be conjugated with desired biomolecules, such as biotin-PEG and avidin. In the preliminary data, the FGNCs can be taken nonspecifically by human aortic endothelial cells and the FGNCs conjugated with avidin can label specifically endogenous biotin within human hepatoma cells. Compare the FGNCs with semiconductor quantum dots and conventional organic dyes, the FGNCs are more biocompatible than quantum dots and more stable than organic dyes. So we believe that the FGNCs have great potential for biomedical applications.**

Keywords—**gold nanoparticles, fluorescent gold nanoclusters**

I. Introduction

Nanoprobe has been used recently in imaging of tracing drug, biomolecules, and cell in vivo by combining medical imaging techniques, such as ultrasound imaging, magnetic resonance imaging (MRI), computed tomography (CT) and position emission tomography (PET). Since 1998, Prof. Alivisatos and Prof. Nie have first applied semiconductor nanoparticle (also called quantum dots) to the biological application [1-2], quantum dots have become gradually as the material that was designed as optical-based nanoprobe. Quantum dots have more advantages than conventional organic dyes, such as no photobleaching, high quantum yields, broad excitation, narrow and symmetrical emission, and excitation only using single excitation. Thus, many studies related with quantum dots in biomedical application have begun to develop. Many products of quantum dots have been commercial at present and provided researchers to design specific nanoprobe. However, the toxicity of quantum dots is the biggest limitation in clinical application, because general commercial quantum dots all contain heavy metal such as cadmium (Cd) or lead (Pb).

On the basis of the toxicity of Cd-based quantum dots, the concept of greener quantum is proposed, like non-Cd-based quantum dots, such as Zn^{2+}-, Cu^{2+}- or Mn^{2+}-based quantum dots [3-6]. Another one is fluorescent gold nanocluster (size is generally smaller than 2 nm). Gold nanoparticles (NPs) show a size-dependent plasmon absorption band when their conduction electrons are confined to dimensions smaller than the electron mean free pathlength (ca. 20 nm)[7]. However, Au nanoparticles smaller than 2 nm (which we term Au nanoclusters) no longer possess plasmon resonance and Mie's theory no longer can be applied [8-10]. Then the size dependent fluorescence and discrete size dependent electronic states are appear [11-12]. Although some synthesized methods of fluorescent gold nanoclusters have been reported [13-18], the producing fluorescent mechanism of fluorescent gold nanocluster is still unclear. And there are rare papers to apply fluorescent gold nanocluster in biological and biomedical application. So in this paper, we are going to describe a simple method to synthesize water-soluble fluorescent gold nanoclusters, and study its optical and physical characterizations of fluorescent gold nanocluster. Finally in this report we will show some examples of fluorescent gold nanoclusters applying in cell targeting and cell imaging that use specific targeting and nonspecific uptake by cell.

II. Materials and methods

A. Chemicals

Didodecyldimethylammonium bromide (DDAB, >98% purity; Fluka), decanoic acid (>98% purity, Aldrich), tetrabutylammonium borohydride (TBAB, >97% purity, Fluka), gold (III) chloride (AuCl3, 99% purity, Strem Chemicals), gold (III) chloride trihydrate (HAuCl4.3H2O), (±)-α-lipoic acid (≥99% purity, Sigma), toluene (Sigma).

B. Synthesis of fluorescent gold nanocluster

Gold nanoparticles prepared from an one-phase reaction. In brief, appropriate amounts of DDAB or decanoic acid were dissolved in toluene as stock solution of 100 mM concentration. Gold precursor solution (25 mM) was then pre-

O. Dössel and W.C. Schlegel (Eds.): WC 2009, IFMBE Proceedings 25/VIII, pp. 108–111, 2009.
www.springerlink.com

pared by dissolving an appropriate amount of gold (III) chloride (AuCl3 or HAuCl4) in the DDAB solution. Gold nanoparticles are etched into small gold nanoclusters (NCs) by the gold precursor solution. The etched gold NCs lose their surface plasmon properties and lead to a yellowish or even colorless transparent solution, whereas the original larger gold nanoparticles possess strong surface plasmon absorption around 520~530 nm. The addition of freshly reduced lipoic acid can replace the surfactants on the etched gold NCs via the formation of strong dithiol - Au bonds, whereby the acid headgroup points towards the solution. Upon such dithiol - related ligand exchange the gold NCs become red - emitting fluorophores. By deprotonization under basic buffer, the etched gold NCs become water - soluble and form a mono - dispersion by electrical repulsion.

C. Characterization of fluorescent Au nanoclusters

The physical characterization of the fluorescent gold nanoclusters was studied by several techniques: transmission electron microscopy (TEM), size exclusion chromatography (SEC), atomic force microscopy (AFM), gel electrophoresis, and UV/vis spectroscopy.

D. Bioconjugation of fluorescent gold nanoclusters

To prove the bioconjugate capability of the fluorescent gold nanoclusters as synthesized in this work, polyethylene glycol (PEG), biotin and avidin were selected as examples for bioconjugation. Water-soluble fluorescent gold nanoclusters are covalently capped by dihydrolipoic acid (DHLA) via thiol-Au bonds. The carboxylic acids on the end of DHLA pointing towards solution are the origin of the negative surface charges of the particles. They also can be used for conjugation with functional moieties by 1-Ethyl-3-[3-dimethylaminopropyl] carbodiimide (EDC) chemistry.

E. Labeling of living cell

For incubation with fluorescent gold nanoclusters HAEC cells were grown in condition medium 200 and serially passaged until they reached passage 8. Fluorescent gold nanoclusters were added to the culture medium (containing serum and antibiotics) and condition medium (serum and antibiotics free medium). After 5 hours of incubation the uptake of fluorescent gold nanoclusters was tested.

III. Results and Discussions

By using UV-visible spectroscopy to measure gold nanoparticle and gold nanoclusters. The gold nanoparticles have a plasma peak at 520 nm (fig. 1a), while gold nanoclusters being obtained by etching gold nanoparticles don't appear the plasma peak. It suggests that the gold nanoparticles can be etched by adding gold precursor. When the surfaces of gold nanoparticles or gold nanoclusters were exchanged by DHLA, the absorption peaks were still similar (Fig. 1c, d). But gold nanoclusters after ligand exchange appear strong red emission around 625nm (Fig. 2). In spite of exciting in different excitation wavelength, the photoluminescence (PL) is still no change. So it suggests that the light from gold nanocluster is fluorescent, but not scattering light from gold

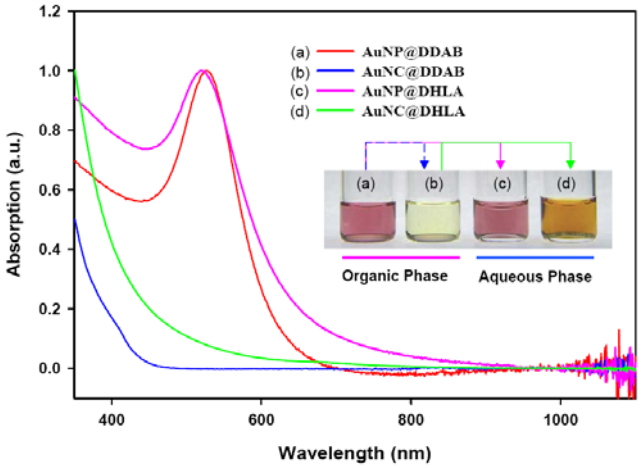


Fig. 1 Absorption spectrum of Au nanoparticles and nanoclusters in organic and aqueous phase.

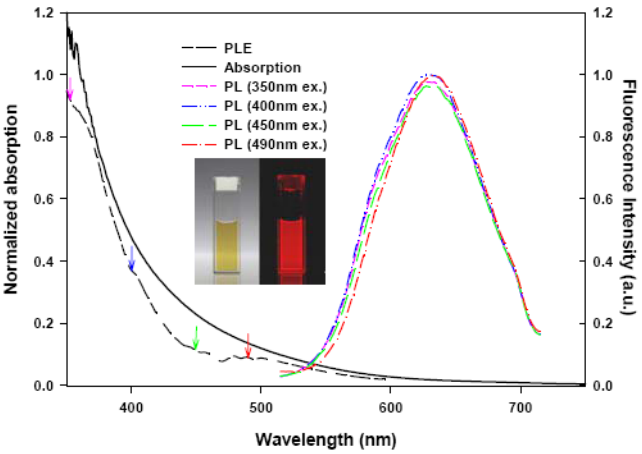


Fig. 2 Absorption, photoluminescence (PL) and photoluminescence excitation (PLE) of fluorescent Au nanoclusters

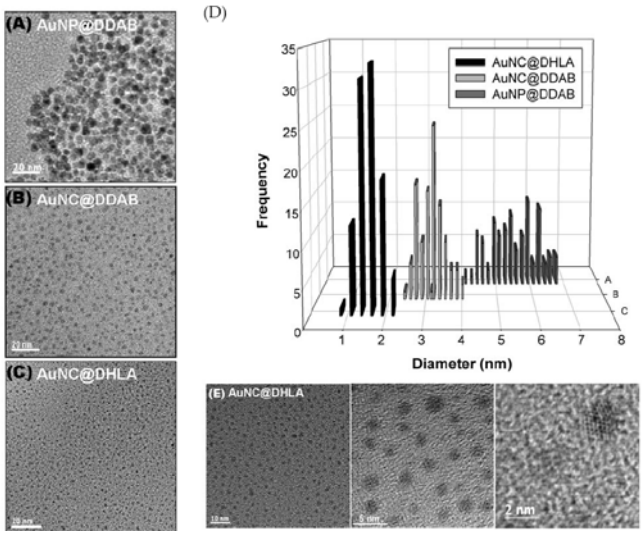


Fig. 3 TEM imaging of different synthetic stage of fluorescent Au nanoclusters.

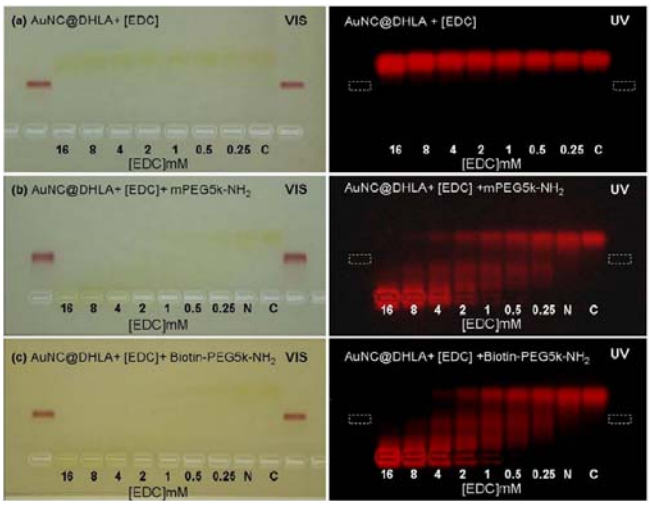


Fig. 4 Gel electrophoresis for probing of the bioconjugation of fluorescent Au nanoclusters

nanocluster. TEM was used for studying the size of gold nanoclusters on the process of different synthesizing stages. TEM images show that the size of gold nanoparticles is around 5.5±0.68 nm, of gold nanoclusters is 3.17±0.35, and of fluorescent gold nanoclusters is 1.56±0.3 (Fig. 3D).

In order to approve that the fluorescent gold nanoclusters can be conjugated with biomolecules for cell labelling application, we use electrophoresis to identify the fluorescent gold nanoclusters can be conjugated with biomolecules (PEG, avidin) which containing amine functional group by EDC chemistry. When fluorescent gold nanoclusters only incubatated with different concerntrations of EDC, the high concentration of EDC can retard the band and it also increase the fluorescent intensity of fluorescent gold nanoclusters (Fig. 4a). When adding PEG-NH2 (Fig. 4b) and biotin-PEG-NH2 (Fig. 4c), the discrete retarded band were obtained with different concentration of EDC. This experiment of electrophoresis shows the fluorescent gold nanoclusters can be conjugated with biomolecules containing amine functional group.

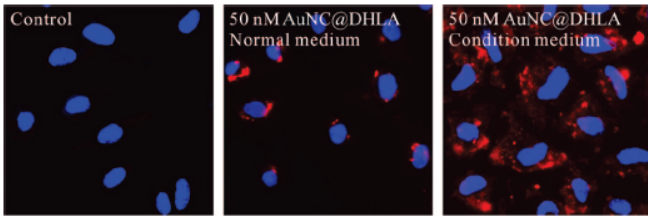


Fig. 5 Uptake of fluorescent Au nanoclusters by HAEC cells.

Finally, the human aortic endothelial cells (HAEC) are used as an example for fluorescent gold nanoclusters that can actually apply for cell labelling. Results are shown in Figure 5. As no functionality had been introduced on these nanoclusters' surface the uptake of the fluorescent gold nanoclusters has to be considered nonspecific.

IV. Conclusions

In this paper we reported the synthesis, characterization, and bioconjugation of fluorescent gold nanoclusters. The fluorescent gold nanoclusters (FGNCs) can be obtained by ligand exchange of reduced dipoic acid. The FGNCs have red emission around 625-650 nm and their size are about 1.56±0.3 nm. The FGNCs have carboxyl groups on the surface, so they can be conjugated with biomolecules containing amine functional group by simple method of EDC chemistry. The FANCs also can be taken nonspecifically by human aortic endothelial cells (HAEC) and they have no any effect of cellular toxicity on HAEC in the preliminary data. Although the FGNCs still have some limitations in biomedical applications, such as low fluorescent quantum yields and not very good photostability comparing to semiconductor quantum dots. However the FGNCs have the advantages of smaller size and nontoxicity comparing to semiconductor quantum dots, so they are still promising nanomaterial for the applications in cell labelling and targeting. So how to enhance the quantum yields and the photostability of the FGNCs are our current projects. We believe the FGNCs have great potential for clinical biomedical applications in the future.

ACKNOWLEDGMEN

This project was financial supported by the National Science Council of The Republic of China(NSC 96-2320-B-033; NSC 97-2627-B-033).

REFERENCES

1. Bruchez, M., Jr.; Moronne, M.; Gin, P.; Weiss, S.; Alivisatos, A. P., Semiconductor nanocrystals as fluorescent biological labels. *Science* **1998,** 281, (5385), 2013-6.
2. Chan, W. C.; Nie, S., Quantum dot bioconjugates for ultrasensitive nonisotopic detection. *Science* **1998,** 281, (5385), 2016-8.
3. Hines, M. A.; Guyot-Sionnest, P., Bright UV-blue luminescent colloidal ZnSe nanocrystals. *Journal of Physical Chemistry B* **1998,** 102, (19), 3655-3657.
4. Hwang, C. S.; Cho, I. H., Characterization of the ZnSe/ZnS core shell quantum dots synthesized at various temperature conditions and the water soluble ZnSe/ZnS quantum dot. *Bulletin of the Korean Chemical Society* **2005,** 26, (11), 1776-1782.
5. Xie, R. G.; Zhong, X. H.; Basche, T., Synthesis, characterization, and spectroscopy of type-II core/shell semiconductor nanocrystals with ZnTe cores. *Advanced Materials* **2005,** 17, (22), 2741-+.
6. Pradhan, N.; Goorskey, D.; Thessing, J.; Peng, X. G., An alternative of CdSe nanocrystal emitters: Pure and tunable impurity emissions in ZnSe nanocrystals. *Journal of the American Chemical Society* **2005,** 127, (50), 17586-17587.
7. Link, S.; El-Sayed, M. A. Optical Properties and Ultrafast Dynamics of Metallic Nanocrystals. *Annu. Rev. Phys. Chem.* **2003**, *54*, 331–66.
8. Alvarez, M. M.; Khoury, J. T.; Schaaff, T. G.; Shafigullin, M. N.; Vezmar, I.; Whetten, R. L. Optical Absorption Spectra of Nanocrystal Gold Molecules. *J. Phys. Chem. B* **1997**, *101*, 3706–3712.
9. Schaaff, T. G.; Shafigullin, M. N.; Khoury, J. T.; Vezmar, I.; Whetten, R. L.; Cullen, W. G.; First, P. N.; GutierrezWing, C.; Ascensio, J.; JoseYacaman, M. J. Isolation of Smaller Nanocrystal Au Molecules: Robust Quantum Effects in Optical Spectra. *J. Phys. Chem. B* **1997**, *101*, 7885–7891.
10. Hostetler, M. J.; Wingate, J. E.; Zhong, C. J.; Harris, J. E.; Vachet, R. W.; Clark, M. R.; Londono, J. D.; Green, S. J.; Stokes, J. J.; Wignall, G. D.; *et al* Alkanethiolate Gold Cluster Molecules with Core Diameters from 1.u5 to 5.2 Nm: Core and Monolayer Properties as a Function of Core Size. *Langmuir* **1998**, *14*, 17–30.
11. Huang, C. C.; Yang, Z.; Lee, K. H.; Chang, H. T. Synthesis of Highly Fluorescent Gold Nanoparticles for Sensing Mercury(II). *Angew. Chem., Int. Ed.* **2007**, *46*, 6824–6828.
12. Chen, S.; Ingram, R. S.; Hostetler, M. J.; Pietron, J. J.; Murray, R. W.; Schaaff, T. G.; Khoury, J. T.; Alvarez, M. M.; Whetten, R.L. Gold Nanoelectrodes of Varied Size: Transition to Molecule-like Charging. *Science* **1998**, *280*, 2098–2101.
13. J. P. Wilcoxon, J. E. Martin, F. Parsapour, B. Wiedenman, D. F. Kelley, *Journal of Chemical Physics* **108**, 9137 (Jun 1, 1998).
14. *Chemical Physics Letters* **2000,** 317, 517-523
15. T. Huang, R. W. Murray, *Journal of Physical Chemistry B* **105**, 12498 (Dec 20, 2001).
16. S. Link *et al.*, *Journal of Physical Chemistry B* **106**, 3410 (Apr 4, 2002).
17. J. Zheng, C. W. Zhang, R. M. Dickson, *Physical Review Letters* **93** (Aug 13, 2004).
18. Kiyohiko Hatake, Nahomi Tokudome, and Yoshinori Ito, *Breast Cancer,* **Vol. 14 No. 2 April 2007**

Use macro [author address] to enter the address of the corresponding author:

Author: Walter H. Chang
Institute: Chung Yuan Christian University
Street: 200, Chung Pei Rd.
City: Chung-Li
Country: Taiwan, R.O.C.
Email: whchang@cycu.edu.tw

Microelectrode Array (MEA) high resolution electrophysiological mapping of cardiac cell, tissue and organ preparations

T. Meyer[1], U. Kraushaar[2] and E. Guenther[2]

[1] Multi Channel Systems MCS GmbH, Aspenhaustr. 21, 72770 Reutlingen, Germany
[2] NMI, Natural and Medical Sciences Institute at the Tubingen University, Markwiesenstr. 55, 72770 Reutlingen, Germany

Abstract— **Microelectrode arrays (MEAs) allow electrophysiological recording from 32 – 252 electrodes in parallel. In addition to field potential data spatial properties such as conduction velocity and propagation patterns can be addressed. These patterns provide insight into mechanisms of the generation of a variety of arrhythmia forms. Here we show data obtained from stem cell derived cardiomyocytes, primary cardiomyocytes, a cardiomyocyte cell line, and surface mappings from atrium and ventricle on isolated hearts.**

Keywords— **Heart, Microelectrode Array, Cardiomyocyte, HL-1, Stem Cells**

I. Introduction

The technology of microelectrode array recordings was first described in 1972 [1] using cultured avian cardiomyocytes. In the following decades MEA technology was widely used for neuronal applications such as hippocampal slices and neuronal networks. However in cardiac research the multitude of electrode allows access to a variety of very useful spatial parameters. Here we introduce recordings from cellular preparations as well as whole organ preparations. In all these cases the recorded parameter is the cardiac field potential [2]. The field potential can be devided into several components, i.e. a rapid component reflecting depolarization driven by sodium channels, a plateau phase reflecting L-type calcium flux and a repolarization wave mediated by the activation of potassium channels. The shape of the field potential is very comparable to an ECG (Figure 1). Electrode diameters of the MEA chips vary between 10 and 100µm, electrode spacings range from 30µm to 700µm. The number of electrodes per array is between 32 and 252. Electrode materials used include Titanium nitrate (TiN), Gold and Platinum black.

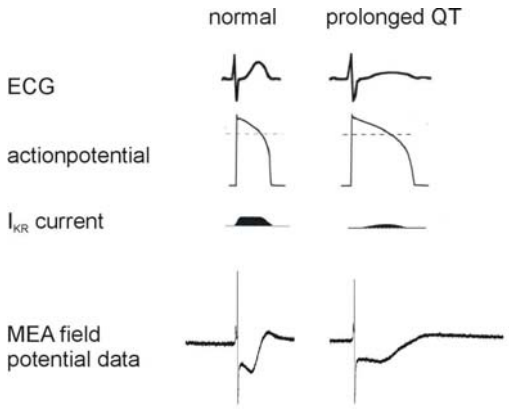


Fig. 1 Top to bottom: Illustration of ECG, transmembrane action potential, I_{KR} current responsible for the repolarization of the action potential and a MEA field potential recording under control conditions and prolonged QT conditions.

II. Results

A: Primary Cardiomyocyte Recordings

Isolated neonatal or embryonic ventricular or atrial cardiomyocytes can be directly plated and cultured on MEAs for several days. These cells couple by gap junctions and form a functional electric syncytium within 3 days of preparation. At an early culture stage multiple pacemakers will trigger activity at various locations within the syncytium. With increasing duration of culture time however the influence of the fastest and strongest pacemaker will synchronize activity over the whole syncytium. The area covered can span several millimeters up to centimeters. The multitude of electrodes allows to obtain a high resolution electrophysiological map. In such a model the pattern of the spreading excitation as well as the speed and direction of propagation can be determined. These data can be acquired either based on spontaneous or evoked excitation. Excitaion can be evoked by electrical stimulation directly applied via MEA electrodes or external stimulation electrodes. A typical field potential signal and

O. Dössel and W.C. Schlegel (Eds.): WC 2009, IFMBE Proceedings 25/VIII, pp. 112–115, 2009.
www.springerlink.com

an excitation pattern are shown in Figure 2. The data shown have been recorded from chicken (gallus gallus) embryo. Cells have been prepared on day 13 of embryonic development and plated on a standard MEA chip (Multi Channel Systems MCS GmbH, Reutlingen Germany) coated with cellulose nitrate. The recording was performed 5 days after plating the cells to allow synchronization of the syncytium.

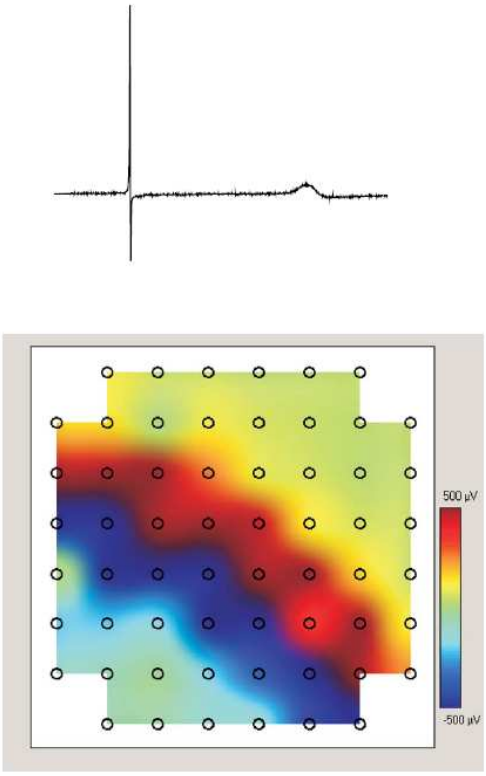


Fig. 2 A typical field potential recorded by a TiN electrode of a MEA from primary cardiomyocytes from chicken embryo (day E13, DIV5) is shown in the top panel. The lower panel displays a snapshot of the propagating signal over the array. Plotted is signal amplitude in µV vs. spatial position on the electrode grid translated into a false color map.

B: HL-1 Cardiac Cell Line

The immortalized murine cardiomyocyte cell line HL-1 [3] has an atrial phenotype. The cells are beating spontaneously with a very variable spontaneous beating frequency. As expected for atrial cardiomyocytes the duration of the action potential is rather short (50-80 ms). In order to obtain better comparable data, the cells have been paced by biphasic voltage pulses applied via the MEA electrodes. Interestingly the origin of excitation was not exactly near the stimulation electrode, but about 1mm apart from it (Figure 3).

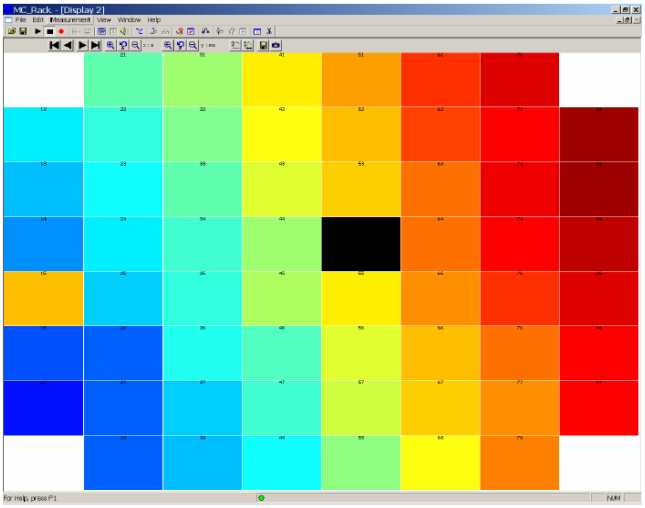


Fig. 3 False colour mapping of the excitation spread on HL-1 cells cultured on a MEA chip. Blue indicates an early detection whereas red indicates a later detection compared to a reference time. Stimulus pulse was applied via electrode 54 (black). Unexpectedly signal propagation wave originates near electrode 82

This indicates the existance of a heterogeneous cell population within the HL-1 line. Only a subpopulation is able to respond to an electrical stimulus and trigger the syncytium. The syncytium itself is substantially less dense than in primary cardiomyocyte cultures. This results in a decreased conduction velocity.

C: Stem Cell derived cardiomyocytes

Stem cell derived cardiomyocytes can be obtained from a variety of sources (Figure 4). Human embryonic stem cells have been differentiated to cardiomyocytes and cultured and recorded by a variety of groups [4;5;6;7;8]. However, due to ethical issues the search for alternatives continues. Murine embryonic stem cells can not replace human cells, so the alternatives remaining were human adult stem cells (such as cardiac stem cells) and cells with induced pluripotency [9; 10]. All of these cells have been successfully cultured and recorded on MEAs. The big advantage of the MEA technology in this respect is the MEA system functioning as an in vitro model for cell transplantation. Parameters such as conduction velocity and direction of signal propagation are good indicators for the proarrhythomgenic potential of the stem cell derived cardiomyocytes when transplanted into native cardiac tissue [11].

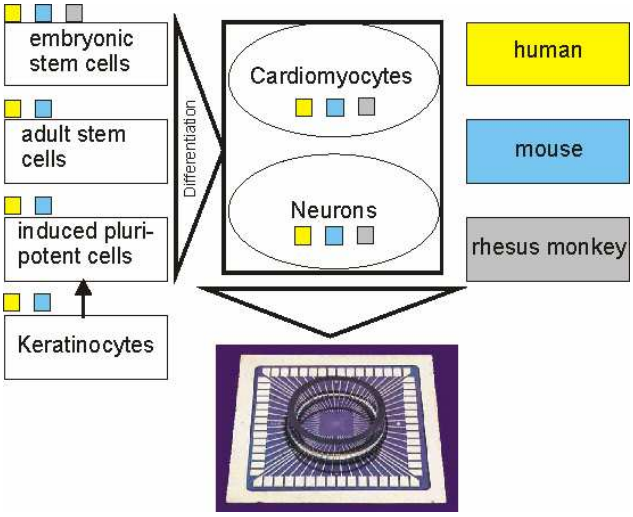


Fig. 4 Schematic overview of stem cell sources and use for MEA applications.

D: Cardiac Surface Mappings

In classical Langendorff preparations an ECG electrode monitors electrical activity of the heart. With the MEA technology a flexible multielectrode array is positioned at the ventricular or atrial surface of the heart (Figure 5).

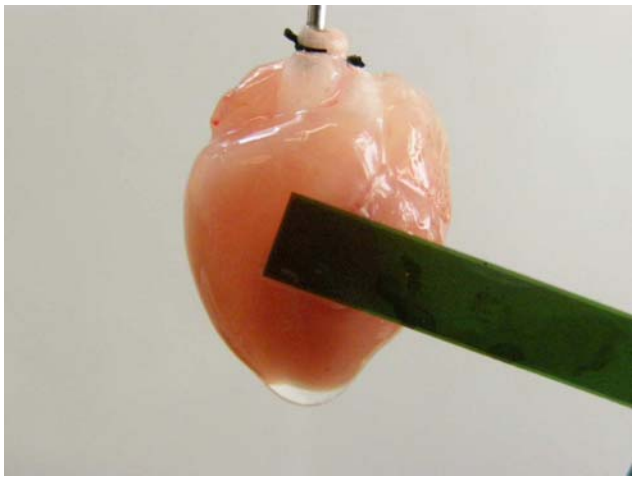


Fig. 5 A flexible MEA positioned on a isolated guinea pig heart retrogradely perfused on a modified Langendorff setup.

Flexible MEAs have 32 and 72 electrodes, respectively, spaced 300µm apart. This allows a high resolution mapping of the spreading electrical signal. Up to 4 flexible MEAs can be positioned at a heart simultaneously. Simple surface contact is sufficient to obtain suitable signals. Due to the versatility of the systems it is easy to map areas around induced lesion or infarcts. This provides the option to study the signal propagation pathway and monitor the risk of reentry cycles. A typical atrial signal as well as the propagation pattern is illustrated in a screenshot of the recording software (MC_Rack, Multi Channel systems MCS GmbH Reutlingen, Germany) (Figure 6).

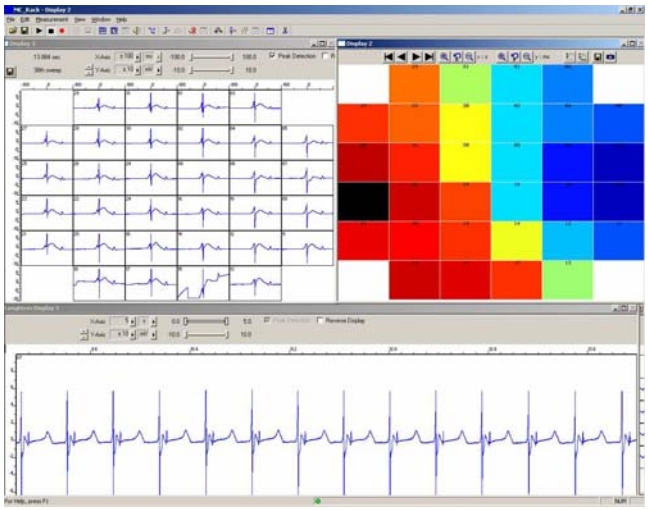


Fig. 6 Screenshot from MC_Rack software while recording from a guinea pig heart atrial surface. Top panel shows triggered display of all channels (left) and false color coded excitation pattern (right). The bottom panel shows a long term plot from one of the electrodes.

III. CONCLUSIONS

The MEA technology offers a versatile and easy to handle approach to electrophysiologically access spatial phenomenons in a wide variety of cardiac preparations. This technology helps to close the gap between cell and tissue as well as between tissue and organ. MEA recordings allow long term monitoring in order to better predict risks of drugs with regards of their arrhythmogenic potential.

ACKNOWLEDGMENT

HL-1 cells were a kind gift of William C. Claycomb.
We thank K. Bernhardt, S. Buckenmaier, J. Nagel and R. Pröbstle for valuable contributions.

REFERENCES

1. Thomas, C. A., Jr., P. A. Springer, et al. (1972). "A miniature microelectrode array to monitor the bioelectric activity of cultured cells." Exp Cell Res 74(1): 61-6.
2. Halbach, M., U. Egert, et al. (2003). "Estimation of action potential changes from field potential recordings in multicellular mouse cardiac myocyte cultures." Cell Physiol Biochem 13(5): 271-84.
3. Claycomb, W. C., N. A. Lanson, Jr., et al. (1998). "HL-1 cells: a cardiac muscle cell line that contracts and retains phenotypic characteristics of the adult cardiomyocyte." Proc Natl Acad Sci U S A 95(6): 2979-84.
4. Itskovitz-Eldor, J. (2003). "Human embryonic stem cells: A potential source for cellular therapy." American Journal of Transplantation: 7.
5. Hescheler, J., M. Halbach, et al. (2004). "Determination of electrical properties of ES cell-derived cardiomyocytes using MEAs." J Electrocardiol 37 Suppl: 110-6.
6. Kehat, I., L. Khimovich, et al. (2004). "Electromechanical integration of cardiomyocytes derived from human embryonic stem cells." Nat Biotechnol 22(10): 1282-9.
7. Beeres, S. L. M. A., D. E. A. Atsma, et al. (2005). "Human Adult Bone Marrow Mesenchymal Stem Cells Repair Experimental Conduction Block in Rat Cardiomyocyte Cultures." J Am Col Cadiol: 10.
8. Gepstein, L. (2008). "Experimental Molecular and Stem Cell Therapies in Cardiac Electrophysiology." Ann N Y Acad Sci 1123: 224-231.
9. Mauritz, C., K. Schwanke, et al. (2008). "Generation of functional murine cardiac myocytes from induced pluripotent stem cells." Circulation 118(5): 507-17.
10. Yamanaka, S. (2008). "Induction of pluripotent stem cells from mouse fibroblasts by four transcription factors." Cell Prolif 41 Suppl 1: 51-6.
11. Pijnappels, D. A., J. van Tuyn, et al. (2007). "Resynchronization of separated rat cardiomyocyte fields with genetically modified human ventricular scar fibroblasts." Circulation 116(18): 2018-28.

Udo Kkraushaar
NMI, Natural and Medical Sciences Institute at the Tubingen University
Markwiesenstr. 55
72770 Reutlingen
Germany
udo.kraushaar@nmi.de

α-fetoprotein analysis in human serum through quartz crystal microbalance

S.L. Huang[1], C.S. Lin[2], Y.S. Lu[1], S.B. Jong[1], M.H. Yang[3], H.Y. Chang[1], H.Y. Hsun[1] and Y.C. Tyan [1*]

[1] Department of Medical Imaging and Radiological Sciences, Kaohsiung Medical University, Kaohsiung, Taiwan

[2] Department of Biomedical Engineering and Environmental Sciences, National Tsing Hua University, Hsinchu, Taiwan

[3] Department of Chemistry, National Sun Yat-Sen University, Kaohsiung, Taiwan

Abstract-**The quartz crystal microbalance (QCM) has been used as the transducer to analyze microelement in term of its physical properties. It has been used for human's microelement assay or immunoassay in liquid phase. This experiment mainly focuses on measuring human serum in gas phase to avoid the problems of variation in viscosity and the need of a lot amount of sample. According to the Sauerbrey equation, the mass change is proportional to the square of basic oscillation frequency that is 10 MHz in this experiment. The QCM electrode provides a gold-plated surface with modify 11-mercaptoundecanoic acid (11-MUA), one of self-assembled monolayer (SAM) compounds. X-ray photoelectron Spectroscopy (XPS) is utilized to characterize 11-MUA onto gold coated QCM surface. XPS spectrums demonstrate 11-MUA existence through peaks shift of C1s and O1s binding energy. Iodine 125 labeled anti-α-fetoprotein (anti-AFP) was immobilized onto the 11-MUA modified chips through reacting -COOH of 11-MUA with 1-ethyl-3-dimethylamino-propyl carbodimide (EDC) and N-hydrocysuccinimide sodium (NHS). The frequency and count rate was measured and compared after AFP immobilization process. The detection limit of QCM biosensor in AFP standard curve detection can reach to 15 ng/mL. Comparing with radioimmunoassay in clinical human serum samples, QCM biosensor method showed a good correlation.**

Keywords—**Quartz crystal microbalance, Self-assembled monolayer, X-ray photoelectron spectroscopy, Radioimmunoassay, α fetal protein**

I. INTRODUCTION

Quartz crystal microbalance (QCM) with A-T cut quartz slide equipped with electrodes has been used in various fields, such as environment protection, chemical technology, medicine, food analysis, and biotechnology [1-8]. It was so widely used in measuring substances in liquid environment. A serious of researches revealed that measurement in liquid environment is so complicated. Several variations such as in both characteristics of crystals themselves and factors of surface interaction in liquid environments need to be controlled and corrected under accurate and precise machines and mathematical formula [9-11]. However, clinical serum samples increase variation in liquid state. Besides, the amount of sample used in aqueous environments often requires more than that can be acquired in clinical collection when it comes to be a clinical immunosensor. Hence, these serious of experiments in our laboratory perform in gas phase to reach the demands of few amount test samples and the same environment when measuring the frequency change. Moisture control on the surface of QCM chips themselves in this experiment is used through freeze-drying method. Comparing to other dry methods, freeze-drying method is capable to dehydrate without deformation of biomaterial substance, such as protein, and enzyme. Considering the activity of antibody and antigen for these experiments and commercial kits, freeze drying method is utilized to sublimate moisture on the surface of QCM chips. Finally, according to the Sauerbrey equation, mass change is proportional to oscillation frequency change of piezoelectric quartz crystal. Sauerbrey equation in gas phase [12]: $\Delta F = -2.3\times10^{-6}\frac{F^2\Delta M}{A}$, ΔF: the frequency change(Hz); F: basic oscillation frequency of piezoelectric quartz (Hz); A: the active area of QCM (cm^2); ΔM: the mass change on QCM (g).

The immobilization methods of antibody in an optimal condition through physical passive adsorption [13], binding protein, and covalence binding have been compared [14-15]. The drawbacks of physical passive adsorption and binding protein method, such as protein A, lead to various bimolecular adsorption investigations in covalence bonding methods, such as 3-aminopropyl triethoxysilane (3-APTES) immobilization through silanization, Lagmur-Blodgett film,

O. Dössel and W.C. Schlegel (Eds.): WC 2009, IFMBE Proceedings 25/VIII, pp. 116–119, 2009.
www.springerlink.com

or SAM. 3-APTES decreases the bioactivity of protein and Lagmur-Blodgett film is less stable than SAM [16-18]. Therefore, an ideal 3-dimensions SAM-formed surface, similar to cellular microenvironment of lipidbilayer structure, offers a suitable intermolecular interaction surface for immobilization of bimolecular. The head group and the length of alkyle chain of SAM affect the display of oriented and ordered monolayer. The functional terminal group and the length of alkyle chain of SAM affect the efficiency of immobilization. Previous studies show that unsymmetrical dialkane sulfides monolayer or short carboxylate chain of disulfide and thiol reveals less dense and ordered than alkanethoil monolayer. [19] Hence, 11-MUA is utilized in this experiment that can be proved its existence onto the QCM chips through X-ray photoelectric spectroscopy [20, 21].

Radioimmunoassay is so sensitive and specific that it has been broadly used in experiments and clinical since it was first discovered by Yalow and Berson in 1960 [22]. Therefore, it has also been widely used in clinical, such as Alpha-fetoprotein (AFP). AFP is a large serum glycoprotein that only produces during the fetus period and the concentration of that decays with the time after being born. Normal levels of alpha-fetoprotein in health human being only grow up slightly during pregnancy. Therefore, it could possibly indicate a pathological process, such as a tumor maker. It also can be of use for the detection of fetal abnormalities, such as Down's syndrome [23]. The clinical normal range for fetus can reach 1 to 10mg/ml and that for adult should under 20 ng/mL.

II. MATERIAL AND METHOD

- Material:

11-mercaptoundecanoic acid (Aldrich Chem.Co, USA),1-ethyl-3(-3-dimethylamino-propyl) carbodimide (Sigma, USA), N-hydrocysuccinimide sodium (Fluka, Switzerland), PBS (pH 7.4, Sigma, USA), alpha-foetoprotein ELSA kit (including :anti-AFP monoclonal antibody coated on ELSA fixed to the bottom of the tube, highly purified human's AFP, and iodine 125 labeled AFP-monoclonal Antibody, Cisbio International, France).

- Instrument:

Frequency measurement: QCM chips (coated with Au, 10MHz, diameter of quartz: 0.8 cm, diameter of Au: 0.36 cm, Taitien, Taiwan) are measured the oscillated frequency through frequency counter (Universal Sensors Inc., U.S.A). Scaler Cobra Ⅱ series Auto-gamma counting system (Packard, USA, Energy window: 15~75 keV, detection efficiency > 75%, resolution < 34%, detector background <25 cpm) was utilized to quantify I-125 labeled anti-AFP on the QCM. X-ray photoelectric spectroscopy (XPS) spectra were acquired with a Physical Electronics PHI 1600 ESCA photoelectron spectrometer (Mg anode: 400W, 15kV, 27mA, base pressure in the chamber: below 2×10^{-8} Pa). Elemental compositions at the surface using C 1s, and O 1s core level spectra were measured and calculated from XPS peak area with correction algorithms for atomic sensitivity. The XPS spectra were fitted using Voigt peak profiles and a Shirley background.

- Methodology:

Measuring original frequency of all QCM chips ensures the stability of frequency and oscillating frequency region before the following procedure. All QCM chips are cleaned with soxhlet extraction process with solution (Methyl Alcohol and Acetone 1:1). Then, QCM chips are cleaned with alcohol (99.99%) All QCM chips are immersed into 0.5 mM 11-MUA alcohol solution for 8 hours and then cleaned with alcohol for removing free 11-MUA. 15 mM EDC and 75 mM NHS are utilized to active –COOH group of 11-MUA for 40 minutes before Dipping the chips into Iodine 125 anti-AFP solution. The chips are dipped into Iodine 125 anti-AFP solution until the saturated state. These chips can be measured the frequency and count rate after washing free Iodine 125 anti-AFP from the chips by sharking in 250 rpm speed. Different concentrations of AFP standard solutions and samples of human being's serum react with anti-AFP immobilized QCM chips for thirty minutes. The frequency is measured and then compared with RIA after washing the chips by sharking in 250 rpm speed till all free substance on the chips are removed.

III. RESULT AND DISCUSSION

- XPS of 11-MUA:

XPS spectrum of 11-MUA onto gold electrode are shown in Figure 1. In the C1s spectrum, the peaks of binding energy are shifted to 285.0 eV in (1) for -C-C-, 286.98 eV in (2) for-C-S-,and 288.8 eV in (3) for O=C-O. In the O1s spectrum, the peaks of binding energy are shifted to 532.0 eV in (1) for O*=C-O (for the *marked O) and 533.2 eV in (2) for O=C-O*((for the *marked O). In

the S 2p spectrum, the peaks of binding energy are shifted to 162.0 eV in (1) for Au-S-C-, 163.2 eV in (2) for -COOH-S-C-, and 169.30 eV in (3) for SO_3^-.

The C 1s, O 1s, and S2p spectrums prove the existence of 11-MUA onto the gold-coated QCM chips. The C 1s core-level spectrum of the peaks at 286.98 eV and the S 2p spectrum of the peaks in 162.0 eV provide the Au-S-$(CH_2)_n^-$ existance. The C 1s core-level spectrum of the peaks at 288.8 eV and the O 1s spectrum of the peaks at 532.0 eV and 533.2 eV provide that the terminal groups of SAM in the QCM chips is carboxylic group. The S 2p spectrum of peak at 163.2 eV could be due to a small number of alkanethiols is physisorbed as a double layer [24]. The longer alkyle chain can increase the efficiency to immobilize more antibodies but it also can cause the increase the possibility of double layers. Therefore, the further study will discuss the effect of length in alkyle chain for antibody immobilization in QCM chips. The S 2p spectrum of peak at 168.5 eV can be attributed to a sulfonite species ($SO3^-$), because the XPS analysis in this 11-MUA modified QCM chip was taken after more than twenty days.

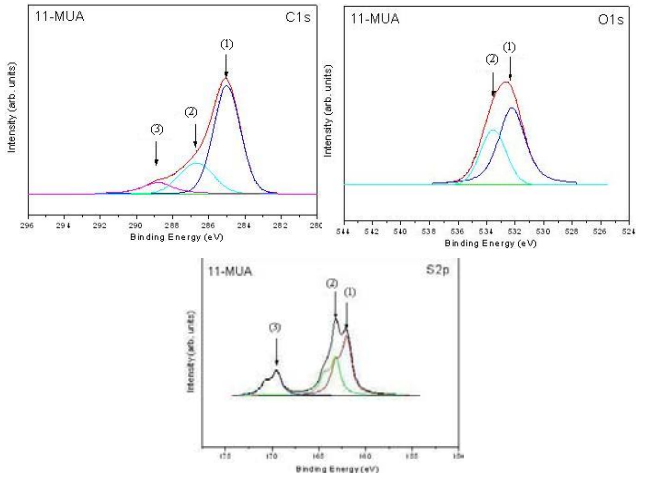


Fig. 1: C1s, O1s and S 2p spectrum of 11-MUA

- The immobilization of iodine 125 labeled anti-AFP

The average and coefficient of variation in frequency difference between pre-iodine 125 labeled anti-AFP immobilization and post-iodine 125 labeled anti-AFP immobilization is 217±28.63 and 13.21%.The average and coefficient of variation in count rate after iodine 125 labeled anti-AFP immobilization is 139±16.9 and 12.2%. Comparing coefficient of variation in frequency change and count rate shows that the frequency measurement method is similar stable to the radioactivity method. The differences or the changes of radiation activity in QCM chips also provide the optimal method for anti-AFP immobilization. Hence, free iodine 125 labeled anti-AFP can be removed clearly from the chips and the chips can be immobilized with saturated anti-AFP with 15 degree and 5 hours.

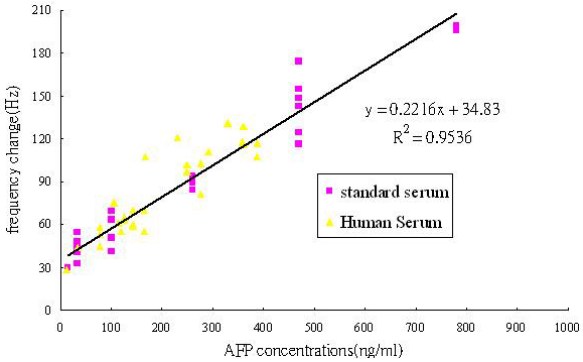


Fig. 2: Frequency changes with the concentrations of AFP standard solution (square) and human being's serum. The regression line is made by frequency changes with the concentrations of AFP standard solution (square)

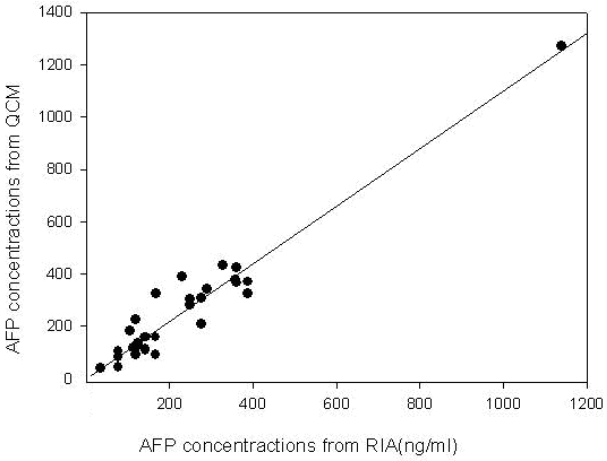


Fig. 3: AFP concentrations measured by RIA and QCM methods.

- Detection of the concentrations of AFP

The regression line of frequency changes (y) with the concentrations of AFP standard solution (x, square) from 15 to 850ng/mL is y=0.2216x+34.83 (R^2=0.9536) in Fig 2. The triangular form in Figure 2 is frequency change with AFP concentration in human serum samples that the data of AFP concentration is from the radioimmunoassay (RIA). In Fig 3 is the relation of data in AFP concentrations between RIA and QCM that is calculated from the formula of y=0.2216x+34.83. The regression line between RIA (x) and QCM methods (y) is y=1.0938x-1.4726 (R^2=0.9332). The result shows a good correlation between RIA and QCM methods. However, it takes longer time to wash the chips for human serum than standard AFP serum to reach

stability in frequency. Finding out a better method for washing the free substance of human serum onto may be more practical for application in clinical.

IV. CONCLUSIONS

XPS prove the existence of 11-MUA onto the gold surface. It also provides there are some double layers in the chips. The further research can study other compounds of SAMs, such as 3-mercaptopropionic acid (3-MPA) that is short alkyle chain in alkanethoil monolayer families to see if the length of alkyle chain affect the efficiency of antibody immobilization [25-26]. Finding out other SAM compounds for immobilizing more antibodies and then increasing the sensitivity for antigen detection needs to be done in the future. The radiation activity in QCM chips really provides the optimal method for anti-AFP immobilization. The detection of AFP shows a good correlation between RIA and QCM method. Improving washing method to remove the free substance of human serum onto may be more practical for application in clinical. The only drawback of application of the QCM chips in clinical is that the quartz body of QCM chips is more frangible than other materials in other method.

REFERENCES

1. King WH (1964) “Piezoelectric Sorption Detector”, Anal.Chem. 36: 1735-1739.
2. Guilbault GG (1983) Determination of formaldehyde with an enzyme coated piezoelectric crystal. Anal. Chem. 55: 1682-1684
3. Guilbault GG, Jordan J (1988) Analytical uses of piezoelectric crystals. CRC Rev. 19: 1-28.
4. Guilbault GG, Luong JH (1988). Gas phase biosensors. J. Biotechnol. 9: 1-10.
5. Guilbault GG, Hock B, Schmid R (1992) PZ immunosensor for atrazine in drinking water. Biosensors Bioelectron. 7: 411-419
6. Fawcett NC, Evans VA, Chen LC, Droza KA (1988) A quartz crystal detector for DNA. Anal. Lett. 21: 1099-1110.
7. Attli B, Suleman A (1996) A piezoelectric immunosensor for the detection of cocaine. Microchemical Journal 54: 174-179.
8. Nie LH, Zhang XT, Yao SZ (1992) Determination of quinine in some pharmaceutical preparations using a ring-coated piezoelectric sensor. J Pharm Biomed Anal 10: 529-533.
9. Muramatsu H et. al., (1988) Computation of equivalent circuit parameters of quartz crystals in contact with liquids and study of liquid properties. Anal.Chem. 60: 2142-2146.
10. Filler RL, Vig JR (1976) The effect of bonding on the frequency vs. temperature characteristics of AT-cut resonators. Defense Technical Information Center.
11. Voinova MV, Jonson M, and Kasemo B (2002) Missing mass effect in biosensor's QCM applications. Biosens Bioelectron 17: 835-841.
12. O'Sullivan CK, and Guilbault GG (1999) Commercial quartz crystal microbalances-theory and applications. Biosens Bioelectron 14: 663-670.
13. Butler JE et al. (1992) The physical and functional behavior of capture antibodies adsorbed on polystyrene. J Immunol Methods 150: 77-90.
14. Muramatsu H, Dicks JM, Tamiya E, and Karube I (1987) Piezoelectric crystal biosensor modified with protein A for determination of immunoglobulins. Anal. Chem. 59: 2760-2763
15. Babacan S, Pivarnik P, Letcher S, and Rand AG (2000) Evaluation of antibody immobilization methods for piezoelectric biosensor application. Biosens Bioelectron 15: 615-621.
16. Lestelius M, Liedberg B, and Tengvall P (1997) In vitro plasma protein adsorption on o-functionalized alkanethiolate self-assembled monolayers. Langmuir 13: 5900-5908.
17. Laibinis PE et al. (1991) Comparison of the structures and wetting properties of self-assembled monolayers of n-alkanethiols on the coinage metal surfaces, Cu, Ag, Au. Journal of the American Chemical Society 113: 7152-7167
18. Karpovich DS, Blanchard GJ, (1994) Direct measurement of the adsorption kinetics of alkanethiolate SAMs on a microcrystalline gold surface. Langmuir 10: 3315-3322.
19. Chaki NK, Vijayamohanan K (2002) Self-assembled monolayers as a tunable platform for biosensor applications. Biosensors and Bioelectronics 17: 1-12.
20. Moulder JF, Stick PE, Soble PE, and Bomben KD (1995) Handbook of X-ray Photoelectron spectroscopy.
21. Catner DG, Hind K, Grainger DW (1996) X-ray photoelectron spectroscopy sulfur 2p study of organic thiol and disulfide binding interaction with gold surface. Langmuir 8: 1247-1250
22. Catt K, Tregear GW (1967) Solid-phase radioimmunoassay in antibody-coated tubes. Science 158: 1570-1572.
23. Wirde M, Gelius U (1999) Self-assembled monolayers of cystamine and cysteamine on gold studied by XPS anD VOLTAMmetry. Langmuir 15: 6370-6378.
24. Gillespie JR, Uversky VN (2000) Structure and function of α-fetoprotein: a biophysical overview. Biochimica et Biophysica Acta 1480: 41-56.
25. Faucheux N, Schweiss R, L.utzow K, Werner C, Grotha T (2004) Self-assembled monolayers with different terminating groups as model substrates for cell adhesion studies. Biomaterials 25: 2721-2730.
26. Patel N et al. (1997) Immobilization of protein molecules onto homogeneous and mixed carboxylate-terminated self-assembled monolayers. Langmuir 13: 6485-6490.

Author: Yu-Chang Tyan
Institute: Department of Medical Imaging and Radiological Sciences
Street: No.100, Shi-Chuan 1st Road, 807
City: Kaohsiung City
Country: Taiwan
Email: yctyan@cc.kmu.edu.tw

Development of a generic multiple frequency signal generator for BioMEMS

N.A. Kadri[1], K.F. Hoettges[2] and M.P. Hughes[2]

[1] Department of Biomedical Engineering, University of Malaya, Kuala Lumpur, Malaysia
[2] Centre of Biomedical Engineering, University of Surrey, Guildford, Surrey, United Kingdom

Abstract—**AC electrokinetics have played an important role in the advancement of BioMEMS research. Although the various AC electrokinetics methods offers a myriad of advantages in conducting bioparticle electrophysiology, the uptake of the technology has been limited only to research centres. One reason is due to the time-consuming procedures involved. This report documents the development of a programmable, multiple frequency signal generator that may be used in any AC electrokinetics experimental setup in conducting parallel electrophysiology assays. The development employs commercially available tools and components, which hopefully encourages the uptake of the various AC electrokinetics methods in conducting BioMEMS research.**

Keywords—**AC electrokinetics, BioMEMS, dielectrophoresis, signal generator**

I. Introduction

The ability of manipulating bioparticles has long been the fascination of scientists and researchers due to its seemingly infinite benefits; be it in the field of medicine, engineering, and biotechnology. A number of authors have described the processes involved in the said manipulation, particularly employing alternating current (AC) electrical fields [1-6]. Unlike its closely related method, the electrophoresis, which employs direct current (DC) electric fields, AC electrokinetics offers precise manipulation of bioparticles in the micrometer and sub-micrometer scale.

Along with the advancement of the microfabrication techniques in the semiconductor industry, researchers are now being presented with a real possibility of developing technology capable of separating, collecting and conducting analysis on bioparticles with a high level of efficiency and accuracy. In addition to the low production cost, this method also has the advantage of being marker-less, and thus further reducing the impact of destructive procedures normally employed in handling bioparticles.

Furthermore, due to the ever-increasing move towards evidence-based medicine in the healthcare industry, there is an almost perpetual demand for simple and automated diagnostic and prognostic systems to be developed [7]. The combination of these demands and technological know-how invariably leads to the birth of biological microelectromechanical systems (BioMEMS), also known as 'lab on a chip', as a promising approach towards the development of the said systems.

There are a number of methods that are commonly grouped as AC electrokinetics techniques, namely dielectrophoresis (DEP), electro-rotation (ROT), travelling-wave dielectrophoresis (twDEP), electro-osmosis, and electro-orientation [5-8]. These methods, though principally different in terms of the employed electrophysiology principles, all shared a common usage of AC electrokinetics as the main drive towards achieving the analytical outcome.

Nevertheless, although these methods offer a number of advantages over routine cell assay methods for cell electrophysiology analysis, the uptake has been low. Most of its usage is confined within research laboratories, due to time-consuming processes involved. This predicament is owed primarily to the limitation imposed on the number of cell assays that can be performed at any one time [2-5,9-11].

Therefore there is an urgent need towards the development of novel bioinstrumentation that allows parallel analyses of bioparticles to be performed, without sacrificing the accuracy and efficiency offered by these methods. The said development will definitely be enhanced by the availability of a generic, programmable, multiple frequency signal generator component that may be used with any of the available AC electrokinetics techniques.

This report documents the development of a 4-channel programmable waveform generator using commercially available tools and components, acting as a proof-of-concept for the development of the aforementioned novel instrumentation.

II. System design

The design of the signal generator system is summarised in the flowchart below (Figure 1). The system should be able to receive an input and produce sinusoidal waveforms at the desired frequency at each of the output channels.

A. User interface and input data entry

MATLAB (The Mathworks, Natick, MA, United States) is the high level programming language of choice in developing the graphical user interface to send input data to the

O. Dössel and W.C. Schlegel (Eds.): WC 2009, IFMBE Proceedings 25/VIII, pp. 120–123, 2009.
www.springerlink.com

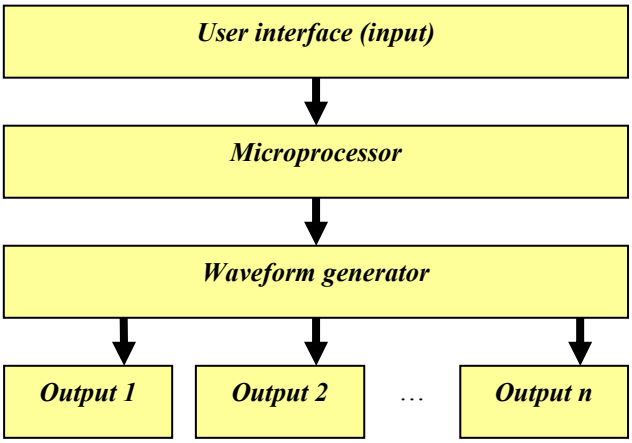


Fig. 1 Flowchart of the programmable signal generator system

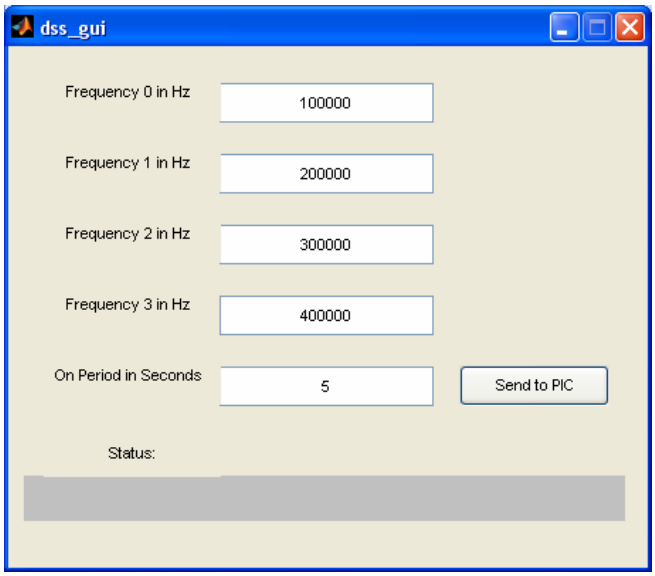


Fig. 2 Graphical user interface of the system

microcontroller (Figure 2). The input data consists of the different frequency values (in Hertz) for each of the channel outputs and the period (in seconds) for the signal to be sent.

B. Microcontroller

A programmable 8-bit, CMOS FLASH-based microcontroller, PIC16F877 (Microchip Technology, Chandler, AZ, United States) is the microcontroller of choice due to its suitable number of output ports available [12]. This is of particular importance since it affects the overall programming of the microcontroller in sending out the appropriate addressing data to the demultiplexer and the subsequent input data to the waveform generator.

C. Demultiplexer

A demultiplexer is a component capable of taking a single data input and producing multiple address inputs to be used in subsequent components in a given electronics circuitry [13]. In this work a SN74154 (Texas Instruments, Dallas, TX, United States) is used for the addressing of the different output channel circuitry.

D. Waveform generator

The choice of waveform generator chip is primarily dependent on the required bandwidth of the output signal. For this work, AD9833 (Analog Devices, Norwood, MA, United States) was used and should theoretically be able to supply a stable signal up to a maximum frequency of 12.5MHz when a 25MHz external oscillator is employed [14].

The chip is controlled by an external serial clock input and accepts 16-bit data word. It has two frequency registers and two phase registers, and thus should be able to act as a dual-output waveform generator.

E. Amplifier

This component by far is the critical consideration in developing any signal generator circuit, especially when a very wide bandwidth and high frequencies are required. A number of considerations, particularly regarding power supply bypass capacitors, ground planes, length of current paths, and termination of input/output pins, must be adhered to in order to remove parasitic inductances and to reduce stray capacitances [15-17].

In this work, two high speed operational amplifiers, LM7372 (National Semiconductor, Santa Clara, CA, United States) and THS4061 (Texas Instruments, Dallas, TX, United States), were used for the amplifier circuitry em-

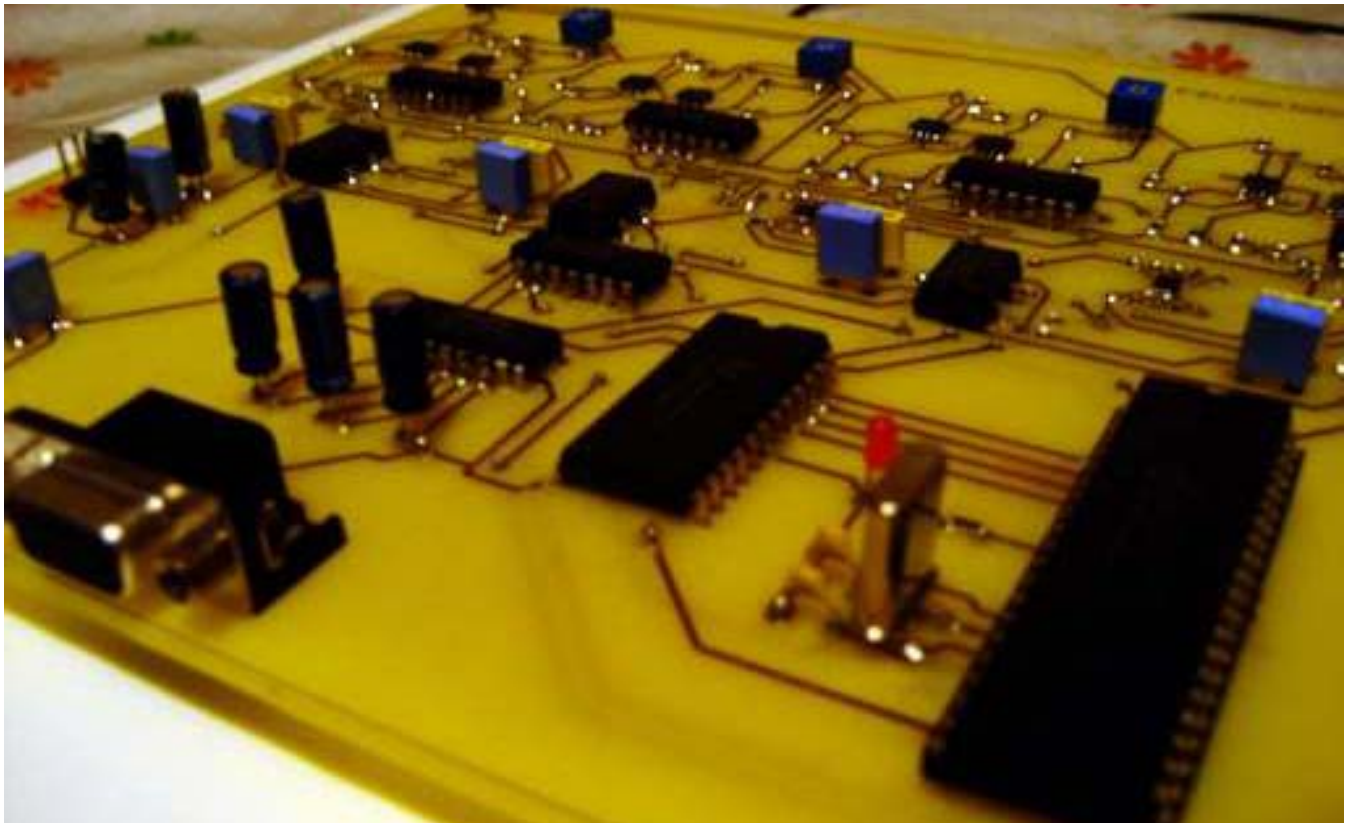


Fig. 3 The signal generator circuit

ploying a 2-stage amplification. This setup was needed to attain a gain of about 20, in order to reach a peak-to-peak potential difference of ±10V.

III. Discussion

Figure 3 shows the produced prototype of the signal generator circuit. The overall system was simulated using Multisim 10.1 (National Instruments, Austin, TX, United States) prior to the actual design and production of the circuit board.

Table 1 Stability of system output

Setting Frequency (kHz)	V_{P-P} (V)	V_{RMS} (V)	Output Frequency (kHz)	Error (%)
1	8.8	3.0	1.0	0.0
5	9.0	3.0	4.9	2.0
10	8.9	3.0	9.8	2.0
20	8.8	3.0	19.5	2.5
50	8.8	3.1	48.7	2.6
100	8.9	3.1	97.8	2.2
200	9.0	3.1	196.8	1.6
500	9.2	3.2	490.6	1.9
1000	9.2	3.4	983.6	1.6

It can be seen from Table 1 that the output frequency closely resembled the setting frequency entered via the graphical user interface with a considerably small error margin for signals up to 1MHz. This may be further corrected by the implementation of offset-reducing circuitry or filtering. The error could even be simply down to the quality of the printed circuit board production, which was done in-house.

IV. Conclusion

The main motivation in producing this report is the lack of availability of documentation on such a simple but an imperative component in developing any AC electrokinetics instrumentation in the literature today. The author is of the opinion that advancement in such a young research area can only be made if the collective knowledge is shared; since many, if not all, of the different techniques in AC electrokinetics and BioMEMS actually shared many common traits, particularly regarding the instrumentation and electronics involved [18].

This short report has shown that the development of a generic, programmable, multiple output signal generator to be used in any AC electrokinetics or BioMEMS setup using commercially available tools and components is highly feasible. The only limitations or variables that need to be taken into consideration are:

- Required output bandwidth
- Type of waveform generator chip used (affects the programming of the microcontroller)
- Type of amplifier used and its associated PCB layout design considerations (affects the output signal stability and the physical size of the system)

This should become an incentive for a BioMEMS-based research to be initiated and run in any laboratories equipped only with basic electronics components and tools, particularly in developing countries where resources are normally scarce.

The PIC program, both in assembler language and hex code, is available from the author as a ZIP file package. Note that the code is written for PIC16F877 microcontroller and may need to be edited to compensate for the difference in input/output addressing if other microprocessors are used.

Acknowledgment

N.A. Kadri would like to thank the Ministry of Higher Education, Malaysia and the University of Malaya, Malaysia for the provision of grants towards the completion of his PhD, of which this report is partly derived from.

References

1. Pohl HA (1978) Dielectrophoresis. Cambridge University Press, Cambridge
2. Fuhr G, Arnold WM, Hagedorn R et al. (1992) Levitation, holding, and rotation of cells within traps made by high-frequency fields. Biochim Biophys Acta 1108(2):215–223
3. Fiedler S, Shirley SG, Schnelle T et al. (1998) Dielectrophoretic sorting of particles and cells in a microsystem. Anal Chem 70(9):1909–1915
4. Morgan H, Hughes MP, Green NG (1999) Separation of submicron bioparticles by dielectrophoresis. Biophys J 77(1):516–525
5. Hughes MP (2002) Strategies for dielectrophoretic separation in laboratory-on-a-chip systems. Electrophoresis 23(16):2569–2582
6. Hughes MP (2003) Nanoelectromechanics in engineering and biology. In Lyshevski SE (Ed.) Nano- and microscience, engineering, technology, and medicine. CRC Press, Boca Raton
7. Pethig R, Markx GH (1997) Applications of dielectrophoresis in biotechnology. Trends Biotechnol 15:426–432
8. Jones TB (1995) Electromechanics of particles. Cambridge University Press, Cambridge
9. Schnelle T, Hagedorn R, Fuhr G et al. (1993) Three-dimensional electric field traps for manipulation of cells - calculation and experimental verification. Biochim Biophys Acta 1157(2):127–140
10. Muller T, Gerardino A, Schnelle T et al. (1996) Trapping of micrometre and sub-micrometre particles by high-frequency electric fields and hydrodynamic forces. J Phys D: Appl Phys 29(2):340–349
11. Green NG, Ramos A, Gonzalez A et al. (2000) Fluid flow induced by nonuniform ac electric fields in electrolytes on microelectrodes. I. Experimental measurements. Phys Rev E 61(4):4011–4018
12. PICmicro™ mid-range MCU family reference manual (1997) Microchip Technology, Chandler
13. SN54154, SN74154 Datasheet (1972, rev. 1988) Texas Instruments, Dallas
14. AD9833 Datasheet (2003) Analog Devices, Norwood
15. AD8007/AD8008 Datasheet (2003) Analog Devices, Norwood
16. Franco S (2002) Design with operational amplifiers and analog integrated circuits. 3rd ed., McGraw-Hill, New York
17. Williams J (1991) High speed amplifier techniques, Application note 47, Linear Technology, Milpitas
18. Yang QH (2005) Design of a four-phase high frequency amplitude-stable power supply. Biomed Microdevices 7(3):243-246

Author: Nahrizul Adib Kadri
Institute: Department of Biomedical Engineering, University of Malaya
City: Kuala Lumpur
Country: Malaysia
Email: nahrizuladib@gmail.com

Precise Deposition of Electrospun Nanofibers and Electrospraying of Nanoparticles as Enabling Techniques for Biomedical Engineering Applications

S. Neubert[1,2], M. Eblenkamp[1], D. Pliszka[2], sS. Sundarrajan[2], S. Ramakrishna[2], and E. Wintermantel[1]

[1] Department and Chair for Medical Engineering, Faculty of Mechanical Engineering, TU Muenchen (TUM), Bolzmannstr. 15, 85748 Garching, Germany
[2] Nanoscience and Nanotechnology Initiative, National University of Singapore (NUS), 2 Engineering Drive 3, Singapore 117576

Abstract— **Electro hydrodynamic methods like electrospinning of nanofibers and electrospraying of ceramic nanoparticle layers find various applications in medical engineering. The aim of this study is the optimization and comparison of the controllability and precision of electrospinning and electrospraying processes. Different methods like for example the specific modification of the electric field by additional electrodes, by changing the collector size etc. and their combinations to control the deposition area of both electrospinning and electrospraying are presented. Stable and precise processes are of highest importance for transferring the techniques of electrospinning and electrospraying from the state of research to mass production.**

Keywords— **electrospinning, electrospraying, nanofibers, titanium dioxide, nanoparticles**

I. Introduction

Both polymer nanofiber membranes and ceramic nanoparticles are widely spread in biomedical engineering for various applications. The precision of the fabrication methods are of high importance because only very well controllable and reliable processes can be applied in mass production of medical engineering products.

Polymer nanofibers can be fabricated with electrospinning method. The nanofiber membranes fabricated by exposing a polymer jet to an electric field are for example used as scaffolds in tissue engineering, as drug delivery systems, for wound dressing and for biosensors [1]. Compositions of the electrospun polymer solution can be modified and adapted to different applications adding carbon-black particles, enzymes, viruses, bacteria, etc [2]. In literature, electrospinning of PCL microfibers was already focused by positioning a metal ring between the needle tip and the collector [3]. Besides, polyethylene oxide (PEO) was electrospun to nanofibers with a water-based polymer solution. The nanofiber spot was focused to a minimum spot of 5 mm [4, 5].

Titanium as well as TiO_2 are biocompatible ceramic materials. Their compatibility with the human body is excellent. Hence, titanium and TiO_2 are widely used as materials for implants [6]. In order to deposit TiO_2 nanoparticles on surfaces, electrospraying technique can be applied. Electrospraying occurs, when the surface tension of the solution is high enough and the solution jet gets broken up into droplets [7]. The advantage of electrospraying in comparison to conventional droplet formation methods like mechanical atomizers is the small size of the droplets (diameter < 1 µm). Additionally, the charged droplets are self-dispersing due to electrostatic forces [7].

Methods to improve the precision of electrospraying and electrospinning are developed in this study and they are finally compared considering the aspect of precision. In order to increase the number of applicable polymers and to guarantee comparability with the electrospraying process, organic solvents are used for electrospinning in this study.

II. Experimental Set-up

A. Electrospinning

In this study, four different polymer compositions were electrospun.

Polycaprolactone PCL (7.5 % wt/wt) was dissolved in chloroform (Merck KGaA, Germany) and methanol (Sigma-Aldrich, Germany). This solution was electrospun with the electrospinning set-up (Fig. 1). An additional ring electrode was applied, whereas the voltage U_1 was equal to U_2. Two parameters were modified: the position of the ring electrode was varied between the positions x=-15 mm and x=0 mm and the voltage was changed in a range between 12 kV and 27 kV.

Poly(vinyl chloride) PVC (Sigma-Aldrich, USA) was prepared in two compositions: For PVC composition 1, PVC (10 % wt/vol) was dissolved in N,N-dimethylformamide (DMF) (Sigma-Aldrich, Germany) and tetrahydrofuran (THF) (Merck, Germany). PVC composition 2 was prepared by dissolving PVC (7 % wt/vol) in N,N-dimethylformamide (DMF), tetrahydrofuran (THF) (Merck, Germany) and dichloromethane (Merck, Germany). Both PVC composition 1 and PVC composition 2 were

O. Dössel and W.C. Schlegel (Eds.): WC 2009, IFMBE Proceedings 25/VIII, pp. 124–127, 2009.
www.springerlink.com

electrospun with the set-up (Fig. 1). The electric field was modified by additional electrodes with $U_1 \neq U_2$, like for instance by tubes with varying diameter and length, rings with different diameters and by metal discs being fixed at the needle as well as by reducing the collector size. Besides, the influence of the distance between the needle tip and the collector Δd on the size of the deposition area was examined.

In order to fabricate a collector with structures at nanoscale, conductive polymer nanofibers were electrospun. (±)-camphor-10-sulfonic acid (β) (CSA)-doped poly(ethylene oxide) (PEO)-polyaniline (PANi) nanofibers were electrospun with a viscous solution being prepared in two steps. First, CSA and PANi (Sigma-Aldrich, USA) were dissolved in chloroform (Merck, Germany) to equal amounts. After filtration, poly(ethylene oxide) (PEO) was added. A PEO-PANi mass ratio of 13 % was chosen. The solution was electrospun with set-up (Fig. 1) without applying any additional electrodes.

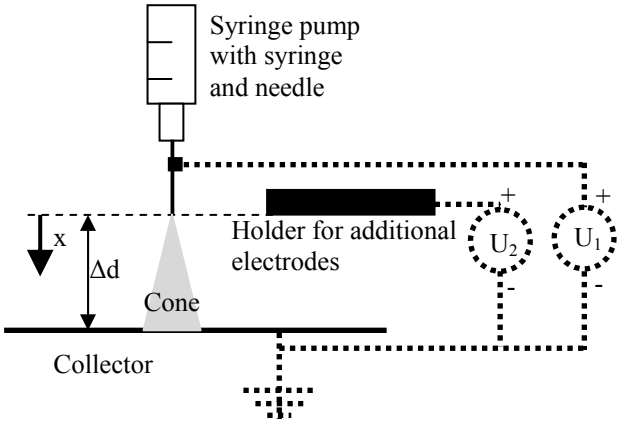


Fig. 1 Set-up used for both electrospinning and electrospraying. For both techniques, the solution is exposed to the electric field between the needle tip and the collector. The process is driven by power supply U_1. In order to modify the electric field, power supply U_2 was used for charging the additional electrodes being positioned coaxially with the needle. For electrospinning, a metal plate is used as collector, for electrospraying metal as well as nanofibers based on conductive polymers are taken as collector. Process parameters are the strength of the electric field, the flow rate of the solution, the solution properties as well as the distance between needle tip and collector Δd.

B. Electrospraying

Titanium dioxide P25 nanoparticles (TiO_2) (5 % wt/vol) were dissolved in methanol (Sigma-Aldrich, Germany) and 3(trimethoxysilyl) propyl (MEMO) (Degussa, Germany) was added in order to avoid agglomerations of nanoparticles. This solution was electrosprayed with set-up (Fig. 1).

As collector, aluminum stripes with a 10 mm width, PEO-PANi membranes as well as PEO-PANi membranes with aluminum foil underneath were used.

C. Characterization

The nanofiber quality was studied with scanning electron microscopy (SEM). The diameter of the electrospun nanofibers were analyzed on basis of the SEM images using image analysis software (Image J, National Institute of Health, Bethesda, MD). Data are presented in means ± standard deviations from multiple analyses.

III. Results and Discussion

First, the precision and efficiency of electrospraying was studied by adapting the collector size and structure to the required surface shape. Therefore, both metallic stripes and conductive polymer nanofibers were used as collector.

By reducing the collector size and by changing the collector shape, the deposition area of the ceramic nanoparticles could be modified and very precise deposition areas could be achieved. For example, an aluminum stripe with 10 mm width was used as collector. The electrospayed TiO_2 nanoparticles were collected by the aluminum stripe with approximately 100 % efficiency. No TiO_2 was found on the surface surrounding the collector consisting of insulating polymer. In addition, it was optically observed that the electrosprayed TiO_2 layer covered the aluminum foil homogeneously.

Hence, controllability and precise nanoparticles deposition of electrospraying could be done by only adapting the size of the metal collector to the demanded width of the ceramic layer. In that way, very precise deposition areas could be achieved at macro scale.

In order to prove the controllability of nanoparticle deposition at micro- and nanoscale too, conductive PEO-PANi nanofiber membranes with the average diameter of 987 ± 179 nm were electrospun and used as collector for the electrospraying process. In order to avoid any external influence, the membrane was placed on an polyethylene support. Also in this case, a nearly 100 % efficiency of electrosprayed nanoparticles was observed.

Studying the deposition of the nanoparticles with the SEM, the top layer of PEO-PANi nanofiber membrane was covered homogeneously with TiO_2 nanoparticles. However, hardly any nanoparticles could be found between the nanofibers (Fig. 2). Interpreting the results of these observations, a precision of nanoparticle deposition down to micro- and nanoscale was achieved by adapting the size and the shapes of the collectors to the required precision of the dimensions of the ceramic layer. Additionally, the required conductivity

of the nanofibers had to be achieved to make electrospraying with homogeneous nanoparticle deposition occur.

It was observed that by using aluminum foil underneath the PEO-PANi nanofiber membrane as collector, the nanoparticle deposition was less homogeneous on the nanofiber surface than by using only conductive nanofibers as collector. The reason for this observation is the overlaying of the electric fields between the needle tip and the conductive nanofiber membrane on the one hand and the aluminum foil underneath on the other hand.

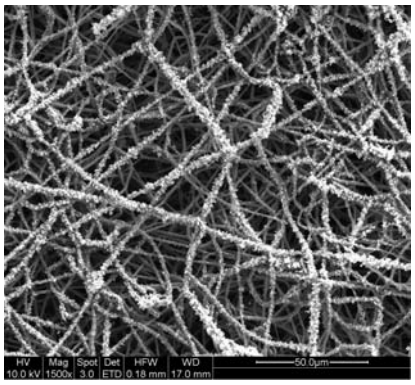


Fig. 2 CSA doped PEO-PANi nanofibers covered with a TiO_2 nanoparticle layer. The layer was fabricated by electrospraying TiO_2 solution onto conductive nanofibers being used as collectors without any aluminum foil underneath. The process of electrospraying can be controlled to precision at micro- and nanoscale by adapting the collector size and shape.

Second, the controllability and the possible precision of nanofiber deposition in the electrospinning process were studied. The conventional electrospinning process being widely used for nanofiber fabrication for example for tissue engineerig is characterized by instabilities due to perturbations like induced vibrations or the shape of the needle tip. This is one reason for the large deposition area of electrospinning. Another reason therefore is the big nanofiber deposition cone. Hence, big spot sizes with up to 100 mm diameter occur. However, biomedical applications like biosensors, scaffolds for tissue engineering, for drug delivery systems etc. require very precise nanofiber deposition in order to realize the complex shapes in mass production. Therefore, various methods were applied.

To attain the aim of minimum deposition areas, the development was done in two steps:

- The deposition area was reduced by increasing the process stability and by reducing the size of the nanofiber deposition spot.
- The quality of the fabricated nanofibers was optimized.

In order to reduce the deposition area of electrospun nanofibers, numerous methods were applied. In the following, the effect of each method is evaluated:

1. *Effect of collector size*
   The reduction of the collector size affected the deposition area only until a certain limit. With using stripes of aluminum foil as collector, the round deposition area was deformed into oval spots, whose axis was only reduced in the direction orthogonal to the stripe direction. Using collectors with a collector size smaller than one square centimeter did not allow any electrospinning to occur because of the weakness of the electric field.
2. *Metal disc at the needle*
   The electric field was made more homogeneous by applying the electric field between the metal disc fixed at the needle and the metal collector because the routes of the electric field lines were made more homogeneous. Hence, the process of electrospinning could be stabilized.
3. *Single ring electrode*
   Electrospinning of PCL nanofibers only occurred, when the ring was positioned above the needle tip. The smaller the distance between the needle tip and the ring was, the more focused the electrospinning was and the thicker the nanofibers became. In that way, the diameter of the nanofiber deposition area could be reduced significantly without any significant influence on the nanofiber quality. It was observed that rings have a stabilizing effect. Even if the electrospinning cone was moving without any additional rings, modifying the electric field with additional electrodes had the effect of stabilizing the electrospinning process.
4. *Combinations of ring and tube electrodes*
   For further focusing of electrospinning, numerous electrodes were combined and tested. In order to maximize the focusing effect, two additional ring electrodes were applied. One additional ring electrode was positioned above, the other one below the needle tip. In order to make electrospinning occur, U_2 charging the additional electrodes had to be set significantly lower than U_1 running the electrospinning process. For electrospinning PVC composition 1 and keeping the Δd constant, nanofiber deposition spots of about 10 mm diameter were achieved. However the nanofiber quality was affected by focusing because the solvent could not evaporate well (Fig. 3).

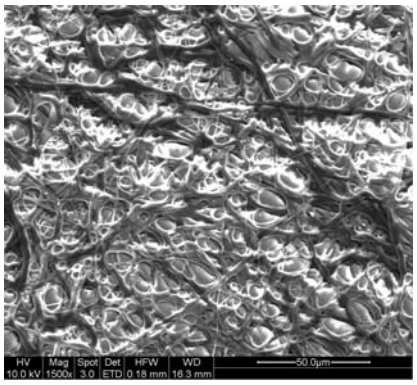


Fig. 3 Nanofibers focused onto a deposition area with 10 mm diameter by two ring electrodes. The solvents could not evaporate fast enough.

5. *Distance between needle tip and collector Δd*
   By reducing Δd, the electrospinning deposition area was reduced because the size of the tailor cone was reduced. However, Δd was not big enough for the solvent evaporation to take place before deposition of nanofibers on the collector (similar to Fig. 3).

Finally, the methods 2 until 5 were combined to design an optimized set-up. As the focusing effect by reducing the collector size (method 1) could not be combined with the methods 2 until 5, the collector size was not reduced.

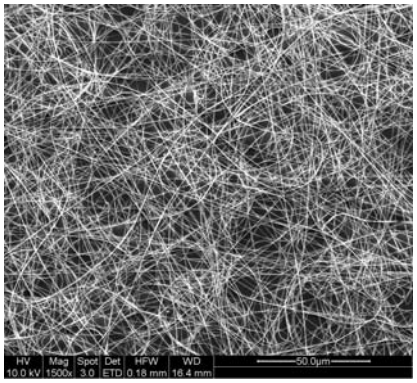


Fig. 4 PVC Nanofibers were achieved by electrospinning a nanofiber stripe with 0.5 mm width.

In the second step, the quality of the nanofibers was optimized by electrospinning PVC composition 2. With dichloromethane and more THF as solvents, the problem of too slow solvent evaporation was avoided and good quality nanofibers could be electrospun (Fig. 4).

With this set-up, nanofiber stripes with a width of 0.5 mm could be achieved by moving the collector under the electrospinning needle. Hence, with the developed means, electrospinning could only be controlled at macro scale in the millimeter range.

IV. Conclusions

Comparing the controllability of material deposition by electrospraying and electrospinning, metal oxide nanoparticle layers could be electrosprayed with a precision at micro- and nanoscales. Due to the long nanofibers, the precision of nanofiber deposition by electrospinning could only be controlled on macro scale, as the smallest deposition area achieved was a stripe with 0.5 mm width. When using hydrodynamic techniques for medical engineering applications, the potential precision of the techniques has to be taken into consideration because precision, controllability and stability of the processes are important for fabrication of biosensors, scaffolds in tissue engineering etc.

Acknowledgment

We acknowledge the funding support from the A*STAR, Singapore, under the project 'Fabrication of Novel Nanocomposite Filter Membranes for Understanding Basic Principles and Their Advanced Technology Applications' (Grant No R-398-000-041-305). In addition, S. Neubert thanks 'Studienstiftung des deutschen Volkes' for the grant supporting his stay at NUSNNI.

References

1. Ramakrishna S, Fujihara K, Teo W-E, Lim T-C, Ma Z (2005) An Introduction to Electrospinning and Nanofibers. World Scientific Publishing Co. Pte. Ltd, Singapore
2. Greiner A and Wendorff JH (2007) Electrospinning: A fascinating method for the preparation of ultrathin fibres. Angew. Chem.-Int. Edit. 46(30):5670-5703
3. Porter MC (1990) Handbook of Industrial Membrane Technology. Park Ridge, NJ: Noyes Publications
4. Deitzel JM, Kleinmeyer JD, Hirvonen JK and Tan NCB (2001) Controlled deposition of electrospun poly(ethylene oxide) fibers. Polymer 42 (19):8163-8170
5. Bellan LM, Craighead HG (2006) 50th International Conference on Electron, Ion, and Photon Beam Technology and Nanofabrication. Baltimore, MD, May 30-Jun 02
6. Wintermantel E, Ha SW (2008) Medizintechnik Life Science Engineering. Springer-Verlag Berlin
7. Jaworek A (2007) Micro- and nanoparticle production by electrospraying. Powder Technol. 176(1):18-35

Author: Sebastian Neubert
Institute: Institute for Medical Engineering, TU München
Street: Bolzmannstr. 15
City: 85748 Garching
Country: Germany
Email: sebastian.neubert@mytum.de

Nanomaterials for Positive Contrast Imaging of MR-Visible Implants

I. Slabu[1], G. Güntherodt[2], T. Schmitz-Rode[1], M. Hodenius[1], N. Krämer[3], G.A. Krombach[3], J. Otto[4], U. Klinge[1,4], and M. Baumann[1]

[1] Applied Medical Engineering, Medical Faculty, Helmholtz Institute, RWTH Aachen University, Germany
[2] II. Physical Institute, RWTH Aachen University, Germany
[3]Department for Radiology, Medical Faculty, RWTH Aachen University, Germany
[4]Department for Surgery, Medical Faculty, RWTH Aachen University, Germany

Abstract— **Each year, about 1.5 million textile meshes are implanted worldwide for abdominal hernia repair. In 10 to 30 % of the cases complications, which are often determined by the mesh, occur. A visualization of the implant helps the surgeon to identify the cause of the suffering and to choose the right treatment. Therefore, superparamagnetic nanoparticles (SPM) are distributed within the filaments of the mesh, which can be then visualized in MRT. Because of the induced susceptibility artefacts of the SPM, the implant can be detected as signal voids in the MR image. Consequently, a homogenous distribution of the SPM within the mesh is of great importance. In this work, the magnetic properties of the particles and of the mesh are analyzed and a method of detecting the incorporated magnetic particles within the filaments of the mesh is developed.**

Keywords— **superparamagnetic nanoparticles, magnetic resonance imaging, inversion recovery with ON-resonant water suppression, superconducting quantum interference device, magnetic force microscopy.**

I. Introduction

Each year, 1.5 million textile meshes are implanted worldwide for fortification of musculature, connective tissue and fascia. In up to 30 % of these cases, the mesh grows in and integrates into the scar tissue, causing severe complications such as migration and erosion, shrinkage and deformation or fistula formation [1]. A post surgery visualization of the implant offers the possibility to identify whether the complication originates from the mesh and to evaluate the properties of the mesh ex-vivo. Following this, the surgeon will decide whether to monitor the complaints, to surgically correct the position of the mesh or to explant the mesh. Thus, the exposure of the patient to redundant surgical interventions can be dramatically reduced. Using the conventional radiological imaging methods such as X-ray, ultrasound, computed tomography and magnetic resonance imaging (MRI), the mesh cannot be distinguished from the ambient tissue. Therefore, superparamagnetic nanoparticles (SPM) are integrated within the filaments of the mesh implant and, as a result, the mesh can be visualized in MRI.

SPM are a contrast agent for magnetic resonance imaging in medical diagnostics and also an important tool in drug targeting and hyperthermia interventions [2]. Quantum size effects and the large surface area of these nanometer sized magnetic particles evoke superparamagnetic phenomena and quantum tunneling magnetization as each particle can be considered as a single magnetic domain. Due to the additional magnetic field susceptibility caused by the SPM, a hypointense signal in MRI is created and the particles can be detected as signal voids in the MR images. However, since air and calcification also show hypointense signals, a method that illuminates the superparamagnetic nanoparticles in the mesh implant with positive contrast, called inversion-recovery ON-resonant water suppression (IRON), is applied [3].

A homogeneous distribution of the SPM in the filaments and an optimal modulation of their magnetic properties are of great importance for a good resolution of the mesh in MRI. Therefore, the physical and chemical properties of differently synthesized nanoparticles are determined and examined for their applicability in MR imaging.

II. Materials and Methods

Fe_3O_4 superparamagnetic nanoparticles are synthesized either as magnetizable nanocolloids that are dispersed in a carrier fluid with chemically coated particles or as a powder without coating treatment using the methods of Shinkai [4] or Khalafalla [5], respectively. As nanoparticles in a ferrofluid tend to agglomerate reducing their surface energy by strong magnetic dipole-dipole attraction, the magnetic fluid is stabilized by coating the particles with dodecanoic acid. By varying the molar ratio between different chemical components during the synthesis operation (e.g. Fe^{2+} NO_2^-) and by adjacent centrifugation, several core sizes of superparamagnetic nanoparticles are fabricated.

The powder is first lyophilized and then, with a pestle, pulverized without utilizing any surfactant. These uncoated nanoparticles build clusters whose sizes are varied by grinding procedures using a flint mill. The particle size distribution and the morphology of ferrofluid particles are exam-

O. Dössel and W.C. Schlegel (Eds.): WC 2009, IFMBE Proceedings 25/VIII, pp. 128–131, 2009.
www.springerlink.com

ined using a transmission electron microscope (TEM) (EM 400 T apparatus, Philips, The Netherlands). The grain distribution of powder is investigated utilizing a laser diffractometer (Mastersizer 2000, Malvern Instruments, Germany). The average particle and grain sizes are listed in Table 1.

Table 1 Average particle and grain sizes for samples synthesized as ferrofluid and powder, respectively.

Sample	Core diameter D_{TEM} [nm]	Grain diameter D_{Laser} [µm]
S1	10.34±3.2	-
S2	5.20±1.6	-
S3	-	27.03±3.65
S4	-	12.17±3.53

For the assembly of textile meshes, a mixture of PVDF-polymer and a small quantity of superparamagnetic iron oxides (SPIOs) (approx. 1 mg/g) is melted down and extruded to filaments. In order to achieve a good contrast in MRI the particles must be adjusted in reference to their dimensions, core shell and solubility within the polymer. Therefore, the susceptibility and saturation magnetization of the particles and of the filaments are determined using a superconducting quantum interference device (SQUID) (MPMS-XL, Quantum Design, USA). The measurements are performed at room temperature varying the magnetic field strength.

The magnetic properties of single SPM and their distribution within an ensemble are determined using a magnetic force microscope (MFM) (DI 3100 Nanoman AFM, Veeco, USA). This method has strong magnetic stray field sensitivity and delivers a high spatial resolution [6]. Figure 1 shows the concept of an MFM sensor: a magnetic tip placed in the stray magnetic field of a spherical nanoparticle. In a first scan an AFM (atomic force microscopy) image is taken to give a reference height. The second scan is performed in MFM mode at the determined reference height line with a lifted cantilever driven at its resonance frequency. The shift of the phase of the driven cantilever is detected. This is the measurement of the derivate of the force acting on the magnetic tip in the direction normal to the surface of the sample.

However, these methods only allow the investigation of small parts of the filaments. Hence, a new inductive method is developed to detect the distribution of the particles within larger regions of the mesh. This is essential for the quality control in clinical applications and manufacture.

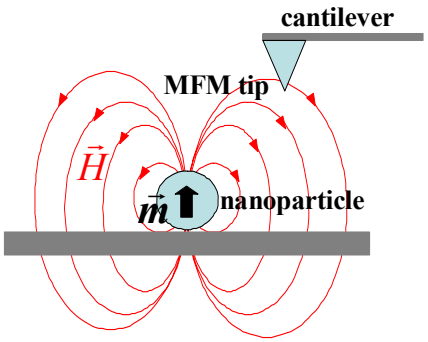


Fig. 1 Schematic diagram of a nanoparticle in MFM: the magnetic tip scans the sample in a reference height line with a lifted cantilever driven at its resonance frequency. The shift of the phase of the driven cantilever is detected.

For a better delineation of the implant from other structures that also create a hypointense signal (e.g. air, calcifications), an MRI method that illuminates the textile structures with positive contrast, called inversion-recovery with ON-resonant water suppression (IRON), is applied. In combination with a spectrally-selective ON-resonant saturation prepulse, the magnetization is inverted. When imaging is performed after these prepulses, a positive signal is obtained from off-resonant protons in close proximity to the magnetic structures [7]. Thus, the mesh appears white while other structures are suppressed. To evaluate the delineation of a mesh, which has SPM embedded and is placed between two pieces of meat, MRI is performed in a 1.5 Tesla scanner (Achieva, Philips, The Netherlands) with a multi-channel receiver coil using both T2*-weighted sequences (TR 285 ms, TE 23 ms, FoV/matrix 200 mm/248, NSA 2, FA 18°), and IRON gradient echo sequences (TR 200 ms, TE 8 ms, FoV/matrix 200 mm/185, NSA 3, FA 18°, offset frequency 180 s^{-1}).

III. Results and Discussion

As shown in Figure 2, sample S1 primarily consists of single Fe_3O_4 particles in the shape of a sphere.

Typical light microscope images of the SPM cluster distribution of a powder with a concentration of 3 mg/g within a 120 µm filament are shown in Figure 3.

The susceptibility measurements reveal a characteristic superparamagnetic behavior with immeasurable coercivity and remanence at 300 K (Fig. 4).

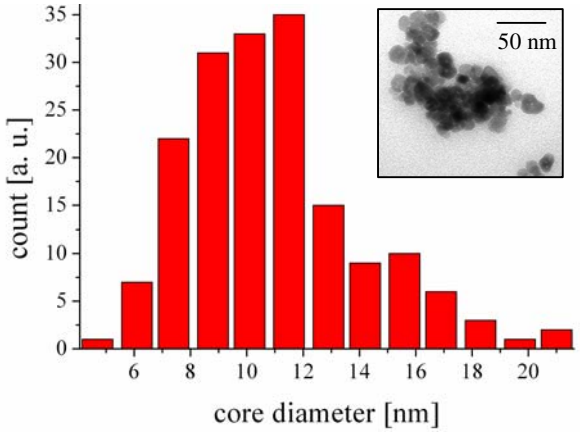


Fig. 2 TEM micrograph determination of Fe_3O_4-core size distribution (sample S1, Table 1).

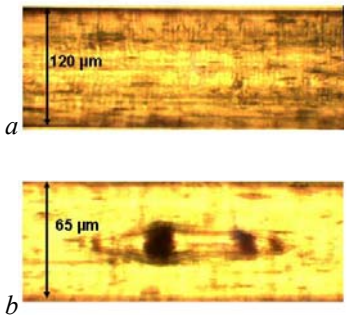


Fig. 3 (a) Light microscope image of a filament containing clustered SPIOs shown as black dashes, (b) an enlarged view of multiple agglomerations of particles.

For superparamagnetic particles, the real magnetic moment at 300 K can be calculated using the Langevin function:

$$M = M_S\left(\coth\left(\frac{\mu H}{k_B T}\right) - \left(\frac{k_B T}{\mu T}\right)\right), \quad (1)$$

where $\mu = M_S \pi D^3/6$ is the true magnetic moment of each particle, k_B is the Boltzmann constant, T is the absolute temperature and M_S is the saturation magnetization. Figure 4 shows the best fit for the Langevin function in Eq. (1). From this data fitting, the mean magnetic moment per particle of sample S3 and S4 for $H \to 0$ (i. e. $M \to M_S\,(\mu H/3k_B T)$), is found to be $1.36 \cdot 10^{-16}$ emu. The initial data is determined by the large particles in the assembly and calculated to $D = 8.87$ nm.

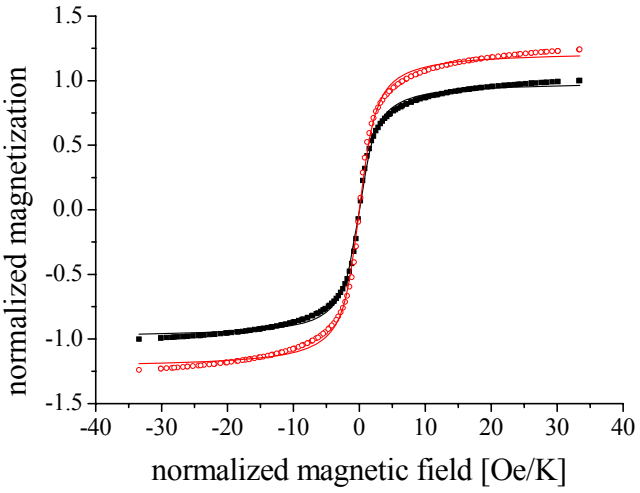


Fig. 4 Normalized magnetization vs. applied magnetic field for particles without coating: experimental data for S3 (red circles) and S4 (black squares), and fitted curves for S3 (red line) and S4 (black line).

Figure 6 shows an AFM/MFM image of clusters of various sizes of SPM in S1 which was put on a silicon wafer and then dried. The sample was magnetized by an external magnetic field that is prior to the measurement oriented horizontally to the substrate plane. The particles can be identified as white structures in the MFM image (Fig. 5, right image). This corresponds to the repulsion between the particles and the MFM tip.

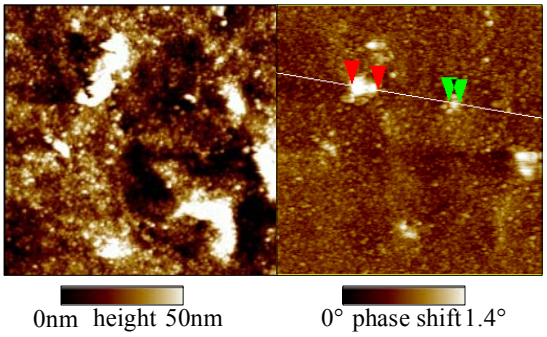


Fig. 5 AFM (left) and MFM (right) images of isolated and clustered particles that are before the measurement magnetized horizontally to the plane. In the MFM image the white color represents repulsion. The sizes of the red and green marked clusters are 500 nm and 215 nm, respectively.

This method is also being applied on the magnetic filaments and connected to light microscopy images, providing an evidence for the fact that the black dashes in Figure 3 can be categorized for sure as magnetic particles and not as material defects.

The images of a PVDF mesh with embedded SPM (mean core size 9.4 nm) in a meat phantom, using T2*-weighted sequences and IRON, are shown in Figure 6. The mesh is made of filaments with a diameter of 120 µm and its size is approx. 2 cm x 0.8 cm.

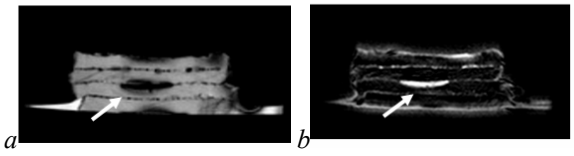


Fig. 6 T2*-weighted sequence (a) and IRON (b) images of a magnetic mesh (arrows) placed in a meat phantom.

In order to quantify the homogeneity of the distribution of the magnetic particles in a larger region within the filaments, an inductive technique is developed which does not require a pretreatment of the sample. The method bases on the magnetic nature of the particles and their effect on the self-inductance of a coil.

IV. Conclusions

This work concentrates on the characterization of superparamagnetic nanoparticles (SPM) which are integrated within textile implants in order to visualize these in MRT. First results show a good resolution of the mesh in a meat phantom for particles of a mean core size of 9.4 nm. Therefore, a method which illuminates the mesh with positive contrast, called inversion-recovery with ON-resonant water suppression (IRON), is applied. Using different methods of synthesis several samples of superparamagnetic Fe_3O_4 nanoparticles are fabricated and characterized. Depending on their structure (e.g. powder, ferrofluid) and size, the SPM have different properties and are investigated in subject to their usability for MRI. The saturation magnetization and susceptibility are measured using a SQUID magnetometer. All samples show a superparamagnetic behavior, though with different values for the magnetic moment. Using the magnetic force microscopy, single SPM and SPM clusters are identified and distinguished. This method is also being applied on the magnetic filaments and matched to light microscopy images. These investigations are required for the setup of a reference database which is necessary for the development of an inductive detector of the magnetic nanoparticles within a mesh. This is most important for the quality control in clinical applications and manufacture as it examines the homogeneity of the distribution of the SPM within larger areas of the filament. By monitoring the mesh after surgery, implant related problems are revealed. This implies a great progress in medical therapy.

Acknowledgment

This project is the winner of the Medical Engineering Innovation Challenge 2007 and is funded by the German Federal Ministry of Education and Research (Ref. 01 EZ 0849).

References

1. Junge K et al. (2004) Decreased collagen type I/III ratio in patients with recurring hernia after implantation of alloplastic prostheses. Langenbecks Arch Surg 389:17-22
2. Berry C C, Curtis S G (2003) Functionalisation of magnetic nanoparticles for application in biomedicine. J Phys D Appl Phys 36:198-206
3. Vlaardingerbroek M T, den Boer J A (2003). Magnetic Resonance Imaging, Springer. Berlin
4. Shinkai M, Honda H, Kobayashi T (1991) Preparation of Fine Magnetic Particles and Application for Enzyme Immobilization. Biocatalysis, 5:61-69
5. Khalafalla S E, Reimes G W (1980) Preparation of dilution-stable aquaneous magnetic fluids. IEEE Trans Magn 16(2):178-183
6. Albrecht M et al. (2005) Scanning force microscopy study of biogenic nanoparticles for medical applications. JMMM 290-291:269-271
7. Korosoglou G et al. (2008) Positive Contrast MR-Lymphography Using Inversion Recovery With ON-Resonant Water Suppression (IRON). J Magn Reson Imag 27:1175-1180

Author: Ioana Slabu
Institute: Institute of Applied Medical Engineering
Street: Pauwelsstr. 20
City: 52074 Aachen
Country: Germany
Email: slabu@hia.rwth-aachen.de

Femtosecond Laser Microstructuring and Bioactivation of Titanium Surfaces for Middle Ear Ossicular Replacement Prosthesis

J. Ilgner[1], S. Biedron[1], D. Klee[2], E. Fadeeva[3], B. Chichkov[3], and M. Westhofen[1]

[1] Department of Otorhinolaryngology, Plastic Head and Neck Surgery, University of Aachen RWTH, Aachen, Germany.
[2] Institute for Technical and Macromolecular Chemistry, University of Aachen RWTH, Aachen, Germany
[3] Laser Zentrum Hannover e.V., Hannover, Germany.

Abstract— **Introduction: While a variety of materials have been evaluated for replacement of human middle ear ossicles following inflammation, titanium and its alloys have shown excellent sound transmission properties and biocompatibility. However, cartilage thickness at the tympanic membrane interface deteriorates over time, while fibrous tissue formation may dislodge the titanium prosthesis. This study was performed to evaluate the effect of microstructures and biologically active nanolayers on titanium surfaces in contact with adjacent biological tissue. Materials and Methods: Titanium samples of 5mm diameter and 0,25mm thickness were structured by means of a Ti:Sapphire femtosecond laser operating at 970nm. The structures applied were lines of cross-sectional parabolic shape of 5µm (parallel), 5µm (cross-hatch) and 10µm width (parallel). The inter-groove distance between two maxima was twice the line width. Nanocoating was applied by means of chemical vapor deposition (CVD) in various layers: Polyethylene Glycol (PEG) only, PEG with RGD peptide sequence and PEG + RGD + Bone Matrix Protein (BMP)-7. Results: Lines smaller than 5µm were not feasible due to the natural irregularity of the basic material with pits and level changes of up to 2µm. Cell culture revealed that microstructures were able to generate oriented cell growth along structured lines. PEG did perform as "stealth" coating to avoid unspecific protein adsorption. Discussion: The results show that microstructures can be applied on titanium surfaces for human implantation with reproducible and constant shapes. Further studies will focus on relative promotion of chondrocyte compared to fibrocyte growth by various concentrations of BMP-7.**

Keywords— **Femtosecond laser, Otology, Microsurgery, Sound transmission, Biosignal.**

I. INTRODUCTION

Up to present, many prosthetic materials have been employed for passive middle ear prostheses that are targeted at restoring sound transmission to the inner ear. Titanium prostheses have become the "gold standard" in microsurgical restoration of middle ear function. They stand out by their excellent biocompatibility as very few foreign body reactions have been reported. They are easy to handle, lightweight, yet stable, and yield excellent results in transmitting sound over the audible frequency range. However, it has been shown that although every care has been taken to achieve an excellent result in terms of function and inflammation-free outcome intraoperatively, about 3 to 4 per cent of operations fail in the long run. Several reasons have been described:

- Insufficient ventilation of the middle ear, resulting in inflammatory reaction and formation of granulating tissue.
- Recurrence of underlying disease, e.g. cholesteatoma.
- Fibrous tissue formation, which may dislodge or deform the prosthetic shaft.
- Atrophy of the replaced or reinforced tympanic membrane, which results in penetration of the prosthesis through the eardrum.

Some attempts have been made in order to overcome some of these complications, e.g. improving middle ear ventilation by T-tubes or altering the superficial structure of the prosthesis in order to increase friction to adjacent cartilage in order to prevent dislodgement.

It is generally accepted that a number of triggers, e.g. mechanical stimulation, implant surface properties etc. can induce a variety of inflammatory reactions, among which are the formation of granulating tissue, seroma or abscess. These reactions eventually lead to failure of the implanted device and to further adverse reactions in the host organism. Thus, the mechanical design and surface properties of the interface between implant and host organism are of prominent importance for successful functional restoration. Various attempts have been made to achieve good compatibility of implanted devices with surrounding structures. Coating a device with a hydrogel layer prevents unspecific protein adhesion and thus effectively reduces fibrous tissue growth. In practice, metal surfaces can be functionalized by Chemical Vapor Deposition (CVD) of amine-functionalized paracyclophane. By means of CVD-coating, the surfaces of e.g. cardiovascular metallic stents have been functionalized by immobilization of thrombin inhibitor r-Hirudin [1]. In another study, intravascular platinum coils for treatment of intra-cerebral aneurysms have been functionalized by CVD-coating in order to immobilize substances stimulating cell growth on the platinum surface [2,3]. Better tissue-interface

O. Dössel and W.C. Schlegel (Eds.): WC 2009, IFMBE Proceedings 25/VIII, pp. 132–135, 2009.
www.springerlink.com

compatibility of titanium hip replacement implants has been achieved by CVD polymerization with amino-functionalized paracyclophane and subsequent immobilization of osteoblast-specific growth factor BMP-2 [4]. On the other hand, structural surface modifications have also been tested extensively. Reich and co-workers have modified an electrode carrier for cochlear implantation with superficial structures [5]. They were able to show that groove structures with a width of 4 to 7 µm reduced fibrous tissue adhesion and could allow for neurite outgrowth to the silicone surface.

However, to our knowledge the effects of microstructuring the interface and chemical bio-functionalization in middle-ear prostheses have not been investigated in depth as yet. In this particular case, cell growth in the interface region between prosthesis and cartilage replacing the tympanic membrane should ideally be calibrated in a way that sound transmission is facilitated while stability of the interface region is increased. As middle ear prosthesis stand out by an interface-to-mass ratio far greater than in e.g. prosthetic replacement of joints for the locomotor system, it seems reasonable to focus on these contact surfaces to the eardrum and stapes structures. But also on non-contact surfaces such as the prosthesis shaft, coating with the ability to down-regulate unspecific protein adhesion and subsequent cell growth is desirable. Thus, the underlying hypothesis for this study is that variations in surface morphology of titanium prostheses for the middle ear as well as hydrogel layers applied to titanium surfaces can modify unspecific protein adsorption and promote cell growth on the interface regions in vitro.

II. Materials and Methods

A. Native Titanium Material

To obtain data on the surface structure of uncoated titanium material, we examined the native surface of a ready-to-use 4.5 mm TORP (total ossicular replacement prosthesis; manufacturer Kurz GmbH, Dusslingen, Germany) under environmental scanning electron microscopy (XL30 ESEM, Philips, Eindhoven, Netherlands). Its morphology was compared to sample material of titanium discs measuring 5.0 mm in diameter and 0.25 mm thickness by the same manufacturer. The titanium platelets were fixed to an electrically conductive base foil, while the TORP prosthesis was arranged on the same base in two different orientations. Electron scanning microscopy examinations were performed under high vacuum at 10kV.

B. Femtosecond Laser Microstructuring

Platelet samples mentioned above were then microstructured by means of a Ti:Sapphire laser with Colquerite amplifier emitting at 980 nm with femtosecond pulses. The characteristics of this laser are that with multiphoton absorption by the target tissue, optical breakdown within the focus area occurs. This process is a) largely non-thermal and b) operates independently of tissue properties. The ablation speed generated by the laser scanner is 0.1mm/s.
Three different structure patterns were generated:

- Linear grooves of 5µm depth and 5µm width, maxima distance 10µm
- Linear grooves of 10µm depth and 10µm width, maxima distance 20µm
- Cross-hatch patterns with dimensions same as a).

Platelets were visually examined for pattern regularity, debris and other abnormalities under ESEM.

C. Chondrocyte Culture

Human ear cartilage was harvested within 24 hours post-mortem in sterile conditions, cut and digested. Chondrocytes were seeded at densities from 0.25 to 2 x 10^4 cells/cm^2 on 48-well tissue culture dishes to examine four different durations (1-4 weeks) as well as on 75ml tissue-culture flasks in order to obtain subcultured cells, In addition, for immunohistochemical analysis cells were stained with antibodies against type I and type II collagen and against DNA (Hoechst, Calbiochem, Nottingham, Great Britain). Phenotype and distribution of cells were monitored by means of light microscopy, epifluorescence microscopy and immunohistochemistry.

III. Results

Regarding the superficial microstructure of native titanium material, the titanium TORP showed marked porosity in the surface of the top plate which is meant to attach to the cartilage-perichondrium graft replacing the defect tympanic membrane. The pores were about 4-5 µm in diameter and about 3 µm in depth (Fig.1).

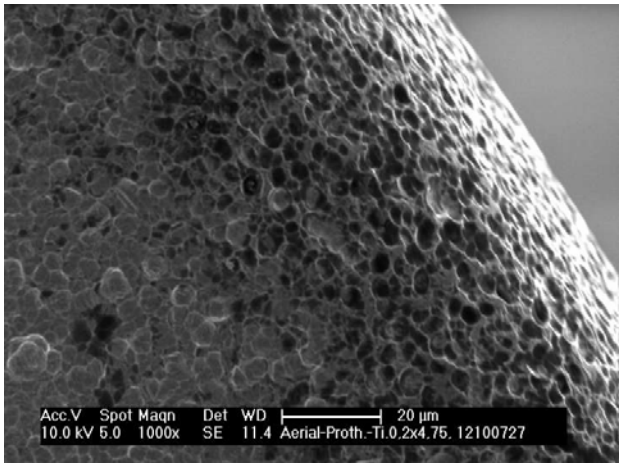


Fig. 1: Native surface of Titanium prosthesis (TORP) top plate. Pits of 4 to 5 µm in diameter reflect particle blasting during the manufacturing process.

In contrast, platelet samples were delivered without further surface alteration: Thus, we detected a relatively homogeneous surface with level irregularities in the range of 2µm (Fig. 2).

Microstructures applied by femtosecond laser ablation showed regular and homogenous lines of 5 µm width, 10µm width and 5µm width in cross-hatch pattern. As predicted, the cross sectional shape of these lines was ellipsoid, resembling the Gaussian energy distribution delivered by the laser system. Marginal debris was present in some of the samples; however, this debris did not markedly alter the surface structure (Fig. 3). After functionalization with amino-paracyclophane and Hydrogel coating with Star-PEG for 15, 30 and 60 minutes exposition, we could visually confirm the integrity of the microstructures under ESEM, which remained largely unaltered independent of the hydrogel layer thickness (Fig. 4).

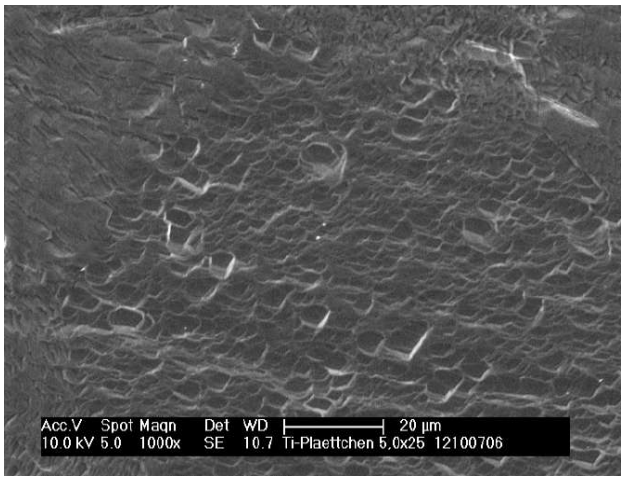


Fig. 2: Native surface of titanium platelet sample: Surface level irregularity of about 2µm.

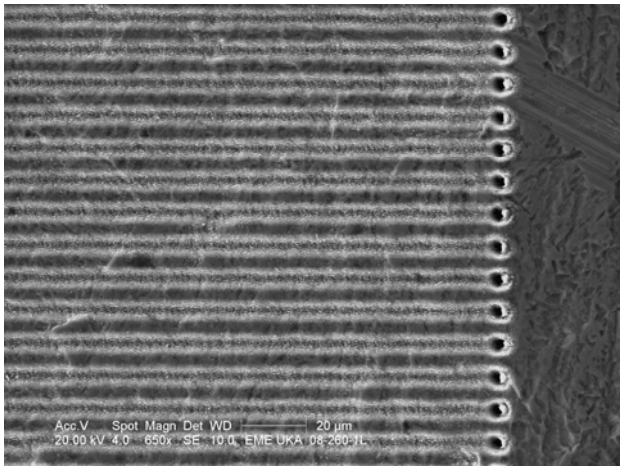


Fig. 3: Linear microstructure on titanium platelet, uncoated, 5µm groove width, 5µm groove depth, 10µm inter-groove distance. ESEM, 20kV, 650x magnification

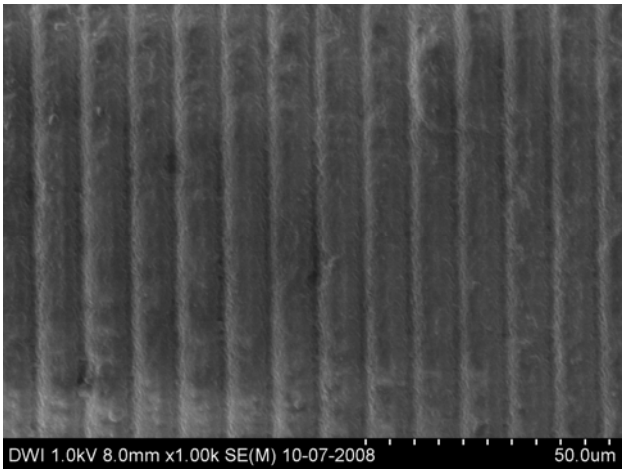


Fig. 4: Linear microstructure on titanium platelet, 5µm groove width, 5µm groove depth, 10µm inter-groove distance, coated with Star-PEG, 30 min. exposition, ESEM, 1kV, 800x magnification.

Examination of cultured ear chondrocytes on titanium surfaces by means of epifluorescence microscopy could be performed without artifacts caused by reflections on the titanium surface. Fluorescence staining yields typical distribution of type I and type II collagen: Ear chondrocytes contain mainly type II collagen. Chondrocyte proliferation is reduced on titanium surfaces. Cells seeded at 2 x 10^4 cells/cm^2 and cultured for 5 days proved best for evaluation of cell-distribution and morphology. At this stage cells began to arrange in chondrone-like groups, as it is known from cartilage in-vivo. While on native titanium surfaces the cell phenotype is similar to cells cultured on polystyrene

tissue culture surfaces, their shape is being influenced by micro-structured surfaces. Nuclei are elongated and oriented along the embossed parts of the structure (Fig. 5). Only few nuclei slip into the grooves. The cell-bodies are arranged in parallel to the surface pattern.

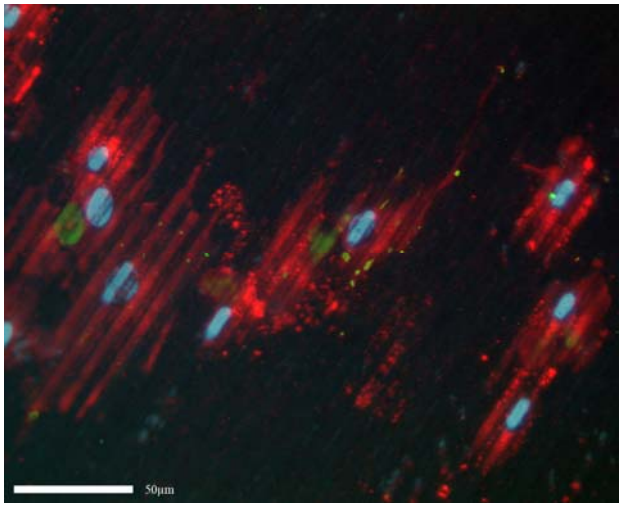


Fig. 5. Human auricular chondrocytes seeded at $2x10^2$ cells/cm² and cultured for 5 days on micro-structured (5µm parallel lines) titanium sample: cells are oriented along the linear groove structure.

IV. Discussion

The results show that medically employed preparations of titanium do not display a totally even surface. Even unprepared titanium platelets possess irregularly shaped plateaus and shallow pits of +/- 2µm difference in level. Although microstructuring titanium surfaces with 2µm grooves were technically feasible, its effect would have been indistinguishable from the effect provided by the native surface. Therefore, we concentrated on the groove structures discussed here.

It is interesting to see that the conventionally manufactured titanium prosthesis displays a similar structure on the top plate with 4 to 5 µm pits caused by particle blasting. However, to our knowledge it has not been proven that this surface modification provides any additional effect of fibrous or cartilaginous tissue formation. In contrast, we could observe that under clinical conditions, a conventional titanium prosthesis which has been fit under a cartilage graft for tympanic membrane replacement shows very little adhesion to the cartilaginous surface especially when there is little surrounding inflammatory reaction (e.g. in cases of dry, non-inflammatory chronic otitis media).

In addition, we could demonstrate that coating the microstructured titanium surfaces with biologically active layers in the nanometer range does not markedly alter the shape of desired structures. Thus it is fair to assume that the effect of biologically active layers can be assessed independently from the effects achieved by the microstructured material itself. Consequently, further evaluation will concentrate on cell culture testing and clinical evaluation of titanium surface modifications, under various surface modifications as well as with different biologically active coatings.

Acknowledgment

This study was funded by the German Research Foundation (Deutsche Forschungsgemeinschaft) as part of the SFB-Transregio program, project No. 37, sub-project B3.

The authors would like to thank the Kurz Company (Kurz GmbH, Dusslingen, Germany) for generously providing the titanium prosthesis and titanium platelet samples.

References

1. Lahann J, Klee D, Plüster W, Höcker H (2001) Bioactive immobilization of r-hirudin on CVD-coated metallic implant devices. Biomaterials 22 .817-826
2. Weiß N. (2004) Verfahren zur Funktionalisierung und bioaktiven Ausrüstung von Implantatoberflächen für eine verbesserte Gewebeintegration. Inaugural Thesis RWTH Aachen.
3. Völker N, Klee D, Höcker H, Langefeld S (2001) Functionalization of silicone rubber for the covalent immobilization of fibronectin. Journal of Materials Science: Materials in Medicine 12 111-119
4. Klee D, Böing J, Höcker H (2004) Surface Modification of Titanium for Improvement of the Interfacial Biocompatibility. Materialwissenschaft und Werkstofftechnik 186-191
5. Reich U, Mueller PP, Fadeeva E, Chichkov BN, Stoever T, Fabian T, Lenarz T, Reuter G (2008) Differential fine-tuning of cochlear implant material-cell interactions by femtosecond laser microstructuring. Journal of Biomedical Materials Research Part B: Applied Biomaterials 87(1) 146-153

Author: Justus Ilgner M.D.
Institute: Dept. of Otorhinolaryngology, Plastic Head and Neck Surgery; University of Aachen RWTH
Street: Pauwelsstrasse 30
City: 52057 Aachen
Country: Germany
Email: jilgner@ukaachen.de

Automation of Chemosensitivity Testing - Enabling Personalized Cancer Therapy

B. Becker[1], D. Grundl[1], S. Etzbach[1], M. Zottmann[1], M. Brischwein[1], and B. Wolf[1]

[1] Heinz Nixdorf-Lehrstuhl für Medizinische Elektronik, Technische Universität München, Munich, Germany

Abstract— **Cell based assays are obtaining greater importance in a plurality of scientific research fields. Due to their high sensitivity towards a great variety of input factors, these assays are also increasingly used in biochemical research, pharmacological drug screening and medical diagnostics.**

For cancer treatment, cellular assays can play a key role to the individualisation of chemotherapy, as different possible drugs can be tested with cells or tissue of a specific patient before commencing the treatment.

Combining cellular assays with laboratory automation equipment like liquid handling systems is the key to large scale chemosensitivity-testing of tumour cells. Therefore our research group has developed an automated high-content online measurement system for cell based assays. The system is comprised of a pipetting robot, sensors for measurement of pH, pO_2, electric signals and cell adhesion, a digital microscope and a climate chamber. The robot is used to supply the cells with nutrient solution or active agents that are to be tested, while the sensors monitor the acidification of the medium, the uptake of oxygen and the adhesion of the cells to the substrate. Reflected light as well as fluorescence imaging during the course of an experiment are possible due to the included microscope. Cells and sensors are arranged in a special 24-well micro plate that is placed at a fixed position within the system. Oxygen and pH values are usually measured every 5 to 15 seconds. The running software also allows planning of experiments over a long period of time (several days to weeks).

Furthermore, this paper shows proof of principle measurements with human cancer cells (MCF-7) treated with different chemotherapeutic agents in different concentrations.

Hence, the feasibility of the working principle could be shown, although the statistical correlation of in-vitro and in-vivo results still has to be proven in clinical trials.

Keywords— **cell based, personalized medicine, chemotherapy, automated**

I. Introduction

Cell based assays are becoming more and more popular in a wide variety of applications. Due to their high sensitivity towards a plurality of compounds and drugs these assays are suitable for applications like pharmaceutical drug screening, chemo- and toxicity testing or environmental monitoring [1,2,3].

The usual approach is the usage of well-known, established cell lines, e.g. for drug discovery or the replacement of animal testing. Cells work as sensor for the impact of drug candidates or potentially toxic agents. Hence the "normal" cellular behavior is known, conclusions about the added substances can be drawn from new behavioral patterns.

For personalized cancer therapy this process has to be reversed. Here, the added drugs and their concentrations are known, while cells / tissue differ from patient to patient. These differences in every individual cancer usually make it difficult for practitioners to choose the right medication.

This is a big problem that could be overcome with the help of cellular assays. Testing cancer biopsies prior to beginning of the treatment could dramatically increase success rates in chemotherapy and avoid ineffective, painful and expensive therapies.

Predictive chemosensitivity testing is neither a technically nor biologically simple task. The test system has to be able to maintain life support for cells over prolonged periods of time and record a variety of cellular parameters. These data have to be examined very carefully regarding different biological effects to indicate the right choice of medication and dosage.

II. Test System

A. General setup

The IMR (Intelligent Microplate Reader) System (Fig. 1) is comprised of a pipetting robot, sensors for measurement of pH, pO_2, bioelectric signals and cell adhesion, a digital microscope, and a climate chamber. IMR follows a strictly modular setup. The sensors are arranged on a modified micro-well-plate. The robot is used to supply the cells with nutrient solution or active agents that are to be tested. Acidification of the medium, the uptake of oxygen and the adhesion of the cells to the substrate are monitored by the sensors. The latter is achieved by an interdigitated electrode structure (IDES), whereas the chemical changes are detected by optodes. Reflected light, as well as fluorescence imaging during the course of an experiment are possible due to the included microscope. All components are arranged in a climate chamber, which provides sterility and keeps environmental parameters (gas, humidity, temperature) constant.

O. Dössel and W.C. Schlegel (Eds.): WC 2009, IFMBE Proceedings 25/VIII, pp. 136–139, 2009.
www.springerlink.com

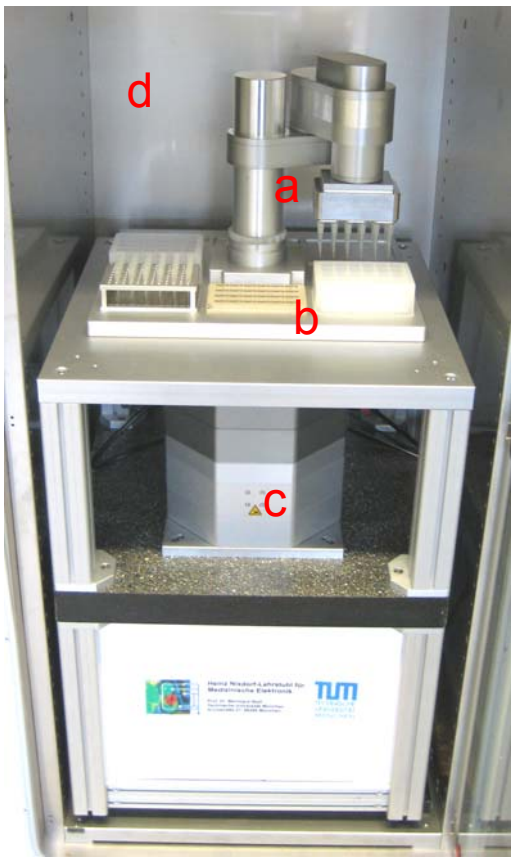


Fig. 1 IMR-System in climate chamber with pipetting robot (a), sensor plate (b), inverted microscope (c) and climate chamber (d)

The system consists of a ground plate where the 24 well micro-plate, as well as storage and waste volumes can be placed. The pipetting robot is mounted on the ground plate and able to reach every position on the plate. From beneath the microscope and the optode read-out system can reach the micro plate through a cutout.

Two setups of the IMR System are used in parallel. One uses an electro-optical system to read out the optodes in the measurement volumes. The other one applies a microscope to access a big variety of optical analysis methods. In both setups the IDES sensor is available for impedance measurements.

B. *General setup*

At the heart of the IMR, a sensorchip-based 24-well-plate with integrated micro fluidics is placed at a fixed position within the device. It provides a means for a well-controlled fluid exchange for every individual cell culture well. Each well consists of three chambers (Fig. 2), at which the central chamber holds cells and sensors. It possesses a very small volume of only 23 µl to allow a higher sensitivity to changes in cell metabolism. Still this volume is large enough to allow cells to form a united structure. This is important as cell collectives behave different than single cells.

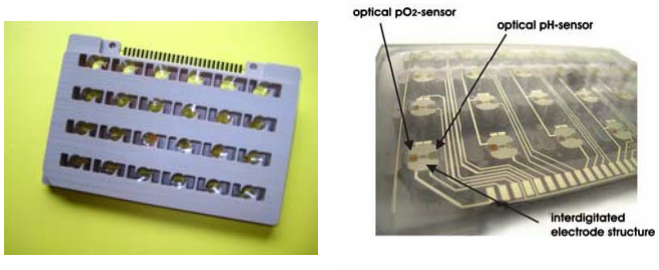


Fig. 2 Micro-well plate including fluidics (left) and sensor structures only (right)

The plate is equipped with micro structured channels for fluid exchange with the other two chambers. Due to the geometrical structure a reproducible exchange of medium from the inflow chamber through the cell culture area to the outflow chamber is achieved, using only hydrostatic pressure differences. Therefore constant and in-vivo like conditions are maintained throughout the experiment.

III. Experiment Results

A. *Experiment setup*

To prove the system's ability of detecting the chemosensitivity of tumor cells, a proof of principle experiment was conducted. Here, the MCF-7 breast cancer cell line was treated with two chemotherapeutic agents (Doxorubicin and Cisplatin). The effectiveness of these drugs in inhibiting and destroying MCF-7 cells is known.

In every well, $4{,}0*10^5$ cells were seeded and incubated for 48 hours. After that time about 60 % of the wells' ground plate area was covered.

Then, the measurement plate was inserted in the IMR-System, where recording of measurement values and the treatment with drugs started. For each drug, 10 wells were used (nutrition medium infused with different concentrations of drugs), while cells in 4 wells were treated with nutrition medium only (control wells).

The experiment went on for 51 hours, during this time medium changes were conducted every 20 minutes.

B. Results

Fig. 3 shows the oxygen uptake rates of wells treated with different concentrations. A clear decrease in metabolic activity can be observed for wells infused with Doxorubicin. This decrease begins eight hours after the treatment with the drug started at the onset of data recording.

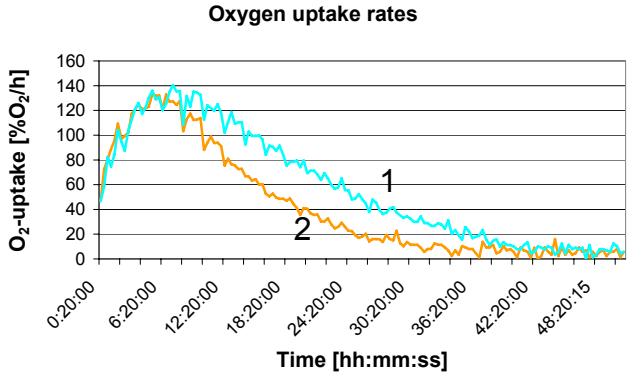


Fig. 3 Oxygen uptake rates for well #21 with 2 uM Doxorubicin (1) and well #17 treated with 5 uM Doxorubicin (2)

The different drug concentrations can be distinguished by the time needed to bring the oxygen consumption rate beneath 20 $\%O_2/h$. This takes 35 hours for 2 uM and 25 hours for 5 uM.

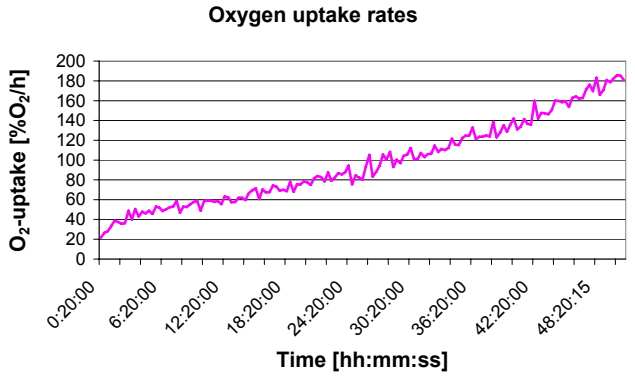


Fig. 4 Oxygen uptake rates for well (#12) without added drug

The control well (Fig. 4), however, shows an ongoing increase in the accumulated respirational activity of the cells.

Looking at the impedance values (Fig. 5) a clear impact of the chemotherapeutic agents can be observed, too. The effect also becomes visible after about 8 hours past the beginning of the experiment.

The two different concentrations can be distinguished clearly, too. 2 uM of Doxorubicin lead to a decrease of 10 %, while 5 uM trigger a decrease of about 20 % of the initial value.

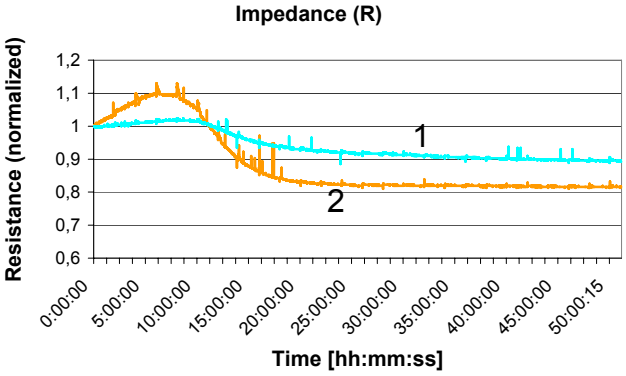


Fig. 5 Impedance values (resistive part) for well #21 with 2 uM Doxorubicin (1) and well #17 treated with 5 uM Doxorubicin (2)

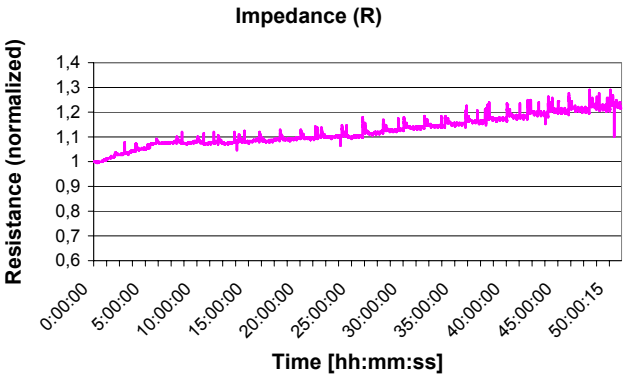


Fig. 6 Impedance values (resistive part) for well (#12) without added drug

As seen in the oxygen uptake values a persisting upward trend throughout the experiment is visible for the no-drug-well (Fig. 6).

In this section only results from Doxorubicin were shown. The very same results were achieved with Cisplatin, but these are omitted here to concentrate on the main information.

IV. Discussion

The impact of the used drugs on the cellular metabolism could clearly be shown using the oxygen uptake rate as well as the acidification rate (not shown above). Also, morphological changes could be detected using impedance sensing. As stronger cellular adhesion to the plate increases resistive impedance values, a growing and more and more strongly adhering cell population could be monitored in the control wells.

Whereas in treated wells, the drug impact becomes effective after a time span of about 8 hours. The reason for this is the time needed to accumulate the agent inside the cells. Then apoptosis is induced when cells try to divide.

This effect can be observed both in the decreasing metabolic activity as well as in a lower resistive part of the impedance. Cells do not divide and apoptotic cells do not adhere to the ground anymore.

V. CONCLUSIONS

The known chemosensitivity of MCF-7 cells towards Doxorubicin and Cisplatin could be observed using the IMR-System, thus showing the system's ability to detect the sensitivity of cellular samples towards specific drugs.

The next steps will be the large scale testing of human tissue samples and the statistical analyses of experimental outcomes with real treatment results.

If a sufficiently high correlation between in-vitro testing and in-vivo results is achieved a new and powerful means for the improvement of cancer treatment will be available.

ACKNOWLEDGMENT

We would like to thank the Bundesministerium für Bildung und Forschung (BMBF) as well as the HP Medizintechnik GmbH for their support.

REFERENCES

1. Brischwein M, Motrescu ER, Otto AM, Cabala E, Grothe H, Wolf B (2003) Functional cellular assays with multiparametric silicon sensor chips. Lab Chip 3(4):234–240
2. Wiest J et al (2005) Cellular assays with multiparametric bioelectronic sensor chips Chimia 59:243–246
3. Brischwein M, Grothe H, Otto AM, Stepper C, Motrescu E, Weyh T, Wolf B (2004) Living cells on chip: bioanalytical applications. In: Mirsky VM (ed) Ultrathin electrochemical chemo- and biosensors. Springer, Berlin, pp 159–180

Author: Bernhard Becker
Institute: Heinz Nixdorf-Lehrstuhl der TU München
Street: Theresienstr. 90 Geb. N3
City: 80333 München
Country: Germany
Email: becker@tum.de

A novel fabrication route to integrating label-free detection of DNA hybridization in microfluidic channel

J.H. Jiang[1], M.L.Bo[1], D.C. Jiang[1], J Wang[1], L. Yang[1], K.-L. Paul Sung[2]

[1] Key Laboratory of Biorheological Science and Technology, Ministry of Education, Bioengineering College, Chongqing University, Chongqing, 400044, China

[2] Departments of Bioengineering and Orthopedics, University of California, San Diego, CA, 92093-0412, USA

Abstract— **We present a fabrication technique to achieve label-free detection of DNA hybridization in microfluidic channel. The label-free detection is based on the electrochemical response of DNA hybridization events on ssDNA doped polypyrrole(PPy)-modified microelectrodes within microfluidic channels. Firstly, the metal microdot(s) as the microelectrodes naked on the inner wall of a microchannle could be made by molding crossed microwires in PDMS via withdrawing and remaining; then a film of PPy and ss-DNA probes is simultaneously electrochemical synthesized on the dot(s) within the microchannle. The label-free detection in thus-formed prototype microchannel device is demonstrated by carrying out hybridization experiments. The described fabrication route enables a fully electronic readout of DNA hybridization events being closely integrated with microfluidic manipulation, rather conveniently and cost-effective.**

Keywords— **polypyrrole, microchannel, label-free detection, soft-lithography, DNA hybridization**

I. Introduction

So far, there have been developed a variety of techniques for enhancing the DNA hybridization and clearly reporting its completion. Among these, two emerging technological goals are being hot pursued, one is to carry out DNA hybridization experiments under microfluidics[1-3] for greatly reducing not only the amounts of regents but also the reaction time; another is to label-free read out the signals of hybridization for avoiding the usage of expensive and time-consuming labeling and fluorescence read-out strategies, and also minimizing the worry that the label itself may alter the binding interaction[4-5]. Many label-free methods such as surface plasmon resonance[6], quartz crystal microgravimetry[7], electrochemical sensing[8-10], fluorescent polymers[11], atomic force microscopy[12], microcantilevers[13], electronic depletion of a field effect transistor[14] and electrostatic repulsion microspheres [15] have been introduced in efforts to circumvent some of the problems inherent to chemical labeling. However, none of these have gained widespread use because each requires either complex device fabrication or sophisticated instrumentation for read-out. In these aspects, the electrochemical and/or electrostatic routes seem to be much promising. For example, a variety of polypyrrole-based electrochemical detection techniques have been proposing towards DNA hybridization label-free readout[16-19].

Moreover, with the rapid advances in microfluidics and microfabrication fields, some label-free detection techniques, e.g. CMOS transistor[20], surface plasmon resonance imaging [21], and electrochemical means [22-23], are being miniaturized and integrated into DNA analytical microfludic devices.

In this paper, we present an easily fabrication technique towards the closely integration of PPy-based label-free detection of DNA hybridization with microfluidical channel.

II. Exprimental methods

There were two main steps taken for the preparation of the above-mentioned microfluidic devices which included PPy-modified microdot(s) in microchannel, and then the DNA hybridization tests could be performed on the base of such microdevice.

A. *The fabrication of microdot(s) in microchannel*

In order to form metal microdot(s) in the inner wall of a microchannel, we use our previously described soft-molding technique route[24], in which its main idea was briefly summarized as that one perfect circle microchannle in PDMS could be realized by just micromolding and withdrawing one piece of microwire. Similar strategy has been taken for the purpose here, two or more pieces of microwires were molding into PDMS block to make them crossing inter-contacted with each other, and then one of them being removed out, the dot(s) crossing on the remaining wire(s) in PDMS would be naked on the inner wall of micro-channel left by the removed one.

The sub-steps of the process were described as following: (i) Aligning cross microwires: The clean microwires (~20-100μm diameter, type 316L stainless steel, commercial available) were aligned on a glass slide, displaying cross-contacted with each other. On them, a specially house-made pane-shaped PMMA ancillary supporting frame was covered and fixed. (ii) Then liquid PDMS (pre-polymer: curing agent = 10:1 w/w, Sylgard 184, Dow Coning Co., Midland, MI, USA) was poured into, and allowed the deployed microwires immerged in. Then PDMS with the immerged cross-aligning microwires was degassed in vacuum and cured for about 2 h at 60.℃. (iii) After curing, the PDMS block with microwires was placed into ethanol pool for a while to swell slightly and wetting the interface,

O. Dössel and W.C. Schlegel (Eds.): WC 2009, IFMBE Proceedings 25/VIII, pp. 140–143, 2009.
www.springerlink.com

then one of the microwires bcured in the PDMS block was drawn out with gentle force, and therefore leading to the formation of microchannel in the PDMS block, and while on the site(s) of the remaining wire(s) cross-contacted by the removed one would be naked in the thus-forming microchannel. Furthermore, small holes (about 0.5-2 mm in diameter) could be pounched vertically to communicats with the inner PDMS channel and they could provide tubing interfaces to chip -to- world; meanwhile the two ends of the remaining wire(s) could be used as leads for loading electricity. The schematic drawing of the preparation process were shown in Fig.1.

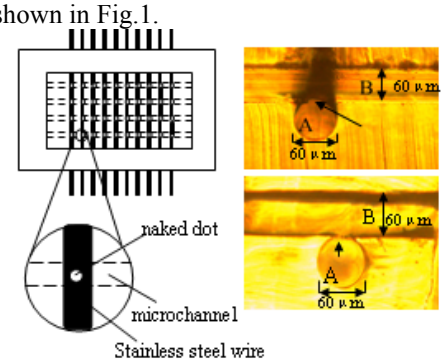


Fig. 1 The preparation of the microdot(s) in microchannel(s)

B. The synthesis of ssDNA doped PPy film on the microdot in microchannel

Before carrying out the synthesis, the above thus-fabricated microdevice should be tubing interfaced onto our own custom-made external microfluidic facilities including high pressure nitrogen source and its regulation valve system, temperature modulation system and placed under an inverted microscopy equipped with CCD camera (Leica DMI 4000B, Germany), and also be linked on three-electrode electrochmical system (CHI 800, CHI, Chenhua, Shanghai, China).

Firstly, introducing diluted PDMS precursor solution (no curing agent) (say, 0.006g PDMS dissolving in 1.8ml THF) into the microchannel pumped with suitable N_2 pressure. This step was expected PDMS film to be deposited onto the metal microdot.

Next, introducing a mixture of oligonucleotide (poly(A_{10}) 1.8nM/ml, Shanghai Sangon Co.Ltd, China) and pyrrole(0.2M, Sinopharm Chemical Reagent Co.Ltd China) and switched on the electrochemical system to carry on the cyclic voltammetric(CV) polymerization of them onto the microdot in microchannel, which was coated on a thin PDMS film in the last step. In this electrochemical process, the microdot linking lead of microwire embedded in PDMS block was used as the working electrode, Pt wire was the counter-electrode, saturated calomel electrode (SCE) as the reference electrode. Its main parameters were as follows: E(V):0~1.2, Scan Rate(V/S):0.01.

C. The hybridization on the ssDNA doped PPy-modified microdot in microchannel

The hybridization events were performed while tracking by CV tests once introducing hybridization solution (SDS 0.5%, 6×SSC, PBS: 0.067M, pH 7.0) containing complementary poly (T_{10}) (1.8 nM/ml) into the above formed microchannel device, under option temperature.

III. RESULTS AND DISCUSSTION

A. The features of the microdot in microchannel

In order to understand the shape and size of the naked microdot formed in the microchannel, we removed all two microwires crossed in the cured PDMS block, and observed the through-holes under the microscopy. The shape of the holes were found to be perfect round as long as the two crossed-microwires were at the same size (Fig.2), and their ubiety in the PDMS block were shown in Fig.1. The diameters of them were measured as seen in Table 1.

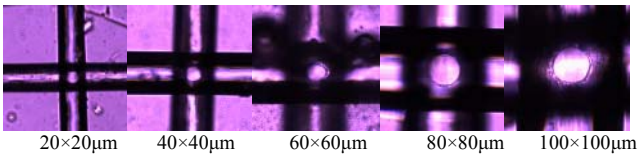


Fig. 2 The through-holes left after removing two cross-contacted microwires in PDMS block

Table 1 The diameters of the through-holes

Size of microwires in crossing (μm)	Diameter of through-hole(μm)	Case numbers
20×20	5.86±1.96	162
40×40	15.00±4.28	340
60×60	17.80±4.21	129
80×80	24.20±8.56	229
100×100	26.45±6.55	157

B. The immobilization of ssDNA in PPy-modified microdot

Before hybridization examination, the known DNA probe should be immobilized on the electrode i.e. the microdot so as to carry on electrochemical test. For achieving this, we firstly introduced the solution of PDMS precursor dissolved in THF via capillary suction into the microchannel. With THF volatilization, there would be deposited a thin film of the PDMS precursor on the bottom wall of the microchannel including the microdot(s). We found it was facilitated the PDMS deposition on when applied a driving pressure of 7.0-9.0kPa in channel. The thickness of such deposited PDMS film was estimated about 2.37μm.

Then, the mixture of ssDNA and pyrrole could be injected into and be given CV monitoring. The ssDNA strands would be entrapped into at the same time the polypyrrole film was formed onto the microdot in microchannel, which

was coated on a thin PDMS film in the last step. In fact, thus-forming hybrid film was robust enough in the microfluidical experiment condition. On one hand, the polypyrrole film was a suitable 3-D network for the keeping ssDNA strands[25], on the other hand, the attachment strength of PPy film onto the microdot could be enhanced by PDMS as the PDMS had cross-linked with them and the surrounding PDMS walls[data not shown]. And there had evidence that under electrochemical potential py monomers could reach to the metal surface of the microdot via penetrating into the PDMS film formed advanced[26]. Furthermore, ssDNA has been demonstrated to be easily entrapped [19,25] in and as a sole dopant [27] in PPy film. Finally, the successfully hybridization signal differentiation in our experiments as following also supported this process.

C. The electrochemical tracking detections before and after DNA hybridization on the microdot in PDMS microchannel

The typical results of the cyclic voltammetric tracking from pyrrole polymerization and ssDNA entrapment to hybridization on the microdot are as shown in Fig.3. The cause of A→B represents the current change of the mixture of poly(A_{10})/pyrrole with the cyclic numbers at room temperature (RT). Note that all current values were collected when the potentials reached at the largest in one of any cycles (the same as following). B→C is during the incubation time (20min) at 43℃ when at B the complementary poly(T_{10}) –contained hybridization solution was introduced into the above same microchannel. C→D represents the current change with the cyclic numbers during which the temperature was reduced from 43℃ to RT. E→F is the case of introducing into fresh hybridization solution after washing out the hybridized one at RT. G→H is the case of introducing again the fresh mixture of poly(A_{10})/pyrrole after washing out old solution at RT. I→J the case of introducing again the fresh complementary poly(T_{10}) –contained hybridization solution after washing at RT. All injection velocity was ~0.167m/s when changing solutions. All the phases was done in the same microchannel, that is, on the same microdot.

Seen from these causes that only the hybridization event occurring at C when incubation at optimal 43℃ could be captured as the highest peak. Compared B→C with H→I, it could be found that the current signal at C when in hybridization increased 32.03 times of the basic current signal at B; In contrast, the current signal at I when in RT increased only 3.51 times of that of at B (see Fig.4). These results showed that the hybridization events on thus-modified microdot in microcannel could enlarge the currents in C-V curves, and the optimal hybridization temperature could also significantly promote this peaking behaviour. It could be believed that this current peaking behaviour is closely related the hybridization event at optimal temperature.

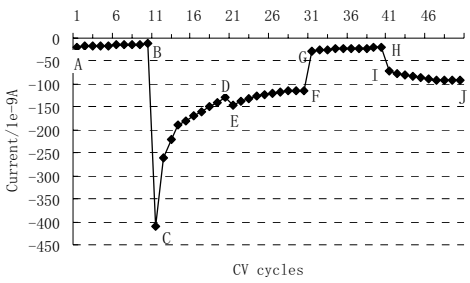


Fig. 3 The current changes during different phases from pyrrole polymerization and ssDNA entrapment to hybridization with the causes of CV cycles in the same one microchannel

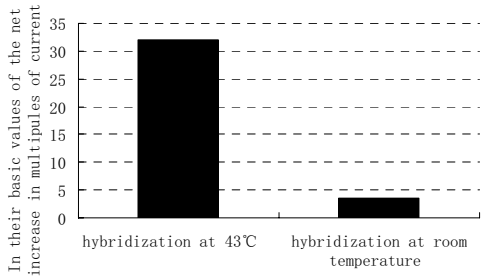


Fig. 4 The increased current peak values at different temperatures when provided the same other hybridization condition

IV. CONCLUSIONS

In this paper, we demonstrated an easy and low-cost fabrication method to the integration of PPy-modified electrode in microchannel, meanwhile, the DNA immobilization and hybridization could be also performed following. Although much work should be added, the marriage of microfluidics with detection technologies such as this will no-doubt provide improvements in miniaturization of bioanalytical methods.

ACKNOWLEDGMENT

This paper was supported by the Key Project for International Science and Technology Collaboration of the Ministry of Science & Technology (2005DFA00190), by NSFC Grant (30870607), CSTC Grant (2008BB5192), and "111 Project" (B06023)

REFERENCES

1. Chung YC, Lin YC, Chueh CD, et al (2008) Microfluidic chip of fast DNA hybridization using denaturing and motion of nucleic acids, Electrophoresis, 29(9): 1859-1865
2. L. Chena, S. Leea, M. Leea, et al (2008) DNA hybridization detection in a microfluidic channel using two fluorescently labelled nucleic acid probes, Biosensors and Bioelectronics, 23:1878–1882

3. Janne Pullat, Wlad Kusnezow, Kaie Jaakson, et al (2008) Arrayed primer extension on in situ synthesized 5'-3' oligonucleotides in microchannels, New Biotech, 25(2/3):133-141
4. Michael Seidel & Reinhard Niessner (2008) Automated analytical microarrays: a critical review, Anal Bioanal Chem 391:1521–1544
5. Rebecca L. Rich, David G. Myszka (2007) Higher-throughput, label-free, real-time molecular interaction analysis, Anal Biochem 361:1–6
6. Alex Ieng Kin Lao, Xiaodi Su and Khin Moh Moh Aung (2009) SPR study of DNA hybridization with DNA and PNA probes under stringent conditions, Biosensors and Bioelectronics, in Press
7. Zhu L, Gao Y, Shen H, Yang Y, et al (2005) A quartz crystal microbalance (QCM) study of single-strand DNA hybridization and hydrolytic cleavage, Journal of Analytical Chemistry, 60(8):780-783
8. Mònica Mir, Ioanis Katakis (2008) Target label-free, reagentless electrochemical DNA biosensor based on sub-optimum displacement, Talanta 75: 432–441
9. Fan, C., Plaxco, K.W. & Heeger, A.J. (2003) Electrochemical interrogation of conformational changes as a reagentless method for the sequence-specific detection of DNA. PNAS, 100: 9134–9137
10. Drummond, T.G., Hill, M.G. & Barton, J.K. (2003) Electrochemical DNA sensors. Nat. Biotechnol. 21:1192–1199
11. Nilsson, K.P. & Inganas, O. (2003) Chip and solution detection of DNA hybridization using a luminescent zwitterionic polythiophene derivative. Nat. Mater. 2: 419–424
12. Zhou, D., Sinniah, K., Abell, C. & Rayment, T. (2003) Label-free detection of DNA hybridization at the nanoscale: a highly sensitive and selective approach using atomic-force microscopy. Angew. Chem. Int. Ed. 42: 4934–4937
13. Zhang J, Lang HP, Huber F, et al. (2006) Rapid and label-free nanomechanical detection of biomarker transcripts in human RNA. Nat. Nanotechnol. 1: 214–220
14. Kamahori, Masao, Ishige, Yu, Shimoda, Maki (2008) Detection of DNA hybridization and extension reactions by an extended-gate field-effect transistor: Characterizations of immobilized DNA-probes and role of applying a superimposed high-frequency voltage onto a reference electrode, Biosensors & Bioelectronics, 23(7):1046-1054,
15. Nathan G. Clack, Khalid Salaita, and Jay T. Groves. (2008) Electrostatic readout of DNA microarrays with charged microspheres. Nature Biotechnology, 26(7):825-830,
16. Chaker Tlili, Nicole J. Jaffrezic-Renault, Claude Martelet, et al. (2008) Direct electrochemical probing of DNA hybridization on oligonucleotide-functionalized polypyrrole, Materials Science and Engineering C 28: 848–854
17. Sungrok Ko, Jyongsik Jang (2008) Label-free target DNA recognition using oligonucleotide-functionalized polypyrrole nanotubes, Ultramicroscopy 108:1328– 1333
18. Bouchet A, Chaix C, Marquette CA, et.al (2007): Cylinder-shaped conducting polypyrrole for labelless electrochemical multidetection of DNA, Biosensors & Bioelectronics, 23(5):735-740
19. Arora Kavita, Prabhakar Nirmal, Chand Subhash, et al.(2007) Immobilization of single stranded DNA probe onto polypyrrole-polyvinyl sulfonate for application to DNA hybridization biosensor, Sensors And Actuators B-Chemical, 126(2): 655-663
20. M. Barbaro, A. Caboni, and D. Loi (2007) A cmos integrated circuit for DNA hybridization detection with digital output and temperature control, Proc. of 3rd IEEE Conference on Ph.D. research in Microelectronics and Electronics, 2007, pp. 137–140
21. Lidija Malic, Teodor Veres, Maryam Tabrizian (2009) Biochip functionalization using electrowetting-on-dielectric digital microfluidics for surface plasmon resonance imaging detection of DNA hybridization, Biosensors and Bioelectronics, in press
22. Zhiwei Zou, Junhai Kai, Michael J. Rust, et al. (2007) Functionalized nano interdigitated electrodes arrays on polymer with integrated microfluidics for direct bio-affinity sensing using impedimetric measurement, Sensors and Actuators A, 136:518–526
23. Peter M. Levine, Ping Gong, Rastislav Levicky, (2008) Real-time, multiplexed electrochemical DNA detection using an active complementary metal-oxide-semiconductor biosensor array with integrated sensor electronics, in press, doi:10.1016/j.bios.2008.10.012
24. Jia Yuefei, Jiang Jiahuan, Ma Xiaodong, et al. (2008) PDMS microchannel fabrication technique based on microwire-molding, Chinese Science Bulletin, 53(24):3928-3936
25. Prabhakar Nirmal, Arora Kavita, Singh Surinder P. et al. (2007) DNA entrapped polypyrrole-polyvinyl sulfonate film for application to electrochemical biosensor, Analytical Biochemistry, 366(1): 71-79
26. Güliz Çakmak, Zuhal Küçükyavuz, Savas Küçükyavuz, et al. (2004) Mechanical, electrical and thermal properties of carbon fiber reinforced poly(dimethylsiloxane)/polypyrrole composites . Composites: Part A, 35:417–421
27. Joseph Wang, Mian Jiang, Antonio Fortes, et al. (1999) New label-free DNA recognition based on doping nucleic-acid probes within conducting polymer films, Analytica Chimica Acta, 402:7–12

Author: Jiahuan Jiang
Institute: Bioengineering College, Chongqing University
Street: Shazheng Street, Shapingba
City: Chongqing
Country: China
Email: jhuan@cqu.edu.cn

Concept of a Microfluidics and Tunneling Effect-Based BioMEMS to Detect Cells

Shengbo Sang, Ulrike Fröber, and Hartmut Witte

Department of Biomechatronics, Ilmenau University of Technology, Max-Planck-Ring 12, Ilmenau D-98693, Germany

Abstract— **A new concept of Biological Micro-Electro-Mechanical Systems (BioMEMS) based on tunneling effect and microfluidics to detect cell is proposed in this paper. It is multilayer structure, one layer is microfluidics and another is tunneling effect-based biosensor. And its key sizes refer to the cell size that will be detected, such as hepatocyte. The crucial material of the BioMEMS is PDMS. The electrokinetic method used to manipulate the cell in microchannel and three main factors (the effective weight of cell, the fluid static pressure and the fluid dynamic pressure) affecting the deformation of membrane have been analyzed and simulated using Ansys® software. The maximum deformation is -0.31 *nm* resulting from the effective weight of hepatocyte in the Z direction when the thickness of membrane is 70 *nm* (PDMS: 60 *nm*, Au: 10 *nm*). At the same condition, the deformations approximate to zero resulting from the fluid static pressure and dynamic pressure. The results prove that the main detection information is from the detected cell and the structure is feasible. This will be a more sensitive and original BioMEMS.**

Keywords— **BioMEMS, microfluidics, tunneling effect, electrokinetics, PDMS, simulation**

I. Introduction

BioMEMS is a heavily researched area with a wide variety of important biomedical applications [1], such as area of research and application in molecules and cells. Professor J. Voldman performs research on BioMEMS, applying microfabrication technology to illuminate biological systems, especially at the cellular level [2]. M. Manimaran *et al.* designed a BioMEMS based microfluidic device as a deformation assay to study the deformability and growth capability of cells through microgaps [3]. A 2-D microcantilever array for multiplexed biomolecular analysis has been researched by M. Yue *et al.* [4]. In general, a BioMEMS is developed made of Microfluidics and Biosensor. Microfluidics provides a powerful platform for biological assays. Examples of bioassays and biological procedures that have been miniaturized into a chip format include cell or molecule counting, cell or molecule sorting, cell or molecule culture, DNA sequencing, polymerase chain reaction (PCR), electrophoresis, DNA separation, enzymatic assays and immunoassays [5–7]. Biosensor offers a way to detect the information of analyte. The tunneling effect was firstly used in the scanning tunneling microscope (STM) in 1986 by Binnig and Rohrer. Subangstrom changes in displacement will induce measurable changes in tunnelling current. This high sensitivity is independent of the lateral size of the electrodes because the tunneling current occurs between two metal atoms located at the opposite electrode surfaces [8–11]. In this paper, a new concept of cell detection BioMEMS based on Microfluidics and Tunneling Effect is proposed.

II. Structure

The BioMEMS studied thoroughly in the paper is a multilayer structure (Fig.1a), one layer is microfluidic structure, and another layer is tunneling effect-based biosensor. Fig.1a is the micromembrane-based tunneling effect biosensor and Fig.1b is the microcantilever-based tunneling effect biosensor. The key sizes of the BioMEMS are based on the size of a detected hepatocyte (diameter is about 16 µm), hence, the membrane is 20 μm × 20 μm (length × width). The microfluidics consists of inlet, outlet and microchannel. The gold is used as electrode.

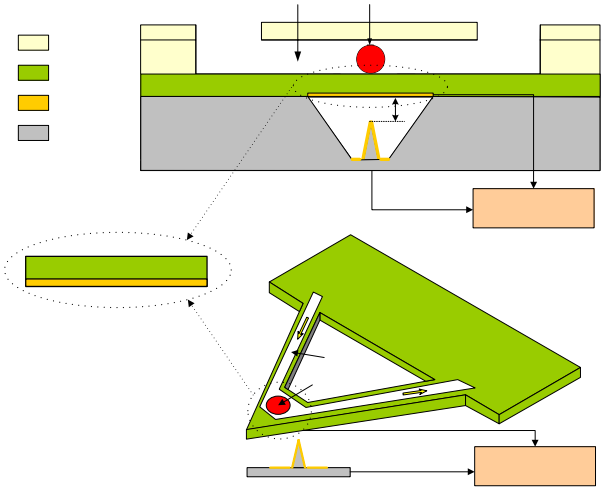


Fig.1 The concept structure of the BioMEMS (two kinds: a and b)

Many handling techniques can be used to manipulate cells or molecules in microchannel, the electric field-based approach is well suited for miniaturization because of relative ease of microscale generation and structuring of an

O. Dössel and W.C. Schlegel (Eds.): WC 2009, IFMBE Proceedings 25/VIII, pp. 144–147, 2009.
www.springerlink.com

electric field on microchip. Three different electrokinetic forces can be employed: electroosmosis [12], electrophoresis [13] and dielectroporesis [14]. Fig.2 is the distribution of electrodes on the bottom wall of the BioMEMS (Fig.1a) studied in the paper. Six electrodes are used to load the solution and cell, trap and fix single cell when they are exerted voltage at different time.

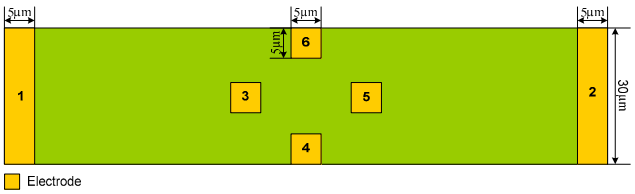


Fig.2 The bottom wall of microchannel in the system (Fig.1a)

Polydimethysiloxane (PDMS) is a biocompatibility transparent material, convenient for direct morphological observations of the cells under a microscope. Also, it has lower stiffness to deflect and high gas permeability suitable to the cell culture for the oxygen supply in closed microdevices. Therefore, it will be used as the material of crucial part, such as membrane, of the BioMEMS. The submaterial of tunnelling effect-based sensor is silicon owing to its mature technology. The glass can be as the microfluidic material.

III. THEORY

1. The tunneling effect

Because the electron has wave and ion characteristics, if a small bias voltage, typically 100 mV, is applied between a sharp conducting tip and a conducting thin film, when the tip and the upper thin film are brought to within 10Å of each other, a tunneling current can flow due to quantum mechanical tunneling effects. The tunneling current is exponentially dependent on the separation between the tip and the upper thin film. The equation for the resulting current is of the form [15]:

$$I = I_0 e^{\left(-\beta\sqrt{\phi}x\right)} \quad (1)$$

Where

I = tunneling current,

I_0 = a constant, relative to material and the tip shape

β = tunneling constant, typically $10.25\sqrt{eV}/nm$

x = separation

ϕ = tunneling barrier, typically $0.5eV$

The detailed theory can be seen in references [16, 17].

2. The electrokinetic method to load the cells

When liquid solution fills a channel, an electric double layer will exist in the interface between liquid and solid. This layer consists of the negative ions of the walls and the positive ions of the solution, attached to each other. If the inlet (electrode 1) and the outlet (electrode 2) of channel is connected to the positive and negative voltage respectively, then the positive ions of solution in the electric double layer will be attracted to the outlet (Fig.3). And the solution and cells will flow toward the outlet by a certain velocity.

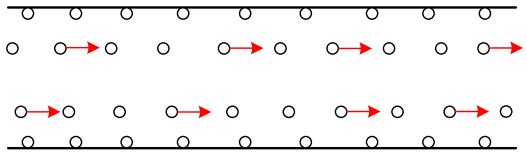


Fig.3 The schematic diagram of fluid using electrokinetic method

3. The method to trap single cell

When the polarized cell moves to the membrane, the four electrodes (electrode 3, 4, 5, 6) shown in Fig.2 are exerted different polar voltage, it will be trapped and fixed in the centre of membrane due to the distribution of electric field on the membrane (Fig.4). It can be seen from Fig.4 that the electric field is smallest in the centre of membrane and the polarized cell will be stabilized in the centre when it locates on the membrane based on the theory of electric field.

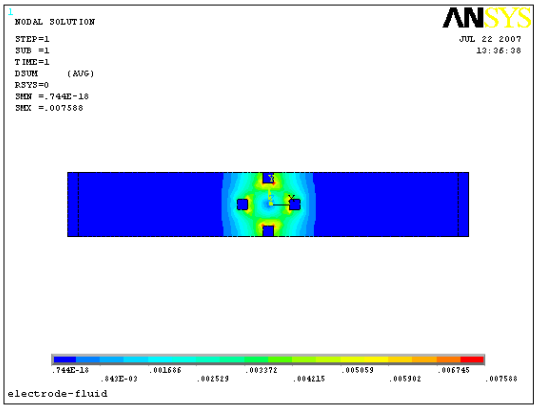


Fig.4 The distribution of electric field in the membrane

IV. THE ANALYSIS AND SIMULATION OF THE EFFECTS ON MEMBRANE

The weight of cell, the fluid static pressure and the fluid dynamic pressure are three main factors to affect the deformation of membrane. In this analysis, the cell is hepatocyte.

1. The first factor: the weight of hepatocyte

The mass of a cell is typically more than 70% water [18], that is to say,

$$M_{water}/M_{wholecell} = 70\% \quad (2)$$

If there is all water in hepatocyte, the mass can be gotten based on the formula:

$$m = 4\rho\pi r^3/3 \quad (3)$$

ρ : the density of water, r : the radius of hepatocyte (about 8 μm) and it is supposed a sphere

The effective weight (F) acting on the membrane is:

$$F = F_1 - F_2 \quad (4)$$

$F_1 = gm_{\text{whole cell}}$: the weight of hepatocyte, $F_2 = \rho vg$: the buoyancy

Based on the formulas (2)(3)(4), the effective weight acting on membrane can be gotten: 8.9964e-12 N.

The deformation of membrane has been simulated when the cell locates on it using Ansys® software. The membrane is made of two layers just like shown in Fig.1: PDMS and Au (Gold). To get perfect result, different thicknesses of membrane: (the PDMS thickness: 60 *nm,* the Au thickness: 10 *nm*), (80 *nm*, 10 *nm*), (50 *nm*, 20 *nm*), (60 *nm*, 20 *nm*), (80 *nm*, 20 *nm*), (100 *nm*, 20 *nm*) and (120 *nm*, 20 *nm*) have been simulated. Fig.5 is the series of simulated results when the effective weight acting on different thicknesses of membrane. With the increase of the PDMS thickness and constant thickness of Au-layer, the deformation becomes smaller. The maximum deformation is -0.31 *nm* in the direction Z when the membrane is (60 *nm*, 10 *nm*), Fig. 6, which is rather large relative to the distance between the membrane and the needle tip (1 *nm* =10Å).

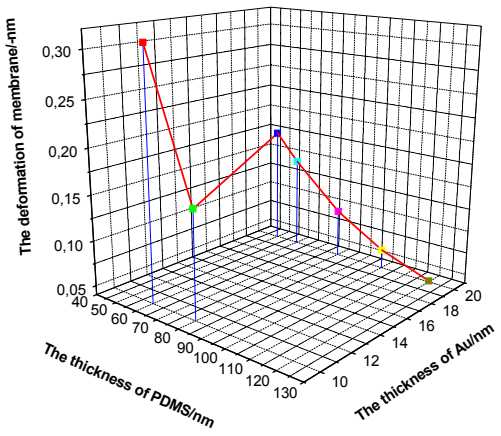


Fig.5 The deformation of membrane as the function of membrane thickness

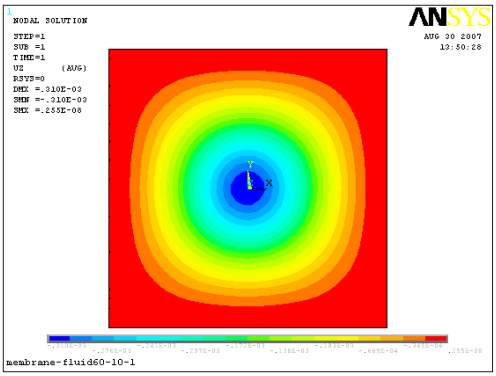


Fig.6 The deflection of (60 *nm*, 10 *nm*) membrane in the Z direction due to the effective weight of hepatocyte

2. The second factor: the fluid static pressure

When the cell is manipulated in the microchannel, the density of solution approximates the density of water. So, the density of solution can be assumed 1 g/cm^2. The fluid static pressure acting on the membrane is:

$$P = \rho hg = 0.245Pa \quad (5)$$

h: the height of the channel, 25 μm.

If the pressure exerts on the (60 *nm*, 10 *nm*) membrane, the maximum deformation is only -0.25×10^{-19} μm, which is quite small compared with the deformation resulting from the effective weight of cell, it can be neglected.

3. The third factor: the fluid dynamic pressure

Because the solution is dynamic, it can exert certain pressure on the bottom wall. In theory, the dynamic pressure is related to the fluid velocity. When the fluid velocity is assumed to be 2 $\mu m/s$, 5 $\mu m/s$, 10 $\mu m/s$, 15 $\mu m/s$, 20 $\mu m/s$ and 40 $\mu m/s$, the pressure on the membrane has been calculated and simulated; it becomes larger with the increase of fluid velocity, and the maximum value can reach to 0.08267 *Pa* when the fluid velocity is 40 $\mu m/s$. The deformation of membrane has been simulated using Ansys® software when the maximum pressure exerts on the easiest deformation membrane (60 *nm*, 10 *nm*), but the deformation approximates to zero and so the effect can also be neglected.

V. Conclusion

There are three main factors: the effective weight of cell, the fluid static pressure and the fluid dynamic pressure, affecting the deformation of membrane. And the fluid dynamic pressure is related to the fluid rate (fluid velocity). If the cell is hepatocyte, the maximum membrane deformation of the BioMEMS shown in Fig.1a is -0.31 *nm* in the Z direction when the thickness of membrane is 70 *nm* (PDMS: 60 *nm*, Au: 10 *nm*). At the same condition, the deformations approximate to zero resulting from the fluid static pressure

and the dynamic pressure. Which can be seen brightly in Fig.7, the comparison of the membrane deformation caused by the three factors, the vertical axis is $|\ln^{|D|}|$ (D: deformation, unite: *nm*) and the vertical value is inversely proportional to the deformation. Hence, the main information is the cell detection and the structure is feasible.

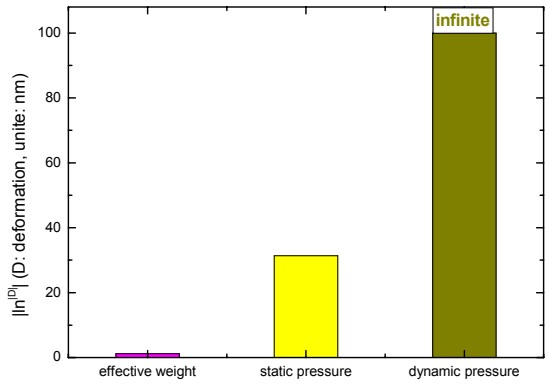


Fig.7 The comparison of the membrane deformation caused by the three factors

ACKNOWLEDGMENT

This research was supported by the Department of Biomechatronics, Faculty of Mechanical Engineering, Ilmenau University of Technology. We would like to thank Dr. Schiling for his useful advice to the paper.

REFERENCES

1. Maruo Ferrari (Ed.), Biomedical Nanotechnology, Vol. I-IV, Kluwer Academic Publishers, 2004,
2. http://www.rle.mit.edu/biomicro
3. M. Manimaran1, F.E.H Tay, K.C. Chaw, "Cell Deformation in Cancer Metastasis: a BioMEMS Based Approach", Journal of Physics: Conference Series 34, 2006, pp.1143–1147
4. Min Yue et al. "A 2-D Microcantilever Array for Multiplexed Biomolecular Analysis", Journal of Microelectromechanical Systems, Vol.13, No.2, 2004, pp.290-299
5. Auroux, P. A., Iossifidis, D., Reyes, D. R., Manz, A., Anal. Chem. 74, 2002, pp.2637–2652
6. Beebe, D. J., Mensing, G. A., Walker, G. M., Annu. Rev. Biomed. Eng. 4, 2002, pp.261–286
7. McDonald, J. C., Whitesides, G. M., Acc. Chem. Res. 35, 2002, pp.491–499.
8. P. Scheeper, J. K. Reynolds, and T.W. Kenny, "Development of a modal analysis accelerometer based on a tunneling displacement transducer," in Int. Conf. Solid-State Sensors and Actuators, Proc., vol. 2, 1997, pp. 867–870.
9. R. L. Kubena, G. M. Atkinson, W. P. Robinson, and F. P. Stration, "A new miniaturized surface micromachined tunneling accelerometer," IEEE Electron Device Lett., vol. 17, 1996, pp. 306–308
10. C. Yeh and K. Najafi, "A low-voltage bulk-silicon tunneling based accelerometer," in Technical Digest, IEEE Int. Electron Devices Meeting (IEDM), Washington, DC, Dec. 1995, pp. 593–596.
11. T.W. Kenny, W. J. Kaiser, S. B.Waltman, and J. K. Reynolds, "A novel infrared detector based on tunneling displacement transducer," Appl. Phys. Lett., vol. 59, 1991, pp. 1820–1822
12. Nazmul Islam and Jie Wu, "Microfluidic Transport by AC Electroosmosis. Journal of Physics: Conference Series 34, 2006, pp.356–361
13. Chan S. Oh "Microfluidic electrophoresis device", US Patent Issued on May 18, 1999, No. 814755 filed on 1997-03-07
14. Ju Hun Yeon & Je-Kyun Park, "Microfluidic Cell Culture Systems for Cellular Analysis", BIOCHIP JOURNAL, Vol. 1, No. 1, 2007, pp.17-27
15. GREGORY T. A. KOVACS, "micromachined transducers sourcebook" , the McGraw-Hill Companies Inc. 1998
16. C. H. Liu, J. D. Grade, A. M. Barzilai, J. K. Reynolds, A. Partridge, H. K. Rockstad, and T. W. Kenny, "Characterization of a high-sensitivity micromachined tunneling accelerometer source," in Proc. Int. Conf. Solid- State Sensors and Actuators, vol. 1, 1997, pp. 471–472.
17. P. R. Scheeper, J. K. Reynolds, and T. W. Kenny, "Development of a modal analysis accelerometer based on a tunneling displacement transducer," in Proc. Int. Conf. Solid-State Sensors and Actuators, vol. 2, 1997, pp. 867–870.
18. Kensal E. van Holde, W. Curtis Johnson and P. Shing Ho, "Principles of Physical Biochemistry", PRENTICE HALL, Upper Saddle River, New Jersey, 1998: 11

Author: Shengbo Sang
Institute: Department of Biomechatronics / Faculty of Mechanical Engineering
Street: Max-Planck-Ring 12
City: Ilmenau
Country: Germany
Email: Shengbo.sang@tu-ilmenau.de

Simulation of Drug Release for the Development of Drug-Eluting Stents – Influence of Design and Manufacturing Parameters on Drug Release Kinetics

N.Grabow[1], S. Siewert[1], K. Sternberg[1], H. Martin[1] and K.-P. Schmitz[1]

[1] University of Rostock, Institute for Biomedical Engineering, Rostock-Warnemuende, Germany

Abstract— **The development of drug-eluting stents (DES) for the inhibition of in-stent restenosis is associated with extensive in vitro testing of the drug release behavior of DES prototypes. Even minor design changes or changes in the manufacturing process often require a large number of in vitro drug release studies to establish their influence on the drug release profile of the DES.**

Numerical analysis of drug release can contribute to the rationalization of the DES design phase, allowing for quick parametric changes in the model and delivering immediate results. In particular, parametric analyses of coating layer architecture, coating material behavior, layer thickness, and drug loading may tremendously reduce the need for prototype manufacture and time-consuming in vitro drug release studies.

In the present study, it is described, how a numerical model can be fitted to in vitro data, and how the influence of important design and manufacturing parameters on the drug release behavior of sirolimus eluting DES can be studied with numerical analysis.

Keywords— **drug-eluting stent, drug release kinetics, coating, finite-element-analysis**

I. Introduction

The development of drug-eluting stents (DES) requires the adaptation of drug release kinetics through a suitable design of the stent platform and the stent coating architecture in order to achieve the desired therapeutic effect [1].

In particular, drug release kinetics of DES and the local concentrations of the pharmaceutical ingredient eluted into the vascular tissue adjacent to the DES must be controlled such, that the maximum therapeutic outcome regarding the inhibition of in-stent restenosis is achieved.

In this context, numerical simulation of drug release behavior can support the design and manufacturing processes of DES. In particular, parametric studies of different DES coating designs, regarding coating layer architecture, coating material behavior, layer thickness, and drug loading, may be a valuable tool to reduce prototype manufacture and time-consuming in vitro drug release studies.

This study describes the simulation and parametric studies of a sirolimus-eluting DES system.

II. Materials and Methods

Stainless steel coronary stents (nominal dimensions = 3.0 x 13 mm) were coated with sirolimus-incorporated polyhydroxybutyric acid in a spray coating process (stent A, drug content = 15 %, nominal coating thickness = 6 µm). Stent B was additionally coated with a 10 µm thick drug-free top coating as a diffusion barrier for drug release retardation, see Fig. 1. The stents were expanded and subjected to an in vitro drug release study according to the conditions described in [2].

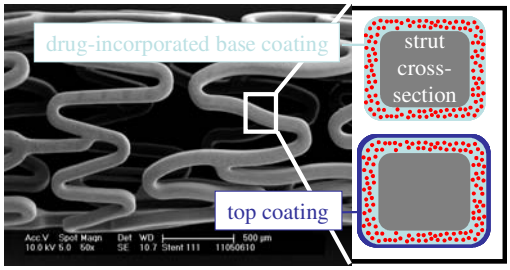


Fig. 1 Electron micrograph of a coated DES (left). Schematic drawing of the coating architecture with/without top coating (right).

For the simulation of drug release behavior, 2-dimensional finite-element-models of coated DES strut cross-sections were created according to the specifications of the manufactured DES prototypes. A transient mass diffusion analysis was performed with the finite-element software ABAQUS (6.4, HKS, Inc., Pawtucket, RI, USA). In a first step, the diffusion coefficients for the polymer matrix and the in vitro drug release medium were determined iteratively by fitting in vitro drug elution data to numerical results. Subsequently, further coating layer design variations and coating manufacturing influences were studied in parametrical simulations.

III. Results

Matching of simulation results with in vitro drug release data of stents A and B, after fitting of the diffusion coefficients in the numerical model, is shown in Fig. 2.

O. Dössel and W.C. Schlegel (Eds.): WC 2009, IFMBE Proceedings 25/VIII, pp. 148–149, 2009.
www.springerlink.com

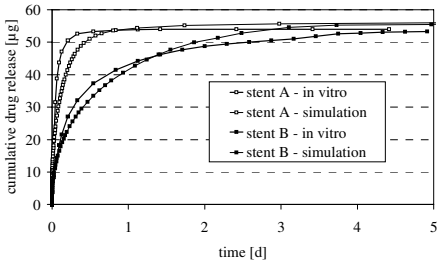


Fig. 2 Overlay of in vitro and simulated sirolimus release curves of DES without (stent A) and with (stent B) release retarding top coating.

Figure 3 shows representative simulated drug release curves for parametric coating design variations regarding top coating thickness and coating thickness distributions, according to Fig. 4.

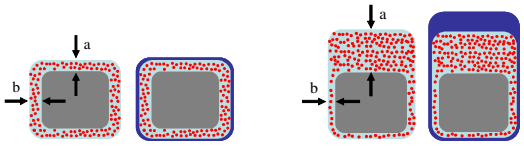


Fig. 4 Uniform coating thickness (a = b, left), and asymmetrical coating thickness distribution (a = 4b, right) in the base and top coating.

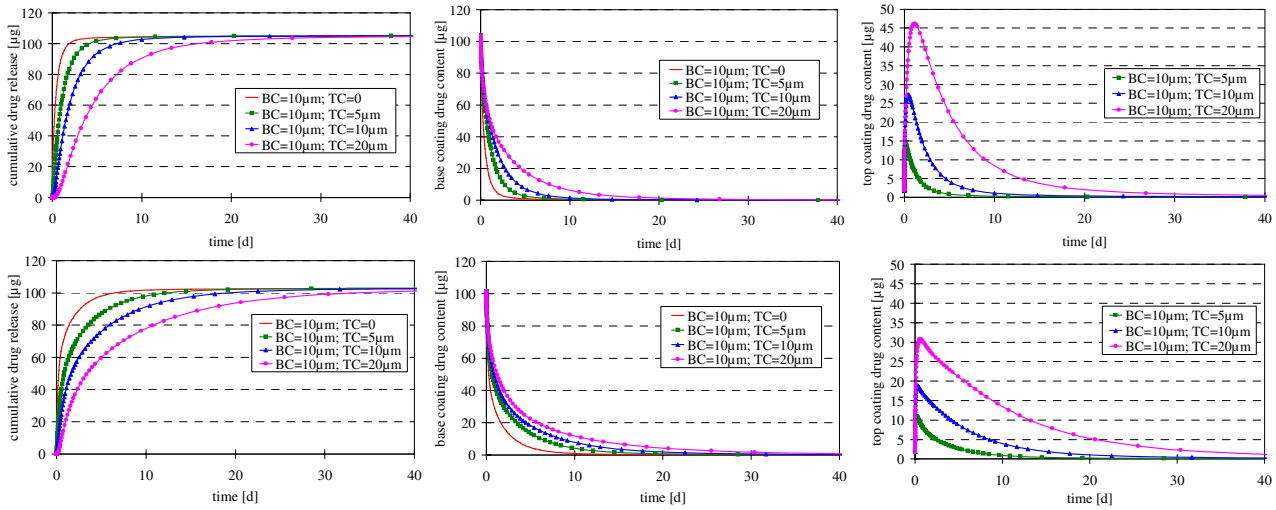


Fig. 3 Simulated drug release at a mean base coating thickness of BC = 10 µm, and a mean top coating thickness range of TC = 0 – 20 µm. The upper row showing results of a uniform coating thickness (a = b), the bottom row showing results of an asymmetrical coating thickness distribution (a = 4b), at constant mean coating thickness. The diagrams show cumulative drug release, drug content in the base coating, and drug content in the top coating (left to right).

IV. Discussion

After determination of the diffusion coefficients by fitting of simulation data to in vitro data, the model can be used to efficiently study influences of important design (layer architecture) and manufacturing parameters (thickness distribution) on the drug release behavior of sirolimus eluting DES. Deviation between in vitro data and simulations may be explained by coating thickness variations of the DES prototypes. Long-term effects on drug release, such as polymer degradation and water uptake, were not accounted for. In a next step, a 3D model shall be created, allowing for geometrical DES design optimization regarding uniform drug concentrations in the surrounding tissue.

Acknowledgment

The Landesregierung Mecklenburg-Vorpommern is gratefully acknowledged for financial support of the study within the program TF-MV, FKZ: V230-630-08-TFMV.

References

1. Schmitz KP, Grabow N, Löbler M et al. (2007) Drug-eluting stent technologies for vascular regeneration. Int J Mater Res 7:637-42
2. Sternberg K, Kramer S, Nischan C et al. (2007) In vitro study of drug-eluting stent coatings based on poly(L-lactide) incorporating cyclosporine A - drug release, polymer degradation and mechanical integrity. J Mater Sci Mater Med 7:1423-32

Address of the corresponding author:

Author: Dr.-Ing. Niels Grabow
Institute: Universität Rostock, Institut für Biomedizinische Technik
Street: Friedrich-Barnewitz-Str. 4
City: D-18119 Rostock-Warnemünde
Country: Deutschland
Email: niels.grabow@uni-rostock.de

Application of an Electronic Nose to Diagnose Liver Cirrhosis from the Skin Surface

K. Witt[1], T. Jochum[2], W. Poitz[3], K.J. Bär[2], and A. Voss[1]

[1] Department of Medical Engineering and Biotechnology, University of Applied Sciences Jena, Germany
[2] Department of Psychiatry, Friedrich-Schiller-University of Jena, Germany
[3] Jenasensoric e.V. Jena, Germany

Abstract—**The human body odor contains of different volatile organic compounds. In patients with liver cirrhosis and patients who are addicted to alcohol the compound of sweat and volatile gases are changed because of the liver dysfunction and remaining alcoholics and alcoholic decomposition products within the blood. This leads to changes of the metabolic balance. Therefore, the purpose of this study was to apply an electronic nose for detecting such metabolic changes at the skin surface. A special applicator was developed to collect and analyze the transpired dermal gases directly on the skin surface. The measured values were analyzed by principal component analysis and quadratic discriminant function analysis. We could show in a pilot study on 25 patients that an electronic nose is able to detect changes in the human body odor and to discriminate between healthy subjects (controls), patients with liver cirrhosis and primed alcoholic addicted patients.**

Keywords—**electronic nose, principle component analysis, liver cirrhosis, alcohol dependency, body odor.**

I. Introduction

An electronic nose represents a modular measurement system that detects volatile components with a sensor set. Sensors are the reactive part and might change their electrical properties in contact with volatile compounds. Such physical changes of the sensors are recorded and transform into an electrical signal.

Electronic noses are applied on many different fields. Interesting for life sciences are e.g. the quality control of food and the application in pharmaceutical industry [1, 2]. Today, the electronic nose have been used in a variety of medical fields, like the detection of mycobacterium tuberculosis in culture and sputum [3], diabetes [4], identification of schizophrenic patients [5], urinary tract infection [6, 7] and bacteria classification [8, 9]. The implementation of an electronic nose in the respiratory analysis showed a high sensitivity and specificity in the detection of lung cancer from exhaled breath [10, 11], asthma [12] and the detection from in vitro to diagnosis mycobacterium tuberculosis [13].

A special application of an electronic nose is the human body odor analysis directly from the skin. The metabolism changes the composition of secretion products from exocrine glands, and therefore, the compounds of volatile gases released by the skin. Diseases of the human organism, particular metabolism diseases, are often adjunctive with typical odors. Therefore the evidence of an ammonia odor could be a renal dysfunction [14] and a of acetone odor diabetes [15].

In this study we applied an electronic nose system based on doped semiconductor metal oxide gas sensors for investigating human body odor in patients with liver cirrhosis, alcohol addicted patients and healthy controls.

II. Methods

A. Patients

The body odor was investigated in 10 patients with liver cirrhosis, 7 alcohol addicted patients with an alcohol concentration between 0.2 and 3.5 ‰ and 8 healthy controls.

The patients and healthy subjects were recruited at the Department of Psychiatry Jena.

Table 1 shows the group mean values and standard deviations of age and BMI.

Table 1 Characteristics of the study population

Groups	N	age [years]	BMI [kg/m^2]
Healthy controls	8	50.88 ± 0.01	25.75 ± 3.65
Alcohol addicted patients	7	53.57 ± 5.32	28.38 ± 9.42
Patients with liver cirrhosis	10	53.50 ± 7.58	27.48 ± 4.71

The sensor head of the electronic nose was placed on the right crook of the arm. The measurements were performed between 9am and 2pm always in the same room. Sensor

O. Dössel and W.C. Schlegel (Eds.): WC 2009, IFMBE Proceedings 25/VIII, pp. 150–152, 2009.
www.springerlink.com

signals of 30 min duration (10 measuring cycles, each 3 min long) were recorded from each patient.

B. *Electronic nose system*

The electronic nose is mainly based on a metal oxide gas sensor placed within a chip holder (Fig. 1) and mounted within a special application tube. The gas sensor consists of an array of three thin oxide layer. This three thin oxide layer are the sensing elements with different sensitivities and selectivities at different temperatures for different gases.



Fig. 1 Sensor chip with sensor box

The interactions between molecules and the sensor array involve reactions on the sensor surface by changing their conductivity. These changes are continuously recorded, conditioned by an amplifier and control system and finally stored on a computer. The integrated platinum heater of the sensor allows operating from 192°C up to 400°C to adapt the sensor's sensitivity to different gas molecules. After each patient measurement the sensor was decontaminated providing comparable measuring conditions.

The structure of the applied electronic nose system is shown in Fig. 2.

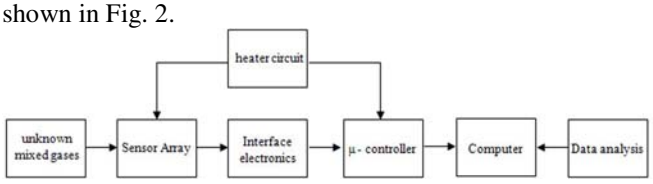


Fig. 2 Configuration of the applied electronic nose system

C. *Data Analysis*

The three sensor signals were analyzed by principal component analysis (PCA). This is an effective method to reduce the multidimensional data space to its main components and therefore improves the human perception ability of the data. PCA determines the linear combinations of the sensor values such that the maximum variance between all data points can be obtained in mutually orthogonal dimensions. This results in the largest variance between sensor values from the first principal odor component and produces decreasing magnitudes of variance from the second to the third and further odor components. To assess dissimilarities in the body odor we reduced in this pilot study the complete sensor signal's information to its first and second principal odor component.

Further on, quadratic discriminant analysis was applied as a statistical analytical technique to test the ability of the electronic nose system for separating the odor of healthy subjects from patients with liver cirrhosis and alcohol addicted patients. The variables used for this purpose are, as mentioned before, the first and second principal odor components.

D. *Results*

The subject characteristics of the 3 groups are shown in Fig. 3. The explained variances of the first two principal components account 97.58% and 2.05%. The cluster of healthy controls (black squares) can be separated from the cluster of patients with liver cirrhosis (red triangles) by quadratic discriminant analysis to 100%. The cluster of patients with liver cirrhosis (red triangles) can also be separated from the cluster of alcohol addicted patients (green crosses) by quadratic discriminant analysis to 100%. Furthermore, it could be demonstrated that the 1st and 2nd principal odor compound differentiate between healthy controls and alcohol addicted patients (green crosses) by quadratic discriminant analysis to 85.71%. Only one patient was misclassified.

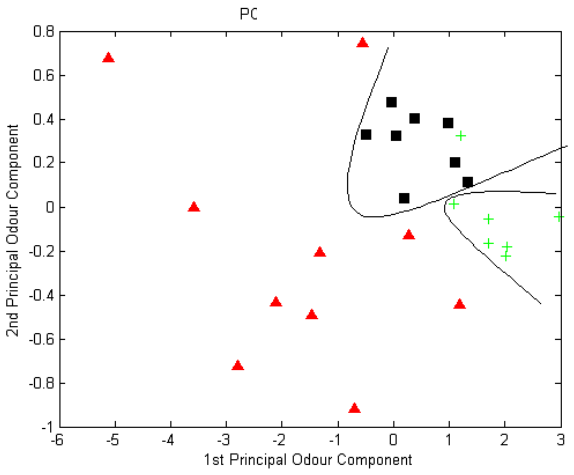


Fig. 3 Scoreplot of the 1st and 2nd principal odor components of the patients with liver cirrhosis (red triangle

points), alcohol addicted patients (green cross points) and healthy controls (black square points)

III. Conclusions

This study shows that an electronic nose is able to classify human body odor of patients with liver cirrhosis and alcohol addicted patients (Table 2).

Table 2 Classification rate of each group with quadratic discriminant analysis using the 1st and 2st principle odor component; 1- healthy controls, 2- patients with liver cirrhosis, 3- alcohol addicted patients

Groups	Classification arte [%]
1 vs. 2	100
2 vs. 3	100
1 vs. 3	85,71

Almost all healthy controls could be discriminated from all patients using the first two principal odor components and quadratic discriminant analysis.

In this study we demonstrated the application of an electronic nose system for analyzing human body odor to identify patients with liver cirrhosis and alcohol addicted patients.

Limitations of this study were the rather low number of patients in every group and the missing correlation with related clinical and biochemical parameters.

Analyzing body odor from the skin surface with an electronic nose system supports us in diagnosing and monitoring different diseases related to alcoholic dependencies.

Acknowledgment

This work was supported by grand from Federal Ministry of Economy and Technology (BMWI) KF 0566901WM7.

References

1. Bourgeoss W, Romain A, Nicolas J et al. (2003) The use of sensor arrays for environmental monitoring: interests and limitations. J. Environ. Monit 6:852–860
2. Tewari J, Irudayaraj J (2005) Floral classification of honey using mid-infrared spectroscopy and surface acoustic wave based z-Nose Sensor . J. Agric. Food Chem. 53:6955-6966
3. Fend R, Kolk A, Bessant C et al. (2006) Prospects for clinical application of electronic-nose Technology to early detection of Mycobacterium tuberculosis in culture and sputum. Journal of clinical Microbiology 44(6): 2039-204
4. Ping W, Yit T, Haibao X et al. (1997) A novel method for diabestes diagnosis based on electronic nose. Biosensors and Bioelectronics B 12(9-10):1031-1036
5. Di Natale C, Paolesse R, D'Arcangelo G et al. (2005) Identification of schizophrenic patients by examination of body odor using gas chromatography-mass spectrometry and a cross-selective gas sensor array. Med Sci Monit 11(8):366-375
6. Lin Y, Guo H, Chang Y et al. (2001) Application of the electronic nose for uremia diagnosis. Sensors and Actuator 76: 177-180
7. Pavlou A, Magan N, McNulty C et al. (2002) Use of an electronic nose system for diagnoses of urinary tract infection. Biosensors and Bioelectronics 17: 893-899
8. Dutta R, Hines E, Gardner J et al. (2002) Bacteria classification using Cyranose 320 electronic nose. BioMedical Engineering 1:4
9. Gibson T, Prosser O, Hulbert J et al. (1997) Detection and simoltaneous identification of microorganisms from headspace samples using an electronic nose. Sensors and Actuators B 44:413-422
10. Machado R, Laskowski D, Deffenderfer O et al. (2005) Detection of lung cancer by sensor array analyses of exhaled breath. American Journal of Respiratory and critical care medicine 171:1286-1291
11. Di Natale C, Macagnano A, Martinelli E et al. (2003) Lung cancer identification by the analyses of breath by means of an array of non-selective gas sensors. Biosensors and Bioelectronics 18: 1209-1218
12. Dragonieri S, Schot R, Mertens J et al. An electronic nose in the discrimination of patients with asthma and controls. J Allergy clin immunol 120:856-862
13. Pavlou A, Magan N, Jones J et al. (2004) Detection of Mycobacterium tuberculose (TB) in vitro and in situ using an electronic nose in combination with a neural network system. Biosensors and Bioelectronics 20: 538-544
14. Voss A, Baier V, Reisch R et al. (2005) Smelling Renal Dysfunction via electronic nose. Annal of Biomedical Engineering 33:656-660
15. http://www.diabetesaction.org

Corresponding author:

Author: Prof. Dr. A. Voss
Institute: University of Applied Siences Jena
Street: Carl-Zeiss-Promenade 2
City: 07745, Jena
Country: Germany
Email: voss@fh-jena.de

Development and Fabrication of Multielectrode Arrays for Immuno-Assisted Whole Cell Detection Systems

A. Steude, O. Pänke, S. Schmidt, and A.A. Robitzki

Centre for Biotechnology and Biomedicine (BBZ), Molecular Biological-Biochemical Processing Technology
University of Leipzig, 04103 Leipzig, Germany

Abstract— **Electrochemical immuno-based biosensors constitute a promising tool for various diagnostic applications. This work aims at the development and fabrication of a novel multielectrode array (MEA) for immuno-assisted whole cell detection systems. The presented MEA is compatible with the 96-well format containing nine wells initially, but allows upscaling for high-throughput screening application. Each well features a gold working electrode permitting surface modification with thiol chemistry, a platinum auxiliary electrode, and an Ag/AgCl reference electrode. The gold surface offers high cleanness and modifiability necessary for voltammetric and impedimetric analyses.**

Keywords— **multielectrode array (MEA), high-throughput screening (HTS), immuno-assisted whole cell detection, voltammetry, impedance spectroscopy (EIS)**

I. INTRODUCTION

The application of electrochemical techniques for specific cell detection is motivated by their potential to detect binding events simply, rapidly, and in a cost-effective manner compared to conventional biochemical assays. The typical design of an electrochemical immuno-based biosensor involves the following elements: (i) immobilization of a cell-specific recognition layer based on antibodies, (ii) binding of target cells, (iii) introduction of an electro-active indicator, and (iv) the electrochemical investigation of the surface. Using multielectrode arrays (MEA) as the transducing unit, high-throughput measurements become feasible.

The aim of this work was the development and fabrication of a novel MEA that permits stable and straightforward modification of the electrode surface with antibodies targeting specific cell surface antigens. The antibody-modified MEA will allow the detection and immobilization of whole cell targets for further analyses. Reports on whole cell detection systems are rarely found in literature but are of high interest. Ribaut et al. [1] for example grafted red blood cells on a gold electrode. Compared to this work we go for specific capture of cells from a mixture of various cells.

The MEA design was focused on simple application and surface recovery for repeated usage. The implementation of Ag/AgCl reference electrodes expands the possible applications allowing voltammetric, amperometric, and impedimetric surface analysis using redox-active reporter compounds. Especially cell-based impedance spectroscopy is potentially useful to give insight into cellular behavior, to detect morphological changes and alterations of the physiological state, or to test the efficiency of drugs and effectors. The cellular sensing method avoids the use of labeled molecules, does not interfere with cellular metabolism *in vitro*, and allows real-time monitoring and analyses of cells.

II. METHODS

A. Design and fabrication of the multielectrode array

The MEA was designed with the AutoCAD software (Autodesk) and fabricated in a clean room facility. The borosilicate substrate (Docter Optics, 49x49x1 mm^3) was cleaned consecutively with acetone, propanol and piranha solution (95 % H_2SO_4 and 30 % H_2O_2 2:1) prior to coating. Afterwards, 3.5 µm positive resist AR-3510 (ALLRESIST) were spin-coated onto the glass substrate (spin-coater SB15, SSE). MEA structures were transferred with custom-made photomasks (MLC Jena), the mask aligner MJB4 (Süss MicroTec AG), UV light exposure (350 nm), and subsequent development of the resist with AR 300-35 (ALLRESIST). The metal layers were deposited by alternating-current-sputtering (BAE 250, BalTec). A 10 nm adhesion layer of chromium was followed by a 500 nm gold layer, and an additional layer of 80 nm platinum. Afterwards the remaining positive resist and the metal sputtered thereon were removed with acetone. 5 µm of the negative resist SU-8 (MicroChem) were deposited for isolation. Parallelization was achieved by implementation of separate test tube chambers from a 96-well-plate.

B. Fabrication of the reference electrodes

Ag wires (Goodfellow) of 0.5 mm in diameter were coated with AgCl by galvanization at 1.2 V in 3 M potassium chloride (KCl) for 1 h. Coated wires were mounted in

O. Dössel and W.C. Schlegel (Eds.): WC 2009, IFMBE Proceedings 25/VIII, pp. 153–156, 2009.
www.springerlink.com

a lid and connected to the potentiostat/frequency response analyzer.

C. *Thiol modification*

Self-assembled monolayers (SAM) were formed by exposing the bare gold working electrodes to a freshly prepared mixture of 0.1 mM 11-mercaptoundecanoic acid and 0.9 mM 6-mercapto-1-hexanol from Sigma Aldrich in ethanol for 72 h. The electrodes were rinsed with ethanol and double distilled water prior to the electrochemical measurements. Surface recovery was feasible by cyclic voltammetry of 1 mM potassium hexacyanoferrate II/III (ferri-/ferrocyanide) 1:1 in 0.1 M KCl from – 800 to 800 mVs^{-1} for four cycles.

D. *Electrochemical measurements*

For electrochemical measurements, the multielectrode arrays were connected to the potentiostat and impedance analyzer CompactStat (Ivium Technologies) using a MEA adapter board (Multi Channel Systems). The Ag/AgCl reference electrodes were directly connected to the CompactStat. Cyclic voltammetry and electrochemical impedance spectroscopy were carried out in 0.1 M KCl containing 1 mM ferri-/ferrocyanide (1:1) as redox compound, unless otherwise stated. Cyclic voltammograms were recorded vs. Ag/AgCl with a scan rate of 100 mVs^{-1}, unless otherwise stated. Four cycles provided stationary cyclic voltammograms. Impedance was recorded for frequencies ranging from 1 Hz to 100 kHz by application of an alternating voltage of 10 mV against the open cell potential.

III. RESULTS AND DISCUSSION

E. *Fabrication of the multielectrode array with implemented Ag/AgCl reference electrodes*

The multielectrode array was made of nine separate measurement chambers in a classical 96-well-format. Each chamber contained a circular working electrode with a diameter of 1.9 mm and an auxiliary electrode forming an open circular ring around the working electrode, which was 7 mm in diameter (Fig. 1A). The surface ratio between auxiliary electrode and working electrode (about 10:1) guaranteed that changes of the electrochemical signals originated from the working electrode.

The electrodes were mounted on the borosilicate glass substrate by consecutive deposition of different metal layers. A layer of chromium facilitated the adhesion of the subsequent layers to the substrate. The second layer consisted of gold forming contact pads, conductor paths, and the working electrodes, which allows covalent modification by thiol chemistry. To prevent additional thiol modification of the auxiliary electrodes, platinum was disposed finally on top.

The geometry of the MEA and the location of the contact pads for auxiliary and working electrodes were compatible to the commercially available adapter boards from Multi Channel Systems. However the utilisation of a reference electrode as a third electrode was not provided by the adapter board. A reference electrode became necessary because analytical measurements with electrochemical turnover of a redox compound demand the control of the working electrode potential (three-electrode system, Fig. 1B). Therefore, a custom-made reference electrode consisting of Ag/AgCl has been connected directly to the electrochemical instrument.

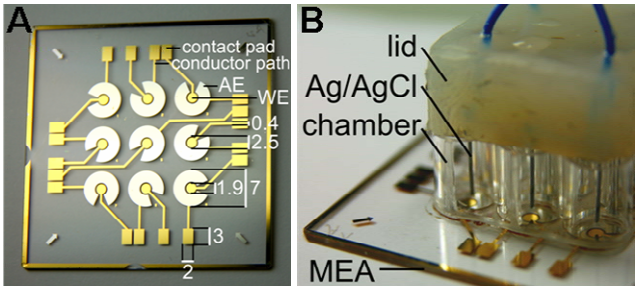


Fig. 1 Fabricated MEA with dimensions in mm (**A**, AE – auxiliary electrodes, WE – working electrodes) and MEA with reference electrodes (**B**, Ag/AgCl)

F. *Characterization of the working electrodes*

The electrochemical conversion of ferri-/ferrocyanide was used to characterize the bare gold working electrodes of the custom-made MEA. Fig. 2A shows a cyclic voltammogram of ferri-/ferrocyanide recorded with the MEA at a scan rate of 100 mVs^{-1}. The corresponding peak currents ($I_{p,ox}$, $I_{p,red}$) were direct proportional to the square root of the scan rate (v) and their ratio was close to one (Fig. 2B) - both characteristics for reversible reactions. On the other hand, the formal potential, which is the average of the peak potentials, remained constant for all scan rates indicating a stable reference system.

The observed peak separation of about 75 mV was close to the theoretical value of 59 mV verifying a clean electrode surface (Fig. 2A) with properties comparable to commercial disk electrodes that are routinely polished for optimal performance (e. g. EasyCon). There are also reports showing sputtered gold electrodes with larger peak separations, e. g. Fragoso et al. [2] found peak separations of about 130 mV.

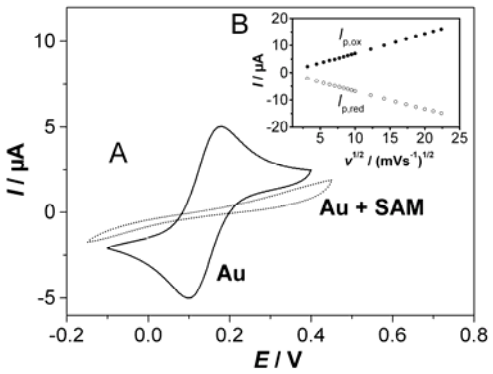


Fig. 2 The MEA was characterized by cyclic voltammetry with 1 mM ferri-/ferrocyanide in 0.1 M KCl at a scan rate v of 100 mVs^{-1}. Cyclic voltammograms of a bare gold working electrode and a thiol-modified electrode (SAM) are displayed in **A**. Peak currents ($I_{p,ox}$, $I_{p,ox}$) for the bare gold electrode are plotted against the square root of the scan rate v (**B**).

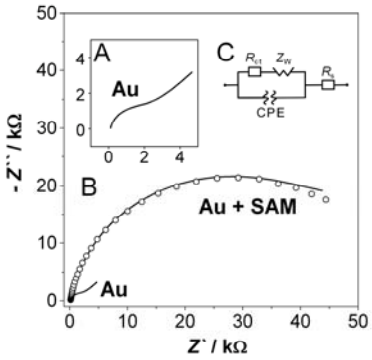


Fig. 3 Impedance spectra were recorded in 1 mM ferri-/ferrocyanide and 0.1 M KCl. The Nyquist plot of a bare gold working electrode showed a typical semicircle (**A**). The diameter of the semicircle increased with thiol modification in comparison to the bare gold electrode (**B**). Data were fitted using an equivalent circuit model (**C**).

A clean electrode surface is a prerequisite for specific modification reactions. Thus, we investigated the accessibility of the electrode surface for thiol reagents. After incubation with a mixture of 0.1 mM 11-mercaptoundecanoic acid and 0.9 mM 6-mercapto-1-hexanol for 72 h, a stable self-assembled monolayer (SAM) was formed (Fig 2A). Distinct peak currents for ferri-/ferrocyanide could not be observed at the modified electrode surface.

The suitability of the fabricated MEA for impedimetric analyses was additionally tested. Impedance spectra were recorded from 1 Hz to 100 kHz with ferri-/ferrocyanide as redox compound. Fig. 3 shows Nyquist plots of impedance spectra recorded for the bare gold electrode and for the thiol-modified electrode. The measured data were analyzed using the equivalent circuit model displayed in Fig. 3C which consists of a charge transfer resistance (R_{ct}) connected in series to the Warburg impedance (Z_W) and both are connected in parallel to a constant phase element (CPE). The solution resistance (R_s) is connected in series to the other circuit elements. The numerical analysis yielded a charge transfer resistance of the bare gold electrode of about 50 Ω/cm^{-2}. After thiol modification, the charge transfer resistance increased 24-fold to a value of 1200 Ωcm^{-2} indicating the formation of a SAM (Fig. 3B). The CPE parameter A, which is similar to a capacitance, showed only a three-fold increase from 2.5 to 7 µFs^{n-1}. The parameter n was 0.9 for both, the bare and the modified electrode, indicating a low surface roughness.

Both, cyclic voltammetry and impedance spectroscopy demonstrated the dramatic reduction of the surface accessibility for ferri-/ferrocyanide after SAM formation and proved the suitability of the presented MEA as a platform for projected applications such as whole cell detection and analysis.

G. Characterization of the reference electrodes

To achieve a compact MEA design, the AgCl-covered Ag wires were inserted as reference electrode directly into the measuring buffer without protecting glass capillary separating the measuring buffer from a particular electrode electrolyte, as usual. Therefore, a sufficient amount of chloride has to be present in the measuring buffer providing a defined and constant reference potential. Using the Nernst equation for the Ag/AgCl reference electrode (Equation 1) and published activity coefficients $y_{Cl^-} = y_{\pm}$ for KCl and NaCl [3-5], the electrode potential can be calculated.

$$E_{Ag/AgCl} = E^{o}_{Ag/AgCl} - \frac{2.3 \cdot RT}{F} \lg\left(y_{Cl^-} c_{Cl^-}\right) \quad (1)$$

Here, $E°$, R, T, F, and c have their usual meaning. The results are summarized in Tab. 1 and agree perfectly with experimental data. Marginal differences between KCl and NaCl were visible under conditions of high ionic strength, where activity coefficients become individual and depend also on the respective cations K^+ and Na^+.

Table 1 Reference potentials for different amounts of KCl and NaCl

c / mol l^{-1}	0.1	0.5	1.0	3.0	3.5
$E_{Ag/AgCl}$ (KCl) / mV	287	251	235	209	205
$E_{Ag/AgCl}$ (NaCl) / mV	287	250	233	203	198

For further verification, we investigated the formal potential of 1 mM ferri-/ferrocyanide at different ionic strength with cyclic voltammetry. As shown in Fig. 4A, the measured formal potential increased from 143 mV at 0.1 M KCl to 284 mV at 3 M. We additionally calculated the for-

mal potentials according to Equation 2 considering equal concentrations of ferri-/ferrocyanide.

$$E'^{\circ} = E_F^{\circ} + \frac{2.3 \cdot RT}{F} \lg \frac{y_{FIII}}{y_{FII}} - E_{Ag/AgCl} \quad (2)$$

The individual activity coefficients y_i were obtained from its mean values $y_\pm$ published in the literature taken into account $y_{FIII} = y_\pm^3$ and $y_{FII} = y_\pm^4$ for ferri- and ferrocyanide, respectively. The formal potential was calculated considering the standard potentials $E° = 361$ mV for ferri-/ferrocyanide [6] and $E° = 222$ mV for Ag/AgCl. The results are presented in Fig. 4 and validate the application of the reference electrode. The small difference between measured and calculated values of about 20 mV was probably due to inaccuracies of the activity coefficients used for calculation. In contrast to the presented experiments, where KCl defined the ionic strength, the activity coefficients of ferri-/ferrocyanide were determined in pure solutions of ferri-/ferrocyanide.

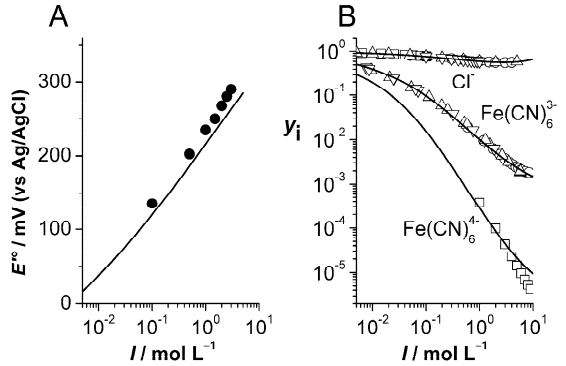


Fig.4 Formal potential $E'°$ of 1 mM ferri-/ferrocyanide, $Fe(CN)_6^{3-/4-}$, at the MEA gold electrodes at different ionic strength I (**A**). The inserted curve was calculated using activity coefficients from the literature [7, 8] (**B**). Different symbols indicate data from different authors. Inserted curves were calculated on the basis of the semi-empiric Davis equation ($\lg y_i = -A\, z_i^2(\sqrt{(I)}/(1+B\sqrt{(I)}) - CI$) allowing the extrapolation of activity coefficients for ferrocyanide, $Fe(CN)_6^{4-}$, at lower I values. The following parameters were obtained: $A/dm^{3/2}mol^{-1/2} = 0.5$ (all anions), $B/dm^{3/2}mol^{-1/2} = 1.08$, 1.25, and $C/dm^3mol^{-1} = 0.037$, 0.001 for Cl^- and $Fe(CN)_6^{3-/4-}$ (both K^+ salts), respectively.

Additional experiments using typical cell culture media based on DMEM, RPMI-1640, or MEM containing 120 to 150 mM chloride in total yielded constant potentials over time (at least for 1 h) and formal potentials for ferri-/ferrocyanide identical to those measured in pure solutions of KCl and NaCl. Thus, protein-rich ingredients such as fetal bovine serum (≤ 10 %) did not affect the stability of the MEA-based measuring system.

IV. CONCLUSIONS

Using clean room techniques we fabricated a novel, recyclable multielectrode array (MEA) in 96-well format as sensor device adaptable to high-throughput measuring systems. Each well contains a gold working electrode and a platinum auxiliary electrode. Additionally, Ag/AgCl reference electrodes were implemented to control the potential at the working electrode which is needed for voltammetric, amperometric, or impedimetric read-out. The reference system was validated by cyclic voltammetry and impedance spectroscopy. Furthermore, the implemented gold working electrodes allow direct surface functionalization. A self-assembled monolayer was successfully immobilized providing a basic prerequisite for further modifications with antibodies allowing specific whole cell detection.

ACKNOWLEDGMENT

This work has been supported by the Deutsche Forschungsgemeinschaft (Graduate School BuildMoNa, GSC 185).

REFERENCES

1. Ribaut C, Reybier K ,Torbiero B et al. (2008) Strategy of red blood cells immobilisation onto a gold electrode: Characterization by electrochemical impedance spectroscopy and quartz crystal microbalance. IRBM 29 (2-3): 141-148
2. Fragoso A, Laboria N, Latta D, O`Sullivan CK (2008) Electron Permeable Self-Assembled Monolayers of Dithiolated Aromatic Scaffolds on Gold for Biosensor Applications. Anal. Chem. 80:2556-2563
3. Lide DR (Editor-in Chief) (1992) CRC Handbook of Chemistry and Physics, 73rd edition, CRC Press, Boca Raton
4. Hornibrook WJ, Janz GJ, Gordon AR (1942) The thermodynamics of aqueous solutions of potassium chloride at temperatures from 15-45° from emf measurements on cells with transference. JACS 64: 513-516
5. Marques A, Ferra MIA, Bandaira MH (2006) Activity coefficients of potassium chloride in aqueous solutions of potassium chloride and potassium phthalate. Portugaliae Electrochemica Acta 24: 295-303
6. Murray RC, Rock PA (1968) The determination of the ferrocyanide-ferricyanide standard electrode potential at 25°C in cells without liquid junction using cation-sensitive glass electrodes. Electrochimica Acta 13: 969-975
7. Robinson RA, Stokes, RH (1959) Electrolyte Solutions. 2nd edition, Butterworths, London
8. Malatesta F, Giacomelli A, Zamboni R (1994) Activity coefficients of electrolytes from the emf of liquid membrane cells. III: $LaCl_3$, $K_3Fe(CN)_6$,and $LaFe(CN)_6$. J Solution Chem 23:11-36

Author: Anja Steude
Institute: Centre for Biotechnology and Biomedicine (BBZ)
Street: Deutscher Platz 5
City: 04103 Leipzig
Country: Germany
Email: anja.steude@bbz.uni-leipzig.de

Sample Preparation on-chip: Accumulation, Lysis of and DNA Extraction from Bacteria

M. Moschallski[1], C. Dorrer[2], M. Kubon[1], P. Rothacher[2], J. Weile[3], B. Hagmeyer[1], K. Fuchsberger[1], K.-H. Boven[4], A. Moeller[4], R. Mohrlok[4] and M. Stelzle[1]

[1] NMI Natural and Medical Sciences Institute at the University of Tübingen, Reutlingen, Germany
[2] Robert Bosch GmbH, Corporate Sector Research and Advance Engineering, Gerlingen, Germany
[3] Robert Bosch Hospital, Stuttgart, Germany
[4] Multi Channel Systems, Reutlingen, Germany

Abstract—

We present a microfluidic chip that collects and accumulates bacteria from a sample by positive dielectrophoresis and subsequently lyses cells to retrieve DNA / RNA. Biological samples containing *Escherichia coli* are transferred to a suitable medium (low conductivity) by on-chip dialysis. This sample is pumped through a microchannel comprising an array of interdigitated electrodes at the bottom. An AC-voltage is applied to the electrodes resulting in an inhomogeneous electric field that extends into the channel and induces dielectrophoretic forces acting on the bacteria. Herringbone- mixer structures between the electrodes induce vortices in the flow and thus rotate the fluid volume from top to bottom. This assures that all bacteria are brought under the influence of the electric field and thus may be trapped. In addition, the herringbone structures induce further inhomogeneities in the electric field. Due to this combined effect, the system allows for the trapping of bacteria even at high flow rates which results in high throughput. Bacteria from several mL of sample are concentrated into 20 µL inside the chamber. This is monitored on-line by measuring the impedance between the electrodes.

In a second step the flow is stopped and the frequency of the electric field is lowered. This induces lysis of the bacteria as a result of a high voltage drop over their cell membrane. The lysis of *E. coli* is monitored using a live-dead staining kit that changes the fluorescence color of bacteria.

The bacteria release DNA which is collected and analyzed further using real time PCR. PCR of the lysate retrieved from the chip showed a signal about 12 PCR cycles earlier than in case of the original *E. coli* suspension. This confirms the accumulation and lysis of bacteria in the chip, the release of DNA and indicates an approximately 4000-fold increase in DNA concentration.

Keywords— **biological sample preparation, accumulation, dielectrophoresis, bacteria lysis, DNA extraction**

I. Introduction

Over the past years, a variety of micro-analysis systems for the detection of DNA or proteins on-chip has been introduced [1], [2]. However, for most of these systems the samples are still prepared manually. These procedures are time consuming and prone to errors. To render these systems viable solutions for clinical applications, the preparation procedure has to be integrated on the microchip. Such an integrated system would then allow for an automatized and reproducible preparation of biological samples and in many cases save time because reactions take place more rapidly on the microscale.

So-called nosocomial or hospital acquired infections are responsible for a large number of deaths and constitute a large burden on health care systems worldwide. Often these infections are particularly difficult to treat due to antibiotic resistances the responsible pathogens have acquired. In order to enable and support an efficient therapy against a particular pathogen, it is necessary to identify pathogens, analyse their DNA or RNA and identify potential resistance genes against certain antibiotics within not more than 1-2 hours time.

To this end the following preparation steps are implemented in a microfluidic system: Pathogens like bacteria have to be concentrated in a small volume and lysed to extract their DNA/RNA. In the present work, dielectrophoresis has been used to accumulate bacteria and other biological particles. Medium with low electric conductivity is required to induce positive dielectrophoretic forces on cells [3], [4]. This is why real biological samples, like for example urine, have to be desalted before dielectrophoresis can be applied. A great advantage of electrical field manipulation of bacteria is that the same electrodes can be used to lyse concentrated bacteria *in-situ* and that no medium changes, like the addition of lysis and washing agents, are required.

O. Dössel and W.C. Schlegel (Eds.): WC 2009, IFMBE Proceedings 25/VIII, pp. 157–160, 2009.
www.springerlink.com

We present a microfluidic cartridge that preconditions urine samples and then accumulates any bacteria contained therein in a small volume, lyses them and extracts their DNA/RNA.

II. MATERIALS AND METHODS

Our microfluidic cartridge works according to the following principles: In a first step the sample flows over a dialysis membrane. Underneath the membrane deionized water is pumped in counterflow in order to desalt the sample. This procedure leaves the sample with a conductivity that is low enough for trapping bacteria using dielectrophoresis. The impedance of the dialysed sample is measured in the accumulation chamber to monitor the progress of dialysis.

The dialysis channel is directly connected to a chamber comprising an array of interdigitated zig-zag-shaped electrodes at the bottom (Fig. 1). An AC-voltage is applied to the electrodes resulting in an inhomogeneous electric field that extends into the channel and results in a dielectrophoretic force acting on the bacteria. The electrodes are flanked by polymeric insulator structures that extend over 1/3 of the channel height. The insulator structures focus the field lines in the remaining channel cross-section, which increases the inhomogeneity of the field and thus the force acting on the bioparticles. The magnitude and direction of this force depend on the voltage amplitude and the frequency of the electric field. At a frequency of 1 MHz and at an amplitude of 30 to 50 V_{pp} bacteria are attracted to areas of high electric field gradient at the edges of the electrodes (positive dielectrophoresis).

Next to focusing the electric field, the polymeric insulator structures act in the manner of a herringbone-micromixer (Fig. 1). Micromixers working according to this principle induce vortices in the flow [5], [6]. In our case, this rotation of the fluid volume assures that all bacteria are transferred to the lower half of the channel, where they are trapped at the edges of the electrodes and of the insulating structures by the dielectrophoretic force.

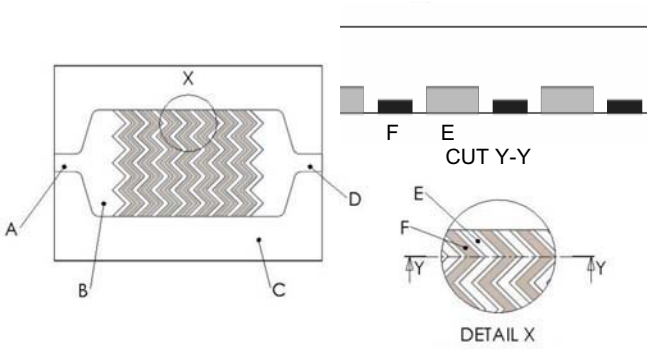


Fig. 1 Top view of the microfluidic chamber (B) on a chip (C) with microfluidic inlet (A) from the dialysis channel, zig-zag-electrodes (F) between insulating structures (E), outlet (D).

When a volume of several mL of bacteria suspension is pumped through the chip in the manner described above, the bacteria are concentrated in the 20 µL volume of the chamber.

The electric impedance between the electrodes is measured over time. This allows us to monitor the accumulation of bacteria with high cytosolic conductivity in a medium of low conductivity.

In a second step the flow is stopped and the frequency of the electric field is lowered to 10 kHz. At this low frequency the bacterial cells are lysed because a major part of the applied potential drops over the cell membrane. This damages the cell membrane if the electric field is strong enough. The lysis of *E. coli* is monitored using the BacLight ™ live-dead staining kit (Invitrogen, Karlsruhe) that changes the fluorescence color of the bacteria. The kit contains green fluorescent Syto 9 which enters viable cells and labels the DNA. As the membrane is damaged, the second dye, propidium iodide, enters the cell and replaces the green label with red fluorescence. This combination of dyes shows viable bacteria in green and lysed ones in red fluorescence.

The bacteria release DNA that is eluted from the microfluidic cartridge and then collected. It is further analyzed using real time polymerase chain reaction (qPCR).

III. RESULTS

Suspensions of *Escherichia coli* in physiological buffer (PBS) were pumped through the microfluidic cartridge.

Dialysis of this sample solution led to a medium conductivity that was decreased below 10% of the original sample conductivity within 15 min.

We performed *simulations* of the flow pattern inside the accumulation chamber using the finite volume code

ANSYS CFX. The simulation results confirmed that, during their trajectory through the chamber, particles are dislocated from the top to the bottom of the channel (Fig. 2). In this way, bacteria are brought closer to the electrodes located at the channel bottom. Additionally, we found that the flow rates in the vicinity of the herringbone structure are considerably reduced, which may also prevent trapped bacteria from being washed away.

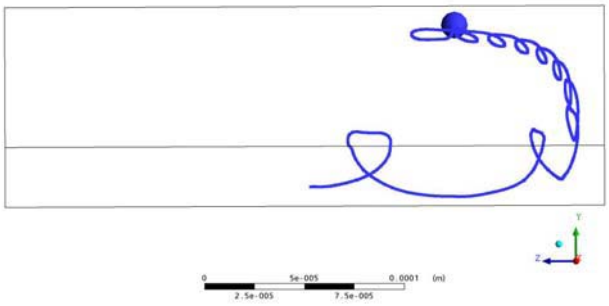


Fig. 2 Simulated trajectory of a particle in the herringbone-micromixer; looking along the channel axis from the outlet towards the inlet, the dot indicates the entrance point of the particle into the channel.

Accumulation of bacteria using dielectrophoresis yielded up to 90% of the sample content. This efficiency was determined by measuring the fluorescence intensity downstream of the accumulation chamber during the accumulation. The values were normalized to the initial intensity in a non-fluorescent channel without electric field applied. Figure 3 shows a fluorescence image of the accumulated *E. coli* between the electrodes captured in the fluorescence microscope.

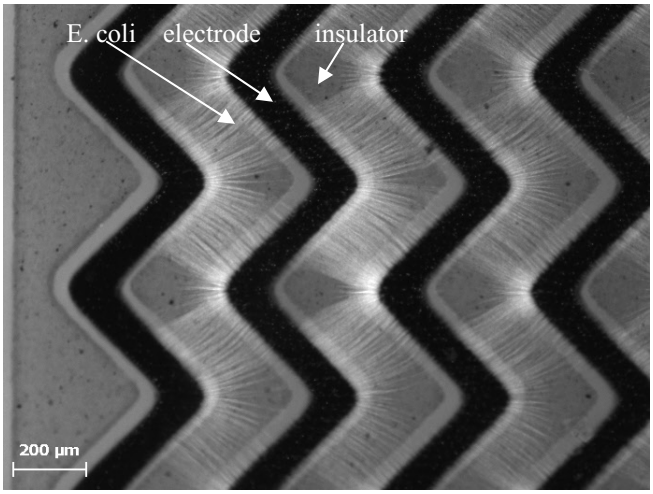


Fig. 3 Fluorescence microscope image using green filter of accumulated *E. coli* (white) aligned along the field lines over the insulator structures (dark grey) between the electrodes (black).

Lysis of *E. coli* was observed as a change from green to red fluorescence as shown in Figure 4.

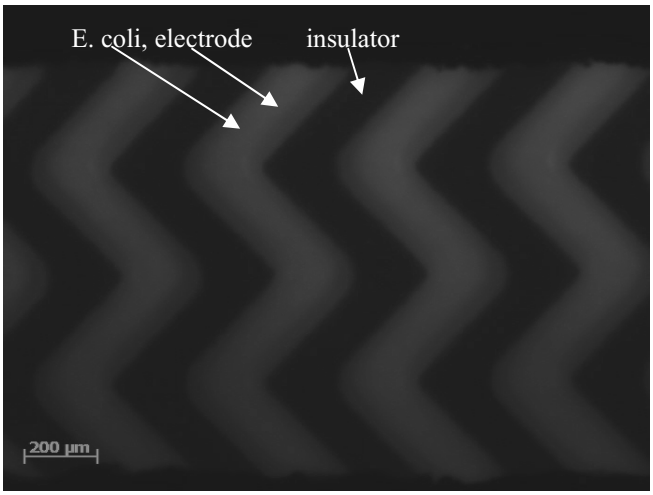


Fig. 4 Fluorescence microscope image of lysed *E. coli* (light) labelled with BacLight™ live/dead kit on top of the electrodes taken with red filter; insulating structures are shown in black.

Real-time-PCR of the lysate retrieved from the chip showed a signal about 12 PCR cycles earlier than in case of the original *E. coli* suspension. This confirms the accumulation and lysis of bacteria in the chip, the release of DNA and indicates a 4000-fold increase of DNA concentration.

IV. CONCLUSIONS

Fluorescence microscope pictures as well as relative real-time PCR quantification show that, using the microfluidic system presented in this work, *E. coli* can be accumulated from physiological samples and that their DNA can be extracted. Three-dimensional structuring of the space between the electrodes leads, firstly, to a mixing effect and, secondly, to increased inhomogeneities in the electric field. Both effects combine to allow for a high sample throughput to retrieve small amounts of relevant sample from high volumes of a sample matrix such as urine. The system yields high DNA concentrations that can be further analyzed either on chip or by conventional methods like qPCR. The procedure can be automatized.

ACKNOWLEDGMENT

Financial support from the BMBF under grant numbers 01EZ0709 and 01EZ0712 is gratefully acknowledged.

REFERENCES

1. Chen, L., A. Manz, and P.J. Day, Total nucleic acid analysis integrated on microfluidic devices. Lab Chip, 2007. 7(11): p. 1413-23.
2. Stoll, D., et al., Protein microarrays: applications and future challenges. Curr Opin Drug Discov Devel, 2005. 8(2): p. 239-52.
3. Arnold, W.M., A.G. Gessner, and U. Zimmermann, Dielectric measurements on electro-manipulation media. Biochim Biophys Acta, 1993. 1157(1): p. 32-44.
4. Lapizco-Encinas, B.H., et al., An insulator-based (electrodeless) dielectrophoretic concentrator for microbes in water. J Microbiol Methods, 2005. 62(3): p. 317-26.
5. Stroock, A.D., et al., Chaotic Mixer for Microchannels. Science, 2002. 295: p. 647-651.
6. Gadish, N. and J. Voldman, High-Throughput Positive-Dielectrophoretic Bioparticle Microconcentrator. Anal. Chem., 2006. 78(22): p. 7870-7876.

Corresponding author:

Author: Meike Moschallski
Institute: NMI Natural and Medical Sciences Institute at the University of Tübingen
Street: Markwiesenstr. 55
City: Reutlingen
Country: Germany
Email: meike.moschallski@nmi.de

Towards Artificial Liver Sinusoids by Dielectrophoretic Cell Assembly in Microfluidic System for Use in Substance Screening

J. Schütte[1], B. Angres[1], K. Benz[1], C. Freudigmann[1], B. Hagmeyer[1], F. Holzner[1], M. Kubon[1], J. Böttger[2], R. Gebhardt[2], H. Becker[3], and M. Stelzle[1]

[1] NMI Naturwissenschaftliches und Medizinisches Institut, Reutlingen, Germany
[2] Institut für Biochemie der Medizinischen Fakultät der Universität Leipzig
[3] microfluidic ChipShop GmbH, Carl-Zeiss-Promenade 10, Jena

Abstract— **We are developing microfluidic systems with 3D-microstructures and integrated electrodes to assemble cells in an organ-like 3D-structure by means of dielectrophoretic and hydrodynamic forces. To further mimic the *in vivo* situation cells are allowed to adhere on liver specific extra cellular matrix proteins. Results showing co-assembly of liver cells in a sinusoid like structure will be presented.**

Keywords— **liver sinusoid, artificial micro organs, dielectrophoresis, microfluidic device, substance screening**

I. Introduction

In vitro toxicity tests used in drug development today mostly rely on 2D-cell cultures which lack predictivity with regard to the *in vivo* situation [1], [2], [3]. A problem encountered with primary hepatocyte cultures is a rapid cell dedifferentiation, which results in a deterioration of liver-specific functions. Thus, not all effects of drugs can be discovered in early drug development. Animal models lack predictivity with respect to toxicity and should be avoided for ethical reasons whenever possible. As a consequence, the pharmaceutical industry today faces considerable risks regarding the safety of patients during clinical trials and the loss of large R&D investments in case of failure of a drug candidate in a late state of drug development.

II. Materials and Methods

A. Dielectrophoresis (DEP)

If particles such as cells are immersed in a buffer solution and subjected to an inhomogeneous electric field a dipole moment is induced which gives rise to a dielectrophoretic force acting on the particle [4], [5], [6] according to

$$F_{DEP} = 2\pi R^3 \varepsilon_m \,\mathrm{Re}\left(f_{CM}\right)\nabla E^2 \qquad (1)$$

where E is the applied rms electric field, R is the particle radius, ε_m is the permittivity of the medium, and $\mathrm{Re}[f_{CM}]$ is the real part of the Clausius-Mossotti factor [4], [7].
AC voltage amplitude applied to the electrodes ranged from $30V_{ss}$ to $200V_{ss}$, frequency was 100 kHz to 1 MHz, depending on cell type. Low conductivity (< 200 µS/cm) medium (10 % sucrose) was employed.

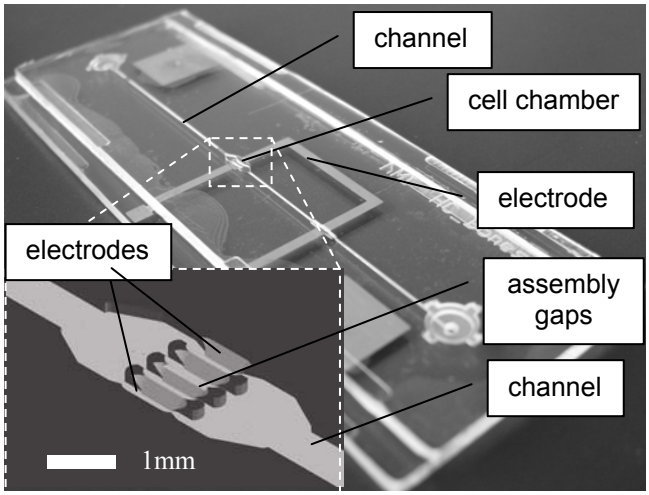


Fig. 1: Microdevice for 3D-assembly of cells into sinusoid like structure by means of DEP. It comprises a microfluidic channel and a cell chamber in the central region of the chip. There, two electrodes establish electrical contact with the medium flowing by. Thus, an electric field may be created, with its maximum strength being located within the assembly gap into which cells are drawn by positive DEP.

Depending on the relative permittivity of the particle and the medium this force may be attractive (positive DEP) or repulsive (negative DEP). In case of our HepaChip design, an inhomogeneous field is created by a 3D-microstructure of the cell chamber with the cell assembly gap located in between the channels and the electrodes (Fig.1).

O. Dössel and W.C. Schlegel (Eds.): WC 2009, IFMBE Proceedings 25/VIII, pp. 161–164, 2009.
www.springerlink.com

B. Design and Numerical Simulation

Electric field distribution, fluid velocity fields, dielectrophoretic force distribution and the resulting particle trajectories were numerically simulated using the multiphysics software package CFD-ACE$^+$ (ESI group).

Different 3D models of the cell chamber were designed and calculations were performed applying appropriate material properties and boundary conditions.

The trapping rate, i.e. the fraction of cells actually immobilized by dielectrophoretic forces in the assembly gap, was calculated and the chip design optimized to maximize trapping rate.

C. Chip fabrication

Chips were fabricated from cyclic olefin copolymer (COC) slides (Topas 5013, Microfluidic ChipShop, Germany) (25 mm x 75 mm) by micro-milling (Fig.1). After completion of channels, cell chamber and fluid ports, a second flat COC slide was glued on top by application of a thin film of UV curable adhesive (Vitralit 1558) [8], [9].

D. Cell culture

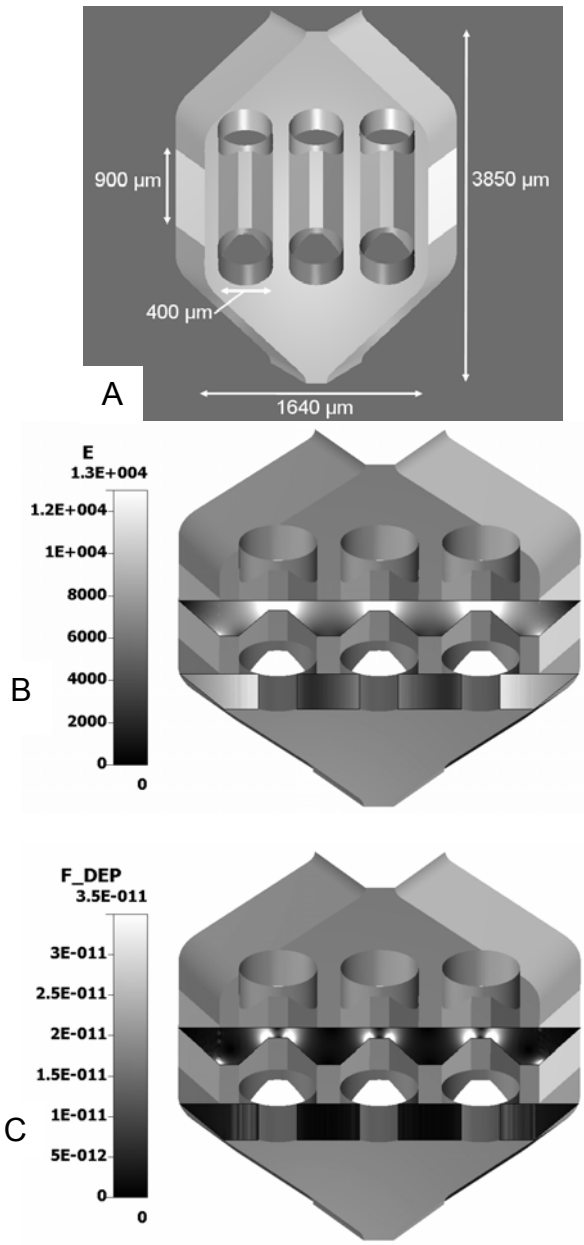
HepG2 cells were cultured in Eagle's Minimum Essential Medium supplemented with 1% non-essential amino acids, 2 mM L-Glutamine, 1 mM sodium pyruvate, 1% penicillin and streptomycin and 10 % fetal calf serum (PAA, Germany). Cell culture was incubated at 37 °C with 5% CO_2. HepG2 cell suspensions were prepared by rinsing the adhered cells with Ca/Mg free phosphate buffered saline and using a solution of trypsine (0.5 mg/ml) and EDTA (0.22 mg/ml) in Ca/Mg free phosphate buffered saline to detach cells from the culture flask. Counting was performed in a cytometer; cells were centrifuged at 250 g for 5 min and resuspended in low conductivity sucrose medium. For fluorescence staining 2 µl of Calcein AM (Invitrogen, Germany) solution were added.

III. Results & Discussion

A. Electric field distribution, dielectrophoretic forces and particle trajectories

Electric field distribution was calculated numerically for a cell chamber comprising three "bone-type" structures. The geometric dimensions of the chamber comprising these structures are shown in Fig. 2A. Shown in Fig. 2B, C are two cross-sections of the cell chamber. Fig. 2B displays the field distribution at the front end of the columns near the entrance of the cell chamber and in the central region across all three assembly gaps, respectively. The electrodes span the length of the assembly gaps and are located on the left and the right chamber wall. As expected, maximum field strength (bright areas) is observed in regions of minimal cross-section of the conductor (buffer medium) between the electrodes, i.e. in the vicinity of the assembly gaps. The dielectrophoretic force, calculated according to Eq. 1, is displayed in Fig. 2C. Again, maximum forces are displayed as bright areas whereas small DEP forces are shown as dark areas. Obviously, the DEP force is confined to the region close to the assembly gap while in a relatively large fraction of the channel cross-section particles will experience only small DEP forces. Further optimization of the 3D geometry of the cell chamber is required to address the complete channel volume by DEP forces. But technologies available for fabrication of these devices also have to be taken into account which may somewhat limit available options.

In Fig. 2D, trajectories of particles are displayed, which start from different locations on the inlet plane (left side) of the cell chamber. This was undertaken in order to assess the trapping rate achievable with this chip design. White arrows indicate some of the trajectories ending on the assembly gap. These trajectories resemble cells trapped by DEP forces. Some trajectories, however, reach the outlet plane (right side) of the simulation space, indicating loss of cells. Simulation results show that with this design about 50 % of all particles entering the cell chamber will be trapped on the assembly gaps and – less desirable – also on the structures in front of and behind the three assembly gaps on both the inlet and the outlet side of the chamber. An even higher trapping efficiency seems achievable with an improved design providing for DEP forces being present within the entire cross-section of the fluid channel.



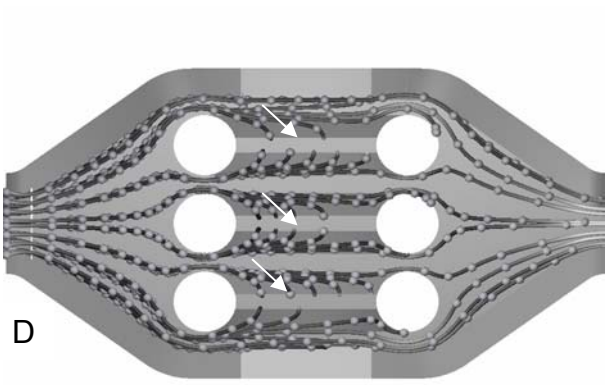


Fig. 2: A) geometric dimensions of simulated cell chamber B) electric field distribution within cell chamber (seen from inlet side). Brighter areas indicate regions of high field strength. Two cross-sections are shown, one near the chamber entrance and a second one in the center of the chamber indicating regions of high field strength in the vicinity of the assembly gaps. C) Dielectrophoretic force distribution: DEP force reaches maxima (shown as bright areas) in the assembly gaps and at the electrode edges. D) Particle trajectories in the cell chamber calculated by multiphysics simulation (seen from top). White arrows indicate trajectories ending on the assembly gaps.

B. Cell assemblies in microfluidic devices

In order to evaluate the results of the simulations, a cell suspension comprising $5x10^5$ HepG2 cells/ml in a 10 % sucrose solution was pumped through the system at a flow rate of 25 µl/min. The low conductivity (<200 µS/cm) of the suspension provided for positive DEP conditions and enabled cells to be accumulated on the assembly gaps. A voltage of 120 V_{ss} was applied.

Over the course of 100 seconds, cells are drawn from the flow channel into the assembly gaps (white arrows). The column structures largely reduce flow velocity and friction forces acting on trapped cells. It is therefore conceivable to turn off the voltage immediately after completion of cell accumulation to exchange DEP buffer with a buffer medium better suited to promote cell adhesion within the assembly gaps.

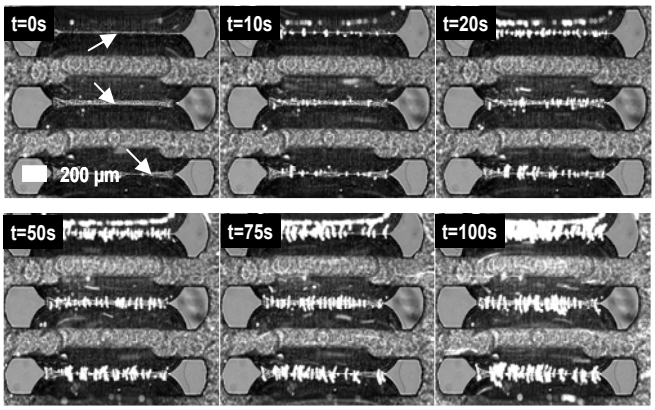


Fig. 3: Micrographs showing accumulation of HepG2 cells (white dots) suspended in a 10 % sucrose solution in a cell chamber comprising three assembly gaps. Voltage amplitude was 120 V_{ss}; flow rate was 25 µl/min. The micrographs are overlays of fluorescence images obtained from calcein staining of cells and transmission microscope images of the chip system to visualize microstructure of the cell chamber.

IV. Conclusions

The 3D assembly of cells by means of dielectrophoresis within a microfluidic system was shown. As was demonstrated both by numerical simulation and by successful cell trapping a dedicated design of a 3D microstructure gives rise to an electric field distribution and to related dielectrophoretic forces which automatically guide cellular assembly into the desired arrangement.

In the future this paradigm will be further exploited to build liver sinusoids by consecutive trapping of hepatocytes and endothelial cells. The channels will then be used to supply nutrients and compounds to be tested as well as to retrieve metabolites for further analysis.

Acknowledgment

Sputter deposition of thin film electrodes in the NMI thin film and microstructure facility by Claus Burkhardt is gratefully acknowledged.

References

1. Thomas, R.J., et al., The effect of three-dimensional co-culture of hepatocytes and hepatic stellate cells on key hepatocyte functions in vitro. Cells Tissues Organs, 2005. **181**(2): p. 67-79.
2. Sivaraman, A., et al., A microscale in vitro physiological model of the liver: predictive screens for drug metabolism and enzyme induction. Curr Drug Metab, 2005. **6**(6): p. 569-91.
3. Gebhardt, R., et al., New hepatocyte in vitro systems for drug metabolism: metabolic capacity and recommendations for application in basic research and drug development, standard operation procedures. Drug Metab Rev, 2003. **35**(2-3): p. 145-213.
4. Pohl, H.A., Dielectrophoresis. 1978, New York: Camebridge University Press. 579.
5. Jones, T.B., Electromechanics of particles. 1995, Cambridge, New York, Melbourne: Cambridge University Press.
6. Kentsch, J., et al., Microdevices for separation, accumulation, and analysis of biological micro- and nanoparticles. IEE Proc Nanobiotechnol, 2003. **150**(2): p. 82-89.
7. Pethig, R., Dielectrophoresis: Using Inhomogeneous AC Electrical Fields to Separate and Manipulate Cells. Critical Reviews in Biotechnology, 1996. **16(4)**: p. 331-348.
8. Kentsch, J., et al. High precision low temperature bonding process for BioMEMS. in Micro Total Analysis Systems 2004. 2004. Malmö: The Royal Society of Chemistry.
9. Kentsch, J., S. Breisch, and M. Stelzle, Low temperature adhesion bonding for BioMEMS. J.Micromech. Microeng., 2006. **16**: p. 802-807.

Corresponding author:

Author: Martin Stelzle
Institute: Natural and Medical Sciences Institute at the University of Tübingen
Street: Markwiesenstraße 55
City: D-72770 Reutlingen
Country: Germany
Email: martin.stelzle@nmi.de

Application of Supported Phospholipids Bilayers for Biosensor based on Imaging Ellipsometry

Y.Y.Chen[1,2], Y.B. Zhang[1,3] , C.X. Wang[1], Z.J. Ding[1], C.H. Huang[1,3] , W.R.Chang[2]*, G. Jin [1,4]*

[1] Institute of Nano-tech and Nano-bionics, Chinese Academy of Sciences, Suzhou 215125, P.R. China
[2]Institute of Biophysics, Chinese Academy of Sciences, Beijing 100101, P.R. China
[3] Graduate University of CAS, Beijing, 100049 P.R. China
[4] Institute of Mechanics, Chinese Academy of Sciences, Beijing 100080, P.R. China

Abstract—**Application of supported phospholipids bilayers (SPB) is presented for biosensor based on imaging ellipsometry. One SPB is prepared by covalent immobilization of phospholipids monolayer on silicon surface, and followed by adsorption of PEG functionalized phospholipids layer. Another is prepared by adsorption of the mixture of phospholipids and PEG functionalized phospholipids on the hydrophilic silicon surface. Results show that obvious resistance to non-specific protein adsorption on SPB is obtained, and proteins covalently immobilized on the bilayers by the terminal carboxyl group of PEG remain higher bioactivity than that immobilized on silicon surface directly.**

Keywords—**imaging ellipsometry, supported phospholipid bilayers, biosensor, microfluidic array.**

I. Introduction

The concept of biosensor based on imaging ellipsometry is reported in 1995 [1]. As the visualization method of biosensor, imaging ellipsometry which combines the power of ellipsometry with microscopy [2] provides a larger field of view for the biosensor (several square centimeters) with a high spatial resolution in the order of micron (laterally) and sub-nanometer (vertically), which makes the biosensor convenient to detect multiple analytes in a microarray simultaneously. Another interesting feature of the biosensor is label free for biomolecule detection, which avoids problems caused by the use of labeling like radioactive isotopes or fluorophores [3]. However, one drawback of the biosensor is that it can not distinguish specific binding and non-specific adsorption. It is necessary to develop a special surface modification to minimize the non-specific binding.

Supported phospholipids bilayers (SPB) at interfaces have actually been shown a good validity in preventing protein adsorption, and have the potential to make the biosensor be developed into highly selective devices for a variety of biological analytes [4-5]. Here the application of two SPB on silicon surface is studied for the biosensor based on imaging ellipsometry. One SPB is prepared by covalent immobilization of a supported phospholipids monolayer on silicon surface, and followed by incubation with PEG functionalized phospholipids in aqueous solution. Another SPB is prepared by adsorption of the mixture of phospholipids and PEG functionalized phospholipids in aqueous solution on the hydrophilic silicon surface.

II. Experiment and discussion

A. Experimental section

Materials: Chemicals used for the buffer preparation were all of analytical grade. Human immunoglobulin G (hIgG), goat anti-hIgG serum, fibrinogen (Fib), anti-Fib, Human serum albumin (HSA) and Bovine serum albumin (BSA) were obtained from Sigma. Fetal bovine serum (FBS) was purchased from Hyclone (USA). L-α-phosphatidylethanolamine (PE) and Tween 20 were purchased from Sigma-Aldrich. 1,2-Diacyl-sn-Glycero-3-Phosphoethanolamine-N-[Methoxy (Polyethylene glycol)-2000] (CH_3-PEG-PE) and 1,2-Distear oyl-sn-Glycero-3-Phosphoethanolamine-N-[Carboxyl (Polyethylene Glycol)-2000] (COOH-PEG-PE) were purchased from Avanti Polar Lipids. 1,2-Dimyristoylphophatidylcholine (PC) was purchased from Lipiod. All lipids were stored at -20 ℃ until use. Dichlordimethylsilane, N-hydroxysuccinimide (NHS) and N-ethyl-N'-(3-diethyl-aminopropyl) carbodiimide (EDC) were from Acros. Milli-Q ultrapure water with a resistivity ~ 18 MΩcm (Millipore, Molsheim, France) was used for all the solutions. Other chemicals used were analytical grade or better.

Imaging ellipsometry: The experiments were carried out with an imaging ellipsometer developed in our laboratory. As an enhancement of traditional ellipsometry, imaging ellipsometry used a CCD camera to image the ellipsometry response of a larger area sample with lateral distribution in different layer thickness, and the result was grabbed as a digital image and stored in a computer with a grayscale format (8 bits, 0–255 grayscale) for further evaluation by an

O. Dössel and W.C. Schlegel (Eds.): WC 2009, IFMBE Proceedings 25/VIII, pp. 165–168, 2009.
www.springerlink.com

image-processing program. Once imaging ellipsometer was fixed, the detected intensity "I" (grayscale) was the function of the layer thickness (d), namely I=f(d), where f() denoted the function relationship which was determined by layers with known intensity and thicknesses, then the unknown thickness of protein layer could be deduced from the detected intensity according to the function.

Microfluidic system: For the fabrication of SPB and the reaction of SPB with protein, a micro-fluidic system [6] in PDMS was used, which includes an 8×6 cell array. When the cell array was attached to the silicon slide surface, 48 individual chambers were formed independently and 48 elliptic spots in the array were patterned onto the silicon surface. Each chamber had two access holes where solution could pass in and out of the chamber through them. By such a micro-fluidic system, different molecules were delivered individually to each spot of the array and immobilized on silicon surface simultaneously. Here it was used for patterning SPB or proteins on silicon surface, transporting of sample solution, reaction of molecular and rinsing.

B. RESULTS AND DISCUSSION

SPB by covalently immobilized on silicon surface:

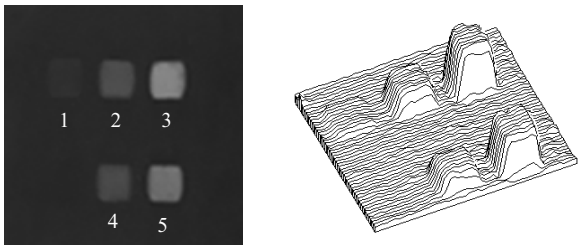
Here SPB consisted of two different phospholipids. One was PE covalently immobilized on silicon surface to form a monolayer, another was PEG functionalized PE adsorbed on the monolayer by hydrophobic interaction to form a SPB. With procedures in Ref.[6], aldehyde groups were introduced on the silicon surface that reacted with amino groups of lipids.

SPB was prepared in the microfluidic system. PE solution(3 mg/ml with the addition of 0.5% Tween 20) was delivered to the silicon surface through the microfluidic system and PE was covalently attached on surface by an imine linkage formed between the aldehyde group on surface and the amine group of PE. After 30 min incubation, buffer was used to rinse the surface, then PEG functionalized PE solution (3 mg/ml)was delivered and incubated with PE monolayer for 30 min to form SPB. Finally SPB was successively rinsed with buffer and purified water.

The ability of SPB on silicon surface to resist non-specific protein adsorption from the aqueous solutions was determined. The PEG grafted on PE is inert, which can avoid protein attaching covalently on bilayer. Fib(1mg/ml), HSA(1mg/ml) and hIgG(1mg/ml) solutions were injected across SPB, respectively. After 30 min incubation, none of the proteins explored caused non-specific adsorption on the bilayer measured with imaging ellipsometry. The adsorption of biomolecules on the bilayer from two more complex solutions, anti-hIgG(10%) and FBS(10%), were studied with imaging ellipsometry, also no adsorption occurred on the bilayers. These results were in agreement with that in other work [7], which indicated that SPB was quite resistant to nonspecific protein adsorption.

hIgG/anti-hIgG binding was employed as a model of antigen-antibody interaction on SPB (the first layer was also PE monolayer and the second layer was COOH-PEG-PE). hIgG solution (0.1mg/ml) was pumped across the bilayers, and then hIgG would be immobilized covalently on surface by stable carbamate bond formed between carboxyl group of PEG chain's end and amino group of hIgG. After incubation for 30 min, BSA solution (10mg/ml) was injected across the bilayers for 30 min. For comparison, hIgG was immobilized covalently on the silicon surface with aldehyde groups directly. Furthermore 10% anti-hIgG in PBS buffer was pumped across hIgG layers for 30 min and rinsed with PBS buffer and purified water. All experiments mentioned above were done on one single silicon slide with the microfluidic system. After dried with a nitrogen blow, the silicon slide was measured with imaging ellipsometry and the result was shown in Fig. 1

The thicknesses of protein layers were calibrated by a traditional ellipsometer (SE400, SENTECH, Germany) equipped with a He-Ne laser (λ=632.8nm, the angle of incidence was 70°). The thickness of SPB-hIgG layers (4.4 nm) was lower than that of hIgG layer (5.0 nm) on silicon slide, but more anti-hIgG (5.7 nm) bound on SPB-hIgG layers than that (4.6 nm) on silicon slide. We repeated the experiment many times and almost same results were obtained, which showed that hIgG molecule attached on phospholipids bilayers can maintain higher bioactivity.



A B

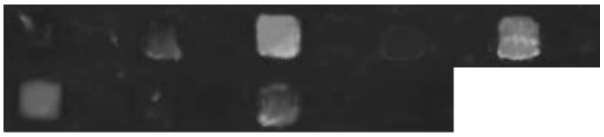
Fig.1. Silicon slide with 5 spots patterned different layers shown in grayscale image (A) and the corresponding thickness distribution image (B). Spot 1 SPB layers, spot 2 SPB-hIgG layers, spot 3 SPB-hIgG/anti-hIgG complex layers, spot 4 hIgG layer, and spot 5 hIgG/anti-hIgG complex layers.

SPB by adsorption on the hydrophilic silicon surface:

In this section, SPB was formed with small unilamellar vesicles (SUVs) fusion on hydrophilic silicon surface. The brief procedure of SUVs preparation was as follows. COOH-PEG-PE was mixed with PC in chloroform. The solvent was then evaporated under a stream of nitrogen followed by desiccation under vacuum at least for 2 hours.

The thin lipid film on the wall of vial was rehydrated in PBS (pH 7.4). The solution was clarified by water bath ultrasonic and extruded at least 11 times through a polycarbonate filter, which had an average pore size of 50 nm.

HSA was chosen as a model ligand to couple to PC/COOH-PEG-PE membrane by activating free carboxyl termini of PEG with NHS/EDC method. With the same procedure of the above section, the non-specific adsorption inhibition and protein bioactivity were studied. Also, the relation between ligand coupling efficiency and the molar content of COOH-PEG-PE was examined, as shown in Fig.2.



A: 1 2 3 4 5
B: 1 2 3 4

Fig. 2 Silicon slide with 9 spots patterned different layers shown in grayscale image. Spot A: 1 Vesicles control (containing 1.5 mol% PE-PEG-COOH). 2 Vesicles containing 0.5 mol% PE-PEG-COOH without NHS/EDC activating. 3 Vesicles containing 0.5 mol% PE-PEG-COOH with NHS/EDC activating. 4 Vesicles containing 1.5 mol% PE-PEG-COOH without NHS/EDC activating. 5 Vesicles containing 1.5 mol% PE-PEG-COOH with NHS/EDC activating. Spot B: 1 negative control. 2 Vesicles containing 4.5 mol%PE-PEG-COOH without NHS/EDC activating. 3 Vesicles containing 4.5 mol%PE-PEG-COOH with NHS/EDC activating. 4 blank control. HSA and anti-HSA were introduced into each spots after forming phospholipid membrane on silica surface (A3, 5 and B3 activating with NHS/EDC, and others were not).

After bumping HSA and anti-HSA across the lipid membrane, there was no obvious grays increase for those lacks of carboxyl activation (as shown in A2, 4 and B2), which illustrated the resistance of SPB to nonspecific adsorption of protein. Moreover, the higher the molar concentration of PEG is, the better the inhibition of SPB to nonspecific adsorption. For those with NHS/EDC activating (as shown in A3, 5 and B3), the amount of protein coupled on SPB was decreasing with the increase of the molar fraction of COOH-PEG-PE. Obviously, there is a trade-off between the better inhibition to nonspecific adsorption of protein and the higher protein bioactivity for the molar concentration of PEG. Here, the protein could be well immobilized and the nonspecific adsorption of protein was reduced below the detection limit when the molar concentration of PEG was as high as 1.5 mol%, which meant it could be used for the biosensor based on imaging ellipsometry.

III. Conclusions

SPB was fabricated on silicon surface for biosensor based on imaging ellipsometry, which was highly protein resistant. Moreover, proteins could be immobilized covalently on the bilayers by the terminal carboxyl group of PEG chain's end, which its bioactivity was higher than that immobilized on silicon surface directly. It showed the biosensor with the potential to be further developed into a sensitive immunoassay technique.

Acknowledgment

The authors would like to gratefully acknowledge financial supports from National High Technology Research and Development Program (863) of China, National Natural Science Foundation of China (10804083, 20845003), Chinese Academy of Sciences((KJCX2.YW.M02 and M04)) and National Post-doctoral Funds.

References

1. Jin G, Tengvall P, Lundstrom I et al, (1995), A biosensor concept based on imaging ellipsometry for visualization of biomolecular interactions. Biochem.232:69-72.
2. Jin G, Jansson R, Arwin H,(1996) Visualization of thin transparent organic films with imaging ellipsometry. Rev. Sci. Instrum. 67:2930-2936.
3. Kanda V, Kariuki J.K, Harrison D.J et al, (2004), Label-free reading of microarray-based immunoassays with surface plasmon resonance imaging.Anal. Chem. 76:7257-7262.
4. Groves, J.T.; Boxer, S.G. (2002) Micropattern formation in supported lipid membranes, Acc Chem Res. 35:149-157.
5. Yang T.L, Jung S.Y, Mao H.B et al, (2001) Fabrication of phospholipid bilayer- coated microchannels for on-chip immunoassays Anal Chem. 73:165-169.
6. Wang Z.H, Meng Y.H, Ying P.Q et al, (2006), A label-free protein microfluidic array for parallel immunoassays. Electrophoresis, 27: 4078-85.
7. Ross E.E, Rozanski L.J, Spratt T et al,(2003) Planar Supported Lipid Bilayer Polymers Formed by Vesicle Fusion. 1. Influence of Diene Monomer Structure and Polymerization Method on Film Properties Langmuir. 19:1752-1765.

Corresponding author: G. Jin

- Institute: Institute of Mechanics,
- Street: Bei-si-huan west road
- City: Beijing 100190
- Country: P. R. China
- Email: gajin@imech.ac.cn

Co-corresponding author: W.R. Chang

- Institute: Institute of Biophysics

- Street: 15 Datun road, Chaoyang district
- City: Beijing
- Country: P. R. China
- Email: wrchang@sun5.ibp.ac.c

Chitosan cushioned air stable single PEGylated phospholipid bilayers

Y. B. Zhang[1,2], Y. Y. Chen[1,3], Z.J. Ding[1], C. X. Wang[1], C. H. Huang[1,2] and G. Jin [4]

[1] Suzhou Institute of Nano-tech and Nano-bionics, CAS, Jiangsu, 215125, P. R. China;
[2] Graduate University of CAS, Beijing, 100049, P. R. China;
[3]Institute of Biophysics, CAS, Beijing, 100101, P. R. China;
[4]Institute of Mechanics, CAS, Beijing, 100190, P. R. China

Abstract—**Air stable single lipid bilayers formation through SUVs fusion methods is still a challenge work. Here soluble LMW chitosan chemically coupled to silicon dioxide surface is cushioned for PEGylated lipid bilayers. Using imaging ellipsometry and spectroscopic ellipsometer, the influence of molar fraction of DSPE-PEG$_{2000}$ for lipid bilayers formation and stability is examined. Under the mushroom phase, PEGylated lipid vesicles may aggregate to multiple bilayers; while entering the brush regime of PEG, vesicles can fused into single lipid bilayers. It is demonstrated both the appropriate mole fraction of PEGylaed lipid and hydrophilic polymer cushion are equally critical for achieving air and wash stable single lipid bilayers. Imaging ellipsometry also show the promise as an easy and useful tool for future air stable lipid bilayers based biosensor.**

Keywords— **air stable, single phospholipid bilayers, chitosan, imaging ellipsometry**

I. Introduction

Artificial biological membranes-supported phospholipid bilayers (SPB) have been used as model membranes, e.g., to study cell-cell recognition in the immune system [1], adhesion of cells [2] and membrane proteins or ion channels based biosensors [3]. Small unilamellar vesicle (SUVs) is used widely for SPB preparation since its easier manipulation and handling. However, vesicles would form multiple lipid bilayers rather than single bilayers after adsorption and fusion onto substrate, which might be troublesome sometimes in the application. Most of published research works on phospholipid membrane are mainly using fluorescence labeling and fluorescence recovery after photobleaching (FRAP) technology, which is never telling the detailed structure of lipid bilayers. In an effort to overcome this problem, we recently designed a polymer cushioned PEGylated lipid membrane for future application in protein sensor. With the hand of imaging ellipsometry, we can examine the thickness of formed lipid bilayers and discriminate the single bilayers or not.

II. Materials and methods

Materials

1,2-Distearoyl-sn-Glycero-3-Phosphoethanolamine-N-[Methoxy(Polyethylene glycol)-2000] (DSPE-PEG$_{2000}$), 1,2-Dimyristoylphophatidylcholine (DMPC) were products of AvantiPolar Lipid, Inc., Alabaster, AL. 3-aminopropyltriethoxysilane (APTES) were purchased from Acros Organics, Belgium. LMW chitosan (MW=10, 000, degree of deacetylation: 85. 31%) was a gift from Jinan Haidebei Marine Bioengineering Co., China.

Methods

LMW chitosan modified silicon substrate

Polished silicon wafers was cleaned with pirahna solution and further modified with APTES according to the protocols described before [4]. NHS activating succinic acids was used as cross-linkers for surface coupling of LMW chitosan.

PEGylated lipid membrane formation

SPB was formed through extruded SUVs fusion method [5]. The substrate dotted with SPB was washed with deionized water and dried with pure nitrogen gas before further detection with imaging ellipsometry or thickness measurement with Woollam M-2000 spectroscopic ellipsometer.

Imaging ellipsometry

The phospholipid membrane array was detected by imaging ellipsometry which was detailed in other places [6]. It was used a CCD camera to image the ellipsometry response of a larger area sample with lateral distribution in different layer thickness, and the result was grabbed as a digital image and stored in a computer with a grayscaleformat (8 bits, 0–255 grayscale) for further evaluation by an image-processing program.

III. Results and discussion

Air-stable chitosan cushioned PEGylated lipid membrane

O. Dössel and W.C. Schlegel (Eds.): WC 2009, IFMBE Proceedings 25/VIII, pp. 169–171, 2009.
www.springerlink.com

Piranha solution treatment can make silicon surface super hydrophilic, with a contact angle lower than 5°. After modified with APTES, the surfaces will loss some extent of hydrophilicity and the contact angle was about 55°. It was reported that either PEG [7] or γ-aminopropylsilane [8] could enhance the air stable of lipid membrane. However, neither PEG nor APTES used in our experiments succeed in showing the air stability of lipid membrane. After doting vesicles on the three different supports: super hydrophilic silicon surface, APTES modified silicon and LMW chitosan coupled surface, only chitosan cushioned PEGylated membranes gave visible lipid layers after washing and drying procedure (Fig. 1).

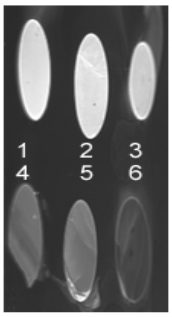


Fig. 1 Air-stable chitosan cushioned PEGylated lipid membrane. The numbers indicate several molar contents of DSPE-PEG_{2000}, which are 0.1, 0.25, 0.5, 1.5, 2.5, 5 mol% successively.

Here we proposed a possible reason for such interesting results as potentially unsymmetrical distribution of PEG in the upper and down layer of lipid membrane. It is not difficult to imagine the steric hindrance of PEG molecules within vesicles, so more PEG moieties may prefer to occupy the out-layers of vesicles. Both Salafsky [9] and Contino [10] had shown that the orientation of the leaflets was preserved upon fusion of proteoliposomes to plain glass. In that case, the out-layer of vesicle should become upper layer of lipid membrane after vesicles adsorption on support, which results in the uneven amount of PEG between upper and lower bilayers. If it is true for above hypothesis and the PEG is in mushroom phase, the much less PEG of lower layer will inevitably fail protecting the lipid membranes when they are exposed to the air/water interface. While the hydrophilic chitosan cushion could increase the bending elastic modulus of the lipid membrane and thus increase the barrier for lipid patches to roll up into sheets and peel away as vesicles.

Single PEGylated phospholipid bilayers

As shown in the Fig. 2, the grayscales of PEGylated lipid membrane decreased while the molar fraction of PEG was increased. SUVs containing PEG lower than 1.5 mol% gave much brighter membranes. The grayscale of lipid membranes containing 0.1 mol% reached as high as the ultimate value. From our observation, we concluded that the membrane was comprised of bilayer aggregates and/or unfused vesicles.

We got a good linear region after curving the thickness of lipid membranes against grayscale values. After calculating thickness of lipid membrane with series PEG content, it was found the membrane thickness was gradually reduced to the normal single bilayers as increasing PEG molar fraction. A supported lipid bilayer is characterized by having a thickness of 4-5 nm. [11] However, the dried PEGylated lipid membrane also showed a thickness around 4 nm (Fig. 3). The polymer moieties have little impact on the thickness of lipid membrane when they are all in dehydration environment. It maybe due to hydrophilic polymer cushion and PEG shielding both upper and down layer, lipid membrane could keep stable in the air condition. (Fig. 4)

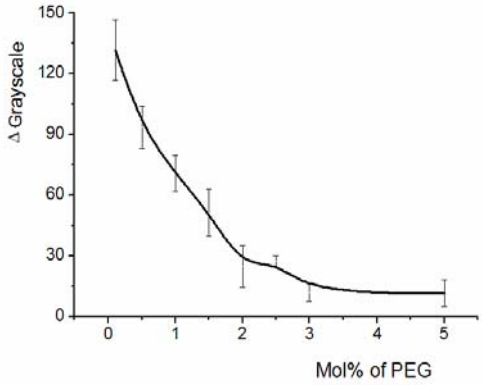


Fig. 2 Grayscales values addition against mole fraction of DSPE-PEG_{2000}.The grayscales values were decreasing as increasing the mole fraction of PEG.

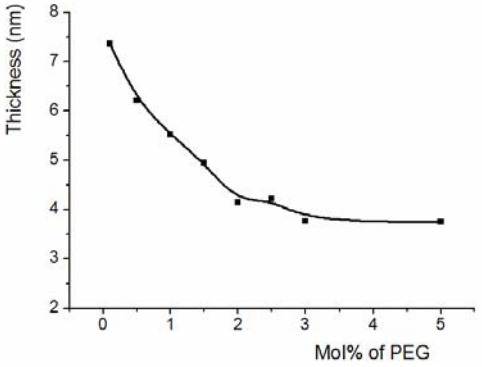


Fig. 3 Membrane thickness against mole fraction of DSPE-PEG_{2000}.The lipid membrane thicknesses were reducing while raising PEG content.

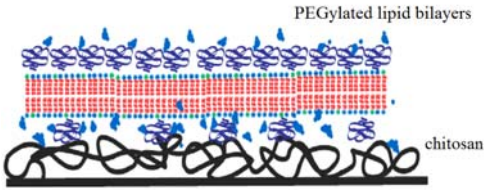


Fig. 4 Schematic chitosan cushioned lipid bilayers.

The transition from mushroom to brush phase happened when molar fraction of PEG_{2000} reached 1.4 mol% [12]. Within the mushroom phase, PEG was in too low density and had little power of stealth effect [13], which was an ability of a PEG-grafted layers to prevent close approach to the liposome surface. In the absence of sufficient grafted polymer, vesicles will adhere to existing lipid bilayers to form multilayer through van der Waals' attraction [14]. As a result, the thickness or grayscales of lipid membrane was much higher than that of single bilayers. When the hydration repulsion of PEG molecules between vesicles and bilayers were improved as raising the PEG amount, the vesicles in the solution would cease to adsorb or fuse onto the formed lipid membrane and the single bilayers could be maintained.

But it seemed too early to say the single lipid bilayer could be formed only if the PEG molar fraction was added above its mushroom-to-brush phase transition concentration. We found PEGylated lipid membrane would be washed away if PEG was added more than 5 mol%, since there was no obvious grayscales addition or thickness detection. We thought that was caused the interactions between polymers and water molecules. Under the vigorously or repeated washing force, PEG will be pulled out from lipid structure, inducing the latter deformation and depletion of lipid membrane.

IV. Conclusions

Here a simple and facile method is used for air and wash stable single lipid bilayer formation. Results demonstrate that the surface density of DSPE-PEG_{2000} is a critical parameter in single lipid bilayers formation visualized by using imaging ellipsometry and spectroscopic ellipsometer. It is suggested the proper molar fraction of PEG for getting single lipid bilayers is around at its mushroom-to-brush phase transition. Furthermore, taking hydrophilic polymers as lipid cushion, like chitosan, is also a key for keeping air stability of lipid membrane.

Acknowledgment

We thank Mr. Tian of Jinan Haidebei Marine Bioengineering Co. for kind gift. The authors would like to gratefully acknowledge financial supports from National Basic Research Program of China 2009CB320300, National High Technology Research and Development Program (863) of China, National Natural Science Foundation of China(10804083, 20845003), Chinese Academy of Sciences((KJCX2.YW.M02 and M04)) and National Post-doctoral Funds.

References

1. McConnell H M, Watts T H, Weis R M et al. (1986) Supported planar membranes in studies of cell-cell recognition in the immune system. Biochim Biophys Acta 864:95-106.
2. Stelzle M and Sackmann E. (1989) Sensitive detection of protein adsorption to supported lipid bilayers by frequency-dependent capacitance measurements and microelectrophoresis. Biochim Biophys Acta 981:135-142.
3. Castellana E T and Cremer P S. (2006). "Solid supported lipid bilayers: From biophysical studies to sensor design." Surf Sci Rep 61: 429–444.
4. Wang Z H and Jin G. (2004) Covalent immobilization of proteins for the biosensor based on imaging ellipsometry. J Immunol Methods 285:237– 243.
5. Lapinski M M, Forero A C, Greiner A J et al. (2007) Comparison of liposomes formed by sonication and extrusion: rotational and translational diffusion of an embedded chromophore. Langmuir 23:11677-11683.
6. Jin G. (2008). Development of biosensor based on imaging ellipsometry. Phys Stat Sol (a) 205:810-816.
7. Albertorio F, Diaz A J, Yang T et al. (2005) Fluid and Air-Stable Lipopolymer Membranes for Biosensor Applications. Langmuir 211:7476-7482.
8. Fang Y. (2006) Spreading and segregation of lipids in air-stable lipid microarrays. J Am Chem Soc 128:3158 -3159.
9.. Salafsky J, Groves J T and Boxer S G. (1996) Architecture and function of membrane proteins in planar supported bilayers: a study with photosynthetic reaction centers. Biochemistry 35:14773-14781.
10. Contino P B, Hasselbacher C A, Ross J B et al. (1994) Use of an oriented transmembrane protein to probe the assembly of a supported phospholipid bilayer. Biophys J 67:1113-1116.
11. Castellana E T and Cremer P S. (2006) Solid supported lipid bilayers: From biophysical studies to sensor design. Surf Sci Rep 61:429–444.
12. Needham D, Kim D H. (2000) PEG-covered lipid surfaces: bilayers and monolayers. Colloid Surfacce B 18:183–195.
13. Lasic D D and Needham D. (1995) The" Stealth" Liposome: A prototypical biomaterial. Chemical Reviews 95:2601-2628.
14. Cevc G and Marsh D. (1987) Phospholipid Bilayers. Physical Principles and Models. Wiley-Interscience, New York.

Corresponding Author: Gang Jin
Institute: Institute of Mechanics, Chinese Academy of Sciences
Street: #15, Bei-si-huan west Road
City: Beijing 100190
Country: P.R. China
Email: gajin@imech.ac.cn

Application of Carbonyl Iron Powder as a Novel Mediator for Arterial Embolization Hyperthermia—Feasibility Investigation

Lingyun Zhao[1], Wei Jiang[2], Yongjian Jin[3], Xiaowen Wang[1], Xufei Wang[1] and Jintian Tang[1]

[1] Institute of Medical Physics and Engineering; Department of Engineering Physics; Tsinghua University, Beijing, China
[2] Department of Biopharmaceutics; Beijing University of Chinese Medicine, Beijing, China
[3] Department of Neurosurgery, 2nd Affiliated Hospital of Tsinghua University, Beijing, China

Abstract— **In this study, we proposed carbonyl iron powder (CIP) as a novel mediator for arterial embolization hyperthermia (AEH). In vitro cytotoxicity study with cultured L929 cells was carried out to test the biocompatibility of the CIP. Effect of alternative magnetic field (AMF) on the temperature rise of CIP was performed by exposing the CIP/Lipiodol suspensions under AMF with different field strength. In vivo heating curve of the hepatic artery after transcatheter arterial embolization (TAE) was also conducted by applying New Zealand half lop rabbits as animal model. Cytotoxicity study demonstrated that CIP showed good biocompatibility. Heating curves, both in vitro and in vivo, revealed that CIP possessed ideal property of inductive heating characteristics under AMF. Our findings suggest that CIP is a very promising mediator candidature of AEH for clinical application.**

Keywords— **Magnetic Inductive Hyperthermia, Arterial Embolization Hyperthermia, Carbonyl Iron Powder, Heating, Cancer Targeted Treatment**

I. Introduction

Magnetic inductive hyperthermia (MIH, also termed as magnetic mediated hyperthermia, MMH) is a new approach for cancer treatment which currently being under clinical trials [1-3]. Selective or targeted hyperthermia can be achieved by heating biocompatible superparamagnetic mediators, which are localized within the tumor tissues, by an externally applied AC magnetic field. For the liver cancer treatment, MIH could be categorized as direct injection hyperthermia (DIH) or AEH, depending on the different administration pathway of the mediator particles. The basis for AEH to tumor treatment is the fact that macroscopic liver tumors derive virtually all their blood supply from the hepatic arterial system, and so any substance infused into the arterial system will have the potential to preferentially target liver tumors [4]. In order to determine whether AEH or DIH produces better tumor response rate, Moroz et al ever conducted in vivo study on small animal models of liver tumors to evaluate tumor response to AEH and DIH [5]. Their findings indicate that AEH is more effective than DIH at moderately elevated temperatures. The possible explanation, as they suggested, may be due to the more widespread particle distribution that can be achieved by TAE which resulting in more extensive and complete treatment of the tumor.

Superparamagnetic mediators or agents play critical role in the AEH, especially the safety concern and heating property. Besides, it was argued by Jones SK that mediator particles for AEH should be micron-sized to ensure that they are trapped in the capillary bed surrounding the tumor rather than passing through to the venous circulation [6]. However, superaramagnetic mediators under clinical trials of MIH are normally nano-sized. Moreover, seldom research was carried out on developing an ideal mediator of micro-size for AEH. ICP (with trade name of Ferronyl®, ISP Pharmaceuticals) has been approved by FDA for dietary iron supplement by oral administration due to its low toxicity and excellent bioavailability [7]. It is elemental iron with high iron content and highly resistant to oxidation. The typical average particle size is about several microns, which potentiates its further application as mediator for AEH. In this study, cytotoxicity and heating property of CIP under AMF has been carried out. Our investigation provides feasibility study on developing a novel and suitable mediator candidature for AEH.

II. Materials and methods

A. Materials

CIP was manufactured by ISP Pharmaceuticals, Wayne, USA. Lipiodol was purchased from Guerbet, France.

B. Morphology and Size Distribution of CIP

Morphology of the CIP particles was observed by scanning electron microscopy (SEM, Jeol JSM 5600LV). The size distribution of the particles was determined by laser light scattering with particle size analyzer (90 Plus, Brookhaven Inst, NY, US) at a fixed angle of 90º at 25ºC.

C. Preparation of ICP Extracts

Samples of sterilized CIP were added to RPIM-1640 cultural medium in a proportion of 1cm^2/mL and incubated for 48h at 37ºC. Serial dilutions were made of extracts from the

O. Dössel and W.C. Schlegel (Eds.): WC 2009, IFMBE Proceedings 25/VIII, pp. 172–175, 2009.
www.springerlink.com

CIP samples, the CIP free cultural medium (negative control) and the 0.02% phenol solution (positive control).

D. Cytotoxicity with Cultured L-929 Cells

This test was conducted according to Evaluation on Biological of Medical Apparatus GB/T 16886.5-1997. L-929 mouse fibroblast cells were used to evaluate cytotoxicity, which was assessed by using the colorimetric MTT assay and compared with that of negative control. MTT assay is based on the reductive capacity of living cells to metabolize the tetrazolium salt, 3-(4,5-dimethythizaol-2-yl)-3,5-diphenyl tetrazolium bromide (MTT), to a chromophore, formazan product, the absorbance of which was determined at 570nm by spectrophotometry of a microplate reader(Bio-Rad Laboratories). The relative growth rate of the cultured cells (RGR) was calculated as the ratio of absorbance of experimental group to that of negative group.

Cytotoxicity could be categorized from Grade 0 to Grade V according to Table 1, in which Grade 0 and I are regarded as no cytotoxicity.

Table 1Cytotoxicity grade based on RGR

Cytotoxicity Grade	RGR
0	≥100
I	75-99
II	50-74
III	25-49
IV	1-24
V	0

E. Preparation of GIP/Lipiodiol Suspensions

CIP/Lipiodiol suspensions were prepared by suspending CIP to 1mL Lipiodiol. The suspensions were then ultrasonicated for 5min followed by agitation on a vortex mixer for one minutes. The formed CIP/Lipiodiol suspensions were subsequently subjected for in vitro heating under AMF or hepetic arterial embolization.

F. Hepatic Arterial Embolization

This experimental study was performed using 16-to 20-week-old New Zealand half lop rabbits weighing 2 to 3kg each. The arterial infusion procedure was designed to mimic that of a possible infusion in a human subject. Upon embolization, each rabbit was subjected to a barbiturate induction general anesthetic. An incision was made in the anesthetized rabbit to expose the right or left femoral artery.

The artery was then punctured by an 18G trochar. The needle was withdrawn and the cannula was left in the artery. A 2.3F cobra catheter was then inserted into the femoral artery. The catheter guided by a guide-wire under Digital subtraction angiography (DSA) was located up to the hepatic artery. After agitation on a vortex, 1mL of CIP/Lipiodiol suspension (60mg of particles) was steadily infused through the catheter, with great care taken to avoid an efflux of the suspension out of the artery. The entire infusion process was confirmed by DSA. After the completion of infusion, the catheter was removed, followed by the ligation of the femoral and closure of the operative wound to complete the operative procedure. After operation, the behavior, appetite and vital signs—especially the rate of respiration—were closely monitored in the rabbits. Embolized rabbits were subjected to the exposure under an AMF.

G. Temperature Measurement

Thermal-couple temperature probe (Model IT-18, Copper-Constantan, Physitemp, New Jersey, USA) was applied during the AEH for the temperature measurement. A 2-cm midline abdominal incision commencing just inferior to the xiphoid process, with peripheral retraction of the abdominal wall, provided to exposure the abdominal viscera. For the purpose of temperature measurement, two or three proves were inserted into the liver tissue and one into the rectum. After insertion of temperature proves the abdominal incision was sutured so that only the prove fibers penetrated the abdominal wall, thereby minimizing heat loss to the environment. The probe fibers were connected to a four-channel millivoltmeter (Model XS01A-4, Beijing Kunlun TianChen Instrument Technology, Co., Ltd, Beijing, China) and the data were collected every 12 seconds by PC with home-written software.

H. Method of Heating

Each embolized rabbit, while still anesthetized, was exposed to the AMF generated by inductive heating device (ShuangPing Instrument Technology, Co., Ltd, ShenZhen, China). After baseline temperature were recorded, the magnetic field was initially set to 2.92 kA/m, alternating at 300kHz, then adjusted up to 8.77kA/m if necessary, until the desired temperature was achieved and maintained for 20min.

III. Results and discussions

A. Morphology and Size Distribution of the CIP

CIP is a grey powder. When examined under SEM, CIP particles are highly spherical (Fig. 1). CIP has a narrow particle size distribution (Fig. 2). The typical average par-

ticle size is about 5 microns, which meets the size requirement as mediator for AEH.

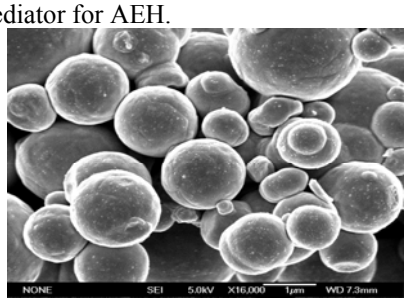


Fig. 1 SEM image of CIP particles

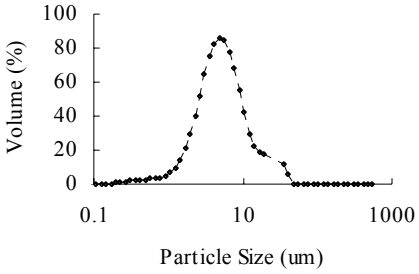


Fig. 2 Size distribution of CIP powders

B. In Vitro Cytotoxicity Assessment

The RGR of L-929 cells and cytotoxicity grade of CIP after 2 and 7 days culture were summarized in Table 2. For any experimental condition, the cytotoxicity grade of CIP particles is within Grade 0 and Grade I, which reveals that the CIP particles showed no cytotoxicity, but significant cytotoxicity occurred in positive control group. This results demonstrates that CIP has excellent biocompatibility for further investigation.

Table 2 In vitro cytotoxicity grade of CIP

	2d		7d	
Group	RGR(%)	CG	RGR(%)	CG
100% Extracts	81.88	1	90.25	1
50% Extracts	100.8	0	102.44	0
Negative Control	100	0	100	0
Positive Control	0	5	0	5

CG: Cytotoxicity grade

C. In vitro Heating Profile of the CIP/Lipiodiol Suspension

Effect of particles content: The heating profile of the CIP/Lipiodiol suspensions with different CIP contents under AMF of 8.77kA and 300kHz was shown in Fig. 2. It is obvious to notice that the heating curve exhibits an asymptote, which signals the equilibrium of the heating process. The curves show that the rate and the equilibrium of the heating depend strongly on the CIP contents, i.e. higher particles content in the suspension can ensure a higher final temperature upon equilibrium.

Effect of field strength of the AMF: Another decisive factor for the heating process is the field strength of the AMF. As can be seen in Fig. 3, higher field strength results in a greater increase in the temperature, which means more energy can be generated by the CIP particles. The rate of temperature rising, as can be reflected by the slope of the profile, becomes faster as well.

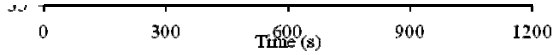


Fig. 3 In vitro heating profile of CIP/Lipiodiol suspensions with various particle contents

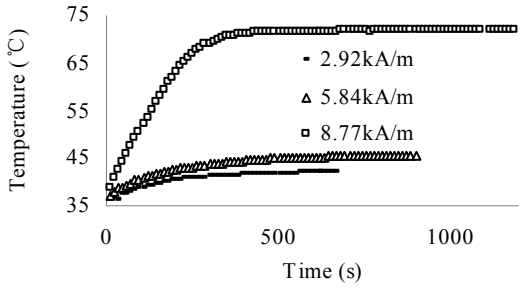


Fig. 4 Effect of field strength of AMF on the in vitro heating profile of CIP/Lipiodiol suspensions

Our findings confirm that the heating profile of a mediator for AEH is dependent on the particle content in the suspension as well as the field parameter of the AMF. Therefore, it is convenient to control the process temperature of the cancer treatment by adopting Lipiodiol suspension with appropriate mediator particles content or adjusting the field parameter of the AMF, or both.

D. In vitro investigations

Fig. 4 shows the TAE of the CIP/Lipiodiol suspension confirmed by DSA. No rabbit died of complications related to the implantation process, the arterial catheterization process. Or the CIP/Lipidiol suspension infusion process during the experiment.

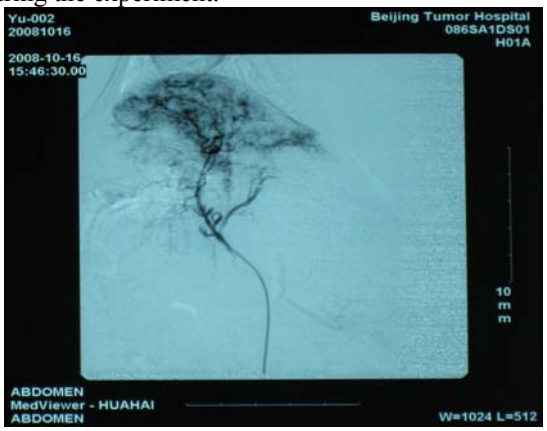


Fig. 5 TAE of the CIP/Lipiodiol suspension confirmed by DSA

In vivo heating profile of the embolized rabbits is demonstrated in Fig.6. The figure shows that the within 4min the-temperature of liver tissue rapidly hit and maintained around 50 ºC whereas there was no observable temperature increase in the rectal prove of any rabbit, which suggests that no significant corporeal heating occurred during the treatment. This observation strongly suggests that CIP has excellent inductive heating characteristics, therefore has great potential as a mediator of AEH for clinical application.

IV. Conclusions

This study systematically investigated the feasibility of applying CIP as a novel, safe while effective mediator for AEH. Preliminary results show that CIP particles are with micron-sized spherical shape and narrow size distribution. It possesses excellent biocompatibility as confirmed by in vitro cytotoxicity test. Both in vitro and in vivo heating profile revealed that CIP has ideal inductive heating characteristics which can guarantee treatment temperature during cancer hyperthermia. Therefore it can be concluded that CIP could be an ideal candidature as AEH mediator. Further investigation on animal tumor model is being carried out to validate the conclusion.

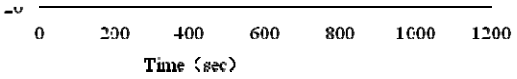


Fig. 6 In vivo heating profile for rabbits subjected to AEH (n=5).

Acknowledgement

This study is supported by China National Natural Science Foundation (No.30571779;PI: Tang Jintian) The authors are grateful of Professor Yang Renjie of Beijing Tumor Hospital for his valuable discussions and excellent technical assistance.

References

1. Landeghem F, Maier-Hauff K, Jordan A et al. (2009) Post-mortem studies in glioblastoma patients with thermotherapy using magnetic nanoparticles. Biomaterials 30: 52-57
2. Johannsen M, Gneveckow U, Thiesen B et al. (2007) Thermotherapy of prostate cancer using magnetic nanoparticles: feasibility, imaging and three-dimensional temperature distribution. Eur Urology 52: 1653-1662
3. Johannsen M, Gneveckow U, Taymoorian K et al (2007) Morbidity and quality of life during thermotherapy using magnetic nanoparticles in locally recurrent prostate cancer: results of a prospective phase I trial. Int J Hyperthermia 23: 315-323
4. Moroz P, Pardoe H, Jones SK et al (2002) Arterial embolization hyperthermia: hepatic iron particle distribution and its potential determination by magnetic resonance imaging. Phys Med Biol 47:1591-1602
5. Moroz P, Jones SK, Gray BN et al (2002) Tumor response to arterial embolization hyperthermia and direct injection hyperthermia in a rabbit liver tumor model. J Surg Oncol 80: 149-156
6. Pardoe H, Clark PR, Pierre TG et al (2003) A magnetic resonance imaging based method for measurement of tissue iron concentration in liver arterially embolized with ferromagnetic particles designed for magnetic hyperthermia treatment of tumors. Mag Res Imaging 21: 483-488
7. www.ispcorp.com

Corresponding author: Tang Jintian
Institute: Medical Physics and Engineering
Street: Tsinghua University
City: Beijing
Country: PR China
Email: tangjt@tsinghua.edu.cn

Development of a Multifunctional Microfluidic System for Studies of Nerve Cell Activity during Hypoxic and Anoxic Conditions

Nazanin Bitaraf[1], Ahmed Ahmed[1], Michael Druzin[2], and Kerstin Ramser[1]

1. Department of Computer Science and Electrical Engineering, Luleå University of Technology, 971 87 Luleå, Sweden
2. Department of Integrative Medical Biology, Section for Physiology, Umeå University, 901 87 Umeå, Sweden

Abstract—**Hemoproteins usually supply cells and tissue with oxygen. A new hemoprotein mainly present in nerve cells called Neuroglobin was recently discovered. Enhanced expression of the protein has been shown to reduce hypoxic neural injury but the mechanism behind this function remains unknown. Methods enabling investigation of the protein in single functional neurons need to be developed. Here, we have studied how the electrical signaling capacity of a neuron was affected by hypoxic environments. Preliminary results show a trend of higher noise-level when a neuron is exposed to hypoxic compared to normoxic surroundings, which implies increased ion-channel activity. The setup used today shows shortages such as reduced control over the oxygen content due to leakage. Therefore, a gas-tight, multifunctional microfluidic system is under development which enables us to study influences of Neuroglobin concentrations on neuronal activity during hypoxia and anoxia. For electrophysiological recordings a patch-clamp micro pipette will be molded into the walls of the microfluidic system. A single biological cell is steered towards the pipette and attached there by means of optical tweezers. The Neuroglobin oxygen binding state will be studied using optical spectroscopy and the neuron environment will be manipulated by applying flows of varying oxygen content through the microfluidic system. This system will constitute a powerful tool in the investigation of the Neuroglobin mechanism of action.**

***Keywords*—Neuroglobin, hypoxia, multifunctional microfluidic system, patch clamp, optical tweezers, optical spectroscopy**

I. INTRODUCTION

The nerve system depends on oxygen for its survival and if the oxygen flow to a cell is restrained the cell may suffer irreparable damage or die. The oxygen supply to tissue and cells is usually provided by hemoproteins.

In 2000, a new hemoprotein was discovered and since this hemoprotein is mainly present in nerve cells it has been named Neuroglobin (Ngb) [1]. Much research has been conducted to learn more about the protein. Its 3D structure and abundance have been studied extensively. The function, on the other hand, is still a matter of debate [2]. Our main interest, i.e. the research performed to unravel Ngb's possible function as a neuroprotectant against hypoxic or ischemic injury, has been examined previously [3]. Evidence was found that neuronal hypoxia induces Ngb expression, and enhanced Ngb expression reduces hypoxic neuronal injury. The challenge that still remains is to investigate the mechanism by which Ngb functions during oxygen deprivation.

Previous research has mainly been implemented on the protein in its purified form and there is a need of better methods to investigate Ngb activity in a functional biological cell. Our research group aims to develop a multifunctional microfluidic system enabling supervision of influences of Ngb concentrations on neuronal activity during hypoxia and anoxia.

II. METHODS

A. Preparation of neurons and solutions

Ethical approval of the procedures described was given by the regional ethics committees for animal research ("Stockholms södra djuförsöksetiska nämnd", approval No. S201/04 and "Umeå djurförsöksetiska nämnd", approval No. A17-05).

Cell preparation

Neurons were prepared from the brains of male Sprague Dawley rats who were decapitated without anesthetics, the brains were rapidly removed and placed in pre-oxygenated ice-cold (4 °C) incubation solution (150mM NaCl, 5mM KCl, 2mM $CaCl_2$, 10mM HEPES, 10mM glucose, 4.93mM Tris-base, pH 7.4) which was also used throughout the entire slicing procedure.

Slicing procedure

A vibratome (Vibratome 100plus, Ted Pella, Redding, CA, USA, or Vibroslicer 752 M, Campden Instruments, Leicestershire, UK) was used to cut 200 - 300 mm thick coronal slices from the part of the block of brain tissue containing the anterior hypothalamus. Slices were then

O. Dössel and W.C. Schlegel (Eds.): WC 2009, IFMBE Proceedings 25/VIII, pp. 176–179, 2009.
www.springerlink.com

allowed to recover for at least one hour in incubation solution at room temperature (21 - 23 °C).

Acute dissociation of MPN neurons

Neurons from the medial preoptic nucleus (MPN) were used here since they have been studied earlier [4] and this area of the brain has shown to contain Ngb [5].
A glass rod (about 0.5 mm in diameter) mounted on a piezoelectric bimorph crystal, was used to apply mechanical vibration at the site of the MPN on the slices. Dissociated cells were then allowed to settle at the bottom of a Petri dish for approximately 10 min.

Recording solutions

Extracellular solution **(**137mM NaCl, 5.0mM KCl, 1.0mM $CaCl_2$, 1.2mM $MgCl_2$, 10mM HEPES, 10mM glucose, pH 7.4(NaOH)) was used for flushing the cells. Amphotericin B (Sigma) was added to the intracellular solution (140mM Cs-gluconate, 3.0mM NaCl, 1.2mM $MgCl_2$, 10mM HEPES, 10mM EGTA, pH 7.2 (CsOH)) from stock solution (6 mg/100 µl DMSO) and added to a final concentration of 120 µg/ml pipette-filling solution.

B. Patch-clamp technique

To be able to register the electrical signals across the plasma membrane of a single neuron, the patch-clamp technique was implemented. [6]

Electric signal recordings were made between a ground electrode placed in the neuron containing Petri dish, which was positioned on the stage of an up-right Olympus BX51Diaphot 200 microscope (Olympus, Japan), and a recording electrode within the recording pipette, which was pulled from borosilicate glass (GC150, Harvard Apparatus Ltd., Edenbridge, Kent, UK), attached to a neuron. The pipettes had a resistance of 3-5 MΩ when filled with intracellular solutions and amphotericin B (Sigma). Signals were recorded using an Axopatch 700A amplifier, a Digidata 1322A interface and pClamp (version 9) software (all from Axon Instruments, Union City, CA).

To allow electric contact with the cell cytoplasm while keeping the cells interior composition intact the perforated patch recording configuration using the perforating antibiotic amphotericin B was used [7].

The recordings were made in the current clamp mode.

C. Oxygen measurement

The neurons surroundings at normal conditions were mimicked by the cell being exposed to normal extracellular solution which had about 19-21% oxygen content. To achieve controlled hypoxic environment around the cell N_2 gas was added to the extracellular solution until an oxygen level of around 3-5 % O_2 was attained, creating an environment similar to that of neurons during hypoxic insult.

The solutions were provided to the cells by a gravity-fed perfusion system with an outlet positioned in close contact to the studied cell. Switching between solutions was controlled by solenoid valves.

The oxygen level was measured with a fiber optic oxygen sensor probe, FOXY AL300, connected to MultiFrequency Phase Fluorometer (both from Ocean Optics, Dunedin, Florida, USA). The neurons were subsequently flushed with each of the solutions to mimic normoxic and hypoxic conditions.

The oxygen leakage in the system was examined by checking the oxygen content repeatedly in the vessel containing the solution compared with the oxygen content at the outlet of the perfusion pipette, i.e. at the cell. The measurements were repeated seven times. The result was expressed as mean ± standard error of mean (SEM).

III. PRELIMINARY RESULTS

The measurements of the oxygen content in the perfusion tank, from where the hypoxic extracellular solution was delivered, and at the outlet of perfusion pipette showed a significant leak of oxygen into the perfusion system which was adding 4,3 ± 0,5 % of oxygen to the extracellular solution. Consequently, the recorded neuron was exposed to oxygen content between 7-9 % during experimental hypoxic condition.

Variations in membrane potentials from a neuron could be observed while performing patch-clamp in the perforated patch mode, see Fig. 1. As Fig. 1a) shows, a higher noise-level could be seen when the cell was exposed to a hypoxic solution compared to a normoxic solution, indicating increased ion-channel activity. This can also be noticed in Figs. 1b) and 1c) which also show that there was no dramatic change due to oxygen manipulation in the release of inhibitory neurotransmitter, gamma-aminobutyric acid (GABA), from adherent presynaptic terminals since the frequency of the spontaneous inhibitory postsynaptic potentials (sIPSPs) did not change.

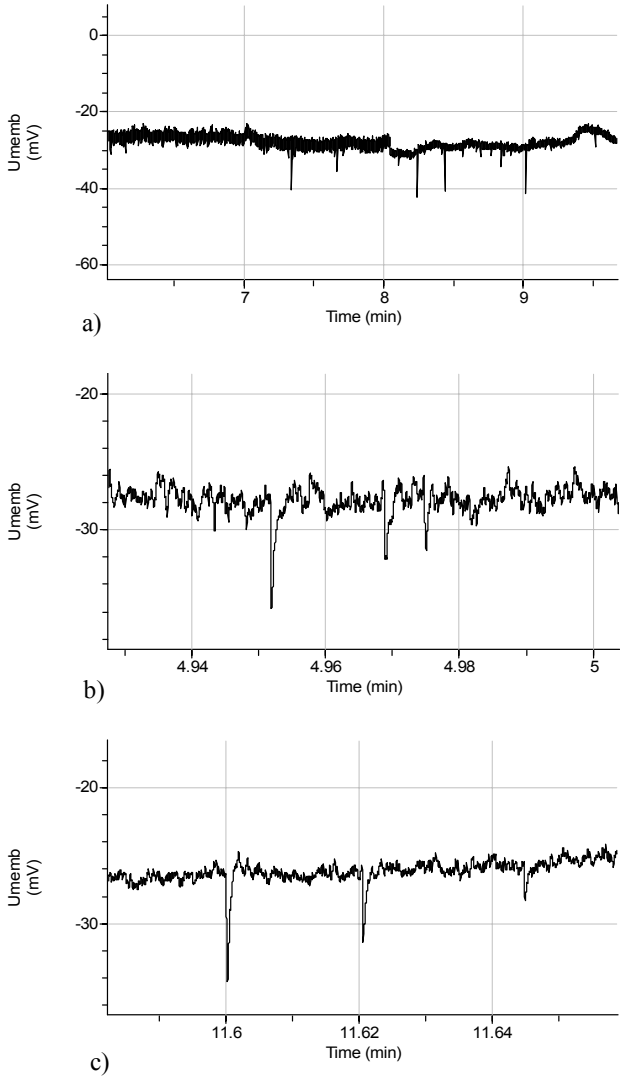


Fig. 1 Variations in the cells membrane potential, Umemb (mV) versus Time (min). 1a) Solutions were changed from hypoxic to normoxic at t = 8.03. Note how the noise of the signal decreases subsequently. 1b) Shows a zoomed in part of a recording of postsynaptic membrane potentials during a hypoxic period. 1c) Shows the same as 1b) but during a normoxic period. For both b) and c) the sIPSCs (fast negative peaks) were mediated by Cl^- entering the cell through GABA-gated ion channels ($GABA_A$ receptors) upon their activation by GABA released from presynaptic terminals..

IV. Discussion of Preliminary Results

The set up used today to maintain a hypoxic environment shows clear shortages as oxygen leaks into the system. Despite of that we have studied how the electrical signaling capacity of a neuron was affected by hypoxic environments by recording the electrical signals of the neuron. The result indicates an increased ion-channel activity during hypoxic conditions. Future experiments will aim at clarification of the ion-channel mechanisms underlying the noise-level changes as well as the possible effects of hypoxia on the neurotransmission. Furthermore, to get better, statistically verified, results more data must be collected.

V. Future Outlook

The preliminary results show that better control over the oxygen content must be achieved. Moreover, for future experiments regarding the role of Ngb during hypoxia, the oxygen binding of Ngb in correlation with the cell signaling should be registered. This can ideally be achieved by optical spectroscopy. Our future approach is to combine the existing patch-clamp setup for electrophysiological recordings with a sealed multifunctional microfluidic system that enables optical monitoring and manipulation of a single neuron. The methods that will be merged into the existing setup are described briefly below.

Microfluidic system

A microfluidic system usually comprises different channels molded into rubber silicon either having reservoirs or sealed in-, and outlets. The microfluidic systems used here are manufactured by soft lithography [8]. In brief, the design is first created with a software drawing program (CAD). Thereafter a high resolution mask is created by e-beam lithography. Polydimethylsiloxane (PDMS) is molded onto the mask and hardened. The PDMS slab is removed from the mask and sealed onto a conventional cover slide.

Optical tweezers

This method refers to optical manipulation by highly focused laser light that enables the steering of cells and particles with high precision in three dimensions without mechanical contact [9]. To achieve gentle optical trapping, near infrared laser light is expanded and focused through a microscope objective having a high numerical aperture (NA). Optical tweezers can easily be implemented into existing setups, in this case to the patch clamp microscope.

Raman spectroscopy and absorption spectroscopy

Raman spectroscopy is a laser based technique. By illuminating molecules with well defined laser light they can be excited into a vibrational state, resulting in an energy change of the outgoing photons. This energy difference gives minute information about the structure and state of molecules. The method is excellent to register the oxygen binding state of hemoproteins, since the porphyrin ring of the protein strongly absorbs several wavelengths in the visible up to the near infrared region. By choosing a wavelength close to an absorption wavelength a resonance effect

can be achieved that is strong enough to register the oxygen content of a cell without interference of other cell components. This has been used to study *Escherichia coli* bacteria that over express Ngb [10].

Absorption spectroscopy is a complementary method by which the oxygenation state of hemoproteins can be registered. Here, the sample is illuminated with the whole visible spectrum and the transmitted light is compared to the ingoing light, concluding which wavelengths have been absorbed by the sample. Since the hemoprotein changes color upon binding to the porphyrin ring the absorption spectrum changes thereafter.

The fusion of the techniques

As mentioned above, the ongoing challenge is the design a closed multifunctional microfluidic system, giving total control over the oxygen content while enabling measurements of both the action potential of a single nerve cell and the oxygen binding state of Ngb. This is not achieved with an ordinary open-flow system. Conventionally, the patch clamp pipette is brought in close contact with the cell by micro-positioning. Here, a single biological cell will be steered with 3D-nanometer precision through the closed multifunctional microfluidic system with optical tweezers and be attached to the patch-clamp micropipette, as seen in Fig. 2. The micropipette is moulded into the PDMS walls of the microfluidic system which has two inlet channels that merge into one. The oxygen content surrounding the cell is controlled by means of changing the flow pressure at one inlet channel, while cutting off the inflow through the other channel. A schematic figure of the setup is shown in Fig. 2.

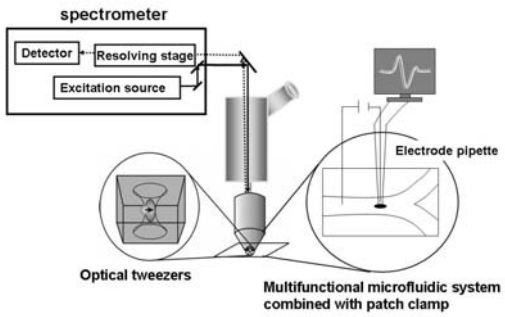


Fig. 2 A schematic graph of the future setup involving a spectrometer, a microscope, optical tweezers and a multifunctional microfluidic system combined with a patch clamp setup.

VI. Conclusions

To be able to study how the electrical signaling capacity of neurons is affected by hypoxic environments and Ngb concentration the existing setup is under improvement. The setup will be equipped with a sealed multifunctional microfluidic system. Furthermore, the system will be equipped with the optical methods described in this paper and thereby creating a powerful tool to establish the mechanism of Ngb's function on the single cell level.

Acknowledgment

The study was supported by grants from Objective 2 Norra Norrland-EU Structural fund and the Swedish Research Council.

References

1. Burmester T, Weich B, Reinhardt S et al. (2000), A vertebrate globin expressed in the brain, Nature 407:520-522
2. Brunori M, Vallone B (2007), Neuroglobin, seven years after, Cell Mol Life Sci, 64:1259-1268
3. Greenberg DA, Jin K, Khan AA (2008), Neuroglobin an endogenous neuroprotectant, Curr Opin Pharmaco l 8:20-24
4. Druzin M, Haage D, Johansson S, (2004), Bicuculline free base blocks voltage-activated K+ currents in rat medial preoptic neurons. Neuropharmacology 46 (2): 285-295
5. Hundahl CA, Allen GC, Nyengaard JR et al. (2008), Neuroglobin in the rat brain, Neuroendochrinology 88(3):173-182
6. Sakmann B and Neher E (1984), Patch Clamp techniques for studying ionic channels in excitable membranes, Ann Rev Physiol 46:455-72
7. Rae J, Cooper K, Gates P et al. (1991), Low access resistance perforated patch recordings using amphotericin B, J Neurosci Methods 37 (1):15-26
8. Enger J, Goksör M, Ramser K et al. (2004) Optical tweezers applied to a microfluidic system, Lab Chip, 4(3):196-200
9. Lang MJ, Block S (2003), Resource Letter: LBOT-1: Laser-based optical tweezers, Am J Phys, 71 (3): 201-212
10. Ramser K, Wenseleers W, Dewilde S et al. (2007), Micro-resonance Raman study of optically trapped Escherichia coli overexpressing human Neuroglobin, J Biomed Opt 12(4):044009

A Novel Microfluidic Based Technique for Encapsulation of Langerhans´ Islets Using High Viscosity Alginate and $BaSO_4$ Nanoparticles

F. Ehrhart[1], Patrick Stumpf[1,4], S. Wiedemeier[2], E. Weyand[3], R. Danzebrink[5], M.M. Weber[3], J. Metze[2], V. Sukhorukov[4], U. Zimmermann[4], and H. Zimmermann[1,6]

[1] Fraunhofer IBMT, Department for Biophysics and Cryotechnology, St. Ingbert, Germany
[2] IBA, Heilbad Heiligenstadt, Germany
[3] University Hospital Mainz, Department for Endocrinology, Mainz, Germany
[4]University Würzburg, Chair for Biotechnology, Germany
[5]Nanogate, Göttelborn, Germany
[6]University of Saarland, Professorship for Molecular and Cellular Biotechnology/Nanotechnology, Saarbrücken, Germany

Abstract— **Transplantation of immunoisolated endocrine tissue could improve the therapy of many diseases, especially the in industrial countries common diabetes mellitus, without use of immunosuppressive treatment. Many efforts have been taken to choose the proper capsule material, to make it biocompatible and to produce it in a standardized way but the capsule production process still needs improvement. Ultra high viscosity alginate is currently the most promising capsule material because its biocompatibility and the crosslinking conditions are biologically agreeable. Common capsule production techniques are e.g. spray-, vibration- or jet-cutting technique but these techniques are not in a closed system and therefore open to contamination and external influence. Here, we want to present a novel, microfluidic based encapsulation machine and first, promising results with different cell types.**

Keywords— **diabetes, alginate, encapsulation, microfluidics, nanoparticles**

I. Introduction

Diabetes is one of the most common diseases in industrial countries. Type 1 diabetes is a complete deficiency of insulin producing β-cells because of pathologic autoimmune activity. External blood glucose supervision and regulation by insulin application is the common therapy but this artificial regulation can never damp metabolic oscillations which lead over long time to vessel damage. Fine vessels in retina and kidney suffer usually first as well as those in external limbs. Transplantation of the missing Langerhans´ islets would usually lead to immunologic rejection and needs immunosuppressive treatment with all its adverse reactions. Encapsulation of Langerhans´ islets in a biocompatible matrix protects them from immunologic attacks and therefore restores insulin supply without immunosuppressive treatment. High viscosity alginate, crosslinked with Barium, is our material of choice because it is long term stable, fully biocompatible and provides nutrient supply and proper insulin release [1]. Since the first try of Lim and Sun (1980) [2] many improvements have been done to make transplantation of encapsulated islets a therapy for human patients, e.g. improved biocompatibility through ultrapure high viscosity alginates [3] or long term stability [4]. Nevertheless, the immunoisolated transplantation is not used for human patients yet because of, *inter alia*, the "open" production of capsules with the spray technology [4,5]. The novel microfluidic encapsulation machine, which we want to present here, is a closed system which reduces the risk of contamination and is able to produce alginate capsules in a safe and reproducible way.

II. Materials and Methods

A. Cells and cell culture

L929 cells, a murine fibroblast cell line, were obtained from DSMZ (Braunschweig, Germany) and cultured in DMEM supplemented with 10% FBS and gentamycine (all cell culture materials were obtained from Gibco/Invitrogen, Karlsruhe, Germany). Twice a week the cell culture was splitted using Trypsin/EDTA. Langerhans islets were provided by university hospital Mainz (department for endocrinology) isolated from Wistar rats by a collagenase digestion according to previously published protocols [6].

Free spheroids were produced by cultivation of cell suspension in a non adhesive petri dish and harvested after 4 days. For further details see [7] and literature cited there.

Cell viability was measured using the protocol described in [6], namely the FDA (fluorescein diacetate) and EB (ethidium bromide) staining.

B. Preparation of cell suspension for encapsulation

Alginate was extracted from raw algae material according to previously published protocols [4]. Alginate solution was prepared by dissolving dry alginate granules in isotonic

O. Dössel and W.C. Schlegel (Eds.): WC 2009, IFMBE Proceedings 25/VIII, pp. 180–182, 2009.
www.springerlink.com

NaCl-solution (all chemicals obtained from Sigma, Schellendorf, Germany it not mentioned otherwise) to get a 0.65% res. 0.7% solution. For Langerhans islets, 0.017% Pluronic was added to the NaCl solution.

Cell suspension in alginate was prepared by collecting cells in a centrifugation tube, discharging of the supernatant and resolving the pellet in alginate solution.

C. Microfluidic encapsulation

The core of the microfluidic encapsulation machine is a microstructured fluidic-chip witch brings two channels, one for alginate and cells and another for the separation of carrier medium, together [8]. The microfluidic chip is made of Teflon as well as the tubing. Several prototypes and demonstration chips were made of transparent Teflon coated Plexiglas instead. In the chip the separation fluid (highly hydrophobic perfluorodecalin, PFD) and cell suspension in alginate solution are brought together forming tiny alginate compartments (about 400µm diameter which is about 10 nl).

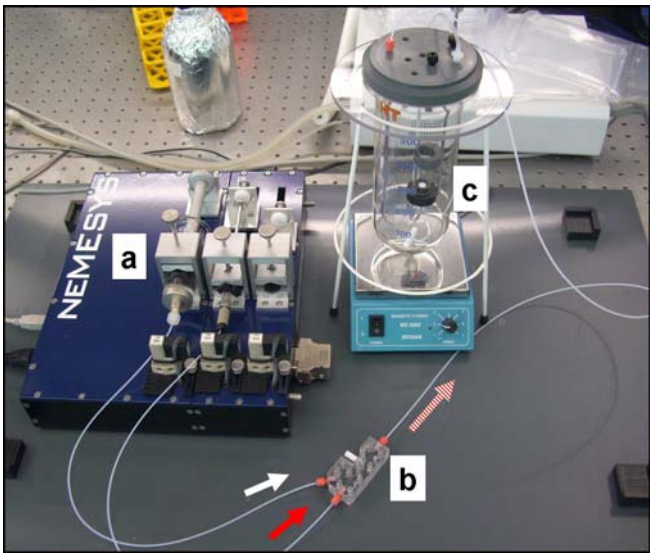


Fig. 1 Microfluidic encapsulation machine – (a) PC driven syringe pump with two syringes filled with alginate/cell suspension or PFD; (b) in the microstructured fluidic chip alginate suspension is aliquoted in tiny compartments of about 10 nl. The picture shows a transparent demonstration microchip instead of the Teflon chip. The alginate compartments are guided into the collecting vessel (c) where the alginate droplets ascend in the heavy PFD until reaching the polymerization solution which is on the top of the PFD.

These compartments are guided into the collecting vessel which is filled to ¾ with hydrophobic PFD, so the alginate compartments detach from the tubing and ascend until reaching the polymerization solution which is on the top of the PFD. Polymerization solution is an isotonic NaCl solution which contains 20mM $BaCl_2$ and 5mM histidine. The alginate compartments polymerize when they contact to the $BaCl_2$-solution and after 20min incubation they can be taken out of the $BaCl_2$-solution, washed with isotonic NaCl-solution and taken up in culture medium. The alginate/cell suspension and the PFD were driven by a PC-controlled syringe pump (NemeSYS, Cetoni, Korbußen, Germany).

Application of nanoscaled $BaSO_4$ particles was performed using a suspension of $BaSO_4$ particles in PFD provided by Nanogate (Göttelborn, Germany). The concentrated suspension was added to the PFD in the collecting vessel and covered with a layer of polymerization solution. Encapsulation was performed the same way, except the washing was done with help of a cell sieve (100µm pores) to get properly rid of the particles.

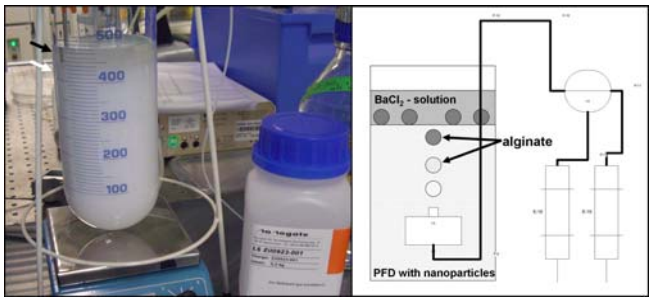


Fig. 2 Application of $BaSO_4$ nanoparticles in the microfluidic encapsulation machine: nanoparticles are suspended in PFD in the collecting vessel (white arrow). Alginate compartments get contact to the particles during ascend to the polymerization solution (black arrow).

III. Results And Discussion

Viability was measured after encapsulation with the microfluidic encapsulation machine and the spray encapsulation machine. Table 1 summarizes the viability data for encapsulated single L929 cells and spheroids. After encapsulation with the microfluidic encapsulation device the viability of the cells is generally lower than with the spray encapsulation machine but about 80% which is still an acceptable value for cell cultivation.

Table 1 Viability [%] of encapsulated L929 cells or L929 spheroids

(n = 3)

	spray encapsulation	microfluidic encapsulation	microfluidic encapsulation with nanoparticles
cells	96,0 ±2,8	83,9 ±10,1	79,0 ±6,7
spheroids	86,4 ±3,6	68,9 ±11,3	71,8 ±8,7

Spheroid viability cannot be measured exactly by optical methods. Viability of complete viable spheroids can vary between 80% and 90% depending on image quality and fluorescence intensity [6].

A possible cause for cell damage may be the shear stress in those tiny tubes. Shear stress is higher in more viscous liquids. Further experiments with shorter tubing will clarify this hypothesis. It was also observed that the cells and spheroids recover if they are cultivated over night in petri dishes with culture medium. The day after encapsulation viabilities were about 5-10% higher.

An experiment of capsule production without use of the polymerization solution, only with $BaSO_4$ nanoparticles in the PFD and isotonic NaCl solution on the top of the PFD, resulted in big clods of partly polymerized alginate without regular shape.

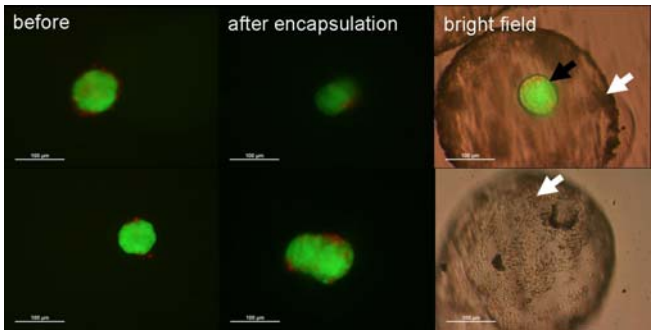


Fig. 3 Langerhans islets before and after encapsulation in alginate using the novel microfluidic encapsulation machine and nanoparticles: FDA and EB staining (living cells fluoresces green, dead red) shows high viability of the islets before and after encapsulation. $BaSO_4$ nanoparticles tend to aggregate or to form a precipitate layer around the capsules which may be a problem for biocompatibility.

Viability of Langerhans islets decreased slightly after encapsulation which is also observed in the former encapsulation machine possibly due to sheer stress. To our experience the islets recover after over night incubation in culture medium. We also observed aggregation of $BaSO_4$ particles on the surface of the alginate capsules which may also affect the image analysis based viability calculation.

Table 2 Viability [%] of Langerhans´ islets before and after microfluidic encapsulation with $BaSO_4$ nanoparticles

	viability [%]
before encapsulation	76,9 ±5,8
after encapsulation	59,9 ±19,9

IV. Conclusion

All our cell models survived the encapsulation with the new microfluidic encapsulation machine with acceptable viability results. The microfluidic encapsulation machine produces alginate capsules which are comparable to those which are made by spray technique but is easier to handle, and to clean. Furthermore, it is a closed system which will pave the way to clinical use.

Acknowledgment

We gratefully thank BMBF (0313680D, 16SV2387) for funding.

References

1. Zimmermann H, Shirley SG, Zimmermann U (2007) Alginate-based encapsulation of cells: past, present, and future. Curr Diab Rep 7(4):314-320
2. Lim F, Sun AM (1980) Microencapsulated islets as bioartificial endocrine pancreas. Science 210:908-910
3. Zimmermann U, Thürmer F, Jork A et al. (2001) A novel class of amitogenic alginate microcapsules for long-term Immunoisolated transplantation. Ann N Y Acad Sci 944:199-215
4. Zimmermann H, Hillgärtner M, Manz B et al. (2003) Fabrication of homogeneously cross-linked, functional alginate microcapsules validated by NMR-, CLSM- and AFM-imaging. Biomaterials 24(12):2083-2096
5. de Vos P, Faas MM, Strand B et al. (2006) Alginate-based microcapsules for immunoisolation of pancreatic islets. Biomaterials 27(32):5603-5617
6. Schneider S, Feilen PJ, Brunnenmeier F et al. (2005) Long-term graft function of adult rat and human islets encapsulated in novel alginate-based microcapsules after transplantation in immunocompetent diabetic mice. Diabetes. 2005 Mar;54(3):687-93.
7. Ehrhart F, Schulz JC, Katsen-Globa A et al. (2008) A comparative study of freezing single cells and spheroids: Towards a new model system for optimizing freezing protocols for cryobanking of human tumours. Cryobiology (in print)
8. Wiedemeier S (2009) Diabetes – Süßes Gift Zucker und seine Folgen – Therapie des Diabetes mellitus mittels immunisolierter Inselzellen. BIOforum 1/2009:14-16

Corresponding author:

Author: H. Zimmermann
Institute: Fraunhofer IBMT
Street: Ensheimerstrasse 48
City: 66386 St. Ingbert
Country: Germany
Email: heiko.zimmermann@ibmt.fraunhofer.de

Analysis of chemotactic activity of mammalian cells in a microfluidic device

A. Lankenau, A. Renner and C. Duschl

Fraunhofer Institute of Biomedical Engineering, Am Mühlenberg 13, 14476 Potsdam, Germany

Abstract— **Local concentration patterns of certain compounds can direct the migration of animal cells and bacteria. This phenomenon is called chemotaxis. The analysis of chemotactic activity is a valuable diagnostic approach for the characterization of immune or tumour cells. Present assay formats are either time consuming or difficult to perform. We present a microfluidic device that allows fast and efficient analysis of the chemotactic activity of cells. Our approach is fully compatible with high-resolution optical microscopy and hence provides access to intracellular processes that may serve as early indicators of directed migration.**

Keywords— **cell migration, cytoskeleton, diffusion, early markers, high-resolution optical microscopy.**

I. Introduction

Most cell types exhibit the ability to sense chemical gradients in their environment and implement these signals into directed migration, which is referred to as chemotaxis. The study of this process is fundamentally important in many areas of biology and biomedicine, like cancer research and immunology. However, the commonly used assays are only of limited use. Transwell systems based on the 'Boyden chamber' [1] generate stable gradients but allow no on-line microscopic observation of migrating cells. Other systems as reviewed in [2] are compatible with microscopy but are difficult to use and cannot warrant full control over the gradient. In recent years, microfluidic devices have been developed to generate stable gradients of chemoattractants over adherent cells and are compatible with high-quality optical microscopy. Inside the system developed by Jeon [3], neutrophils were efficiently induced to migrate along a gradient of IL-8 but the system is very sophisticated and likely to be susceptible to technical pertubations. This also applies to the system by Shamloo [4], which allowed detailed morphological studies of HUVEC cells using high-resolution fluorescence microscopy. We developed a microfluidic device even simpler than the trident-shaped channel described by Nie [5]. However, the main goal of our approach is to identify early markers for chemotactic activity in order to accelerate its analysis with respect to current protocols. Cell shape, organization of the cytoskeleton or the expression of migration-associated proteins could serve as parameters that indicate chemotactic activity long before a cell has migrated a measurable distance. For monitoring such parameters, the device was designed in order to be fully compatible with high-resolution optical microscopy. For performing the assay, cells were flushed into the chip and adhered to the bottom of a "Y-Type" microfluidic channel (width: 500 µm, height: 100 µm) with two input streams and one output stream. As the flow in the microfluidic channel is laminar and thus transport between parallel streams occurs only via diffusion, gradients of chemoattractants can be produced and positioned with high precision and stability. Adherent cells sensing this gradient migrate towards the attractant, whereas cells outside the gradient area migrate randomly. Using this straightforward setup, we induced chemotaxis of human HFF-1 fibroblasts in a gradient of EGF. From time-lapse recordings and subsequent image analysis, chemotactic parameters were determined in dependence of the cells' positions in the gradient.

II. Results

Chemotaxis experiments were performed in a Y-shaped microchannel (length: 2 mm, width: 500 µm, height: 100 µm). Seeding of human HFF-1 fibroblasts on the bottom of the microchannels was achieved by introducing them through the two inlet ports employing a very low flow rate. For enhancing cell adhesion, a monolayer of the extracellular matrix (ECM) component fibronectin was formed beforehand by flushing the channel with a 10 µg/ml protein solution for ½ hour. Through the parallel injections of the plain cell medium on one inlet port and the medium containing the chemoattractant epidermal growth factor (EGF) (concentration: 10 ng/ml) on the other inlet port, a diffusion-driven EGF concentration gradient could be established. The concentration profile fitted well to the 1-dimensional solution of Fick's 2nd law (see Figure 1) and its steepness decreased downstream along the channel according to the time needed for a particular volume element to be transported. The concentration gradient was highly stable and could be maintained without interruption for several hours. A fully automated optical microscope allowed the monitoring of the concentration gradient (if a fluorescent probe was used) and the migration of the live cells in the microchannel over these periods. As the steepness of the gradient varied over the width of the channel, it was divided into five sections and chemotactic

O. Dössel and W.C. Schlegel (Eds.): WC 2009, IFMBE Proceedings 25/VIII, pp. 183–184, 2009.
www.springerlink.com

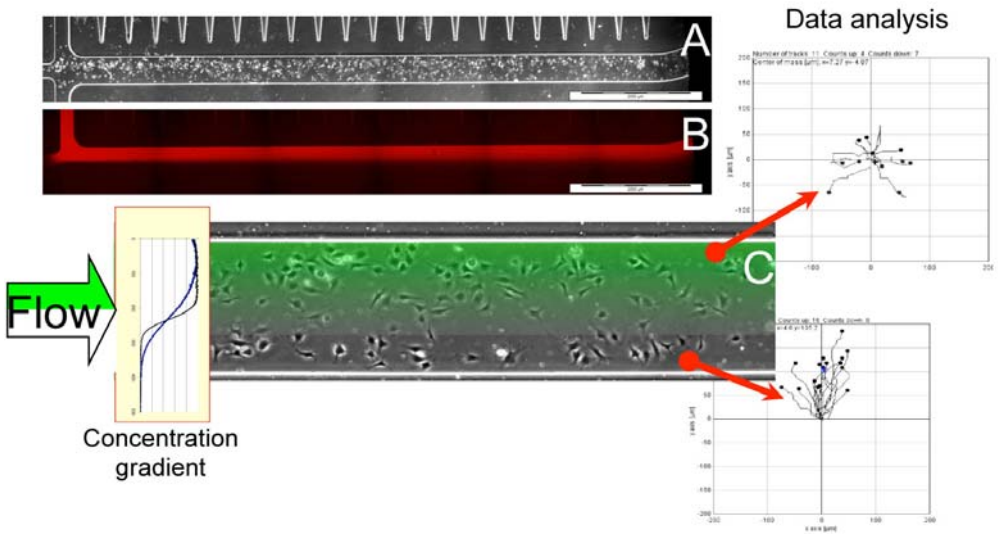


Fig. 1 Chemotaxis Assay in a Microfluidic Channel: Parquetted phase contrast (top) and fluorescence (bottom) micrographs of HFF1cells in a 20mm long microfluidic channel. Human HFF-1 fibroblasts show positive chemotaxis in a FITC-labelled EGF (epidermal growth factor) concentration gradient (c_0= 100 ng/ml). Two representative track plots are shown (right). Chemotactic activity was highest in the segment with the lowest absolute concentration and negligible in the sector where the concentration saturates, with intermediate activity in the regions between.

response was separately evaluated in these regions (see Figure 1). Track plots where the starting positions of all cells of one section were set to a common origin give a comprehensive overview of the migration pattern of the cells. Interestingly, chemotactic activity was highest in the segment with the lowest absolute concentration and negligible in the sector where the concentration saturates. Intermediate activity was measured in the regions between. By plotting the relative concentration gradient ($\frac{dc}{dy}\frac{1}{c}$), it becomes clear that chemotactic activity or the chemotactic index CI scales well with this parameter (CI=Δy/d with Δy being the cellular displacement towards the gradient and d being the total migration distance). Another aspect that is worth being mentioned concerns the behaviour of cells when traversing more then one segment. The migration velocity or CI per time unit remained constant after a distinct acceleration phase, irrespective in which segment the cell was migrating. It appeared that the chemotactic activity of a cell is determined by the properties of the gradient during its start and the cell possesses a kind of chemotactic memory. In order to demonstrate the compatibility of our set up with high-resolution optical microscopy, we introduced fibroblasts that express actin-GFP and performed live cell imaging of single cells (results not shown). In the future, we plan to exploit the translocation of other migration-related proteins, which may indicate the beginning of chemotactic migration. We expect this to dramatically reduce the time required for functional chemotaxis assays and additionally to yield more significant information about chemotactic processes.

III. Conclusions

A microfluidic device is presented that allows the characterization of chemotactic activity of adherent cells. Our approach is fully compatible with high-resolution optical microscopy and hence allows the use of intracellular markers for an early detection of chemotactic activity.

Acknowledgment

We are grateful for financial support from the European Commission – FP6: NEST project “Control Cancer Stem”.

References

1. a) BOYDEN S., J Exp Med. 1962 Mar 1;115:453-66., b) Partsch G, Schwarzer C.,J Biolumin Chemilumin. 1991 Jul-Sep;6(3):159-67.
2. Bignold LP., J Immunol Methods. 1988 Apr 6;108(1-2):1-18.
3. Li Jeon N, Baskaran H, Dertinger SK, Whitesides GM, Van de Water L,Toner M., Nat Biotechnol. 2002 Aug;20(8):826-30.
4. Shamloo A, Ma N, Poo MM, Sohn LL, Heilshorn SC., Lab Chip. 2008 Aug;8(8):1292-9.
5. Nie FQ, Yamada M, Kobayashi J, Yamato M, Kikuchi A, Okano T., Biomaterials. 2007 Sep;28(27):4017-22.

An Adjustable Optofluidic Micro Lens Enhancing Single Cell Analysis Systems

M. Rosenauer and M.J. Vellekoop

Institute of Sensor and Actuator Systems, Vienna University of Technology, Vienna, Austria

Abstract— **In this contribution we present experimental results of a hydrodynamically adjustable optofluidic micro lens with the ability to focus light three-dimensional. This liquid-core/liquid-cladding lens utilizes two fluids with different refractive indices. The principle of variable curvature radii of the lens body is successfully demonstrated. By integrating the 3D fluidic lens in a flow cytometer the measurement sensitivity of the system can be increased substantially. We developed a novel single cell analysis device combining 3D hydrodynamic focusing of the analyte and 3D focusing of the incident light beam for optical measurements.**

Keywords— **Optofluidics, Micro Lens, Rapid Prototyping, Single Cell Analysis**

I. Introduction

In the last years various successful implementations of optical microfluidic systems in point-of-care (POC) diagnostics have been demonstrated [1]. The rapidly increasing number of publications in the field of optical lab-on-a-chip (LOC) [2] illustrates the great interest of the scientific community in the topic. Nevertheless, the transformation of proof-of-principle devices into commercially relevant micro-systems often faces the challenging points of fabrication costs, measurement sensitivity and portability.

The name LOC determines the integration of many useful items from a laboratory. To implement optical elements, like lenses, waveguides, light sources and detectors, many approaches have been presented to overcome the above mentioned problems. In optical single cell analysis (fluorescence spectroscopy or absorbance detection) the detection sensitivity is often determined by the quality of light guidance, the optical path length and the visual range of the optical inspection region. To exchange expensive bulky laboratory equipment with low-cost, but also less sensitive detection devices, one has to integrate better light guiding elements. With 2 ½ dimensional fabrication methods it is very difficult to fabricate micro lenses with the possibility to focus light three-dimensional. Various approaches have been presented to overcome these difficulties in terms of light focusing and guiding [3]. In this contribution we present a hydrodynamic micro lens with the possibilities not only to focus the incident light three-dimensional but also with a tunable focal length.

II. Optofluidic Principle of the 3D Lens

Liquid-core/liquid-cladding (L^2) optical elements [4 - 6] have recently attracted great interest because of simple reversible altering of optical element parameters (lens curvature, waveguide dimension, refractive index) by adjusting flow rates of the fluid streams in the micro-channel system.

Figure 1 depicts the formation of a 3D optofluidic lens [7]. The design utilizes three inlets for lens core and cladding flows and one outlet. Furthermore, two 90-degree curves bend the core/cladding interface wall for each lens component as a result of the Dean-vortices [8]. By combining the channels a transversal biconvex lens is generated. The fluid streams are now driven through a horizontal expansion region where the flow profile is widened in the center producing the three dimensional character of the optofluidic lens.

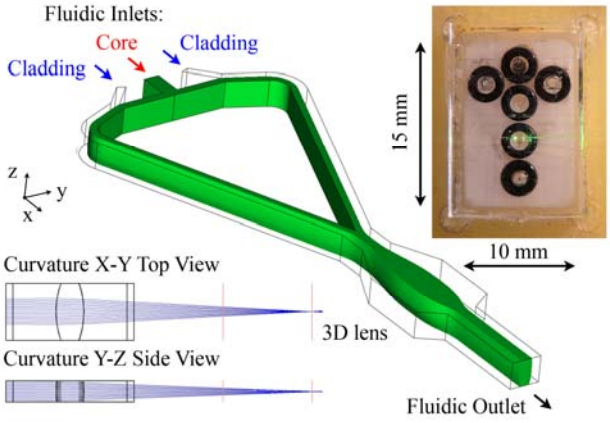


Fig. 1 Schematic illustration of the reconfigurable optofluidic lens. By altering the flow rates of the fluidic inlets the curvature in X-Y and Y-Z plane is tunable in the range of 100-1600 µm. In the fluidic simulation (COMSOL Multiphysics) the optical interface and thus the lens body (green) is defined as the derived surface with a refractive index $n_3 = (n_1 + n_2) / 2$. By importing the geometry data of the CFD-simulation (Computational Fluid Dynamics / Finite-Element-Method) and defining the source parameter (fiber source, NA = 0.22, λ = 532 nm) we simulated the optical system by ray tracing (ZEMAX EE). Inset: Micrograph of the fabricated device spring-mounted on a custom-made holder utilizing rubber o-rings and PTFE – tubes for the fluidic interconnection.

O. Dössel and W.C. Schlegel (Eds.): WC 2009, IFMBE Proceedings 25/VIII, pp. 185–188, 2009.
www.springerlink.com

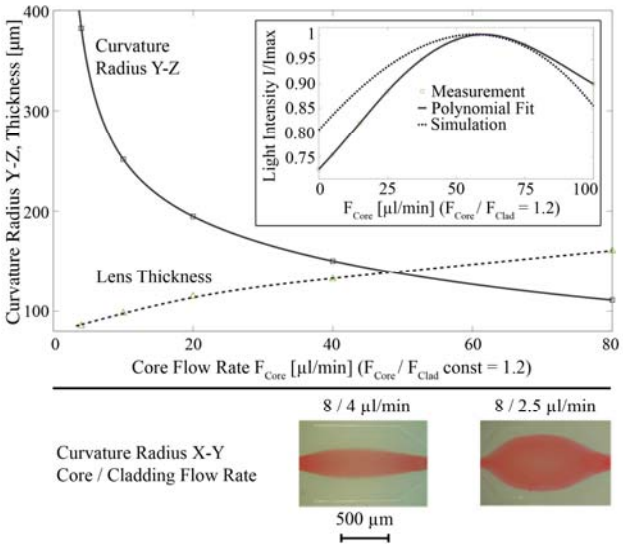


Fig. 2 (Top) Curvature radius of the liquid lens (Y-Z) as a function of the core flow rate. Below F_{Core} = 5 µl/min the lens shape is influenced by discontinuous pumping distortions; above F_{Core} = 70 µl/min the lens height decreases and the form misshapes to a non-cylindrical lens. The curvature of the lens in the X-Y plane is invariant to absolute changes in flow rates. The thickness of the lens increases nearly linear with increasing flow rates. Inset: Comparison of light intensity measurement and ray tracing simulation of the light irradiance over the glass fiber core area. (Bottom) Curvature radius of the lens (X-Y) at two distinct flow rate ratio. The core flow (red ink) rate is fixed which reshapes the lens in the X-Y plane. The transversal lens is not altered as a function of the relative flow rate.

For the measurement experiments the device was fixed on a plastic holder (Figure 1) to achieve sealed fluidic interconnections to syringes. The flow rates at the different inlets were applied by syringe pumps. As light source we used a fiber-coupled solid-state laser (532nm, 50/150 µm). The fiber end was cleaved and inserted into the fiber trench. A Si-photodetector connected to a multimode fiber was applied to measure the focused light. The used fluids are Benzothiazole (core, n = 1.64) and a mixture of ethanol and trichloro-trifluoroethan (cladding, n = 1.36). We measured the focused light intensity to evaluate the quality of the optofluidic lens in the Y-Z plane (Figure 2, Top). The measurement results confirm the simulations which are performed by calculating the integrated irradiance over the outlet fiber core area. The difference results from non-perfect channel sidewall quality caused by the resolution of the prototyping method and from the non-continuous flow rates of the syringe pumps used for the measurement. We also evaluated the horizontal lens characteristics (X-Y plane) at two distinct flow rate ratios (Figure 2, Bottom). The results confirm the functionality of the presented optofluidic lens and enable novel designs like the one we present in section IV.

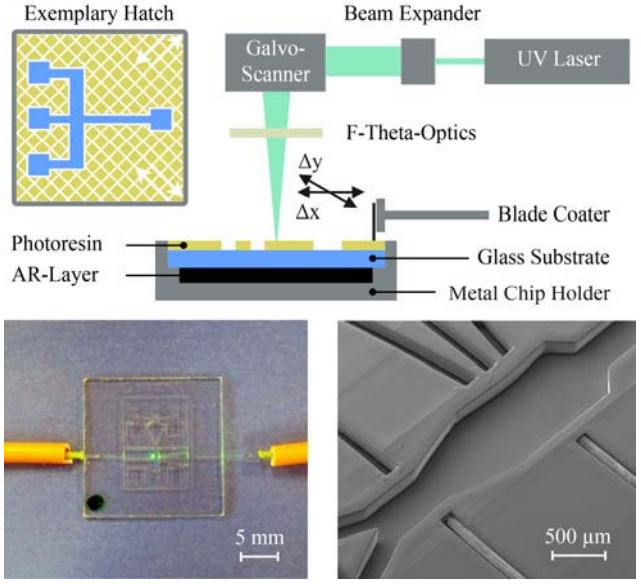


Fig. 3 (Top) Schematic micro-stereolithography setup for the fabrication of single-layer devices. An UV-absorber coating is deposited on the bottom of the substrate to reduce back-reflections. (Bottom) Photograph of the glass substrate with an additive laser-structured photoresin layer and inserted glass fibers. Details of the expansion chamber are illustrated in the SEM (scanning electron microscope) image.

III. Device Fabrication

Micro-stereolithography is a versatile tool to manufacture prototypes in a fast and quality-reliable manner [9, 10]. The standard stereolithography technique allows fabricating a structured design layer by layer by laser induced polymerization. The deflectable laser beam transforms a photosensitive liquid (Renshape SL-7870, cured density ρ = 1.15 g cm^{-3}) to a solid spot. The resin is polymerized by a focused UV-laser beam (spot size d = 3-4 µm, P_{CW} = 800 µW, v = 150 mm s^{-1}) which follows a scanning hatch pattern resulting from the channel design. By utilizing the micro-stereolithography setup (Figure 3) with a custom-made metal chip holder we have simplified substrate alignment and resin coating for our application compared to conventional techniques [9].

With these adaptations the fabrication duration is under 1.5 hours from the CAD-data to the ready-to-use optofluidic device. Without a resin cover layer the removal of the unpolymerized resin is simple. By conventional solvent treatment the uncured liquid resin is dissolved and the structure cleansed before the final UV curing. The structured microchannels built on the glass substrate are capped with a PDMS lid and top-clamped with a PMMA slide. The fabricated results are shown in Fig. 3.

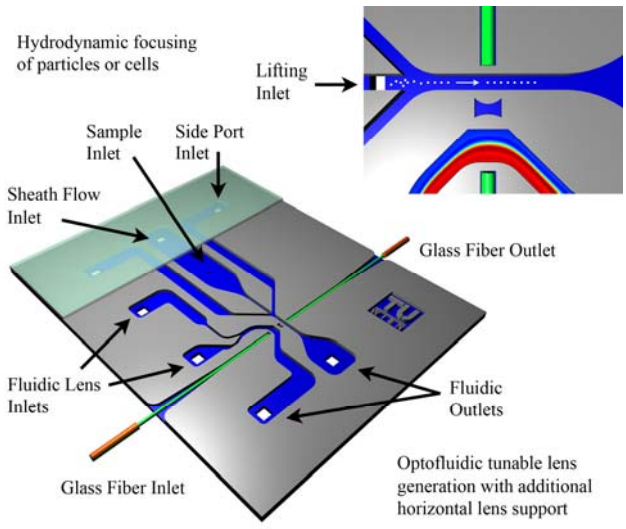


Fig. 4 Rendered image of the design of the flow cytometric device with an integrated optofluidic lens system to focus the analytical incident light three-dimensional on the cells or particles. The sample suspension is hydrodynamically focused in the center of the microfluidic channel. The sample is enfolded within the sheath flow which decreases the width of the sample stream and holds the sample on the bottom of the channel. The lifting stream raises the sample to the center of the channel and the side ports quench the centered sample stream to a defined width lining up the cells or particles after each other. The detailed inset shows the fluidic lens generation by driving the optical fluids through the 90° bend and arching the fluidic interface to a convex form in both optical planes. The biconcave resin/air lens utilizes additional focusing in the horizontal plane to support the curvature of the fluidic lens in the X-Y plane. By bringing these to designs together it is possible to achieve a single focal length in both planes (horizontal X-Y and vertical Y-Z). For this specific application (single cell analysis) with fixed focal length due to fixed particle position we introduce a half-adjustable fluidic lens (fixed X-Y / variable Y-Z curvature).

IV. Single Cell Analysis Device Design

The application of a 3D optofluidic lens in combination with 3D hydrodynamically centered single cells or particles enables sensitive (bio)-analytical measurements. To expand the overlapping area of focal lengths of the two lens curvatures (X-Y and Y-Z) it is necessary to "amplify" the fluidic lensing effect in the X-Y plane with an additional solid lens. The flexibility of the lens shaping is still given and the focal length overlap is increased. We introduce a novel device design where this adapted form of the lens generation technique is implemented (Figure 4). The difference in focal length is balanced with an additional air/resist (n = 1.6) lens.

The hydrodynamic focusing of the cell or particle suspension is described in detail in [11]. The used buffer fluid as well as the cell or particle suspension should have a similar density (ρ = 1.05 g cm^{-3}) to avoid sedimentation. The buffer fluid surrounds the sample at all sides and prevents channel clogging. The shape, size and position of the sample suspension stream can be controlled by the relative flow rate ratios of the buffer to the sample flows. The influence of rectangular sideport/sample junctions on the shape of the sample stream by creating an hour-glass shaped profile is reduced by an 45° angle between side port and sample channel [8].

In Figure 5 a close-up of the optical inspection region is illustrated. The optical fluids (Benzothiazole n = 1.64, Trichloro-trifluoroethan n = 1.36) are driven through the 90 ° channel bend causing a deformation of the fluidic interface. The used flow rates are $F_{Core} = F_{Cladding}$ = 15 µl/min. Using these flow rates the diffusive mixing in the laminar regime is insignificant. The curvature radius of the horizontal lens (r_{X-Y} = 250 µm) is smaller and not distinct enough to have the focal point exactly in the middle of the analytical channel. Therefore, an additional horizontal lens achieves the focusing effect. As a result of the increased centrifugal force in the center of the channel due to the parabolic velocity profile the vertical lens (r_{Y-Z} = 70 µm) originates and focus the light on the particles. The refraction at the air/resist lens is included in the calculation. Both lens geometries (X-Y + air/resist and Y-Z) achieve a single focal length. The irradiance [W/m²] reaches a maximum at the centered particle and increases the reachable fluorescent emission or absorption sensitivity. To our knowledge this is the first time that a design with 3D light and particle focusing for single cell analysis is presented. Measurements to confirm the simulation results are currently conducted.

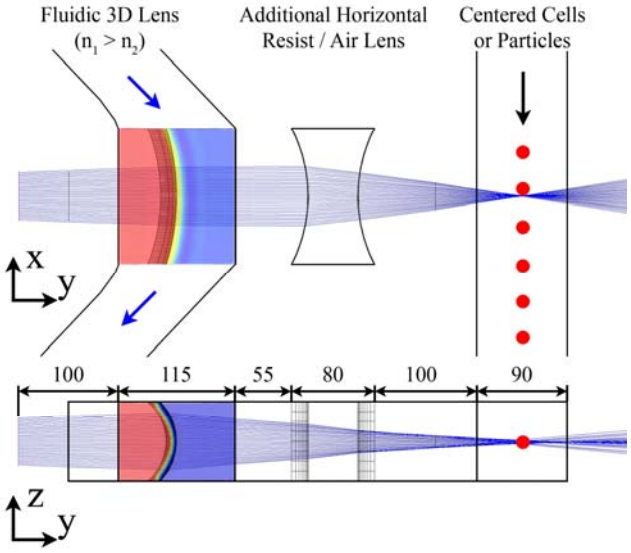


Fig. 5 Illustration of the fluidic and ray tracing results of the optical inspection region. The interfaces of the optical fluids in both planes are depicted and enable 3D light focusing. The light source is a conventional glass fiber (NA = 0.22) inserted in fiber notches on the fabricated device.

V. CONCLUSIONS

We have developed a novel microfluidic device with 3D light focusing characteristics fabricated by fast high quality micro-stereolithography. The fluid channel design introduces three-dimensional micro lens shaping which enables new areas of microfluidic optical applications. We fabricated our microfluidic device in a very promising rapid prototyping technique: micro-stereolithography. We achieved resolutions down to 20 µm in a total process time of 1.5 hours. The measurement results of this 3D optofluidic lens chip are in very good agreement with the conducted simulations.

By adapting the 3D lens shaping principle with an additional fixed "focus amplification" lens we increased the tunability in focal length and the measurement sensitivity in the flow cytometric device. For the presented single cell analysis application with a fixed centered particle position we introduced a half-adjustable fluidic lens (fixed X-Y / variable Y-Z curvature). The performed simulations show that this combination of 3D hydrodynamic and optical focusing creates an incident excitation light spot with highly increased irradiance compared to conventional planar single cell analysis devices.

ACKNOWLEDGMENT

For the sensor fabrication and the technical support we thank M. Spitzbart (Department of Micro- and Nanosystems, University of Applied Sciences Wr. Neustadt), J. Stampfl (Institute of Materials Science and Technology, Vienna University of Technology), E. Svasek and P. Svasek (ISAS Technology Lab and ZMNS, Center of Micro- and Nanostructures, Vienna University of Technology). The SEM image analysis was carried out using facilities at the University Service Centre for Transmission Electron Microscopy (USTEM, Vienna University of Technology).

REFERENCES

1. Myers F B, Lee L P (2008) Innovations in optical microfluidic technologies for point-of-care diagnostics. Lab Chip 8:2015–2031
2. Hunt H C, Wilkinson (2008) Optofluidic integration for microanalysis. Microfluid Nanofluid, 4:53-79
3. Kuiper S, Hendriks B H W et al (2004) Variable-focus liquid lens for miniature cameras. Appl Phys Lett 85:1128-1130
4. Wolfe D B, Conroy R S, Garstecki et al (2004) Dynamic control of liquid-core/liquid-cladding optical waveguides, PNAS 101:12434-12438
5. Tang S K Y, Stan C A, Whitesides G M (2008) Dynamically reconfigurable liquid-core liquid-cladding lens in a microfluidic channel. Lab Chip 8:395-401
6. Mao X, Waldeisen J R, Juluri B K, Huang T J (2007) Hydrodynamically tunable optofluidic cylindrical microlens. Lab Chip 7:1303-1308
7. Rosenauer M, Vellekoop M J (2008) Three-dimensional hydrodynamically adjustable lens chip fabricated by rapid prototyping, Proc. of MicroTAS, San Diego, USA, 2008, pp. 59-61
8. Sudarsan A P, Ugaz V M (2006) Fluid mixing in planar spiral microchannels. Lab Chip 6:74-82
9. Bertsch A, Jiguet S, Bernhard P, Renaud P (2003) Microstereolithography: a review. Mat Res Soc Symp Proc 758: LL1.1.1.
10. Rosenauer M, Spitzbart M, Zoppel S, Vellekoop M J (2008) Ultra rapid high quality prototyping for optical microfluidic analysis devices, Proc. of Eurosensors, Dresden, Germany, 2008, pp.785-788
11. Hairer G, Vellekoop M J (2009) An integrated flow-cell for full sample stream control. Microfluid Nanofluid: DOI 10.1007/s10404-009-0425-6

Author: Michael Rosenauer
Institute: Institute of Sensor and Actuator Systems / TU Vienna
Street: Gusshausstrasse 27-29 / E366
City: Vienna
Country: Austria
Email: michael.rosenauer@tuwien.ac.at

Artificial urinary bladder – focal technical challenges

M. Roth[1], D. Kirchleitner[1], D. Jocham[1] and H. Wassermann[2]

[1] University of Luebeck, Department of Urology, Luebeck, Germany

[2] University of Applied Sciences, Institute for Sensor Technology, Munich, Germany

Abstract— **The design of an artificial urinary bladder for the treatment of patients after bladder excision is been challenged by various aspects from an engineering point of view. Focal technical challenges are at least that the system has to imitate the functionality of the human bladder, it has to be safe, reliable and small in construction size. The materials have to be bio-compatible and feasible for an usage for several years. The technical solutions for these challenges are presented based on results from the research towards the fully implantable artificial urinary bladder.**

Keywords— **artificial organ, prosthesis, urinary bladder.**

I. Bladder cancer and the fully implantable artificial urinary bladder concept

The incidence of urinary bladder cancer amounts to more than 28,750 people in Germany annually, worldwide 356,000. [1,2]

For those patients, the radical excision of the bladder is often inevitable and following this severe surgery, the patients can be treated with cystoplasty using gastrointestinal segments. However, the presence of such segments in the urinary tract has been associated with many complications. [3]

One option for the treatment of patients after bladder excision is the utilization of an artificial urinary bladder system, whereas extensive research on artificial bladders began around the year 1960. Despite numerous attempts, the challenge of substituting a biological reservoir by an artificial system has not yet been solved satisfactorily. [4]

One approach for the development of an artificial urinary bladder is currently being administered by a research group of the Clinic of Urology, University of Luebeck in cooperation with Munich University of Applied Sciences, Institute for Sensor Technology:

The 'artificial urinary diversion system'

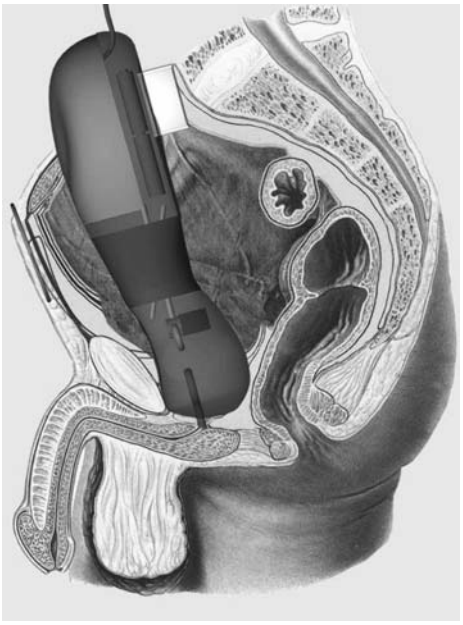


Fig. 1 Schematic depiction of the implanted system

Foremost intention of this research initiative is to imitate the functionality of the human bladder and to overcome the technical disadvantages of other artificial urinary bladder concepts.

The technical design concept is a closed capsular system which is fully implanted in the patient's body without any exterior connections (wires, switches etc.)

This system is patented (EP 1161202B1), has been distinguished by several awards and was funded by the German Federal Ministry of Education and Research (BMBF). [5]

O. Dössel and W.C. Schlegel (Eds.): WC 2009, IFMBE Proceedings 25/VIII, pp. 189–191, 2009.
www.springerlink.com

II. Selected technical challenges for any bladder subsitute and engineering solutions within the fully implantable artificial urinary bladder

A. Focal technical challenges for any bladder substitute

Selected challenges from an engineering point of view for any artificial urinary bladder system include at lease the following: [4, 6 and 7]:

1. Functionality and patient safety

Obviously, any bladder substitute has to imitate the functionality of the human organ. However, this is a serious engineering challenge, e.g. as the urine needs to be stored within a feasible reservoir, which has to prevent urinary encrustation and capsule formation as both could impair the normal functioning of the reservoir. Furthermore an active reservoir emptying is necessary in order to avoid large residual volumes after implantation and subsequent encrustations. [8, 9]

The foremost claim is to prevent any patient damage due to technical failures of the system. Results from previous projects report severe technical problems, e.g. especially for a highly sophisticated design concept there is a high risk of mechanical dysfunction. [10]

2. Bio- and Human-compatibility

Seemingly, the system has to be implanted into humans and therefore the artificial system requires an adequate compatibility to the patients requirements, namely:

- Feasible shape of the artificial urinary diversion system, whereas there have been two principal design concepts in previous attempts, the fixed volume models in opposition to expandable models. [4, 6]
- Anastomosis between living tissue and the prosthesis, especially the connection between the ureters and the urethra to the artificial system. [4]
- Soft-tissue response to the synthetic biomaterials, as the human body tends to show an inflammatory reaction to the alloplastic material. [6]

3. Optimization of technical concept

Any technical system is to be optimized by engineering methods, however especially an artificial organ requires particular endeavors in order to minimize design space, system weight etc.

B. Engineering Solutions for the depicted technical challenges within the fully implantable artificial urinary bladder

For the technical challenges named above, the engineering solutions within the fully implantable artificial urinary bladder are presented as feasible solutions for the identified challenges.

1. Functionality and patient safety

This artificial organ is a closed capsular system which is fully implanted in the patient's body without any exterior connections. In terms of the mode of operation, the urine - as produced by the kidneys - is stored in an artificial reservoir and the fill level is monitored by the central logic of the system. An alarm signal is given to the patient via remote control when necessary. Following this alarm, the patient can deliberately empty the reservoir by activating the pump-valve-actuators.

Patient safety is realized by means of redundancy of electrical systems, bypass options and emergency functionality. The urinary diversion system contains anti-reflux valves in order to avoid a backflow of urine to the kidneys. System inspection and medical examination by a physician, e.g. renal endoscopy, are possible due to the technical design of the reservoir, the valves and pump.

2. Bio- and Human-compatibility

The shape of the urinary diversion system was developed in cooperation with the Institutes of Anatomy and Pathology of the University of Luebeck. The outer shell is derived from a sixth-degree polynomial and was verified in dead-body studies. Furthermore, the system is divided into three major modules: reservoir, control section and actuators. For each of the three modules, different sizes exist and hence it is possible to adapt the whole artificial system to the anatomical requirements of each individual patient.

Anastomosis is currently the foremost challenge from the medical point of view, however extensive own research efforts challenge this problem, and emerging surgical and material concepts appear promising.

The semi-rigid outer shell is made of polyurethane material, whereas the feasibility and reliability of the polyurethane material were tested and proven by means of long-term tests with over 85,000 load-cycles equaling a durability of 15 years.

3. Optimization of technical concept

The system is powered by lithium-polymeric batteries and recharged by means of sub-cutaneous energy transfer using an inductive principle. Therefore a separate recharge device was developed which needs to be placed in reach of

an implanted coil. Battery loading will require approximately three hours and during the normal course of operation, the artificial organ is operational for five to seven days of normal usage.

This artificial urinary bladder is intended to be tightened at the patient's promontory of sacrum and symphysis pubica, therefore the total weight of the system can be absorbed by a feasible fixation, however the system is also optimized in terms of constructed system weight.

III. Conclusions

Focal technical challenges from an engineering point of view for any artificial urinary bladder system were identified. Extensive research has been done and technical feasible solutions are being developed for the 'artificial urinary diversion system'. This artificial urinary bladder is expected to be fully functional by end 2009 and subsequently the clinical validation phase is to be initiated.

Acknowledgment

We thank all project partners and all persons involved in the development of the 'fully implantable artificial urinary bladder'

References

1. Robert Koch Institute (2008) Cancer in Germany, p. 82
2. Parkin DM, Bray F, Ferley J, Pisani P (2002) Estimating the world cancer burden, Globocan 2002
3. Zoeller G, Ringert RH (2004) Harnblasenkarzinome und andere Urothelkarzinome, Onkologie, pp. 1203 ff
4. Desgrandchamps F, Griffith DP (1999) The artificial bladder, European Urology 35, pp. .257-266
5. Wassermann H, Jocham D; following patents are relevant: US 20070073413A1, DE 19912472.8, EP 1161202B1, WO 2000056246A1
6. Gurpinar T, Griffith DP (1996) The prosthetic bladder, World Journal of Urology 14, pp. 47-52
7. Rohrmann D (2003): The artificial urinary bladder; in Atala A and Slade D (eds): Bladder disease – Research Concepts and clinical applications, Kluwer Academic, 2003, pp 885 - 893
8. Griffith DP, Gleeson M (1995): The prosthetic bladder; in Fitzpatrick JM, Krane RJ (eds): The Bladder, Churchill Livingstone, 1995, vol 39, pp 475-492
9. Rohrman D, Albrecht D (1996) Alloplastic replacement of the urinary bladder, Journal of Urology 156, pp. 2094-2097
10. O'Sullivan DC, Barrett DM (1994): Prosthetic bladder: In vivo studies on an active negative-pressure-driven device, Journal of Urology 151, pp. 776-780

Matthias Roth
c/o University of Munich
Institute for Sensor Technology
Lothstr. 64
80335 Munich
Germany
Matthias.Roth@medizin.uni-luebeck.de

Design and Performance of an improved active subretinal chip

Steffen Kibbel[1], Alex Harscher[1], Walter-G. Wrobel[1], Eberhart Zrenner[3], Albrecht Rothermel[2]

[1] Retina Implant AG, Reutlingen, Germany
[2] Institute of Microelectronics, University of Ulm, Germany
[3] Centre for Ophthalmology, University of Tübingen, Germany

Abstract— **The aim of the subretinal implant is to restore visual perception in blind patients suffering from retinitis pigmentosa (RP) and – at a later stage – age-related macular degeneration (AMD). Electrical stimulation of the remaining retinal neurons can restore meaningful visual perceptions [1, 2]. Our retina implant, consisting of a light sensitive CMOS chip (1,500 pixels) and 16 separate direct stimulation electrodes, is presently being tested successfully in a clinical pilot study with 12 patients. A detailed analysis of the data obtained sofar led to a redesign of the CMOS chip [4]. Results of the technical characteristics of this next generation retina chip are presented here. The chip was designed in cooperation with the Institute of Microelectronics at the University of Ulm. Tests in vitro show that the chip performs according to its specifications. Implants with an inductively coupled power supply equipped with the novel chip are in production and will soon be ready for extensive testing in vivo.**

Keywords— **retina implant, subretinal implant, active medical device, visual prosthesis, retinitis pigmentosa, AMD, CMOS, photoarray.**

I. Introduction

Stimulation of retinal neurons via subretinal electrodes has proven to partially restore vision in a reproducible way. Within a clinical pilot study, 11 patients with RP were provided with the implant for at least 4 weeks each. Some patients have been able to localize objects, to differentiate e.g. fork and knife and even to read white letters on a dark background. Furthermore visual acuity could be measured using a standard visual test [5]. These experiments were performed with a light sensitive CMOS chip [3] with all electrodes providing stimulation pulses simultaneously. Clinical data indicated that sequential stimulation might lead to even better efficiency and higher spatial resolution [5]. Moreover minimize chemical reactions, no DC potential should appear at any terminal of the chip. Mainly for these reasons, a new retinal implant was designed [4, 6] and realized implementing the novel features described here. So far, our active subretinal implant is being wire-controlled and energy and control signals are supplied by an external supply unit. This led to mechanical load on the cable and is a potential risk for inflammation for the patient. The new implant is controlled by an inductively coupled power supply, hence fully implantable. To improve stability against electrochemical corrosion, the power supply was realized free of DC driven components. The amount of charge as a key factor of stimulation efficiency is proportional to the stimulation voltage amplitude. Thus a biphasic stimulation pattern is realized that guarantees a charge balanced stimulation with maximum charge transfer for a given electrode impedance. Reliability and hence testability is of great importance for medical implants. To verify function and performance of the implant a novel test strategy was implemented.

II. Methods

A. Chip Design

A block diagram of the architecture is shown in Fig. 1. A rectifier generates internal DC supply from the external AC supply. As no external components (e.g. capacitors) can be connected to the chip, V_H and V_L are required to be piecewise linear voltages which are constant during chip operation and stimulation (for several ms), and change polarity fast (within about 100 ns). Internal DC supply is connected to the photo sensors, amplifiers, and digital control. The output drivers are directly connected to the external AC supply subdermally placed behind the ear. This way the DC to AC signal conversion in the output drivers is supported, and the current flowing through the on chip rectifier is minimized.

The chip comprises 40 x 40 pixels of size 70 x 70 μm^2. Every pixel includes a logarithmic photo sensor, an amplifier, some logic circuits and the output drivers. The fractal TiN electrode has a geometric surface of 50 x 50 μm^2 leaving
15 x 48 μm^2 for the photo diode. The design is fabricated in a 0.35 µm CMOS technology comprising optical design features. Total chip size is 3.0 x 3.5 mm^2 with an active pixel area of 2.8 x 2.8 mm^2. Chip thickness is 70 µm. The

O. Dössel and W.C. Schlegel (Eds.): WC 2009, IFMBE Proceedings 25/VIII, pp. 192–195, 2009.
www.springerlink.com

chip is operated with DC free square wave voltage of ± 2V

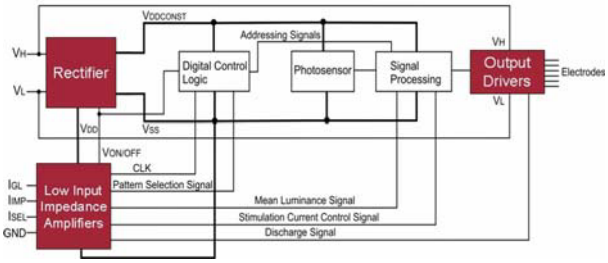


Fig. 1 Chip architecture

A digital controller addresses the pixels sequentially, which reduces the peak supply current. Four different addressing algorithms (operation modes) are implemented. Three control signals are required to operate the chip. The brightness reference level is defined by the analog signal I_gl. Stimulation timing and amplitude limit is defined by an analog signal I_imp that also defines the waveform of the stimulation current. Due to an end to end current mirror design, the maximum output stimulation current is proportional to I_imp. The operating pattern is chosen by the 2-bit binary signal I_sel.

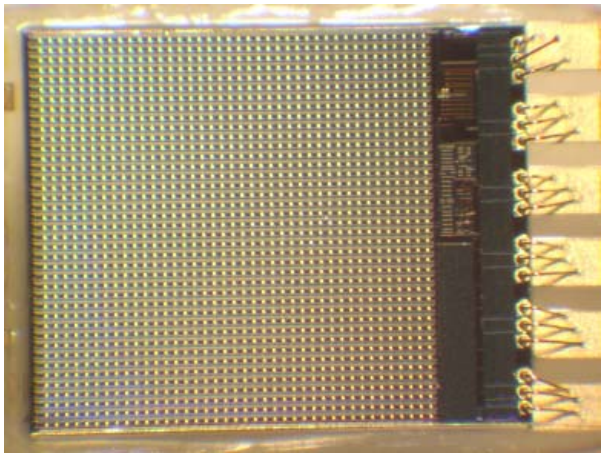


Fig. 2 Retina Chip with 1600 pixels

Electrical connection of the chip with its carrier, which is a polyimide multilayer flexible ribbon, is realized via conventional gold wire bonding onto each of the six 3-fold contact pads (see Fig 2). The chip is encapsulated with silicone along the edges and on the contact pads. A flexible cable connects the chip to a subcutaneous hermetically sealed HF power supply (Fig. 3).

Fig. 3 Implant with HF power supply

B. Modes of operation

The results of our pilot study are suggesting preferentially a sequential chip operating mode since sequential stimulation of neuronal cell assemblies takes the refractory period of nerve cells into account. Four different sequential operating modes have been realized. The stimulating algorithms are hardware implemented and can be selected by the binary signal I_sel. For safety reasons the least charge emitting mode is selected by default if I_sel is disconnected.

The output drivers generate charge balanced biphasic (anodic and cathodic) voltage and current pulses at the output electrodes. In all stimulating modes 4 x 4 pixels are combined to a subunit that is always activated at the same time. Nonetheless, each pixel generates a stimulation amplitude controlled by the local logarithmic photo sensor and the mean luminance control signal (I_gl).

In mode 1 the four blocks in the respective corners of the active area are activated simultaneously. This enables the patient to get an orientation of the chip position in the eye.

Mode 2 activates the pixel subunits linewise according to a conventional TV screen.

Mode 3 sets 5 subunits simultaneously active for a burst sequence of 5 pulses while in the intermediate breaks between two pulse series a second group of subunits is activated. The so called burst mode is proposed to show the lowest stimulation thresholds, defined as the smallest output signal to evoke a visual sensation, elicited by a short charge transfer per pixel.

Mode 4 is optimized for a maximum distance between the sequentially activated subunits.

Given a particular setting for I_imp, a hardware implemented technical test mode can be activated. When the chip runs in this test mode, the electrode discharge transistors remain switched on during stimulation. As a result, stimulation current is flowing through the chip GND terminal and can be measured by the aid of an external shunt resistor in the GND line.

This additional test feature works for all of the above described operation modes. Once the chip is implanted, this test mode is not accessible any more. The test mode is of great importance to establish a reproducible implant manufacturing and to test the chip intraoperatively.

C. Test feature

For a functional test of the chip circuitry before implantation, the chip is activated in the above described test mode. Thus the output signal is switched OFF and the output current is directed to Chip GND. In a first step, by setting I_gl to an appropriate (high) value, the output drivers can be tested independently from illumination, because all amplifiers are driven with a large differential input voltage. In a second step, by setting I_gl to the operating value, photo sensors and amplifier offset characteristics are verified. In this mode, homogenous illumination conditions will be applied. In a third step, by using uneven illumination, the different addressing patterns can be tested. This testing parameter set serves as control for correct operation of all individual pixel group circuits. In the test mode, no load is applied to the pixel amplifier outputs and no information about the charge transfer into the tissue is given.

III. Measurements

A. Dry Measurements with tungsten probe

The performance of a single pixel cell was measured with a standard tungsten tip and a model load of 10 kΩ and 20 nF in series. Output current and voltage at maximum brightness are shown in Fig. 4. The biphasic pulse causes a charge transfer maximum of 8 nC for the anodic part and 16 nC for the cathodic one (see Fig. 5).

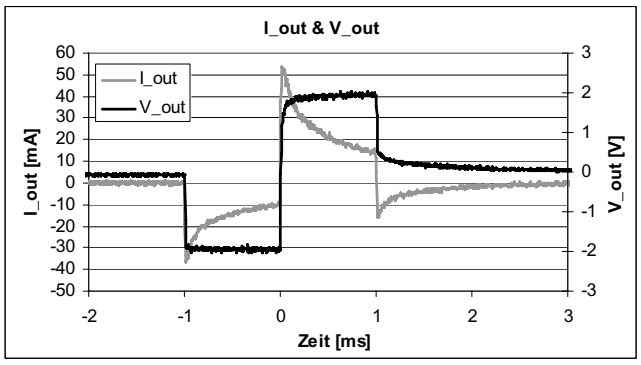


Fig. 4: Output current and voltage with model load.

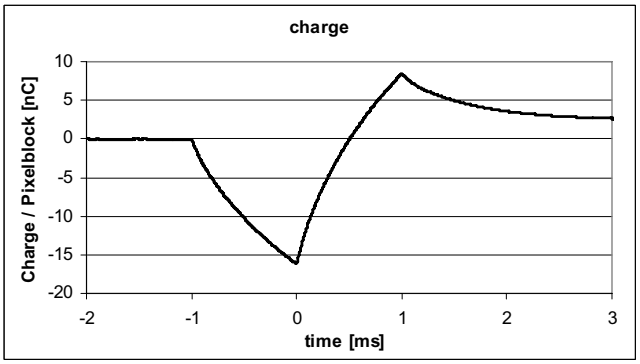


Fig. 5: Charge transfer with model load.

B. Measurements in saline solution

Encapsulated chips were activated in PBS to measure the performance in vitro. Voltage drop across a shunt resistance between reference electrode and GND provides the signal shape and amplitude for the different operation modes at various illumination conditions. As an example, the output signal of a pixel subunit with the chip operating in line mode with maximum input at the differential amplifier is shown in Fig. 6.

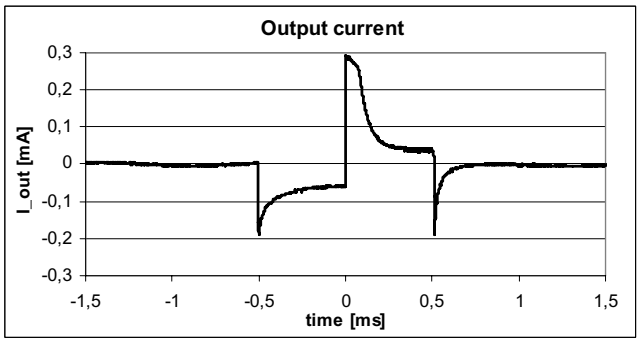


Fig. 6: Output current of one pixel subblock emitted in saline solution.

The reference current I_gl defines the reference level for the ambient brightness situation when adjusted between 60 µA and 200 µA.

By integration of the current pulse the charge emitted into the retinal tissue can be calculated. This charge transfer indicates the strength of stimulation. To illustrate theadaption to different light levels, the anodic charge transfer is plotted vs. illuminance of the ambient light. Fig. 7 shows the output characteristic for three different values of I_gl.

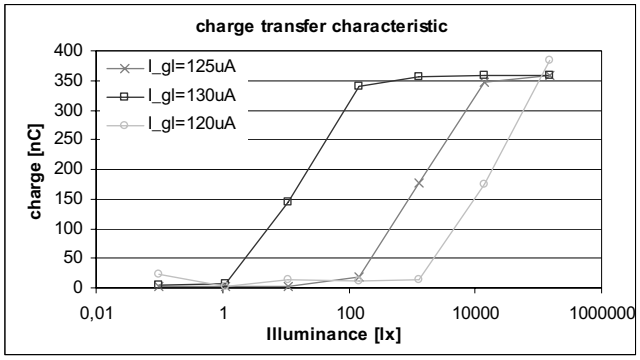


Fig. 7: Output characteristic measured in-vitro for three different settings of I_gl.

A decrease of I_gl shifts the working range of the amplifier towards higher illumination. Hence by adjustment of I_gl, the patient can adapt the chip output to the ambient brightness.

IV. Conclusions

A novel retina implant with an improved CMOS photo chip is presented here. The basic chip concept is based on sequential stimulation of 1600 pixels in four different modes of operation.

The improved retinal implant consists of an implantable power supply, flexible ribbon and a CMOS photo chip. Its characteristics have been tested showing suitability for implantation within the ongoing pilot study in the near future.

Acknowledgment

The authors gratefully acknowledge funding by German ministry for research and education (FKZ 0315113) and express sincere appreciation to the staff of the Institute of Microelectronics at the University of Ulm for the chip design and continuing support regarding chip characterization.

References

1. E. Zrenner, et al. (2007) Psychometric analysis of visual sensations mediated by subretinal microelectrode arrays implanted into blind retinitis pigmentosa patients, ARVO Annual Meeting e-Abstract 6592007
2. E. Zrenner (2007) Restoring neuroretinal function: new potentials, Doc Ophthalmol Vol. 115, pp. 56 - 59
3. Dollberg, H. G. Graf, B. Höfflinger, W. Nisch, J. D. Schulze Spuentrup, K. Schumacher (2003) A fully testable retina implant, IASTED International Conference on Biomedical Engineering 2003, pp. 255-260
4. A. Rothermel, V. Wieczorek, L. Liu, A. Stett, M. Gerhardt, A. Harscher, S. Kibbel (2008) A 1600-pixel subretinal chip with DC-free terminals and 2V supply optimized for long lifetime and high stimulation efficiency, IEEE Int. Solid-State Circuits Conf. Dig. Tech. Papers Feb. 2008, pp. 144-145
5. E. Zrenner, et al. (2009) ARVO Annual Meeting e-Abstract 4581, 2009
6. A. Rothermel, L. Liu, N. Pour Aryan, M. Fischer, J. Wuenschmann, S. Kibbel, A. Harscher (2009) A 1600-pixel subretinal chip with DC-free terminals and 2V supply optimized for long lifetime and high stimulation efficiency, IEEE Journal of Solid-State Circuits Jan. 2009, pp. 290-300

Author: Steffen Kibbel
Company: Retina Implant AG
Street: Gerhard-Kindler-Str. 8
City: 72770 Reutlingen
Country: Germany
Email: steffen.kibbel@retina-implant.de

An intelligent implant system for monitoring and biofeedback therapy of snoring

Dan Anker Hofsøy[1], Johannes Clauss[1, 2] and Bernhard Wolf[1]

[1] Heinz Nixdorf Lehrstuhl Medizinische Elektronik, Technische Universität München, Deutschland
[2] Sense Inside GmbH im Innovationszentrum Medizinische Elektronik, München, Deutschland

Abstract— **The problem of snoring increases as a result of an older and more overweight population. In Germany alone, there are more than 8 million habitual snorers.**

This project aims at helping those who are troubled by snoring or mild to moderate obstructive sleep apnea (OSA) by offering a long-term miniaturized monitoring system in combination with biofeedback therapy for use at home.

By using an accelerometer mounted in a removable headband (i.e. fixed to the skull), head position and the vibrations from snoring were successfully recorded. In addition, respiration frequency was derived from the head breathing movements as well as the heart rate from blood pulse movements while sleeping.

This allows innovative new ways of home monitoring with minimum annoyance to the snorer. One aspect is to use the miniaturized sensor in an intelligent implant system for long-term screening at home; another is to evaluate both the compliance and efficacy of therapy methods over a longer period of time.

The headband was fitted with a biofeedback signal in order to perform positional therapy, since many snorers and OSA patients have the problem predominantly in the supine position. Within 10 seconds after a positional change to the supine position, the biofeedback signal starts up and the snorer is in this way encouraged to change position.

Since a position change happens in a light sleep phase, the biofeedback therapy is applied with minimal disturbance to the sleep quality of the snorer. The first trials has shown promising results and further studies will be conducted to verify the effect.

Keywords— **snoring, accelerometer, monitoring, biofeedback, implant system.**

I. Introduction

A. Motivation

At the Heinz Nixdorf Lehrstuhl Medizinische Elektronik (HNLME), a sensor platform was initially developed in order to monitor and give therapy to bruxism patients. The sensor system was made small enough to be used in implants worn by tooth-grinding patients, and communicates with an external box recording the bruxism events and delivering biofeedback therapy when bruxism occurs [1].

This project was started to investigate if a similar miniaturized platform could be used for the purpose of detecting parameters related to the epidemic problem of habitual snoring.

B. Medical background

When we go to sleep, the muscles in the throat relax and so the upper airway consisting of soft structures becomes narrower. If the narrowing is greater than normal, it can cause the airway behind the tongue to collapse. Snoring arises when these structures strike each other and start to vibrate during breathing.

Lugaresi et al. found in a study examining 5,783 individuals that 24.1 % of the male and 13.8 % of the female population were snoring on a regular basis and are so-called habitual snorers. Age and overweight are important contributors to snoring – more than 60 % of men and about 40 % of women between 60 and 65 years of age were habitual snorers [2]. Use of alcohol before bedtime and sleeping on the back are other significant risk factors, because of the relaxing effect and gravity influence on the soft structures respectively.

Similar to snoring is the so-called obstructive sleep apnea (OSA), which can be found in 10 to 20 % of regular snorers, and in 2 to 7 % of the general population [3]. Patients with OSA almost always have habitual snoring, and habitual snoring is believed to be a precursor to OSA [4]. In the case of OSA, the tongue gets sucked backwards and completely blocks the collapsible part of the airway. After about 10 seconds the brain reacts with a loud gasp when the oxygen level gets too low. This pattern could happen 30 times per hour in the night without any recollection in the morning.

OSA normally leads to excessive daytime sleepiness and hence significantly increases the chance of being involved in a car accident. In the USA, 1400 lives and $11.1 billion could be saved every year, if all OSA patients had received a diagnosis and been treated according to their condition [5]. But approximately 70 to 80 % of OSA patients have not even been diagnosed [3]. It is therefore desired to include the possibility of screening for OSA with the system.

As in the case of snoring, more than half of the OSA patients have the problem predominantly in the supine position (i.e. when sleeping on their back) [3, 4, 6].

O. Dössel and W.C. Schlegel (Eds.): WC 2009, IFMBE Proceedings 25/VIII, pp. 196–199, 2009.
www.springerlink.com

II. Methods

A headband prototype was chosen as an initial test system, since it must not be individually prepared like an implant and can therefore easily be used on multiple test persons. Also, the test circuit can be easily modified and the use of an external receiver box is not needed.



Fig. 1 Headband prototype

A. Sensor system

An accelerometer was found suitable for the purpose of snore detection. Up to now, most devices use a microphone to detect the sound of snoring. This requires a sound level through the air and the microphone must therefore be attached externally on the patient. An accelerometer, on the other hand, detects the vibrations from snoring as changes in acceleration and can therefore be built into a closed implant system. It has also the ability to detect other important parameters like breathing movement.

The so-called MEMS (micro electro-mechanical system) process has made it possible to manufacture accelerometers with footprint less than 10 mm^2, which has open up for new innovative uses in the consumer market like the Nintendo Wii remote or automatic change of screen view on mobile phones and cameras. The size and low power consumption enables the usage of these accelerometers also in implant systems.

The accelerometer chosen for testing was a conventional 3-axis MEMS with high sensitivity and extremely low noise, which are important for the first testing.

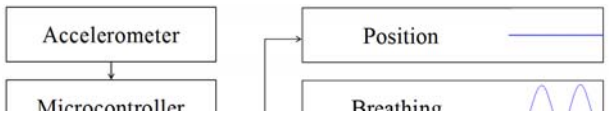


Fig. 2 Recording and processing of accelerometer output

The output from the accelerometer is digitally sent to the microcontroller which saves the sampled data to the microSD card, as demonstrated in Figure 2. A Matlab graphical user interface (GUI) is used to select the desired data from the microSD card and digital filtering is applied in order to discriminate between the different measurement parameters. The applied filters are Butterworth 10^{th} order band-pass filter, demonstrated used on the different parameters in Figure 4. The signal processing is kept simple so that it can be transferred to the microcontroller in a wireless implant system later on.

A microphone circuit was included in the prototype as reference to the accelerometer recording of snoring.

B. Positional therapy

An important feature of the sensor system is its ability to determine the *head* position when sleeping – most measurement systems use *body* position as reference, which is considered a limitation since the gravity influence on the upper airway is not considered [6].

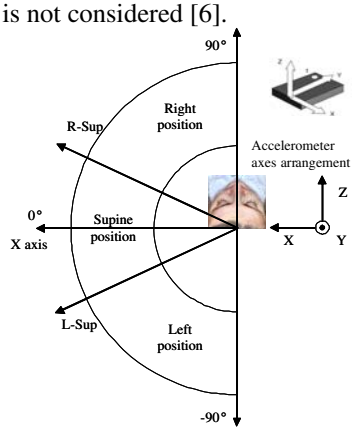


Fig. 3 X axis used to detect sleep position

The DC signal from the X axis of the accelerometer is used for this purpose as shown in Figure 3. The signal output will equal 0g for supine sleeping position, and -1g and +1g for right and left lateral position respectively. L-Sup and R-Sup defines the range of supine head position. Y axis determines if the patient is lying down or sitting upright.

The system has a built-in biofeedback signal, which will be evaluated as positional therapy. The positional snorer or OSA patient will learn by a signal – with minimal sleep disturbance and the possibility of individually adjusted therapy magnitude – to avoid critical sleeping positions such as the supine position, and the monitoring system is able to document it.

III. Results

A. Monitoring

Six persons have been tested with the sensor system, of which three were habitual snorers. Figure 4 shows the results of normal sleep with the raw signal from the Y axis of the accelerometer, and the digitally filtered snoring, heart rate and breathing signals consecutively.

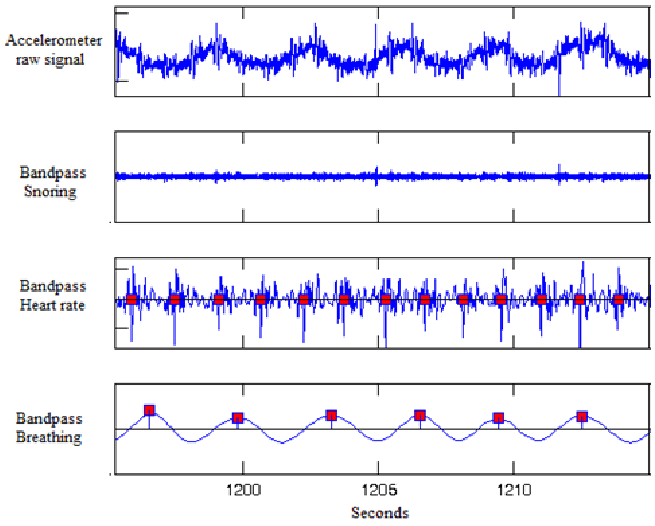


Fig. 4 Raw signal of normal sleep filtered

The heart rate signal and breathing frequency has been successfully derived from peak detection – the raw signal is filtered and the peaks are found from the quadratic signal. The peak values have to be within certain values or else they are considered noise or disturbance.

In Figure 5, a recording of a habitual snorer is shown. On the raw signal, snoring, breathing movements and also heart rate are optically viewable. Filtering discriminates these parameters well, but the heart rate has some noise influence from snoring. The heart rate can however be derived from the heart beats between the snoring events. A microphone signal is used as reference to the accelerometer snoring signal.

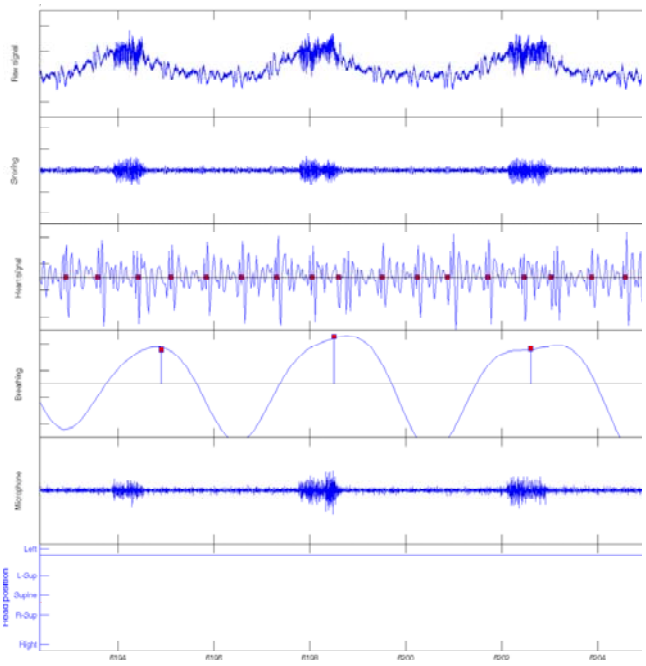


Fig. 5 Snoring in lateral position left

B. Positional therapy

Figure 6 shows how the biofeedback signal was turned on 10 seconds after the patient turned from the right lateral to the supine position. The signal lasted until the patient turned over to the left lateral position.

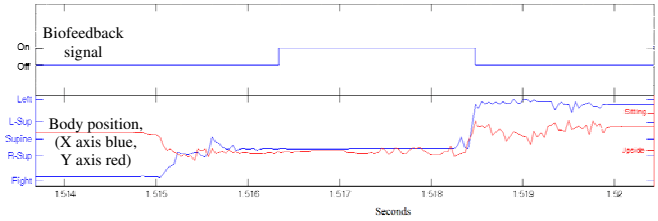


Fig. 6 Biofeedback therapy of supine sleep

Sleeping position from one night without therapy and one with therapy enabled are represented in Figure 7. The patient slept 11.68 % in the supine position without biofeedback therapy. With biofeedback therapy enabled, the patient was five times prevented from remaining in the supine position (indicated by arrows) and had a total of 0.85 % supine sleep.

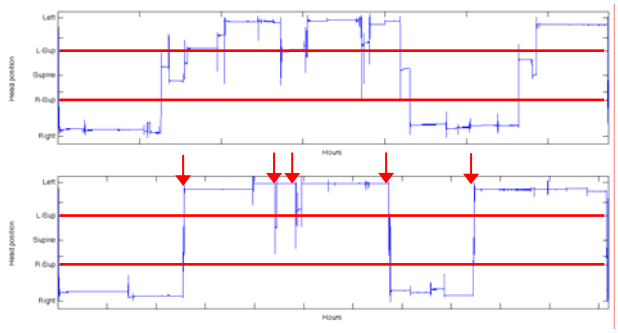


Fig. 7 One night without (top) and with biofeedback therapy (bottom)

IV. Discussion

It was demonstrated that recording of important parameters for monitoring of snoring and OSA events is possible with a single accelerometer placed in a headband. The results, however, are transferable to a head worn closed implant system, since they both measure the vibrations on the bones connected to the soft tissues in the mouth where snoring emerges.

The use of accelerometers for the purpose of assisting OSA diagnose has also been demonstrated by Sanchéz Morillo et al., who placed a sensor system with an accelerometer between neck and thorax [7]. Our sensor system will be further miniaturized and focus on long-term monitoring of snoring and OSA together with existing or new therapy approaches, comfortable and cost-effective at home. This possibility currently does not exist and is often demanded in articles [6, 8].

The first trials on test persons with the positional biofeedback therapy included in the sensor system show promising results. A similar kind of therapy has been described in an article by Oksenberg et al.; they set off an acoustical alarm when the patient slept in the supine position. In this way, the average supine sleeping time was reduced from 51.4 % to 2.1 % [6].

The long-term compliance of the biofeedback signal tested is believed to be good and will be documented in later studies. This is important, since for example a vest worn by patients in the night to avoid the supine position was proven effective but rejected by 72.4 % of the patients, because of its low wearing comfort [8].

76 % of snorers are believed to be snoring mainly in the supine position [4] and can therefore be treated with a positional therapy approach. Few studies have been conducted on snorers to confirm this – a thoroughly study with the sensor system is possible and will be conducted.

According to sleep experts, positional therapy would be especially welcomed by patients with positional OSA, since they usually receive the so-called CPAP (Continuous Positive Airway Pressure)-Therapy when diagnosed. A CPAP device delivers a positive airway pressure with a respiratory mask throughout the night, so that the airway can not collapse. Many patients find this kind of treatment unpleasant and in the case of a positional OSA condition, the CPAP device could be avoided with the use of an efficient and monitored positional therapy instead, which will be tested with the presented system.

References

1. Clauss JF, Scholz A, Gruber H-G, Probst A, Wolf B. (2005) Telemetric diagnosis system for bruxism and sleep diseases. The 3rd European Medical and Biological Engineering Conference (EMBEC'05). Prague: IFMBE Proceedings 11(1). ISSN: 1727-1983
2. Lugaresi E et al. (1980) Some epidemiological data on snoring and cardiocirculatory disturbances. Sleep 3(3): 221-224
3. Punjabi N (2008) The Epidemiology of Adult Obstructive Sleep Apnea. Proc Am Thorac Soc 5: 136-143
4. Nakano H et al. (2003) Effects of Body Position on Snoring in Apneic and Nonapneic Snorers. Sleep 26(2):169-172
5. Sassani A et al. (2004) Reducing Motor-Vehicle Collisions, Costs, and Fatalities by Treating Obstructive Sleep Apnea Syndrome. Sleep 27(3): 453-458
6. Oksenberg A, Silverberg D S (1998) The effect of body posture on sleep-related breathing disorders: facts and therapeutic implications, Sleep Medicine Reviews 2(3):139-162
7. Sanchéz Morillo D et al. (2007) Monitoring and Analysis of Cardio Respiratory and Snoring Signals by using and Accelerometer, EMBS 2007, Proceedings of the 29th Annual International Conference of the IEEE EMBS; 3942-3945 DOI 10.1109/IEMBS.2007.4353196
8. Wendel S et al. (2007) Efficacy and long-term compliance of the vest preventing the supine position in patients with obstructive sleep apnea. Laryngo-Rhino-Otol 86:579-583

Author: Dan Anker Hofsøy
Institute: Heinz Nixdorf Lehrstuhl Medizinische Elektronik, TU-München
Street: Theresienstrasse 90
City: Munich
Country: Germany
Email: hofsoey@tum.de

Driving force of a neutrophile in liquid using concentration Marangorni effect for developing microcapsule for Drug Delivery Systems

M. Tamagawa[1] and K. Matsumura[1]

[1] Graduate School of Life Science and Systems Engineering, Kyushu Institute of Technology, Kitakyushu, Japan

Abstract— **This paper describes the effects of gradient of cytokine concentration on chemotaxis of neutrophile by observing the motion in liquid with adding cytokine concentration. The aim of this investigation is to control of microcapsule motion in liquid by concentration gradient for drug delivery systems**

Keywords— **DDS, Chemotaxis, Marangorni effect, ,Driving force, Micromachine**

I. Introduction

Inflammation reaction is very important role as immune response in human body. In this reaction, once the inflammation occurred, the cytokine (chemokine) is delivered from the inflammation place, then neutrophile aggregate at the place to cure. The neutrophile moves the place that has large gradient of cytokine concentration. This is so called chemotaxis of neutrophile, but the driving force of this motion in liquid is not elucidated yet. In the previous investigations, the motion of neutrophile has been considered to be amebic swimming in liquids as same as amebic motion on solids. Generally, the particulate in liquid on the gradient of concentration has the force by Marangoni effects. So the netrophile has the driving force of the motion in liquids by both amebic motion and Marangoni effects (Fig.1).

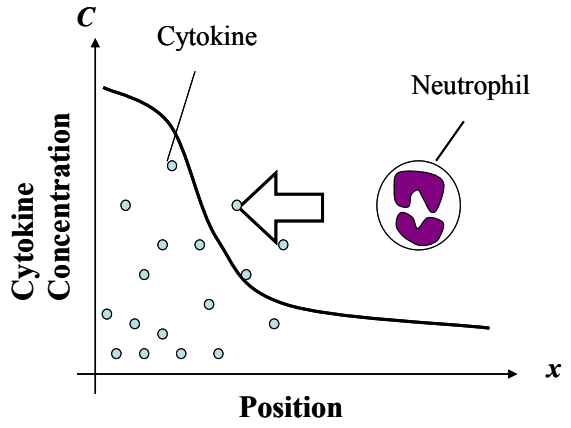


Fig. 1 Concept of chemotaxis using concentration Marangoni effect

This mechanism has possibilities to be applied to the drug delivery systems. Once the chemokine or concentration is generated at the affected part, the capsule with chemotactic function moves to this place automatically.

In the previous experiments, the effects of gradient of cytokine concentration on chemotaxis of neutrophile were investigated by observing the motion in liquid with adding cytokine concentration. Then the motion of neutrophile in the physiological salt was taken by CCD camera on microscope. Using PTV measurements, the average velocity of neutrophile was obtained with changing the cytokine concentration.

In this paper, the model of membrane for sensing is discussed by comparing with inorganic particulate model in water. Then the cytokine with fluorescent material (FITC) is observed in the microscope and the motion of neutrophile are analyzed.

II. Driving Force by Surface Tension Gradient

Suppose that the particulate sphere in liquid under the surface tension gradient as shown in Fig.2. The driving force F of particulate in liquid by the surface tension is obtained from the following equation,

$$F = -\nabla G(x) = -4\pi R^2 \left(\frac{d\sigma}{dx} \right)$$

where G indicates kinematic potential. And surface tension on the sphere is generally defined as follows;

$$\sigma = \sigma\left(C(x), T(x)\right)$$

where C and T indicates concentration and temperature.

Then the gradient of surface tension is expressed as follows if the temperature is constant,

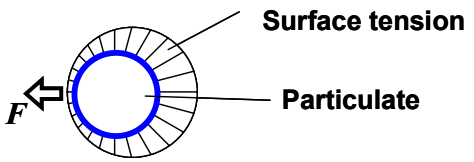


Fig. 2 Driving force by surface tension gradient

O. Dössel and W.C. Schlegel (Eds.): WC 2009, IFMBE Proceedings 25/VIII, pp. 200–201, 2009.
www.springerlink.com

$$\left(\frac{d\sigma}{dx}\right)=\left(\frac{\partial\sigma}{\partial C}\right)_T\left(\frac{dC}{dx}\right)$$

From this relation the driving force of particulate is dependent on the concentration gradient. Our supposition is that the driving force of neutrophlie is caused by the concentration gradient, so called Marangoni effect.

III. Observation of Concentration Diffusion and Neutrophile Motion by Fluorescence

To prove the neutrophile motion by concentration gradient, the experimental observation was done using the simple system as shown in Fig. 3. In this system, after dropping the cytokine IL-8 at the side of liquid area of neutrophile suspension, the concentration of cytokine diffused to the suspension liquid. The motion of neutrophile is taken by the video movie at the center of the liquid area in Fig.3. The cytokine with fluorescent material (FITC) is observed as intensity level in CCD image. Figure 4 shows diffusion process of cytokine and motion of neutrophile. It is considered that the cytokine with fluorescence is attached to the membrane of neutrophile. It is found that the high intensity region can be observed around the neutrophile. After taking CCD image, the intensity analysis for diffusion was done. Figure 5 shows concentration gradient history at the center of membrane and surrounding fluid. It is found that there is difference of the concentration gradient between membrane and surrounding fluid. As described above equation, it is important to find the difference because of the driving force depends on this gradient. These results mean that the surface tension between the membrane and the liquid is different. So the important mechanism of the driving force is hidden in the structure of the membrane of the neutrophile.

IV. Conclusions

From the experiments, the diffusion process of concentration is different between on the membrane and around the membrane. The difference of diffusion process corresponds to the surface tension difference, which leads to driving force by Marangroi effect.

We acknowledge the financial support of the grant in aids by a Grant-in-Aid for Scientific Research from the ministry of Education, Culture, Sports, Science and Technology, Japan (Scientific Research (B) (2)19360088, Exploratory Research 19656051).

1. Tamagawa M., Mukai, K., Furukawa, Y., , Proc. of Fifth East Asian Biophysics Symposium & Forty-Fourth Annual Meeting of the Biophysical Society of Japan, 2006

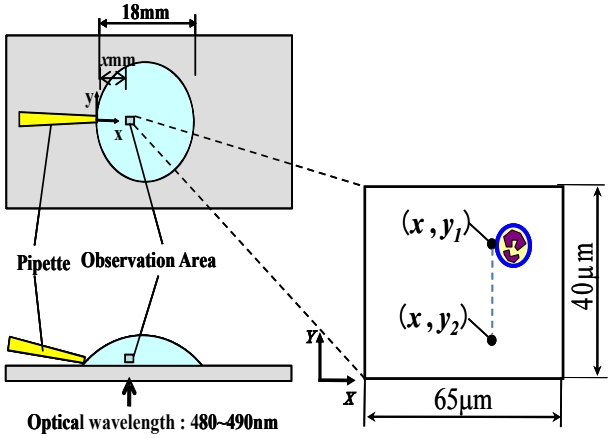


Fig. 3 Observation of neutrophile motion by concentration (cytokine) gradient

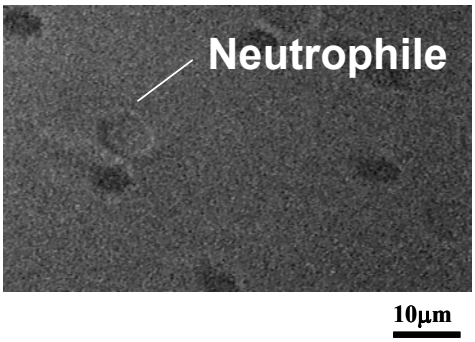


Fig. 4 Observation of neutrophile motion by concentration (cytokine) gradient

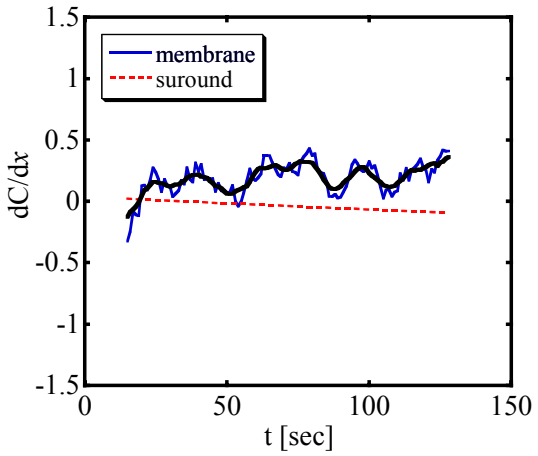


Fig. 5 Concentration gradient at the center of membrane and surrounding fluid

Cellular Uptake of Gold Nanoparticles into Normal and Cancer Cells

Jade Trono[1], Kazue Mizuno[1], Noritaka Yusa[2], Takehisa Matsukawa[3], and Mitsuru Uesaka[2]

[1] Department of Nuclear Engineering and Management, The University of Tokyo, Tokyo, 113-8654, Japan
[2] Nuclear Professional School, The University of Tokyo, Ibaraki, 319-1188, Japan
[3] Juntendo University School of Medicine, Tokyo, 113-8421, Japan

Abstract— **Gold nanoparticles intracellular uptake was investigated using both normal and cancer human cells. Cell uptake was analyzed using Atomic Absorption Spectrometry (AAS). It was found that combining 20nm gold nanoparticles with longer incubation time and lower concentration can optimize the uptake of gold nanoparticles by cancer cell. The findings of this study will help in the design and optimization of the nanoparticles uptake for therapeutic and diagnostic applications of X-ray Drug Delivery System.**

Keywords— **Gold nanoparticle uptake, GNP contrast agent, radiosensitizer, dose enhancer.**

I. Introduction

The introduction and development of gold nanoparticles has led to studies dealing with its potential for medical imaging and diagnostic applications. Several studies have been conducted evaluating factors that will potentially determine the uptake and uptake mechanism of nanoparticles and/or modified nanoparticles by the cell [1,2,3,4]. Gold nanoparticles have been actively investigated in a wide variety of biomedical applications for several reasons: it has the advantage of small size which is highly tunable (1-100nm) [5], capable of evading the immune system [5], easy to characterize by UV-vis spectrophometry, ICP-AES or ICP-MS, and TEM[3]. Our particular interest on using gold lies on its size tunability and its potential use either as radiosensitizer/dose enhancer in the treatment of cancer or as contrast agent for diagnostic imaging of cancer. It has been demonstrated that 2mm gold can be used as internal fiducial marker of tumors [6]. It was also evaluated numerically that gold nanoparticles can be used as contrast agent [7].

Our group is developing pinpoint keV/MeV X-ray source for X-ray DDS (Drug Delivery System) [8]. The X-ray DDS uses advanced nano-scaled polymers which contain and deliver drug or contrast agent to cancers. Figure 1 and 2 shows the mechanism of X-ray DDS and the schematic diagram of the future pinpoint X-ray source with DDS, respectively [8]. This new modality combining physical energy (via pinpoint X-ray source) and drug (via DDS) in one compact system is very important for inspection and therapy of cancer. The in-vitro evaluation on the combination of gold nanoparticles and physical energies via X-ray DDS is necessary for the development of a safe and effective treatment and/or imaging modality. Fundamental studies on uptake of nanoparticles, investigating factors such as size, incubation time and concentration play an important role in the design of safe nanoparticles for diagnostic and therapeutic applications.

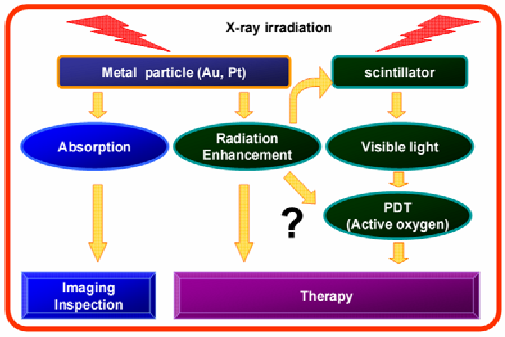


Fig. 1. Mechanism of X-ray DDS

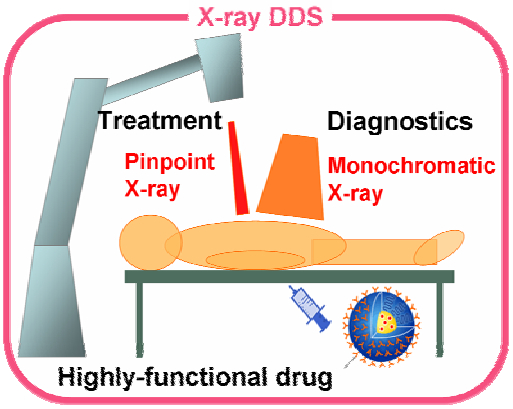


Fig 2. Schematic diagram of the future pinpoint X-ray source and DDS

In this paper, we present result on the uptake of several cell lines, taking into account factors such as gold nanoparticle size, incubation time and concentration. We aim to compare how normal and cancer cell uptake of gold nanoparticles are affected by these factors and how we can use the combination of these three factors to optimize gold nanoparticles uptake of cancer cells.

O. Dössel and W.C. Schlegel (Eds.): WC 2009, IFMBE Proceedings 25/VIII, pp. 202–205, 2009.
www.springerlink.com

II. Materials and Methods

A. Chemicals

Gold nanoparticles (5, 10, 20, 50nm) were supplied from British Biocell International. Prior to use in cell experiments, gold nanoparticles used were initially characterized using AAS (atomic absorption spectroscopy), UV-vis spectrometry and TEM.

B. Apparatus

The gold content of samples was determined using a AAnalyst 800 atomic absorption spectrometer (Perkin-Elmer) with THGA graphite furnace, gold hollow-cathode lamp and AS-800 autosampler. All analyses were performed at wavelength of 242.8nm using 0.7nm slit width. New graphite tubes were conditioned by heating and the machine is recalibrated prior to use. For the evaluation of peak profiles, the calculation of peak area and permanent storage peak profiles, AAWinlabTM software was used. Argon was used as the inert gas.

C. Cell line, culture and sample preparation

We used both normal and human cancer cells for these experiments. PK-1, PK-45, Panc-1, WI-38, NB1RGB and HeLa were purchased from Riken cell bank (RIKEN, Tsukuba). PK-1, PK-45, Panc-1 are all human pancreas cancer cells while WI-38, NB1RBG are finite normal human cells. PDL of WI-38 and NB1RGB is 35 and 40 respectively. HeLa was used as control experiment to check and compare reported results. Initial experiments were also conducted to check for aggregation of 20nm gold nanoparticles using different media with serum, checking for aggregation at several intervals from 0-48 hours. It was found (results not included) that gold nanoparticles aggregate within three hours when combined with MEM, MEM-alpha, DMEM media. Gold nanoparticles were also observed to aggregate in PBS (Phosphate buffer saline). Also, toxicity via MTT assay and colony assay were also conducted and the results did not indicate cellular toxicity, similar to other reported results [1-4].

The cell medium for all cell lines (except HeLa) used is RPMI-1640 (GIBCO, 11875, RPMI-1640), supplemented with 10% serum (HYCLONE, SH30396.03, Fetal Bovine Serum). The cell medium for HeLa was DMEM (GIBCO, 61965, DMEM) supplemented with 10% serum (HYCLONE, SH30396.03, Fetal Bovine Serum). Cells were continuously subcultured in T-25 flask (BD Falcon, 353108) and prior to achieving confluency, cells were seeded into 60mm dishes (BD Falcon, 353002, T-25) for gold treatment. To ensure uniform cell count during experiment, samples are prepared per condition per cell type. Six dishes were prepared for one treatment condition: one for control, one for cell counting and the remaining for gold treatment. While the cells were on the exponential phase, gold colloid was diluted with media (2.5mL) to achieve the desired concentration. Dishes were stored in a humidified atmosphere at 37°C, 5% CO_2 in air. Treatment duration time depends on the condition to be tested.

After gold treatment, cells were washed with 1mL Dulbecco Phosphate Buffered Saline (SIGMA, D8537, DPBS) thrice. Cells were collected from the dish by trysinization, using trypsin-EDTA solution (0.05% trypsin, 0.02% EDTA, T3924, SIGMA), counted (Nucleocounter) and transferred to 1.5mL eppendorf tubes. The cell solution was homogenized using sonicator (HandSonic).

D. Gold measurement

The concentration of gold nanoparticles used was verified using AAS. Cell digestion was initially performed but results showed that homogenized and digested samples gave no significant difference in the detected Au content of the samples. In AAS analysis, five-point calibration curve using 1000ppm Au standard diluted to maximum of 100ppb was used. The gold content of samples was determined by AAS as previously described [9] with minor modification. Samples were diluted 1 to 50 fold by mixing 0.5% HCl. Using an autosampler, 20uL of diluted sample and 5uL of matrix modifier (0.1% palladium and 0.06% magnesium nitrate in 1.5% HNO3) were injected in the graphite furnace to measurement the gold content of the sample. Two replicates were taken for each sample analyzed.

III. Results and Discussion

The effect of gold nanoparticles size, incubation time and concentration on the uptake of normal and cancer cell lines used were investigated. For diagnostic and medical purposes, uptake data are presented in gold amount (nmol) per cell, and not as number of gold particles per cell. The concentration of gold detected in the sample using AAS is simply divided by the number of cells present in the sample.

A. Dependence on Gold nanoparticles size

Cell samples were treated with 12μM gold nanoparticles colloid of various sizes mixed with media for 24 hours. In figure 3a, a plot of the Au content of cells versus size shows that the uptake is dependent on size. Among the gold nanoparticles used, 5 and 10nm gold nanoparticles had

significantly lower uptake as compared to 20 and 50nm. This trend is observed on all cells used in the experiment, with 20nm gold nanoparticles uptake higher than 50nm. Based on these results and to simplify succeeding experiments, we will be using 20nm gold nanoparticles.

For comparison purposes, we also presented data as number of gold nanoparticles per cell (figure 3b). In order to extract the number of nanoparticles up taken by each cell, the number of nanoparticles must be calculated based on the concentration of Au found in the sample. This was done by using the diameter and concentration of gold nanoparticles to calculate the number of atoms per particle. Our result was quite different from the results reported in ref 3 (figure 3b). It was reported that the maximum cells uptake occur at 50nm. If the number of gold particles up taken will be considered, based from our results, 5nm gold nanoparticles have the highest probability of entering the cells. The number of gold particles entering the cells decreases drastically as the gold nanoparticles size increases.

B. Dependence on incubation time

Cells were treated with 47µM 20nm gold nanoparticles from 1 to 48 hours. For therapeutic and diagnostic purposes, incubation time will dictate the optimum condition (ie, cancer cell is loaded with sufficient gold nanoparticles). Figure 4 shows the uptake of gold nanoparticles increases significantly between 1 to 12 hours. Although both normal and cancer cells uptake almost similar quantities of gold on the first 12 hours, it was observed that between 12-48 hours, cancer cells continue to uptake 20nm gold nanoparticles while normal cells gradually slow and approach plateau. Previous reported results indicated that HeLa cell approaches plateau within 4-7 hours [3]. Our results showed that HeLa cell uptake slowed after 24 hours.

C. Dependence on concentration

The effect of concentration of gold nanoparticles uptake of the cell was also investigated (fig 5). Cells were treated with 12, 24, 47 and 94 µM of 20nm gold nanoparticles for 24 hours. It was previously found that uptake is also dictated by the amount of gold present in the solution. For smaller concentrations, increasing the incubation time will

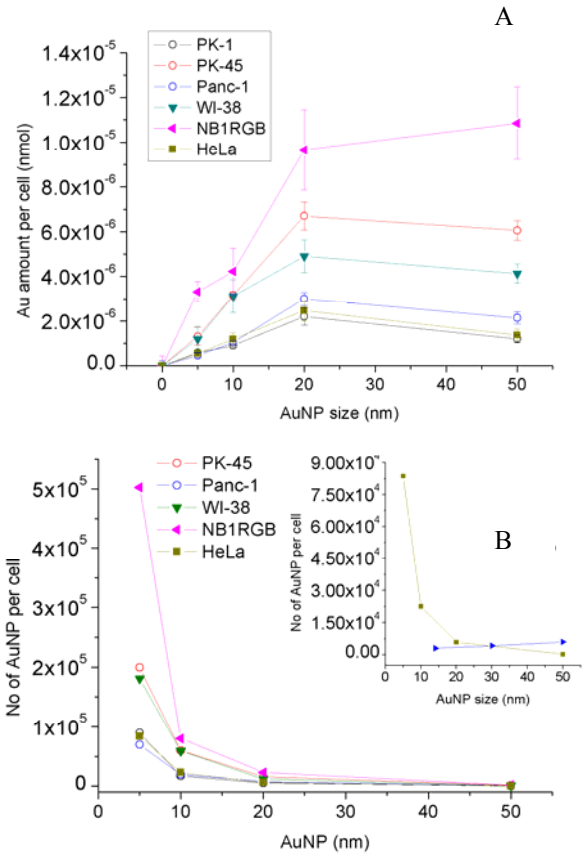


Fig 3. Uptake dependence on gold nanoparticle size. Y-axis is presented in (A) nmol per cell, (B) no of AuNP (gold nanoparticles) per cell. Inset in (B) is the result of HeLa compared to ref 3.

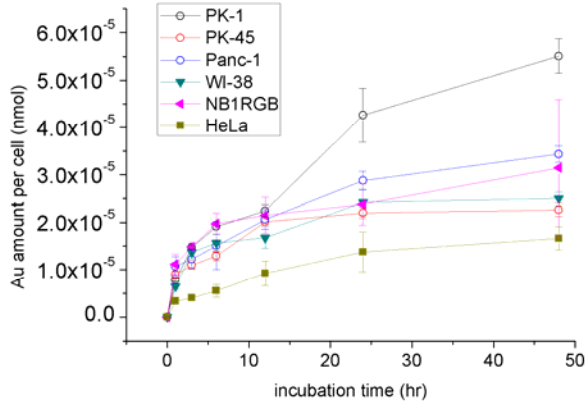


Fig 4. Dependence on incubation time

not increase the gold nanoparticles uptake of the cell from our previous results. From figure 5, the uptake of gold-nanoparticles increases as the concentration is increased. It was hypothesized in ref 3 that the uptake mechanism is via receptor-mediated endocytosis (RME). RME is an endocytotic mechanism in which specific molecules enter the cell. Cells have a limited number of receptors on the membrane, and through these receptors the gold nanoparticles enter the cell. If there are fewer gold nanoparticles in the sample, we expect that the gold nanoparticles have a small probability of getting near the receptors; hence the uptake on lower concentrations is low. However, for the case when there are abundant gold nanoparticles on the solution, nanoparticles are abundantly available in the solution and these receptors will be able to take-in nanoparticles easily. As such, approaching the plateau of uptake could mean two things, one is that there are few nanoparticles in the solution, second is that the cells are already saturated with gold nanoparticles that some are released back into the solution.

From figure 5, it was observed that both cancer and normal cells have similar uptake at lower concentrations, but as concentration was increased, the uptake of normal cells is higher compare to cancer cells. Referring to figure 4, there is significant difference in uptake of normal and cancer cells at longer incubation time. These experimental conditions can be combined in order to optimize uptake of gold nanoparticles by cancer cells.

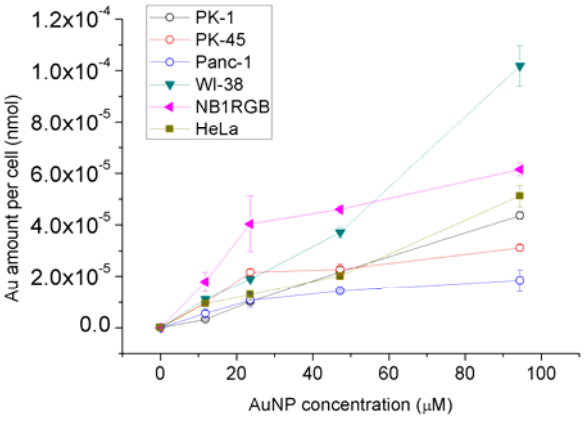


Fig 5. Dependence on gold nanoparticle concentration

IV. Summary

We aim to develop gold nanoparticles DDS for non-invasive imaging for future dynamic tracking radiation therapy. As one of the subjects forwards it, we are analyzing the uptake of gold colloids to cancer cells. We are going to continue this study using other gold nanoparticles sizes to find the optimized sizes for several cells.

From our present results, we were able to optimize gold nanoparticles uptake of cancer cells by combining experimental conditions that can help optimize the uptake. 20nm gold nanoparticles particles at lower concentration and longer incubation time (more than 24 hours) can help optimize uptake of cancer cells as compared to the uptake of normal cells. Optimizing uptake to only cancer cells is one of the many factors which will be considered in conducting in-vivo and pre-clinical experiments.

Further investigations will be conducted combining gold nanoparticles and ionizing radiation in cancer cells via X-ray DDS for verification of radio-sensitization effect for safe and effective use of gold nanoparticle-based agents in the near future.

References

1. J.A. Khan, B. Pillai, T.K. Das, Y. Singh, S. Maiti (2007). "Molecular Effects of Uptake of Gold Nanoparticles in HeLa Cells," *ChemBioChem*, **8**, 1237-40.
2. B.D. Chithrani, W.C. Chan (2007). "Elucidating the Mechanism of Cellular Uptake and Removal of Protein-Coated Gold Nanoparticles of Different Sizes and Shapes," *Nanoletters,* **7-6**, 1542-1550.
3. B. D. Chithrani, A.A. Ghazani, W.C Chan (2006). "Determining the Size and Shape Dependence of Gold Nanoparticle Uptake into Mammalian Cells," *Nanoletters,* **6-4**, 662-668.
4. J. Xing, J. Zeng, J. Yang, T. Kong, T. Xu, W. Roa, X. Wang, J. Chen (2007). "Gold-based Nanoparticles for breast cancer diagnosis and treatment," IEEE International Symposium on Circuits and Systems, 2882-2885.
5. M. Chang, A. Shiau, Y. Chen, C. Chang, H. Chen, C. Wu (2008). "Increased apoptotic potential and dose-enhancing effect of gold nanoparticles in combination with single-dose clinical electron beams on tumor-bearing mice," *Cancer Sci.* **99-7**, 1479-1484.
6. Shirato, H., T. Harada, et al. (2003). "Feasibility of insertion/implantation of 2.0-mm-diameter gold internal fiducial markers for precise setup and real-time tumor tracking in radiotherapy." *International Journal of Radiation Oncology Biology Physics* **56**(1): 240-247.
7. Yusa, N., M. Jiang, et al. (2009). "Numerical evaluation of the effectiveness of colloidal gold as a contrast agent." *Radiological Physics and Technology* **2**(1): 33-39.
8. M. Uesaka, K. Mizuno, A. Sakumi, J. Meiling, N. Yusa, N. Nishiyama, K. Kataoka, K. Nakagawa (2007). "Pinpoint KeV/MeV x-ray sources for x-ray drug delivery system," Proceedings of Proceedings in Accelerator Physics.2007, 2793-2795.
9. J.J.M. de Llano, E.J. Andreu, A. Pastor, M. de la Guardia, E. Knecht, (2000). "Electrothermal Atomic Absorption Spectrometric Diagnosis of Familial Hypercholesterolemia." Anal Chem, 72, 2406-2413.

Author: Jade Dungao Trono
Institute: Department of Nuclear Engineering and Management, School of Engineering, The University of Tokyo
Street: 7-3-1 Hongo, Bunkyo-ku,
City: Tokyo
Country: Japan
Email: trono@nuclear.jp

Study to trap fluid microcapsules in artificial blood vessel by producing local acoustic radiation force

Kohji Masuda[1], Ryusuke Nakamoto[1], Yusuke Muramatsu[1],
Yoshitaka Miyamoto[2], Keri Kim[3] and Toshio Chiba[3]

[1] Graduate School of Bio-Applications and Systems Engineering, Tokyo Univ. of Agri. &Tech., Tokyo, Japan
[2] School of Medicine, Nagoya University, Nagoya, Japan
[3] National Center for Child Health and Development, Tokyo, Japan

Abstract—**Microcapsules of µm order collapse themselves after ultrasound emission. Applying this technique as drug delivery system (DDS), not only local medication but also gene therapy method should be possible. However, it has been limitation to enhance the efficiency of medication because capsules suspension spreads in human body after the injection, where motion of capsules in blood flow cannot be controlled. To affect behavior of microcapsules, acoustic radiation force was introduced. We have observed the local aggregation of microcapsules by producing local acoustic radiation force in the artificial blood vessel. Then we estimated amount of trapped capsules by optical image processing. We confirmed fluid microcapsules of similar diameter with red blood cell were trapped in the middle of the path and by ultrasound of sinusoidal signal of 1 MHz. The condition to trap capsules was indicated by higher sound pressure and lower flow velocity.**

Keywords— **drug delivery system, microcapsule, acoustic radiation force, artificial blood vessel, trapping**

I. Introduction

Making use of the phenomena that microcapsules or microbubble of µm order collapse themselves after ultrasound emission near their resonant frequency, physical DDS (Drug Delivery System) has been proposed. To minimize the side effect of medication, drug should affect only to the target area, not to other parts inside human body. Though recent mainstream of research in DDS is focused on the gene transduction by using gene vector, it takes time and cost for development. The microcapsules, which can contain the specified drug inside the shell, have the possibility to correspond to various kinds of medications. Also the feature to use the microcapsules is easily detected and actuated by ultrasound. The distribution of capsules inside the body is easily recognized by echogram (B-mode image) because the brightness of echogram varies according to the density of capsules. However, because of the diffusion of capsules after injection, it was difficult to enhance the efficiency of medication. If the density of capsules inside human body can be controlled, the amount of drug would be minimum. Then we have noticed that microbubble aggregates in water by the effect of Bjerknes force [1,2] which is produced by pressure gradient of ultrasound and the oscillation of diameter in microbubble. Since the oscillation in microcapsule is smaller than in microbubble, because of the shell, a microcapsule is thought to receive the acoustic radiation force [3,4] to be pushed out with acoustic propagation. In this paper we describe our attempt [5,6] to trap fluid microcapsules in an artificial blood vessel by acoustic radiation force.

II. Method

Fig.1 shows behavior of fluid microcapsules under ultrasound emission. Considering the shape of a microcapsule as sphere, the acoustic radiation force F_{ac} acts to push the capsules to the direction of acoustic propagation. On the other hand, when the microcapsules are put in flow, a capsule should receive the flow resistant F_d. Thus, if F_d and F_{acx} in Fig.1 are similar, the acoustic radiation force balances with the flow resistant to trap fluid microcapsules.

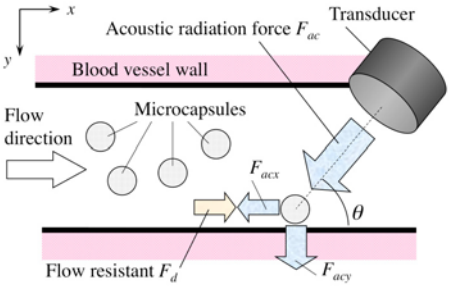


Fig. 1 Behavior of fluid microcapsules under ultrasound emission.

We used microcapsule F-04E which shell is made of PVC (polyvinyl chloride) with specific gravity as 0.0225 and average of diameter as 3.5 µm. We sieved it as the range of diameter is from 4 to 20 µm to be applied to use *in vivo*. We have prepared the artificial blood vessel, which is made of PEG (polyethylene glycol), including a straight path as the schematic view shown in Fig.2. The external size is 80 mm x 55 mm x 10 mm and the inner diameter of the path is 2 mm. It is placed in the bottom of water tank,

O. Dössel and W.C. Schlegel (Eds.): WC 2009, IFMBE Proceedings 25/VIII, pp. 206–207, 2009.
www.springerlink.com

which is filled with water. By using an optical microscope (KH-7700, Omron, Japan), behavior of microcapsules is observed and recorded.

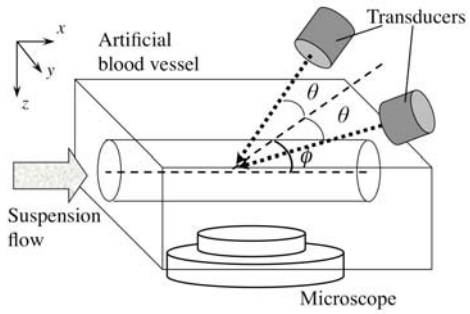


Fig. 2 Schematic view of the experiment to trap capsules.

We introduced two transducers to be focused at the same point with their angle and 2θ as shown in Fig.2. The plane which includes axes of the transducers is set $\phi = 50$ deg to prevent physical intervention between the transducer and an edge of the water tank. The transducer includes a concavity ceramic disc with the diameter of 25 mm. Ultrasound is emitted by amplifying sinusoidal signal to the amplitude 210 kPa where the focal area of ultrasound is created in 60 mm from the surface of the transducer with the half width of sound pressure in 8 mm.

III. Results

We observed the focused area under emission of sinusoidal ultrasound with frequency as 1 MHz, flow velocity as 20 mm/s and angle θ as 30 deg. Fig.3 shows time series microscopic images of the area where capsules are trapped in the middle of the path. Thus we confirmed the possibility to trap fluid microcapsules which sizes are similar to red blood cell under ultrasound emission.

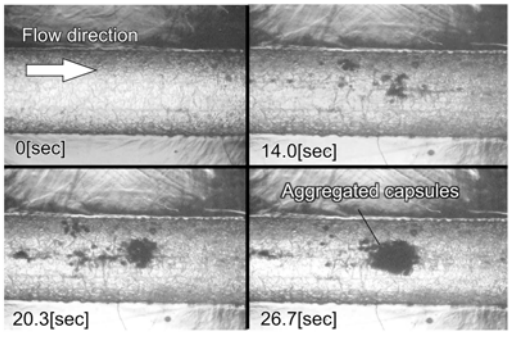


Fig. 3 Time series microscopic images where fluid microcapsules are trapped at the focused area under ultrasound emission (210kPa, 1MHz)

Then we measured amount of trapped capsules by calculating occupied area by capsules in the microscopic images when the amount of capsules is saturated. We experimented in various flow velocities and sound pressures. Fig.4 shows the occupied area by capsules versus flow velocity with parameter of sound pressure. When sound pressure is increased, much more amount of capsules was trapped. In the same sound pressure, the amount of capsules in 10 mm/s was more than in 20 mm/s.

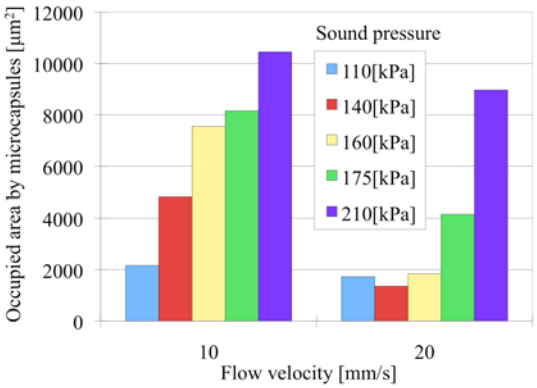


Fig. 4 Occupied area by microcapsules in the microscopic images versus flow velocity with parameter of sound pressure.

IV. Conclusions

In this study, we have experimented to trap fluid microcapsules in artificial blood vessel. We confirmed the capsules with diameter of 3.5 μm were trapped in the middle of the path and by ultrasound of sinusoidal signal of 1 MHz. The condition to trap capsules was indicated by higher sound pressure and lower flow velocity. We are going to apply the experiment by varying other parameters and to investigate the mechanism of the phenomena.

References

1. H. Mitome: Japanese Journal of Applied Physics, Vol.40 (2001) pp.3484-3487.
2. T. Lilliehorn, U. Simu, M. Nilsson, M. Almqvist, T. Stepinski, T. Laurell, J. Nilsson and S. Johansson: Ultrasonics, Vol.43 (2005) pp.293-303.
3. Y. Yamakoshi and T. Miwa: Japanese Journal of Applied Physics, Vol.47 (2008) pp.4127-4131.
4. T. Kozuka, K. Yasui, T. Tuziuti, A. Towata and Y. Iida: Japanese Journal of Applied Physics, Vol.47 (2008) pp.4336-4338.
5. Y. Muramatsu, S. Ueda, R. Nakamoto, Y. Nakayashiki, K. Masuda and K. Ishihara: Proc. of Euro. Med. & Biol. Eng. Conf. (2008) pp.1589-1593.
6. K.Masuda, Y.Muramatsu, S.Ueda, R.Nakamoto, Y.Nakayashiki and K.Ishihara: Japanese Journal of Applied Physics, Vol.48 (2009) in press

Diamond microelectrodes for amperometric detection of secretory cells activity

A. Pasquarelli[1], V. Carabelli[2], Y. Xu[1], Z. Gao[1], A. Marcantoni[2], E. Kohn[1] and E. Carbone[2]

[1] Institute of electron devices and circuits, University of Ulm, Ulm, Germany
[2] Department of Neuroscience, NIS Centre, University of Torino, Torino, Italy

Abstract — **Diamond is the only transparent semiconductor electrode material used in heavy duty electrochemistry and therefore also an attractive material for microelectrode arrays in biochemistry. Three configurations are described: (1) single crystalline diamond (SCD), with a substrate size of less than 4mm x 4mm, serving as ideal reference material, (2) nanodiamond (NCD) thin films on silicon substrates, representing an application of the commonly used diamond MEMS technology and (3) NCD thin films on sapphire, sapphire being the standard substrate for GaN optoelectronics and electronics. A basic electrode array (quadropole MEA) has been developed for this investigation. For optimized deposition conditions, the influence of grain boundaries could be widely suppressed and comparable electrode characteristics could be obtained for all cases. In the diamond-on-Si case, fragile membranes need to be etched for optical transparency. Full advantage of the diamond electrode properties combined with the biological requirements is therefore only obtained by the diamond-on-sapphire system. Preliminary results of the amperometric detection of secretory cells activity are presented including a first comparison with discrete carbon fiber electrodes.**

Keywords— **Diamond, MEA, Neurotransmitters, RedOx.**

I. Introduction

Recordings of action potentials, synaptic transmission and hormone release are fundamentals for determining the state of neurons and neuroendocrine cells [1]. Modern techniques make use of metallic and CMOS microarrays, which record extracellular action potentials by capacitive charge transfer between cells and microelectrodes [2] or by modulating the channel current of a FET with the membrane voltage of the cell in contact with the device [3]. In both cases the extracellular signals are well resolved in time and amplitude (1-10 ms; 20-100 μV) and furnish important details about the functional state of neurons and excitable cells. Nevertheless these devices show serious limitations: they are opaque, poorly biocompatible and only conditionally stable in biological media.

Diamond is a semiconductor with extreme properties: it is chemically inert, remains stable in a range of pH 0 to pH 14 and is not wet-chemically etched, it can be electrically highly insulating or quasi-metallically conducting by doping and is optically transparent over a very wide range from the far infrared to deep-UV (225 nm). It possesses a large potential window of hydrolysis (approx. 3 V) and is the only semiconductor material used in heavy duty electrochemistry like waste water purification and electroanalysis of hazardous substances [4]. It offers thus electrical conductivity together with high electrochemical activity (charge transfer), inhibition of hydrolysis in a wide potential window and at the same time chemical resistance [5]. The industrially relevant configuration is nanocrystalline diamond (NCD) deposited onto silicon substrates by chemical vapour deposition (CVD) and has indeed gained strong interest as substrate and functional material for biological and biochemical applications especially in the field of biosensors [6].

In electrochemistry, doped diamond belongs to the family of redox electrodes and is thus primarily suitable for amperometric applications. Since hydrolysis appears at a much wider potential window, with respect to most other materials, diamond electrodes allow the detection of several analytes with redox potentials well beyond the water dissociation potential (1,23 V). Its high electrochemical activity makes diamond also very sensitive and fast in temporal response.

Under these premises the amperometric detection of neurotransmitter release appears as a straight-forward application for diamond microelectrodes. Here we focused on the development of devices for the fast quantal detection of catecholamines released from adrenal chromaffin cells.

Presently, the mostly used technique to resolve single secretory events is the amperometric detection of catecholamines using carbon-fiber microelectrodes polarized to +650-800 mV to detect the target molecules by electrochemical oxidation [7, 8]. Amperometric burst-signals can be recorded for seconds or minutes depending on the stimulus. Each spike monitors the fusion of single vesicles and the release of catecholamines. Despite their high time resolution, high-sensitivity and not being invasive, discrete carbon fibers have serious drawbacks, being limited in use with single cells and due to the difficult use in combination with a lateral glass-pipette microelectrode, for simultaneous amperometric and patch-clamp recordings.

Aware of these issues we have developed a concept for-transparent planar diamond microelectrodes, which leave

O. Dössel and W.C. Schlegel (Eds.): WC 2009, IFMBE Proceedings 25/VIII, pp. 208–211, 2009.
www.springerlink.com

the entire working field free of obstacles, thus allowing concurrent amperometric, patch-clamp and fluorescence measurements from the same cell. In this concept NCD is nucleated and grown on sapphire substrates, which are commonly used as substrates for GaN based electronics. Thus, this concept allows potentially also the integration of electrode arrays with GaN-based field effect transistor electronics as already demonstrated in a first proof-of-concept experiment of a discrete GaN-based ISFET with diamond electrode [9].

II. Materials and Methods

A. Test Device on single crystalline Diamond

Starting from a Sumitomo HTHP synthetic Ib diamond substrate of 4 mm x 4 mm in size, we have deposited a 180 nm thick mono-epitaxial layer of Boron-doped diamond with an impurities concentration of ~10^{20} cm^{-3} by Microwave Plasma Enhanced CVD (MW-PECVD), to obtain a quasi-metallic conducting layer with a sheet resistivity of ~600Ohm/□. This conducting layer was processed by means of lithographic and dry chemical techniques to obtain four independent circular microelectrodes of 16 µm diameter. The surface was then terminated in oxygen plasma to enhance the cell adhesion without the use of biological substrates (laminin, polylysine, collagen etc.), which adversely affect the amperometric operation of the planar electrodes.

The last step consisted in packaging and bonding the 4 mm large array onto a custom-made carrier based on Roger 4000 dielectric material, which shows very low leakage currents even in the presence of humidity, and finally fitting a glass ring to provide an adequate perfusion chamber.

B. Devices on nanocrystalline Diamond

The above described electrode array process has been transferred to two NCD configurations. The first one being a standard diamond-on-Si MEMS process by using a Hot-filament CVD (HF-CVD) process on 4″ diameter substrates. Here firstly, after nucleation by bias enhancement (BEN), a 1 µm buffer layer was grown followed by a 200 nm thick quasi-metallically Boron-doped electrode layer. Obviously in these cases the conducting layer was not mono-epitaxial because of the NCD nature of the underlying insulating layer. However, depending on the outgrowth conditions and doping profiles employed, the influence of the grain boundaries on the electrochemical characteristics (mainly the background current in the absence of redox reactions and water dissociation potential window, as shown in Fig.1) could be widely suppressed. Nevertheless, a wet-chemical process had been used to remove any graphitic clusters.

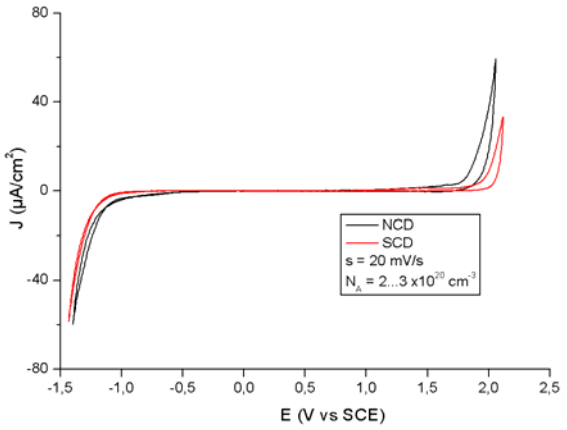


Fig. 1: Cyclic voltammetry scan showing the hydrolysis potential window of SCD and NDC electrodes.

To enable fluorescence labeling and optical detection a membrane of 3 mm in diameter had been etched by an Inductively Coupled Plasma etching process (ICP).

It turned out that the mechanical membrane stability is critical, especially in the case of ultrasonic cleaning. For higher mechanical stability essentially thicker membranes and thus diamond films would be needed, however reducing the transparency due to increased scattering at the grain boundary network.

Thus as alternative concept, diamond has been deposited onto a sapphire wafer. Such wafers are the standard substrate for GaN based optoelectronics and electronics and are available for large diameters with high crystalline quality.

Sapphire is highly transparent and electrically highly insulating. Onto such substrates thin diamond layers with high electrochemical quality could be deposited by HF-CVD.

In the case discussed here we prepared a 400 nm thick intrinsic nucleation and buffer layer, capped with a 300 nm thick quasi-metallically Boron doped film. With sapphire being perfectly transparent in the visual and near UV range (the spectral regions of interest for fluorescence), this new chip is very robust and can be sonicated without any danger.

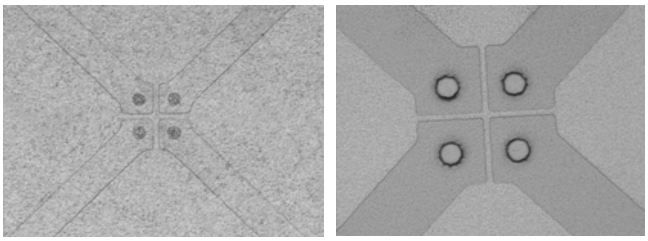


Fig. 2: NCD devices on silicon (left) and on sapphire substrate (right). The apertures are 16µm and the pitch 50µm, in both cases.

III. Results

Instrumentation: The front-end consists in a four channel custom-made voltage-biased current amplifier (trans-resistance configuration) with a gain of 10^8 V/A. The background noise has a spectral density of 50 fA/sqrt(Hz). All signals are low-pass filtered at 1kHz by means of a 4th order Bessel-filter and then acquired using a National Instruments USB-6216 unit sampling with 16 bits resolution at rate of 4kHz per channel. The acquisition is controlled with a LabView application program developed by the authors. When operated with a Tyrode solution and an Ag/AgCl ground-electrode, the overall background noise of the measurement system resulted lower than 10 pA peak-to-peak.

Characterization: First we performed a series of cyclic-voltammetry measurements to detect a) possible artefacts due to inorganic and organic substances used in the sequential steps of cell manipulation and b) the oxidation activity of adrenaline on our microelectrodes.

It turned out that our standard Tyrode buffered solution (pH 7.4), does not produce artefacts, DMEM culture solution produces little oxidation artefacts at ~900 mV, and poly-L-lysine spoils completely the redox properties of the diamond electrodes turning it into a fairly linear ohmic solid/liquid interface. The oxidation activity of 1 mM adrenaline in Tyrode buffer could be observed starting at 400 mV and peaking around 650 mV (Fig.3), confirming the potential suitability of our devices for the target application.

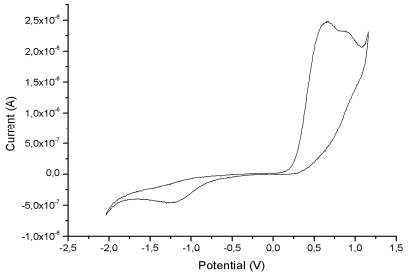


Fig. 3 Cyclic voltammetry of 1mM Adrenaline in Tyrode buffer solution with NCD working-electrodes against Ag/AgCl reference electrode. Scan speed is 50 mV/s.

The reproducibility of oxidation activity detection was tested by sequentially applying, through a micro-perfusion, 1mM adrenaline and saline rinsing solutions. This experiment showed negligible loss of sensitivity due to accumulation of educts from the oxidation reaction (fouling).

Electrodes on sapphire have been investigated to analyze the transparency in the spectrum range of interest. A comparison of simulated data with experimental results shows some absorption at short wavelengths (Fig. 4), mainly due to the silicon interlayer used to facilitate the initial diamond nucleation. It is evident that further optimization is needed to achieve overall transmittance properties suitable for fluorescence detection.

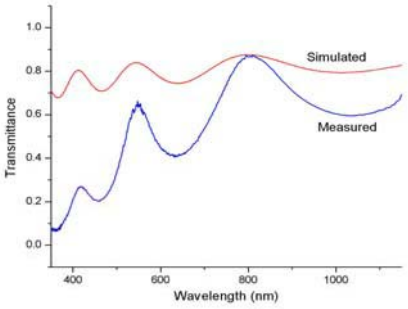


Fig. 4: Transmittance of the NCD on sapphire device. Comparison of simulated and measured data show absorption at shorter wavelengths.

The basic electrochemical behavior was also investigated, showing negligible dark current and sensitive response to application of 1mM adrenaline drops.

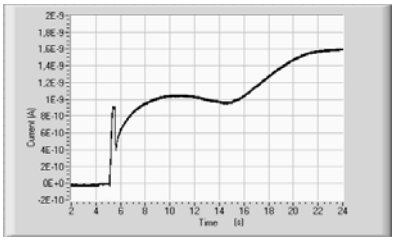


Fig. 5: Response of one NCD on sapphire electrode to two drops (dispensed at the times of 5 and 15 s) of 1 mM adrenaline solution.

Cell measurements: For testing the diamond microelectrodes we chose isolated chromaffin cells prepared from mouse adrenal glands. After removal, the glands were placed in Ca^{2+} and Mg^{2+}free Locke's buffer containing (in mM): 154 NaCl, 3.6 KCl, 5.6 $NaHCO_3$, 5.6 glucose, and 10 HEPES, pH 7.2, at room temperature. The glands were then decapsulated, and the medulla was precisely separated from the cortical tissue. Medulla digestion was achieved for 60 min at 37°C in the Locke's buffer mentioned before containing 20U/ml of papain (Worthington Biochemical Corp., Lakewood, NJ). The cell suspension was then centrifuged for 5 min at 900 rpmi, washed two times, and resuspended in 2 ml DMEM supplemented with 15% foetal calf serum (FCS).

After placing an isolated cell onto one electrode and setting the biasing voltage between 650 and 800 mV, the cell was depolarized by adding an external solution containing

135 mM TEACl and 10 mM $CaCl_2$. In these conditions Ca^{2+} influx through voltage-dependent Ca^{2+}-channels caused exocytosis by vesicle fusion and consequent release of catecholamines. The SCD electrodes could clearly detect several quantal release events over a time span of more than two minutes, after which exocytosis was limited by Ca^{2+}-channel inactivation. The device could detected amperometric spikes of 5 to 80 pA peak amplitude and duration spanning between few milliseconds and several tens of milliseconds, accounting for vesicles of different sizes and/or different location of the exocytotic events on the cell membrane (Fig. 6-left).

Also the NCD on silicon device could clearly detect events of catecholamine quantal release. The "dark current" was negligible (~10 pA) and the background noise level was the same as with the SCD device (Fig. 6-right).

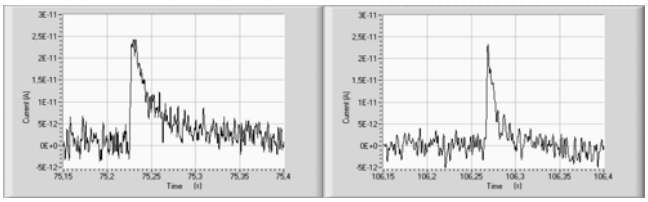


Fig. 6 Single quantal release event recorded left with an SCD microelectrode and right with an NCD on silicon device. Noise level, reaction time and sensitivity are very similar.

IV. DATA ANALYSIS AND DISCUSSION

Amperometric spikes were analyzed by means of IGOR macros. The analysis of individual exocytotic events was performed by measuring the following parameters: maximum oxidation current (I_{max}), spike width at half height ($t_{1/2}$), total charge of the spike (Q), ascending slope of the spike (m) and time to reach the peak (t_P). Preliminary results, obtained by comparing time course and amplitude of the spikes simultaneously recorded by NCD and classical carbon fibers, gave similar values in the two recording conditions. For example, mean quantity of charge (Q) was 0.43 and 0.47 pC (NCD versus carbon fiber), $t_{1/2}$ was 10.8 versus 8 ms, t_P was 3.6 versus 3.9 ms.

These promising results suggest that our planar diamond-based devices allow accurate measurements of single exocytotic events, with high time resolution, comparable to those of classical carbon fibers. However the advantage of measuring secretion from a planar detecting area is that it can be shaped to simultaneously monitor vesicle fusion from different membrane areas of the same cell. Future prototypes will be designed to the purpose.

V. CONCLUSION

These preliminary results of the diamond-on-sapphire technology may also be compared to first proof-of-concept results obtained for a diamond electrochemical electrode directly integrated with a GaN-based FET structure (an InAlN/GaN HEMT structure) realized in the concept of an extended gate ISFET (EG-ISFET) [9]. Clearly, here also a high water dissociation window of approx. 3 V is obtained and an electrode background current of less than 1 nA/mm². Moreover this device has been successfully operated in the amperometric mode as electrode and in the potentiometric mode as ISFET. Obviously a final goal is the integration of such a new dual mode device into biochip arrays, opening new fields for biosensors applied to biomedicine.

ACKNOWLEDGMENT

Work supported by the Ateneo Italo-Tedesco and the Deutscher Akademischer Austausch Dienst (DAAD), in the frame of the Vigoni program, to EC and EK, the Regione Piemonte (grants. A28-2005 to VC and D14- 2005 to EC).

REFERENCES

1. Carbone E et al. (2006) T-type channels-secretion coupling: evidence for a fast low-threshold exocytosis *Pflügers Archiv European Journal of Physiology*. **453:** 373-383.
2. Schätzlhauer R, Fromherz P. (1998) Neuron-silicon junciton with voltage-gated ionic currents. *Europ J. Neuroscience,* **10**: 1956-1962.
3. Fromherz P. Neuroelectronic interfacing: semiconductor chips with ion channels, nerve cells and brain. In: *Nanoelectronics and Information Technology*. Ed Waser R, Wiley-VCH, Berlin 2003, p. 781-810
4. Kraft A, Stadelmann M, Kirstein W. (2000) Use of diamond electrodes for electrolytic water purification and disinfection by anodic oxidation. *Galvanotechnik*. 91(2):334-339.
5. Show Y et al (2003) Characterization and Electrochemical Responsiveness of Boron-Doped *Nanocrystalline Diamond Thin-Film Electrodes. Chem. Mater.,* **15**: 879-888.
6. Yang W et al. (2002) DNA-modified nanocrystalline diamond films as stable, biologically active substrates. Nature Materials, 1, 253-257.
7 Kawagoe et al. (1991). Etched carbon-fiber electrodes as amperometric detectors of catecholamine secretion from isolated biological cells *Anal Chem*. **63**: 1589-1594
8 Chow et al. (1992). Delay in vesicle fusion revealed by electrochemical monitoring of single secretory events in adrenal chromaffin cells. *Nature* **356**: 60-63
9. Dipalo M et al. (2009) Combining diamond electrodes with GaN heterostructures for harsh environment ISFETs, Diamond and Related Materials, DOI: 10.1016/j.diamond.2009.01.011.

Author: Alberto Pasquarelli
Institute: Electron Devices and Circuits, University of Ulm
Street: Albert Einstein Allee 45
City: Ulm
Country: Germany
Email: alberto.pasquarelli@uni-ulm.de

Local electrical stimulation of single myocytes using three-dimensional electrode arrays with small interelectrode distances

D. Braeken[1], R. Huys[1], D. Jans[1], Josine Loo[1], D. R. Rand[1], G. Borghs[1], G. Callewaert[2] and C. Bartic[1]

[1] Bioelectronic Systems, IMEC, Kapeldreef 75, 3001 Leuven, Belgium
[2] Neurophysiology Lab, Subfaculteit Geneeskunde, KULeuven, E. Sabbelaan 53, 8500 Kortrijk, Belgium

Abstract— **In this paper, we describe the localized and selective electrical stimulation of single cells using a three-dimensional electrode array. The chip consisted of 84 nail-like electrodes with a stimulation surface of 0.8 μm^2 and interelectrode distances as small as 3 μm. Immunohistochemical staining of actin filaments in cells on these electrode arrays showed a tight coupling between the cell membrane and the chip surface. Selective and localized stimulation of primary embryonic cardiomyocytes using biphasic voltage pulses was achieved. The response of the cells to the applied electrical field was monitored using calcium imaging. An increase in relative $[Ca^{2+}]_i$ of 200% was seen upon applying stimulation pules of 1.2 V. Arrays of these three-dimensional electrodes could ultimately be used as a tool to selectively electroporate the membrane of single cells for genetic manipulation or to obtain electrical access to the inner compartment of the cell.**

Keywords— **Electrical stimulation, three-dimensional electrodes, microfabrication, embryonic cardiomyocytes.**

I. INTRODUCTION

Microfabrication of multi-electrode arrays offers a growing amount of solutions to various challenges in many fields of biomedical research. Microelectrode arrays (MEAs) represent a new tool for the long-term recording of electrical field potentials of excitable cells due to the non-invasive contact [1]. Microelectrode chips with planar electrodes are also used for the electrical stimulation of cells or tissues, e.g. for long-term potentiation studies in acute brain slices or for the selective electroporation of the cell membrane in DNA transfection studies. Localized electroporation and transfection in adherent cells using MEAs has been reported before [2,3]. However, MEAs still suffer from several drawbacks. An important disadvantage is the poor electrical coupling of a planar electrode with the cell membrane. This leads to a significant loss in the efficiency of electrical stimulation. Also, the majority of MEAs that are currently available are passive arrays with large electrode dimensions, even larger interelectrode distances, and a limited number of electrodes, all of which makes them non-ideal for single-cell experiments. Thus, the electrode-membrane coupling can be improved using three-dimensional electrodes with sizes that are smaller than the cell itself.

In this paper, we show that the cell membrane of cultured embryonic cardiomyocytes formed a tight engulfment around the nail-shaped electrodes, suggesting a strong coupling. Next, we demonstrate the electrical stimulation of single cells using biphasic voltage pulses between two three-dimensional electrodes located close to each other, creating a local electrical field. Changes in the relative intensity of the fluorescent Ca^{2+} indicator Fluo-4 from stimulated cells were recorded to assess intracellular $[Ca^{2+}]$ changes.

II. METHODOLOGY

A. Fabrication of passive electrode array and electrical stimulation set-up

The fabrication of the micronails is comparable to the method by Huys *et al.* [4] based upon the standard CMOS dual damascene copper process. However, tungsten was used instead of copper to reduce cytotoxicity. The electrodes were fabricated by etching of a layer of 100 nm TiN, resulting in planar electrodes. The nails were then fabricated by using lithography with a light-field mask on circles of 1.2 μm centered around the TiN electrodes, followed by a time-controlled oxide etch to remove the field oxide. This resulted in nails (500 nm to 1 μm high) with flat TiN electrodes on top and electrical connection in the tungsten shaft insulated by SiO_2, and planar connections on the bottom. Figure 1A shows a fragment of the 8 inch wafer with individual chips. Chips were diced and then packaged on a printed circuit board by flip-chip and epoxy-underfill (Figure 1B). A glass ring was placed on top of this printed circuit board to confine the culture medium.

O. Dössel and W.C. Schlegel (Eds.): WC 2009, IFMBE Proceedings 25/VIII, pp. 212–215, 2009.
www.springerlink.com

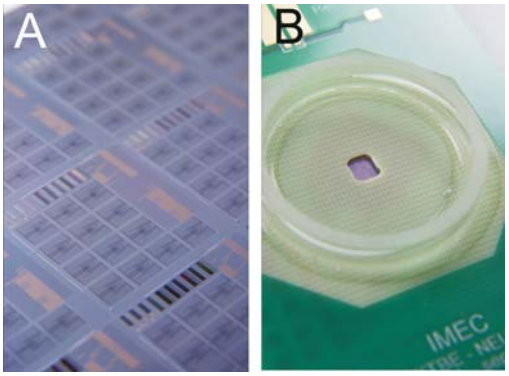


Fig. 1. A. Individual chips on the 8 inch wafer. B. Packaged chip on the printed circuit board with culture chamber.

Bipolar electrical stimulation was performed by connecting two nail electrodes with a local battery-powered opamp, operating in unity-gain feedback mode. The culture medium was not connected to a reference electrode; thus, charge displacements in the culture medium due to the stimulation pulses only occurred between the electrodes. Pulses were generated with the Clampex software using episodic stimulation of biphasic pulse trains with a pulse width of 1 ms, and amplitudes ranging from 100 mV to 2 V, with increasing amplitudes. The signals are generated by an acquisition system (Digidata 1440 from Axon Instruments) (Figure 2).

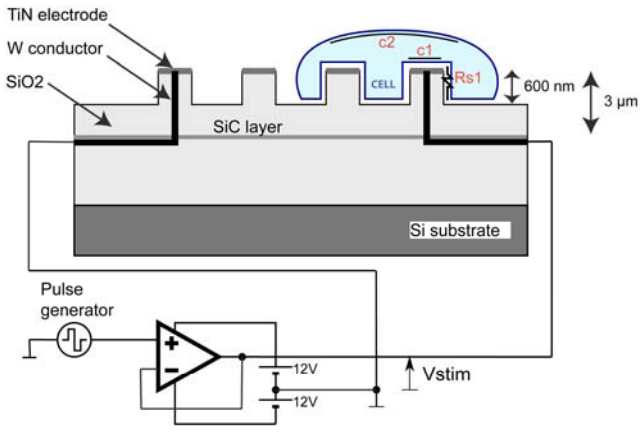


Fig. 2. Electrical stimulation set-up. The membrane capacitance c1 is the membrane situated above the nail electrode and c2 is the capacitance of the upper part of the membrane. Rs1 is the seal resistance.

B. Cell culturing

Hearts of 16-day old Wistar rat embryos were removed under sterile conditions and placed in Ca^{2+}- and Mg^{2+}-free HBSS solution as described previously [5]. After removing excess blood, the heart was chopped in small fragments of 1 mm^2 pieces and collected in a Falcon tube. Trypsin-EDTA (0.05%) was then added to the tube. After 8 minutes of incubation at 37°C, the supernatant was discarded. Enzymatic dissociation was done by the addition of DNAse Type II solution (10,000 units/ml) that was incubated for 3 minutes at 22°C. Next, 2.5 ml of trypsin-EDTA was added and incubated for 8 minutes at 37°C. The supernatant was collected and added to Ham's F10 medium containing 0.5% insulin, transferrin and selenite solution (ITS) and 33% fetal calf serum and kept on ice. The collected cells were then centrifuged for 10 minutes at 4°C and 200 g and resuspended in Ham's F10 medium containing 0.5% ITS and 5% FCS. For the remaining tissue, this trypsinization step was repeated at least 5 times. The collected cell suspensions were then seeded on 30 mm culture dishes and incubated for 70 minutes at 37°C and 5% CO_2 for differential adhesion. After this plating step, the cells were collected and centrifuged for 10 minutes at 22°C and 200 g. The pellet was then resuspended in cell medium. The cells were plated on uncoated devices at cell densities of 40,000 cells/ml.

C. Calcium Imaging

Fluo-4 AM was dissolved in DMSO containing 20% (w/v) Pluronic to obtain a final concentration of 5 µM Fluo-4. The cells were first transferred to Ca^{2+}-free KREBS solution (135 mM NaCl; 5.9 mM KCl; 2 mM EGTA; 1.2 mM $MgCl_2 \cdot 6H_2O$; 11.6 mM HEPES; 11.5 mM glucose; pH 7.3), and incubated with the Fluo-4 and PI solution for 30 minutes at 37°C. Afterwards, the cells were rinsed with a 1.5 mM Ca^{2+} KREBS solution (135 mM NaCl; 5.9 mM KCl; 1.5 mM $CaCl_2$; 1.2 mM $MgCl_2 \cdot 6H_2O$; 11.6 mM HEPES; 11.5 mM glucose; pH 7.3). Cells were then excited at 488 nm (Fluo-4) using a LED-based Zeiss Examiner Imaging system in the upright configuration. Data were processed using the Zeiss Examiner software.

D. Immunohistochemical stainings and scanning electron microscopy

Cells were fixated using 4% paraformaldehyde solution and permeabilized in PBS containing 0.5% TX-100 for 5 min. After washing (3 times in PBS), cells were blocked overnight at 4°C followed by a 1.5 h incubation at 23°C in the same blocking solution containing the first antibody. After washing, immunoreactivity was revealed by incubation (1 h, 23°C) with Alexa488 conjugated secondary antibodies (Invitrogen). To label actin filaments, Alexa488 conjugated phalloidin was included in the incubation mix; nail electrodes were stained with Alexa555-labeled laminin,

coated prior to cell seeding. Cells were then washed 3 times with PBS and rinsed 3 times with water. The substrates were examined using an Axioskop FS2 Mot (Zeiss) equipped with a Pascal LSM5 confocal scanning unit. For SEM imaging, the cells were post-fixated for 2 h using 2% OsO_4 (Sigma) and washed with PBS. Next, the water is substituted by ethanol using replacement series. The samples were incubated twice for 10 to 15 min in 30%, 50%, 70%, 90% and 100% ethanol and were subjected to critical point drying. Test substrates with uniform nail electrode arrays were used for morphological characterization.

III. RESULTS AND DISCUSSION

A. Morphological characterization of cultured cardiomyocytes on nail electrode arrays

Embryonic cardiomyocytes were seeded on test nail electrode arrays to determine their morphological behavior on three-dimensional structures of various sizes. Figure 3 shows staining of the actin filaments of cultured cardiomyocytes (green) on nail electrodes of (red) after 5 days in culture (DIV).

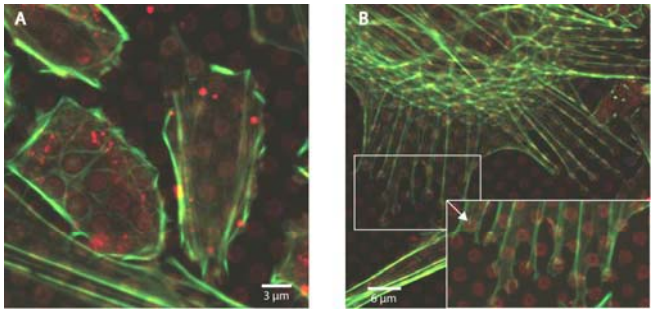


Fig. 3. A. Immunohistochemical staining of actin filaments (green) in cultured embryonic cardiomyocytes (5 DIV) and fluorescently-labeled laminin on nail electrodes (red). B. Membrane protrusions, indicated by actin filament staining, extend out to the nail structures.

From these images, it is clear that the cell membrane engulfs the nail-shaped electrodes (Figure 3A), as actin filaments are seen enveloping the electrodes. This behavior of the actin filaments was even observed with a configuration in which the interelectrode distance was rather small (3 µm). Moreover, the shape of the total cell was determined by the underlying structure of the three-dimensional electrodes.

Long protrusions of the cell membrane specifically reach out for nail electrodes as indicated by the actin filament staining in Figure 3B. This process has been described previously as contact guidance [6] and is deemed beneficial because strong coupling between the cell membrane and the electrode is a desired result. Contact guided outgrowth of the cell was also seen after SEM imaging of the chips after fixation and critical point drying of cultured cardiomyocytes on test structures (Figure 4).

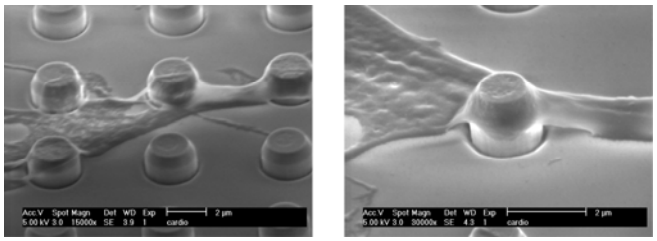


Fig. 4. Scanning electron microscopy images of cultured embryonic cardiomyocytes on nail electrodes (5 DIV).

B. Electrical stimulation of single myocytes on a passive nail electrode array

In order to follow changes in intracellular [Ca^{2+}] after electrical stimulation of the cultured myocytes, cells were loaded with the Ca^{2+}-sensitive fluorophore Fluo-4. Electrical stimulation was performed by applying biphasic voltage pulses between two nail electrodes, one of which was situated underneath the cell. Figure 5 shows the response of the relative intracellular [Ca^{2+}] ($\Delta F/F_0$) upon increasing voltage pulses applied through the nail electrodes. At amplitudes of 1.2 V, a strong increase in the intracellular [Ca^{2+}] was seen. The decrease of the Ca^{2+} signal was slow and incomplete, suggesting that local perforation of the membrane was achieved. However, the opening of voltage-gated Ca^{2+} channels could not be excluded from these experiments. Figure 5 also indicates that the stimulation was very localized, as neighboring cells did not react to the electrical stimulus (regions 4-7). This demonstrates the limited range the electrical field creates at the tip of the stimulating small nail electrode. This localized effect can be explained by the large sealing resistance Rs1 between the membrane and the electrode and the capacitive divider c2/c1 + c2, which determines that 99% of the voltage existed across the small part of the membrane above the nail electrode (Figure 2). More experiments are underway to clarify the exact nature of the electrical field and to characterize the electrical coupling between the cell and the electrode.

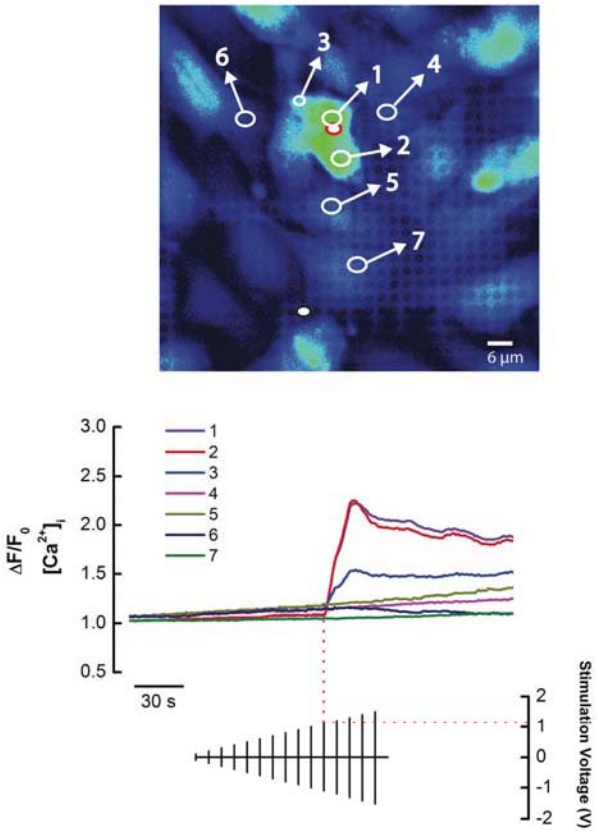


Fig. 5. Electrical stimulation of single cardiomyocytes by voltage stimulation and the changes in intracellular $[Ca^{2+}]_i$. Regions 1-3 were taken in the cell on top of the electrode (white cirle with red outline). Other regions (4-7) were taken in neighbouring cells. The white circle with black outline represents the second electrode.

IV. CONCLUSIONS

We have fabricated a passive electrode array consisting of 84 three-dimensional nail-shaped electrodes using standard CMOS-compatible processing. Staining of actin filaments in embryonic cardiomyocytes suggested strong engulfment of the electrodes by the cell membrane and contact guided behavior on the surface of the nail beds. Electrical stimulation using biphasic voltage pulses showed the possibility of localized Ca^{2+} influxthrough pores created in the membrane.

ACKNOWLEDGMENT

This work was funded by the European Seventh Framework Programme project 'Brain Storm' (215486).

REFERENCES

1. Stett A, Egert U, Guenther E et al. (2003) Biological application of microelectrode arrays in drug discovery and basic research. Anal. Bioanal. Chem. 377 (3): 486-495
2. Lin YC, Li M, Wu C C, (2004) Simulation and experimental demonstration of the electric field assisted electroporation microchip for in vitro gene delivery enhancement. Lab Chip 4 (2): 104-108
3. Jain T, Muthuswamy J (2008) Microelectrode array (MEA) platform for targeted neuronal transfection and recording. IEEE Trans. Biomed. Eng. 55 (2): 827-832
4. Huys R, Braeken D, Van Meerbergen B et al. (2008) Novel concepts for improved communication between nerve cells and silicon electronic devices. Solid-State Elect. 52(4): 533-539
5. Krause M, Ingebrandt S, Richter D et al. (2000) Extended gate electrode arrays for extracellular signal recordings Sens. Actuat. B Chem. 70 (1-3): 101-107
6. Weiss P, Garber B (1952) Shape and Movement of Mesenchyme Cells as Functions of the Physical Structure of the Medium: Contributions to a Quantitative Morphology. Proc Natl Acad Sci USA 38 (3): 264-280

On-Surface Amplification of L-Glutamate Using a Patterned Bi-enzymatic System

D.R. Rand[1,2], D. Braeken[1], Y. Mulla[1], G. Borghs[1,2], and C. Bartic[1,2]

[1] IMEC v.z.w., Kapeldreef 75, 3001 Leuven, Belgium
[2] Katholieke Universiteit Leuven, Department of Physics and Astronomy, Celestijnenlaan 200D, 3001 Leuven, Belgium

Abstract— **We present a method for the amplification of L-glutamate directly on a surface. Our strategy is based on the surface patterning of a bi-enzymatic system consisting of glutamate oxidase (GLOD) and glutamic-pyruvate transaminase (GPT). This bi-enzymatic system amplifies L-glutamate via a recycling process. The surface chemistry on Ta_2O_5 was optimized for maximal enzyme loading. Enzyme activity was determined using a colormetric assay for the presence of GLOD. Co-immobilization of GLOD and GPT results in at least a doubling of the signal. Furthermore, increasing the surface concentrations of each enzyme leads to amplification levels that approach those obtained in solution. These enzymes can be patterned on substrates using a flip chip bonder for aligned microcontact printing. This bi-enzymatic system can be applied to biosensor surfaces for the *in vitro* detection of L-glutamate.**

Keywords— **Glutamate oxidase, glutamic-pyruvate transaminase, quartz crystal microbalance, microcontact printing.**

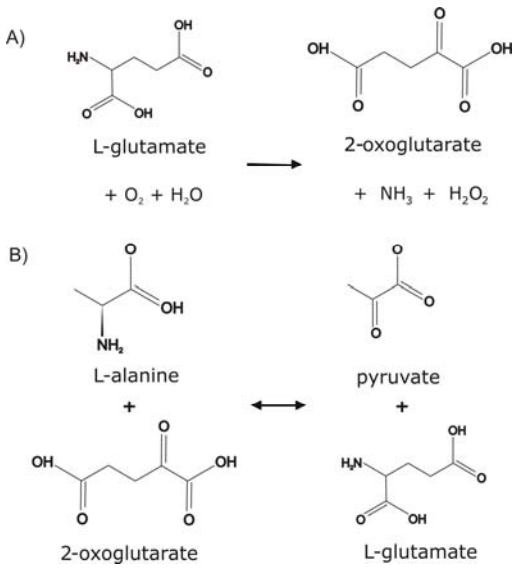


Fig. 1 Schematic of the reaction mediated by A) glutamate oxidase and B) glutamic-pyruvate transaminase.

I. Introduction

Microelectronic biosensor technology detects the presence of specific molecules by triggering a change in the electronic properties of a solid-state device [1]. Frequently, biosensors implement enzymes as recognition elements because their product can be readily and accurately measured, they demonstrate extreme selectivity for a substrate, and are commercially available. Neurotransmitter detection is important when investigating neurological disorders, such as Alzheimer's disease, that require monitoring neuronal activity at the synaptic level. L-glutamate is a key neurotransmitter involved in learning and memory processes [2]. Although several enzymes catalyze L-glutamate [3, 4, 5], glutamate oxidase (GLOD) is favorable because its activity does not rely on co-factors and only requires oxygen and water (Fig. 1A). Moreover, coupling GLOD with a second enzyme, glutamic-pyruvate transaminase (GPT), regenerates L-glutamate [6] (Fig. 1B) and allows for the amplification of a detectable moiety (NH_3, H_2O_2). Ultimately exploiting this dual enzyme system on a sensor surface can increase signal levels from the small amount of secreted L-glutamate from cultured neurons (*in vivo* L-glutamate concentrations in brain extracellular fluid are estimated at 0.5-2μM [7, 8, 9]). Because enzymatic reactions should occur as close as possible to the active area of the biosensor transducer, an important consideration is the enzyme surface immobilization. Self-assembled monolayers (SAMs) can provide the necessary functional groups and order for binding enzymes [10]. Furthermore, because the ultimate goal is *in vitro* L-glutamate detection, the surface must also permit cell attachment and proliferation. A polymer that is frequently used in cell culturing is poly-L-lysine (PLL), which improves cell adhesion to solid substrates due to its positive surface charge [11].

Several multiple enzyme systems for the detection of neurotransmitters have previously been used [12, 13, 14]. However, many of these systems rely on multilayers, which may hinder neurotransmitter diffusion to the electrode surface, or co-deposition with a polymer from solution, which may lead to uncontrolled enzyme distribution. Alternatively, microcontact printing is an effective method for depositing molecules on surfaces, such as the patterning of PLL for neuronal guiding [15] and various proteins and enzymes [16].

O. Dössel and W.C. Schlegel (Eds.): WC 2009, IFMBE Proceedings 25/VIII, pp. 216–219, 2009.
www.springerlink.com

In this paper, we show that a bi-enzymatic system can be spatially patterned onto surfaces using microcontact printing. Tantalum pentoxide, chosen for its sensitivity to H^+ ions, served as the substrate to which the bi-enzymatic system was anchored. The surface chemistry was optimized for maximal enzyme loading. Enzyme patterning was achieved using stamps made from a UV-sensitive siloxane polymer prepared on rigid SiO_2 substrates together with an aligned microcontact printing method that uses a flip chip bonder. This bi-enzymatic system was shown to amplify L-glutamate at least two-fold. This strategy can eventually be applied to biosensor surfaces for the *in vitro* detection of L-glutamate, and can easily be extended to include different neurotransmitters by choosing an enzyme system that catalyzes the neurotransmitter of choice.

II. Materials and Methods

A. Surface chemistry

Tantalum pentoxide surfaces (100 nm on SiO_2) were cleaned using a solution of sulfuric acid and hydrogen peroxide (3:1, v/v) for 15 min followed by a UV/ozone treatment for 15 min. Samples were then immersed in an aqueous alcohol silane solution containing 2% 11-(triethoxysilyl)undecanal (TESU, 95%, ABCR) for 5 min. After rinsing with ethanol, the samples were baked on a hotplate at 110°C for 30 minutes. Poly-L-lysine (PLL, 70 kDa, Sigma) was either adsorbed onto clean Ta_2O_5 substrates directly or was covalently bound to the TESU self-assembled monolayer (SAM) by immersion of the substrates in a 1:1 (v/v) solution of PLL (4 mg/mL in 10 mM borate buffer, pH 8) and cyanoborohydride (CNBH, coupling buffer, Sigma) for 30 min, followed by rinsing with borate buffer. Some PLL surfaces were then subjected to a glutaraldehyde (GA, solution, 25% in water, 2.6 M, Sigma) treatment, which involved submersion of substrates in a 1:1 (v/v) solution of GA (5% in water) and CNBH for 30 min, followed by rinsing with water. Glutamate oxidase (GLOD, from *Streptomyces* sp., Yamasa Corporation) and glutamic-pyruvate transaminase (GPT, from porcine heart, 108 U/mg protein, Sigma) were coupled to these TESU, PLL, or GA surfaces.

B. Glutamate oxidase assay

The activity of immobilized GLOD was determined using the Amplex Red glutamic acid/glutamate oxidase assay kit (Invitrogen). The reaction solution contained 100 µM Amplex Red reagent (10-acetyl-3,7-dihydroxyphenoxazine), 0.25 U/mL horseradish peroxidase, 0.5 U/mL GPT, 40 µM L-glutamic acid, and 200 µM L-alanine. For each assay, 150 µL of the reaction solution was applied to 1 cm^2 substrate samples. After incubation for 30 minutes at 37°C in a dark environment, 100 µL of the solution was collected from the sample and transferred to a micro-titer plate (Nunc). Absorbances were measured with a spectrophotometer (Biotech) at a wavelength of 571 nm.

C. Microcontact printing

Stamps for use in the flip chip bonder were made by UV-sensitive polydimethylsiloxane (PDMS, WL-5351, Dow Corning) spin coated onto a Si wafer substrate. A Carl Suss flip chip bonder (Suss Microtec) was used for aligned microcontact printing. Stamps were cleaned with ethanol, dried with N_2, and inked with a GLOD solution (in PBS, 150 mM, pH 7.4) for 1 min. The enzyme solution was removed and the stamp was dried with N_2. Inked PDMS stamps were placed on the upper arm of the flip chip bonder and a PLL-coated Ta_2O_5 substrate was placed on the lower chuck. After alignment was accomplished visually, the stamping program was initiated (600 s, 25°C, 5 kg). This process of inking, aligning, and stamping was then repeated for GPT on the same substrate. When not in use, all PDMS stamps were stored in water.

III. Results and Discussion

A. Surface chemistry

The surface chemistry on Ta_2O_5 substrates was evaluated by quartz crystal microbalance (QCM). The resonance frequency of the Ta_2O_5-coated crystal depends on its total oscillating mass and a decrease in that frequency translates to additional mass. The Sauerbrey equation can be applied assuming the mass added onto the crystal is a thin and rigid layer [17]:

$$\Delta m = \frac{C \cdot \Delta f}{n} \quad (1)$$

where Δm is the change in mass, C = 17.7 ng Hz^{-1} cm^{-2} for a 5 MHz quartz crystal, Δf is the change in frequency, and n = 1, 3, 5, 7 is the overtone number (for all results, n=3).

Figure 2 shows the binding capacity of PLL onto clean or TESU-treated Ta_2O_5. The results indicate that more PLL binds to TESU than adsorbs onto bare Ta_2O_5. This is due to the amino groups on PLL covalently binding to the aldehyde groups of TESU. However, this result is also crucial because PLL is necessary for the eventual *in vitro* cell culturing of these substrates. Thus, maximal PLL loading and neuron viability can be attained in this one surface chemistry step. Figure 2 also shows the binding capacity of GLOD and GPT to TESU. As expected, GPT has a higher

loading capacity to TESU than GLOD due to the more numerous amino groups on GPT. However, once GA is introduced onto the surface, the binding capacity of GLOD approaches that of GPT. Finally, the QCM results indicate that GPT can also bind to a GLOD surface, which demonstrates the importance for precise enzyme placement through patterning.

B. Aligned microcontact printing of the bi-enzymatic system

Stamps for microcontact printing were made by spin coating UV-sensitive PDMS onto a Si wafer. In this way, the thin and rigid stamps would not interfere with focusing on the flip chip bonder. The stamp processing was optimized for relief feature isolation as well as maximal enzyme transfer. Figure 3 shows scanning electron micrographs of the stamps. The relief features have excellent uniformity and resolution. Their height of ~10 μm proved sufficient for stamping as substrates showed no evidence of enzyme except where the relief features of the stamp made contact with the substrate. Furthermore, Fig. 3 shows that the relief feature surfaces are flat, which is necessary for even inking and transfer of the enzyme solution.

Figure 4 shows examples of aligned microcontact printing done using a flip chip bonder. Stamps coated with an enzyme solution were aligned to PLL-coated substrates. Glutamic-pyruvate transaminase (red) was aligned and printed, followed by GLOD (green) in a shift of either 30μm (Fig. 4A) or 25 μm (Fig. 4B). In order to visualize the pattern, GPT and GLOD were fluorescently labeled. As can be seen, the precise alignment of each enzyme can be achieved. Furthermore, the entire surface of the relief features successfully transferred the enzymes. Because the

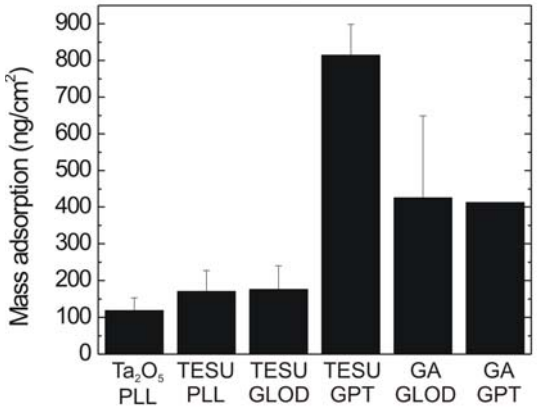
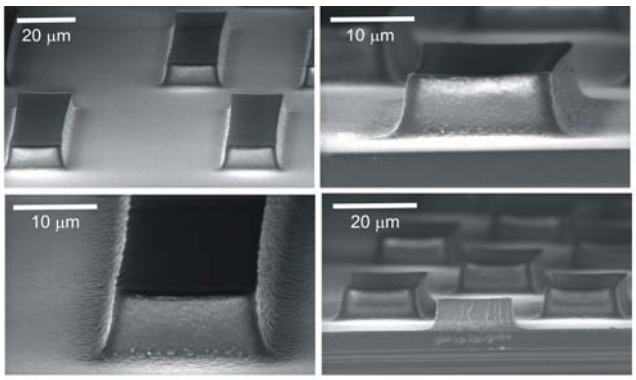


Fig. 2 Quartz crystal microbalance results of the surface chemistry on Ta_2O_5-coated crystals.



F*ig. 3 Scanning electron micrographs of patterned poly(dimethylsiloxane) stamps.*

substrate was first coated with PLL, a necessary step that provides a surface suitable for both enzyme adsorption and cell attachment, the surface contains three distinct compositions: PLL, GLOD, and GPT.

C. Amplification of L-glutamate by an immobilized bi-enzymatic system

Glutamate oxidase and GPT were co-immobilized on the same substrate in order to investigate L-glutamate amplification. Glutamate oxidase (1 mg/mL) and GPT (1 or 2 mg/mL) were stamped onto separate 1x1 cm^2 PLL-coated substrates and placed next to each other. The results, shown in Fig. 5A, indicate that not only does amplification increase with immobilized GPT concentration, but that amplification levels are able to reach those attainable when GPT is in solution. Lower levels of amplification seen with immobilized enzymes could be explained by the fact that immobilization may lead to a decrease in enzyme activity, or that the amount of enzyme transferred to the surface is distinctly less than the enzyme inking concentration. The results of the GLOD assay performed on microcontact

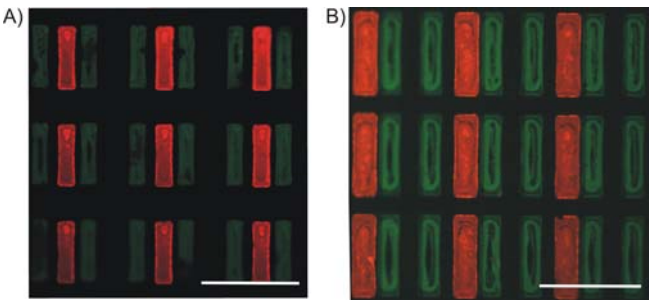


Fig. 4 Aligned microcontact printing. The substrate was coated with poly-L-lysine (black, background), followed by the successive printing of glutamate oxidase (green) and glutamic-pyruvate transaminase (red). Scale bars are 100 μm.

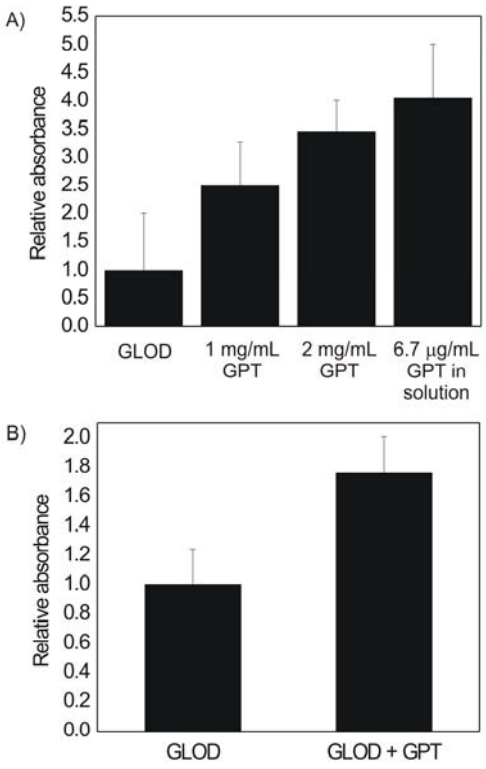


Fig. 5 Amplification of L-glutamate when glutamate oxidase (GLOD, 1 mg/mL) and glutamic-pyruvate transaminase (GPT, 1 or 2 mg/mL) are stamped on A) separate substrates B) the same substrate. Error bars are coefficients of variation.

printed substrates like those shown in Fig. 4 indicate there is approximately a doubling of the signal when both GLOD and GPT are on the surface compared with the signal obtained from just GLOD (Fig. 5B).

IV. Conclusions

The immobilization of a bi-enzymatic system consisting of GLOD and GPT to Ta_2O_5 substrates was characterized and optimized for enzyme loading. Quartz crystal microbalance results indicate that while GPT has a higher binding capacity than GLOD on TESU. Furthermore, the underlying SAM proves essential for maximal PLL loading. Lastly, because GPT is able to bind to GLOD surfaces, it is important to be able to control precisely their position on the substrate.

Patterned enzyme surfaces were subject to a GLOD assay in order to assess L-glutamate amplification. Poly-L-lysine-coated substrates were microcontact printed using the flip chip bonder. The dual enzyme surfaces show approximately a doubling of the signal with respect to those substrates stamped with only GLOD. The results indicate that these patterned surfaces could prove advantageous for the *in vitro* detection and amplification of L-glutamate on biosensor surfaces.

Acknowledgment

We thank the IWT Artificial Synapse (ASAP) project (SBO 050151) for funding.

References

1. Willner I, Katz E, Willner B (1997) Electroanal 9:965-977
2. Manahan-Vaughan D, Ngomba RT, Storto M, et al. (2003) Neuropharmacology 44:17-25
3. Petach, HH, Driscoll J (1994) Biotechnol Bioeng 44:1018-1022
4. Nikolelis DP (1987) Analyst 112:763-765
5. Dremel BAA, Schmid RD, Wolfbeis OS (1991) Anal Chim Acta 248:351-359
6. Valero E, Garcia-Carmona F (1998) Anal Biochem 259:265-271
7. Parrot S, Sauvinet V, Riban V, et al. (2004) J Neurosci Meth 140:29-38
8. Zhang S, Takeda Y, Hagioka S, et al. (2005) Brain Res Brain Res Protoc 14:61-66
9. Benveniste H, Drejer J, Schousboe A, et al. (1984) J Neurochem 43:1369-1374
10. Willner I, Riklin A, Shoham B, et al. (1993) Adv Mater 5:912-915
11. Richert L, Lavalle Ph, Vautier D, et al. (2002) Biomacromolecules 3:1170-1178
12. Garguilo MG, Michael AC (1993) J Am Chem Soc 115:12218-12219
13. Hu Y, Mitchell KM, Albahadily FN, et al. (1994) Brain Res 659:117-125
14. Upadhyay S, Ohgami N, Kusakabe H, et al. (2006) Sensor Actuator B 119:570-576
15. James CD, Davis R, Meyer M, et al. (2000) IEEE T Bio-med Eng 47:17-21
16. Bernard A, Delamarche E, Schmid H, et al. (1998) Langmuir 14:2225-2229
17. Sauerbrey G (1959) Z Phys 155: 206-222

The role of microrheological red blood cell properties in efficiency of drug transport and their delivery to cellular targets

A.V. Muravyov, S.V. Cheporov, F.A. Chuchkanov, A.A. Muravyov
State pedagogical university, Yaroslavl, Russia, alexei.47@mail.ru

Abstract. The purpose of this study was to estimate effect of drugs on red blood cell (RBC) microrheological properties. Despite of simplification, mature erythrocytes retain a number of molecular components of signaling pathways and so drugs can affect on cellular function including their flow deformation and O_2-transport capacity. It was found that hormones: epinephrine (10^{-6} M) and insulin (70 pM) changed red blood cell deformability (RBCD) and aggregation (RBCA). It was shown that RBCD and RDCA were variable under adenylyl cyclase (AC) activation by forskolin or dibutyryl cAMP (dB-cAMP; 10^{-4} M), therefore one of the cellular molecular target for RBC microrheological change can be AC. It was found that all four phosphodiesterase (PDE) inhibitors: IBMX, vinpocetine, rolipram, pentoxifylline decreased RBCA significantly (by 30-50%, $p<0.01$) and quite the contrary they increased RBCD (by 15-24%, $p<0.05$). Therefore PDEs might be considered as red blood cell molecular targets for some drugs. We have obtained data showing that Ca^{2+} blocker verapamil and calcium chelator EGTA decreased RBCA and increased RBCD significantly ($p<0.05$). Calcium ionophore (A23187), on the contrary, increased aggregation and red cell rigidity. Therefore Ca^{2+} channels of the red cell membrane can be also considered as molecular targets red cell microrheology modification. Of these, particular interest presents erythrocyte protein tyrosine kinases and phosphatases, because of their possible roles in the modulation of erythrocyte morphology, deformability and metabolic functions. We inhibited red cell tyrosine phosphatase activity by N-vanadat (10^{-4} M) and obtained an increase of RBCD. The similar effects on the RBCD were obtained under red cell incubation with Epoetin-beta and cisplatin that can stimulate tyrosine kinase activity. The obtained data reveals evidence that some elements of erythrocyte signaling pathways can be the molecular targets for microrheological active drugs.

1. Introduction

Blood flow in microcirculation, tissue perfusion and oxygenation depend on red blood cell (RBC) microrheological properties; namely deformability and aggregation [1, 2]. Drugs and signaling molecules can affect microrheological properties of blood cells including their aggregation and deformation [3, 4]. It is known that at the capillary level the blood flow efficiency depends on red cell microrheological properties [5], and the change of these mechanical properties can influence not only upon the tissue oxygenation [6] but also the drug delivery into tissue microregion, namely to target cells. According to the red cell microrheological changes after drug treatment it is possible to suppose three variations of drug effect on red cell fluidity: 1) Drug doesn't exert influence significantly upon the red cell aggregation and deformation and their transport capacity doesn't change – it is *neutral effect*; 2) Drug decreases red cell fluidity and increases red cell aggregation – it is *negative* effect; and 3) drug increases red cell fluidity and decreases red cell aggregation (RBCA) – it is *positive* drug effect. One of the known rheologically "positive" drugs is pentoxifylline [1, 3]. The main mechanism of pentoxifylline blood rheological efficiency is connected with its phosphodiesterase (PDE) inhibitory activity [7]. The other drug, having phosphodiesterase as intracellular targets, can be microrheologically active both in vitro and in vivo.
The aim of this study was to investigate hemorheological effect of drugs and regulatory pathways that was associated with their action.

2. Materials and Methods

2.1. Preparation of blood samples

Venous blood samples were obtained from healthy adults (men, n=28; age range 19-25 years) via withdrawal into sterile vacuum tubes containing heparin (1.5 mg/ml blood). Red blood cells were separated from the blood by centrifugation at 1,400 g for 15 min and washed 3 times with 10 mM phosphate buffered saline (PBS) (pH=7.4). The washed RBCs were then resuspended in PBS at a hematocrit of approximately 40%.

2.2. Protocols for in vitro studies

In each of the research sessions RBC suspensions were divided into some aliquots and exposed to: 1) Epinephrine (1.0 μM); Insulin (70 pM); 2) dibutyril cAMP – permeable cAMP analog (100 μM); Forskolin – cell adenylyl cyclase activator (10 μM); 3) Vinpocetine – inhibitor of PDE1, 10 μM; Rolipram – inhibitor of PDE4, 10 μM; Isobutyl-methyl-xanthine (IBMX) – nonselective PDE inhibitor, 100 μM; Pentoxifylline – nonselective PDE inhibitor, 10 μM; 4) cell tyrosine phosphatase activity inhibitor - N-vanadat (100 μM); recombinant human erythropoetin (Epoetin-beta, 10 I.E./ ml); cellular protein kinase activator – Phorbol 12-myristate 13-acetate (PMA, 10 μM); cisplatin as an activator of cell tyrosine kinase, 0.10 μM; 5) Verapamil, 10 μM; EGTA, 1.0 mM; calcium ionophore A23187, 10 μM at 37°C for 15 min. The remaining aliquot (red cell suspension with PBS) was kept at 37°C for 15 min and served as the control. Following treatment or control periods, the red blood cells were resuspended in autologous plasma at a hematocrit of 0.5% or 40% and then used for aggregation and deformability measurements. All drugs and chemical compounds were purchased from Sigma.

2.3. Red blood cell microrheology measurement

Red blood cell aggregation (RBCA) in native plasma was assessed by of the Myrenne Aggregometer which provides an index of RBC aggregation facilitated by low shear. In brief, the

O. Dössel and W.C. Schlegel (Eds.): WC 2009, IFMBE Proceedings 25/VIII, pp. 220–222, 2009.
www.springerlink.com

suspension was subjected to a short period of high shear to disrupt pre-existing aggregates, following which the shear was abruptly reduced to 3 s^{-1} and light transmission through the suspension that was integrated for ten seconds; the resulting index, termed «M1» by the manufacturer and «ARBC» herein, increased with enhanced RBC aggregation. To work out in detail the red cell aggregation process was used a direct microscopic methods with computer image analysis.

To estimate deformability RBCs were placed into flow microchamber. Cells were attached to bottom part of chamber with "one point" and then were deformed by shear flow, under constant shear stress (τ). According to the parallel plate flow chamber, then relationship of shear stress τ, flux Q and chamber's sizes is [8]: $\tau = 6\eta Q/wh^2$,

where **η** is the viscosity of the perfusate, and **w** is the width and **h** is the height of the flow passageway. In our experiments, η = 1,07 mPa.s, w = 0.90 cm, h = 0.01 cm.

2.4. Miscellaneous techniques

Plasma protein concentrations were measured by the Biuret method, whole blood and red cell suspension hematocrites were determinated via the microhematocrit methods (i.e., 12,000 x g for 7 minutes).

2.5. Statistics and data presentation

Results are presented as mean SEM. Differences between the mean values were evaluated using an ANOVA test. Values of $p<0.05$ indicate statistical significance and are not adjusted via the Bonferroni method.

3. Results

3.1. Effect of epinephrine and insulin on red blood cell deformability and aggregation

Initially, the experiments were designed to evaluate the microrheological effect of adrenergic receptor agonists as an extracellular part of molecular signaling pathway. RBC incubation with epinephrine resulted in significant rise aggregation by 50% ($p<0.01$) (fig.1). While insulin decreased red cell aggregation markedly (fig. 1).

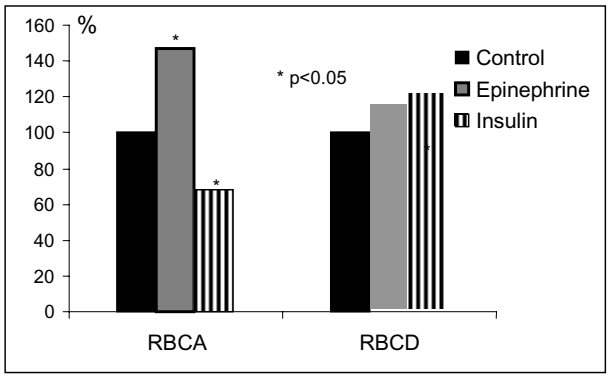


Fig. 1. Red blood cell deformability and aggregation changes under incubation with (vs control): Epinephrine 10^{-6} M and Insulin (70 pM)

3.2. Effect of adenylyl cyclase stimulation on red blood cell deformability and aggregation

The diterpene forskolin has been reported to activate *adenylyl* cyclase (AC) in a manner consistent with an interaction at the catalytic unit [9]. In addition AC stimulation and cAMP level rise in red cells can be achieved using stable analog of cAMP (dB-cAMP) or prostaglandin E_1 (PGE_1) [10]. RBCs incubation with forskolin facilitated an increase of RBC deformability (by 17%: I.E. from 0.194±0.006 to 0.227±0.008; $p<0.05$) and some more significant deformability rise after RBC incubation with dB-AMP was found (by 27% (from 0.194±0.006 to 0.246±0.007; $p<0.01$). PGE1 also stimulated RBCD by 22% (fig. 4).

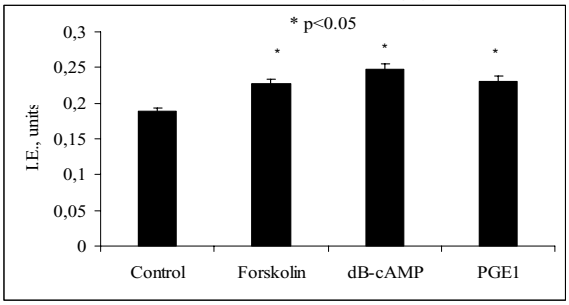


Fig. 2. Red blood cell deformability change (vs. control) under incubation with: forskolin (10 μM), dB-cAMP (100 μM); prostaglandin E1 (PGE_1, 10^{-10} M)

Red cell aggregation was significantly decreased at these conditions. The aggregation reduction (vs. control) made up from 29% (forskolin) to 36% (PGE1, $p<0.01$).

3.3. Effect of phosphodiesterase (PDE) activity inhibition on red blood cell deformability and aggregation

All drugs having PDE activity increased red cell deformability in the similar value (fig. 6). Some more changes of deformability was found after RBC incubation with pentoxifylline – 25% ($p<0.05$) and IBMX incubation was accompanied by 15% rise of RBC deformability only (fig. 3).

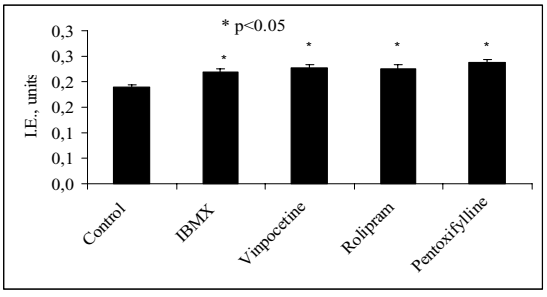


Fig. 3. Red blood cell deformability change (vs. control) under incubation with: IBMX (100 μM), vinpocetine (10 μM); rolipram (10μM), pentoxifylline (10μM)

Above mention drugs with PDE inhibitory activity reduced red cell aggregation in vitro. The most significant effect was found under cell incubation with pentoxifylline and inhibitor PDE_1 – vinpocetine. Taken as a whole RBCA reduction averaged 34 and 38% ($p<0,05$) under these conditions.

3.4. Role Ca2+ in red cell microrheological property changes

Ca^{2+} entry blocking into the red cells by verapamil or its chelating in medium by EGTA led to significant RBCA decrease and deformability rise (fig. 4). It has been found that the rise of Ca^{2+} influx, stimulated by A23187 [28] was accompanied by an increase of RBCA, whereas red cell deformability was changed insignificantly (fig. 8).

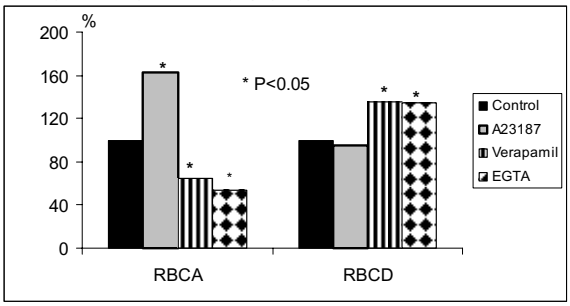


Fig. 4. Red blood cell deformability (RBCD) and aggregation (RBCA) changes (vs. control) under incubation with: A23187 (10 μM), verapamil (10 μM) and EGTA (1.0 mM)

3.1. Protein kinase as target for drug modification of red cell deformability

We inhibited red cell tyrosine phosphatase activity by N-vanadat (fig. 7). The latter is expected to lead to activate tyrosine kinases, a dissociation of ternary complex (band 3 - band 4.1R - spectrin and an increase of red cell membrane plasticity [11]. The similar effects on the RBCD were obtained under red cell incubation with Epoetin and phorbol 12-myristate 13-acetate (PMA; fig. 7). PMA is an activator of cellular protein kinase, mainly PKC and after red cell incubation with this compound (10 μM) was found a little rise of cell deformability, while tyrosine kinase activation by N-vanadat, Epo and cisplatin was accompanied by a significant increase of this RBC rheological property (by 17 and 21%, p<0.05).

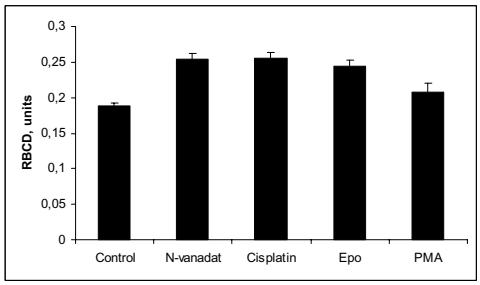


Fig. 7. The changes of RBCD under cell incubation with N-vanadat, cisplatin, Eportin-beta (Epo) and phorbol 12-myristate 13-acetate (PMA)

The obtained data reveals evidence that some elements of erythrocyte signaling pathways can be the molecular targets for microrheological active drugs.

[1] G. Pindur, A. Sander, U.T. Seyfert, J. Fung. The effect of pentoxifylline on the deformability of erythrocytes in erythrocyte concentrates in additive solution *Anasthesiol Intensivmed Notfallmed Schmerzther.* 36 (2001), Suppl 1, S59-61.

[2] J.J. Bishop, S. A. Popel, M. Intaglietta, and P.C. Johnson. Effect of aggregation and shear rate on the dispersion of red blood cells flowing in venules *Am J Physiol Heart Circ Physiol*.- 2002.- Vol.283.- H1985-H1996.

[3] E. Ernst. Pentoxifylline for intermittent claudication: a critical review Angiology 1994, 45, 339-345.

[4] Hines P., Zen Q., Burney S., Shea D., Ataga K., Orringer E et. al. Novel epinephrine and cyclic AMP-mediated activation of BCAM/Lu-dependent sickle (SS) RBC adhesion // *Blood,* 2003.- V.101.- N8.- P.3281-328.

[5] A.R. Priers, T.W. Secomb. Rheology of the microcirculation. Clinical Hemorheology and Microcirculation 29 (2003), N3-4, P. 143-148.

[6] F. Jung, W.Erdlenbruch, Koscielny, H. Kiesewetter. Influence of hyper-/isovolaemic haemodilution with hydroxyethyl starch on blood fluidity, blood flow and tissue oxygen tension in patients with POAD stage II *Clin. Hemorheol*. 15 (1995) N3, P. 415.

[7] Endres S., Semmler J., Eisenbut T., Sinba B. The role of cyclic adenosine 3',5'-monophosphate in suppression of tumor necrosis factor-α synthesis: effect of pentoxifylline. *Leukocytes and Endothelial Interactions*. Prous Science. Barselona, 1995, P. 59-69.

[8.]G.M. Artmann, Microscopic photometric quantification of stiffness and relaxation time of red blood cells in a flow chamber, *Biorheology* 32 (1995), N5, 553-570.

[9] S.A. Morris, J.P. Bilezikian, Evidence that forskolin activates turkey erythrocyte adenylate cyclase through a noncatalytic site, *Arch Biochem Biophys*. 220 (1983), N2, 628-636.

[10] K. Oonishi, N. Sakashita, N. Uysaka, Regulation of red blood cell filtrability by Ca2+ influx and cAMP-mediated signaling pathways, *Am. J. Physiol*. 273 (1997), (Cell. Physiol. 42), C1828-C1834

[11] S. Manno, Y. Takakuwa, N. Mohandas, Modulation of erythrocyte membrane mechanical function by protein 4.1 phosphorylation, *J Biol Chem.* 280 (2005), 7581-7587.

A polymer based local drug delivery system on plasma activated silicon implant surfaces

H.W. Rohm[1], K. Sternberg[1], T. Stöver[2], G. Paasche[2], S. Barcikowski [3], A. Hahn[3], and K.-P. Schmitz[1]

[1] University of Rostock/Institute for Biomedical Engineering, Rostock, Germany
[2] Hannover Medical School, Hannover, Germany
[3] Laser Zentrum Hannover e.V., Hannover, Germany

Abstract— **Medical implants which include a local drug delivery system are a growing area in implant development. For many implant applications silicone is used as material because of its chemical inertness and good biological performance. However the choice of silicone as material brings up some challenges when a local drug delivery system should be applied. To enhance adhesion of a drug containing polymeric coating silicone was activated by aid of plasma chemistry. This treatment leads to reactive groups which can be used for further modification. After an additional treatment with 3-Aminopropyl-triethoxysilane (APTS) polymers activated by 1-[3-Dimethylamino)propyl]-3-ethylcarbo-diimide hydrochloride (EDC) were coupled to the surface to give a polymeric monolayer. Afterwards a polymer coating with Dexamethasone incorporation was applied to the silicone by a spray coating technique. Coatings on the basis of PLLA and P(4HB) show an increased mechanical stability. Investigations on the release of Dexamethasone from these coatings show as well that the conducted work is a good basis for further developments.**

Keywords— **Cochlear implant, plasma, silicone, local drug delivery.**

I. Introduction

Modern medical implants evolve into multifunctional implants, which are not only able to fulfill their principal duties but are also capable of being local drug delivery systems. For example cochlear implants (CI) have become a well accepted instrument for the effective treatment of sensory deafness. Thereby the quality of the signal transmission highly depends on channel separation and impedance. One factor that affects the impedance is the growth of connective tissue around the electrodes after traumatic insertion into the inner ear. Therefore it is desirable to apply drugs with antiproliferative effects on fibroblasts. It was already shown, that Dexamethasone a synthetic glucocorticoid effectively suppresses the growth of connective tissue.[1]

For a successful suppression it is necessary to supply Dexamethasone continuously over an extended period of time. Therefore it is desirable to combine a drug reservoir with the implant for local drug delivery. To establish such a drug reservoir on implants different approaches are imaginable. The incorporation of drugs into polymer coatings is a very promising way. Besides the benefit that the drug is fixed on the implant's surface and relatively protected against mechanical stress, a polymer coating allows to control the drug release characteristics in a wide range. So a tailor made drug delivery system for the desired application can be obtained.[2]

Due to the poor adhesion on silicones that most polymeric coatings show a chemical modification of the CI's silicone surface is required. Plasma chemistry allows to activate the relatively chemical inert silicone surface to produce functionalities that can be used for further surface modification.[3] For example a polymer monolayer can be applied to form an interface for adhesion enhancement.

II. Materials and methods

Chemicals were used as received without further purification: 3-Aminopropyl-triethoxysilane (APTS; 99 %, Aldrich), N-Hydroxysuccinimide (NHS; Merck, for synthesis), 1-[3-(Dimethylamino)propyl]-3-ethylcarbodiimide hydrochloride (EDC; for synthesis, Merck), Dexamethasone (>97 %, Fluka), ethanol (95 %, central pharmacy university Rostock), methanol (LiChrosolv, Merck), chloroform (p.a., J. T. Baker), ultra pure water ($\sigma = 0.05$ µS/cm at 25 °C, Ultra clear, SG Wasseraufbereitung und Regenerierstation GmbH, Germany), Poly-L-lactide (PLLA, Resomer L214, Boehringer-Ingelheim Pharma), Poly-4-hydroxy-butyric acid (P(4HB), Tepha Inc.).

Silicone samples were washed with methanol prior to use and dried in a vacuum drying cabinet at 40 °C for at least 48 h. The silicone samples were modified using a radio frequency plasma generator (Diener electronic GmbH + Co. KG). The plasma was generated at a pressure of 0.3 mbar and 180 W of generator power using Oxygen as process gas. The samples were treated 20 min. After treatment with an oxygen-based plasma the silicone samples were quickly immersed into a solution of 10 % of APTS in ethanol and heated under reflux for at least 3 h. Then the samples were removed from solution, rinsed with ethanol and dried in

O. Dössel and W.C. Schlegel (Eds.): WC 2009, IFMBE Proceedings 25/VIII, pp. 223–225, 2009.
www.springerlink.com

vacuum. The desired polymer was dissolved in chloroform and EDC/NHS was added. The solution was agitated at 50 °C for 30 min. Then APTS treated silicon samples were immersed into this solution and kept at this temperature for additional 16 h. Afterwards the solution was removed and the silicon samples were rinsed with Chloroform and dried in vacuum. Drug containing polymer coatings were applied using a spray coating process. Therefore the used polymers were dissolved in Chloroform and a solution of Dexamethasone in ethanol was added to give a weight ratio of polymer to drug of 70/30 (w/w).

Release of Dexamethasone from polymer coatings was studied by means of HPLC. Therefore a HPLC device from Knauer (Berlin) equipped with a Eurospher 100 C18, 120 x 4 mm ID column was used. It was run isocratic at 23 °C, with a mixture of methanol and ultra pure water (50/50, v/v) as mobile phase. Flow rate was 1 ml/min and detection wavelength was set to 254 nm. Standards of Dexamethasone were used with concentration of 0.1, 0.5, 1.0, 2.0, 5.0 and 10 µg/ml. Coated silicone pieces were placed into capped glass vials and 1 mL of isotonic (0.9 %) NaCl solution was added. Vials were placed into an oven at 37 °C and shaken gently. After a designated period of time the silicone pieces were removed from solution. The solution was subjected to HPLC measurement. Silicone pieces were placed into a new vial and another 1 mL of NaCl solution were added.

Contact angle measurements were made using the Contact Angle System, dataphysics instruments GmbH, (model: OCA 20). Ultra pure water was chosen as probe liquid and sessile drop measurements were performed at room temperature. Drop volume was about 7 µl.

IR-spectra were recorded on a Hyperion 2000 IR-microscope that is coupled to a Bruker Equinox 55 FTIR spectrometer. Measurements were done with Ge-ATR-optics at a contact pressure of 0.8 N. IR-Spectra were recorded in a range from 600 to 4000 cm^{-1} by aid of OPUS software.

III. Results

After activation by O_2-plasma a clear decrease in contact angle can be observed (see Tab. 1). This decrease is sign for an increased hydrophilic character which is affiliated with the creation of –OH-groups on the silicone surface. Although simple and efficient, activation by O_2-plasma produces a thin layer, which quickly loses its hydrophilic character unless kept under water. Therefore the subsequent derivatisation with APTS was accomplished to create more persistent $–NH_2$-groups at the silicone's surface. As expected an increased contact angle can be observed after treatment with APTS. These $–NH_2$-groups were used to bind a polymeric monolayer of P(4HB) and PLLA, respectively to the silicone surface. The monolayer acts as a mediator between the silicone of the implant and the polymeric coating that is applied in order to increase the coating's adhesion to the implant. The coupling of P(4HB) and PLLA, respectively to the silicone's surface can be observed by a change in contact angle, too. Thereby the degree of change reflects the hydrophilic character of the polymers used. While PLLA is more hydrophobic and shows a wider angle P(4HB) shows a more hydrophilic character and therefore a narrowed angle.

Table 1 Contact angles against water (at 23 °C) of untreated silicone in comparison to that after several surface modification steps and coupling of polymeric layers, respectively.

	Contact angle in °
Untreated	90±6
O_2-plasma treated	61±5
After coupling of APTS	95±7
After coupling of PLLA	81±5
After coupling of P(4HB)	75±8

The coupling of P(4HB) and PLLA, respectively to the activated and modified silicone surface can also be traced by FTIR-ATR-spectroscopy. The IR-spectrum reveals a new vibration band at ~1650 cm^{-1} which can be affiliated to carbonyl groups of the polymers. Therefore it can be assumed that a monolayer of the polymer used has been attached to the modified silicone surface.

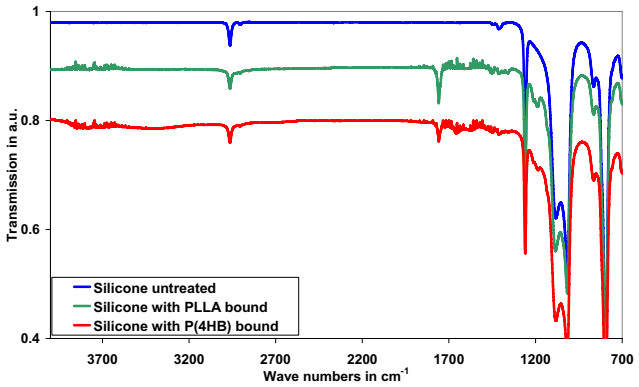


Fig. 1 FTIR spectra of untreated silicone, after binding of PLLA and P(4HB), respectively.

The polymeric monolayer allows applying a polymeric coating wherein Dexamethasone is incorporated by means of spray coating. From this coating the drug can be released.

Depending on the polymer the release can be tuned to match the application's needings.

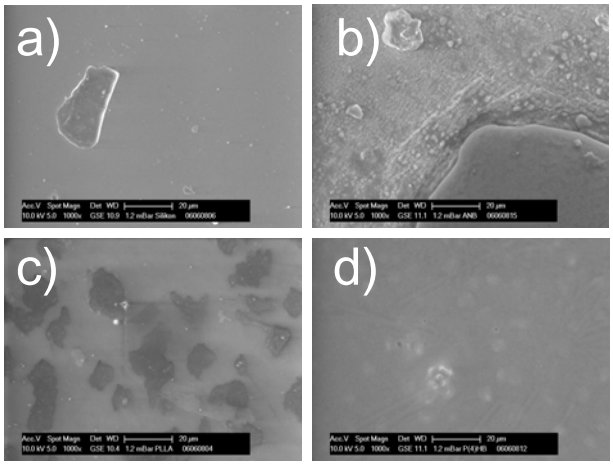


Fig. 2 ESEM images of silicone a) untreated, b) after polymer coupling, c) with PLLA/Dexamethasone coating, d) with P(4HB)/Dexamethasone coating.

The release of Dexamethasone from the polymeric coating is highly dependent on the polymer that is used. As can be seen from the release study (Fig. 3) Dexamethasone is released very quickly from the P(4HB) coating (green line). In less than 5 h all incorporated Dexamethasone is released into the medium. In contrast PLLA shows a slow release of Dexamethasone over several days (red line). This behavior might be explainable when the ESEM images are taken into account (Fig. 2).

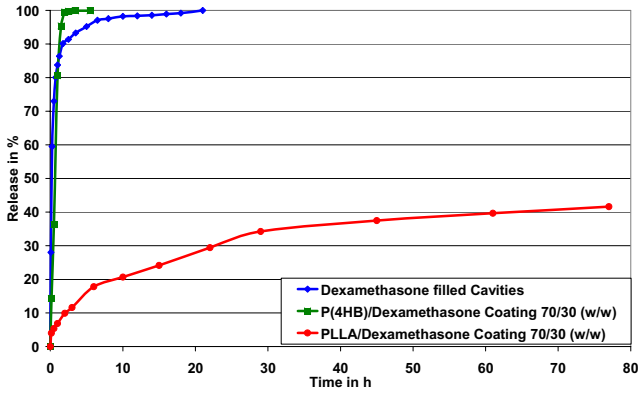


Fig. 3 Release of Dexamethasone from polymeric coatings in comparison to Dexamethasone filled cavities.

As can be seen the PLLA/Dexamethasone coating (c) shows dark domains which can be assigned to the incorporated drug. This local concentration and the more hydrophobic character leads to the slower release of Dexamethasone from the coating. In opposition to that the P(4HB) coating with incorporated Dexamethasone shows no distinct domains where the drug might be concentrated. It seems that the drug is uniformly distributed over the whole area. In addition with the higher hydrophilicity the release of Dexamethasone is accelerated compared to the PLLA coating. This release is even faster than the direct release from drug filled cavities (blue line), because in the case of drug filled cavities the drug is locally concentrated in the cavities and not smoothly distributed over the whole surface as it is the case with the P(4HB) coating.

IV. Conclusions

Silicone surfaces can be activated by aid of O_2-plasma. Subsequent treatment with APTS allows to attach a polymer monolayer of P(4HB) or PLLA, respectively after polymer activation by 1-[3-(Dimethylamino)propyl]-3-ethylcarbodiimide hydrochloride (EDC) and N-Hydroxysuccinimide (NHS). This monolayer forms a good base for a drug containing polymer coating that can be applied by spray coating. By use of PLLA as polymer matrix a slow drug release over several days can be achieved which is essential for a use in a local drug delivery system in the inner ear.

Acknowledgment

This work is supported financially through the DFG as a part of the SFB/TR 37.

References

1. Stöver T, In vitro neurite outgrowth induced by BDNF and GDNF in combination with Dexamethasone on cultured spiral ganglion cells *Laryngo-Rhino-Otol*. **2007**, 86(5), 352-357.
2. Sternberg K, In vitro study of drug-eluting stent coatings based on poly(L-lactide) incorporating cyclosporine A - drug release, polymer degradation and mechanical integrity. *J. Mater. Sci. Mater. Med.* **2007**, 18, 1423-1432.
3. Donzel C, Hydrophilic Poly(dimethylsiloxane) Stamps for Microcontact Printing *Adv. Mater.* **2001**, 13, 1164-1167.

Author: Henning W. Rohm
Institute: Institute for Biomedical Engineering
Street: Friedrich-Barnewitz-Str. 4
City: 18057 Rostock
Country: Germany
Email: henning.rohm@uni-rostock.de

Particle-Size Distribution of Dextran- and Carboxydextran-Coated Superparamagnetic Nanoparticles for Magnetic Particle Imaging

K. Lüdtke-Buzug, S. Biederer, T.F. Sattel, T. Knopp, and T.M. Buzug

Institute of Medical Engineering, University of Lübeck, Lübeck, Germany

Abstract— **During the last few years, nanosized superparamagnetic materials based on iron-oxide, so called SPIOs, became more and more interesting due to an increasing variety of applications from cancer therapy to contrast enhancement in magnetic resonance imaging. Superparamagnetic iron-oxide based contrast agents like Resovist™ had been widely established in radiological imaging of the reticuloendothelial system.**

Recently, a novel imaging technique called magnetic particle imaging (MPI) has been proposed for determination of the spatial distribution of iron-oxide nanoparticles. In first publications of MPI, Resovist™ plays a key role. Unfortunately, however, Resovist™ has been withdrawn by Bayer Schering Pharma in the end of 2008. Therefore, the analysis of an acceptable surrogate agent is presented in this paper.

By means of dynamical light scattering and magnetic particle spectroscopy it will be demonstrated that dextran-coated iron oxide nanoparticles can be synthesized with similar particle size distribution and analogous magnetic properties compared to the carboxydextran-coated Resovist™.

Keywords—Resovist, superparamagnetism, SPIO, magnetic nanoparticles, magnetic particle imaging, photon cross correlation

I. Introduction

In the last few years, nanoparticles have been advanced to one of the most interesting materials [1-3]. Especially in medicine, these particles are in the focus of research for new active agents that may carry therapeutic substances [4] or act as tracer material for imaging purposes [5]. Magnetic nanoparticles, for instance, play a key role in magnetic resonance imaging (MRI) where they are used as contrast media leading to improved resolution of the acquired images [6].

A well established nanoparticle-based contrast agent in MRI is Resovist™ (Bayer Schering Pharma) [7]. This agent falls into the category of superparamagnetic iron-oxide nanoparticles, so-called SPIOs. It consists of magnetite covered with carboxydextran, which prevents the particles from agglomeration. Due to structure and size of these particles, Resovist™ is a reticuloendothelial system (RES) specific MRI contrast media, originally used for imaging of liver lesions [8].

Recently, Resovist™ has been used to demonstrate the feasibility of magnetic particle imaging (MPI) [9-11]. MPI is a new modality, which is directly based on the nonlinearity of the magnetization curve of the nanoparticles that can be described by Langevin's theory of superparamagnetism. However, Resovist™ does not meet all expectations for MPI and, unfortunately, it has been withdrawn by Bayer Schering Pharma in the end of 2008.

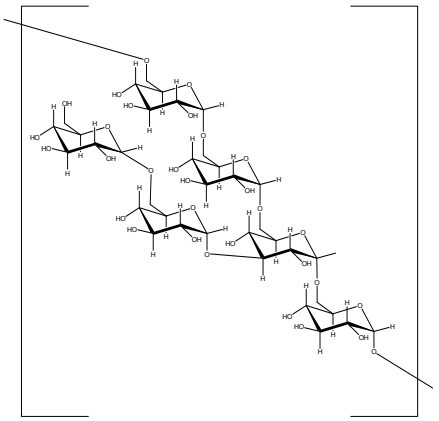


Fig. 1 Schematic representation of the structure of a dextran unit.

In this contribution, it will be shown that dextran-covered iron-oxide nanoparticles are acceptable candidates for a surrogate. In Fig. 1 a, dextran unit is shown schematically. For optimal imaging results in MPI, a narrow particle size distribution and a high magnetization response is required. A brief overview of the synthesis strategy, the particle size spectroscopy and, the quantification concept for the magnetic response is given. Resovist™ and new dextran-coated iron-oxide nanoparticles are quantitatively compared.

II. Material and Methods

As mentioned in the introduction, a surrogate for the recently withdrawn contrast agent Resovist™, a suspension of carboxydextran-coated iron-oxide nanoparticles in water, is desired for a variety of MRI and MPI applications. In this section, the synthesis of an alternative agent with similar imaging properties is proposed. Two properties of the

O. Dössel and W.C. Schlegel (Eds.): WC 2009, IFMBE Proceedings 25/VIII, pp. 226–229, 2009.
www.springerlink.com

substitute are of special importance: the hydrodynamic diameter and the characteristic magnetization, which is determined by the magnetic core diameter. Both parameters are of particular interest for medical imaging.

For MPI it is not the mean but rather the particle size distribution that essentially affects the overall magnetization signal and, hence, the imaging quality. In this section, two methods for the spectral analysis of the synthesized nanoparticles are briefly discussed: photon cross-correlation spectroscopy (PCCS) [12] and magnetic particle spectroscopy (MPS) [13].

A. Synthesis of Dextran-Coated SPIOs

Iron oxide nanoparticles can be synthesized in microemulsions, sol-gels or by gas deposition [14,15]. The strategy proposed here consists of the classical precipitation of iron oxide in an alkaline solution in presence of dextran, i.e.

$$Fe^{2+} + 2\,Fe^{3+} + 8\,OH^- \xrightarrow[\text{temperature}]{\text{at room}} Fe(OH)_2 + 2\,Fe(OH)_3$$

$$Fe(OH)_2 + 2\,Fe(OH)_3 \xrightarrow[\text{for 30-60 minutes}]{\text{heating (~70 °C)}} Fe_3O_4 + 4\,H_2O$$

However, a homogeneous mono-modal particle size distribution requires a chain of separation and purification steps. The molecular weight of dextran used for the particles analyzed here is 70,000 daltons. For more details of the synthesis see [16].

B. Photon Cross Correlation Spectroscopy (PCCS)

Dynamic light scattering can be used for spectroscopy of particle size distribution. Spectrometers that are commercially available (see Fig. 2, Nanophox, Sympatec, Clausthal-Zellerfeld, Germany) are either based on photon-correlation spectroscopy (PCS) or photon cross-correlation spectroscopy (PCCS). For the results presented in the next section, PCCS is used. PCCS allows for simultaneous measurement of particle size distribution and stability in the range of 1 nm to some micrometers in suspensions [12].



Fig. 2 PCCS particle size spectrometer.

The fundamental principle of PCCS is a 3D cross-correlation technique in a special scattering geometry.

The particle-size spectroscopy via light scattering is briefly motivated here (for details see e.g. [12,17]). The key idea is the measurement of the decay of the cross-correlation function calculated from the scattered coherent laser-light signals acquired with two detectors under a certain angle focused on the 3D scatter volume (see Fig. 3).

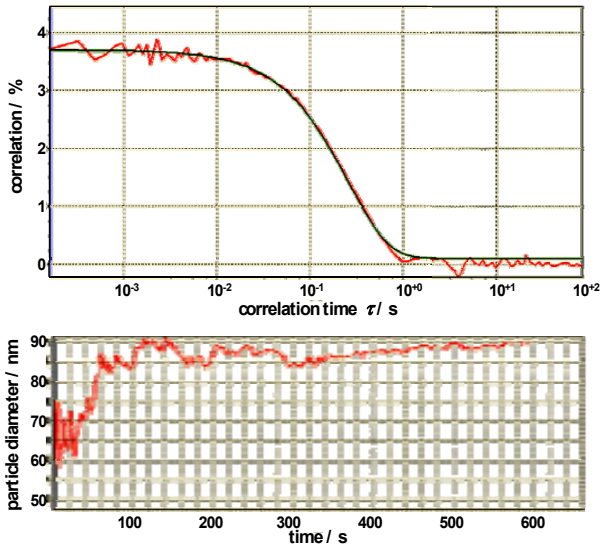


Fig. 3 Example of the correlation function (red: measured data; black: data fit) and convergence of the hydrodynamic particle diameter versus measurement time.

The reason for the correlation decay of the scatter signals lies in the *Brownian* motion of the particles under investigation, i.e. the random movement of the nanoparticles suspended in the liquid.

For small *Reynolds* numbers, the mean squared shift, $\langle x^2 \rangle$, of the particles is related to the diffusion coefficient, D, and the dynamic viscosity, η, of the liquid by

$$< x^2 >= Dt = \frac{k_B T}{\gamma} t\,, \tag{1}$$

where k_B is the *Boltzmann* constant and T the liquid temperature. For spherical particles, the fluid coefficient, γ, is given by the *Stokes* equation, i.e. $\gamma = 6\pi\eta r$. This leads to the *Einstein-Smoluchowski* relation

$$D = \frac{k_B T}{3\pi\eta d_h}\,, \tag{2}$$

where d_h is the desired hydrodynamic particle diameter. The hydrodynamic diameter, in turn, can be determined by the cross-correlation of the scattered light. It has been shown by *Schätzel* [17] that precise filtering of the single scattered fractions from the intensity is possible and that the

hydrodynamic diameter, d_h, of the particle can be estimated by

$$\ln\left(g_2(\tau)-1\right) \propto D(d_h), \tag{3}$$

where $g_2(\tau)$ is the cross-correlation of the scatter signals shown in Fig. 3.

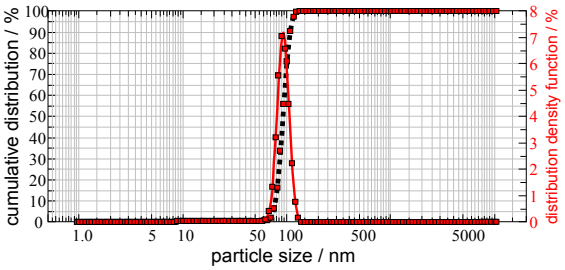


Fig. 4 Example for a distribution density function and the corresponding cumulative distribution of a nanoparticle suspension (distribution density function: red solid line; cumulative distribution: black dotted line).

The correlation fit was carried out by non-negative least squares (see Fig. 3, upper graph). The data acquisition time was set to 600 s. The temperature of the cuvette was constantly held at $T = 298$ K. The dynamic viscosity was $\eta = 0.89$ mPa s. In Fig. 4, the distribution density function and the cumulative distribution of a nanoparticle suspension can be seen.

C. *Magnetic Particle Spectroscopy (MPS)*

In the past, different strategies have been proposed to obtain an estimate of the mean particle's core diameter. Typically, transmission electron microscope (TEM) images are analyzed or relaxation experiments are carried out. However, image analysis of TEM leads to poor statistics and relaxation is a rather indirect method to obtain an estimate of the paramagnetic core diameter, d_c.

In this contribution, magnetic particle spectroscopy (MPS) shall be understood as measurement of the remagnetization dynamics, $M(t)$. Tthat can be described by Langevin's theory of paramagnetism,

$$M(t) = m_s c\left(\coth\left[\frac{m_s \mu_0 H(t)}{k_B T}\right] - \frac{k_B T}{m_s \mu_0 H(t)}\right), \tag{4}$$

where μ_0 is the permeability of vacuum, k_B the *Boltzmann* constant, T the temperature in Kelvin and, c the particle concentration. The magnetic moment at saturation, m_s, of the particles is given by

$$m_s = \frac{1}{6}\pi d_c^3 M_s, \tag{5}$$

where M_s is the saturation magnetization of magnetite.

Obviously, the paramagnetic core diameter, d_c, can be obtained as the solution of the inverse problem given by the measured data, $M(t)$ (for a detailed description of the spectrometer that has been set up in our lab see [13]). Essentially, MPS consists of a zero-dimensional version of a magnetic particle imaging (MPI) device [9,11]. In a shielded chamber the particle suspension sample is subjected to an oscillating magnetic field, $H(t)$, at 25 kHz. Due to the nonlinearity of the magnetization curve given by equation (4) a decay of the harmonics in the measured magnetization response can be detected and exploited to determine an estimate of the particle core size.

III. Results and Discussion

With the proposed technique to synthesize and purify dextran-coated iron-oxide nanoparticles, we are able to design an acceptable tracer for MPI. It is competitive to Resovist™ with respect to particle size and magnetization response. In [16], we have already reported on the relatively large variance of the hydrodynamic particle diameter of Resovist™.

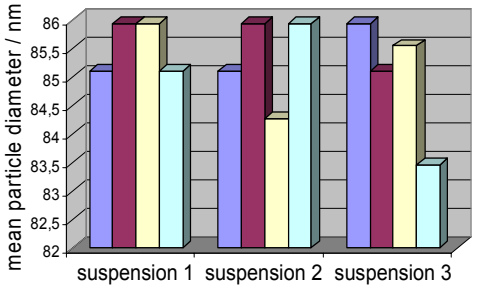


Fig. 5 Variation of mean hydrodynamic particle diameter d_h of three suspensions in four independent PCCS measurements.

In Fig. 5, the variation of the mean hydrodynamic particle diameter can be seen of the dextran-coated particles, which have been synthesized in our lab. In independent measurements of three independent water-based suspensions, the particles show a good uniformity of the mean hydrodynamic diameter (MHD). However, the particle distribution is not mono-disperse. In our PCCS measurements, we found a variation of the MHD from 83 nm to 86 nm. For different lots of Resovist™, we measured a MHD variation from 56 nm to 86 nm [16]. The standard deviation depends highly on the purification strategy. Since the hydrodynamic particle diameter is important for the biocompatibility in a certain metabolic process, the second important parameter is the magnetization response measured with MPS, which, in turn, yields an estimate of the particle core diameter.

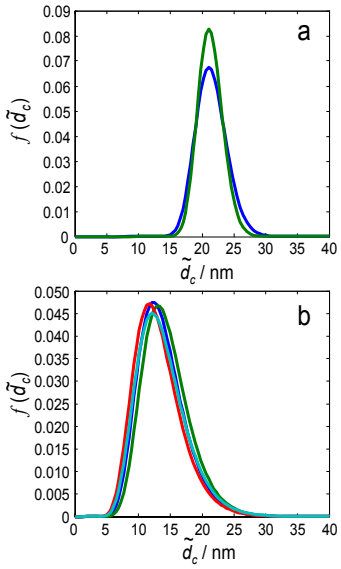


Fig. 6 Distribution of the estimated particle core diameter $\tilde{d}_c$ for a) the dextran-coated nanoparticles and b) the carboxydextran-coated nanoparticles.

In Fig. 6, the distribution of the estimated particle core diameter $\tilde{d}_c$ for dextran-coated nanoparticles (a) and carboxydextran-coated nanoparticles (b) is shown. For the best dextran-covered particles, the estimated mean core diameter was $\tilde{d}_c = 21.13$ nm with a standard deviation of 1.93 nm. For the different lots of Resovist™, the best estimated particle core diameter was $\tilde{d}_c = 13.57$ nm with a standard deviation of 3.69 nm. In both cases, 'best' means the smallest standard deviation.

IV. Conclusions

It has been shown that dextran-coated iron-oxide nanoparticles can be synthesized and purified with an acceptably narrow mono-modal particle size distribution. Therefore, this contrast media is an adequate chemical substitute for the carboxydextran-coated Resovist™ in MPI measurements. Moreover, our particles have a slightly larger iron-oxide core diameter, leading to a better magnetization response as required for MPI tracers. Thus, an improvement of imaging quality can be achieved.

Acknowledgement

The authors are financially supported by the Innovation Foundation of the State Schleswig-Holstein (grant number 2008-60).

References

1. Paschen H, Coenen C, Fleischer T, Grünwald R, Oertel D, Revermann C (2004) Nanotechnologie – Forschung, Entwicklung, Anwendung. Springer-Verlag, Berlin, Heidelberg, New York
2. Leyendecker S (2008) Nanomaterialien in Architektur, Innenarchitektur und Design. Birkhäuser, Basel
3. Bönnemann H, Brijour W, Brinkmann R (1991) Angew. Chemie 103(10):1344-1346
4. Gulyaev A E et al. (1999) Significant transport of doxorubicin into brain with polysorbate 80-coated nanoparticles. Pharm. Res. 16(10): 1564-1569
5. Lanza G M, Lamerichs R, Caruthers S, Wickline A S (2004) Molekulare Bildgebung in der MRT mit paramagnetischen Nanopartikeln. MEDICAMUNDI 6:11-17
6. Groman E V, Josephson L, (1983) US Patent 4.770.183
7. Reimer P et al. (1996) Neue MR-Kontrastmittel in der Leberdiagnostik. Erste klinische Ergebnisse mit hepatobiliärem Eovist (Gadolinium-EOB-DTPA) und RES-spezifischem Resovist. Der Radiologe, 36(2):124-133
8. Hamm B, Reichel M, Vogl T, Taupitz M, Wolf K J (1994) Superparamagnetische Eisenpartikel. Klinische Ergebnisse in der MR-Diagnostik von Lebermetastasen. Fortschr Röntgenstr; 160:52-58
9. Gleich B, Weizenecker J (2005) Tomographic imaging using the nonlinear response of magnetic particles. Nature, 435:1214-1217
10. Knopp T, Biederer S, Sattel T, Weizenecker J, Gleich B, Borgert J, Buzug T M (2009) Trajectory Analysis for Magnetic Particle Imaging. Physics in Medicine and Biology, 56(2):385-397
11. Sattel T, Knopp T, Biederer S, Gleich B, Weizenecker J, Borgert J, Buzug T M (2009) Single-Sided Device for Magnetic Particle Imaging. Journal of Physics D: Applied Physics 42(2):1-5
12. Witt W, Aberle L, Geers H (2003) Measurement of particle size and stability of nanoparticels in opaque suspensions and emulsions with photon cross correlation spectroscopy. Particulate Systems Analysis, Harrogate, UK
13. Biederer S, Sattel T F, Knopp T, Lüdtke-Buzug K, Gleich B, Weizenegger J, Borgert J, Buzug T M (2008) A Spectrometer for Magnetic Particle Imaging. Proc. 4th European Congress for Medical and Biomedical Engineering, Springer IFMBE Series, 22:2313-2316
14. Demirer M (2006) Controlled synthesis of superparamagnetic iron oxide nanoparticles in the presence of poly(acrylic acid). Master thesis, Koc University
15. Gupta A K, Gupta A (2005) Synthesis and surface engineering or iron oxid nanoparticles for biomedical applications. Biomaterials 26:3995-4021
16. Lüdtke-Buzug K, Biederer S, Sattel T, Knopp T, Buzug T M (2008) Preparation and Characterization of Dextran-Covered Fe_3O_4 Nanoparticles for Magnetic Particle Imaging. Proc. 4th European Congress for Medical and Biomedical Engineering, Springer IFMBE Series, 22:2343-2346
17. Schätzel K J (1991) Mod Optics 38:1849

Corresponding author:

Kerstin Lüdtke-Buzug
Institut für Medizintechnik
University of Luebeck
Luebeck
Germany
E-mail: luedtke-buzug@imt.uni-luebeck.de

Size depended electrical properties of Hydroxyapatite nanoparticles

V. Bystrov [1], N. Bystrova [1,2], Yu. Dekhtyar [3], A. Karlov[4], A. Katashev [3], C. Meissner [3], E. Paramonova [1], N. Polyaka [3], A Sapronova [1].

[1] Institute of Mathematical Problems of Biology, Puschino, Russia,

[2] Institute of Experimental and Theoretical Biophysics, Puschino, Russia,

[3] Riga Technical University, Riga, Latvia,

[4]Centre for Orthopaedy and Medical Material Sciences, Tomsk, Russia

Abstract— **Hydroxyapatite (HAp) nanoparticles is widely in use to fabricate implants. Computer simulation was employed to understand the HAp clusters structural and electrical (dipole momentum and polarization – surface charges) properties. A size (X) of the simulated cluster has an influence on its dipole momentum, polarization and as the result on the electron work function (φ). Saturation of hydrogen bonds and the size of the cluster have an influence on its surface polarization. Values of φ were experimentally estimated owing to photoelectron emission measurements. The magnitude of φ was demonstrated positive correlation on X. The nanoparticles demonstrated a capability to be gathered within conglomerates. This property is confirmed by calculated surface disordering of HAp nanoparticles leading to its higher interaction.**

Keywords— **Surface charge; Hydroxyapatite; nanoparticle; electron work function; polarization**

I. Introduction

Bone diseases are often treated owing to inserting of implants into the humans. The bone cells that couple regenerating bone tissue with an implant should be adhered on its surface [1]. Such a process depends particularly on a surface charge of the implant. Bone implants have a trend to be fabricated from nanoparticles of hydroxyapatite (HAP). A size of the particles affects its surface dilatation and perhaps density of electrical charge [2]. As the result, interaction with the cells is influenced (i). Electrical communications between HAP nanoparticles could provide their conglomeration (ii). Both (i) and (ii) affect quality of the implant.

The present paper is directed to:

- computational simulation of HAP ($Ca_5(PO_4)_3$ OH) ions positioning influence on the dipole momentum and polarization of the nanoparticles surface;
- experimental estimation of the HAP nanoparticles electron work function and its influence on conglomeration.

II. Computational simulation

Dipole momentum (D) and polarization (P) of HAP nanoparticles (clusters) surface was simulated owing to quantum and molecular mechanics methods. Hyperchem, Crystals software and home made programs were in use.

Simulation was provided to the clusters:

- cut off from the infinitive crystal; clusters did not have saturated hydrogen bonds,
- relaxed after the cut off procedure,
- having saturated hydrogen bonds.

The clusters had symmetry $P6_3$ /m and cell parameters sizes presented in the Table 1. The simulation results for the clusters are presented in the Table 2. WdV is the Wan der Vaals volume of calculated cluster. The number of included OH channels in the nanostruscture characterizes each cluster.

Simulation demonstrated that the density of the positively charges ions (protons) situated at the surface became higher for the HAP clusters having smaller sizes. The clusters demonstrated the different behavior of D and P, however their values for the P are decreased with cluster size. The saturation of the broken bonds by H leads to rise

O. Dössel and W.C. Schlegel (Eds.): WC 2009, IFMBE Proceedings 25/VIII, pp. 230–232, 2009.
www.springerlink.com

both D and P, while the P had the same behavior with cluster size.

Table 1 Sizes of clusters

"Name" of the clusters	N_{chan}	Quantity of the el. crystal cells	Sizes of the single cell, nm			V cluster, nm^3
			a	b	c	
Big cluster	36	5x5x3	0.94	0.94	0.68	45.064
Small cluster	2	3x2x2	0.94	0.94	0.68	7.448

Table 2. Dipole moment and polarization of the clusters

Number of cluster OH channels	UNSATURATED HYDROGEN BONDS		
	Volume V (VdW), nm^3	Dipole moment, D	Polarization, $*10^{-3}$ C/m^2, P=3.336*D/V
2	4.58	6.56	4.781
3	7.03	11.48	5.445
6	11.50	15.36	4.456
9	19.24	10.96	1.901
12	24.44	15.56	2.124
15	29.66	27.79	3.126
18	34.87	25.93	2.480
24	43.58	17.32	1.326
30	52.81	19.32	1.221
36	64.44	5.83	0.302
Number of cluster OH channels	SATURATED HYDROGEN BONDS		
	Volume V (VdW), nm^3	Dipole moment, D	Polarization, $*10^{-3}$ C/m^2, P = 3.336*D/V
2	5.029	10.85	7.107
3	7.719	21.14	9.137
6	12.60	25.60	6.78
9	20.82	31.72	5.08
12	26.44	41.55	5.24
15	32.08	55.30	5.75
18	37.76	62.37	5.51
24	47.21	70.80	5.00
30	57.10	82.45	4.81
36	70.25	47.42	2.25

The above data evidence that saturation of hydrogen bonds and the size of the cluster has an influence on its surface layer polarization. To estimate the latter electron work function measurements were supplied.

III. Electron work function

The HAP nanoparticles were fabricated due to mechanical-chemical technology. For this powders of $Ca(H_2PO_4)$ – (class pure for analysis) and CaO (class – for spectral analysis) were mixed with water in a mortar during 10-30 minutes. Mechanical activation (4-10 minutes) of mixtures was provided in a planetary mill owing to rotation of a titanium drum (850 revolutions/minute) filled with titanium carbonitride balls. The obtained particles were selected by grids within fractions.

To verify HAP crystalline origin of nanoparticles X-ray diffraction (DRON-3 equipment, Cu-cathode, radiation was filtered by the Ni-filter, tube voltage – 30 kV, anode current – 8 mA, speed of a counter/detector – 2 grad/min, vertical aperture height – 0.5 mm) was applied. The nanopowders had typical spectra of crystalline HAP.

Infra red spectroscopy was applied to test chemical content of HAP.. Measurements were done owing to spectrometer Specord -75 DR in a range 400…4000 cm^{-1}. The specimens were mixed with annealed KBr powder and pressed in tablets.

An electron work function (φ) was applied to characterize charge of the surface. For this photoelectron spectroscopy (ultraviolet range) was employed to estimate Nanopowders were mixed with ethanol to reach a cream-like emulsion. The latter was deposed on a glass wafer and dried during 1 hour at room temperature and atmosphere. After that the specimens were placed in a photoelectron emission spectrometer for measurements at vacuum condition (10^{-4} Pa). The values of φ were estimated with the uncertainty that did not exceed ± 0.04 eV.

The magnitudes of φ were directly proportional to the typical sizes (X) of the nanoparticles (Fig. 1) that is in accord with the above computational simulation results in respect with behavior of P values, when the cluster size is larger.

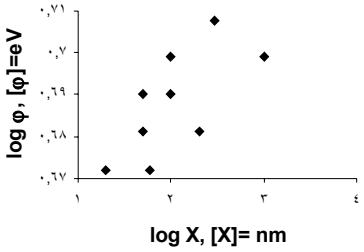


Fig. 1. Correlation of φ on X.

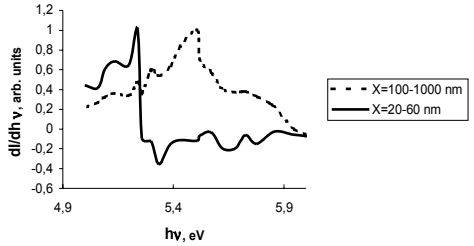


Fig. 2. Derivations dI/dhν for different X.

A derivation of the emission current (I) to a photon energy (hν) demonstrated a sharp maximum at 5.2 eV for the powders sized to $\approx 20 - 60$ nm. However the particles belonged to the range of size ≥ 100 nm indicated the maximum at 5.5 eV that had a scattered structure (Fig. 2). By this reason one could conclude that correlation of φ on X was stipulated by the alteration of electron density of states depended on X.

Conglomeration

To verify conglomeration of the nanoparticles the nanopowders were stored 6 months at room conditions and after that the transmission electron microscope IEM – 1200 EX – IEOL, (120 keV) was employed to estimate the typical size of conglomerates.
Because the sizes of the particles were spread within the fractions, they had different electrical charge and therefore had a possibility to gather within conglomerates after storage. The typical size (X*) of the conglomerate positively correlated on φ. (Fig. 3).

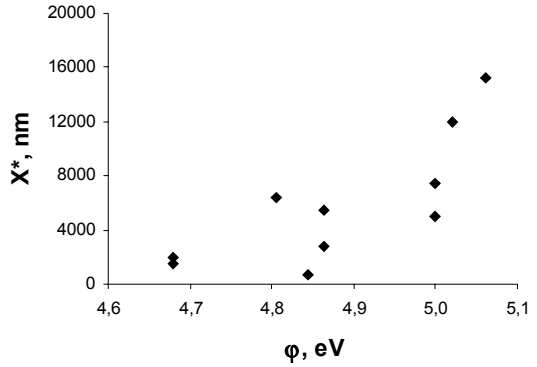


Fig. 3. Sizes of conglomerates in dependence on φ by the native nanoparticles.

Conclusion

1. Increasing of the HAP nanoparticles size influence on the nonlinear behavior of the dipole momentum, decrease the polarization of their surface layer and increase of the electron work function.
2. The electron work function by the native nanoparticles has an influence on their conglomeration. The particles characterized with higher values of electron work function fabricated greater conglomerates.

ACKNOWLEDGMENTS

The research had been worked in the frames of the EC project NMP3-CT-2003- 504937.

References

1. *Biomaterial science.* Ed. B.D. Ratner et al. Academic Press. London 1996.
2. *Electronic properties of two-dimensional systems.* TY. Ando, et al. Reviews of modern physics. V. 54, No. 2, 1982.

Microscale Organization of Chondrocyte Array in Hydrogel by Dielectrophoresis

S. Miyata and Y. Takeuchi

Department of Mechanical Engineering, Faculty of Science and Technology, Keio University, Yokohama, Japan

Abstract— **Recently, microfabrication tools have been utilized to quantify the role of the cellular microenvironment on cell activity and function. Improving tissue regeneration by cell culture on scaffold material will also require tools to control cellular organization in 3-dimentional (3-D) condition. Our objective was to improve cartilage tissue engineering using 3-D cell organization technology. In this study, we developed an anisotropic cartilaginous tissue by cell patterning within hydrogel slabs using dielectrophoretic (DEP) forces. Our data indicate that the embedded chondrocytes remained viable and reconstructed cartilaginous tissue along the patterned cell array. DEP cell patterning may become a useful approach for reconstructing anisotropic structure in cartilage regeneration.**

Keywords— **tissue engineering, cartilage, chondrocyte, dielectrophoresis, MEMS**

I. Introduction

Recently, tissue-engineering approaches to restore articular cartilage defects has been developed; this approach involves culturing autologous chondrocytes *in vitro* to create a three dimensional tissue and subsequently implanting the cultured tissue. Chondrocytes organization in the articular cartilage varies with depth from articulating surface as well as with phase of maturation [1]. This organization is related to cell biosynthesis and tissue anisotropy. Therefore control of cellular organization is important to improve cartilage tissue engineering. The random encapsulation of chondrocytes within hydrogels has been already useful in 3-D culture of chondrocytes. Recently, a novel micro-particle patterning technique was developed that utilizes DEP forces to rapidly manipulate living cells [2].

The objective of this study was to investigate the ability of DEP cell patterning within hydrogel to modulate chondrocyte organization, proliferation, and sulfated glycosaminoglycan (sGAG) synthesis.

II. Materials and Methods

A. Cell Patterning Chamber

A patterning chamber was developed to establish a highly non-uniform electric field in rectangular volume. The chamber was formed by sandwiching a 500 μm silicon gasket between two glass slides coated with a conductive material, indium tin oxide (ITO). The bottom glass was micro-patterned with a 5-10 μm film of SU-8 photoresist to insulate specific areas of the conductive surface and expose line-shape parallel electrode array, 20 μm wide and spaced 80 μm apart (Fig. 1a). High electric field is localized at the line-shape electrodes and living chondrocytes are localized to the region of low electric field (Fig. 1b). The chamber components were sterilized with 70% ethanol and assembled followed by low-conductivity (LC) buffer rinses.

B. Chondrocyte Isolation and Patterning in Hydrogel

Articular cartilage was harvested form articular joints of bovine (3-6 weeks old) from a local abattoir, and chondrocytes were isolated from cartilage explants by enzymatic digestion.

Cell-suspended agarose gels were prepared as described previously [3]. Briefly, isolated bovine chondrocytes were suspended in LC buffer and mixed in a 1:1 ratio with 3% low-melting agarose to produce 1.5% agarose solution having a cell density of 1.0×10^7 cells/ml.

The chondrocyte/agarose solution was introduced in the chamber. A sine-wave AC potential of 0, 10, 20 $V_{p\text{-}p}$, 10 kHz was applied via a function generator and amplifier that caused rapid cell localizing to the region of low electric field. After cell patterning, the chondrocyte/agarose solution in the chamber was gelled at 4°C for 20 min.

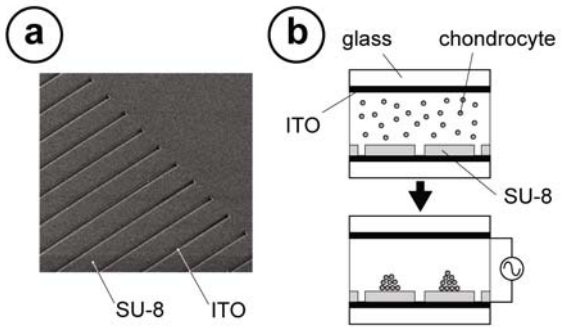


Fig. 1 SEM image of micropatterned electrode array (a) and the cross section of DEP-patterning chamber indicating cellular localization.

O. Dössel and W.C. Schlegel (Eds.): WC 2009, IFMBE Proceedings 25/VIII, pp. 233–234, 2009.
www.springerlink.com

Chondrocyte-patterned agarose constructs were cultured in DMEM/F12 with 20% FBS and 50 μg/ml ascorbic acid for 7 days.

C. Cell Proliferation and Biochemical Composition

After 7 days culture, the constructs were stained with Safranin-O to evaluate sGAG distribution. Total DNA content was determined by fluorometric DNA assay by Hoechst33258. The cell number in the cultured construct was calculated from the total DNA content divided by cellular content of DNA (7.7 pg) [4]. Sulfated GAG content was determined by DMMB dye binding assay.

III. Results and Discussion

Following DEP cell patterning in the agarose gel, cell arrays were retained and the chondrocyte remained alive. Moreover, the chondrocytes patterned in agarose gel were viable during 7 days culture. The chondrocytes patterned in agarose gel reconstructed anisotropic cartilaginous tissue along cell alignment, while the chondrocytes randomly seeded in agarose showed dispersed matrix syntheses.

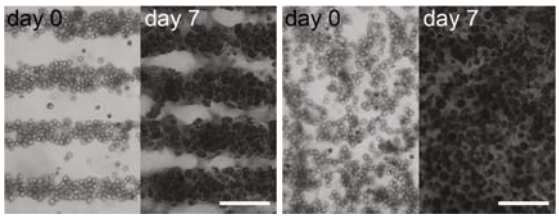
The cell number of the construct did not change significantly according to the amplitude of applied AC potential (Fig. 3). Sulfated GAG content (per one cell) of the specimens applied AC 20 $V_{p\text{-}p}$ showed lower values than that of other specimens. This result suggested that the applied AC voltage might decrease the chondrocyte activity. In the future, we plan to evaluate the effect of amplitude of AC potential on chondrocyte activity.

IV. Conclusions

In this study, chondrocyte clusters were organized in agarose gel by DEP cell patterning. The chondrocytes patterned in agarose reconstructed anisotropic tissue using. Finally, this DEP cell-patterning methodology could become a useful approach for reconstructing anisotropic structure in cartilage regeneration.

References

1. Jadin KD, Wong BL, Bae WC et al (2005) Depth-varying density and organization of chondrocytes in immature and mature bovine articular cartilage assessed by 3D imaging and analysis. J Histochem Cytochem 53:1109-119
2. Albrecht DR, Underhill GH, Wassermann TB et al (2006) Probing the role of multicellular organization in three-dimensional microenvironments. Nature Method 3:369-375
3. Miyata S, Numano T, Homma K et al (2007) Feasibility of noninvasive evaluation of biophysical properties of tissue-engineered cartilage by using quantitative MRI. J Biomech 40:2990-2998
4. Kim YJ, Sah RL, Doong JY et al (1988) Fluorometric assay of DNA in cartilage explants using Hoechst 33258. Anal Biochem 174: 168-176



(a) (b)

Fig. 2 Chondrocytes array organized in hydrogel. Cell-patterned agarose gel (a) and cell-unpatterned agarose gel (b). bars: 100 μm.

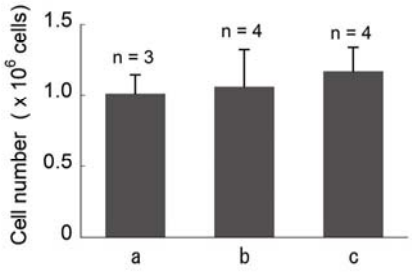


Fig.3 Cell number of chondrocyte-patterned hydrogel after 7 days culture. Chondrocytes were patterned by DEP at AC 0 (a), 10 (b), and 20 (c) $V_{p\text{-}p}$.

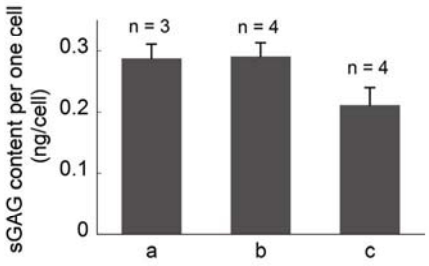


Fig. 4 Sulfated GAG content (per one cell) of chondrocyte-patterned hydrogel after 7days culture. Chondrocytes were patterned by DEP at AC 0 (a), 10 (b), and 20 (c) $V_{p\text{-}p}$.

Corresponding author:
Shogo MIYATA
Faculty of Science & Engineering, Keio University,
3-14-1 Hiyoshi, Kohoku-ku, Yokohama 223-8522, Japan
E-mail：miyata@mech.keio.ac.jp

Iron oxide nanoparticles conjugated with trastuzumab as an immunospecific probe for detecting HER2 antigen

S. Rasaneh[1], H. Rjabi[1], H. Babaei[2]

1. Department of Medical Physics,School of Medical Sciences, Tarbiat Modares University,Tehran-Iran
2. Radioisotope Department, Nuclear science and technology research institute, Tehran , Iran

Abstract—**In this study we synthesized dextran coated iron oxide nanoparticles conjugated to trastuzumab (anti - HER2) and checked it for detecting HER2 antigen in 5 cancerous cell lines with colorimetric methods. The results suggest that the trastuzumab conjugated to iron oxide nanoparticles may be considered for further investigation as an alternative test for checking the HER2 expression level of cancer cells. The complex can provide the possibility of in vivo imaging of the tumors using magnetic resonance imaging (MRI).**

Keywords— **Iron oxide nanoparticles, trastuzumab, HER2 antigen, breast cancer**

I. Introduction

Breast cancers can be categorized as being HER2 positive or HER2 negative[1] and it is very important to accurately determine HER2 tumor status before treatment. Two main methods used for HER2 testing are immunohistochemistry (IHC) and fluorescence in-situ hybridization (FISH).[2] In the present study we synthesized dextran coated iron oxide nanoparticles and conjugated it to trastuzumab and applied the complex against the HER2 receptor in 5 cell lines to discover the level of this antigen on the surface of these cells. The aim was to check the complex as an alternative technique to measure the HER2 status of tumors in in-vitro condition.

II. Material and methods

Ferric chloride hexahydrate ($FeCl_3.6H_2O$), ferrous chloride tetrahydrate ($FeCl_2 \cdot 4H_2O$), ammonia solution (25% wt) and dextran (14 kDa) and all chemical agents were purchased from Fluka chemical corp. The monoclonal antibody, trastuzumab was purchased in 150 ml vial from Genentech Inc, South San Francisco, USA.

Dextran-coated iron oxide nanoparticles were prepared using the co-precipitation method. The particle core and hydrodynamic size were determined by transmission electron microscopy and dynamic light scattering. The toxicity and uptake of iron oxide nanoparticles was checked on MCF7, A431, SW480, RAJI and LOVO cell lines using MMT and colorimetric techniques. The nanoparticles were conjugated to trastuzumab using periodat method. The stability of the complex was checked in citrate buffer and human serum up to 72 hours in $37c^0$. The uptake of complex by MCF7, A431, SW480, RAJI and LOVO cell lines were measured using spectrophotometer based colorimetric technique.

III. Results

The particle core size and hydrodynamic size were 4±2 nm and 33.9±17 nm respectively. Nanoparticles were nontoxic to the cell below the 0.6 mg/ml concentration. After coupling to the antibodies, the molar antibody/nanoparticle ratio was 2.0-2.3. The complex was stable up to 72 hrs (89± 1.2% in buffer and 86±3.5% in human serum.

The complex could discover that the MCF7 cells considerably over express HER2. The level of expression was lower in SW480, A431 and RAJI cell lines as expected. The complex showed almost negligible HER2 in LOVO cell line.

IV. Conclusions

The results suggest that the trastuzumab conjugated to iron oxide nanoparticles may be considered for further investigation as an alternative test for checking the HER2 expression level of cancer cells. The stability of the complex in human blood serum provides the possibility of in vivo imaging of the tumors using magnetic resonance imaging (MRI).This could be useful for detecting tumors and also sub-typing the tumors based on their distinct receptor expression.

O. Dössel and W.C. Schlegel (Eds.): WC 2009, IFMBE Proceedings 25/VIII, pp. 235–236, 2009.
www.springerlink.com

REFERENCES

1. Romond EH, Perez EA, Bryant J et al(2005) *Trastuzumab plus adjuvant chemotherapy for operable HER2-positive breast cancer.* N Engl J Med 353:1673-1684

2. Carlson RW, Moench SJ, Hammond MEH(2006) *HER2 testing in breast cancer: NCCN Task Force report and recommendations*. J Natl Compr Canc Netw 4:1- 22
3.

Use macro [author address] to enter the address of the corresponding author:

Author: Hessein Rajabi
Institute: Tarbiat Modares university
City:Tehran
Country: Iran
Email: hrajabi@modares.ac.ir

Determination of Tannic Acid Precipitated with Bovine Serum Albumin by Visible Light Scattering by a Flow-injection System

Tzong-Jih Cheng, Chien-Yu Chung, Po-Chung Chen, and Richie L.C. Chen*

Department of Bio-Industrial Mechatronics Engineering, College of Bio-Resources & Agriculture, National Taiwan University, Taiwan.

Abstract—**A flow system, coupled with visible light scattering method, was developed for tannin determination based on the ability of the tannic acid to precipitate bovine serum albumin (BSA). The amount of precipitated tannic acid-BSA is measured directly by scattering intensity of visible light (600 nm), which is properly related to the tannic acid concentration and conformed by a particle sizing method. Scattering signals were non-significant compare with background produced by BSA in both solutions lower than pH4 and higher than pH8. The tannic acid-protein precipitates on pipeline wall and sensing cell could be effectively removed by 22 cm of SDS stream. The system performed a linear detection range 70-100 g/ml of tannic acid with a detect limit 40 μg/ml in pH5 solution. It also could be used in medium solution with detection ranges were over 420-500 g/ml and 700-1000 μg/ml in pH6 and pH 7, respectively. The proposed method had good correlations ($r^2 > 0.97$) with the ferrous tartrate method in analysis of both one tannic acid and two tea tannins samples.**

Keywords—**tannic acid, precipitation, light scattering.**

I. Introduction

Tannins are polyphenolic compounds occurring in the barks and fruits of many kinds of plants. The content of tannins in tea or wine is partly responsible for its flavor. Therefore, tannin content is the most reasonable and important parameter to evaluate the quality of tea and the commercialized products, there are also plenty reports claiming the physiological effects and healthy aspects of tea tannin [**1**]. As the consequence, a trustful and convenient quantification method for tea tannin is valuable and urgently demanded for both the quality control and health concerns.

Methods used for quantitative analysis of tannins can be classified as: (1) general phenolic methods, (2) functions group methods, (3) HPLC and (4) protein precipitation. In general, phenolic methods among the most useful of these reactions for analytical purposes are the tendency for phenolic group to be oxidation. Widely used method based on redox chemistry includes the Prussian blue method and the Folin method [**2**] differences in the redox potential & stoichiometry for different phenolics leads to differential responses with redox assays. General phenolic methods can be useful screening plants for the presence of phenolics. Functional group methods are much more selective than the general methods, and provide both quantitative & qualitative information about tannins in an extract. However, the specificity of these methods can lead to problems with interpretation. Hydrolyable tannins can be fractionated by HPLC to provide both qualitative and quantitative information. HPLC of condensed tannins had proved more difficult than HPLC of hydrolysable tannins. Good separations of monomeric flavonoid are easily achieved. However, separation of the high molecular weight polymeric procyaidins has not been successful [**3**]. Although the ability to precipitation protein is the defining characteristic of tannins, the detailed chemistry of the interaction is still only partly understood. Numerous methods for determining tannins which take advantage of the interaction between tannin and protein have been devised. The radial diffusion [**4**] is easy but inconvenient; the protein-precipitation phenolics method [**5**] is robust and gives excellent results with many types of tannins; the radiochemical method [**6**] is very sensitive but requires specialized equipment; a similar but less sensitive method can be done with blue dye-labeled protein [**7**]. Qualitative assessments of binding can be made with electrophoretic methods [**8**].

In recently, several methods for tannin analysis such as colorimetric, UV spectrophotometric, chromatographic, enzymatic and nuclear magnetic resonance techniques are also available. The spectrophotometric vanillin method is commonly used to determine tannin in plants because of its sensitivity, specificity and simplicity, but it is difficult to perform reproducibly and to standardize properly [**9**]. A Fourier transform infrared spectroscopy was used in an investigation of interaction between polyphenols (tannins) with gelatin [**10**]. An indirect spectrophotometric method also had bee proposed for quantitative determination of tannic acid. [**11**]. Scattering technique had been applying to many applications relating to biochemical analysis and materials [**12**]. We also had reported a preliminary study in formation of tannin-albumin nano-particles by a scattering technique [**13**]. A study based on nephelometry was recently reported for investigating interaction of BSA with tannins from different sources [**14**]

The purpose of this work was simply to update a traditional protein precipitation method for tannins

O. Dössel and W.C. Schlegel (Eds.): WC 2009,IFMBE Proceedings 25/VIII, pp. 237–240, 2009.
www.springerlink.com

determination that is labour-intensive nature. For this purpose, a visible light scattering technique was used to develop an on-line sensing system for real-time monitoring precipitating tannins with BSA, followed by direct measurement of precipitated BSA by a scattering model in a fluorometer, with no need for any subsequent process.

II. Materials and methods

A. Chemicals

Tannic acid, Ammonium ferrous sulfate hexahydrate, potassium sodium (+)-tartrate tetrahydrate (Wako Co., Japan), Bovine Serum Albumin (fraction V), SDS, triethanolamine (Sigma, USA) and all other chemicals were of reagent grade and used as received. All solutions used in the experiments were prepared with deionized water made with Milli-Q water purification system (Millipore, USA). Acetic buffer (0.2 M, pH 5.0) was prepared by diluting 11.4 ml of acetic acid and dissolving 9.68 g of sodium chloride in water until in 1 liter solution. SDS solution was prepared by diluting 50 ml of trithanoamine and dissolving 10 g SDS in water and brought up to 1 liter. Tannin (10 mg/ml tannic acid) and BSA (1.0 mg/ ml) standard solutions were prepared by dissolving solids in the dispersant and subsequently filtering through the 0.22 m filter for analysis in particle sizing . The solutions were further diluted with the dispersant to suitable concentrations in a cuvette. Ferrous tartrate stock solution was prepared by dissolving 0.1 g of ammonium ferrous sulfate hexahydrate and 0.5 g of potassium sodium (+)-tartrate tetrahydrate in 100 ml of the phosphate buffer (0.1M, pH 6.8).

B. Flow injection assembly

Conventional flow-injection tubing (silicon or Teflon tubes with 1mm i.d.) and polypropylene connectors were used to assemble the system. The carrier (deionized water), reagent (BSA in various pH of buffer solution) and sample streams were driven (0.5~1.0 ml/min for each) with a signal-controllable three-channel peristaltic pump (SMP23S, Tokyo Rika Co., Japan). Into the carrier stream, 20μl of sample solution was injected and merged with the reagent stream. After mixing in the 20 cm coiled tube (the mixing coil), the resulting sample plug was delivered through a fluorometric detector (FP-1520, Jasco Co., Japan) to monitor the light scattering (= 600 nm).

C. Determination of aggregates size and scattering responses

Scattering intensity of was obtained with a particle sizer (Coulter N4 Plus) equipped with a 5-mW semiconductor laser (633 nm); the aperture of its optical system was 200 μm. The correlators were aligned at 90º and performed in logarithmic mode. The nonnegative least squares algorithm was used to analyze the particle distributions. Weight of light scattering was calculated with the correlators of the stated particle sizer. All the optical measurements were conducted at ambient temperature with a 1*1-cm plastic cuvette.

III. Results and discussion

A. Characteristics of scattering signals in the FIA system

The aggregation between tannic acid and BSA was on-line measured according to formation of aggregates in solution, which were determined directly by light scattering method. A flow-injection scattering measurement was built allowing the analysis in continuous scattered light resulted from the formation of micro- or nano-particles of tannin-BSA aggregates, which were not so easy to precipitate in short time if without centrifugation even though in acid solution (e.g., typical value of pH5.0 for the precipitation method). Precipitation time of tannin-BSA aggregates was found about 40 min in stationary acid solution (pH5.0) from scattering signal (not shown here). Comparatively, the precipitation was hardly observed in medium and base solutions.

Responses of scattering light for high concentrations (1 mg/ml) of tannic acid mixed with 1 mg/ml of BSA in the flow injection system were obtained. The repeatability of response was very good despite of high concentration of tannic acid. However, base line of response was significantly elevated following with the first injection of samples and could not reset to initial level by carrier solution. It was also found that base line shift was more significant in acid solutions than medium and base solutions. The base-line shift could be slightly improved by a following injection of a short segment of SDS stream.

The studies of flow injection variables were the injected reagent volume, the precipitation coil length, coil length of regeneration reagent and the flow rate of the sample and water dilution streams. The effect of the precipitation coil length was investigated at constant flow-rate (1.2 ml/min). Reactor coil length as short as possible was preferred for this study because the tannin-protein precipitation reaction almost occurs in a moment. Moreover, long reactor coil

increased the residence time of the precipitate in the sensing cell to an extent that caused partial adsorption on the inner walls of the tubing. A mixing coil length of 10 cm was thus chosen based on above considerations and implement possibility of the flow injection system.

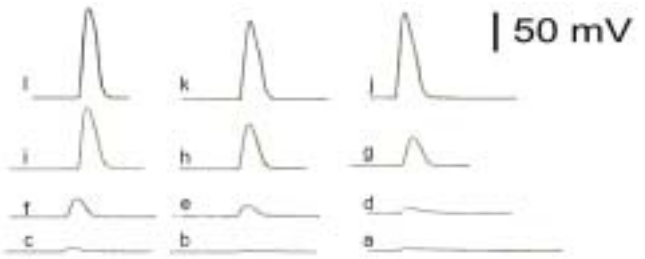


Fig. 1 IDose-dependent FIAgram of tannic acid. Different concentrations of tannic acid were injected at the indicated times (the arrows). Flow rate: 1.2 ml/min; BSA concentration: 1 mg/ml. Concentration of tannic acid, (a): 0, (b): 30, (c): 40, (d): 50, (e): 60, (f): 70, (g): 80, (h): 90, (i): 100, (j): 150, (k): 200, (l): 300.

B. Dose-dependent scattering intensity of tannic acid in an acid solution

The pH5.0 acetate acid was primarily chosen, where BSA was shown to be stable and to have a strong ability to bind and precipitate condensed tannins [15]. Under these conditions, the refraction index of solvated particles and viscosity of solution are insignificant different, and the intensity of the scattering light is proportional to the concentration of dispersed insoluble aggregates. Under these conditions, the control solution showed that the solvent did not precipitation protein in absence of tannic acid and no precipitation was observed in the tannic acid without BSA, even with higher concentrations than those used in the study.

The profiles of the appearance of the tannin-protein aggregates resulting from the interaction between BSA and different concentrations of tannic acid at pH5 are shown in Fig. 1. Peak height of scattering response was increased with concentration of tannic acid. The baseline scattering of the FIAgram (Fig. 1a or b) was from 1 mg/ml of BSA. The typical FIA peak profiles revealed the reproducible dose-dependent scattering effect of tannin on the aggregation with BSA. In the following paragraphs, peak heights were used to optimize the proposed method.

The dose-dependent scattering effect was also verified by a particle sizer. Both the weight (or intensity) of light scattering and particle size in solution were dependently increasing with tannic acid concentrations in acid solution (pH5). This result consisted with that from FIA analysis in acid solution (pH5) and previous study [Lin, 2003] using dynamic scattering technique in medium solution (pH7.0). The calibration curve of tannic acid in pH5 is shown in Fig. 2. The linear detection range was from 70 to 200μg/ml with low-detection limit of 40 μg/ml.

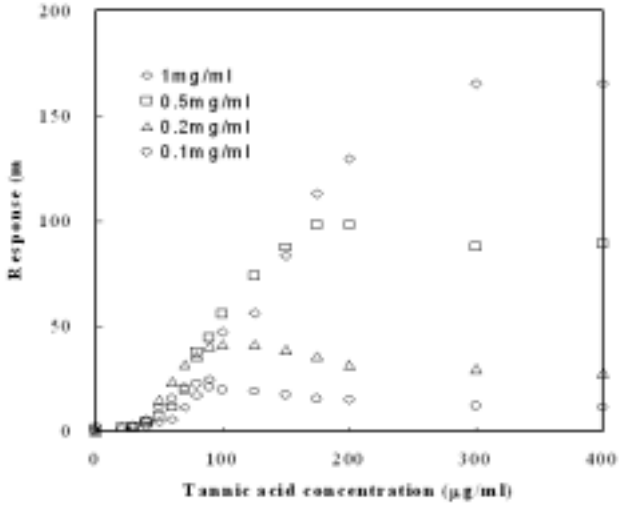


Fig. 2 Dynamic ranges for tannic acid with different concentrations of BSA. BSA concentration: ○= 0.1 mg/ml, = 0.2 mM, □= 0.5 mg/ml, ●= 1 mM; flow rate: 1.2 ml/min. BSA was dissolved in ??M phosphate buffer (pH 5.0).

C. Effect of BSA Concentration on Calibration Curve in an acid solution

Light scattering responses of both BSA (1 mg/ml) and tannic acid (1 mg/ml) were only 2.5 mV and almost non-significant in solution from pH4 to pH9, respectively. These results also consistence with our previous report [13] showed particle size of tannic acid is only three tenth of BSA in neutral solution (pH6.8). According that study [13], background signal of scattering is dominated by BSA but tannic acid because scattering intensity produced by tannic acid is about 1/729 of by BSA based on theory calculation according to the Rayleigh equation. Therefore, intensity of light scattering was mainly contributed from BSA molecules or BSA-tannin aggregating particles, and independent with pH value as well as ion strength of solutions.

A few parameters of these calibration curves were listed at Table 1. Scattering responses were increasing and were then slightly decreasing with increase of tannic acid concentrations. These results indicated that sensitivity, detection ranges and up-detection limit were improved as increasing BSA concentration. Blank response of scattering

light was linearly increased with BSA concentrations (see Table 1) in range of 0.1~ 1.0 mg/ml. For utility, BSA concentration could be preset according to requirement of intended detection limit and ranges.

Table 1 Effect of BSA concentration

BSA concentration (mg/ml)	Blank response[1] (mV)	Parameters of calibration curve[2]			
		Slope (mV/mL/mg)	Low-detection limit[3] (mg/ml)	Up-detection limit (mg/ml)	Detection range[4] (mg/mL)
0.1	0.25	0.44	30	80	50
0.2	0.50	0.64	30	90	60
0.5	1.24	0.83	40	150	110
1.0	2.40	0.93	70	200	130

[1] Intensity of light (600 nm) scattering in a FIA system.
[2] From linear calibration curves, all of their $r^2 > 0.97$.
[3] Obtained from calibration curves based on SNR>3.
[4] Detection range = Up-detection limit – Low-detection limit. *Effect of Reagent pH on System Characteristics*

In order to explore the potential of the scattering technique to quantitative determination of tannic acid in physiological or other reality conditions, experimental conditions were extended up to pH9. Effect of reagent pH was investigated with 1.0 mg/ml of BSA in acetic acid or phosphate acid of different pH. Background signals induced from BSA molecules was almost same in various reagent pH, so the FIAgram will not be easily disturbed by the transient pH change of the injected sample plug. The pH value of solution significantly dominated scattering intensity produced by tannic acid-BSA aggregates. Scattering responses will be appeared in acidic solution (pH5 ~ pH7) but non-significant in basic solutions (> pH7) and strong acidic solution (< pH5) even though BSA concentration was larger than 1 mg/ml. Calibrations curves only be obtained from pH 5 to pH6 solutions This phenomena implied that aggregation between tannic acid and BAS as well as producing light scattering effect are significant in acidic solutions (pH5~pH7).

This system performed good sensitivity in acidic solution (pH5~pH6) but in medium solution (pH7). The pH5 solution performed better performances than others based on consideration of mentioned analytical parameters. Even thought detection range of this FIA system was not sufficient wide than other analytical methods of tannic acid, this minor weak is easy to be improved by an automatic dilution procedure. Comparing with our previous report, this study performed lower detection limit (700 μg/ml) and wider detection range (30% of up-detection limit) in medium solution (pH7). It will be useful to physiological and beverage applications.

IV. CONCLUSIONS

The flow injection system with light scattering technique proposed in this study was shown to be a simple and reliable method to on-line determine tannic acid. Sustained on-line work can achieved based on that the absorption of BSA-tannic acid aggregates on inner wall of sensing cell and flow pipe can be effectively eliminated by a sufficient length of SDS stream tailed after BSA-tannic acid mixture. This system showed a good correlation with the ferrous tartrate methods in assay both tannic acid and tea tannins. It performs a better analytical characteristic in pH5 solution, and also could be used in medium solution (pH7). This capacity for used in medium solution will be conducive to be as a tool for investigating tannins (or polyphenols) interact with interesting biochemical molecules in physiological condition in our future works.

REFERENCES

1. Haslam E (1996) Natural polyphenols (vegetable tannins) as drugs: possible modes of action. J. Nat. Prod. 59: 205-215.
2. Swain, Hillis WE (1959) J. Sci. Food Agric. 10: 63.
3. TanninBook p.37
4. Hagerman J (1987) Chem. Ecol. 13: 437-449.
5. Hagerman AE, Butler (1978) J. Agric. Food Chem. 26: 809-812.
6. Hagerman AE, Rice ME, Ritchard N.T. (1978) J. Agric. Food Chem. 26: 809-812
7. Asquith, Bulter (1985) J. Chem. Ecol. 11: 1535-1544.
8. Austin et al. (1989) J. Chem. Ecol. 15: 1335-1347.
9. Deshpande S.S., Cheryan M., Salunkhe D.K. (1986) CRC Crit. Rev. Food Sci. Nutr. 24: 401.
10. Edelmann A et al. (2002) Toward the Optical Tongue: Flow-Through Sensing of Tannin-Protein Interactions Based on FTIR Spectroscopy. J. AM. CHEM. SOC. 124: 14741-14747.
11. Ratnavathi CV et al. (1998) Microassay for the quatitation of protein precipitation polyphenols: use of bovine serum albumin-benzidine conjugate as a protein probe. Food Cemistry. 61: 373-380.
12. Cao A (2003) Light Scattering - Recent Applications. Analytical Letters 36: 3185–3225.
13. Lin H-C, Chen P-C, Cheng T-J, and Chen RLC (2004), Formation of tannin–albumin nano-particles at neutral pH as measured by light scattering techniques. Analytical Biochemistry 325: 117–120.
14. Carvalho E, Mateus N , de Freitas V (2004) Flow nephelometric analysis of protein–tannin interactions. Analytica Chimica Acta 513: 97–101.
15. de Freitas V, Mateus N (2001) J. Agric. Food Chem. 49: 940.

Author: Tzong-Jih Cheng (Associate Professor)
Institute: BIME, National Taiwan University
Street: 1, Sec. 4, Roosevelt Rd.
City: Taipei
Country: Taiwan
Email: tzongjih@ntu.edu.tw

Magnetron Enhanced Plasma-Polymerization for Biocompatible Sensor Coatings and Membranes on Polymeric Based Materials

F.Olcaytug[1], L. Ledernez[1], G. Dame[1], P. Zahn[1], H. Yasuda[1,2] and G.Urban[1]

[1]IMTEK, Department of Microsystems Engineering, Laboratory for Sensors, University of Freiburg, Freiburg, Germany

[2]Center for Surface Science & Plasma Technology, Department of Chemical Engineering, University of Missouri-Columbia, Columbia, MO, USA

***Abstract*— One of the key questions in the application of miniaturized sensors and actuators for acute and/or chronic use in living-body environment is the biocompatibility. In case of gas sensors additionally a very fine balance between the biocompatibility of the device and the gas (e.g. O2, NO, CO) permeability of its coating must be maintained. In many sensor configurations polymeric substrate materials are used. Here, we present the application of a unique deposition technique for nano-films with thickness ranging between 10 and 200 nm on top of flexible polymeric foils used as substrates in the technology of a variety of biosensors and lab-on-chip structures. The method employs a 15 kHz magnetron-enhanced glow discharge plasma-polymerization process using methane as precursor. It is configurable for laboratory scale batch sizes but also for continuous industrial coating lines. Unsurpassed results of this processing technique have been documented with contact lenses already. Hence, we tested depositions with this process on top of PMMA, polyimide and polystyrene foils of different surface morphology. Compatibility of the process and of the coatings with these materials, adherence in dry and aqueous environment were checked. Antibacterial behaviour of the films were tested by immersing the coated samples in a bio-film reactor for 48 hours as well as for 7 days in E-coli bacteria solutions. After the inoculation time samples were rinsed and treated in an ultrasonic bath. Colonies formed on different culture media out of the rinsing water were enumerated. Number of colony forming units, depending on inoculation time and coating conditions, has been investigated. Remarkable reduction of bacterial attachment was proven with film thicknesses as low as about 15 nm, which allows a reasonable gas permeation rate. Hence, the technology provides production of antibacterial and gas permeable membranes for miniaturized sensors and sensor arrays on chip.**

Keywords— **biocompatible coatings, antibacterial, gas-sensors, gas permeability, glow discharge, plasma polymerization.**

O. Dössel and W.C. Schlegel (Eds.): WC 2009, IFMBE Proceedings 25/VIII, p. 241, 2009.
www.springerlink.com

Fully electronic cellular migration assays with field-effect transistor arrays

S. Ingebrandt[1,2]*, S. Schäfer[2], R. Stockmann[2], A. Offenhäusser[2]

[1] Department of Informatics & Microsystem Technology, University of Applied Sciences Kaiserslautern, Zweibrücken, Germany
[2] Institute of Bio- and Nanosystems (IBN2), Forschungszentrum Jülich GmbH, Jülich, Germany

Abstract— **We describe a novel method for the non-invasive, electronic monitoring of cellular migration. Planarized open-gate field-effect transistor (FET) chips are utilized for the migration measurements. These chips were developed, fabricated, and previously used for the extracellular recording from electrogenic cells. A miniaturized and portable 16-channel amplifier system capable of monitoring the transistor transfer function (TTF) of the devices was developed. Proof-of-principle assays with rat embryonic fibroblast cells are presented.**

Keywords— **Field-effect transistor, transfer function, cellular migration.**

I. Introduction

Cellular migration and adhesion plays a key role in inflammation, wound healing, and metastasis. Electronic assays for monitoring adhesion and migration were introduced many years ago. The usually used Electric Cell-Substrate Impedance Sensing (ECIS) system is commercially available [1] and its feasibility for biomedical and pharmacological studies was successfully demonstrated [2-4].

In our recent publications we reported about the use of an impedance readout principle for our field-effect transistor (FET) arrays, which even enables cellular adhesion assays on a single cell level [5-7]. The special resolution of our system is therefore about one order of magnitude better compared to the ECIS system. When monitoring the transfer function in a time-dependent manner over an extended period of time, cellular migration down to an individual cell and even subcellular compartment level can be monitored. An un-hindered migration is only recordable with our recent design of planarized open-gate transistors minimizing the topological features on the chip surface.

II. Materials and Methods

A. FET devices

For the migration assays we used a newer design of our standard 16-channel open-gate FET devices [8]. These chips were fabricated in the clean room facilities of IBN at the Forschungszentrum Jülich. The 16 transistors (4×4) in the arrays had a pitch of 200 µm in the center of a 5×5 mm^2 silicon chip. Gate lengths of 1 to 3 µm and gate widths of 6, 12, or 25 µm were used for this design. The gate oxide consisted of thermally grown SiO_2 with a thickness of 10 nm. We introduced a planarization step to fabricate ultra-flat surfaces having maximum topographical features in the open-gate area of only 30 nm (Fig. 1). Contact lines were passivated by a sufficiently thick layer of thermal oxide, raising the gate area onto a plateau. Those planar FETs are mandatory to monitor cellular migration under minimized topographical influence.

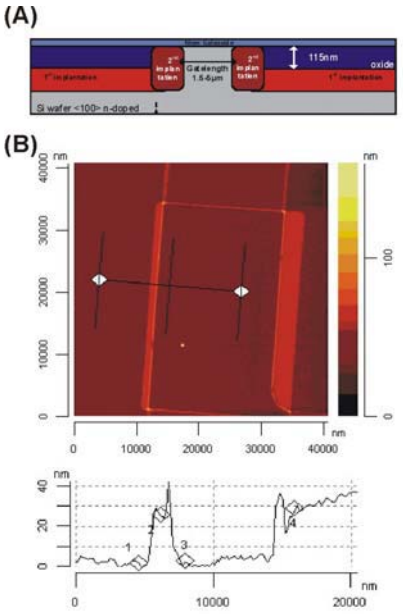


Fig. 1 (A) Schematical cross-section through a gate area of the ultraflat FET chip. (B) AFM image with line scan of a gate area. Largest feature sizes are bird beaks of only 30 nm height.

B. Cell culture

Cellular migration is strongly linked to the cells' ability to adhere to a surface. We recently described time-dependent adhesion and detachment measurements with our FET arrays [7]. In addition, time-dependent transfer function measurements can be used to observe cell migration.

O. Dössel and W.C. Schlegel (Eds.): WC 2009, IFMBE Proceedings 25/VIII, pp. 242–244, 2009.
www.springerlink.com

For those experiments, fibroblasts were chosen as cell system, as they are very motile and a preferred model system in migration research. Fibroblasts are mainly present in the connective tissue. They play an essential role for synthesis of the extracellular matrix, e.g. by producing collagen. This is especially important for healing processes after tissue rupture. The fibroblasts were taken from the umbilical cord of the rat and plated onto the fibronectin coated chips in numbers of 2000 to 15000 cells per chip (Fig. 2). They were cultured for 1 to 2 days at 37°C in an incubator. To stimulate cellular migration, 50nM epidermal growth factor (EGF) was added 1 hour before the measurement. As culture medium for the fibroblasts we used endothelial cell growth medium containing a supplemental mixture (basic fibroblastgrowth factor (human, recombinant) 1.0ng/ml medium; endothelial cell growth supplement/Heparin 4µl/ml medium; epidermial growth factor (human, recombinant) 1.0ng/ml medium; hydrocortisone 1µg/ml medium; phenolred 0.62ng/ml medium; fetal calf serum 20µl/ml medium).

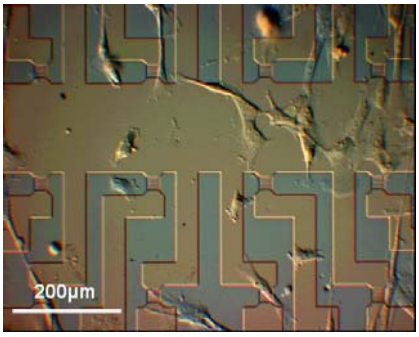


Fig. 2 Fibroblasts were cultured on fibronectin-coated transistor chips (differential interference contrast microscopy (DIC)).

C. Readout system

For signal recording a miniaturized 16-channel amplifier system was developed [5-7, 9]. The portable amplifier offered electronic characterization of the FETs and recordings in potentiometric and impedimetric mode. The whole amplifier unit was operated by a microprocessor and the data were transferred via an USB connection to the PC. The read-out software was implemented in Delphi® 5.0 (Borland Software Corporation). For all experiments, we used an Ag/AgCl wire as reference electrode.

In the potentiometric readout mode, the FETs were operated in the constant-voltage mode. By applying a constant drain-source voltage V_{DS} and a constant gate-source voltage V_{GS}, the working point of the device was set. At the first operational amplifier (OP), changes in the drain-source current ΔI_{DS} were converted into an output voltage v_{out}.

In our latest amplifier version for impedimetric readout, 16 independent, frequency-selective amplifiers were additionally included into the system. This allowed simultaneous operation of all 16 readout channels. The scan of the transfer function can be done by feeding a sinodal test signal V_{mod} with 10 mV amplitude and varying frequency from 1 Hz – 1 MHz to the reference electrode. The FETs were operated in the same working point as for the dc-readout. Test signals of exact amplitude, frequency and phase were provided by a direct-digital-synthesis device. Frequency-selective amplification was performed via a frequency multiplier, which was built-in into a capacitive de-coupled amplification cascade. By a right selection of stimulation voltage and sampling frequency for the data, a simultaneous readout of impedimetric and potentiometric signals is possible, too.

III. RESULTS AND DISCUSSION

As we described previously, by means of the TTF method it is possible to determine the attachment or de-attachment of an individual cell to the gate area of a single transistor in a time-dependent readout mode [7].

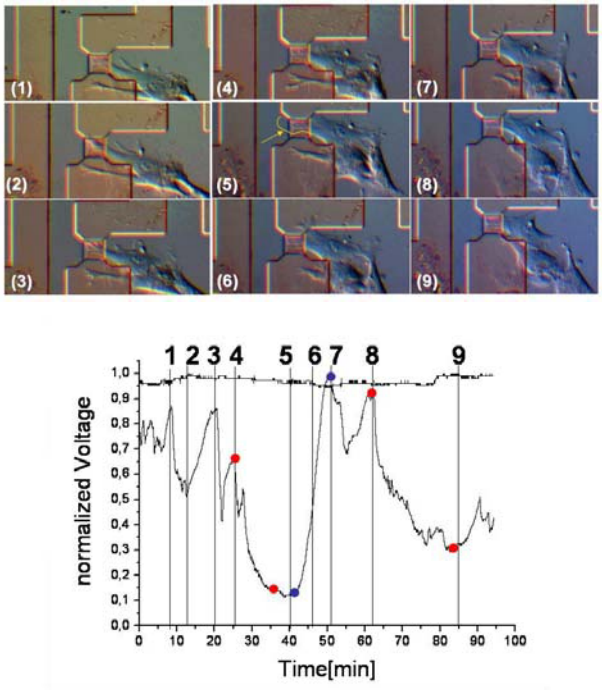


Fig. 3 Upper images: DIC images taking during a migration measurement. One fibroblast cell is getting into contact with a FET gate. Lower graph: Corresponding transfer function signal of this transistor. The cell is getting into contact, retracting and getting into contact again. A second recording of a transistor having no cell attached is shown, too.

For the migration assays described here we read out only 1 data point per s and per channel. The total assay time was up to two ours. While accomplishing the transfer function measurements, a time series of photographs was taken with one photograph per minute to correlate cell motion and electronic signal. In Fig. 3 one exemplary recording is shown. A fibroblast cell is getting into contact with a FET gate. The transistor even records the initial contact when parts of the cell's membrane adhere to the gate. Between 30-40 min the cell's membrane covered the whole gate and thereafter the cell retracted its membrane again. In addition the almost silent recording from another channel having no cell attached is shown. This exemplary recording demonstrates the capability of the system to record cellular migration down to a subcellular level.

IV. CONCLUSIONS

We developed a portable system utilizing the transistor-transfer function method to electronically observe cell-substrate binding events to the gate structure of 16-channel FET chips. When we record signals over an extended period of time (several hours), fully electronic cellular migration assays are possible.

In future we will develop chip designs, which offer many more readout channels. In addition we will develop a 'water proof' preamplifier head stage, which will offer migration and growth studies inside an incubator during cell culture. Additionally, we will apply our method to many different biomedical and pharmacological assays.

ACKNOWLEDGMENT

We thank Nico Hersch for the cell culture of the fibroblast cells and B. Hoffmann and R. Merkel (all IBN-4, Forschungszentrum Jülich (FZJ)) for fruitful discussions. We also thank G. Wrobel, S.Eick and B. Hofmann (all IBN-2, FZJ) for their help in the initial phase of the project. In addition we thank Dieter Lomparski (IBN-2, FZJ) for the software, and Norbert Wolters and Ralph Otto (IBN-TA, FZJ) for the design and realization of the amplifier unit. This work was funded by the Helmholtz Association of German Research Centers.

REFERENCES

1. Applied BioPhysics at www.biophysics.com
2. Giaever I and Keese C R (1991) Micromotion of Mammalian-Cells Measured Electrically. Proc. Natl. Acad. Sci. U. S. A. 88:7896-7900
3. Giaever I and Keese C R (1993) A Morphological Biosensor for Mammalian-Cells. Nature 366:591-592
4. Lo C M, Keese C R and Giaever I (1995) Impedance analysis of MDCK cells measured by electric cell-substrate impedance sensing. Biophys. J. 69:2800-2807
5. Ingebrandt S, Han Y, Nakamura Fet al (2007) Label-free detection of single nucleotide polymorphisms utilizing the differential transfer function of field-effect transistors. Biosens. Bioelectron. 22:2834-2840
6. Ingebrandt S, Wrobel G, Eick Set al (2007) Probing the Adhesion and Viability of Individual Cells with Field-Effect Transistors, TRANSDUCERS 07 and EUROSENSORS XXI, The 14th International Conference on Solid-State Sensors, Actuators and Microsystems,, Lyon, France, pp 803-806
7. Schäfer S, Eick S, Hofmann Bet al (2009) Time-dependent observation of individual cellular binding events to field-effect transistors. Biosens. Bioelectron. 24:1201-1208
8. Offenhäusser A, Sprössler C, Matsuzawa Met al (1997) Field-effect transistor array for monitoring electrical activity from mammalian neurons in culture. Biosens. Bioelectron. 12:819-826
9. Ingebrandt S, Han Y H, Sakkari M Ret al (2005) Electronic detection of nucleic acid molecules with a field-effect transistor, Materials Research Society Symposium Proceedings, Semiconductor Materials for Sensing, Warrendale, pp 307-312

Author: Prof. Dr. Sven Ingebrandt
Institute: University of Applied Sciences Kaiserslautern
Street: Amerikastr. 1
City: Zweibrücken
Country: Germany
Email: sven.ingebrandt@fh-kl.de

Artificial Urinary Diversion System – kinematic requirements on fixation

D. Kirchleitner[1], M. Roth[1], D. Jocham[1] and H. Wassermann[2]

[1] Department of Urology, University of Luebeck, Luebeck, Germany
[2] Institute for Sensor Technology, University of Applied Sciences Muenchen, Muenchen, Germany

Abstract— **A German research group develops a new artificial urinary bladder – the Artificial Urinary Diversion System – to treat patients after excision of the human bladder suffering from end-stage bladder disease. The research project implies the development of a feasible fixation element guaranteeing a determined position of the implanted artificial organ in the abdomen of the patient. Hence it is crucial to define the kinematic requirements on the fixation considering the possible anatomical locations for fixating an artificial bladder with a special technical means. The Promontory of sacrum and the symphysis pubica are both possible anatomical locations. Due to this, the kinematic requirements on the fixation element are based on the range of motion of the human spine as well as the interaction between the implanted artificial bladder and adjacent human organs. The kinematic requirements can be considered as basis in the development process of the fixation for the Artificial Urinary Diversion System.**

Keywords— **artificial organ, artificial urinary bladder, prosthetic bladder, urological prosthesis, fixation**

I. Introduction

Worldwide the number of patients suffering from bladder cancer amounts to 356,000 incidences per year [1]. For 20 to 30% of them, the course of disease requires a bladder excision and subsequently a bladder substitution [2]. The golden standard in present surgical processes for bladder replacement systems play separated segments of large or small intestine. These surgeries have a decent risk for complications. A high rate of follow-up problems results in physical damages of the patients and further surgeries are often inevitable. Conventional bladder substitutes can also cause serious restrictions for quality of life of the patients [2].

A new realistic approach for the treatment of patients after bladder excision was launched in 1994 by a research group of the Clinic of Urology, University of Luebeck in cooperation with Munich University of Applied Sciences Institute for Sensor Technology. The fully implantable Artificial Urinary Diversion System according to patent EP 1161202B1 could overcome the disadvantages of conventional bladder substitutes [2].

The artificial bladder provides adequate urine storage, has no exterior connections (wires, switches) and its structure is bio and human compatible. Moreover, this alloplastic system enables the patient to start volitional the evacuation of urine.

The alloplastic bladder is characterized by modular design principle consisting of urine pouch, control and actuation module. For each of the modules, different sizes exist and hence this modular design concept enables the adaption of the whole artificial system to the anatomical requirements of each individual patient.

The prosthetic bladder requires a fixation in the abdomen of the human body. Rohrmann reported about migration of a previous developed and in a female patient implanted prosthetic bladder through the skin in 2003 [3]. This system was implanted without any fixation towards the position in the abdominal section. Furthermore, the Artificial Urinary Diversion System has a higher mass inertia in cases of acceleration of the trunk compared to the human bladder. The fixation could avoid the inacceptable displacement and therefore the damage of adjacent organs in such cases. Thus possibilities for a fixation were investigated and kinematic requirements defined. This report represents the results of the research.

II. Study Approach

Fixation guarantees a determined position of the artificial system in the abdominal section of the human body with a special technical means. Therefore it is crucial to first define possible anatomical fixation locations and then kinematic requirements on the fixation element.

At the beginning of the study, we defined the construction space for the artificial system. The final design of the system was validated by severe investigations with human dead-body studies. Finally, the definition of the design space allows investigating possibilities for fixating the artificial urinary bladder.

The requirements for fixating an artificial system as the artificial urinary bladder are also derived from comparable surgery methods, e. g. sacrocolpopexy or sacrohysteropexy.

Further needs on the design of the fixation element were defined due to investigations of the kinematics of the human

O. Dössel and W.C. Schlegel (Eds.): WC 2009, IFMBE Proceedings 25/VIII, pp. 245–247, 2009.
www.springerlink.com

lumbar spine and interaction between the artificial bladder and adjacent abdominal organs.

III. RESULTS

The results are divided in three interdependent parts. Firstly, possible anatomical locations for fixating the artificial bladder are presented. Secondly, the requirements on the fixation element specified by the main kinematics of the spine and thirdly, interaction between artificial bladder and adjacent abdominal organs are reported.

A. Anatomical locations for fixation

There are two anatomical locations for fixating an artificial urinary bladder, predetermined and limited by the available construction space for the whole capsular system:

- The upper one is promontory of sacrum – it could be mainly responsible for fixating the position
- The lower one is symphysis pubica – it could be mainly responsible for bearing the weight of the artificial system

The combination of these both fixation points and a special fixation element guarantees a determined position of the artificial system in the abdominal section. This is depicted in figure 1.

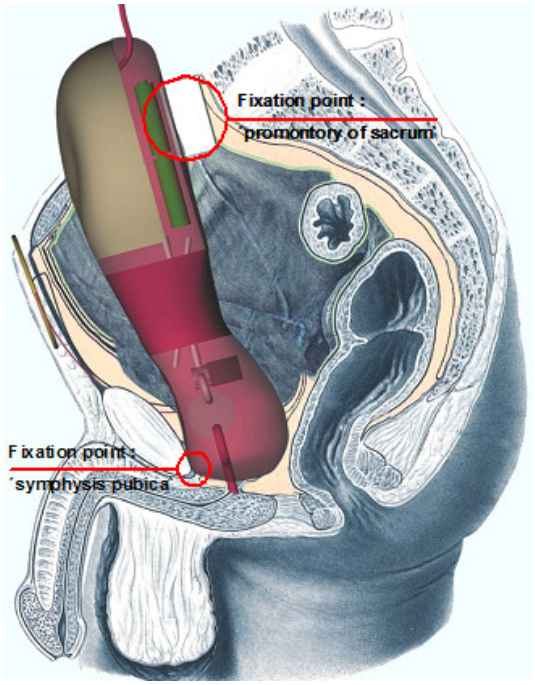


Fig. 1 Side view artificial urinary bladder implanted in male pelvis

The application of both fixation points minimizes the risks of inacceptable displacement of the artificial bladder and therefore high stress and strain at the fixation location in cases of loading. Theses cases of loading could be caused by motion of the trunk.

The anastomosis of the fixation element to the tissue of promontory of sacrum and symphysis pubica is comparable to state of the art surgery methods, e. g. sacrocolpopexy or sacrohysteropexy.

B. Kinematics of the human spine

The previous part A depicts the possibility of fixating the Artificial Urinary Diversion System at the intervertebral disc between fifth lumbar vertebra (L5) and sacrum (S1) and at symphysis pubica. Thus it is crucial to identify following basic kinematics of the human spine for all six degrees of freedom as requirements on the fixation element:

- Flexion/ Extension
- Lateral bending
- Axial rotation

The depicted spinal motions could happen during normal daily movements or sport activities of the patients. Therefore the requirements on the fixation element are partially based on the range of motion of the human spine. The basic kinematics of the human spine and the maximum range of motion were investigated in several in vitro and in vivo studies in the past [4, 5, 6].

Furthermore, the mobility of the sacroiliac joint needs to be considered for the basic motions of the human spine named above. The range of motion of this joint was investigated in vitro by Kisslinger et al. in 1990 [7]. Further results on in vivo experiments were reported by Wilke et al. in 1997 [8]. The studies depict that the consideration of this motion is unimportant due to the marginal mobility of the sacroiliac joint.

C. Organ interaction

The third part relates to the investigation of the interaction between the artificial bladder and adjacent organs. The interaction is caused by motions of the trunk based on the kinematics of the spine (as depicted in part B) and especially lumbar spine motions.

The excision of the human bladder and the subsequent implantation of the Artificial Urinary Diversion System alter the natural structure in the abdominal section of the human body due to the semi flexible outer shell. In cases of loadings especially caused by motions of the lumbar spine the semi flexible capsule interacts with the tissue of the adjacent abdominal organs. The fixation needs to be as

flexible as necessary to avoid pains for the patient as well as damages to the technical system. The term "pain" was defined by a commission of experts in 1979 [9]: "An unpleasant sensory and emotional experience associated with actual or potential tissue damage, or described in terms of such damage."

Hence it is crucial to investigate the organ interaction to define further requirements on the fixation and also on the outer shell of the artificial bladder.

IV. DISCUSSION

The investigation reports about the first development steps in the process of the fixation of the Artificial Urinary Diversion System. The kinematic requirements on the fixation demand mainly on the three problem fields depicted in the chapter above. Besides this, there are further requirements, e. g. on ergonomics of assembling the fixation element the surgery. Furthermore, the element has to be bio and human compatibility.

The weakest point in terms of physical force compensation of the fixation is the anastomosis to the living tissue of promontory of sacrum and symphysis pubica. It is crucial to create a connection with high rigidity but without damaging the living tissue. As a consequence, this could cause serious restrictions for the patients, e. g. a limitation of certain activities. Hence investigations of static and dynamic load capacity of this special anastomosis are inevitable in order to further investigate the physical load situation.

V. ACKNOWLEDGMENTS

We thank all project partners and all persons involved in the development of this project.

VI. CONCLUSION

The requirements on the fixation are mainly based on the anatomical fixation locations, kinematics of the human spine and organ interaction. The fixation of the Artificial Urinary Diversion System at promontory of sacrum and symphysis pubica with a fixation element is an innovative, safe and simple technique that is comparable with state of the art surgery methods.

REFERENCES

1. Parkin DM, Bray F et al. (2002) Estimating the world cancer burden. Globocan 2002
2. Wassermann H (2003) Kuenstliches Harnableitendes System. Medizintechnik in Bayern, Muenchen
3. Rohrmann D (2003) The artificial urinary bladder. In: Atala A, Slade D (eds) (2003) Bladder disease – Research Concepts and clinical applications. Kluwer Academic 56:885-893.
4. White A A, Panjabi M M (1978) The basic kinematics of the human spine. Spine 3:12-20
5. Yamamoto I, Panjabi M et al. (1998) Three-dimensional movements of the whole lumbar spine and lumbosacral joint. 14:1256-1260
6. Ochia R S, Inoue N et al. (2006) Three dimensional in vivo measurement of lumbar spine segmental motion. Spine 31:2073-2078
7. Kissling R, Brunner Ch et al. (1990) Zur beweglichkeit der iliosakralgelenke in vitro. Z Orthop Ihre Grenzgeb 128:282-288
8. Wilke H-J, Fischer K et al. (1997) In-vivo-messung der dreidimensionalen bewegung des iliosakralgelenks. Z Orthop Ihre Grenzgeb 137:550-556
9. Bonica J J (1979) Pain terms: A list with definitions and notes on usage. Pain 6:247-252

Daniel Kirchleitner
c/o University of Munich
Institute for Sensor Technology
Lothstr. 64
80335 Munich
Germany
daniel@kirchleitner.de

Compact Drug Delivery System for Analysis Arrays

M. Scheuenpflug[1] and T.C. Lueth[1]

[1] MIMED, Micro Technology and Medical Device Engineering, Prof. Dr. Tim C. Lueth, Technische Universität München, Boltzmann-straße 15, D- 85748 Garching, Germany

Abstract— **This article presents a novel compact dosing system for the delivery of drugs to analysis arrays. State of the art systems are characterized by large dimensions and inflexible use. The new dosing system can be controlled by a standard PC. Due to its dosing rate of minimal 200 nl per second, the fluid reservoir of 20 ml, the reliability and repeat accuracy, the system can be used for many kinds of dosing jobs in biology, chemistry or medicine. The miniaturization of the dosing system allows the matrix combination of many pumps to parallelize analyze jobs on multi-well plates.**

Keywords— **Microfluid, Dosing, Drug delivery,**

I. Introduction

Fluid handling systems are used for biochemical examinations [1] like the drug delivery or the monitoring of cell metabolism for the test of cytostatic drugs. The support of liquid culture medium and medicine has to be error free provided for more than 24 hours, to keep the cell medium in the bio arrays vivid. A compact and easy to use system for the examination different cytostatic drugs on multiple test samples out of one biopsy is missing. One aspect is the missing unit for the drug delivery.

State of the art dosing systems have large dimensions and are difficult in handling and service or are not able to provide an autarkic fluid supply of lower than 20 µl per minute for 24 hours.

Peristaltic pumps like they are produced from different companies [2] provide a very large range of dosing rates. Due to the use of silicon tubes with different inner diameter no internal reservoir is given. The fluidic system has to be connected with long tubes, which makes it accident-sensitive for blocking by gas bubbles. Especially at small tube diameters the capillary forces increase. Thus even small gas bubbles can cause a blocking of the fluid transport.

Piston pumps [3, 4] on the other hand are working in the fitting area of dosing rates for analysis systems. Though they are not designed for parallel dosing jobs, their lateral dimensions are big. When 12 or more micro reactors have to be supplied with drugs, long capillary tubes have to be used to get over the long distances. The problem of blockings in the tubes still exists, what makes the system not more suitable for this application.

Especially since the development of MEMS has increased, various micropumps and micro dosing systems have been developed. Zengerle et. al. [5, 6] developed a silicon micropump. Other micropumps are already commercial available [7]. Especially for dosing this kind of actuation is often not specialized. The actuators are often only controllable in an open loop. A defined dosing volume in only hardly reachable

II. Objective

Objective of this research is the development of a compact and easy to use fluid support system, which is, due to its size, suitable for parallelized analysis jobs. In contrast to state of the art fluid handling systems the new development provides more than 10 ml dosing volume in a compact system of the size of only a filled glass syringe [8]. This correlates with a 48 hours use of cytostatic drug test in Molecular Devices' CytoSensor microphysiometer (Fig. 2). The setup can be easily controlled with standard PCs.



Fig. 1: Picture of the compact dosing system at MIMED with installed glass syringe.

O. Dössel and W.C. Schlegel (Eds.): WC 2009, IFMBE Proceedings 25/VIII, pp. 248–250, 2009.
www.springerlink.com

III. Setup

The system consists of an actuation module, which is docked onto a conventional glass syringe. The cylindrical drive module is connected to the stepping motor driver. The actuator runs an inverted drive screw, which itself pushes the plunger into the syringe and displaces the fluid in the syringe. The layout with the small stepper motor [9] implemented in the inverted driving screw allows the dosing system to keep the lateral dimensions of 40 mm in diameter. Besides, the stiffness of the power train allows a precise dosing performance (Fig. 1). To maximize the dosing accuracy and to reduce the play at the change of load, the power train is prestressed. Therefore the screw of the screwdriver is divided and pushed apart by a spring. Thus always the outer shoulder of the thread is in mesh, play in changing the drive directions can be minimized. Besides manufacturing tolerances in the long drive nut can be eliminated without an effect to the dosing accuracy.

The connection of a conventional glass syringe is done by a bayonet lock. Within a turn of about 30° the syringe is placed on a stopper and hence docked onto the pump. A locking device is realized by a flexible silicon inlay in the bayonet lock. It fixes the syringe in the bayonet and presses the syringe onto the actuator at the same time.



Fig. 2: CytoSensor microphysiomete from Molecular Devices as a typical device for analysis arrays.

IV. Material and methods

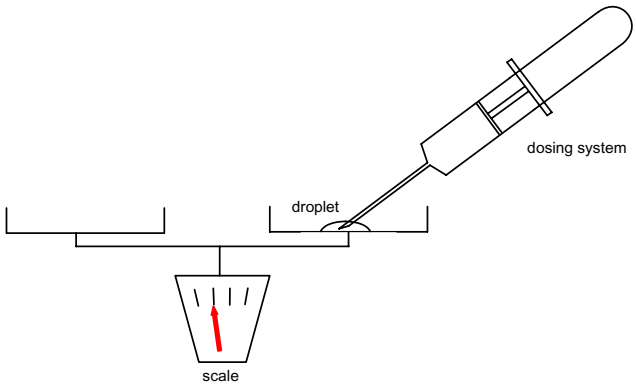


Fig. 3: Dosing experiment with dosing of water into a droplet on the precision scale.

For measurements of the dosing accuracy the prototype of the dosing system is fixed in a framework. A hypodermic needle with an inner diameter of 0.4 mm and a length of 20 mm is attached to the 20 ml glass syringe. The system is placed at a precision scale with the needle dipping into a small droplet on the platform of the scale (Fig. 3). This setup avoids inaccuracies caused by the surface tension of the fluid. Thus even small dosed volumes can be detected reliably. The stepper motor is controlled with a defined count of pulses of a fixed frequency. The out of the reservoir of the syringe displaced fluid is measured with a precision scale. At a step of 9° and a gear reduction of 1024:1 the reduced volume in the syringe is calculated [10] and compared with the measurement.

For the characterization of the dosing system two experiments are most important. The repeat accuracy shows the reliability of the system and the delivery volume provides information about the minimal possible dosing rate.

The repeat accuracy was determined by using a 500 step-pulse with 20 Hz, 60 Hz and 100 Hz. The dosed volume is measured with the precision balance. For the delivery volume measurements with different step-pulses (100, 200, 300, 400, 500, 600, 800, 1000 steps) at a frequency of 100 Hz are made.

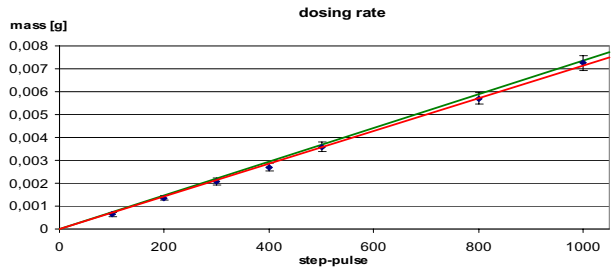


Fig. 4: Measurement of the dosing rate. The dosed mass of deionized water is given over the number of pulses to the stepping motor.

The repeat accuracy shows with 3.56 mg to 3.59 mg and the root mean square deviation of 0.22 mg to 0.24 mg no significant difference between the different pulse-frequencies. The overall repeat accuracy is 3.58 mg with a root mean square deviation of 0.22 mg dosed mass. The averaged dosing volume per step-pulse is 7.16 nl (Fig. 4).

All dosing experiments are done according to the norm DIN 8655, which rules the calibration of piston-operated volumetric apparatus. Facts like the evaporation rate, the number of measurements and the maximal tolerable RMS-value of readings are defined in this norm. This makes the measurements comparable to other studies. The results of the experiments according to DIN 8655 are shown in Fig. 5.

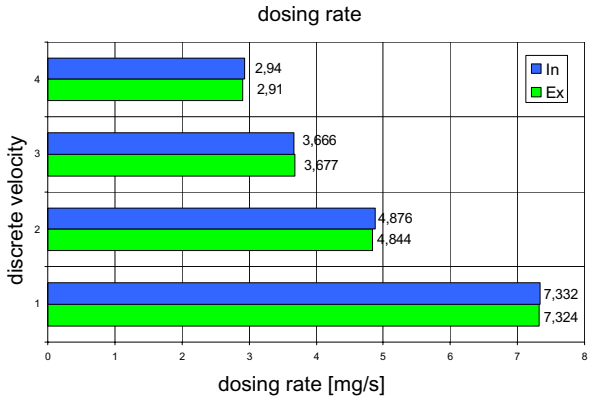


Fig. 5: Results of the experiment of the dosing rate following the DIN 8655

V. Results

Tests of the compact dosing system showed a reliable function of the system. The repeat accuracy over 105 measurements is with a root mean square of 0.22 mg, this is less than 6.2 %, extremely high. The reachable dosing rate is much lower as the required dosing rate at the CytoSensor microphysiometer from Molecular Devices with 10 µl per minute. The needed space for the dosing system was reduced to a tube of 30 cm length and a diameter of 40 mm. The experiment has shown that the dosing system is applicable for the supply of fluids to bio-chemical arrays.

With a minimal dosing rate of 200 nl per second and the construction conditioned reliability this system differs extremely from commercial available systems.

Acknowledgment

Special thanks to the Dr. Johannes Heidenhain-Stiftung for granting the project.

References

1. Eklund SE, Taylor D, Kozlov E, Prokop A, Cliffel DE, “A microphysiometer for simultaneous measurement of changes in extracellular glucose, lactate, oxygen, and acidification rate,” in Anal Chem., 2004 Feb 1;76(3):519-27.South J, Blass B (2001) The future of modern genomics. Blackwell, London
2. Watson & Marlow, http://www.watson-marlow.com, 2009
3. BBraun Perfusor, http://www.bbraun-shop.de/shop/?productId=PRID00000461, 2009
4. D. Heise, J. Rathgeber, and D. Kettler, "Fehlerquellen und Gefahren beim Einsatz von Motorspritzenpumpen," Der Anaesthesist, vol. 47, no. 1, pp. 54-58, 1998.
5. M. Zhu, P. Kirby, M. Wacklerle, M. Herz, and M. Richter, "Optimization design of multi-material micropump using finite element method," Sensors & Actuators: A. Physical, vol. 149, no. 1, pp. 130-135, 2009
6. R. Zengerle, S. Kluge, M. Richter, and A. Richter, "A bidirectional silicon micropump," *IEEE Micro Electro Mechanical Systems, 1995, MEMS'95, Proceedings*.
7. Bartels Mikrotechnik, http://www.bartels-mikrotechnik.de, 2009
8. Eric R. Lee, “Microdrop generation”.CRC Press, 2003.
9. Stölting H, Kallenbach E, “Handbuch elektrische Kleinantriebe“, Hanser Verlag, 2002d
10. Niemann G, Winter H, Höhn B-R, “Maschinenelemente Band 1: Konstruktion und Berechnung von Verbindungen, Lagern, Wellen“, Springer, 2005.

Corresponding author:

Author: Michael Scheuenpflug
Institute: Department of Micro Technology and Medical Device Engineering, TU München
Street: Boltzmannstraße 15
City: 85748 Garching
Country: Germany
Email: scheuenpflug@tum.de

Effect of Polymer Molecular Weight on Morphology and Particle Size of Chitosan Microspheres Prepared via Spray Drying Method

S. Taranejoo[1,2], M. Rafienia[3], M. Janmaleki[1], M. Kamali[4], and L. Sadeghzadeh[1]

[1] Nanomedicine and Tissue Engineering Research Center, Shahid Beheshti University (M.C), Tehran, Iran
[2] School of Chemical Engineering, University of Tehran, Tehran, Iran
[3]Faculty of Medicine, Isfahan University of Medical Science, Isfahan, Iran
[4]Baghiatallah University of Medical Sciences, Tehran, Iran

Abstract— **chitosan microspheres for biological applications were prepared by spray-drying method. Two kinds of chitosan with different molecular weigh were used and their characteristics were compared. Scanning electron microscopy was applied to study morphology of the particles. We saw most of the chitosan microparticles had spherical or pseudo-spherical shape. It is found out that Smoothness and sphericity of the particles were significantly increased by the enhancement of chitosan molecular weight.**

Keywords— **Chitosan, Microsphere, Morphology, Smoothness**

I. INTRODUCTION

Chitosan, poly(D-glucosamine), has many applications in the medical and pharmaceutical fields because of its non-toxicity, mucoadhesion, biocompatibility and biodegradability features [1], [2], [3], [4].

Chitosan may be utilized in different drug delivery routs such as nasal, transdermal, vaginal, and oral [5]. For some of these routs, chitosan has been administered in micro or nanoparticles powder forms [6].

Microparticle-based drug delivery systems have many advantages, i.e. easier assessment of mass transfer performance, defined kinetics modeling, and controlled drug release [7]. In these systems, drug delivery performance and release profile are affected by the particle characteristics [8]. In this paper, we used spray drying method for preparation of chitosan microparticles .The main objective of this study is the evaluation of chitosan molecular weight (MW) on final properties of microparticles such as particle size and surface morphology. For this purpose, we used two kinds of chitosan with different MW and investigated the influence of MW on the mentioned particle parameters.

II. MATERIALS AND METHODS

A. Materials

Two types of chitosan with different MW are used. The low MW chitosan was obtained from Chitotech Co. Iran. The other with Medium MW was purchased from Sigma-Aldrich Chemie (Steinheim, Germany). The degree of deacetylation of both kinds of chitosan were more than 75%. TPP and acetic acid was supplied from Merck Co.

B-Methods

Preparation of chitosan microparticles: Two samples were prepared by spry drying methods as follows. Formulations of these samples are presented in table 1. Chitosan is dissolved in 2% acetic acid solution. TPP is dissolved in water in order to make 1wt% TPP solution and pH adjusted 4.0. 20 cc of TPP solution added to 200cc of chitosan solution under the sonication power of 45 w and magnetic stirrers. Crosslinking time was fixed on 60 min. the suspension of crosslinked chitosan were then spray dried (Buchi® Mini spray drier, type 190, Switzerland) through a 0.2 mm nozzle at a feed rate 2.4 ml/min. The driving pressure was 8 bar. Temperature was maintained at 120ºC.

Table 1. Formulation of preparation of chitosan microsphere

Sample	*Chitosan con. (wt%)*	*TPP con.(wt%)*	*Chitosan/TPP (V/V)*	**Polymer MW**
1	0.2	1	10	Low
2	0.2	1	10	Medium

Characterization: The spray-dried microparticles were studied using scanning electron microscopy (SEM). Samples were coated by a thin gold layer observed with microscope (25kV)(Philips XL30.

The particle size of microparticles was quantified using optical inverted microscope (Nikon TE 2000-J)

O. Dössel and W.C. Schlegel (Eds.): WC 2009, IFMBE Proceedings 25/VIII, pp. 251–252, 2009.
www.springerlink.com

III. Results and Discussion

Figure 1 shows SEM microphotographs of the chitosan microspheres. The surface morphology of these spray dried chitosan microparticles illustrates increasing of smoothness and sphericity of the microspheres with the enhancement of chitosan molecular weight. It should be noted that most of the particles had spherical and pseudo-spherical structure. As it can be seen from these images, MW had more effect on surface characteristics than the size of the particles.

On the other hand, using optical microscopy revealed that with a reduction in chitosan molecular weight, the average particle size was decreased from 1.3 to 1.1.

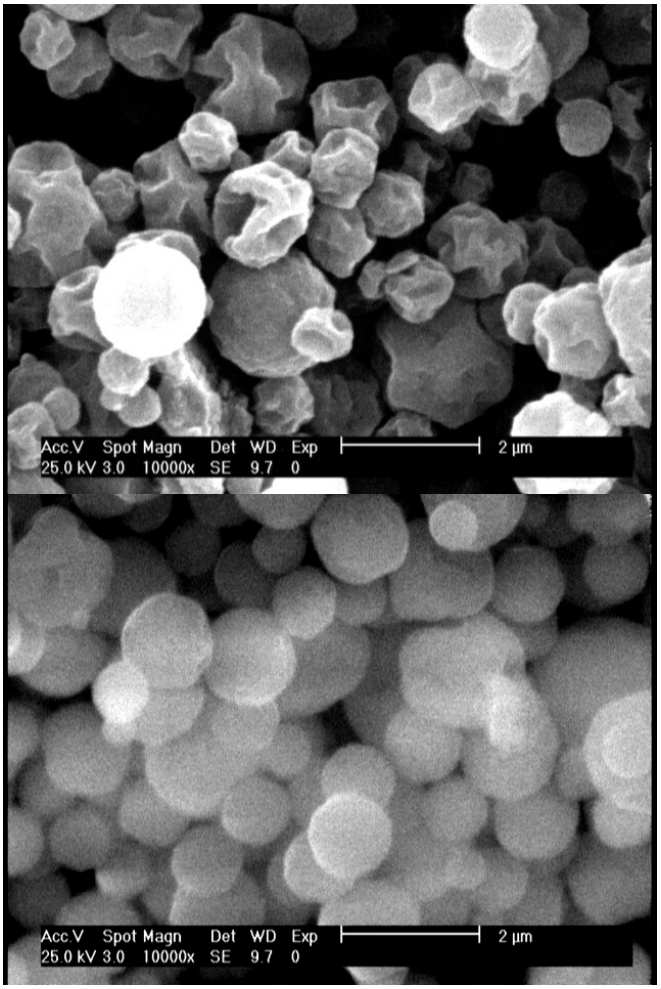


Fig.1. Scanning electron microscope pictures of TPP cross-linked chitosan microspheres, prepared from sample 1(A),and sample 2 (B).

IV. Conclusion

The present study demonstrated influence of polymer MW on the characteristics of chitosan–TPP microspheres prepared by spray-drying method. The result shows that MW significantly affects on morphology of the particles. As the MW increased, the smoothness and sphericity of the particles were increased. Furthermore, the reduction of the MW causes smaller microparticles.

Acknowledgement

The authors are grateful to Dr. Peirovi the chief of Nanomedicine and Tissue Engineering Research Center, for his sincere support and guidance.

Reference

1. Zhao K S, Asami K, Lei J P. (2002) Dielectric analysis of chitosan microsphere suspensions: Study on its ion adsorption. Colloid Polym Sci 280: 1038–1044
2. Pavanetto J, Perugini P, Conti B et al. (1996) Evaluation of process parameters involved in chitosan microsphere preparation by the o/w/o multiple emulsion method. J microencapsulation, 13(6): 679 – 688
3. Wu J, Wei W, Wang L Y et al. (2008) Preparation of uniform-sized pH-sensitive quaternized chitosan microsphere by combining membrane emulsification technique and thermal-gelation method. Colloids and Surfaces B 63(2): 164-175
4. Majeti N V, Kumar R. (2000) A review of chitin and chitosan applications. Reactive Polymers 46(1): 1-27
5. Valenta C. (2000) The use of mucoadhesive polymers in vaginal delivery. Advanced Drug Delivery Reviews 57(11): 1692-1712
6. Panos, I, Acosta N, Heras A.(2008) New Drug Delivery Systems Based on Chitosan**.** Current Drug Delivery Technologies 5(4): 331-341(9)
7. Lin L C, Chang S J, Chen S F et al. (2006) Effects of pH $Na_5P_3O_{10}$/NaOH reaction solution on the properties of chitosan microspheres, Biomedical Engineering Applications, Basis and Communications 18: 167–177
8. Chen S, Liu M, Jin S. (2006) 187-195 Preparation of ionic-crosslinked chitosan-based gel beads and effect of reaction conditions on drug release behaviors. International Journal of Pharmaceutics 311: 187–195

Author: Mohammad Rafienia
Institute: Tissue Engineering Lab., Faculty of Medicine, Isfahan University of Medical Science
Street: Soffe
City: Isfahan
Country: Iran
Email: rafie_med@yahoo.com

The Use of Body Motion for Powering Biomedical Devices

E. Romero[1,2], R.O. Warrington[2] and M.R. Neuman[3]

[1] Mechanical Engineering Department (Faculty on Leave), Turabo University, Puerto Rico, USA
[2] Mechanical Engineering Department, Michigan Technological University, Houghton, USA
[3] Biomedical Engineering Department, Michigan Technological University, Houghton, USA

Abstract— **Powering electronic devices from environmental sources such as light and temperature gradients has been demonstrated with commercially viable products such as solar-powered calculators and thermal-powered wristwatches. A new electromagnetic generator approach presented here is found to have the potential to power miniature medical devices. The power output from harvesting environmental energy is proportional to the acceleration-squared-to-frequency (*ASTF*) and the quality (*Q*) factor of the system. Human-based activities exhibit large *ASTF* values and low *Q* factors while machines are typically associated with low *ASTF* values and high *Q* factors.**

This paper reviews the generation limits of energy harvesting, the possibilities of energy generation from body motion, and the development of a new oscillating generator. The device presented is composed of a rotor with a multipole permanent magnet (PM) ring with an eccentric weight and a stator with a radial gear-shaped planar coil. The oscillations of the rotor due to the eccentric mass when subject to body motion induce a voltage on the planar coil. As much as 2.35μW of power has been produced with a preliminary prototype placed laterally on the hip while walking. It is estimated that energy from human motion could generate as much power as 1mW/cm^{3}with such a device.

Keywords— **MEMS, Energy Harvesting, Body Motion, Power Supply**

I. Introduction

Powering portable electronic devices using energy harvesting technology has become an interesting option due to the almost infinite lifetime and the independence from fuels. A solar powered calculator is a prime example of the use of environmental sources to power electronic devices. Passive energy scavenging from human bodies has also been demonstrated as a viable alternative to energize portable devices such as electronic self-winding and thermal-powered wristwatches. Motion is an especially attractive environmental energy source because of its pervasiveness and the knowledge gained from considerable research conducted in this area using electromagnetic, piezoelectric, and electrostatic transduction techniques.

Autonomous wearable microsystems for environmental monitoring and data processing with wireless transmission have been successfully implemented as watch-sized micro instrumentation devices [1]. These microsystems are commonly powered by batteries that often tend to be larger than the rest of the device, especially for systems that operate for long periods of time. For instance, cardiac pacemaker batteries fill about half the total volume of pacemakers [2]. Most autonomous systems face limitations due to battery lifetime and size. A trade-off of these two factors has typically governed the size, useful life, and capabilities of the system. Researchers have tried to merge energy scavengers into biomedical devices in order to avoid battery limitations, such as using electronic self-winding wristwatch generators for powering pacemakers [3], or for powering artificial organs employing piezoelectric generators inside a shoe [4]. However, traditional technology for biomedical devices is either power hungry, or the energy generated by the scavengers is too small. Therefore, portable microsystems have to follow low-power design approaches in order to minimize power consumption and extend battery life. At the same time their low power consumption has opened the possibility of exclusively using energy scavenging for powering them. It can even be expected that in the near future hybrid approaches that combine batteries and energy scavenging can avoid these technological limitations. An example of this path is the well-known electronic self-winding wristwatch mechanism, where a motion-based electrical generator is coupled with a rechargeable battery.

II. Available energy

Motion-based harvesters use the force generated due to the acceleration of a proof mass as the movement needed for scavenging energy by several transduction mechanisms. Fig. 1 presents common energy harvester geometries. The displacement of the proof mass inside the generator is used by the transduction mechanism to produce electrical energy. Electromagnetic generators employ the relative displacement of the proof mass to induce a voltage. Electrostatic devices make use of the changing distance to induce a charge. Piezoelectric transduction converts an applied mechanical stress in a piezoelectric material to produce an electrical potential.

O. Dössel and W.C. Schlegel (Eds.): WC 2009, IFMBE Proceedings 25/VIII, pp. 253–256, 2009.
www.springerlink.com

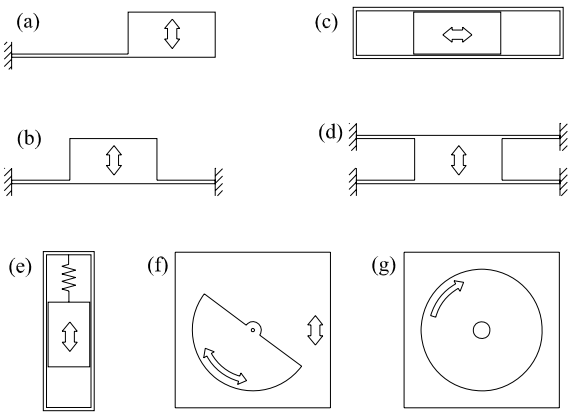


Fig. 1 Common geometries: (a) cantilever beam, (b) out-of-plane plate, (c) free-sliding mass, (d) in-plane plate, (e) spring-mass system, (f) oscillating rotational, and (g) continuous rotation generator [5,6]

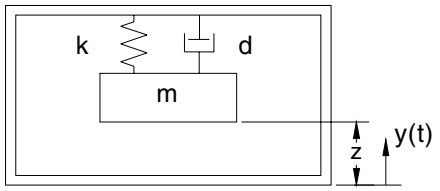


Fig. 2 Basic inertial generator

A basic inertial generator can be modeled as a mass-spring-damper system, as shown in Fig. 2. This system is composed of a proof mass m, an elastic joint element with stiffness k, and a damper of a damping constant d. The damping on an energy harvester device is due to the combination of the mechanical losses and the energy extracted. The power dissipated into the damper is [7]:

$$P_d = \frac{m\xi_t Y_o^2 \omega_r^3 \omega^3}{[1-\omega_r^2]^2 + [2\xi_t \omega_r]^2} \quad (1)$$

ξ_t is the total damping ratio ($\xi_t = d_t/(2m\omega_n)$), ω_r is the ratio of input frequency ω over natural frequency ω_n Using the acceleration relationship ($a = Y_o\ \omega^2$) and making the input frequency ω equal to the natural frequency ω_n ($\omega_r = 1$) the above equation becomes:

$$P_d = \frac{1}{2} m \frac{a}{\omega^2} \frac{1}{2\xi_t} \quad (2)$$

The last term of Eq. (2) is viewed as the quality factor Q ($Q = 1(2\xi_t)^{-1}$). Eq. (2) illustrates that the power that goes into an energy harvester can be estimated as proportional to the proof mass, the acceleration-squared-to-frequency (*ASTF*), and the Q factor. Therefore, high accelerations and low frequencies produce larger ratios of *ASTF* that are related to a higher available power. Human-based activities belong to the category with large *ASTF* values and low Q while machines are typically associated with the opposite, low *ASTF* and high Q factors. Table 1 summarizes some vibration sources in terms of the frequency, acceleration and acceleration-squared-to-frequency. According to Table 1, the *ASTF* values can be as low as 0.001 for machines, to values as high as 30 for human activities.

Table 1 Acceleration, frequency and *ASTF* values from various sources

Source	Acceleration (G's)	Frequency (Hz)	ASTF
Idle Car (Dashboard)	0.04	38	0.0006
Idle Car (Hood)	0.2	38	0.016
Idle Car (Engine)	0.3	38	0.036
Accelerating Car (Dashboard)	0.12	34	0.006
Accelerating Car (Engine)	0.8	13	0.752
Accelerating Car (Window)	0.06	37	0.001
Driving Car (Hood)	0.7	37	0.202
Driving Car (Dashboard)	0.6	37	0.148
Walking (Below Knee)	1.5	1.2	28.6
Walking (Elbow)	0.6	0.9	6.1
Walking (Shoulder)	0.4	0.9	2.7
Walking (Wrist)	0.4	1.8	1.3
Walking (Head Side)	0.2-0.3	1.8-2.5	0.3-0.5
Keyboard Typing (Back of Hand)	0.8	1.5	6.5

Rearranging Eq. (2) for volumetric power density where $m=\rho V$ (mass = density·volume) leads to:

$$\frac{P_d}{V} = \frac{1}{2} \frac{a^2}{\omega} \rho Q \quad (3)$$

The volumetric power density equation produces the plot of Fig. 3 (using Table 1 as a reference, choosing Q factors from 0.1-1000 and assuming a mass density of 10 g/cm^3 for simplicity). This graph indicates the available energy for a given combination of *ASTF* and Q factors. To clarify, this volumetric power density only considers the volume enclosed by the proof mass and not the generator overall volume as commonly specified. Then, the power limit for an inertial microgenerator based on human motion is found to be close to 1mW/cm^3 (*ASTF* = 0.5, typical for walking, and Q = 1). Therefore, according to the results presented in Fig. 3, energy harvesting from human-based activities could generate as much power as machine-based generators [8].

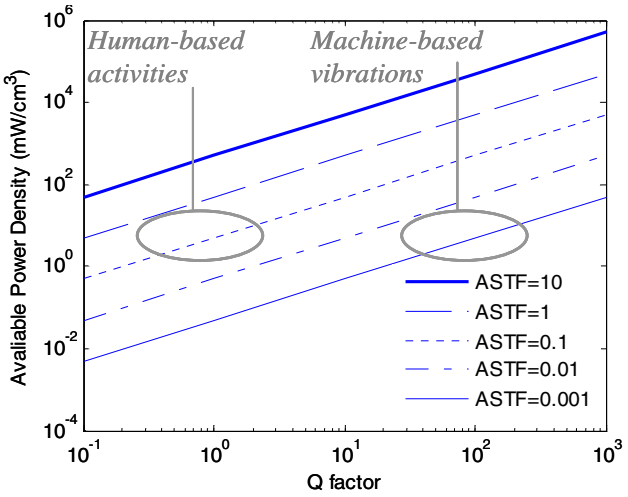


Fig. 3 Available power for vibration-based generators at resonance

III. Generator Design and Results

Human body motion exhibits broad spectral frequency content; hence the above expressions only represent simplified relations that describe the limits of available raw power. Energy generation from human-based activities then poses a challenge to traditional harvesters due to the large displacements and broad frequency spectrum. Hence the need for a generator design that fits the constraints of this type of motion. One such design that is not restricted to operate with small displacements or at fixed frequencies is the pendulum mechanism, which has been extensively used on self-winding wristwatches. The electromagnetic generator design presented here is found to be well suited for these conditions. This energy harvester is designed as a simplified electrical generator that follows the design of small wind-powered generators having multiple arrangements of magnets and coils on their periphery.

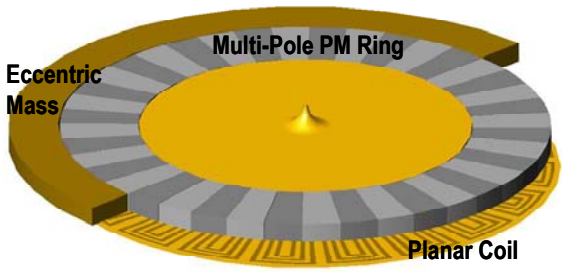


Fig. 4 Generator design

The design of our generator, as shown in Fig. 4, consists of three main components: a rotor composed of a multipole NdFeB permanent magnet (PM) ring with an eccentric weight, a stator with a gear-shaped, multilayer radial planar coil, and a jewel bearing arrangement, not shown. It produces energy by induction when the eccentric weight rotates as a result of an external movement creating a changing magnetic flux on the coils. A preliminary meso-scale prototype (1.5cm^3, 2.2g mass) composed of 20 discrete pole-pairs NdFeB PM (2x1x1mm) inserted in a 25mm slotted PMMA disc with an eccentric brass mass and fitted with a steel spindle was built to test the design concept, Fig. 5. The spindle was mounted between sapphire jewel bearings that were encased in PMMA packaging. The gear-shaped radial planar coil was manufactured using photolithography on a copper-clad polyimide film, Fig. 6.



Fig. 5. From left to right, photo of a prototype generator next to a 2-layer thin-film coil and a multipole NdFeB PM rotor (assembled with individual 1mm^3 magnets). The rotor is fitted with a steel spindle; an eccentric mass can partially be seen behind the magnets.

A maximum power output close to 3.5μW at 2.7Hz has been recorded on a laboratory shaker giving a power density of 2.3μW/cm^3 (10-layer coil, 200μm linewidth and 4 turns, 20 pole-pairs NdFeB PM of 2x1x1mm), Fig.7. Open-circuit voltage of 2.7mVrms was recorded for a 2-layer planar coil (100μm linewidth and 9 turns) with only one pole-pair NdFeB PM (5x1x1mm) when the harvester was placed temporally on the head while walking. It is estimated that the open-circuit voltage for a 4-layer planar coil with 20 pole-pairs can reach 100mV$_{rms}$ for a power output on the order of 100μW when placed on the head. A test performed with 20 pole-pairs NdFeB PM (2x1x1mm) prototype and a 2-layer coil oriented vertically on the lateral hip produced 2.35μW of power (1.6μW/cm^3) while walking, Fig. 8.

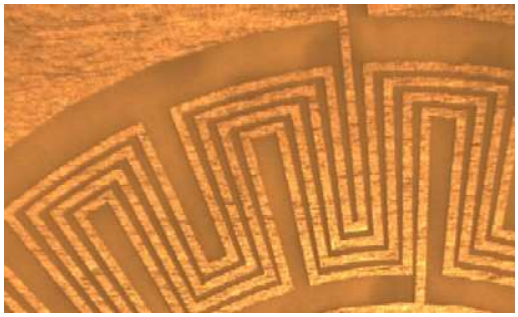


Fig. 6 Photo of a fabricated gear-shaped radial planar coil made of a copper-clad polyimide film with 25µm thick polyimide, 18µm thick copper, 200 µm linewidth, 4 turns, 25mm coil diameter and 4mm radial length

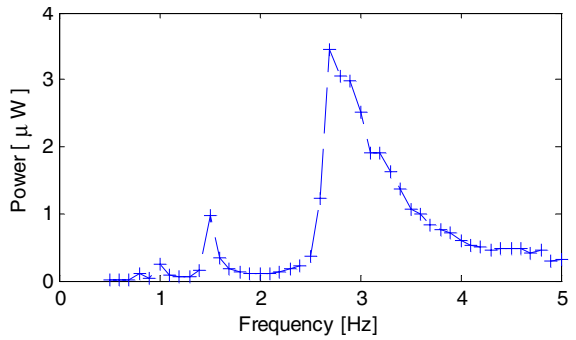


Fig.7 Power output spectrum for 20 pole-pairs NdFeB PM (2x1x1mm) and a 10-layer coil (200µm linewidth,4 turns). R_{load}=44Ω, R_{coil}=44Ω, V_{rms}=10.4mV, P_{pk}=3.45µW

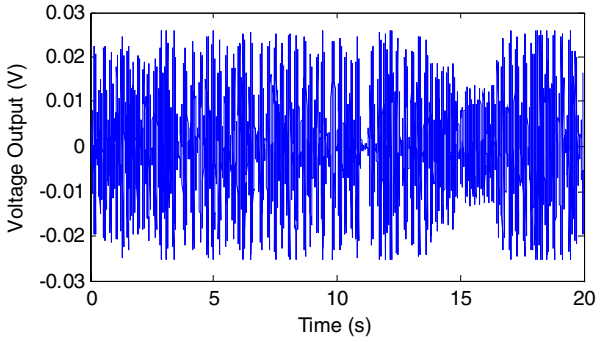


Fig. 8 Voltage output while walking with the prototype generator positioned vertically on the lateral hip. The prototype was tested with a 2-layer coil (200µm linewidth and 4 turns) and 20 pole-pairs NdFeB PM (2x1x1mm). R_{load}=10.5Ω, R_{coil}=11.5Ω, V_{rms}=10.4mV, P=2.35µW

IV. Conclusions

The electromagnetic generator approach presented here is found to be well suited for the large displacements and broad frequency spectrum inherently associated with body movements. The power output from harvesting energy from a moving proof mass is proportional to the *ASTF* and the *Q* factor of the system. Human-based activities exhibit large *ASTF* values and low *Q*, while machines are typically associated with low *ASTF* values and high *Q* factors. This makes it possible to scavenge energy from body motion at comparable levels to that obtained from machines.

This paper reviewed the available energy generated from body motion and the development of a new oscillating generator for human activities. The device presented is composed of a rotor with a multipole PM ring with an eccentric weight and a stator with a radial gear-shaped planar coil. The oscillations of the rotor due to the eccentric mass when subject to body motion induced a voltage on the planar coil. 2.35µW of power have been produced with a preliminary 1.5cm^3 prototype placed vertically on the side of the hip while walking. It is estimated that human motion could generate as much power as 1mW/cm^3.

Acknowledgment

This work was supported by the National Science Foundation under Award Number EEC-0096866.

References

1. Najafi K (2000) Low-power micromachined microsystems, Proc. Int. Symp. on Low Power Electronics and Design, pp 1-8
2. Mallela VS, Ilankumaran V, Rao NS (2005) Trends in cardiac pacemaker batteries. Indian Pacing and Electrophysiology J 4:201-212
3. Goto H, Sugiera T, Harada Y, Kazui T (1999) Feasibility of using the automatic generating system for quartz watches as a leadless pacemaker power source. Med and Biol Eng and Comp 37:377-380
4. Antaki JF, Bertocci GE, Green E et al. (1995) A gait-powered autologous battery charging system for artificial organs. ASAIO J 41:M588-M595
5. Yeatman EM, Mitcheson PD, Holmes AS (2007) Micro-Engineered Devices for Motion Energy Harvesting. IEDM 2007, pp 375-378
6. Arnold DP (2007) Review of Microscale Magnetic Power Generation Magnetics. IEEE Transactions 43:3940-3951
7. El-Hami M, Glynne-Jones P, White NM et al. (2001) Design and fabrication of a new vibration-based electromechanical power generator. Sensors and Actuators A 92:335-342
8. Romero E, Galchev T, Aktakka E et al. (2008) Micro Energy Scavengers. Electronic Proc. COMS 2008
9. Roundy S, Wright PK, Rabaey JM (2003) Energy Scavenging for Wireless Sensor Networks with Special Focus on Vibrations. Kluwer, Norwell

Author: Edwar Romero
Institute: Michigan Technological University
Street: 722 M&M Bldg, 1400 Townsend Dr.
City: Houghton, MI 49931
Country: USA
Email: eromeror@mtu.edu

Economic feasibility studies in the field of Active Implants and Biosensors over Simulations: A methodology for structured and valid results

Ch. Elsner[1], D. Häckl[1] and H. Wiesmeth[1]

[1] Center for Healthcare Management at the Leipzig Graduate School of Management, Leipzig, Germany

Abstract— **The market for active implants and biosensors is of high interest for medical industries. In many cases developments are triggered more by technical feasibility or opinion leader decisions than economic feasibility. As payors and health economic considerations are getting more important in terms of business planning and mid-term reimbursement, exact and (scientific) valid economic feasibility studies are getting more important for all parties.**

Unfortunately, literature mostly provides only single economic considerations targeted on single specific aspects (e.g. cost savings from reduced rehab in a special patient cohort with stroke). To make business planning and payor presentation / negotiation more effective and base the results on more valid information, the Center for Healthcare Management in Leipzig developed a methodology to collect relevant data for those health economic feasibility studies and normalize it to common parameters. This way semi-automated meta-studies can be exported from the database on selected questions and relevant studies.

In a second step, a simulation-tool allows custom-tailored health economic feasibility study results e.g. in terms of a specific population mix of the investigation and/or targeted outcome parameters (e.g. saved cost at Provider, saved transportation cost, reduced rehab-rate in Population etc.). This way product development can already address market-related needs in a very early stage and later products can be marketed more targeted e.g. to a specific population-mix of a single healthcare provider or comparing different outcome parameters.

Keywords— **Economic feasibility, Health Economics, Active Implants, Simulation, Biosensors**

I. Introduction

If one compares the approach taken for economic feasibility studies in the pharmaceutic industries with those taken for Health-Technology Assessment (HTA) in the Medical Devices Industries, there is a huge gap: At this point of time HTA seems to be no integral part of the Device Development in most Research Groups or Companies.

But looking at the market for the reimbursement regulations and the payor´s decision-makers, health economic feasibility analysis becomes an important topic for Providers and Payors in establishing new therapeutic options for patients. The parties having this as part of their business-planning process, normally have small in-house solutions based on a very basic set of considerations. Normally they integrate just prominent and common values form "Landmark Publications" and "Average Populations".

In practice these "Business-Plans" are good for some plain bottom line argumentation in a high level management decision – but they start to fail in specific questions e.g. for specific cost savings for single parties (e.g. "How much money is saved due to altered drug-therapy with the device?"), they fail in the question for a sensitivity analysis (e.g. Taken the worst case studies in the market, how much would the technology still save?) and last, they fail in the adaption to mixed target populations or to specific cost views (e.g. "How much will be saved with the technology in the specific population of the Payor XY at the Provider XZ?").

To overcome those problems and to have a reusable, valid and common datamodel for health economic questions and product development related considerations, at the Center for Healthcare Management in Leipzig a methodology and softwaretool was developed to allow structured simulations for specific health economic questions.

II. Built structure and methodology

The Approach to build the simulation is a 4 step way. Figure 1 shows the schematic process in an overview.

In a first step the different datasources are identified and structured in the central database. Normally there are 4 differents kinds of data being integrated in the dataset.

O. Dössel and W.C. Schlegel (Eds.): WC 2009, IFMBE Proceedings 25/VIII, pp. 257–258, 2009.
www.springerlink.com

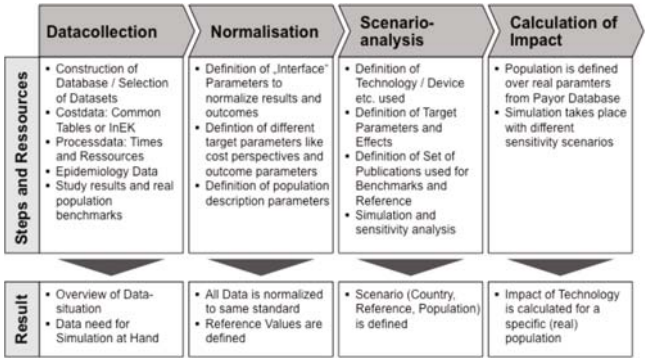


Fig. 1 Approach to build the simulation

Costdata from common cost tables on wages, treatment-cost and cost of equipment, Data on Process Workflows mostly from specific studies (e.g. How long does it take to perform an ECG?), Data on population epidemiology like incidence and prevalence rates for targeted illnesses, and last Data on specific effects of the Technology to investigate in the Simulation.

In a second step the data is "normalized". That means, that all input and outcome values are projected to a similar "normalized" set of parameters. This Normalisation process would for example project different studies comparing the impact of a HF-Monitoring system to the two parameters "Number of Hospitalisations" and "Length of Stay" with and without the technology and would make it compareable to other studies dealing with a compareable technology. The data is then extracted in an XML Format and stored to the database.

```
<Define_Value>XYZ Study</Define_Value>
<Content_Type>LOS without Monitoring<Content_Type>
<Value_MID>11</Value_MID>
<Value_MAX>17</Value_MAX>
<Value_MIN>7</Value_MIN>
</Content_Type>
<RefTime>12 month</RefTime>
<RefPopulation>Post Infarction</RefPopulation>
<Evidence>I b</Evidence>
```

Fig. 2 Coding example in XML Format

In a third step the Scenarioanalysis takes place, which can be different for different adaptions of the simulation. In this step, the technology used or compared are specified, the reference and benchmark publications are chosen and the simulation is run with a different set of minimum and maximum parameters form the chosen publications.

In the forth and last step the simulation is custom-tailored to a specific population-mix according to the parameters delivered e.g. from the payor and the impact on the whole population and single patients is calculated.

III. CONCLUSIONS

With the tool and methodology a custom-tailored health economic feasibility study e.g. in terms of a specific population mix of the investigation and/or targeted outcome parameters (e.g. saved cost at Provider, saved transportation cost, etc.) can be produced.

With the tool and methodology HTA can be integrated in the product development cycle more effectively. New scientific evidence and market-related needs can be integrated fast and easy in a very early stage and products can be marketed more targeted e.g. to a specific population-mix of a single healthcare provider.

The developed data scheme seems to be feasible to extract relevant information from the publications. Mapping the Information from the references still needs sort of interpretation which needs to be commented in both the schemes.

Further developments may include also geoinformation to allow e.g. for telemedical measures the impact projections not only in different target populations but also for different regions and population densities and medical infrastructures.

Author: Dr. Christian Elsner
Institute: Center for Healthcare Management
Street: Jahnallee 57
City: 04109 Leipzig
Country: Germany
Email: christian.elsner@hhl.de

Dual phosphatidylglyceroglycerol-based thermosensitive liposomes for MR-guided chemothermotherapy

T. Wang[1,4], M. Hossann[2], M. Peller[3], H. M. Reinl[3], M. Reiser[3], R. D. Issels[1,4] and L. H. Lindner[1,4]

[1] Department of Internal Medicine III, University Hospital, Grosshadern, Munich, Germany
[2] Max Planck Innovation GmbH, Munich, Germany
[3] Department of Clinical Radiology, University Hospital, Grosshadern, Munich, Germany
[4] CCG Hyperthermia, Institute of Molecular Immunology, Helmholtz Center Munich – German Research Center for Environmental Health, Munich, Germany

Abstract— **Phosphatidylglyceroglycerol (DPPGOG)-based thermosensitive liposomes (TSL) with either encapsulated proton (^{1}H) magnetic resonance (MR) contrast agent gadodiamide (Gd-DTPA-BMA) or doxorubicin (DOX) have been proposed for noninvasive online temperature monitoring and drug release respectively during tumor treatment using chemotherapy combined with hyperthermia. The technique exploits the fact that water exchange between the TSL interior and exterior is increased and/or the encapsulated Gd-DTPA-BMA or DOX is released near the gel-to-liquid crystalline phase transition temperature of TSL, and thus shortens the ^{1}H MR longitudinal relaxation time (T_1) of tissue and increases drug delivery to tissue. In this work, DPPGOG-TSL with encapsulated Gd-DTPA-BMA were mixed with those with encapsulated DOX. The resulting suspension was characterized in vitro by measuring the temperature dependence of the T_1 and DOX fluorescence intensity while temperature was increased from 30 and 46 °C. The measurements revealed that from 37 to 44 °C, the T_1 markedly decreased and DOX fluorescence intensity increased since encapsulated Gd-DTPA-BMA and DOX were simultaneously rapidly released.**

Keywords— **phosphatidylglyceroglycerol, thermosensitive liposomes, gadodiamide, longitudinal relaxation time, proton magnetic resonance.**

I. Introduction

Thermosensitive liposomes (TSL) were designed for enhanced local drug release by hyperthermia (HT), exploiting the fact that TSL-encapsulated drugs are released around the gel-to-liquid crystalline phase transition temperature (T_m) of the lipids [1]. Recently, a new thermosensitive liposomal formulation based on synthetic 1,2-dipalmitoyl-*sn*-glycero-3-phosphoglyceroglycerol (DPPGOG) has been introduced [2]. These DPPGOG-TSL offer the advantage of a prolonged plasma circulation time without the use of poly(ethylene glycol) (PEG)-modified lipids, an efficient and fast drug release around 42 °C without the help of lyso-phosphatidylcholines, and an improved stability at 37 °C compared with the TSL formulations known so far.

In our early work, in vitro stability and content release properties of the DPPGOG-TSL with encapsulated doxorubicin (DOX) have been studied [3]. Moreover, DPPGOG-TSL with encapsulated proton (^{1}H) magnetic resonance (MR) longitudinal relaxation time (T_1)-shortening contrast agent gadodiamide (Gd-DTPA-BMA) have also been characterized in vitro and in vivo [4,5]. In this work, DPPGOG-TSL with encapsulated DOX were mixed with those with encapsulated Gd-DTPA-BMA. The resulting "dual" DPPGOG-TSL were characterized by measuring both the temperature dependence of the T_1 and DOX fluorescence intensity increase during drug release from 30 to 46 °C. The purpose of this work was to explore the potential of the dual DPPGOG-TSL for simultaneous drug release and noninvasive temperature monitoring during chemotherapy combined with HT [6,7].

II. Materials and methods

All ^{1}H MR T_1 measurements were performed on a 0.47 T-NMR-Analyzer (Minispec NMS120, Bruker, Karlsruhe, Germany) in combination with a water bath and a thermostat. DOX release was determined with a fluorescence spectrometer (Varian Cary Eclipse).

The DPPGOG-TSL with encapsulated DOX and Gd-DTPA-BMA (OMNISCAN™, GE Healthcare, USA) were prepared separately by successive lipid film hydration, extrusion, and dialysis as described detailed in [3,4]. For measurement, both DPPGOG-TSL formulations were diluted to the same phospholipid concentration in fetal calf serum (FCS)/HN buffer 1:1 (v/v).

To measure the temperature dependence of the T_1 of dual DPPGOG-TSL, the temperature of a sample was increased from 30 to 46 °C. The sample was incubated for 10 minutes at the desired temperature in order to reach the thermal

O. Dössel and W.C. Schlegel (Eds.): WC 2009, IFMBE Proceedings 25/VIII, pp. 259–260, 2009.
www.springerlink.com

equilibrium and the T_1 was acquired once at this temperature. To measure the DOX release at the same temperature, a subsample was subsequently taken and cooled down immediately in an ice-water bath. Afterwards, the corresponding DOX fluorescence intensity was determined.

III. Results and discussion

The temperature dependence of the T_1 of dual DPPGOG-TSL is shown in Figure 1. T_1 values ± standard deviation (SD) of a sample were measured while heated from 30 to 46 °C. During heating from 37 to 44 °C, the encapsulated Gd-DTPA-BMA was rapidly released from dual DPPGOG-TSL due to the gel-to-liquid crystalline phase transition of phospholipid membrane. The rapid Gd-DTPA-BMA release resulted in the drastic "sigmoid" T_1 shortening of the sample. The release began at approximately 38.6 °C with a T_1 of 1440 ± 30 ms, reached a turning point at 39.6 °C with 503 ± 7 ms, and ended at 41.5 °C with 404 ± 6 ms.

For comparison, the temperature dependence of the released DOX fluorescence intensity of dual DPPGOG-TSL is also plotted in Figure 1. Released DOX fluorescence intensity ± SD of the same sample were measured while heated from 30 to 46 °C. Similarly, the encapsulated DOX was rapidly released from dual DPPGOG-TSL during heating from 37 to 44 °C. The release began at approximately 38.6 °C with a released DOX fluorescence intensity of 54 ± 1 a.u., reached a turning point at 39.6 °C with 135 ± 2 a.u., and ended at 41.5 °C with 229 ± 4 a.u..

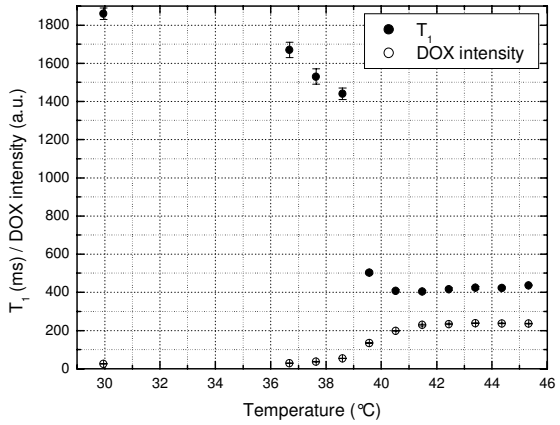


Fig. 1 Temperature dependence of the T_1 and DOX fluorescence intensity of dual DPPGOG-TSL while heated from 30 to 46 °C

IV. conclusions

The dual DPPGOG-TSL with encapsulated Gd-DTPA-BMA and DOX were successfully characterized in vitro by measuring the temperature dependence of the T_1 and released DOX fluorescence intensity of dual DPPGOG-TSL samples between 30 and 46 °C. Below 37 °C, the DPPGOG-TSL released negligible amounts of Gd-DTPA-BMA or DOX. From 38 to 44 °C, DTPA-BMA and DOX were rapidly released. These preliminary results showed that the dual DPPGOG-TSL are promising and have the potential to provide a novel tool for simultaneous noninvasive MR thermometry and drug dosimetry during tumor treatment using chemotherapy combined with HT.

Acknowledgment

The authors thank Dr. Hansjörg Eibl (Max Planck Institute for Biophysical Chemistry, Göttingen, Germany) for the synthesis of DPPGOG and Anja Zengerle for technical assistance. This work was financially supported by the Helmholz Gemeinschaft (VH-VI-140) and the German Research Foundation (SFB 455).

References

1. Yatvin MB, Weinstein JN, Dennis WH et al. (1978) Design of liposomes for enhanced local release of drugs by hyperthermia. Science 202:1290–1293
2. Lindner LH, Eichhorn ME, Eibl H, et al. (2004) Novel temperature-sensitive liposomes with prolonged circulation time. Clin Cancer Res 10:2168–2178
3. Hossann M, Wiggenhorn M, Schwerdt A et al. (2007) In vitro stability and content release properties of phosphatidylglyceroglycerol containing thermosensitive liposomes. Biochim Biophys Acta 1768:2491–2499
4. Wang T, Hossann M, Reinl HM et al. (2008) In vitro characterization of phosphatidylglyceroglycerol-based thermosensitive liposomes with encapsulated ^{1}H MR T_1-shortening gadodiamide. Contrast Media Mol Imaging 3:19–26
5. Peller M, Schwerdt A, Hossann M et al. (2008) MR characterization of mild hyperthermia-induced gadodiamide release from thermosensitive liposomes in solid tumors. Invest Radiol 43:877–892
6. Viglianti BL, Abraham SA, Michelich CR et al. (2004) In vivo monitoring of tissue pharmacokinetics of liposome/drug using MRI: illustration of targeted delivery. Magn Reson Med 51:1153–1162
7. Viglianti BL, Ponce AM, Michelich CR et al. (2006) Chemodosimetry of in vivo tumor liposomal drug concentration using MRI. Magn Reson Med 56:1011–1018

Author: Tungte Wang
Institute: Department of Internal Medicine III, University Hospital Grosshadern, University of Munich
Street: Marchioninistrasse 15
City: D-81377 Munich
Country: Germany
Email: tungte.wang@med.uni-muenchen.de

Monitoring adherent cell cultures in microtiter-plates by a wireless sensory system

J. Wissenwasser[1], M. Milnera[1], L. Farmer[2], C. Höpfner[2], M. Vellekoop[3] and R. Heer[1]

[1] Nano-Systems, [2] Life Science of the Austrian Research Centers GmbH, Vienna, Austria
[3] Inst. of Sensor and Acutator Systems, University of Technology, Vienna, Austria

Abstract — **The development of drugs, medicine products or chemicals demands high throughput systems and processes for the active substance testing at cells and tissues. Some systems, where Interdigitated Electrode Structures (IDES) are integrated in the bottom of the wells of customized microtiter-plates, are already available. In this work we present a sensor system which is based on insets for state-of-the-art micro-titer-plates. Each inset is carrying electronic circuitry and an IDES acting as sensor. These units work without a permanent energy source and communicate through a wireless interface with a reader based on Radio Frequency Identification RFID. Alterations of the cell metabolism are simultaneously reflected by changes of the electrical impedance which is measured by the sensors. Thus, this non-invasive monitoring system allows keeping track on the effects of toxic substances within the same cell culture up to two weeks.**

Keywords— **Biosensor, wireless, RFID, Impedance measurement, cell cultures**

I. Introduction

Impedance measurements with Interdigitated Electrode Structures (IDES) are suitable to monitor concentration, proliferation and the physiologic condition of adherent cell cultures. Mostly the impedance is measured with sinusoidal probe signals at frequencies between 1 kHz and 1 MHz. The isolating properties of the cell membranes affect the overall impedance of the sensor system. This reflects morphological changes. Details on this already established technique can be found in e.g.[1], [2], [3] and [4].

II. Sensor Design

The basic layout of an IDES uses electrodes with comb-shaped electrode-areas. The "fingers" of those electrodes are interdigitated.

Most layouts, like in [2] or [3], rely on fingers whose electrode and gap widths are as large or even larger than the cells´ diameters. The gaps and widths range from 23 µm [3] to 50 µm [2]. The sensors used in this work are designed with an electrode width of 50 µm and an electrode-electrode-gap of 50 µm. In chapter IV an impedance model will be discussed.

A. Production details

The glass AF45 from Schott AG (www.schott.ag) with a thickness of 0.5 mm is used as substrate. The metallization layers are fabricated using a LOR (lift off resist)-process. The glass substrates are spincoated with lift off resist *LOR 3A* and positive-tone photoresist *AZ MiR 701* by MicroChemicals GmbH (www.microchemicals.com). The positive resist is patterned by photolithography. During the development of the resist, the lift off resist is underetched. Subsequently, a 10 nm thick Ti adhesion layer followed by a 150 nm thick Au-layer is deposited by a Sputter-process. The underetched resist forms a *shadow mask* for the metal deposition and allows a perfect lift off of the residual resists together with the excessive metallization by an acetone-treatment.

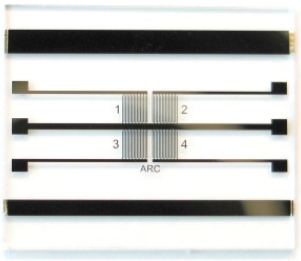


Fig 1: Sensor element with a overall size of 15x18 mm^2 carrying 4 sensor fields à 1.8 x 2 mm^2. The fingers in each sensor field have widths and gaps of 50 µm.

The sensor element shown in Fig 1 carries four individually addressable fields with a common line in the middle. Each of them measures 1.8 x 2 mm^2. The rather broad metal strips on the top and the bottom are introduced to facilitate the lift-off process.

B. Sensor device assembly

The system-concept provides sensor devices to be used as detachables on the measurement device, a so called tag, which is introduced in the next chapter. Fig 2 shows the components of such a sensor device.

O. Dössel and W.C. Schlegel (Eds.): WC 2009, IFMBE Proceedings 25/VIII, pp. 261–264, 2009.
www.springerlink.com

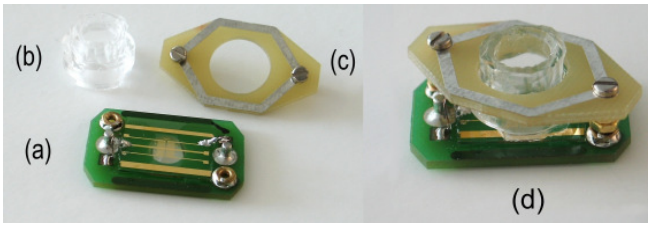


Fig 2: Sensor device components. (a) PCB with jackets and the sensor element glued on it, (b) PDMS-tube, (c) clamp plate, (d) assembled device.

A printed circuit board (PCB, Fig 2a) of type FR4 (epoxy resin impregnated fiberglass) is used as carrier. The sensor is bonded on it with silicone (polydimethylsiloxane, PDMS, derivative *TSE399* from *GE Bayer Silicones*). The PCB has a window underneath the sensor fields, thus an inverted microscope can be used for optical checks. Jackets for the mechanical and electrical connection to the tags are placed on the left and the right side of the PCB. The electrical connections to the metal pads of the sensor fields are done with thin Ag-coated copper wires.

The tube, which forms the well for the uptake of cells, (Fig 2b) is also made of a PDMS (*Sylgard 184 silicone elastomer* from *Dow Corning*). PDMS is a well known material for the production of microfluidic channels [5] and to our knowledge no negative effects on cell growth have been found so far. The clamp plate (Fig 2c) is screwed on the carrier and fixes the PDMS tube on the sensor. This clamping technique allows a disassembling to provide access to the sensor surface for, e.g., cleaning procedures or microscopic investigations. The volume of the well, which is formed by the sensor element as the bottom and this tube, allows a filling volume of 300 µl to 400 µl. The exposed bottom area is 50 mm^2 at the actual tube diameter of 8 mm.

III. IMPEDANCE MEASUREMENT SETUP

A. Measurement device

The overall system has a modular design with the sensor device as a detachable element. It is mounted onto a tag, which contains all the electronics to measure the impedance of the sensor device's fields with a sinusoidal probe signal at a frequency of 10 kHz and a voltage amplitude of 50 mV. The measurement system was demonstrated (with 1 kHz signal frequency) and described in [6].

Data transfer from and energy-transfer to the tag are established via an RFID-interface at 13.56 MHz which is an already established technique for sensory systems [7], [8]. Fig 3 shows the realization of a RFID tag without and with the sensor device.



Fig 3: A single tag (left) and with a sensor device attached on it (right).

This tag is designed to fit into a well of a 6-well microtiter-plate. The plate acts as handling device and protection unit against possible contamination of the adhered cell culture.

Like the sensor's carrier the tag has a window in the middle to provide access for inspections with an inverted microscope. This can be done while leaving the sensor elements in the titer-plate which simplifies handling.

B. Measurement system and test setup

The measurement itself needs a RFID-based reader system where six antenna coils are positioned directly underneath the wells of the microtiter-plate. Fig 4 shows a schematic and the realized system.

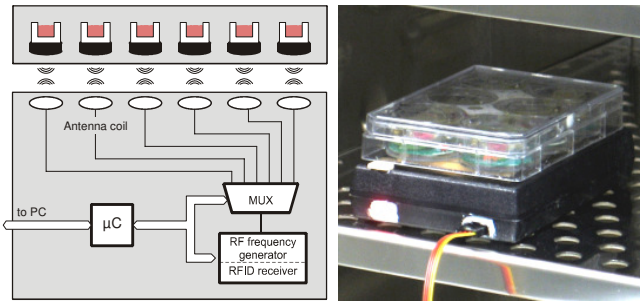


Fig 4: Left: Schematic of the reader unit with a microtiter-plate on it. Right: Real system inside a CO_2-incubator.

IV. IMPEDANCE MODEL

A simple impedance model with an electrical equivalent circuit is introduced to discuss the impedance measurements on cell cultures. The influence of the cells on the measured impedance is mostly determined by their cell membranes. Generally their electrical properties evoke higher impedance than the surrounding culture medium at certain frequencies. If the cells adhere on the electrodes the electric current will then mainly pass at the residual electrode area which causes an increased ohmic resistance compared to a cell-free electrode at low frequencies 2].

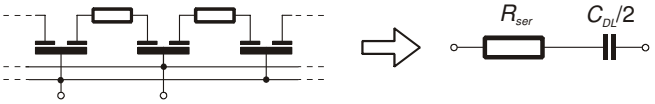


Fig 5: Impedance model. On the left side the impedance parts are shown in their position on the electrodes, the right side is the overall impedance.

Fig 5 shows a simple model to describe the ionic conductivity of the culture medium, represented by R_{ser}, and the electrochemical double layer (DL), represented by $C_{DL}/2$. The DL exists on both electrodes, so this representation shows the effective value of two capacitors lying in series if both electrode areas are of the same size, which is the case for our sensor fields. The electrical impedance is given by

$$Z = R_{ser0} + (j\omega \cdot C_{DL}/2)^{-1} \quad (1)$$

The DL has a penetration depth of 1 to 2 nm from the electrodes into the culture medium and should not be affected by the cell membranes, which are located about 15 nm and more above the electrodes [2], [9]. Our measurement results confirm this assumption.

Fig 6 shows a section of an IDES-simulation for two electrodes on the bottom with voltages $+V$ and $-V$ applied.

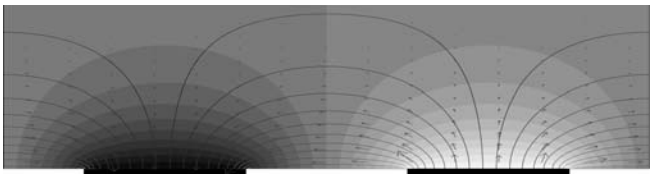


Fig 6: Cutout of IDES-model with two electrodes (black), current density vectors (arrows of proportional length), potential ranges (contour) and electrical displacement (continuous lines). Width-to-Height-ratio is 2.

The sensitive height of an IDES is about the same length as the center-to-center-distance of the electrode-fingers which is 100 µm in our sensor design. This means that also the sensing of all kind of influence due to the properties of culture medium is limited to that height.

V. RESULTS AND DISCUSSION

All tests were performed in an incubator at 37 °C in a 5 % CO_2 atmosphere. As test system mouse embryo cells, 163-CCL Balb/3T3 clone A31, obtained from the American Type Culture Collection. They were cultured in DMEM (**D**ulbecco´s **M**odified **E**agle **M**edium) supplemented with 10 % fetal bovine serum (FBS) and antibiotics. Only one sensor field per sensor element was in use.

The results of the first experiment are shown in Fig 7. 150 µl culture medium per sensor device (without cells) were used to detect each sensor's blank impedance. It took about 2 h until the values were stable. The serial capacitance of samples #c0 and #c1 were about half the value of the other sensors. Further experiments showed that this was caused by a residual contamination which was left after the cleaning in an ultrasonic bath with acetone, isopropyl and DI water.

With the initial values of the higher capacitances of about 90 nF the area-related double layer capacitance C_{DL}' can be calculated. The active area of one electrode is the 4th part of the whole sensor-field-area of 1.8 x 2 mm^2.

$$C_{DL}' = (2 \cdot 90\ \text{nF}) / (9 \cdot 10^{-7}\ \text{m²}) = 200\ \text{mF/m²} \quad (2)$$

This meets the reported range from 50 to 500 mF/m^2 in [10] quite well.

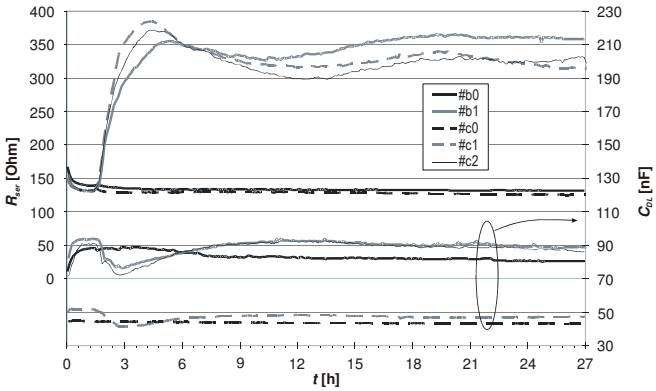


Fig 7: First experiment. Impedance model data vs time.

After 2 hours 150 µl cell suspension with $5 \cdot 10^4$ cells per sample were added to the samples #c0 to #c2. This resulted in confluent layers without further cell growth. Samples #b0 and #b1 got 150 µl medium without cells and were used as reference blanks to detect changes of the culture medium.

It is quite interesting that during the settling time of the cells the capacitance value dropped, but later recovered to values close to their previous data and did not further change much. It may be that during cell settling the DL was disturbed. In parallel the resistances increased, reached peak values and then relaxed at values around 300 Ω. It is not yet clear what causes this behaviour. One explanation could be the transition of the cell shape from spherical to flat in the adhered state.

In a second test four of the previous sensors devices were cleaned and two of them reloaded with $5 \cdot 10^2$ cells per well. With a doubling time of about 18 h at least

$18\,\mathrm{h} \cdot \log_2(5{\cdot}10^4/5{\cdot}10^2) \approx 120\,\mathrm{h}$ would be necessary to achieve the same signal level as in the first measurements.

The measurement was again started with culture medium to provide reference levels. Here it can be seen that C_{DL} is comparable to the values of the cleaned sensors of the first measurement. 4 hours later $5{\cdot}10^2$ cells/well were seeded at samples #c0 and #c1 in a suspension of 150 µl culture medium. The blanks #b0 and #b1 did only get culture medium without cells.

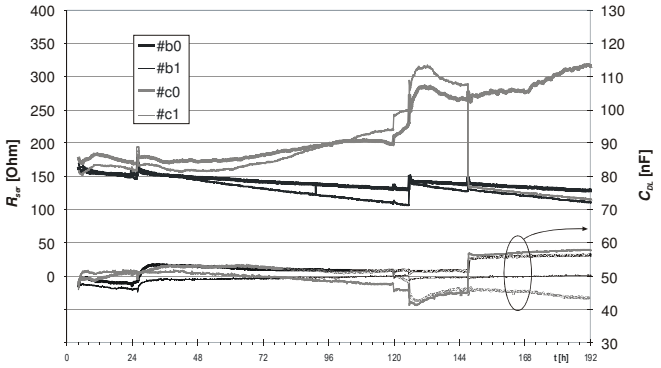


Fig 8: 2nd experiment. Impedance model #0 data vs time.

After 24 hours, the culture medium was exchanged. It was found that about 30 µl culture medium per well evaporated during the first day. After 119 hours an optical check was done where about 50 % confluence was found on all three samples. It has already been shown that during these checks the temperature is reduced to room temperature, so that impedance changes occur ([2], [3]). After 125 h culture medium was changed again. The ohmic part on all samples changed significantly. This can be explained by two reasons: The initial change was because the new medium had a lower ionic concentration as the evaporated and therefore the ionic resistance increased. This can be evaluated by the relative changes of the blank resistances compared to the changes of the sensors with cell cultures. The DL is not that sensitive to changes of the ion concentration [10]. The second reason is that after 4 days the culture medium did not have enough nutrients for further cell growth. The new medium allowed the cells to grow again.

After 145 h culture medium was changed again where 0.1 vol% of Triton X-100 were added at the samples #b0 and #c1. Triton X-100 dissolves membrane proteins and cells die. The serial resistance of #c1 drops within 10 minutes to the value range of the blanks. Further C_{DL} sightly increases on both samples while the second blank #b1 was still at the same value. This is a hint that the Triton X-100 may influence the EcDL. The same behaviour was in principle shown in [2].

The samples #b1 and #c0 did not get the Triton X-100-treatment and #c0 showed cell growth for 2 further days. This also assures the previous assumption that the late medium change suppressed proliferation. The experiment was then stopped after an overall time of 8 days.

VI. CONCLUSION

A wireless impedance measurement system was presented which is able to detect cell growth on multiple sensors. The assembled sensor devices were demonstrated to be useable for long-term measurements. Furthermore the effect of evaporated culture medium and its replacement by fresh medium on the measured impedance has been shown.

This shows that the parallel measurement of blanks (sensors with culture medium without cells) is a necessity to allow a differentiation of the impedance change due to cell growth and the properties of the culture medium.

REFERENCES

1. J. Wegener et al.: *Electric Cell-Substrate Impedance Sensing (ECIS) as a Noninvasive Means to Monitor the Kinetics of Cell Spreading to Artificial Surfaces.* Exp. Cell Res. 259, 158-166, 2000
2. R. Ehret et al.: *Monitoring of cellular behaviour by impedance measurements on interdigitated electrode structures.* Biosens. Bioelec 12, 29-41, 1997
3. L. Ceriotti et al.: *Assessment of cytotoxicity by impedance spectroscopy*. Biosensors and Bioelectronics 22 (2007) 3057–3063
4. P. Van Gerwen et al.: *Nanoscaled interdigitated electrode arrays for biochemical sensors*. Sensors and Actuators B 49, 73-80, 1998
5. G. M. Whitesides. *The origins and the future of microfluidics.* Nature 442, p368-373, 2006
6. J. Wissenwasser et al.: *Online-Monitoring von Zellkulturen für High-Throughput Systeme auf der Basis von RFID-Technologie*. Tagungsband Informationstagung Mikroelektronik ME 08, ISBN: 978-3-85133-049-6
7. K. Finkenzeller: *RFID Handbuch*. 4. Auflage, ISBN-10: 3-446-40398-1, ISBN-13: 978-3-446-40398-7, Carl Hanser Verlag München Wien
8. US 2007/0001850 A1: *Wireless Temperature Monitoring For An Electronic System.*
9. R. Zaidel-Bar et al.: *Hierarchical assembly of cell–matrix adhesion complexes*. Biochemical Society Transactions, 32:416–420, 2004
10. Haman C. et al.: *Elektrochemie I*, 2. Auflage, VCH Verlagsgesellschaft mbH, 1985, ISBN: 3-527-21100-4

Author: Jürgen Wissenwasser
Institute: Nano-Systems, Austrian Research Centers GmbH – ARC
Street: Donau-City-Straße 1
City: A-1220 Wien
Country: Austria
Email: juergen.wissenwasser@ait.ac.at

In-vitro characterization of an implantable thermal flow sensor for hydrocephalus

J. Burger[1], T. Bork[1], A. Hogg[2], M. Lempen[2], D. Mueller[2], D. Joss[3], T. Bardyn[4], P. Buechler[4], H. Keppner[3] and Y. Tardy[1]

[1] Codman Neuro Sciences sàrl, Le Locle, Switzerland
[2] Berne University of Applied Sciences, Biel, Switzerland
[3] Neode, Haute Ecole ARC Ingénierie, La Chaux-de-Fonds, Switzerland
[4] Institute for Surgical Technologies and Biomechanics ISTB, University of Bern, Bern, Switzerland

Abstract— **An implantable thermal flow sensor for the treatment of hydrocephalus has been developed. The sensor uses passive telemetry at 13.56 MHz for power supply and read out of the measured flow rate. The in vitro performance of the sensor has been characterized using artificial Cerebrospinal Fluid (CSF) with increased protein concentration and artificial CSF with 10% fresh blood. No drift could be observed in the flow sensor measurement which could be associated to a deposition of proteins at the sensitive surface walls of the packaged flow sensor.**

Keywords— **implant, flow sensor, hydrocephalus, protein adsorption**

I. INTRODUCTION

Hydrocephalus is one of the most common congenital disorders of the central nervous system. Cerebrospinal Fluid (CSF) is produced by secretory cells of the choroid plexus at a rate of approximately 20 ml per hour, circulates through the ventricular system and is finally absorbed into the venous system via the superior sagittal sinus.

Hydrocephalus occurs when there is an imbalance between the amount of CSF that is produced and the rate at which it is absorbed. The occurrence of hydrocephalus in newborn children is about 1 out of 500 – 2'000 [1, 2]. The treatment of hydrocephalus requires the implantation of a shunt for fluid drainage. Per year, more than 100'000 shunt valves are implanted worldwide. However, malfunctioning of the shunt catheter cannot be excluded which might lead to severe complications especially for children [3].

In order to allow a better management of hydrocephalus shunted patients, a thermal flow sensor which will be implanted close to the shunt valve has been developed. The sensor will allow an improved long-term monitoring of the functioning of the valve as well as a better understanding of the flow of CSF. Whereas microsystems including pressure sensors have been developed for intracranial pressure monitoring [4-6], flow sensing of CSF is currently done using MRI methods [7].

II. MATERIALS AND METHODS

A. Sensor description

The implant consists of three main parts: a thermal flow sensor, a microcontroller and a RF section (Fig. 1). The flow sensor (Sensirion AG, Stäfa, Switzerland) is realized on a CMOS silicon chip that contains the sensor as well as all necessary electronics to treat the sensor signal (ADC, linearization, amplification, temperature compensation, calibration memory). The sensors have been calibrated with a specification requirement of +-10% for a flow range between 2 ml/h and 40 ml/h.

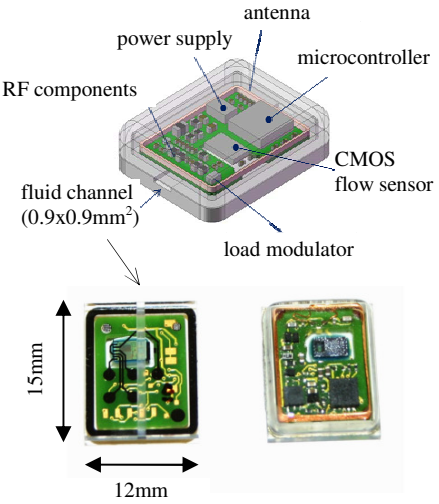


Fig.1: Components of the implantable thermal flow sensor. The height of the encapsulated implant is 4.5 mm. Bottom left: Bottom view of the packaged sensor showing the rectangular flow channel. Bottom right: Top view of the packaged flow sensor

One of the key features of the sensor is the thermal flow measurement which is done through the Pyrex glass substrate of 100 um thickness. Using this configuration, the thermal sensors and the heaters are not directly exposed to

O. Dössel and W.C. Schlegel (Eds.): WC 2009, IFMBE Proceedings 25/VIII, pp. 265–268, 2009.
www.springerlink.com

the body fluids. Therefore, no coating or passivation of the sensors and heaters is needed and electrical feed-throughs to the fluidic chamber are avoided. In that way, a highly reliable and long-term biocompatible implant could be realized which is especially important as the sensor will be inside the body for up to 10 years or even longer [8].

In order to provide the implant with energy and to read out the measured flow rate, passive telemetry is used at a RF frequency of 13.56 MHz [9]. The RF section of the implant is responsible for extracting energy for the implant, for transmitting the level of RF induced voltage to the microcontroller as well as for modulating the FSK signal for communication with the external reading unit.

B. In-vitro characterization of the implantable flow sensor

Thermal flow sensors with sensing and heating elements attached to the walls of the fluid channel are sensitive to modifications of the sensing surface area. A potential protein or blood component adsorption especially during the first days after implantation with a risk of elevated protein concentration and blood within the CSF could have an influence on the flow sensor response.

In order to investigate the sensor performance under worst case situations, the flow rate of the sensor was measured using elevated protein concentration and blood content in CSF.

The composition of normal CSF is close to that of ultrafiltrate of plasma and has a protein concentration of less than 0.5% of plasma [10]. The protein concentration is low with about 0.2 g/l. In order to accelerate the protein absorption, a protein concentration increased by a factor of 10 to reach 2 g/l was used for the artificial CSF in these tests.

Due to patients who have hydrocephalus as a result of a haemorrhagic event such as periventricular haemorrhage in the premature neonate, or subarachnoid haemorrhage in the adult, CSF containing a profile of proteins different from that of “normal” CSF must be taken into consideration as well.

For the testing, the following solutions were used:

- artificial CSF with 2 g/l protein (Albumin from human serum)
- artificial CSF with 2 g/l protein (Albumin from human serum) and 10% fresh blood
- sterile water with 0.65% Sodium azide as reference solution

In order to simulate a potential protein deposition that might affect the sensor function after e.g. a subarachnoid haemorrhage, fresh human blood was drawn from a vein and added immediately to the warmed artificial CSF solution in order to avoid clotting. As the mixture tends to degrade after about 24hrs at 37ºC due to break up of red blood cells, the solution was changed daily.

Table 1 Composition of artificial Cerebrospinal fluid

Chemical Name	Formula	Conc. in CSF [g/l]
Sodium chloride	NaCl	8.660
Potassium chloride	KCl	0.224
Calcium chloride dihydrate	$CaCl_2$-$2H_20$	0.206
Magnesium chloride hexahydrate	$MgCl_2$-6H20	0.163
Sodium phosphate monobasic monohydrate	NaH_2PO_4-H_20	0.027
Di-Sodium hydrogen phosphate heptahydrate, acs	Na_2HPO_4-$7H_20$	0.214
Sodium Azide 0.1 M Solution	N_3Na	0.77 ml
D-(+)-Glucose	$C_6H_{12}O_6$	0.600
Urea	CH_4N_2O	0.201
Albumin (from human serum)		2.000
Gamma-globulin from human blood		0.015

C. Fluidic test setup

The fluidic circuit for characterization of the implantable flow sensors consists of a tubing pump which pulls the test liquids artificial CSF, artificial CSF with 10% fresh blood and sterile water as reference solution through three parallel fluidic circuits (Fig. 2). The test setup was kept in an oven at 37ºC. Once a day, the flow sensor measurement was

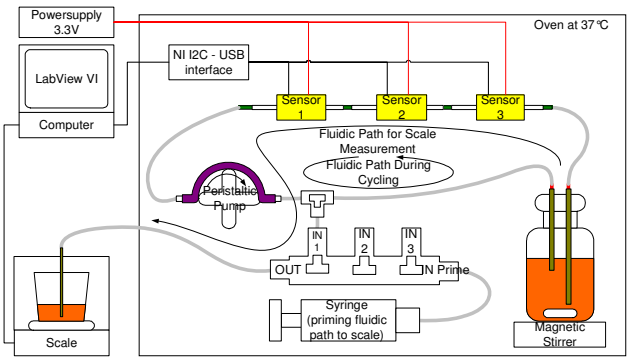


Fig. 2: Test setup for in-vitro characterisation of the implantable flow sensor. Only one fluidic circuit is shown

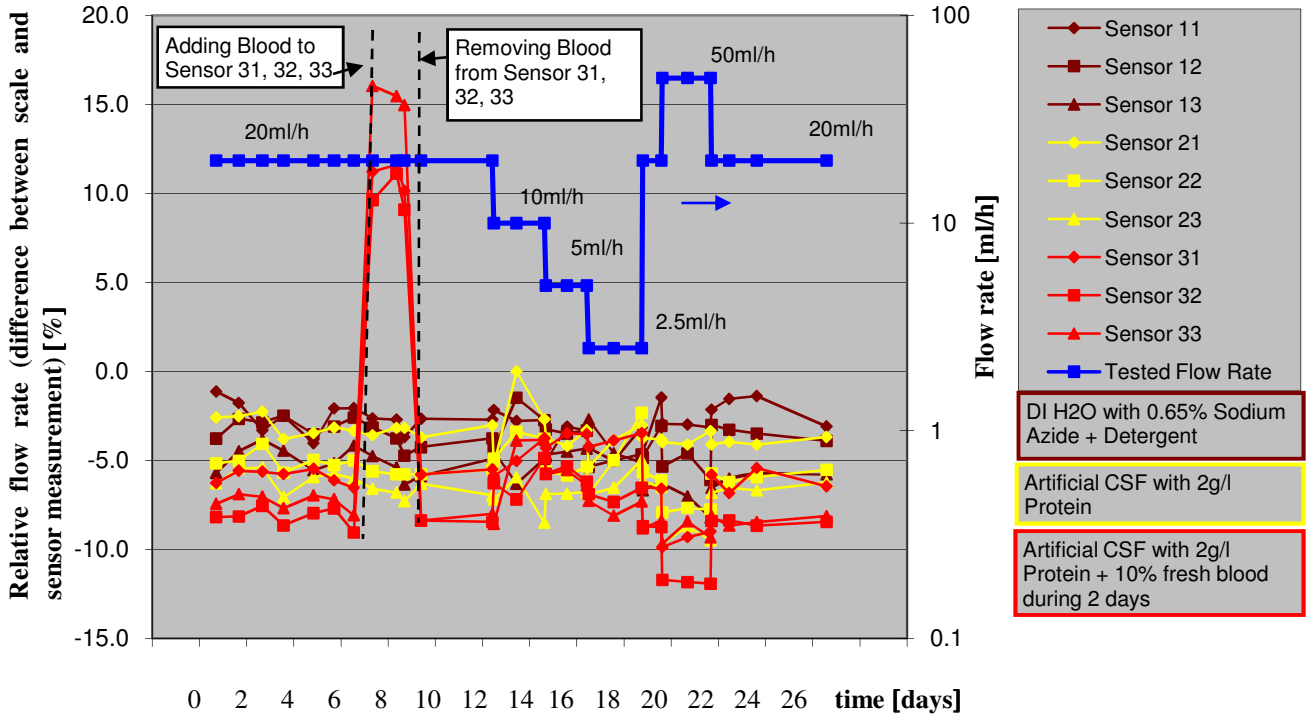


Fig. 3: Relative flow rate of the implantable thermal flow sensor as a function of time. In test circuit 3 (sensors 31, 32, 33), 10% fresh blood was temporarily added.

compared to a reference scale measurements (gravimetric method). During a period of 180 s, the flow sensor reading was taken at a frequency of 10 Hz and averaged. The scale reading was taken in parallel and the flow was calculated by taking the start reading and the end reading of the balance. A relative flow rate in % was calculated by taking

$$\frac{\text{flow rate (flow sensor)} - \text{flow rate (scale)}}{\text{flow rate (scale)}} \cdot 100$$

In order to simulate a continuous use of the flow sensor during the test period of 26 days, the heater of the flow sensor was periodically turned on for 5 minutes and then turned off for 10 minutes in between the scale measurements. The power consumption of the CMOS flow sensor was measured to be 16.3 mW at a supply voltage of 3.3 V. The power consumption of the ultra-low power microcontroller was 2.87 mW.

III. RESULTS

In Fig. 3 the relative flow rate for all sensors for a test period of 26 days is shown as the difference between the flow sensor measurement and the comparative scale measurement. Within those 26 days the flow rate has been varied from the nominal flow of 20 ml/h down to 2.5 ml/h and up to 50 ml/h in order to characterize the relative flow rate of the flow sensors at different flow rates within the operating range. It can be seen that there is no apparent drift in any of the 3 fluidic circuits, especially when only comparing the beginning and the end of the testing where the 20 ml/day flow rate was tested.

The average of all relative flow rates (261 values) shown in Fig. 3 is offset by –5.4% for a test temperature of 37°C. As the flow sensors have been calibrated at a temperature of 22ºC, the influence of temperature on the difference between the scale measurements and the flow sensor measurements was evaluated.

For that purpose, 3 sensors have been characterized at 2 different flow rates of 5 ml/h and 10 ml/h at temperatures 22ºC and 37ºC. The temperature offset of the relative sensor flow rates at 37°C is about 6.3% compared to the relative sensor flow rates at 22°C.

A temperature compensation of the offset of –5.4% at 37°C with the temperature offset of +6.3% leads to a compensated average of all relative flow rates of +0.9%.

The reference liquid containing sensors (brown in Fig. 3) as well as the CSF/protein containing sensors (yellow in

Fig. 3) are maintaining essentially the same difference between sensor and scale measurements throughout the test.

Only the sensors of the fluidic circuit that had temporarily 10% fresh blood added to it (red in Fig. 3) show an increase of relative flow rate of ~20% to ~25% during the time the blood is present. If blood components were deposited on the channel wall, this additional layer would decrease the heat that is transferred to the fluid which would result in a decreased measured flow rate of the flow sensor.

The observed increase of flow rate can be explained by the settling of the heavier red blood cells on the bottom of the flow channel due to the low flow rate used. This sedimentation could be observed visually in the channel tubing. The viscosity of this sediment becomes more elevated resulting in a lower flow rate near the bottom of the flow channel. Since the overall volume of fluid passing through the channel is kept constant by the peristaltic pump, the flow rate at the top of the flow channel, where only the lower viscous CSF-plasma mix is flowing, increases accordingly.

Comparing the relative flow rates before and after the blood was added/removed even the flow sensors in the fluidic circuit with artificial CSF and 10% blood don't exhibit a drift. Furthermore when looking at Fig 3 one can see that there is no major influence on the relative flow rate when tested between 2.5 ml/day and 50 ml/day. All measured differences between sensor and scale measurements for all sensors remain within 0% to –10% except sensor 32 with ~-12% during the 50ml/day measurement.

This deviation might be explained by a misaligned fluidic connection it was found to be very important to have a laminar flow at the sensor location which is depending on the fluidic connection and the flow rate used.

IV. CONCLUSIONS

No drift could be observed in the flow sensor measurements which could be associated to a deposition of proteins even though the tested protein level was about 10 times higher than the normal protein level in human beings. Even if a protein layer has been deposited on the flow channel wall during the 26 days of exposure, its thickness is not sufficient to have an influence on the sensor reading.

Blood which is not homogeneously mixed in the fluid can temporarily disturb the flow sensor reading. However in a real life situation this is not relevant as the patient is moving and the fluid remains mixed. Blood does not create any permanent sensor changes due to deposition of blood components on the flow channel wall.

The flow sensor specification requirement of +-10% for a flow range between 2 ml/h and 40 ml/h. could be confirmed at test conditions of 37°C.

ACKNOWLEDGEMENT

This research was supported by the Swiss innovation promotion agency (grant CTI #8558.1 LSPP-LS).
The authors would like to thank J. Sounggalon Siringoringo for the three dimensional view of the implant and Dr. Roger Bayston for the recommendations concerning the test liquids and their preparation.

REFERENCES

1. Murshid WR, Jarallah JS, Dad MI (2000), Epidemiology of infantile hydrocephalus Saudi Arabia: birth prevalence and associated factors, Pediatr Neurosurg 2000;32:119–123.
2. Persson E-K; Anderson S, Wiklund L-M, Uvebrant P, Hydrocephalus in children born in 1999-2002: epidemiology, outcome and ophthalmological findings. Child's Nervous System, 23 (10), pp. 1111-1118
3. Oikonomou J, Aschoff A, Hashemi B, Kunze S (1999), „New Valves - New Dangers? 22 Valves (38 Probes) Designed in the Nineties in Ultralong-Term Test (365 Days)", European Journal of Pediatric Surgery 9, Suppl. I, pp. 23-26
4. Ko WH, Leung A M, Cheng E and Lorig R J (1981), Intracranial pressure telemetry system: I Hardware development , *Biotelem. Patient Monit.* 8 (3), pp. 131-150
5. Munshi I, Lathrop D, Madsen JR, Frim DM (1998), "Intraventricular Pressure Dynamics in Patients with Ventriculopleural Shunts: A Telemetric Study" , Pediatr Neurosurg 28, pp. 67-69
6. Ginggen, A.; Tardy, Y.; Crivelli, R.; Bork, T and Renaud, P (2008), A Telemetric Pressure Sensor System for Biomedical Applications, Biomedical Engineering, IEEE Trans Biomed Eng 55 (4) pp. 1374 – 1381
7. Linninger, A.A.; Xenos, M.; Zhu, D.C.; Somayaji, M.R.; Kondapalli, S.; Penn, R.D. (2007), Cerebrospinal Fluid Flow in the Normal and Hydrocephalic Human Brain, IEEE Trans Biomed Eng 54 (2), pp. 291 - 302
8. T. Bork (2007), "Thermal Flow Sensor Having Streamlined Packaging ", US Patent No. 7,181,963 B2
9. Neukomm P A, Furrer D (2003), "Design Rule for a Weakly Coupled Inductive Link avoiding the "Black Hole" in Passive Telemetry Data Transmission for an Implantable Thermal Flow Sensor", Proceedings of the 1^{7th} Conference of the International Society on Biotelemetry ISOB 17, Sept 1-5, 2003, Brisbane,
10. Kuschinsky W. (1996), Blood-Brain Barrier and the Production of Cerebrospinal Fluid , In: Comprehensive Human Physiology (Edited by: Greger R, Windhorst U), Volume 1, Berlin, Springer, pp. 545-558

Author: Juergen Burger
Institute: Codman Neuro Sciences sàrl
Street: Girardet 29
City: CH-2400 Le Locle
Country: Switzerland
Email: jburger@its.jnj.com

Concentration-dependent multi-parametric functional screening of CNS drugs with neuronal networks on microelectrode arrays

O.H.-U. Schroeder[1], A. Gramowski[1,2], K. Jügelt[1] and D.G. Weiss[2]

[1] NeuroProof GmbH, 18119 Rostock, Germany
[2] Institute of Biological Sciences, Cell Biology and Biosystems Technology, University of Rostock, 18051 Rostock, Germany

Abstract—**Functional screening of CNS drugs with neuronal network cultures on microelectrode arrays can elucidate different modes of action for a given substance at different concentrations. This concentration-dependent profiling of CNS drug candidates is a new feature of this technology.**

Keywords— **Functional screening, neuronal network cultures, microelectrode arrays, multiple mode of action, concentration dependent mode of action, high content screening HCS.**

I. Introduction

Neuronal networks of primary tissue-specific cell cultures grown on microelectrode arrays (MEAs) are an attractive alternative for substance screening in drug development and safety pharmacology. The activity pattern changes obtained from these networks following chemical stimulation are both reproducible and substance-specific, so that MEAs are applicable as a new read-out system for cell-based drug screening.

The development of new chemical entities for treatment of disorders of the central nervous system with high efficacy and minor side effects is a high risk job today. Attrition rates of these drugs are as high as 90 %; insufficient efficacy and adverse side effects being the most frequent reasons of failure. The lack of predictive and reliable biological models is the bottleneck in preclinical research of such drugs. Functional screening of neuronal networks can provide new insights into these complex problems. Therefore, we have been investigating the limitations and prospects of this technology.

CNS drugs very often show multiple modes of action, whereby the wanted and most specific effect is assigned to a specific concentration range - the therapeutic range. We analyzed in detail the patterns of electrical activity changes for a wide range of substances and determined their concentration-dependent modes of action. We demonstrate biphasic behavior for many parameters for substances such as fluoxetine, agmatine and others. For fluoxetine for example, a network behavior is shown that is typical for SSRIs at concentrations equivalent to the therapeutic range. We postulate that a substance has multiple modes of action if the concentration-response of its spike rate curve is biphasic.

II. METHODS

A. Neuronal Network Cultures

Primary neuronal cells from NMRI mice were cultured on MEA neurochips. The spike train data were recorded with a standard setup (Gramowski et al. 2004). We used the microelectrode array (MEA) neurochip technology consisting of the MEAs from CNNS, UNT (Denton Texas, USA), the MEA workstation from Plexon, Inc. (Dallas, TX, USA), and analyzing software (Plexon, Inc., and NeuroProof GmbH, Rostock, Germany). The results shown here originate from frontal cortex tissue. Preliminary tests were run to estimate the optimal range of the concentration-response curve. In doing so, preliminary EC_{10}, EC_{50}, and EC_{90} were determined if possible. Subsequently, at least 8 more tests with defined increasing concentrations were conducted. A stable activity phase of at least 30 minutes was analysed for every application phase (Fig. 1). For this study we tested the following substances: agmatine (AGM), bicuculline (BCC), clonazepam (CLO), dermorphine (DER), diazepam (DIA), endomorphine (EM1), fluvoxamine (FLV), fluoxetine (FLX) and valproate (VPA).

B. Data Analysis

Chemically stimulated networks require a specific data analysis approach due to their spontaneous and complex network behaviour (Fig. 2). Certain spike train parameters such as peri-stimulus histograms are not suited in this case. We work with a parameter-free non-classical statistical classification approach. A good starting point for investigating network behaviour is to classify substance-specific network responses independent of the individual network culture specificity. Since substance-specific responses are concentration-dependent one has to decide for which concentration a comparison of substance-specific activity patterns should be performed. This is especially important since substances often act via different modes of action at different concentrations. For this reason we classified sub-

O. Dössel and W.C. Schlegel (Eds.): WC 2009, IFMBE Proceedings 25/VIII, pp. 269–272, 2009.
www.springerlink.com

stance-specific activity patterns at different concentrations to reflect the full dynamic range of a substance.

C. Spike Train Features

For each of these substances' addition phases spike train features were calculated for stable activity periods. Computation of spike train features was performed to characterize effects such as general activity, burst structure, regularity of oscillation and synchronicity. We constructed spike train features known from literature (see Brown et. al. 2004 and Gramowski et. al. 2004) and also heuristic ones. Since it is very difficult to assess the significance and relevance of features in advance, we have constructed spike train features in a gun-shot manner. Some spike train features are parameter-dependent. For example, the CV-Net and CV-Time spike train features (see Gramowski et al. 2004) are strongly parameter dependent, since the so-called bin parameter is crucial for the values of these features. Another important spike train feature is the so-called contrast, which is the absolute value of the difference of the number of spikes of two consecutive intervals divided by the number of spikes in both intervals. This spike train feature also depends strongly on the length of the bin intervals. Since this parameter is continuous, one can construct an infinite number of such contrast features. In conclusion, it becomes obvious that the most important step in data mining of spike train data is the assessment of spike train features, which we performed by feature selection. All parameters have to be normalized to the native situation as baseline of activity.

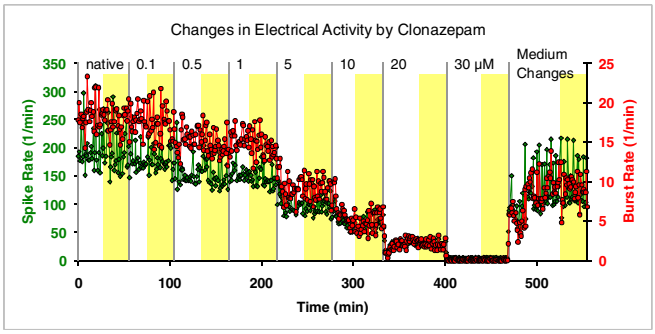


Fig. 1. Example of a standard experimental protocol. Spike train features are computed for stable activity phases after substance application (highlighted).

D. Feature Selection

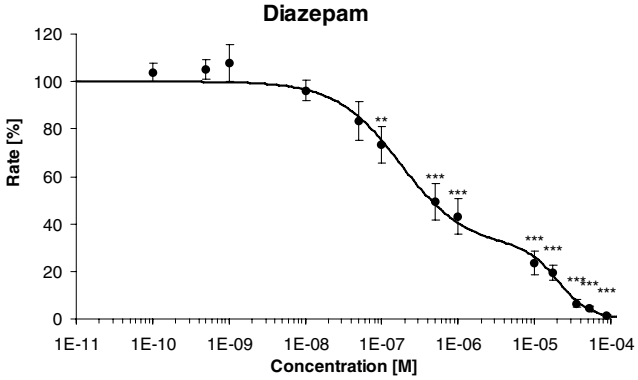
Feature selection is a widely accepted method in bioinformatics and a wide range of different approaches have been proposed (Gyon et. al 2003). One method of feature selection can be performed by measuring the significance of a feature by a so-called feature score. We calculated rankings of features by different feature scores. Different scores were assessed with classification experiments. The 40 most suitable parameters were selected and their total correct predictions were compared. In this manner we obtained the best results for a MDL (minimal description length) modified algorithm.

E. Machine Learning and Cross Validation

Data records were trained with an artificial network algorithm called resilient back propagation. Then, cross-validation was conducted where in each test the concentration datasets from one experiment were excluded as a whole. The best features of the categories general activity, oscillation, synchronicity, and burst structure were analyzed separately.

III. RESULTS

We compared the concentration-dependent spike rate responses of diazepam, fluoxetine and agamatine. It is known that all three substances have multiple modes of action. Although diazepam has only two different modes of action related to different subtypes of the GABA-A receptor (Walters et. al. 2000), we can see a shoulder at the high concentration range. We postulate that ideally a selective substance with a single mode of action should have a sigmoidal spike rate concentration curve.



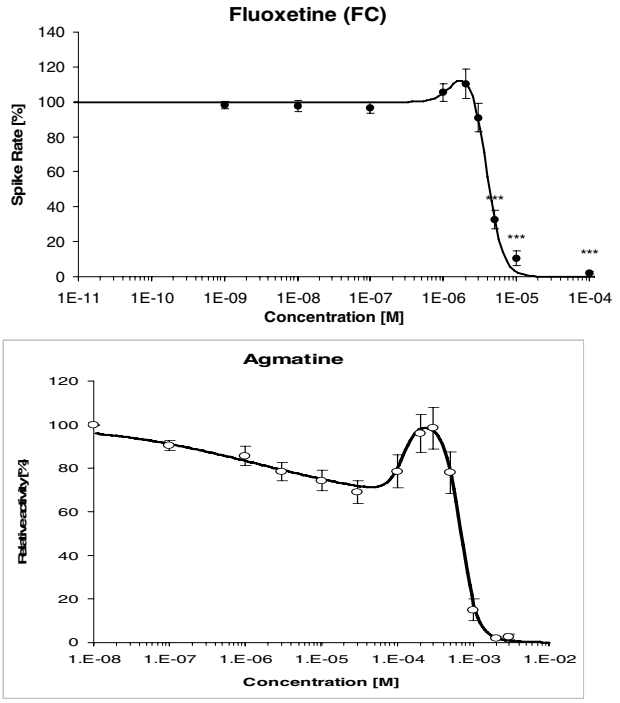


Fig.2 Concentration-response curves demonstrating the concentration dependence of selected parameters.

We got 84 data records to perform a classification for fluoxetine (see table 1). Fluoxetine was classified against a training set of bicuculline (BCC), dermorphine (DER), diazepam (DIA), endomorphine (EM1), fluvoxamine (FLV), and valproate (VPA). Fluoxetine was classified in the majority of cases as fluvoxamine with 33 hits, what can be expected. The highest similarity was achieved at the concentrations from 0.1 to 5 µM, this coincides with the therapeutic range (0.48 to 1.6 µM serum concentration). At the highest concentration we found a certain similarity to valproate and at low concentrations to dermorphine.

Table 1 Classification experiment for different concentrations of fluoxetine

FLX(µMo)	DS	BCC	DER	DIA	EM1	FLV	VPA
1E-09	6	0	33	17	0	17	33
0.000001	12	0	42	0	0	17	42
0.001	12	0	25	17	8	17	33
0.01	8	0	38	13	13	38	0
0.1	**12**	**0**	**17**	**8**	**33**	**17**	**25**
1	**12**	**0**	**8**	**8**	**17**	**58**	**8**
2	6	17	0	0	17	50	17
3	4	0	0	0	0	100	0
5	6	17	0	17	0	50	17
10	6	0	17	17	0	17	50
Sum	84	2	20	10	11	33	24

IV. CONCLUSIONS

These data show that different modes of action of substances imply different activity patterns. Therefore, the assignment of functionality patterns has to be made concentration dependent. In this manner higher resolution of the substance profiling is obtained. This shows the high capacity of functional screening with microelectrode arrays for drug profiling. The dependency of function and concentration in neuronal networks is not yet understood. The investigation of these phenomena is expected to deliver new insights into the dynamics of neuronal networks.

ACKNOWLEDGMENT

We would like to thank Kristine Gürtler for technical assistance. This work was supported by the European Union Grant NORMOLIFE (LSHC-CT-2006-037733). We received further support from the “Landes-Forschungsschwerpunkt Innovationsnetzwerk Biosystemtechnik” grant of the European Regional Development Found (ERDF).

REFERENCES

1. Brown, E. N., Kass, R. E., Mitra, P. P. Multiple neural spike train data analysis: state-of-the-art and future challenges. Nature Neuroscience 7, (2004), 46-461
2. Gramowski, A., Jügelt, K., Weiss, D. G. and Gross, G. W. Substance identification by quantitative characterization of oscillatory activity in murine spinal cord networks on microelectrode arrays. Eur J. Neurosci. 19, (2004). 2815-2825

3. Guyon I., Elisseeff A., An introduction to variable and feature selection. J. Machine Learning Research 3, (2003), 1157-1182
4. Walters RJ, Hadley SH, Morris KD, Amin J (2000) Benzodiazepines act on GABAA receptors via two distinct and separable mechanisms. Nat Neurosci 3: 1274-1281.

Author: Olaf H.-U. Schroeder
Institute: NeuroProof GmbH
Street: Friedrich-Barnewitz-Str. 4
City: 18119 Rostock
Country: Germany
Email: olaf.schroeder@neuroproof.com

Electric Field Characteristics of Bipolar Impedance Sensors

P. Kassanos[1], R.H. Bayford[2], and A. Demosthenous[1]

[1] Department of Electronic and Electrical Engineering, University College London, London, UK
[2] Department of Natural Sciences, Middlesex University, Middlesex, UK

Abstract— **There has been an increased interest in the last decade on Lab-on-a-Chip (LOAC) technologies, which concentrate on the detection and manipulation of biomolecules. Impedance detection plays a vital role in these developments. There are various types of impedance sensors, with four electrode systems being the focus of the work presented here. However, in order to optimize a tetrapolar system, the bipolar needs to be examined first. The electric field properties and characteristics of bipolar systems and in particular, the effect of the electrode width, W, and separation, D, are examined in this paper. This is performed using conformal mapping techniques, which are compared with the Finite Element Method (FEM). An analytical numerical equation for the electric field is derived and examined.**

Keywords— **Conformal Mapping, FEM, Impedance Biosensor, Bipolar, Tetrapolar.**

I. INTRODUCTION

Electrochemical impedance spectroscopy (EIS) and its application to biosensors, plays an important role in the development of Lab-on-a-Chip (LOAC) technologies. It is a promising and powerful technique offering the advantages of low cost, analytical time-reduction, portability, high miniaturization and most importantly, label-free detection. There are two electrode (bipolar) [1], interdigital [1-5], three electrode (tripolar) [6] and four electrode (tetrapolar) [6] sensors. This paper concentrates on planar technology compatible sensors.

In contrast to past trends where the electrode position was effectively arbitrarily chosen, in recent years there has been an increased interest in the optimization of such sensors [1-5, 7-9]. Finite Element Modeling (FEM) has been usually applied to quantify the response of such devices [5, 7-8]. However, this technique does not allow one to obtain an analytic numerical solution to the problem and allows optimization in a trial and error type approach. The conformal mapping (CM) technique has been widely applied in the field of transmission lines [10] and allows such analytical numerical expressions to be obtained. Thus, it allows a more elaborative sensor optimization process to take place. However, it appears from the bibliography that its application is limited to 2D homogenous isotropic half-spaces [1-4, 9-11]. Two of the earliest examples of the application of these techniques in the field of biosensors are presented in [1] and [3]. CM allows the mapping of a geometry, in which the solution of a problem is complex, into another geometry, in which the problem is simpler. The problem is then solved in the transformed domain and the obtained results can subsequently be back-transformed to the original plane [9, 11]. In this paper, the Schwarz-Christoffel transformation for polygonal boundaries is examined. For an n-sided polygon, with vertices t_1, t_2, …, t_n and with corresponding exterior angles f_1, f_2, …, f_n, the Schwartz-Christoffel mapping, transforming the interior of a polygon into a semi-infinite half-plane, is defined as [11]:

$$z(t) = C_1 \int_{t_o}^{t} \prod_{j=1}^{n} (t - t_j)^{-\phi_j / \pi} dt + C_2 \qquad (1)$$

The constant C_1 defines the scale and orientation of the polygon, while C_2 gives its position. The value of C_2 can be found from: $z(t_o)=C_2$. The confinement of the electric field is determined by the width and separation of the injecting electrodes [1] and of course by the boundaries of the 2D space investigated. In [1], an electric field confinement threshold of 80% was applied. Using this, a number of sensors providing this threshold value at a specific height above the sensors surface, were designed. Similar threshold values have been used in [2, 5]. Our work concentrates on the detection of cancer biomarkers, more specifically hCGβ, a protein. According to [2], the binding region for protein detection is located up to a height of 100nm from the sensor surface. As it appears from [2], this characteristic pushes the dimensions of the sensor in the nanometer range.

The focus of this work is the optimization of planar tetrapolar impedance sensors. However, in order to get to the optimized tetrapolar system, the bipolar field characteristics need to be investigated. This is conducted using conformal mapping methods developed in Matlab (Mathworks Inc.) and the FEM package Comsol Multiphysics (Comsol AB, Stockholm, Sweden).

II. CONFORMAL TRANSFORMATION MATLAB MODEL

A starting point in the design of such a sensor is the investigation of the electric field confinement in terms of the electrode width, W, and separation, D. Considering only

O. Dössel and W.C. Schlegel (Eds.): WC 2009, IFMBE Proceedings 25/VIII, pp. 273–276, 2009.
www.springerlink.com

two electrodes of length infinitely large compared to D and W, a 2D approximation is valid. In order to simplify the problem, the electrodes may be considered of having zero thickness. This approximation is valid, provided that the thickness is infinitely small compared to the rest of the electrode dimensions. The model can be defined as a semi-infinite Cartesian half-space, with the two electrodes placed on the x-axis, which extends to ±∞ and the y-axis extending between 0 and +∞, as shown in Fig. 1a. We wish to evaluate the electric and current density distribution throughout this space and be able to obtain an analytic mathematical expression for these. In order to achieve this, the half-space is mapped into the interior of a rectangle using (1), as described in [11]. The exterior angles of a rectangle are equal to π/2 and the points at ∞ can be ignored [11]. For ease, the fixed point between the two planes t_p is chosen to be 0, making C_2=0. Additionally, t_a=-1/k, t_b=-1, t_c=1 and t_d=1/k. Since the starting plane is the semi-infinite half-plane and the rectangle is the "destination", we have the liberty of setting C_1 equal to 1/k. By manipulating the denominator, the transformation finally becomes:

$$z(t) = \int_0^t \frac{dt}{\sqrt{(1-t^2)(1-k^2t^2)}} \tag{2}$$

The above integral is an elliptic integral of the first kind. Of particular importance is the complete elliptic integral with the upper limit t of (2) equal to 1 (which gives K(k)) and equal to 1/k (which gives K(k)+iK'(k)). K(k) and K'(k) are related through

$$K'(k) = K(k') \tag{3}$$

with

$$k' = \sqrt{1-k^2} \tag{4}$$

Following the transformation, the corners of the rectangle in the transformed space (Fig. 1b) are ±K(k), K(k)+jK'(k) and –K(k)+jK'(k). If an electrode in the original plane (Fig. 1a) lies between ±D/2 and ±(D/2+W), in order to make these into the required values (±1, ±1/k) for the transformation, the T-plane is normalized by D/2 and therefore

$$k = \frac{D}{D+2W} \tag{5}$$

with 0<k<1. From this transformation, the electrodes are mapped to the sidewalls of the rectangle and the entire semi-infinite half-space is now confined within it. By setting a potential difference between these two electrodes in the transformed space, a uniform electric field is established

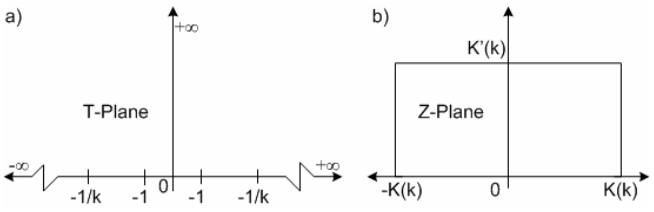


Fig. 1 a) The original plane, b) The transformed plane

similar to that of a perfect parallel plate capacitor. If the potential at one electrode is set to 1V and to the other at 0V then the potential at any point can be found by [12]

$$V_z = \frac{V_1(x-x_2) - V_2(x-x_1)}{x_1 - x_2} = -\frac{(x-K(k))}{2K(k)} \tag{6}$$

According to [11], the electric field in the original plane is equal to the electric field on the transformed space multiplied by the complex conjugate of the derivative of the mapping function. Hence,

$$E_t = -\nabla V_t = -\nabla V_z \cdot \overline{f'(z(t))} \tag{7}$$

with t=x+iy. In the transformed plane, the x-component of the electric field (the y-component is zero) is equal to $\nabla V_z = -\frac{1}{2K(k)}$, i.e. a constant. Therefore,

$$E_t = \frac{1}{2K(k)} \cdot \overline{\frac{1}{\sqrt{(1-t^2)(1-k^2t^2)}}} \tag{8}$$

Additionally, the current density may be calculated by

$$J = \sigma E \tag{9}$$

For x=0 in the T-plane the field lines reach maximum volume penetration, the y-component of the electric field is equal to zero and the x-component is equal to

$$E_{tx} = \mathrm{Re}(E_t)_{x=0} = \frac{1}{2K(k)\sqrt{1+y^2+k^2(y^4+y^2)}} \tag{10}$$

As it can be seen from the above equation, the electric field value is directly related to the width and separation of the electrodes through the value of k. At t=±(1+0j) and t=±(1/k+0j), (8) goes to ∞, as expected, since these are the locations of the electrode edges. Having calculated the above, it is necessary to multiply the coordinate system by D/2 and the electric field by 2/D, in order to de-normalize the calculated values. Furthermore, the inverse of the transform is the Jacobi elliptic function and is denoted as

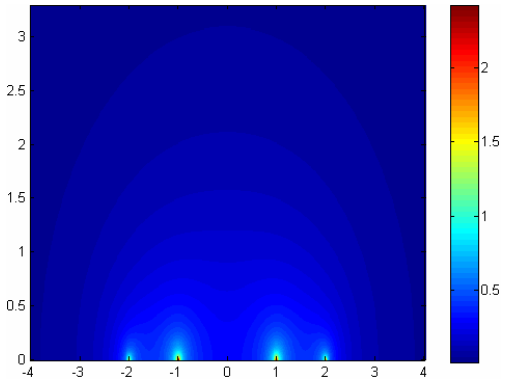


Fig. 2 2D color map of the distribution of Enorm

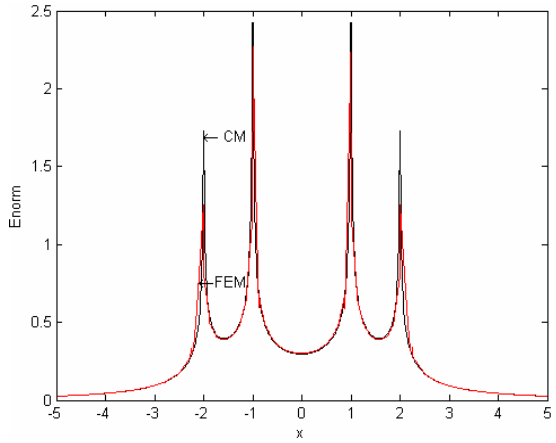


Fig. 3 Comparison of Enorm obtained from FEM and conformal mapping, for y=0.

$$T(z) = sn(z) \tag{11}$$

In the rectangular space (Fig. 1b), lines of constant x are isopotential lines and lines of constant y are field lines. The complete elliptic integrals as well as the Jacobi elliptic functions were calculated using the functions provided in [13].

III. Results

The color map of Fig. 2 (calculated using (8)), illustrates the 2D distribution of Enorm. The data of this figure were subsequently compared and verified with Comsol Multiphysics 3.5. For y=0, these are compared in Fig. 3. In order to investigate the effect of the geometry to the electric field confinement, (10) was used in order to calculate the electric field. Since, the maximum values of the field lie at x=0, the value at this point can be considered as 100%. Hence, the percentage of the field at each height, with respect to that on the surface, can be calculated. Subtracting 100 from all the data points then gives the percentage confinement of the field at each height. The normalized results obtained from this are shown in Fig. 4. By setting a threshold level of 80%, the 80% confinement of the field was plotted as a function of k (Fig. 4 inset). By setting W=100nm, D was calculated for each value of k. This allowed the de-normalization of the electric field and the coordinates. The de-normalized height giving the required 80% confinement was then plotted in Fig. 5 against D. In order to investigate the effect of the W to the confinement, D was set equal to 100nm, and W was calculated for each value of k using (5). De-normalizing the field appropriately gives then the required characteristic curve (Fig. 5). Fig. 6 was plotted using (11) and illustrates the isopotentials and field lines of the normalized geometry (this is the same geometry as that of Fig.1-3).

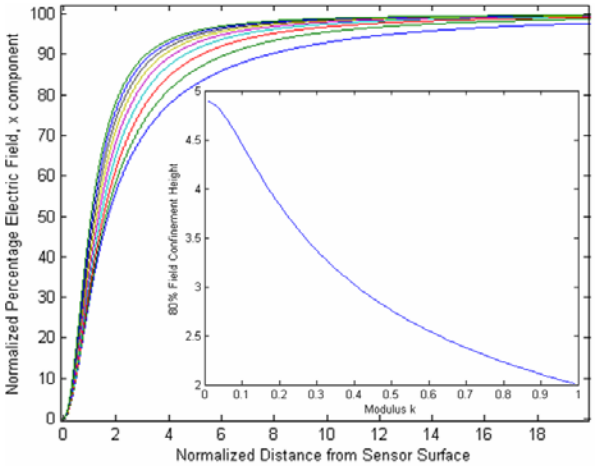


Fig. 4 The percentage of the electric filed vs. height. The inset shows the behavior of the 80% confinement level against k

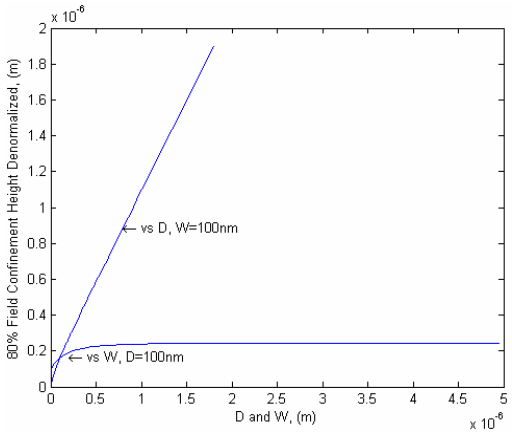


Fig. 5 80% confinement height against D for W=100nm and against W for D=100nm

IV. Discussion and Conclusion

Fig. 1a, illustrates the normalized space, where an electrode begins from ±1 and ends at ±1/k. For a value of k=0.5, this is equal to ±2. This is shown in Fig. 2 and 3, as the electric field is particularly strong at points ±1 and ±2, which correspond to the electrode edges. As it is evident from Fig. 3, the conformal mapping model results seem to agree quite accurately with the results obtained from the same model geometry examined using FEM. Therefore, this may serve as a validation of the results presented here. In Fig. 4, a value close to 100% corresponds to a near-zero field value. The inset figure shows the height at which the threshold of 80% is reached. Comparing these, it is observed, that large k means small field confinement. Fig. 5 indicates that for the same values of k, a smaller range of values of D (with W=100nm) is obtained than the values obtained for W (for D=100nm). Additionally, the confinement height seems to have a linear relationship with D, increasing linearly. Similarly, increasing W seems to increase the confinement height as well. However, in this case, the response seems to saturate after a certain value of W. Therefore, increasing both D and W increases the confinement of the electric field.

This analysis provides design guidelines for the development of bipolar sensors. Previous work [7-8] is currently being combined with the methodology presented here, as a means of optimizing a tetrapolar electrode system. Simultaneously, tank models are being performed in order to validate the results.

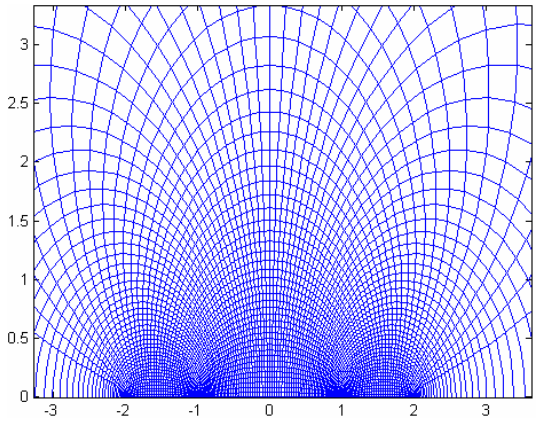


Fig. 6. Equipotential and field lines, derived using (11)

Acknowledgment

This work was supported by the UK Engineering and Physical Sciences Research Council (EPSRC).

References

1. Jacobs P, Varlan A, Sansen W (1995) Design optimization of planar electrolytic conductivity sensors. Med & Biol Eng & Comp 33: 802-810
2. van Gerwen P, Laureyn W, Laureys W et al. (1998) Nanoscaled interdigitated electrode arrays for biochemical sensors. Sens. Actuators B 49:73-80
3. Olthius W, Streekstra W, Bergveld P (1995) Theoretical and experimental determination of cell constants of planar-interdigitated electrolyte conductivity sensors. Sens. Actuators B 24-25:252-256
4. Timmer B, Sparreboom W, Olthius W, et al. (2002) Optimization of an electrolyte conductivity detector for measuring low ion concentrations. Lab Chip 2:121-124
5. Radke S M, Alocilja E C (2004) Design and fabrication of a microimpedance biosensor for bacterial detection. IEEE Sensors J 4:434-440
6. Grimnes S, Martinsen O G (2000) Bioimpedance & Bioelectricity Basics. Academic Press, London
7. Kassanos P, Bayford R H, Demosthenous A (2008) Comparison of tetrapolar injection measurement techniques for coplanar affinity-based impidimetric immunosensors, Proc. BioCAS, Baltimore, USA, 2008, pp. 317-320
8. Kassanos P, Bayford R H, Demosthenous A (2008) Towards an optimized design for tetrapolar affinity-based impedimetric immunosensors for lab-on-a-chip applications, Proc. BioCAS, Baltimore, USA, 2008, pp. 141-144
9. Sun T, Morgan H, Green N G (2007) Analytical solutions of ac electrokinetics in interdigitated electrode arrays: Electric field, dielectrophoretic and traveling-wave dielectrophoretic forces. Physical Review E 76:046619-1-04661918
10. Gevorgian S S, Martinsson T, Linner P L J, Kollberg E L (1996) CAD models for multilayered substrate interdifital capacitors. IEEE Trans. Microwave Theory and Techniques 44:896-904
11. Schinzinger R and Laura P A A (1991) Conformal Mapping: Methods and Applications. Elsevier, Amsterdam
12. Hayt W H Jr (1989) Engineering Electromagnetics. McGraw-Hill, Singapore
13. Driscoll T A (2008) Schwartz-Christoffel Toolbox for Matlab at http://www.math.udel.edu/~driscoll/SC/index.html

Author: Panagiotis Kassanos
Institute: Electronic & Electrical Eng., University College London
Street: Torrington Place, WC1E 7JE
City: London
Country: UK
Email: p.kassanos@ee.ucl.ac.uk

Hemodynamic response with an artificial myocardial assistance in chronic animal examination

Y. Shiraishi[1], T. Yambe[1], Y. Saijo[2], M. Shibata[1], H. Liu[1], T. Sugai[2], A. Tanaka[3], S. Konno[1], A. Baba[4], T. Fujimoto[4], K. Imachi[2], M. Yoshizawa[5], S. Nitta[1], H. Sasada[6], K. Tabayashi[7], Y. Sato[8], M. Umezu[8], D. Homma[9]

[1] Institute of Development, Aging and Cancer, Tohoku University, Sendai, Japan
[2] Graduate School of Biomedical Engineering, Tohoku University, Sendai, Japan
[3] Fukushima University, Sendai, Japan
[4] Shibaura Institute of Technology, Tokyo, Japan
[5] Cyber Science Center, Tohoku University, Sendai, Japan
[6] Graduate School of Agriculture, Tohoku University, Sendai, Japan
[7] Graduate School of Medicine, Tohoku University, Sendai, Japan
[8] TWIns, Waseda University, Tokyo, Japan
[9] Toki Corporation, Tokyo, Japan

Abstract— **Thromboembolic and haemorrhagic complications are the primary causes of mortality and morbidity in patients with artificial hearts, which are known to be induced by the interactions between blood flow and artificial material surfaces. The authors have been developing a new mechanical artificial myocardial assist device by using a sophisticated shape memory alloy fibre in order to achieve the mechanical cardiac support from outside of the heart without a direct blood contacting surface. The original material employed as the actuator of artificial myocardial assist devices was 100um fibred-shaped, which was composed of covalent and metallic bonding structure and designed to generate 4-7 % shortening by Joule heating induced by the electric current input. Prior to the experiment, the myocardial streamlines were investigated by using a MDCT, and the design of artificial myocardial assist devices were refined based on the concept of Torrent-Guasp's myocardial band theory. As the hydrodynamic or hemodynamic examination exhibited the remarkable increase of cardiac systolic work by the assistance of the artificial myocardial contraction in the originally designed mock circulatory system as well as in the acute animal experiments, the chronic animal test has been started in a goat. Total weight of the device including the actuator was around 150g, and the electric power was supplied percutaneously. The device could be successfully installed into thoracic cavity, which was able to be girdling the left ventricle. In the chronic animal trial, the complication in respect to the diastolic dysfunction by the artificial myocardial compression was not observed. Systolic pressure and aortic flow waveforms were elevated by the assistance using the device contraction synchronously by around 5%. And blood pressure response against the increase of aortic pressure was investigated under the myocardial assisted condition in order to examine the vascular tone which was controlled by vagal nervous activity.**

Keywords— **Artificial myocardium, shape memory alloy fibre, chronic animal experiment, myocardial band, hemodynamics, blood pressure response.**

I. Introduction

Chronic heart failure (CHF) is functionally and structurally characterized by pathophysiological remodeling of the ventricle. In general, ventricular assist devices (VADs), such as artificial hearts, are used for the surgical treatment of the patients with the final stage of severe heart failure [1-4]. However, thromboembolic and haemorrhagic complications are still the primary causes of mortality and morbidity in patients with VADs, which are known to be induced by the interactions between blood flow and artificial material surfaces. Several concepts of the mechanical assistance from outside of the ventricle have been presented so far, such as Anstadt's ventricular cup, providing a solution to these problems without direct contacting surfaces against blood [5-12]. And also some new devices, such as Myosprint, demonstrated improvements in eliminating mitral regurgitation in dysfunctional left ventricle as well as in preventing the ventricular enlargement which was to compensate for the reduction in cardiac function [13-14]. Although the passive implantable devices, which are girdling the ventricle from the outside, have been already applied for clinical trials in patients with chronic congestive heart failure for the passive assistance as well as for the prevention of enlargement of the left ventricle to compensate for the reduction in cardiac function, there might be a limitation to passive assistance in the case of sudden changes of cardiac contractile function, such as angina of effort. We have been developing an artificial myocardial assist device by using a covalent type nano-tech shape memory alloy fibre, which is capable of assisting natural cardiac contraction from outside of the ventricular wall as shown in Figure 1. The purpose of this study was to examine the function of the artificial

O. Dössel and W.C. Schlegel (Eds.): WC 2009, IFMBE Proceedings 25/VIII, pp. 277–280, 2009.
www.springerlink.com

myocardium, which was designed to assist the heart synchronously with native contraction, and its feasibility in chronic animal experiments.

II. Materials and methods

A. Myocardial assist device description

The artificial myocardium consists of ten shape memory alloy fibres which were covered by silicone rubber as shown in Figure 2. Special features of the shape memory alloy fibre material (Biometal®) which was to be employed as the actuator of the artificial myocardium were as follows: a) composition of covalent and metallic bonding structure, b) 4-7 % shortening by Joule heating induced by the electric current input, c) linear characteristics of electric resistance against shortening, d) strong maximum contractile force of 10N with 100um-fibre, e) high durability of over one billion cycles, f) contractile frequent response by 1-3 Hz, g) selectable maltensitic temperature by fabrication processing from 45 to 70 Celsius, and h) elective diameter size smaller than 30um [15-17]. The contraction of the device can be controlled by an originally-designed microcomputer system. The device is controlled and performed by electrical signal input, which is supplied percutaneously. Each signal for the contraction is regulated by the controller and synchronized with native electrocardiogram (Figure 3 and 4). Originally-designed ladder-shaped hinges were constructed on the parallelly-linked shape memory alloy fibres belt, specifically on the surface attaching to the left ventricular free wall in order to simulate the wall-thickening effect as well as to promote the mechanical shortening perpendicularly to the left ventricular long axis.

B. Mechanical design of the device based on the anatomical examination of native heart

Myocardial streamline was confirmed by the MDCT investigation in a healthy goat heart which was extracted and unfolded based on the Torrent-Guasp's myocardial band concept as shown in Figure 5 [17]. The orientation of the device contraction might promote native systolic function while avoiding both the external and internal critical structures of the heart. The myocardial streamline was detected from the data with plastic markers plot by MDCT, and the angular configuration to the left ventricular long axis was calculated.

C. Experimental procedure

The chronic animal experiments were performed in healthy female adult Japanese Saanen goats (n=2), which weighed 45 kg. Implantation of the device was performed as

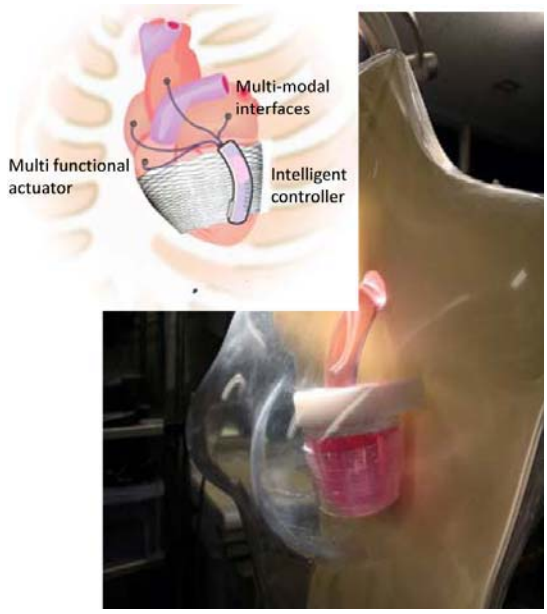


Fig. 1 Schematic illustration and an installation in the mock of an artificial myocardium attached on the ventricular wall; the synchronous contraction can be achieved according to the natural physiological demand.

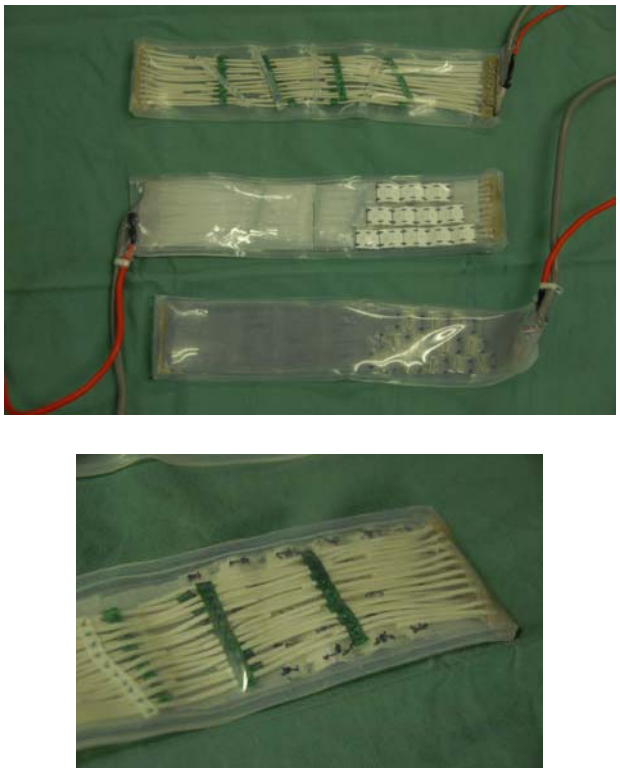


Fig. 2 Several types of myocardial assist device developed for the feasibility study in chronic animal experiments (top), and the details of the connection of shape memory alloy fibres covered with silicone tubing (bottom).

part of an open-chest cardiac procedure on a beating heart under the normal inhalation and anesthesia followed by endotracheal intubation using 2.5% halothane. The band-shaped myocardial assist device was installed into the thoracic cavity girdling from the apex to the base and one of the ends was parallel to the left ventricular long axis myo cardial streamline on its free wall side. Coronary vasculature was visually identified and avoided on the exterior of the heart during the implantation. There was no direct suture on the tissue or muscles with the device. Prior to the measurement, postoperative care without mechanical assistance was carried out for one week. These animal trials were electively terminated after postoperative one month.

All animals received humane care in accordance with "the Guideline for the Care and Use of Laboratory Animals" published by the National Institute of Health (NIH publication 85-23, revised 1985) as well as with "the Guidelines for Proper Conduct of Animal Experiments" formulated by Science Council of Japan (2006) and the guidelines determined by the Institutional Animal Care and Use Committee of Tohoku University.

III. Results and Discussion

A. Hemodynamic effects

There were no serious infections and surgical procedural failures in the implantation of the device from the beginning and throughout the study in all cases. Left ventricular and aortic pressures were obtained and remarkably increased by the mechanical assistance as shown in Figure 6. Each waveform was calculated as the average of the data in the period of 90sec. 'Control' indicates the waveforms taken without assistance, while 'Assisted' were with mechanical contraction. There were no significant changes in the left ventricular end diastolic pressure, so that it was suggested that there might not be any diastolic dysfunction during the mechanical assistance using the artificial myocardium. As a result, systolic pressure was increased from 110 to 118 mmHg (7%), and assisted flow rate was elevated for 70msec, which was equivalent of the mechanical contractile duration (Figure 7). Consequently, the assistive effect on cardiac output during the assistance was calculated to be 3% higher than control condition without mechanical contraction.

B. Blood pressure response associated with vascular tones

As shown in Figure 7, blood pressure response associated with vascular tone affected by vagal nervous activity under the intravenous administration of methoxamine hydrochloride might be changed by the myocardial assistance.

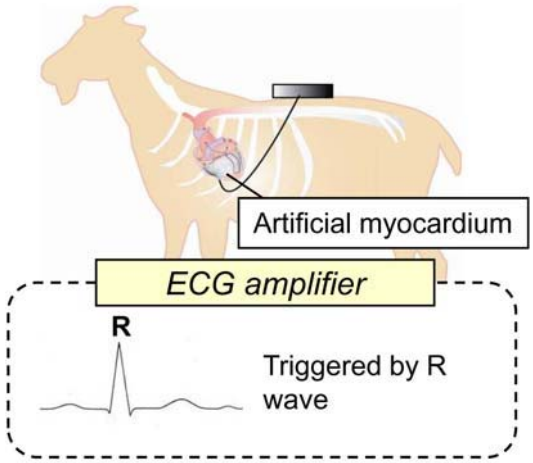


Fig. 3 Schematic illustration of the signal connection for the control of mechanical myocardial contraction in the animal experiments.

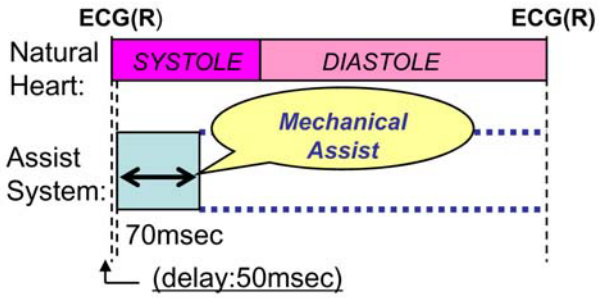


Fig. 4 Schematic drawing of the contraction signal input for the artificial myocardium synchronized with electrocardiogram (ECG-R).

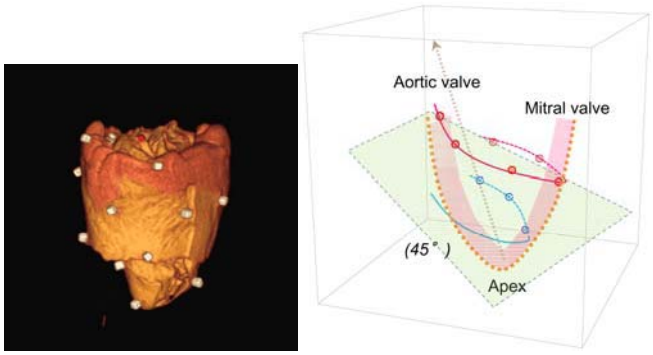


Fig. 5 MDCT examination of the healthy goat heart unfolded by the Torrent-Guasp's concept and reconstructed with plastic markers (left), and the native myocardial streamline orientation calculated from the data as the reference of implantation of the artificial myocardium (right).

IV. Conclusions

The first animal trials of the artificial myocardium using shape memory alloy fibre demonstrated both feasibility and efficacy in healthy adult goats. The result indicated the development of the active ventricular assist device was useful because of its ability to consistently reduce or eliminate the complications in relation to thrombosis or hemolysis along with simple mechanism for the effective actuation.

Acknowledgment

The authors acknowledge the support of Grand in Aid for Scientific Research of and Ministry of Education, Culture, Sports, Science and Technology (17790938, 19689029, 20659213). And we thank Mr. K. Kikuchi and Mr. T. Kumagai for kind support of animal cares as well as experimental preparations.

References

1. Hosenpud JD, et al. (1998) The registry of the international society for heart and lung transplantation: fifteenth official report–1998, J Heart Lung Transplant 17:656–68.
2. Rose EA, et al. (2001) Long-term use of a left ventricular assist device for end-stage heart failure, New Eng J Med 345:1435-43.
3. Long JW, et al. (2005) Long-term destination therapy with the Heartmate XVE left ventricular assist device: Improved outcomes since the REMATCH study, Congest Heart Fail 11:133-8.
4. Drakos SG, et al. (2006) Effect of mechanical circulatory support on outcomes after transplantation, J Heart Lung Transplant 25:22-8.
5. Shimizu T, et al. (2002) Fabrication of pulsatile cardiac tissue grafts using a novel 3-dimensional cell sheet manipulation technique and temperature-responsive cell culture surfaces, Circ Res 90(3):e40.
6. Shiraishi Y, et al. (2005) Development of an artificial myocardium using a covalent shape-memory alloy fibre and its cardiovascular diagnostic response, Conf Proc IEEE Eng Med Biol Eng 1(1), 406-408.
7. Yambe T, et al. (2004) Artificial myocardium with an artificial baroreflex system using nano technology, Biomed Pharmacother 57 Suppl 1:122s-125s.
8. Wang Q, et al. (2004) An artificial myocardium assist system: electrohydraulic ventricular actuation improves myocardial tissue perfusion in goats, Artif Organs 28(9):853-857.
9. Anstadt GL, et al. (1965) A new instrument for prolonged mechanical massage, Circulation 31(Suppl. II):43.
10. Anstadt M, et al. (1991) Direct mechanical ventricular actuator, Resuscitation 21:7-23.
11. Kawaguchi O, et al. (1997) Dynamic cardiac compression improves contractile efficiency of the heart, J Thorac Cardiovasc Surg 113:923-31.
12. Fukamachi K, McCarthy PM. (2005) Initial safety and feasibility clinical trial of the Myosprint device, J Card Surg 20:S43-S47.

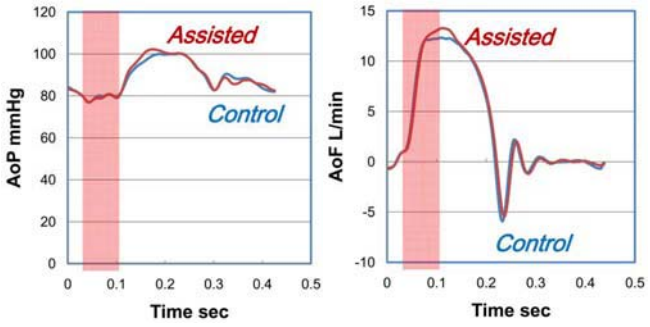


Fig. 6 Changes in hemodynamic waveforms obtained at a goats with the mechanical assistance by using the artificial myocardium. Each waveform was calculated as the average of the data in the period of 90 sec. 'Control' indicates the waveforms taken without assistance, while 'Assisted' were with mechanical contraction. The area colorized shows the duration of signal input for 70msec from 50msec subsequent of electrophysiological cardiac contraction detected by 'ECG-R'.

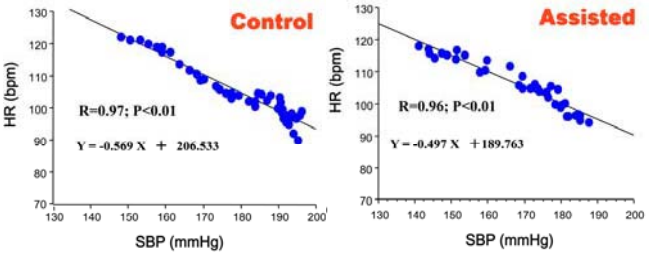


Fig. 7 Changes in blood pressure response calculated by the hemodynamic waveforms obtained at a goats with the intravenous administration of methoxamine hydrochloride under the control condition (without assistance) and the assisted condition. These response exhibited that the dynamic characteristics of vascular tones controlled by barorelfex systems might be interactively reconstructed by the direct myocardial assistance.

13. McCarthy PM, et al. (2001) Device-based change in left ventricular shape: A new concept for the treatment of dilated cardiomyopathy, J Thorac Cardiovasc Surg 122:482-490.
14. Buehler WJ, Gilfrich J, Wiley KC. (1963) Effect of low-temperature phase changes on the mechanical properties of alloys near composition TiNi, J Appl Phys 34:1465.
15. Homma D, Miwa Y, Iguchi N, et al. (1982) Shape memory effect in Ti-Ni alloy during rapid heating, Proc of 25th Japan Congress on Materials Research..
16. Sawyer PN, et al. (1976) Further study of NITINOL wire as contractile artificial muscle for an artificial heart, Cardiovasc Diseases Bull. Texas Heart Inst 3: 65.
17. Buckberg G, et al. (2008) Structure and function relationships of the helical ventricular myocardial band.J Thorac Cardiovasc Surg 136(3):578-89

Author: Yasuyuki Shiraishi
Institute: Institute of Development, Aging and Cancer, Tohoku University
Street: 4-1 Seiryo-machi, Aoba-ku
City: Sendai 980-8575
Country: Japan
Email: shiraishi@idac.tohoku.ac.jp

Implantable sensor system for the monitoring of bone healing

M. Sattler[1,2], J. Clauss[1,2], M. Schmidhuber[1], J. Belsky[3] and B. Wolf[1]

[1] Heinz Nixdorf Lehrstuhl Medizinische Elektronik, Technische Universität München, Deutschland
[2] Sense Inside GmbH im Innovationszentrum Medizinische Elektronik, München, Deutschland
[3] NetPensum GmbH, Wien, Österreich

Abstract — **A continuous monitoring of the healing process of bone fractures by active, microelectronic implants is a potential measure to prevent complications. So far bone healing is monitored by diagnostic methods such as X-ray, CT and MRT. For ascertaining the permitted stress of implants, e. g. in dental surgery, heretofore clinical experiences are consulted. For these and further parameters a capture by measurement engineering would be preferable.**

An active, autonomously working implant for direct mounting at bone fractures was developed. It contains a sensor, an electronic control circuit, a radio system and a battery for power supply. The oxygen saturation of the extracellular tissue fluids at the site of fracture is measured periodically. Via a radio transmitter in the implant, an external receiver and a data transmission computer with wireless LAN connection to the internet, the measured values are sent to a web server with a marginal time lag. From there the data are retrieved with a web browser. The implant is coated with a biocompatible synthetic resin in order to avoid any contact between the electronic circuitry and the body tissue.

The system was tested in-vivo by implantation into artificial bone defect at the cranial calvarium of sheep. The preliminary test validated the functionality of the data transmission system and the biocompatibility of the implant. A close contact between implant and surrounding tissue was verified by visual inspection after sacrificing the animal. However, the correlation between the dissolved oxygen saturation and the healing process could not be confirmed as yet. Because the measured values were subject to drift and the used sensor could not be calibrated in-situ, a physiological interpretation of the data is not possible.

Keywords — **Bone Healing, Active Implants, Telemonitoring, Dissolved Oxygen**

I. Introduction

The healing of bone fractures is a lengthy and complicated process, which has to be occupied and monitored. Only this way a satisfying healing of fractures can be assured. It is important to know the toughness of the healing fracture for choosing the point in time to remove osteosynthesis material or which type of physical therapy has to be applied. So far, the healing process is evaluated by clinical experience because clinical criteria are very vague [1].

Nowadays bone healing is monitored by diagnosis methods like X-ray techniques, computer tomography (CT) and magnet resonance tomography (MRT). All these procedures have several disadvantages like the harmful X-ray or varying interpretation of the photos, wherefore a new basic approach for the monitoring of bone healing shall be investigated. An implantable, autarchic working measurement system shall acquire the advancement of the healing by measuring parameters of fluids in-vivo. The gathered information shall be available to the medicating physician via telemedical technologies. The physician can evaluate the data and will be able to configure the therapy for the patients accordingly.

At the beginning of the study, the dissolved oxygen saturation is assumed to be an indicator for the progress of bone healing. At the Heinz Nixdorf Lehrstuhl für Medizinische Elektronik of the Technische Universität München an amperometric oxygen sensor, based on the Clark principal, was developed, which is successfully applied for the analysis in cell-based systems [2]. Hence this oxygen sensor is used in the performed measurements.

The challenges in this study were manifold. The battery-powered implant had to perform regular measurements and data transmissions for one month. To achieve a long battery lifetime, an intelligent power management had to be included in the system. Additionally the implant must have a biocompatible surface because it was tested in-vivo at the cranial calvarium of sheep and neither the animal nor the device was allowed to be attacked by harmful fluids or materials. Finally the data transmission from the implant through the animal tissue and skin to the extern receiver and the following transmission to the web server had to be built up reliably.

The purpose of this study was to develop and test the whole implant and the data transmission system and not primarily the measurement of the oxygen saturation.

II. Materials and methods

A. Overview of the project

In this study, which was based on an ethics proposal, a new developed implant system for monitoring of bone heal-

O. Dössel and W.C. Schlegel (Eds.): WC 2009, IFMBE Proceedings 25/VIII, pp. 281–284, 2009.
www.springerlink.com

ing is tested in-vivo. The implant is mounted at a bone fracture at the cranium of sheep where it measures the oxygen saturation of the extracellular tissue fluids. The data are transmitted to a wireless receiver in the animal facility, which is connected via USB to an external transmission computer. This PC has access to the internet and stores the measurement values at a web server. With a web browser the healing progress can be supervised (Fig. 1).

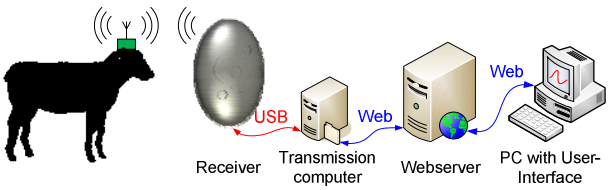


Fig. 1 Data transmission chain of the project.

B. Sensor system and analog electronics

The implant shall deliver information of physiological actions of bone healing by means of an amperometric oxygen sensor. For this purpose a planar sensor at a ceramic substrate is controlled by a potentiostat regulating circuit. The analysis of the signals is assumed by an analog-to-digital converter. Its data are gathered by a downstreamed electronics and are transmitted to a receiver which is located in the animal facility.

After the integration of the sensor on the printed circuit board (PCB) of the implant (Fig. 2) the functionality of the sensor and the circuit is verified by a test. Thereby, phosphate buffered saline (PBS) is used as dissolution because PBS is a common buffered solution for cells and the implant is utilized in a cell-physiological environment. A saturated PBS solution with 100 % dissolved oxygen is applied to the sensor. Afterwards an oxygen-free solution, made of PBS with sodium sulfite (Na_2SO_3), is tested on the sensor. The accomplished measurements with both solutions are prosperous.

The measured voltage is indirect proportional to the current. The current is proportional to the oxygen partial pressure of the ambience in the so-called diffusion-limited range of the sensor.

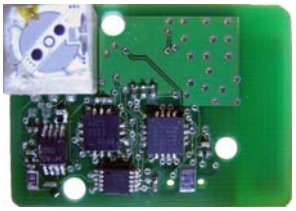


Fig. 2 Uncoated implant. Upper left side: Ceramic chip on plastic socket. The oxygen sensor is positioned in the center of this chip.

C. Digital electronics and power management

The core of the implant is a microcontroller, which controls the sensor, reads out the measurement values regularly and sustains the communication via a radio transceiver with a miniaturized chip-antenna to the external receiver.

The implant contains a battery for power supply of the circuit and the sensor. Because of the small dimensions of the implant and the associated little capacity of the battery, an intelligent power management is needed. The microcontroller always switches off those parts of the electronics that are not used currently. Thus an average current consumption of the complete implant of approximately 100 µA is ensured. On grounds of the battery capacity of 950 mAh a theoretical operating time of 9500 h can be calculated. The real uptime can be estimated to about 3000 to 4000 hours, because of the irregular load and due to the fact that battery voltage decreases significantly before the end of the runtime.

D. Miniaturized implant and biocompatible coating

In order to produce a minimized electronics (24 mm x 33 mm), the battery could not be mounted on the PCB. It had to be connected with wires (Fig. 3).

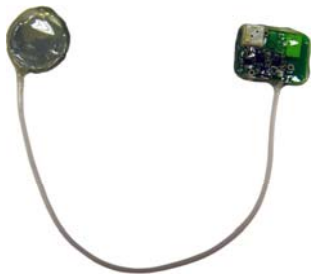


Fig. 3 Coated ovine implant. Left side: battery; Right side: electronics with sensor.

The electronics and the battery were coated with a biocompatible synthetic resin for protecting the circuit electrically and mechanically and to defend the test animal from harmful substances. Fig. 4 displays the encapsulated outskirt area of the ceramic chip.

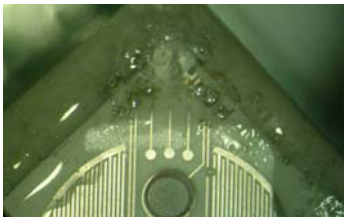


Fig. 4 Partial view of the encapsulated sensor chip.

For perpetuating the flexibility of the battery wires, they were passed in a biocompatible tube. At both ends it was encased with resin.

The mounting holes were obturated with bushings, made of the medical plastic polyetheretherketone (PEEK). The sensor socket that sticks out of the resin was produced with the same material.

E. Surgical implantation

Before the implantation of the device at the cranial calvarium of the subjects, it was disinfected with povidone-iodine. An artificial bone fracture was created that was big enough to accommodate the sensor chip and its socket. The implant was mounted with screws on the cranium (Fig. 5) and the extern battery of the electronics was put in the adipose tissue in the neck of the animal.

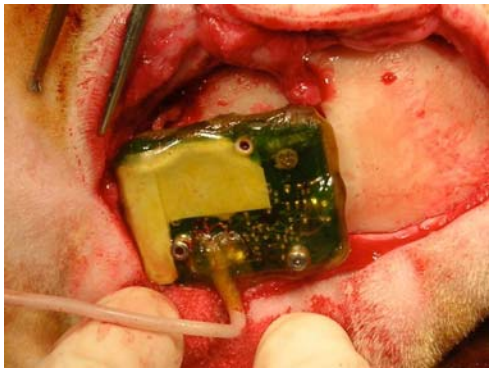


Fig. 5 Implant at the cranial calvarium of a sheep

F. Communication and software

The implant uses a wireless transmission chain to send the measurement values out of the sheep body. The radio signals are received by a device that is placed in the animal facility at a height of about 2 m. It is connected with a USB cable to a computer, placed outside of the facility. A software reads out the information automatically from the receiver. This PC has access to the local available WLAN and can save the information at a web server. Alternatively a cell phone connection could be established to the server. The windows software of the transmission computer offers an interface for an individual configuration of the automatic data transfer to the web server. Additionally a graphical preview of the values is possible.

The web server provides the user with a web interface that allows a real-time analysis of the test results. A graphical diagram permits a fast and simple interpretation of the data right on the website, without any complex post-processing.

III. Results

In the described study an electronically functional active implant with an operational power management was developed. The radio transmission of measurands from the implant at the fracture through the animal tissue and skin to an extern receiver and the following transfer of the data to a web server were proven successfully. Besides, a technique for a manually applicable, biocompatible coating with synthetic resin was investigated.

At the end of the trial, the measurands stored in the database of the web server were analyzed. All data since the activation of the implant, which took place before the implantation, were considered. Fig. 6 shows exemplary the measurands of the implant of sheep 1, which are standardized to the measurement progress and are not conditioned.

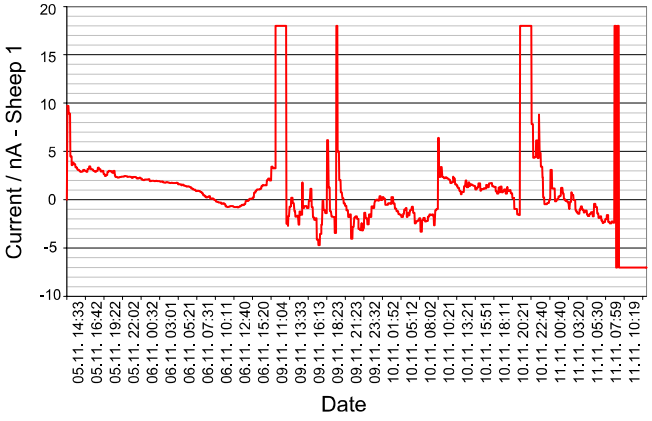


Fig. 6 Measurands of sheep 1

The measured curve degrades slightly during the course of the days und shows some intense steps. In the first third of the diagram, a continuous drift is noticeable. Here, the sensor is suggested to work properly. During the rest of the measurement time, the values oscillate heavily, therefore it is presumed, that the sensor is not functional any more. The peaks are supposed to be the effect of a signal malfunction.

Consequently the applied sensor, which is suitable in cell-based analysis, is not useful for measurements in implants.

IV. Discussion and Conclusions

The current measured by the implant should lie in the range from 0 nA … 18 nA. A slow drift of the current at constant oxygen values in the environment of the sensor is possible. Due to the fact that the sensor can't be recalibrated after the implantation, a signal drift is not distinguishable

from the actual changes of the measured parameters at the present measurement period. Without the possibility of an in-situ calibration of the sensor, an interpretation of the data is not possible at the physiological level.

The sensors in the sheep were functional from 16 to 72 hours. Negative values report a malfunction of the implant circuit or the sensor. The investigation of the implants after the devotement of the subjects showed that fluids intruded into some of the implants. The electronics of the implant and the power management are working correctly if the coating is leak-proof.

By reason of the missing possibility to calibrate the utilized oxygen sensor, the measured values could not be consulted for propositions to bone healing.

Further experiments with an improved sensor system and an impervious coating are intended.

Acknowledgment

The authors would like to thank cellasys GmbH for the provision of the sensors and for their kind support.

References

1. Rössler H, Rüther W (2005) Orthopädie und Unfallchirurgie. Elsevier GmbH, Urban & Fischer Verlag, München
2. Schmidhuber M, Wiest J, Brischwein M, Otto A M, Grothe H, Wolf B (2007) Multiparametric sensor chips for the metabolic analysis of live cells, 25th DECHEMA annual convention of biotechnologists, Köln, 30.5.-01.06.2007

Author: Martin Sattler
Institute: Heinz Nixdorf-Lehrstuhl für Medizinische Elektronik, TU München
Street: Theresienstr. 90
City: Munich
Country: Germany
Email: martin.sattler@mytum.de

Spontaneous Activity of Rat Embryonic Cardiac Myocytes

D. Jans[1,2], D. Braeken[2], D. Rand[2], C. Bartic[2] and G. Callewaert[1,2]

[1] K.U. Leuven, Subfaciliteit Geneeskunde Campus Kortijk, Etienne Sabbelaan 53, B8500 Kortrijk, België
[2] IMEC, Bioelectronics Systems Group, Kapeldreef 75, B3001 Heverlee, België

Abstract— **Rat embryonic cardiac myocytes display a spontaneous activity, which manifests itself as a repetitive change in a number of cellular properties, resulting in an oscillatory contractile behavior with a beating frequency of about 1 Hz. Fluo-4 loaded cardiac cells in primary culture demonstrated large fluctuating increases of the intracellular free calcium concentration. Long-term recordings of extracellular field potentials with microelectrode arrays from 60 planar electrodes showed repetitive electrical membrane depolarizations that coincided with the whole-cell Ca^{2+} transients. Whole-cell patch clamp analysis revealed the existence of regular membrane depolarizations. A close correlation between the three processes was noticed. Such a correlation was confirmed in the absence of extracellular calcium, which reversibly halted the appearance of the whole-cell Ca^{2+} transients and the electrical processes. Involvement of membrane depolarizations was suggested, because cellular depolarization prevented the spontaneous activity of the cardiomyocytes. In conclusion, our experiments suggest that the oscillations in intracellular calcium and the membrane depolarizations that we observe in rat embryonic cardiac myocytes reflect Ca^{2+} influx after membrane depolarization. The processes responsible for the membrane depolarizations remain to be elucidated.**

Keywords— **embryonic cardiomyocytes, multi-electrode arrays, patch-clamp, intracellular calcium**

I. Introduction

Generation of spontaneous electrical activity in the adult heart originates in the sinoatrial nodal cells located in the right atrium. These cells lack a stable resting membrane potential. Instead, spontaneous depolarizations take place because of three processes that coordinate to reverse the ratio of outward versus inward positively charged ion currents in favor of the inward currents: (1) slowdown of the repolarizing outward directed K^+ current; (2) activation of a depolarizing Na^+/Ca^{2+} exchanger current; and (3) opening of hyperpolarizing-activated channels that create a slowly depolarizing inward current [1]. These three processes, mentioned in accordance to their importance, serve a pacemaking system to initiate rhythmic activity to these cells and the whole heart.

Embryonic hearts are spontaneous active as well, but the mechanisms involved appear to differ from the adult heart. Several authors attempted to elucidate the underlying processes by either using primary cultures [2] or stem-cell derived cardiomyocytes [3]. Even though several steps are identified at the moment a full picture is still lacking. The purpose of this work was to investigate the processes by applying innovative approaches for electrophysiological research and combining them with traditional methods.

II. Materials and methods

A. Primary Culture of Embryonic Cardiac Cells

Pregnant female Wistar rats (E16) were terminated by carbon dioxide inhalation. Available embryos were removed under sterile conditions and transferred to a Ca^{2+}- and Mg^{2+}-free HBSS solution. The ventricles of the dissected rat embryonic hearts were chopped in small fragments and collected in a Falcon tube. Enzymatic digestion was initialized in a 5 mL trypsin-EDTA (0.05%) solution for 8 min at 37°C. After removal of the supernatant, free DNA from the heart pieces was digested in the presence of 100 µl DNAse type II (10,000 units/mL, Sigma) for 3 min at room temperature. Consequently, the heart fragments passed six cycles of trypsin-EDTA treatment at 37°C each one 8 minutes. After every treatment, the supernatant was recovered in 4 mL cardiac culture medium, enriched with 33% fetal calf serum (FCS, Gibco) and kept on ice. Next, the collected cells in the six tubes were centrifuged at 200g for 10 minutes at 4°C. The cell pellets were resuspended in Hams F10 cardiac culture medium, enriched with 5% FCS, 0.5% mixture of insulin, transferring and selenite and 0.1% penicillin/streptomycin and plated for 90 minutes in small dishes for selective adhesion of accompanying fibroblasts. Subsequently, the cells in the solutions on top was recollected and centrifuged at 200g for 10 minutes at 22°C. The cell pellets were resuspended in 1 mL of cardiac culture medium and counted. Cells were seeded at a density of 100,000 cells/mL and incubated at 37°C. Cells were used for experiments after minimally 2 days of culture and up to 14 days. Culture medium was refreshed twice a week.

B. Ca^{2+} Imaging

We used Fluo 4 as Ca^{2+} sensitive fluorescent dye. Fluo 4-AM (Invitrogen, Belgium) was dissolved in DMSO contain-

O. Dössel and W.C. Schlegel (Eds.): WC 2009, IFMBE Proceedings 25/VIII, pp. 285–288, 2009.
www.springerlink.com

ing 20% (w/v) pluronic acid to obtain a final concentration of 5 µM Fluo 4 (Fluo 4 stock solution). Cells were loaded by incubating the cells with 10 µL of a Fluo 4 stock solution in 500 mL culture medium for 30 minutes at 37°C. Afterwards, the cell were rinsed with appropriate buffer solution and transferred to the measuring unit. Changes in the free intracellular calcium concentration of the cells were visualized on a confocal microscope (Pascal LSM5, Zeiss, Germany) by illumination with the Argon laser at 488 nm and emission detection at 520 nm.

C. Solutions and Chemicals

An isotonic solution for perfusion of the cells during control conditions consisted of the following components (in mM): 135 NaCl, 5.9 KCl, 1.5 $CaCl_2.2H_2O$, 1.2 $MgCl_2$, 11.6 Na^+HEPES^- and 11.5 glucose; pH = 7.43. A depolarizing (high K^+) solution was composed as follows (in mM): 135 KCl, 5.9 NaCl, 1.5 $CaCl_2.2H_2O$, 1.2 $MgCl_2$, 11.6 Na^+HEPES^- and 11.5 glucose; pH = 7.43. The Ca^{2+}-free solution contained (in mM): 135 NaCl, 5.9 KCl, 2 EGTA, 1.2 $MgCl_2$, 11.6 Na^+HEPES^- and 11.5 glucose; pH = 7.43.

Caffeine was ordered from Sigma, Belgium.

D. Whole-cell Patch Clamping

Patch clamp experiments were carried out in the current clamp mode, using the whole-cell patch clamp technique. Quartz glass pipettes with an inner diameter of 1 mm and a series resistance of 2-5 MΩ were pulled with a Zeitz micropipette puller. The pipettes were filled with a solution of the following composition: 140 mM KCl, 5 mM EGTA, 5 mM NaCl, 5 mM Na_2ATP, 10 mM K^+HEPES^-, 1 mM $MgCl_2$, pH = 7.4. After the formation of a gigaseal, the membrane was ruptured using ZAP pulses and changes in the membrane potential of the clamped cells were recorded in continuous current clamp mode.

E. Multi-electrode Array (MEA) Recordings

Microelectrode array chips (MEAs) were purchased from Multichannel Systems (Reutlingen, Germany). Different layouts were used including HEXA-MEA, High-density MEA, and the standard 8x8 MEA. Prior to cell seeding, the surface of the MEAs was made hydrophilic by UV/O3 exposure for 5 minutes. Chips were sterilized using an ethanol-based solution (ethanol:water, 70:30, v/v), rinsed 3 times with DI water and dried in air. Field potential recordings were performed using the upright 60-MEA set-up, combined with the MC Rack software.

III. Results and Discussions

A. Cellular activity in control conditions

Embryonic cardiac cells, cultured for 3 days on an HEXA-MEA, were mounted on the stage of the confocal microscope and continuously perfused with control buffer solution. The temperatures of both the incoming perfusion solution and the measuring chamber were kept constant at 37°C. Figure 1, panel A displays a typical Ca^{2+} imaging recording of the embryonic cardiac cells.

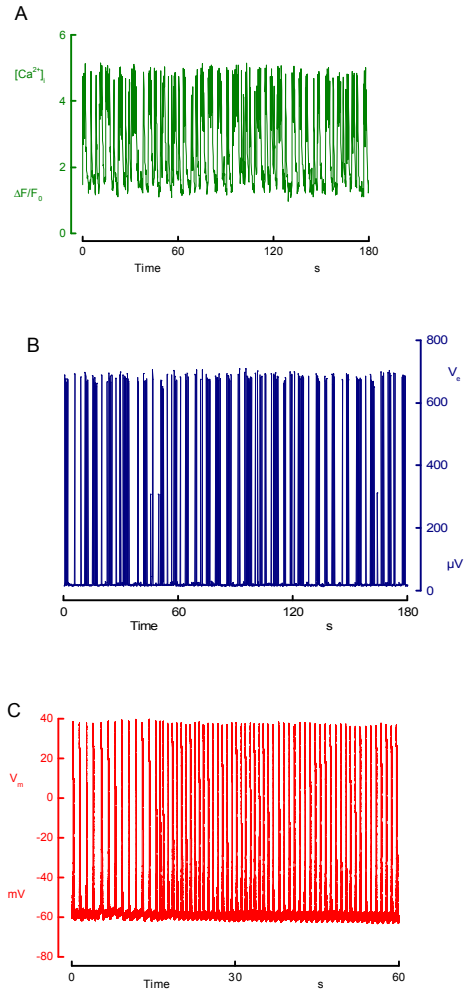


Fig. 1 - A - $[Ca^{2+}]_i$ changes of rat embryonic cardiac cells - B - Extracellular field potentials - C- Changes of the membrane potential in function of time.

It is possible to observe large changes in the free intracellular Ca^{2+} concentration ($[Ca^{2+}]_i$) that appear in a regular time frame.

The changes in intracellular Ca^{2+} may be involved in both the electrical activity as well as the contraction of the muscular filaments. Therefore, we recorded simultaneously the extracellular field potentials of cells. Figure 1, panel B displays a typical recording of one sensor. Repetitive fast upstrokes of short duration with amplitudes of about 700 µV are observed.

In addition, a cardiac cell located on top of a sensor was assessed for patch clamping. Whole cell depolarizations with amplitudes of 100 mV are noticed to occur in a steady way.

Figure 2 illustrates the strong correlation between the observed processes.

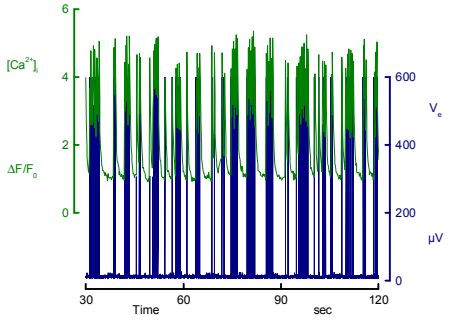


Fig. 2 - Simultaneous recordings of the changes in $[Ca^{2+}]_i$ and of the extracellular field potentials.

B. The nature of the extracellular field potential

The upper panel of Fig. 3 shows two typical extracellular field potentials manifesting as a biphasic record, consisting of a fast component followed by a less pronounced phase.

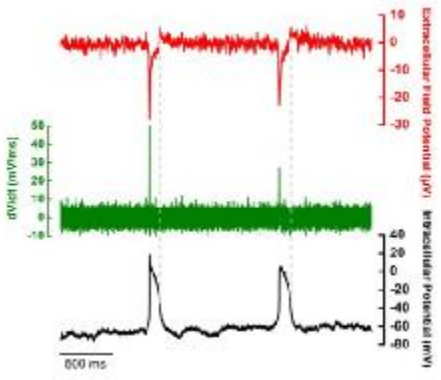


Fig. 3 - Simultaneous recordings of the extracellular voltage (upper panel) and the whole cell membrane potential (lower panel). In between the first derivative of the intracellular voltage.

The fast component likely represents firing of action potentials in the vicinity of the electrode. The fast fluctuations are caused by the inward and outward currents that flow during the action potential. The shape, polarity and amplitude of the extracellular field potential signal depend on several parameters, including passive circuit currents and the distance of the cell to the electrode. From the simultaneous recorded action potentials it can be observed that the first phase of the extracellular field potential correlates with the onset of the action potential, whereas the amplitude depends on the rising time of the action potential (first derivative, dV/dt). In addition, the plateau phase of the field potential nicely corresponds with the repolarizing phase. Therefore, these observations indicate that extracellular field potentials include several properties of the electrical activity of the cells that can be identified after careful analysis, thereby adding the increase in spatial information compared to patch clamp, because of the great number of cells that can be analyzed simultaneously.

Figure 4 shows extracellular field potentials and intracellular Ca^{2+} transients of cardiomyocytes cultured on top of the HEXA-MEA. We analyzed the electrical activity at 9 different locations within the monolayer. The observed planar electrodes had different dimensions (30 µm for E14 and E26; 20 µm for E17, E23, E24, and E25; and 10 µm for E33, E34, and E35).

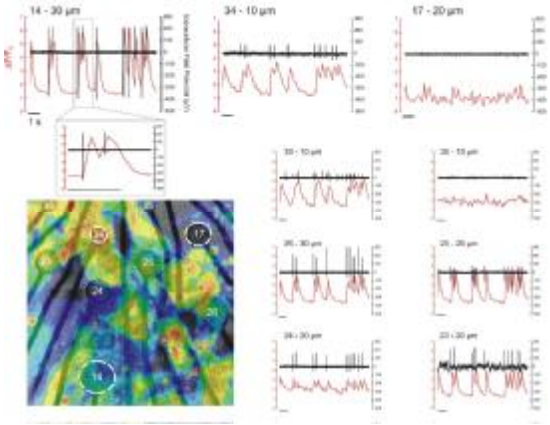


Fig. 4 - Changes in $[Ca^{2+}]_i$ and of the extracellular field potentials recorded at 9 different electrodes.

In addition, $[Ca^{2+}]_i$ changes were monitored and regions of interests were selected that corresponded to the positions and the dimensions of the electrodes mentioned above. With the exception of E17 and E35, which were void of cells, synchronized spontaneous field potentials were recorded, indicating that cells were electrically coupled within the monolayer. For all field potentials analyzed, a close correlation was found between their amplitude and the diameter of the electrode. This is related to the lower impedance of large electrode surfaces. It is also apparent that concomitant with field potentials rhythmic changes in intracellular Ca^{2+} were recorded. The whole-cell Ca^{2+} transients either started from

the resting Ca^{2+} level (base-line Ca^{2+} transient) or from an elevated plateau level (plateau Ca^{2+} oscillation). Base-line Ca^{2+} transients were always preceded by large amplitude field potentials. In the interpretation of the field potential as related to the first derivative of the action potential, these findings indicate that base-line Ca^{2+} transients are triggered by propagating full action potentials.

C. Dependency on extracellular calcium

From the early stages of cardiogenesis, mammalian cardiomyocytes have both an excitable membrane and a functional sarcoplasmatic reticulum (SR) suggesting that these whole-cell Ca^{2+} transients reflect Ca^{2+} influx via voltage-operated Ca^{2+} channels and subsequent Ca^{2+}-induced Ca^{2+} release from the SR. Field potentials recorded during plateau Ca^{2+} oscillations, on the other hand, frequently displayed a lower amplitude and their onset followed the increase in $[Ca^{2+}]_i$. These findings indicate that these field potentials reflect slow membrane depolarizations driven by spontaneous Ca^{2+} release from the SR. These experiments thus suggest that in embryonic cardiomyocytes global Ca^{2+} signals can be generated by two different mechanisms (action potential and SR-driven).

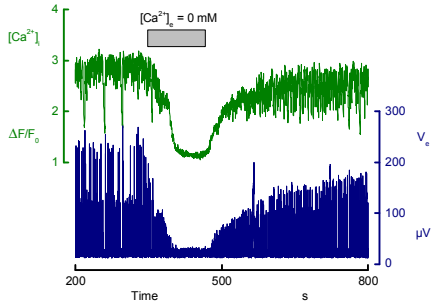


Fig. 5 - Effect of extracellular calcium on the changes in $[Ca^{2+}]_i$ and of the extracellular field potentials.

If whole-cell Ca^{2+} transients are driven by Ca^{2+} influx activated by propagating action potentials, blocking Ca^{2+} influx should result in the disappearance of spontaneous activity. As shown in Fig. 5, a solution void of calcium in contact with the cardiomyocytes ceased their spontaneous activity. Cellular activity could be restored after perfusing the cells with the Ca^{2+}-containing control solution.

D. Dependency on membrane depolarizations

We created conditions in which the cardiac cells were fully depolarized by exposing the cells to a perfusion solution with a high K^+ concentration. In the presence of high K^+ the generation of field potentials was inhibited while $[Ca^{2+}]_i$ strongly increased towards an elevated plateau level (Fig. 6). These data indicate that whole-cell Ca^{2+} transients in embryonic cardiomyocytes are driven by action potentials.

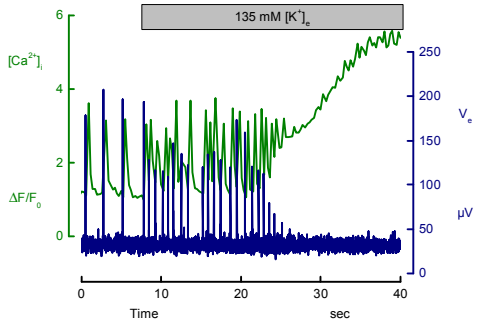


Fig. 6 - Effect of high external K^+ on the changes in $[Ca^{2+}]_i$ and the extracellular field potentials.

IV. CONCLUSIONS

There exists an increased interest to use MEA recordings for obtaining information about the cellular electrical activity. Advantageous is the amount of spatial information that becomes available. The signal recorded with MEA sensors revealed all phases of the intracellular action potential. Combining MEA recording with Ca^{2+} imaging revealed that the whole-cell Ca^{2+} transients in cultured cardiomyocytes were accompanied by electrical activity. Both activities strongly depended on influx through voltage-gated ion channels. However, the origin of the spontaneous activity is not clear at the moment.

ACKNOWLEDGMENT

We acknowledge both the Catholic University of Leuven (K.U. Leuven, Belgium) and the Institute for Microelectronics (IMEC, Heverlee, Belgium) for financial support and IMEC for the accommodation. All experiments were performed at IMEC.

REFERENCES

1. Maltsev VA and Lakatta EG (2007) Heart, Lung and Circulation 16:335-348
2. Sasse P, et al (2007) Intracellular Ca2+ oscillations, a potential pacemaking mechanism in early embryonic heart cells. J Gen Physiol 130:133-144
3. Banach K, et al (2003) Development of electrical activity in cardiac myocytes aggregates derived from mouse embryonic stem cells. Am J Physiol Heart Circ Physiol 284: H2114–H2123

The Design and Construction of a Set of Modular Synthetic BioLogic Devices for Programming Cells

B. Wang[1], R. Kitney[1], M. Buck[2], M. Jovanovic[2], N. Joly[2], E. James[2]

[1]Department of Bioengineering, Imperial College London, London, UK
[2]Division of Biology, Imperial College London, London, UK

Abstract— **Modularity is an essential property for rationally engineered standard parts and devices. This principle is now being extended to biological based parts and devices for programming cells. However, the design principles and building blocks which are currently in Synthetic Biology are somewhat limited. In addition, it is important to explore the underlying mechanisms of existing, natural biological systems in order to utilise them in designing novel genetic circuit modules. In this paper, we will describe a set of modular synthetic biological parts and devices that are based in rational design. Particularly, a modular tight-controlled and hypersensitive genetic circuit with digital logic AND function is rationally designed and engineered. They use a sigma factor 54 (σ^{54}) dependent hetero-regulation module in the *hrp* (hypersensitive response and pathogenicity) gene regulatory system for Type III secretion in *Pseudomonas syringae*. Their inputs and outputs are both promoters and thus do not rely on specific inducible promoters and could drive various cellular responses. It shows that the *hrp* system has significant potential for building a range of biological parts and devices with good performance and flexibility.**

Keywords— ***hrp* gene regulation, modularity, rational design, genetic devices.**

I. Introduction

Synthetic biology has great potential to extend or modify the behaviour of organisms and to engineer them to perform new tasks through the design and construction of new biological parts, devices and systems, and the redesign of existing, natural biological systems. The long-term goal is to program cells using genetic circuits in the way which is similar in concept to how computers are programmed today. Up to now various biological parts and devices have been designed and built by synthetic biologists [1]. For example, genetic circuits which mimicking digital logic gates [2] and biological oscillators designed to behave like their electronic counterpart [3]. Their initial applications are also demonstrated in some pioneering research such as the *Escherichia coli* can be programmed as biosensors to invade cancer cells upon specific environmental stimulations [4]. However, the design principles and building blocks which are currently available in synthetic biology are somewhat limited. Most of the devices are designed to use specific inputs to drive specific outputs, which make them difficult to incorporate and reuse in other circuit programs. By contrast, modular devices can be easily connected to other modules, and connected to different inputs to drive various outputs. In addition, it is important to explore the underlying mechanisms of existing, natural biological systems in order to utilise them in designing novel genetic circuit modules with good performance, as they are usually evolved to behave with optimized functions.

In this paper, we have designed and constructed a set of modular logic devices using genetic modules in the *hrp* (hypersensitive response and pathogenicity) gene regulation system for Type III secretion in *Pseudomonas syringae*, whose inputs and outputs are both promoters. The output promoter is only turned on when a specific logic combination of input promoters is active. The main advantage is that they use a σ^{54} dependent, high-order hetero regulation module in the system, which can be tightly controlled and is highly sensitive. Their input-output relationships sare modelled with mathematical descriptions.

II. Materials and Methods

A. Hrp gene regulation system

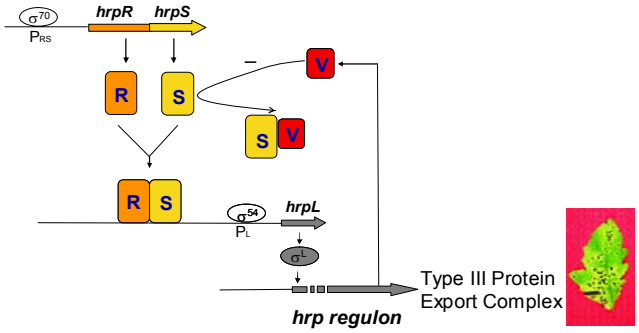
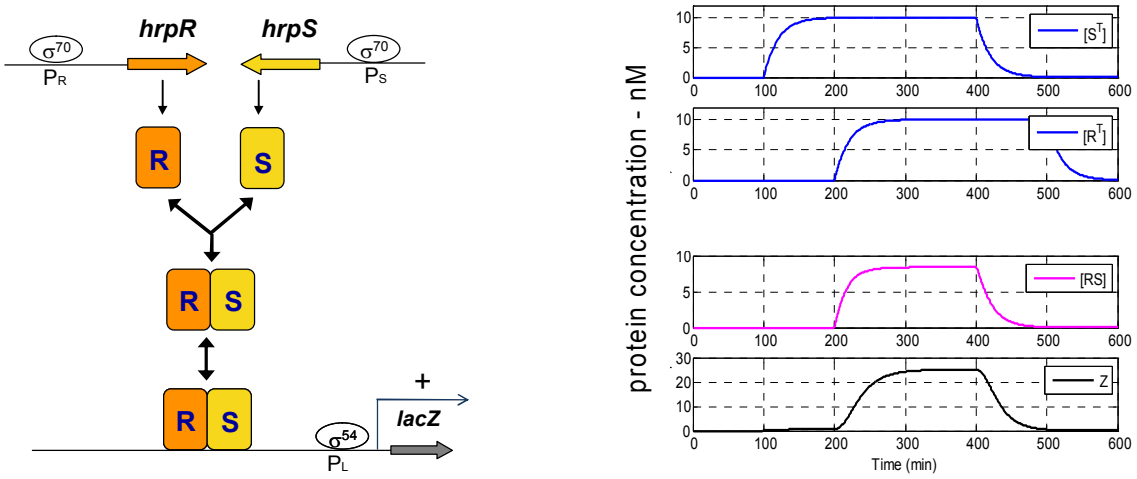


Fig.1. The extracted *P. syringae hrp* gene regulation model, which determines its ability to cause disease in host plants and to elicit the HR (hypersentive response) in non-hosts [6]. The σ^{54} dependent *hrpL* promoter is the primary regulator of this system, which is activated by the high order heterogeneous protein complex HrpRS (AAA+ protein family). HrpV plays as the negative regulator of *hrpL* promoter by interacting with HrpS.

O. Dössel and W.C. Schlegel (Eds.): WC 2009, IFMBE Proceedings 25/VIII, pp. 289–292, 2009.
www.springerlink.com

The ability of *P. syringae* to cause diseases in host plants and to elicit the HR (hypersensitive response) in non-hosts is controlled by the *hrp* and *hrc* (hypersensitive response and conserved) genes residing in pathogenic gene clusters of its Type III protein secretion systems [7]. Based on current knowledge of the *hrp* gene regulation and our experimental data, HrpR, HrpS, and HrpV proteins have been identified as the primary regulatory components for the σ^{54} dependent *hrpL* promoter, which controls the expression of *hrp* gene clusters (Fig. 1).

B. Modelling



(a) (b)

Fig.2. The modelling of the system when promoter *hrpL* is only regulated by the regulatory factors – HrpR and HrpS. (a) is the schematic view of the system setup which shows the main biochemical reactions and interactions in the system. (b) is the simulation results which displays the dynamic evolution of protein concentrations of interest. $[S^T]$, $[R^T]$ are the total concentrations of protein HrpR and HrpS, and [RS] and [Z] represent the levels of protein complex HrpRS and protein lacZ.

Table 1 The primary biochemical reactions in the model of the system and their corresponding modelling equations. mRNA(Z) denotes the mRNA for protein Z. K denotes synthesis rate constant for protein or mRNA and D denotes degradation rate constant. K_{RS_on} and K_{RS_off} are the association and dissociation rate constants of protein-promoter complex. n_{rs} is the Hill coefficient.

Reactions	Notes	Equations	
$mRNA(R) \xrightarrow{K_R} mRNA(R) + R$	synthesis of protein R from mRNA(R)	$\frac{d[R]}{dt} = K_R[mRNA]_R - D_R[R] - K_{RS_on}[R][S] + K_{RS_off}[RS]$	(1)
$mRNA(S) \xrightarrow{K_S} mRNA(S) + S$	synthesis of protein S from mRNA(S)	$\frac{d[S]}{dt} = K_S[mRNA]_S - D_S[S] - K_{RS_on}[R][S] + K_{RS_off}[RS]$	(2)
$R + S \underset{K_{RS_off}}{\overset{K_{RS_on}}{\rightleftharpoons}} RS$	association of protein R and S, and dissociation of RS complex	$\frac{d[RS]}{dt} = K_{RS_on}[R][S] - K_{RS_off}[RS] - D_{RS}[RS]$	(3)
$n_{rs}RS + P_{hrpL} \underset{K_{RSP_off}}{\overset{K_{RSP_on}}{\rightleftharpoons}} n_{rs}RSP_{hrpL}$	activator RS binds to promoter *hrpL*		
$n_{rs}RSP_{hrpL} \xrightarrow{K_{mZ_RS}} mRNA(Z) + n_{rs}RSP_{hrpL}$	synthesis of mRNA(Z) from binding complex of RS and *hrpL*	$\frac{d[Z]}{dt} = \frac{K_Z[RS]^{n_{rs}}}{KD_{RS}^{n_{rs}} + [RS]^{n_{rs}}} - D_Z[Z]$	(4)
$mRNA(Z) \xrightarrow{K_Z} mRNA(Z) + Z$	synthesis of Z from mRNA(Z)		

A quantitative dynamic model based on protein and protein-promoter interactions for the *hrp* gene regulatory module was built (Fig. 2, Table 1) [8]. In this case, HrpR (R) and HrpS (S) are expressed under two inducible promoters. R binds S to form a heterogeneous protein complex HrpRS (RS), which then binds to the DNA binding sites in the *hrpL* promoter to activate the transcription of downstream *lacZ* gene. The simulation results correlate well with the experimental data (not shown here). Consequently, a series of important functions and properties of the regulatory system

are identified. The most efficient components or sensitive parameters in the system, with the desired properties, have been identified using sensitivity analysis. We found that the cooperativity and binding affinity between the proteins HrpR and HrpS are the most sensitive factors contributing to the system transfer – the switching of system steady state from low to high level. These results were then used to guide the device circuit design.

C. Experiments

As the *hrp* gene regulatory system comprises multiple components that interact and regulate each other, we concluded that multiple-input combinatorial logic devices could be constructed using the existing properties of the system. Using the modelling and experimental results, a set of modular parts and devices were designed and constructed using subsets of the regulatory network. These include a 2- and 3-input AND gates, a 2-input AND, but with one input inverted (Fig. 5), etc. These different genetic parts are constructed through standard molecular biology and genetic engineering techniques – and later transformed into the same *E. Coli* MC4100 cell strain to form a functional device like the genetic logic AND gate (Fig. 3 (a)).

III. Results

First, a genetic AND gate was constructed by fusing *hrpR* and *hrpS* genes on two independent inducible promoters - *pLac* and *pBAD* promoters which can be induced by IPTG and arabinose, respectively. The output was connected to the expression of lacZ enzyme and assayed by using the Miller procedure. The results are shown in Fig. 3. From the titration chart of the device behaviour, it can be seen that the circuit behaves as a digital AND gate, where the output is at high level when only the two inputs are activated.

In order to fully characterize the device, the output reporter *lacZ* is then swapped with *GFP* (green fluorescent protein) gene, which allows the dynamic, quick and automated assay of the system output. The initial result of full characterization is displayed in Fig. 4. It shows that the device behaves as a good AND gate, with sharp switching between the low and high levels.

Fig. 5 shows the designs of the two- and three-input modular AND gate but with one input inverted, and their modelling results based upon available experimental data.

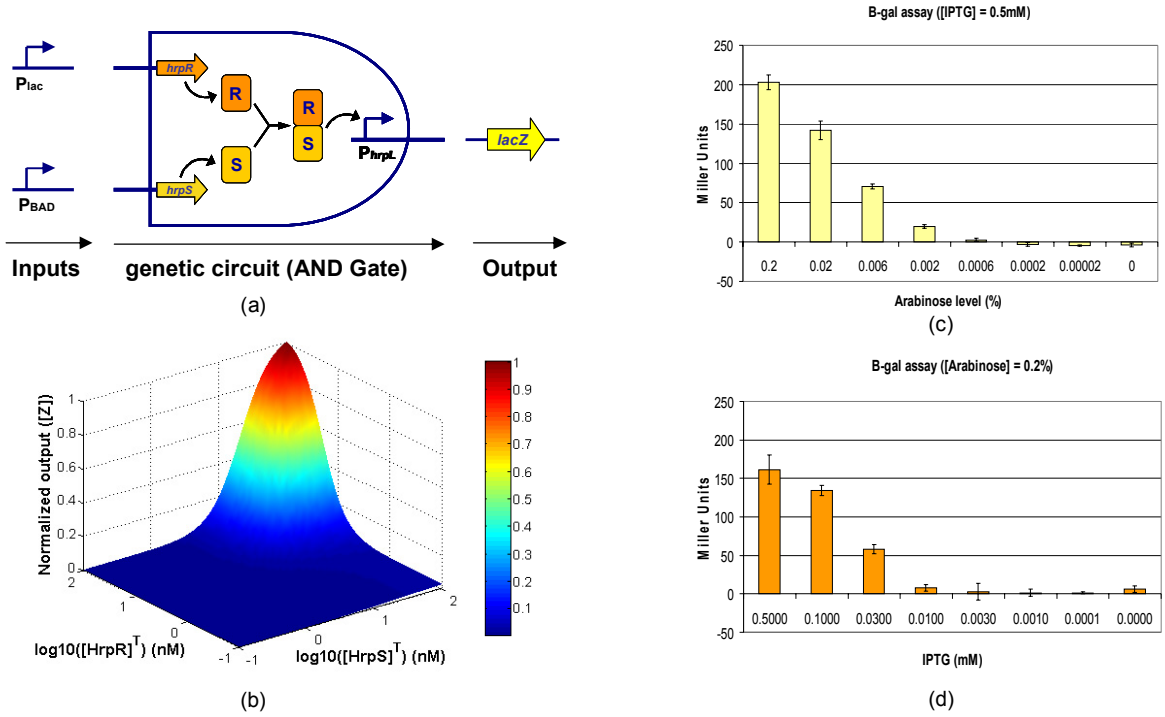


Fig.3. Engineering a modular genetic AND gate. (a) the AND gate comprising two genes *hrpR*, *hrpS,* and one promoter *hrpL*. (b) the modelling of this genetic AND gate system transfer function. (c) and (d) the initial experimental characterization results of the system input-output relationships (in *E.Coli*, MC4100 Ø*hrpL-lacZ,* LB media), which shows a sharp switching between the high and low levels.

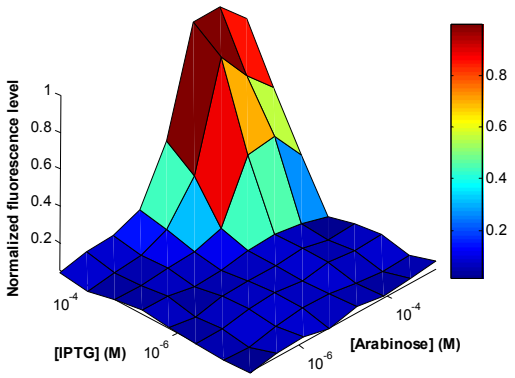


Fig.4 The initial full characterization of the engineered genetic AND gate using *GFP* (green fluorescent protein) as the reporter gene. The chart shows the system output (normalized fluorescence level) versus various concentration levels of the two input inducers – arabinose and IPTG (in *E.Coli*, MC4100, M9 supplemented minimal media with 0.01% glucose. Cells are assayed at mid log phase with 8x8 various combinations of induction at 30˚C.).

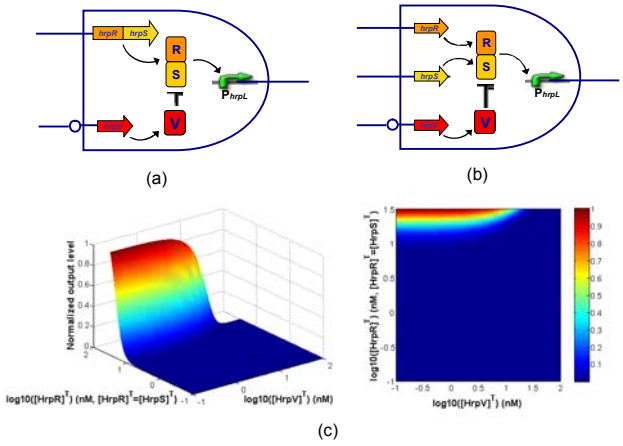


Fig.5 The two- and three-input modular AND gate but with one input inverted. The top, (a) and (b), are the schematic view of the device working mechanism, which is through the co-regulation of the σ^{54} dependent *hrpL* promoter by the two positive regulators (HrpR and HrpS) and the one negative regulator (HrpV). The bottom (c) is the system transfer function from the modelling (the vertical axis is the output level and the horizontal axes are the input levels).

IV. Conclusions

We have designed and constructed a set of modular biologic devices and demonstrated that exploring existing natural biological systems not only helps to explain the underlying mechanisms, but, also, to inform the design of new biological parts and devices. The system described has many advantages, such as the σ^{54} dependent activation [5] and potential hypersensitive response property (the high order heterogeneous protein complex HrpRS activator), which absolutely requires an activator with the default activity close to zero. This greatly increases the tightness and sensitivity of transcription activation. Moreover, these components are designed to be modular and can, potentially, be easily incorporated into larger and more complex systems. The research shows that the *hrp* system has significant potential for building a range of biological parts and devices with good performance. Future work will include the detailed full characterization of these devices and their practical applications for programming cells.

Acknowledgment

The authors would like to thank Dr. Joerg Schumacher, Dr. Vincent Rouilly, Kirsten Jensen and Matthieu Bultelle for their inspiring discussions, advice and support for this work. The experiment work done in Professor Martin Buck's lab is sponsored by the BBSRC.

References

1. Voigt, CA. (2006) Genetic parts to program bacteria. Curr Opin Biotech 17:548-557
2. Anderson, J. C. et al. (2007). Environmental signal integration by a modular AND gate. Mol Syst Biol 3.
3. Kitney, R. I., P. S. Freemont and V. Rouilly (2007). Engineering a molecular predation oscillator. Synthetic Biology, IET 1(1.2): 68-70.
4. Anderson, J. C., E. J. Clarke, A. P. Arkin and C. A. Voigt (2006). Environmentally Controlled Invasion of Cancer Cells by Engineered Bacteria. Journal of Molecular Biology 355(4): 619-627.
5. Buck, M. et al. (2006). A second paradigm for gene activation in bacteria. Biochem. Soc. Trans. 34(Pt 6): 1067-1071.
6. He, S.-Y. et al (2003). Type III protein secretion in Pseudomonas syringae. Microbes and Infection 5(4): 301-310.
7. Collmer, A., J. L. Badel, A. O. Charkowski, W.-L. Deng, D. E. Fouts, A. R. Ramos, A. H. Rehm, D. M. Anderson, O. Schneewind, K. van Dijk and J. R. Alfano (2000). Pseudomonas syringae Hrp type III secretion system and effector proteins. Proc Natl Acad Sci USA 97(16): 8770-8777.
8. Alon, U. (2007). An introduction to systems biology: design principles of biological circuits. London, Chapman & Hall/CRC.

The address of the corresponding author:

Professor Richard Kitney
Department of Bioengineering
Imperial College London
Exhibition Road
London, SW7 2AZ
r.kitney@imperial.ac.uk

An Innovative Rotational Magnetic System to Enhance Cell Transfection with Magnetic Nanoparticles

Dahmani Ch.[1], Helling Fl.[1], Weyh Th.[1], and Plank Ch.[2]

[1] Technische Universität München, Heinz Nixdorf-Lehrstuhl für Medizinische Elektronik, Munich, Germany
[2] Klinikum Rechts der Isar, Institute for Experimental Oncology, Munich, Germany

Abstract— **The use of nanoparticles combined with magnetic fields has gained in importance in medical diagnosis and therapy over the last years. It has also contributed to the improvement of pharmaceutical research and biological methods [6]. In fact, researchers are not only able to target cells with active agents bound to magnetic nanoparticles that are controlled and guided by external magnetic fields, but they also can enhance reproducibly the rate of cell transfection by coating magnetically activated nanoparticles with DNA and pulling the resulting complex through the cell membrane to the inner parts of different kinds of cells. This technique is used to produce proteins for clinical or research applications, to add genetic markers to cell lines and more generally to study DNA replication, recombination and mutation.**

For this application, mainly static magnetic fields have been used, whereas new experiments suggest the use of pulsing fields, with a certain amplitude and a certain frequency, to best improve the transfection rate.

Using fields that change over time necessitates strong electromagnets that are specially conceived for the transient application and really demand a sophisticated design and a strict temperature control due to the emerging eddy currents [3]. These cause a heating of the system that not only leads to instabilities in the resulting magnetic field and the overall experimental parameters but also represents a disturbing factor for the activity of the treated cells and even a danger for their viability.

We developed a new system that delivers the needed field characteristics without using electromagnets and therefore excludes their drawbacks and limitations. As a matter of fact, we conceived a new rotational permanent magnet system based on a brush-less motor that assures the exposure of the magnetic nanoparticles to well defined pulses, which should enhance the efficiency of cell transfection independently of electromagnets´ considerations. Moreover, not only adherent cell cultures can be targeted by the elaborated system, also cells in suspension are easily exposed to the necessary magnetic pulses in the designed setup.

Keywords— **superparamagnetic nanoparticles, cell transfection, magnetofection, magnetic field pulses.**

I. INTRODUCTION

Whereas chemical as well as physical processes, including electroporation, are considered to be established techniques for improving cell transfection, the use of superparamagnetic nanoparticles combined with magnetic fields to do so, generally referred to as "magnetofection", is still in the intensive study stadium.

Till now, mainly static magnetic fields have been investigated and have shown great improvement rates, explained by the drag forces acting on the magnetic nanoparticles that are drawn to and through the cell membrane, where they can deposit their DNA load and enhance transfection. It is furthermore believed that pulsed magnetic fields will not only drag the transported DNA faster to the cells but would also create transient cell membrane openings [7], so called pores, either through the direct impact on the membrane or through the activation of a certain vibration mechanism due to the resulting repeated "pulling and pushing"-action on the nanoparticles, driven by the applied magnetic force:

$$F = \mu * \text{grad}\,(B)$$

Where μ is the magnetic moment of the nanoparticle and B is the flux density of the magnetic field [1][2][5].

Recent research work at the Department of Chemical Engineering at the National Chung Cheng University of Taiwan has shown improved transfection rates using magnetic pulses with - and even without - nanoparticles [1].

In the light of this new evidence, we tried to also improve the transfection effect by conceiving a magnetic pulsing system that should overcome the drawbacks of using electromagnets. These are subject to very strict construction constraints and are limited due to the rapid heating of the system which raises its resistance and therefore reduces the applied electric current, resulting in fluctuations in the experimental parameters and eventually erroneous predictions.

The idea behind the new concept is the use of permanent magnets that should be moved in a rotating system to produce the needed magnetic pulses without the inconvenience of electromagnets.

O. Dössel and W.C. Schlegel (Eds.): WC 2009, IFMBE Proceedings 25/VIII, pp. 293–296, 2009.
www.springerlink.com

II. Materials and Methods

A. Use of magnetic pulses to improve cell transfection

Chao-Bin Chen et al. have proved the increased efficiency of cell transfection when it is performed using magnetic nanoparticles dragged by external magnetic field pulses. Although the mechanisms behind this phenomenon are still a field of study, it can be believed that the pulses produce a bombardment of magnetic nanoparticles that push these tiny DNA carriers into the cell inner medium, where they can release their charge. Or the particles are simply dragged to the membrane where they can deposit the carried DNA, without even entering the intracellular space. One might also think of an induced mechanical membrane vibration due to the pulses, which would enlarge the membrane pores for a very short period of time and result in the diffusion of the DNA to the cell inner part. Either way, the obtained results were proven for adherent cells and cells in suspension, in some cases reaching a raise of 19 to 90 % in the transfection efficiency [1].

The pulses used in these experiments had magnitudes of 0.2 to 0.66 T and were spaced by 6 seconds in time. The pulse delivering magnetizer needed a 1100V DC source, which lets us easily expect high eddy currents and a rapid heating of the device.

B. The new system to generate the needed magnetic pulses

Eddy currents and the resulting heating in electromagnets generate a variation in the electric current [3], which not only leads to instabilities in the developed magnetic field and the overall experimental parameters but also represents a danger and a disturbing factor for the treated cells.

To exclude the drawbacks of electromagnets in the process of enhancing cell transfection with magnetic pulses, we elaborated a new concept that would only involve permanent magnets and still generate the necessary variable field. To be able to deliver pulsing fields with these magnets, we needed a comparable mechanical system that assures a very rapid transient change in the magnetic flux density surrounding the nanoparticles.

An eventually translational movement of a permanent magnet would not be as fast as needed and therefore could not deliver the needed changes in terms of field strength.

The approach that is most likely to generate the intended pulses is thus a rotating system which keeps the flux density in the targeted region varying rapidly over the time. The estimated pulse magnitude should hereby exceed $6*10^{-3}$ to $7*10^{-2}$ T and the pulse duration should ideally be in the range of 10^{-5}s to 10^{-1}s [7].

C. Simulation and technical realization

The concept was first proven through simulations to predict the behaviour of the flux density in the targeted sites and adjust frequencies and amplitudes.

The conceived system has been implemented in COMSOL Multiphysics and consisted of two permanent magnet rods (10 x 20 x 120 mm) rotating counter-clockwise and separated by 20 mm. Each of them had a remanent flux density of 1.43T, which is the highest achieved value for industrial usage.

The two magnet rods were placed following 4 possible arrangements, as depicted in Figure 1, with a magnetization along the width and along the depth, in parallel and anti-parallel direction.

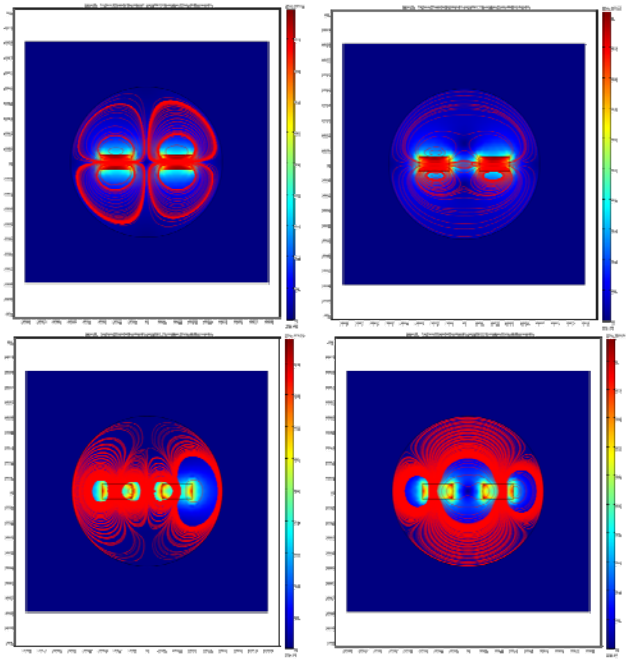


Fig. 1 magnetic flux density distribution and magnetic field lines of the simulated magnet dispositions (top: magnetization along width, parallel and anti-parallel, bottom: magnetization along depth, parallel and anti-parallel)

The rotation was modeled using a deformed mesh application mode, in which the center part of the geometry, containing the rotating magnets and the space between and surrounding them (indicated through the index "rot"), rotates with a rotation transformation relative to the default coordinate system (indicated through the index "stat"). The rotation of the deformed mesh is defined by the transformation

$$\begin{bmatrix} x_{rot} \\ y_{rot} \end{bmatrix} = \begin{bmatrix} \cos(\omega t) & -\sin(\omega t) \\ \sin(\omega t) & \cos(\omega t) \end{bmatrix} \cdot \begin{bmatrix} x_{stat} \\ y_{stat} \end{bmatrix}$$

where ω is the angular frequency.

The rotating magnetization was also implemented following the same transformation [4].

The results of the simulation were then used to construct the system involving two permanent magnet cuboids made out of Neodymium-Iron-Boron (NdFeB) with a 10 micron coating of Nickel (Ni+Cu+Ni) and having a residual induction of B_r = 1.43T. The magnet control was performed using a brush-less motor system carrying out rotations of up to 4000 turns per minute, which corresponds to a maximum frequency of 2 x 4000/60s = 133.33Hz.

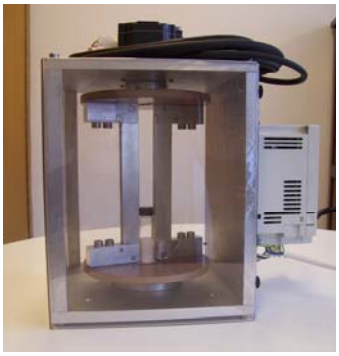


Fig. 2 The constructed rotating magnetic system

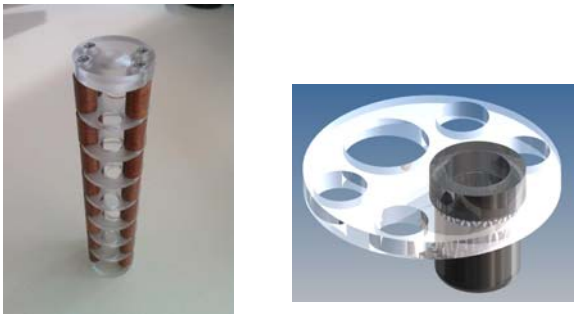


Fig. 3 Conceived and developed sample recipient (right) and multi-recipient holder (left) for the cells to be transfected

III. RESULTS

The conceived rotating magnetic system was evaluated throughout the simulations and generated optimal results in both embodiments shown in figures 3 and 4, with the plotted field characteristics, respectively calculated at the center between the two magnets and at a space point shifted 5mm in the x-direction from the center.

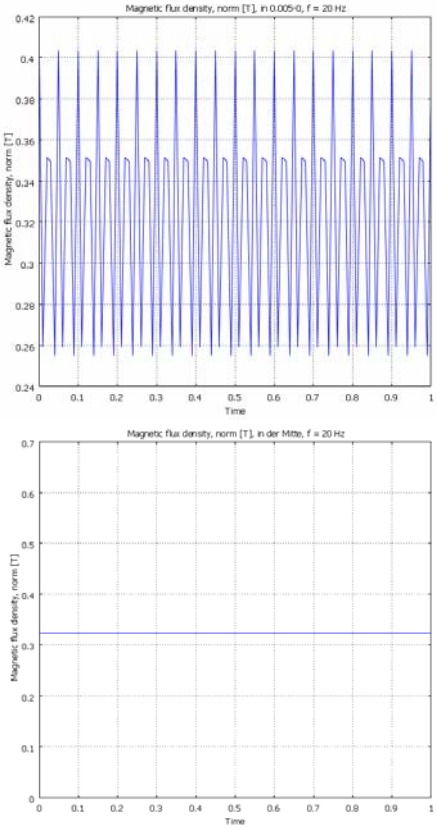


Fig. 4: Magnetic flux density at the point (5mm|0) (top) and at the center of the system (bottom), the magnetization is along the depth, in parallel arrangement.

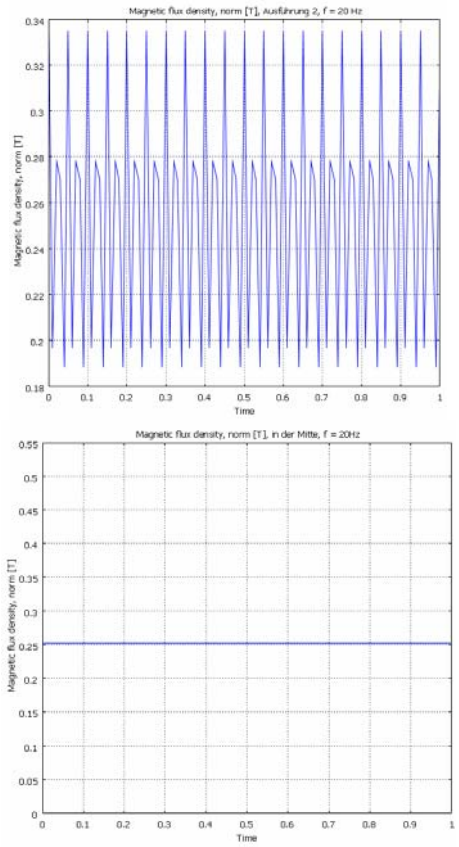


Fig. 5: Magnetic flux density at the point (5mm|0) (top) and at the center of the system (bottom), the magnetization is along the width, in parallel arrangement.

The developed system produced the expected pulse forms, durations (10^{-5}s < t_{pulse} < 10^{-1}s, as described in [7]) and magnitudes (B > 7*10^{-2}T). Moreover, not only adherent cell cultures could be targeted by the elaborated system, also cells in suspension were easily exposed to the necessary magnetic pulses in the designed setup.

The system has been successfully tested and assures its functions without any intervention of electromagnets. It is suited for adherent cells and cells in suspension that can be placed in a flacon between the two magnet rods.

IV. Discussion

Through this new concept, we have been able to reach the effect of varying magnetic fields without using electromagnets and thus assuring the exclusion of their drawbacks like heating and resulting fluctuations in the electric current, which not only leads to instabilities in the resulting magnetic field and the overall experimental parameters but also represents a danger and a disturbing factor for the treated cells.

The developed rotating system delivers the needed magnetic pulses to improve cell transfection, in the presence and also in the absence of magnetic nanoparticles.

Though this enhances transfection efficiency, independently of the supposed biological theory explaining the phenomenon behind it, we believe that profoundly understanding the mechanisms of transfection –which is still in progress till now– would surely lead to the development of even more efficiency enhancing techniques.

Engineering can deliver solutions to well defined biological problems and known aims, but it can only generate the optimal technical approach, when all biological aspects are studied and phenomena are understood.

Acknowledgment

We want to thank Comsol Multiphysics for providing us with their simulation software.

References

1. Chao-Bin Chen, Ji-Yao Chen and Wen-Chien Lee. Gene transfer mediated by impulsed magnetic field. Revised manuscript for publication in Biomacromolecules, March 2007

2. Bernhard Gleich, Aktiver Wirkstofftransport mit magnetischen Feldern, 2007, pp 72

3. Eberhard Kallenbach, Rüdiger Eick, Peer Quendt, „Elektromagnete. Grundlagen, Berechnung, Konstruktion, Anwendung“, Vieweg+Teubner Verlag, 2003, pp 189-190

4. Comsol Multiphysics, Modeling Guide. 2009.

5. Alexiou, Christoph, et al. “A High Field Gradient Magnet for Magnetic Drug Targeting”, IEEE Transactions on applied superconductivity, Vol. 16, No. 2, pp 1527-1530 (2006)

6. Eugenii Katz and Itmar Willner, Integrierte Hybridsysteme aus Nanopartikeln und Biomolekülen: Synthese, Eigenschaften und Anwendungen, Angewandte Chemie, 2004, 116, 6166-6235

7. Timothy E. Vaughan and James C. Weaver ”Energetic Constraints on the Creation of Cell Membrane Pores by Magnetic Particles“, Biophysical Journal, Volume 71, August 1996, pp 616-622

PROTMINE: A Web Service Based Tool to Interpreter Clinical Proteomic Data

M. Giacomini[1], S. Ravaschio[1], S. De Nadai[1], A. Petretto[2], and G. Melioli[2]

[1] Department of Communication Computer and System Science, University of Genova, Genova, Italy
[2] Central Laboratory, Giannina Gaslini Institute, Genova, Italy

Abstract— **Nowadays scientific research improvements allow a lager information quantity, especially since Internet has been developed. In this paper we will deal with Proteomics data management, this branch studies protein elements which can be found in a living organism or in a biological system. This project was born at the same time Visual Studio and SQL Server had been used to build up a web site for the Proteomic data management. This idea has been developed by the "Giannina Gaslini" Institute of Genoa and the "Department of Communication Computer and System Sciences" (DIST) of University of Genoa. The projects name is "Protmine".**

Keywords— **Clinical Proteomics; Web Service.**

I. INTRODUCTION

Humans have been "manually" extracting information from data for centuries, but the increasing volumes of data in modern times has called for more automatic approaches. As data sets and the information extracted from them have grown in size and complexity, direct hands-on data analysis has increasingly been supplemented and augmented with indirect, automatic data processing using more complex and sophisticated tools, methods and models. The proliferation and increasing power of computer technology has aided data collection, processing, management and storage. However, the captured data needs to be converted into information and knowledge to become useful. The development of Internet has allowed to collect the data also in Biological area, especially in Proteomics.

Proteomics is the large-scale study of proteins, particularly their structures and functions. Proteins are vital parts of living organisms, as they are the main components of the physiological metabolic pathways of cells. The proteome is the entire complement of proteins, including the modifications made to a particular set of proteins, produced by an organism or system. This will vary with time and distinct requirements, or stresses, that a cell or organism undergoes.

Proteomics is often considered the next step in the study of biological systems, after genomics. It is much more complicated than genomics, mostly because while an organism's genome is more or less constant, the proteome differs from cell to cell and from time to time. This is because distinct genes are expressed in distinct cell types, meaning that even the basic set of proteins which are produced in a cell needs to be determined.

The EMBL-EBI lies in the 55 acres of landscaped parkland in rural Cambridgeshire that make up the Wellcome Trust Genome Campus. The EMBL-EBI grew out of EMBL's pioneering work to provide public biological databases to the research community. The EMBL-EBI provides a unique environment for bioinformatics research, for example:

- to provide freely available data and bioinformatics services to all facets of the scientific community in ways that promote scientific progress;
- to contribute to the advancement of biology through basic investigator-driven research in bioinformatics;
- to provide advanced bioinformatics training to scientists at all levels, from PhD students to independent investigators;
- to help disseminate cutting-edge technologies to industry.

The International Protein Index (IPI) provides a top level guide to the main databases that describe the human, mouse and rat proteomes. IPI is built from the protein sequence data taken from the UniProt Knowledgebase, Ensembl and RefSeq databases, which are combined to create proteome sets for each species that combine a level degree of completeness with a low level of redundancy. Stable identifiers (with incremental versioning) allow the tracking of sequences in IPI between IPI releases, while cross-references are provided between equivalent entries in the source databases.

II. MATERIALS AND METHODS

Effectively, it's been created a web site application on the server of the MEDINFO Laboratory of the DIST (http://www.medinfo.dist.unige.it/Protmine), developed in ASP.NET 2.0 environment.

SQL (Structured Query Language) is a database computer language designed for the retrieval and management of data in relational database management systems, database

O. Dössel and W.C. Schlegel (Eds.): WC 2009, IFMBE Proceedings 25/VIII, pp. 297–298, 2009.
www.springerlink.com

schema creation and modification, and database object access control management.

SQL is a programming language for querying and modifying data and managing databases. SQL was standardized first by the ANSI and (later) by the ISO. Most database management systems implement a majority of one of these standards and add their proprietary extensions. SQL allows the retrieval, insertion, updating, and deletion of data. A database management system also includes management and administrative functions. Most -- if not all -- implementations also include a Command-line Interface (SQL/CLI) that allows for the entry and execution of the language commands, as opposed to only providing an API intended for access from a GUI.

Microsoft Visual Studio is an Integrated Development Environment (IDE) from Microsoft. It can be used to develop console and Graphical user interface applications along with Windows Forms applications, web sites, web applications, and web services in both native code together with managed code for all platforms supported by Microsoft Windows, Windows Mobile, Windows CE, .NET Framework, .NET Compact Framework and Microsoft Silverlight.

Visual Studio includes a code editor supporting IntelliSense as well as code refactoring. The integrated debugger works both as a source-level debugger and a machine-level debugger. Other built-in tools include a forms designer for building GUI applications, web designer, class designer, and database schema designer. It allows plug-ins to be added that enhance the functionality at almost every level - including adding support for source control systems to adding new toolsets like editors and visual designers for domain-specific languages or toolsets for other aspects of the software development lifecycle.

The Department of Experimental Medicine of Gaslini Hospital produces an Excel file, using the ProteomeLabTM PF2D Protein Fractionation System of Beckman Coulter. It's a partially automated system which allows the separation of a protein blend by two steps: first considering the iso-electric point of proteins and then, set a range of pH, evaluating the strength of hydrophobic bonds, using chromatography. Due to this system it's possible to identify the single proteins contained and mixed in the blood sample by searching and analysing the peptides which belong to them [1].

III. RESULTS

At present we are in the testing phase for data collection and comparison. Specifically more than 150 protein lists have been successfully uploaded by people from clinical laboratories of the Gaslini Institute. In this phase we are comparing these lists mainly according to cellular protein location and protein function in order to verify if significant differences in the profiles of these characteristics can be correlated with specific clinical status in which the samples are collected.

A news about Protmine is the use of the EBI Web Service. Now we can construct a smaller database and we have a faster elaboration and consultation.

A further advantage: we have always data up-to-date, because we communicate in real time with the EBI service.

The organization of the proteomic community is of high level also as regards computer data management, so that many web based tools are available. Specifically, EBI support data integration with their databases in many ways. We decided to use web services maintained by EBI servers. This decision is due to their complete and non redundant content , their speedy answer, completely acceptable within the time requirements of this project.

At DIST Server, a MS SQL Server DB has been set up in order to collect experimental data (mainly list of proteins identified in clinical samples) and to correlate them with relevant clinical information of the sample. A web based interface allows people from clinical laboratory to submit the collected lists and to compare results within different experiments. EBI web services are interrogated to collect proteomic data chosen by experimental people in order to support data mining reasoning rules.

Further investigation with modern data mining tools like Artificial Neural Networks will be tried.

REFERENCES

1. Levreri I., Musante L., Petretto A., Bruschi M., Candiano G., Melioli G., (2005) - Separation of human serum proteins using the Beckman-Coulter PF2DTM system: analysis of ion exchange-based first dimension chromatography. Clin Chem Lab Med, 43(12):1327-1333

Corresponding Author: Mauro Giacomini
Institute: DIST – University of Genova
Street: Via All'Opera Pia 13
City: 16145 Genova
Country: Italy
Email: Mauro.Giacomini@dist.unige.it

Silicon Based Multi Parametric Biohybrid Microsensor Chips

Y. Eminağa[1], J.Wiest[2], M. Remm[1], M. Brischwein[1] and B. Wolf[1,3]

[1] Heinz Nixdorf-Lehrstuhl für Medizinische Elektronik, Technische Universität München, Munich, Germany
[2] cellasys GmbH im Innovationszentrum Medizinische Elektronik, Munich, Germany
[3] Zentralinstitut für Medizintechnik der Technischen Universität München (IMETUM), Munich, Germany

Abstract — **The Heinz Nixdorf-Lehrstuhl für Medizinische Elekronik at Technische Universität München has developed silicon based biosensor chips for monitoring activities of cell cultures, which combine the thin-film bio sensors with those based on semiconductor technology. The O_2/ISFET sensors (ion-sensitive field-effect transistor) and the pn temperature diode use the semiconductor properties of the silicon substrate, while the amperometric sensor and the IDES (integrated electrode structures) were realized on the surface of the silicon wafer using platinum structures. These perform dissolved oxygen concentration measurement, pH measurement, impedance measurement and temperature measurement, integrated on the same chip.**

Keywords — **Silicon Biosensors, ISFET, O_2-FET, pH, cellular respiration.**

I. Introduction

Biomedical analysis techniques require the development of smart sensors with low cost, low power consumption and ease of use. Various sensors have been developed to cover the needs of the biomedical research field. In these researches, biological cell cultures are analyzed under different conditions. The biochemical activities of these cultures change parameters of the environment which they live in. This environment can be enclosed and protected from any outer effects, so any changes by the living biological cells can be detected using various detecting methods. One of these methods is electrochemistry, which covers the detecting of electrical signals caused by chemical reactions. [1]

Semiconductor sensors have not only the advantage that they have smaller dimensions than the sensors made with other materials but also the possibility to integrate several sensor types on the same chip. Miniature electronic circuits and structures e.g. memory or amplifiers can be produced on the same wafer with the sensor at the same time. On the other hand, only mass produced semiconductor sensors are economically producible. Alternatively, researches are also done using thin film technology to produce sensors on glass or ceramic. [2]

Because of rapid development in the field of the semiconductor production with its high quality at small dimensions, the silicon sensors are not to be ignored. Therefore the Heinz Nixdorf-Lehrstuhl für Medizinische Elekronik has developed silicon based biosensor chips for monitoring activities of cell cultures.

II. Materials and Methods

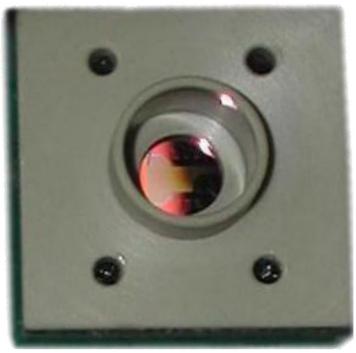


Fig. 1 The Si-Biosensor chip

The silicon biosensor chip is fixed on a PLCC68-compatible printed wire board (24mm x 24mm) and is electrically contacted by wire-bonding. To create a culture vessel, the chip is encapsulated by injection molding. The diameter of the chip area grown with cells is 6 mm and the volume for cell culture media is 7mm^2. Figure. 1 shows the packaged sensorchip. Changes in extracellular acidification, cellular respiration and adhesion/morphology of cell cultures can be monitored at the same time on the same chip. The measurement parameters and the corresponding sensor for its detection are listed in the following table.

Table 1 Types of microsensors on the chip

Parameter	Used microsensor	Number of sensors
Reference Transistor	MISFET	1
Temperature	PN-diode	1
Impedance	IDES	1
pH value	ISFET, O_2-FET	4 2
Dissolved oxygen	Amperometric oxygen sensor, O_2-FET	1 2

O. Dössel and W.C. Schlegel (Eds.): WC 2009, IFMBE Proceedings 25/VIII, pp. 299–302, 2009.
www.springerlink.com

A. IDES Sensor

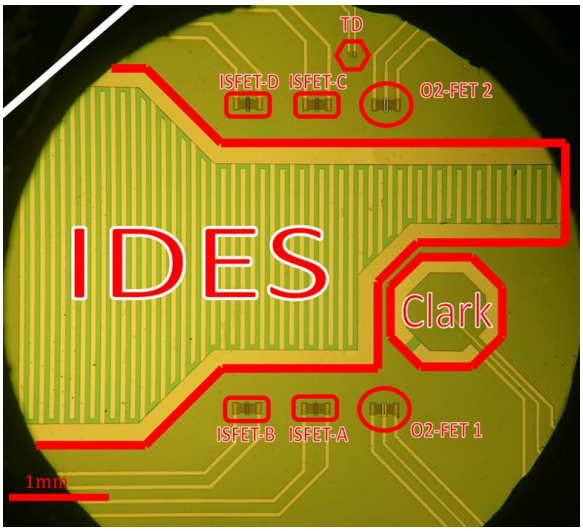


Fig. 2 The Si-Biosensor chip with the IDES in the middle

Changes in cellular growth condition (which are interpreted toward cellular adhesion / morphology / proliferation) are detected with an IDES sensor. The impedance of the cell layer is measured. [3] A 30mV sinusoidal voltage with the frequency of 10 kHz is applied and the resulting impedance is determined. A drugs effect on the growth conditions of living cells can be detected with this IDES sensor. [4]

B. Temperature Diode

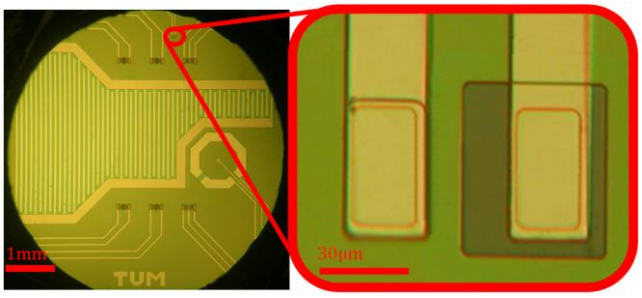


Fig. 3 The PN-temperature diode

For control purposes the temperature on the biosensor chip is also monitored. For this purpose a temperature dependent PN-diode is used.

C. Amperometric dissolved oxygen sensor

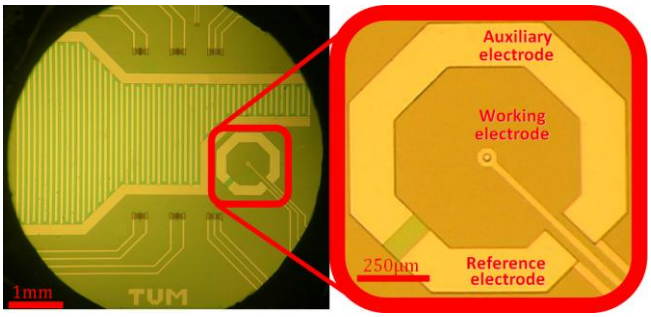


Fig. 4 The amperometric dissolves oxygen sensor

Dissolved oxygen is reduced electrochemically via a negative potential applied to the work electrode. An electric current measured between the work and the auxiliary electrode is proportional to the reduced oxygen. This enables the change of the cellular respiration to be detected, when the cells are responding to drugs. [5]

D. ISFET Sensor

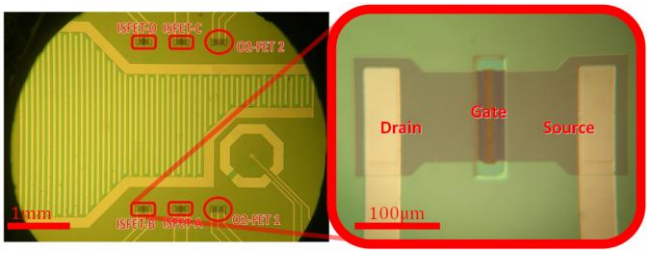


Fig. 5 The pH ISFET sensor

The working principle of the ISFET sensor was introduced and describes for the first time by Bergveld in 1979. [6] The ISFET is simply a MISFET (metal insulator semiconductor FET) without its gate contact. Instead of the metallic gate contact an ion-sensitive layer is used, on which the ions of the cell culture medium build an electric potential. This potential makes the underlying semiconductor conductive and allows current to flow through the activated n-channel between source and drain depending on the pH value of the medium.

A drug has effects toward the proton ion channel of a cell and shifts the hydroxide concentration of the culture medium which is detected with the ISFET sensor.

E. O_2-FET Sensor

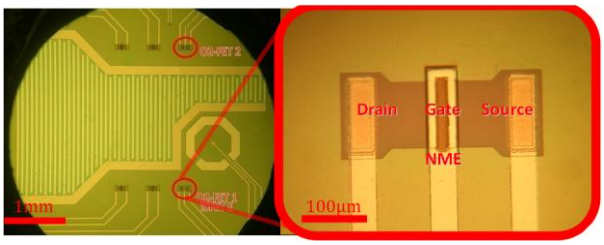


Fig. 6 The O_2-FET sensor

Since the ISFET sensor was developed primary to measure the pH value of fluidic media, it was not possible to use it for measuring dissolved oxygen. This problem was solved by additional use of a ring shaped NME surrounding ISFETs ion-sensitive area as described by Lahmann [7]. Thus the ISFET was developed further to an O_2-FET and successfully evaluated. Additionally the neighboring amperometric dissolved oxygen sensor confirms the results of the O_2-FET sensor.

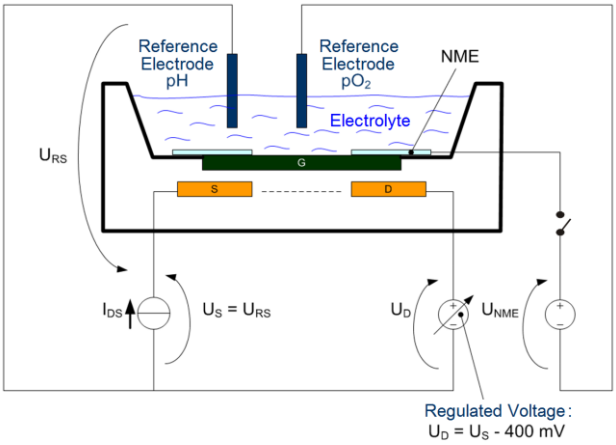


Fig. 7 The functional principle of the O2-FET sensor

The measurement system has two isolated electrical circuits. The first one is an ISFET controlling circuit. The second one is a simple amperometric oxygen sensor circuit; the NME and a reference electrode have contact to the measuring electrolyte. With this unique simple modification the O_2-FET is now able to measure pH and dissolved oxygen even quasi parallel. If zero volts at the NME are applied, the O_2-FET works as a pH ISFET sensor and if -600mV are applied; the O_2-FET works as a sensor for dissolved oxygen. The operating point -600mV was determined by cyclic voltammetry with oxygen saturated and oxygen depleted phosphate buffered saline (PBS). [8]

III. Resullts

Extracellular acidification and cellular respiration of the cell caltures are the main parameters to monitor on the sensor chip, therefore the results of the sensors used for measuring dissolved oxygen and pH value will be presented in more detail.

- Amperometric dissolved oxygen sensor

The work electrode of the amperometric dissolved oxygen sensor has a diameter of 35 m, with a limit current of about -8nA. That is about the same ratio of 0.2nA/ m as Bahr [9] has calculated. After successful measurements on several chips, the best choice for an operating point is at -600mV. This value is located in the plateau region of all sensors we tested. The plateau region, where the limit current flows, has an average width of 600mV.

- ISFET pH sensor

It is remarkable that beside the usual pH sensitivity in the triodic transistor operating mode (45mV/pH) the sensor has a much higher pH dependent signal in the weak inversion mode. In this region a sensitivity of 3V/pH value at a working of I_{DS}= -22nA was successfully achieved. The senstivity of the ISFET sensor in the weak inversion region was comfirmed by using different pH valued PBS media (phosphate buffered saline) for several cycles.

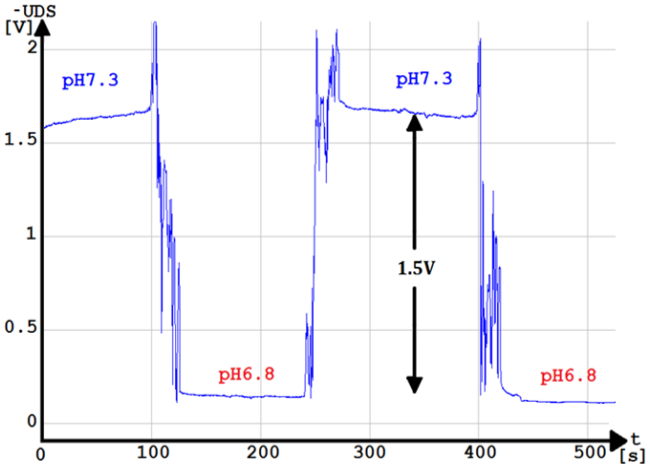


Fig. 8 Measuring pH value using ISFET sensor in the weak inversion region at a working point of I_{DS}=-22nA

Figure 8 shows an example measurment using two PBS media with a difference of 0.5 pH between them. The resulted signal was stabilized within 5 seconds.

- O_2-FET sensor

A cyclic potential U_{NME} switching between zero and -600mV is applied. This electrical potential is repeated during the measurement.

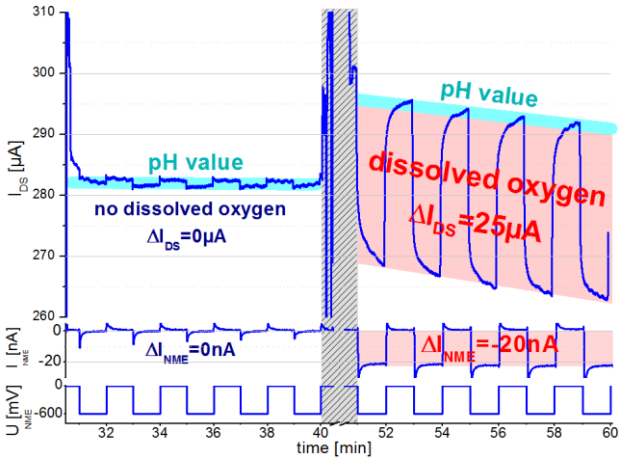


Fig. 9 Measuring dissolved oxygen using O_2-FET

As shown in figure 9, the dissolved oxygen concentration corresponded to the amplitude of the top-down source drain current peaks in each cycle of the NME voltage. The amplitude of such a peak correlated with the higher oxygen concentration in the medium. In oxygen saturated medium, the amplitude was 27 A; while in oxygen depleted medium it was 2 A. This amounted to a difference of 25 A between oxygen saturation and depletion. This measured current is a thousand times bigger than the current measured with the amperometric oxygen sensor. In other words, the O_2-FET works like an amplifier for electrochemical currents.

The measured I_{NME} is the current of the applied cyclic voltage U_{NME}. If there is no dissolved oxygen, there will also be no I_{NME} current. A current of about -20nA corresponds to 100% air saturated oxygen. This is can be used as a control measurement for the current peak meathode described before.

Table 2 Sensitivity of the sensors

Sensor	Oparating point	Sensitivity
IDES	U=30mV@10kHz	-80mΩ/mM NaCl
Temperature Diode	I_{TD}=1 A	-100mV/°C
Amper. Oxygen Sensor	U_{NME}=-600mV	-8nA@100%O_2
ISFET-Sensor	I_{DS} = 1mA	+45mV/pH
	I_{DS} = -22nA	-3V/pH
O_2-FET	U_{DS}= -1.5V U_{NME} = 0,-600mV	-25µA@100%O_2 -20nA@100%O_2

IV. Conclusions

With the presented biosensor chip, field and laboratory measurements can be done now directly on living cells. It is possible to prove the effectiveness of a drug on cancer cells and determine their response to chemotherapeutics in an in-vitro environment without using any animals. Micro-organisms e.g. algae can also be populated to measure its metabolic reactions as an evidence of their vitality and give conclusions on water quality. [10] So, any cells reacting to certain substances can be used as living mediators, by monitoring their metabolic activity with silicon sensors in dependency on the substance concentration.

References

1. Wolf B., Kraus M., Brischwein M., et al. (1998) Biofunctional hybrid structures - cell-silicon hybrids for applications in biomedicine and bioinformatics. Bioelectrochemistry and Bioenergetics, 46:215-25
2. Wiest, J., Stadthagen T., Schmidhuber M., et al. (2006) Intelligent mobile lab for metabolics in environmental monitoring. Analytical Letters, 39:1759-1771
3. Brischwein M., Grothe H., Otto A.M., et al. (2004) Ultrathin Electrochemical Chemo- and Biosensors. ed. V.M.Mirsky, p. 159
4. Ehret R., Baumann W.H., Brischwein M., et al. (1997) Monitoring of cellular behavior by impedance measurements on interdigitated electrode structures. Biosensors &Bioelectronics, 12:29-41
5. Wiest J, Brischwein M, Grothe H, et al., (2005) Planar Microsensors for measurement of cellular respiration. SENSOR 2005 Proceedings II: 249-254
6. Bergveld P. (2003) Thirty years of ISFETOLOGY What happened in the past 30 years and what may happen in the next 30 years. Sensors and Actuators B; Chemical, vol. 88:1-20
7. Lehmann M., Baumann W., Brischwein M., et al (2001) Simultaneous measurement of cellular respiration and acidification with a single CMOS ISFET. Biosensors & Bioelectronics 16:195–203
8. Wiest J., Brischwein M., Ressler J., et al. (2005) Cellular Assays with Multiparametric Bioelectronic Sensor Chips. Chimia 2005;59:243-6.
9. Bahr L. (2002) Evaluirung planarer Sensorstrukturen zur Messung der zellulären Respiration. Heinz Nixdorf-Lehrstuhl für Medizinische Elektronik, Technische Universität München
10. Otto A., Brischwein M., Niendorf A., et al. (2003) Microphysiological testing for chemosensitivity of living tumor cells with multiparametric microsensor chips. Cancer Detection and Prevention 27:291-296

Address of the corresponding author:

Author: Yazay Eminağa
Institute: Heinz Nixdorf-Lehrstuhl für Medizinische Elektronik, Technische Universität München
Street: Theresienstr. 90
City: Munich
Country: Germany
Email: eminaga@tum.de

Stent-Based Plasmid Gene Delivery into Porcine Coronary Artery

L.H. Zhang[1], T. Luo[2], C. Zhang[1], P. Luo[2], X. Jin[1], H.F. Sun[1], C.X. Song[1,*], and R.L. Gao[2,*]

[1]The Institute of Biomedical Engineering, Peking Union Medical College & Chinese Academy of Medical Sciences (PUMC & CAMS), Tianjin 300192, China; [2] Fu-Wai Hospital for Cardiovascular Disease, PUMC & CAMS, Beijing 100037, China. *Corresponding authors

***Abstract*—We successfully tethered plasmid gene on coronary stents using a novel antibody-tethering strategy and demonstrated highly site-specific gene delivery without systemic vector spreading in a porcine coronary stenting model. The novel system showed long-term therapeutic effects on the inhibition of restenosis when an inducible NOS (iNOS) cDNA was tethered on the stent.**

***Key Words*—Intravascular gene delivery, stent modification, restenosis, plasmid gene expression**

I. INTRODUCTION

Despite remarkable success of percutaneous coronary intervention (PCI) with stenting, restenosis has remained the major drawback that has absorbed intensive research work. With better understanding of the pathophysiology and molecular mechanism of restenosis, gene therapy has emerged as a promising approach aimed at modification of cellular processes that give rise to restenosis. Success of gene therapy requires the combination of a therapeutic gene, an appropriate gene vector and a device to deliver the vector into the diseased vascular site [1]. Coronary stents have shown great potential as an ideal platform for localized delivery of vectors to the vascular wall [2]. Stent-based gene delivery utilizing antibody-tethering approach reported by Levy group [3] has been demonstrated to be feasible to deliver viral vector with reporter gene, avoiding gene vectors eluting easily from stents, thus achieving high levels of regional arterial gene expression. In our most recent study, a tri-complex (pDAC) composed of plasmid DNA-antiDNA Antibody-Cationic lipid was successfully tethered on collagen-coated stent using the novel antibody-tethering strategy. The new system showed highly localized gene delivery and efficient plasmid gene (GFP reporter) transfection in cell culture and in a locally infused rabbit carotid model.[4]

The aim of the present study is to evaluate (i) *in vivo* transfection of plasmid gene delivered by the pDAC-stent system in a pig coronary PCI-stenting model; (ii) long-term therapeutic effect of the pDAC-stent system carrying an iNOS as therapeutic gene for the inhibition of restenosis after coronary stenting for 28 days in pigs.

II. EXPERIMENTAL METHODS

A. Materials

A monoclonal Mouse anti-Bovine DNA antibody (IgM) recognizing double-stranded and single-stranded DNA was obtained from US Biological (Swampscott, MA, USA)(1mg/ml). N-Succinimidyl-3-(2-pyridyldithiol)-propionate (SPDP) was obtained from Pierce Chemical (Rockfold, IL, USA). Lipofectamine™ 2000 Transfection Reagent, Superscript ™III First-Strand cDNA Synthesis System and Trizol were purchased from Invitrogen (Invitrogen, Carlsbad, CA, USA). Plasmid encoding a green fluorescent protein (GFP) with enhanced fluorescence (*pEGFP-C1*) was purchased from Clontech (Palo Alto, CA, USA). GFP expression was assessed using fluorescent microscopy with a filter calibrated to detect fluorescent isothiocyanate (FITC; Nikon Inc., Melville, NY,USA). Mustang® 316L stainless steel coronary stents (2.5×13mm) were a gift from MicroPort Medical (Shanghai) Co., Ltd. pcDNA3.1-iNOS was a gift from Professor Gao Runlin (Fu-Wai Hospital for Cardiovascular Disease, Beijing, China).

B. Protocol for preparing the pDAC-tethered stents

The pDAC-tethered stents were prepared as previously described [5]. Briefly, a collagen-coated stent was reacted with SPDP followed by reduction with dithiothreitol to introduce SH-group on the stent (SH-stents). Separately, the anti- DNA antibody was reacted with SPDP to introduce dithiol groups on the antibody molecules (S-S-antibody). The S-S-antibody was then chemically linked on the SH -stents by the established thiolexchanging reaction. The anti-DNA antibody-bound stent was incubated in a pEGFP or a cDNA plasmid encording an inducible nitric oxide synthase (p-iNOS) solution at 37 ◦C for 1 h followed by an extensive rinse with PBS. The stent was further incubated with Lipofectamine™ 2000 Reagent at room temperature for approximately 35 min before PCI surgery.

C. PCI procedure

The Administrative Committee on Animal Research in the Institute of Biomedical Engineering approved all the protocols for the animal experiments. Angioplasty was performed on mini-swines (male, 25–305 kg) using a quantitative coronary angiography system. The stents were

O. Dössel and W.C. Schlegel (Eds.): WC 2009, IFMBE Proceedings 25/VIII, pp. 303–305, 2009.
www.springerlink.com

implanted into right carotid arteries (RCA) and left anterior descending coronary artery (LAD) via 8F large lumen guiding catheters. Stents with collagen coating only were used as the control and implanted in the same way. After the surgery, all swines were given penicillin (4.8 million unit/day) intramuscularly for up to 3days. No systemic anticoagulants were given after the procedures. Euthanasia was performed with a continuous infusion of thiopental after 7days post implantation for the pEGFP-stenting groups or 28 days for the p-iNOS-stenting groups. Stents and tissue samples such as stented arteries, arterial segments distal to the stents, surrounding organs were retrieved and evaluated for gene expression. Representative arterial samples were embedded in frozen section media, and subjected to cryosectioning, then fixed in 4% paraformaldehyde, and examined using fluorescence microscopy for GFP. For the iNOS–stenting samples, RT-PCR analysis was performed.

D. RT-PCR analysis

In brief, total RNA was extracted using the TRIzol reagent® (Invitrogen, Germany) according to the manufacturer's instructions and the integrity of RNA was checked on 2% agarose gel electrophoresis. Reverse transcription reaction was performed using a SuperScript III First-strand Synthesis System for RT-PCR (Invitrogen, Carlsbad, CA). The iNOS primers used for these analyses were 5'-AGCGGTAACAAAGGAGATAGA-3' forward (F1); and 5'-AACCACTCG TATTTGGGATG-3' reverse (R1). Glyceraldehyde-3 phosphate dehydrogenase(GAPDH) was chosen as an internal control in the RT-PCR reaction. PCR conditions include denaturation (94°C for 5min); annealing (57°C for 30 s); extension (72°C for 30 s); number of cycles (30). The PCR product was resolved by 1% TAE-agarose gel electrophoresis and photographed under UV light using a Gel Doc 1000 system (Bio-Rad).

E. Histology and morphology

Representative arterial samples were fixed by 4% paraformaldehyde, followed with routine dehydration, embedding, cutting with microtome, dewaxing, staining with hematoxylin-eosin and observing under optical microscope for assessing the neointimal proliferation.

III. RESULTS AND DISCUSSION

A. Gene transfection by pEGFP -tethered stents

Repeat angiography was performed 15 minutes after stent implantation to confirm vessel patency and stent position. The angiography showed well-opened coronary ostia with good antegrade flow, no residual stenosis and no stent migration. All animals survived until necropsy with no significant adverse events noted. The stented arteries were anatomized under a surgical microscope and showed no evidence of vessel thrombosis. The pigs that had been implanted with the pEGFP-tethered stents showed complete endothelialization around the stent struts. The artery segments, which had been in close contact with the antibody-immobilized/ pEGFP-tethered stents, showed strong fluorescent signal in the intimal and medial layer (Figures1A and 1B). By contrast, the arterial segments 1 cm distal to the pEGFP-tethering stents revealed only weak autofluorescence (Figure 1C). These data demonstrated that plasmid DNA carried on coronary stents by the novel antiDNA antibody-immobilization and DNA- tethering approach avoided DNA leaching in blood circulation during the PCI procedure, that ensured highly site-specific gene transfection without distal vector spreading.

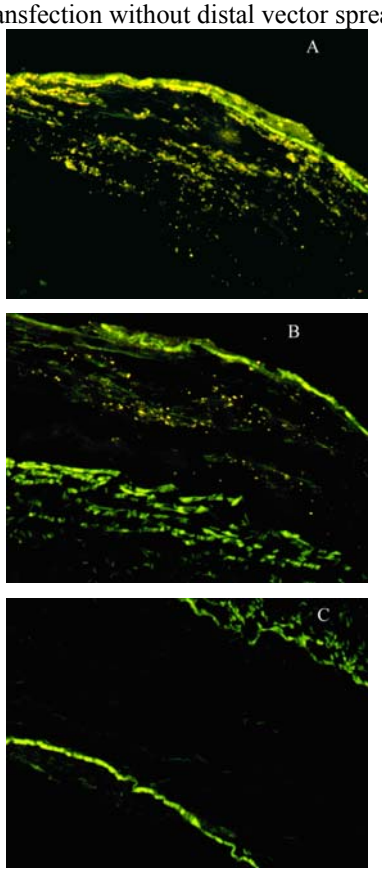


Fig. 1: Pig coronary gene transfection 7days after stenting. A&B: Stented arteries with pEGFP-tethered stents. GFP-positive cells were detected as a strong green fluorescence located in the intimal (A) and medial layers (B). C: The arterial segments of 1 cm distal to the pEGFP tethered stent showed only autofluroscence.

B. Gene expression by p-iNOS-tethered stents

All animals survived the 28 days until the time of euthanasia, and their weights at that time did not vary significantly among the groups. The stented arteries showed no obvious evidence of vessel thrombosis. RT-PCR results

from the stented arteries showed 515bp ladders, which are in accordance with the pre-designed iNOS primers, indicating iNOS gene expression in the stented coronary arteries (fig 2A). By contrast, there was no expression of iNOS in the tissue samples of control arteries, arterial segments 1cm distal to the stents, peri-stent myocardiac tissue and distal organs (lung, liver, and kidney) (Fig. 2B). In Fig. 2B the expression of a control housekeeping gene, GAPDH, was detected in all samples, indicating the experimental system was intact and the RNA extraction was successful. The results well support the hypothesis that there was no gene leaching from stent during the course of PCI surgery. The novel antiDNA antibody-immobilization and DNA-tethering approach may enable us to deliver therapeutically efficient amount of cDNA plasmid specifically into the stented artery site to maintain long-term (for at least 28 days as evidenced here) gene transfection and expression.

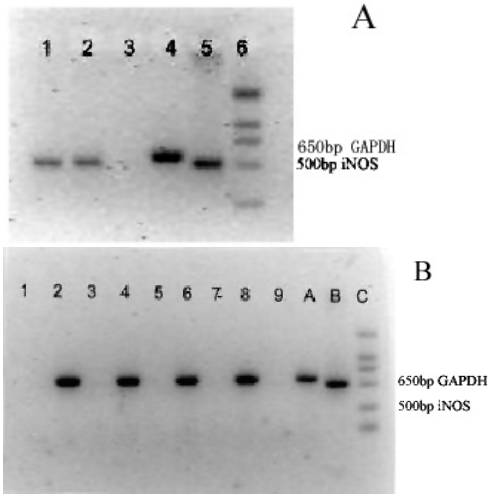


Fig. 2: RT-PCR results for tissue samples 28 days after implantation of p-iNOS-tethered stents: A. Lane 1-2: stented arteries; lane 3-4: control arteries; lane 5: p-iNOS standard; lane 6: DNA markers. B. Lanes 1-2, arteries 1cm distal to the p-iNOS-tethered stents; lane 3-4: peri-stent myocardiac tissue; lane 5-6: liver; lane 7-8: lung; lane 9-A: kidney; lane B: p-iNOS; lane C: DNA markers.

C. Inhibition effect on neointimal proliferation

Figure 3 showed representative photomicrographs of porcine coronary arteries 28 days after stented with the p-iNOS-tethered stents. Some of the cut stent struts remain in the sections (black rectangles) and in some areas the spaces occupied by the stent struts can be identified (unoccupied rectangles). As shown by figure 3, the control artery was observed significant neointimal proliferation (A). As a contrast, arteries treated with the p-iNOS tethered stents showed no significant stenosis and neointimal proliferation (B). A non-injured coronary artery is shown where no evidence of neointimal growth is seen (C).

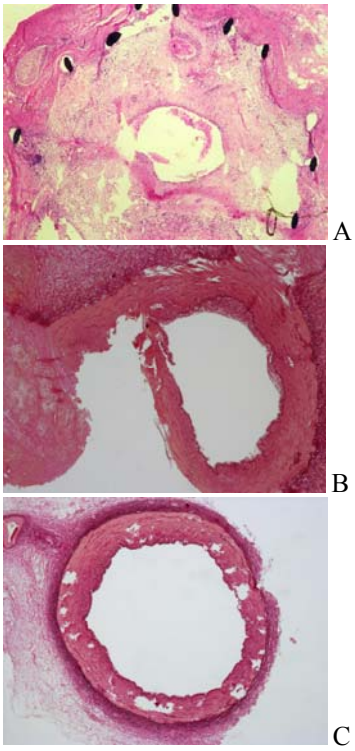


Fig. 3: Representative light micrographes of cross section of porcine coronary arteries 28 days after stent implantation (hematoxylin and eosin staining): A. Stented coronary artery from control group; B. Stented coronary artery from p-iNOS-stethered group; C. Non-injured coronary artery.

IV. Conclusion

In conclusion, the new anti-DNA antibody immobilized and iNOS cDNA tethered coronary stent showed highly localized gene delivery and long-term therapeutic effect after interventional stenting in pig coronary artery for 28 days. Further studies on this novel intravascular gene delivery system should focus on biocompatible modification on metal surface for antibody immobilization so that eliminating the use of collagen coating that may evoke an allergic response.

Aknowledgment

The project was financialy supported by the National Natural Sciense Foundation of China (NSFC) grant #50830106 and #50473059.

References

1. Sharif F, Daly K, Crowley J, et al. Current status of catheter-and stent-based gene therapy. *Cardiovasc Res* 2004; 64: 208–216.
2. Klugherz BD, Jones PL, Cui X, et al. Gene delivery from a DNA controlled-release stent in porcine coronary arteries. Nat Biotechnol 2000; 18: 1181–118
3. Klugherz BD, Song C, DeFelice S, et al. Gene delivery to pig coronary arteries from stents carrying antibody-tethered adenovirus. Hum Gene Ther 2002; 13: 443–454.
4. X Jin[1], L Mei, CX Song, et al.: Anti-DNA antibody modified coronary stent for site-specific plasmid DNA delivery. J Gene Med 2008, 10 (4): 421-429

Disruption of Microvessels by Focused Ultrasound with Microbubbles to Cause the Extravasation of Macromolecules and Observed by Two-photon Fluorescence Microscopy

Kuo-Wei Lu[1] , Chi-Hsun Huang[1] , Chun-Chin Wang[2] , and Win-Li Lin[1,3]

[1] Institute of Biomedical Engineering, National Taiwan University, Taiwan
[2] Department of Physics, National Taiwan University, Taiwan
[3] Medical Engineering Research Division, National Health Research Institutes, Taiwan

Abstract— In this study, we investigated the permeability variation of blood vessels produced by focused ultrasound in presence of micro-bubbles (MB). Both diameter and radius of curvature for the ultrasound transducer are 1.6 cm, and the driving frequency of the transducer is 1.0 MHz. The parameters of ultrasound sonication are pulse length 10 ms, duty cycle 1%, sonication duration 60s, and peak negative pressure 0.6 MPa. The ultrasound contrast agent (UCA), SonoVue, was used as the MB to enhance the microvessels permeability. We used rhodamine-labeled dextrans as macromolecular drug carrier, and observed their transport *in vivo* by two-photon fluorescence microscopy (TPM). The results of this study display that focused ultrasound with MB can disrupt the blood vessel walls for the normal tissue and cause the extravasation of macromolecules and the whole process can be observed from the real-time TPM image.

Keywords— focused ultrasound, blood vessels, microbubbles, two-photon fluorescence microscopy.

I. INTRODUCTION

Heat, mechanical force and cavitation are the three major effects as ultrasound interacts with tissue. When a bubble appears in an ultrasound beam, the bubble oscillates with the acoustic pressure and its size grows. The bubble may collapse as the acoustic pressure is high enough and the oscillation is long enough, and the collapse is called inertial cavitation. For a cavitation, it can produce high temperature, shock waves, high velocity microjets, etc. surrounding the bubble. The results of oscillation and inertial cavitaion are the potential sources of changing the structure of the endothelial wall to increase the permeability of blood vessels. The ability to monitor biological phenomena *in vivo* at nanometer-scale is the key factor to understand biological mechanisms and provides potential applications in medical sciences. Due to nonlinear optical effects, two-photon fluorescence microscopy (TPM) allows us to obtain cellular imaging at the depth of several hundred microns in in-vivo organs of small animals. Furthermore, the point-like excitation nature of TPM results in the images with excellent contrast with minimum photo-damage and disturbance. In this study, we observed the transportation of macromolecules in normal tissues and blood vessels by TPM, and further investigated the transport phenomenon variation of macromolecules when the tissues were exposed to ultrasound sonication with the injection of microbubbles.

II. METHODS AND METERIALS

A. Experimental Animals and Dorsal Skin Fold Window Chamber

Male BALB/c mice weighing from 30 to 40g were used in this study. Each mouse was anesthetized through IP injection of Trichloroacetaldehyde Monohydrate (400mg/kg) and the body temperature was maintained around 37℃. Dorsal skin fold window chamber (Department of Physics, National Taiwan University, Taiwan) was surgically implanted, and it was compatible with TPM and transducer cone.

O. Dössel and W.C. Schlegel (Eds.): WC 2009, IFMBE Proceedings 25/VIII, pp. 306–309, 2009.
www.springerlink.com

B. Ultrasound Transducer

A spherical focused ultrasound transducer (Olympus, Waltham, MA) was used in this study. Both diameter and radius of curvature for the transducer are 1.6 cm, and the driving frequency is 1.0 MHz. A function generator was connected to power amplifier (Advanced Surgical System, Tucson, AZ) to drive the ultrasound transducer to generate pulsed waves at focal region.

C. Two-photon Fluorescence Microscopy

Ti-Sapphire laser was used in the two-photon fluorescence microscopy (TPM) as light source, and the output power is 10mW. After travelling through the optical lens, the incident light transmits to microscopy and excites the skin of the mouse inside the chamber window. The reflected fluorescence and second-harmonic signals are collected by 40× objective, and they are amplified by Photomultiplier to be readily analyzed.

D. Experimental Setup

In order to do ultrasound sonication and observe the tissue simultaneously, we combined the ultrasound transducer with TPM. Figure 1 shows the arrangement of the combination system for experiments. The ultrasound transducer was mounted with a removable cone filled with distilled and degassed water and its tip capped with a polyurethane membrane. The transducer was arranged under the chamber and targeted to the region inside the circular incision of the chamber.

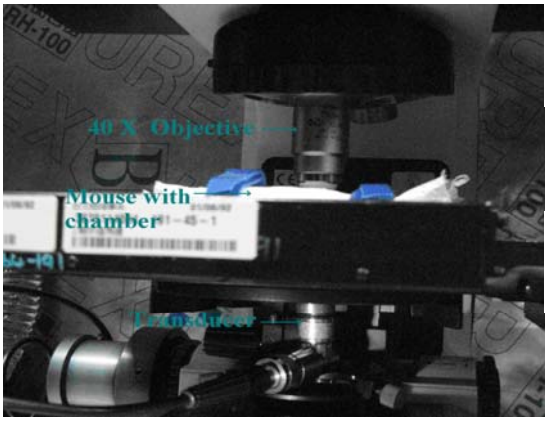


Fig. 1 is the schematic diagram to show the combination of ultrasound transducer and two-photon microscopy.

E. Ultrasound Sonication

Focused ultrasound with pulsed waves was applied with burst length 10 ms, duty cycle 1%, repetition frequency 1 Hz, and sonication duration 60s. Maximum negative acoustic pressure at the focal zone is 0.6 MPa.

F. Image Acquisition

Ultrasound contrast agent (UCA), SonoVue (Bracco International, Amsterdam, The Netherlands), and Dextran 70kDa Rhodamine B (Maximum absorption wavelength is 545nm, maximum emission wavelength is 570nm), Invitrogen (Carlsbad, CA 92008, USA) were used in this study. Mice with skin chamber were injected with the solution of UCA (100 μ L/kg) and Dextran 70kDa Rhodamine B (5mg/mL) through tail vein about 8 minutes before sonication. Mice were positioned on the stage of TPM, and sonicated after finding blood vessels. The TPM images were recorded from the moment of finding blood vessels to 30 minutes after sonication. Image were acquired with an in-plane resolution of 256x256 pixels with a field of view of 110x110 μ m and an optical slice thickness of 4 μ m.

G. Image Analysis

We evaluated the sonication effect on blood vessels by analyzing the fluorescence intensities inside and outside the vessels. We can obtain red, green, blue lights and second-harmonic signals from TPM, and ImageJ (National Institute of Health, USA) was used to analyze the images. Two regions of interest (ROI) were selected in the time-lapse red light image. Figure 2 shows two ROI in the image. First ROI is a 27.5 by 5 μ m rectangle with 3 μ m away from the vessel, and second ROI is a 31 μ m diameter circle with 26 μ m away from the vessel.

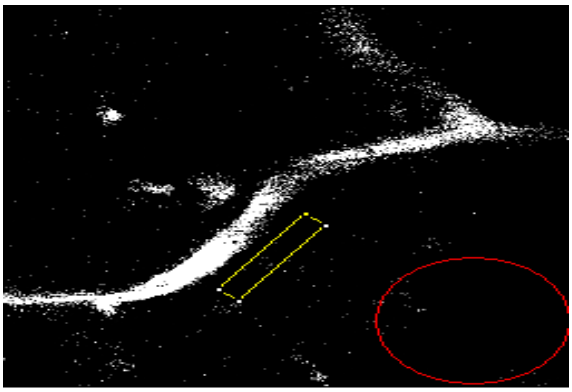
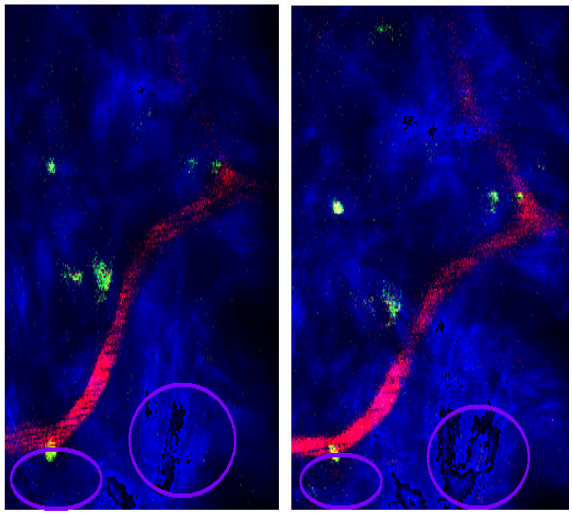


Fig. 2 is the image of two regions of interest. First ROI (yellow) is a 27.5 by 5 μm rectangle with 3 μm away from the vessel, and second ROI (red) is a 31 μm diameter circle with 26 μm away from the vessel.

III. RESULTS

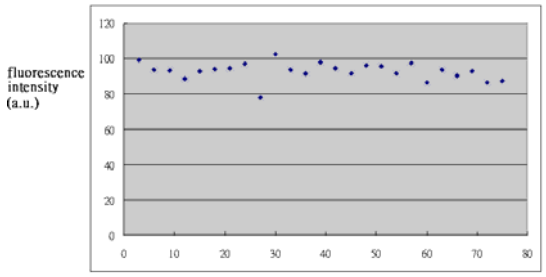
Figure 3 shows the difference between before and after the sonication. The results display that many red spots appeared at the circled region after sonication. The results indicate that dextrans extravasated from the blood vessel after sonication.



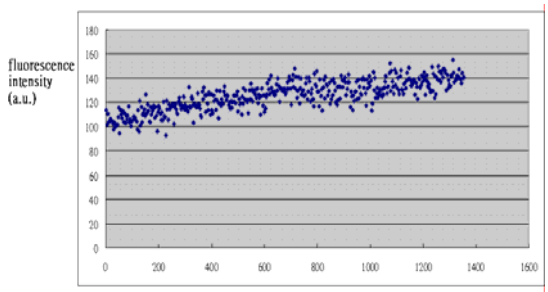
(a) (b)

Fig. 3 is the image of the vessel and its surrounding. (a) before, and (b) after sonication. Two circled regions were used to compare the two images.

Figure 4 shows the fluorescence intensity of red light in first ROI (27.5 by 5 μm rectangle with 3 μm away from the vessel) before and after sonication. The fluorescence intensity was about 90 before sonication, and it was about 100 when the sonication was just finished. The fluorescence intensity increased to about 140 at 30 minutes after the sonication. The results indicate that dextrans didn't extravasate before sonication, and extravasated continuously after sonication.



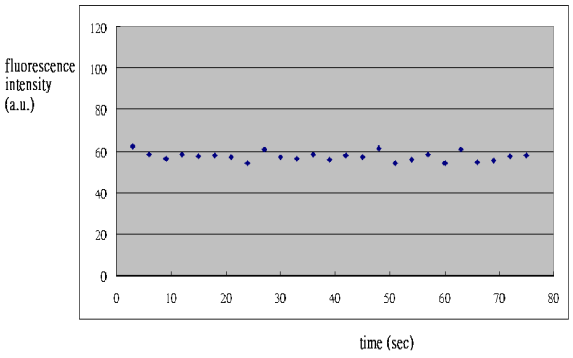
(a)



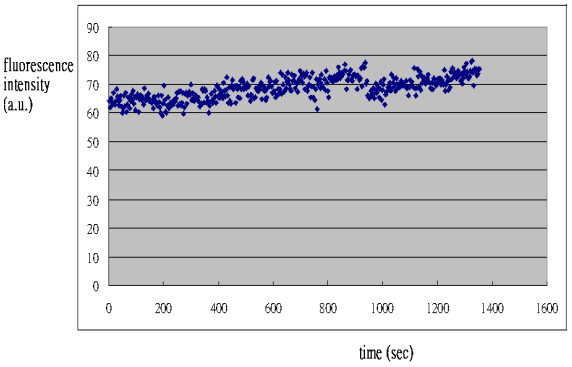
(b)

Fig. 4 is the fluorescence intensity of red light in first ROI (27.5 by 5 μm rectangle with 3 μm away from the vessel) (a) before, and (b) after sonication.

Figure 5 shows the fluorescence intensity of red light in second ROI (a 31 μm diameter circle with 26 μm away from the vessel) before and after sonication. The fluorescence intensity was about 60 before sonication, and it was about 65 when the sonication was just finished. The fluorescence intensity increased up to about 75 at 30 minutes after sonication. The results indicate that dextrans didn't appear in this region before sonication and they transport to this region after sonication.



(a)



(b)

Fig 5. The fluorescence intensity of red light in second ROI (31 μm diameter circle 26 μm away from the vessel) (a) before sonication, (b) after sonication.

IV. DISCUSSION AND CONCLUSION

In this study, we employed a 1.0 MHz spherical ultrasound transducer and injection of microbubbles (MB) to produce cavitation to change the structure of the endothelial cells of normal capillaries. The tight junction between endothelial cells of normal capillaries is less than 2 nm, and 12nm diameter Dextran (70kDa Rhodamine B) cannot extravasate. After sonication, dextrans appeared outside the capillaries. The results indicate that the pores of normal capillaries were enlarged or new large pores were produced after sonication. In conclusion, we used two-photon fluorescence microscopy (TPM) to observe the variation of permeability of the normal tissue capillaries. Tumor microvessels are leaky, and the pore sizes of tumor microvessels vary from 100 nm to 780nm in diameter. The findings of this study are important and this method can be further used to observe the variation of transport properties of tumor microvessels with ultrasound sonication for enhancing nanodrug delivery.

ACKNOWLEDGMENT

This study was supported by grants from the National Science Council (no. NSC: 95-2221-E-002-030, and no. NSC: 96-2628-E-002-007-MY3) and the National Health Research Institutes (no. NHRI: 96A1-MEPP13-014) of Taiwan.

REFERENCES

1. Stieger SM, Caskey CF, Adamson RH, Qin S, Curry FR, Wisner ER, Ferrara KW. Enhancement of vascular permeability with low-frequency contrast-enhanced ultrasound in the chorioallantoic membrane model. *Radiology 2007*; **243**: 112-21.
2. Matthew R. Dreher , Wenge Liu , Charles R. Michelich , Mark W. Dewhirst , Fan Yuan , Ashutosh Chilkoti. Tumor Vascular Permeability, Accumulation, and Penetration of Macromolecular Drug Carriers. *Journal of the National Cancer Institute 2006*, **98**: 336-344.
3. Seong Hoon Jang, M. Guillaume Wientjes, Dan Lu, and Jessie L.-S. Au. Drug Delivery and Transport to Solid Tumors. *Pharmaceutical Research 2003*; **20**: 1337-1350.

Corresponding Author: Win-Li Lin
Institute: Institute of Biomedical Engineering, National Taiwan University
Street: No. 1,Sec. 1.,Jen-Ai Rd., Taipei, Taiwan.
City: Taipei City
Country: Taiwan
Email: winli@ntu.edu.tw

Micro– and Nanosensors for Medical Applications

Urban Gerald A.

IMTEK Albert Ludwigs Universität Freiburg
Freiburg Institute of Advanced Studies FRIAS
Georges Koehler Allee 103, 79110 Freiburg/Germany

Recent progress in microsystems technologies has raised the expectation to get a comprehensive insight into metabolic events of patients. Such micro– and nanobiosensors in combination with appropriate micro fluidics enable the simultaneous description and moreover monitoring of gene, protein expression and metabolic states in a biosystem.

At present, all intermediate acute testing of metabolic parameters are made using small POC analysers which work with miniaturized sensor arrays (1).

To detect a variety of metabolic parameters precisely and selectively in a complex analyte matrix biosensors (2) have to be used.

Chiefly miniaturized glucose sensors faced an immense boom due to monitoring of diabetic patients at home allowing a more precise adjustment of insulin.

Such microbiosensors can be also integrated to analyze different blood parameters at once (3) and implemented in a microfluidics long term monitoring of body fluids was accomplished (4).

The next step in the field of biosensors will use nanotechnology: An example for the use of nanotransducers are cantilever based sensors which utilize a micromechanically produced cantilever in a similar manner as for production of AFM probes. The sensitivity can be tuned down to single molecule interaction analysis. Multifunctional cantilevers have a great potential in diagnostics for label-free, non-amplified parallel analysis by individual immobilization of biomolecules on their surface for gene expression or proteomics. (5-7) of biological samples. The cantilever consists of micromachined silicon which can be produced by standard silicon technology (8).Recently the field of nanobiosensors emerged rapidly with different technologies to get insight into cellular metabolic events (9).

Also electrochemical sensing methods can be scaled down (10). Special attention was laid on carbon nanotubes modification of electrochemical working electrodes (11). A very exciting field is the use of nanowires as new tool for biosensing (12).

However, such tools are still in its infancy with excellent potentials to be established in the future.

References

1. http://www.roche.de/diagnostics/labor/index_poc.htm
2. D. Thevenot, K. Thot, R. Durst, G. Wilson, Electrochemical Biosensors: Recommended Definitions and Classifications, Pure appl. Chem. Vol 71, no 12 (1999) 2333-2348
3. I. Moser, G. Jobst, G.A. Urban, Biosensor Arrays for Simultaneous Measurement of Glucose, Lactate, Glutamate, and Glutamine (2002). Biosensors & Bioelectronics 17/4, 297-302.
4. Rhemrev-Boom MM, Korf J, Venema K, Urban G, Vadgama P., A versatile biosensor device for continuous biomedical monitoring. Biosens Bioelectron. 2001 Dec;16(9-12):839-47
5. Zhang, J., Lang, H. P., Bietsch, A., Huber, F., Certa, U., Güntherodt, H.-J., Hegner, M. Gerber, Ch. (2006) *Rapid and label-free nanomechanical detection of biomarker transcripts in human RNA,* Nature Nanotechnology, 1 ,214-220.
6. Huber, F., Hegner, M., Gerber, Ch.,Güntherodt, H.J., Lang, H.P. (2005) *Label free analysis of transcription factors using microcantilever arrays,* Biosens. Bioelectron. 21 (8) 1599-1605
7. Christiane Ziegler, Cantilever-based biosensors, Analytical and Bioanalytical Chemistry 379,7-8 (2004), 946-959
8. www.concentris.com
9. Tuan Vo-Dinh, Paul Kasili, Musundi Wabuyele, Nanoprobes and nanobiosensors for monitoring and imaging individual living cells , Nanomedicine: Nanotechnology, Biology, and Medicine 2, 22– 30, 2006.
10. A. Martin Pumera, Samuel S´anchez, Izumi Ichinose, Jie Tang, Review , Electrochemical nanobiosensors, Sensors and Actuators B: Chemical ,Volume 123, Issue 2, 1195–1205, 2007.
11. M. Musameh, J. Wang, A. Merkoci, Y. Lin, Low-potential stable NADH detection at carbon-nanotube-modified glassy carbon electrodes, Electrochem. Commun., 4, 743–746, 2002.
12. G. Zheng, F. Patolsky and C.M. Lieber, Nanowire biosensors: a tool for medicine and life science, Nanomedicine: Nanotechnology, Biology and Medicine, Volume 2, Issue 4, Page 277, 2006.

O. Dössel and W.C. Schlegel (Eds.): WC 2009, IFMBE Proceedings 25/VIII, p. 310, 2009.
www.springerlink.com

Ferroelectric Nanoparticles for Contrast Enhancement Microwave Tomography: Feasibility Assessment for Detection of Lung Cancer.

S. Semenov[1], N. Pham[1], S. Egot-Lemaire[1]

[1] Keele University / School of Medicine, Stoke-on-Trent, UK

Abstract— **Microwave Tomography (MWT) has recently attracted a significant interest for its potential biomedical applications. It has been shown that MWT might be applicable for non-invasive assessment of functional and pathological conditions of various soft tissues, including tissue malignancies. Since within this imaging modality tissues are differentiated and, consequentially can be imaged based on the contrast in dielectric properties, the diagnostic potentials of MWT are based on the contrast in dielectric properties between normal and malignant tissue. However, giving complexity of MWT imaging, especially for such inhomogeneous objects as human torso, it is desirable to enhance a natural dielectric contrast.**

We suggest using ferroelectric nanoparticles for contrast enhancement of MWT. Here we report some of our experimental results of dielectric properties of various ferroelectric nanoparticles and further computer simulations for an assessment of an enhanced diagnostic power of MWT using a simplified chest model with lung cancer. This initial feasibility study demonstrates that ferroelectric nanoparticles might significantly improve a diagnostic power of MWT.

Keywords— **nanoparticles, ferroelectric, microwave tomography**

I. INTRODUCTION

Microwave Tomography (MWT) is an emerging biomedical imaging modality with attractive potentials for non-invasive assessment of functional and pathological conditions of various soft tissues. Since within the MWT tissues are differentiated and, consequentially can be imaged based on the contrast in dielectric properties, the diagnostic potentials of MWT are based on the contrast in dielectric properties between normal and malignant tissue. It has been demonstrated that dielectric properties of malignant tumors and normal tissues are different in the breast [1-6], liver [1,7,8] and lung [1,9]. MWT of biological objects, especially a large scale, high contrast parts of human body, such as torso, possesses very complicated problem of so called diffraction tomography. Therefore, it is desirable to enhance a natural dielectric contrast to improve a diagnostic power of MWT.

We suggest using ferroelectric nanoparticles for contrast enhancement of MWT. Ferroelectrics, having high values of dielectric properties as compared with biological tissues, present interesting enhancement potentials. In this report we present some of our experimental results of dielectric properties of various ferroelectric nanoparticles and further computer simulations for an assessment of an enhanced diagnostic power of MWT using a simplified chest model with lung cancer.

The biocompatibility and biosafety issues are out of the scope of this feasibility study. Our overall concept is similar to drug loaded cancer specific magnetic nanoparticles approach (for example, [13]), but using ferroelectric instead of magnetic core in complex nanoparticles.

II. METHODS

The Methods section has two subsections. Subsection A covers experimental methodology used to study dielectric properties of ferroelectric nanoparticles. Images reconstruction method and simulation model used in this study are presented in subsection B.

A. Experimental methods

Two commercially available nanoparticles were used: calcium titanate ($CaTi0_3$) and barium titanate ($BaTiO_3$). Nanoparticles were supplied in powder with particles size of 50nm. We suspended the particles in glycerol to form a suspension of desired viscosity and stability to conduct dielectric measurements. At least three sets of the suspensions with three different volume fractions of nanoparticles were measured. Measurements were conducted using coaxial probe technique, presented elsewhere [10]. All measurements were performed at temperature 24 ± 1^0 [C]. Further measured data was analyzed and dielectric properties of nanoparticles were retrieved from measured bulk properties of suspensions using different approaches of effective media approximation of dielectrics.

B. The model and image reconstruction method

2D Chest model comprises of a cylindrical thorax area (with radius 15cm) with outermost ribs shell (ε=10+j2), the lung tissue itself (ε=33+j12) and a two-ventricular chamber model of the heart with myocardium of ε=58+j21 Two small inclusions simulate cancer areas: one with -15% dielectric contrast against normal lung tissue [1,11] and another one with enhanced contrast. The 2D imaging chamber

O. Dössel and W.C. Schlegel (Eds.): WC 2009, IFMBE Proceedings 25/VIII, pp. 311–313, 2009.
www.springerlink.com

was a cylinder with 64 transmitters/receivers positioned on the perimeter at a central cross-section of the chamber. The chamber was filled with matching solution of ε=33+j12. Frequency was 1GHz. We've simulated a whole cycle of tomographic measurements from each transmitter using direct solver with polar grids 512*256.

For image reconstruction we used iterative 2D Newton approach with Tikhonov regularization presented elsewhere [12]. We use 256*128 polar grids to solve direct problem for each transmitting antenna at each iteration and 64*64 Cartesian grids to solve inverse problem. The starting point for image reconstruction was always a homogeneous media with known dielectric properties of matching solution. Regularization parameters were chosen by a trial method.

III. RESULTS

Some of our experimental results are summarized in Table 1. The retrieved dielectric properties of 50nm sized calcium titanate ($CaTi0_3$) and barium titanate ($BaTiO_3$) nanoparticles are presented at frequencies 1GHz and 2.45GHz. Those two frequencies are within the "optimal" range for microwave biomedical imaging. As can be seen, the dielectric properties (both real and imaginary parts) are of high contrast as compared with dielectric properties of biological tissues, for example with of ε=56+j23 of muscle tissues at 1GHz. The contrast is even more pronounced if compared with low water content tissues, such as fat or bone.

	1GHz		**2.45GHz**	
	ε'	**ε''**	**ε'**	**ε''**
$CaTi0_3$	135	52	97	45
$BaTiO_3$	128	122	67	72

Table 1. Retrieved dielectric properties of ferroelectric nanoparticles (particle size of 50nm) at 24 ± 1^0 [C].

Those findings were further used in a simplified 2D model of chest with two areas simulating a lung cancer. It has to be emphasized that lung cancer imaging is one of the most challenging problem of MWT: small areas of diagnostic interest are within a high contrast dielectric "shield" presented by a complex ribs area. The model incorporates two cancer areas: the larger one (R=10mm) with small -15% contrast at [X;Y]=(-9.0;3.0)cm (see Figure 1) and the smaller one (R=5mm) with ferroelectric nanoparticles enhanced contrast at [X;Y]=(-5.0;8.25). The assumption for the second one was that the ferroelectric nanoparticles occupy 50% of tumor volume (volume fraction of 0.5). As can be seen, the contrast enhanced tumor are confidently reconstructed on both ε' and ε', being even smaller, than non-enhanced area.

This is initial feasibility study. The study does not address neither details of very complicated and challenging technical problems of MWT chest imaging nor biocompatibility and biosafety issues.

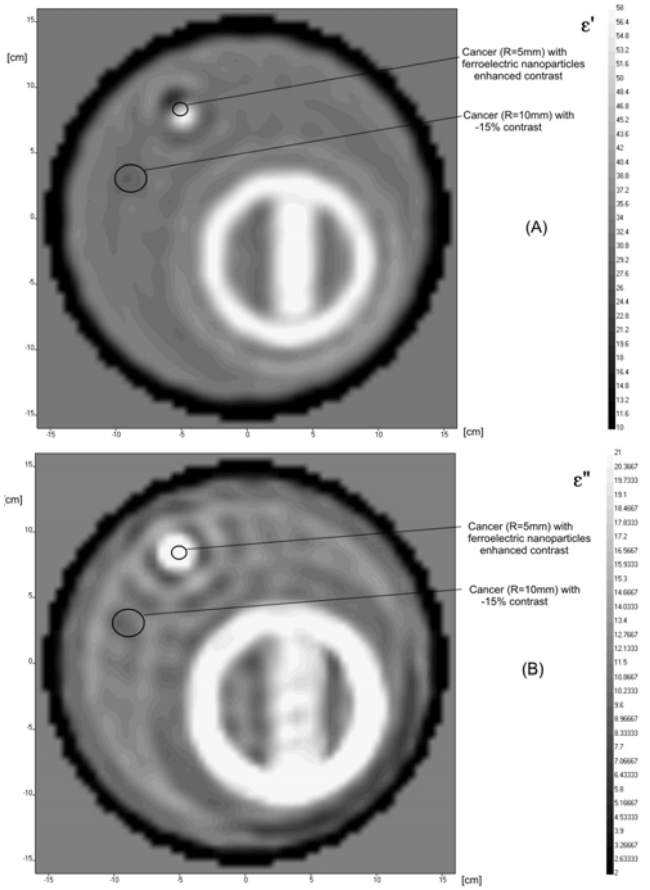


Figure 1. Reconstructed MWT images of 2D chest model with two simulated cancer areas: one with 15% dielectric contrast at [X;Y]=(-9.0;3.0)cm and Radius=10mm and 2nd one with ferroelectric nanoparticles (with 0.5 volume fraction) enhanced contrast at [X;Y]=(-5.0;8.25) cm and Radius=5mm. Frequency 1GHz. Results presented for ε' – top of the Figure (1A) and for ε" – bottom of the Figure (1B).

IV. CONCLUSIONS

This initial feasibility study demonstrates that ferroelectric nanoparticles might significantly improve a diagnostic power of MWT.

ACKNOWLEDGMENT

The work was supported by Keele University, School of Medicine, ISTM, UK.

REFERENCES

1. Joines W.T., Zhang Y., Li C., Jirtle R.L. (1994) The measured electrical properties of normal and malignant human tissues from 50 to 900 MHz, *Med.Phys*, **31**, 4, 547-550.
2. Surowiec A.J., Stuchly S.S., Barr J.R., Swarup A. (1988) Dielectrical properties of breast carcinoma and the surrounding tissues", *IEEE Trans. BME.,* **35**,4, 257-263.
3. Chaudhary S.S., Mishra R.K., Swarup A., Thomas J.M. (1984) Dielectric properties of normal and malignant human breast tissues at radiowave and microwave frequencies *Indian J. Biochem., Biophys*., **21**, 76-79.
4. Joines W.T., Jirtle R.J., Rafal M.D., Schaefar D.J. (1980) Microwave power absorption differences between normal and malignant tissue, *J. Radiation Oncology Biol. Phys*., 6, 681-687.
5. Lazebnik M, McCartney L, Popovic D, Watkins C, Lindstrom MJ, Harter J, Sewall S, Magliocco A, Booske JH, Okoniewski M and SC Hagness (2007) A large-scale study of the ultrawideband microwave dielectric properties of normal breast tissue obtained from reduction surgeries, *Phys.Med.Biol*, 52, 2637-2656.
6. Lazebnik M, Popovic D, McCartney L, Watkins CB, Lindstrom MJ, Harter J, Sewall S, Ogilvie T, Magliocco A, Breslin TM, Temple W, Mew D, Booske JH, Okoniewski M and SC Hagness (2007) A large-scale study of the ultrawideband microwave dielectric properties of normal, benigh and malignant breast tissues obtained from cancer surgeries", *Phys.Med.Biol*, **52**, 6093-6115.
7. Smith S.R., Foster K.R, Wolf G.L. (1986) Dielectric properties of VX-2 carcinoma versus normal liver tissue", *IEEE Trans. BME*, 33, 5 522-524.
8. O'Rourke AP, Lazebnik M, Bertram JM, Converse MC, Hagness SC, Webster JG and DM Mahvi (2007) Dielectric properties of human normal, malignant and cirrhotic liver tissue: *in vivo* and *ex vivo* measurements from 0.5 to 20GHz using a precision open-ended coaxial probe, *Phys.Med.Biol*, **52**, 4707-4719.
9. Marimoto T., Kimura S., Konishi Y., Komaki K., Ugama T., Monden Y., Kinochi Y., Iritana T. (1993) A study of electrical bio-impedance of tumors", *J. of Investigative Surgery*, **6**, 25-32.
10. Agilent Technology. "Agilent Basics of measuring the dielectric properties of materials" Application note http://cp.literature.agilent.com/litweb/pdf/5989-2589EN.pdf
11. Semenov S.Y., Bulyshev A.E., Posukh V.G., Williams T., Sizov Y.E., Souvorov A.E., Repin P.N., Voinov B.A. (2003) Microwave Tomography for Detection of Tissue Malignancies: Lung, Liver and Kidney Sites", in "Progress in Electromagnetics Research Symposium, 2003", Honolulu, Hawaii, USA October 13-16, 2003.
12. Souvorov A E, Bulyshev A E, Semenov S Y, Svenson R H, Nazarov A G, Sizov Y E and Tatsis G P (1998) Microwave tomography: a two-dimensional Newton iterative scheme *IEEE Trans. MTT* **46** 1654-59.
13. R Jurgons, C Seliger, A Hilpert, L Trahms, S Odenbach and C Alexiou (2006) Drug loaded magnetic nanoparticles for cancer therapy *J. Phys.: Condens. Matter* **18**, S2893–S2902.

MEA Neurosensor, the Tool for Synaptic Activity Detection: Acute Amyloid-β Oligomers Synaptotoxicity Study

I. Benilova[1,2,3], I. Kuperstein[1,2], K. Broersen[4,5], J. Schymkowitz[4,5], F. Rousseau[4,5], C. Bartic[3,6], and B. De Strooper[1,2]

[1] Center for Human Genetics, KU Leuven, [2] Department for Molecular and Developmental Genetics VIB, Leuven, Belgium, [3] IMEC, Leuven, Belgium; [4] Switch Laboratory, VIB; [5] Vrije Universiteit Brussel, Belgium; [6] Department of Physics and Astronomy – KU Leuven, Leuven Belgium

Abstract— **Microelectrode arrays were used for monitoring the impact of Alzheimer's amyloid oligomers on hippocampal neurons. Micromolar concentrations of Aβ 42 oligomers, but not fibrils, potently inhibited spontaneous electrical activity of the cells; the effect was partially reversible. The significance of the method for Alzheimer's disease research is studied.**

Keywords— **MEA, amyloid, oligomers, synapse, Alzheimer.**

I. Introduction

Alzheimer's disease (AD) is a neurodegenerative disorder characterized by neurofibrillar tangles and amyloid plaques consisting of aggregated amyloid-β peptide [1]. Neurotoxicity is believed to be associated with soluble Aβ oligomers [2-4] whereas mature Aβ fibrils in contrast are largely inert [5]. Molecular mechanisms and neurophysiology behind the synaptic impairment leading to dementia remain to a large extent unexplored.

Microelectrode array (MEA) devices are a valuable tool for non-invasive extracellular monitoring of synaptic activity in developing and mature neuronal networks. Two-dimensional MEA-supported neuronal culture is a useful model to study acute synaptotoxicity in vitro.

The goal of this work was to determine an acute effect of soluble Aβ oligomers and insoluble fibrils on hippocampal cultures using MEA chip.

II. Methods

A. Neuron culture and MEA

Multielectrode culture chambers (HexaMEA/ITO; 60 TiN electrodes arranged in a recording area 700 um × 5 mm, Multichannel Systems GmbH, Germany) were exposed to UV/ozone for 5 min, sterilized in ethanol, and coated with Poly-L-Lysine; then filled with Neurobasal medium (NB; Invitrogen, supplemented with 12.5 uM L-glutamate, B27 (Invitrogen) and 0.5 mM L-glutamine) pre-incubated at 37ºC in 5% CO_2.

Hippocampal neurons were isolated from E17-18 FVB mouse embryos as described [6], and plated at ca. 1000 cells/mm^2 on the MEA substrates. The culture chambers were then sealed with semi-permeable Teflon film [7].

Spontaneous electrical activity was recorded in 8-11 days old neuron cultures which already possessed a developed network of functional synapses [8].

During recordings, a temperature controller from Multichannel Systems was used to maintain MEA platform at 37ºC.

B. Amyloid preparation

Aβ 42 oligomers were prepared from rPeptides monomers using HFIP-based procedure followed by Tris buffer. Fibrils were obtained by incubation of the monomers for 2 weeks at room temperature.

C. Data analysis

MEAs allow simultaneous recording from multiple firing sites, thus revealing a pattern of activity across the population of neurons. Most of experiments were done on 8 days old cultures whose firing pattern is characterized by comparatively sparse spike trains.

Firing rate is an important component of neural coding [9-10]. Prone to alteration by electrical and chemical stimuli [11], the frequency of action potentials (or spikes) provides a quantitative evaluation of cell electrical output.

By use of MC_Rack 3.5.10 software (Multichannel Systems), we computed the rate of firing by integrating all spikes picked up by every single electrode (n) over 60 s. Detection threshold was set at a triple noise level.

III. Results

Treatment with 1-20 uM Aβ 42 oligomers readily altered firing rate in a concentration-dependent manner. The lethal concentration of Aβ 42 (20 uM) caused immediate silencing of the network (Fig.1) whereas the effect of sub-lethal low

O. Dössel and W.C. Schlegel (Eds.): WC 2009, IFMBE Proceedings 25/VIII, pp. 314–316, 2009.
www.springerlink.com

uM range concentrations (<2 uM) was only observed after overnight treatment.

As shown in Fig.3, Aβ 42 oligomers, but not fibrils rapidly and significantly inhibit synaptic activity, supporting the data obtained by other electrophysiological methods [3].

Inhibition of spontaneous electrical activity in neuronal networks by Aβ 42 oligomers was partially or completely reversible. After 30 min of incubation with amyloid, the cells were extensively washed in NB medium, and firing recovery was checked during the following 24 h. Neurons treated with 5 uM of Aβ 42 oligomers, restored their electrical activity within 12-24 h.

To verify specificity of the Aβ 42 oligomers effect, anti-Aβ antibodies were added to neuronal cultures prior to Aβ 42 oligomers treatment. Amyloid injury was prevented by both general sequence-specific anti-Aβ 6E10 antibody and by anti-oligomers A11 antibody in agreement with previous investigations [12], Fig. 3.

In another set of experiments, oligomers were pre-incubated with 6E10 antibody prior to cells treatment. Treatment with immunodepleted Aβ 42 oligomers did not affect spike rate during at least 30 min of recording (116.7±8.3%, *n*=5) in contrast to cells treated with Aβ 42 oligomers only (45.2±11.4%, *n*=10), p=0.0005.

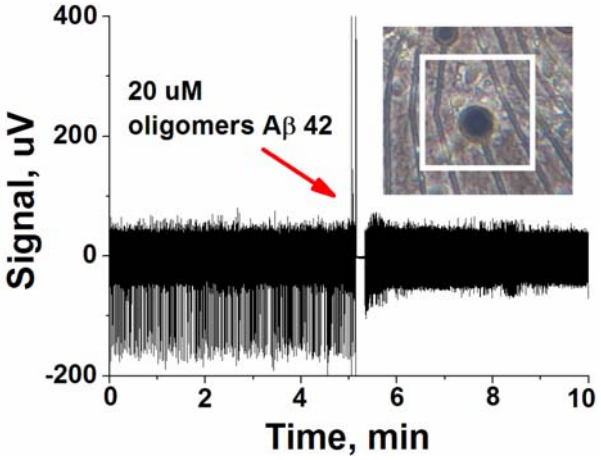


Fig. 1 20 uM of Aβ 42 oligomers quazi-immediately suppresses spontaneous electrical activity of hippocampal neurons. Inset: MEA electrode to which correspond the recorded datastream.

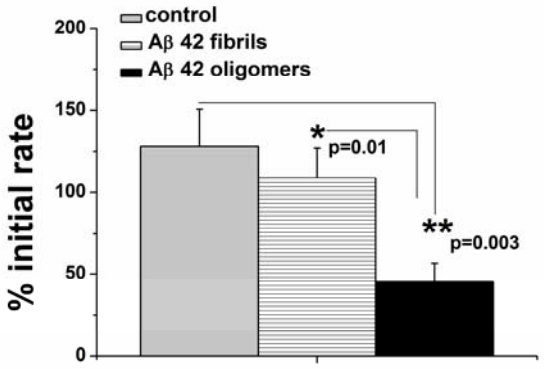


Fig. 2 Aβ 42 oligomers, but not fibrils, rapidly inhibit network firing. Concentration of amyloid species: 5 uM. Values are % of baseline ± s.e.m., 2-3 independent experiments, *n*=10-15.

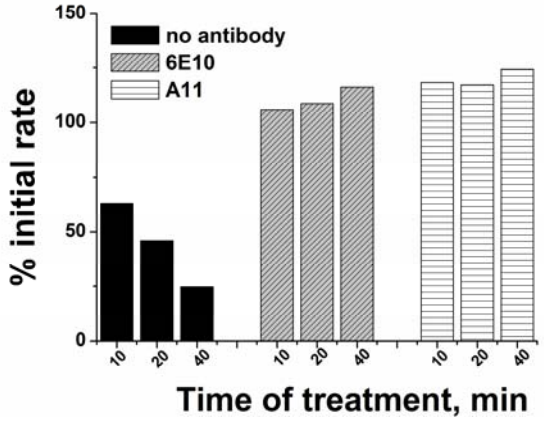


Fig. 3 Sequence-specific anti-Aβ antibody 6E10 and anti-oligomers A11 antibody prevent amyloid injury in hippocampal neurons. Antibodies were pre-incubated in culture chamber for 30 min prior to 5 uM Aβ 42 oligomers injection. Values are % of baseline, average activity across 1 chip.

IV. Conclusions

Microelectrode array (MEA) is a unique, sensitive and easily operating method for simultaneous recording of spontaneous synaptic activity of neuronal networks in culture. MEA-based sensor allows monitoring of subtle changes in electrical output of hippocampal neurons under treatment with various Aβ 42 preparations. Taking into consideration dynamics of Aβ aggregation, detection of acute effects of the oligomeric preparations is essential for careful comparison of synaptotoxicity potential of oligomers species during the aggregation process. The method will allow to follow

synaptotoxicity under sub-lethal concentrations of Aβ oligomers species and to discriminate cell death from the net synaptotoxic effects.

ACKNOWLEDGMENT

This work was supported by the IWT SBO 050151 Artificial Synapse grant and by Methusalem grant (Prof. Bart De Strooper) of the Flemish government.

REFERENCES

1. Hardy J, Selkoe D. The amyloid hypothesis of Alzheimer's disease: progress and problems on the road to therapeutics (2002) Science 297:353-356
2. Lue L, Kuo Y, Roher A et al (1999) Soluble amyloid β peptide concentration as a predictor of synaptic change in Alzheimer's disease. Am J Pathol 155:853-862
3. Selkoe D (2008) Soluble oligomers of the amyloid beta-protein impair synaptic plasticity and behavior. Behav Brain Res 192:106-113
4. Martins I, Kuperstein I, Wilkinson H et al (2008) Lipids revert inert Abeta amyloid fibrils to neurotoxic protofibrils that affect learning in mice. EMBO J 27:224-233
5. Aksenov M, Aksenova M, Butterfield D et al (1996) Glutamine synthetase-induced enhancement of beta-amyloid peptide A beta (1-40) neurotoxicity accompanied by abrogation of fibril formation and A beta fragmentation. J Neurochem 66:2050-2056.
6. Banker G, Goslin K (1998) Culturing nerve cells. The MIT press.
7. Potter S, DeMarse T (2001) A new approach to neural cell culture for long-term studies. J Neurosci Meth 110: 17–24
8. Martel M, Wyllie D, Hardingham G (2009) In developing hippocampal neurons, NR2B-containing N-methyl-d-aspartate receptors (NMDARs) can mediate signaling to neuronal survival and synaptic potentiation, as well as neuronal death. Neuroscience 158:334-343
9. Gerstner W, Kreiter A, Markram H et al (1997) Neural codes: Firing rates and beyond. PNAS 94:12740-12741
10. Lisman J (1997) Bursts as a unit of neural information: making unreliable synapses reliable. Trends Neurosci 20:38-43
11. Yaksi E, Friedrich R (2006) Reconstruction of firing rate changes across neuronal populations by temporally deconvolved Ca^{2+} imaging. Nature Methods 3:377-383
12. Meyer J, Kamp F, Bartels et al (2008) MEA supported cortical cultures as a novel tool in Alzheimer's research. 6th Int. Meeting on Substrate-Integrated Microelectrodes Proc., Reutlingen, Germany, 2008, pp 224-225.

Corresponding authors:

Author: Carmen Bartic
Institute: the Interuniversitair MicroElectronica Centrum (IMEC)
Street: Kapeldreef, 75
City: Leuven
Country: Belgium
Email: barticca@imec.be

Author: Bart De Strooper
Institute: Flanders Institute for Biotechnology (VIB)
Street: Herestraat, 49
City: Leuven
Country: Belgium
Email: bart.destrooper@med.kuleuven.be

Development of Tri-component Copolymer Rods as Implantable Drug Delivery Systems for Liver Cancer Therapy

N. Nasongkla[1], P. Akarajiratun[1], and S. Hongeng[2]

[1]Department of Biomedical Engineering, Faculty of Engineering, Mahidol University, Nakorn Pathom, Thailand
[2]Department of Pediatrics, Faculty of Medicine, Ramathibodi Hospital, Mahidol University, Bangkok, Thailand

***Abstract*—** Tri-component copolymers of poly(ε-caprolactone)-random-poly(D,L-lactide)-block-poly(ethylene glycol)-block-poly(ε-caprolactone)-random-poly(D,L-lactide) (PLCA-PEG-PLCA or PLEC) were used as a material to develop cylindrical polymeric rods and were used as the implantable drug delivery system. PLEC was successfully synthesized and the copolymer ratio and molecular weight were controllable. Trypan blue was selected as a model drug and the release profiles of trypan blue were carried out at 20 and 30 % loading. The release rate of trypan blue was found to directly depend on the amount of lactide in PLEC and the amount of trypan blue.

Keywords— Drug delivery system, cancer, copolymer**,** polymeric rod, implantation

I. INTRODUCTION

Cancer is the second highest cause of death in US today, and more than half a million people die from this disease each year.1 Among a variety of cancer types, liver cancer is one of the most deadly forms. Current treatment for liver cancer includes surgical resection, systemic or regional chemotherapy, arterial embolization, cryotherapy and radiation therapy. Even though surgical resection demonstrates the improvement in the therapeutic outcome, for the majority of patients, resection may not be possible due to factors such as age, health, multiple tumor sites and advanced cirrhosis. A small portion of cancer cells can survive a standard treatment, especially at locations close to blood vessels. Subsequently, the remaining cancer cells cause the tumor recurrence that requires further treatment. Therefore, it is necessary to develop intratumoral drug delivery as a local drug therapy for the treatment of liver cancers. This controlled release drug delivery system is required to deliver appropriate amount of drugs for a desire period of time.[1,2] A successful drug delivery device for local chemotherapy has to be able to precisely control the concentration of anticancer drugs within their narrow therapeutic windows. Polymeric rods will be fabricated in the shape of a cylindrical rod (1.6 mm in diameter and approximately 1 cm in length), which will be implanted directly inside the tumor. This therapy has potential advantages in that the local delivery can reduce drug dosage, toxicity and side effects usually associated with systemic chemotherapy.

Polymers have been efficiently used as materials for a variety of drug delivery systems, for example, polymer implant [3], and nanoparticles [1,4-7]. In this study, polyester was selected as a material for this drug delivery system due to its well-known biocompatibility and biodegradation.[8,9] Poly(ε-caprolactone) (PCL) and poly(D,L-lactide) (PLA) are biodegradable polyester that can be degraded by the hydrolysis of ester linkages. Poly(ε-caprolactone) (PCL) is the excellent biodegradable polymer with good biocompatibility and non-toxicity.[5] However, the degradation rate of poly(ε-caprolactone) is very slow, and its biodegradation half time is longer than one year owing to its strong crystallinity and hydrophobicity.[10,11] It has been reported that poly(D,L-lactide) (PLA) is more susceptible to hydrolysis than PCL.[4] Thus the degradation half time of PCL can be reduced. Poly(ethylene glycol) (PEG) was selected as the third component in the polymers to increase the hydrophilicity of the polymer matrix. This approach is rationally chosen to solve the inhomogeneity dispersion of external excipient materials such as sodium chloride and sugar in drug delivery systems.[12-14] To combine these advantages, copolymerization is a proper approach to achieve the desired properties of polymers. The tri-component copolymer of poly(ε-caprolactone)-random-poly(D,L-lactide)-block-poly(ethylene glycol)-block-poly(ε-caprolactone)-random-poly(D,L-lactide) (PLEC) was used to entrap drugs in a cylindrical polymeric rods. The rate of drug release will be controlled by varying the overall drug loading content and copolymer composition.

II. MATERIALS AND METHODS

Materials

Stannous (II) octoate ($Sn(Oct)_2$, from Aldrich) was used as received. Poly(ethylene glycol) (PEG, MW = 1000 Da) was purchased from Sigma (USA). ε-Caprolactone monomer (CL, from Aldrich) was dried in calcium hydride and distilled under vacuum. D,L-Lactide (LA, from Aldrich) was recrystallized from dry ethyl acetate. Toluene was dried by refluxing with sodium. Other reagents were used as received.

Polymerization of poly(ε-caprolactone)-random-poly(D,L-latide)-block-poly(ethylene glycol)-block-poly(ε-caprolactone)-random-poly(D,L-latide) (PLEC)

PLEC with different compositions was synthesized by ring opening polymerization of D,L-lactide and ε-caprolactone using PEG (Mw = 1000) as a macro-initiator

O. Dössel and W.C. Schlegel (Eds.): WC 2009, IFMBE Proceedings 25/VIII, pp. 317–320, 2009.
www.springerlink.com

and stannous octoate as a catalyst.[15],[6] D,L-Lactide and PEG were weighted in the dry two-necked round bottomed flask and the mixture was dried under reduced pressure overnight. Then dry argon was purged into the reaction flask. Dry ε-caprolactone and toluene (used as a solvent) were introduced into the flask through the dry glass syringe. The mixture was dried by azeotropic distillation under reduced pressure to remove the trace of water. The flask was immersed in an oil bath and maintained at 140 °C. Stannous octoate was introduced into a polymerization flask and the reaction was carried out for 48 h. The product was obtained by precipitating the toluene solution of the raw product by cold methanol. The copolymer composition was controlled by monomer feeding ratio. Thus, the desired hydrophilicity, degradation rate and drug release rate can be obtained.

Preparation of PLEC microparticles

PLEC microparticles were prepared by solvent evaporation method. PLEC was dissolved in methylene chloride and added into 1% poly(vinylalcohol) aqueous solution drop by drop while mixed vigorously by a homogenizer (Heidolph, Germany) at 8000 rpm for 4 min to form an oil/water emulsion. The mixture was then stirred overnight in the excess of 1% poly(vinylalcohol) aqueous solution to remove the residue methylene chloride. Finally, microparticles were corrected by centrifugation, washed with distilled water, and freeze-dried to give a powder like sample. The microparticles size was measured by a light microscope (Model CKX41, Olympus).

Fabrication of polymeric rods

Polymeric rods were prepared using a compression-heat-molding procedure that has been developed recently.[3] Briefly, lyophilized trypan blue particles were mixed with PLEC microparticles with the final loading density at 20 and 30 % w/w. Then the well-mixed particles were placed in a stainless steel mold and heat at 90 °C for 2 hours. The compression pressure at 4.6 x 10^6 Pa was introduced to the system by applying the constant weight on the mold.

Trypan blue release study

Polymeric rods are weighed prior to the drug release. The rods are placed in 20 mL glass vials and submerged in 15 mL phosphate-buffered saline (PBS) pH 7.4. The vials are placed in an orbital shaker (Model ES-20/60, BioSan) at 37 °C and rotated at 100 rpm. A buffer solution was removed periodically for UV measurement at trypan blue maximum absorption wavelength (λ_{max} = 586 nm). The cumulative released of trypan blue is calculated by the summation of each individual sample release. The release profile is obtained by plotting the amount of released trypan blue as a function of time.

III. Results and Discussion

PLEC was synthesized by ring opening polymerization of D,L-lactide and ε-caprolactone at 140 °C. Poly(ethylene glycol) (HO-PEG-OH, Mn = 1,000 Da) was used as a macro-initiator and stannous (II) octoate as a catalyst. PLEC was selected as a material for polymeric rods. Its properties such as hydrophilicity, degradation rate and drug release directly depend on its copolymer composition. The degree of polymerization of ε-caprolactone and D,L-lactide in PLEC was calculated by comparing integral intensity of characteristic resonance of the CL proton at 3.9 ppm (-C(=O)-$(CH_2)_4$C**H**$_2$-O-), D,L-lactide proton at 5.1 ppm (-C(=O)-C**H**(-CH_3-)) and PEG resonance at 3.55 ppm (-O**C**H_2CH_2-) in the ^{1}H NMR spectrum (Figure 1).

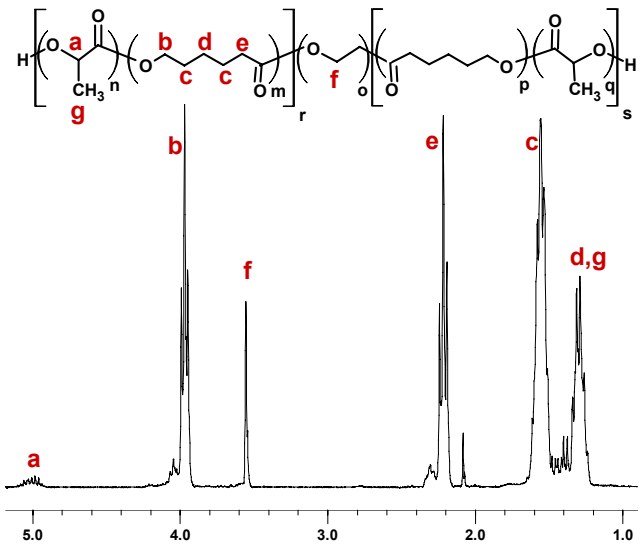


Fig. 1 ^{1}H NMR spectrum of PLEC in $CDCl_3$.

PLECs with different properties such as drug release rate, hydrophilicity and degradation rate can be prepared by varying the molar ratio of D,L-lactide and ε-caprolactone monomer as shown in Table 1. It should be noted that PEG was kept constant at 1000 Da for all three polymers. The function of PEG is to increase the hydrophilicity of polymers. The D,L-lactide percentage is increased from 0, 11 and 26.5 % mol for PLEC 1, 2 and 3, respectively. The molecular weight of PLEC was controlled approximately at 20 kD. For all PLEC, a unimodal distribution was observed in the size exclusion chromatograms (data not shown).

Table 1 Chemical composition of PLEC as determined by ^{1}H NMR

PLEC	PEG	LA		CL		MW of PLEC
	kDa	MW (kDa)	mol %	MW (kDa)	mol %	(kDa)
1	1000	0	0	22.47	100	23.47
2	1000	1.86	10.92	24.02	89.08	26.87
3	1000	3.8	26.54	16.66	73.46	21.46

PLEC was successfully fabricated into microparticles using the single emulsion procedure. An analysis by light

microscope showed that these particles have a spherical shape and the average diameter is 3-5 μm based on the image analysis of 50 particles with the average diameter of 3.8 μm (Figure 2A). The image also demonstrates that there is no residue poly(vinyl alcohol) which can possibly become a impurity in the rods. The micro-scale size allows a homogenous dispersion of microparticles with lyophilized trypan blue particles which consequently leads to a homogenous distribution of trypan blue through out polymeric rods. The PLEC microparticles and trypan blue were vigorously mixed by a vortex technique. The mixture was then molded into a rod shape at 90 °C with a constant compression pressure at 4.6 MPa. After 2 h annealing, the mold was allowed to cool down and the polymeric rods were obtained with 20% and 30 % trypan blue loading (Figure 2B).

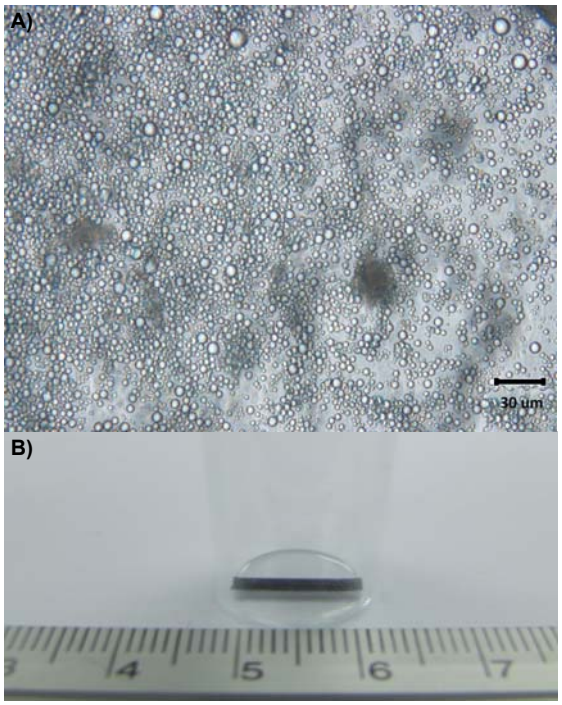


Fig. 2 A) Light microscope analysis of PLEC microparticles. B) PLEC polymeric rod contains trypan blue.

Figure 3 demonstrates the release studies of trypan blue containing polymeric rods (PLEC 1 to 3) in PBS buffer at 37 °C. Buffer solution was periodically refreshed, removed buffer solution was measured the UV-Vis absorption at wavelength of 586 nm. Trypan blue concentration in each period was calculated and plotted between the accumulative concentration and time. Each data was obtained in triplicate. All PLEC rods with 20 and 30 % trypan blue loading showed similar release pattern, i.e. fast release at the early release time and subsequently reach the slow release after 36 h. The percentage of D,L-lactide in PLEC obviously had the effect on the trypan blue release rate. For example, PLEC rods (20 % trypan blue loading, Figure 3A) with 0% D,L-lactide showed the slowest release with 46 % trypan blue release which is probably due to the high hydrophobicity and crystallinity of poly(ε-caprolactone). Introduction of D,L-lactide into these polymers also brings up the hydrophilicity and amorphous property. Trypan blue release from PLEC 2 rods (D,L-Lactide 11%) and PLEC 3 rods (D,L-Lactide 26.5%) increases to 70 and 80% within 36 h. Similar results were also observed for PLEC rods with 30 % trypan blue loading. The faster release of trypan blue from D,L-lactide containing polymers is due to the transformation from the crystalline (PLEC 1) to an amorphous polymer (PLEC 2 and 3) as previously reported.[16,17] The crystalline region can entrap drugs inside the rods which will lower the release rate. On the contrary, an amorphous region allows drugs to easily diffuse through the polymer matrix increasing release rate of drugs.

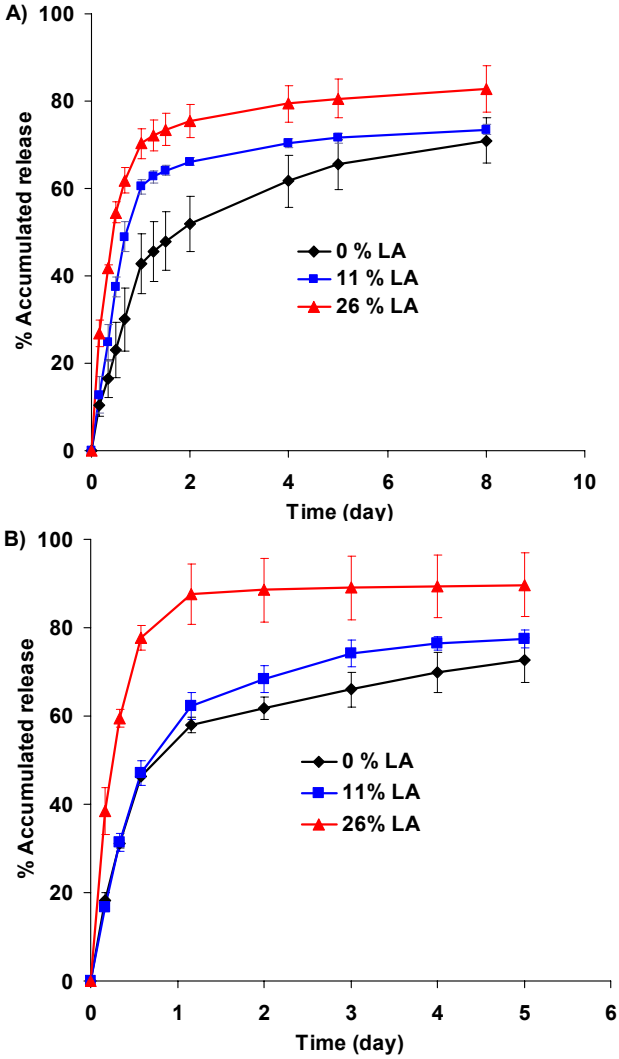


Fig. 3 Trypan blue release profiles from polymeric rods containing different amount of D,L-lactide. Trypan blue loading in all polymeric rods is A) 20 and B) 30 % w/w. All polymers have the same molecular weight at 20 kDa.

Figure 4 demonstrates the effect of trypan blue loading (20 and 30 % trypan blue loading) on the release profiles of polymeric rods. Increasing amount of trypan blue loading leads to the faster release for 0, 11 and 26.5 % D,L-lactide containing polymeric rods. For polymeric rods with 0 % D,L-lactide, trypan blue was found to release at 40 and 60 % after 1 day for polymeric rods with 20 and 30 % loading, respectively. Similar results were obtained for polymeric rods with 11 and 26.5 % D,L-lactide.

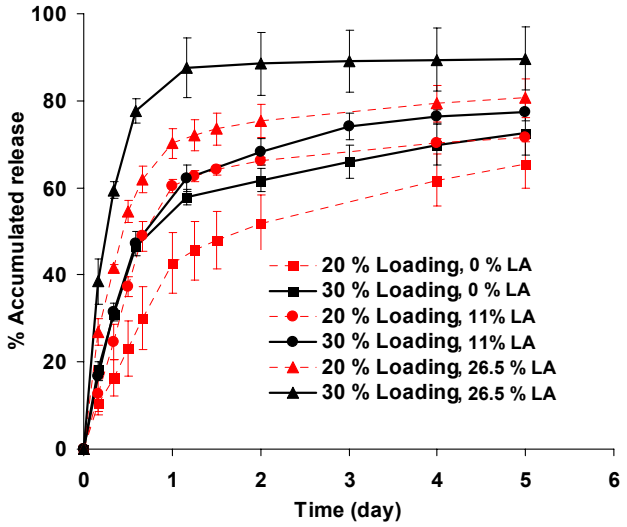


Fig. 4 Effect of trypan blue loading on the release profiles of polymeric rods with 0, 11 and 26.5 % D,L-lactide. Polymeric rods contain different amount of trypan blue at 20 and 30 % w/w. All polymers have the same molecular weight at 20 kDa.

Conclusion

PLEC was successfully used as a material to fabricate polymeric rods. Utilization of tri-component copolymers leads to the adjustable trypan blue release without using the external excipient molecules such as sodium chloride and sugar. Trypan blue release rate can be controlled by co-polymer ratio and trypan blue loading. Trypan blue release rate directly relates to the amount of D,L-lactide in the polymers and trypan blue loading.

Acknowledgment

We thank Dr. Jinming Gao at University of Texas Southwestern Medical Center for helpful discussions and Dr. Jitladda Tangpakdee-Sakdapipanich at Mahidol University for the help in the polymer characterization. This research is supported by Thailand Research Fund and Commission on Higher Education for N. N..

References

1. Nasongkla N, Bey E, Ren J, Ai H, Khemtong C, Guthi JS, Chin SF, Sherry AD, Boothman DA, Gao J (2006) Multifunctional polymeric micelles as cancer-targeted, mri-ultrasensitive drug delivery systems. Nano Lett 6: 2427-2430
2. Baker R (1987) Controlled release of biologically active agents. New York, Wiley
3. Qian F, Nasongkla N, Gao J (2002) Membrane-encased polymer millirods for sustained release of 5-fluorouracil. J Biomed Mater Res 61: 203-211
4. Sutton D, Wang S, Nasongkla N, Gao J, Dormidontova EE (2007) Doxorubicin and beta-lapachone release and interaction with micellar core materials: Experiment and modeling. Exp Biol Med (Maywood) 232: 1090-1099
5. Nasongkla N, Shuai X, Ai H, Weinberg BD, Pink J, Boothman DA, Gao J (2004) cRGD-functionalized polymer micelles for targeted doxorubicin delivery. Angew Chem Int Ed Engl 43: 6323-6327
6. Shuai X, Ai H, Nasongkla N, Kim S, Gao J (2004) Micellar carriers based on block copolymers of poly(epsilon-caprolactone) and poly(ethylene glycol) for doxorubicin delivery. J Control Release 98: 415-426
7. Sutton D, Nasongkla N, Blanco E, Gao J (2007) Functionalized micellar systems for cancer targeted drug delivery. Pharm Res 24: 1029-1046
8. Okada H: One- and three-month release injectable microspheres of the lh-rh superagonist leuprorelin acetate. Adv Drug Deliv Rev 1997;28:43-70.
9. Shameem M, Lee H, DeLuca PP (1999) A short term (accelerated release) approach to evaluate peptide release from plga depot-formulations. AAPS PharmSci 1: E7
10. Schindler A, Jeffoat R, Kimmel GL (1977) Contemporary topics in polymer science. New York Plenum Press
11. Karjalaimen T (1996) Mechanical properties of e-caprolactone and lactide copolymers after hydrolysis in vitro. J Appl Polym Sci 59: 5
12. Weinberg BD, Ai H, Blanco E, Anderson JM, Gao J (2007) Antitumor efficacy and local distribution of doxorubicin via intratumoral delivery from polymer millirods. J Biomed Mater Res A 81: 161-170
13. Qian F, Saidel GM, Sutton DM, Exner A, Gao J (2002) Combined modeling and experimental approach for the development of dual-release polymer millirods. J Control Release 83: 427-435
14. Qian F, Stowe N, Saidel GM, Gao J (2004) Comparison of doxorubicin concentration profiles in radiofrequency-ablated rat livers from sustained- and dual-release plga millirods. Pharm Res 21: 394-399
15. Lang MD, Wang SG (1999) Synthesis and identification of pcl/peo/pla tri-components copolymer. J Biomater Sci, Polym Ed 4: 12
16. Zhanga L, Hua Y, Jiang X, Yanga C, Luc W, Yang YH. (2004) Camptothecin derivative-loaded poly(caprolactone-co-lactide)-b-peg-b-poly(caprolactone-co-lactide) nanoparticles and their biodistribution in mice. Journal of Controlled Release 96: 14
17. Zhang Y, Wang C, Yang W, Shi B, Fu S (2005) Tri-component diblock copolymers of poly(ethylene glycol)–poly(e-caprolactoneco-lactide): Synthesis, characterization and loading camptothecin. Colloid Polym Sci 283: 5

Microchip-Integrated EOSCs (Electrolyte Oxide Semiconductor Capacitors) as Devices for High Efficiency and Selective Electroporation of Mammalian Cells

M. Maschietto[1,§], S. Girardi[1,§], M. Dal Maschio[1,2] and S. Vassanelli[1,¶]

[1] Department of Human Anatomy and Physiology – Institute of Physiology, University of Padova, Padova, Italy
[2] IIT – Italian Institute of Technology, Genova, Italy

Abstract— **Electroporation is a widely used technique for the delivery of molecules in cultured cells. In the last years microchips have been developed for electroporating cells growing in adhesion to the chip substrate. Most part of these devices are based on metal electrodes. Here we show an innovative use of a silicon microchip featuring 64 insulated EOSCs (Electrolyte Oxide Semiconductor Capacitors) to electroporate single or a few mammalian CHO-K1 cells with high efficiency and selectivity. The use of low-voltage pulses allows to maintain a higher cell viability than standard electroporation of cell suspensions. By means of the viability dye Trypan Blue we provide evidencies of both reliability and selectivity of our device. The microchip is presented here as an efficient tool for the delivery of a DNA plasmid to induce the production of the fluorescent protein EYFP, suggesting its possible general use in exogenous genes expression experiments. Finally, we report the application of our device for live imaging *in vitro* by means of the actin cytoskeletal probe Phalloidin. These results open new perspectives on the possibility of performing alternative live stainings avoiding the chemical fixation of the cells, that is necessary in standard immunofluorescence protocols.**

Keywords— **Electroporation, EOSC, gene expression, live imaging**

I. Introduction

Electroporation is one of the most widely used physical approaches for the delivery of molecules in cell cultures. In the last years many devices have been developed for the electroporation of cells growing in adhesion. Several of them are based on MEA (MultiElectrodes Arrays): low-voltage electrical pulses are applied by means of small metal electrodes, inducing transient pores on the plasmatic membrane of cells growing on them. These devices allow to transfect different kinds of mammalian cells with a variety of molecules and to perform selective electroporations, confined to groups of few cells [1, 2] or to single cells [3], with reduced voltage amplitude respect to standard electroporation of cell suspensions.

In the present work we show that silicon microchips can be used to perform electroporation of the epithelial cell line CHO-K1. The microelectronic basic unit of the device is represented by a stimulation site (EOSC - Electrolite Oxide Semiconductor Capacitor): capacitors are organized in two linear arrays of 32 elements each [4]. EOSCs were previously used to stimulate nerve cells from *Lymnaea stagnalis*, adopting specific stimulation protocols in order to open ion channels and to avoid the formation of pores in the plasmatic membrane attached to the microchip surface [5].

Starting from this point, we wanted to verify the possibility to use EOSCs to perform high-efficiency electroporation of CHO-K1 cells, by proper modulations of slope and frequency of the stimulus. Our data confirm that both slow- and fast-slope stimuli induce pores formation in the plasmatic membrane, allowing the transfection of CHO-K1 with different kinds of molecules, comprising markers for live imaging. Moreover, fast-slope combined with high frequency allows exogenous genes expression, favoured, perhaps, by poration of the nuclear membrane. Our results demonstrate that the approach is selective, reliable and may provide a new mean for simultaneous and multiple delivery trials on the same culture.

II. Materials & methods

A. Microchip

The microchip is based on two linear arrays, each consisting of 32 octagonal EOSCs of about 30 to 50 μm width (Fig. 1a) [4]. A plastic chamber is mounted on the chip to allow the cell culture (Fig. 1b).

The waveform generator Agilent 33250A 80 MHz (Agilent Technologies) has been used to generate electroporation voltage protocols, that were monitored by an Agilent 54641A 350 MHz oscilloscope (Agilent Technologies). Each EOSC was manually selected through connectors on the board contacting the chip (Fig. 1c).

§ These authors contributed equally to this work.
¶ Corresponding author.

O. Dössel and W.C. Schlegel (Eds.): WC 2009, IFMBE Proceedings 25/VIII, pp. 321–324, 2009.
www.springerlink.com

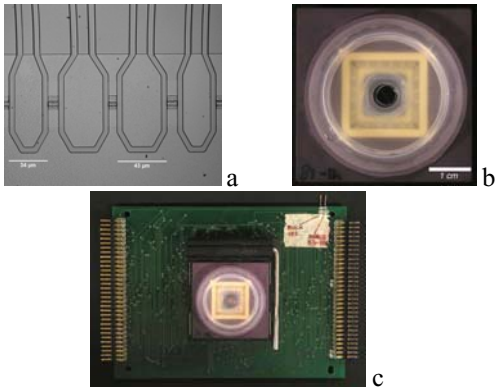


Fig. 1 (a) Detail of a part of an array showing octagonal EOSCs of two different dimensions (34 and 43 μm). (b) Plastic chamber mounted on the microchip, featuring two linear EOSCs arrays. Scale bar 1 cm. (c) Board with inserted chip. On the left a series of connectors are arranged in two parallel arrays for the manual selection of the EOSCs.

B. Electroporation protocols

Two different protocols were used to electroporate cells two days after plating:

1) slow-slope and low-frequency stimulus;

2) fast-slope and high-frequency stimulus.

In both protocols the voltage amplitude range was ± 4 V, according to the limits of tolerance of the device [6].

C. Cell line and molecules

All the experiments were performed with epithelial CHO-K1 cells that were plated and grown in adhesion to the chip surface.

The efficiency of the protocols in electroporating the cells was verified by means of three kinds of molecules, solubilized in a high ionic strength buffer [3]:

a) Trypan Blue (subsequently named TB), a vital stain capable of entering a cell only if the plasmatic membrane is porated. It is used with protocol 1) to show the reliability of EOSCs in electroporation and the selectivity;

b) an expression plasmid for the fluorescent protein EYFP: it is introduced in the cells by means of protocol 2) in order to show that EOSCs allow to perform gene expression experiments. The expression of EYFP is verified 24 h after the electroporation;

c) Fluorophore-conjugated Phalloidin (subsequently named PH; Molecular Probes®): it specifically binds to the cytoscheletal protein actin. It is used with protocol 1) to demonstrate the real possibility of performing live imaging experiments with our devices.

III. Results

A. Microchip-integrated EOSCs can be used to electroporate mammalian cells with high efficiency

Fig. 2 represents an example of electroporation of CHO-K1 cells by means of protocol 1), where all the EOSCs have been selected and TB has been used as a marker. By comparing Fig. 2a (visible light, before electroporation) with Fig. 2b (UV light, after electroporation) it is clear that the electroporation is specific, as transfected cells are present only on the EOSCs. Furthermore the efficiency is high, being estimated to be 81% (SD = 8) from a series of 10 experiments with different chips.

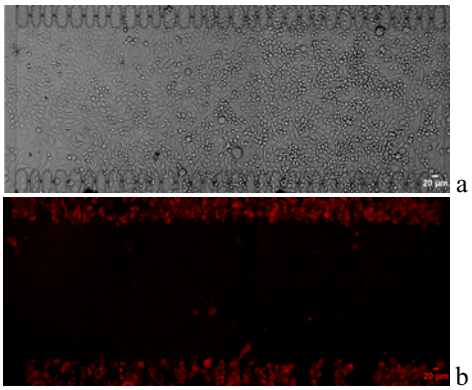


Fig. 2 Central area of the chip with the two linear arrays of 32 EOSCs. CHO-K1 cells are growing on the entire chip surface (a), but only those that are covering the EOSCs are fluorescent (b), indicating that TB has been selectively transfected by electroporation. Scale bars 20 μm.

B. The electroporation of CHO-K1 cells by means of EOSCs is selective

As each EOSC is insulated from its neighbours, it is possible to choose the sites obtaining selective electroporations. We applied protocol 1) with TB only to a few sites. Fig. 3a represents the superimposition of visible and UV light pictures: only the cells covering the selected sites (number 1, 3 and 5) are fluorescent, indicating that only those cells have been electroporated. This is confirmed by the fluorescence intensity plot profile over the red line in Fig. 3a. The line was drawn to cover the EOSCs from 2 to 4. The plot highlights that no fluorescence appears in correspondence of the cells covering the non-selected spots (Fig. 3b).

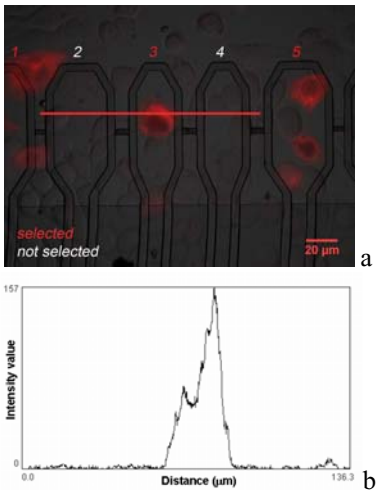


Fig. 3 (a) Group of 5 EOSCs after the electroporation of CHO-K1 with TB selecting only sites 1, 3 and 5. Notable is the selectivity of the device. Scale bar 20 µm. (b) The selectivity of the electroporation is evidenced in the plot of the fluorescence intensity along the red line shown in (a), covering both selected and not-selected spots: fluorescence is completely absent from the cells on non-selected EOSCs (numbers 2, 4).

C. EOSCs are reliable devices for inducing protein expression in CHO-K1 cells by electroporation

As the previous results demonstrate that our microchip is a reliable tool to electroporate mammalian cells, we verified the possibility to realize transfections with biologically useful molecules, like genes. Fig. 4a shows an example of EYFP expression in CHO-K1 after the electroporation of the plasmid containing the corresponding coding gene, using the protocol 2). A magnification of the spots in the blue square is shown in Fig. 4b.

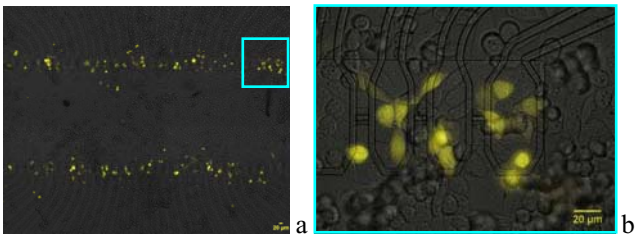


Fig. 4 Example of EYFP expression in CHO-K1 after electroporation. (a) Superimposition of visible and UV light images of the entire arrays. (b) Magnification of the spots in the blue square in (a). Scale bars 20 µm.

The expression of EYFP indicates that the plasmids passed through both the plasmatic membrane and the nuclear one. This suggests that the fast-slope high-frequency stimulus may create pores also in the nucleus, allowing the exogenous gene to be expressed.

Noteworthy is also the good efficiency of transfection: from ten experiments it has been calculated as 61.21% (SD = 17.62). The variability can be justified considering that plasmid DNAs present multiple coiled-coil structures with variable dimensions: depending on the pores diameter, some big molecules may not enter the cell, decreasing the efficiency of the electroporation.

It is important to note that a high transfection efficiency implies also that a large portion of electroporated cells remains fully viable.

D. Live imaging experiments

Other biologically interesting molecules that are usually introduced into the cells are fluorescent citoplasmatic markers. They are widely used to perform cell imaging experiments: this application usually requires the chemical fixation of the cells with substances (like formaldehyde) that kill the cells and may introduce artifacts by altering the intracellular structures. We therefore verified if electroporation mediated by EOSCs can be used to introduce fluorescent markers in cells, avoiding fixation and keeping them alive. To this aim, electroporations of CHO-K1 were performed with the cytoscheletal marker PH that binds specifically to actin.

Fig. 5a is an example of transfection of PH by means of protocol 1): even in this case it is possible to detect the fluorescence in almost all the cells growing on the EOSCs. The typical PH pattern is more visible in the magnification in Fig. 5b: also some filamentous structures (the so-called “stress fibers”) become visible.

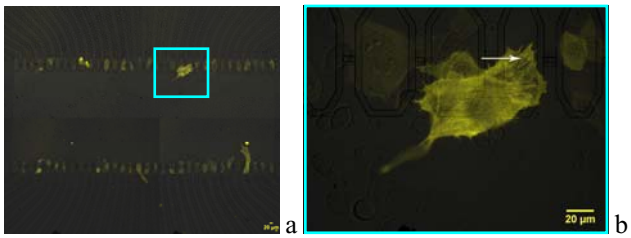


Fig. 5 Electroporation of CHO-K1 with fluorescent Phalloidin. (a) Almost all the cells covering the EOSCs were electroporated. (b) Magnification of the spots in the blue square in (a), where the distribution of actin in a cell is visible. The white arrow points out the so-called “stress fibers” made of actin filaments. Scale bars 20 µm.

The efficiency of the electroporation with PH calculated from a series of 10 independent trials with different chips is 89% (SD = 11). The results indicate that high efficiency transfections and high quality images can be obtained using our device with intracellular markers, providing a new easy-to-use tool to realize live imaging experiments.

IV. Conclusions & perspectives

The present work proposes the use of EOS capacitors integrated in a silicon microchip to perform electroporations of mammalian cells growing in adhesion.

The results demonstrate the reliability of the device that allows to obtain high transfection efficiencies with different molecules, like plasmids coding for exogenous genes or markers for live imaging experiments, while keeping the cells healthy.

Furthermore, the independence of each EOSC in the arrays allows to perform selective electroporations, opening the possibility to make multiple transfections of different molecules at the same time on the same chip.

Our trials with the actin marker Phalloidin were made to demonstrate that EOSCs are reliable tools to introduce markers for intracellular structures. Therefore, this system could be used to track the turnover of a labeled protein in time-lapse experiments. To this respect, the approach could be considered as an easy-to-use and less invasive alternative to microinjection [7].

The validation of the technique with primary cells is in progress.

Acknowledgments

We would like to thank Prof. Peter Fromherz for providing us with the microchips.

We thank also Maria Cristina Bazan and Onelia Gagliano for their precious contributions to realize this work.

References

1. Jain T, Muthuswamy J. (2007) Microsystem for transfection of exogenous molecules with spatio-temporal control into adherent cells. Biosens. Bioelectron. 22: 863-870.
2. Jain T, Muthuswamy J. (2008) Microelectrode array (MEA) platform for targeted neuronal transfection and recording. IEEE Trans. Biomed. Eng. 55: 827-832.
3. Vassanelli S, Bandiera L, Borgo M, Cellere G, Santoni L, Bersani C, Salamon M, Zaccolo M, Lorenzelli L, Girardi S, Maschietto M, Dal Maschio M, Paccagnella A. (2008) Space and time-resolved gene expression experiments on cultured mammalian cells by a single-cell electroporation microarray. N. Biotechnol. 25: 55-67.
4. Schmidtner M, Fromherz P. (2006) Functional Na+ channels in cell adhesion probed by transistor recording. Biophys. J. 90: 183-189.
5. Schoen I, Fromherz P. (2007) The mechanism of extracellular stimulation of nerve cells on an electrolyte-oxide-semiconductor capacitor. Biophys. J. 92:1096-1111.
6. Wallrapp F, Fromherz P. (2006) TiO2 and HfO2 in electrolyte-oxide-silicon configuration for applications in bioelectronics. J. Appl. Phys. 99: 114103.
7. Theiss C, Meller K. (2002) Microinjected anti-actin antibodies decrease gap junctional intercellular commmunication in cultured astrocytes. Exp. Cell Res. 281: 197-204.

Corresponding author:

Author: Vassanelli Stefano
Institute: Dept. Human Anatomy and Physiology – Inst. Physiology
Street: via Marzolo 3
City: Padova, 35131
Country: Italy
Email: stefano.vassanelli@unipd.it

Sensors for Healthcare Monitoring – Proteins, Viruses and Blood-Group-Typing

F.L. Dickert[1], P.A. Lieberzeit[1], A. Seifner[1], R. Schirhagl[1] and Christof Jungbauer[2]

[1]University of Vienna, Department of Analytical Chemistry and Food Chemistry, Vienna, Austria
[2]Blood Donation Center, Austrian Red Cross, Vienna, Austria

Abstract— **Molecular imprinting strategies could successfully be applied to bioanalytes of different dimensions, ranging from proteins, as insulin, to picornaviruses, Human-Rhino-Virus (HRV) or Foot-Mouth-Disease-Virus (FMDV) to cells, e.g. yeast-cells or even highly flexible erythrocytes. Blood cell surface patterning of pre-polymers could be achieved via coatings with selective recognition properties. Polymer layers coupled with mass-sensitive quartz crystal micro balances (QCMs) lead to a selective sensor system concerning blood group typing. Thus, blood groups A_1, A_2 and B can be distinguished by the imprinted layers acting as synthetic antibodies. Further development of synthetic receptor sites were realized by generating plastic replica of immunoglobulin-Y (IgY), resulting in an antibody-like structure integrated on the polymer surface. For this purpose nano-particles from polymers were imprinted with natural immunoglobulin. After removing the template these patterned particles were pressed in a pre-polymer resulting in a synthetic receptor having antibody properties. The sensitivity to the allergen sesame protein was even higher than to the natural analogue.**

Keywords— **Molecular Imprinting, Insulin, HRV, Erythrocytes, Plastic Antibodies.**

I. Introduction

The development and improvement of Molecularly Imprinted Polymers (MIPs) for their use in selective sensors gets increasing interest [1]. The analyte chemical properties are casted into a polymer-system resulting in selective layers that are inexpensive, easy-to-use and provide long-term-stability. The idea of polymer imprinting is schematically presented in Fig. 1. Combining such layers with Quartz-Crystal-Microbalances (QCMs), analytical systems are resulting in a smart combination of selectivity and sensitivity [2]. Extracting of analytes leads to a lowering of QCM resonance frequency.

For medical purpose online-monitoring is an interesting task, e.g. for insulin. Therefore, a sensor system based on molecularly imprinted layers was developed for this protein. Human rhino virus (HRV) as well as foot-and-mouth disease virus (FMDV) lead to potential risks for health and are also economically threatening. For both viruses, HRV and FMDV several serotypes belonging to distinct groups are known. The HRV e.g. can be divided into major (91 serotypes) [3] and minor (10 serotypes) group [4]. With the help of sensitive layers, generated by a stamp imprinting technique, viruses should be specifically extracted in respect to serotypes.

Concerning molecular recognition of whole cells, not only yeast cells [5], but also erythrocytes are used for imprinting procedures in spite of their high flexibility [6]. Besides blood groups A, B, AB and O, there are several subgroups. The blood groups A_1 and A_2 (22 % of European population are possessing A_2) are differing in A-antigen density [7]. In clinical practice, blood groups are determined by antibodies immobilized on dextran gel. In this way a reversible procedure is proposed without antibody consumption.

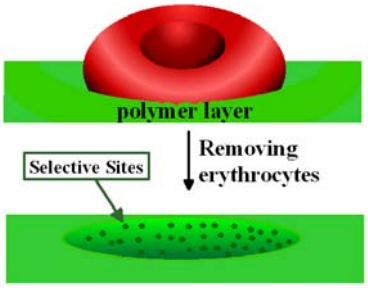


Fig 1: Schematic presentation of imprinting process. Red blood cells are embedded into the polymerizing monomer/crosslinker-mixture. After removing the template the generated synthetic receptor sites can re-include red blood cells, again.

Further progress in substituting natural receptors by synthetic analogues is realized by generating polymeric replicae of natural antibodies. For this purpose, polymer nanoparticles are printed with natural immunoglobulins. Washing out these templates, cavities can be generated with complementary structure. These particles can be used for imprinting a pre-polymer-layer on a QCM leaving behind antibody-like structures on the surface after curing the polymer. This procedure which can be applied for all kinds of antibodies, reveals several advantages such as robust handling and is cost effective as compared to the natural analogues.

II. Experimental

Quartz crystal microbalance and measurements: 10 MHz-QCMs were used in this work. The quartz crystal microbalances are made of quartz blanks (thickness: 168

O. Dössel and W.C. Schlegel (Eds.): WC 2009, IFMBE Proceedings 25/VIII, pp. 325–328, 2009.
www.springerlink.com

µm, diameter: 15.5 mm). Dual electrode arrangements were screen printed, compensating for physical interferences. Measurements were carried out with a home-made measuring-cell and electronics connected to a peristaltic pump. Data aquistion was done via a frequency counter (HP53131A) and HP-IB bus.

Imprinting: For generating insulin- and glargin-selective coatings, stamp imprinting technique is employed with insulin crystals. After hardening the polyurethane pre-polymer the printing insulin crystals were removed with sodium dodecyl sulfate and HCl to create selective interaction sites.

For preparing both HRV/MKDV- and insulin-imprints, polyurethane, consisting of bisphenol A, phloroglucinol and hexamethylene diisocyanate 24:28:48 % (w/w) dissolved in 200 µL THF and prepolymerized to the gel point at 70°C was used. Stamps for viruses were prepared by adhering them on a glass plate.

The polymer composition used for blood cell-imprinting is given by a mixture at of 95 mg 1-vinyl-2-pyrrolidone, 5 mg N,N'-methylenebisacrylamide and 1 mg azobisisobutyronitrile (AIBN). The imprinting process was performed at 70° in a thin pre-polymer directly on a QCM followed by UV initiated polymerization around the embedded red blood cells. Removing of erythrocytes can be realized by carefully rinsing the imprinted layers with water.

Plastic replicae of immunoglobulin-Y (IgY) were generated via imprinted nano-particles from copolymers of 1-vinyl-2-pyrrolidone, methacrylic acid and N,N'-1,2 dihydroxy-ethylene-bis(acrylamide) acting as cross-linker. The ingredients were solved in water at 70°C, the solution was adjusted to pH 7. After adding the template IgY and potassium peroxydisulfate as initiator the polymerization was performed to the gel-point by UV-light. Precipitation polymerization is performed in acetonitrile. Particles were generated in a size of some hundred nanometers. The QCM-electrodes were coated with the same prepolymer as in the case of nano-particles. The QCM-electrodes were printed with the particles prepared. After curing the polymer and washing steps it was ready for use.

Surface characterization: For the characterization of the modified polymer surfaces, Contact Mode Atomic Force Microscopy was applied (Veeco Nanoscope IVa).

Chemicals: All chemicals were purchased from Fluka, Aldrich and Merck and whole blood in EDTA tubes were obtained from Red Cross, Vienna.

III. Results and Discussion

Bionalytes are ranging from proteins in a diameter of some nano-meter to cells in a size of some micro-meter.

Insulin: The well-being of man is strongly dependent on hormone concentration. Thus, insulin concentrations were monitored by QCM sensors as it is important for diabetes. The native insulin and the depot insulin were of interest.

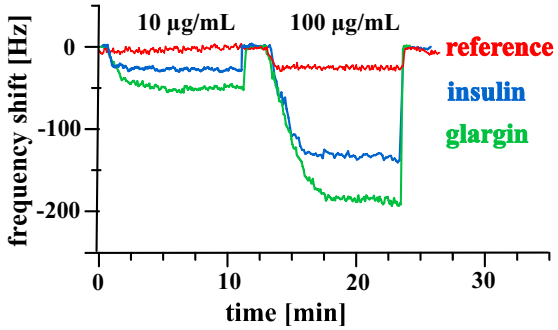


Fig. 2: QCM-measurements with insulin- and glargin-imprinted layers exposed to the respective analyte at different concentrations are given. The reference electrode shows only minor responses, representing non-specific interactions, the imprinted layers were exposed to 10 and 100 µg/mL insulin/glargin.

In Fig 2, insulin- and glargin-imprinted polyurethane layers on a QCM are shown. The non-imprinted reference electrodes guarantee via difference measurements an elimination of temperature influences, mainly due to viscosity.

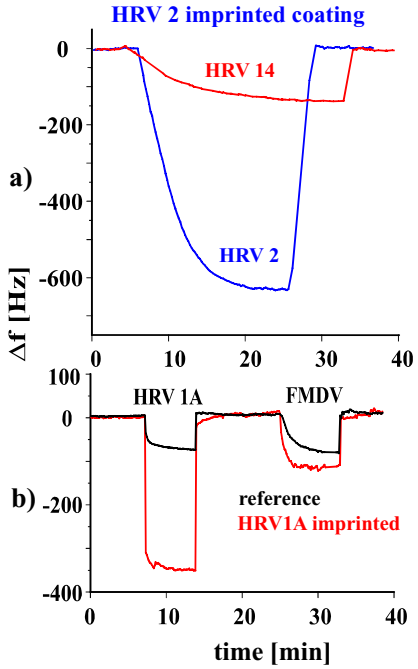


Fig. 3: HRV-measurements of imprinted layers on a QCM possessing dual electrode geometry. a) HRV 2 imprinted sensor coating, exposed to HRV 2 and HRV 14 (virus concentration: $3.2 \cdot 10^{10}$ particles/mL). b) HRV 1a imprinted sensor layer, exposed to HRV 1a- and FMDV at similar concentrations ($2 \cdot 10^{12}$ particles/mL).

Insulin consists of 51 amino acids. The native insulin and the depot insulin differ only by three amino acids. Figure 2 shows differences between the patterned QCM-coatings. Cross sensitivities between insulin or glargin, when the differently templated layers are appreciable. Thus, sensor arrays allows the analysis of insulin mixtures. Furthermore, the sensor responses in Fig. 2 will exceed some hundreds of Hz at higher concentrations. This cannot be explained by mono layers of insulin. Obviously an aggregation of adhered insulin molecules will occur.

Viruses: Human rhinoviruses (HRV) are particles which show an approximately larger diameter than insulin. All HRVs in a variety of approximately 150 different serotypes have an identical diameter of 30 nano-meter. In Fig. 3a, 10 MHz QCM-measurements with HRV-imprinted polyurethane layers are given. The sensor layer imprinted with the serotype, HRV 2 yields a sensor response of 600 Hz, whereas the frequency response to HRV 14 with the same particle diameter is appreciable smaller and can be clearly distinguished. Thus, it can be concluded that in spite of the identical size the different surface structure of proteins leads to the effects observed. Furthermore, in contrast to natural antibodies the template strategy characterizes the whole surface of the viruses and not only receptor sites. The effect of size is given in Fig. 3b where HRVs and FMDVs are compared. The FMD virus has a diameter of 25 nano-meter being smaller by 5 nano-mater compared to HRV. The sensor response is significant concerning distinguishing these types of picornaviruses. The FMD virus gives only an unspecific response as the non-imprinted layer.

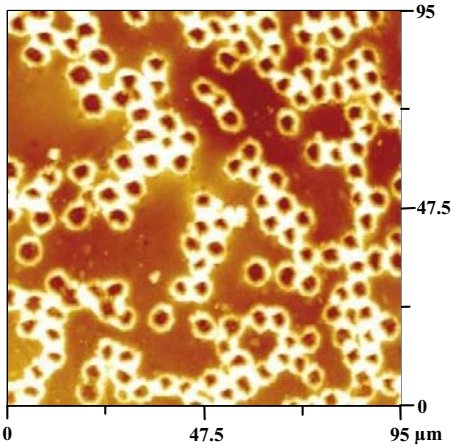


Fig. 4: Atomic Force Microscopy in Contact Mode of erythrocyte imprints in polyvinylpyrrolidone. The imprints in the polymer layer are 8 µm in diameter and some hundred nano-meter in depth.

Erythrocyctes: In Fig. 4 the image of an erythrocyte-imprinted polymer layer on a QCM can be seen. Cavities corresponding to red blood cell imprints of approximately 8 µm in diameter are visualized. A re-inclusion is possible and proves the molding process to be successful. Measurements with blood-cell imprinted layers with A_1- and A_2-erythrocytes were performed, which is shown in Fig. 5. The erythrocyte concentration used for all blood groups were identical to be $3.5 \cdot 10^8$ cells/mL. Obviously, when the analyte to be is identical to the template erythrocytes the highest frequency response is obtained (15 kHz for A_1-imprinted layers and 20 kHz for A_2-imprinted layers). Non-template blood groups give only minor frequency changes. These results show that molecular imprinting is not only applicable to detect geometrical differences as shown in comparing HRV and FMD viruses but also for flexible cells. Both blood and even sub blood groups can be distinguished due to the antigens on the cell surfaces.

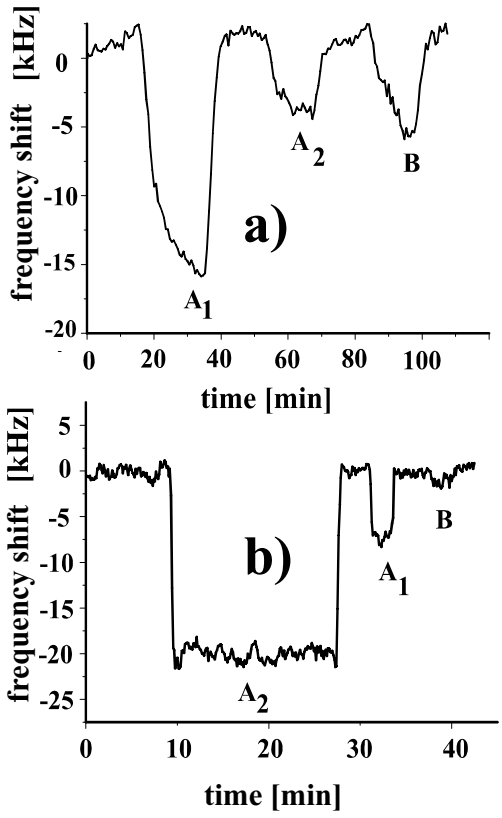


Fig. 5: Difference-measurements with A_1- and A_2-erythrocytes imprinted polyvinylpyrrolidone-layers. The concentration of cells amounts to $3.5 \cdot 10^8$ cells/mL for all blood groups. The template erythrocytes show the most prominent frequency decays, followed by blood group B for A_1-imprinted layers (a) and A_2-imprinted films (b).

Immunoglobulin-Y: Further development of QCM-selective layers could be realized to substitute natural immunoglobulin-Y by their plastic replicae. The realization was done by a double printing process. At first nanoparticles were prepared in presence of IgY acting as template. After washing out the adhered IgY the nano-particles were assembled on a flat surface and pressed in a pre-polymer. The nanoparticles have the advantage they are easily removed from the polymer surface due to their small interaction surface. In this way the identical surface recognition properties of IgY are transferred to the QCM-coating. When the immunoglobulin will act as antibody to some protein the synthetic coating will have the identical receptor properties. Thus, if a natural antibody is available the synthetic replica is easily to be prepared.

This idea can be used for detecting allergens which are getting more and more important. Sesame proteins are widely spread in food and it is interesting to have a sensor to this protein. In Fig. 6 an extract of sesame as analyte is used and a concentration dependent effect is observed. The synthetic IgY shows even an sensitivity which is higher by a factor of 3-4 in comparison to the natural IgY which can be followed from the porous structure of the nano-particles. Thus, the replicae are more easily accessible by analytes.

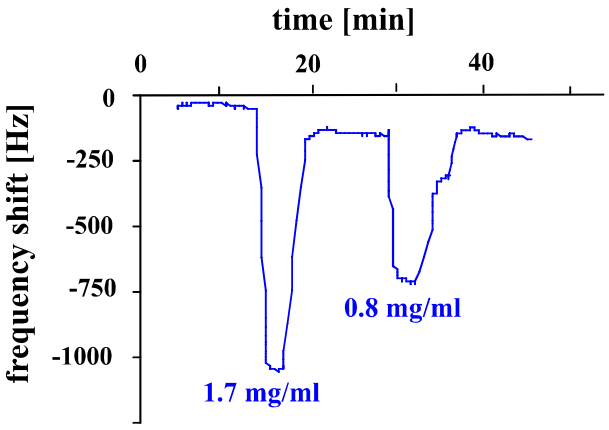


Fig. 6: Frequency response of a 10 MHz QCM coated with IgY plastic replicae to sesame protein, reversible responses are shown.

IV. Conclusion

The concept of Molecular Imprinting could effectively be applied for bioanalytes of different sizes ranging from a few nano-meter for proteins up to erythrocytes with 7-8 µm. Mass-sensitive detection is a label-free strategy which can universally be used and leads to a frequency diminishing of the QCM-resonance frequency according to mass loading. Selectivity is obtained by synthetic receptors which are generated by molding pre-polymers with the bioanalytes. This strategy can be used without knowing an exact structure of the analyte. The monomers are chosen to have only a similar polarity and form especially hydrogen bonding to the bioanalytes. During the curing process they will reorientate in a way that guarantees an optimized fit between analyte and polymeric cavity. Intermolecular binding and geometrical reorganization between host and guest will occur.

Thus, not only the different sizes of HRV and FMD viruses can be differentiated but also serotype recognition which is only based on their surface structure. In this respect a special challenge is blood typing, too. These cells are completely flexible and thus, only the nature of antigens on the cell surface is important.

The next step in developing sensitive materials is to use the natural evolution in respect to antigen antibody recognition. The receptor sites of immunoglobulin were cast in polymers. This can be done by a double imprinting process using nano-particles and thus more stable and better available systems as in nature are generated.

References

1. Dickert, F.L., Hayden, O., Halikias, K.P. (2001) Synthetic receptors as sensor coatings for molecules and living cells. Analyst 126:766-771
2. Dickert F.L., Hayden O., Bindeus R., Mann K.-J., Blaas D., Waigmann E. (2004) Bioimprinted QCM sensors for virus detection-screening of plant sap. Analytical and Bioanalytical Chemistry 378: 1929-1934
3. Vlasak M., Roivainen M., Reithmayer M., Goesler I., Laine P., Snyers L., Hovi T., Blaas D. (2005) The minor receptor group of human rhinovirus (HRV) includes HRV23 and HRV25, but the presence of a lysine in the VP1 HI loop is not sufficient for receptor binding, J. Virol. 79: 7389-7395
4. Greve J.M., Davis G., Meyer A.M., Forte C.P., Yost S.C., Marlor C.W., Kamarck M.E. (1989) Cell 56: 859–867
5. Seidler K., Lieberzeit P.A., Dickert F.L. (2009) Application of yeast imprinting in biotechnology and process control. Analyst 134: 361-366
6. Hayden O., Mann K.-J., Krassnig S., Dickert F.L. (2006) Biomimetic blood-group typing. Angew. Chem. Int. Ed. 45: 2626-2629
7. Furukawa K., Clausen H., Hakomori S.-I., Sakamoto J., Look K., Lundblad A., Mattes M.J., Lloyd K.O. (1985) Analysis of the specificity of five murine anti-blood group A monoclonal antibodies, including one that identifies type 3 and type 4 A determinants. Biochemistry 26: 7820-7826

Author: Franz L. Dickert
Institute: Analytical Chemistry and Foodchemistry
Street: Waehringer Str. 38
City: A-1090 Vienna
Country: Austria
Email: Franz.Dickert@univie.ac.at

The interaction between charged macroions induced by rod-like ions

K. Bohinc[1], A. Iglič[1], S. Maset[2] and S. May[3]

[1] Faculty of Electrical Engineering, Tržaška 25, University of Ljubljana, 1000 Ljubljana, Slovenia
[2] Department of Mathematics and Informatics, University of Trieste, Trieste, Italy
[3] Department of Physics, North Dakota State University, Fargo, ND 58105-5566, USA

Abstract— **We study a model for the interaction between two planar, like-charged macroions, separated by an aqueous solution containing rod-like counterions. Each counterion consists of two positive charges that are separated by a fixed distance. This is a specific case of ions that possess a spatially extended electric charge distribution. Such systems are not well described by mean-field theory. We thus suggest a density functional approach that accounts for charge-charge correlations within each rod-like ion but still neglects correlations between different ions. Our approach results in an integral-differential equation that can be solved numerically. The solution shows that orientational ordering of rod-like ions in the electric field between the two macroions gives rise to an attractive macroions-macroions interaction. We demonstrate that the attraction arises for sufficiently long rod-like ions and high surface charge densities of the two macroions.**

Keywords— **Electrostatics, biomaterials and biological interfaces.**

I. Introduction

Electrostatic interactions between macroions in aqueous solution containing microions are ubiquitous in all living cells [1, 2]. The macroions appear as charged lipid membranes, DNA, colloidal particles, cytoskeletal molecules, proteins, viruses, and even entire cells. Microions such as multivalent metal ions, dendrimers, charged micelles, and polyelectrolytes mediate electrostatic interactions between the macroions. For example, divalent diamin ions induce the aggregation of rodlike M13 viruses [3], multivalent ions mediate network formation in actin solutions [4], multivalent counterions condense DNA [5, 6], and positively charged colloids form complexes with DNA[7, 8].

Mean-field Poisson-Boltzmann theory does not predict attraction between like-charged surfaces [9]. Hence, attraction must be caused by charge-charge correlations. Indeed, accounting for inter-ionic correlations between (multivalent) counterions and charged surfaces leads to the possibility of attractive forces [10, 11, 12]. The Monte-Carlo (MC) simulations of Guldbrand et al. [13] first confirmed the existence of an attraction between like-charged surfaces of high surface charge density, immersed into a solution composed of point-like divalent ions. These and other [14, 15, 16] MC simulations showed that attractive interactions between equally charged surfaces may arise for high surface charge density, low temperature, low relative permittivity and polyvalent point-like counterions. Various theoretical approaches exist that characterize the role of charge-charge correlations between different point-like ions [17, 18, 15, 19] (i.e inter-ionic correlations).

Another possibility for the appearance of attractive interactions between like-charged surfaces finds its origin in the internal structure of multivalent ions [20, 21, 22]. Here, individual charges within an ion are spatially separated through non-electrostatic (i.e. steric) interactions [21, 23]. In this case, *intra-ionic* correlations add to the presence of inter-ionic correlations. In fact, intra-ionic correlations alone are sufficient to change repulsive into attractive interactions.

In the present work we consider two like-charged surfaces with one species of rod-like ions between them. Each rod consists of two elementary charges separated by a fixed distance. We extend the Poisson-Boltzmann approach to rod-like ions, resulting in an integral-differential equation that can be solved numerically. The solution allows us to characterize the local concentration and orientational ion distributions as well as the corresponding free energy for arbitrary rod-length. We note that the macroion-imposed orientational restrictions of the rod-like ions are fully accounted for in our model.

II. Theory

We represent the two like-charged macroions by two equally charged planar surfaces, each of surface area A and surface charge density σ. Each rod-like ion carries two positive elementary charges, separated by a fixed distance l. The distance between the two surfaces of the macroions is denoted by D as illustrated in Figure 1. In our model the electrostatic field of the system varies only along the x-axis, the normal direction between the two charged surfaces. We assume that there is no electric field behind each of the two charged planar surfaces (which is appropriate if inside the macroions the dielectric constant is much smaller than in the aqueous region between the surfaces). The rod-like ions are characterized by their positional and orientational degrees of

O. Dössel and W.C. Schlegel (Eds.): WC 2009, IFMBE Proceedings 25/VIII, pp. 329–331, 2009.
www.springerlink.com

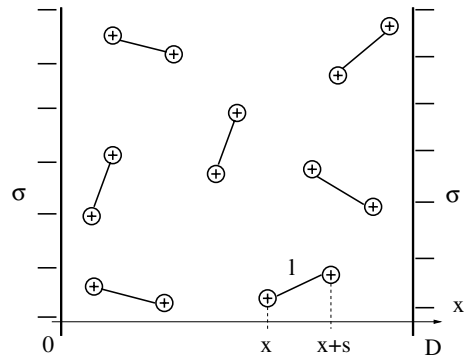


Fig. 1: Schematic illustration of two like-charged planar surfaces with surface charge density σ, interacting in a solution containing rod-like ions. Each ion consists of two elementary charges separated by a fixed distance l. For one particular ion the two locations of its two charges, x and $x+s$ are indicated.

freedom. We describe them by referring to one of the two charges of each ion as a reference charge, denoting the local concentration of all the reference charges by $n(x)$. The location of the second charge of a given rod-like ion is then specified by the conditional probability density $p(s|x)$, denoting the probability to find the second charge at position $x+s$ if the first resides at x. The product between the local concentration of reference charges and conditional probability density defines particle distribution function $n(x,s) = n(x)\,p(s|x)$. At any given position x, we require the normalization condition $1/(2l)\int_{-l}^{l} ds\, p(s|x) = 1$ to be fulfilled. Note also that $p(s|x) = 0$ for $|s| > l$.

The Helmholtz free energy of the system, measured per unit area of the surface and divided by the thermal energy unit, kT, consists of two contributions: electrostatic and entropic (the latter accounting for both the translational and orientational entroy of the rod-like ions)

$$\frac{F}{AkT} = \int_{-\infty}^{\infty} dx \left\{ \frac{\Psi'(x)^2}{8\pi l_B} + \int_{-l}^{l} ds\, n(x,s)\left[\ln(\lambda n(x,s)) - 1 + U(x,s)\right] \right\}. \quad (1)$$

Here Ψ denotes the reduced electrostatic potential. Also, as a measure of the dielectric constant ε within the aqueous solution, we use the Bjerrum length $l_B = e^2/(4\pi\varepsilon\varepsilon_0 kT)$ where ε_0 is the permittivity in vacuum and e is the elementary charge. Note that the constant λ must be chosen so as to ensure overall charge neutrality of the system. Finally, the function $U(x,s)$ is a non-electrostatic external potential that acts on the rod-like ions; it ensures that the rod-like ions cannot penetrate beyond the rigid macroion surfaces. We also note that the local charge density $\rho(x) = (e/l)\int_{-l}^{l} ds\,[n(x,s)+n(x-s,s)]$ explicitely accounts for both charges of each rod-like ion.

Minimization of the free energy in Eq. 1 results in a Boltzmann distribution for $n(x,s)$ which upon insertion into Poisson's equation $\Psi''(x) = -4\pi l_B \rho(x)/e$ yields the following integral-differential equation for the reduced electrostatic potential

$$\Psi''(x) = -\frac{8\pi l_B}{\lambda}\frac{1}{2l}\int_{max[-l,-x]}^{min[l,D-x]} ds\, e^{-(\Psi(x+s)+\Psi(x))} \quad (2)$$

Note that the integration limits embody the potential $U(x,s)$; i.e. they account for the orientational constraints imposed by the rigid surfaces. The boundary conditions at the charged surfaces read

$$\Psi'(x=0) = -4\pi l_B\sigma/e \qquad \Psi'(x=D) = 4\pi l_B\sigma/e. \quad (3)$$

Subject to these boundary conditions we have solved the integral-differential equation (Eq. 2) numerically, and we have determined the corresponding free energy F in Eq. 1.

III. Results and Discussion

Fig. 2 shows the electrostatic free energy F/AkT as a function of the distance D between the two like-charged surfaces for two different lengths of the rod-like ions, $l =$ 2 nm (left) and $l = 5$ nm (right). Different curves correspond to different σ as indicated in the caption of Fig. 2. For small surface charge densities σ, the electrostatic free energy

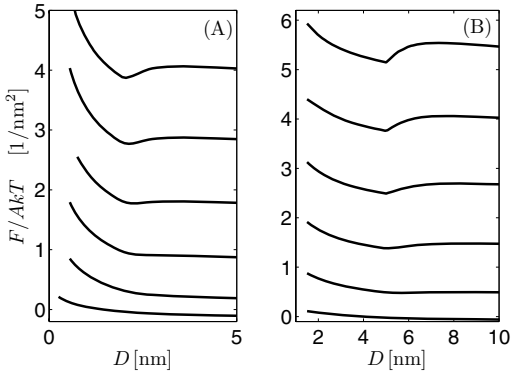


Fig. 2: The electrostatic free energy F as a function of the distance between the two like-charged surfaces for $l = 2$ nm (A) and $l = 5$ nm (B). The different curves correspond to different surface charge densities ranging from $\sigma = 0.01\,\mathrm{As/m^2}$ (bottom curve in (A) and (B)) to $\sigma = 0.16\,\mathrm{As/m^2}$ (top curve in (A) and (B)), changing in increments of $\triangle\sigma = 0.03\,\mathrm{As/m^2}$.

monotonously decreases with increasing distance D, indicating repulsion between the surfaces. Above a sufficiently high σ, however, a minimum at a finite distance $D = D^{eq}$ develops, indicating an attractive interaction for sufficiently large distances $D > D^{eq}$. We note that the critical surface charge density σ, above which a finite equilibrium separation develops, decreases with growing l. That is, longer rod-like ions are more potent to mediate attractive interactions between like-charged surfaces. We also note that once the optimal separation D^{eq} becomes finite, is roughly equals the rod length l. This indicates a bridging effect as the mechanism for the attraction. Specifically, there are two energetically favorable ion orientations, one parallel to the surfaces and the other one normal (this is schematically illustrated in Fig. 3). The latter of the two preferred orientations embodies the bridging and gives rise to an equilibrium separation that roughly corresponds to the length l of the rod-like ions. An analogous conclusion has been drawn for spherical ions [24].

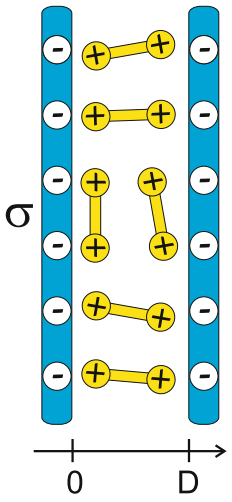


Fig. 3: Schematic illustration of the bridging mechanism. For long rod-like ions, there exists a stable equilibrium between the two macroions at $D \approx l$. Here, the rod-like ions preferentially orient either parallel or normal to the macroion surfaces. Those aligning in normal direction give rise to the bridging equilibrium.

IV. Conclusion

In summary, we have extended the Poisson-Boltzmann formalism to account for the presence of rod-like ions, resulting in an integral-differential equation for the electrostatic potential. This integral-differential equation can be viewed as a modified Poisson-Boltzmann equation that includes all intra-ionic (but still neglects inter-ionic) correlations. We have demonstrated that rod-like ions are capable of producing attractive interactions between like-charged surfaces, given the surface charge density of the macroions and the length of the rod-like ions are sufficiently large. The attraction is caused by the bridging of some rod-like ions between the two surfaces. Previous work for a related system [25] has shown that our modified Poisson-Boltzmann approach agrees well with Monte-Carlo simulations for a rod length $l \gtrsim 1.5\,\text{nm}$. We are thus confident that the present approach correctly captures the underlying physics of ionic solutions composed of sufficiently long rod-like ions.

Acknowledgment

SM thanks NSF for support through grant DMR-0605883.

References

1. Evans D F and Wennerström H 1994 *The colloidal domain, where physics, chemistry, biology and technology meet* (New York: VCH)
2. McLaughlin, S. 1989 *Annu. Rev. Biophys. Biophys. Chem.* **1989 18, 113**.
3. Butler J C, Angelini T, Tang J X and Wong G C L 2003 *Phys. Rev. Lett.* **91** 028301
4. Angelini T E, Liang H, Wriggers W and Wong G C L 2003 *Proc. Natl. Acad. Sci. U S A* **100** 8634
5. Bloomfield V A 1996 *Curr. Opin. Struct. Biol.* **6** 334
6. Teif V *Biophys. J.* 2005 **89(4)** 2574
7. Rädler J O, Koltover I, Salditt T and Safinya C R 1997 *Science* **275** 810
8. Gelbart W M, Bruinsma R, Pincus P A and Parsegian V A 2000 *Physics today* **53** 38
9. Safran S A 2003 *Statistical thermodynamics of surfaces, interfaces, and membranes* (Colorado: Westview Press)
10. Carnie S and McLaughlin S 1983 *Biophys. J.* **44** 325
11. Kirkwood J K and Shumaker J B 1952 *Proc. Natl. Acad. Sci. USA* **38** 863
12. Oosawa F 1968 *Biopolymers* **6** 1633
13. Guldbrand L, Jönsson B, Wennerström H and Linse P 1984 *J. Chem. Phys.* **80** 2221
14. Svensson B and Jönsson B 1984 *Chem. Phys. Lett.* **108** 580
15. Moreira A G and Netz R R 2001 *Phys. Rev. Lett.* **87** 078301
16. Reščič J and Linse P 2000 *J. Phys. Chem. B* **104** 7852
17. Grosberg A Y, Nguyen T T and Shklovskii B I 2002 *Rev. Mod. Phys.* **74** 329
18. Netz R R 2001 *Eur. Phys. J. E* **5** 557
19. Levin Y 2002 *Rep. Prog. Phys.* **65** 1577
20. Bohinc K, Iglič A and May S 2004 *Europhys. Lett.* **68(4)** 494
21. May S, Iglič A, Reščič J, Maset S and Bohinc K 2008 *J. Chem. Phys. B* **112** 1685
22. Kim Y W, Yi J and Pincus P A 2008 *Phys. Rev. Lett.* **101(20)** 208305
23. Maset S and Bohinc K 2007 *J. Phys. A: Math. Theor.* **40** 11815
24. Urbanija J, Bohinc K, Bellen A, Maset S, Iglič A, V. Kralj-Iglič and P B S Sunil 2008 *J. Chem. Phys.* **129(10)** 105101/1-5
25. Maset S, Reščič J, May S, Pavlič J I and Bohinc K 2009 *J. Phys. A: Math. Theor.* **42** 105401

Integration of Micro Fluidic Bio-chip Design and Automatic fluorescent Identification for Rapid Sperm Mobility Assessment

Li-Chern Pan[1], Fang-Chi Hsu[2],Yun-Ying Wu[3], Fan-Gang Tseng[4], *Member, IEEE,* Da-Jen Yao[5],Yieh-Loong Tsai[6], Jiann-Loung Hwang[7]

[1]Department of General Education, Taipei Medical University, Taipei, Taiwan
[2]Departmentof Public Health, Taipei Medical University, Taipei, Taiwan
[3]Graduate Institute of Biomedical Informatics, Taipei Medical University, Taipei, Taiwan
[4] Division of Mechanics, Research Center for Applied Sciences, Academia Sinica, Taipei, Taiwan, ROC,
[5] Department of Engineering and System Science, National Tsing Hua University, Hsinchu, Taiwan,
[6,7] Department of Obstetrics and Gynecology, Shin Kong Wu Ho-Su Memorial Hospital, Taipei, Taiwan,

Abstract—**Since male abnormality has now been reported to account at least thirty percent of couples with fertility problem. Therefore, distinguishing and classification of sperm has become more and more important, especially when Assisted Reproductive Technology (*ART*) like *in vitro* fertilization (IVF) is involved. However, traditional sperm sorting methods all requires manual selection, which is tedious and often cause sperm damage during the screen process. Although, new design from our recent study, seemed to point for a possibility to make these kind of MISS device capable of separating sperms into various mobility sub-class. In addition, the Hoechst 33258 and propidium iodide double staining results, also confirmed that the most motile and health sperm is indeed able to leave the laminar stream and being sorted out at outlet-h, with least dead sperm or debris. Meanwhile, we observed the dead sperm had been dominate from clear red stains and live sperm are not as active as is corresponded with more diffused blue stains. In order to confirm the real sorting situation, we counted the amount of sperm in collected sample by flow cytometry and tried to establish the statistic model. Though the flow cytometry, we could detect the sperm fluorescent distribution and count the size of sperm population. Nevertheless, *t*-test with 95% confidence level also shown significant difference in live/dead sperm ratio. Therefore, from the combined result among flow cytometry, fluorescent stain, and the statistic model test, it is confirmed that live sperms were able to cross the laminar stream created by the device and reach the sorting chamber with corresponding range from non-motile sperms to debris, as well as from living to dead ones. It is concluded that the proposed method is cost effective and is possible to serve as a protocol for rapid sperm quantitative assessment.**

Keywords—Sperm motility; Micro fluidic device; Fluorescence

I. Introduction

Infertility has become a common problem for married couples for the past few decades. Moreover, male abnormality is reported to account for about thirty percent in couples with less-than-normal fertility [1]. Therefore, distinguishing and classification of sperm quality has become more and more important. However, traditional sperm sorting methods, such as swim-up and migration-sedimentation, requires manual selection, which is tedious and often cause sperm damage during preparation [2].

In 2002, B. Cho, et al. [3] proposed a gravity-driven pumping system that is integrated with micro channel for sperm selection. Subsequently, they further improved this system and turn it into a Microscale Integrated Sperm Sorter (MISS). In Particular, Bovine Serum Albumin (BSA) coating in the structured PDMS micro-channels was used to elevate the surface hydrophilicity for the reduction of cell nonspecific adsorption [4].

Although, based on the assumption that sperms with higher mobility are potentially able to cross more stream lines in shorter time span, the design is able to separate some live sperms from the major stream line. However, due to the single threshed design, it often poses limitation not only in workable input sperm density range, but also in the ability to spate sperms with wide spectrum of mobility differences.

Therefore, we propose a novel laminar stream micro fluidic device with multiple thresholds. So that, sperms with higher mobility will spend least among of time in crossing the stream lines, and be collected in one duct. On the other hand, sperms with lower mobility or even the debris will end up in the different collecting ducts.

O. Dössel and W.C. Schlegel (Eds.): WC 2009, IFMBE Proceedings 25/VIII, pp. 332–335, 2009.
www.springerlink.com

II. Materials and Methods

The fabrication processes started with the formation of a master mold by using SU-8 photoresist on silicon wafer for 50μm deep (Fig. 1). The compartment for the definition of reservoirs was then miller-machined on acrylic substrate. PDMS was first molded in the acrylic compartment, and then been cut into desired length. Afterwards, PDMS reservoir mold and SU-8 micro channel mold were then assembled and connected after O_2 plasma treatment. Finally, PDMS device was fabricated by molding on the assembled master mold coated with Teflon, then cut off from the reservoirs to open the channel at lateral and bonded on glass substrate after O_2 plasma treatment. The dimensions of all the reservoirs are 6000 μm length and 2100 μm width. The Physical dimensions for the inlets and outlet reservoirs are 3mm and 2mm height, respectively. Furthermore, in order to become more hydrophilic and be able to prevent the molecular nonspecific absorption problem, these channels and reservoirs are to be coated with 1% Bovine Serum Albumin (BSA) solution before the experiment.

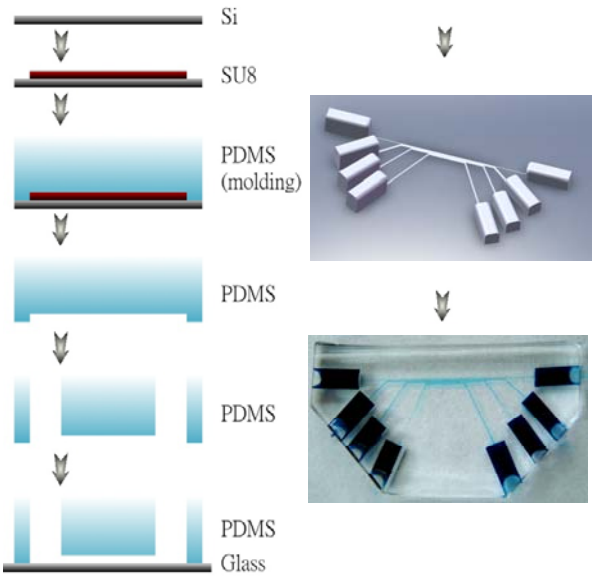


Fig. 1 The schematic of major fabrication processes.

In current design four pairs of parallel chambers in this device were used (See Fig. 2 for details). Since, the inlet reservoir is higher than the outlet ones, driven by gravity and surface tension, the test fluid would flow from the inlet (left) to outlet (right) [4]. Also, with the assumption that sperms with higher mobility are potentially being able to cross the stream lines in shorter period of time, the sorting process begins with the loading of the sample into the inlet reservoir, meanwhile with the medium been loaded into three other inlet reservoirs at the same time. Therefore, sperms with various mobility levels are to be collected from far left outlet with major popular with normal motility, to weaker motility, in the following two outlets to the right and mostly nonmotile on the far right outlet.

To assess the sorting function quantitatively, video recordings will be made at the 4 outlet reservoirs. From right to left, with outlet-e representing outlet at the far right hand side of outlet port, outlet-f representing outlet at the middle right, outlet-g representing outlet at the middle left, and outlet-h representing the one at the far left hand side of the outlet port.

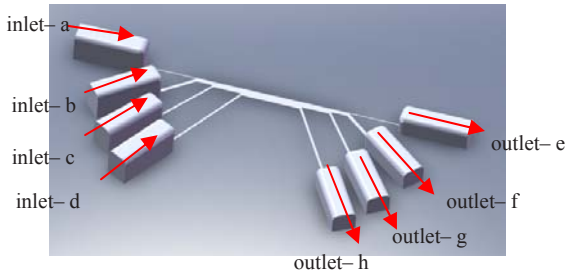


Fig. 2 Top view of the fabricated mold and flow device.

To test whether the BSA coating is complete or not, we injected the Bovine serum albumin conjugated to fluorescein isothiocyanate (BSA-FITC) into the channel. As shown in Fig. 3, the inner surface of the device channel had been coated uniformly, as is presented by green fluorescence with BSABSA-FITC staining. Therefore, in turn proves that the channel is hydrophilic and is ready for subsequent experiment.

Moreover, to differentiate live sperm from the dead ones, we used Propidium Iodide (PI) to stain the nucleus of the dead and damaged sperm (which will be presented as red fluorescence). And with Hoechst 33258 to cross the complete cell membrane and stained the DNA in living sperm [5]. Fresh boar semen from Animal Technology Institute (ATIT) of Taiwan was used throughout the experiment. Video recording were taken soon as the original sample was injected into one inlet, and the diluted version of the same semen to three other inlet reservoirs.

Meanwhile, at outlet-e, we observed the dead sperm had been dominate from clear red stains and live sperm are not as active as is corresponded with more diffused blue stains. In order to confirm the real sorting situation, we counted the amount of sperm in collected sample by flow cytometry and tried to establish the statistic model. Though the flow cytometry, we

could detect the sperm fluorescent distribution and count the size of sperm population, as is shown in figure 5. Nevertheless, *t*-test with 95% confidence level also shown significant difference in live/dead sperm ratio

III. Results and Discussion

From the initial video recording, it is observed that the input test flow is composed of motile sperms, non-motile sperms, as well as debris. However, at the last port side to the right, live sperms were mostly being sorted out and moved away from the stream lines, with all other non-motile ones and debris limited to the exit at the upper streamline.

When eye-ball counting with a five-point tentative motility scale, with 0 representing sperm at the non-motile status and 5 for most motile ones, the most motile sperms were being sorted out at outlet-*h* on the far left hand side, where the highest threshold occurred. As is showed in Fig.4, most of the catch is live and over which 70% is over scale 4, but with far less head counts than rest of the three outlets. Meanwhile, the ratio of non motile sperms and debris is relatively high at the outlet-e, because many motile sperms are collected on the way through outlet-g and outlet-*f*.

In addition, from Hoechst 33258 staining results, it is confirmed that the most motile and healthy sperm (Fig. 5(a)) is indeed would leave the laminar stream and being sorted out at outlet-*h*, with least dead sperm or debris (Fig. 5(b)). Meanwhile, at outlet-*f*, we observed the dead sperm had been dominate from clear red stains (Fig. 5(c)) and live sperm are not as active as is corresponded with more diffused blue stains (Fig. 5(d)).

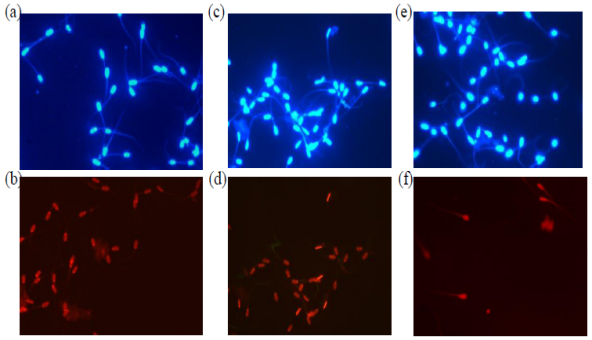


Fig. 4 Fluorescence images of live sperm in blue, and dead sperm debris with in red from (a) inlet-a with Hoechst 33258 staining; from (b) inlet-b with Propidium Iodide staining; from (c) outlet-e with Hoechst 33258 staining; from (d) outlet-e with Propidium Iodide staining; from (e) outlet-h with Hoechst 33258 staining; from (f) outlet-h with Propidium Iodide staining.

Subsequently, the vitality counts of sperm passed though micro fluidic device were evaluated in use of fluorescence microscope as well as flow cytometry. The *t*-test result showed that the counts of dead and live fluorescent-labeled sperms under fluorescence microscope are highly correlated with 95% confidence level. When comparing the quantitative results from flow cytometry with the automatic image system (see figure 6). It showed that the live/dead sperm ratio in outlet-*h* was larger than original input sperm sample and three other outlets. In addition, the similar result had been found in both methods.

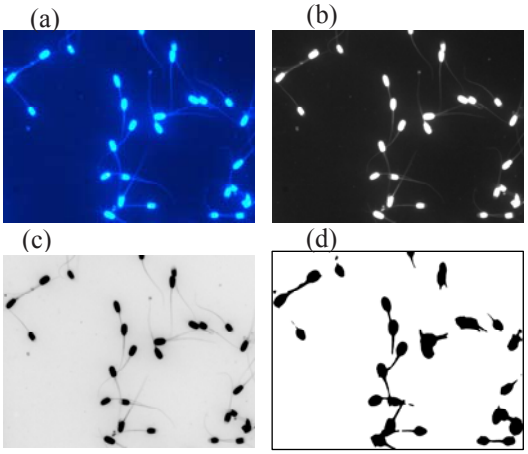


Fig. 5 Fluorescent sperm image processed from original in (a) to black/white in (b) for target identification, and to (c) for gray levels adjustment, and final down graded to (d) for fast target tracking.

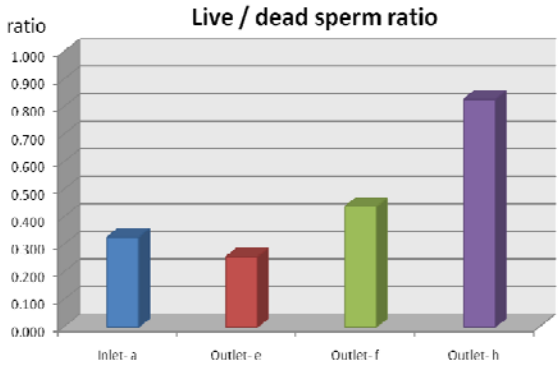


Fig. 6 Percentage distribution of live / dead sperm ratio under 4 different threshold levels under a five-points tentative mobility scale.

IV. Conclusions

In this study a modified laminar-stream-based micro fluidic system has been proposed. This device is designed to make possible the separation of sperm into multiple dynamic ranges. More importantly, is to use fluorescence marker for accurate target sperm identification. From the combined result among flow cytometry, fluorescent stain, and the statistic model test, it is concluded that live sperms were able to cross the laminar stream created by the device and reach the sorting chamber with corresponding range from non-motile sperms to debris, as well as from living to dead ones. Therefore, the proposed method is cost effective and is possible to serve as a protocol for rapid sperm quantitative assessment.

Acknowledgment

This experiment was made possible by grant support from National Science Council of Taiwan (97-2320-B-038-003-MY3), as well as Shin Kong Wu Ho-Su Memorial Hospital of Taiwan (SKH-TMU-98-14).

References

1. S. S. Howards, "Treatment of male infertility," N Engl J Med, vol. 332, pp. 312-7, Feb 2 1995.
2. R. R. Henkel and W.-B. Schill, "Sperm preparation for ART," Reproductive Biology and Endocrinology, vol. 1, 2003.
3. B. Cho, T. Schuster, X. Zhu, D. Chang, G. D. Smith, and S. Takayama, "A microfluidic device for separating motile sperm from nonmotile sperm via inter-streamline crossings," 2nd Annual International IEEE-EMBS Special Topic Conference on Microtechnologies in Medicine & Biology, pp. 156-159, 2002.
4. B. S. Cho, T. G. Schuster, X. Zhu, D. Chang, G. D. Smith, and S. Takayama, "Passively driven integrated microfluidic system for separation of motile sperm," Analytical Chemistry, vol. 75, No. 7, pp. 1671-1675, Web Release Date: February 22, 2003.
5. T.L. Wu, D. J. Yao, F.G. Tseng, L.C. Pan, “Laminar Stream Defined Passive Fluidic Device for Motile Sperm Separation”, IEEE 1st Annual International Conference Nano/Molecular Medicine Engineering (IEEE Nanomed), 2007.
6. Garner D.L. , Johnson LA. , “Viability assessment of mammalian sperm using SYBR-14 and propidium iodide” , Biol Reprod 1995;53:276-84.
7. B. S. Cho, T. G. Schuster, X. Zhu, D. Chang, G. D. Smith, and S. Takayama, "Passively driven integrated microfluidic system for separation of motile sperm," *Analytical Chemistry,* vol. Vol. 75, No. 7, pp. 1671-1675, 2003.

Corresponding author:

Author: Dr. Yieh-Loong Tsai
Institute: Shin Kong Wu Ho-Su Memorial Hospital of Taiwan, Fu Jen Catholic University of Taiwan
Street: No. 95, Wen Chang Road, Shih Lin District
City: Taipei
Country: Taiwan
Email: M002044@ms.skh.org.tw

Interfacing metallic ohmic contacts in biocompatible ceramic substrates with diamond surfaces for biosensing applications

M.A. Neto[1], E.L. Silva[1], A.J.S. Fernandes[2], F.J. Oliveira[1], R.F. Silva[1]

[1] University of Aveiro/Dept. of Ceramics & Glass Engineering, CICECO, Aveiro, Portugal
[2] University of Aveiro/Dept. of Physics, I3N, Aveiro, Portugal

Abstract— **The development of biosensors for in vivo applications requires the deposition of metallic contacts on biofunctionalized, biocompatible surfaces. For improved performance the metallic contacts should not interfere with the biosensing zone of the sensors. Owing to their biological compatibility with human tissues and fluids, diamond, titanium and silicon nitride ceramics (Si_3N_4) are potential candidates to be incorporated in implantable biosensors. The easy formation of titanium carbide under carbon saturated atmospheres, make titanium the right choice for diamond nucleation and growth. The same applies to the well studied Si_3N_4 ceramics used as substrates for diamond growth. The fabrication of biocompatible ceramic substrates with incorporated titanium contacts and chemically vapour deposited low resistivity boron doped diamond surfaces is the aim of the present work.**

In this work, Ti contacts were diffusion bonded to a Si_3N_4 ceramic substrate forming electrical contacts through the thickness of the insulating substrate. The hot filament chemical vapor deposition (HFCVD) technique was then used to produce well adherent polycrystalline diamond coatings on those ceramic-metal substrates. Raman scattering evidenced different carbon content sp3/sp2 ratios depending of the crystalline nature of the coatings. The 1332 cm^{-1} raman line exhibits small shifts indicating low residual stresses at the diamond/substrate interface enven near the ceramic-metal contacts. Four-point probe measurements showed linear I-V responses of these contacts under reverse and forward bias. Electrical resistivity as low as 0.02 Ω.cm was achieved. This is characteristic of an ohmic behavior suggesting that this new approach has potential for use with ac signals such is the case of implantable biodevices for real time monitoring.

Keywords— **Biosensors, CVD diamond, titanium, biocompatible, silicon nitride ceramic**

I. Introduction

Implantable biosensors, requires the development of biocompatible/biosensing electrically conductive surfaces. The biological activity on the sensor is monitored though its conversion into an electrical signal. Usually, adherent ohmic contacts are fabricated on these surfaces to collect the signal but they must not interact with the biosensitive surface and with the surrounding biological environment.

Synthetic CVD diamond surfaces have an enormous potential in this field due to their extreme chemical inertness and low electrical resistivity when doped with boron. Moreover, these surfaces can be easily functionalized to achieve specific immobilization and recognition of several types of biomolecules, such as proteins and enzymes [1, 2]. However, the usual method of contact fabrication uses noble metals (Au, Ag, Pt) deposited on the sensitive surface [3]. This could hamper signal acquisition. Another major problem facing the effective application of these surfaces is their need for a suitable substrate material that will give the desirable structural strength to the biosensor. Additionally, this material should not only stimulate diamond growth but must also be non toxic with minimum immune responses. In this context, the current work presents the fabrication of a new type of ohmic contacts in biocompatible/bioinert silicon nitride (Si_3N_4) ceramic substrates [4, 5]. Recent studies have shown the excellent affinity of these ceramics for diamond nucleation and growth [6, 7]

Schottky and ohmic contacts can be obtained at a metal-semiconductor junction. However, the former has a rectifier behavior, conducting electricity in one way, whereas the later can conduct under forward and reverse bias. In this sense, ohmic contacts are preferable in most applications that require ac electrical signals.

II. Materials and methods

Silicon nitride (Si_3N_4) ceramic discs (∅16 mm) were prepared by pressureless sintering [7] where samples are placed in a controlled nitrogen atmosphere furnace at 1750ºC for during 2 h. Four 1.6 mm diameter holes were then drilled in the ceramic discs and filled with Ti rods. The samples were afterwards placed inside a vacuum furnace and heated to 1200 ºC for 1h.

Adequate cutting, grinding and polishing procedures enable the production of several 1 mm thick Si_3N_4-Ti samples. To accomplish proper diamond nucleation and growth on these materials, the ceramic-metal substrates were mechanically abraded with diamond powder prior to deposition. The samples were placed in a HFCVD reactor for 3 h at substrate temperatures of 800ºC and 700ºC, respectively for

O. Dössel and W.C. Schlegel (Eds.): WC 2009, IFMBE Proceedings 25/VIII, pp. 336–338, 2009.
www.springerlink.com

microcrystalline (MCD) and nanocrystalline (NCD) diamond growth. Boron was added to the system through a bubbler in a concentrated solution of 10000 ppm of boron oxide in ethanol. The transport gas was argon that was kept at a constant flow rate of 1.5 ml/min. The CH_4/H_2 flow ratios used were 0.04 and 0.07, respectively for MCD and NCD depositions with a total flow of 100 ml/min.

SEM and optical microscopy helped exposing the crystalline nature of the diamond surfaces as well as the quality of the ceramic-metal interfaces. UV-Raman spectroscopy assisted on the carbon sp^2/sp^3 content characterization of the resulting films.

Electrical resistivity measurements of the diamond coatings and the I-V behavior of the metal-diamond junction were done using a home built four-point probe apparatus (Fig 1). The four equally spaced stainless steel needles were made to contact with the diamond surface and with the Ti contacts.

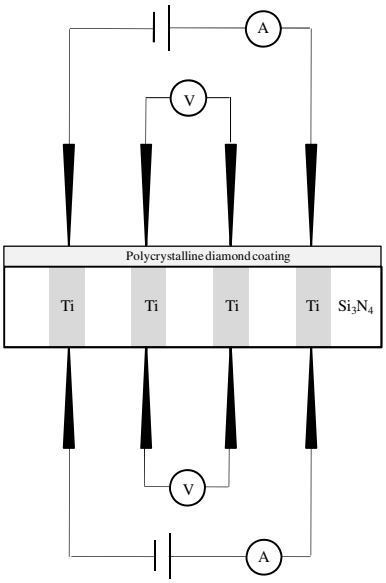


Figure 1 Shematic drawing of the four-point probe apparatus for I-V measurements on the ceramic-metal-diamond sample

For sheet resistances lower than 100 Ω this configuration enables measuring resistivity more accurately than the alternative two-point configuration.

III. Results and discussion

The optical micrograph of Fig 2 represents the top surface of the metal-ceramic interface before diamond coating. It is clear that the Ti rod diffusion bonded well to the ceramic material. No significant reaction of Ti with Si could be observed. The diffusion bounding technique for joining Ti with silicon nitride proved to be an effective way to attain stable and clean metal to ceramic contacts.

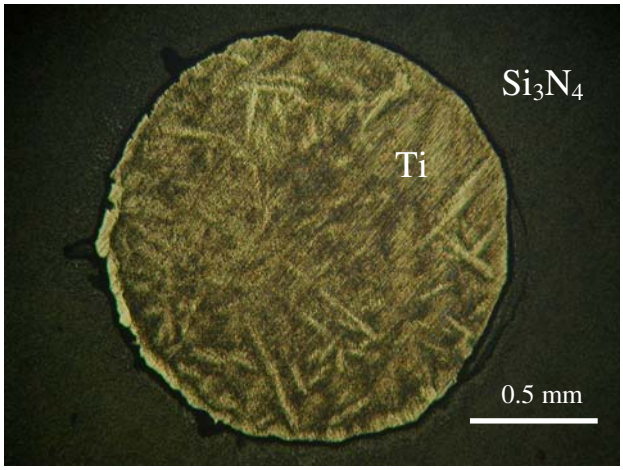


Figure 2 Titanium contact on the Si_3N_4 disc

Diamond growth on these samples was successfully realized. The diamond coatings were characterized by having thicknesses of 1 μm and 3 μm, for NCD and MCD samples, respectively. Their surface morphologies are illustrated in Fig 3.

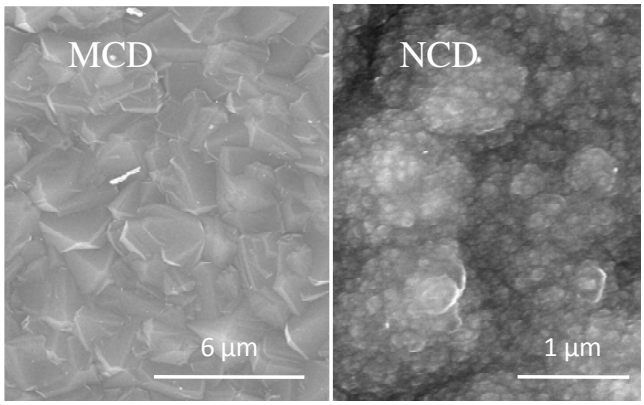


Figure 3 Top surface SEM micrographs of MCD and NCD coatings

These two types of diamond coatings are also structurally different, as observed from the Raman spectra (Fig 4). Whereas MCD spectrum is characterized by a sharp and dominant 1332 cm^{-1} diamond line, for the NCD Raman spectrum intergranular graphitic and non diamond phases dominate. The fact that both coatings have the diamond

Raman line very close to 1332 cm^{-1} is an indication of low residual stress at the diamond/substrate interface.

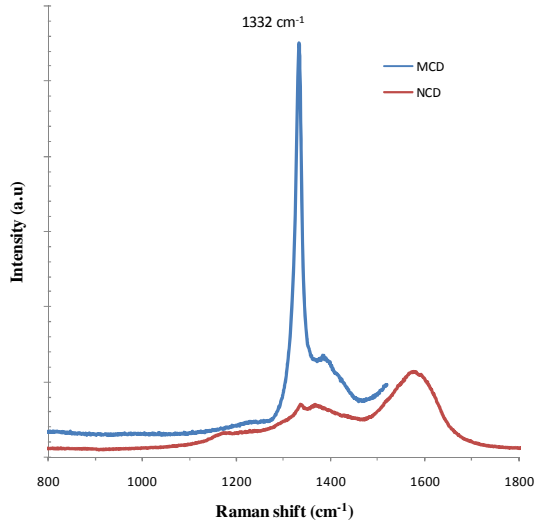


Figure 4 Raman spectra for both microcrystalline (MCD) and nanocrystalline (NCD) diamond coatings

The four-point probe measurements showed low resistivity diamond layers deposited on the ceramic-metal substrates. Typical values of 0.02 Ω.cm and 1.2 Ω.cm were respectively achieved for the MCD and NCD samples. They are comparable to results reported by others for heavily boron doped diamond grown on different substrates [8].

This same characterization of the Ti-diamond junction evidenced a characteristic ohmic performance for both groups of coatings under forward and reverse bias (Fig 5).

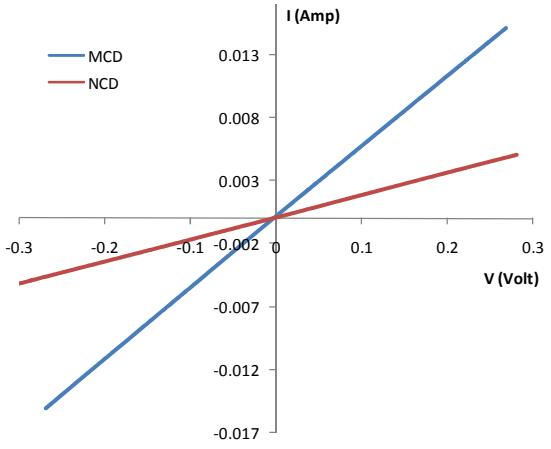


Figure 5 I-V performance of the Ti-diamond junction for MCD and NCD type diamond coatings

Even though the electrical resistivity of the boron doped coatings is already low, this value can be further reduced by heating the samples at temperatures where the bonded hydrogen can be removed. It is known that atomic hydrogen can passivate most donor and acceptor states in a variety of semiconductors [9]. In boron doped diamond, B-H pairs are easily formed in hydrogen rich atmospheres [10], therefore passivating the boron acceptor states.

IV. CONCLUSIONS

The results presented in this work demonstrate the feasibility to produce biocompatible ceramic-metal substrates that will serve as a starting point for future implantable devices such as biosensors. Titanium is considered a good choice for diffusion bonding to the silicon nitride ceramics. Also, it is a proper metal for nucleation and growth of diamond coatings and, at the same time, it creates ohmic contacts with deposited boron doped diamond. An electrically conductive diamond surface ready for biofunctionalization by adequate biomolecule immobilization and fully separated from the ohmic contacts was obtained.

ACKNOWLEDGMENT

M. A. Neto would like to acknowledge FCT the grant SFRH/BPD/45610/2008.

REFERENCES

1. Haertl A, Schmich E, Garrido J et al. (2004) Nat. Matters 3:736
2. Clare T, Nichols B, Abbott N et al. (2005) Langmuir 21:6344
3. Alexander M, Latto M, May P et al. (2003) Diamond and Related Materials 12:1460–1462
4. Hernández P, Taboada C, Leija L et al. (1998) Sensors and Actuators B 46:133–138
5. Kue R, Sohrabi A, Nagle D et al. (1999) Biomaterials 20:1195-1201
6. Amaral M, Oliveira F, Belmonte M et al. (2003) Surface Engineering 19:410-416
7. Belmonte M, Fernandes A, Costa F et al. (2003) Diamond and Related Materials 12:733–737
8. May P, Ludlow W, Hannaway M et al. (2008) Diamond and Related Materials 17:105:117
9. Pearton S (Ed.) Hydrogen in Compound Semiconductors, Trans. Tech. Publications, Mater. Sci. Forum (1994):148-149
10. Chevallier J, Theys B, Lusson A et al. (1998) Phys. Rev. B 58:7966

Author: Miguel Angelo da Costa Neto
Institute: University of Aveiro – Ceramics Engineering Dept.
Street: Campus Santiago
City: Aveiro
Country: Portugal
Email: mangelo@ua.pt

Chemical Modification of Surfaces for Biochemical and Medical Sensor Applications

V.C. Ayala[1], K. Moosmann[2], O. Prucker[2], J. Rühe[2], and L.M. Reindl[1]

[1] Laboratory for Electrical Instrumentation, IMTEK, University of Freiburg, Freiburg, Germany
[2] Chemistry and Physics of Interfaces, IMTEK, University of Freiburg, Freiburg, Germany

Abstract— **Portable microacoustic sensors capable of detection on the molecular level have recently become of increasing interest. Thin-film acoustic sensors based on GaN substrates are of particular merit because of their high chemical stability, high acoustic wave velocity and their ability to detect molecules in liquids. In this paper the use of sensitive layers for selective particle detection, as well as an investigation into the binding affinity of GaN, are presented. A sensitive layer for detection of diols, such as sugars or neurotransmitters, has been realized by attaching a polymer layer to the surface. A final cytotoxicity test has also been conducted on all of the presented substrates. In this work layers were successfully attached to a substrate and characterized, exhibiting long term chemical stability as well as good homogeneity and roughness making them adequate for future applications in microacoustic sensors. The cytotoxicity test yielded negative results, indicating that toxins are not liberated to the medium, thereby contaminating the sample. These types of sensors find their application in the quantification of samples and analysis of their chemical properties.**

Keywords— **Sensitive layers, microacoustic sensors, gallium nitride, photochemistry.**

I. INTRODUCTION

In recent years the detection of molecules with masses less than 10^{-7} kg has become desirable. An approach to make this possible is the application of microacoustic sensors. Microacoustic sensors are capable of detecting mass using the relationship between frequency change and mass loading on a surface. In 1959, G. Sauerbrey published the linear relationship between the frequency of a resonator and the mass attachment to the surface [1]. When an electric potential is applied to a piezoelectric material an acoustic wave is generated. With a periodic excitation and reflection of the acoustic wave, it is possible to produce a characteristic resonance frequency in a resonator. To detect specific molecules, a sensitive layer is attached to the piezoelectric material, where a selective binding is produced. When the molecules get attached to the layer, the mass loading causes a change in the characteristic resonance frequency of the sensor. With these types of sensors it is possible to quantify substances, as well as study their chemical properties. Microacoustic sensors have the advantage of high portability which allows point-of-care treatment and enables several applications, such as food technology, environmental and process monitoring, genetic engineering and biotechnology.

There are various types of microacoustic sensors, whereby those based on bulk acoustic waves (BAW) allow propagation of the wave through a piezoelectric material. In the case of resonators based on surface acoustic waves (SAW), the wave propagates on the surface. Acoustic waves can present two polarizations: longitudinal and transversal. For biological applications, transversal waves are needed in order to avoid a damping of the wave into the material. Longitudinal waves are normally used for gas sensors [2].

Different materials can be used as piezoelectric substrates. Quartz is the standard material used to stimulate BAWs, exhibiting a centre frequency below 100 MHz. SAW resonators have the advantage of working at higher frequencies, which enables the detection of smaller molecules. One of the materials used to excite SAWs is lithium tantalate ($LiTaO_3$). This material has the advantage of having a high dielectric permittivity which is comparable to that of water. This reduces the dielectric losses of the liquid into the substrate surface [3]. Another piezoelectric material that is currently being researched is zinc oxide (ZnO). It is commonly applied in thin-film bulk acoustic resonators (FBAR). The main advantage of FBARs is that they can have resonance frequencies as high as 10 GHz.

FBARs are also constructed with the material used in this work, gallium nitride (GaN). Depending on the crystal orientation of the layer´s grown, it is possible to generate transversal and longitudinal waves in GaN, which makes them suitable for the detection of liquids and gases respectively. GaN films (~2 μm) can be grown on sapphire (Al_2O_3) and on silicon (Si), where the substrate determines the crystal orientation of GaN. This was studied by growing GaN on different orientations of Al_2O_3 [4]. To generate transversal waves, a-plane GaN is grown on r-plane Al_2O_3. For longitudinal waves, c-plane GaN is grown on c- or a-plane Al_2O_3 and also on Si.

Depending on the type of resonator, sensitive layers are placed in corresponding locations. In the case of SAW resonators, such as a delay line design, they are placed between two interdigital transducers (IDT) (see bottom half of

O. Dössel and W.C. Schlegel (Eds.): WC 2009, IFMBE Proceedings 25/VIII, pp. 339–342, 2009.
www.springerlink.com

Fig. 1) while for BAW resonators they are placed on top of the electrodes (see Fig. 1 upper half). To attach the sensitive layers, chemisorption is used as it has a longer stability compared to physisorption.

In this paper, the molecular binding affinity of GaN as well as the characterization of a boronic acid containing polymer is presented. With the mentioned polymer it is possible to detect diols, such as carbohydrates (glucose, fructose), neurotransmitters (adrenaline, dopamine), glycoproteins and nucleotides. The attachment of molecules to gold (Au) surfaces for the use in electrodes is also presented. Finally a study of the cytotoxicity of GaN is discussed.

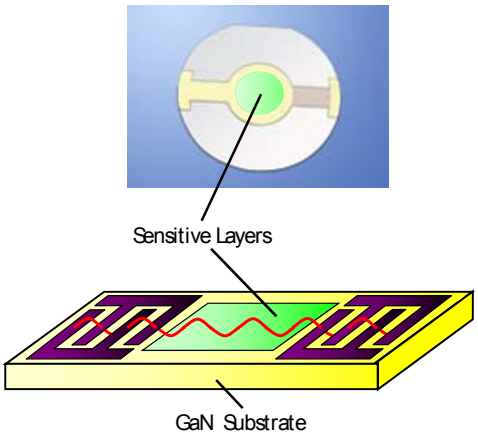


Fig. 1 Sensitive layers on BAW (upper) and SAW (lower) acoustic sensors

II. Materials and Methods

A. Layers on GaN

In this work, the binding affinity of GaN was investigated. For this purpose, Al_2O_3 substrates with a 2.5 µm thick a-plane GaN layer were used. The surface of GaN was first activated with piranha solution generating hydroxyl groups $(OH)^-$ [5]. Benzophenone silane (BPS) was then attached to these groups, allowing further binding of polymers by exposure to UV-light. In this case hepta-decafluorodecyl acrylate (fluoropolymer) was the polymer used [6]. After binding BPS to the surface, fluoropolymer was spin-coated (B.L.E. Delta 10). Some samples were illuminated (60 min, λ=365 nm), while the controls were not. Nonattached polymer was removed by washing. The characterization of the layer was carried out using X-ray photoelectron spectroscopy (XPS, Physical Electronics 5600 ci).

After the chemical attachment verification, experiments with a diol capturing polymer were carried out. In this case the surface was hydroxylated and BPS was attached. Next, *N,N*-dimethylacrylamide, 4-vinylphenylboronic acid and 4-methacryloyloxy benzophenone P(DMAA-*co*-VPBA-*co*-MABP) was spin-coated (60 mg/ml, 3000 rpm) on a-plane GaN/Al_2O_3, c-plane GaN/Si (2 µm film thickness) and Si substrates. The polymer was then photochemically functionalized by exposing it to UV-light for 60 min. Nonattached polymer was removed by washing. After the polymer attachment a characterization of the polymer was conducted by measuring the layer thickness and the polymer roughness. The layers were characterized with atomic force microscopy (AFM, Nanoscope III, Digital Instruments) in tapping mode and XPS.

B. Layers on gold

In the case of BAW resonators, it is possible to grow the sensitive layers on Au. To functionalize the Au surface, benzophenone disulfide (BPdiS) dissolved in toluene was used. After the BPdiS attachment, fluoropolymer was attached. Nonattached polymer was removed by washing. XPS analysis was carried out to characterize the layer.

C. Cytotoxicity test to GaN

In order to corroborate the cytotoxicity of the GaN substrates, a lactate dehydrogenase (LDH) assay was carried out. For this test, mouse fibroblast cells L929 were used on samples of GaN/Al_2O_3, GaN/Si, Al_2O_3 and Si. The samples were incubated 24 hrs in cell culture medium, after which the medium was extracted and added to the L929 cells and allowed to incubate for 48 hrs. The results were obtained by measuring the concentration of LDH enzyme, indicating the cell death and cell lysis.

III. Discussion and Results

The GaN surface hydroxylation was verified with contact angle measurements against water. Before hydroxylation, the GaN surface is hydrophobic and after the immersion in piranha solution it becomes hydrophilic indicating the $(OH)^-$ attachment.

Benzophenone has been chosen as the desired photolinker due to its greater thermal stability, weak sensitivity to ambient light, chemical inertness in the absence of light and long term chemical stability.

A fluoropolymer was chosen due to its facilitation of detection with XPS analysis. Fig. 2 and Fig. 3 show the XPS analysis of the GaN activated surfaces. The samples that were illuminated after the polymer deposition show a stronger F1s peak (Fig. 2) as compared to those of the reference samples (Fig. 3). This fact becomes much clearer if the F1s peaks are compared to signals that originate from the

substrate alone e.g. the N1s at ~400 eV. In this way, very little adsorption is observed in the reference samples. In the illuminated samples, the F1s peak is larger, corroborating an appropriate attachment to the surface.

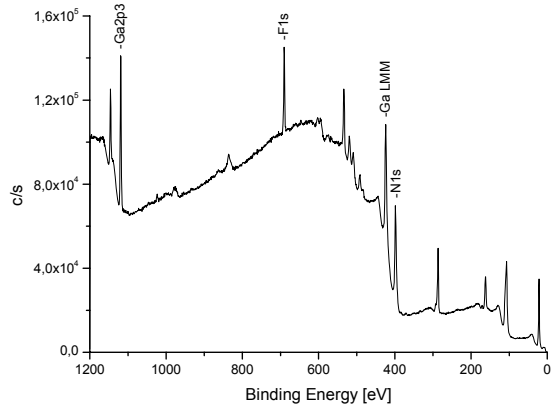


Fig. 2 XPS analysis of GaN substrate deposited with a fluoropolymer after illumination

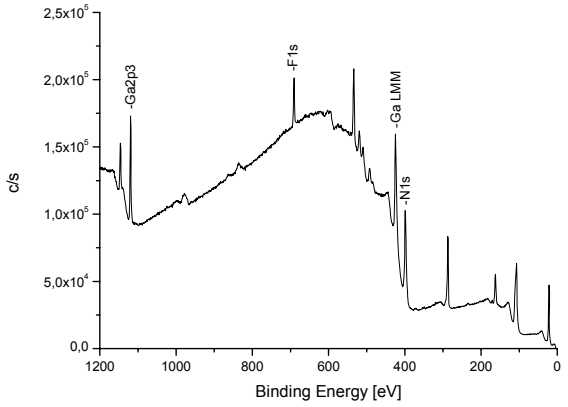


Fig. 3 XPS analysis of a GaN substrate reference sample deposited with fluoropolymer (not illuminated)

The characterization of the diol capturing polymer was carried out with AFM and ellipsometry. The AFM results showed a polymer roughness of 5 nm in a 50 µm scan size. This polymer layer also exhibited a long term chemical stability, i.e. the coating did not deteriorate after 3 weeks.

This polymer was spin-coated at different rotation speed and different concentration. A concentration of 60 mg/ml at 3000 rpm was chosen because it showed favorable homogeneity on the polymer film. The polymer thickness showed a dependence on the concentration and rotation speed. The thickness was measured with ellipsometry as well as with AFM, and developed a 125±3 nm thick layer at 3000 rpm.

The polymer attachment is achieved by exposure to UV-light. The advantage of this photochemical functionalization is that by use of a photomask it is possible to area selectively activate the desired locations.

The diol attachment to the polymer was previously studied. A 500 nm thick polymer layer was deposited on Si. Dopamine was bonded to the polymer adding 4 nm to the layer thickness. The roughness and homogeneity achieved make the diol capturing polymer adequate for future application in microacoustic devices.

The tests carried out with BPdiS on Au layers showed an adequate attachment to the surface.

For the cytotoxicity tests, a positive and a negative control were used. The positive control consisted of PVC strips with organo-zinc and the negative control of Thermanox plastic coverslips. In Fig. 4 the results of the test are presented. It can be observed that the cell death of the tested materials is comparable to the negative control. A negative result is also shown for GaN substrates, indicating that there was no release of toxins from the medium that could contaminate the sample.

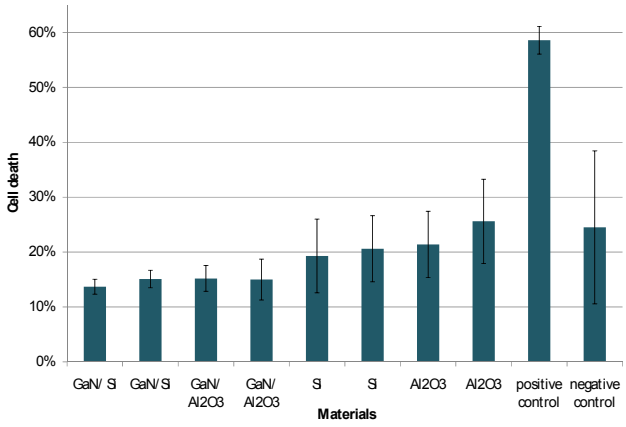


Fig. 4 Results of cytotoxicity test on various substrates

IV. Conclusions

In this work the surface activation of GaN and Au was studied. Chemical adhesion of molecules to a GaN surface was successfully carried out using a fluoropolymer and successively activated to Au surfaces.

A sensitive polymer layer for diol detection using a boronic acid-based polymer was successfully developed and attached to a GaN surface. Its characterization showed

a long term chemical stability as well as high surface homogeneity.

The cytotoxicity of GaN was also investigated and proved to release no toxins into the surrounding medium.

It can be conclude that the application of the presented sensitive layer on GaN substrates is promising for future applications in microacoustic devices.

ACKNOWLEDGMENT

The author would like to thank M. Welsche and D. Eisele for their insightful discussions as well as N. Schatz for her technical assistance.

REFERENCES

1. Sauerbrey G (1959) Verwendung von Schwingquarzen zur Wägung dünner Schichten und zur Mikrowägung. Zeit für Phys 155:206–222
2. Länge K, Rapp B, Rapp M (2008) Surface acoustic wave biosensors: a review. Anal Bioanal Chem pp 1509–1519 DOI 10.1007/s0021600819115
3. Dickert F, Tortschanoff M, Bulst W, Fischerauer G (1999) Molecularly Imprinted Sensor layers for the Detection of Polycyclic Aromatic Hydrocarbons in Water. Anal Chem 71:4559–4563
4. Kim Y, Lim G, Choi K, Chung S, Kim H, Park H, Park HS (2002) SAW Characteristics of GaN Epitaxial Films Deposited on Different Plane Sapphire Substrates using MOCVD. IEEE Ultrasonics Symp pp 427–430
5. Baur B, Steinhoff G, Hernando J, Purrucker O, Tanaka M, Nickel B, Stutzmann M, Eickhoff M (2005) Chemical functionalization of GaN and AlN surfaces. Appl Phys Lett 87 263901:1–3 DOI 10.1063/1.2150280
6. Jeyaprakash J, Samuel S, Ruehe J (2004) A Facile Photochemical Surface Modification Technique for the Generation of Microstructured Fluorinated Surfaces. Langmuir 20:10080–10085

Minimizing Stress Exposure to Cells Using Novel Microfluidic Cell Capture Devices

G. Kijanka‡, I.K. Dimov‡, R. Burger, and J. Ducrée

Biomedical Diagnostics Institute, National Centre for Sensor Research, Dublin City University, Glasnevin, Dublin 9, Ireland
‡These authors contributed equally

Abstract— **Microfluidics offers a unique environment to capture cells and assess cell function. Although many devices have been developed in recent years, maintaining cell integrity remains problematic. In this study, we develop two different microfluidic devices which capture cells with high efficiency, while exposing cells to minimal stress. Both systems are based on a sedimentation principle. The first device utilizes gravity to capture cells within a trench-like structure, while the second device sediments cells in an artificial gravity field induced by centrifugal forces. These novel microfluidic devices can be applied directly to the biomedical field as they enable cell manipulation under relatively stress free conditions.**

Keywords— **Cell Capture, Sedimentation, Lab-in-a-Trench, Centrifugal Microfluidics.**

I. INTRODUCTION

Microfluidic devices offer a unique method to investigate the behavior of individual cells. Subsets of cell populations involved in pathological processes can be monitored and a personalized medical approach can be tailored individually to the patient's needs. Although there are many different microfluidic cell trapping techniques currently available [1], they frequently encounter problems such as cell activation prior to investigation and low capture efficiencies.

In this current study, we describe two methods of cell capture based on a sedimentation approach which expose cells to minimal stress and captures cell with exceptionally high efficiencies. The first method captures cells within a deep trench based on gravitational sedimentation, whereas the second method uses centrifugally driven sedimentation to capture cells within retention structures under stagnant flow conditions.

The unique design of these microfluidic devices enables processing of cells within the chip. Distinct subsets of cell populations can be monitored through real time imaging and techniques such as immunofluorescence and PCR can be used to assess cell function. Both of these microfluidic chips encompass key features which are required for maintaining the physiological integrity of cells.

II. MATERIALS AND METHODS

A. Device fabrication

The microfluidic devices were fabricated using standard SU-8 lithography and subsequent casting into PDMS. Briefly, moulds were created using negative photoresist, SU8-3050 (Microchem U.S.A.) and SU8-2150 (Microchem U.S.A.). Photoresist was spun onto silicon wafers using a spinner (P6700 Specialty Coating Systems, Inc., U.S.A.). The wafers were then soft baked at 95 ºC for 15 min and UV-exposed at 9.5 mW/cm^2 using a Karl-Süss KSM MJB-55W mask aligner. The wafers were subsequently baked for 6 min at 65 ºC and 12 min at 95 ºC, allowed to cool down to room temperature, and developed in Microposit EC Solvent developer (Chestech Ltd., UK). The SU-8 moulds were then coated with Perfluorosilane and spin coated with degassed PDMS prepolymer (Sylgard 184, Dow Corning). Cured PDMS was peeled off the mould and the devices were assembled using O_2 plasma treatment.

B. Cell culture

CO_2 independent medium (Gibco) containing 10% heat inactivated FBS and 1% Penicillin-Streptomycin solution (Invitrogen) was used for routine maintenance of HeLa cell line. HeLa cells were cultivated in a cell incubator at 37 ºC and a CO_2 level of 5%. For cell capture experiments approximately 200 cells / μL were loaded onto the chip. Cell numbers were quantified using a hemocytometer. All on-chip cell capture experiments were performed at 37 ºC.

C. Flow control

Gravitational Sedimentation: A pipette tip was inserted into the inlet port of a primed microfluidic device. An open fluid column within the pipette tip maintains the fluid flow within the microfluidic chip. The flow velocity is determined by the height of the open fluid column. Injected HeLa cells were trapped by sedimentation within trench structures.

*Centrifugal Sedimentation: A r*otation frequency of 20 Hz was used to establish an artificial gravity field within the

O. Dössel and W.C. Schlegel (Eds.): WC 2009, IFMBE Proceedings 25/VIII, pp. 343–346, 2009.
www.springerlink.com

centrifugal microfluidic disc to sediment silica beads and trap these in retention structures under stagnant flow conditions.

D. Microscopy & Imaging

The microfluidic device was mounted on a thermally controlled inverted fluorescent microscope (Olympus IX81) fitted with an incubation chamber (Solent Scientific). All bright field acquisitions were obtained with a CCD sensor (Hamamatsu C4742-80-12AG) using 10x magnification. When scanning multiple cell retention structures, a programmed motorized stage was used to position and focus the objective over each structure. Image analysis and motorized stage programming was done using the software Cell R (Olympus).

III. Results and Discussion

A. Cell capture in a microfluidic trench structure

The microfluidic structure consists of a chamber with a trench (220µm deep, 100 µm x 400 µm wide). The key characteristic of the trench structure is the ability to capture cells by sedimentation (Fig. 1A). Cells introduced into the microfluidic device flow over the trench structure and sediment into the bottom, where they are effectively captured. In experiments with 1.5-µm silica beads and input flow speeds of 20 μm / sec the capture efficiency was close to 100%. Experiments with HeLa cells also demonstrated similar results (Fig. 1B).

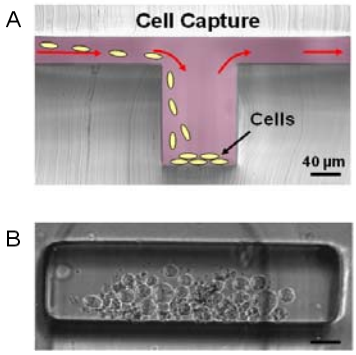


Fig. 1 Cell capture based on sedimentation of cells to the bottom of a trench structure (A). Photograph of HeLa cells trapped within a trench (from above) (B).

B. Flow velocity and shear stress

We simulated flow velocities within the microfluidic channel and trench structure based on a computational fluid dynamics approach [2] (Fig. 2A). The simulation revealed decreasing flow velocities with increasing depth as fluid flows over the trench. At the base of the trench structure, flow velocities were calculated to be three orders of magnitude lower then the flow velocity at the top of the trench (Fig. 2B). Cells entering the low flow velocity region are effectively retained at the base of the trench.

Fluid shear stresses exerted on cells tend to modify certain cell types [3] and might introduce bias to microfluidic bioassays. In a recent paper, Khabiry *et al* have characterized flow patterns in microfluidic grooves showing shear stress sheltering and weaker flows at the bottom of deep grooves [4]. Such shear-protected regions have a clear advantage over other microfluidic cell retention methods for biomedical applications. This also has a positive effect on microfluidic cell culture as the cell adherence to channel surfaces improves with decreasing shear stress [5].

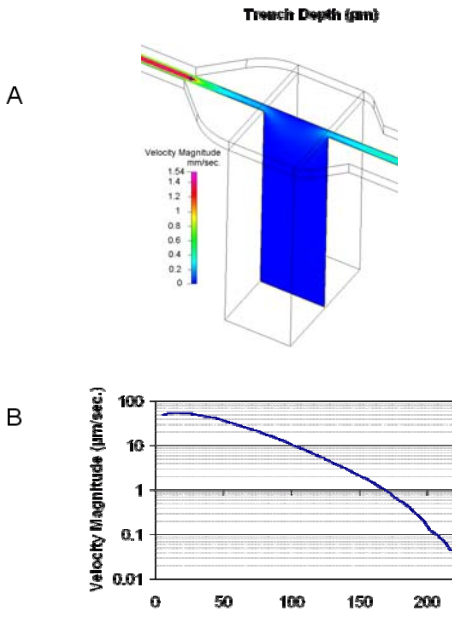


Fig. 2 Computational fluid dynamics (CFD) simulation of flow velocity within the microfluidic channel and trench (A). Cell capture is achieved with flow velocity approximately 3 orders of magnitude lower at the base of the trench than the flow sensed at the top of the trench (B).

C. *Centrifugal microfluidics for cell capture*

The centrifugal microfluidic platform combines the inherent features of microfluidic devices such as miniaturization, integration, automation and parallelization with the independence of an external displacement pump for flow generation [6]. Here, we incorporate V-shaped retention elements, which are widely used in pressure driven microfluidic systems [7], into centrifugal platform technology. As shown in Figure 3, pressure driven cell capture systems create dynamic flow lines within the liquid which influence the direction of flowing cells in and around the V-shaped structures, thus leading to low capture efficiencies of approximately 16-20%, only.

In contrast to the pressure driven microfluidic systems, our centrifugal microfluidic device sediments cells under stagnant flow conditions. Cells thus follow straight (radial) paths, with theoretical capture efficiencies of 100% (Fig. 4A). In practice, we performed experiments using 10-µm silica beads spun at a rotation frequency of 20 Hz and obtained capture efficiencies greater than 85% (Fig. 4B). Although there are no dynamic flow lines under stagnant flow conditions, additional effects such as the surplus of particles captured in one V-shaped retention element, Coriolis-effect or others, may cause deflection of the sedimenting particles, reducing the capture efficiency from the theoretical 100% to the experimental 85%.

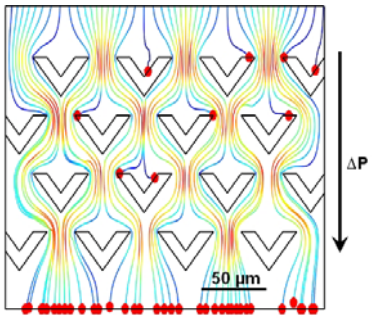


Fig. 3 Simulation of particle flow lines in a pressure driven cell retention structure. The arrow ΔP indicates the direction f the flow.

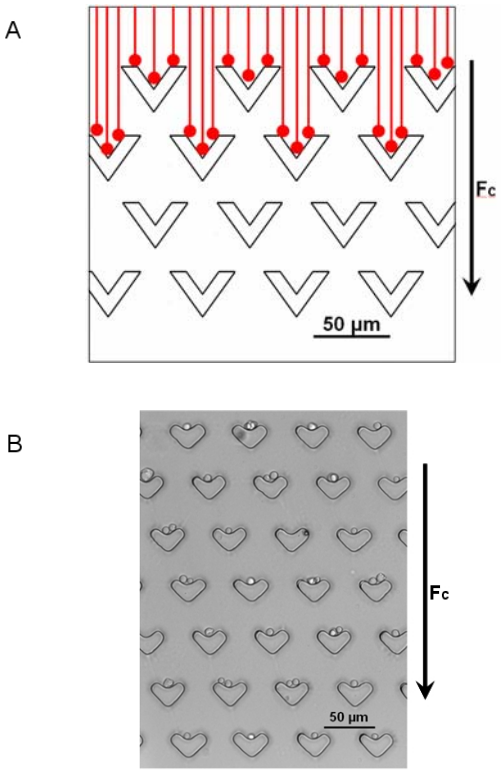


Fig. 4 Centrifugal driven systems can sediment particles at stopped flow and thus do not create flow lines and particles merely sediment due to their higher density with respect to the liquid (A). Photograph of a cell retention structure on a centrifugal chip capturing 10-µm silica beads (B). The arrow F_c indicates the direction f the centrifugal force.

IV. Conclusions

In this study, we demonstrate two novel approaches for cell capture in a microfluidic chip. In both of our microfluidic devices, high capture efficiencies are obtained and the pathological effects of shear stress are minimized. These microfluidic devices may be applied in the biomedical field where maintaining the physiological integrity of cells is essential.

ACKNOWLEDGMENT

This work was supported by the Science Foundation Ireland under Grant No. 05/CE3/B754.

REFERENCES

1. Johann R M (2006) Cell trapping in microfluidic chips. Anal Bioanal Chem 385: 408-412.
2. Chung T (2002) Computational Fluid Dynamics. Cambridge University Press.
3. Lawler K, Foran E, O'Sullivan G et al. (2006) Mobility and invasiveness of metastatic esophageal cancer are potentiated by shear stress in a ROCK- and Ras-dependent manner. Am J Physiol Cell Physiol 291: C668-677.
4. Khabiry M, Chung B G, Hancock M J et al. (2009) Cell Docking in Double Grooves in a Microfluidic Channel. Small. In Press.
5. Lu H, Gaudet S, Schmidt M A et al. (2004) A microfabricated device for subcellular organelle sorting. Anal Chem 76: 5705-5712.
6. Ducrée J, Haeberle S, Lutz S et al. (2007) The centrifugal microfluidic bio-disk platform. J. Micromech. Microeng. 17: 103-115.
7. Di Carlo D, Wu L Y, and Lee L P (2006) Dynamic single cell culture array. Lab Chip 6: 1445-1449.

Address of the corresponding author:

Author: Gregor Kijanka
Institute: Biomedical Diagnostics Institute, Dublin City University
City: Dublin
Country: Ireland
Email: gregor.kijanka@dcu.ie

Development of EGFR-Targeting Nanomedicine for Effectively and Noninvasively Treats Lung Cancer Patients by Aerosol Delivery

Ching-Li Tseng[1], Yueh-Hsiu Wu[2], Su-Wen Yu[1], Kai-Chiang Yang[2], and Feng-Huei Lin[1,2]

[1] National Health Research Institutes/ Division of Medical Engineering Research, Miaoli, Taiwan, ROC.
[2] National Taiwan University/ Institute of Biomedical Engineering, Taipei, Taiwan, ROC.

Abstract—**Lung cancer is a harmful form of cancer. The long-term survival rate of lung cancer patients treated by conventional modalities remains far from satisfactory. Encapsulated anticancer drugs in nanocarriers, can protect not only the integrity of drugs during transport but also the normal tissues from the toxicity.** To develop an effective drug delivery system for lung cancer therapy, gelatin nanoparticles (GPs) were modified with NeutrAvidin^{FITC}-biotinylated epidermal growth factor (bEGF) to form EGF receptor (EGFR)-seeking nanoparticles (GP-Av-bEGF). Cisplatin, **a key drug used in the chemotherapy with sever side effect,** was incorporated in the nanocarriers for active targeting to reduce toxicity. **Furthermore, these nanocarriers were given to mice via inhalation of** aerosol droplets which were generated by a nebulizer and delivered to mice model of lung cancer via aerosol. **To summarize,** the *in vivo* targeting ability of GP-Av-bEGF was examined by **fluorescence images obtained from live mice showed that these nanoparticles could target the cancerous lungs in a more specific manner** by aerosol delivery. And **gelatin nanoparticles loaded with cisplatin and decorated with EGF tumor-specific ligand (GP-Pt-bEGF) were also successfully developed. Their *in vitro* and *in vivo* targeting ability and anticancer effect were confirmed. This treatment showed that GP–Pt–bEGF had stronger antitumor activity and was less toxic compared with other cisplatin formulas. Furthermore, these formulations were given to mice with lung cancer via aerosol delivery and showed that inhaled GP–Pt–bEGF could target EGFR-overexpressing cells to achieve high cisplatin dosage in cancerous lungs. The aerosol delivery of nanocarriers was demonstrated here. Simple aerosol delivery of targeted drug carriers may prove useful for the clinical treatment of lung cancer patients to eliminate patient complaints associated with the frequent intravenous injection.**

Keywords—**gelatin nanoparticles, EGFR, tumor targeting, cisplatin, aerosol delivery**

Ⅰ. Introduction

Lung cancer is one of the most harmful forms of cancer. The long-term survival rate of lung cancer patients treated remains far from satisfactory. Systemic drug delivery is rarely successful because only a limited dosage of the chemotherapeutic drugs target lung tumor sites, even when administered at a high dose. Most chemotherapeutic drugs act on normal cells, inhibiting their growth; this makes the patient extremely weak and can even result in death. Cisplatin (*cis*-diammine-dichloroplatinum (II); CDDP) is accepted as a standard first-line treatment for advanced non-small cell lung carcinoma (NSCLC)[1]. Chemotherapy with cisplatin is associated with sever side effects, such as anemia, nausea, vomiting, neurotoxicity and nephrotoxicity[2]. Due to these side effects, alternative methods of administering toxic cisplatin are needed. Specific drug delivery systems (DDS) have been investigated. Sever polymer were developed as drug carriers, In this study, gelatin was selected as the raw material to prepare the drug carrier because of its biocompatibility and biodegradability[3]. There have been few published studies on the formulation of gelatin nanoparticles (GPs) with cisplatin. Another way to reduce the side effects of drugs is active targeting. A tumor-specific ligand can be employed for more specific recognition of and interaction with cancer cells, reducing the effect on normal cells. The overexpression of epidermal growth factor receptor (EGFR) on human tumors, especially on NSCLC, has been reported. In the present study, epidermal growth factor (EGF) was conjugated with the gelatin-cisplatin nanocomplex as a targeting vehicle for lung cancer treatment. The objective of the present work was to evaluate the anticancer efficiency and specific targeting ability of a cisplatin-gelatin nanomedicine with affinity for EGFR. We developed a gelatin nanoparticle (GP) complex with CDDP (GP-Pt) surface-modified with NeutrAvidin^{FITC}-biotinylated epidermal growth factor (bEGF), abbreviated as GP-Pt-bEGF, to target the tumor site and be taken up by EGFR-mediated endocytosis in tumor cells overexpressing EGFR.

Ⅱ. Materials and methods

Schematic diagram of different particles is showed in Fig.1. In brief, GPs were prepared as previous description by two step desolvation method. 5% (w/v) aqueous gelatin solution was heated to 50°C, and mixed with acetone. The resulting precipitate was collected and redissolved at 50°C in water. Acetone was then added to the redissolved gelatin solution at pH 2.5. The resulting nanoparticles were cross-linked by adding glutaraldehyde and stirring overnight. Finally, the acetone was removed and the fabricated GPs were purified and resuspended in deionized water. These

O. Dössel and W.C. Schlegel (Eds.): WC 2009, IFMBE Proceedings 25/VIII, pp. 347–350, 2009.
www.springerlink.com

particles were stored at 4°C for further applications. Thereafter, CDDP was dissolved in a GPs suspension to react at 37°C for 3 days, and then unbound CDDP was removed. The GPs with incorporated CDDP are named GP-Pt. The preparation of NeutrAvidin^{FITC}-biotinylated EGF modified nanocarriers were the same as previous study[4]. First, the GP-Pt suspension was reacted with 2-iminothiolane for 1 h at 37°C. The nanoparticles were washed 3 times by PBS and collected in Amicon Ultra-4 filter devices, the amino groups on the surface of GP-Pt were converted to thiol groups for ligand conjugation. In a separate reaction mixture, NeutrAvidin^{FITC} (1mg/ml) was dissolved in sodium phosphate buffer containing Sulfo-MBS for activation. The solution was mixed thoroughly and left to react at R.T. for 1 h. The activated NeutrAvidin^{FITC} was purified on a gel filtration column, and then mixed with the thiolated nanoparticles and reacted overnight at 4°C. The unbound NeutrAvidin^{FITC} derivative was separated by and the complex of NeutrAvidin^{FITC} with GP-Pt nanoparticles was prepared. After the surface modification of the NeutrAvidin^{FITC} on GP-Pt nanoparticles, biotinylated EGF (bEGF) was added to bind with the NeutrAvidin^{FITC} on the particle surface. The biotinylation of EGF was performed by biotinylation reagent (Sulfo-NHS-LC-biotin) prior to its conjugation with NeutrAvidin^{FITC}. The solution was thoroughly mixed and incubated for 30 min at R.T. The free bEGF was separated by size exclusion chromatography. The bEGF modified GP-Pt complex is abbreviated as GP-Pt- bEGF. The targeting efficiency of the developed GP-Av-bEGF *in vivo* was evaluated by an *in vivo* imaging system. The *in vivo* anticancer effect was evaluated by intratumoral injection in a mouse subcutaneous model. Aerosol delivery was adopted to allow inhaled chemotherapy for metastatic lung cancer. The mice were treated with one of the different cisplatin formulations once via aerosol delivery. SCID mice were used to induce pulmonary metastases by lung adenocarcinoma cells (A549) injection into tail vein. After that, mice were exposed to the aerosol. An ultrasonic nebulizer was used to generate aerosol particles. Different formulations of aqueous solution (CDDP, GP–Pt, or GP–Pt–bEGF) were used for inhalation. The control group was treated with H_2O. Cisplatin concentrations in the blood and lungs were measured with ICP-AES.

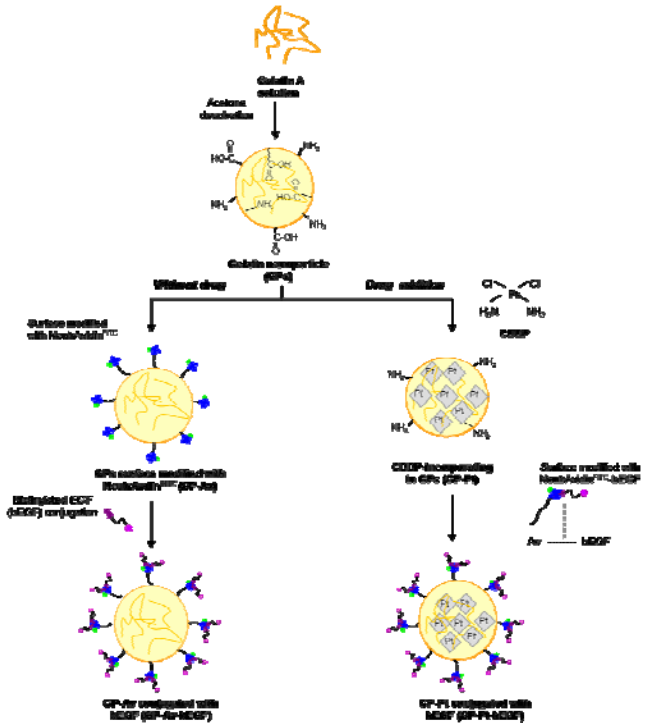


Fig. 1. Schematic diagram of different process of GPs with or without CDDP incorporation with Neutr^{Avid}inFITC-biotinylated EGF conjugation

III. Results

A. In vivo targeting via aerosol delivery

Fig. 2 shows the distribution of the nanoparticles in live mice 24 h latter following aerosol delivery. The distribution profile of the GP-Av-bEGF in organs following aerosol administration in the mice is shown in Fig. 3. The accumulation of fluorescent signals differed significantly between the normal and cancerous lungs at 24 h after inhalation. The relative percentage of GP-Av-bEGF fluorescent signals attained a maximum value of 368.3% ±15.67% in the cancerous lungs at the time point of 24 h, while the fluorescence intensity was only 103.87%±39% in the normal lungs. This indicating that the GP-Av-bEGF was specific to the tumor tissue.

B. In vivo anticancer activity and inhalation efficiency

The antitumor efficacy of variant CDDP formulas was evaluated in a subcutaneous cancer model. All drugs were administered twice in 1 week. Fig. 4(a) shows the growth curves of A549 tumors in SCID mice after intratumoral

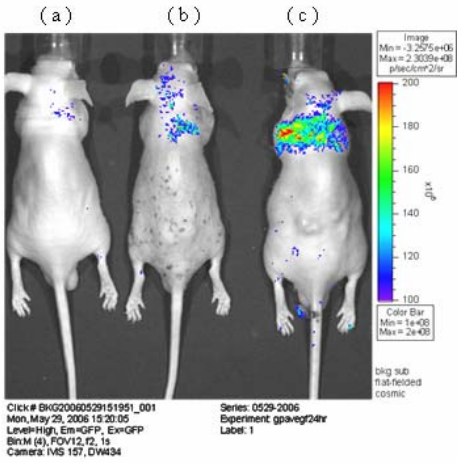


Fig. 2 The *in vivo* fluorescence images of tumor-induced mice following aerosol delivery 24h latter by treatment with different nanoparticles solution: PBS treated group (a), GP-Av-treated group (b), and GP-Av-bEGF conjugate-treated group (c). FITC green fluorescence spectra were obtained from live mice xenografted with the human lung adenocarcinoma cells (A549).

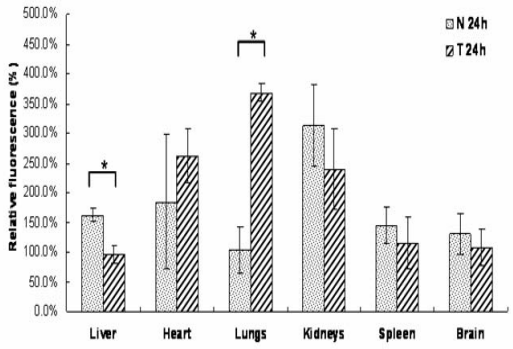


Fig. 3 Distribution of GP-Av-bEGF administered by inhalation to normal and tumor-bearing mice after 24 hr. The distribution to each organ is presented as a relative percentage of that in the normal mice that were not treated. *p < 0.05

administration of PBS, CDDP, GP-Pt or GP-Pt-bEGF. A significant antitumor effect of CDDP in mice treated with GP-Pt-bEGF was observed after 4 days and up to 17 days of treatment. By 17 days after injection, the average tumor volume in GP-Pt-bEGF was only 31.82±20.47 % of the initial tumor volume whereas the average tumor volume in PBS-treated mice grew rapidly and reached 201.92±49.01%. Notably, GP-Pt-bEGF nanoparticles showed greater anti-tumor efficacy than did CDDP or GP-Pt. GP-Pt showed delayed antitumor efficacy after 10 days of treatment. Changes in the body weight after injections are depicted in Fig. 4(b). No significant difference was observed between mice treated with GP-Pt, GP-Pt-bEGF or PBS. The body weight loss was tolerable. At the end of the study, mice receiving CDDP had weight lost of 26.59±7.99%. The decreases in body weight in the CDDP group may result from the toxicity of CDDP. From Fig. 5(a), the serum Pt assay result, free CDDP showed shorter blood retention time than GP-Pt or GP-Pt-bEGF. The free CDDP treated group had high serum Pt concentration in the initial half-hour (91.07±26.43 ppb), but it decreased quickly from 24 to 48h. The GP-Pt treated one showed highest Pt concentration in plasma in the initial half-hour. The GP-Pt-bEGF treated mice also represented a longer retention time and higher Pt concentration existence in the circulation system than free CDDP. After inhalation, GP-Pt and GP-Pt-bEGF showed a very long blood retention profile compared with free CDDP. The GP-Pt-bEGF treated group exhibited the highest concentrations of Pt in the lungs at 0.5 hr and 24 hr after inhalation of all the animals given variant form of CDDP (Fig. 5 (b)).

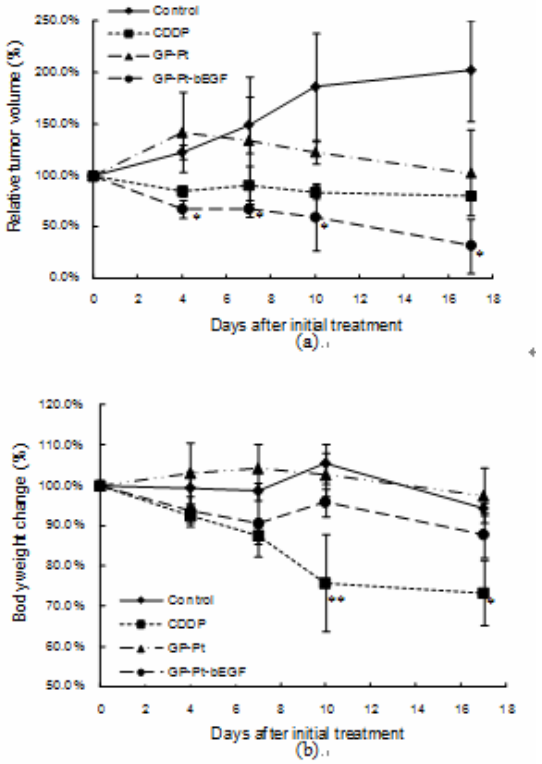


Fig. 4 (a) In *vivo* anti-tumor effects and (b) body weight change caused by different formulations in A549-bearing SCID mice (female, *n* =5) treated with PBS as control group (♦), CDDP (■), GP-Pt (▲) or GP-Pt-bEGF (●). Each drug was administered at the dose of 12 mg/kg on a CDDP basis. *p < 0.05, **p < 0.01.

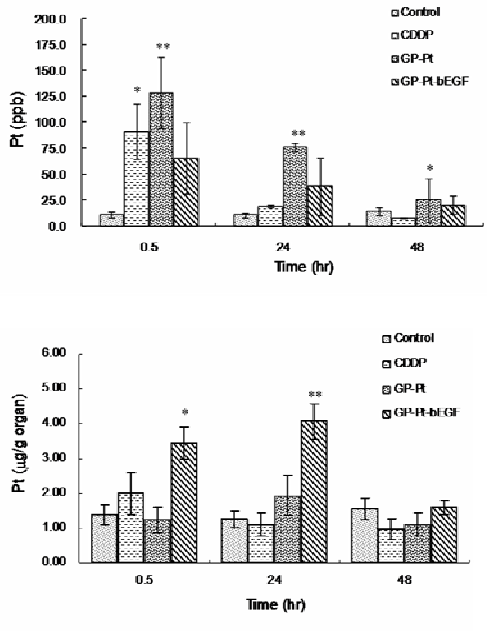


Fig. 5 Time profiles of Pt concentration in the plasma (a) and lungs (b) after a single inhalation of PBS (control) and various cisplatin formulations: CDDP, GP-Pt and GP-Pt-bEGF at an equivalent dose of 12mg /kg CDDP). *p < 0.05

Ⅳ. Discussion

From the results of Fig. 3 and 6, the particles and drug accumulation in cancerous lung were much higher at 24 hr rather than 0.5 h. According to this, we hypothesized that some fraction of the GP-Av-bEGF or GP-Pt-bEGF was not trapped by the epithelial cells immediately after inhalation but entered into blood circulation; once these particles approached the lung region again, they could be recognizes and taken up by cancer cells with EGFR-overexpression. This tendency was only observed in the lung cancer group while there was no difference in the normal mice. This observation reveals that the highly accumulation in the lungs of EGF-modified nanocarreirs should depend on EGF ligand guiding, not only the effect of local delivery via inhalation. From the serum content results (Fig. 6), CDDP was quickly removed from the circulation after inhalation, but CDDP-incorporated in carriers (GP-Pt and GP-Pt-bEGF) could still be found at a high serum level after 24 h; it showed a stable existence with a long blood retention profile. From Fig. 4, it suggests that GP-Pt-bEGF is a superior CDDP formulation compared to the free drug and non-ligand modified drug carrier (GP-Pt). A previous study has shown that activation of the EGFR could increase the sensitivity of cancer cells to CDDP and enhance cell apoptosis [5]. Base on this concept, the GP-Pt-bEGF is more toxicity then other formulas due to the EGF enhanced apoptosis. The antitumor efficacy in subcutaneous cancer model also proved GP–Pt–bEGF had stronger antitumor activity and was less toxic compared with other cisplatin formulas. The cisplatin dosage for inhalation and the optimal time course for treatment are being studied to further confirm the anti-cancer effect of aerosol chemotherapy in the lung cancer mouse model. The present study demonstrates that CDDP agents can be delivered with a high degree of specificity to a selected lung lobe via EGFR targeting. We believe that the application of targeting agent, GP-Pt-bEGF, by aerosol delivery may have better therapeutic effects in humans than in mice.

Ⅴ. Conclusions

A polymer–anticancer drug conjugate, gelatin nanoparticle (GPs), was developed as a carrier of CDDP to enhance its therapeutic effects and reduce its side effects. GP-Pt-bEGF with EGFR affinity produced Pt concentration in cells highly expressing EGFR. The *in vivo* anticancer experiment showed that GP-Pt-bEGF had stronger antitumor activity and was less toxic than free CDDP and GP-Pt in a subcutaneous model. Inhalation of drug aerosols is a modern pathway to combat lung diseases; these formulations were given to mice with lung cancer via aerosol delivery. This treatment showed that GP-Pt-bEGF could target the EGFR-overexpressing cells via inhalation to achieve high dosage in the cancerous lungs and may reduce the side effect of cisplatin. Their in vitro and in vivo targeting ability and anticancer effect were confirmed. The aerosol delivery of the nanodrug carrier was demonstrated. Simple aerosol delivery of targeted drug carriers may prove useful for the clinical treatment of lung cancer patients in the future.

Reference

1. Giaccone G (2004) Twenty-five years of treating advanced NSCLC: what have we achieved? Ann Oncol 15:S81-S83
2. Uchino H, Matsumura Y, Negishi T et al (2005) Cisplatin-incorporating polymeric micelles (NC-6004) can reduce nephrotoxicity and neurotoxicity of cisplatin in rats. Br J Cancer 93:678-687
3. Vandervoort J, Ludwig A (2004) Preparation and evaluation of drug-loaded gelatin nanoparticles for topical ophthalmic use. Eur J Pharm Biopharm 57:251-261
4. Tseng C-L, Wu SY-H, Wang W-H et al (2008) Targeting efficiency and biodistribution of biotinylated-EGF-conjugated gelatin nanoparticles administered via aerosol delivery in nude mice with lung cancer. Biomaterials 29:3014-3022
5.Cenni B, Aebi S, Nehme A et al (2001) Epidermal growth factor enhances cisplatin -induced apoptosis by a caspase 3 indenpented patyway. Cancer Chemother Pharmacol 47:397-403

Amperometric Microbiosensors Based on PQQ-Dependent Glucose Dehydrogenase towards the Development of an ATP Biosensor for in vitro Analysis

C. Weber[1], E. Gauda[2], E. Hecht[1], B. Mizaikoff[1], and C. Kranz[1,*]

[1] Institute of Analytical and Bioanalytical Chemistry, University of Ulm, Germany
[2] Johns Hopkins Hospital, Division of Neonatology Research Laboratories, Baltimore, USA

Abstract— **An amperometric biosensor for adenosine-5`-triphosphate (ATP) was developed applying a competitive assay of two glucose converting enzymes. Hexokinase and pyrroloquinoline quinone (PQQ)-dependent glucose dehydrogenase were entrapped by pH-shift induced deposition of Resydrol at a platinum microelectrode with a diameter of 25 µm. Different mediators for the PQQ-dependent glucose deydrogenase (GDH) catalyzed reaction were used applying potentials not higher than 400 mV vs. Ag/AgCl reference electrode. The obtained biosensor is selective to ATP and sensitive to it at physiological concentrations down to the nanomolar range.**

Keywords— **ATP, PQQ-GDH, hexokinase, Resydrol, microbiosensor.**

I. Introduction

Adenosine-5`-triphosphate (ATP) is involved in numerous biological energy metabolism and signaling processes. For instance, ATP plays an important role as an excitatory neurotransmitter in the central nervous system of mammalians [1] and is discussed as a regulating factor for the reflex control in the carotid body [2]. However, ATP is also a target molecule in environmental analysis [3], food control [4] and drug design [5] as a marker of fungal contamination or inhibitor of enzymes, respectively. Therefore various analytical techniques for detection of ATP have being developed based on liquid chromatography [6], fluorescence [7], bioluminescence [8] and colorimetry [9]. Unfortunately, most of these methods lack of sensitivity, are cost-intensive or destructive for the examined tissue.

However, for the analyses of cellular processes in clinical microbiology the detection and quantification of ATP with a suitable temporal and spatial resolution is inevitable. Therefore utilizing miniaturized electrochemical sensors seems to be a very promising approach. As ATP and its metabolic products cannot be electrochemically converted directly at suitable potentials, electrochemical transducers such as microelectrodes are combined with either a consecutive or a competitive enzyme assay. A number of ATP-biosensors have been already published mainly based on two different approaches: One approach uses an enzyme assay based on glycerole kinase and glycerol-3-phosphate oxidase [10], using glycerole as cosubstance; the second type of ATP biosensors is based on the conversion of glucose by enzymes like the competitive enzyme assay glucose oxidase and hexokinase [11], [12]. For both detection schemes an additional constituent is required as a co-substrate of the ATP converting type of kinase so that both require further additives that can contaminate the analyzed sample. These types of biosensors are consequently a priori not reagentless. The contamination with glycerol may be more disadvantageous in comparison to glucose since glucose is practically present in almost all biological samples. Another disadvantage of these enzyme assays is the dependence on the oxygen concentration as these reactions are based on dissolved oxygen as electron acceptor generating hydrogen peroxide (H_2O_2), which is further converted by a third enzyme or is detected at the electrode surface. Unfortunately, a potential of 600 mV is required in order to oxidize the generated hydrogen peroxide leading to co-oxidation of other biomolecules, like catecholamines or ascorbic acid, which might be present in the solution.

Therefore a biosensor based on a competitive assay of hexokinase and PQQ-dependent glucose dehydrogenase was developed. Using this dual enzyme electrode oxygen concentrations are no limiting steps in the detection of ATP and lower potentials avoiding interferences by co-oxidation can be applied.

II. Experimental

A. Chemicals

Pyrroloquinoline quinone-dependent glucose dehydrogenase from microorganism (≥ 850 U/mg) was purchased by Toyobo, Japan. Glucose oxidase type X-S from *Aspergillus niger* (136.1 U/mg), hexokinase from *Saccharomyces cerevisae* (457 U/mg protein), adenosine-5`-triphosphate, glucose, sodium hydrogenphosphate and dihydrogenphophate, magnesium chloride, N-Methylphenazonium methyl sulfate (PMS), Potassium hexacyanoferrate(II) and (III), Chromium(III) nitrate nonahydrate and ferrocenemethanol were purchased from Sigma, Germany. Resydrol AY498w/35WA was obtained from Cytec, USA. For the preparation of all solutions HPLC water was used.

O. Dössel and W.C. Schlegel (Eds.): WC 2009, IFMBE Proceedings 25/VIII, pp. 351–354, 2009.
www.springerlink.com

B. Apparatus

A three-electrode set-up equipped with an Ag/AgCl reference electrode, a platinum counter electrode and platinum microelectrodes (diameter 25 µm) as working electrodes was used for amperometric measurements and immobilization procedures. For cleaning purpose of the microelectrodes in 0.5 M sulfuric acid, a $Hg/HgSO_4$ reference electrode was used, respectively. Platinum microelectrodes were fabricated by sealing a microwire into a borosilicate capillary and consecutively grinding and polishing steps until a disk electrode was exposed.

Electrochemical measurements were conducted with either a potentiostat (CH660) or a bipotentiostat (CH842) from CH Instruments, USA. AFM imaging was performed with a PicoPlus/Agilent 5500 from Agilent Technologies, USA, using Pico View, SPM Control Software (Agilent Technology).

C. Immobilization Procedure

Especially for miniaturized biosensors a non-manual immobilization procedure for the enzymes is required. A pH-shift induced precipitation of the anodic electrodeposition paint Resydrol was used.

In order to immobilize the mediator layer directly at the electrode surface, chromium hexacyanoferrate layer was electrochemically deposited at the microelectrode as previously published by Tseng et al. [13].

For immobilization of the enzyme PQQ-GDH 3 cycles of a multipotential profile (1.9 V for 0.3 s, -0.3 s for 5 s) was applied to an enzyme/polymer solution (2900 U PQQ-GDH and 70 µl Resydrol per mL).

ATP sensors were obtained by immobilizing additionally hexokinase in the Resydrol polymer film.

The biosensor can be either used immediately after preparation or can be stored in 0.1 M phosphate buffer (pH 7.4) containing 5 mM Mg^{2+}, 5 mM glucose and 2 mM ferrocenemethanol.

D. Characterization

The permeability of Resydrol polymer films were examined by cycling the electrode before and after the precipitation in 10 mM ferrocyanide dissolved in 0.5 M KCl solution. The thickness (height profile) of the polymer deposition was detected by AFM.

Prior to the development of the ATP sensor, several mediators were investigated due to their compatibility with the immobilized enzymes and their kinetics in the mediating process: two soluble mediators, N-methylphenazonium methyl sulfate (PMS) and ferrocenemethanol and an immobilized mediator, chromium ferricyanide were tested.

The characterization of the biosensors performance was conducted at constant potential amperometry in an electrochemical flow cell using solutions with different concentrations of glucose or ATP and 1 mM glucose, respectively. The applied potential was chosen in respect to the used mediator. For ferrocenemethanol and the chromium hexacyanoferrate layer a potential of 400 mV and for PMS a potential of 100 mV was applied.

III. Results and Discussion

The electrochemical detection of ATP based on a competitive system of hexokinase and PQQ-glucose dehydrogenase is complex as shown in the following reaction schemes:

- Catalyzed by hexokinase: glucose + ATP → glucose-6-phosphate + ADP
- Catalyzed by PQQ-GDH: glucose + $^1/_n$ oxidized mediator → gluconolactone + $^1/_n$ reduced mediator
- At the electrode surface: $^1/_n$ reduced mediator → $^1/_n$ oxidized mediator + e^-

Both reactions require glucose as a substrate. When the ATP converting reaction, catalyzed by hexokinase, consumes glucose the local glucose concentration is reduced and the electrochemical signal due to the glucose oxidation, catalyzed by PQQ-GDH, decreases. Consequently, the reduction of the glucose signal is proportional to the local ATP concentration.

Hexokinase and PQQ-dependent glucose dehydrogenase are dependent on magnesium ions as an essential cofactor. For hexokinase the optimum concentration of Mg^{2+} is around 5 mM [14], the required magnesium concentration for PQQ-GDH is lower [15]. A pH of 7.4 was chosen for the amperometric measurements due to the optimum pH for the hexokinase-catalyzed reaction [16]; PQQ-GDH is also active in this pH-range.

Due to the complexity of the sensor design the performance of the biosensor depends on a number of variables:

Optimization of the deposition: The number of entrapped enzyme molecules is foremost controllable by the size of the polymer precipitation whereas the size and the permeability of the polymer bulk can be influenced by several factors:

- the concentration of the EDP solution
- the applied potential (a minimum potential of 1.7 V vs. Ag/AgCl reference electrode is required)
- the duration of the pulse
- the number of the applied cycles

These factors influence the deposition based on a pH shift in the vicinity of the electrode surface (data are not shown). Applying three cycles of a potential pulse profile of 1.9 V for 0.3 s and -0.3 s for 5 s resulted in the optimized deposition regarding film thickness and permeability (Figure 1 and 2).

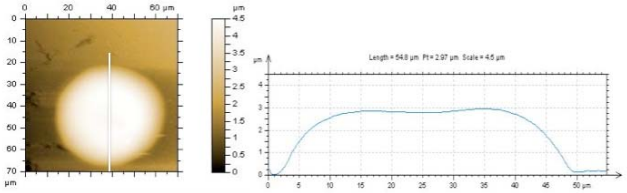


Figure 1: AFM images of Resydrol precipitation applying 3 cycles of 1.9 V for 0.3 s and -0.3 V for 5 s vs. Ag/AgCl reference electrode in a 70 µl/ml Resydrol solution (scan speed 1.6 line/s); left: AFM image (white line indicates cut for height profile); right: height profile of the polymer film

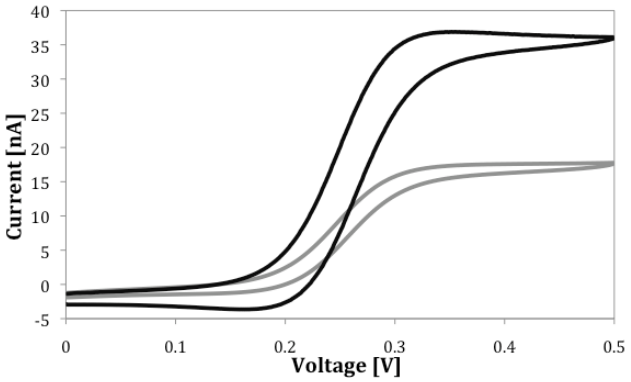


Figure 2: CVs recorded at a Pt microelectrode before (▬) and after (▬) precipitation of Resydrol layer (applying 3 cycles of 1.9 V for 0.3 s and -0.3 V for 5 s vs. Ag/AgCl reference electrode in a 70 µl/ml Resydrol) in 10 mM ferrocyanide and 0.5 M potassium chloride solution vs. Ag/AgCl-reference electrode; scan rate 0.1 V/s

Optimization of the glucose sensor: Since the ATP-sensing scheme is preliminary dependent on the glucose oxidation catalyzed by PQQ-GDH, in a first step the glucose microbiosensor was optimized in respect to the effect of different mediator systems: ferrocenemethanol and PMS as soluble mediators and a chromium hexacyanoferrate(III) layer at the platinum surface as an immobilized mediator. The response of a biosensor towards a target molecule depends strongly on the properties, especially the kinetics, of the mediator. Figure 3 shows the sensitivity of the PQQ-dependent glucose dehydrogenase based glucose sensors in respect to the used mediators.

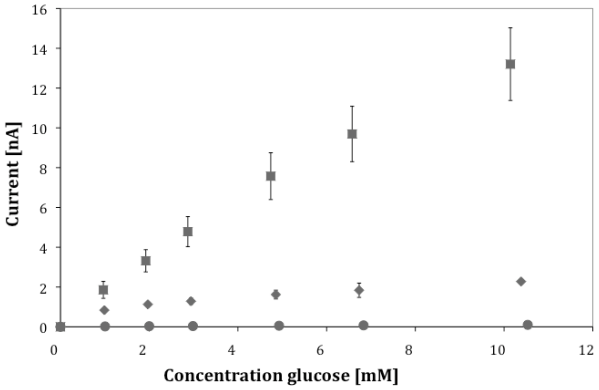


Figure 3: Calibration curves for PQQ-dependent glucose dehydrogenase based glucose sensors using different mediators: 2 mM ferrocenemethanol (■) at 400 mV; 1 mM PMS at 100 mV(◆), immobilized chromium hexacyanoferrate(III) at 400 mV(●)

Chromium hexacyanoferrate(III) was used as an immobilized mediator. Amperometric measurements were performed at 400 mV vs. Ag/AgCl reference electrode but compared to the free-diffusing mediators N-methylphenazonium methylsulfate (PMS) and ferrocenemethanol the sensitivity was low and not adaptive for an ATP biosensor for physiological ATP concentrations. PMS measurements were conducted at preferrential low potential of 100 mV vs. Ag/AgCl reference electrode. However, PMS is light-sensitive, biochemically active and shows a slow response towards glucose addition (not shown) and was still less effective as an electron acceptor towards glucose. Ferrocenemethanol showed a sensitivity of 1.5 nA/mM ± 0.4 nA/mM in a linear range of 0-5 µM glucose.

First developments towards an oxygen independent ATP-sensor: The concentration of hexokinase was varied in order to improve the response towards ATP. The immobilization of PQQ-dependent glucose dehydrogenase and hexokinase was performed in consecutive layers. Sensitivity up to 290 pA/µM ATP could be reached in a delimited linear range when using 4300 U hexokinase per mL for immobilization.

IV. Conclusion

An oxygen independent biosensor for adenosine triphosphate (ATP) was designed by immobilizing a competitive assay of two enzymes at the surface of a platinum microelectrode: pyrroloquinoline quinone-dependent glucose dehydrogenase (PQQ-GDH) catalyzes the oxidation of glucose to gluconolactone using an artificial redox mediator while hexokinase transfers a phosphate group of ATP to

glucose resulting in adenosine diphosphate and glucose-6-phosphate and reduces therefore the amount of glucose available for the conversion by PQQ-GDH. Hence, a decrease in response at the amperometric biosensor is obtained in the presence of ATP.

For the gentle immobilization of enzymes fundamental aspects concerning the fabricated microelectrodes and the immobilization procedure were optimized and implemented. In order to improve the ATP detection the effect of different mediators for the PQQ-GDH-based system were investigated and the effect of different hexokinase concentrations were examined.

ACKNOWLEDGEMENTS

The authors are grateful to M. Bunz for technical assistance in fabricating microbiosensors. Financial support was generously provided by NIH within project R01 HL080725.

REFERENCES

1. Devlin, T. M., (2006) Textbook of Biochemistry With Clinical Correlations. Wiley-Liss, Hoboken, NJ
2. Masson, J.-F.; Kranz, C.; Mizaikoff, B. & Gauda, E. B. (2008) Amperometric ATP Microbiosensors for the Analysis of Chemosensitivity at Carotid Bodies. Anal. Chem. 80: 3991-3998
3. Jørgensen, P. E.; Eriksen, T. & Jensen, B. K. (1992) Estimation of Viable Biomass in Wastewater and Activated Sludge by Determination of ATP, Oxygen Utilization Rate and FDA Hydrolysis. Wat. Res. 26: 1495-1501
4. Stannard, C. J. & Wood, J. M. (1983) The Rapid Estimation of Microbial Contamination of Raw Meat by Measurement of Adenosine Triphosphate (ATP). J. Appl. Microbiol. 55: 429-438
5. Shukla, S.; Wu, C. P. & Ambudkar, S. V. (2008) Development of inhibitors of ATP-binding cassette drug transporters: present status and challenges. Expert Opin Drug Metab Toxicol 4: 205-223
6. Schweinsberg, P. D. & Loo, T. L. (1980) J. Chromatogr. 181: 103-107
7. Foy, G. P. & Pacey, G. E. (1996) Determination of ATP using chelation-enhanced fluorescence. Talanta 43: 225-232
8. Lundin, A. & Thore, A. (1975) Analytical Information Obtainable by Evaluation of the Time Course of Firefly Bioluminescence in the Assay of ATP. Anal. Biochem. 66: 47-63
9. Kunst, A.; Draeger, B. & Ziegenhorn, J., (1984) Colorimetric Method with Glucose oxidase and Peroxidase.
10. Katsu, T.; Yang, X. & Rechnitz, G. A. (1994) Amperometric Biosensor for Adenosine-5`-Triphophate Based on a Platinum-Dispersed Carbon Paste Enzyme Electrode. Anal. Lett. 27: 1215-1224
11. Scheller, F. & Pfeiffer, D. (1980) Glucose Oxidase-Hexokinase Bienzyme Electrode Sensor for Adensosin Triphosphate. Anal. Chim. Acta 117: 383-386
12. Kueng, A.; Kranz, C. & Mizaikoff, B. (2004) Amperometric ATP Biosensor Based on Polymer Entrapped Enzymes. Biosens Bioelectron 19: 1301-1307
13. Tseng, T.-F.; Yang, Y.-L. & Lou, S.-L. (2007) Chromium Hexacyanoferrat Modified Biosensor Based on PQQ-Dependent Glucose Dehydrogenase. International Conference of the IEEE EMBS 29: 2681-2684
14. Compagnone, D. & Guibault, G. G. (1997) Glucose Oxidase/Hexokinase Electrode for the Determination of ATP. Anal. Chim. Acta 340: 109-113
15. Yamada, M.; Inbe, H.; Tanaka, M.; Sumi, K.; Matsushita, K. & Adachi, O. (1998) Mutant isolation of the Escherichia coli quinoprotein glucose dehydrogenase and analysis of crucial residues Asp-730 and His-775 for its function. J. Biol. Chem. 273: 22021-22027
16. Domenech, M. d. (1980) Specifity of Hexokinase towards Some Uncommon Substrates and Inhibitors. FEBS Lett. 119: 174-176

Corresponding author:	C. Kranz
Institute:	Analytical and Bioanalytical Chemistry
Street:	Albert-Einstein-Allee 11
City:	89081 Ulm
Country:	Germany
Email:	christine.kranz@uni-ulm.de

Remote Controlled Drug Release Induced by a Rotating Magnetic Field

W. Andrä [1], T. Gesener [1], A. Raabgrund [1] and M. E. Bellemann [1]

[1] Department of Medical Engineering and Biotechnology, University of Applied Sciences, Jena, Germany

Abstract— **A novel type of a medical capsule is described which is suitable to perform remote controlled drug release at predetermined positions in the gastrointestinal tract without the use of ionizing radiation. This capsule is based on magnetically generated heating effects and completely consists of biocompatible parts. Theoretical estimations show that the maximum depth of the capsule below the abdominal wall (range of operation) is mainly ruled by the weight and the cautionary conditions of a spinning magnet needed for the thermally produced drug ejection. In vitro experiments confirmed the theoretical predictions. A maximum depth of about 12 cm for ambulatory measuring units and of about 20 cm for stationary units, respectively, can be expected.**

Keywords— **Magnetic marker monitoring, gastrointestinal tract, human drug absorption, drug targeting, range of operation.**

I. Introduction

Targeted drug delivery in the digestive tract is a goal set already for a long time. To date, only the method of physiological triggering is practically applied. However, the shortcomings of this way are well known [1].

There is, however, another possibility: the remote controlled drug release (RCDR), which was already tried many times. More than 30 different types of capsules that might be suitable for RCDR, can be found in the literature [2]. However, at present only one, the so called Enterion™ capsule, is widely applied in numerous phase I clinical studies [3]. Most of the RCDR capsules are based on magnetic principles and use the heating of a small part, e. g. a spring latch filament, as a suitable means to trigger the release mechanism. However, two problems are not satisfyingly solved up to now:

(i) monitoring the capsule without using ionizing radiation;
(ii) reducing capsule parts which are only needed for the releasing mechanism (batteries, electronic circuits, etc.), in favor of the drug load.

We developed a special capsule (Figure 1) in order to simultaneously solve the two mentioned problems. It uses a small permanent magnetic sphere for both the monitoring procedure as well as for the RCDR method. The sphere is turned by the action of a rotating magnetic field. The detection of the capsule position is based on the so called rotating magnetic marker monitoring (RMMM) already successfully tested with volunteers [4]. Later, this technique was developed for use with a small unit which can be fixed at a belt [5]. The application with respect to RCDR was already demonstrated with in vitro experiments [6]. However, it was not yet evaluated for its range of operation (the depth in a human body up to which the drug release can be performed). The aim of this paper is to determine this range.

II. Materials and methods

For the investigated capsules, the standard size 000 (length: 28 mm; diameter: 9.9 mm) was chosen. Due to the double wall structure shown in Figure 1, the diameter of the rotating sphere is restricted to about 5 mm. An essential element is the low-boiling liquid which is heated by the friction of the rotating sphere up to the evaporation temperature. The evaporating liquid expands the swelling bag and expels the agent from the capsule. The rotating magnetic field is, in our equipment, generated by a small cylindrical magnet (diameter = height = 2 cm or 3.5 cm, respectively) consisting of NdFeB. It is turned by an electric motor (idle-running speed: 24000 rpm corresponding to a rotational frequency v = 400 Hz).

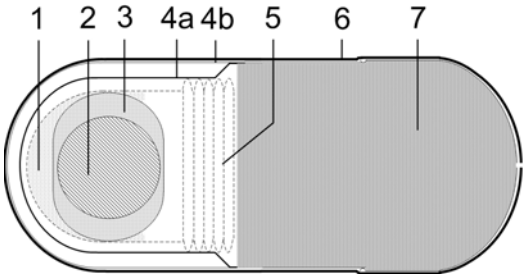


Fig. 1 Investigated capsule, consisting of a NdFeB sphere (2), an oil bearing (3), a low-boiling liquid (1) enclosed in an expandable bag (5) made of polyethylene foil, and the agent container (7). The double wall structure (4a, 4b) and the bearing case are made of hard gelatin. A coating (6), e. g. made of ethylcellulose, protects the gelatin against the aqueous environment.

O. Dössel and W.C. Schlegel (Eds.): WC 2009, IFMBE Proceedings 25/VIII, pp. 355–358, 2009.
www.springerlink.com

For monitoring the sphere serves as magnetic marker during the RMMM procedure. For that purpose, the external magnetic field H_R rotates slowly (less than 10 times per second). As soon as the capsule has arrived at its destination, faster rotation of H_R is started to perform the drug release.

As low-boiling fluid a mixture of ethanol and ether (boiling temperature: 65 °C) was used in this study, but alternatives are possible. Therefore, the temperature rise from body temperature is ΔT = 28 K. In the close-fitting bearing the effective viscosity of the oil is different from the nominal value because the thickness of fluid is only about a tenth of a millimeter between the surface of the sphere and the walls of the bearing case. In consideration of this fact, the frictional torque was directly measured with the sphere being inside the capsule by means of a purpose-built apparatus [7].

Two properties of the rotating field are crucial: the field strength H_R and the rotational frequency v. The field strength is needed to overcome the frictional torque acting on the sphere by the bearing fluid. This torque increases with the rotational frequency. Due to the fact that H_R is decreasing with increasing distance between the sphere and the spinning magnet, the range of operation D is limited.

A. Theoretical consideration

To estimate the maximum distance between the sphere and the source of the rotating field up to which the RCDR procedure operates, we start with the following assumption. The needed increase of temperature ΔT from body temperature up to the evaporation temperature is determined by the stationary equilibrium of supplied heat power L_i and the outflow of heat. The latter one is ruled by the thermal resistance of the capsule R_{th}. This consideration yields

$$L_i = \Delta T/R_{th} \ . \tag{1}$$

L_i is generated by the frictional torque G_R of the sphere acting during its rotation in the bearing liquid.

$$L_i = 2\pi \cdot v \cdot G_R \ . \tag{2}$$

The torque exerted by the rotating magnetic field is

$$G_H = \mu_0 \cdot m \cdot H_R \cdot \sin(\delta) \ , \tag{3}$$

where δ is the lag angle between H_R and the magnetic moment m of the rotating sphere. For a safe rotation of m the angle δ must remain below $\pi/2$. The rotating field is assumed to be generated by a primary dipole m_P perpendicular oriented to its rotational axis. If the capsule is placed on this rotational axis with the sphere located in the distance D from m_P, then

$$H_R = m_p/(4\pi \cdot D^3) \ . \tag{4}$$

Then, the corresponding range of operation $D^{(L)}$ results in

$$D^{(L)} \le [\mu_0 \cdot m \cdot m_p \cdot R_{th} \cdot v/(2 \cdot \Delta T)]^{1/3} \ . \tag{5}$$

This range of operation increases with increasing frequency. As a second condition, the magnetic torque must be sufficiently large to overcome the frictional torque acting on the rotating sphere. Neglecting the influence of static friction this torque can be described by [8]

$$G_R = 12\pi \cdot \eta \cdot V \cdot v \ , \tag{6}$$

where η means the viscosity and V the volume of the sphere. A consideration similar to that sketched above leads to

$$D^{(G)} \le [\mu_0 \cdot m \cdot m_p/(48\pi^2 \cdot V \cdot \eta \cdot v)]^{1/3} \ . \tag{7}$$

This range of operation increases with increasing frequency. Combining the equations (5) and (7) the maximum operational range as a function of the frequency results as the crossing point of the two curves given by the corresponding equations.

$$D = [\mu_0 \cdot m \cdot m_p]^{1/3} \cdot [R_{th}/(96\pi^2 \cdot F \cdot \Delta T \cdot V \cdot \eta)]^{1/6} \ . \tag{8}$$

Associated with this D value is the optimum frequency

$$v = [\Delta T/(24\pi^2 \cdot R_{th} \cdot V \cdot \eta)]^{1/2} \ . \tag{9}$$

B. Experimental determination of the operational range

The capsule was kept in a bath of controlled temperature (37 °C). A cylindrical permanent magnet was fixed on the axis of an electric motor with the direction of the primary magnetic moment m_P perpendicular to the rotating axis. The release of a model drug was tried with different distances D between the center of the spinning magnet and the sphere inside the capsule (Fig. 2).

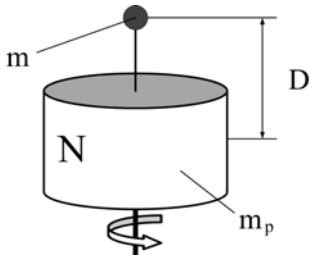


Fig. 2 The cylindrical permanent magnet (NdFeB) acts as source of the rotating field H_R. For the theoretical consideration, it may be approximated by a dipole with the magnetic moment m_P perpendicularly oriented to the rotational axis. The north pole of m_P is indicated by the letter N, the south pole is hidden. The field strength of H_R acting of the magnetic moment m decreases with increasing distance D according to equation (4).

For a given frequency each experiment was started with large *D*. Initially, drug release was not performed. Then, the attempt was repeated with decreasing *D* until release was observed. The procedure was carried out for two different sizes of the primary dipole.

III. Results

A typical series of successful drug release is shown in Fig. 3. The theoretically derived curves are plotted in Fig. 4 and Fig. 5 with the parameter values corresponding to our experimental conditions. Included in these figures are experimental results obtained with decreasing distance *D*. The open circles represent releasing attempts without success. The full circle indicates the successful experiment with the largest distance.

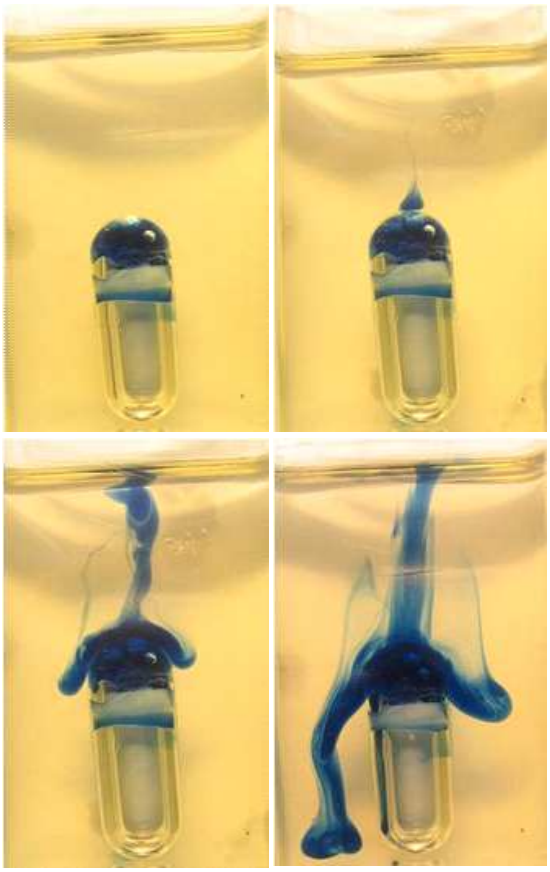


Fig. 3 Typical sequence of a successful release of a model drug (edible oil colored with Sudan Blue). The top left hand corner of the sequence shows the capsule before the start of the rotating field. In this state, a part of the model drug is visible only inside the upper cap whereas the main part is hidden by the double wall structure.

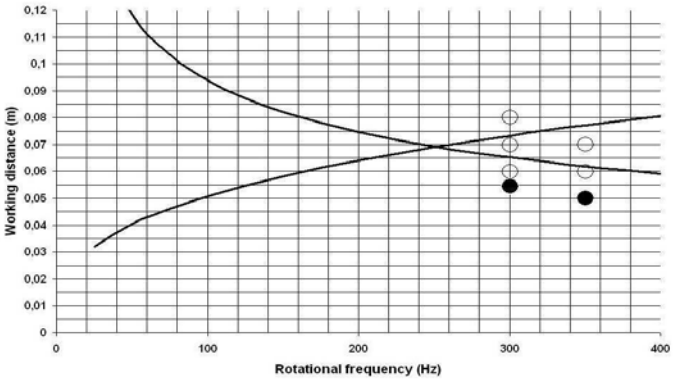


Fig. 4 Range of operation (working distance) *D* as function of the rotational frequency. As explained above, the increasing and the decreasing curves *D(v)* correspond to the requirement of minimum heat power and of minimum magnetic torque, respectively. The calculations are based on the following values of parameters used in equation (8): magnetic moments m = 0,065 Am^2; m_p = 5.7 Am^2; thermal resistance R_{th} = 150 K/W; required increase of temperature ΔT = 28 K; volume of the sphere $V = 6{,}5 \cdot 10^{-8}$ m^3; viscosity of the bearing oil η = 0.2 Pa·s. Circles show experimentally determined *D* values with (●) and without (○) successful release.

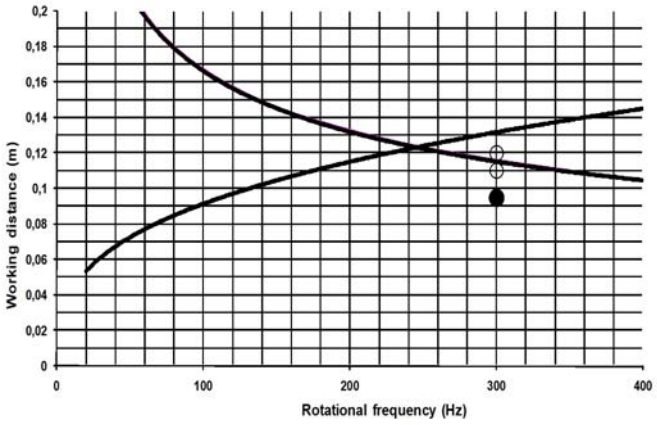


Fig. 5 The range of operation (working distance) *D* as function of the rotational frequency. The increasing and decreasing curves represent the theoretical functions given in equations (5) and (7), respectively. The same values of parameters are taken as used in Fig. 4, except the value of m_P = 34,8 Am^2.

IV. Discussion

First of all, the reproducibility of the RCDR procedure was investigated by performing 20 experiments with a distance *D* = 5 cm and a frequency of 350 Hz using the parameters given in Fig. 4. In 15 cases, we performed successful release with more than 70 % of the agent expelled.

Afterwards, we performed experiments to determine realistic D values. In the first series, the magnetic moment of the spinning primary magnet was m_P = 5.7 Am^2. The corresponding results are indicated in Fig. 4 by open circles (no release) and full circles (successful release). In a second series, the same procedure was performed using a primary magnet with m_P = 34.8 Am^2 (see Fig. 5).

The experimentally determined values of the operational range were always smaller than the theoretically expected ones. There are different reasons to explain his effect.

- The consideration leading to equation (1) neglects the contributions to the needed heat caused by the specific heat as well as by the evaporation heat of the liquid. Further, the thermal equilibrium state assumed in equation (1) is approached exponentially with time. For all practical purposes, however, a finite waiting time is required. The consequence of these two aspects is a fictitious increase of the temperature rise ΔT.
- The real frictional torque is larger than theoretically assumed for two reasons. Additionally to the viscous friction there is a static friction and the viscous friction may be enhanced by turbulent flow of the bearing liquid. Both effects may be expressed by an enlarged η value.
- Finally, due to imperfect isolation of the capsule, the thermal resistance R_{th} may be smaller than assumed.

All the above mentioned deviations lead to a smaller range of operation than expected. However, due to the 6th root in equation (8) only a moderate deviation may be expected. Our experimentally determined operational distances were 15 % to 20 % less than the theoretically predicted values.

Generally, there are possibilities to enlarge the operational distance by choosing appropriate parameters. However, some of the parameters given in equation (8) are restricted by practical reasons. This particularly applies to the upper limit of the magnetic moment m and the volume V of the sphere, which are limited by the capsule size. The thermal resistance R_{th} cannot essentially be enhanced due to the restricted isolation capability of the capsule construction. The lower limit of the temperature rise ΔT is given by the condition that spontaneous ejection of drug must strictly be excluded. The upper limit of the frequency v is restricted by technical reasons and, as a consequence of equation (9), determines the lower limit of the viscosity η as well.

Only the magnetic moment m_P of the primary dipole can generally be enlarged, whereby the range of operation is increased. The comparison of Fig. 4 and Fig. 5 shows that this tendency is experimentally confirmed.

Larger magnets, however, need a special fixation and owing to the strong magnetic forces, precaution should be taken in these cases. An operational range of about 20 cm seems to be practicable with stationary equipment.

References

1. Van den Mooter G. (2006) Colon drug delivery. Expert Opin. Drug Deliv. 3: 111-125
2. Andrä W, Werner C. (2007) Remote-controlled drug delivery in the gastrointestinal tract. In: Magnetism in Medicine, WILEY-VCH, Weinheim, pp. 499-510
3. Wilding I R, Prior D V. (2003) Remote controlled capsules in human drug absorption (HAD) studies. Critical Reviews in Therap. Drug Carrier Systems 20: 405-431
4. Andrä W, Danan H, Eitner K et al (2005) A novel magnetic method for examination of bowel motility. Med. Phys. 32: 2942-2944
5. Andrä W, Bellemann M E, Brand M et al (2008) Magnetic marker monitoring using a permanent magnetic sphere oriented by a rotating magnetic field. EFMBE Proceedings 22: 1137-1140
6. Dutz S, Andrä W, Steinke et al (2008) Remote controlled drug release and marker mponitoring using the same magnetic mechanism. Biomed. Technik 52 (Supplementary CD
7. Steinke F, Andrä W, Heide et al (2007) Rotating magnetic macrospheres as heating mechanism for remote controlled drug release. JMMM 311: 216-218
8. Landau L D, Lifshitz E M (1978) Lehrbuch der theoretischen Physik Bd. 6, Akademie-Verlag, Berlin

Author: Matthias E. Bellemann
Institute: University of Applied Sciences
Street: Carl-Zeiss-Promenade 2
City: 07745 Jena
Country: Germany
Email: bellemann@fh-jena.de

Microfluidics for Drug Delivery

S. Haeberle[1], D. Hradetzky[1], A. Schumacher[1], M. Vosseler[1], S. Messner[1], and R. Zengerle[1,2]

[1] Hahn-Schickard-Gesellschaft, Institute of Micromachining and Information Technology (HSG-IMIT), Wilhelm-Schickard-Str. 10, 78052 Villingen-Schwenningen, Germany
[2] Laboratory for MEMS Applications, Department of Microsystems Engineering (IMTEK), University of Freiburg, Georges-Koehler-Allee 106, 79110 Freiburg, Germany

Abstract— **Drug delivery, i.e. the way a pharmacologically active substance is delivered to the body, has a significant impact on the therapeutic value of medication. The paper gives an overview on different drug delivery schemes and describes the limitations of the oral route, which is the current gold standard in the market. Following these limitations, plenty of alternative (parenteral) drug delivery technologies are currently under development. Many of them require the precise handling of small liquid volumes using small sized and low energy consuming devices. So microfluidics is a key enabling technology for these upcoming drug delivery devices.**

Ease of use and autonomous operation are the most important aspects for high acceptance and compliance of the patients. So for short term therapy (e.g. antibiotics), the devices should be small and portable. For long term therapy (e.g. cardiac), implantable devices are favorable since they can operate autonomously and deliver precise doses exactly to the target site (local therapy). The paper describes two examples for microfluidic drug delivery devices in more detail, namely the intra-oral transmucosal *IntelliDrug system* and the transdermal *ChronopaDD* device.

Keywords— **microfluidics, drug delivery, microsystems**

I. Introduction

Due to the demographic change and the therewith related prevalence of chronic diseases, the health care market is facing increasing cost pressure within the upcoming years. Nevertheless, people demand high standard treatment to maintain or improve their health condition. Facing this situation and looking from a technology perspective, drug delivery is one of the most obvious and close to market domains where innovative products can make an important difference.

Looking at the drug delivery market in more detail, three main drivers for innovation can be identified:

1. **New types of drugs**: future biopharmaceutical drugs cannot be delivered via the oral route (first pass metabolism). Consequently, parenteral delivery routes will be increasingly addressed in the future.
2. **New types of therapy**: adopting the drug dosage to the patient (personalized medicine) and time of the day (chronotherapy) is required for the upcoming more sophisticated medication scenarios.
3. **Patent expiration**: many patents of current block buster drugs will expire within the upcoming years, leading to increased competition from generic manufacturers. One possible strategy for pharmaceutical companies is to add a new drug delivery technology to their existing drug.

Based on these considerations, we discuss the chances of different drug delivery technologies and pathways to meet these challenges with a clear focus on microfluidic approaches.

II. State of the art in Drug Delivery

An ideal drug delivery technology enables the optimum medication of every patient. Therefore, the plasma level, i.e.
concentration of drug in the circulatory system, hast to be permanently maintained within the therapeutic window (see 0).

The therapeutic window can alter from patient to patient (personalized therapy) and over the course of the day (chronotherapy). Many state of the art delivery systems are not able to maintain this optimum delivery scheme. Consequently, the different drug delivery technologies can first be classified regarding their flexibility in transient delivery schemes as described within the following section.

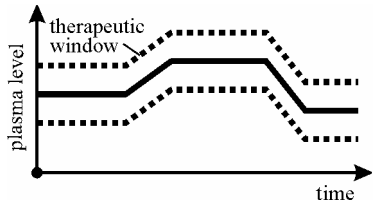


Fig. 1. Course of plasma level for an optimum drug delivery.

O. Dössel and W.C. Schlegel (Eds.): WC 2009, IFMBE Proceedings 25/VIII, pp. 359–362, 2009.
www.springerlink.com

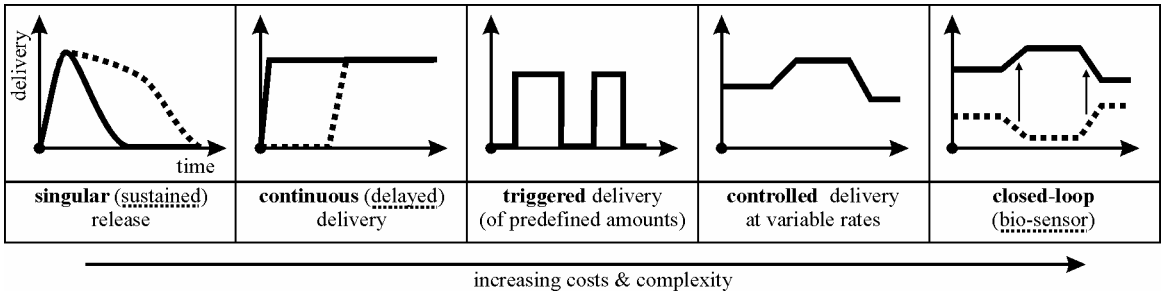


Fig. 2. Classification of different drug delivery schemes regarding delivery profiles.

A. *Classification of Drug Delivery Devices*

Different drug delivery schemes are depicted in 0. They range from basic singular release, over continuous delivery, to more complex and time controlled delivery of predefined amounts. The ultimate closed-loop approach (right), where the drug release is directly triggered by a biosensor measuring relevant physiological parameters (e.g. glucose level in diabetes care) could not be realized so far due to missing long-term stable *in vivo* biosensors. Thus, the controlled delivery at variable rates is the most complex delivery scheme today.

Based on these considerations, we can categorize the capabilities of the different pathways to deliver the drug to the body (see 0). Basically, the drug can either be administered directly (injectable, implantable) or indirectly (oral, inhalable, transmucosal, transdermal). The different pathways are assessed concerning their potential to meet the future challenges in drug delivery:

- **Delivery scheme**: complex profiles possible?
- **Bioavailability**: efficiency of absorption to body
- **Macromolecules**: suitable for biopharmaceuticals?
- **Autonomous** operation possible?

Type	Oral	Inhalable	Injectable[1]	Transmucosal	Transdermal	Implantable
delivery scheme[2]						
bioavail-ability	low	good	high	good	middle / good [3]	high
macro-molecules	O	+	++	+	+[4]	++
auto-nomous	no	no	yes[3]	yes[4]	yes[4]	yes

[1]including intravenously (IV); [2]most complex; [3]portable infusion pumps; [4]see examples in this paper

Fig. 3. Different pathways for drug delivery.

B. *Oral Drug Delivery – Limitations of the Gold Standard*

The oral route (taking pills) is the gold standard in drug delivery with a market share of approximately 40 % [1]. It is based on the absorption of the active agent within the stomach, the small intestine or the colon. However, the transit time through the gastrointestinal tract depends on multiple factors, like activity or food consumption, and therefore it is hardly reproducible even in a single individual, and thus the bioavailability is quite low. Due to the first pass metabolism, also future macromolecular biopharmaceuticals can hardly be administered via this route. So-called "intelligent pills" could be a possible solution to overcome this drawback [2, 3]. However, they are technically complex and thus seem to be applicable in high-price niche applications only.

Consequently, alternative approaches to the oral route are required to meet the future challenges described before. These novel devices should be small and low energy consuming for portable use on the one hand, and allow the precise and controllable dosage of small amounts of liquids

on the other hand. Both challenges can be met by microfluidics as described by some examples within the following section.

III. Microfluidic Drug Delivery Approaches

Several microfluidic drug delivery devices have already been proposed within the last years. Straight forward approaches are based on the integration of micropumps [4, 5] or other means of liquid propulsion (like osmosis [6] or electrolysis [7]) into delivery systems. For further miniaturization, also new materials like hydrogels for direct stimuli response [8-11] or electroactive polymers ("micro muscles") [12-15] are intensively investigated. Another very promising and already commercialized [16] technology is the release of drug from microcavities by thermal disruption [17-20] or resorption [21] of a thin membrane.

A comprehensive overview of microfluidic and MEMS-based drug delivery devices can be found in recent review papers [22-27]. In the following, two concrete examples of microfluidic drug delivery devices are presented, that are currently under development at HSG-IMIT. Namely, the miniaturized intra-oral transmucosal delivery device *IntelliDrug* and the transdermal delivery device *ChronopaDD.*

A. IntelliDrug: Intra-Oral Transmucosal Delivery Device

The different mucous membranes (buccal, anal, nasal, and vaginal) are promising interfaces to deliver drugs to the vascular system. They are available anytime for drug delivery and therefore allow automated drug delivery in principle. Especially the buccal mucosa features additional advantages as the easy accessibility of the quasi-implant for refilling, and the available high absorptive surface area.

To take advantage of these opportunities, a highly miniaturized and self-contained delivery device for the oral cavity has been developed by a multinational EU-consortium (FP6-IST project "IntelliDrug" FP6-IST-002243). The *IntelliDrug* device is an integrated, controlled drug delivery system to be implanted into the human denture and delivers the drug through the buccal mucosa. The challenges for such a system are the minimal space requirements (volume of few mm^3) and the harsh environment in the oral cavity regarding chemical stability and mechanical loads up to 250 N. The main target application is the treatment of chronic diseases.

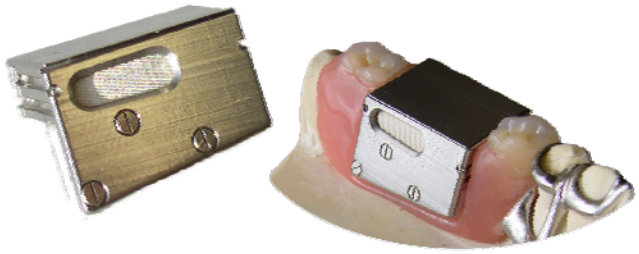


Fig. 4. Intra-oral transmucosal drug delivery device (*IntelliDrug*).

Due to the limited space, the *IntelliDrug* system is designed to deliver a maximum amount of drug solution with a minimum amount of energy. Thus, the system concept comprises an osmotic pump [28] for liquid propulsion (i.e. no energy consumption) and a normally closed 2/2 microvalve. Additionally, a flow and filling level sensor are integrated to monitor the delivered amounts. 0 shows the final prototype of the system developed in the *IntelliDrug* project (integrated in a partial denture on the right).

B. ChronopaDD: Transdermal Device for Chronotherapy

Another promising pathway for drug delivery is the human skin. It allows the administration from an extracorporeal device without using intravenous pathways. Based on mechanical penetration of the stratum corneum by micro needles, a universal pathway for drugs into the vascular system can be established. This pathway offers possibilities for self administrated drug delivery and opens up a large range of applications, e.g. pain therapy, hypertension treatment, rheumatism.

Currently we develop the *ChronopaDD* called transdermal drug delivery device where all components, like the pump, drug reservoir and interface are located within a patch like system. Using this device, a well defined volume of liquid drug will be delivered at a pre-defined time to the vascular system. For example a patch for hypertension or rheumatism treatment can be attached in the evening and delivers the drug at two o'clock in the morning, where the therapeutic effect is best. A drug containing bag and a one-time actuator are integrated in a disposable plastic housing (0, top). The drug is delivered through the stratum corneum by polymer micro needles (0, bottom).



Fig. 5. Transdermal delivery device (*ChronopaDD*)

IV. Conclusion

Due to the current drivers in the drug delivery market (new types of drugs & therapies, patent expiration), we think that future drug delivery devices will be more sophisticated in terms of delivery schemes and medication scenarios. Thus, microfluidics certainly is one of the enabling technologies for these new technologies, since it meets the challenges in size, energy and precision.

Based on these considerations, we assessed the different possible pathways for drug delivery and presented two new microfluidic approaches, namely the *IntelliDrug* device for oral transmucosal, and the *ChronopaDD* device for transdermal delivery. Both approaches enable automated and thus patient independent operation which is important for e.g. elderly patients who often forget to take their medication. Additionally, both allow complex transient delivery schemes.

Overall, we see two possible directions in "microfluidics for drug delivery". Firstly, adding additional functionality and precision to conventional extracorporeal drug delivery devices for short term therapy; and secondly, innovative and highly miniaturized systems for implantable scenarios in long term therapy.

Acknowledgment

Parts of this work have been supported under the Sixth Framework Program, project IntelliDrug, (contract: FP6-IST-002243, see www.intellidrug.org). We also like to thank the Landesstiftung Baden-Württemberg gGmbH for funding the development of the transdermal device.

References

1. Market Study (2008) Drug Delivery Technologies - Current Market Dynamics, Future Market Opportunities and Lifecycle Strategies. Arrowhead Publishers.
2. Deo S, et al. (2003) Responsive drug delivery systems. Analytical Chemistry 75:207A-213A.
3. Philips (2009), intelligent pill technology (iPill), www.research.philips.com.
4. Nisar A, et al. (2008) MEMS-based micropumps in drug delivery and biomedical applications. Sensors and Actuators B-Chemical 130:917-942.
5. Geipel A, et al. (2007) A novel two-stage backpressure-independent micropump: modeling and characterization. Journal of Micromechanics and Microengineering 17:949-959.
6. Wright JC, et al. (2001) An in vivo/in vitro comparison with a leuprolide osmotic implant for the treatment of prostate cancer. Journal of Controlled Release 75:1-10.
7. Su YC, et al. (2004) A water-powered micro drug delivery system. Journal of Microelectromechanical Systems 13:75-82.
8. Ehrick JD, et al. (2005) Genetically engineered protein in hydrogels tailors stimuli-responsive characteristics. Nature Materials 4:298-302.
9. Guiseppi-Elie A, et al. (2002) A chemically synthesized artificial pancreas: Release of insulin from glucose-responsive hydrogels. Advanced Materials 14:743-+.
10. Obaidat AA, et al. (1997) Characterization of protein release through glucose-sensitive hydrogel membranes. Biomaterials 18:801-806.
11. Hoffman AS (2002) Hydrogels for biomedical applications. Advanced Drug Delivery Reviews 54:3-12.
12. Low LM, et al. (2000) Microactuators toward microvalves for responsive controlled drug delivery. Sensors and Actuators B-Chemical 67:149-160.
13. Miller LL (1988) Electrochemically Controlled Release of Drug Ions from Conducting Polymers. Molecular Crystals and Liquid Crystals 160:297-301.
14. Xu H, et al. (2006) Polymer actuator valves toward controlled drug delivery application. Biosensors & Bioelectronics 21:2094-2099.
15. Smela E (1999) Microfabrication of PPy microactuators and other conjugated polymer devices. Journal of Micromechanics and Microengineering 9:1-18.
16. microCHIPS Inc. (2009), www.mchips.com.
17. Santini JT, Jr., et al. (1999) A controlled-release microchip. Nature 397:335-338.
18. Santini JT, et al. (2000) Microchips as controlled drug-delivery devices. Angewandte Chemie-International Edition 39:2397-2407.
19. Li YW, et al. (2004) In vivo release from a drug delivery MEMS device. Journal of Controlled Release 100:211-219.
20. Prescott JH, et al. (2006) Chronic, programmed polypeptide delivery from an implanted, multireservoir microchip device. Nature Biotechnology 24:437-438.
21. Grayson ACR, et al. (2003) Multi-pulse drug delivery from a resorbable polymeric microchip device. Nature Materials 2:767-772.
22. Langer R (2003) Where a pill won't reach. Sci Am 288:50-57.
23. Martin FJ, et al. (2001) Microfabricated drug delivery systems: concepts to improve clinical benefit. Biomed Microdevices 3:97-108.
24. Razzacki SZ, et al. (2004) Integrated microsystems for controlled drug delivery. Advanced Drug Delivery Reviews 56:185-198.
25. Staples M, et al. (2006) Application of micro- and nano-electromechanical devices to drug delivery. Pharmaceutical Research 23:847-863.
26. Lavan DA, et al. (2003) Small-scale systems for in vivo drug delivery. Nature Biotechnology 21:1184-1191.
27. Nuxoll EE, et al. (2009) BioMEMS Devices for Drug Delivery Improved Therapy by Design. Ieee Engineering in Medicine and Biology Magazine 28:31-39.
28. Theeuwes F, et al. (1976) Principles of Design and Operation of Generic Osmotic Pumps for Delivery of Semisolid Or Liquid Drug Formulations. Annals of Biomedical Engineering 4:343-353.

Author: Stefan Haeberle
Institute: HSG-IMIT
Street: Wilhelm-Schickard-Str. 10
City: D-78052 Villingen-Schwenningen
Country: Germany
Email: stefan.haeberle@hsg-imit.de

Cell Based Assays for Label Free Investigation of Living Cells

J. Wiest[1], M. Schmidhuber[2], D. Grundl[2], F. Demmel[2], M. Zottmann[2], H. Grothe[2], M. Brischwein[2], and B. Wolf[2]

[1] Innovationszentrum Medizinische Elektronik - cellasys GmbH, Munich, Germany
[2] Heinz Nixdorf-Lehrstuhl für Medizinische Elektronik, Technische Universität München, Munich, Germany

Abstract— **Label free cell based assays are introduced and the corresponding developments at the *Heinz Nixdorf-Lehrstuhl für Medizinische Elektronik* are presented. A new BioChip-G platform for use with standard microscopes and first result measuring the vitality of 3T3 fibroblasts are shown. Further applications of label free cell based assays are discussed.**

Keywords— **biosensors, label-free, electrochemical, optical, biochip.**

I. Introduction

The development of cell based assays for investigation of whole cells is a logical step after preparation of analytical tools for genomics or proteomics. Furthermore it is possible to design such systems biocompatible and label-free. That allows moving from conventional endpoint assays toward cell based assays which are able to monitor various parameters of living cells[1]. Different systems for life cell monitoring are available[2].

The systems which were developed at the *Heinz Nixdorf-Lehrstuhl für Medizinische Elektronik* of *Technische Universität München* incorporate microsensors for label-free detection of e.g. cellular respiration (pO_2 sensors), extracellular acidification (pH sensors), changes in cellular morphology (impedance sensors) and electro-physiological activity of the cells (micro-electrode arrays)[3-9].

II. BioChip-G

Figure 1 shows one of these multi-parametric sensorchips (the glass-based so-called BioChip-G). The microsensors for pO_2 (cellular respiration), pH (extracellular acidification), impedance (morphological changes) and temperature have been manufactured by thin film technology on the sensorchip surface within a diameter of 12mm where the living cells are cultivated. The bulk material is glass which allows optical access towards the cells cultivated on the BioChip-G. For data acquisition and processing an adapter box is used to connect the microsensors to a modified read out electronic device (not shown but described in Wiest et al.[10]).

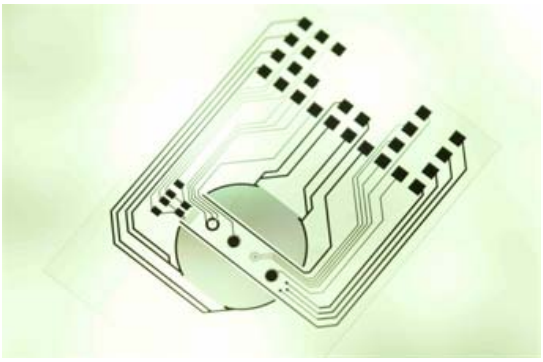


Fig. 1: BioChip-G: The circular cell culture area has a diameter of 12mm. Inside this area are two interdigitated electrode structures for measurement of changes in cellular morphology, two dissolved oxygen sensors for measurement of cellular respiration, two pH sensors for measurement of extracellular respiration and one temperature sensor.

To allow an easy combination of the BioChip-G with standard inverted microscopes a flat connection unit was realized to connect the electrochemical microsensors but also to allow connection of a fluid interface. Figure 2 shows the connector unit with a size of 48 x 36 x 11 mm³.



Fig. 2: Connector unit with BioChip-G: On the right side a flat cable for the seven microsensors is connected. On the left side a fluid interface with inflow and outflow is shown. The unit can be placed on a standard inverted microscope for optical access towards the cells.

O. Dössel and W.C. Schlegel (Eds.): WC 2009, IFMBE Proceedings 25/VIII, pp. 363–364, 2009.
www.springerlink.com

Measurements with 3T3 fibroblasts (DSMZ no. ACC 173) where performed using the system. As media Dulbecco's MEM + 4mM L-Glutamin + 50µg/ml gentamicin + 5 % fetal bovine serum was used. After three days of preincubation the biochips where connected to the read-out system and cellular vitality was monitored. After three hours 5µM HgCl was added. With this low concentration, toxicodynamic effects to the cells are detected, which shows the high sensitivity of this cell based system. Five hours later the experiment was stopped adding 0,7% Triton X-100 to the media.

III. Results and Discussion

Cellular vitality was monitored using the incorporated microsensors. Microscopic images with a standard laboratory microscope where taken at the beginning (figure 3) and at the end (figure 4) of the experiment.

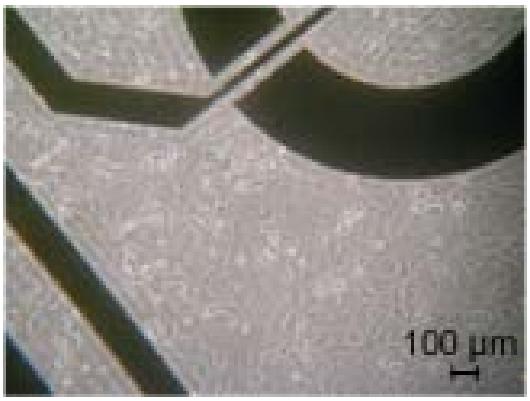


Fig. 3: Microscopic image of vital 3T3 fibroblasts on a BioChip-G.

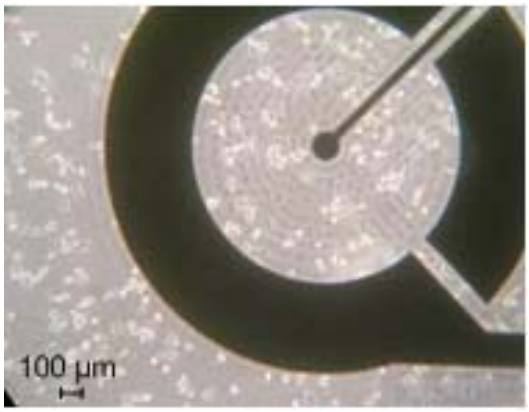


Fig. 4: Microscopic image at the end of the experiment.
No vital 3T3 fibroblasts can be identified on the BioChip-G.

The corresponding signals from the microsensors show similar results. The acidification rate is high at the beginning of the experiment and almost zero at the end of the experiment. For statistical correlation, however, more experiments have to be performed.

The new platform can be used in various applications which include for example chemosensitivity[4], environmental monitoring[10] or as an alternative method for animal experiments[11].

Aknowledgment

Authors like to thank the *Bayerisches Wirtschaftsministerium* (TOU-0805-0007) for funding and Prof. Jürgen Frank (director zet life science laboratory) for helpful discussions and support.

References

1. Wilson GS, Gifford R. (2005) Biosensors for real-time in vivo measurements. Biosensors & Bioelectronics. 20:2388-2403
2. Spegel C, Heiskanen A, Skjolding LHD, Emneus J. (2008) Chip based electroanalytical systems for cell analysis. Electroanalysis. 20:680-702
3. Wolf B, Kraus M, Brischwein M et al. (1998) Biofunctional hybrid structures - cell-silicon hybrids for applications in biomedicine and bioinformatics. Bioelectrochemistry and Bioenergetics. 46:215-225
4. Henning T, Kraus M, Brischwein M, Otto AM, Wolf B. (2003) Relevance of tumor microenvironment for progression, therapy and drug development. Anti-Cancer Drugs. 15:7-14.
5. Brischwein M, Motrescu ER, Cabala E et al. (2003) Functional cellular assays with multiparametric silicon sensor chips. Lab Chip. 3:234-240.
6. Otto AM, Brischwein M, Motrescu ER, Wolf B. (2004) Analysis of Drug Action on Tumor Cell Metabolism Using Electronic Sensor Chips. Arch Pharm Pharm Med Chem. 337:682-686.
7. Wiest J, Brischwein M, Ressler J et al. (2005) Cellular Assays with Multiparametric Bioelectronic Sensor Chips. Chimia. 59:243-246.
8. Wolf B, Brischwein M, Lob V, Ressler J, Wiest J. (2007) Cellular signaling: aspects for tumor diagnosis and therapy. Biomedizinische Technik. 52:164-168.
9. Lob V, Geisler T, Brischwein M, Uhl R, Wolf B. (2007) Automated live cell screening system based on a 24-well microplate with integrated micro fluidics. Medical & Biological Engineering & Computing. 45:1023-1028.
10. Wiest J, Stadthagen T, Schmidhuber M et al. (2006) Intelligent mobile lab for metabolics in environmental monitoring. Analytical Letters. 39:1759-1771.
11. Wiest J, Grundl D, Schmidhuber M et al (2008) Cell based assay for label-free, long-term investigation of living cells as alternative testing method for toxicity, ALTEX, Suppl. Linz, 1, 77-78

Author: Dr. Joachim Wiest
Institute: cellasys GmbH – R&D
Street: Karlstrasse 96
City: Munich
Country: Germany
Email: wiest@cellasys.com

Silicon Based Devices for Intracellular applications

R. Gómez-Martínez[1,2], M. Duch[1], A. Sanchez[1], J. A. Plaza[1], and J. Esteve[1]

[1] Instituto de Microelectrónica de Barcelona, IMB-CNM (CSIC) / Micro and Nanosystems Department, Cerdanyola, Spain
[2] CIBER de Bioingeniería, Biomateriales y Nanomedicina (CIBER-BBN), Spain

Abstract— **Recent advances in microtechnology and nanotechnology have enabled Microelectromechanical Systems (MEMS) and nanoparticles to be used as interfaces in cell biology. Complex silicon based MEMS can be precisely micro-nanomachined offering higher performance and versatility. The development of intracellular silicon based devices is the key to providing real-time monitoring of activity within individual living cells.**

Keywords— **Silicon, microdevices, Cells, MEMS/NEMS.**

I. Introduction

Microsystems technologies have allowed the development of a great number of devices powerful for the characterization, monitoring and manipulation of single cell and culture cell. Semiconductor technologies beginning ~40 years ago can now be used to mass-produce complex structures very precisely at the micron and submicron scale, reaching an integration level of tens of millions of components in a square millimeter of silicon. Microelectronic fabrication technique was a field that advanced rapidly due to the precipitate interest of the integrated circuit industry. Usually, MEMS research has been applied to develop devices on micron scale, such as sensors, switches, micro particles, micro needles, microchips, etc. These devices are fabricated by the applications of different procedures as: photolithography, oxidation, sputtering, chemical vapor deposition and ion implantation [1].

In recent years microfabrication and micromachining techniques have been progressively integrated into biological studies opening new opportunities in cell biology [2,3]. A lot of examples of devices developed based on MEMS technology can be found in the literature. Silicon Microelectromechanical Systems have been applied to the nanomechanical analysis of cells [4, 5], the weighing of single cells [6] or for cell manipulation and positioning [7,8]. Similarly, the biomolecular application of BioMEMS has been demonstrated in molecular recognition [9, 10] or cell manipulation [11]. Additionally, some devices work as a microelectrodes array, microsensors or fluidic Microsystems but always from a non invasive point of view [12, 13]. On the other hand, there are a lot of examples of the application of micro/nano particles for different biological and medical applications: molecular marks, separation, concentration of cells, etc. These micro/nano particles can be made of several materials, with different sizes and properties (especially magnetic and fluorescent ones [14]). Up to now, only nanoparticles used as a markers (quantum dots and gold nanoparticles [15]) have been introduced in the cells or biological system for use in imaging [16, 17], diagnosis [18] or drug delivery [19].

In this work we show the combination of nano and micro technologies to obtain micro particles and barcodes devices based on silicon, polysilicon or combination of different materials with dimensions between 1 and 3 μm and 3 μm x 11 μm, which could contain functional nano devices. These objects, silicon based IntraCellular Chips (ICCs), that take advantage of MEMS (well-controlled shape and size, versatility and mass-production and chemical properties of material) but that are small enough to be internalized within living cells, organs or tissue. These devices could be used to monitoring intracellular parameters, including: cell behavior, chemical stimulus, movement, drug delivery etc.

II. Materials and methods

A. Fabrication and design.

Micro/Nano particles

Silicon microdevices were manufactured by combining photolithographic techniques with silicon microelectronic and microfabrication technologies (Fig. 1). This technology is essentially based on the combination of a device layer and a sacrificial layer coated onto a silicon wafer. The vertical dimensions of the chip are fixed with nanometer precision by the thickness of the device layer (silicon or polysilicon) while photolithographic techniques define the micrometric or even sub-micrometric lateral dimensions. The devices were then obtained by vertical dry etching of the device layer, followed by their release from the wafer substrate by etching the sacrificial layer (silicon oxide). Finally, the devices were suspended in ethanol and collected by ultrasound. This approach yielded more than 150 million devices per processed 4-inch wafer, each of a controlled and repro-

O. Dössel and W.C. Schlegel (Eds.): WC 2009, IFMBE Proceedings 25/VIII, pp. 365–368, 2009.
www.springerlink.com

ducible shape and dimensions. After testing different shapes and dimensions, devices with lateral dimensions or a diameter of 1.5-3 µm and with a thickness of 0.5 µm (polysilicon) or 1.5 µm (silicon) were selected for further study (Fig. 2).

In addition, a nickel layer was deposited by electroless on the surface of the single silicon micro particles (Fig. 2) in order to provide them magnetic properties. This will allow to detect and manipulate the particles magnetically from outside of the cell.

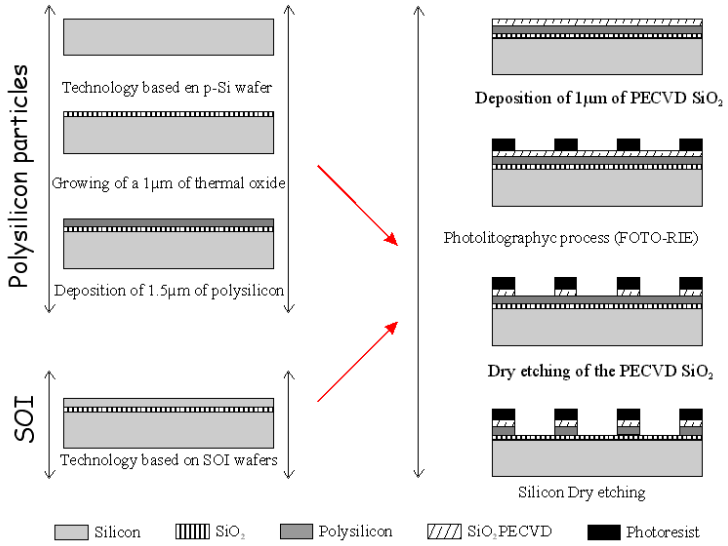


Figure 1. Scheme of the fabrication process of the silicon and polysilicon micro-objects

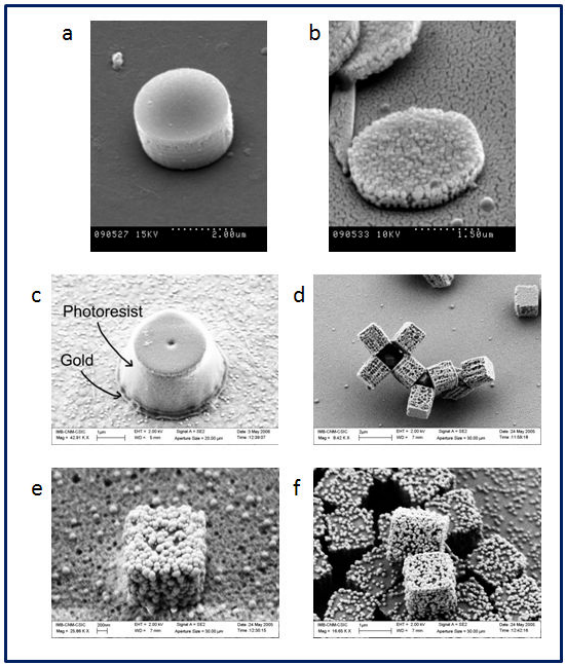


Figure 2. (a) 1.5 µm thick and 2 µm diameter silicon micro-object , (b) 0.5 µm thick and 2µm diameter polysilicon micro-object, (c) 20 nm gold disc with photoresit on top, (d) free 1 µm size silicon micro-particle, (e) nickel dots on the surface of a 1 µm silicon particle, (f) silicon micro-particle cover by electroless nickel layer.

Barcodes Devices

Some devices based on polysilicon to be used as barcode were also fabricated. A first barcode generation is based on a matrix concept, this divided into a regular 4 x 2 grid (Fig. 3) that contains a total of 8 bits (1 or 0) to give a binary data to the barcode reader, which means 256 different codes. Barcodes have to be asymmetric in order to allow the correct reading of data; for this reason, the barcodes have been designed with a start marker to help the user to read the message in its correct orientation. As most cell studies are performed using light and confocal microscopes, features smaller than 1 µm could be difficult to identify. Thus, considering the code visibility, the lateral dimensions of the barcodes were fixed to 10 µm x 6 µm. In contrast, the thickness of the barcode was fixed to submicron dimensions, 500 nm, according to the small volume criteria. Due to the submicron range of the thickness of the barcode, the maximum volume of an individual barcode was 30 μm^3; thus, the volume of the barcode is approximately 20 to 500 times smaller than that of many typical cells. Barcode microdevices were fabricated using the combination of a device layer and a sacrificial layer coated onto a silicon wafer.

A Plasma enhanced chemical vapor deposition (PECVD) silicon oxide layer was deposited on the front side of the wafer to be used as a sacrificial layer. The next step was the deposition of the device layer, a 0.5 µm thick Low-pressure chemical vapor deposition (LPCVD) polysilicon layer. The barcodes were patterned by a photolithographic step and a posterior dry etching. The etching uniformity through the whole wafer and the vertical profile of the etching were required due to the extremely small dimensions of the codes (10 x 6 x 0.5 µm). Barcodes were patterned by vertical silicon/polysilicon dry etching using an optimized Bosh process recipe. Finally, the codes were released by the etching of the silicon oxide sacrificial layer in vapors of acid fluoride.

A second generation of barcodes have been design and fabricated based on 3D silicon etching process (Fig. 4) . The proposed technology is also based on silicon micromachining in order to obtain micrometer-sized structures with well-controlled. A silicon wafer is used as substrate, then by varying etching condition, such us vertical or non-vertical etch profile. Non vertical profile defines Bit=0 and vertical profiles defines Bit=1. Compare to 2D barcodes, 3D barcodes offer less sensitive reading, due to the spatial orientation of the code respect to the reader.

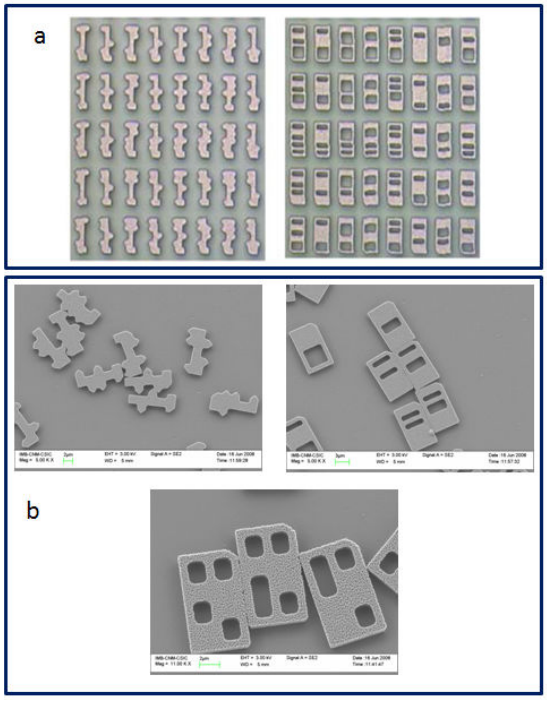


Figure 3. (a) Optical and (b) SEM images of barcodes polysilicon devices

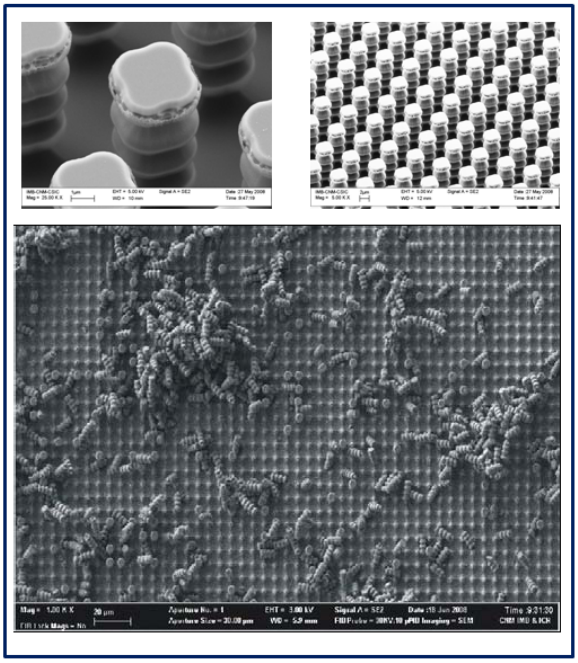


Figure 4. SEM images of a 3D silicon barcode.

III. CONCLUSIONS

For instance, ICCs microdevices and barcodes have been manufactured of silicon, polysilicon, or in combination of different materials. The devices show a high control on their shapes and dimensions. Our results suggest that silicon based top-down fabricated ICCs (1.5 - 3 μm) could be internalized, using techniques as fagocytosis or lipofection by eukaryotic cells and suggest that functionalized ICCs could be used as intracellular sensors or actuators. Devices composed of different materials open the door to their use for different biological purposes. ICCs conjugate mass production, biocompatibility and potential functionalization of their surfaces. In addition, ICCs offer higher flexibility and versatility in shape, size and materials because they take advantages of the MEMS technologies. Hence, it has the potential to generate more complex intracellular devices in the future as MEMS or NEMS.

ACKNOWLEDGMENT

This study was financed by the Spanish government through the MINAHE 2 project MECTEC2005-07996-CO2-01, MINAHE 3 project MEC-TEC2008-06883-CO3-01, the health researchproject SAF2007-66175 (to EJdlR), and the INTRACELL project CSIC-200550F0241 8 (to JE, EJdlR & FSB). We also wish to thank the MEC-GICSERV program and the IMB-CNM clean room staff.

REFERENCES

1. R. Jeager (1993) Introduction to microelectronic fabrication, Addison-Weslet, Reading, MA.
2. Withesides G. M. (2003) The 'right' size in nanobiotechnology. Nature Biotech. 21:1161-1165.
3. Weibel, D. B., Di Lucio, W. R. and Whitesides, G. M. (2007). Nature Rev. Microbiol. 5:209-218.
4. Bao, G. & Suresh, S. (2003) Cell and molecular mechanics of biological materials. Nature Mater. 2:715-725.
5. Cross, S. E., Jin, Y. S., Rao, J. et al (2007). Nanomechanical analysis of cells from cancer patients. Nature Nanotechn. 2:780-783.
6. Burg, T. P. et al. (2007) Weighing of biomolecules, single cells and single nanoparticles in fluid. Nature 446:1066-1069.
7. Lee, H., Liu, Y., Ham, D. et al (2007). Integrated cell manipulation system—CMOS/microfluidic hybrid. Lab Chip 7:331-337.
8. Gray, D.S., Tan, J.L., Voldman, J. et al (2004). Dielectrophoretic registration of living cells to a microelectrode array. Biosens. Bioelectron. 19:1765-1774 .
9. Fritz, J. et al (2000) Translating Biomolecular Recognition into Nanomechanics. Science 288: 316-318.
10. Shekhawat, G., Tark, S. H. and Dravid, V. P. (2006) MOSFET-Embedded Microcantilevers for Measuring Deflection in Biomolecular Sensors. Science 311:1592-1595.
11. Striemer, C. C., Gaborski, T. R., McGrath, J. L. & Fauchet, P. M. Charge- and size-based separation of macromolecules using ultrathin silicon membranes. Nature 445, 749-753 (2007).
12. Wolf B., Brischwein M., Baumann W., et al (1998) Monitoring of cellular signalling and metabolism with modular sensor-technique: the PhysioControl-Microsystem (PCM®), Biosens. Bioelectron. 13:501–509.
13. S. Hediger, A. Sayah, M.A.M. Gijs, (1999) Fabrication of a novel microsystem for the electrical characterisation of cell arrays", Sensors and Actuators B: Vol. 56, 1-2, 1:175-180.
14. OV Salata, "Applications of nanoparticles in biology and medicine", J. of Nanobiotechnology., 2:3, 2004.
15. Y.W. Lin, M.J. Huang and H.T. Chang (2003) Analysis of double-stranded DNA by microchip capillary electrophoresis using polymer solutions containing gold nanoparticles, J. of Chromatography A, Volume 1014, Issues 1-2:47-55.
16. Bruchez, M., Jr., Moronne, M., Gin, P., et al (1998) Semiconductor Nanocrystals as Fluorescent Biological Labels. Science 281:2013-2016.
17 Heller, D. A. et al.(2006) Optical Detection of DNA Conformational Polymorphism on Single-Walled Carbon Nanotubes. Science 311:508-511.
18. Wagner, V., Dullaart, A., Bock, A. K. et al (2006) A. The emerging nanomedicine landscape. Nature Biotech. 24:1211-1217.
19.. Akin, D. et al (2007) Bacteria-mediated delivery of nanoparticles and cargo into cells. Nature Nanotechn. 2: 441-449.

Use macro [author address] to enter the address of the corresponding author:

Author: Rodrigo Gómez-Martínez
Institute: Centro Microelectronico de Barcelona, IMB-CNM (CSIC)
Street: Campus UAB s/n 08193
City: Bellaterra / Barcelona
Country: SPAIN
Email: Rodrigo.gomez@imb-cmn.csic.es

Cell Select – A New Concept for Collecting of Rare Cell Populations *in vivo*

S. Pietschmann[1], R. Martin[2], T. Schoen[2], J.P. Spatz[2], and U. Pison[1]

[1] Charité-Universitätsmedizin Berlin, Department Anesthesiology, Berlin, Germany
[2] Max-Planck-Institute for Metals Research & University of Heidelberg, Germany

Abstract— **Diagnostic procedures seek to provide measures of analytes, cells and their components, morphological structures or molecular fingerprints to guide therapy. Such procedures are limited by the concentration of analytes or cells, the dimension of morphological structures and the identification of a given molecular state with a distinct state of health or disease. To improve diagnostic procedures the increase of analyte and cell concentration in blood, tissue or other body fluid samples is desirable. Material science and engineering could construct new devices that may enable the enrichment of analytes and cells *in vivo* or *ex vivo* for subsequent testing.**

We functionalized two kinds of substrates with specific antibodies (IgG) that were directed against distinct cell surface antigens. One substrate was characterized by nano-patterned gold dots, the other by a solid gold surface. Mouse monoclonal IgG, directed either against CD4 or HLA-G cell surface epitopes, was covalently bound to gold islands or solid gold surfaces using linker chemistry. With both kinds of substrates and three types of linker specific cells were enriched and collected out of samples that resemble *in vivo* conditions: CD4+ lymphocytes in blood samples and trophoblasts under flow conditions. Using ^{125}J-labelled IgG we demonstrated stable binding of antibodies to substrate (5,6 to 10,2 ng/mm^2, depending on linker type) with less than 10 % loss of ^{125}J-IgG over a time frame of 30 days.

We conclude that nano-patterned and solid gold surfaces could be functionalized with antibodies for collecting of rare cell populations in biological samples. Biopsy devices may be constructed for the enrichment of cells *in vivo*, if unspecific reactions could be ruled out.

Keywords— **biopsy device, point-of-care-diagnostic, prenatal diagnostic, trophoblast, disseminated tumor cells.**

I. Introduction

For the guidance of therapy various diagnostic procedures are used that include chemical and cellular analyses and imaging technologies. To obtain samples of tissue, cells or analytes out of the body of animal or men for subsequent testing, biopsy devices are frequently used in medicine. In order to obtain a biopsy sample, the biopsy device must be inserted into the body to reach the appropriate compartment for sampling tissue, cells or analytes of interest. One major limitation of biopsy in general is that the obtained sample does not include the tissue, cell or analyte of interest. To increase the probability that the material of interest is sampled in an appropriate concentration to be detectable in subsequent testing multiple biopsies could be taken or the sample volume could be increased. The number of biopsies and increasing sampling volume, however, is limited in living animal and human. Thus, new biopsy devices are desirable that have the capacity to enrich rare analytes or cell populations *in vivo*.

We present first data on a new concept for collecting of rare cell populations under *in vivo* conditions that should enable the construction of improved biopsy devices. Such devices are especially useful for point-of-care-diagnoses in cancer patients and for non-invasive prenatal diagnoses [1-3].

II. Materials and Methods

Materials: All chemicals were analytical grade and purchased from Sigma-Aldrich or Pierce. Anti human CD4-IgG was purchased from Becton Dickinson, Europe. The anti human HLA-G antibody was obtained from EXBIO Praha, Czech Republic.

Substrate preparation and functionalization: Two types of substrates were prepared for cell experiments. One was a gold wire with 1 mm diameter that had a solid gold surface. The other type was nano-patterned gold islands on glass which was obtained using micelle nanolithography as described elsewhere [4]. The distance between the gold nanodots were adjusted to 30 nm, 60 nm or 120 nm, respectively. The glass area not covered by gold nanodots was blocked by PEG against non-specific adsorption of proteins and cells [5]. To both types of substrates mouse monoclonal IgG antibodies were covalently bound using three different linker types, type 1, 2 and 3.

Binding capacity and stability of IgG: Mouse monoclonal IgG antibodies were iodinated by the lactoperoxidase glucose oxidase method using Bio-Rad Enzymobeads. Free Na^{125}J was separated from ^{125}J-IgG on a Bio-Gel PGDG column. Fractions that contained radioactivity that was > 88% precipitable by trichloroacetic acid were combined and used for binding studies on solid gold surfaces and using the three linker types. Specific activities ranged from 0,7 to 1,6 µCi/µg protein. Radioactivity was counted using gamma scintillation.

O. Dössel and W.C. Schlegel (Eds.): WC 2009, IFMBE Proceedings 25/VIII, pp. 369–371, 2009.
www.springerlink.com

Cell experiments: Cell experiments were carried out using human blood samples or AC1M32, a trophoblast-hybrid cell line. Heparinised human blood samples were incubated for 30 minutes with anti-CD4 IgG functionalized solid gold surfaces at room temperature under continuous agitation. After incubation substrates were washed three times in phosphate buffered saline and incubated for 10 minutes with Alexa-Fluor 488-anti-CD4 IgG before microscopy. The trophoblast-hybrid cells were incubated under flow (2 to 300 ml/min) and no-flow conditions with substrates that carried nano-patternd gold dots or a solid gold surface and that were functionalized with anti-HLA-G IgG, respectively. Cells were counted using transmitted light microscopy.

III. Results and Discussion

Substrate preparation and functionalization: Solid gold surfaces that were given in our case by gold wires could be easily functionalized with antibodies. Other geometric forms like gold foils, tubes or gold cylinders are possible alternatives and are simple to produce.

Micelle nanolithography revealed substrates with nano-patterned gold dots. The advantage of this technique is that the distance between the dots could be adjusted in the nanometer range for the reassembling of biological surfaces that favor cellular attachment and growth. Both types of substrates could serve as a sustained basis for various linker types for the covalent bonding of antibodies and other molecules for the targeting of cells and analytes (Fig. 1).

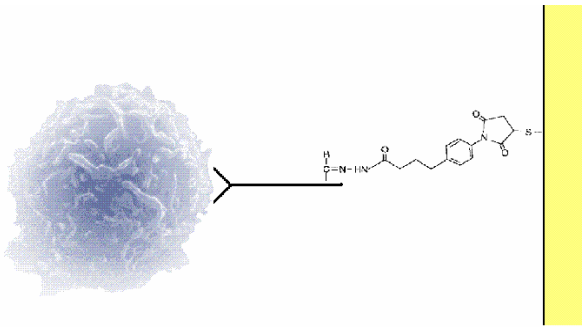


Fig. 1: Conceptual scheme for how to collect cell population in biological samples. Antibody directed against specific cell surface epitope is covalently bound through linker to solid or nano-structured gold.

Binding capacity and stability of IgG: Mouse monoclonal IgG antibodies that were iodinated with ^{125}J bound to gold surfaces with capacities that depend on the linker type (Table 1). Linker type 1 revealed the highest binding capacity on solid gold substrates (10,2 ng/mm^2 surface). Using the other two linker types we found binding of 5,6 and 9,7 ng/mm^2, respectively. The stability of binding over time was very strong. Detachment of IgG was less than 10 % and after 2 weeks no significant further dissolution of IgG was measured. These data indicate that the linker type influences binding capacity but not detachment.

Table 2 ^{125}J-IgG binding to solid gold surfaces and stability of binding

Linker Type	^{125}J-IgG after binding [ng/mm^2]	^{125}J-IgG after 2 weeks [ng/mm^2]
Type 1	10,2	9,6
Type 2	5,6	4,9
Type 3	9,7	8,7

Cell experiments: Gold wires with aCD4-IgG bound to their surfaces were covered after 30 minutes of incubation in a heparinised human blood sample with only one single cell type – CD4+lymphocytes (Fig. 2). The identity of the cell type was verified using Alexa-Fluor 488-anti-CD4 IgG and fluorescence microscopy.

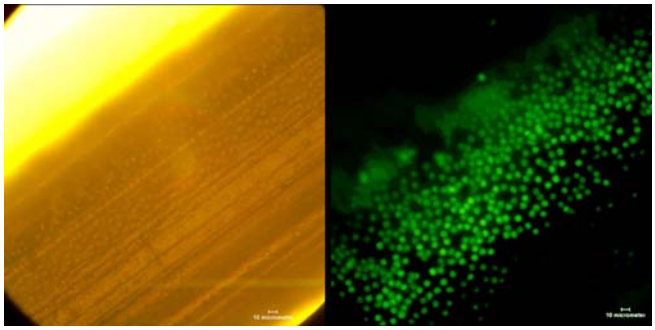


Fig. 2: CD4+ cells are enriched on solid gold substrates. Substrate was functionalized with mouse-anti-human-CD4-IgG and cells were enriched out of a regular blood sample. Left– picture taken in transmitted light setting; right – picture taken with fluorescent light setting

Trophoblast-hybrid cells (AC1M32) were binding to substrates that carried nano-patternd gold islands or a solid gold surface and were functionalized with anti-HLA-G IgG. The amount of cell binding depended on the distance of the gold nano dots, but significant cellular binding also occurred on solid gold surfaces (Fig. 3).

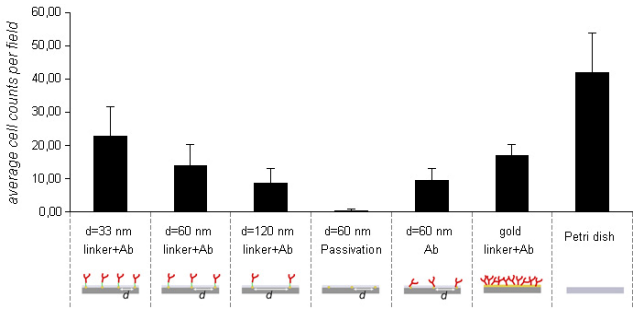


Fig. 3: Trophoblast-hybrid cells (AC1M32) bind to nano-patterned gold dots or solid gold surfaces that were functionalized using anti-HLA-G IgG. The distance of gold dots strongly influences the amount of cell binding.

Under flow conditions between 2ml/min and 300ml/min we observed cell adherence. However, the highest the flow rate, the lowest the number of cells which adhere.

IV. Conclusions

We conclude that nano-patterned and solid gold surfaces could be functionalized with antibodies for collecting of rare cell populations in biological systems. PEG passivated nano-patterned gold surfaces may have advantages compared to solid gold, since less amount of antibody is required for the same effect and the specificity of the surfaces might be substantially higher. Solid gold surfaces, however, are easier and cheaper to produce.

Prior *in vivo* use of this technology as a biopsy device certain tests have to demonstrate safety and experimental data should be provided on selectivity and specificity.

Acknowledgment

Financial support from the BMWI (ZIM), BMBF (Go-Bio) and the Max Planck Society is acknowledged.

References

1. Torricelli F, Pescucci C (2001) Isolation of fetal cells from the maternal circulation: Prospects for the non-invasive prenatal diagnosis. Clin Chem Lab Med 39:494-500
2. Joyce JA, Pollard JW (2009) Microenvironmental regulation of metastasis. Nature Reviews Cancer 9:239-252
3. Oudejans CBM, Tjoa ML et al. (2003) Circulating trophoblast in maternal blood. Prenatal Diagnosis 23:111-116
4. Lohmueller T, Bock E, Spatz JP (2008) Synthesis of quasi-hexagonal ordered arrays of metallic nanoparticles with tuneable particle size. Adv Mater 20:2297-2302
5. Blümmel J, Perschmann N et al. (2007) Protein Repellent Properties of Covalently Attached PEG Coatings on Nanostructured SiO_2 Based Interfaces. Biomaterials 28:4739-4747

Address of the corresponding author:

Prof. Dr. med. Ulrich Pison
Charité-Universitätsmedizin Berlin
Augustenburger Platz 1
13353 Berlin
Germany
ulrich.pison@charite.de

Combined AFM-SECM: Towards a novel platform for imaging microbiosensors

Justyna Wiedemair[1], Jong-Seok Moon[1], D. E. Eaton[2], Boris Mizaikoff[3], Christine Kranz[3]

[1] School of Chemistry and Biochemistry,
Georgia Institute of Technology,
Atlanta 30311, GA, U.S.A

[2]School of Physiology,
Emory University,
Atlanta xx, GA, U.S.A

[3]Institute of Analytical and Bioanalytical Chemistry
University of Ulm
Albert-Einstein-Allee 11
89081 Ulm, Germany

Abstract— **The combination of atomic force microscopy (AFM) and scanning electrochemical microscopy (SECM) has emerged as a versatile tool for simultaneous measurement of topographical and electro(chemical) properties at the sample surface. In particular, the implementation of a miniaturized amperometric biosensor into AFM-SECM probes is an attractive method to obtain laterally resolved information on biologically/biomedically relevant processes. However, improvement of the electrochemical transducer is a requirement for more complex biosensor architectures.**

Keywords—AFM-SECM, microbiosensor, ion-induced deposition (IBID), imaging microbiosensor

2. INTRODUCTION

Combining scanning probe techniques such as scanning force microscopy (AFM) and scanning electrochemical microscopy (SECM) has gained considerable interest in recent years. We have demonstrated AFM-SECM probes with tip-integrated micro-/nano-electrodes that are recessed from the apex of the AFM tip [1-3]. AFM-SECM probes with the electroactive area at the apex of the combined probe [4-6] have been demonstrated. Although these probes show a superior resolution in electrochemical imaging, they are not suitable for further modification as the tip apex is in contact with the sample surface (contact mode) or touching the surface (intermittent mode), and hence, the biosensor layer immobilized at the combined probe might suffer damage or got removed. With an electroactive area recessed from the probe we could successfully demonstrate the integration of enzymatic biosensors, and simultaneously imaging topography and glucose transport through a artificial membrane in intermittent mode AFM [7]. Recently, we focused on implementing more complex biosensor architectures such as a detection scheme for ATP sensing at AFM-SECM tips. However, given the competitive nature of the enzymatic conversion, signals obtained from the transducers in the size of several hundred nanometers are in the low pico- to femto-ampere range, and due to the scanning nature of the experiment provide an unfavorable signal-to-noise ratio. In addition, if these small electrodes are employed as transducer for the design of more complex biosensors involving more biological components, only small amounts of biomolecules can be immobilized Hence, we present strategies for improved tip-integrated electrochemical transducer platforms enabling more complex biosensor architectures.

Focused ion beam induced deposition

An elegant way of increasing the transducer surface without losing significantly the lateral resolution for the electrochemical imaging is based on localized metal deposition using focused ion beam (FIB) technology. Besides the possibility of three-dimensional structuring using a focused ion beam, deposition can be achieved using additional chemistries within the FIB chamber [8, 9]. During the deposition process, a precursor is vaporized into a high vacuum environment in the vicinity of a substrate. Precursor molecules adsorbed to the sample surface are dissociated into smaller chemical structures and individual elemental con-

O. Dössel and W.C. Schlegel (Eds.): WC 2009, IFMBE Proceedings 25/VIII, pp. 372–375, 2009.
www.springerlink.com

stituents by exposing the surface to a focused ion beam. The IBID process can be described as a localized chemical vapor deposition process, whereby the interaction of incident ions, sputtered material, and secondary electrons with the precursor causes fragmentation and formation of volatile and non-volatile species. The on-volatile fragments form three-dimensional structures at the sample surface with a geometry controlled by the selected pattern. A scheme of the IBID process is shown in Figure 1.

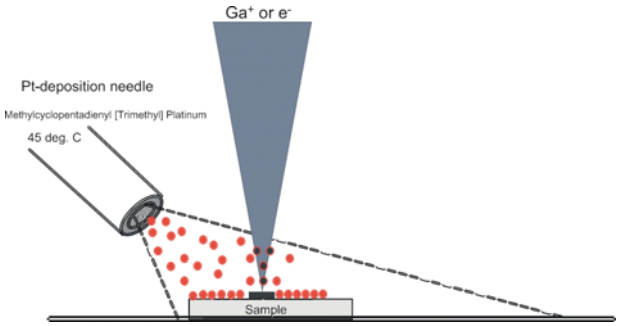


Figure 1: Scheme of the ion beam induced Pt deposition process

As organometallic precursor for the deposition of platinum composites methylcyclopentadienyl [trimethyl] platinum (C9H16Pt) has been used. The material formed during the decomposition process includes a substantial amount of carbon impurities given the organometallic nature of the precursor. Additionally, gallium ions are implanted in the matrix as a second contaminant, since a focused gallium ion beam is used during IBID. Platinum fractions varying from 15 atomic% (at%) to 50 at% are reported in literature depending upon the deposition conditions (7, 19, 20).
Prior to the deposition of IBID, cantilever were coated with a metal layer (typically gold or platinum) and consecutively insulated with PECVD silicon nitride or vapor deposited parylene coating as previously published. Focused ion beam milling was used to expose frame electrodes at AFM-SECM probes. (). Protruding PtC frames were deposited at AFM tip-integrated Au frame electrodes via IBID. *Figure 4.4A* shows representative CVs recorded in Ru(NH3)63+/2+ solution before and after the deposition of the PtC frame; the corresponding SEM images are shown in *Figure 3* The limiting steady-state current observed increases approx. 4-fold after the deposition of the PtC composite material. Considering the well-defined sigmoidal shape of the CV, which indicates fast electron transfer at the heterogeneous interface this is very encouraging meaning that IBID has the capability to enable increasing the tip-integrated electrode area.

3. MATERIALS AND METHODS

Chemicals

Hexaammineruthenium(III) trichloride ($Ru(NH_3)_6^{3+/2+}$, , potassium chloride were obtained from Sigma-Aldrich, (St. Louis, MO). Aqueous solutions were prepared with deionized water (Millipore, Billerica, MA) with resistance of 18.2 M Ω cm at 25 °C. All solutions were sparged with argon (Airgas, Marietta, GA).

1. Ion beam induced deposition of Pt/C

Ion beam induced deposition was performed with a Quanta 200 3D DualBeam (FIB/SEM) system (FEI Company, Hillsboro, OR) equipped with a gas injection system (GIS). The organic precursor used for deposition was methylcyclopentadienyl [trimethyl] platinum ($C_9H_{16}Pt$), which was heated to 39 °C and evaporated into the vacuum chamber through a gas injection system. A dwell time of 200 ns and a relative interaction diameter of 150 % (beam overlap of 0 %) of the gallium beam was used for depositions ATP microbiosensor was rinsed with phosphate buffer and stored for 2 hours at 4°C prior electrochemical analysis.

2. Electrochemical Experiments

Electrochemical measurements were performed with a CHI 842 bipotentiostat equipped with a Faraday cage and preamplifier (CH instruments, Austin, TX). All experiments were performed in a three electrode set-up with the AFM-SECM tip integrated IBD electrode as working electrode, a Ag/AgCl reference electrode and a Pt counter electrode.

3. AFM Imaging

Imaging was obtained using an AFM (model 5500, Agilent Technologies, Chandler, AZ) equipped with a liquid cell. The 5500 AFM operates in a “top-down” configuration with the AFM probe mounted on the piezo-scanner for imaging of the sample surface. The AFM was placed in a vibration isolation chamber (Agilent Technologies, Chandler, AZ), and additionally in a Faraday cage (home-built) in order to reduce environmental vibration and electromagnetic noise. AFM images were post-processed with the PicoScan 5.3.3 software (Agilent Technologies, Chandler, AZ) for tilt correction or flattening of the image background.

4. RESULTS AND DISCUSSION

Figure 2 shows representative CVs recorded in Ru(NH3)63+/2+ solution before and after the deposition of the PtC frame. The limiting steady-state current observed increases approx. 4-fold after the deposition of the PtC composite material. Considering the well-defined sigmoidal shape of the CV, which indicates fast electron transfer at the heterogeneous interface has the capability to enable increasing the tip-integrated electrode area. Approximately a 4-times increase of the steady state current is achieved.

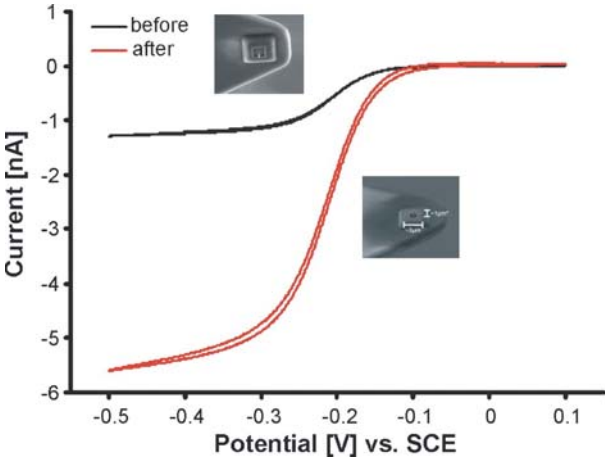


Figure 2: CVs recorded at tip-integrated AFM-SECM probe before and after the deposition of PtC layer via IBID in 5 mM $Ru(NH_3)_6^{3+/2+}$ containing 0.5 M KCl supporting electrolyte (scan rate 0.1 V s^{-1}). (B) Corresponding top-view SEM images showing the PtC frame.

Combined AFM-SECM imaging was performed to demonstrate that increasing the electroactive area of the integrated electrode, while only increasing slightly the outer diameter of the frame-shaped electrode does not significantly reduce the electrochemical localization power. Simultaneously recorded contact mode AFM images and feedback mode electrochemical surface properties are shown in Figure 3.

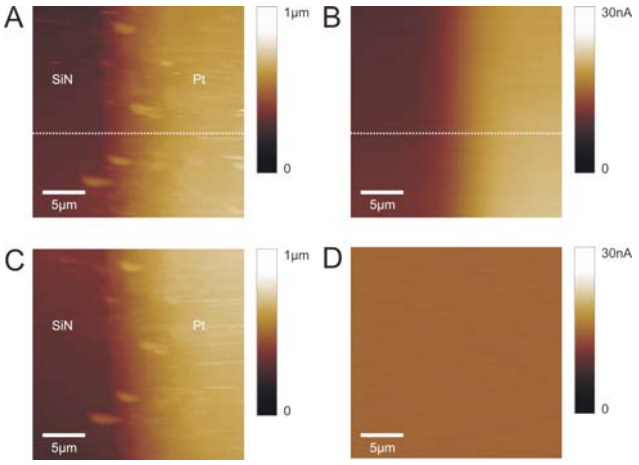


Figure 3: Simultaneous AFM-SECM imaging of elevated platinum features on a silicon nitride substrate. Topography (A and C) and current (B and D) images are shown. The tip-integrated PtC electrode was biased at -0.45 V (A and B) and 0 V (C and D) vs. AgQRE, respectively, in a 5 mM $Ru(NH_3)_6^{3+/2+}$ solution containing 0.5 M KCl. The tip was scanned in contact mode AFM with a scan rate of 0.72 lines s^{-1} (original scan size: 45 × 45 µm^2). The edge length of the PtC frame electrode was 3.3 µm and the tip length 1.2 µm.

Images were recorded at two different electrode biases to proof the electrochemical functionality of the IBID electrode. The electrode was biased at -0.45 V vs. AgQRE (A and B) for the reduction of $Ru(NH_3)_6^{3+/2+}$. The elevated platinum grid (sample) leads to a positive feedback effect resulting in a localized current increase. As expected, the insulating silicon nitride substrate results in a negative feedback effect as seen by the decreased current. As a control experiment the tip was biased at 0 V, where no considerable reduction of $Ru(NH_3)_6^{3+/2+}$ occurs. Correspondingly, the current image (D) shows no differences in current level depending on electrical properties of the surface, although the AFM tip was still scanned across the step of the grid as seen in the topography (C). This result demonstrates that AFM-SECM imaging is possible with AFM tip-integrated PtC electrodes while maintaining sufficient electrochemical spatial resolution to clearly resolve the step matching the topography. Starting and end points of the grid step are marked and overlap for both the current and the topography.

As the deposited Pt/C composite electrodes are characterized by a significant carbon content, their electrochemical behavior towards oxidation of hydrogen peroxide, one of the prominent electroactive by-products of oxidoreductase-catalyzed reactions, is less favorable. Hence, further treatment such as thermal annealing, ozone/UV treatment or post-deposition milling will be applied to remove carbon

from the electrode surface, and to enhance the kinetics of the H_2O_2 oxidation.

ACKNOWLEDGMENT

The authors are thankful for access to the MIRC cleanroom facility and the FIB Center at Georgia Tech. Financial support was generously provided by the National Institutes of Health (NIH, grant #EB000508).

REFERENCES

1. Kranz, C.; Friedbacher, G.; Mizaikoff, B.; Lugstein, A.; Smoliner, J.; Bertagnolli, E. Integrating an Ultramicroelectrode in an AFM Cantilever: Combined Technology for Enhanced Information, Anal. Chem. 2001, *73*, 2491-2500.
2. Kueng, A.; Kranz, C.; Mizaikoff, B.; Lugstein, A.; Bertagnolli, E. Combined scanning electrochemical atomic force microscopy for tapping mode imaging, Appl. Phys. Lett. 2003, *82*, 1592-1594.
3. Kueng, A.; Kranz, C.; Lugstein, A.; Bertagnolli, E.; Mizaikoff, B. Integrated AFM-SECM in tapping mode: Simultaneous topographical and electrochemical imaging of enzyme activity, Angew. Chem., Int. Ed. 2003, *42*, 3238-3240.
4. Macpherson, J. V.; Unwin, P. R. Combined Scanning Electrochemical-Atomic Force Microscopy, Anal. Chem. 2000, 72, 276-285.
5. Fasching, R. J.; Tao, Y.; Prinz, F. B. Cantilever tip probe arrays for simultaneous SECM and AFM analysis, Sens. Actuators, B 2005, *B108*, 964-972.
6. Frederix, P. L. T. M.; Bosshart, P. D.; Akiyama, T.; Chami, M.; Gullo, M. R.; Blackstock, J. J.; Dooleweerdt, K.; de Rooij, N. F.; Staufer, U.; Engel, A. Conductive supports for combined AFM-SECM on biological membranes, Nanotechnology 2008, *19*, 384004/384001-384004/384010.
7. Kueng, A.; Kranz, C.; Lugstein, A.; Bertagnolli, E.; Mizaikoff, B. AFM-tip- integrated amperometric microbiosensors: High-resolution imaging of membrane transport, Angew. Chem., Int. Ed. 2005, *44*, 3419-3422.
8. Young, R. J.; Puretz, J. Focused ion beam insulator deposition, J. Vac. Sci. Technol., B: Microelectron. Nanometer Struct. 1995, *13*, 2576-2579.
9. Edinger, K.; Melngailis, J.; Orloff, J. Study of precursor gases for focused ion beam insulator deposition, J. Vac. Sci. Technol., B: Microelectron. Nanometer Struct. 1998, *16*, 3311-3314.
10. Vila, A.; Hernandez-Ramirez, F.; Rodriguez, J.; Casals, O.; Romano-Rodriguez, A.; Morante, J. R.; Abid, M. Fabrication of metallic contacts to nanometer-sized materials using a focused ion beam (FIB) Mater. Sci. Eng., C 2006, *26*, 1063-1066.1066.
11. Telari, K. A.; Rogers, B. R.; Fang, H.; Shen, L.; Weller, R. A.; Braski, D. N. Characterization of platinum films deposited by focused ion beam-assisted chemical vapor deposition, J. Vac. Sci. Technol., B: Microelectron. Nanometer Struct. 2002, *20*, 590-595.
12. Langford, R. M.; Wang, T. X.; Ozkaya, D. Reducing the resistivity of electron and ion beam assisted deposited Pt, Microelectron. Eng. 2007, *84*, 784-788.

Microfluidic Platform for Investigating Small Blood Vessels

Conrad Lochovsky[1], Andrei Vagaon[2], Sanjesh Yasotharan[3], Darcy Lidington[2], Julia Voigtlaender-Bolz[2,4], Steffen-Sebastian-Bolz[2], and Axel Günther[1,5]

[1]Institute for Biomaterials and Biomedical Engineering
[2]Department of Physiology
[3]Division of Engineering Science, University of Toronto, Canada
[4]St. Michael's Hospital, Toronto, ON, Canada
[5]Department of Mechanical and Industrial Engineering, University of Toronto, Canada

Abstract— **Small resistance arteries, with diameters between 60 - 250 microns, play a key role in regulating peripheral vascular resistance by dynamically changing the artery diameter (tone), an important factor in the development of hypertension. We present a microfluidic device that allows functional and structural assays to be routinely conducted on small blood vessels, while overcoming several limitations that are associated with conventional cannulation procedures. The presented microfluidic platform was fabricated using standard multilayer soft lithographic techniques and is to our knowledge the first scalable approach with the potential to provide routine screening on an organ level. Mouse mesenteric arteries were used to obtain aggregate dose-response relationships for phenylephrine, a vaso-constrictor. Results demonstrated viability on chip and were consistent with measurements obtained in conventional cannulation systems. The presented approach may allow standardization in microvascular research and accelerate the discovery of antihypertensive drugs.**

Keywords— **microfluidics, resistance artery function, hypertension**

I. Introduction

Small resistance arteries (SRAs), with diameters between 60µm and 250µm, are crucial components of the cardiovascular system, and play a key role in regulating peripheral vascular resistance by dynamically changing the artery diameter (tone), an important factor in the development of hypertension [1]. The current understanding of small artery structure and function is also limited by the lack of experimental tools for probing it. Traditional methods employed to study 1-2mm segments of resistance arteries excised from mice are expensive, time-consuming, and conducted manually, requiring a highly specialized training. Despite the clinical and economical importance of cardiovascular diseases, the development pipelines of major pharmaceutical companies currently lack innovative antihypertensive drugs.

We present a microfluidic device that allows functional and structural assays to be conducted on small blood vessels, while overcoming the aforementioned limitations [2]. The platform is highly robust and scalable, allowing the opportunity for long-term culture of small blood vessels.

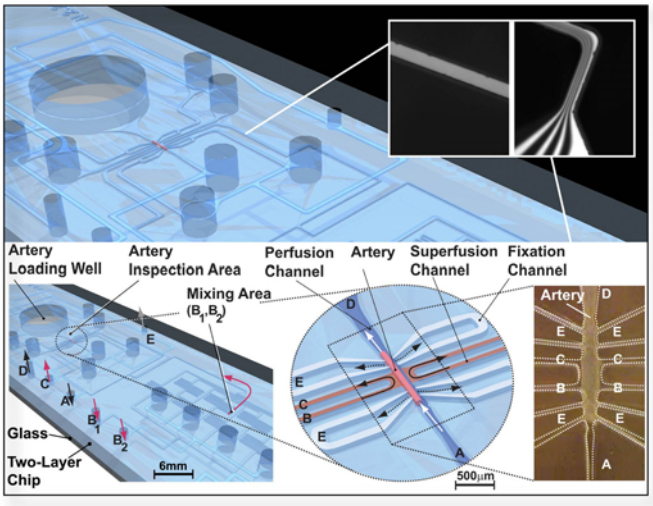


Fig. 1 Rendered image of the microfluidic chip with perfusion inlet (A) and outlet (D). The superfusion inlet consists of a drug-containing stream (B_1) that interdiffuses with stream (B_2), passes the outer wall of a loaded mesenteric artery and leaves through port (C). Ports (E) allow fixation of the artery segment and prevent cross-talk.

II. Chip Design and Fabrication

The microfluidic device was fabricated using standard multilayer soft lithography techniques. Figure 1 illustrates key device features of the device that is to our knowledge the first scalable platform with the potential to provide routine screening on an organ level. An approximately 1mm long resistance artery segment is introduced through a 5mm diameter loading well. Pressure-driven flow is used to guide it through the loading channel (labeled A) to the inspection area. The artery is then spatially fixed by applying suction pressures (E) at its end points.

O. Dössel and W.C. Schlegel (Eds.): WC 2009, IFMBE Proceedings 25/VIII, pp. 376–377, 2009.
www.springerlink.com

Subsequently, the center of the artery segment is subjected to a microenvironment mimicking physiological conditions by simultaneously superfusing the outer vessel wall (B C), perfusing the inside vessel lumen (A D) and applying a defined pressure difference across the vessel wall (transmural pressure). Unwanted crosstalk between the two streams is completely prevented by the fixation channels (E), which was simulated using a multi-physics analysis package (Comsol, Fig. 2a,b) and experimentally verified using fluorescence microscopy.

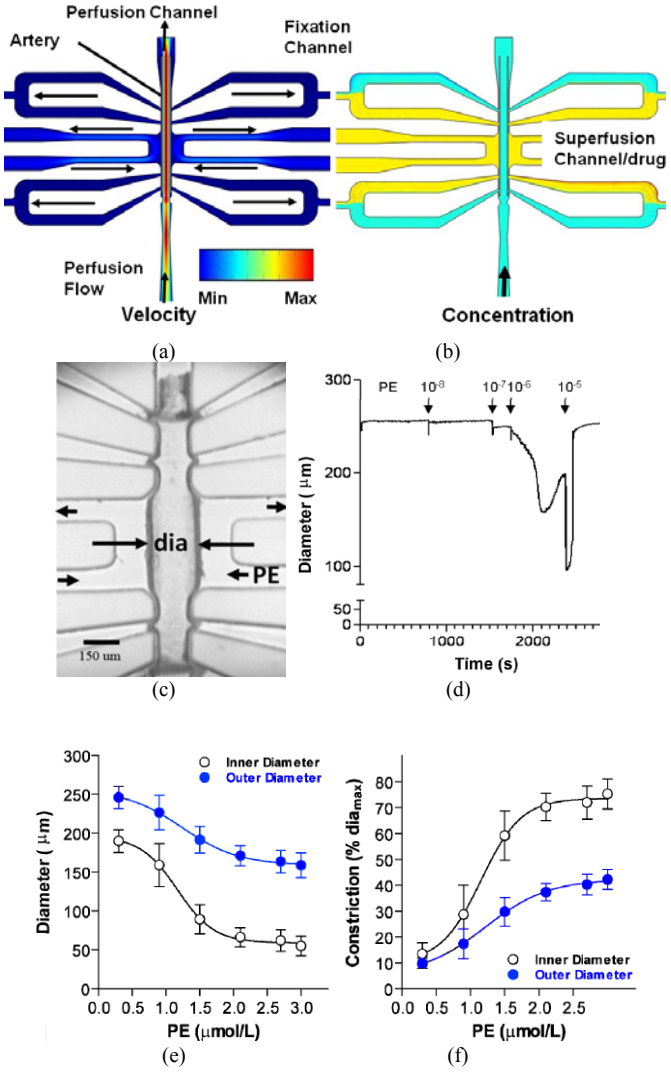


Fig. 2 Numerically obtained velocity (a) and concentration field (b) indicating the complete separation of the perfusing stream (center) and the superfusing streams. (c) Micrograph of perfused and superfused artery. (d) Single representative measurement of the artery diameter (tone) in response to step changes in the concentration of phenylephrine (PE) in the superfusing stream, and (e,f) aggregate dose response curves.

The temperature, flow rates, pressures and compositions of the superfusing/perfusing streams can be adjusted independently.

III. Results and Discussion

The microfluidic device was assessed by loading mesenteric arteries from mice, and performing functional assays to determine vessel viability after loading. Two individual feed streams (B_1 and B_2) were mixed on chip. By changing the relative flow rates of the feed streams via computer-controlled syringe pumps, the concentration of active substances in the resultant superfusion was selected, and the dynamic evolution of artery tone was recorded on an inverted microscope. An aggregate dose-response curve for phenylephrine (PE), a vaso-constrictor which acts on the smooth muscle cells of blood vessels, was derived from multiple sets of time-resolved brightfield measurements demonstrating viability of the vessel after loading (Fig.2d). Aggregate vessel response obtained with the microfluidic platform (Fig. 2e,f) was consistent with measurements obtained in conventional cannulation systems [3,4]. The presented microfluidic chip provides a versatile platform that can be easily adapted to a variety of animal-derived small resistance arteries. The scalable chip-based approach may allow standardization in microvascular research by replacing the current manual approaches and potentially accelerates the discovery of antihypertensive drugs.

Acknowledgment

We acknowledge financial support from the National Sciences and Engineering Research Council of Canada and are grateful for in-kind contributions provided by Quorum Technologies (Guelph, Ontario, Canada) and Nanopoint Imaging (Honolulu, Hawaii, USA).

References

1. Smith RET, Ashiya M (2007) *Nature Rev. Drug Discovery* **6** (8), 597
2. Guenther A, Bolz StS (2008), US provisional patent 61/073244
3. Halpern W, Osol G, Coy GS (1984), *Annals of Biomedical Engineering* **12** (5), 463.
4. Mulvany MJ, Halpern W (1976), *Nature* **260** (5552), 617.

Corresponding author:

Dr. Axel Guenther
Department of Mechanical and Industrial Engineering
Institute of Biomaterials and Biomedical Engineering
University of Toronto
5, King's College Road
Toronto, Ontario, Canada
Email: axel.guenther@utoronto.ca

Characterization of Electron Conduction in Unsaturated Organic Monolayers on Silicon(111) Using Electrical Impedance Spectroscopy

T.C. Chilcott, H.G.L. Coster, and D. Zamri

School of Chemical and Biomolecular Engineering, University of Sydney, Sydney, NSW 2006, Australia

Abstract— **Electrical impedance spectroscopy (EIS) studies of monolayers comprised of molecules of *Geranyllinalool* and *Isophytol* revealed structural and molecular organizational details that were compatible with crystallographic dimensions of these molecules. *Geranyllinalool* ($C_{20}H_{34}O$) and *Isophytol* ($C_{20}H_{40}O$) differ principally in the structures of their hydrocarbon backbones. Several carbon-carbon bonds in the *Geranyllinalool* backbone are double bonds (unsaturated) whereas those bonds in *Isophytol* are single (saturated). Even though the *Geranyllinalool* monolayers were thicker than the *Isophytol* monolayer, EIS further revealed that their conductivities were an order of magnitude higher than those of the *Isophytol* monolayers. This is consistent with the electron enriched double bonds in the *Geranyllinalool* backbone providing a better conduction path than the electron depleted single bonds in the *Isophytol* backbone. The study reveals that unsaturated organic monolayers can improve the electrical connectivity of the semiconductor-biological interface whilst maintaining biocompatibility and passivity.**

Keywords— **biosensors, monolayers, impedance, silicon, electron condution.**

I. INTRODUCTION

The future of biosensor and stimulatory electrodes lies in improving the interface between conventional electronics and targeted biological events.

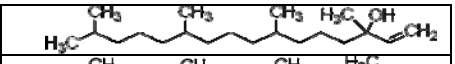
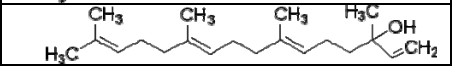
Conventional electronics utilizes semiconductors (silicon) and metals (e.g. gold) which electrically interact with each other via electron conduction but neither interacts as directly with the bulk aqueous biological environment where conduction is ionic. Silicon oxidizes to form a layer of SiO_2 whereas gold forms an "ionic double layer" in which ions form one layer in the aqueous phase and electrons form the other layer in the gold. Although the "ionic double layer" and the SiO_2 layer are only nanometers in thickness, they are very poor conductors of both electrons and ions. Neither provides the means of sensing biologically based electron transfers.

Successful detection of DNA-mediated electron transfers (see [1] and [2]) have been possible on gold but only after the interface was functionalized with single-stranded DNA probes distributed in an otherwise biologically passivated organic monolayer [3]. EIS unambiguously correlated an 8-fold increase in conductance with DNA-mediated electron transfers. Substantial capacitive changes, that were indicative of structural and/or dielectric variations arising from the formation of the double helices, were also correlated with the transfers. However, a specific characterization was complicated by the persistence of a modified ionic double layer and effects arising from the rough surfaces of gold.

Here we present an EIS study of electron transfers in organic monolayers attached directly to atomically flat silicon (i.e. no SiO_2 layer) without the complications associated with gold and the use of biologically incompatible ferric cyanide as an electro-catalyst in the aqueous phase [4].

The EIS study establishes procedures for studying structural and functional features of functionalized monolayers, such as those that facilitate DNA-mediated electron transfers.

Table 1 Molecular structure of *Isophytol* and *Geranyllinalool* highlighting the different types of carbon-carbon bonding in the hydrocarbon backbones

Isophytol	
Geranyllinalool	

II. EXPERIMENTAL

A. Silicon-Carbon Chemistry

Methods of attachment of organic monolayers to silicon are described in detail elsewhere [5]. Highly doped Si(111) wafers (0.01-0.1 Ωm) were cleaned in "Piranha" solution at 90℃ for 30 min and rinsed thoroughly with Milli-Q water and then etched in deoxygenated NH_4F solution for 20 min to generate hydride terminated Si(111) surfaces. The freshly etched surfaces were then converted to a Si-C linked monolayer through hydrosilylation in deoxygenated solutions of either *Geranyllinalool* or *Isophytol* by photochemical activation under UV light for 2-10 hours. The functionalized silicon wafers were then rinsed with hexane, dichloromethane, tetrahydrofuran and ethanol prior to drying thoroughly under a stream of nitrogen.

O. Dössel and W.C. Schlegel (Eds.): WC 2009, IFMBE Proceedings 25/VIII, pp. 378–381, 2009.
www.springerlink.com

B. *Electrical impedance measurements*

Impedance measurements were performed with an Inphaze Impedance Spectrometer (Inphaze Pty Ltd., Sydney, Australia) over a frequency (ω) range of 6 mHz to 100 kHz using the Inphaze 3-electrode electrochemical cell (Fig. 1). Gallium-indium eutectic was applied to the non-functionalized side of the wafer which was then placed on the working electrode where a low-ohmic contact was formed.

Ac electric current used for impedance measurements was injected into the wafer via the working electrode and the counter electrode immersed in a 100mM KCl electrolyte that also made contact with the functionalized surface of the wafer. A Ag|AgCl reference electrode (type LF-2 from Innovative Instruments Inc. 8533 Queen Brooks Ct.Tampa, FL 33637, USA) was located in an electrolyte filled recess in the chamber and monitored the electric potential response of the system to the *ac* current.

The chamber also featured a mechanism for sealing a precisely defined area of the functionalized surface while minimizing deformation of that surface. The significance of the rectilinear gasket and recessed reference electrode are described in detail elsewhere ([6], [7]).

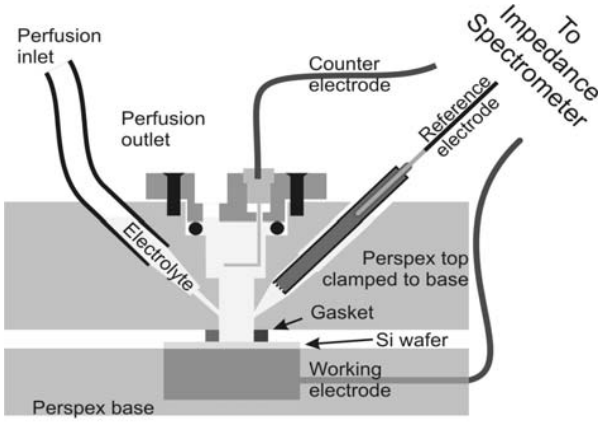


Fig. 1 Electrochemical Cell for monolayer characterisations (adapted from [7])

A systematic study of alkyl (saturated) monolayers of hydrocarbon chain length ranging from 10 to 18 carbons [8] has provided accurate estimates of the thicknesses of these layers using electrical impedance spectroscopy (EIS) and X-ray reflectometry (XRR) to better than an Angstrom resoltion. The EIS estimates were based on measurements of the capacitance per unit area, C, of the layer in contact with a KCl electrolyte, in which the thickness is given by;

$$d = \varepsilon \varepsilon_0 / C \qquad (1)$$

where ε is the dielectric constant of the layer (≈2.05) and ε_0 is the permittivity of free space (=8.85x 10^{-12} Fm^{-1}).

The conductance measurements for these layers were consistent with them acting as an insulator between the silicon and electrolyte.

III. Results and Discussion

The impedance data of the monolayer-electrolyte systems are shown in Fig 2 as dispersions of the conductance and capacitance with frequency ω The dispersion for both the *Geranyllinalool* and *Isophytol* systems converge at high frequencies yielding the conductance and capacitance values for the electrolyte (1st circuit element shown in Fig. 3).

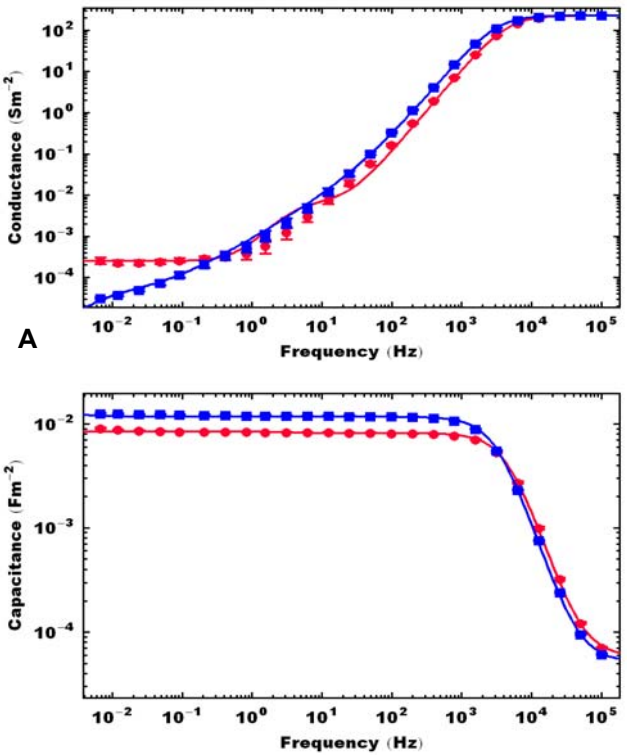


Fig. 2 Conductance (A) and capacitance (B) dispersions with frequency obtained from the impedance measurements of *Geranyllinalool* (●) and *Isophytol* (■) monolayers in contact with a 100mM KCl electrolyte. Convergence of data at high frequencies yields properties of the electrolyte whilst divergence at low frequencies reveals differences in properties of the monolayers.

The dispersions diverge at low frequencies revealing different conductive and capacitive properties of the *Geranyllinalool* (●) and *Isophytol* (■) monolayers. A Maxwell-Wagner model was readily fitted to the *Geranyllinalool* (●) data (Fig 3A). However, the divergence of the conductance data for the *Isophytol* (■) monolayers at very low frequencies (see Fig. 2A) could only be explained by a frequency (ω) dependent conductance element (g_3 in Fig. 3B). However, the capacitance dispersion in this frequency range was independent of frequency (see Fig. 2B) and yielded a capacitance value for the *Isophytol* monolayer (c_3 in Fig. 3B) that was independent of frequency.

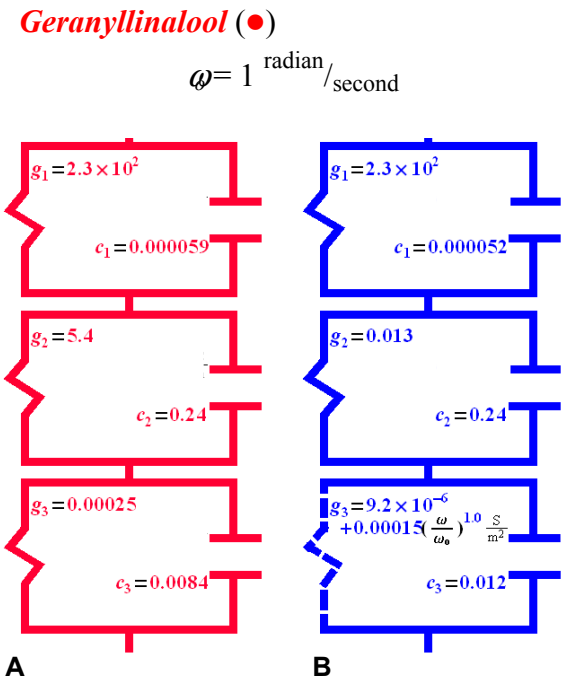


Fig. 3 Circuit diagrams for generating theoretical curves shown in Fig. 2 for the *Geranyllinalool* (A) and *Isophytol* (B) monolayer-electrolyte systems. The 1st circuit element yields conductance (g_1) and capacitance (c_1) values for the bulk electrolyte that are constant in frequency. The 3rd circuit element reveals capacitance values (c_3) that are constants in frequency for both monolayers. Whilst the conductance value (g_3) for the *Geranyllinalool* monolayer is also constant the conductance value for the *Isophytol* (B) monolayer includes a frequency (ω) dependent component. The 2nd circuit element is attributed to an interfacial layer between the electrolyte and monolayer.

An additional Maxwell Wagner element (2nd circuit element in Fig. 3) was required to fit the conductance and capacitance dispersions with frequency at mid-frequencies. Its electrical properties are indicative of an interfacial layer between the electrolyte and monolayer but are such that the layer does not contribute substantial to the total impedance of the systems, especially at low frequencies where electrical properties are indicative of the low conducting monolayers.

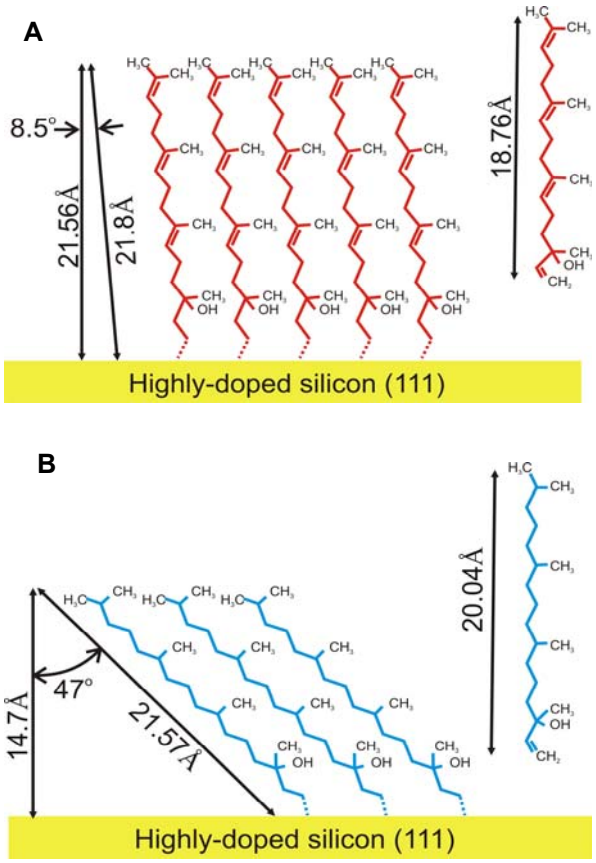


Fig. 4 Schematic of structures for *Geranyllinalool* (A) and *Isophytol* (B) monolayers. Thicknesses of the monolayers were etimated from the capacitance values obtained for the 3rd circuit elements shown in Fig. 3, assuming a dielectric constant of 2.05. Molecular dimensions are based on crystallographic studies and take into account reorientation of terminal groups upon reacting with the silicon.

The capacitance values for the monolayers (3rd circuit element in Fig. 3) provide a means of estimating the thicknesses of the layers using Eqn. 1. Schematics of the layers based on these thickness values and molecular lengths based on crystallography [9] are depicted in Fig. 4. These indicate that the *Geranyllinalool* molecules in the monolayer stand almost vertically whereas the *Isophytol* (B) molecules are orientated at an angle of approximately 47° to the normal. These canting orientations are consistent with expectations that the double C-C bonds in the *Geranyllinalool* molecule

would result in a more rigid hydrocarbon backbone than one comprised exclusively of single bonds such as the backbone of the *Isophytol* molecule.

Another expectation is that the electron rich double bonds in a backbone would also enhance electron transport through the monolayer. Indeed a comparison of the conductance values for the 3rd circuit in Fig. 3 (i.e. g_3) reveals that the conductance of the *Geranyllinalool* monolayer is at least an order of magnitude larger than the conductance of the thinner *Isophytol* monolayer.

The conductivities of the monolayers provide a comparison of the electron transference properties that is independent of the monolayer geometries. Conductivity in the "one-dimension" experimental system used in this study is given by;

$$\sigma = g_3 \, d_3 \qquad (2)$$

which yields a substantially larger conductivity value for the unsaturated monolayer as depicted in Fig. 5.

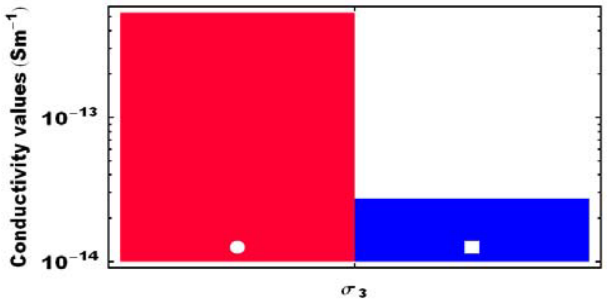


Fig. 5 Conductivity values for the *Geranyllinalool* (●) and *Isophytol* (■) monolayers calculated using Eqn. (2). Value of g_3 for the *Isophytol* monolayer was the projected *dc* value (i.e. ω=0)

IV. Conclusions

Electrical impedance spectroscopy facilitates precise characterizations of structural and functional features of functionalized monolayers that have been attached directly to atomically flat silicon.

Such characterizations can proceed without complications associated with oxidized layers, ionic double layers, rough surfaces and electro-catalysts in the aqueous phase.

Unsaturated organic molecules substantially enhance electron transfers.

Future work will explore roles that unsaturated organic molecules can play in coupling conventional electronics (silicon semiconductors) to targeted biological events.

Acknowledgment

We acknowledge the technical support of David Ta-Yuan Wang of Inphaze Pty Ltd.

References

1. Levicky R, Herne TM, Tarlov MJ, Satija SK (1998) Using self-assembly to control the structure of DNA monolayers on gold: A neutron reflectivity study. Journal of the American Chemical Society, 120:9787-9792
2. Arkin MR, Stemp EDA, Holmlin RE, Baron JK, Hormann A, Olson EJC, Barbara PF (1996) Rates of DNA-mediated electron transfer between metallointercalators. Science, 475-480
3. Chilcott TC, Wong ELS, Böcking T, Coster HGL (2008) Electrical characterizations of biomimetic molecular layers on gold and silicon substrates, Physiol. Meas., 29, S307–S319
4. Kelley SO, Boon EM, Barton JK, Jackson NM and Hill MG 1999 NucleicAcids Res. 27 4830-4837
5. Böcking T, James M, Coster HGL, Barrow KD, Chilcott TC (2004) Structural Characterization of Organic Multilayers on Silicon (111) Formed by Immobilization of Molecular Films on Functionalized Si-C Linked Monolayers, Langmuir 20(21): 9227-9235
6. Chilcott TC, Wong ELS, Böcking T, Coster HGL (2008) Electrical characterizations of biomimetic molecular layers on gold and silicon substrates, Physiol. Meas., 29, S307–S319
7. Chilcott TC, Wong ELS, Coster HGL, Coster AFC, James M (2009) Ionic double layer of atomically flat gold formed on mica templates Electrochimica Acta 54:14,3766-3774
8. Wong ELS, James M, Chilcott TC, Coster HGL, (2007) Characterisation of Alkyl-Functionalised Si(111) using Reflectometry and AC Impedance Spectroscopy, Surface Sciences 601:5740-5743
9. Geranyllinalool molecular structure retrieved from http://www.thegoodscentscompany.com/data/rw1041741.html and isophytol molecular structure retrieved from http://www.pherobase.com/database/synthesis/synthesis-detail-isophytol.php

The study of micro liter Insulin injection system by Osmotic pressure for Diabetes therapy

Toshiaki Nagakura[1], Kazuki Inada[1], Yuuto Susuki[1], Naohiro Yoshida[1],

Akira Yamada[2], Masashi Ikeuchi[3], Koji Ikuta[3]

[1]Dept. of Biomedical Engineering, Osaka Electro-Communication University, Japan

[2]Cardiovascular Physiology Okayama University Graduate School of Medicine, Dentistry and Pharmaceutical Sciences, Japan

[3]Dept. of Micro System Engineering, Nagaoya University, Japan

Abstract— **There is diabetes mellitus more than 15 million people, and this disease cause various serious complication. Diabetes mellitus therapy is insulin injection therapy, but the quantity of insulin is decided by experience. So it has danger of hypoglycemia attack. Then it is expected for insulin therapy to be done by measuring blood sugar level, but it is not still practical method. We developed that insulin valve system driven by osmotic change (blood sugar level change). This system actuation was confirmed by preliminary experiment. We tried to fabricate the small size valve system which could control micro liter insulin injection. The smaller osmotic valve, the better for a treatment of diabetes mellitus therapy. We tried to confirm that this small valve could control blood sugar level of rat.**

Keywords— **Osmotic pressure, Osmotic valve, Diabetes mellitus, Insulin, semipermeable membrane**

I. Introduction

In 2006, according to the World Health Organization, at least 171 million people worldwide suffer from diabetes mellitus. Type 2 diabetes mellitus accounts for the great majority of cases of diabetes. Diabetes mellitus is not the disease that merely blood sugar level raises but a disease to cause severe complications. And the diabetes causes a serious circulatory disease such as myocardial infarction, cerebral infarction and chronic renal failure. The major complications are neuropathy, retinopathy and nephropathy. The retinopathy lead to blindness, and the nephropathy lead to chronic renal failure and dialysis therapy. Therefore diabetes mellitus increases both medical cost and serious damage of patients.

The usual therapy for diabetes mellitus is insulin injection therapy. However, dosage of insulin is decided by experience of medical doctor. And it is reported that progress of complications become slow progress by intensive blood sugar level control [1]. But it is needed for patients enough intelligence and patience in this intensive therapy. This therapy sometimes cause extremely harmful hypoglycemic attack. Thus a device of blood sugar level control is needed. The artificial pancreas, which provides insulin by measuring blood sugar level, has been developed. Even this portable artificial pancreas is not used in practical therapy. The easy and effective instrument for insulin substitution therapy is expected for diabetes mellitus treatments.

II. Principle

We have studied for the osmotic valve for insulin therapy. This micro valve is filled with a solution, covered with a semi-permeable membrane. This semi-permeable membrane changes the inside volume of solution according to the concentration of an outside solution. This volume change is not required energy supply and the regulation system. We applied this valve to the insulin injection system worked by the changing of blood sugar.

Human osmotic pressure (π) consists of 4 components. These are Sodium (Na), Potassium (K), Blood Urea Nitrogen (BUN) and Blood Sugar (BS).

$$\pi = 1.8(Na+K) + BUN/2.8 + BS/18 \ (mOsm)$$

π	: Serum Osmotic pressure	285-295 [mOsm/kg] (mOsm/l)
Na	: Sodium	135-145 [mmol/l]
K	: Potassium	3.5-5.0 [mmol/l]
BS	: Blood sugar	75-100 [mg/dl]
BUN	: Blood urea nitrogen	10-20 [mg/dl]

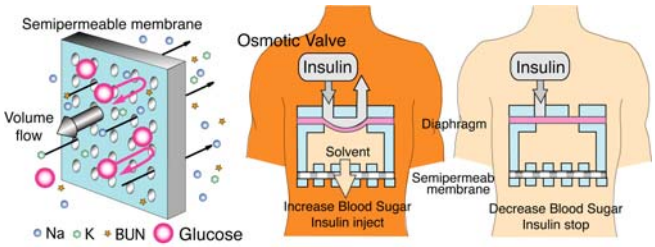


Figure 1. The principle osmotic valve. The molecule of glucose is larger than that of Na, K, BUN. The osmotic valve works during high concentration (blood sugar high) and closes valve during low concentration automatically.

O. Dössel and W.C. Schlegel (Eds.): WC 2009, IFMBE Proceedings 25/VIII, pp. 382–383, 2009.
www.springerlink.com

As for the glucose, molecular weight is greater than 3 of others. If the permeable membrane which does not pass glucose is used, solvent transfers through memblane depending on a change of glucose concentration. The osmotic valve works during high glucose concentration. The diabetes mellitus is the disease that only blood sugar control is out of order. Furthermore other components are regulated by homeostasis. This principle is shown in Figure 1. We confirmed that the function of osmotic valve by preliminary experiment of rat implanted this osmotic valve.

III. Method

This osmotic valve is made by 3D micro stereo-lithography that is irradiated by ultraviolet laser at photosensitive resin [2]. The fabrication process is shown in Figure 2. Our osmotic valve implanted in subcutis of rat could deliver insulin according to the change of blood sugar concentration. This osmotic valve has various advantages in down sizing, such as driving speed, the efficiency of osmotic valve. In the medical devices, the smaller size is the less invasive. We report that the optimization of an osmotic valve to keep adequate blood sugar level in rat that was reported at Transducers 2003 [3].

We tried to improve the fabrication for down size osmotic valve. We made the permeable membrane from the cellulose that was used as a medical material, and used elastic rubber as a diaphragm membrane. We made the smallest osmotic valve in our study. Then we studied whether this small osmotic valve can be used as clinical usage.

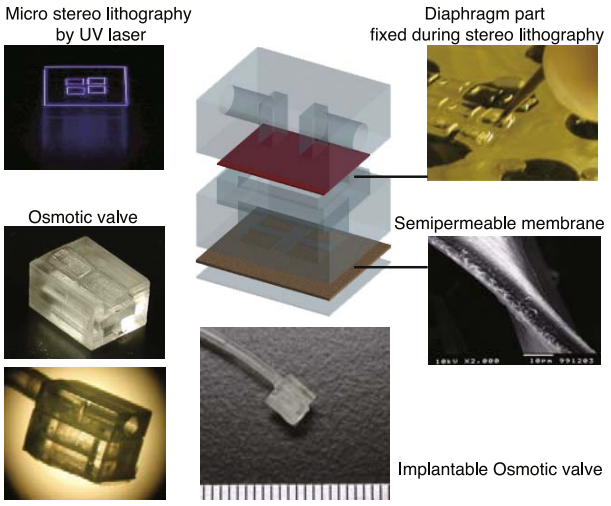


Figure 2. The structure of osmotic valve made by 3D micro stereo-lithography that is irradiated by ultraviolet laser at photosensitive resin. The size of osmotic valve was 3.0x4.0x3.5mm.

IV. Results

At first we let an anesthetized rat eat a glucose solution, and a blood sugar level was raised. We implanted osmotic valve in subcutis of rat (10 weeks 153g female rat). The osmotic valve injected insulin solution much quantity during high blood sugar concentration and control blood sugar of rat. This valve could control micro liter insulin solution.

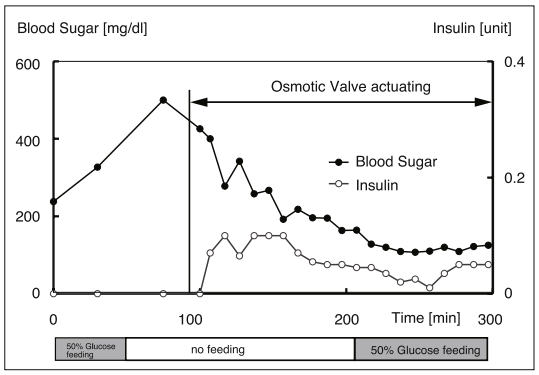


Figure 3. The result of experiment of osmotic valve implanted in subcutis of rat. The osmotic valve worked during high blood sugar concentration and control blood sugar of rat.

V. Conclusions

We investigated that system element for optimized diabetes mellitus therapy. One of important element is the size of osmotic valve. The smaller size, the less invasive. We confirmed that smallest of our studied osmotic valves could work and control blood sugar of rat. The insulin solution of this experiment was be substantially dilute solution. We think that it can work for human diabetes mellitus therapy.

Acknowledgment

The present study was partially funded by Research Grant Japan Science and Technology Agency (JST) Novel Measuring and Analytical Technology Contributions to the Elucidation and Application of Life Phenomena “New Principle Measurement Tools using Optical-driven Nano Machine” (2004-)

References

1. UK Prospective Diabetes Study (UKPDS) Group, Intensive blood-glucose control with sulphonylureas or insulin compared with conventional treatment and risk of complications in patients with type 2 diabetes (UKPDS 33). LANCET; 352(9131): 837, 1998.
2. K. Ikuta, S. Maruo, Y. Fukaya and T. Fujisawa, New micro stereo lithography for freely movable 3D structure -Super IH process with submicron resolution-, Proceedings of the IEEE International Workshop on Micro Electro Mechanical Systems (MEMS98), 290-295, 1998.
3. T. Nagakura, S. Maruo, K. Ikuta, THE STUDY OF MICRO BLOOD SUGAR CONTROL DEVICE WITHOUT ENERGY SUPPLY FOR DIABETES THERAPY, Transducers' 03, The12th International Conference on Solid-State Sensors Actuators and Microsystems Technical Digest, Volume 2/2, p.1209-1212, 2003

Amperometric Monitoring of Substance-P Levels in Biological Fluids

J. Horak, B. Enderle, H. Bakirci and G.A. Urban

IMTEK-Albert-Ludwigs-University Freiburg, Laboratory for Sensors, Freiburg, Germany

Abstract— **In this paper, a foil-based microfluidic chip (Fig. 1) for rapid determination of the neuropeptide Substance-P (SP) level in biological fluids is presented. Compared with standard ELISA methods, the miniaturization allows reducing the assay preparation and the measurement time. Due to the high variability levels and the extremely poor stability of SP in blood plasma, such improvement is crucial in point of care diagnostics of SP-induced inflammatory and immune diseases. The measurement is realized by a competitive immunoassay based on the sequenced immobilization of primary and secondary capture antibody into the capillary channel of the sensor (Fig. 2). Subsequent oxidation of hydrogen peroxide generated by the SP-labeled glucose oxidase mixed with the plasma sample resulted in a current signal inversely proportional to SP concentration. The measured 160 pg/ml in human sample (Fig. 3) was repeatable and reproducible by the corresponding optical ELISA kit on microtiter plates. Combined sensitive detection limit of 10 pg/ml and two minutes response demonstrates that this on-chip immunosensing technique is ideally suited for clinical application.**

Keywords— **Capillary competitive immunoassay, Substance-P, microfluidic system, amperometry.**

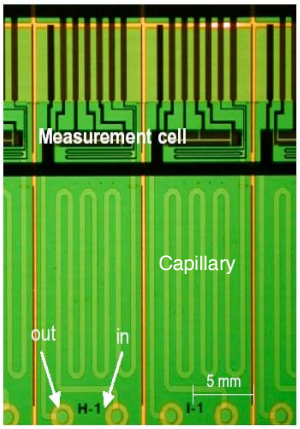


Fig. 1 Section of a wafer originally comprising 30 sensor chips.

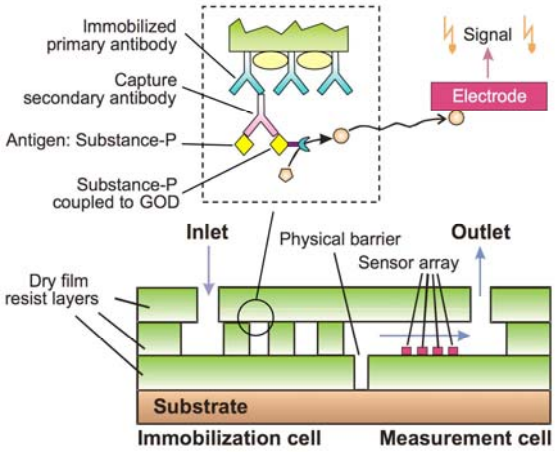


Fig. 2 Functional principle of capillary amperometric immunoassay.

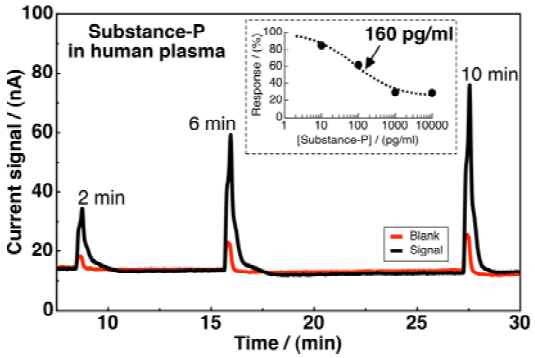


Fig. 3 Stop-flow amperometric measurement of human plasma sample with respective accumulation time of 2, 6 and 10 min (black curve). The inset shows the standard curve determined with synthetic Substance-P.

O. Dössel and W.C. Schlegel (Eds.): WC 2009, IFMBE Proceedings 25/VIII, p. 384, 2009.
www.springerlink.com

High Throughput Microelectrode Array Platforms for Quantitative Pharmacology, Toxicology, and Drug Development Using Spontaneously Active Neural Tissue

Guenter W. Gross

Professor of Neuroscience, Department of Biological Sciences
Director, Center for Network Neuroscience
University of North Texas
Denton, TX 76203

Primary cell cultures, derived from dissociated murine central nervous system tissue, form stable, spontaneously active networks on microelectrode arrays (MEAs) that provide long-term action potential readout from many discriminated units and simultaneous optical information on cell condition and general network morphology. The spontaneous activity is driven by competing ignition sites (burst leaders) that form a primary, monosynaptically connected circuit (1). Such cell group activity represents a window to the internal dynamics of self-organized networks, but also provides reproducibility and fault tolerance through the use of ensemble activity. In addition to supporting theoretical studies, it is now clear that these networks can be used in pharmacology, toxicology, and as tissue-based biosensors. Experimental evidence shows such models to be "histiotypic", as their responses are highly similar to those of the parent tissue *in vivo.* The networks, which consist of non-neuronal glia cells as well as brain region-specific different neuronal subtypes, reliably report a range of toxic responses: cytotoxicity (death of all cells), neurotoxicity (death of subtypes of neurons), and functional toxicity (loss of electrical function in the absence of cell death). Reproducible dose response curves for many compounds have been obtained (2) and dissociation constants for bicuculline, gabazine, and trimethylolpropanephosphate have been calculated from network activity changes (3). However, before such systems can be used effectively for rapid toxicity screening or for drug development, it is essential to develop high throughput platforms.

Approaches to high throughput have commenced at UNT with the development and testing of 8-network platforms served by a liquid handling robot (BioTek Precision 2000). Eight recording arrays, with 32 microelectrodes each, reside on a single glass plate, are seeded at the same time and grow under a common medium during 3-4 weeks of development. The networks are confined to separate, 1 ml medium pools upon assembly of the recording chamber. Automated dose response data have been obtained, and continual recording periods of up to 20 days have been achieved with robotic osmolarity maintenance and medium changes. The remaining challenges lie in life support engineering, the precision of robotic pipetting, in automated data acquisition, processing, and display, and the development of an effective user interface. Coupling to inverted microscopes is also a remaining engineering problem.

In light of the accelerated production of new chemical and pharmaceutical compounds, present testing systems are overwhelmed. As the extensive use of animals is ethically problematic, rapid screening with neuronal networks in vitro is a viable answer. Ten mouse embryos can provide enough tissue to seed up to 1,000 networks if most regions of the brain and spinal cord are used. Remaining cell pools can be frozen and saved for subsequent analyses. This approach provides a high efficiency of tissue utilization.

Supported by the Texas Advanced Technology Program, Plexon Inc., Dallas, and the Charles Bowen Endowment to the CNNS.

(1) Ham, M., Bettencourt, L. M., McDaniel, D, and Gross, G.W. (2008). Spontaneous coordinated activity in cultured networks: Analysis of multiple ignition sites, primary circuits, and burst phase delay distributions. J. Computational Neuroscience 24: 346-357.

(2) Gross, G.W and Gopal, K.V. (2006) Emerging histiotypic properties of cultured neuronal networks. In: M. Taketani and M. Baudry (eds) Advances in Network Electrophysiology using Multi-Electrode Arrays. Springer, pp 193-214.

(3) Rijal-Oli, S. and Gross, G.W. (2008) Determination of dissociation constants using spontaneous neuronal network activity recorded with microelectrode arrays *in vitro.* Journal of Neuroscience Methods 173: 183–192

O. Dössel and W.C. Schlegel (Eds.): WC 2009, IFMBE Proceedings 25/VIII, p. 385, 2009.
www.springerlink.com

Author Index

A

Ahmed, Ahmed 176
Akarajiratun, P. 317
Ambrosi, A. 41
Andrä, W. 355
Angres, B. 161
Ayala, V.C. 339

B

Baba, A. 277
Babaei, H. 235
Bähr, J. 37
Bakirci, H. 384
Bär, K.J. 150
Barcikowski, S. 223
Bardyn, T. 265
Bartic, C. 212, 216, 285, 314
Baumann, M. 128
Bayford, R.H. 273
Becker, B. 77, 84, 136
Becker, H. 161
Bellemann, M.E. 355
Belsky, J. 281
Benilova, I. 314
Benz, K. 161
Biederer, S. 61, 226
Biedron, S. 132
Biehl, M. 57
Bitaraf, Nazanin 176
Bo, M.L. 140
Boettcher, M. 101
Bohinc, K. 329
Borgert, J. 61
Borghs, G. 212, 216
Bork, T. 265
Böttger, J. 161
Boven, K.-H. 157
Braeken, D. 212, 216, 285
Brasil, L.M. 53
Brischwein, M. 30, 136, 299, 363
Broersen, K. 314
Buck, M. 289
Buechler, P. 265
Burger, J. 265
Burger, R. 343
Buzug, T.M. 61, 226
Bystrov, V. 230
Bystrova, N. 230

C

Callewaert, G. 212, 285
Carabelli, V. 208
Carbone, E. 208
Carvalho, J.C. 53
Carvalho Júnior, J.C. 53
Ch., Dahmani 293
Ch., Plank 293
Chailapakul, O. 80
Chang, H.Y. 116
Chang, J. 104
Chang, W.R. 165
Chang, Walter H. 108
Chen, Po-Chung 237
Chen, Richie L.C. 237
Chen, She 34
Chen, Y.Y. 165, 169
Chen, Yun-Chu 8
Cheng, Tzong-Jih 237
Cheporov, S.V. 220
Chiba, Toshio 206
Chichkov, B. 132
Chilcott, T.C. 378
Chuchkanov, F.A. 220
Chung, Chien-Yu 237
Clauss, J. 281
Clauss, Johannes 196
Coster, H.G.L. 378

D

Dal Maschio, M. 321
Dame, G. 241
Danzebrink, R. 180
Dekhtyar, Yu. 230
de la Escosura-Muñiz, A. 41
Demmel, F. 98, 363
Demosthenous, A. 273
De Nadai, S. 297
De Strooper, B. 314
Dickert, F.L. 325
Dimov, I.K. 343
Ding, Z.J. 165, 169
Dorrer, C. 157
Druzin, Michael 176
Duch, M. 365
Ducrée, J. 343
Duschl, C. 49, 101, 183

E

Eaton, D.E. 372
Eblenkamp, M. 124
Egot-Lemaire, S. 311
Ehrhart, F. 180
Elsner, Ch. 257
Eminağa, Y. 299
Enderle, B. 384
Esteve, J. 365
Etzbach, S. 136

F

Fadeeva, E. 132
Farmer, L. 261
Fernandes, A.J.S. 336
Fl., Helling 293
Flurschütz, T. 45, 91
Freudigmann, C. 161
Fröber, Ulrike 144
Fuchsberger, K. 157
Fujimoto, T. 277

G

Gao, R.L. 303
Gao, Z. 208
Gauda, E. 351
Gebhardt, R. 161
Gerald A., Urban 310
Gesener, T. 355
Giacomini, M. 297
Girardi, S. 321
Gleich, B. 61
Gómez-Martínez, R. 365
Grabow, N. 148
Gramowski, A. 269
Gross, Guenter W. 385
Grothe, H. 363
Gruhl, F.J. 69, 73

Grundl, D. 30, 84, 91, 98, 136, 363
Guenther, E. 112
Günther, Axel 376
Güntherodt, G. 128

H

Häckl, D. 257
Haeberle, S. 359
Hagmeyer, B. 157, 161
Hahn, A. 223
Harscher, Alex 192
Hecht, E. 351
Heer, R. 261
Hodenius, M. 128
Hoettges, K.F. 120
Hofsøy, Dan Anker 196
Hogg, A. 265
Holzner, F. 161
Homma, D. 277
Hongeng, S. 317
Höpfner, C. 261
Horak, J. 384
Hossann, M. 259
Hradetzky, D. 359
Hsu, Fang-Chi 332
Hsun, H.Y. 116
Huang, C.H. 165, 169
Huang, Chi-Hsun 306
Huang, S.L. 116
Hughes, M.P. 120
Huys, R. 212
Hwang, Jiann-Loung 332

I

Iglič, A. 329
Ikeuchi, Masashi 382
Ikuta, Koji 382
Ilchmann, F. 37, 77, 84
Ilgner, J. 132
Imachi, K. 277
Inada, Kazuki 382
Ingebrandt, S. 242
Irnich, Werner 22
Ishikawa, M. 5
Issels, R.D. 259

J

Jäger, M.S. 49, 101
James, E. 289
Janmaleki, M. 251
Jans, D. 212, 285
Jaruwongrungsee, K. 80
Jiang, D.C. 140
Jiang, J.H. 140
Jiang, Wei 172
Jin, G. 165, 169
Jin, Gang 19, 34
Jin, X. 303
Jin, Yongjian 172
Jocham, D. 189, 245
Jochum, T. 150
Joly, N. 289
Jong, S.B. 116
Joss, D. 265
Jovanovic, M. 289
Jügelt, K. 269
Jungbauer, Christof 325

K

Kadri, N.A. 120
Kamali, M. 251
Karlov, A. 230
Kassanos, P. 273
Katashev, A. 230
Kawada, H. 5
Keatch, R.P. 87
Keppner, H. 265
Kibbel, Steffen 192
Kijanka, G. 343
Kim, Keri 206
Kirchleitner, D. 189, 245
Kirschbaum, M. 49
Kitajima, H. 5
Kitney, R. 289
Klee, D. 132
Klein, S. 26
Klinge, U. 128
Knopp, A. 26
Knopp, T. 61, 226
Kohn, E. 208
Konno, S. 277
Krämer, N. 128
Kranz, C. 351
Kranz, Christine 372
Kraushaar, U. 112
Krombach, G.A. 128
Kubon, M. 157, 161
Kuperstein, I. 314
Kurz, R. 95

L

Länge, K. 69, 73
Lankenau, A. 183
Lautram, N. 65
Le, H.R. 87
Ledernez, L. 241
Lee, Chin-Hsien 108
Lempen, M. 265
Li, Yen Kuang 8
Liang, X.F. 104
Lidington, Darcy 376
Lieberzeit, P.A. 325
Lin, C.S. 116
Lin, Cheng-An J. 108
Lin, Feng-Huei 347
Lin, Win-Li 306
Lindner, L.H. 259
Liu, H. 277
Liu, Li 34
Löbler, M. 65
Lochovsky, Conrad 376
Loo, Josine 212
Lu, Kuo-Wei 306
Lu, Y.S. 116
Lüdtke-Buzug, K. 61, 226
Lueth, T.C. 248
Luo, P. 303
Luo, T. 303

M

Mackay, R.E. 87
Maltez, M. 41
Marín, S. 41
Marcantoni, A. 208
Martin, H. 148
Martin, R. 369
Maschietto, M. 321
Maset, S. 329
Masuda, Kohji 206
Matsukawa, Takehisa 202
Matsumura, K. 200
May, S. 329
Meissner, C. 230
Melioli, G. 297
Meng, YongHong 34
Merkoçi, A. 41
Messner, S. 359
Metze, J. 180
Meyer, J. 77, 84
Meyer, T. 112
Milnera, M. 261
Miyamoto, Yoshitaka 206
Miyata, S. 233
Mizaikoff, B. 351
Mizaikoff, Boris 372
Mizuno, Kazue 202
Moeller, A. 157
Mohrlok, R. 157
Moon, Jong-Seok 372
Moosmann, K. 339

Moschallski, M. 157
Mueller, D. 265
Mulla, Y. 216
Muramatsu, Yusuke 206
Muravyov, A.A. 220
Muravyov, A.V. 220

N

Nagakura, Toshiaki 382
Nair, Vignesh Janardhanan 1
Nakamoto, Ryusuke 206
Nasongkla, N. 317
Nasongkla, Norased 11
Nestler, B. 26
Neto, M.A. 336
Neubert, S. 124
Neuman, M.R. 253
Nitta, S. 277
Niu, Yu 19, 34
Nuntawong, N. 80

O

Offenhäusser, A. 242
Olcaytug, F. 241
Oliveira, F.J. 336
Otto, J. 128
Otto, K.-H. 26

P

Paasche, G. 223
Pan, Li-Chern 332
Pänke, O. 153
Paramonova, E. 230
Pasquarelli, A. 208
Paul Sung, K.-L. 140
Peller, M. 259
Pérez-López, B. 41
Perrier, T. 65
Petretto, A. 297
Pham, N. 311
Pietschmann, S. 369
Pison, U. 369
Plaza, J.A. 365
Pliszka, D. 124
Poitz, W. 150
Polyaka, N. 230
Prommas, J. 80
Prucker, O. 339

R

Raabgrund, A. 355
Rafienia, M. 251
Ramakrishna, S. 124
Ramser, Kerstin 176
Rand, D. 285
Rand, D.R. 212, 216
Rapp, B.E. 69, 73
Rapp, M. 69, 73
Rasaneh, S. 235
Ravaschio, S. 297
Reindl, L.M. 339
Reinl, H.M. 259
Reiser, M. 259
Remm, M. 299
Renner, A. 183
Rjabi, H. 235
Robitzki, A. 95
Robitzki, A.A. 153
Rocha, A.F. 53
Rohm, H.W. 65, 223
Romero, E. 253
Rosa, S.S.R.F. 53
Rosenauer, M. 185
Roth, M. 189, 245
Rothacher, P. 157
Rothermel, Albrecht 192
Rousseau, F. 314
Rühe, J. 339

S

Sadeghzadeh, L. 251
Saijo, Y. 277
Sanchez, A. 365
Sang, Shengbo 144
Sapronova, A. 230
Sasada, H. 277
Sato, Y. 277
Sattel, T.F. 61, 226
Sattler, M. 281
Saulnier, P. 65
Schäfer, S. 242
Scheuenpflug, M. 248
Schirhagl, R. 325
Schmidhuber, M. 37, 45, 77, 98, 281, 363
Schmidt, S. 153
Schmitz, K.-P. 65, 148, 223
Schmitz-Rode, T. 128
Schoen, T. 369
Scholz, O. 57
Schroeder, O.H.-U. 269
Schumacher, A. 359
Schymkowitz, J. 314
Schütte, J. 161
Sebastian-Bolz, Steffen 376
Seifner, A. 325
Semenov, S. 311
Shibata, M. 277
Shiraishi, Y. 277
Sickinger, A. 95
Siewert, S. 148
Silva, E.L. 336
Silva, R.F. 336
Slabu, I. 128
Song, C.X. 303
Spatz, J.P. 369
Stöver, T. 223
Stelzle, M. 157, 161
Sternberg, K. 148, 223
Steude, A. 153
Stockmann, R. 242
Stuke, M. 101
Stumpf, Patrick 180
Su, Hung-Ju 8
Sugai, T. 277
Sukhorukov, V. 180
Sun, H.F. 303
Sundarrajan, S. 124
Susuki, Yuuto 382

T

Tabayashi, K. 277
Takeuchi, Y. 233
Tamagawa, M. 200
Tanaka, A. 277
Tanaka, Y. 5
Tang, Jintian 172
Taranejoo, S. 251
Tardy, Y. 265
Th., Weyh 293
Thuvvakkadan, Sandeep 1
Trono, Jade 202
Tsai, Yieh-Loong 332
Tseng, Ching-Li 347
Tseng, Fan-Gang 332
Tsutsui, S. 5
Tuantranont, A. 80
Tyan, Y.C. 116

U

Uesaka, Mitsuru 202
Umezu, M. 277
Urban, G. 241
Urban, G.A. 384

V

Vagaon, Andrei 376
van den Driesche, S. 15

Vassanelli, S. 321
Vellekoop, M. 261
Vellekoop, M.J. 15, 185
Voigtlaender-Bolz, Julia 376
Voss, A. 150
Vosseler, M. 359

W

Wang, B. 289
Wang, C.X. 165, 169
Wang, Chun-Chin 306
Wang, H.J. 104
Wang, J. 140
Wang, T. 259
Wang, Xiaowen 172
Wang, Xufei 172
Warrington, R.O. 253
Wassermann, H. 189, 245
Weber, C. 351
Weber, M.M. 180
Weile, J. 157
Weiss, D.G. 269
Weizenecker, J. 61
Westhofen, M. 132
Weyand, E. 180
Whei Chen-Yang, Yui 8
Wiedemair, Justyna 372
Wiedemeier, S. 180
Wiesmeth, H. 257
Wiest, J. 37, 45, 91, 98, 299, 363
Wintermantel, E. 124
Wissenwasser, J. 261
Witarski, W. 15
Witt, K. 150
Witte, Hartmut 144
Wolf 30
Wolf, B. 37, 45, 77, 84, 91, 98, 136, 281, 299, 363
Wolf, Bernhard 196
Wong-ek, K. 80
Wrobel, Walter-G. 192
Wu, Jui-Chuang 8
Wu, Yueh-Hsiu 347
Wu, Yun-Ying 332

X

Xu, Y. 208

Y

Yamada, Akira 382
Yambe, T. 277
Yan, XiYun 34
Yang, Den-Kai 8
Yang, Kai-Chiang 347
Yang, L. 140
Yang, M.H. 116
Yao, Da-Jen 332
Yasotharan, Sanjesh 376
Yasuda, H. 241
Yeh, Hung-I 108
Yoshida, Naohiro 382
Yoshizawa, M. 277
Yu, Su-Wen 347
Yusa, Noritaka 202

Z

Zahn, P. 241
Zamri, D. 378
Zengerle, R. 359
Zhang, C. 303
Zhang, L.H. 303
Zhang, X. 30
Zhang, Y.B. 165, 169
Zhao, Lingyun 172
Zhao, Q. 87
Zimmermann, H. 180
Zimmermann, U. 180
Zottmann, M. 45, 77, 91, 136, 363
Zrenner, Eberhart 192